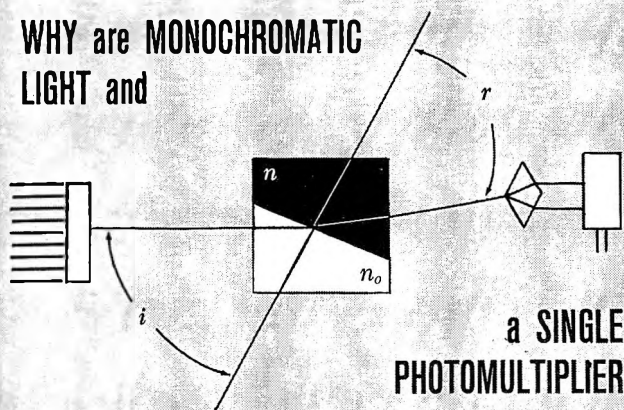


THE JOURNAL OF PHYSICAL CHEMISTRY

Volume 69, Number 10 October 1965

Nonstereospecific Mechanisms in the Photolysis of Cyclic Ketones Robert L. Alumbaugh, Glyn O. Pritchard, and Bruce Rickborn	3225
The Kinetics of the Reaction of Selenium(IV) with 2,3-Diaminonaphthalene Peter Cukor and Peter F. Lott	3232
Thermodynamics of Aqueous Solutions of Noble Gases. I. A. Ben-Naim	3240
Thermodynamics of Aqueous Solutions of Noble Gases. II. Effect of Nonelectrolytes A. Ben-Naim	3245
Thermodynamics of Aqueous Solutions of Noble Gases. III. Effect of Electrolytes A. Ben-Naim and M. Egel-Thal	3250
Chemisorption of Oxygen on Zinc Oxide Rimantas Glemza and R. J. Kokes	3254
Binary Mixtures of θ -Solvents Mitsuo Abe and Hiroshi Fujita	3263
Investigation of the Metallic Phases in Reduced, Impregnated Nickel and Nickel-Copper Silica-Alumina Catalysts Harold E. Swift, Frank E. Lutinski, and William L. Kehl	3268
Structure and Properties of Amorphous Silicoaluminas. II. Lewis and Brønsted Acid Sites J. J. Fripiat, A. Léonard, and J. B. Uytterhoeven	3274
The Role of Amino Groups in Water Absorption by Keratin J. D. Leeder and I. C. Watt	3280
The Electronegativity of Groups James E. Huheey	3284
Effects of Additives on the Radiolysis of Cyclohexane Vapor at 100° Leslie M. Theard	3292
The Outer Coordination Sphere. I. Nuclear Magnetic Resonance Relaxation Time Effects Produced by Paramagnetic Ions with Nonlabile Inner Coordination Spheres Thomas R. Stengle and Cooper H. Langford	3299
Mathematical Analysis of Multicomponent Free-Diffusion Experiments J. L. Duda and J. S. Vrentas	3305
Oxidation and Chemiluminescence of Tetrakis(dimethylamino)ethylene. I. Reversible Reactions of Oxygen with Tetrakis(dimethylamino)ethylene and <i>n</i> -Decane Carl A. Heller and Aaron N. Fletcher	3313
The Dynamics of Cryosorption Pumping S. H. Bauer and Peter Jeffers	3317
The Reduced Thermodynamic Functions for the Significant Structure Theory of Simple Liquids Teresa S. Ree, Taikyue Ree, Henry Eyring, and Richard Perkins	3322
Voltage Transients of Freshly Produced Noble Metal Electrode Surfaces R. S. Perkins, R. C. Livingston, T. N. Andersen, and H. Eyring	3329
Electrosorption of Ethylene on Platinum as a Function of Potential, Concentration, and Temperature E. Gileadi, B. T. Rubin, and J. O'M. Bockris	3335
Electron Density Shifts during Chemical Bond Formation P. R. Smith and J. W. Richardson	3346
On the Nature of Valence-Shell Molecular Orbitals Dean W. Robinson	3357
The <i>P-T-x</i> Phase Diagram of the System Zinc-Tellurium F. A. Kröger	3367
A Study of the Radical Termination Mechanisms in the Radiolysis of Crystalline Choline Chloride Margaret A. Smith and Richard M. Lemmon	3370
Definitive Test of the Onsager Reciprocal Relations in Isothermal Ternary Diffusion of Water-Sodium Chloride-Potassium Chloride Donald G. Miller	3374
Reactivity and Surface Composition. Anodic Methanol Oxidation on Platinum-Gold Alloys M. W. Breiter	3377
The Gel Melting Point as a Measure of the Tacticity of Poly(methyl methacrylate) Charles F. Ryan and Paul C. Fleischer, Jr.	3384
Kinetics of Ion Exchange in the Phosphonic Resin Bio-Rex 63 C. Heitner-Wirguin and V. Urbach	3400
A Gas Phase Electron Diffraction Investigation of Iron Pentacarbonyl M. I. Davis and H. P. Hanson	3405
Esin and Markov Effect for Adsorbed Organic Ions and Molecules R. G. Barradas, P. G. Hamilton, and B. E. Conway	3411
Nuclear Magnetic Resonance Study of Aluminum Alkyls Kermit C. Ramey, James F. O'Brien, Ichiro Hasegawa, and Alfred E. Borchert	3418

WHY are MONOCHROMATIC LIGHT and



a SINGLE PHOTOMULTIPLIER

VITAL to AUTOMATIC DIFFERENTIAL REFRACTOMETRY?

MONOCHROMATIC LIGHT?

The use of monochromatic light eliminates the dispersion effect found in instruments employing polychromatic light. Only the use of monochromatic light permits differential refractometers to be calibrated in terms of absolute refractive index difference.

A SINGLE PHOTOMULTIPLIER?

Drift due to temperature changes, spectral shifts, and fatigue are eliminated with the use of a single photomultiplier tube. This also permits measurement of highly absorbing and turbid samples, a capability not provided by other photo-detectors.

The end result is an instrument with greater accuracy, more sensitivity, extended range and increased stability . . . the Phoenix Differential Refractometer. Want more reasons? Write for Bulletin R-2000.



PHOENIX PRECISION INSTRUMENT COMPANY
A Subsidiary of CENCO INSTRUMENTS CORP.
3803-05 N. 5th Street, Phila., Penna. 19140, U.S.A.

4754 p-Terphenyl, scint. \$9.00/100g
3917 Cobalt carbonyl, toluene susp. \$75.00/35g abs.

RARE & FINE CHEMICALS

RARE CHEMICALS

FINE

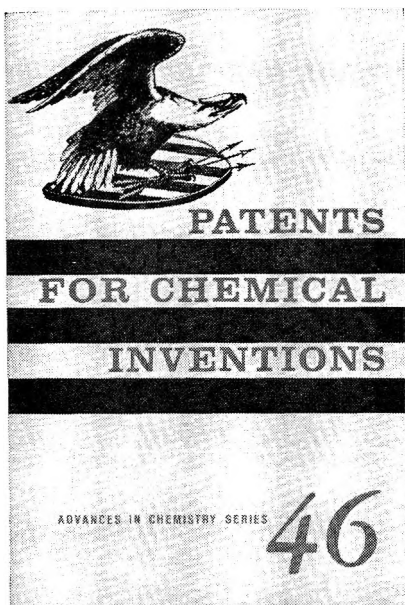
CATALOG NUMBER 5

SEND FOR CATALOG #5

TELEPHONE 516-433-8184
AREA CODE 516
GENERAL 3-6262

TELEX: 01-26464
CABLE: KALABOR PLAINVIEW NEW YORK

LABORATORIES, INC.
121 EXPRESS STREET, ENGINEERS HILL, PLAINVIEW, NEW YORK



Do you know how to protect your idea or invention . . .

or how to avoid the pitfalls that have lost rights and fortunes for many inventors in the past? Are you familiar with the requirements for patentability? Do you know what steps to take if your idea involves a new use for an old product, is related to prior art, or deals with homologs, isomers, or other analogs?

PATENTS FOR CHEMICAL INVENTIONS discusses these and many other pertinent questions. It will help you in your contacts with your employer and your patent attorney and will help you understand patent literature.

Though it contains legal abbreviations and terminology, this 117-page book is not a treatise on patent law. It is written for the technically trained man—the research chemist and director—whose very profession provides more than the usual opportunities for conceiving patentable ideas. It presents the broad range of problems concerned with the nature of invention, ownership, inventorship, priority interpretations, documents, signatory formalities during prosecution, etc. Shop rights, employer assignment agreements, the status of the chemist hired to invent, and many other important aspects are discussed.

You will want to have **PATENTS FOR CHEMICAL INVENTIONS** for your own personal reference. It is No. 46 in the Advances in Chemistry Series, 117 pp., cloth bound, \$4. Order your copy today.

Special Issues Sales/American Chemical Society 1155 Sixteenth St., N.W., Washington, D.C. 20036

The Adsorption and Oxidation of Hydrocarbons on Noble Metal Electrodes. I. Propane Adsorption on Smooth Platinum Electrodes	S. B. Brummer, J. I. Ford, and M. J. Turner	3424
Rare Gas Sensitized Radiolysis of Methane	Vincenzo Aquilanti	3434
Anion Exchange in Concentrated Solutions	C. H. Jensen and R. M. Diamond	3440
Properties of Partially Localized Adsorbed Monolayers	William A. Steele	3446
Vaporization Catalysis. The Decomposition of Gallium Nitride	Richard C. Schoonmaker, Albert Buhl, and James Lemley	3455
Potential Curves and Bond Strength of PO	Ran B. Singh and D. K. Rai	3461
Infrared Spectroscopic Investigations of Zeolites and Adsorbed Molecules. I. Structural OH Groups	C. L. Angell and Paul C. Schaffer	3463
The Heat Capacity of Potassium Hexabromorhenate(IV) from 7 to 300°K. Manifestation of Thermal History Behavior. Antiferromagnetic Anomaly near 15°K. Entropy and Free Energy Functions	R. H. Busey, R. B. Bevan, Jr., and R. A. Gilbert	3471
Temperature Dependence of the Viscoelastic Behavior of Polystyrene	Donald J. Plazek	3480
Spectroscopy of Titanium, Zirconium, and Hafnium Oxides in Neon and Argon Matrices at 4 and 20°K.	William Weltner, Jr., and Donald McLeod, Jr.	3488
A Small Angle X-Ray Scattering Study of the Colloidal Nature of Petroleum	C. W. Dwiggin, Jr.	3500
Ionization Potentials of Aromatic Amines	P. G. Farrell and J. Newton	3506
A Proposed Model for Electron Injection into Some Organic Semiconductors in the Dark	M. E. Green	3510
The Thermodynamics of the Scandium-Hydrogen System	M. L. Lieberman and P. G. Wahlbeck	3514
Dissociation of Phosphoric Acid Solutions at 25°	K. L. Elmore, J. D. Hatfield, R. L. Dunn, and A. D. Jones	3520
Catalytic Deuterium-Exchange Reactions with Organics. XX. A π -Complex Mechanism for the Isomerization and Isotope Exchange of <i>cis</i> - and <i>trans</i> -Stilbenes on Platinum Catalysts	J. L. Garnett and W. A. Sollich-Baumgartner	3526
Heats of Formation of Solid Solutions in the Systems (Na-Ag)Cl and (Na-Ag)Br	O. J. Kleppa and S. V. Meschel	3531
Diffusional Processes in Knudsen Cells	N. A. Gokcen	3538
The Solubility of Hydrogen in Liquid Sodium	D. W. McClure and G. D. Halsey, Jr.	3542
Radiolysis of Liquid Nitrogen Tetroxide	Thomas C. Castorina and Augustine O. Allen	3547
Nuclear Magnetic Resonance Spectra of Phenyl- and Diphenylacetylene	S. Castellano and J. Lorenc	3552
Further Studies on the Decarboxylation of β -Resorcylic Acid in Polar Solvents	Louis Watts Clark	3565
Activity Coefficients and Molal Volumes of Two Tetraethanolammonium Halides in Aqueous Solutions at 25°	Wen-Yang Wen and Shuji Saito	3569
X-Ray and Thermodynamic Studies of the Absorption of Hydrogen by Gold-Palladium Alloys	Arnulf Maeland and Ted B. Flanagan	3575
Diffusion of Hydrogen in the α -Phase of the Palladium-Hydrogen System	J. W. Simons and Ted B. Flanagan	3581
Adsorption Studies on Heterogeneous Titania and Homogeneous Carbon Surfaces	W. R. Smith and D. G. Ford	3587
Sulfur in the Burnt Gas of Hydrogen-Oxygen Flames	C. P. Fenimore and G. W. Jones	3593
Soret Coefficients and Heats of Transport of Some Aqueous Electrolytes at 9°	B. D. Butler and J. C. R. Turner	3598
The Mercury-Photosensitized Decomposition of Perfluoropropene	Julian Heicklen and Vester Knight	3600
The Heats of Formation and Polymerization of Carbon Suboxide	B. D. Kybett, G. K. Johnson, C. K. Barker, and J. L. Margrave	3603
The Reduction of CuO _{0.67} in Hydrogen	A. W. Czanderna	3607
The Lattice Energies of the Alkaline Earth Halides	Thomas E. Brackett and Elizabeth B. Brackett	3611
Vapor Spectra and Heats of Vaporization of Some Purine and Pyrimidine Bases	Leigh B. Clark, Gary G. Peschel, and Ignacio Tinoco, Jr.	3615

For your own information program...

try this formula

**Journal of the American Chemical Society,
cutting across all fields of chemistry,
plus another ACS research journal
such as:**

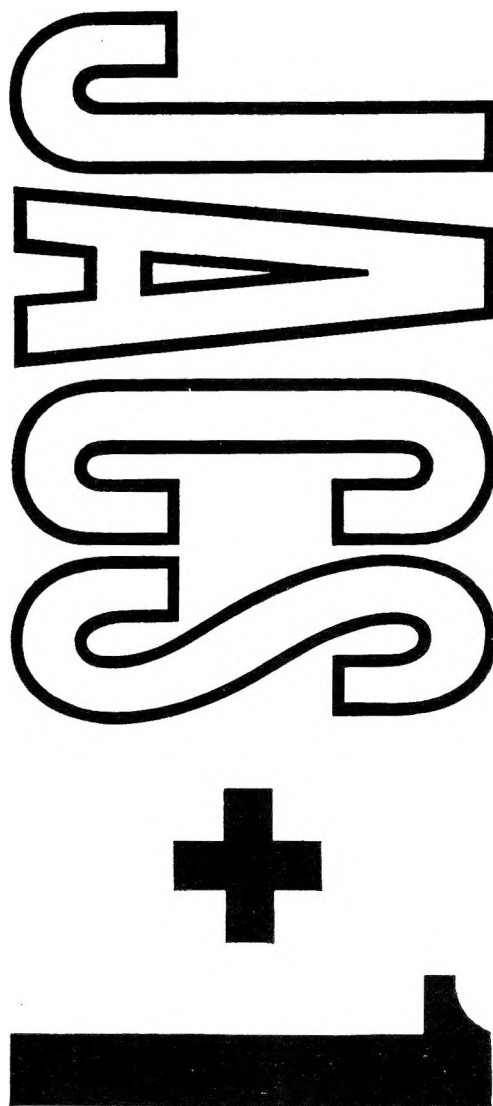
The Journal of Physical Chemistry
The Journal of Organic Chemistry
Biochemistry
Inorganic Chemistry
Journal of Medicinal Chemistry
Chemical Reviews
Analytical Chemistry
Journal of Chemical Documentation
Journal of Agricultural and Food Chemistry
Journal of Chemical and Engineering Data
I&EC Process Design and Development
I&EC Fundamentals
I&EC Product Research and Development

Each of these more specialized ACS journals extends or supplements the general-interest articles found in JACS. Important new work in your field is reported in JACS and in one or more of these journals. You need JACS and another one (or two). Find your own formula... then apply it regularly to keep your knowledge up to date.

Order from:

American Chemical Society

1155 Sixteenth Street, N.W.
Washington, D. C. 20036



Abstractors Needed for Chemical Abstracts

IF you are a chemist who can read:

Albanian	Dutch	Portuguese
Azerbaijani	Flemish	Romanian
Belorussian	French	Russian
Bulgarian	Georgian	Slovak
Chinese	Italian	Swedish
Czech	Japanese	Ukrainian
Danish	Polish	

IF you are a subject expert in one of these fields regardless of your language abilities:

Crystallography	Nuclear phenomena
Dyes	Nuclear technology
Electron paramagnetic resonance	Pharmacodynamics
Electrophotography	Physiological biochemistry
Endocrinology	Physical chemistry
Enzymes	Plant biochemistry
Graphic arts	Radiation biochemistry
Hormones	Reaction mechanisms
Metallurgy	Semiconductors
Nuclear magnetic resonance	Solid State

. . . CHEMICAL ABSTRACTS can use you as an abstractor. You can learn to make effective abstracts with the help of instructions sent with the first assignment. Further assistance is provided as needed. Thousands of chemists in every branch of the science have become qualified abstractors this way.

Assignments of chemical papers and patents, both as to number and kind, are always flexible enough to fit the interests and available time of the individual. Abstractors are furnished with papers or patent specifications to be abstracted.

The publication of chemical papers is growing at an increasing rate throughout the world. This new information needs to be promptly brought to the attention of chemists.

If you would like to help, write to Fred A. Tate, Acting Editor, Chemical Abstracts Service, The Ohio State University, Columbus, Ohio 43210.

SPECIAL NOTICE

CA has an urgent need for chemists who are interested in and able to abstract patents in the French and Flemish languages.

Nonstereospecific Mechanisms in the Photolysis of Cyclic Ketones¹

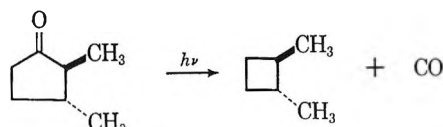
by Robert L. Alumbaugh, Glyn O. Pritchard, and Bruce Rickborn

Department of Chemistry, University of California, Santa Barbara, California (Received May 27, 1965)

Photolysis of either *cis*- or *trans*-2,6-dimethylcyclohexanone gave the same major products in the same product ratios. The products were identified as *cis*- and *trans*-1,2-dimethylcyclopentane (equal amounts from either starting ketone), *cis*- and *trans*-2-heptene, *cis*- and *trans*-2-methyl-5-heptenal, the geometrical isomer of the starting ketone, and probably propylene and *cis*- and *trans*-2-butene. The observed lack of stereospecificity rules out a concerted mechanism and lends strong support to the intermediacy of diradicals. The effects of pressure, added gases, and added radical sources have been examined. It is concluded that ketone geometrical isomerization occurs primarily through the acyl-alkyl diradical intermediate rather than by a chain process involving α -hydrogen abstraction.

Srinivasan² has recently reviewed the photochemistry of the cyclic ketones, concluding that concerted, stereospecific mechanistic pathways are followed in the photolytic decomposition at 3130 Å. The evidence for these mechanisms appears to be particularly strong for cyclopentanone and cyclohexanone, where it is proposed that decomposition occurs from an excited singlet state, and that the vibrational energy possessed by the excited molecule at the moment of decomposition determines its product distribution. This theory is in contradistinction to the intuitively more apparent diradical mechanism, previously proposed by Benson and Kistiakowsky³ and by Blacet and Miller.⁴

Srinivasan² has suggested a possible definitive experiment to distinguish between the two mechanisms. The compound 2,3-dimethylcyclopentanone exists as two geometric isomers; photolysis of either of these isomers would produce a single 1,2-dimethylcyclobutane if the decomposition is stereospecific. If the



reaction proceeds through a diradical intermediate that is sufficiently long-lived to undergo rotation, both isomers of the disubstituted cyclobutane could be produced. The work reported in this paper was instigated prior to Srinivasan's suggestion. The materials that we have used *cis*- and *trans*-2,6-dimethylcyclohexanone, have the added advantage of symmetry

(1) A preliminary report of this work has appeared in *Chem. Ind.* (London), 1951 (1964).

(2) R. Srinivasan, *Advan. Photochem.*, **1**, 83 (1963); further reference to this author's works are not made individually as they are all discussed in this chapter.

(3) S. W. Benson and G. B. Kistiakowsky, *J. Am. Chem. Soc.*, **64**, 80 (1942).

(4) F. E. Blacet and A. Miller, *ibid.*, **79**, 4327 (1957).

about the carbonyl function, which ostensibly should lead to a fairly simple distribution of products.

Experimental Section

Apparatus. All the experiments reported herein were carried out in a conventional high-vacuum system for gas phase investigations. The cylindrical quartz reactor (10 cm. in length, 5 cm. in diameter) was maintained at the desired temperature by an external vapor jacket. Most of the experiments were carried out at 100°, and the sections of the apparatus where materials of low volatility were handled were grease free. The reaction volume was 156 ml. and it was fully illuminated. The dead space, which was less than 10% of this volume, was also maintained at the reaction temperature. The light source was a British-Thomson-Houston high-pressure Hg arc (Type ME/D, 250 w.). The light beam was collimated by a quartz lens and passed through a Corning 9863 blue glass filter. A photographic spectrum of the lamp⁵ indicates two emission bands in the region of 2900 Å. (the low wave length absorption limit of these experiments) with a continuum starting below 3000 Å. and progressing to longer wave lengths. The upper absorption limit of the photolyses was thus determined by the upper limit for the ($\pi^* \leftarrow n$) transition of the carbonyl chromophore. The ultraviolet spectra of the two ketones were recorded in *n*-octane. The *cis* ketone has a λ_{\max} at 2858 Å. (ϵ 18.8) and at 3130 Å. (ϵ 6.1). The respective figures for the *trans* ketone are λ_{\max} 2952 Å. (ϵ 27.8) and 3130 Å. (ϵ 15.9). The increased overlap of the σ -electrons of the α -methyl group in the axial position (*trans* ketone) with the π -bond of the carbonyl function apparently lowers the energy required for the ($\pi^* \leftarrow n$) transition, shifting λ_{\max} to a longer wave length and increasing the absorption intensity.

Materials. The methods reported in the literature for the preparation of 2,6-dimethylcyclohexanone normally result in a mixture in which the more stable *cis* isomer predominates.⁶ In this work the 2,6-dimethylcyclohexanone was prepared by reduction of the corresponding phenol using rhodium-on-alumina catalyst. This procedure gave a mixture of ketones and alcohols which was then fully reduced to a mixture of isomeric alcohols with lithium aluminum hydride. The alcohols were separated by preparative vapor phase chromatography and subsequently oxidized by the Jones procedure⁷ to the isomerically pure ketones.⁸ Attempts to purify the ketones directly by distillation led to isomerization.

Analysis. Product analysis was effected mainly by vapor phase chromatography and n.m.r. spectrometry, supplemented when necessary by low-temperature

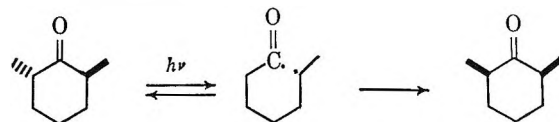
fraction in Ward-Leroy stills,⁹ mass spectrometry, and infrared spectroscopy. The primary products, *cis*- and *trans*-2-heptene, *cis*- and *trans*-1,2-dimethylcyclopentane, *cis*- and *trans*-2-methyl-5-heptenal, and the two isomeric ketones, were analyzed on a 26-ft. triscyanoethoxypropane column at 100° and 30 p.s.i. of head pressure. The decarbonylated products were further fully resolved on a 20-ft. dioctyl phthalate column at 70° and 50 p.s.i. CO was separated at -195° and identified by mass spectrometry.

The further characterization of the products will be discussed in the next section.

Results

It may be concluded from the over-all lack of stereospecificity (see Table I) that the primary products are formed through ring opening between the C-1-C-2 carbons giving the acyl-alkyl diradical. This diradical can ring close to the starting ketone (or its geometrical isomer), undergo internal hydrogen abstraction to give unsaturated aldehydes, or decarbonylate to form the 2,6-heptane diradical. This second diradical can abstract a hydrogen to form the isomeric heptanes, collapse to cyclic hydrocarbons, or cleave further to give propylene and butene.

Ketone Photoisomerization. The thermally attained equilibrium mixture of 2,6-dimethylcyclohexanone contains about 90% of the *cis* isomer at 100°. Consequently, most of the experiments relating to ketone photoisomerization were carried out with the *trans* material. Table I clearly demonstrates that the observed lack of stereospecificity is not due to ketone isomerization, which amounts to only 3.5 and 2% from *trans* and *cis*, respectively, in 10 min. at 100°. Thermal equilibration of *trans* to *cis* amounted to only 1%/hr. at 100°, as shown by dark runs in the same system. In this study we were not able to determine the diradical fraction that reverts to the starting isomer on ring closure, but by analogy with the cyclo-



pentanes (see below), it would appear that either mode is equally probable. We have also clearly shown¹ that

(5) H. O. Pritchard, private communication.

(6) E.g., H. Conroy and R. A. Firestone, *J. Am. Chem. Soc.*, **78**, 2290 (1956).

(7) K. Bowden, I. M. Heilbron, E. R. H. Jones, and B. C. L. Weedon, *J. Chem. Soc.*, 39 (1946).

(8) B. Rickborn, *J. Am. Chem. Soc.*, **84**, 2414 (1962).

(9) D. J. Leroy, *Can. J. Res.*, **B28**, 492 (1950).

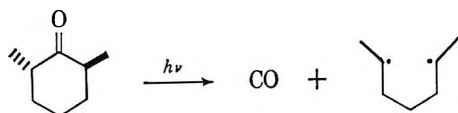
Table I: Product Ratios in the Photolysis of 2,6-Dimethylcyclohexanone at 3130 Å. and 100°

	Run no.										
	1 ^a	2	3	4	5	6	7 ^b	8	9	10	11
	<i>trans</i>					<i>cis</i>					
	Ketone pressure, mm.										
37	38	6	6	37	37	41	39	39	38	6	
Time, min.											
a	10	30	30	30	150	180	10	30	150	30	
1,2-Dimethylcyclopentane, <i>trans</i> : <i>cis</i>	..	1.04	1.00	0.96	1.02	1.04	1.08	0.96	0.98	0.92	0.88
2-Heptene, <i>trans</i> : <i>cis</i>	..	2.03	1.90	2.03	2.08	2.03	2.08	2.08	2.03	1.86	1.78
1,2-Dimethylcyclopentane : 2-heptene	..	0.41	0.40	0.38	0.38	0.38	0.43	0.34	0.38	0.35	0.39
2-Methylheptenal, <i>trans</i> : <i>cis</i>	..	2.57	2.39	2.51	2.57	3.00	2.85	2.39	2.57	2.70	2.40
C ₇ fraction : 2-methylheptenal	..	0.86	3.34	...	1.50	2.05	7.45	0.5	1.0	1.30	3.79
2,6-Dimethylcyclohexanone, % <i>trans</i> ^c	94	96.5	89.5	88	90.5	71	62	2	4.5	6.5	...

^a Dark run at 100° for 6 hr. ^b The temperature of this run was 153 ± 1°. ^c These values have in all cases except for the dark run been corrected for the small amount of thermal equilibration that occurred during the photolyses.

any possible equilibration *via* a process involving abstraction of an α -hydrogen is at most of very minor importance.

Dimethylcyclopentanes. These products were characterized by comparison with pure standard samples. The *trans*/*cis* ratio of unity obtained for their production is the focal point of this work, and the conclusion that photodecarbonylation to a diradical occurs is inescapable. It is of interest that the subsequent ring-



closure reaction, besides lacking stereospecificity due to rapid rotation about the carbon-carbon bonds, is also nonstereoselective. In other words, the greater stability of *trans*-dimethylcyclopentane is not reflected in this ring closure step; the observed result is anticipated for processes with negligible activation energies.

Heptenes. 1-Pentene is a product of the photolysis of cyclohexanone, and in like manner heptene is to be expected in the present system. Characterization was effected by the use of lower and higher olefins than C₇ and by comparison of v.p.c. retention times. Catalytic reduction of the photolysis product eliminated the two peaks attributed to isomeric heptenes and gave rise to a new peak of comparable magnitude and the same retention time as *n*-heptane on two different columns.

The n.m.r. spectrum of the total condensable photolysis product showed a broad, unresolved band at 5.38 p.p.m. (TMS = 0). The absence of absorption between 4.6 and 4.96 p.p.m. is taken as strong evidence that this fraction contained no terminal methylene product.^{10,11} This evidence, coupled with the formation of 1-pentene in the photolysis of cyclohexanone

allows the conclusion that the C₇ olefins formed are *cis*- and *trans*-2-heptene.¹²

The 2:1 ratio of *trans*- to *cis*-2-heptene closely resembles the ratio for the photostationary state of 2-pentene determined by Hammond, Turro, and Leermakers,¹⁴ leading one to question whether the heptene ratio is kinetically determined or due to photosensitized isomerization. The latter seems unlikely in view of the relatively slow rate of attainment of photoequilibrium in the 2-pentene system¹⁴ and the fact that the olefin ratio in the present study was invariant with time.

The data in Table I indicate that the ratio of 1,2-dimethylcyclopentane to 2-heptene is invariant with changes in temperature, pressure, and time. The temperature independence of this ratio is in agreement with that found in the photolysis of cyclohexanone.⁴ This constancy is strong evidence that these two hydrocarbon products share a common precursor (the hydrocarbon diradical). Olefin formation by internal hydrogen abstraction is favored over cyclization, as noted previously by Dunbar and Kutschke for cyclohexanone.¹⁵

(10) L. M. Jackman, "Applications of NMR Spectroscopy in Organic Chemistry," Pergamon Press, Ltd., London, 1959.

(11) The n.m.r. spectra of 1-hexene and 1-octene showed absorption multiplets centered at 4.7 and 5.2 p.p.m., while 2-octene absorbed between 5.28 and 5.56 p.p.m.

(12) Precise assignment of geometry was not possible at the time these experiments were performed since standard samples were not available; the major isomer has been assigned the *trans* configuration on the basis of our expectation that the more stable isomer should predominate from mechanistic grounds. This assignment is in keeping with the shorter retention time observed and reported lower boiling point¹³ of the *trans* isomer.

(13) "Selected Values of Properties of Hydrocarbons and Related Compounds," API Project 44, Carnegie Institute of Technology, Pittsburgh, Pa., 1956.

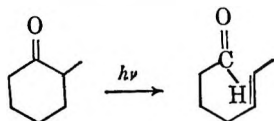
(14) G. S. Hammond, N. J. Turro, and P. A. Leermakers, *J. Phys. Chem.*, **66**, 1144 (1962).

Heptenals. The formation of 4-pentenal and 5-hexenal in the photolyses of cyclopentanone and cyclohexanone, respectively, suggests that in the present system 2-methyl-5-heptenal should be formed. Vapor phase chromatography of the photolyses mixture gave two peaks which were tentatively identified as aldehydes; this was verified by observing under maximum resolution the aldehydic proton region of the n.m.r. spectrum. Two incompletely resolved doublets, with the same area ratios as the v.p.c. curves, were found at 9.58 ($J = 1.7$ c.p.s.) and 9.62 p.p.m. ($J = 1.7$ c.p.s.). Catalytic reduction led to the loss of the two v.p.c. peaks with the concurrent formation of a new peak of comparable area; the n.m.r. spectrum of this reduction product showed a clean doublet centered at 9.64 p.p.m. (TMS = 0) with $J = 1.8$ c.p.s. The n.m.r. spectrum of the original photolysis mixture was, as previously noted, free of absorption in the terminal methylene region.

On the basis of this evidence and the reasoning presented earlier with regard to the geometries of the 2-heptenes,¹² we have assigned the structures of the major and minor isomers as *trans*- and *cis*-2-methyl-5-heptenal, respectively.

We see in Table I that the ratio of *trans*- to *cis*-2-methyl-5-heptenal is, within experimental error, independent of the starting ketone isomer, changes in pressure, temperature, and photolysis time. Again this is consistent with a diradical but not a concerted mechanism.

Srinivasan² has emphasized the probable occurrence of concerted processes from an investigation of the liquid phase photolysis of 2-methylcyclohexanone, claiming that of the two possible isomeric 5-heptenals



only one is formed. We have reinvestigated this system¹⁶ and found that both isomers are formed, in a similar ratio to that noted for the 2-methyl-5-heptenals in the present work.

Some relative product distributions are recorded in Table II. It is seen that increasing pressure (runs 3 and 5) tends to decrease C₇-compound formation, while increased temperature has the opposite effect (runs 6 and 7). Analogous behavior has been reported for cyclohexanone.²

Secondary Products. The v.p.c. traces of the reaction mixtures indicated the presence of numerous minor products. The formation of lower olefinic products is generally observed in the photolysis of

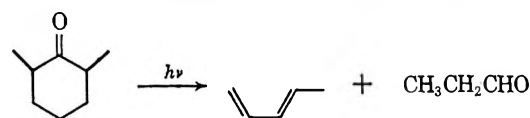
Table II: Product Distribution

Run no.	%			Decompn.*
	C ₇ fraction	2-Methyl-heptenal	2,6-Dimethyl-cyclohexanone	
2	3	3.5	93.5	10
3	25	7.5	67	40
5	13.5	9	77.5	30
6	40	19.5	40.5	72
7	74.5	10	12.5	92
8	1	2	97	5
9	7	7	36	18
10	17.5	13.5	69.5	34.5

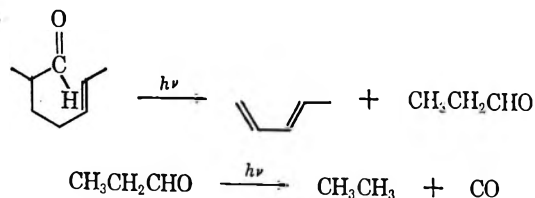
* The per cent decomposition includes products formed by photolytic decomposition plus any measurable photochemical equilibration of the ketones and is based on v.p.c. curve area measurements of the condensable fraction; the numbers are therefore only relative, as the sensitivities of all the compounds were not known.

cyclic ketones,² and the present system proved no exception. Distillates taken at -150 and -80° were subjected to mass spectrometry, but the resultant spectra were complicated and indicative of complex mixtures. The -150° fraction contained ethane, and possibly some propylene, while the -80° fraction appeared to contain 2-butene and 1,3-pentadiene. These products were all of minor importance, but nevertheless it is reasonable to expect their occurrence. Similar products, and particularly ethylene and propylene, are found in the photolyses of cyclohexanone, 2-methylcyclohexanone, and cycloheptanone,² again in minor amounts. With cyclohexanone the formation of ethylene and propylene is only one-twelfth as important as the C₅ products.

The ethane likely arises from the photolysis of propanal, which may be formed directly by a Norrish III mechanism or more probably from the Norrish II



photolysis of 2-methyl-5-heptenal. The ethane and

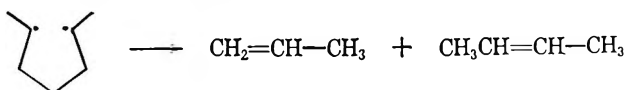


(15) J. R. Dunn and K. O. Kutschke, *Can. J. Chem.*, **32**, 725 (1954).

(16) Unpublished results.

1,3-pentadiene were more evident in runs at high conversion, suggesting that they are not formed in a primary process.¹⁷

Propylene and the isomeric 2-butenes formed in this system presumably arise from the further decomposition of the heptane 2,5-diradical.



The complexities of these systems are well exemplified by a recent reinvestigation of the photolysis of cyclopentanone,¹⁸ where at about 20% conversion more than 40 minor products were obtained, including 1-butene, *cis*- and *trans*-2-butene, ethylene, ethane, propane, propylene, and acetaldehyde.

Added Gases. Two experiments each with the *trans*-ketone were carried out in the presence of di-*t*-butyl peroxide and of oxygen (Table III).

Table III: Photolysis of *trans*-2,6-Dimethylcyclohexanone with Added Gases at 100°

	Run no.			
	12	13	14	15
	Time, min.			
	180	30	180	30
	<i>p</i> (ketone), mm.			
	14	10	28	19
	<i>P</i> (added gas), mm.			
	61 ^a	74 ^a	70 ^b	125 ^b
1,2-Dimethylcyclopentane, <i>trans:cis</i>	2.30	2.20	0.85	0.90
2-Heptene, <i>trans:cis</i>	2.30	1.80	2.20	2.20
1,2-Dimethylcyclopentane: 2-heptene	0.39	0.35	0.22	0.25
2-Methylheptenal, <i>trans:cis</i>	1.30	3.50	1.90	2.30
C ₇ fraction :2-methylheptenal	129	18.6	9.14	1.80
C ₇ , %	84	66	69	19
<i>trans</i> -Ketone, %	90	90	53	89

^a Di-*t*-butyl peroxide. ^b Oxygen.

Photodecomposition of the peroxide occurs at the wave lengths used¹⁹ (ethane was produced in blank runs with the peroxide alone) and it was anticipated that the methyl radicals formed might react with the diradical intermediates and alter some of the product ratios given in Table I. No definite conclusions can be reached, although it is noteworthy that the per cent ketone isomerization in the 180-min. run 12 was much reduced. Reaction of the methyl radicals with the initially formed acyl-alkyl diradical would result in diminished ring closure to the *cis* isomer. Alternatively, the peroxide may efficiently quench the excited ketone, leading to reduced decomposition;

however, the ketone isomerization obtained in run 13 is normal (cf. Table I). The ratios for the heptenals also appear to be scattered, and no definite explanation can be offered for the anomalous increase in the *trans/cis* dimethylcyclopentane ratios of runs 12 and 13 (it is considered likely that in the presence of peroxide some new product is formed with the same v.p.c. retention time as the *trans* compound). The data in Table I indicate that the C₇/aldehyde ratios increase with time (and temperature, run 7), largely due to secondary photodecomposition of the aldehyde, a process which will obviously be of greater consequence in longer runs. With added peroxide, aldehyde loss is further enhanced by hydrogen abstraction by CH₃ radicals to generate the acyl radical, or by addition to the double bond.

Cremer and Srinivasan,²⁰ in a recent investigation of the photolysis of cyclohexanone in the liquid state, have observed a leveling off in the 5-hexenal yield with increasing time. This observation, it was suggested, provides evidence for the selective quenching by the hexenal of the particular excited electronic state of the ketone which is the precursor of the aldehyde. An alternate explanation is that photolysis (or consumption by free-radical processes) of the aldehyde becomes increasingly important as its concentration increases, and an approximate photostationary state is established. It is clear that in a prolonged experiment the aldehyde yield will eventually decrease (run 7, Table II). The ensuing complications caused by the photolysis of 4-pentenal in cyclopentanone experiments even at low per cent conversions have been emphasized by Butler and his co-workers.¹⁸ It is also relevant to note that 2-butenal is a relatively efficient quencher of triplet acetone at 3130 Å., whereas the upper singlet state is unaffected.²¹ In the photolysis experiments with added peroxide, and in other work in which the peroxide was pyrolyzed at 153° in the absence of ultraviolet light, a new product was encountered which was identified as 2,2,6-trimethylcyclohexanone

(17) The Norrish II mechanism for 2-methyl-5-heptenal is particularly appealing because of the formation of a conjugated diene. Also a type II, rather than a type III, mechanism occurs in the photolysis of 2-methylcyclohexanone [C. H. Bamford and R. G. W. Norrish, *J. Chem. Soc.*, 1521 (1938)]. A type I mechanism for the decomposition of 2-methyl-5-heptenal appears to be unimportant. Probable products would be 2-heptene and/or 2,5-heptadiene. Additional production of 2-heptene by a secondary process can be ruled out by the constancy of our product ratios with time.

(18) J. N. Butler, A. J. Drake, J. C. Mitchell, and P. Singh, *Can. J. Chem.*, **41**, 2704 (1963).

(19) D. H. Volman and W. M. Graven, *J. Am. Chem. Soc.*, **75**, 3111 (1953).

(20) S. Cremer and R. Srinivasan, *ibid.*, **86**, 4197 (1964).

(21) R. E. Rebert and P. Ausloos, *ibid.*, **86**, 4803 (1964).

on the basis of identical v.p.c. retention time with a known sample. This product would be expected from methyl radical abstraction of the α tertiary hydrogen followed by radical recombination. As noted previously,¹ ketone isomerization by a chain process initiated in like manner appears to be ruled out on the basis that the extent of isomerization is unaffected by the added free-radical source.

A comparison of runs 14 and 15 in the presence of O₂ (Table III) with similar experiments without added gas (Table I) indicates very little change in most of the ratios, although the dimethylcyclopentane/heptene and the 2-methyl-5-heptenal *trans/cis* ratios are somewhat lower. Srinivasan's investigation² of the photolysis of cyclopentanone in the presence of oxygen similarly indicated very little effect on product formation. This, coupled with the observation that the time between collisions in the system was $\sim 10^{-8}$ sec. and the knowledge that alkyl radicals react with oxygen at every collision at moderate pressures, led Srinivasan to abandon the diradical hypothesis and postulate a concerted mechanism for cyclopentanone photodecomposition.²² In view of the evidence which we have presented on the photoisomerization of the 2,6-dimethylcyclohexanones, we must conclude the existence of the acyl-alkyl diradical, and assume that it is short-lived, or invoke steric or other considerations to explain the negligible reaction with oxygen under the conditions used. Similar conclusions apply to the heptane 2,5-diradical that we have postulated. The time required for internal rotation in either diradical should be of the order of 10^{-12} sec., so that intramolecular recombination or disproportionation may occur in a time appreciably less than 10^{-8} sec.²³

Examination of runs 3, 5, 11, and 15 (all at 30 min.) shows a twofold increase in the C₇/2-methylheptenal ratio for the experiments conducted at low pressure (6 mm.). At the wave lengths employed in this study, the ketone will contain ~ 95 kcal. mole⁻¹ excess energy following absorption; after C-1-C-2 bond dissociation, the excess vibrational energy in the diradical will be about 20 kcal. mole⁻¹. The fraction of this energy which gives rise to C-1-C-6 bond fission (decarbonylation) is subject to removal by quenching, leading to the observed pressure effect. The value for *D* (CH₃-CO) in acetyl is not known exactly but a reasonable estimate would be 15 ± 4 kcal. mole⁻¹,²⁴ and we may assume that this value will approximate that for *D*[CH₃CH(CH₂)₃CHCH₃-CO]. The activation energy for isomerization to 2-methyl-5-heptenal will be much less (CH₃ + cyclohexane \rightarrow CH₄ + C₆H₁₁ has *E* ~ 8 kcal. mole⁻¹) so that any quenching effect on the rate of this process will be relatively much less

pronounced. This picture assumes that the rate of ring closure (C-1-C-2 bond formation) of the diradical is not pressure sensitive, which is borne out by the observed extents of ketone isomerization.

Discussion

Srinivasan² has found similar pressure effects to those discussed here in the photolysis of cyclopentanone, both with varying ketone pressure and in the presence of added gases. An increase in the total pressure favors the formation of pentenal at the expense of processes which lead to carbon monoxide, while the ratio of the decarbonylation products (C₂H₄/cyclobutane) remains relatively constant. On the basis of a concerted mechanism, this behavior is rationalized by assuming that decomposition occurs from an excited singlet state, which may exist long enough to undergo collisions, and the vibrational energy possessed by the molecule at the instant of decomposition will determine its photolysis mode; the aldehyde would thus be formed from the lower vibrational levels of the excited electronic state. Similar effects are reported in the photolysis of cyclohexanone.

Increase of temperature and decrease of wave length in the photolysis of cyclopentanone, and increase of temperature in the photolysis of cyclohexanone, lead to increased decarbonylation at the expense of aldehyde formation. These results have been interpreted as further support for the concerted mechanism² with decarbonylation occurring from the higher vibrational levels of the electronically excited ketone. It is also apparent that increased energy input (whether photolytic or thermal) will affect the subsequent decomposition mode of the diradical formed by C-1-C-2 bond fission; the increased energy content of the diradical will enhance decarbonylation at any given pressure.

With the higher energy states involved in radiolytic studies, a direct comparison with photolyses is often difficult. However, Singh and Freeman²³ have concluded that the 5-hexenal formed in the γ -radiolysis of cyclohexanone implies C-1-C-2 bond cleavage. It is interesting that the 5-hexenal/CO ratio is about one-fifth as large as in the liquid phase photolysis,² a result which is consistent with both the concerted and diradical mechanisms. More recently, the 12 products identified in the γ -radiolysis of liquid cyclopentanone²⁵

(22) Srinivasan² correlates the behavior of alkyl monoradicals with methylene in similar systems, but there is no clear evidence of the rapid reaction of CH₂ and O₂; cf. W. B. deMore and S. W. Benson, *Advan. Photochem.*, **2**, 219 (1964).

(23) A. Singh and G. R. Freeman, *J. Phys. Chem.*, **69**, 666 (1965).

(24) T. L. Cottrell, "The Strengths of Chemical Bonds," Butterworth and Co. (Publishers) Ltd., London, 1958, p. 197; J. A. Kerr and J. G. Calvert, *J. Phys. Chem.*, **69**, 1022 (1965).

have been largely accounted for in terms of a free-radical mechanism.

Srinivasan has commented that there are some minor interpretive difficulties with the concerted mechanism that he has proposed for the photolytic decomposition of cyclopentanone, and by extrapolation for other cyclic ketones. It is noted that the ratio of ethylene to cyclobutane depends upon the geometry of the system, and that the Arrhenius plot of CO/pentenal leads to an activation energy difference of 2.5 kcal. mole⁻¹. This is a surprisingly small activation energy difference for pathways which are so profoundly affected by changes in pressure, etc., especially when it is noted that the work of Rabinovitch and his co-workers²⁶ indicates that from 10 to 20 kcal. mole⁻¹ of excess vibrational energy may be transferred at each collision. Also Butler and co-workers¹⁸ have observed a decrease in the ethylene/cyclobutane ratio of 33% while varying the extent of decomposition of cyclopentanone from 0.025 to 0.75%; although this change is contrary to that expected from the photodecomposition of 4-pentenal, such decomposition at these small conversions is strongly implied. It is apparent that deductions based upon CO/pentenal ratios may be suspect, and that ethylene/cyclobutane ratios depend upon factors other than the geometry of the system.

Between 20 and 30% of the initially excited cyclopentanone molecules return to the ground state without decomposition,² by a path which is not affected by the pressure. More recent studies²⁷ indicate that cyclopentanone does not undergo fluorescence stabilization, the fluorescence efficiency being independent of cyclopentanone or added gas pressure. It is pointed out²⁷ that this situation is possible when decomposition competes with fluorescence (at nearly identical rates) from all vibrational levels of the excited state. The inherent lack of selectivity in this suggestion is not compatible with the concerted mechanism for photodecomposition. We may also note that our experi-

ments indicate that the fraction of diradicals that undergo ring closure to the isomeric ketone is independent of the pressure.

The almost negligible effect of added oxygen on the photocomposition of the cyclic ketones suggests the unimportance of the triplet state, although the phosphorescence of cyclopentanone as a solute in the liquid and solid phases has been observed.²⁸ Further, it has been pointed out that the use of oxygen as a diagnostic test for the triplet state is not efficacious in every case.²⁹ However, radiolytic studies on the quenching effects of oxygen dissolved in liquid cyclohexanone suggest that the lowest triplet state is the precursor of about 70% of the 5-hexenal formed in the system.²³ This observation, together with the fact that the total emission from the triplet state of acetone is rapidly quenched by small amounts of oxygen, implies that singlet processes are of greater importance than triplet processes in the photochemistry of cyclic ketones. Our experiments conclusively prove that, in the case of 2,6-dimethylcyclohexanone, photodecomposition occurs exclusively *via* a diradical mechanism. Furthermore, the fact that 2-methylcyclohexanone gives not one but two unsaturated aldehydes suggests that this is the general mechanism for photolysis of cyclic ketones.³⁰

Acknowledgment. We wish to thank Mr. M. J. Perona for carrying out some of the experiments.

(25) W. W. Bristone, M. Katayama, and C. N. Trumbore, *J. Phys. Chem.*, **69**, 807 (1965).

(26) B. S. Rabinovitch and M. C. Flowers, *Quart. Rev. (London)*, **18**, 122 (1964).

(27) S. R. LaPaglia and B. C. Roquette, *Can. J. Chem.*, **41**, 287 (1963).

(28) S. R. LaPaglia and B. C. Roquette, *J. Phys. Chem.*, **66**, 1739 (1962).

(29) D. W. Setser, D. W. Flaczek, R. J. Cvetanović, and B. A. Rabinovitch, *Can. J. Chem.*, **40**, 2179 (1962).

(30) R. Srinivasan and S. E. Cremer [*J. Am. Chem. Soc.*, **87**, 1647 (1965)] have reiterated their suggestion of a concerted mechanism, once again quoting stereoselectivity in the liquid phase photolysis of 2-methylcyclohexanone.

The Kinetics of the Reaction of Selenium(IV) with 2,3-Diaminonaphthalene

by Peter Cukor

Department of Chemistry, St. John's University, Jamaica, New York

and Peter F. Lott

Department of Chemistry, University of Missouri at Kansas City, Kansas City, Missouri
(Received October 4, 1964)

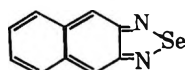
The kinetics and mechanism of the reaction between 2,3-diaminonaphthalene (DAN) and selenous acid were investigated. The rate of the reaction was studied as a function of concentration, pH, temperature, and ionic strength. The results indicate that the reacting species are the monoprotonated diamine and undissociated selenous acid. The rate law may be written as

$$R = k \left[\frac{1}{\frac{K_{\text{H}_2\text{SeO}_3}}{K_{\text{DAN}}} + \frac{[\text{H}^+]}{K_{\text{DAN}}} + \frac{K_{\text{H}_2\text{SeO}_3}}{[\text{H}^+]}} \right] [\text{DAN}][\text{H}_2\text{SeO}_3]$$

Experimentation was performed under darkroom conditions because of the sensitivity to light of 2,3-diaminonaphthalene.

Introduction

The discovery of new reagents for the determination of trace quantities of elements has been a subject of continuing interest in analytical chemistry. Interest in reagents for selenium analysis has been particularly keen because of the nutritional aspects of this element.¹ Trace quantities of selenium are commonly determined by the reaction of Se(IV) with certain *ortho* aromatic diamines to form compounds known as piaszelenols; 3,3'-diaminobenzidine has been the most generally used diamine for this purpose.² In order to discover a still more sensitive reagent, other *ortho* aromatic diamines have been investigated and recent research has shown that 2,3-diaminonaphthalene (DAN) is a superior reagent.³⁻⁶ The piaszelenol formed in the reaction of selenium with DAN is the compound 2,1,3-naphtho(2,3-*c*)selenadiazole having the structural formula



Previously, speculation has been made that as a general mechanism, piaszelenol formation proceeds through an oxidation-reduction phenomenon⁷; re-

cently, Barcza⁸ partially investigated the kinetics of the reaction of selenous acid with *o*-phenylenediamine and indicated that it proceeded through a molecular mechanism.

Reported herein is a study of the kinetics and possible mechanism of the reaction of Se(IV) with 2,3-diaminonaphthalene. It is felt that the elucidation of the mechanism of the reaction will be helpful in searching for better reagents to be used in selenium analysis, as well as in explaining certain difficulties and peculiarities that occur in the determination of selenium with *ortho* aromatic diamines.

- (1) H. K. King, *Sci. Progr.* (London), **50**, 629 (1962).
- (2) W. C. Broad and A. J. Barnard, Jr., *Chemist-Analyst*, **50**, 124 (1961).
- (3) C. A. Parker and L. G. Harvey, *Analyst*, **87**, 558 (1962).
- (4) P. F. Lott, P. Cukor, G. Moriber, and J. Solga, *Anal. Chem.*, **35**, 1159 (1963).
- (5) P. Cukor, J. Walezyk, and P. F. Lott, *Anal. Chim. Acta*, **30**, 473 (1964).
- (6) W. H. Allaway and E. Cary, *Anal. Chem.*, **36**, 1359 (1964).
- (7) L. S. Efron and Z. V. Todres-Selektor, *Zh. Obshch. Khim.*, **27**, 483 (1959).
- (8) L. Barcza, *Mikrochim. Ichnoanal. Acta*, 136 (1964).

Experimental Section

Reagents. A solution of 1 mg./ml. of selenium was prepared by dissolving 1.621 g. of selenous acid (Fisher Certified) in 1.00 l. of distilled water.

2,3-Diaminonaphthalene solution was made by dissolving 0.10 g. of the recrystallized reagent in 100 ml. of 0.1 *N* HCl using a magnetic stirrer. Because of its sensitivity to light, this solution was freshly prepared each day and stored in a darkroom. The commercially available 2,3-diaminonaphthalene (Aldrich Chemical Co.) was recrystallized by dissolving in 4 *N* HCl and precipitating with 6 *N* NaOH. Then the white solid was filtered by suction and washed free of base, dried, and stored in a desiccator. The melting point of the reagent was 190–191°; the corresponding value reported in the literature was 190–194°. ⁹

Apparatus. Spectrophotometric measurements for the kinetic studies were obtained on a Beckman Model DU spectrophotometer, equipped with a double row of Beckman Thermospacers. The reaction was carried out in a 1-cm. absorption cell at a temperature constant to $\pm 0.1^\circ$. Ultraviolet and visible spectra were recorded on a Bausch and Lomb 505 recording spectrophotometer.

Procedure. The experimental work was carried out in a conventional photographic darkroom; a flashlight was used when necessary to read the instrument scales. The acidity of the reaction mixtures was adjusted by using either sodium hydroxide or hydrochloric acid. The experiments were performed at the desired bath temperatures of either 20, 30, 40, or 50°. In order to maintain proper control of the temperature, measurements to be made at 20° occasionally had to be carried out at slightly higher temperature because of the higher ambient temperature.

Kinetic Measurements. To a series of 100-ml. volumetric flasks containing approximately 80 ml. of distilled water and 5.85 g. of NaCl (to ensure constant ionic strength), the desired volume of selenous acid was added and the flasks were transferred to the constant temperature bath. When thermal equilibrium was reached, the contents were transferred into 150-ml. beakers and the appropriate volume of DAN solution (also thermally equilibrated) was added. The acidity was adjusted to the desired value, the contents of the beaker were transferred to the appropriate volumetric flask, and the solution was diluted to 100 ml. with distilled water. The acidity of the sample was rechecked.

The reaction was followed by absorbance measurements at 380 μ , the characteristic wave length for the absorption of the piaszelenol. The ultraviolet and visible spectra of DAN and its piaszelenol have been reported previously. ⁴

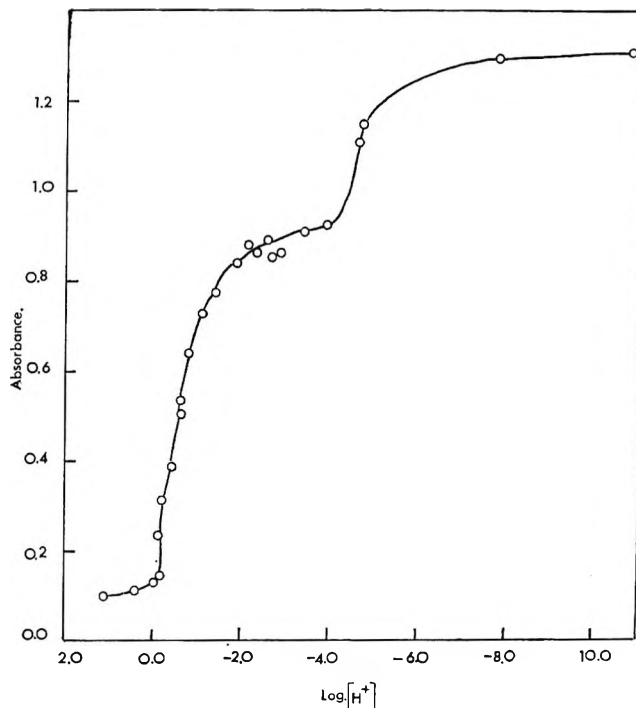


Figure 1. Effect of hydronium ion concentration on absorbance of 2,3-diaminonaphthalene. Conditions: DAN 0.316 μ mole/ml.; temperature 29.8°.

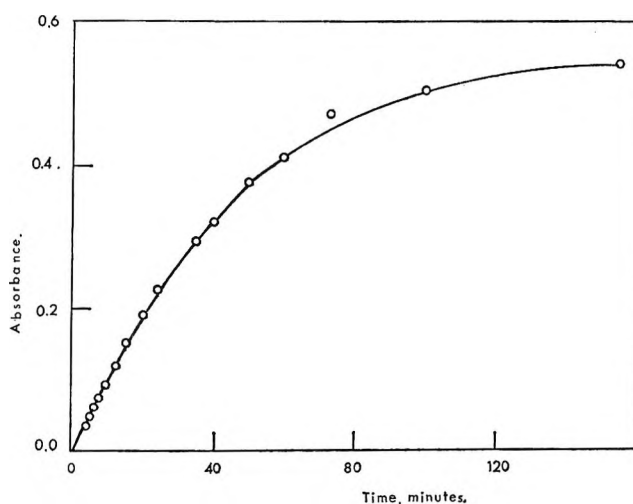


Figure 2. Absorbance of piaszelenol vs. time. Conditions: selenous acid 0.313 μ mole/ml.; DAN 0.316 μ mole/ml.; pH 1.5; temperature 29.2°.

Job's Method of Continuous Variations. To a series of 100-ml. volumetric flasks containing about 85 ml. of distilled water and 5.85 g. of NaCl, respectively, 0.10, 0.25, 0.75, or 0.90 ml. of 1.25×10^{-2} *M* selenous acid solution was added. The flasks were immersed in

(9) F. Sachs, *Ber.*, 39, 3021 (1906).

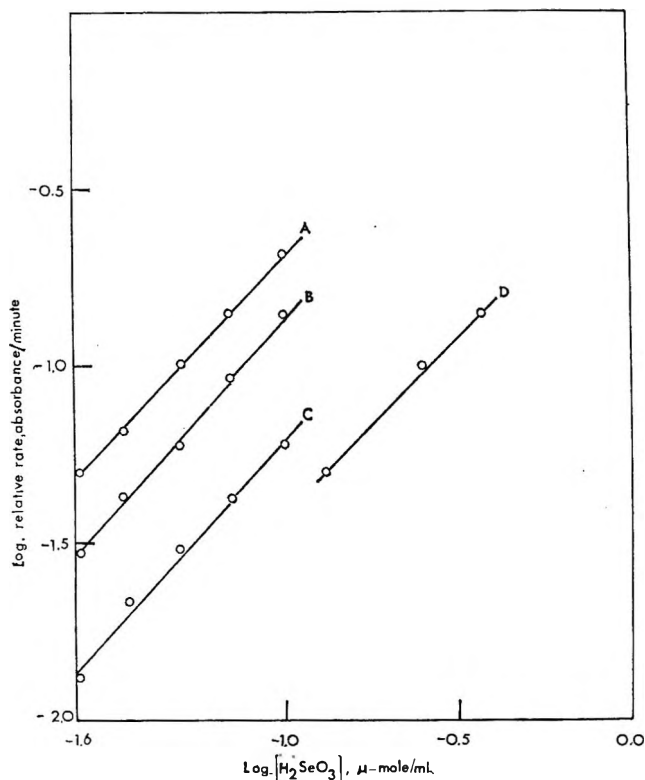


Figure 3. The order of the reaction in selenous acid. Conditions: A: pH 1.1, DAN 0.26 μ mole/ml., slope 1.05; B: pH 2.6, DAN 0.26 μ mole/ml., slope 1.10; C: pH 3.0, DAN 0.26 μ mole/ml., slope 1.10; D: pH 1.7, DAN 0.033 μ mole/ml., slope 0.95; temperature 29.2°.

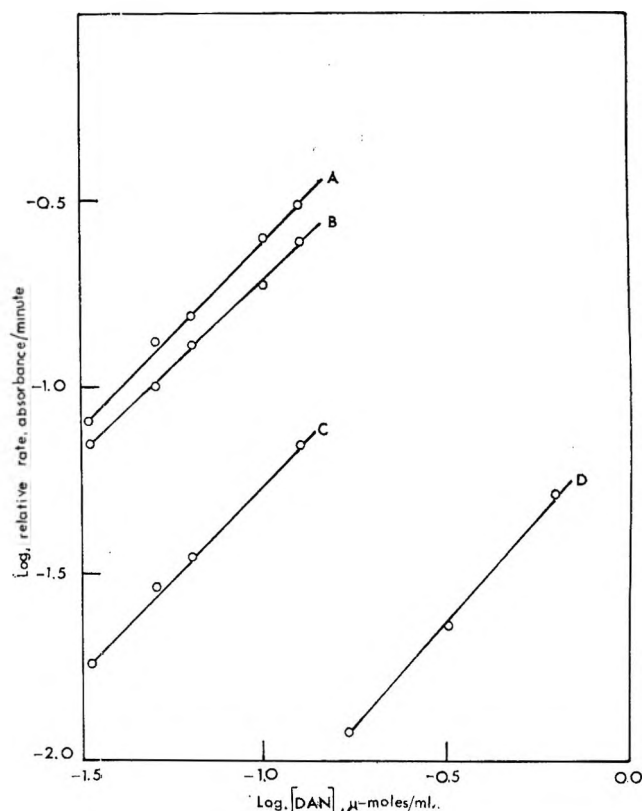


Figure 4. The order of the reaction in 2,3-diaminonaphthalene. Conditions: A: pH 1.9, selenous acid 0.25 μ mole/ml., slope 0.95; B: pH 0.6, selenous acid 0.25 μ mole/ml., slope 0.95; C: pH 2.9, selenous acid 0.25 μ mole/ml., slope 1.10; D: pH 0.5, selenous acid 0.125 μ mole/ml., slope 1.10; temperature 29.2°.

the constant temperature bath until thermal equilibrium was established. Then the samples were transferred to 150-ml. beakers and 1.80, 1.50, 1.00, 0.50, or 0.20 ml., respectively, of $6.25 \times 10^{-3} M$ DAN solution was added to make the total amount of DAN and selenous acid 12.5 μ moles in each beaker. The acidity of the samples was adjusted to a desired value. The solutions were returned to the volumetric flasks, diluted to volume with distilled water, and placed in the constant temperature bath. The absorbance was measured every 0.5 hr. until constant readings were obtained. The entire procedure was repeated to obtain another set of data corresponding to 25 μ moles/100 ml. of total selenous acid and 2,3-diaminonaphthalene. These samples contained 0.10, 0.20, 0.30, 1.00, or 1.50 ml. of selenous acid and 3.80, 3.60, 3.40, 2.00, or 1.00 ml. of DAN, respectively.

Ionization Constants of 2,3-Diaminonaphthalene. About 90 ml. of distilled water was placed in a 100-ml. volumetric flask containing 5.85 g. of NaCl. After the contents of the flask reached thermal equilibrium at 29.8°, 5 ml. of DAN solution was added. The acidity

of the samples was adjusted to desired values and the solution was diluted to 100 ml. with distilled water. The absorbance was measured at 340 $m\mu$, which is a characteristic absorption wave length of DAN, for a number of acidity values ranging from 12 N to $10^{-11} N$ in hydrogen ion concentration. The results are reported in Figure 1 and show the first and second dissociation constants of the diprotonated base to be 0.312 and 0.0077 at 29.8°. The constants were obtained directly from the graph.

Results and Discussion

The Order of the Reaction. The reaction can be followed by measuring the formation of the piaszelenol as a function of time. A typical plot of the absorbance of the piaszelenol *vs.* time at constant pH is shown in Figure 2. The relative rate of the reaction is determined by measuring the initial slope of such curves. Pseudo orders for DAN and selenous acid are obtained by finding the slope of the logarithmic plot of this relative rate *vs.* the logarithm of the concentration of

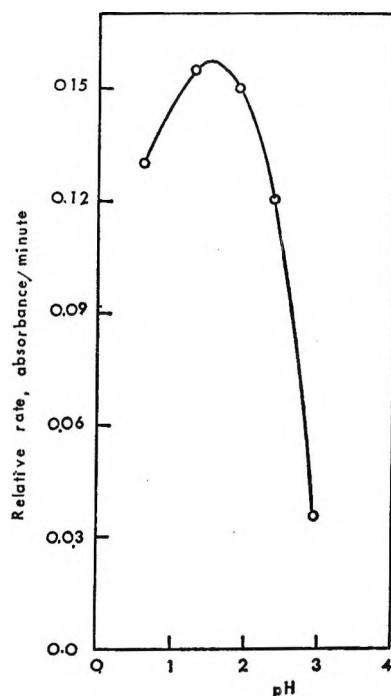


Figure 5. Dependence of rate on acidity. Conditions: selenous acid 0.25 μ mole/ml., DAN 0.0632 μ mole/ml., temperature 29.2°.

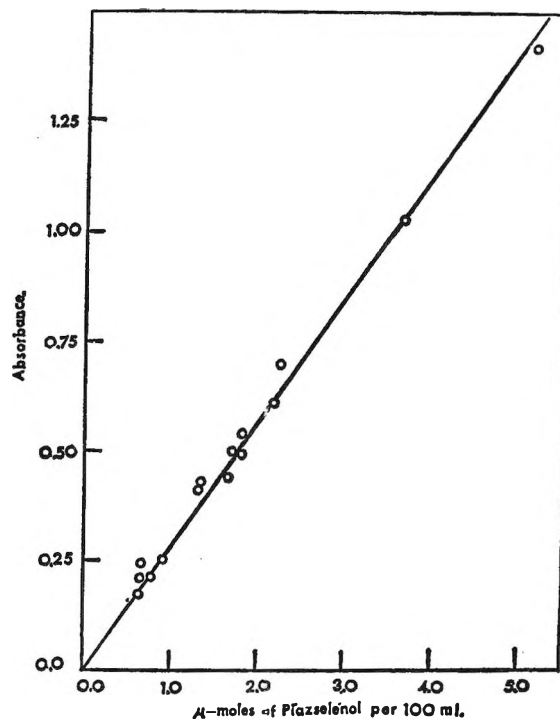


Figure 7. Calibration curve.

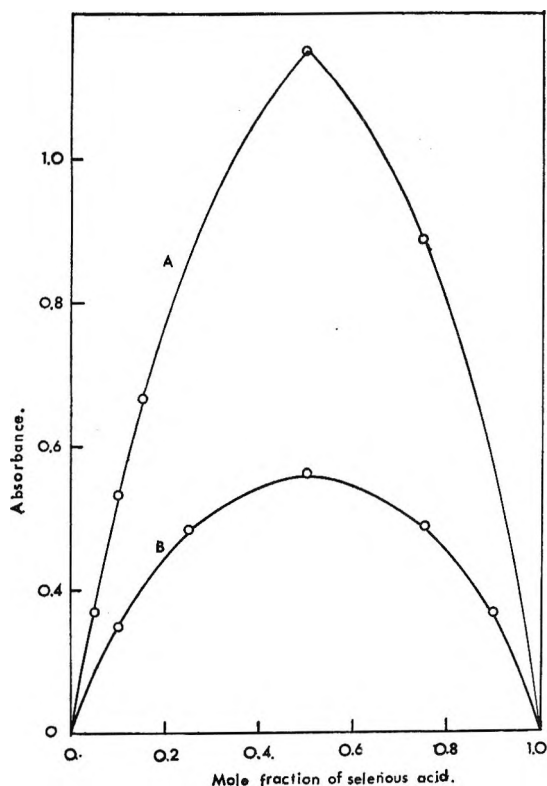


Figure 6. Job's method of continuous variations. Conditions: pH 1.5, temperature 29.8°, total concentration of selenous acid and DAN: curve A, 0.25 μ mole/ml.; curve B, 0.125 μ mole/ml.

the minimum reagent, while keeping the other reagent in large excess. In this way the isolation method of Ostwald is used in conjunction with the differential method of van't Hoff.¹⁰ Figures 3 and 4 show that the reaction follows pseudo-first-order kinetics for both selenous acid and DAN.

The rate of the reaction is also affected by the acidity of the media. Figure 5 shows the dependence of the rate on pH. The maximum type curve obtained points to two opposing effects: one accelerating and the other hindering the rate of the reaction.

The first-order kinetics for each reagent is also confirmed by substituting the data into the integrated rate expressions. This is complicated by the fact that the course of the reaction can be followed only by measuring the absorbance of the product formed, that the reaction reaches an apparent equilibrium, and that after standing for several hours the color fades owing to secondary reactions which destroy the product.

The Apparent Equilibrium Constant of the Reaction. To overcome these difficulties, the apparent equilibrium constant of the reaction

$$K_{app} = \frac{[X]}{[H_2SeO_3-X][DAN-X]}$$

(10) K. J. Laidler, "Chemical Kinetics," McGraw-Hill Book Co., Inc., New York, N. Y., 1950, p. 18.

(where X is the concentration of the piazselenol at equilibrium) was determined and used to prepare a calibration curve of the molar piazselenol concentration *vs.* absorbance. The equilibrium constant was obtained by applying Job's method of continuous variations.¹¹ A typical pair of curves is shown on Figure 6. Table I summarizes these data. To prepare the calibration curve, the corresponding absorbance at equilibrium was plotted against the concentration of the piazselenol (Figure 7).

Table I: Job's Method of Continuous Variations to Determine the Apparent Equilibrium Constant as a Function of Temperature

pH	Temp., °C.	K_{app}^a
0.9	29.8	9.35
1.5	29.8	10.40
1.5	40.1	23.50
1.5	50.0	45.00
2.3	29.8	9.72

^a K_{app} entries are averages of two determinations.

Rate Constants. The molar concentration of piazselenol corresponding to the absorbance reading at any time was obtained from Figure 7 and these data in conjunction with the known initial concentration of DAN and selenous acid were substituted into the integrated rate equations. Figure 8 shows pseudo-first-order integrated rate plots, and Figure 9 shows the second-order rate plot when both reagents are present in equal concentrations. The second-order rate constants and the experimental conditions under which they were obtained are summarized in Table II. Also included in Table II are the "true rate constants" which are derived from the reaction mechanism and include the equilibrium considerations occurring throughout the reaction.

Figure 10 shows the effect of temperature on the rate of the reaction at constant pH; the Arrhenius equation parameters calculated by the method of least squares are summarized in Table III.

The dependence of the rate constant on the ionic strength of the solution also was investigated and the results shown in Figure 11 indicate that the ionic strength has little influence on the rate of the reaction. The slight decrease in the value of k' with increasing ionic strength could be due to solubility effects. According to the Brønsted-Bjerrum "activity-rate theory" at least one of the reacting species must be a neutral molecule. To investigate the possible reacting species,

Table II: Second-Order Rate Constants

pH	Temp., °C.	H ₂ SeO ₃ , μmole/ml.	DAN ⁰ , μmole/ml.	$k' \times 10^2$, ^a ml./μmole min.	$k \times 10^2$, ^b ml./μmole min.
1.5	25.0	0.313	0.0316	2.87	...
1.5	25.0	0.0313	0.316	3.02	...
1.5	25.0	0.125	0.125	2.48	...
2.3	22.5	0.313	0.0316	2.48	...
2.3	22.5	0.0313	0.316	2.50	...
2.3	22.5	0.125	0.125	2.70	...
0.9	22.0	0.313	0.0316	1.20	...
0.9	22.0	0.0313	0.316	0.98	...
0.9	22.0	0.125	0.125	1.15	...
1.5	29.2	0.313	0.0316	3.44	3.90
1.5	29.2	0.0313	0.316	3.10	3.72
1.5	29.2	0.125	0.125	3.29	3.95
2.3	29.2	0.313	0.0316	2.53	4.05
2.3	29.2	0.0313	0.316	2.69	4.32
2.3	29.2	0.125	0.125	2.92	4.70
0.9	29.2	0.313	0.0316	2.62	3.66
0.9	29.2	0.0313	0.316	2.12	2.96
0.9	29.2	0.125	0.125	2.46	3.45
Av. $k = 3.88$					
1.5	37.5	0.313	0.0313	6.00	8.80
1.5	37.5	0.0313	0.316	5.60	8.20
1.5	37.5	0.125	0.125	6.71	9.80
2.3	37.5	0.313	0.0316	5.40	8.65
2.3	37.5	0.0313	0.316	6.10	9.75
2.3	37.5	0.125	0.125	5.90	9.45
0.9	37.5	0.313	0.0316	6.00	8.75
0.9	37.5	0.0313	0.316	6.00	6.75
0.9	37.5	0.125	0.125	6.10	8.80
Av. $k = 8.97$					
1.5	45.0	0.313	0.0316	12.60	...
1.5	45.0	0.0313	0.316	11.70	...
1.5	45.0	0.125	0.125	11.60	...
2.3	45.0	0.313	0.0316	8.40	...
2.3	45.0	0.0313	0.316	8.30	...
2.3	45.0	0.125	0.125	7.90	...
0.9	45.0	0.313	0.0316	10.80	...
0.9	45.0	0.0316	0.313	10.10	...
0.9	45.0	0.125	0.125	10.20	...

^a k' entries represent the average values of triplicate runs.
^b k is "true second-order rate constant" derived from reaction mechanism.

Table III: Arrhenius Equation Parameters

pH	E_{act} , cal.	A , ml./μmole min.
0.9	18,400	5.00×10^{11}
1.5	13,800	3.55×10^8
2.3	11,700	7.90×10^6

(11) A. K. Majumdar and M. M. Chakrabartty, *Anal. Chim. Acta* 19, 372 (1958).

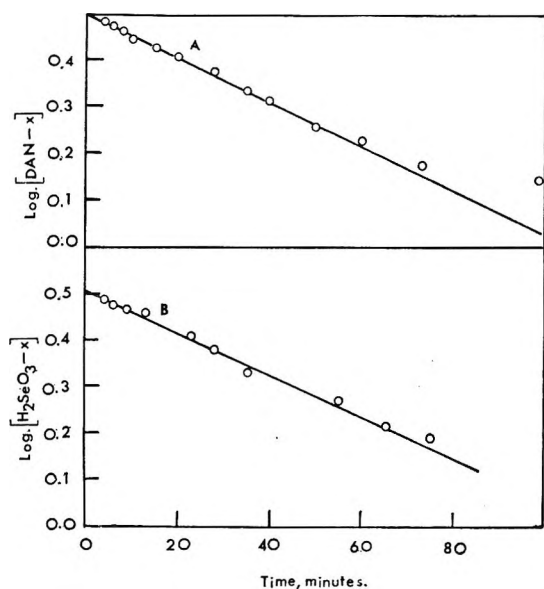


Figure 8. Pseudo-first-order integrated rate plots. Conditions: curve A: selenous acid in large excess; curve B: DAN in large excess; temperature 29.2°; pH 1.5; concentration of excess reagent 0.313 μ mole/ml; concentration of minimum reagent 0.316 μ mole/ml.

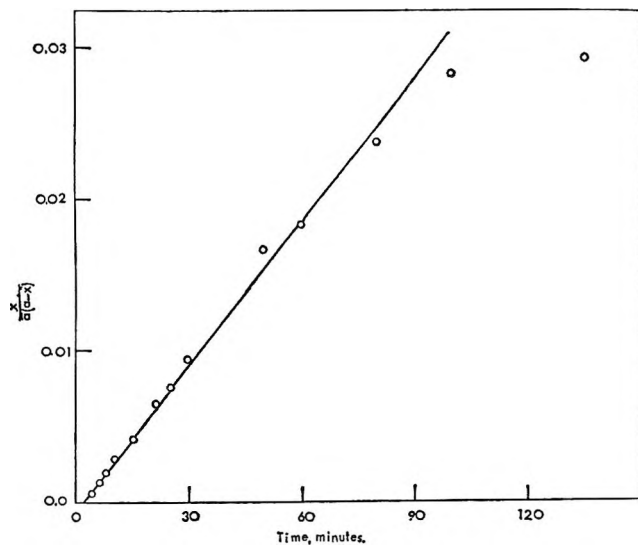


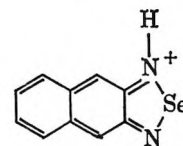
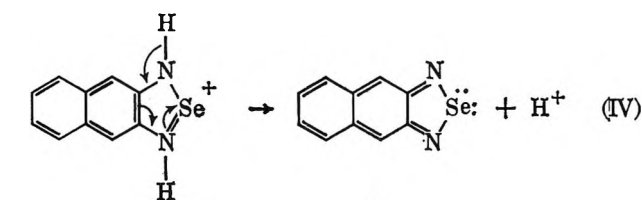
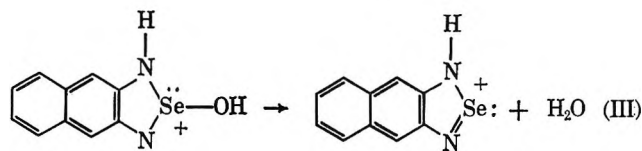
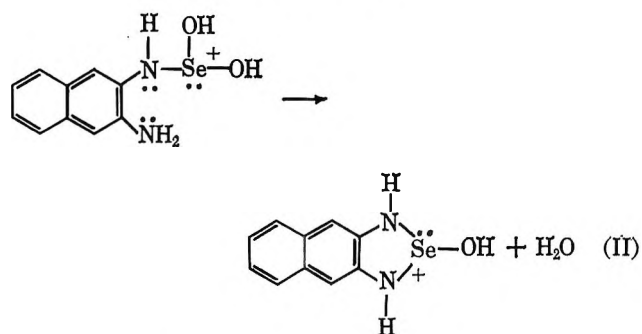
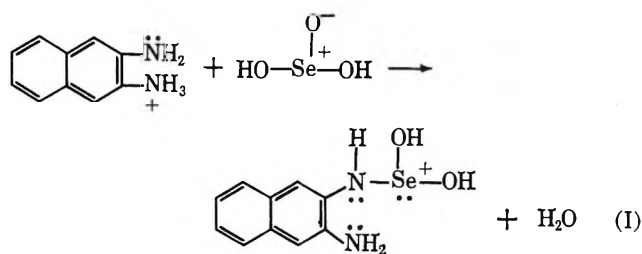
Figure 9. Second-order integrated rate plot. Conditions: temperature 29.2°; pH 1.5; concentration of both selenous acid and DAN 0.125 μ mole/ml.

the distribution of ions and molecules as a function of pH was calculated (Figure 12).

The ionization constants for selenous acid were taken from the data of Kolthoff and Stenger.¹² In order to obtain a maximum type of rate dependence on pH as shown in Figure 5, the reacting species would have to be either monoprotonated 2,3-diaminonaphthalene and selenous acid or diprotonated 2,3-diaminonaphthalene

and biselenite ion. The ionic strength study eliminated the second possibility.

Mechanism. On this basis the course of the reaction can be described by the mechanism



As indicated in the mechanism, the final product found in the reaction is probably the protonated pi-azselenol, as after washing with water and isolation of the product the pi-azselenol thus recovered neither re-dissolved in water or in certain organic solvents such as benzene in which the protonated form dissolved.

If the first step of the above reaction mechanism

(12) I. M. Kolthoff and V. A. Stenger, "Volumetric Analysis," 2nd Ed., Vol. 1, Interscience Publishers, Inc., New York, N. Y., 1947, Table 11.

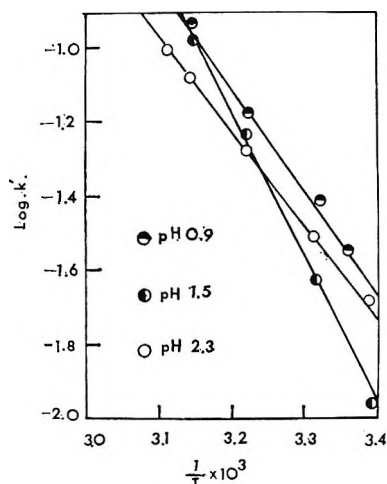


Figure 10. The dependence of rate constant on temperature.

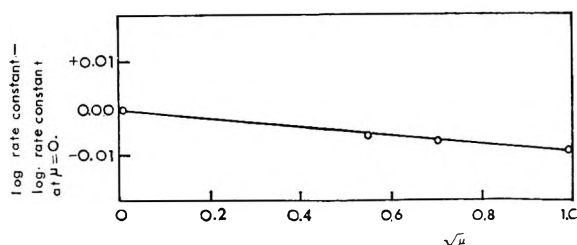


Figure 11. Dependence of apparent second-order rate constant of ionic strength. Conditions: pH 1.9; temperature 29.2°; selenous acid 0.25 μ mole/ml.; DAN 0.25 μ mole/ml.

were the rate-determining step, or if the first step were a rapid equilibrium followed by a slow rate-determining step, in either case the rate expression would be written as

$$R = k'[\text{DANH}^+][\text{H}_2\text{SeO}_3] \quad (1)$$

Thus there is no immediate way of differentiating between these two possible mechanisms. Furthermore, no intermediates were found by a continuous scanning of the spectrum throughout the reaction.

Table IV: The Effect of Oxidized or Reduced Species on the Rate of the Reaction

Conditions for the reaction of selenous acid	DAN	Rate compared to regular conditions
In the presence of $\text{NH}_2\text{OH}\cdot\text{HCl}$	Air oxidized	Slower
In the presence of $\text{NH}_2\text{OH}\cdot\text{HCl}$	Regular condition	Same
Regular condition	Air oxidized	Slower
In the presence of NH_2NH_2	Regular condition	No reaction
In the presence of NH_2NH_2	Air oxidized	No reaction

To investigate the possibility of an oxidation-reduction mechanism, reduced species of selenous acid and oxidized species of DAN were added to the reaction mixture. The data obtained are summarized in Table IV and show no substantial change in the reaction rate. This fact would rule out an oxidation-reduction mechanism.

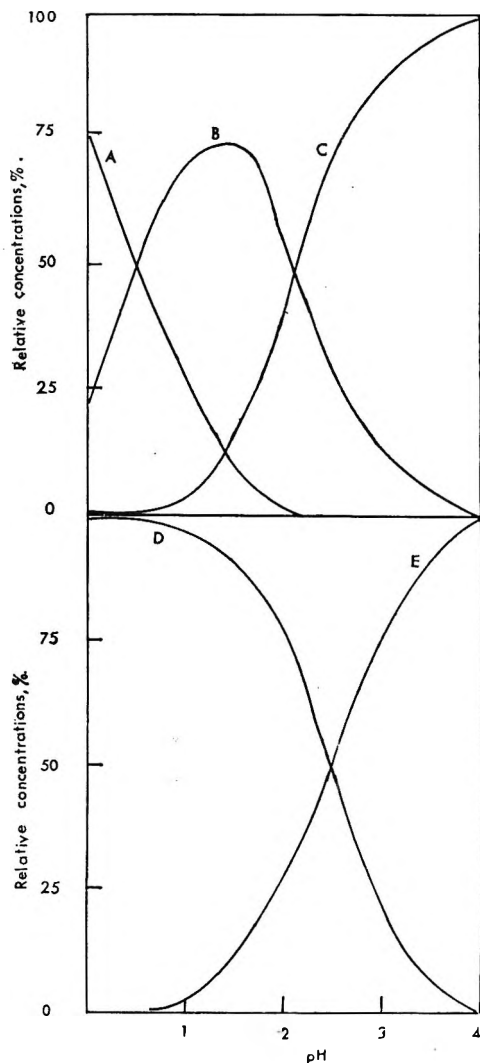


Figure 12. Distribution of different species of DAN and selenous acid: A, DANH_2^{2+} ; B, DANH^+ ; C, DAN; D, H_2SeO_3 ; E, HSeO_3^- .

It should be noted that the rate does not change in the presence of hydroxylamine hydrochloride; thus this reagent may be used safely in the analytical procedure to prevent the oxidation of 2,3-diaminonaphthalene.⁶ Hydrazine, on the other hand, probably reduces selenium to its elemental state and therefore prevents the reaction from occurring.

Rate Law. Substituting the equilibrium constants

$$K_{\text{H}_2\text{SeO}_3} = \frac{[\text{HSeO}_3^-][\text{H}^+]}{[\text{H}_2\text{SeO}_3]} \quad K_{\text{DAN}} = \frac{[\text{DANH}^+][\text{H}^+]}{[\text{DANH}_2^{2+}]}$$

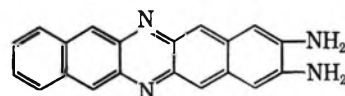
into eq. 1, the expression obtained for the rate of the reaction is

$$R = k \left[\frac{1}{\frac{K_{\text{H}_2\text{SeO}_3}}{K_{\text{DAN}}} + \frac{\text{H}^+}{K_{\text{DAN}}} + \frac{K_{\text{H}_2\text{SeO}_3}}{\text{H}^+}} \right] [\text{DAN}][\text{H}_2\text{SeO}_3] \quad (2)$$

The quantity k is the "true second-order rate constant" for the reaction and can be obtained by multiplying the apparent rate constant listed in Table II by the fraction appearing in eq. 2. The constancy of the "true rate constant" in Table II confirms the rate law. The relative standard deviation for the "true rate constant" is 10% in contrast to 15% for the experimental rate constant.

Light Sensitivity of 2,3-Diaminonaphthalene. Parker and Harvey³ previously reported a higher fluorescence of a reagent blank containing DAN when the piaz-selenol reaction was carried out in daylight. Although the effect of daylight on the reagent was not critical in certain analytical work,⁴ in following the reaction kinetics it was observed that in daylight the rate was not reproducible and the order of the reaction in 2,3-diaminonaphthalene varied between 1.0 and 0.7. In the absence of light, however, reproducible rates were observed.

Samples of DAN exposed to daylight and ultraviolet light decomposed slowly and after a period of several hours started to form brown precipitates. On the basis of C,H,N microanalysis and infrared spectral data, the precipitate was classified as a polymer of DAN probably having the type structure



The formation of this polymer would decrease the concentration of DAN available for reaction and might be responsible for the irreproducibility of kinetic results in daylight. In analytical work where the stoichiometric excess of DAN is large,⁴ such small changes in concentration do not affect the analytical results.

Conclusion. The reaction mechanism postulated in this work is believed to be generally applicable to the reaction between selenous acid and different *ortho* aromatic diamines. Since the rate of the reaction at a given pH depends on the amount of monoprotonated diamine and undissociated selenous acid present in the reaction mixture, diamines which are ionized to a greater extent at low pH would have a faster reaction rate and might be better analytical reagents for selenium. Further studies along this line are being pursued.

Acknowledgment. This investigation was supported by research grant GM 12830-01 from the National Institutes of Health, U. S. Public Health Service.

Thermodynamics of Aqueous Solutions of Noble Gases. I

by A. Ben-Naim

Department of Physical Chemistry, The Hebrew University, Jerusalem, Israel (Received December 16, 1964)

The thermodynamic behavior of aqueous solutions of noble gases is discussed in terms of a "two-structure" model for liquid water. The entropy and enthalpy of solution are treated as composed of two terms, the "static" and the "relaxation" one. The first refers to a solution in which the chemical equilibrium between the various forms is "frozen in." The latter arose from the shift in the equilibrium concentrations of the two forms toward the more ordered one. The origin of the "stabilization of the structure of water" by the noble gas, based on the compact nature of the clusters of water molecules, is discussed.

I. Introduction

Aqueous solutions of noble gases reveal many anomalous properties. In particular, the entropy and enthalpy of solution of the gases are appreciably lower in water than in other solvents.

The first attempt at a complete analysis of the properties of aqueous solutions of noble gases was done by Eley¹ although several authors²⁻⁴ had dealt before him with different aspects of the problem.

Eley regarded the process of solution in any solvent as comprised of two steps, the first consisting of the creation of a cavity suitable for accommodating a gas molecule (process C) and the second consisting of the introduction of the gas molecule into this cavity (process A). The enthalpy of solution, ΔH_s , is therefore the sum of two contributions

$$\Delta H_s = \Delta H_C + \Delta H_A$$

Usually, $\Delta H_C > 0$, whereas $\Delta H_A < 0$. In addition, $|\Delta H_C|$ was estimated to be greater than $|\Delta H_A|$ and thus $\Delta H_s > 0$. To account for the negative ΔH_s in water, Eley assumed the existence of natural cavities, so that $\Delta H_C \approx 0$ and thus $\Delta H_s \approx \Delta H_A < 0$ which is a plausible explanation of the sign of ΔH_s . However, the experimental value of $|\Delta H_s|$ is too high to have its origin solely in the interaction between the gas and the water. This led Lange and Watzel⁴ to the suspicion that formation of a chemical bond might be involved in the process of solution.

A different approach was that of Frank and Evans,⁵ who suggested that the entropy and enthalpy phenomena might be accounted for by the assumption

that the gas molecule introduced into water builds up a so-called microscopic "iceberg" around it. This elucidates immediately the pronounced negative entropy and enthalpy of solution in water. However, Frank and Evans confessed not having a satisfactory explanation for the cause of the formation of the icebergs by the inert molecules.

The next development was the attempt to compare the properties of water solutions of rare gases with the properties of their crystalline hydrates. Claussen and Polglase⁶ proposed that the water structure around solute molecules (especially paraffin gases) is the same as the structure in the crystalline hydrates, previously described by Claussen.⁷ They remarked that their model, although successful in the case of methane, ethane, and propane, failed for *n*-butane solution, the butane molecules being too big to fit the cavities. They also pointed out that no hydrates of *n*-butane were known, in contrast with the simpler paraffins. However, as the thermodynamic properties of *n*-butane solutions are not essentially different from those of the other gases, one can hardly accept the forwarded explanation unless one assumes that the origin of the *n*-butane phenomena differs from that of the other gases.

(1) D. D. Eley, *Trans. Faraday Soc.*, **35**, 1281 (1939).

(2) J. A. V. Butler, *ibid.*, **33**, 229 (1937).

(3) J. Uhlig, *J. Phys. Chem.*, **41**, 1215 (1937).

(4) E. Lange and R. Watzel, *Z. physik. Chem. (Leipzig)*, **A182**, 1 (1938).

(5) H. S. Frank and M. W. Evans, *J. Chem. Phys.*, **13**, 507 (1945).

(6) W. F. Claussen and M. F. Polglase, *J. Am. Chem. Soc.*, **74**, 4817 (1952).

(7) W. F. Claussen, *J. Chem. Phys.*, **19**, 259, 662, 1425 (1951).

The principal disadvantage of this model, and of similar ones,^{8,9} is their restriction to the case of definite radii for the cavities.

The purpose of this paper is to discuss the entropy and enthalpy of solution of noble gases in water. This will be done by using a model for liquid water which is similar to some models recently used to describe the properties of pure water and of aqueous solutions of nonelectrolytes.¹⁰⁻¹³

It will be shown that the so-called¹³ "stabilization of the structure of water" by nonelectrolytes plays an essential role in the elucidation of the origin of the anomalous thermodynamic behavior of aqueous solutions of noble gases.

II. Reformulation of the Problem in Terms of a "Two-Structure" Model for Liquid Water

The model used here is the same as used in a previous work.¹³ Liquid water is assumed to consist of two kinds of molecules in chemical equilibrium: the monomeric water molecules (*p* molecules), that is, molecules not linked by hydrogen bonds to other molecules and clusters of water molecules linked together by hydrogen bonds (*c* molecules). Unlike other models, the present one assumes only that the molecules in the cluster are linked tetrahedrally by hydrogen bonds. The spatial structure is not specified and might be icelike, clathratelike, or any other structure. For the sake of simplicity we assume that the clusters are of spherical shape and that they are of equal size (the generalization to many kinds of clusters merely adds details which are not essential to the conclusions).

The chemical reaction is thus $c \rightleftharpoons np$, where *c* is a cluster built by *n* water molecules. We denote by n_p and n_c the number of molecules present in the two forms and by n_w the total number of water molecules, so that $n_w = n_p + nn_c$.

Let *s* be a nonelectrolyte, present in a small concentration in water. Specifically, we shall deal with noble gas solutes, but our general requirement will be that only a weak interaction exists between solute and water molecules, so that new kinds of water molecules are not formed. (Had *s* been an electrolyte, the "two-structure" model could hardly have been used since the molecules in the hydration shell cannot be identified with one of the two original forms.)

The partial molecular quantity \bar{E}_s corresponding to an extensive variable *E* is given by

$$\bar{E}_s \equiv \left(\frac{\partial E}{\partial n_s} \right)_{n_w} = \left(\frac{\partial E}{\partial n_s} \right)_{n_c n_p} + \left(\frac{\partial E}{\partial n_c} \right)_{n_s n_p} \left(\frac{\partial n_c}{\partial n_s} \right)_{n_w} + \left(\frac{\partial E}{\partial n_p} \right)_{n_s n_c} \left(\frac{\partial n_p}{\partial n_s} \right)_{n_w} \quad (1)$$

In what follows, the pressure and temperature will always be held constant and therefore be omitted from the notation. Using the condition $n_w = n_p + nn_c$ we get

$$\bar{E}_s = \left(\frac{\partial E}{\partial n_s} \right)_{n_c n_p} + (\bar{E}_c - n\bar{E}_p) \left(\frac{\partial n_c}{\partial n_s} \right)_{n_w} \quad (2)$$

where \bar{E}_c and \bar{E}_p have their usual meaning. We denote

$$E_s^* = \left(\frac{\partial E}{\partial n_s} \right)_{n_c n_p} \quad \Delta E_s^r = (\bar{E}_c - n\bar{E}_p) \left(\frac{\partial n_c}{\partial n_s} \right)_{n_w}$$

and obtain

$$\bar{E}_s = E_s^* + \Delta E_s^r \quad (3)$$

In this notation \bar{E}_s is divided into two parts. The static one, E_s^* , may be interpreted as that partial molecular quantity which would have been measured, had the equilibrium $c \rightleftharpoons np$ been "frozen in." The additional one, the relaxation term, ΔE_s^r , is the contribution to \bar{E}_s which arises from the displacement of the equilibrium concentrations of *c* and *p* caused by the addition of *s*.

In the same manner the partial molecular entropy, enthalpy, and free energy are given by

$$\bar{S}_s = S_s^* + \Delta S_s^r \quad (4)$$

$$\bar{H}_s = H_s^* + \Delta H_s^r \quad (5)$$

$$\mu_s = \mu_s^* + \Delta \mu_s^r \quad (6)$$

The division of the process of dissolution into two parts, suggested by the last relations, proves helpful in the interpretation of the thermodynamic quantities associated with aqueous solutions of noble gases. This division into two parts can be pictured as follows. Suppose the reaction $c \rightleftharpoons np$ reaches equilibrium only in the presence of a catalyst. Starting with a system described by n_c , n_p , and n_s at equilibrium in the presence of a catalyst, the first step consists of removing the catalyst and transferring dn_s molecules of *s* into the system. In the second step, the catalyst is introduced again. Inspection of relations 4-6 reveals that while \bar{H}_s and \bar{S}_s have contributions from both steps, only the first contributes to the partial molecular free energy. This peculiarity of the behavior of μ_s arises from the

(8) H. S. Frank and A. S. Quist, *J. Chem., Phys.*, **34**, 604 (1961).

(9) D. N. Glew, *J. Phys. Chem.*, **66**, 605 (1962).

(10) G. Wada, *Bull. Chem. Soc. Japan*, **34**, 955 (1961).

(11) H. S. Frank and W. Y. Wen, *Discussions Faraday Soc.*, **24**, 133 (1957).

(12) G. Némethy and H. A. Scheraga, *J. Chem. Phys.*, **36**, 3382, 3401 (1962).

(13) A. Ben-Naim, *J. Phys. Chem.*, **69**, 1922 (1965).

condition of chemical equilibrium, $\mu_c = n\mu_p$, so that the last relation reduces to¹⁴

$$\mu_s = \mu_s^* \quad (7)$$

In the present formulation, Eley's treatment might be broadly identified with the use of static terms only, while in that of Frank and Evans, the relaxation terms are stressed.

It is to be realized that the relaxation terms of \bar{S}_s and \bar{H}_s play the role of the "iceberg-building" contribution to the entropy and enthalpy of solution.

In the next section we shall turn to deal with the central problem of the present subject, *i.e.*, to examine under what conditions $(\partial n_c / \partial n_s)_{n_w} > 0$. This problem is related to the question raised by Frank and Evans⁵ as to the cause of the "iceberg" formation. It was discussed for a special case in the preceding paper¹³ and was also treated by several authors using different approaches.¹⁵

III. The Stabilization of the Structure of Water by Noble Gases

In the previous paper,¹³ we have dealt with the "stabilization effect" (S.E.) on the structure of water by nonelectrolytes. We confined the discussion to the case where no penetration of solute molecules into the cavities of the "open-structure" clusters occurs. In this section we shall show that additional contribution to the stabilization effect is gained when "s-penetration" occurs. Experimental evidence, mainly from partial molar volume measurements, indicates that s-penetration is very probable. It is reasonable that, for small-size molecules having a weak interaction with the solvent, this penetration does not affect the structure of the clusters.

As before,¹³ we shall examine the sign of $(\partial \Delta\mu / \partial n_s)_{n_c n_p}$ instead of investigating directly the derivative $(\partial n_c / \partial n_s)_{n_w}$. This will be done by using the transformation¹³

$$\left(\frac{\partial n_c}{\partial n_s}\right)_{n_w} = -(\mu_{\infty} - 2n\mu_{op} + n^2\mu_{pp})^{-1} \left(\frac{\partial \Delta\mu}{\partial n_s}\right)_{n_c n_p} \quad (8)$$

where $\Delta\mu = \mu_c - n\mu_p$ and $\mu_{ij} = \partial \mu_i / \partial n_j$.

We have shown¹³ that for very low concentrations of the solute and for sufficiently large, compact clusters of molecules, $(\partial \Delta\mu / \partial n_s)_{n_c n_p}$ is negative provided that the difference between the interaction energy of the water-water and water-solute pairs fulfill a certain condition. Hereafter, we shall call this effect the indirect S.E. (I.S.E.).

We shall now restrict the discussion to the additional contribution to $(\partial \Delta\mu / \partial n_s)_{n_c n_p}$ which arises from the molecules occupying the cavities of the clusters.

This contribution will be referred to as the direct S.E. (D.S.E.).

For this purpose we start with an aqueous solution of a noble gas described by n_c, n_p, μ_s, V , and T , where μ_s is the chemical potential of the gas s . The following hypothetical process will be used. First we freeze the chemical equilibrium $c \rightleftharpoons np$; then we remove all the molecules (p and s) which are in the surroundings of the clusters. We are left with a system of n_c clusters, containing s molecules at a given chemical potential μ_s . At this stage we shall calculate the partition function of the system, in particular, the contribution of the inner s molecules to the term $(\partial \Delta\mu / \partial n_s)_{n_c n_p}$. Finally, the p and s molecules are reintroduced; this brings us back to the initial state.

At the intermediate stage we have a system consisting of n_c clusters (including s molecules) of equal size in the gas phase of volume V and temperature T .

Let ν be the number of cavities in a cluster (ν is proportional to n for large n). Assuming that the cavities are equivalent, the partition function of this system is the same as that of a system of n_c absorbents each having ν sites which are occupied by s molecules at constant chemical potential μ_s . The partition function of this system is¹⁶

$$\Gamma(n_c, V, \mu_s, T) = \exp[(PV - \mu_c^g n_c) / kT] = \gamma^{n_c} / n_c! \quad (9)$$

where

$$\gamma = \sum_{j=0}^{\nu} q(j) \lambda_s^j, \quad q(0) = V / \Lambda_s^3, \quad \lambda_s = \exp(\mu_s / kT)$$

and μ_c^g is the chemical potential of c in this state. $q(j)$ is the partition function of a cluster containing j molecules in its cavities. If we assume that the system is sufficiently dilute, we can put $PV / kT = n_c$ in (9) and obtain

$$\mu_c^g = kT \ln n_c - kT \ln \gamma \quad (10)$$

By the assumption made above and since s is an inert gas molecule, we can write

$$q(j) = q(0) \frac{\nu!}{j!(\nu-j)!} (q_s e^{-\epsilon/kT})^j \quad (11)$$

where q_s is the partition function of s molecule in its cavity and ϵ is its total interaction energy with the cavity. Thus, combining (9) and (11), we get

(14) Application of this result to solubility of noble gases in water will be discussed elsewhere.

(15) For references see ref. 13.

(16) T. L. Hill, "An Introduction to Statistical Thermodynamics," Addison-Wesley Publishers, Reading, Mass., 1960, p. 138.

$$\begin{aligned}\gamma &= q(0) \sum_{j=0}^{\nu} \frac{\nu!}{j!(\nu-j)!} (q_s \lambda_s e^{-\epsilon/kT})^j \\ &= q(0) (1 + q_s \lambda_s e^{-\epsilon/kT})^{\nu}\end{aligned}\quad (12)$$

Inserting (12) in (10), we get

$$\mu_c^g = kT \ln \rho_c \Lambda_c^3 - kT \ln (1 + q_s \lambda_s e^{-\epsilon/kT})^{\nu} \quad (13)$$

where $\rho_c = n_c/V$.

Since the process of removing and then reintroducing the surrounding p and s molecules leaves the state of the system unchanged, the term $-kT \ln (1 + q_s \lambda_s e^{-\epsilon/kT})^{\nu}$ is exactly the contribution of s-penetration to the chemical potential of c. The appropriate contribution to the S.E. is thus

$$\begin{aligned}-\frac{\partial}{\partial n_s} [kT \ln (1 + q_s \lambda_s e^{-\epsilon/kT})^{\nu}] &= \\ \frac{-\nu kT q_s e^{-\epsilon/kT} \partial \lambda_s}{1 + q_s \lambda_s e^{-\epsilon/kT} \partial n_s} &= \frac{-\nu q_s e^{\mu_s/kT}}{e^{\epsilon/kT} + q_s \lambda_s} \frac{\partial \mu_s}{\partial n_s}\end{aligned}\quad (14)$$

Since from the stability condition¹⁷ $(\partial \mu_s / \partial n_s) > 0$, we thus conclude that (a) the penetration of s molecules into the cavities of the "icelike" form gives an additional negative contribution to $(\partial \Delta \mu / \partial n_s)_{n_c, n_p}$, which is proportional to ν (i.e., to n for large n) and (b) the D.S.E. is larger the greater the interaction energy of s with its cavity (note that $\epsilon < 0$).

IV. Discussion

a. *Enthalpy of Solution.* Following Eley's arguments on the enthalpy of solution, it is probable that the value of $|\Delta H_s^*|$ is of the order of $|\Delta \bar{H}_s^{\circ}|$ in other liquids. Thus, an explanation of the high negative value of $\Delta \bar{H}_s^{\circ}$ may be primarily based upon the corresponding relaxation term.

Let us write $\Delta \bar{H}_s^{\circ}$ (in any standard states chosen) in the form

$$\begin{aligned}\Delta \bar{H}_s^{\circ} &= \bar{H}_s^{\circ} (\text{in water}) - \bar{H}_s^{\circ} (\text{in gas phase}) \\ &= H_s^* + \Delta H_s^{\ddagger} - \bar{H}_s^{\circ} (\text{in gas phase}) \\ &= \Delta H_s^* + \Delta H_s^{\ddagger}\end{aligned}\quad (15)$$

where

$$\begin{aligned}\Delta H_s^{\ddagger} &= (\bar{H}_c - n\bar{H}_p) \left(\frac{\partial n_c}{\partial n_s} \right)_{n_w} = \\ &= -(\bar{H}_c - n\bar{H}_p) (\mu_{cc} - 2n\mu_{cp} + n^2\mu_{pp})^{-1} \left(\frac{\partial \Delta \mu}{\partial n_s} \right)_{n_c, n_p}\end{aligned}$$

(Note that $\Delta \bar{H}_s^*$ and $\Delta \bar{H}_s^{\ddagger}$ refer to the same state chosen for $\Delta \bar{H}_s^{\circ}$.) Since $\bar{H}_c - n\bar{H}_p < 0$ and $(\mu_{cc} - 2n\mu_{cp} + n^2\mu_{pp}) > 0$, the relaxation term ΔH_s^{\ddagger} is negative (for sufficiently large n). This result reveals the source

of the anomalous, large negative enthalpy of solution of noble gases. The extra term ΔH_s^{\ddagger} which is characteristic of liquid water depends on $(\bar{H}_c - n\bar{H}_p)$ and is greater the larger the clusters.

It is, however, impossible to predict the dependence of ΔH_s^{\ddagger} on the magnitude of the interaction energy between s molecules and water molecules since the S.E. arises from two different sources: the I.S.E. was found to be greater the weaker the interaction between solute and water,¹³ while the D.S.E. has the opposite dependence on this interaction energy.

b. *Entropy of Solution.* In an analogous manner, the entropy of solution can be written in the form

$$\Delta \bar{S}_s^{\circ} = \Delta S_s^* + \Delta S_s^{\ddagger} \quad (16)$$

where

$$\begin{aligned}\Delta S_s^{\ddagger} &= -(\bar{S}_c - n\bar{S}_p) (\mu_{cc} - \\ &= 2n\mu_{cp} + n^2\mu_{pp})^{-1} \left(\frac{\partial \Delta \mu}{\partial n_s} \right)_{n_c, n_p}\end{aligned}$$

Since the "icelike" form is expected to be more "ordered," i.e. $(\bar{S}_c - n\bar{S}_p) < 0$, the relaxation term of $\Delta \bar{S}_s^{\circ}$ gives a negative contribution to $\Delta \bar{S}_s^{\circ}$. (Obviously, since $\mu_c = n\mu_p$, it follows that $\Delta H_s^{\ddagger} = T\Delta S_s^{\ddagger}$, thus ΔH_s^{\ddagger} and ΔS_s^{\ddagger} are not independent and have the same sign.)

However, in contrast with $\Delta \bar{H}_s^{\circ}$, where we assumed that ΔH_s^{\ddagger} is the predominating term, both ΔS_s^* and ΔS_s^{\ddagger} seem to contribute appreciably to the large negative entropy of solution. The reason for this conclusion comes from the following experimental fact. $\Delta \mu_s^{\circ}$ is known to be large and positive.^{1,5} We write $\Delta \mu_s^{\circ} = \Delta \bar{H}_s^{\circ} - T\Delta S_s^{\circ}$. Using (15) and (16) and noting that $\Delta H_s^{\ddagger} = T\Delta S_s^{\ddagger}$, we get

$$\Delta \mu_s^{\circ} = \Delta \mu_s^* = \Delta H_s^* - T\Delta S_s^* \quad (17)$$

Following Eley's arguments,¹ ΔH_s^* should have a negative value (since no appreciable amount of energy has to be supplied to create cavities) so that we must be led to the conclusion that it is a high negative value of ΔS_s^* which is responsible for the large positive $\Delta \mu_s^*$.

It is customarily stated in the literature that the high positive value of $\Delta \mu_s^{\circ}$ is caused by an entropy effect rather than by an energy effect. This may be formally right. It is, however, misleading to understand by "entropy effect" that part of the entropy change which accompanies a structural shift in the solvent. The contribution of the relaxation term of $\Delta \bar{H}_s^{\circ}$ to $\Delta \mu_s^{\circ}$ is exactly counterbalanced by the corresponding part of the entropy change.

(17) I. Prigogine and R. Defay, "Chemical Thermodynamics," Longmans, Green and Co., London, 1954, Chapter XV.

V. Comparison with Other Approaches

As we have already noted, Eley's treatment¹ is essentially equivalent to the treatment which considers only static terms. Strictly speaking, Eley did not base his arguments on a "two-structure" model but assumed that water consists of a definite number (n_H) of natural holes, the gas molecules being distributed only among them, and that the insertion of the solute does not perturb the state of water (in particular it was assumed that $\partial n_H / \partial n_s = 0$); thus the partition function for the solution had the form¹

$$Q(T, V, n_s, n_w) = \frac{n_H!}{n_s!(n_H - n_s)!} q_w^{n_w} q_s^{n_s}$$

These assumptions have not been made in the present treatment. The gas molecules may be found everywhere in the solvent, in the natural cavities, or in the neighborhood of monomeric water molecules; and the relaxation terms take into account the change in the state of water caused by the introduction of the solute.

On the other hand, the treatment of Frank and Evans⁵ is primarily concerned with the relaxation term. As Frank and Evans' original statement of the iceberg formation has been interpreted in various ways by different authors, it is instructive to quote it at this point: "When a rare gas atom or a nonpolar molecule dissolves in water at room temperature, it modified the water structure in the direction of greater crystallinity—the water, so to speak, builds a microscopic iceberg around it."

A close comparison of the present approach with that of Frank and Evans reveals an essential difference between the two. The net effect in the two cases is that the solute molecule brings about an increase in the total amount of "order" in the water. The present approach views the equilibrium between *already existing* water species as being shifted, upon introduction of gas, in the direction of the "better ordered" form. By our arguments in section III, this *pre-existence* of the more ordered form is a necessary condition for this shift (for some experimental support see ref. 18 and 19). According to Frank and Evans, an iceberg is built *around* the molecule. No matter what structure this iceberg has, the statement leaves us with the impression that an "active building" of a new form is taking place. Many authors have interpreted the statement in this sense, and the impression of the active building is even augmented upon finding that some^{20,21} discuss it together with the effect of ions upon water structure (*i.e.*, building of hydration shells, especially when dealing with entropies of solution).

Since the pre-existence of icebergs was not assumed

explicitly by Frank and Evans, the reason for their formation is unclear if we remember that we are dealing with a relatively inert molecule. In our approach the condition $\mu_c = n\mu_p$ is satisfied, and all that is required is that the gas molecule cause a small shift of the equilibrium concentrations of c and p .

The estimation of the order of magnitude of the relaxation term has, of course, to be done by using a specific model for liquid water. It is worthwhile to mention here that Frank and Quist⁸ made this kind of estimation by applying Pauling's model for water and calculating the partial molar entropy of the solute. They found that the excess entropy is composed of two terms, analogous to our static and relaxation ones, which have nearly equal values. This is qualitatively the same result as that drawn by us in examining the two terms. The reason for the shift of the equilibrium concentration in Frank and Quist's model is, however, different from ours. As already noted, Pauling's model suffers from the restriction of definite radii of the cavities so that the phenomena displayed by larger molecules cannot be discussed. Moreover, this model cannot be used either for high concentration of solute^{18,19} or at high temperatures.

A different mechanism of a dynamical nature, has been brought forward by Frank and Wen,¹¹ who described the formation and annihilation of clusters as caused by local fluctuation in the energy. They reached the conclusion that a solute molecule present at the boundaries of such a cluster promotes the formation of the icelike clusters. An extension of Frank and Wen's idea was made by Némethy and Scheraga,¹² who have recently described a model of liquid water consisting of five molecular species, differing by the number of hydrogen bonds supplied by them. This model was then applied to the effect of inert solute upon the structure of water.

Némethy and Scheraga start from a consideration of "energy levels" assigned to the various forms. Changes of these energy levels lead, through the change in the partition function of the system, to a redistribution of water molecules between the various forms. Our treatment, on the other hand, is concerned with the examination of the chemical potentials of the various forms. Changes of the chemical potentials provide a direct cause for the shift in the equilibrium concen-

(18) A. Ben-Naim and S. Baer, *Trans. Faraday Soc.*, **60**, 1736 (1964).

(19) A. Ben-Naim and G. Moran, *ibid.*, **61**, 821 (1965).

(20) R. A. Robinson and R. H. Stokes, "Electrolyte Solutions," Butterworth and Co. Ltd., London, 1959, p. 14.

(21) J. P. Hunt, "Metal Ions in Aqueous Solution," W. A. Benjamin, New York, N. Y., 1963, p. 41.

trations of the various forms. In addition, the examination of the chemical potentials of the various forms is simpler than the evaluation of the partition function of the system since it requires less detailed information on the structure of water.

VI. Conclusion

The thermodynamic behavior of aqueous solutions of noble gases was discussed in terms of a "two-structure" model for liquid water. It was shown that a satisfactory qualitative explanation of the entropy and enthalpy of solution can be given by regarding the thermodynamic functions of solution as composed of two parts, the static and the relaxation one. This division proves to be helpful also for interpretation of

experimental results. The occurrence of the relaxation part was based on the assumption that liquid water contains large compact clusters of water molecules connected by hydrogen bonds. This property is one which distinguishes water from other liquids. The penetration of solute molecules into the cavities of the relatively open structure of the clusters was shown to enhance the stabilization effect but, by no means, is the essential cause for it.

Acknowledgments. The author wishes to express his thanks to Professor G. Stein and Dr. S. Baer for suggesting the problem and for numerous helpful discussions on the subject. Indebtedness is expressed to Dr. A. Treinin for discussion on different parts of this work.

Thermodynamics of Aqueous Solutions of Noble Gases. II.

Effect of Nonelectrolytes

by A. Ben-Naim

Department of Physical Chemistry, The Hebrew University, Jerusalem, Israel (Received March 11, 1965)

The solubility of argon was measured in water and in dilute aqueous solutions of nonelectrolytes: methanol, ethanol, 1-propanol, 1-butanol, glycerol, *p*-dioxane, glucose, and sucrose. The entropy and enthalpy of solution of argon were calculated from the temperature dependence of the solubility. The difference in these quantities in solution of nonelectrolyte and in pure water is interpreted in terms of a "two-structure" model for liquid water and is attributed to the difference in the degree of crystallinity of the various solvents.

Introduction

The thermodynamic behavior of aqueous solutions of noble gases reveals many anomalous properties when compared with other solvents.¹⁻³ In an attempt to find their origin we examined in detail the effect of added solutes on the thermodynamic functions of solutions of argon in water. This investigation is con-

cerned with the effect of nonelectrolytes. A qualitative interpretation of the results, based on a "two-structure" model for liquid water, is suggested.

(1) D. D. Eley, *Trans. Faraday Soc.*, **35**, 1281 (1939).

(2) H. S. Frank and M. M. Evans, *J. Chem. Phys.*, **13**, 507 (1945).

(3) (a) A. Ben-Naim, *J. Phys. Chem.*, **69**, 1922 (1965); (b) A. Ben-Naim, *ibid.*, **69**, 3240 (1965).

Experimental Section and Results

The solubility of argon was measured in pure water and in dilute solutions of nonelectrolytes. The details of the method have been described elsewhere.⁴ Measurements were done at five temperatures between 5 and 25°. Several measurements were performed at each temperature, and the mean values obtained are recorded in Table I in terms of the Ostwald absorption coefficient.⁵

Table I: Values of $\gamma \times 10^3$ for Argon in Water and in Aqueous Solutions of Nonelectrolytes

	Temp., °C.				
	5	10	15	20	25
Pure water	48.07	43.36	39.56	36.63	34.08
Methanol $x = 0.015$	49.60	45.00	41.35	38.45	35.96
Ethanol $x = 0.015$	49.80	45.05	41.30	38.33	35.85
1-Propanol $x = 0.015$	48.45	44.05	40.55	37.75	35.45
1-Butanol $x = 0.015$	48.00	43.55	40.10	37.25	34.90
Glycerol $x = 0.015$	43.80	39.80	36.70	34.10	31.93
<i>p</i> -Dioxane $x = 0.015$	46.24	42.40	39.35	36.96	35.00
Glucose 0.5 <i>m</i>	41.55	37.93	34.90	32.45	30.40
Sucrose 0.5 <i>m</i>	38.80	35.47	32.75	30.60	28.85

The value of γ for pure water at 10° was found to be slightly lower than that published previously.⁴ Distilled water and Analar grade materials were used. During outgassing, a small change of concentration might have occurred; however, no correction for this was taken into account.⁶ As we were primarily interested in the changes of the thermodynamic functions of solution upon adding the solute, we found it convenient to plot $\Delta\mu_t^\circ$ vs. T , where $\Delta\mu_t^\circ$ is defined by

$$\Delta\mu_t^\circ = \Delta\mu_s^\circ (\text{in water} + \text{nonelectrolyte}) - \Delta\mu_s^\circ (\text{in pure water})$$

$\Delta\mu_s^\circ$ is the standard free energy of solution of argon given by⁷ $\Delta\mu_s^\circ = -RT \ln \gamma$ and γ is the Ostwald absorption coefficient.⁵

Values of $\Delta\bar{S}_t^\circ$ and $\Delta\bar{H}_t^\circ$ were calculated from the slopes of the curves (measured with an accurate tangentimeter⁸) in Figure 1 and are given in Table II. The pertinent relations are (for more details see the Appendix)

$$\Delta\mu_t^\circ = -RT \ln \gamma/\gamma_0$$

$$\Delta\bar{S}_t^\circ = R \frac{\partial}{\partial T} (T \ln \gamma/\gamma_0) - RT \frac{\partial}{\partial T} (\ln \rho/\rho_0)$$

$$\Delta\bar{H}_t^\circ = \Delta\mu_t^\circ + T\Delta\bar{S}_t^\circ$$

where γ_0 and γ refer to a solution of argon in pure water and in a solution of a nonelectrolyte, respectively. ρ_0 and ρ are the corresponding densities of the solvents.

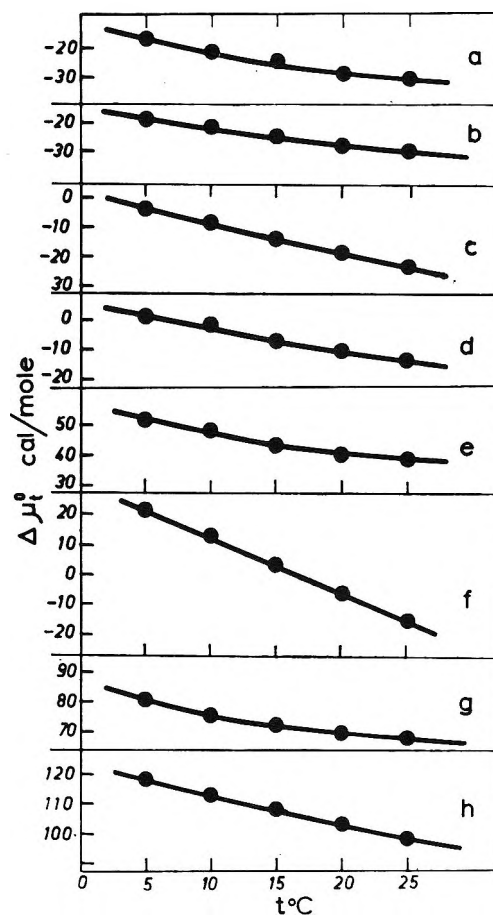


Figure 1. Values of $\Delta\mu_t^\circ$ as a function of temperature for the transfer of argon from pure water into an aqueous solution of nonelectrolytes (x is the mole fraction of the nonelectrolyte): a, methanol ($x = 0.015$); b, ethanol ($x = 0.015$); c, 1-propanol ($x = 0.015$); d, 1-butanol ($x = 0.015$); e, glycerol ($x = 0.015$); f, *p*-dioxane ($x = 0.015$); g, glucose (0.5 *m*); h, sucrose (0.5 *m*).

(4) A. Ben-Naim and S. Baer, *Trans. Faraday Soc.*, **59**, 2735 (1963).

(5) J. H. Hildebrand and R. L. Scott, "The Solubility of Nonelectrolytes," 3rd Ed., Reinhold Publishing Corp., New York, N. Y., 1950, p. 4.

(6) A. Ben-Naim and S. Baer, *Trans. Faraday Soc.*, **60**, 1936 (1964).

(7) R. P. Bell, *ibid.*, **33**, 496 (1937).

(8) H. J. G. Hayman, F. Deutsch, and H. Tabor, *J. Sci. Instr.*, **34**, 307 (1957).

The calculated thermodynamic functions correspond to the process

argon (in pure water) \longrightarrow

argon (in water + nonelectrolyte)

at an equal molar concentration of argon in the two liquids.

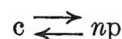
Table II: Values of $\Delta\mu_t^\circ$ (cal./mole), $\Delta\bar{S}_t^\circ$ (cal./mole deg.), and $\Delta\bar{H}_t^\circ$ (cal./mole) for the Transfer of Argon from Pure Water into the Various Solutions of Nonelectrolytes

	Methanol, $x = 0.015$				
$\Delta\mu_t^\circ$	-17.8	-21.9	-26.0	-29.2	-31.5
$\Delta\bar{S}_t^\circ$	1.00	0.91	0.73	0.55	0.37
$\Delta\bar{H}_t^\circ$	260	236	184	132	79
	Ethanol, $x = 0.015$				
$\Delta\mu_t^\circ$	-18.7	-21.9	-25.1	-27.9	-29.7
$\Delta\bar{S}_t^\circ$	0.73	0.64	0.55	0.46	0.37
$\Delta\bar{H}_t^\circ$	184	159	133	107	81
	1-Propanol, $x = 0.015$				
$\Delta\mu_t^\circ$	-4.1	-8.7	-14.2	-18.7	-23.3
$\Delta\bar{S}_t^\circ$	1.05	1.00	0.98	0.92	0.87
$\Delta\bar{H}_t^\circ$	288	274	268	251	236
	1-Butanol, $x = 0.015$				
$\Delta\mu_t^\circ$	0.9	-2.3	-7.7	-11	-14.2
$\Delta\bar{S}_t^\circ$	0.87	0.82	0.73	0.64	0.59
$\Delta\bar{H}_t^\circ$	243	230	202	176	162
	Glycerol, $x = 0.015$				
$\Delta\mu_t^\circ$	51.6	48.0	43.0	40.2	38.4
$\Delta\bar{S}_t^\circ$	0.75	0.68	0.47	0.24	0.08
$\Delta\bar{H}_t^\circ$	260	240	178	111	62.2
	<i>p</i> -Dioxane, $x = 0.015$				
$\Delta\mu_t^\circ$	21.5	12.8	3.2	-6.4	-15.5
$\Delta\bar{S}_t^\circ$	1.8	1.8	1.8	1.8	1.8
$\Delta\bar{H}_t^\circ$	522	522	522	521	521
	Glucose, 0.5 <i>m</i>				
$\Delta\mu_t^\circ$	80.4	74.9	71.7	69.0	67.6
$\Delta\bar{S}_t^\circ$	1.19	0.87	0.55	0.37	0.32
$\Delta\bar{H}_t^\circ$	417	321	230	177	163
	Sucrose, 0.5 <i>m</i>				
$\Delta\mu_t^\circ$	118.4	112.9	107.9	103.3	98.7
$\Delta\bar{S}_t^\circ$	1.14	1.05	1.00	0.96	0.87
$\Delta\bar{H}_t^\circ$	435	410	396	385	358

Discussion

It has been previously^{3,9} found convenient to divide the partial molar quantities of the gas into two parts: a static and a relaxation part. This was done using a "two-structure" model for liquid water. This model is, no doubt, the simplest one by which one can describe

the properties of pure liquid water, yet it seems that it furnishes a satisfactory explanation for some anomalous properties of pure water and aqueous solutions of nonelectrolytes. Liquid water is regarded³ as being composed of monomeric water molecules (p) and "icelike" clusters of water molecules (c), containing n molecules linked together by hydrogen bonds. The "chemical" reaction is



Let n_p and n_c be the number of moles of the two species, respectively. If the solution contains n_s moles of gas (*i.e.*, argon) and n_w moles of water ($nn_c + n_p = n_w$) then the partial molar quantity \bar{E}_s , corresponding to any extensive function E , can be represented by

$$\bar{E}_s = \left(\frac{\partial E}{\partial n_s} \right)_{n_w} = \left(\frac{\partial E}{\partial n_s} \right)_{n_c n_p} + (\bar{E}_c - n\bar{E}_p) \left(\frac{\partial n_c}{\partial n_s} \right) = E_s^* + \Delta E_s^r$$

(The pressure and temperature are held constant and are omitted from the notation.)

The static term, E_s^* , refers to a solution where the equilibrium between the two forms is "frozen in," while the relaxation term, ΔE_s^r , takes into account the change in the distribution of water molecules between the two forms. For the sake of comparison with experimental results, the interpretation of the relaxation terms should be considered. The "two-structure" model is useful for detecting the origin of the anomalous thermodynamic behavior of aqueous solution of noble gases. However, liquid water consists of clusters of different size and shape. The relaxation term should thus be modified so as to take into account the change in the concentration of the various clusters present. In the following discussion, we still use a single relaxation term. In fact, it expresses the change of the thermodynamic functions due to the change of the concentration of *all* the clusters present. The static term retains its usual meaning; it refers to a solution where the equilibrium between *all* kinds of clusters is frozen.

Entropy and Enthalpy of Transfer of Argon from Pure Water into a Solution of a Nonelectrolyte. Table II shows that $\Delta\bar{S}_t^\circ$ and $\Delta\bar{H}_t^\circ$ are always positive for nonelectrolyte solutions although the effect on the structure of water might be different for each nonelectrolyte. A qualitative interpretation can be given by defining the quantities

(9) A. Ben-Naim, *J. Chem. Phys.*, **42**, 1512 (1965).

$$\Delta\bar{H}_t^* = H_s^* \text{ (in water + nonelectrolyte) - } \\ H_s^* \text{ (in pure water)}$$

$$\Delta H_t^r = \Delta H_s^r \text{ (in water + nonelectrolyte) - } \\ \Delta H_s^r \text{ (in pure water)}$$

$$\Delta S_t^* = S_s^* \text{ (in water + nonelectrolyte) - } \\ S_s^* \text{ (in pure water)}$$

$$\Delta S_t^r = \Delta S_s^r \text{ (in water + nonelectrolyte) - } \\ \Delta S_s^r \text{ (in pure water)}$$

so that the following relations hold

$$\Delta\bar{S}_t^\circ = \Delta S_t^* + \Delta S_t^r$$

$$\Delta\bar{H}_t^\circ = \Delta H_t^* + \Delta H_t^r$$

$$\Delta H_t^r = T\Delta S_t^r$$

(Note that ΔS_t^* , ΔS_t^r , ΔH_t^* , and ΔH_t^r refer to the same standard state chosen for $\Delta\bar{S}_t^\circ$ and $\Delta\bar{H}_t^\circ$.)

These three relations contain four unknowns— ΔS_t^* , ΔS_t^r , ΔH_t^* , and ΔH_t^r —of which ΔH_t^* seems the simplest to interpret. We assume, following Eley's view,¹ that most of the gas molecules occupy empty cavities in both pure water and in dilute solutions of a nonelectrolyte. Since the major part of ΔH_s^* is determined by the interaction energy between the gas molecule and its cavity, we should expect that the difference between ΔH_s^* in pure water and ΔH_s^* in dilute solutions of a nonelectrolyte will be very small. Thus, if we put $\Delta H_t^* \approx 0$ the last relations can be solved to obtain

$$\Delta S_t^r = \Delta\bar{H}_t^\circ / T$$

$$\Delta S_t^* = \Delta\bar{S}_t^\circ - \Delta S_t^r$$

Values of ΔS_t^* and ΔS_t^r calculated on the basis of this assumption are given in Table III. These values, although approximate, seem to have a significant meaning.

First, we see that the sign of ΔS_t^* is positive for methanol, ethanol, 1-propanol, and 1-butanol solutions, while negative for glycerol, glucose, and sucrose solutions. If we assume again that the major part of ΔS_t^* is determined by the change in the total number of cavities, the sign of ΔS_t^* for the first four solutes might indicate that these solutes increase the number of cavities while glycerol, glucose, and sucrose reduce the number of cavities. This conclusion is in accord with the view that solute molecules containing inert groups "stabilize the structure of water" while the other solutes have an opposite effect. (An exception is the behavior of *p*-dioxane. Using a different set of meas-

Table III: Approximate Values of ΔS_t^* (cal./mole deg.) and of ΔS_t^r (cal./mole deg.) for the Transfer of Argon from Pure Water into the Various Solutions of Nonelectrolytes (x Is the Mole Fraction of the Nonelectrolyte)

	Temp., °C.				
	5	10	15	20	25
Methanol, $x = 0.015$					
ΔS_t^*	0.06	0.08	0.09	0.1	0.1
ΔS_t^r	0.94	0.83	0.64	0.45	0.26
Ethanol, $x = 0.015$					
ΔS_t^*	0.07	0.08	0.09	0.095	0.1
ΔS_t^r	0.66	0.56	0.46	0.37	0.27
1-Propanol, $x = 0.015$					
ΔS_t^*	0.015	0.031	0.05	0.063	0.078
ΔS_t^r	1.04	0.97	0.93	0.86	0.79
1-Butanol, $x = 0.015$					
ΔS_t^*	-0.003	0.008	0.027	0.037	0.047
ΔS_t^r	0.873	0.81	0.7	0.6	0.54
Glycerol, $x = 0.015$					
ΔS_t^*	-0.185	-0.17	-0.15	-0.14	-0.13
ΔS_t^r	0.935	0.85	0.62	0.38	0.21
<i>p</i> -Dioxane, $x = 0.015$					
ΔS_t^*	-0.075	-0.045	-0.011	+0.022	0.052
ΔS_t^r	1.87	1.84	1.81	1.78	1.73
Glucose, 0.5 <i>m</i>					
ΔS_t^*	-0.29	-0.26	-0.25	-0.23	-0.22
ΔS_t^r	1.48	1.13	0.8	0.6	0.54
Sucrose, 0.5 <i>m</i>					
ΔS_t^*	-0.42	-0.40	-0.37	-0.35	-0.33
ΔS_t^r	1.56	1.45	1.37	1.31	1.2

urements, we concluded that *p*-dioxane probably has a destabilizing effect on the structure of water.¹⁰)

It should be noted that ΔS_t^* refers to the transfer of argon from pure water into an aqueous solution of a nonelectrolyte, the molar concentration of the gas being the same in the two solvents. Thus, if we take the same volumes of pure water and of the aqueous solution of nonelectrolyte, the total number of water molecules in the latter will be less than that in pure water, and we might expect that the total number of cavities will also be reduced by the presence of the added solute. The sign of ΔS_t^* for the first four solutes indicates that for a low concentration of these solutes the stabilizing effect of the structure of water is even larger than the above-mentioned opposite effect, so that the net effect is that the total number of cavities

(10) A. Ben-Naim and G. Moran, *Trans. Faraday Soc.*, 61, 821 (1965).

increases. Obviously, for a high concentration of solutes the destabilizing effect would be the predominating one.

As for the relaxation term, Table III shows that for all the solutions its sign is positive. Now, since we have shown³ that ΔS_s^r is negative for a noble gas in pure water, the above result means that the absolute value of the relaxation term in the solution is smaller than that in pure water. This seems to contradict the conclusion we have drawn previously^{3,7} that the relaxation term is greater the greater the "degree of crystallinity" of the solvent. However, it should be emphasized that the above conclusion was drawn for pure water only, using a two-structure model (*i.e.*, one kind of clusters), and this must not be the case if the change of the "degree of crystallinity" is due to the presence of an additional solute. A proper interpretation of this result should take into account some factors which might change when passing from one solvent to another. Let us write ΔS_t^r in the form⁸

$$\Delta S_t^r = \Delta \left[(\bar{S}_c - n\bar{S}_p) \left(\frac{\partial n_c}{\partial n_s} \right)_{n_w} \right] = \Delta \left[-(\bar{S}_c - n\bar{S}_p) (\mu_{cc} - 2n\mu_{cp} + n^2\mu_{pp})^{-1} \times \left(\frac{\partial (\mu_c - n\mu_p)}{\partial n_s} \right)_{n_c n_p} \right]$$

All the factors in the last bracket might be affected by the addition of the solute. Moreover, for treating a real case, one should consider the sum of such terms over all kinds of clusters present. Thus, an interpretation of the sign of ΔS_t^r seems to be impossible at this stage.

Conclusion

From the temperature dependence of the solubility of argon in water and in aqueous solutions of nonelectrolytes, we calculated that the entropy and enthalpy change accompanied the transfer of argon from pure water into the corresponding nonelectrolytic solution.

The division of ΔS_t° and of $\Delta \bar{H}_t^\circ$ into two parts was found to be useful for the interpretation of the experimental results. A qualitative correlation with the "degree of crystallinity" of the solvent was found. The results obtained in this manner lead to a classification of the various nonelectrolytes into two categories: those which stabilize the structure of water and those which destabilize it.

Acknowledgment. The author wishes to express his thanks to Professor G. Stein and Dr. S. Baer for their continuous interest in this work.

Appendix

Derivation of the Thermodynamic Functions for the Transfer of Argon from Pure Water to an Aqueous Solution of Nonelectrolyte. Let μ_s^g and μ_s^l be the chemical potential of the gas *s*, in the gas and liquid phases, respectively. Assuming ideal behavior in the two phases, one can write

$$\mu_s^g = \mu_s^{\circ g} + RT \ln c_s^g \quad (1)$$

$$\mu_s^l = \mu_s^{\circ l} + RT \ln c_s^l \quad (2)$$

where c_s^g and c_s^l are the molar concentrations of the gas *s* in the two phases, respectively. $\mu_s^{\circ g}$ and $\mu_s^{\circ l}$ are formally defined by

$$\mu_s^{\circ g} = \lim_{c_s^g \rightarrow 0} [\mu_s^g - RT \ln c_s^g] \quad (3)$$

$$\mu_s^{\circ l} = \lim_{c_s^l \rightarrow 0} [\mu_s^l - RT \ln c_s^l] \quad (4)$$

One usually proceeds to interpret $\mu_s^{\circ l}$ and $\mu_s^{\circ g}$ as being the chemical potentials of *s* at a hypothetical ideal state of $c_s^l = 1$ and $c_s^g = 1$, respectively. However, for the purpose of interpretation, a simpler significance can be related to the difference $\Delta \mu_s^\circ = \mu_s^{\circ l} - \mu_s^{\circ g}$.

To do this let us recall that at equilibrium we have $\mu_s^l = \mu_s^g$, and thus from (1) and (2) we get

$$\Delta \mu_s^\circ = -RT \ln (c_s^l/c_s^g)_{eq} = -RT \ln \gamma \quad (5)$$

where γ is the Ostwald absorption coefficient. By subtracting (2) from (1) and using (5) we get

$$\mu_s^l - \mu_s^g = \Delta \mu_s^\circ + RT \ln (c_s^l/c_s^g) = -RT \ln \gamma + RT \ln (c_s^l/c_s^g)$$

We immediately recognize that $\Delta \mu_s^\circ = -RT \ln \gamma$ is the change of free energy which accompanies the transfer of the gas *s* from one phase to the second whenever $c_s^l/c_s^g = 1$. This is true no matter what the values of the concentrations, c_s^l and c_s^g , provided that they are low enough to ensure the validity of (1) and (2) and that they are equal to each other.

In the same manner one can consider the transfer of *s* from one solvent, *l*₁, to a second solvent, *l*₂, and get

$$\Delta \mu_t^\circ \equiv \mu_s^{\circ l_2} - \mu_s^{\circ l_1} = (\mu_s^{\circ l_2} - \mu_s^{\circ g}) - (\mu_s^{\circ l_1} - \mu_s^{\circ g}) = -RT \ln (\gamma_2/\gamma_1)$$

where γ_1 and γ_2 are the Ostwald absorption coefficients in the two solvents, respectively.

$\Delta \mu_t^\circ$ is simply the change of free energy which accompanies the process

argon (in solvent l_1) \rightarrow argon (in solvent l_2)

where the molar concentration is the same (low enough) in the two solvents; *i.e.*, $c_s^{l_1} = c_s^{l_2}$.

In the same manner by differentiation (1) and (2), with respect to the temperature and by substituting $c_s^{l_1} = c_s^{l_2}$, we get the changes of entropy and enthalpy which accompany the same process mentioned above.

$$\Delta \bar{S}_t^\circ = R \frac{\partial}{\partial T} (T \ln (\gamma_2/\gamma_1)) - RT \frac{\partial}{\partial T} (\ln (\rho_2/\rho_1))$$

$$\Delta \bar{H}_t^\circ = \Delta \mu_t^\circ + T \Delta \bar{S}_t^\circ$$

The term $RT[\partial \ln (\rho_2/\rho_1)]/\partial T$ which arises from the volume change of the solvents has, in most cases, a negligible value.

Thermodynamics of Aqueous Solutions of Noble Gases. III.

Effect of Electrolytes

by A. Ben-Naim and M. Egel-Thal

Department of Physical Chemistry, The Hebrew University, Jerusalem, Israel (Received March 11, 1966)

The solubility of argon was measured at five temperatures between 5 and 25° in water and in aqueous solutions of electrolytes: LiCl (1 *m*), NH₄Cl (1 *m*), NaCl (1 *m*), KCl (1 *m*), KBr (1 *m*), NaI (1 *m*), and KI (1, 2, and 4 *m*). The entropy and enthalpy of solution of argon were calculated from the temperature dependence of the solubility. The difference in these quantities in solution of electrolytes and in pure water is interpreted in terms of a "two-structure" model for liquid water and is attributed to the decrease of the "degree of crystallinity" of the water caused by the added electrolytes.

Introduction

Effects of electrolytes on the structure of water have been extensively studied both theoretically and experimentally. On the other hand, aqueous solutions of noble gases reveal some anomalous thermodynamic behavior, the origin of which has been related to the special structure of water.¹⁻³ It is, therefore, interesting to examine the effect of electrolytes on the thermodynamic functions of solution of the gases in water.

The solubility of gases in electrolytic solutions was studied by many authors who were primarily interested in "salting-out" effects of the various salts. The temperature dependence of the solubility in these solutions was rarely examined.⁴⁻⁷

Frank and Evans,² in a discussion of the anomalous

thermodynamic behavior of aqueous solutions of noble gases, calculated some values of the entropy change on transferring the gas from pure water to an aqueous electrolytic solution. However, their conclusions rest upon earlier experimental results which seem to be insufficiently accurate for this purpose. Their interpretation was based on the "iceberg-building" idea. The change of the thermodynamic

- (1) D. D. Eley, *Trans. Faraday Soc.*, **35**, 1281 (1939).
- (2) H. S. Frank and M. M. Evans, *J. Chem. Phys.*, **13**, 507 (1945).
- (3) A. Ben-Naim, *J. Phys. Chem.*, **69**, 1922, 3240 (1965).
- (4) A. Eucken and G. Herzberg, *Z. physik. Chem. (Leipzig)*, **195**, 1 (1950).
- (5) T. J. Morrison and F. Billett, *J. Chem. Soc.*, 3819 (1952).
- (6) T. J. Morrison and N. B. B. Johnstone, *ibid.*, 3655 (1955).
- (7) F. A. Long and W. F. McDevitt, *Chem. Rev.*, **51**, 114 (1952).

functions associated with the transfer of the gas from pure water to an aqueous solution of the various electrolytes was attributed to the relative ease of ice-berg formation in the different solvents.

The purpose of this investigation is to examine the change of the thermodynamic functions of solutions of argon upon the addition of various electrolytes. The results obtained are interpreted by using a "two-structure" model for liquid water; a model which was recently applied³ to describe the thermodynamic behavior of aqueous solutions of noble gases.

Experimental Section and Results

The solubility of argon was measured in pure water and in aqueous solutions of several electrolytes. The experimental details together with an estimation of the accuracy of the results have been described elsewhere.⁸ Measurements were done at five temperatures between 5 and 25°. The mean values obtained from two or three experiments at each temperature are given in Table I. Distilled water and Analar grade materials were used. During outgassing, a small change of concentration may have occurred; however, no correction for this was taken into account.⁹

Table I: Values of $\gamma \times 10^3$ for Argon in Water and in Aqueous Solutions of Electrolytes

	Temp., °C.				
	5	10	15	20	25
Pure water	48.07	43.36	39.56	36.63	34.08
LiCl, 1 m	37.01	33.83	31.25	29.19	27.47
NH ₄ Cl, 1 m	38.20	34.91	32.23	30.08	28.27
NaCl, 1 m	33.15	30.44	28.16	26.33	24.77
KCl, 1 m	33.79	31.10	28.85	27.05	25.51
KBr, 1 m	34.07	31.24	28.94	27.11	25.57
NaI, 1 m	33.25	30.86	28.57	26.90	25.50
KI, 1 m	33.41	30.83	28.68	26.98	25.57
KI, 2 m	24.53	22.91	21.58	20.54	19.68
KI, 4 m	14.17	13.48	12.96	12.59	12.32

As we were primarily interested in the changes of the thermodynamic functions of solution on addition of the salt, we found it convenient to plot $\Delta\mu_t^\circ$ vs. T , where $\Delta\mu_t^\circ$ is defined by

$$\Delta\mu_t^\circ = \Delta\mu_s^\circ (\text{in water} + \text{electrolyte}) - \Delta\mu_s^\circ (\text{in pure water})$$

$\Delta\mu_s^\circ$ is the standard free energy of solution of argon given by $\Delta\mu_s^\circ = -RT \ln \gamma$, γ being the Ostwald absorption coefficient.¹⁰

Values of $\Delta\bar{S}_t^\circ$ and $\Delta\bar{H}_t^\circ$ were calculated from the slopes of the curves in Figures 1 and 2 and are given in

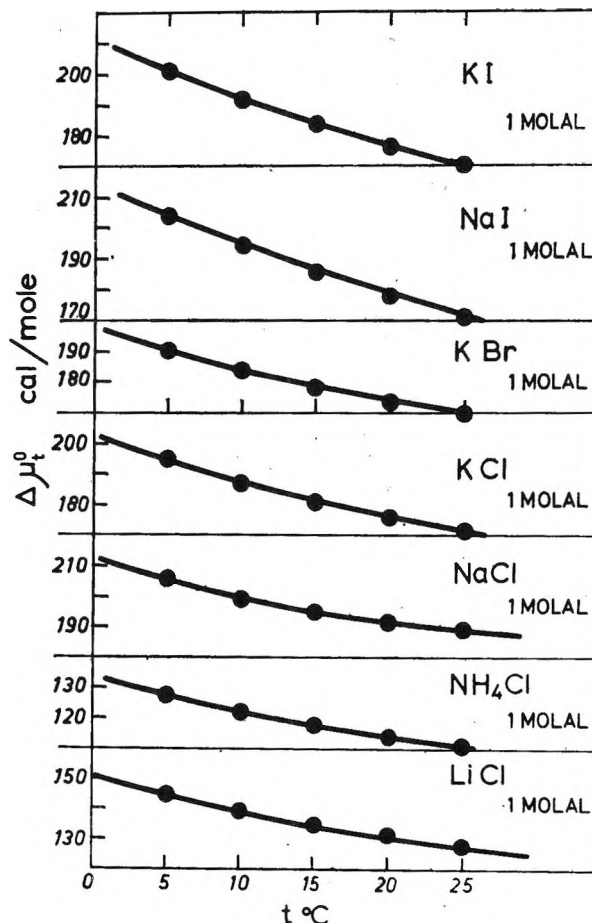


Figure 1. Values of $\Delta\mu_t^\circ$ (cal./mole) as a function of temperature for the transfer of argon from pure water into an aqueous solution of electrolytes.

Table II. The pertinent relations are (for more details see the Appendix of the preceding paper¹¹)

$$\Delta\mu_t^\circ = -RT \ln (\gamma/\gamma_0)$$

$$\Delta\bar{S}_t^\circ = R \frac{\partial}{\partial T} (T \ln (\gamma/\gamma_0)) - RT \frac{\partial}{\partial T} (\ln (\rho/\rho_0))$$

$$\Delta\bar{H}_t^\circ = \Delta\mu_t^\circ + T\Delta\bar{S}_t^\circ$$

(8) A. Ben-Naim and S. Baer, *Trans. Faraday Soc.*, **59**, 2735 (1963).

(9) A. Ben-Naim and S. Baer, *ibid.*, **60**, 1736 (1964). It should be noted that the accuracy of the solubility measurement is sufficient to draw a conclusion on the direction of change of the thermodynamic functions of solution of the gas, caused by the addition of the salt. It is, however, not suitable for calculating accurate values of the "salting-out" coefficients for the various salts. For this purpose an exact determination of the salt concentration is needed. The concentration of our solutions was slightly changed while outgassing (about 1%). Nevertheless, approximate values of the salting-out coefficients for some of the salts were found to be in agreement with those of Morrison and Johnstone.⁶

(10) J. H. Hildebrand and R. L. Scott, "The Solubility of Nonelectrolytes," 3rd Ed., Reinhold Publishing Corp., New York, N. Y.: 1950, p. 4.

(11) A. Ben-Naim, *J. Phys. Chem.*, **69**, 3245 (1965).

γ_0 and γ refer to a solution of argon in pure water and in an electrolytic solution, respectively. ρ_0 and ρ are the corresponding densities of the solvents. The thermodynamic functions $\Delta\mu_t^\circ$, $\Delta\bar{S}_t^\circ$, and $\Delta\bar{H}_t^\circ$ refer to the process of transferring argon from pure water into an electrolytic solution, the molar concentration of the gas being the same in the two liquids.

Discussion

A qualitative interpretation of the calculated thermodynamic functions is suggested based on the so-

Table II: Values of $\Delta\mu_t^\circ$ (cal./mole), $\Delta\bar{S}_t^\circ$ (cal./mole deg.), and $\Delta\bar{H}_t^\circ$ (cal./mole) for the Transfer of Argon from Pure Water into the Various Solutions of Electrolytes

	Temp., °C.				
	5	10	15	20	25
LiCl, 1 m					
$\Delta\mu_t^\circ$	144.4	139.4	134.8	131.2	127.5
$\Delta\bar{S}_t^\circ$	1.14	1.02	0.84	0.73	0.71
$\Delta\bar{H}_t^\circ$	461.3	428.1	376.7	345.1	339.1
NH ₄ Cl, 1 m					
$\Delta\mu_t^\circ$	127.0	121.6	117.0	113.3	110.6
$\Delta\bar{S}_t^\circ$	1.26	1.04	0.84	0.71	0.58
$\Delta\bar{H}_t^\circ$	477.4	415.9	358.9	321.3	283.4
NaCl, 1 m					
$\Delta\mu_t^\circ$	205.7	198.8	194.2	191.0	188.7
$\Delta\bar{S}_t^\circ$	1.64	1.23	0.89	0.60	0.20
$\Delta\bar{H}_t^\circ$	661.6	546.9	450.5	366.8	248.3
KCl, 1 m					
$\Delta\mu_t^\circ$	194.7	186.9	180.5	175.0	170.9
$\Delta\bar{S}_t^\circ$	1.76	1.53	1.24	0.99	0.77
$\Delta\bar{H}_t^\circ$	684.0	619.9	537.6	465.1	400.4
KBr, 1 m					
$\Delta\mu_t^\circ$	190.1	183.7	178.7	173.7	170.0
$\Delta\bar{S}_t^\circ$	1.42	1.23	1.07	0.94	0.83
$\Delta\bar{H}_t^\circ$	584.9	531.8	486.9	449.1	417.3
NaI, 1 m					
$\Delta\mu_t^\circ$	203.8	194.2	186.0	178.2	171.8
$\Delta\bar{S}_t^\circ$	2.10	1.88	1.74	1.50	1.31
$\Delta\bar{H}_t^\circ$	787.6	726.2	687.1	617.7	562.2
KI, 1 m					
$\Delta\mu_t^\circ$	201.1	191.5	183.7	176.4	170.0
$\Delta\bar{S}_t^\circ$	2.06	1.83	1.59	1.43	1.30
$\Delta\bar{H}_t^\circ$	773.8	709.4	641.6	595.4	557.4
KI, 2 m					
$\Delta\mu_t^\circ$	371.5	358.7	346.4	335.4	324.9
$\Delta\bar{S}_t^\circ$	2.84	2.62	2.48	2.28	2.16
$\Delta\bar{H}_t^\circ$	1161	1100	1061	1003	969
KI, 4 m					
$\Delta\mu_t^\circ$	674.1	656.3	638.0	619.7	601.4
$\Delta\bar{S}_t^\circ$	3.86	3.86	3.86	3.86	3.83
$\Delta\bar{H}_t^\circ$	1750	1750	1750	1750	1750

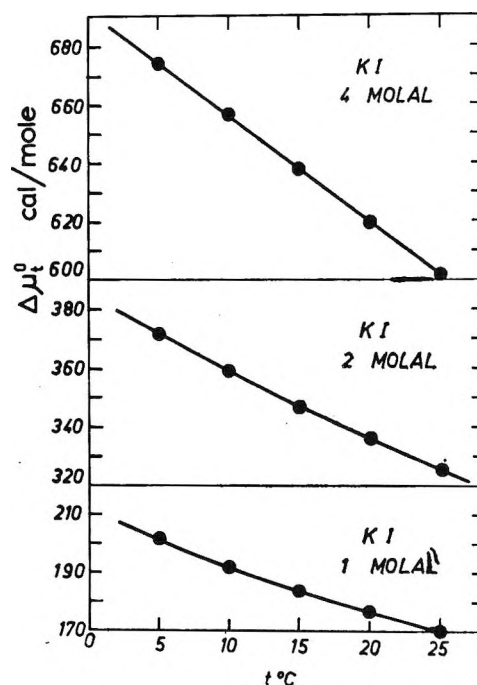


Figure 2. Values of $\Delta\mu_t^\circ$ (cal./mole) as a function of temperature for the transfer of argon from pure water into an aqueous solution of KI at different concentrations of the salt.

called "two-structure" model for liquid water. In this model, the standard entropy and enthalpy of solution of the gas can be written in the form^{8,11}

$$\Delta\bar{S}_s^\circ = \Delta S_s^* + \Delta S_s^r$$

$$\Delta\bar{H}_s^\circ = \Delta H_s^* + \Delta H_s^r$$

where ΔS_s^* and ΔH_s^* refer to a solution in which the chemical equilibrium between the various forms is "frozen in." ΔS_s^r and ΔH_s^r are the contribution to $\Delta\bar{S}_s^\circ$ and $\Delta\bar{H}_s^\circ$ arising from the shift in the equilibrium concentrations of the various forms caused by the addition of the gas. (For more details see preceding papers.^{8,11,12})

We define further

$$\Delta S_t^* = S_s^* (\text{in water} + \text{electrolyte}) - S_s^* (\text{in pure water})$$

$$\Delta S_t^r = \Delta S_s^r (\text{in water} + \text{electrolyte}) - \Delta S_s^r (\text{in pure water})$$

$$\Delta H_t^* = H_s^* (\text{in water} + \text{electrolyte}) - H_s^* (\text{in pure water})$$

$$\Delta H_t^r = \Delta H_s^r (\text{in water} + \text{electrolyte}) - \Delta H_s^r (\text{in pure water})$$

(12) A. Ben-Naim, *J. Chem. Phys.*, **42**, 1512 (1965).

For dilute solutions of electrolyte, we assume^{11,12} that the main change in the enthalpy of transfer of argon is caused by the change in the relaxation term ΔH_t^r , so that $\Delta H_t^* \approx 0$. This assumption allows the calculation of ΔS_t^* and ΔS_t^r which, although being only approximate values, have a significant meaning. Some values of ΔS_t^* and ΔS_t^r are given in Table III.

Table III: Approximate Values of ΔS_t^* (cal./mole deg.) and of ΔS_t^r (cal./mole deg.) for the Transfer of Argon from Pure Water into the Various Solutions of Electrolytes at 15°

	LiCl	NH ₄ Cl	NaCl	KCl	KBr	NaI	KI
ΔS_t^*	-0.47	-0.41	-0.67	-0.63	-0.62	-0.65	-0.64
ΔS_t^r	1.31	1.25	1.56	1.87	1.69	2.39	2.23

^a Concentration is 1 *m* for all the salts.

Table III shows that the sign of ΔS_t^* is always negative, while that of ΔS_t^r is always positive. The first result means that the static partial molar entropy of the gas decreases upon transferring the gas from pure water into an electrolytic solution, the molar concentration of the gas being the same in the two solutions. This is in accord with Eley's view¹ that the entropy of solution is primarily determined by the number of empty cavities. Thus, if we assume that the ions break the structure of water, *i.e.*, reduce the number of cavities, the static partial molar entropy should decrease.

On the other hand, the positive value of ΔS_t^r is qualitatively in agreement with the previously suggested explanation³ that the relaxation term depends on the size of the clusters of water molecules. It was found that for sufficiently large clusters, the so-called stabilizing effect³ becomes proportional to the number of molecules building the cluster.

As ions are supposed to break the structure of water, we conclude that the sign of ΔS_t^r is due to the decrease of the mean cluster size in electrolytic solutions. Thus, the signs of both ΔS_t^* and ΔS_t^r are qualitatively explainable by the decrease of the "degree of crystallinity"¹³ of water caused by the addition of electrolyte.

From Figure 1, one can see that the differences between values of $\Delta\mu_t^\circ$ for the different electrolytes are significant. This is not the case for $\Delta\bar{S}_t^\circ$ and $\Delta\bar{H}_t^\circ$. These quantities are calculated from the slopes of the experimental curves. The differences between the slopes of most of the curves are within the experimental error.

Conclusion

From the temperature dependence of the solubility of argon in water and in aqueous solutions of electrolytes the entropy and enthalpy changes which accompany the transfer of argon from pure water into the corresponding electrolytic solution were calculated.

The division of $\Delta\bar{S}_t^\circ$ and of $\Delta\bar{H}_t^\circ$ into two parts was found to be useful for the interpretation of the experimental results. A qualitative correlation with the "degree of crystallinity" of the solvents was found. The results obtained are in accord with the assumption that the ions break the structure of water.

Acknowledgment. We wish to express our thanks to Professor G. Stein and Dr. S. Baer for their continuous interest in the work and for helpful discussions.

(13) Note that changes of the "degree of crystallinity" of water should not be confused with the ordering effect induced by the ions in building up their hydration shell. In the model used here, the degree of crystallinity is qualitatively identified with the total concentration of the icelike form of water. The water molecules in the hydration shell are not identified with one of the two forms. Thus, the use of the "two-structure" formalism includes implicitly the assumption that the number of water molecules in the hydration shell of an ion does not change by the introduction of the gas molecules. All changes of the "degree of crystallinity" refer to the water molecules outside the hydration region. Thus, although ions may cause a net increase of "order" in the water, the "degree of crystallinity" of these solutions will be less than that of pure water.

Chemisorption of Oxygen on Zinc Oxide

by Rimantas Glemza and R. J. Kokes

Department of Chemistry, The Johns Hopkins University, Baltimore, Maryland 21218
(Received December 28, 1964)

Measurements of the adsorption of oxygen at low pressures ($<10 \mu$) on sintered zinc oxide pellets and the concomitant conductivity change have been made as a function of temperature, amount of oxygen, pretreatment, and doping. The results are consistent with the suggestion that the stable form of chemisorbed oxygen between -80 and 150° (type A) is different from the stable form of chemisorbed oxygen above 300° (type B). Details of the results suggest: (a) A is an intermediate in the formation of B; (b) A is formed by reaction with conduction electrons; (c) B is formed by reaction of A with ionized donors.

Introduction

There is considerable experimental evidence¹⁻⁵ that the strongly chemisorbed oxygen on zinc oxide at room temperature (type A) is different from the strongly chemisorbed oxygen on zinc oxide at about 400° (type B). Apparently, type A adsorption serves as an electron trap whereas type B adsorption does not.⁴ In a brief note the authors⁶ have noted that conductivity changes on adsorption at 353° suggest that first oxygen reacts with conduction electrons to form A; then, B is formed by the reaction of donors with A. Such a set of consecutive reactions is consistent with the observations that B has little effect on the conductivity, provided there is a substantial concentration of un-ionized donors.

Peers⁶ has criticized the above picture on two counts. First, he suggests that the transient conductivities observed are artifacts due to surface effects which would disappear if the conductivity was measured at high frequencies. However, recent high frequency measurements of conductivity⁷ show that this criticism is invalid. Peers also maintains that the donors are completely ionized at room temperature. This conclusion (apparently based on data for zinc oxide deliberately doped with metallic zinc^{8,9}) is correct for deliberately doped samples at 353° but is *not* valid at room temperature. From the equilibrium constant quoted in ref. 9, we find 25 to 50% ionization at room temperature for the donor concentrations cited in ref. 4. Finally, it should be noted that the samples used in ref. 4 and 5 were not doped with metallic zinc; hence, arguments based on data for such doped samples cannot be legiti-

mately applied to our samples because in the doped samples, the "interstitial zinc is certainly not the usual donor in zinc oxide."⁸ Thus, the objections⁶ to the tentative picture advanced in ref. 5 are by no means compelling.

It is imprudent to attempt to correlate the conductivity of sintered pellets *ab initio* to the properties of the bulk material, but the pellet conductivity does serve as a useful parameter in kinetic studies. In an attempt to elucidate the mechanism of chemisorption on zinc oxide, we have studied oxygen adsorption by pellets and the concomitant conductivity changes as a function of temperature, coverage, oxidation state, and doping. Throughout these studies, the conductivity was viewed as a kinetic parameter, and no attempt was made to relate quantitatively the conductivity (*by itself*) to bulk properties. This paper summarizes the results of these studies.

Experimental Section

ZnO-I was a sample of the SP 500 pigment manufactured by the New Jersey Zinc Co. ZnO-II was

- (1) S. R. Morrison, *Advan. Catalysis*, **7**, 213 (1955).
- (2) T. I. Barry and F. S. Stone, *Proc. Roy. Soc. (London)*, **A255**, 124 (1960).
- (3) T. I. Barry and K. Klier, *Discussions Faraday Soc.*, **31**, 219 (1961).
- (4) R. J. Kokes, *J. Phys. Chem.*, **66**, 99 (1962).
- (5) R. Glemza and R. J. Kokes, *ibid.*, **66**, 586 (1962).
- (6) A. M. Peers, *ibid.*, **67**, 2228 (1963).
- (7) H. Saltsburg and D. P. Snowden, *ibid.*, **68**, 2734 (1964).
- (8) D. G. Thomas, *J. Phys. Chem. Solids*, **3**, 229 (1957).
- (9) A. R. Hutson, *Phys. Rev.*, **108**, 222 (1957).

prepared by the decomposition of zinc oxalate in oxygen at 450° followed by calcination in air for 16 hr. The batch of ZnO-II was divided into two parts; ZnO-II P was slurried with 100 ml. of distilled water; ZnO-II Li was slurried with the same volume of LiNO₃ solution. Each slurry was evaporated to dryness and calcined in air at 500° for 16 hr. The composition of the solution was such that ZnO-II Li should contain 0.25 mole % Li. ZnO-II P served as a control.

Preparation of pellets was essentially the same as that reported earlier⁵ with one modification. The preliminary low temperature sintering of the pellet in the die was carried out at 420° for 5 hr. rather than 500° for 16 hr. Then, the pellet was sintered in air for 16 hr. at 800°. Electrical measurements were also described earlier. As before $\sigma = 1000/R$ where R is the resistance, determined potentiometrically, between the two inner leads.

Throughout these experiments, the pellet was connected to the vacuum system *via* a trap kept at -195°. Initially, the samples were evacuated at room temperature. Then the temperature was increased in stages to 510°, and the evacuation was continued for 16 hr. Typical parameters of the samples after this preliminary treatment are shown in Table I.

Table I: Catalyst Properties

Sample	Surface area, m. ² /g., B.E.T.	Total surface area, m. ²	Conductivity ^a after initial treatment	Con- ductivity ^a after hydrogen treatment
ZnO-I C	0.22	2.4	38	90
ZnO-I K	0.42	4.4	...	126
ZnO-I T	28	118
ZnO-I V	0.26	2.7	22	102
ZnO-II P	1.68	13.9	28	...
ZnO-II Li	0.84	7.0	0.036	...

^a All conductivities in this table were measured at 510° after evacuation for 16 hr.

In an attempt to erase any differences in the surface structure due to uncontrollable variables in the pretreatment, all ZnO-I samples were subjected to an alternate oxidation-reduction treatment. (This was a precautionary measure; even without this pretreatment the same qualitative results were obtained.) The procedure following the initial treatment was: (a) exposure to oxygen at 20 mm. at 470° for 1 hr. plus a 16-hr. evacuation at 510°; (b) exposure to hydrogen at 15 mm. for 5 min. at 420° plus a 1-hr. evacuation (repeated twice) followed by a 16-hr.

evacuation at 510°; (c) exposure to oxygen at 470° for 10 min. to 24 hr. at pressures from 10 to 60 mm. followed by a 16-hr. evacuation at 510°.

The effect of (a) and (b) on the conductivity of the sample can be seen by reference to Table I. By varying the severity of the oxidation treatment in step c, we can vary the value of σ by several orders of magnitude. We shall find it convenient in what follows to define the "oxidation state" of a given sample by the value of σ .

For the ZnO-II samples, only oxygen pretreatment at 470° was used. This modified procedure was adopted because it was feared that hydrogen pretreatment of the easily reducible¹⁰ lithium-doped samples would make comparisons of doped to undoped samples invalid.

Preliminary experiments at room temperature showed that stray laboratory light caused an irreversible increase in the conductivity. This effect was not reversible in the dark at room temperature, but the conductivity could be restored by heating to 500° in the dark. Such photoeffects are well established for zinc oxide.^{11,12} For all the runs reported herein, the catalyst was carefully shielded from light.

It was also found in these experiments that the conductivity did not respond instantaneously to temperature changes. For example, it was established that a temperature change from 510 to 360° required about 2 hr. for temperature equilibrium. In this particular case, about 95% of the total conductivity change occurred by the time temperature equilibrium was established; an additional 5% change occurred in the next 22 hr., and then the conductivity remained steady. The origins of this drift are obscure, but it was established experimentally that the conductivity and adsorption kinetics were unaffected by the changes in the catalyst that give rise to this slow drift.

Results

Chemisorption at Room Temperature. Figure 1, curve A, shows a plot of adsorption of oxygen *vs.* (for convenience) the square root of time. If we assume the effective area of an oxygen molecule is comparable to that of a nitrogen molecule, the amount ultimately adsorbed in Figure 1 corresponds to a coverage of 0.03% of the surface. Kinetic studies revealed that at a fixed coverage the rate of adsorption of this type A oxygen increased with increasing pressure and that for a fixed pressure the rate of adsorption

(10) P. M. G. Hart and F. Sebba, *Trans. Faraday Soc.*, 56, 557 (1960).

(11) D. B. Medved, *J. Phys. Chem. Solids*, 20, 255 (1961).

(12) G. Heiland, E. Mollwo, and F. Stöckmann, *Solid State Phys.*, 8, 191 (1959).

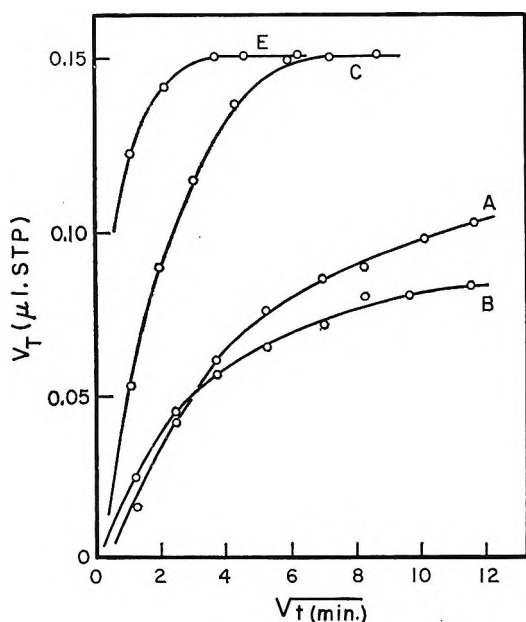


Figure 1. Adsorption kinetics at several temperatures: A, 25°; B, 150°; C, 320°; E, 465°. The size of the oxygen inlet was 0.150 μ l. for all runs.

increased by a factor of at least five when the coverage was changed from 0.200 to 0.050 μ l.

Simultaneous conductivity measurements for a run at room temperature in which 0.38 μ l. of oxygen was adsorbed resulted in a reduction in σ to about 1% of the initial value. Then, the sample with 0.38 μ l. of adsorbed oxygen was isolated from the pumps, heated to 450°, and cooled to room temperature; by this procedure, the conductivity was restored to its initial value. Presumably,⁵ this behavior means that A was converted into B at high temperature. The adsorption kinetics at room temperature on the surface containing 0.38 μ l. of B were identical with those for a clean surface. By way of contrast 0.38 μ l. of A would reduce the rate to less than 20% of the value for a clean surface; hence, this amount of B has no effect on the rate.

It was possible to obtain a calibration curve of σ/σ_0 vs. the volume A. (σ_0 is the conductivity of a pellet with no chemisorbed A.) Such a curve could be constructed either from a single kinetic run in which A rapidly changes with time or from the steady values of A after a series of stepwise additions of oxygen. Either procedure gave the same curve; hence, at room temperature, there is a one-to-one correspondence between σ/σ_0 and the amount of A.

The change in σ/σ_0 on oxygen adsorption could conceivably be due to the chemisorbed gas itself acting as an insulator between particles. Since chemisorbed

carbon dioxide has no effect at any temperature even when $\theta \approx 0.50$, we believe that such an effect is unlikely.

Effect of Temperature. The effect of temperature on the adsorption kinetics is shown in Figure 1. Qualitatively, these results are consistent with those reported earlier for unsintered samples⁴ insofar as an isobar with 10 min. or more allowed for equilibration would show a minimum in the neighborhood of 150°.

Until the adsorption is 85% complete, the kinetics follow the Elovitch equation, $dq/dt = ae^{-bq}$, when q is the amount adsorbed and a and b are constants. Similar behavior has been reported by several authors^{2,3,13} for this system. Values of a and b are quite sensitive to the oxidation state of the sample; a change of 25% in σ_0 changes a by an order of magnitude and b by a factor of three. Accordingly, it is of some interest to compare these values obtained by Barry and Stone.² At 384° and an initial pressure of 3.0 μ they found values of 5.1×10^{-6} cc./sec. for a and 8.6×10^3 cc.⁻¹ for b . Their samples had roughly 3 times the area of our samples. If we correct for this, our values of a and b correspond to $a = 4 \times 10^{-6}$ cc./sec. and $b = 5 \times 10^3$ cc.⁻¹. Thus, on the basis of the Elovitch parameters alone, this sample, which was adopted as our standard, was roughly comparable in oxidation state to that used by Barry and Stone.²

Figure 2 shows the σ/σ_0 kinetics corresponding to the adsorption kinetics shown in Figure 1. For a given run there is presumably a one-to-one relation between a decrease in σ/σ_0 and an increase in the amount of type A adsorption. Since, however, this relation between σ/σ_0 and A changes somewhat with temperature, only qualitative comparisons can be drawn between runs at widely different temperatures. At 25 and 150° (curves A and B) there is a monotonic decrease of σ/σ_0 with time. The run at room temperature was continued for 48 hr.; after 2 hr., adsorption was complete, and there was no further change in σ/σ_0 . For runs between 150 and 260° the adsorption was not complete within 5 hr. so that σ/σ_0 continued to decrease with time. At this point, the residual gas phase was removed by brief evacuation; thereafter, σ/σ_0 remained constant. At these coverages even prolonged evacuation at 25 to 260° failed to cause an increase in σ/σ_0 ; hence, A is essentially irreversibly adsorbed.

At 320° and above (curves C, D, and E), σ/σ_0 initially decreases as adsorption proceeds, but after adsorption is nearly complete (compare Figures 1

(13) T. I. Barry, *Actes Congr. Intern. Catalyse*, 2°, Paris, 1960, 2, 1449 (1961).

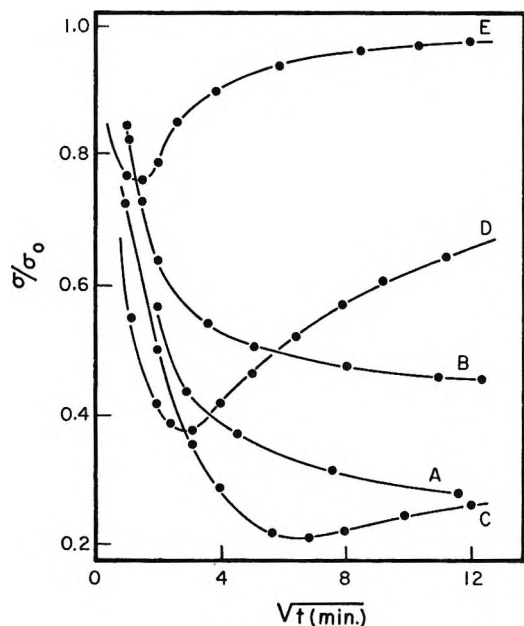
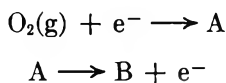


Figure 2. Conductivity kinetics at several temperatures: A, 25°; B, 150°; C, 320°; D, 385°; E, 465°. The size of the oxygen inlet was 0.150 μ l. for all runs.

and 2) σ/σ_0 starts to increase. Figure 3 shows σ/σ_0 kinetics for two runs at 360°. Curve I shows the normal kinetics for an adsorption experiment. Between points M and N, the sample was evacuated, and the lack of abrupt change in the curve suggests that, even at 360°, the adsorption is irreversible. Curve II shows an interrupted run. To obtain these data, the adsorption was terminated by evacuation at $\sqrt{t} = 2 \text{ min.}^{1/2}$. Shortly after the evacuation was started, a minimum occurred. Thus, the onset of the minimum coincides with unavailability of gas phase oxygen. Evacuation was terminated at point R, and no pressure buildup above 0.01 μ was observed.

Although these results do not identify the nature of the adsorbed species, they suggest the following two-step mechanism



The first step, which is accompanied by a decrease in the conductivity, cannot be reversed by evacuation below 380° and apparently (Figure 1) has an activation energy of the order of 3 kcal. between 150 and 460°. The second step, which restores the conductivity, is also irreversible and has such a high activation energy that it is unobservable below 260°. At 320° and above, adsorption still occurs *via* the formation of A. As long as the rate of formation of A from the gas phase is greater than the rate of reaction

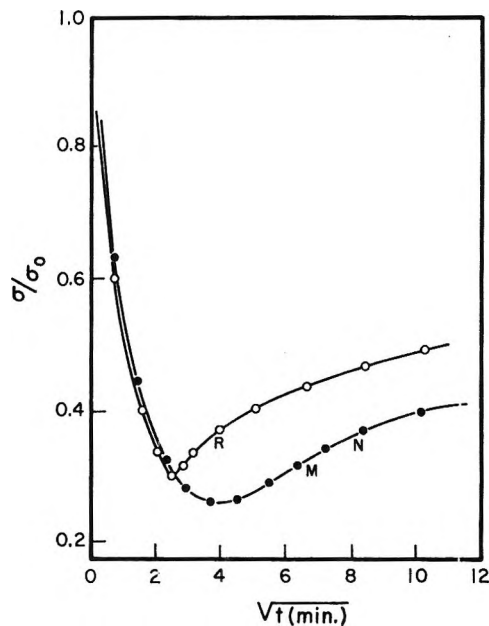


Figure 3. Conductivity kinetics at 360°: closed circles, adsorption of 0.150 μ l. of oxygen; open circles, adsorption of 0.150 μ l. of oxygen, evacuation at $\sqrt{t} = 2 \text{ min.}^{1/2}$.

to form B, the net amount of A increases and σ/σ_0 decreases. When, however, the pressure falls to a low enough value, either by depletion of gas phase oxygen or by evacuation, the rate of formation of A becomes less than its rate of reaction, the net amount of A decreases, and the conductivity increases.

The data in Table II, which summarizes the σ/σ_0 kinetics for a narrow range of temperatures, permits us to make the above picture more quantitative. In the second column, we have listed values of t_m , the time at which the minimum occurs. Adsorption occurs beyond this point, but when the pressure falls to less than 0.01 μ the adsorption effectively ceases; at approximately this time, t_a , the rate of conductivity recovery, $\dot{\sigma}/\sigma_0$, is a maximum. Values of this maximum rate are listed in Table II. Since t_m shifts to lower values at higher temperatures, it appears that the formation of B does indeed have a higher temperature coefficient than the rate of adsorption. A crude estimate of this temperature coefficient from an Arrhenius plot for the maximum rates tabulated in Table II yields an activation energy of 30–35 kcal. Such a high value suggests a bulk process rather than a surface process.

Effect of Inlet. The effect of the size of the inlet on the conductivity kinetics is summarized by the data in Figure 4 and Table III. The dependence of the adsorption kinetics on inlet is typical: the initial rate is greater for the greater inlet, but for the greater inlet a longer time is required for complete adsorption. This

Table II: Conductivity Kinetics^a

t , °C.	t_m , min.	t_a , min.	$(\dot{\sigma}/\sigma_0)_M \times 10^3$, min. ⁻¹
320	40	55	0.7
340	20	30	1.8
360	12	25	4.0
380	8	15	7.0

^a See text for definitions. Constant inlet is 0.150 μ l.

Table III: Conductivity Kinetics^a

Inlet, μ l.	t_m , min.	t_a , min.	$(1 - \sigma/\sigma_0)_M$	$\dot{B}_M \times 10^3$ μ l./min.
0.090	9	14	0.41	0.55
0.150	12	25	0.69	0.66
0.235	24	45	0.83	1.0
0.425	70	120	0.92	1.4

^a See text for definitions. Constant temperature 360°.

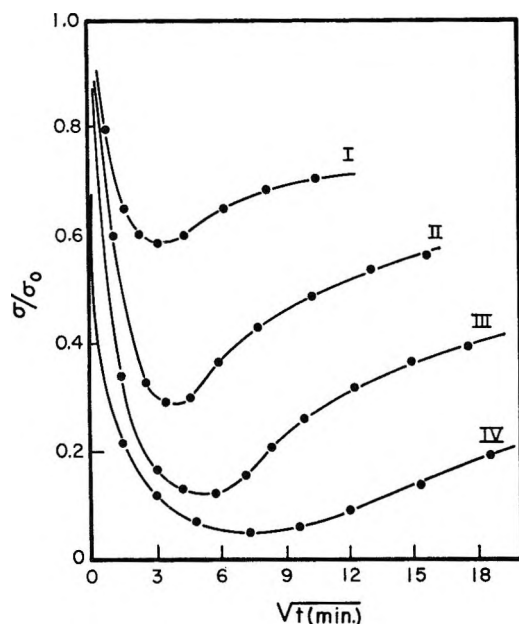


Figure 4. Conductivity kinetics at 360° for various oxygen inlets: I, 0.090 μ l.; II, 0.150 μ l.; III, 0.230 μ l.; IV, 0.420 μ l.

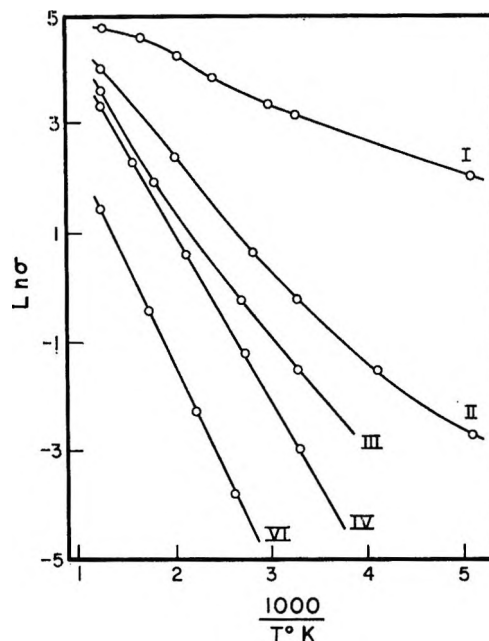


Figure 5. Dependence of conductivity on temperature for various oxidation states. (See Table IV.)

behavior is reflected in the conductivity kinetics. The initial fall in σ/σ_0 is more rapid for the larger inlet, but the minimum occurs later since adsorption continues for a longer time.

The effect of A on the rate of conversion to B can be estimated from the maximum rate of change of conductivity after the minimum. At this point $\dot{B} \cong -\dot{A}$ since adsorption is effectively complete. Since σ/σ_0 is nonlinear in A when A is large, direct comparison of the rates of conductivity change is misleading. In the last column of Table III, we have listed the corresponding \dot{B}_M estimated from σ/σ_0 vs. A curves at 25°. In the penultimate column we have listed values of $1 - (\sigma/\sigma_0)$ when the conductivity return rate is a maximum. Since $1 - (\sigma/\sigma_0)$ is a monotonic function that increases with A, the data show that \dot{B}_M increases as A increases.

Effect on Oxidation State. The effect of the oxidation state on the conductivity-temperature dependence is

shown in Figure 5. These measurements were made on a single sample pretreated in various ways. Sample I was reduced in hydrogen and received no oxidation; the other samples were subjected to exposures at 470° to oxygen at ~ 30 mm. for times ranging from 10 min. to 24 hr. The severity of the oxidation increased in the order II through VI. As shown in Figure 5, the conductivities for this single sample differ by a factor ranging from 20 at 500° to 10^4 at room temperature. These curves approximate crudely an Arrhenius plot; the corresponding activation energies range from ~ 0.25 e.v. for the strongly oxidized samples to ~ 0.05 e.v. for the unoxidized samples. No attempt is made to attach theoretical significance to these energy values, but it is worth noting that an increase in the experimentally determined activation energies often accompanies processes known to reduce the non-stoichiometry.¹⁴

To a very large degree, both the adsorption and conductivity kinetics for a given sample are uniquely determined by the value of σ . For example, for 90% of the range studied after the minimum, the conductivity kinetics can be characterized by an empirical equation of the form

$$\sigma/\sigma_0 = \frac{1}{\beta} \ln(t + \bar{t}) + I$$

where β , \bar{t} , and I are constants (see Figure 8). It was found that for a sample with $\sigma = 39$ (at 510°) the value of β at 360° was 9.4. This sample was then severely oxidized and reduced—a procedure varying σ by a factor of nearly 30. It was then reoxidized under controlled conditions to $\sigma = 38$ (at 510°), and the conductivity kinetics were redetermined. Values of I and \bar{t} were virtually unchanged, and the value of β was 8.6; the adsorption kinetics were likewise similar.

Even though we attach little theoretical significance to the magnitude of σ , it is reasonable to suppose that for a given degassed sample, σ serves as a gauge of the effective electron concentration and, *via* this, the donor concentration. On this basis Table IV and Figure 6 provide a summary of the adsorption and conductivity kinetics as a function of the native donor concentration in zinc oxide. The relation of σ/σ_0 to the amount of type A adsorption changes with the extent of oxidation; nevertheless, the qualitative trends are clear from Figure 6. With increasing oxidation the minimum is delayed, and the rate of conductivity recovery is reduced.

Kinetic parameters for these samples are listed in Table IV. The adsorption kinetics by themselves have no unusual features; hence, we can adequately characterize the adsorption rates by $t_{1/2}$, the time required for half the gas to adsorb. Since the adsorption involves reaction of electrons with oxygen, we expect

Table IV: Conductivity Kinetics^a

Sample	σ_0^b	$t_{1/2}^c$	$t_{1/2} \times \sigma_0^d$	t_m^c	$(\sigma/\sigma_0)_M \times 10^2$
I	89.0	~0.4	36	2	3.0
II	23.8	1.3	31	9	7.0
III	16.6	2.0	33	12	4.0
IV	12.1	4.5	52	24	2.2
V	5.5			55	0.2
VI	1.86	22	41	~300	~0.01

^c Temperature 360°; inlet 0.150 μ l. ^b Conductivity at 360°.

^d See text for definitions. The time is measured in minutes.

^e Average = 39 \pm 6.

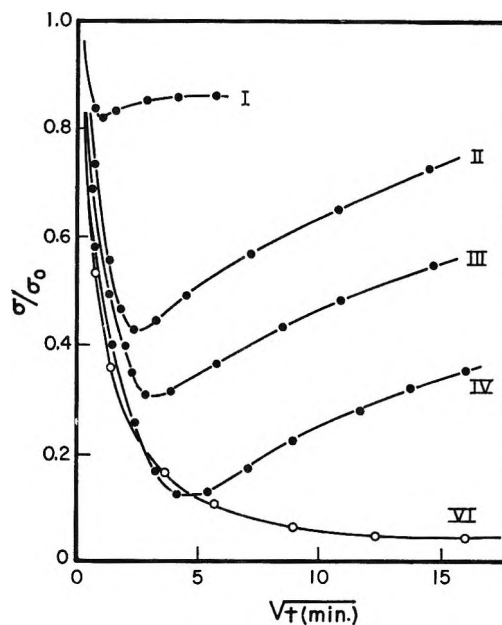


Figure 6. Conductivity kinetics at 360° for various oxidation states; 0.150- μ l. inlet. (See Table IV.)

the adsorption rate to decrease as the conductivity decreases. Comparison of columns 2 and 3 of Table IV shows this expected trend; in fact, the product of $t_{1/2}$ and the initial conductivity, σ_0 , is nearly constant (column 4) even for a 50-fold variation in σ_0 ; apparently, the rate of adsorption is roughly proportional to σ_0 . This is consistent with the supposition that σ_0 serves as a qualitative indicator of the electron concentration.

The change in oxidation state also affects the rate of conversion of A to B. This can be seen by reference to the maximum rates for conductivity recovery listed in the last column of Table IV. To see the effect of oxidation on \dot{B}_M , we must recognize that the effect of a given amount of A on σ/σ_0 is rather small for the reduced catalysts compared to that for the oxidized catalyst (see Figure 6). When this is taken into account, we find that (even including sample I) $\dot{B}(\max)$ decreases as the conductivity decreases. Thus, the rate of formation of B decreases as the concentration of donors and/or electrons decreases. Since the overall effect of the formation of B is to increase the electron concentration by an irreversible step, it appears that the rate of production of B increases with increasing concentration of ionized or un-ionized donors rather than electrons. The fact that t_m increases as the conductivity decreases requires, of course, that, for a given time, \dot{B} is more inhibited by a drop in conductivity than the adsorption rate.

(14) A. W. Smith and H. Wieder, *J. Phys. Chem.*, 63, 2013 (1959).

It should be noted that although \dot{B} for sample I was initially rapid, it rapidly fell to almost zero. This was unexpected and remains unexplained.

Effect of Doping. The kinetics of oxygen adsorption were studied for samples of ZnO-II both undoped and doped with lithia. For the undoped sample, the surface area was about five times that of the samples of ZnO-I already discussed; moreover, the mode of preparation was quite different. Nevertheless, the qualitative behavior was similar insofar as simultaneous measurements of oxygen adsorption and conductivity revealed a minimum in σ/σ_0 when adsorption was virtually complete.

Table V summarizes the results for doped and undoped catalysts. Doping with lithium showed the expected¹⁵ decrease in conductivity and surface area (Table I) compared to that of the undoped sample. As expected the presence of the acceptor, lithium, increases the half-time for adsorption, $t_{1/2}$, just as the oxidation does; moreover, the time required to reach the minimum is also considerably longer than for the undoped catalyst. The maximum rate of increase in conductivity, however, is greater for the lithium-doped catalyst. If we take into account the fact that σ/σ_0 is a more sensitive function of A for sample Li than for sample P, we find that the maximum \dot{B} is about twice as great for the lithium-doped catalyst.

Table V: Conductivity Kinetics for Doped Samples^a

Sample	σ_0	$t_{1/2}$	t_m	$(\dot{\sigma}/\sigma_0)_M \times 10^4$
ZnO-II P	1.5	2	9	0.5
ZnO-II Li	5.7×10^{-3}	33	90	0.7

^a Temperature 360°. Inlet 0.150 μ l.

The effect of lithium doping on the kinetics has a simple interpretation. The oxidation state studies suggest that A increases with increasing electron concentration and B increases with increasing donor concentration (ionized and/or un-ionized). Addition of lithium, an acceptor, decreases the electron concentration and hence decreases the rate of adsorption. On the other hand, the work of Hauffe and Gensch¹⁶ suggests that doping with lithium results in an increase in the concentration of ionized donors. Accordingly, the increase in \dot{B} for lithium-doped catalysts implies that it is the ionized donors that enhance the rate of formation of B; such would be expected if B is the result of reaction of A with ionized donors.

Quantitative Experiments. If the general form of the

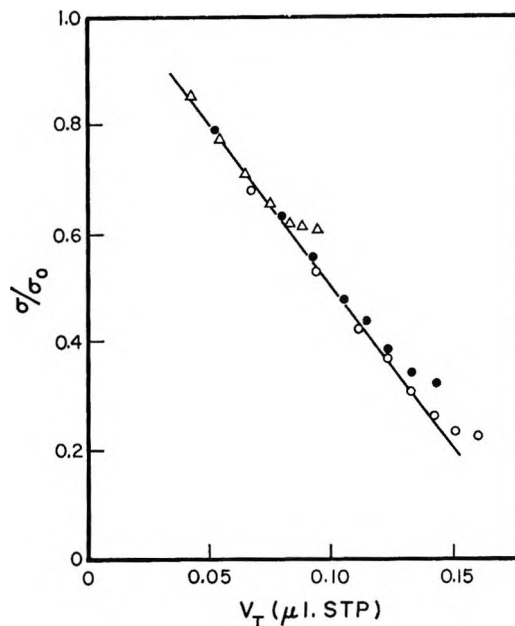


Figure 7. Calibration curve for σ/σ_0 vs. A at 343°: Δ , 0.086 μ l. of oxygen; \bullet , 0.150 μ l. of oxygen; \circ , 0.229 μ l. of oxygen.

assumed mechanism is correct insofar as the rate of adsorption to form A is rapid compared to the rate of formation of B, the initial decline in σ should be due solely to the formation of A. Thus, for a series of runs like those shown in Figure 4, a plot of σ/σ_0 vs. V_T , the total amount of oxygen adsorbed, should yield a single curve, independent of inlet, in the initial stage of adsorption. In the latter stages of adsorption, departures from this curve will be observed because V_T then includes B as well as A. Figure 7 shows a plot of σ/σ_0 vs. V_T in the early stages of adsorption for three different inlets at 340°. In the early stages of adsorption, the points do indeed define a single plot. Such a plot constitutes a calibration curve for σ/σ_0 vs. A at 343° and enables us to ascertain the concentration of A on the surface from the value of σ/σ_0 . Since B is equal to $V_T - A$, this means we can determine A and B as functions of time throughout the run.

At each of four temperatures, 321, 343, 365, and 385°, a series of runs with inlets of 0.09, 0.15, and 0.23 μ l. were carried out on a catalyst in a given oxidation state. At each temperature, a calibration curve for σ/σ_0 vs. A was constructed. (It was not linear at all temperatures.)

The kinetics of the conductivity return follow the

(15) E. Molinari and G. Parravano, *J. Am. Chem. Soc.*, **75**, 5233 (1953).

(16) K. Hauffe and C. Gensch, *Z. physik. Chem. (Leipzig)*, **195**, 116 (1950).

empirical equation cited earlier. The fit is excellent at 364, 365, and 385°, as may be seen by reference to Figure 8, but not quite as good at 321°. This equation, which has the form of an integrated Elovitch equation, is viewed as empirical; moreover, from the range in which it applies, it is clear that the usual interpretation should not be applied to the parameters β , \bar{t} , and I . Nevertheless, it serves as a concise way of summarizing the results, and for this reason, the constants for all these runs are listed in Table VI.

Table VI: Elovitch Constants

$V_T, \mu\text{l.}$	β	\bar{t}	I
$t = 343^\circ$			
0.086	29.4	8	0.488
0.150	12.3	9	-0.012
0.229	10.7	12	-0.275
$t = 364^\circ$			
0.090	20.7	0	0.460
0.154	10.4	-2	0.031
0.236	8.07	5	-0.322
$t = 385^\circ$			
0.083	26	-5	0.601
0.150	10.4	-2.5	0.174
0.232	7.5	-3.5	0.156

With the aid of the calibration curves of the type depicted in Figure 7, it was possible to translate the

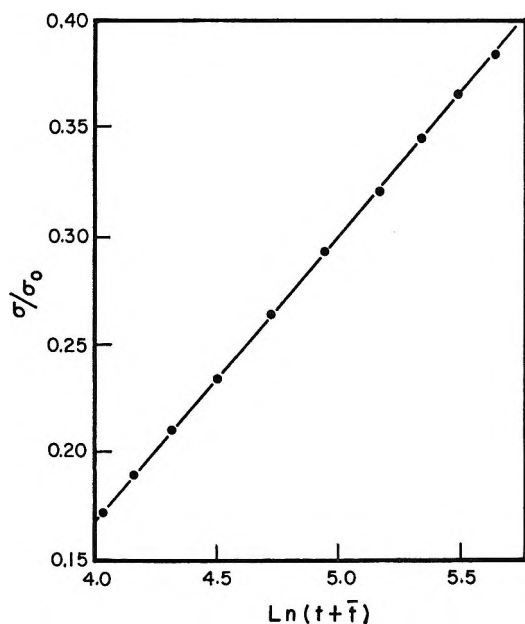
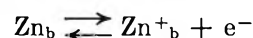


Figure 8. Elovitch plot of conductivity kinetics at 360°; inlet 0.236 $\mu\text{l.}$

σ/σ_0 kinetics into kinetics for the appearance of B. In view of the nearly linear relation between σ/σ_0 and A , this resulted in an Elovitch-type equation for B. It was not possible to find a kinetic expression of the form $\dot{B} = kA^m B^n$, that adequately described the kinetics.

Discussion

The electrical conductivity of zinc oxide presumably arises from an equilibrium of the type¹⁷



where Zn_b and Zn^{+b} indicate un-ionized and ionized donors produced by deviations from stoichiometry. It has been suggested⁵ that type A oxygen is an adsorbed O^- ion formed by direct interaction with free electrons, whereas type B oxygen is formed by transport of donors to the surface and their reaction with type A oxygen to form a surface complex of the type Zn^+O^-_s . Such a reaction with donors (whether they are ionized or un-ionized) has no bearing on the overall reaction) will yield the observed conductivity restoration provided the above equilibrium lies to the left.

It seems reasonable to assume that the slow kinetic step in the over-all reaction of donors with A is the transport of ionized donors to the surface. If this transport is effected by the boundary layer field rather than diffusion, we can write for J_s , the flux of donors

$$J_s = - \frac{|e|D}{kT} (\text{Zn}^{+s}) \left(\frac{dV}{dx} \right)_s$$

where $|e|$ is the electronic charge, V is the potential, and the other symbols have their usual significance. In this equation we have made use of the relation between mobility and the diffusion coefficient.¹⁸ Let us treat only the case when adsorption is complete; then, after a time t_0 a steady state is reached and $J_s = -\dot{A} = \dot{B}$. The net charge density at the surface is $|e|A$, and, if it is treated as a continuous distribution, we can write

$$\dot{A} = - \frac{|e|D}{kT} (\text{Zn}^{+s}) \frac{4\pi A |e|}{K}$$

or an integration

$$\ln \frac{A}{A(t_0)} = - \frac{\pi 4e^2 D}{KkT} \int_{t_0}^t (\text{Zn}^{+s}) dt$$

(17) We represent the ionized donors by Zn^+ for simplicity. The argument is essentially the same for any native donors, e.g., oxygen vacancies.⁸

(18) W. J. Moore, "Physical Chemistry," 3rd Ed., Prentice-Hall, Inc., Engelwood Cliffs, N. J., 1962, p. 340.

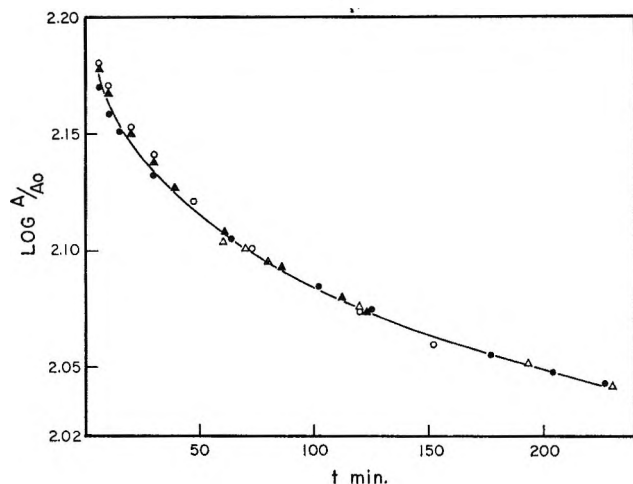


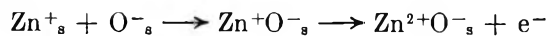
Figure 9. Plot $\log A/A_0$ vs. time at 360° : ●, interrupted run, initial inlet $0.511 \mu\text{l}$, $\log A_0 \equiv -3$; ▲, interrupted run, initial inlet $0.268 \mu\text{l}$, $\log A_0 \equiv -3.048$; ○, interrupted run, initial inlet $0.164 \mu\text{l}$, $\log A_0 \equiv -3.101$; △, regular run, initial inlet $0.239 \mu\text{l}$, $\log A_0 \equiv -2.886$.

If the steady state is rapidly achieved, the preceding equation will not be a sensitive function of t_0 for an experiment in which at $t = 0$ an amount of oxygen A is suddenly put on the surface. This ideal experiment can be approximated by interrupted experiments of the type shown in Figure 3; of course, in such experiments A_0 must be treated as an adjustable parameter. Figure 9 shows such plots for several such runs together with a plot for a regular run. The

values of the constants A_0 for each run were chosen so that they could be represented on the same plot. The surprising feature of this curve is that the integral in the last equation is apparently independent of the amount of adsorbed oxygen. This suggests that the surface concentration of ionized donors is determined largely by bulk processes.

The above treatment, admittedly speculative, can be applied to data for the runs summarized in Table VI. Once again, all data at the same temperature fall on the same curve suggesting that bulk processes determine the surface concentration of donors.

Although the above interpretation is consistent with the available data, it is by no means unique. For example, if donor ionization is complete at the higher temperatures, it is possible to explain the conductivity data by the alternative mechanism



It seems clear that the ionization of such a surface defect-pair (with over-all neutrality) would proceed more readily than further ionization of Zn^+_{s} . In either case, however, B is a surface complex formed by the migration of donors to the surface and reaction with A.

Acknowledgment. Acknowledgment is made to the donors of the Petroleum Research Fund, administered by the American Chemical Society, for support of this research.

Binary Mixtures of Θ -Solvents

by Mitsuo Abe and Hiroshi Fujita

Department of Polymer Science, Osaka University, Osaka, Japan (Received December 31, 1964)

A Θ -solvent may be obtained by mixing two pure solvents which bring a given polymer to Θ -conditions at different temperatures. The present study is concerned with the phase equilibrium and the viscosity behavior of *cis*-1,4-polybutadiene and polystyrene in such mixed Θ -solvents. These are methyl isoamyl ketone (MIAK) + methyl *n*-propyl ketone (MNPK) and diethyl ketone (DEK) + MNPK for polybutadiene, and cyclohexane (CH) + methylcyclohexane (MCH) and diethyl malonate (DEMT) + diethyl oxalate (DEOT) for polystyrene. These three pure Θ -solvents for polybutadiene are first reported in this study. When the volume fraction of one component is taken as the composition variable, the compositional variation of the Θ -temperature (determined from phase separation experiments) in the mixture DEK + MNPK is linear. The compositional variations of the Θ -temperature in the other mixtures can be described by concave or convex downward curves depending on the kind of mixture. If the data for T_c^{-1} vs. $M^{-1/2}$ (T_c is the consolute temperature and M is the molecular weight of the polymer) are interpreted in terms of Flory's theory for two-component systems, it is found that the values of the energy of mixing parameter κ_1 for polybutadiene in DEK, MIAK, MNPK, and any binary mixture of them are nearly identical. On the other hand, the κ_1 for polystyrene in the system DEMT + DEOT is about one-half that for the same polymer in the system CH + MCH. Viscosity measurements show that for polybutadiene the values of K_Θ (defined by the relation $[\eta]_\Theta = K_\Theta M^{1/2}$) in the three pure Θ -solvents and binary mixtures of them follow a linear correlation line of slightly negative slope when plotted against Θ . However, for polystyrene those in the mixtures CH + MCH and DEMT + DEOT fall on different correlation lines, one having a small negative slope and the other with essentially zero slope. From these results it is inferred that in a series of Θ -solvents, pure or mixed, which have similar energetic interactions with the given polymer, the factor K_Θ would change with Θ in a regular fashion. Correlation lines would have negative, zero, or positive slopes depending on the value of the parameter κ_1 .

Introduction

The most commonly used method for obtaining a Θ -solvent is to mix a good solvent with an appropriate amount of a nonsolvent. In this paper, we present another way of obtaining mixed Θ -solvents and describe the phase equilibrium and viscosity behavior of *cis*-1,4-polybutadiene and polystyrene in such solvents. Our method consists of mixing two pure solvents which resemble one another both chemically and physically and which bring a given polymer to the Θ -state at widely different temperatures. It might be expected that for a given polymer a binary mixture so prepared would show a series of Θ -temperatures between those

of the component solvents when the composition is varied over the entire range. Also, for the polymer in such a mixed solvent, the theory for two-component systems may be applied with fair confidence.

Experimental Section

Materials. A Phillips sample of *cis*-1,4-polybutadiene was separated into a number of fractions by using a successive precipitation and solution method. Three that had relevant molecular weights were chosen for the present study. The calculation of the viscosity-average molecular weight of each fraction was made by using a relation deduced by Danusso, *et al.*,¹ for

benzene solution. The microstructure of the chosen fractions, determined by an infrared analysis according to Ohtsuka,² was as follows: 1,4-*cis*, 94.6%, 1,4-*trans*, 1.4%, and 1,2-vinyl, 4.1%. Each sample was freeze-dried from a benzene solution. One per cent (w./w.) phenyl- β -naphthylamine (PBNA) was added, and the sample was stored in a freezer at about -25° until used.

For polystyrene three fractions were selected from our sample stock. Their average molecular weights were estimated from the limiting viscosity numbers in toluene, using a relation derived by Kawahara.³ Each sample was also freeze-dried from a benzene solution, but no antioxidant was added.

All the solvents which were used carefully purified in accordance with the method typical of each. PBNA, 0.1% (w./v.), was added to the polybutadiene solvents.

Component Pure Θ -Solvents. The only pure Θ -solvent which had been known for *cis*-1,4-polybutadiene was isobutyl acetate found by Danusso, *et al.*¹ We therefore began this study by seeking two or more pure Θ -solvents for this polymer. After extensive solubility tests, we eventually found that three aliphatic ketones—diethyl ketone (DEK), methyl isoamyl ketone (MIAK), and methyl *n*-propyl ketone (MNPK)—were capable of being Θ -solvents for the polymer at or near room temperature. Here DEK and MNPK are isomers. We then proceeded to determine the Θ -temperatures of these three ketones by the application of the familiar phase separation method due originally to Shultz and Flory.⁴ The results obtained were 10.3° for DEK, 12.6° for MIAK, and 59.7° for MNPK.

As pure Θ -solvents for polystyrene the following four organic liquids were chosen from the literature: cyclohexane (CH),⁵ methylcyclohexane (MCH),⁵ diethyl malonate (DEMT),^{6,7} and diethyl oxalate (DEOT).⁶ The Θ -temperatures of these solvents were redetermined in our phase separation tubes and found to be 34.5° for CH, 70.5° for MCH, 34.2° for DEMT, and 55.8° for DEOT. Some of these values differ slightly from the reported values.

Binary Mixtures of Θ -Solvents. For polybutadiene binary mixtures of DEK and MNPK and of MIAK and MNPK were examined over the entire range of composition. Since, as noted above, DEK and MNPK are isomers, their binary mixtures are expected to behave thermodynamically like one-component systems. For polystyrene, mixtures of CH and MCH and of DEMT of DEOT were studied as a function of composition. The Θ -temperature of a given polymer in each of these mixtures was determined as in the component-pure Θ -solvents, *i.e.*, by Flory's phase separation method.

Viscometry. Limiting viscosity numbers of the chosen fractions of polybutadiene and polystyrene in some of these pure and mixed Θ -solvents were measured, using a capillary viscometer of the Ubbelohde type. The upper bulb of the viscometer was *ca.* 2 ml., and the flow time for benzene at 30° was 160.1 sec.

Results and Discussion

Variation of the Θ -Temperature with Composition. Figure 1 shows plots of T_c^{-1} vs. $M_v^{-1/2}$ for *cis*-1,4-polybutadiene in MNPK, MIAK, DEK, four mixtures of MNPK and MIAK, and two mixtures of MNPK and DEK. Here T_c is the consolute temperature (degrees Kelvin) for a given polymer fraction in a given solvent, and M_v is the viscosity-average molecular weight of that fraction. The plots in each solvent follow a straight line, in agreement with the theory of Flory.⁵ It can be observed that the solid lines drawn in the figure are parallel to each other. It is legitimate to assume that this behavior is valid also for the three mixtures of MNPK and MIAK in which T_c was de-

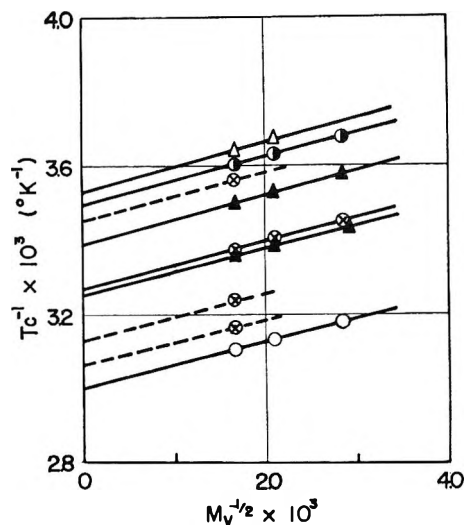


Figure 1. Plots of T_c^{-1} vs. $M_v^{-1/2}$ for *cis*-1,4-polybutadiene in various solvents; T_c is the consolute temperature in degrees Kelvin: O, MNPK; ●, MIAK; ▲, DEK, ⊗, MNPK + MIAK; ▲, MNPK + DEK.

- (1) F. Danusso, G. Moraglio, and G. Gianotti, *J. Polymer Sci.*, **51**, 475 (1961).
- (2) S. Ohtsuka, Y. Tanaka, T. Yoshimoto, and M. Fujimori, *Kobunshi*, **13**, 252 (1964).
- (3) K. Kawahara, *Makromol. Chem.*, **73**, 1 (1964).
- (4) A. R. Shultz and P. J. Flory, *J. Am. Chem. Soc.*, **74**, 4760 (1952).
- (5) P. J. Flory, "Principles of Polymer Chemistry," Cornell University Press, Ithaca, N. Y., 1953.
- (6) G. V. Schulz and H. Baumann, *Makromol. Chem.*, **60**, 120 (1963).
- (7) T. A. Orofino and J. W. Mickey, Jr., *J. Chem. Phys.*, **38**, 2512 (1963).

terminated for only one polymer fraction and then extrapolate to infinite molecular weight as indicated by the dashed lines in the figure. If we apply Flory's theory of phase equilibrium for a homogeneous polymer in a single solvent, the parallel feature of the plots for T_c^{-1} vs. $M_v^{-1/2}$ implies that the values of $\Psi_1\theta$ for *cis*-1,4-polybutadiene in these pure and mixed solvents are substantially equal to each other. Here Ψ_1 is the entropy of mixing parameter for a given polymer-solvent pair, and θ is its Θ -temperature in degrees Kelvin. The energy of mixing parameter, κ_1 , for the given polymer-solvent pair at a given absolute temperature T can be calculated from the expression $\kappa_1 = \theta\Psi_1/T$.⁵ Thus, the data of Figure 1 indicate that for *cis*-1,4-polybutadiene, all the tabulated pure and mixed solvents have nearly the same Ψ_1 -values when compared at the same temperature. However, this statement is based on the assumption that each mixed solvent may be regarded as a one-component system.

Figure 2 shows plots for T_c^{-1} vs. $M_v^{-1/2}$ on polystyrene in CH, DMT, DEOT, one mixture of CH and MCH, and one mixture of DMT and DEOT. Again Flory's expectation is well obeyed, but here the slope of the straight line is solvent dependent. The slopes of the system CH-MCH and the system DMT-DEOT differ by a factor of about two although within each system the slope is independent of composition. Applying Flory's theory, this result implies that in either of the two systems the parameter κ_1 of the solvent (pure or mixed) for polystyrene is independent of composition, but its value for the system DMT-DEOT is nearly one-half that for the system CH-MCH when compared at the same temperature. Recently, from precise second virial coefficient-temperature data in the region encompassing the Θ -temperature, Orofino and Mickey⁷ have shown that the values of the parameter κ_1 for polystyrene in DMT, CH, and 1-chloro-*n*-undecane, which all have nearly the same Θ -temperatures for this polymer, are 0.17, 0.38, and 0.19, respectively. This result indicates that, when compared at the same temperature, the values of κ_1 of DMT and 1-chloro-*n*-undecane for polystyrene are nearly equal and about one-half that of CH for the same polymer. Our conclusion from phase separation experiments is consistent with this deduction from a different type of measurements.

Besides their theoretical interpretation, the data of Figures 3 and 4 demonstrate that now we can bring either polystyrene and high *cis*-polybutadiene to the Θ -state at any desired temperature in the range 35–70° for polystyrene and 10–60° for polybutadiene. The linear or nearly linear dependence of θ on the volume fraction suggests that, in contrast to a conventional

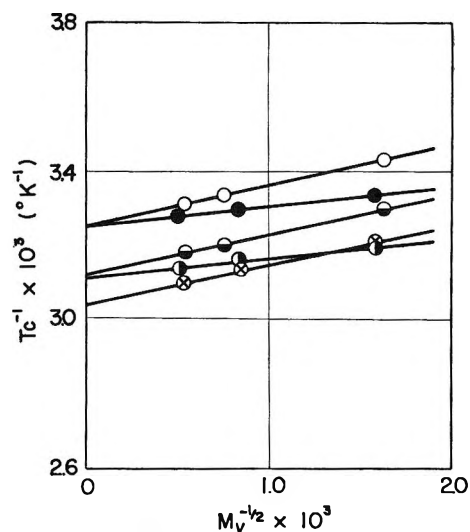


Figure 2. Plots of T_c^{-1} vs. $M_v^{-1/2}$ for polystyrene in various solvents: ●, CH; ○, DMT; ⊗, DEOT; ⊙, CH + MCH; ◐, DMT + DEOT.

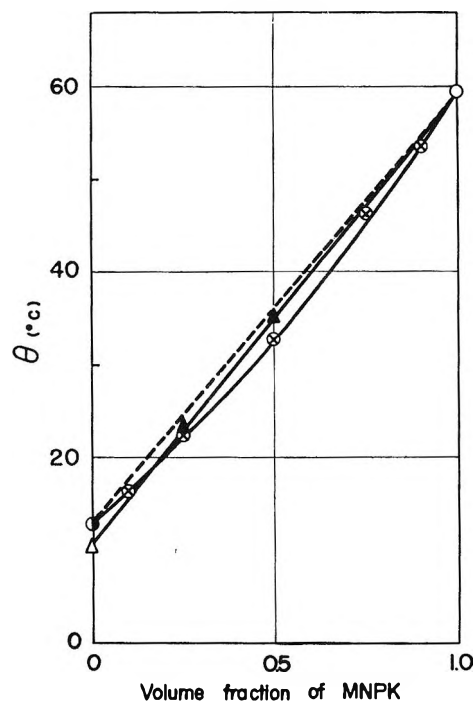


Figure 3. Variation of Θ -temperature for *cis*-1,4-polybutadiene with solvent composition: ○, MNPK; ●, MIAK; Δ, DEK; ⊗, MNPK + MIAK; ▲, MNPK + DEK.

mixed Θ -solvent composed of a good solvent and a nonsolvent, the Θ -temperature of this novel type of mixed solvent is relatively insensitive to a slight variation of the relative amounts of its components, and thus it is easily handled experimentally.

Viscosity Data. By way of an example, Figure 5

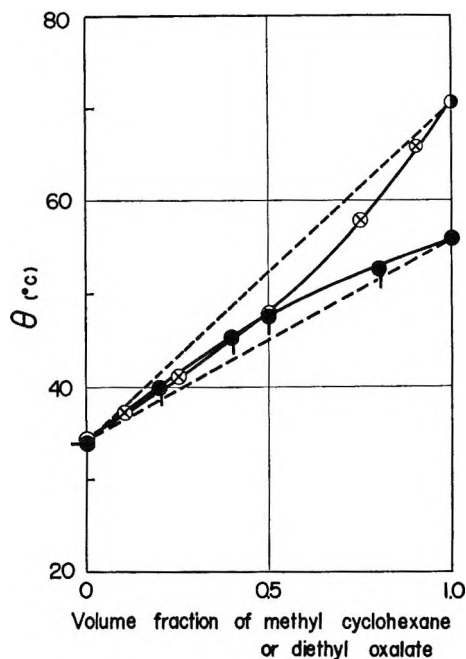


Figure 4. Variation of θ -temperature for polystyrene with solvent composition: O, CH; \square , MCH; \diamond , CH + MCH; \bullet , DENT; \circ , DEOT; \circ , DENT + DEOT.

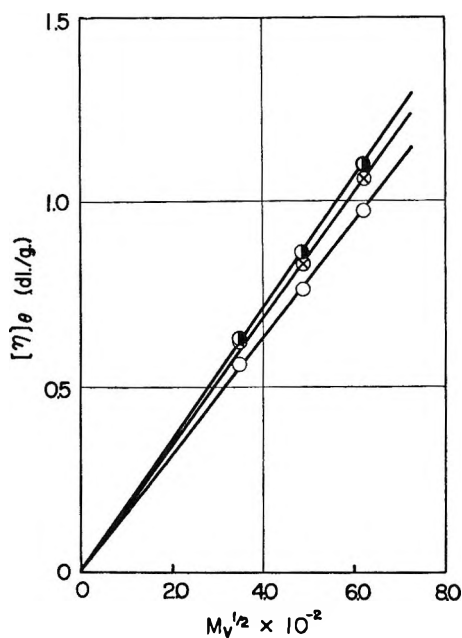


Figure 5. Linear relation between $[\eta]_{\theta}$ and $M_v^{1/2}$ for *cis*-1,4-polybutadiene in three θ -solvents: O, MNPK at 59.7°; \square , MIAK at 12.6°; \diamond , MNPK + MIAK (50-50 by volume) at 32.7°.

shows plots of $[\eta]_{\theta}$ vs. $M_v^{1/2}$ for *cis*-1,4-polybutadiene in MNPK, MIAK, and 50-50 mixture (by volume) at the respective θ -temperatures. Here $[\eta]_{\theta}$ is the usual notation for the limiting viscosity number in deciliters

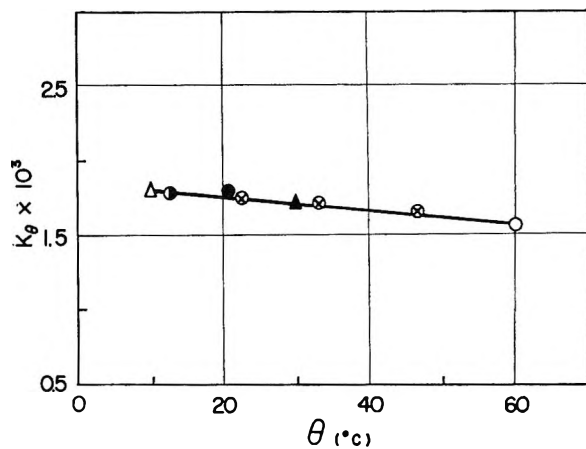


Figure 6. Temperature dependence of K_{θ} for *cis*-1,4-polybutadiene: O, MNPK; \square , MIAK; \triangle , DEK; \diamond , MNPK + MIAK; \blacktriangle , MNPK + DEK; \bullet , isobutyl acetate (Danusso, *et al.*).

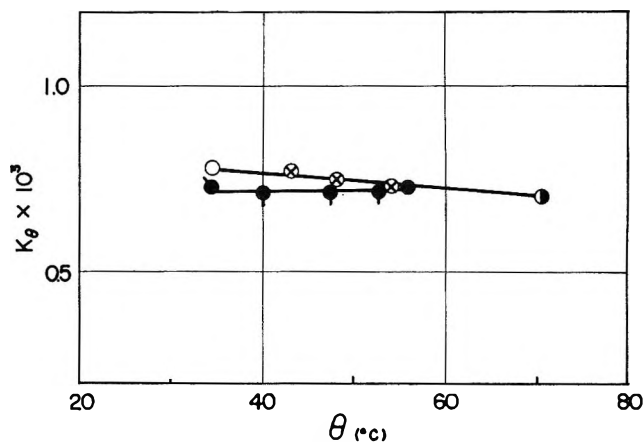


Figure 7. Temperature dependence of K_{θ} for polystyrene: O, CH; \square , MCH; \diamond , CH + MCH; \bullet , DENT; \circ , DEOT; \circ , DENT + DEOT.

per gram under θ -conditions. It is observed that each plot obeys the relation $[\eta]_{\theta} = K_{\theta}M_v^{1/2}$, in agreement with the current theory of dilute polymer solutions.⁵ Similar results were obtained in all other cases examined viscometrically. The values of K_{θ} deduced from these results are summarized in Table I. Figure 6 shows plots of K_{θ} against θ for *cis*-1,4-polybutadiene, and Figure 7 shows the corresponding plots for polystyrene.

It can be seen that the plots for polybutadiene fall well on a single straight line having a small negative slope. From this behavior we may be tempted to conclude that, at least in the range of θ indicated, the factor K_{θ} for *cis*-1,4-polybutadiene depends essentially on temperature only. This conclusion appears to be

Table I: Values of K_{Θ} in Various Θ -Solvents

Θ -Solvent	Θ , °C.	$K_{\Theta} \times 10^4$
<i>cis</i> -1,4-Polybutadiene		
DEK	10.3	1.81
MIAK	12.6	1.78
MIAK + MNPK (3/1) ^a	22.3	1.75
DEK + MNPK (3/2)	30.0	1.74
MIAK + MNPK (1/1)	32.7	1.71
MIAK + MNPK (1/3)	46.2	1.67
MNPK	59.7	1.57
Polystyrene		
CH	34.5	0.779
CH + MCH (2/1) ^a	43.0	0.776
CH + MCH (1/1)	48.0	0.748
CH + MCH (1/2)	54.0	0.730
MCH	70.5	0.696
DEMT	34.2	0.718
DEMT + DEOT (4/1) ^a	40.0	0.712
DEMT + DEOT (1/1)	47.4	0.715
DEMT + DEOT (1/4)	52.6	0.714
DEOT	55.8	0.730

^a Composition in volume ratio.

strengthened by the fact that the K_{Θ} value obtained by Danusso, *et al.*,¹ with another Θ -solvent, isobutyl acetate, comes close to the straight line relationship for the K_{Θ} values obtained with ketones. However, it can be realized from Figure 7 that this correlation of K_{Θ} values occurs since, as noted above on the basis of the Flory theory of phase equilibrium, the values of κ_1 for pairs of *cis*-1,4-polybutadiene and MIAK, MNPK, DEK, and any binary mixture of them are almost the same. In fact, Figure 7 indicates that the

values of K_{Θ} for polystyrene in the systems CH-MCH and DEMT-DEOT follow different correlation lines, corresponding to the difference in κ_1 between the two systems. The correlation line for the system CH-MCH has a negative slope, while that for the system DEMT-DEOT has virtually zero slope. Very recently, Orofino and Ciferri⁸ found an increase of K_{Θ} with Θ when they studied polystyrene in three pure Θ -solvents 1-chloro-*n*-decane ($\Theta = 6.6^\circ$), 1-chloro-*n*-undecane ($\Theta = 32.8^\circ$), and 1-chloro-*n*-dodecane ($\Theta = 58.6^\circ$). Since these solvents are chemically similar, it was not unexpected that K_{Θ} showed a regular correlation with Θ . However, it must be emphasized that this is the first example for polystyrene which exhibited a correlation line of positive slope. Finally, we wish to remark that a recent report of Ueda, *et al.*,⁹ on polyvinyl acetate showed different temperature coefficients (negative) for K_{Θ} in Θ -solvents of alcohol and ketone types. Summarizing, it may be concluded that in a series of Θ -solvents, either pure or mixed, which have similar energetic interactions with a given polymer, the factor K_{Θ} will change with Θ in a more or less regular fashion and that the slope of the correlation line will be positive, zero, or negative depending on the value of the parameter κ_1 .

Acknowledgments. The assistance of Miss T. Yamashita is gratefully acknowledged. Part of this study was supported by a grant from the Japan Synthetic Rubber Co.

(8) T. A. Orofino and A. Ciferri, *J. Phys. Chem.*, **68**, 3136 (1964).

(9) M. Ueda, K. Kajitani, and S. Matsumoto, paper read at the 13th Polymer Symposium held in Tokyo, Nov. 1964.

Investigation of the Metallic Phases in Reduced, Impregnated Nickel and Nickel-Copper Silica-Alumina Catalysts

by Harold E. Swift, Frank E. Lutinski, and William L. Kehl

Gulf Research & Development Company, Pittsburgh, Pennsylvania (Received January 18, 1965)

An investigation of the reduced copper-nickel silica-alumina system has revealed the presence of a copper-nickel alloy phase which was identified by X-ray diffraction. In addition to the copper-nickel phase, metallic nickel and copper may be present on the catalyst surface. To make the system more complex there is also a nickel phase that is not removed by carbon monoxide. Such a phase was found on nickel silica-alumina catalysts. Hydrogen chemisorption, carbon monoxide extraction, cyclohexane dehydrogenation, and *n*-octane hydrocracking studies indicate that the properties of the nickel silica-alumina catalyst system are greatly modified by the addition of copper to the system.

Introduction

The physicochemical and catalytic properties of nickel-copper alloys have been discussed very extensively in the literature. Of particular interest in many of these studies has been the relationship between the d-band character of the alloys and their catalytic activity towards certain chemical reactions.¹⁻¹⁶ Most of the work has been done with unsupported alloys, and the subject of supported alloys, especially in impregnated catalysts, has received little attention. Studies using nickel-copper alloys supported on kieselguhr³ and alumina^{17,18} have been reported. These supported nickel-copper alloys were prepared by the precipitation of mixed carbonates from an aqueous solution containing nickel and copper nitrates onto the support, followed by drying and reduction with hydrogen.

Alloys of Pt-Rh, Pd-Rh, Pt-Ru, and Os-Pt on impregnated alumina catalysts have also been reported.¹⁹ However, the existence and nature of the alloys were definitely not established, and Bond states²⁰ that supported alloys are naturally suspect.

The work presented in this paper is concerned primarily with the examination of the metallic phase or phases formed on reduction of impregnated nickel and nickel-copper silica-alumina catalysts. It has been found that a nickel-copper alloy phase is formed when impregnated nickel-copper silica-alumina catalysts are reduced with hydrogen.

Experimental Section

The catalysts used in this study were prepared by impregnating various supports with an aqueous solu-

- (1) G. Reinacker and G. Vormum, *Z. anorg. allgem. Chem.*, **283**, 287 (1956).
- (2) G. Reinacker and E. A. Bommer, *ibid.*, **242**, 302 (1939).
- (3) G. Reinacker and R. Burmann, *J. prakt. Chem.*, **158**, 95 (1941).
- (4) G. C. Bond and R. S. Mann, *J. Chem. Soc.*, 3566 (1959).
- (5) G. C. Reinacker and S. Unger, *Z. anorg. allgem. Chem.*, **274**, 47 (1953).
- (6) W. K. Hall and P. H. Emmett, *J. Phys. Chem.*, **62**, 816 (1958); **63**, 1102 (1959).
- (7) R. J. Best and W. W. Russell, *J. Am. Chem. Soc.*, **76**, 838 (1954).
- (8) D. A. Dowden, *J. Chem. Soc.*, 242 (1950).
- (9) P. H. Emmett and N. Skau, *J. Am. Chem. Soc.*, **65**, 1029 (1943).
- (10) C. L. McCabe and G. D. Halsey, *ibid.*, **74**, 2732 (1952).
- (11) O. Beeck, *Record Chem. Progr. (Kresge-Hooker Sci. Lib.)*, **8**, 105 (1957).
- (12) O. Beeck and A. W. Ritchie, *Discussions Faraday Soc.*, **8**, 159 (1950).
- (13) P. B. Shallcross and W. W. Russell, *J. Am. Chem. Soc.*, **81**, 4132 (1959).
- (14) W. K. Hall, F. E. Lutinski, and J. A. Hassell, *Trans. Faraday Soc.*, **60**, 1823 (1964).
- (15) W. K. Hall, F. J. Cheselske, and F. E. Lutinski, *Actes Congr. Intern. Catalyse, 2e, Paris, 1960*, **2**, 2199 (1960).
- (16) N. A. Scholtus and W. K. Hall, *Trans. Faraday Soc.*, **59**, 969 (1963).
- (17) P. Fuderer-Leutic and I. Brihta, *Croat. Chem. Acta*, **31**, 75 (1959).
- (18) P. W. Reynolds, *J. Chem. Soc.*, 242 (1950).
- (19) T. J. Gray, N. G. Masse, and H. G. Oswin, *Actes Congr. Intern. Catalyse, 2e, Paris, 1960*, **2**, 1697 (1960).

tion of nickel and/or copper salts to the point of incipient wetness. The catalysts were then oven dried at 115° for 18 hr. and calcined at 500° for 24 hr. De-ionized water was used in all of the impregnations. The salts used were Fisher Certified nickel nitrate hexahydrate and cupric nitrate trihydrate. The silica-alumina support that was used in most of the preparations was American Cyanamid Triple A (nominally 25% Al₂O₃-75% SiO₂) which had a surface area of 342 m.²/g. after being calcined at 540°. The other silica-alumina supports were prepared at this laboratory from silica-alumina co-gels. The 80% Al₂O₃-20% SiO₂ support had a surface area of 322 m.²/g. while the 50% Al₂O₃-50% SiO₂ had a surface area of 399 m.²/g. These surface areas were measured after the samples were calcined at 480°. Davison Grade 70 silica gel had a reported surface area of 340 m.²/g. η -Alumina obtained from the Davison Co. had a surface area of 214 m.²/g. after calcination at 540°. The catalysts studied in the present work were: 6 wt. % nickel on silica, alumina, and silica-alumina; 6 wt. % copper on silica-alumina; 6 wt. % nickel-0.5 wt. % copper (10:1 mole ratio) on silica-alumina; 6 wt. % nickel-3.2 wt. % copper (2:1 mole ratio) on silica-alumina; 6 wt. % nickel-6.5 wt. % copper (1:1 mole ratio) on silica, alumina, and silica-alumina; and 6 wt. % nickel-13.0 wt. % copper (1:2 mole ratio) on silica-alumina.

The surface areas of the calcined, supported catalysts were determined by the B.E.T. method, using a nitrogen adsorbate.

The method of preparation and notes on purity of the unsupported nickel-copper alloys are described in detail elsewhere.^{6,21} The compositions of the alloys were 72.4 mole % nickel and 53.8 mole % nickel with surface areas of 1.62 and 0.89 m.²/g., respectively. Nickel powder (analyzed to be 100% nickel) was prepared by the reduction of nickelous hydroxide and had a surface area of 1.30 m.²/g. The surface areas of the alloys were obtained using a krypton adsorbate after the samples had been reduced with hydrogen for 4 hr. at 500°.

The X-ray diffraction patterns were obtained with a Norelco diffractometer, using nickel-filtered Cu K α radiation. A gas proportional counter detector was used in conjunction with a pulse height analyzer, the window of which was set to discriminate somewhat against fluorescent Ni K α radiation, and the diffraction patterns were obtained as strip chart recordings of the output of a counting rate meter.

Metallic nickel was removed from the catalysts after the standard reduction pretreatment by flowing carbon monoxide, at a space velocity of approximately 300, over the samples at 80° usually for 6 hr. The

pretreatment consisted of reducing the catalysts at 500° for 4 hr. at a space velocity of approximately 300. The amount of nickel removed was determined by decomposing the carbonyl at 300° in a glass tube which was weighed before and after the carbonyl was decomposed. The carbon monoxide was C.P. grade, obtained from the Matheson Co., and was dried by passing it over thoroughly dried molecular sieves.

Catalysts were evaluated for hydrocracking and dehydrogenation activity by using an atmospheric pressure, bench scale catalyst screening unit. The dehydrogenation reaction studied was the conversion of cyclohexane to benzene. The following conditions were used to carry out the reactions: reaction temperature 300°, liquid hourly space velocity 2.36 hr.⁻¹, carrier flow 32 cc. STP/min., reaction time 1 hr., carrier gas hydrogen, catalyst weight 1 g., reactor bed volume 12 cc., cyclohexane charge weight 2.36 g. *n*-Octane was used as the charge for the hydrocracking reaction which was carried out under the following conditions: reaction temperature 400°, liquid hourly space velocity 0.432 hr.⁻¹, carrier flow 32 cc. STP/min., reaction time 2 hr., carrier gas hydrogen, catalyst weight 5 g., reactor bed volume 12 cc., *n*-octane charge weight 2.16 g.

Pure grade 99 mole % minimum cyclohexane and *n*-octane obtained from the Phillips Petroleum Co. were dried with molecular sieves and injected into the feed gas stream by a positive displacement pump. The catalysts were pretreated with the carrier gas at 500° for 2 hr. before the charge was introduced. The per cent conversion was calculated from the total moles of gaseous and liquid products collected. Products in the gas phase were analyzed by mass spectroscopy while the liquid collected was analyzed by gas chromatography.

The amount of hydrogen adsorbed on approximately 6-g. samples was measured in a volumetric adsorption system, described previously.²² The standard sample pretreatment consisted of a 4-hr. reduction at 500° in flowing hydrogen at a space velocity of approximately 300, followed by 1-hr. evacuation at 500° to a pressure approaching 10⁻⁶ torr. The hydrogen was obtained from the Air Reduction Co. and was purified by passing it through a Deoxo unit, a magnesium perchlorate drying tower, and an activated charcoal trap at -195°.

(20) Cited from G. C. Bond, "Catalysis by Metals," Academic Press Inc., New York, N. Y., 1962, p. 485.

(21) W. K. Hall and L. Alexander, *J. Phys. Chem.*, **61**, 242 (1957).

(22) D. S. MacIver and H. H. Tobin, *ibid.*, **65**, 1665 (1961).

Results

X-Ray Diffraction Analyses. In reduced nickel silica-alumina preparations containing between 5 and 10 wt. % nickel, metallic nickel was always found, even when no effort was made to protect the sample from oxygen while the X-ray pattern was being obtained. The strongest line of the X-ray pattern of this nickel was easily observed since its peak intensity was approximately three times that of the background intensity.

A reduced sample of 6 wt. % copper on silica-alumina contained both metallic copper and copper oxide. The identity of the oxide is somewhat uncertain, but it was probably Cu_2O . This sample turned green during a 1-month exposure to air at room temperature. X-Ray diffraction analysis indicated a substantial decrease in the concentration of metallic copper, but there was no corresponding increase in the intensity of the oxide pattern. The green compound is apparently amorphous to X-rays.

In all preparations containing both nickel and copper on silica-alumina, the metallic phase formed during reduction in hydrogen was a solid solution, or alloy, of copper and nickel. This solid solution was homogeneous in the preparations containing nickel and copper in the molar proportions 1:1 and 2:1. When the nickel-copper mole ratio was 1:2 the solid solution was inhomogeneous, and the range of variation of the composition was calculated to lie between 20 Ni-80 Cu and 60 Ni-40 Cu. These calculations were based on the shape and position of the (111) X-ray diffraction line, assuming a linear relation between composition and lattice dimension in the copper-nickel system. It was also observed that the intensity of the pattern of the alloy phase in the 2:1 molar ratio preparation was not sufficient to account for all of the metal in this sample. Part of the metal apparently is present in a form that is amorphous to X-rays.

All of the above reduced nickel-copper samples were treated with carbon monoxide, and some nickel was removed in each case, as shown in Table I. X-Ray analysis of each of these samples after the carbon monoxide treatment failed to show any observable change from the pattern of the reduced sample before carbon monoxide treatment. These results imply that the extracted nickel was not removed from the bulk structure but was taken either from surface layers of the alloy crystals or from amorphous nickel phases which were not observed in the X-ray patterns.

A well-crystallized, homogeneous solid solution was observed in the reduced sample of equimolar nickel-copper on silica gel, but only a very weak indication of the nickel-copper component was observed in the

Table I: Removal of Nickel from Nickel and Nickel-Copper Silica-Alumina Catalysts by Carbon Monoxide

Wt. % Ni	Wt. % Cu	Ni-Cu mole ratio	% of total nickel removed
6.0	0.0	∞	78 ± 3
6.0	0.5	10:1	52
6.0	3.2	2:1	12
6.0	6.5	1:1	9
6.0	13.0	1:2	5

diffraction pattern of the reduced sample containing equimolar proportions of nickel-copper on Davison $\eta\text{-Al}_2\text{O}_3$. It is not clear whether the observed phase in this latter preparation is copper, a copper-rich solid solution, or an inhomogeneous alloy.

Two preparations of unsupported nickel-copper alloys containing 72.4 and 53.8 mole % nickel were also examined. In both cases the alloys were well-crystallized and homogeneous, as judged from the shape of the X-ray diffraction lines. Furthermore, treatment of these samples with carbon monoxide to remove nickel did not appear to alter the bulk composition of the crystals that produced the X-ray patterns.

Removal of Nickel by Carbon Monoxide from Reduced, Impregnated Catalysts. Treatment of reduced nickel and nickel-copper silica-alumina catalysts with carbon monoxide resulted in the removal of metallic nickel in the form of nickel carbonyl. Table I gives the results obtained from carbon monoxide extraction experiments on catalysts containing varying nickel-copper compositions. These results show that, as the copper content increases, the amount of nickel removed by carbon monoxide decreases. Treatment of a reduced nickel silica-alumina catalyst with carbon monoxide resulted in the removal of approximately 78% of the total nickel present. The remaining 22% of the nickel was not removed by reacting with carbon monoxide even after an additional reduction treatment. Examination of the nickel silica-alumina catalyst by X-ray diffraction after the sample had been treated with carbon monoxide showed that the metallic nickel phase was absent. No identifiable ionic nickel diffraction lines were observed even though approximately 22% of the nickel remained. A detailed investigation of the state of this nonremovable nickel was not made, but the fact that X-ray diffraction lines attributed to this phase were not observed is an indication that the nickel is associated with the support in the form of an amorphous complex that is not readily reduced to metallic nickel with hydrogen.

The removal of nickel by carbon monoxide from impregnated catalysts has been reported to be quantitative.²³ This is true for nickel silica catalysts if treated for a sufficient period of time, but it is not true for nickel impregnated on alumina-containing carriers. It has been found that, as the alumina content of the support is increased, the fraction of the nickel that can be removed by carbon monoxide decreases, as illustrated in Table II.

Table II: Removal of Nickel from Various Impregnated Carriers by Carbon Monoxide^a

Carrier	% of total nickel removed
75% SiO ₂ -25% Al ₂ O ₃	78
50% SiO ₂ -50% Al ₂ O ₃	62
20% SiO ₂ -80% Al ₂ O ₃	54
Davison γ -Al ₂ O ₃	45

^a All samples contain 6 wt. % nickel.

Removal of Nickel from Unsupported Nickel-Copper Alloys by Carbon Monoxide. Experiments were carried out to determine whether carbon monoxide would remove nickel from unsupported nickel-copper alloys at 80°. Two samples of different composition were treated with hydrogen for 4 hr. and then treated with carbon monoxide. Care was taken to exclude air from the samples after the hydrogen reduction and during the carbon monoxide treatments.

The results shown in Table III indicate that nickel is slowly removed from the unsupported alloys over a relatively long period of time.

To normalize the data, the per cent of the total nickel content removed per square meter of surface

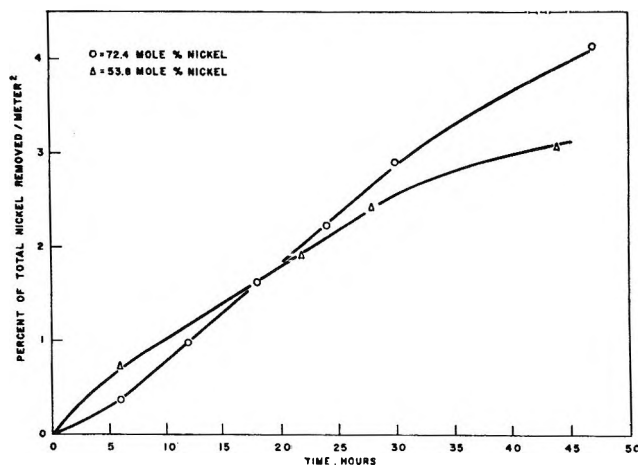


Figure 1. Removal of nickel from unsupported nickel-copper alloy samples with carbon monoxide.

was plotted as a function of time in Figure 1. From such a plot it can be seen that the per cent of the total nickel removed per square meter of sample is fairly linear and nearly the same for both samples for the first 30 hr. After 30 hr. the rate of nickel removal begins to decrease, and an appreciable difference between the two samples appears. This type of behavior suggests that the nickel removed is taken from the surface layers of the alloy crystallites, leaving a copper rich surface through which other nickel atoms must diffuse in order to be extracted. This conclusion is supported by the X-ray diffraction results which show that the bulk composition of the crystals (*i.e.*, beneath the surface layers) is not altered significantly.

The rate at which nickel was removed by carbon monoxide from nickel powder was much faster than from the alloys. After 6 hr. 18% of the total nickel per square meter was removed, while less than 1% was removed from the two unsupported alloys.

Hydrogen Chemisorption Studies. Hydrogen chemisorption measurements were made in order to obtain information about the metallic phases formed on reduced nickel, nickel-copper, and copper silica-alumina catalysts. These results are summarized in Table IV. These measurements were carried out at 100 mm. and 0° since it was found that a maximum occurred in the hydrogen isobar at this temperature for a reduced nickel silica-alumina catalyst. The values contained in Table IV were obtained from rate plots (V_{H_2} cc. STP/m.² vs. time) after 200 min.

Of the catalysts studied the reduced nickel silica-alumina catalyst adsorbed far more hydrogen than any of the others. After treatment with carbon mon-

Table III: Removal of Nickel from Unsupported Nickel-Copper Alloys and Nickel Powder by Carbon Monoxide

Sample	% of total nickel removed	Time, hr.
Nickel powder	5.50	6
	0.38	6
	1.00	12
	1.63	18
	2.25	24
	2.93	30
72.4 mole % Ni	4.15	48
	0.73	6
	1.93	22
	2.40	28
	3.08	44
53.8 mole % Ni		

(23) See ref. 11, p. 40.

Table IV: Hydrogen Chemisorption Measurements

Wt. % Ni	Wt. % Cu	Ni:Cu mole ratio	V_{H_2} adsorbed ^a after reduction	V_{H_2} adsorbed ^a after extraction with CO
6.0	0.0	∞	2.34×10^{-3}	0.05×10^{-3}
6.0	6.5	1:1	0.99×10^{-3}	0.63×10^{-3}
0.0	6.0	0	0.32×10^{-3}	^b
Silica-alumina		...	0.05×10^{-3}	^b

^a In cc. STP/m.². ^b Not measured.

oxide this catalyst adsorbed very little hydrogen, the amount being about the same as that adsorbed by the silica-alumina support.

The reduced nickel-copper silica-alumina catalyst adsorbed less than half the amount of hydrogen adsorbed by the nickel silica-alumina catalyst. After treatment of the supported nickel-copper catalyst with carbon monoxide (which removed approximately 9% of the total nickel) the sample still adsorbed an appreciable amount of hydrogen. It is likely that this hydrogen is adsorbed entirely on the alloy phase whereas the hydrogen adsorbed on the catalyst before the carbon monoxide treatment is adsorbed on both the extractable nickel and the nickel-copper alloy. However, most of this decrease in hydrogen chemisorption could also be attributed to the removal of nickel atoms from the supported nickel-copper alloy phase, leaving a copper-rich surface.

The reduced copper silica-alumina catalyst adsorbed about half the amount of hydrogen that was adsorbed on the carbon monoxide treated nickel-copper silica-alumina catalyst.

Catalyst Activity Studies. The results of cyclohexane dehydrogenation and atmospheric pressure *n*-octane hydrocracking experiments are summarized in Tables V and VI, respectively. These results indicate clearly that the addition of copper to the nickel silica-alumina system greatly decreases the dehydrogenation and hydrocracking activity of the catalyst. For the 2:1 to 1:2 nickel-copper silica-alumina catalysts the variation of catalytic activity with the nickel-copper mole ratio is not very great, especially in the case of the dehydrogenation activity. The copper silica-alumina catalyst and the silica-alumina support exhibited no hydrocracking and dehydrogenation activity under the conditions used.

Treatment of the reduced nickel silica-alumina catalyst with carbon monoxide (which removed 78% of the total nickel) resulted in a catalyst which was much less active than the untreated sample. It is interesting that the resulting material still exhibited hydro-

Table V: Cyclohexane Dehydrogenation

Wt. % Ni	Wt. % Cu	Ni:Cu mole ratio	% con. g. ⁻¹ hr. ⁻¹	Selec-tivity ^a	% con. g. ⁻¹ hr. ⁻¹ after CO ext.	Selec-tivity ^a
6.0	0.0	∞	35.0 ± 1.0	92	2.0	100
6.0	0.5	10:1	22.5 ± 1.0	83	5.0	53
6.0	3.2	2:1	17.5 ± 1.0	82	15.5	79
6.0	6.5	1:1	16.5 ± 1.0	82	15.5	82
6.0	13.0	1:2	19.0 ± 1.0	83	19.0	87
0.0	6.0	0	0.0 ± 1.0	..	0.0	...

^a To benzene.

Table VI: *n*-Octane Hydrocracking

Wt. % Ni	Wt. % Cu	Ni:Cu mole ratio	% con. g. ⁻¹ hr. ⁻¹	% con. g. ⁻¹ hr. ⁻¹ after CO ext.
6.0	0.0	∞	8.0 ± 0.30	1.00
6.0	0.5	10:1	6.60	1.50
6.0	3.2	2:1	4.70	4.25
6.0	6.5	1:1	3.60	3.00
6.0	13.0	1:2	2.80	3.70
0.0	6.0	0	0.00	0.00

cracking and dehydrogenation activity even after all the nickel that was capable of forming nickel carbonyl had been removed. Treatment of the 2:1, 1:1, and 1:2 nickel-copper silica-alumina catalysts with carbon monoxide (which removed 12, 9, and 5% of the total nickel, respectively) resulted in a slight decrease or no change of activity compared to the activity of the catalysts before treatment with carbon monoxide. The one exception was the hydrocracking activity of the carbon monoxide treated 1:2 nickel-copper catalyst. This result is not explainable but may be related to the inhomogeneity observed only in the case of this particular catalyst.

The products of the hydrocracking experiments were periodically examined by mass spectrometry. For the reduced nickel and 10:1 nickel-copper silica-alumina catalysts the main product formed was methane. However, for the 2:1 to 1:2 nickel-copper silica-alumina catalysts the major product was propane, and very little methane was produced. Treatment of the latter catalysts with carbon monoxide had very little effect on the product distributions. Propane was also the major product of the carbon monoxide treated 10:1 nickel-copper silica-alumina catalyst. It was interesting to find that a carbon monoxide treated nickel silica-alumina catalyst produced con-

siderably more C₄ hydrocarbons (*i.e.*, *n*-butanes, isobutane, and butenes) than the untreated nickel silica-alumina catalyst.

The catalytic activity results reported in Tables V and VI are in units of per cent total conversion per gram of catalyst per hour. A comparison of specific activities (per cent conversion per square meter of metallic phase per hour) would be much more meaningful, but without a knowledge of the metal surface areas (the surface areas of the nickel and nickel-copper phases) specific activities could not be obtained.

Discussion

The experimental results of this work indicate that nickel-copper alloys will form on silica-alumina upon reduction of impregnated nickel-copper silica-alumina catalysts. The main evidence for this alloy formation is provided by the X-ray diffraction analyses. In addition to the nickel-copper alloy phase, there are likely to be metallic nickel and copper phases on the silica-alumina surface, depending on the concentrations used to impregnate the silica-alumina. To make the system more complex there is also a nickel phase that is not removed by carbon monoxide even after repeated reductions. Such a phase was found in nickel silica-alumina catalysts. Apparently, this nickel is ionic and is complexed with the silica-alumina in some way. The data presented in Table II show that, as the alumina content of the support is increased in catalysts containing 6 wt. % nickel, the fraction of nickel removed with carbon monoxide decreased. This cannot simply be the result of a decrease in nickel surface area since it was recently reported that for reduced impregnated catalysts containing 10 wt. % nickel the nickel surface areas decreased in the order: Ni on Al₂O₃ > Ni on SiO₂ > Ni on SiO₂-Al₂O₃.²⁴ It has been reported that in impregnated nickel alumina catalysts nickel oxide may combine chemically with the alumina support to form nickel aluminates^{25,26} which is not easily reduced with hydrogen. Therefore, the most logical conclusion to be deduced from the results shown in Table II is that the amount of nickel chemically associated with alumina increases as the alumina content of the support increases.

The reaction of metallic nickel with carbon monoxide to form nickel carbonyl was used in an attempt to obtain quantitative information about the amount of "free nickel" on reduced nickel-copper silica-alumina catalysts. Such a technique has been used to separate metallic nickel from a mixture of nickel and nickel subsulfide.²⁷ The data in Table III show that after 45 hr. approximately 4% of the nickel present can be removed from unsupported nickel-copper alloys. It

is reasonable to expect that the nickel could come from the surface layers of the alloy crystals or from unalloyed nickel phases which might be present together with the alloy. The X-ray diffraction analyses indicate that the unsupported reduced alloys were homogeneous and contained no observable metallic nickel. However, amorphous unalloyed nickel phases in amounts sufficient to account for much of the extractable nickel would probably be undetectable by X-ray diffraction, and could be present. Therefore, the amount of nickel removed from the nickel-copper silica-alumina catalysts can be considered only as a semiquantitative estimate of the "free nickel" present on the silica-alumina.

According to the electron band theory the catalytic activity of transition metals for hydrogen transfer type reactions, such as hydrogenation-dehydrogenation is due to the partially empty d-bands of the metals. Adding various amounts of I-B metals, such as copper, to the transition metals results in the gradual filling of the d-band vacancies with a corresponding decrease in catalytic activity. The results obtained from the dehydrogenation and hydrocracking experiments show a marked decrease in activity as copper is added to the nickel silica-alumina system. These results also support the conclusion that the nickel and copper are combining on the silica-alumina surface. If the nickel and copper were not combining, such a striking decrease in activity would not be expected. It is interesting to note that for the 2:1 to 1:2 nickel-copper catalysts the major product produced from the hydrocracking of normal octane was propane, whereas methane was the principal product formed over the nickel and 10:1 nickel-copper catalysts. This change in selectivity also suggests the presence of a different major metallic phase in the 2:1 to 1:2 nickel-copper catalysts compared to the catalysts where nickel is the dominant metallic phase.

A decrease in hydrogen chemisorption as copper is added to the nickel silica-alumina system would be expected on alloy formation according to the electron band theory. This decrease in adsorption is due to an increase in the energy of activation for adsorption as the d-band of nickel is progressively filled by the valence electrons of copper. For copper the d-band is filled,

(24) W. F. Taylor, D. J. C. Yates, and J. H. Sinfelt, *J. Phys. Chem.*, **68**, 2962 (1964).

(25) S. Yoshitomi, Y. Morita, and K. Yamamoto, *Bull. Japan Petrol. Inst.*, **5**, 27 (1963).

(26) K. Morikawa and F. Nozaki, *Kogyo Kagaku Zasshi*, **64**, 1562 (1961).

(27) E. H. M. Badger, R. H. Griffith, and W. B. S. Newling, *Proc. Roy. Soc. (London)*, **A197**, 184 (1949).

and hydrogen is not readily adsorbed on the copper silica-alumina sample.

Alloys may be more common on reduced supported metal oxide catalysts than has been realized. This idea was expressed recently by Endter, who reported that platinum-aluminum alloys were formed during the preparation of a platinum alumina catalyst used in the synthesis of hydrogen cyanide.²⁸

Acknowledgment. The authors wish to express their appreciation to Dr. W. K. Hall of Mellon Institute, Pittsburgh, Pa., for the unsupported nickel-copper alloy samples and to Miss Winifred Roensch for the X-ray diffraction analyses.

(28) F. Endter, presented at the 147th National Meeting of the American Chemical Society, Philadelphia, Pa., April 5-10, 1964.

Structure and Properties of Amorphous Silicoaluminas. II. Lewis and Brønsted Acid Sites

by J. J. Fripiat,¹ A. Léonard, and J. B. Uytterhoeven

Laboratoire de Physico-Chimie Minérale, Agronomic Institute of the University of Louvain, Héverlé-Louvain, Belgium (Received February 8, 1965)

The schematic structures derived previously from coordination number measurements and infrared spectroscopy suggested different possible origins for Brønsted and Lewis acid sites in silicoaluminas with compositions ranging from pure silica to pure alumina. To check these hypotheses, cation-exchange capacities and ammonia adsorption isotherms were measured, and infrared spectra of adsorbed species were recorded. The comparison between structural and adsorption data shows the existence of two probable Lewis acid types located either on silicon atoms in high alumina samples or on aluminum atoms in low alumina samples. The critical composition is somewhat lower than 40% in Al_2O_3 . Brønsted acid sites originate from isomorphic substitution of silicon by aluminum in the tetrahedral network.

Introduction

Acid properties of silicoalumina surfaces are due to Brønsted or Lewis sites according to the hydration state and to the surface structure, which reflects to some extent the organization in the bulk. Therefore, it appears interesting to relate the schematic structures obtained previously² from X-ray fluorescence spectroscopy and from infrared to acid properties.

The coordination numbers of aluminum and silicon were obtained from the comparison of the angular positions of the Al $K\alpha$ and Si $K\alpha$ lines with the angular positions of the corresponding lines in materials of

known structures where aluminum or silicon have the coordination numbers 0, 4, or 6, respectively. For aluminum the results were expressed in terms of relative contents in fourfold coordinated atoms ($\% \text{Al}^{\text{IV}}$). This was justified by the distribution of aluminum atoms into two main types of sites where they are either tetrahedrally or octahedrally coordinated with respect to oxygen atoms. Infrared spectroscopy in the Si-O

(1) The University of Louvain and M.R.A.C. Tervuren.

(2) A. Léonard, S. Suzuki, J. J. Fripiat, and C. De Kimpe, *J. Phys. Chem.*, **68**, 2608 (1964).

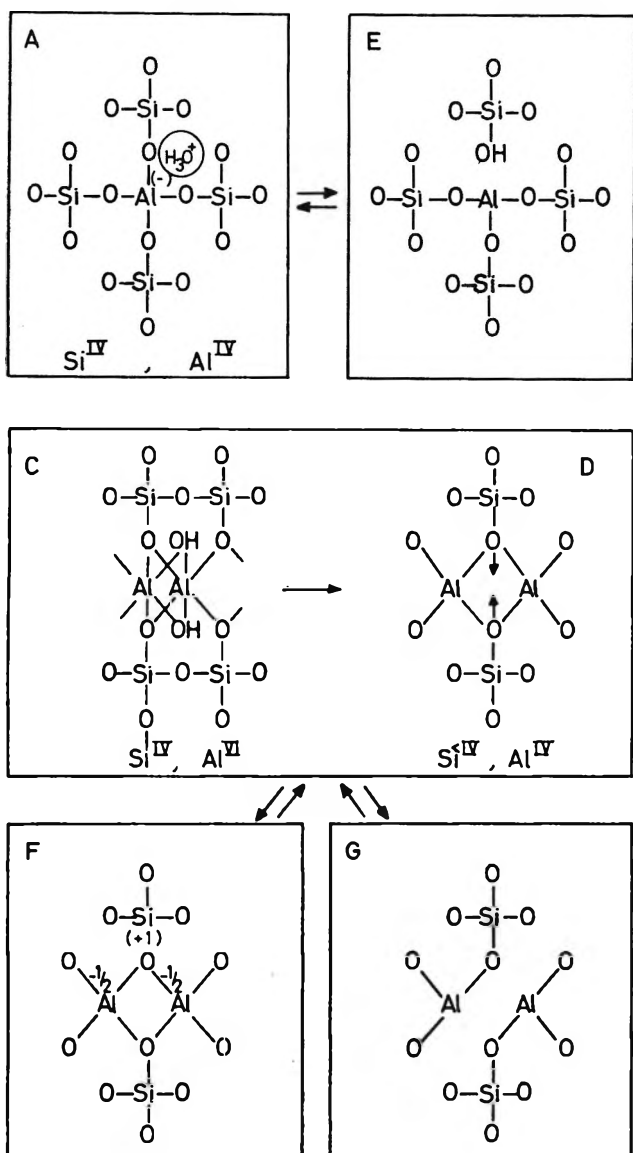


Figure 1. Schematic structures.

stretching region was used essentially to check these data.

The schematic structures proposed in the first paper² are represented in Figure 1A, C, and D.

As far as aluminum is concerned, three different oxygen environments were actually taken into consideration, corresponding, respectively, to aluminum tetrahedra sharing corners with silicon tetrahedra (A), to aluminum octahedra (C), or to aluminum tetrahedra sharing edges (D). The distribution of these different types depends on the aluminum content and the pre-treatment temperature. Hydrated silicoaluminas rich in alumina (>80% Al_2O_3) contain essentially aluminum octahedra (C), which, by dehydration, are converted

into aluminum tetrahedra sharing edges (D). Samples poor in alumina (<30% Al_2O_3) contain essentially tetrahedral aluminum of the A type regardless of the hydration level. Samples in the medium composition range contain a mixture of both C and A structures. In silicoaluminas of the D type, the apparent silicon coordination number is smaller than 4.

This second contribution aims to correlate these different structures with their surface acid properties. Ammonia has been chosen to distinguish between Brønsted and Lewis sites according to the findings of Mapes and Eischens³ that infrared spectra of adsorbed NH_3 or NH_4^+ indicate the dominant type of acid sites. Numerous attempts to relate acidity and composition have already been made,⁴⁻⁷ but it is believed that the direct information obtained on aluminum and silicon coordination numbers will permit a more detailed and firmer analysis of the phenomena.

Experimental Section

Samples. The samples were prepared by hydrolysis of aluminum isopropoxide and ethyl orthosilicate, dried, and calcined at different temperatures, ranging between 100 and 700°. Their compositions [$\text{Al}_2\text{O}_3/(\text{Al}_2\text{O}_3 + \text{SiO}_2$ and water contents)], their relative Al^{IV} contents, and the silicon coordination numbers (Si c.n.) were reported previously.² Their B.E.T. (N_2 at -196°) surface areas are shown in Table I.

Cation-Exchange Capacities and Ammonia Adsorption Isotherms. The cation-exchange capacities (c.e.c.) were determined, according to MacKenzie,⁸ for the samples dried at 100° by adsorption of NH_4^+ from solution and subsequent determination by the micro-Kjeldahl technique. The results are contained in Table I.

NH_3 adsorption isotherms were run at 20 or 350°. All the isotherms display the behavior shown in Figure 2; the adsorption may be split into a reversible and an irreversible process. The amount of irreversibly adsorbed NH_3 was obtained by lowering the NH_3 pressure to zero, by outgassing the samples, and by measuring the NH_3 held by the solid at 20 or 350°. This was made as follows. After outgassing, the glass bulb containing the sample was sealed, removed from the adsorption apparatus, and broken in an acid solution, and

(3) J. E. Mapes and R. P. Eischens, *J. Phys. Chem.*, **58**, 1059 (1954).

(4) T. Milliken, G. A. Mills, and A. G. Oblad, *Discussions Faraday Soc.*, **8**, 270 (1950).

(5) M. W. Tamele, *ibid.*, **8**, 270 (1950).

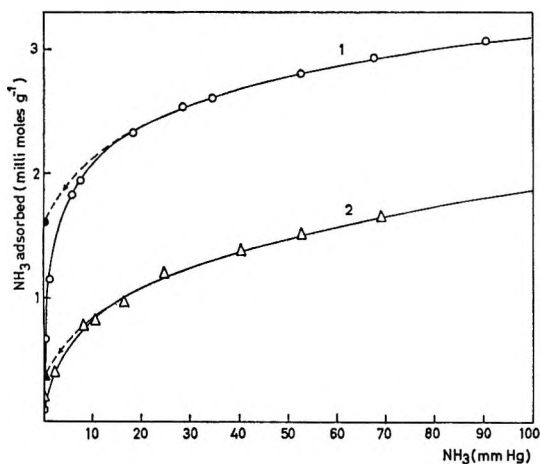
(6) J. D. Danforth, *J. Phys. Chem.*, **59**, 564 (1955); presented at the 2nd International Congress on Catalysis, Paris, 1960.

(7) J. Turkevich, F. Nozaki, and D. Stamires, Proceedings of the 3rd International Congress on Catalysis, Amsterdam, 1964; Preprints, Vol. I, p. 33.

(8) R. C. MacKenzie, *Clay Minerals Bull.*, **1**, 203 (1950).

Table I: B.E.T. Surface Areas ($\text{m}^2 \text{g}^{-1}$) and Cation-Exchange Capacities (c.e.c.) (mequiv./g.)

Compn., % $\text{Al}_2\text{O}_3/$ ($\text{Al}_2\text{O}_3 + \text{SiO}_2$)	B.E.T. surface area					C.e.c. ^a
	Pretreatment temp., °C.					
	100	200	350	470	700	
0	466	675	828	773	672	0.02
17.7	239	86	81	115	83	1.02
33.2	231	101	124	131	191	1.08
59.4	304	156	196	222	297	0.60
66.6	326	213	223	231	277	0.48
81.4	327	251	278	299	287	0.18
100.0	302	235	257	226	170	0.01

^a Samples dried at 100°.**Figure 2.** Typical isotherms obtained for NH_3 adsorption and desorption. Samples were pretreated at 100°; NH_3 was adsorbed at 20°; 1, 33.2% Al_2O_3 ; 2, 81.4% Al_2O_3 samples.

the NH_3 content was measured by distillation. Reversibly adsorbed NH_3 will be, rather arbitrarily, defined as the difference between the amount adsorbed under a NH_3 pressure of 50 mm. and the irreversibly adsorbed quantity. The results expressed either per gram or per unit surface area are shown in Table II.

Infrared Spectroscopy. The samples were pressed in thin wafers and introduced into a vacuum-tight infrared cell and outgassed at the desired temperature, as usual. The NH_3 pressure in the cell was increased and then decreased and the outgassing was again performed under various conditions. After each adsorption or desorption step, the spectra were recorded in the 5.5–7.5- μ range, using CaF_2 optics. The instrument setting was as follows: slit, 1.5 \times standard; period, 2 sec.; gain, 4%; scanning speed, 0.1 μ /min.

Figure 3 shows some of the spectra obtained under these conditions. The assignments of the bands are as follows: 1452 cm^{-1} , deformation vibration of NH_4^+

Table II: NH_3 Adsorption^a

Outgassing temp., °C.	$\text{Al}_2\text{O}_3/(\text{Al}_2\text{O}_3 + \text{SiO}_2)$, %								
	0		33.2		81.4		100		
	Ir	Rev	Ir	Rev	Ir	Rev	Ir	Rev	
Adsorption at 20°									
100	σ	0.80	3.45	4.16	2.88	0.65	2.18	0.33	1.38
	q	0.61	2.67	1.59	1.11	0.35	1.18	0.17	0.69
200	σ	0.44	2.74	4.16	5.18	0.80	2.88	0.31	1.53
	q	0.49	3.03	0.69	0.87	0.33	1.20	0.12	0.60
350	σ	0.39	1.77	2.20	3.00	0.65	1.85	0.42	1.54
	q	0.45	2.44	0.45	0.62	0.29	0.85	0.18	0.66
470	σ	0.28	1.66	1.29	2.48	0.94	1.16	0.41	2.02
	q	0.20	2.14	0.29	0.52	0.47	0.58	0.16	0.76
700	σ	0.01	0.94	0.42	1.21	1.06	1.39	0.60	1.74
	q	0.01	1.05	0.12	0.39	0.49	0.66	0.17	0.49
Adsorption at 350°									
350	σ	0	0.14	1.47	2.14	0.08	0.23	0.04	0.49
	q	0	0.20	0.31	0.44	0.05	0.11	0.02	0.21
470	σ	0.01	0.22	0.57	1.66	0.10	0.29	0.09	0.34
	q	0.01	0.28	0.12	0.36	0.05	0.14	0.03	0.13
700	σ	0	0	0.09	0.39	0.11	0.67	0.04	0.31
	q	0	0	0.03	0.13	0.05	0.33	0.01	0.09

^a σ , 10^{14} molecules/ cm^2 ; q , 10^{-3} mole adsorbed/g.; Ir, irreversibly adsorbed (determined by distillation after outgassing at the adsorption temperature); Rev, NH_3 adsorbed at 50 mm. minus Ir.

perturbed by hydrogen bonding with water or ammonia,^{9,10} 1420 cm^{-1} , deformation vibration of unperturbed NH_4^+ ; 1592–1595 cm^{-1} , deformation vibration of chemisorbed NH_3 ; $\approx 1632 \text{ cm}^{-1}$, deformation vibration of water and/or NH_3 physically adsorbed. The shoulder observed scarcely at 1705 cm^{-1} has not been assigned. From the spectra shown in Figure 3 it appears that in a sample poor in alumina (17.7% Al_2O_3), outgassed at 100°, NH_3 is adsorbed mainly as NH_4^+ (curve 1). By outgassing the same sample at higher temperature (curve 2), the band assigned to chemisorbed NH_3 appears, while the water deformation band disappears accordingly and the 1420- cm^{-1} component due to free NH_4^+ becomes clearly visible. At still higher temperature (curve 3) the contribution of free NH_4^+ becomes much weaker.

According to recent results from this laboratory,¹¹ the ratio of the absorption coefficients of the NH_3 and NH_4^+ deformation bands ($\text{NH}_3:\text{NH}_4^+$) is of the order of magnitude of 1:7.

The relative intensities of the 1592–1595- cm^{-1} and of the 1420–1452 cm^{-1} bands must be corrected ac-

(9) M. Mortland, J. J. Fripiat, J. Chaussidon, and J. Uytterhoeven, *J. Phys. Chem.*, **67**, 248 (1963).

(10) P. Cloos and M. Mortland, 13th National Clay Conference, Madison, Wis., 1964, in press.

(11) M. Van Tongelen, private communication.

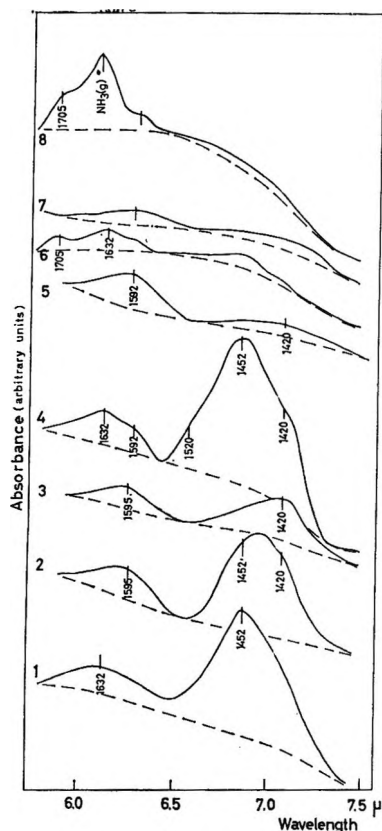


Figure 3. Infrared spectra of adsorbed NH_3 . The frequencies of the main bands are expressed in cm^{-1} . 17.4% Al_2O_3 sample: 1, pretreated at 100° , NH_3 adsorbed and outgassed at 20° ; 2, pretreated at 120° , NH_3 adsorbed and outgassed at 120° ; 3, pretreated at 370° , NH_3 adsorbed and outgassed at 210° . 33.2% Al_2O_3 sample: 4, pretreated at 100° , NH_3 adsorbed and outgassed at 20° ; 5, pretreated at 375° , NH_3 adsorbed and outgassed at 375° . 81.4% Al_2O_3 sample: 6, pretreated at 100° , NH_3 adsorbed and outgassed at 20° ; 7, pretreated at 300° , NH_3 adsorbed and outgassed at 300° ; 8, pretreated at 100° , NH_3 adsorbed at 100° , 94 mm. of NH_3 present in the cell. All the pretreatments were carried out *in vacuo*.

cordingly to estimate the relative $\text{NH}_3\text{-NH}_4^+$ contents. This leads to the conclusion that progressive dehydration of the 17.4% Al_2O_3 sample results in a decrease in chemisorbed NH_4^+ and in a strong increase in chemisorbed NH_3 .

As shown by curves 4 and 5 in Figure 3, these phenomena are still better pronounced for the 33.2% Al_2O_3 sample while, according to curves 6, 7, and 8 obtained with a sample much richer in alumina (81.4% Al_2O_3), the formation of NH_4^+ is no more noticeable even after outgassing at 100° while NH_3 is the most abundant chemisorbed species. Other spectra, recorded for intermediate compositions, show transition stages between the well-delineated cases depicted in Figure 3.

If the spectra were recorded with gaseous NH_3 still

in the cell, the sharp peak at 1630 cm^{-1} due to the gas emerges from the diffuse $6\text{-}\mu$ band.

Discussion

In accordance with the already emphasized importance of hydration states,² the relations between the proposed A, C, and D structures (Figure 1) must be discussed, taking into account the pretreatment temperature.

In samples dried at 100° , the A structure is dominant for alumina contents lower than 33%; above this composition, the A and C structures may exist simultaneously in different regions of the solid. Cationic-exchange sites are associated with aluminum tetrahedra sharing corners with silicon tetrahedra since an unambiguous linear relation is observed between the relative Al^{IV} content and the c.e.c., as shown in Figure 4A.

To obtain additional information on the meaning of this, it is interesting to consider the change, with respect to the water content, of the irreversible adsorption of NH_3 by the silica gel and the silicoalumina bearing, in the hydrated state, the highest negative charge [$\text{Al}_2\text{O}_3/(\text{Al}_2\text{O}_3 + \text{SiO}_2) = 33.2\%$]. A linear relation is observed between the amount of irreversibly adsorbed NH_3 and the water content of the silicoalumina; the thoroughly dehydrated sample has still a definite sorption capacity. Irreversible adsorption is not observed for the silica gel at zero water content (Figure 4B).

According to the infrared spectra, NH_3 irreversibly adsorbed by the thoroughly dehydrated 33.2% Al_2O_3 sample is probably in the NH_3 form while, at higher

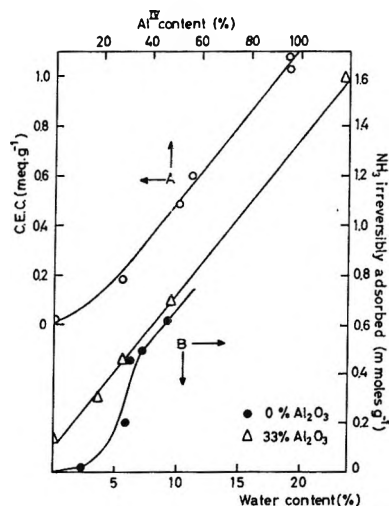


Figure 4. A. Variation of the c.e.c. against the Al^{IV} relative contents for the various compositions dried at 100° . B. Variation of the amount of NH_3 irreversibly adsorbed by silica gels and by the 33.2% Al_2O_3 samples with respect to their water contents.

hydration level, chemisorbed NH_3 is transformed noticeably into NH_4^+ . It follows that dehydrating samples with this composition results in the conversion of Brønsted into Lewis adsorption sites. In order to explain this phenomenon, the A structure shown in Figure 1 must be necessarily converted into a structure which contains Lewis sites.

It has been demonstrated in the first paper² that fourfold coordinated aluminum surrounded by Si tetrahedra is not affected by the water content for compositions in Al_2O_3 lower than 33%. It is, however, hard to believe that the charge-balancing proton, or hydronium, in the structure, will be maintained outside the lattice at high temperature. Therefore, the transformation of the A structure into the E structure, as shown in Figure 5, is suggested to occur upon water removal. Brønsted sites should then be associated with A structures while potential Lewis sites, generated by removing water, should be accounted for by E structures. This is also in agreement with the reversible transformation of Lewis into Brønsted sites on rehydration for samples rich in silica as emphasized by Basila, *et al.*¹²

The opposite process which would lead to the formation of Lewis sites on silicon atoms and to the formation of AlOH groups is ruled out in this case for two reasons: (1) McDonald^{13,14} and Basila^{15,16} have found that in cracking catalysts $\text{Al}_2\text{O}_3/(\text{Al}_2\text{O}_3 + \text{SiO}_2) = 25\%$ outgassed at high temperature, the OH groups are very similar to those observed in silica gel; (2) thermal stability of surface OH associated with aluminum is lower than that of silanols.¹⁷

The situation for samples richer in aluminum appears to be quite different. At high hydration level and for the 81.4% Al_2O_3 sample dried at 100°, the relative Al^{IV} content was found by Léonard, *et al.*² to be of the order of magnitude of 30%; the C structure in which aluminum is octahedrally coordinated is therefore dominant. Dehydration leads to the progressive transformation of C into D structure, characterized by aluminum tetrahedra sharing edges and silicon coordination numbers smaller than 4. This has been tentatively interpreted as a partial abstraction of the oxygen atom linking alumina to silica from the coordination shell of silicon. For this 81.4% Al_2O_3 sample, as shown in Table II, the surface density in NH_3 irreversibly adsorbed increases markedly upon dehydration. The relation between this increase and the extent of transformation of C into D structure, expressed by the relative Al^{IV} content, appears in Figure 5 as roughly linear. Accordingly, infrared spectra of adsorbed NH_3 show a very low degree of conversion of adsorbed species into NH_4^+ and rela-

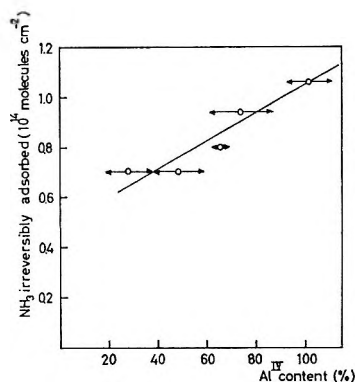


Figure 5. Variation of the surface density in NH_3 irreversibly adsorbed by the 81.4% Al_2O_3 samples, pretreated at increasing temperatures, with respect to their Al^{IV} contents. Arrows indicate deviations with respect to the average results in coordination number measurements.

tively higher NH_3 contents after outgassing at 400° (Figure 3).

In order to explain NH_3 chemisorption in samples rich in alumina, the D structure must be thus considered as generative of Lewis acid sites: two possibilities exist which are schematically represented in Figure 1 by the F and G structures, both being induced by the interaction of NH_3 with the surface. According to F, silicon would be a Lewis site and the charge balance should be internally compensated. In this situation, aluminum is fourfold coordinated and the silicon coordination number decreases to 3. Due to its higher electronegativity, silicon is probably a stronger Lewis acid than aluminum. In the G structure, aluminum would be the Lewis site and the strain existing in aluminum tetrahedra sharing edges should be released. In both cases, the extent of the transformation of D into F or G would be a function of the adsorbate basic strength. In the pure alumina sample, dehydration also converts octahedral aluminum into tetrahedrally coordinated atoms but the increase in surface density of irreversibly adsorbed NH_3 does not follow the extent of this transformation.¹⁸

The different properties of the 100% Al_2O_3 sample and the 81.4% Al_2O_3 silicoalumina suggest a probable

(12) M. R. Basila, T. H. Kantner, and K. H. Rhee, *J. Phys. Chem.*, **68**, 3197 (1964).

(13) R. S. McDonald, *ibid.*, **62**, 1168 (1958).

(14) R. S. McDonald, *J. Am. Chem. Soc.*, **79**, 850 (1957).

(15) M. R. Basila, *J. Chem. Phys.*, **35**, 1151 (1961).

(16) M. R. Basila, *J. Phys. Chem.*, **66**, 2223 (1961).

(17) J. J. Fripiat, 12th National Clay Conference, Atlanta, Ga., 1963, Pergamon Press Ltd., London, 1964, pp. 327-358.

(18) It will be shown elsewhere that coordination measurements for aluminas cannot be interpreted in terms similar to those used for silicoaluminas.

influence of silicon in the latter and a possible intervention of structure F.

Moreover, if the surface densities of NH_3 irreversibly adsorbed by the 81.4% Al_2O_3 and 33.2% Al_2O_3 samples are compared, as shown in Table III, the high alumina

Table III: Ratio of Surface Densities of NH_3 Irreversibly Adsorbed by the 81.4% Al_2O_3 and 33.2% Al_2O_3 Samples (σ for 81.4% $\text{Al}_2\text{O}_3/\sigma$ for 33.2% Al_2O_3)

Pretreatment temp., °C.	— NH_3 adsorption temp.—	
	20°	350°
350	0.29	0.05
470	0.73	0.17
700	2.52	1.24

composition appears to be markedly favored by pretreatment carried out at high temperature. In addition, since the silicon coordination number decreases at high temperature, the F structure seems more probable than the G structure. Silicon being fourfold coordinated in the low alumina composition, irrespective of the water contents, Lewis sites on silicon would be restricted to samples rich in alumina and pretreated above 400°.

In summary, two types of Lewis sites would exist in silicoaluminas according to their compositions: they are represented by the E and F structures in Figure 1. The $\text{A} \rightleftharpoons \text{E}$ and $\text{D} \rightleftharpoons \text{F}$ transformations are probably reversible.

Brønsted sites, localized on aluminum, might be alternatively considered: (1) as resulting from E struc-

ture on water addition to the calcined material or, (2) as a result of the ionization of water molecules during the formation process from ethyl silicate and aluminum isopropoxide hydrolysis, this ionization being required for balancing the charge of isolated aluminum tetrahedra. Catalysis chemists will probably consider the first alternative while specialists of aluminosilicate structures will retain the second one.

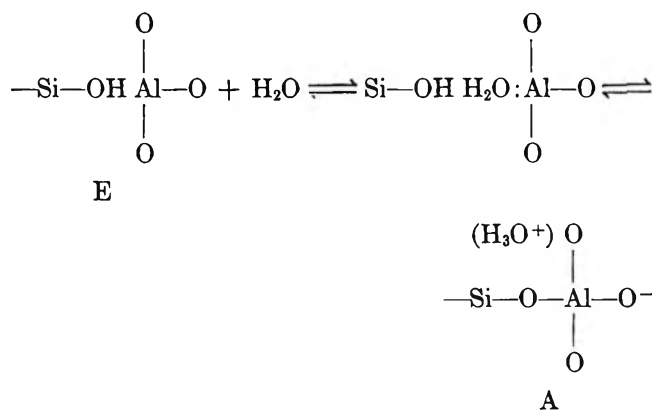
The question is still open whether aluminum exists as a trigonally coordinated atom in the E structure or not. The answer could be given by careful bond length measurements but, as a matter of fact, aluminum coordination numbers significantly lower than 4 have never been observed in this work. Unfortunately, it is impossible for technical reasons to perform such measurements on samples pretreated at high temperature and having chemisorbed ammonia.

So far the NH_3 reversible adsorption has not been considered in this discussion. Results of Table II indicate that, with the exception of pure silica, the amount of NH_3 reversibly adsorbed reaches a maximum for the two silicoaluminas pretreated at 200°. A maximum is also observed for the pure alumina pretreated at 470°. It might be suggested that water and reversibly adsorbed ammonia molecules compete on the surface until the water surface density decreases to zero. Then the coordination mechanism suggested by Hsieh¹⁹ could take place: ammonia molecules interact with NH_4^+ and polarized chemisorbed NH_3 molecules to which they are bound.

Conclusions

Structural data derived from coordination measurements and NH_3 irreversible adsorption determinations suggest the existence of two probable types of Lewis acids on dehydrated silicoalumina surfaces. In high alumina samples, silicon atoms would be the Lewis sites while in low alumina samples, $[\text{Al}_2\text{O}_3/(\text{Al}_2\text{O}_3 + \text{SiO}_2) < 33.1\%]$, the aluminum atoms would constitute these sites. In hydrated samples, regardless of the composition, Brønsted sites originate from isomorphic substitutions of silicon by aluminum in the tetrahedral network as shown by the close relation between cation-exchange capacity and relative contents in aluminum atoms in fourfold coordination.

(19) P. H. Hsieh, *J. Catalysis*, **2**, 211 (1963).



The Role of Amino Groups in Water Absorption by Keratin

by J. D. Leeder

Division of Textile Industry, C.S.I.R.O. Wool Research Laboratories, Belmont, Victoria, Australia

and I. C. Watt

Division of Textile Physics, C.S.I.R.O. Wool Research Laboratories, Ryde, New South Wales, Australia
(Received February 15, 1965)

The effect of amino groups in keratin on the keratin-water isotherm has been investigated by measuring isotherms of a series of partially deaminated wools. A plot of residual amino group content against equilibrium water content is linear at humidities up to 80% relative humidity. Extrapolation of this plot to zero amino group content enables an isotherm to be constructed for wool containing no amino groups. The reduction in water content can be expressed as a Langmuir isotherm at relative humidities below 25%. At higher humidities the absorption of a second and third water molecule on each amino group causes deviations from the Langmuir isotherm and variations in the over-all energy of attachment of water molecules with change of water content. Above approximately 80% relative humidity additional absorption of water on water within the wool also occurs.

Introduction

It is generally accepted that proteins absorb water vapor by binding water molecules to hydrophilic sites at low relative humidities, followed by condensation or multimolecular absorption as the humidity increases.¹⁻⁴ At present no clear-cut distinction can be made between bound water and mobile or condensed water, the relative proportions of each varying with the total moisture content of the system.⁵

Chemical and physical modifications of keratin have been related to changes in shape of the keratin-water isotherm.⁶ Changes in the polar nature of wool result in variation of water content at low relative humidities, while physical changes which modify the forces opposing swelling of the keratin network result in deviations from the normal isotherm at high humidities, *i.e.*, in the solution region proposed by Katz.⁷ For the keratin-water system the solution region has been defined as the 80-100% relative humidity range.⁶

The main polar groups in proteins are the free amino, carboxyl, and hydroxyl groups of the amino acid side chains. Mellon, *et al.*,⁸ found that benzoylation of amino groups in casein reduced the water content, particularly at low relative humidities, while Kanagy and Cassel⁹ obtained similar results with collagen after

deamination, acetylation, and esterification treatments. When applied to wool, deamination¹⁰ was reported to give no change in the isotherm. However, Watt and Leeder⁶ have shown that acetylation and esterification result in significant reductions in water content at low humidities although increased water uptake may occur at high humidities owing to structural changes brought about by the chemical reaction.

Modification of the hydrophilic properties of wool by chemical reactions which introduce new groups can give effects other than the desired specific reaction. For instance, Leeder and Lipson¹¹ found that acetyla-

- (1) A. B. D. Cassie, *Trans. Faraday Soc.*, **41**, 450, 458 (1945).
- (2) L. Pauling, *J. Am. Chem. Soc.*, **67**, 555 (1945).
- (3) A. D. McLaren and J. W. Rowen, *J. Polymer Sci.*, **7**, 289 (1951).
- (4) J. J. Windle, *ibid.*, **21**, 103 (1956).
- (5) M. Feughelman and A. R. Haly, *Textile Res. J.*, **32**, 966 (1962).
- (6) I. C. Watt and J. D. Leeder, *Trans. Faraday Soc.*, **60**, 1335 (1964).
- (7) J. R. Katz, *ibid.*, **29**, 279 (1933).
- (8) E. F. Mellon, A. H. Korn, and S. R. Hoover, *J. Am. Chem. Soc.*, **69**, 827 (1947).
- (9) J. R. Kanagy and J. M. Cassel, *J. Am. Leather Chemists' Assoc.*, **52**, 248 (1957).
- (10) J. B. Speakman, *J. Soc. Chem. Ind. (London)*, **49**, T209 (1930).
- (11) J. D. Leeder and M. Lipson, *J. Appl. Polymer Sci.*, **7**, 2053 (1963).

tion and esterification treatments alter the density of wool such that sorption properties, particularly rate of absorption, are changed. The new groups may be hydrophilic to an unknown extent, so it would be advantageous to investigate the effect of polar groups on the keratin-water isotherm by using reactions designed to remove these polar groups, without leaving bulky substituents in their place.

The attachment of water to amino groups in proteins occurs with an energy of binding higher than the energy needed to attach to other hydrophilic groups¹² so modification of this group should have a greater effect than modification of other hydrophilic sorption sites. The effect of deamination on water sorption by keratin is reported in this paper.

Experimental Section

Absorption isotherms were measured at 35° as previously described,¹³ using a quartz spiral spring balance. The wool was from the same source as that used in earlier work⁶ and was given a similar cleaning procedure.

Deamination Treatments.¹⁴ Deamination was carried out with van Slyke reagent as follows. Samples (5 g.) of wool were treated with 165 ml. of 25.6% aqueous sodium nitrite + 35.3 ml. of glacial acetic acid at 20° for (a) 1 day, (b) 2 days, (c) 4 days, (d) 8 days, and (e) 16 days, with daily changes of reagent. Treatments d and e were washed with water and carded on a small mechanical carding machine every 4 days to assist in obtaining even and exhaustive treatment. The Orange II-formic acid dye uptake method of Maclaren¹⁵ was used in the estimation of total basic group content.

Table I contains the results of analyses for residual basic groups in the deaminated wools.

Table I: Basic Groups Analysis of Deaminated Wools

Treatment	Total basic groups, mequiv./g.
Untreated	0.83
Treatment a	0.49
Treatment b	0.42
Treatment e	0.34
Treatment d	0.17
Treatment e	0.10

For the purpose of the present work, it will be assumed that deamination only modifies amino groups. Amino acid analyses (kindly carried out by Mr. A. S. Inglis) indicate reaction with tyrosine, but diazotization

of tyrosine occurs in the *ortho* position,¹⁶ probably leaving the phenolic hydroxyl unchanged as a water sorption site.

Results and Discussion

Comparison of the activation energies of diffusion and heats of hydration for the wool-water system with the values obtained for the individual polar groups enabled Watt, *et al.*,^{17,18} and Speakman¹² to show that initial uptake of water vapor by dry wool is most likely to occur on the polar amino, carboxyl, and hydroxyl groups. The heats of hydration for these groups have been set at 16.8 kcal./mole for NH₃⁺ groups, 7.4 kcal./mole for COO⁻ groups, and 5.7 kcal./mole for OH groups,¹² while the activation energy of drying of wool increases from approximately 5 kcal./mole at 5% water content to approximately 16 kcal./mole at dryness.¹⁷

This suggests that at low relative humidities water is first sorbed onto amino groups, then onto carboxyl and hydroxyl groups as the water content of the system increases. Removal or inactivation of these polar groups would therefore be expected to have a profound effect on the wool-water isotherm, particularly in the low humidity region.

The curves in Figure 1 compare the water vapor isotherms for the three deaminated wool samples a, c, and e with that for untreated wool.

The isotherms are considerably modified by deamination, but the reduction in water content is not proportional over the entire isotherm. For treatment e the equilibrium water content (e.w.c.) is reduced by approximately 30% at low humidities, while at 80% relative humidity the reduction is of the order of 17%. These changes are contrary to those observed by Speakman,¹⁰ probably owing to the more severe deamination conditions used in the present study since increased severity of treatment results in greater reductions in water content. It is possible that conformational changes in the keratin structure occurred during the deamination treatment as indicated by the increased water uptake in the solution region of the isotherms. Any effect on the wool-water isotherm owing to degradative action will be restricted to the solution

(12) J. B. Speakman, *Trans. Faraday Soc.*, **40**, 6 (1944).

(13) I. C. Watt, *Textile Res. J.*, **32**, 1035 (1962).

(14) G. H. Elliott and J. B. Speakman, *J. Soc. Dyers Colourists*, **59**, 185 (1943).

(15) J. A. Maclaren, *Arch. Biochem. Biophys.*, **86**, 175 (1960).

(16) J. S. L. Philpot and P. A. Small, *Biochem. J.*, **32**, 542 (1938).

(17) I. C. Watt, R. H. Kennett, and J. F. P. James, *Textile Res. J.*, **29**, 975 (1959).

(18) I. C. Watt, *ibid.*, **30**, 443 (1960).

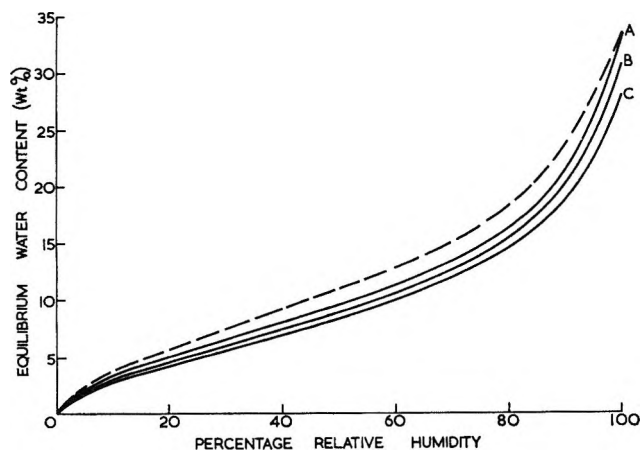


Figure 1. Water absorption isotherms at 35°: curve A, treatment a; curve B, treatment c; curve C, treatment e; - - -, unmodified wool.

region of the isotherm,⁶ *i.e.*, above 80% relative humidity.

The curves in Figure 1 indicate less water uptake in the solution region as the severity of treatment increases despite an expected increase in degradation. However, the reduced water content and consequent reduction in swelling of the fibers delays the onset of the solution region and decreases the water uptake at high humidities.

Deamination with the van Slyke reagent converts some amino groups to hydroxyl groups,^{9,10} so not all the amino groups will be converted to nonpolar residues. However, Valentine¹⁹ has shown that hydroxyl groups have very much lower sorbing powers than amino groups at 65% relative humidity, so any effect of new hydroxyl groups will be of secondary importance at this stage and will not affect the general conclusions of the present paper.

From the sorption isotherm data for the treated wools and the corresponding amino group analyses from Table I, values of equilibrium water contents have been taken at selected relative humidities and plotted against the number of residual basic groups in the manner used by Mellon, *et al.*,⁸ for benzoylated casein (see Figure 2).

The relationship in each case is linear except at the highest humidities, where structural modifications affect the water content. This linear relationship is significant since it demonstrates that even at low humidities all the amino groups are equally accessible to water vapor despite the complex morphological structure of wool keratin.

Extrapolation to zero basic group content at each relative humidity enables the isotherm shown as curve B of Figure 3 to be constructed. The difference be-

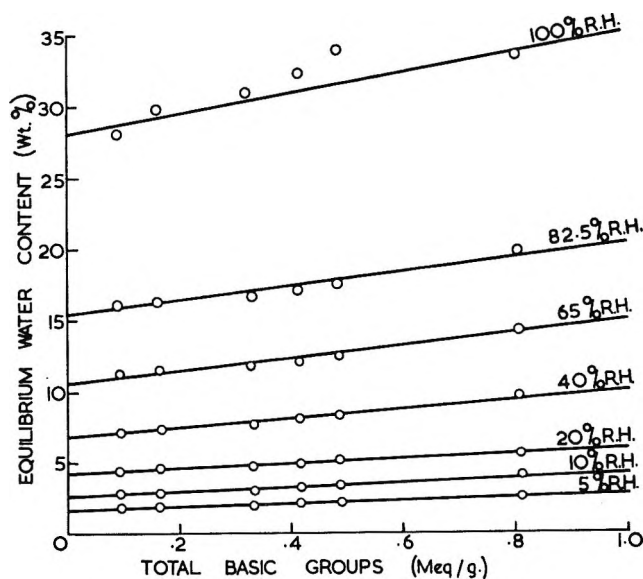


Figure 2. Equilibrium water content at 35° vs. residual amino group content, at various relative humidities.

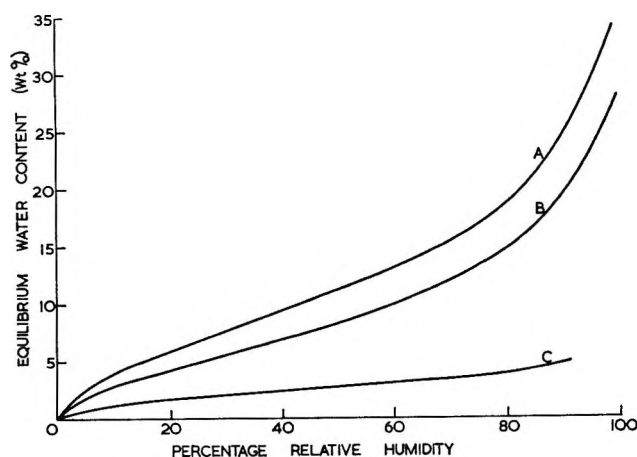


Figure 3. Water absorption isotherms at 35°: curve A, unmodified wool; curve B, wool containing no amino groups; curve C, difference curve, representing contribution of amino groups to the wool-water isotherm.

tween this isotherm and the isotherm of unmodified wool is represented by curve C of Figure 3. This curve may be considered as the water vapor isotherm of the amino groups in keratin. The curve no longer has a pronounced sigmoidal shape and may represent an isotherm of the Langmuir type for monomolecular absorption. For a Langmuir isotherm there is a linear relation between the reciprocal of the amount absorbed and the reciprocal of the relative pressure.

Curves A and C of Figure 3 are replotted in this way to give the corresponding curves A and C of Figure 4.

(19) L. Valentine, *Ann. Sci. Textiles Belges*, 4, 206 (1955).

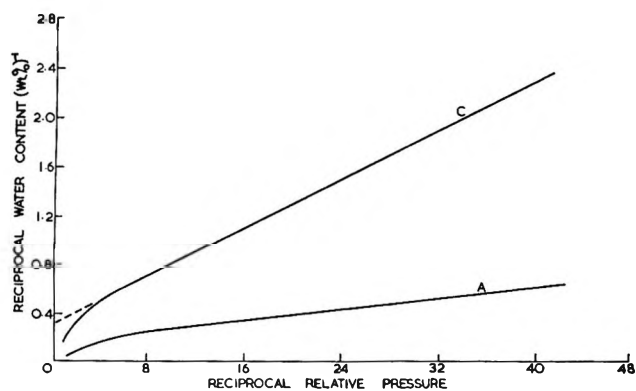


Figure 4. Reciprocal water content vs. reciprocal relative pressure for curves of Figure 3: curve A, unmodified wool; curve C, contribution of the amino groups.

The dotted line is an extrapolation of the linear portion of curve C. For curve C the relation is linear up to 25% relative humidity, but at higher pressures there is a greater uptake than would be expected for a simple Langmuir isotherm. The Langmuir plot for unmodified wool (curve A of Figure 4) shows a very limited linear region.

A Langmuir isotherm implies that there is a definite number of sites available for absorption and that each site is independent of its neighbors. Deviations from the Langmuir isotherm at high water vapor pressures may occur for several reasons. For example, if swelling of the wool makes the amino groups accessible to more than one water molecule, the ratio of new sites becoming available to the number of existing unfilled "Langmuir" sites may become appreciable. It is also possible that multimolecular absorption occurs at high relative humidities. On the other hand, interaction between the absorbed water molecules may occur when a large proportion of the available sites becomes occupied.

The linear portion of curve C, Figure 4, can be extrapolated to zero reciprocal relative pressure. From the intercept on the ordinate the saturation value can be calculated to be approximately 3.4% water content. This corresponds to the value obtained at 70% relative humidity for the amino groups represented by curve C of Figure 3.

The average number of water molecules associated with each amino group at various water vapor pressures can be calculated. At 25% relative humidity, where the amino group absorption deviates from the Langmuir isotherm, there are approximately 1.4 water molecules per amino group, while at 65% relative humidity a value of approximately 2.6 water molecules per amino group is obtained. This latter value is in excellent agreement

with that arrived at by Mellon, *et al.*,⁸ for amino groups in casein.

The amino group is capable of forming three hydrogen bonds,²⁰ so a completely accessible group would probably associate with three water molecules. This saturation of amino groups occurs at approximately 80% relative humidity (from curve C of Figure 3). Above 80% relative humidity the additional absorption probably represents attachment of water to water already on the amino groups. The extrapolation of the Langmuir plot (curve C, Figure 4) predicts a value of 2.7 water molecules for each amino group at saturation. Therefore, any interaction between the three possible water molecules has not prevented the available sites from being utilized; *i.e.*, the energy of interaction between sorbed water molecules is secondary in value to the energy of interaction between amino groups and water molecules.

The high energy of bonding of 16.8 kcal./mole of water to an amino group would only be true for one water molecule. It is possible that a single water molecule could be attached through two, or even three, hydrogen bonds to an amino group at low humidities, resulting in a high energy of attachment. Nuclear magnetic resonance studies²¹ and measurement of activation energies of drying¹⁷ have shown that there is a smooth decrease in energy of binding of water to keratin with increase in water content, indicating that each increment of water reduces the average strength of attachment of water molecules already present in the wool. However, this will have no effect on the low humidity region of the isotherm.

The attachment of water to specific groups in wool at humidities up to 80% relative humidity can be equated with these changes in energy of binding as follows. For amino groups, initial absorption from dryness would occur with high energy of binding; whereas, when two and finally three water molecules become associated with each amino group as sorption proceeds, the average energy of binding of each water molecule would be expected to decrease. There would not be sharp changes in experimentally observed binding energies as absorption increased from 1 to 2 to 3 water molecules per amino group since, at any particular humidity, there would be certain proportions of amino groups having one, two, and three associations with water molecules, depending on the energy of attachment and the accessibility and steric environment of each particular amino group.

(20) O. L. Sponsler, J. D. Bath, and J. W. Ellis, *J. Phys. Chem.*, **44**, 996 (1940).

(21) G. W. West, A. R. Haly, and M. Feughelman, *Textile Res. J.*, **31**, 899 (1961).

Thus, binding of water by amino groups constitutes a large percentage of the over-all sorption capacity of wool and is proportionately greater at low humidities.

This result is in contrast to the deduction of Breuer²² that peptide groups are the primary water-binding sites. Other hydrophilic side chains and the peptide groups all contribute to water absorption²³ but not to a greater extent than the amino side chains, especially at low humidities.

Previous work⁶ has shown that "solution" or "condensation" absorption becomes a measurable component of the water content at 80% relative humidity; *i.e.*, incoming sorbate molecules condense on water already present in the wool, so the present results may indicate that attachment of water to specific sorption sites is the main mechanism of sorption up to as high as 80% relative humidity, multimolecular absorption only occurring at higher pressures. It has been shown²⁴⁻²⁶ that volume swelling is less than volume sorption at low water contents, and does not become proportional to volume sorption until 20% water con-

tent, *i.e.*, at 80% relative humidity for unmodified wool. This reduced swelling is partly due to filling of voids and partly due to "electrostriction" of water molecules around charged groups in the protein.^{27,28}

It is significant that electrostriction of water by the amino groups would only occur up to the point where they become saturated with water molecules. Above 80% relative humidity, swelling is proportional to volume absorption, and it is in this region that electrostriction by the amino groups is no longer operative.

(22) M. M. Breuer, *J. Phys. Chem.*, **68**, 2067 (1964).

(23) J. D. Leeder and I. C. Watt, in preparation.

(24) F. L. Warburton, *J. Textile Inst. Trans.*, **38**, T65 (1947).

(25) J. L. Morrison and J. F. Hanlan, *Nature*, **179**, 528 (1957).

(26) J. H. Bradbury and J. D. Leeder, *J. Appl. Polymer Sci.*, **7**, 545 (1963).

(27) J. T. Edsall in "The Proteins," Vol. 1B, H. Neurath and K. Bailey, Ed., Academic Press, Inc., New York, N. Y., 1953, p. 565.

(28) J. H. Bradbury, *J. Appl. Polymer Sci.*, **7**, 557 (1963).

The Electronegativity of Groups

by James E. Huheey¹

Division of Chemistry, Worcester Polytechnic Institute, Worcester, Massachusetts (Received February 15, 1965)

The electronegativities of 99 groups have been calculated by assuming variable electronegativity of the central atom in the group and equalization of electronegativity in all bonds. The resulting values are compared with those obtained by previous methods. It is suggested that one of the most important aspects of the electronegativity of groups is the relatively low values of the charge coefficients which have the effect of promoting charge transfer.

Electronegativity was originally defined² as an invariant property of atoms. Recently, several workers³⁻⁷ have suggested that the electronegativity of an atom depends upon the environment of that atom in a molecule. For example, Walsh³ concluded that the electronegativity of carbon was dependent upon the hybridization of the atom. Sanderson⁴ suggested

that the electronegativity of an element depended upon its oxidation state, and Pritchard and Sumner⁵ in-

(1) Department of Chemistry, University of Maryland, College Park, Md.

(2) L. Pauling and D. M. Yost, *Proc. Natl. Acad. Sci. U. S.*, **14**, 414 (1932); L. Pauling, "The Nature of the Chemical Bond," 3rd Ed., Cornell University Press, Ithaca, N. Y., 1960.

roduced variable electronegativity in a molecular orbital context. Recently, Iczkowski and Margrave⁶ defined electronegativity as the derivative of ionization energy with respect to charge. These ideas have been extended by Jaffé and co-workers,⁷ who introduced the idea of *orbital electronegativity*. In this treatment, the electronegativity of an atom depends upon the nature of the orbital involved and upon the occupancy of that orbital.

Sanderson^{4,8} has proposed that electronegativity is equalized upon covalent bond formation. He suggested that the equalized value is equivalent to the geometric mean of the values of the constituent atoms. Iczkowski and Margrave⁶ and Jaffé⁷ have suggested that electronegativity is equalized to give a minimum in the ionization potential and electron affinity energy. The ionization potential (I) and electron affinity (A) obey the relationship

$$E = k'q + k''q^2 + k''' \quad (1)$$

where E is the energy of the atom and q is the charge on the atom. The minimum for the sum of the I - A energies for a diatomic molecule will occur when the charge on each atom causes its electronegativity to equal that of the other atom.

If the neutral atom is defined as zero energy, eq. 1 can be written in terms of partial charge⁹ as

$$E = a\delta + \frac{b}{2}\delta^2 \quad (2)$$

where δ is the partial charge resulting from electron gain or loss and where¹⁰

$$a = \frac{I - A}{2} \quad (3)$$

$$b = I + A \quad (4)$$

The orbital electronegativity is defined⁷ as

$$\chi = dE/d\delta = a + b\delta \quad (5)$$

where a may be termed the "inherent electronegativity" which corresponds approximately to the fixed electronegativity of previous workers, and b may be termed the charge coefficient.

Estimation of charge transfer is now simply a matter of setting the electronegativity function of one atom equal to that of the other and solving for the value of δ . For example, the partial charges on the atoms of the hydrogen chloride molecule can be calculated¹¹

$$\chi_{\text{H}} = 7.17 + 12.85\delta_{\text{H}} \quad (6)$$

$$\chi_{\text{Cl}} = 9.38 + 11.30\delta_{\text{Cl}} \quad (7)$$

$$\delta_{\text{H}} + \delta_{\text{Cl}} = 0 \quad (8)$$

$$7.17 + 12.85\delta_{\text{H}} = 9.38 - 11.30\delta_{\text{H}} \quad (9)$$

$$\delta_{\text{H}} = \frac{2.21}{24.15} = +0.092 \quad (10)$$

Values obtained by this method are generally somewhat lower than previous estimates.^{2,12} In the example given, the valence state chosen for chlorine was $s^2p^2p^2p^1$. Undoubtedly, the bonding orbital contains some s character which will increase the electronegativity of the chlorine.

The assumption of electronegativity equalization ignores energies arising from electrostatic ("ion-ion") interactions¹³ and changes in overlap.¹⁴ For bonds which have a high degree of ionic character this is serious, but for predominantly covalent bonds the errors incurred are small. The errors resulting from neglect of changes in electrostatic and overlap terms have opposing effects and tend to cancel each other; both approach zero as δ approaches zero.

These recent advances in our understanding of electronegativity make possible a better estimate of the distribution of charges in molecules. The electronegativity of an atom will increase as the charge density decreases because of reduced shielding.⁴ Since this will affect all orbitals in the atom, one can compute the electronegativity of a group if it is possible to compute the charge induced on the central atom by the substituent groups. Jaffé and co-workers^{7b} have thus been able to use a reiterative method to calculate the electronegativities of groups.

Previous efforts to obtain group electronegativities

(3) A. D. Walsh, *Discussions Faraday Soc.*, **2**, 18 (1947).

(4) R. T. Sanderson, *J. Chem. Educ.*, **31**, 2 (1945).

(5) H. O. Pritchard and F. H. Sumner, *Proc. Roy. Soc. (London)*, **A235**, 136 (1956).

(6) R. P. Iczkowski and J. L. Margrave, *J. Am. Chem. Soc.*, **83**, 3547 (1961).

(7) (a) J. Hinze and H. H. Jaffé, *ibid.*, **84**, 540 (1962); (b) J. Hinze, M. A. Whitehead, and H. H. Jaffé, *ibid.*, **85**, 148 (1963); (c) J. Hinze and H. H. Jaffé, *J. Phys. Chem.*, **67**, 1501 (1963).

(8) R. T. Sanderson, "Chemical Periodicity," Reinhold Publishing Corp., New York, N. Y., 1960.

(9) Jaffé and co-workers⁷ used the occupancy number (n) in setting up their relationships. In the present discussion, the partial charge (δ) is used instead. Otherwise, the methods are the same.

(10) The sign convention used here for ionization energies and electron affinities is to assign a negative sign to an exothermic reaction and a positive sign to an endothermic reaction when written as: $X \pm e^- \rightarrow X^\mp$.

(11) For convenience, all electronegativities will be used on Mulliken's scale. The relationship between this scale and that of Pauling is: $\chi_{\text{P}} = 0.336(\chi_{\text{M}} - 0.615)$ (ref. 7).

(12) For a review of methods based on fixed electronegativity values see H. O. Pritchard and H. A. Skinner, *Chem. Rev.*, **55**, 745 (1955).

(13) R. P. Iczkowski, *J. Am. Chem. Soc.*, **86**, 2329 (1964).

(14) H. P. Pritchard, *ibid.*, **85**, 1876 (1963).

have been largely empirical in nature. For example, estimates have been obtained from infrared,¹⁵ solubility,¹⁶ basicity and coupling potential,¹⁷ and n.m.r.¹⁸ data. Clifford¹⁶ has pointed out that reasonable values may often be obtained by simply averaging the individual electronegativity values of the atoms comprising a group.

It is the purpose of this paper to apply the recently developed methods to the calculation of electronegativities of groups. The present method does not appear to differ significantly from that of Jaffé, in principle, but permits simple and straightforward computations.

Methods

The values of ionization potential and electron affinity computed by Jaffé and co-workers⁷ have been used to derive values of a and b for appropriate valence states for various atoms. These values are listed in Table I.

For the illustration of the calculation of group electronegativity, the methyl group will be used as an example. The electronegativity of this group is not that of unbonded tetrahedral carbon ($\chi_{C_{te}}$) *per se* but the adjusted electronegativity of a carbon atom in the environment of three hydrogen substituents.^{19,20}

Not only will the inherent electronegativity differ from that of carbon, but the ability of the peripheral hydrogen atoms to absorb or dispense charge will cause a great difference in the charge coefficient of the group.

The calculation for the methyl group involves the following steps.

(1) Calculation of the charge distribution and resultant adjusted electronegativity of a neutral methyl group (free radical)

$$\chi_{C_{te}} = 7.97 + 13.27\delta_C = \chi_H = 7.17 + 12.85\delta_H \quad (11)$$

$$\delta_C + 3\delta_H = 0 \quad (12)$$

$$7.97 - 3(13.27)\delta_H = 7.17 + 12.85\delta_H \quad (13)$$

$$\delta_H = \frac{0.80}{52.66} = 0.015 \quad (14)$$

$$\chi_{CH_3} = 7.37 = a_{CH_3} \quad (15)$$

(2) Calculation of the charge distribution of either the methyl cation or the methanide anion. For the methyl cation, the same equations hold except that

$$\delta_C + 3\delta_H = +1 \quad (16)$$

Solving, we get

$$\delta_H = +0.27 \quad (17)$$

$$\chi_{CH_3^+} = 10.63 \quad (18)$$

Table I: Electronegativities of Some Common Elements

At. no.	Element	Hybridization ^a	a	b
1	H	s	7.17	12.85
3	Li	s	3.10	4.57
4	Be	di	4.78	7.59
5	B	tr	6.33	9.91
		te	5.99	8.90
6	C	p	5.80	10.93
		te	7.98	13.27
		tr	8.79	13.67
		di	10.39	14.08
		s	14.96	12.10
7	N	p	7.39	13.10
		23% s	11.21	14.64
		te	11.54	14.78
8	O	p	9.65	15.27
		20% s	14.39	17.65
		te	15.25	18.28
		26.4% s	15.50	18.37
9	F	p	12.18	17.36
11	Na	s	2.80	4.67
12	Mg	di	4.09	6.02
13	Al	tr	5.47	6.72
		te	5.38	5.59
14	Si	te	7.30	9.04
15	P	p	6.08	9.31
		te	8.90	11.33
16	S	p	7.39	10.01
		te	10.14	10.73
17	Cl	p	9.38	11.30
		te	11.84	10.87
32	Ge	te	8.07	6.82
35	Br	p	8.40	9.40
50	Sn	te	7.90	5.01
53	I	p	8.10	9.15

^a Symbols are as follows: s and p represent the unhybridized orbitals; di = sp, digonal; tr = sp², trigonal; te = sp³, tetrahedral.

Similarly, for the methanide ion we get

$$\delta_H = -0.24 \quad (19)$$

$$\chi_{CH_3^-} = 4.05 \quad (20)$$

Now, these three values of χ for the methyl group lie

(15) (a) R. E. Kagarise, *J. Am. Chem. Soc.*, **77**, 1377 (1955); (b) J. V. Bell, J. Heisler, H. Tannenbaum, and J. Goldenson, *ibid.*, **76**, 5185 (1954); (c) J. K. Wilmshurst, *J. Chem. Phys.*, **26**, 426 (1957); (d) J. K. Wilmshurst, *Can. J. Chem.*, **35**, 937 (1957); (e) J. K. Wilmshurst, *J. Chem. Phys.*, **28**, 733 (1958).

(16) A. F. Clifford, *J. Phys. Chem.*, **63**, 1227 (1959).

(17) D. H. McDaniel and A. Yingst, *J. Am. Chem. Soc.*, **86**, 1334 (1964).

(18) B. P. Dailey and H. N. Shoolery, *ibid.*, **77**, 3977 (1955).

(19) This approach to group electronegativity seems to have been suggested first by Wilmshurst²⁰ and was further developed by Hinze, Whitehead, and Jaffé.^{7b}

(20) J. K. Wilmshurst, *J. Chem. Phys.*, **27**, 1129 (1957).

on a straight line when plotted *vs.* charge, and we can get the slope of that line to give

$$\chi_{\text{CH}_3} = 7.37 + 3.24\delta_{\text{CH}_3} \quad (21)$$

For more general cases, we have the following situations.

(1) *Group-WX*. Using the set of equations

$$a_w + b_w\delta_w = a_x + b_x\delta_x \quad (22)$$

$$\delta_w + \delta_x = 0 \quad (\text{radical}) \quad (23)$$

$$\delta_w + \delta_x = 1 \quad (\text{cation}) \quad (24)$$

$$\delta_w + \delta_x = -1 \quad (\text{anion}) \quad (25)$$

we obtain

$$\chi_{-WX} = \frac{a_w b_x + a_x b_w + b_w b_x \delta_{WX}}{b_x + b_w} \quad (26)$$

(2) *Group-W < X*. Using the equations

$$a_w + b_w\delta_w = a_x + b_x\delta_x = a_y + b_y\delta_y \quad (27)$$

$$\delta_w + \delta_x + \delta_y = 0 \quad (\text{radical}) \quad (28)$$

$$\delta_w + \delta_x + \delta_y = 1 \quad (\text{cation}) \quad (29)$$

$$\delta_w + \delta_x + \delta_y = -1 \quad (\text{anion}) \quad (30)$$

we obtain

$$\chi_{-WXY} = \frac{a_w b_x b_y + a_x b_w b_y + a_y b_w b_x + b_w b_x b_y \delta_{WXY}}{b_x b_y + b_w b_x + b_w b_y} \quad (31)$$

(3) *Group-W < Y*. Using the equations

$$a_w + b_w\delta_w = a_x + b_x\delta_x = a_y + b_y\delta_y = a_z + b_z\delta_z \quad (32)$$

$$\delta_w + \delta_x + \delta_y + \delta_z = 0 \quad (\text{radial}) \quad (33)$$

$$\delta_w + \delta_x + \delta_y + \delta_z = 1 \quad (\text{cation}) \quad (34)$$

$$\delta_w + \delta_x + \delta_y + \delta_z = -1 \quad (\text{anion}) \quad (35)$$

we obtain

$$\chi_{WXYZ} = \frac{a_w b_x b_y b_z + a_x b_w b_y b_z + a_y b_w b_x b_z + a_z b_w b_x b_y + b_w b_x b_y b_z \delta_{WXYZ}}{b_x b_y b_w + b_x b_z b_w + b_x b_y b_z + b_y b_z b_w} \quad (36)$$

Discussion

Before examining the results of the present series of computations, it will be profitable to examine briefly the differences between a system of electronegativities,

based on an invariant value for each element,^{2,12} and one which allows the electronegativity to vary as a function of charge. If the latter concept has any validity, it may be surprising that a fixed scale has any meaning whatsoever. For example, most elements approximately double their electronegativities as the partial charge approaches +1 (occupancy approaches zero) whereas their electronegativities essentially disappear as the partial charge approaches -1 (occupancy approaches 2). That both systems give similar qualitative results stems from the fact that the charge coefficient (*b*) is of the same order of magnitude for most elements. Thus, the electronegativities of the elements increase and decrease at approximately the same rate, and for simple qualitative calculations they can be (and *have* been) ignored in diatomic molecules. This can be demonstrated by the following calculation. Consider, for example, the diatomic molecule AB. The charge on A can be found as before

$$\chi_A = a_A + b_A\delta_A = \chi_B = a_B + b_B\delta_B \quad (37)$$

$$\delta_A = -\delta_B \quad (38)$$

$$\delta_A = \frac{a_B - a_A}{b_A + b_B} \quad (39)$$

If all values of *b* were equal, eq. 39 would become

$$\delta_A = \frac{a_B - a_A}{K} = K'(\Delta\chi) \quad (40)$$

Such a linear dependence of ionic character on differences in electronegativity has been suggested by Gordy,²¹ and Wilmshurst²² has suggested that the ionic character is best given by

$$\delta_A = \frac{\chi_B - \chi_A}{\chi_A + \chi_B} \quad (41)$$

Equation 41 was proposed on an empirical basis but actually is closely related to eq. 39. Written in terms used in the present paper, it becomes

$$\delta_A = \frac{a_B - a_A}{a_A + a_B} \quad (42)$$

since *a* represents the Mulliken electronegativity of A and B. This expression is roughly proportional to eq. 39 because the values of *a* and *b* for an element parallel each other.

The electronegativity of a group of more than one element does not have a charge coefficient similar to a single atom. It is found that the charge coefficient

(21) W. Gordy, *J. Chem. Phys.*, **14**, 304 (1946); **19**, 792 (1951).

(22) J. K. Wilmshurst, *ibid.*, **30**, 561 (1959).

Table II: Group Electronegativities

Group	% s ^a	a	b	x _P ^b	x _J ^c	x _C ^d	x _S ^e	Other
BeH	50	5.67	4.77	1.89		1.81	1.76	
BeF	50	7.04	5.28	2.16		2.65	2.34	
BeCl	50	6.63	4.54	2.02		2.18		
BeBr	50	6.40	4.20	1.94		2.01		
BeI	50	6.29	4.15	1.91		1.96		
BeCH ₃	50	6.60	2.27	2.01		2.10		
MgH	50	5.07	4.10	1.50		1.69	1.61	
MgF	50	6.17	4.47	1.87		2.54	2.14	
MgCl	50	5.93	3.93	1.79		2.06		
MgBr	50	5.77	3.67	1.73		1.90		
MgI	50	5.68	3.63	1.70		1.85		
MgCH ₃	50	6.22	2.11	1.88		2.06		
BH ₂	33	6.82	3.75	2.09		2.12	2.11	
BF ₂	33	9.31	4.42	2.92		3.24	3.08	
BCl ₂	33	8.20	3.47	2.55		2.61		
BBr ₂	33	7.68	3.09	2.38		2.39		
BI ₂	33	7.46	3.03	2.30		2.32		
B(CH ₃) ₂	33	7.26	1.38	2.23		2.24		
CH ₃	25	7.37	3.24	2.27	2.30	2.28	2.27	2.34 ^f 2.63 ^g
CH ₃ CH ₂	25	7.40	1.85	2.28		2.29		
(CH ₃) ₂ CH	25	7.41	1.30	2.28		2.29		
(CH ₃) ₃ C	25	7.42	1.00	2.29		2.29		
CH ₂ F	25	8.38	3.46	2.61	2.61	2.70		
CHF ₂	25	9.55	3.73	3.00	2.94	3.12		
CF ₃	25	10.90	4.03	3.46	3.29	3.55	3.49	
CF ₃ CF ₂	25	10.73	2.28	3.40		3.49		
(CF ₃) ₂ CF	25	10.67	1.59	3.38		3.47		
(CF ₃) ₃ C	25	10.63	1.22	3.37		3.46		
CF ₃ CH ₂	25	9.23	2.09	2.90		3.01		
(CF ₃) ₂ CH	25	10.11	1.54	3.19		3.31		
CH ₂ Cl	25	7.97	3.13	2.47	2.47	2.46	2.44	2.48 ^f 2.74 ^g
CHCl ₂	25	8.54	3.03	2.66	2.63	2.65	2.63	2.62 ^f 2.88 ^g
CCl ₃	25	9.07	2.93	2.84	2.79	2.83	2.82	2.76 ^f 3.03 ^g
CH ₂ Br	25	7.74	2.95	2.40	2.40	2.38		2.44 ^f
CHBr ₂	25	8.05	2.73	2.50	2.49	2.48		2.55 ^f
CBr ₃	25	8.32	2.53	2.59	2.57	2.59		2.65 ^f
CH ₂ I	25	7.65	2.94	2.37	2.38	2.36		
CHI ₂	25	7.88	2.69	2.44	2.44	2.43		
CI ₃	25	8.08	2.48	2.51	2.50	2.51		
CHFCl	25	8.99	3.34	2.82		2.89		
CHClBr	25	8.28	2.87	2.58		2.57		
CHBrI	25	7.96	2.71	2.47		2.46		
CFCI ₂	25	9.23	3.05	2.90		2.99		
CClBrI	25	8.46	2.64	2.64		2.64		
CH ₂ OH	25	8.77	2.74	2.74		2.52		
SiH ₃	25	7.20	3.14	2.21		2.22	2.22	
SiF ₃	25	10.58	3.88	3.35		3.49	3.40	
SiCl ₃	25	8.88	2.86	2.78		2.78		
SiBr ₃	25	8.17	2.48	2.54		2.53		
SiI ₃	25	7.94	2.42	2.46		2.45		
Si(CH ₃) ₃	25	7.36	0.99	2.27		2.28		
GeH ₃	25	7.52	2.63	2.32		2.28	2.28	
GeF ₃	25	10.29	3.13	3.25		3.55	3.49	
GeCl ₃	25	8.91	2.43	2.79		2.84		
GeBr ₃	25	8.30	2.15	2.58		2.59		
GeI ₃	25	8.09	2.11	2.51		2.52		

Table II (Continued)

Group	% s ^a	a	b	χ_P^b	χ_I^e	χ_C^d	χ_B^c	Other		
Ge(CH ₃) ₃	25	7.47	0.93	2.19		2.29				
SnH ₃	25	7.51	2.31	2.32		2.27	2.27			
SnF ₃	25	9.89	2.69	3.11		3.54	3.48			
SnCl ₃	25	8.74	2.15	2.73		2.82				
SnBr ₃	25	8.21	1.93	2.55		2.58				
SnI ₃	25	8.02	1.90	2.49		2.50				
Sn(CH ₃) ₃	25	7.47	0.89	2.30		2.29				
NF ₂	17.8	11.46	5.40	3.64		3.62	3.60			
NCl ₂	(25)	9.98	4.01	3.14		2.99				
NH ₂	22.9	8.39	4.47	2.61	2.82	2.50	2.47	1.7 ^h	2.99 ⁱ	3.40 ^g
NHCH ₃	(22.9)	7.91	2.20	2.45		2.40		3.0 ^h		
N(CH ₃) ₂	23.0	7.75	1.46	2.40		2.37		3.0 ^h		
NHC ₂ H ₅	(23.0)	7.75	1.46	2.40		2.37		3.0 ^h		
N(C ₂ H ₅) ₂	(23.0)	7.64	0.87	2.36		2.34		3.0 ^h		
NHOH	(22.9)	10.01	3.56	3.16		2.75				
NHNH ₂	(22.9)	8.45	2.63	2.63		2.55				
PF ₂	19.5	10.42	4.83	3.29		3.29	3.15			
PCl ₂	14.8	8.70	3.67	2.71		2.65	2.62			
PBr ₂	16.6	8.24	3.25	2.56		2.43				
PH ₂	5.4	6.95	3.67	2.13	2.06	2.16	2.16			
P(CH ₃) ₂	13.7	7.39	1.40	2.28		2.25				
P(C ₂ H ₅) ₂	(13.7)	7.43	0.85	2.29		2.27				
OF	18.6	12.95	8.70	4.14 ^j		3.70	3.70			
OCl	26.2	11.72	7.00	3.73		3.23				
OBBr	(25)	10.73	6.21	3.40		3.06				
OH	20.0	10.21	7.44	3.51	3.53	2.86	2.78	2.3 ^h	3.6 ^k	3.89 ^g 3.51 ⁱ
OCH ₃	26.4	8.59	2.75	2.68		2.52	2.48	3.0 ^h		
OC ₂ H ₅	(26.4)	8.15	1.68	2.53		2.44	2.41	3.0 ^h		
OCF ₃	(26.4)	11.75	3.30	3.74		3.54				
SH	3.7	7.52	5.66	2.32	2.35	2.33	2.32	2.45 ⁱ	3.2 ^k	
SCH ₃	20.6	7.91	2.48	2.45		2.31	2.31	2.6 ^h		
SC ₂ H ₅	(20.6)	7.74	1.58	2.39		2.31				

^a Group II elements assumed to be sp; group III elements assumed to be sp²; group IV elements assumed to be sp³. Bond angles used to estimate s character in elements of groups V and VI: C. A. Coulson, "Valence," Oxford University Press, London, 1952, p. 193. Values in parentheses are assumed where no data on bond angles were available. ^b Calculated inherent electronegativity (*a*) in Pauling units for purposes of comparison to literature values given in following columns. ^c Calculated by Jaffé (ref. 7). ^d Calculated by the method of Clifford (ref. 16) using electronegativity values of Jaffé (ref. 7) except for elements of groups V and VI. Values for these elements were those given by E. J. Little and M. M. Jones, *J. Chem. Educ.*, **37**, 231 (1960). ^e Calculated by the method of Sanderson (ref. 8) using the same values as in *d*. ^f See ref. 15a. ^g See ref. 20. ^h See ref. 15b. ⁱ See ref. 18. ^j Reference 23 cites a value of 3.40 in error. ^k See ref. 17.

decreases approximately inversely as the number of atoms in the group. This can be shown simply by assuming that

$$b_w = b_x = b_y = b_z \quad (43)$$

Equation 35 becomes

$$\chi_{wxyz} + \frac{a_w + a_x + a_y + a_z + b\delta}{4} \quad (44)$$

or for the more general case

$$\chi = \frac{\Sigma a}{n} + \frac{b}{n} \delta \quad (45)$$

Term two of eq. 45, which now represents *b* of the group, is inversely proportional to *n*. Under such conditions the charge coefficient can no longer be ignored, even for rough qualitative calculations. A low value of *b* has the effect of increasing the apparent electronegativity of those groups bonded to a more electropositive element and of decreasing the apparent electronegativity of groups bonded to a more electronegative element. In other words, the low value of *b* "buffers" the electronegativity of the group, and it takes a larger shift in charge to pull it up or down to equalize the electronegativity of the element to which it is bonded. This

has been pointed out previously by Sanderson⁸ and may readily be seen from the equation for ionicity⁷

$$i = \frac{a_A - a_B}{b_A + b_B} \quad (46)$$

The group electronegativities calculated by the present method are given in Table II.²³ First, it may be noted that the values obtained are approximately the same as those obtained by the method of Clifford.¹⁶ This would be expected if all elements had the same value for b (*cf.* first term, eq. 45).

Although Sanderson^{4,8} did not discuss group electronegativity *per se*, his method may be used to calculate such values. It will be noted that values obtained by this method also are generally in good agreement with the results of the present method.

Secondly, it can be seen that the charge coefficient (b) is as important in determining the electronegativity of a group as is its inherent (uncharged) electronegativity (a). For example, the methyl group is generally considered to be a better electron donor than the hydrogen atom. However, the inherent electronegativity of the methyl group is slightly higher than hydrogen as might be expected from the higher electronegativity of carbon ($\chi_C = 7.97$; $\chi_H = 7.17$). However, when bonded to more electronegative groups (as is usually the case), the methyl group can better absorb the increasing positive charge; and, for partial charges in excess of about +0.02, the methyl group is less electronegative, as is observed experimentally. This effect is portrayed graphically in Figure 1, where the electronegativities of hydrogen and alkyl groups have been plotted as functions of charge. Initially, the higher ("carbon-rich") members of the aliphatic series have higher electronegativities, but, because their slopes (b) are small, hydrogen soon overtakes them.

Figure 2 illustrates the same phenomenon with respect to negative groups. In plots of this type, the ionic character can be obtained by superposing the slopes of the two groups or elements, one gaining and the other losing electrons (*cf.* ref. 7). For illustrative purposes, fluorine has been added to Figure 1 and hydrogen to Figure 2.

Because of the variation of electronegativity with charge, single values for electronegativity have little value in themselves. This is especially true for groups. The Pauling unit values given in Table II (the "inherent" electronegativity) are useful in the following context. If two groups or atoms have the same inherent electronegativity, they will form a nonpolar bond. If they do not have identical values, the relative values of a determine the direction of bond

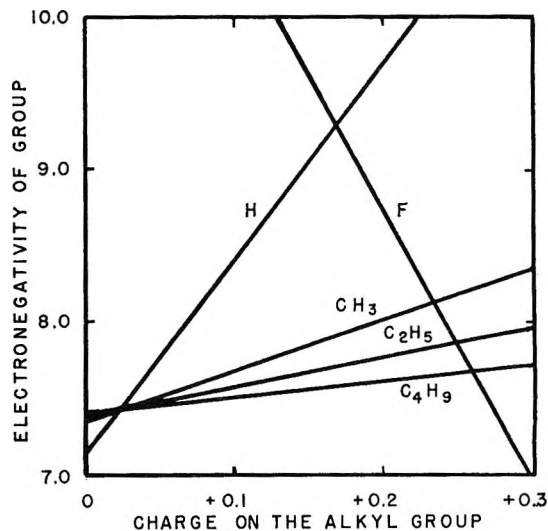


Figure 1. Electronegativity of hydrogen and alkyl groups plotted as a function of partial charge.

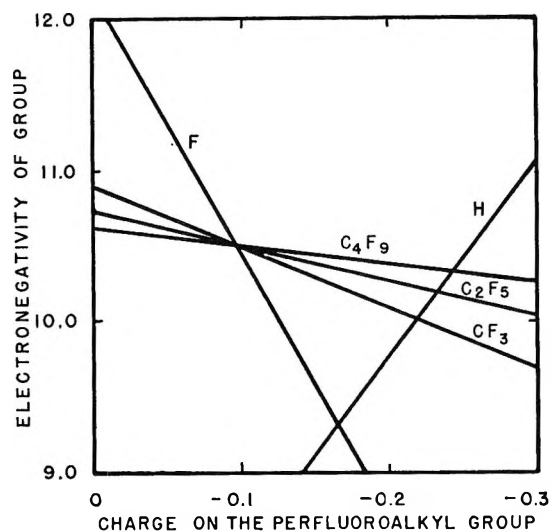


Figure 2. Electronegativity of fluorine and perfluoroalkyl groups plotted as a function of partial charge.

polarity, but it is necessary to utilize both a and b to determine *how* polar a particular bond will be.

It may be surprising to some that certain groups (*e.g.*, OF, OCl) appear to have *greater* electronegativities than any of the component atoms (O = 3.5, F = 3.9, Cl = 3.0, Pauling scale). However, it should be kept in mind that the commonly accepted fixed values for electronegativities are *average* values for various oxidation and valence states. The electronegativities of elements in groups V and VI will be especially suscep-

(23) Preliminary results for perhalo groups have been published previously: J. E. Huheey, *J. Phys. Chem.*, 68, 3073 (1964).

tible to variation in electronegativity through changes in *s* character. For example, depending upon whether it is using pure *p* orbitals or *sp*³ hybrid orbitals, oxygen can have an electronegativity of 3.04 to 5.93.⁷

Comparison of values from previous workers with those given here provides little information. The differences between the various sets of data reflect not only varying approaches to the problem but also the lack of a uniform scale with which to work. The electronegativities of the elements, presumably well known, differ by 0.1–0.2 unit, depending upon which scale is used, and this variability is often reflected in postulated group electronegativities. The values tabulated in Tables II and III represent those given by the original authors with the exception that values of χ_s and χ_c have been recalculated using the same values of *a* as used in the present series of calculations.

Despite the general irregularity, there seems to be good agreement between the values obtained here and

those from carbonyl frequency data^{15a} and from phosphoryl frequency data^{15b} with the exceptions of the anomalous values for OH and NH₂ of the latter. Values of other workers tend to be high, and this is probably a reflection of the treatment of electronegativity as an invariant value, neglecting the charge coefficient (*b*). As shown in the discussion above, the value of *b* greatly affects the amount of charge an atom or group can absorb and therefore affects its apparent electronegativity.

One of the advantages of the use of variable electronegativity is that it allows charged groups to be treated quite simply. The electronegativity equations for such groups are calculated as before, and the formal charge of the group is equated to δ to determine the electronegativity of the charged group. Electronegativities for some charged groups are given in Table III. It should be emphasized again that the single values given are based on the assumption of unit charge and that polarity in the bond between the group and a substrate will modify this.

One difficulty inherent in the present method is that isomeric groups will yield identical electronegativities (assuming that the hybridization does not differ). This is in contradiction to the empirical observation that a group such as FCH₂CH₂CH₂ has a quite different electronegativity from the CH₃CH₂CHF group. This "dilution" of polar effects is a result of the fact that electronegativity is not 100% equalized.¹⁴ By including a correction for the slight inequality of electronegativity, it should be possible to obtain better values for group electronegativities. Attempts are currently being made to correct this difficulty.

Acknowledgment. The author wishes to thank Dr. W. D. Hobey for stimulating discussions of the subject of electronegativity. Obviously, this does not imply agreement with all of the ideas presented here. C. A. Keisling helped with the figures.

Table III: Electronegativities of Charged Groups

Group ^a	<i>a</i>	<i>b</i>	χ^b	χ_P^c	χ_{it}^d
NH ₃ ⁺	8.15	3.32	11.47	3.65	3.3
NH ₂ CH ₃ ⁺	7.85	1.88	9.73	3.06	
NH(CH ₃) ₂ ⁺	7.77	1.49	9.26	2.91	
N(CH ₃) ₃ ⁺	7.65	1.01	8.66	2.70	
N(CH ₂ H ₆) ₃ ⁺	7.56	0.59	8.15	2.53	
N(<i>i</i> -Pr) ₃ ⁺	7.52	0.40	7.92	2.46	
N(<i>t</i> -Bu) ₃ ⁺	7.52	0.33	7.85	2.43	
OH ₂ ⁺	9.27	4.75	14.02	4.51	3.8
OHCH ₃ ⁺	8.31	2.26	10.57	3.35	
O(CH ₃) ₂ ⁺	8.01	1.49	9.50	2.99	
O(C ₂ H ₅) ₂ ⁺	7.78	0.88	8.66	2.70	

^a All groups assumed to be tetrahedral. ^b Value of χ for $\delta = +1$. ^c Electronegativities of charged groups in Pauling units. ^d See ref. 17.

Effects of Additives on the Radiolysis of Cyclohexane Vapor at 100°

by Leslie M. Theard

Sandia Laboratory, Albuquerque, New Mexico (Received February 19, 1965)

Effects of benzene, ethylene, propylene, cyclohexene, nitric oxide, iodine, and hydrogen iodide on the γ -radiolysis of cyclohexane vapor at 100° have been studied in an effort to determine some details of the radiation-induced energy degradation processes. Benzene, the olefins, and iodine markedly reduce the yield of hydrogen to a comparable degree, while nitric oxide reduces hydrogen considerably less, and hydrogen iodide increases hydrogen. Of the gaseous hydrocarbon products, determined in the presence of all the additives studied except ethylene and propylene, the unsaturated products (ethylene, propylene, and acetylene), which comprise the major fraction, are practically unaffected by benzene, cyclohexene, or nitric oxide. Iodine and hydrogen iodide do not affect the yields of ethylene and acetylene, but they reduce the yield of propylene. Yields of ethane and propane are reduced by several additives but are unaffected by hydrogen iodide. The observed additive effects on the gaseous products appear to be unattributable to ionization transfer. The olefins and benzene apparently reduce hydrogen yield by two processes which are suggested to be scavenging of hydrogen atoms and scavenging of ionic precursors of hot hydrogen atoms, where the scavengeable ions are not also precursors of gaseous hydrocarbon products. The increase of hydrogen yield by hydrogen iodide is explained by an electron-capture mechanism from which it is estimated that *ca.* 36% of the hydrogen yield for pure cyclohexane arises from neutralization of positive ions. Depression of hydrogen yield by iodine is explained by a combination of electron capture and hydrogen atom scavenging. It is suggested that reduction of the yield of propylene by I₂ and HI is attributable to electron capture and that reduction of the yields of ethane and propane by several additives is effected by scavenging of ethyl and propyl radicals.

Introduction

Studies of the radiolysis of cyclohexane vapor²⁻⁸ have been relatively limited, whereas studies of the radiolysis of cyclohexane liquid⁹ and effects of additives have been extensive and have provided insight into the nature of some important radiation-induced elementary processes. Included among these processes are energy (excitation or ionization) transfer^{2,10,11} and ion neutralization.¹²

In a study of the α -radiolysis of gaseous mixtures of cyclohexane and benzene, Ramaradhy and Freeman⁶ suggested that the depression of $G(\text{H}_2)$ by benzene is attributable principally to the transfer of energy, probably in the form of ionization, from cyclohexane to benzene. To the contrary, in a study of the γ -radiolysis of vapor phase cyclohexane-benzene mixtures, Dyne, *et al.*,⁶ suggested that energy (excitation or

ionization) transfer cannot account for depression of hydrogen by benzene. In another study of the latter system, Blachford and Dyne⁷ explained hydrogen

(1) This work was supported by the United States Atomic Energy Commission. Reproduction in whole or in part is permitted for any purpose of the U. S. Government.

(2) J. P. Manion and M. Burton, *J. Phys. Chem.*, **56**, 560 (1952).

(3) V. P. Henri, C. R. Maxwell, W. C. White, and D. C. Peterson, *ibid.*, **56**, 1953 (1952).

(4) J. M. Ramaradhy and G. R. Freeman, *J. Chem. Phys.*, **34**, 1726 (1961).

(5) J. M. Ramaradhy and G. R. Freeman, *Can. J. Chem.*, **39**, 1769 (1961).

(6) P. J. Dyne, J. Denhartog, and D. R. Smith, *Discussions Faraday Soc.*, **36**, 135 (1963).

(7) J. Blachford and P. J. Dyne, *Can. J. Chem.*, **42**, 1165 (1964).

(8) R. D. Doepker and P. Ausloos, Abstracts, 148th National Meeting of the American Chemical Society, Chicago, Ill., 1964, p. 48V.

(9) For a recent paper containing pertinent references see S. Z. Toma and W. H. Hamill, *J. Am. Chem. Soc.*, **86**, 1478 (1964).

depression as resulting from ion-molecule addition reactions of ion fragments (C_2-C_3) with benzene, as suggested by Borkowski and Ausloos¹³ for the *n*-butane-benzene system.

In the present study, effects of a variety of additives on cyclohexane vapor radiolysis have been studied in an effort to understand better the nature of the processes responsible for the additive effects. Effects of benzene, ethylene, propylene, and cyclohexene suggest that reduction of the yield of hydrogen is unattributable to charge transfer and is partially attributable to hydrogen atom scavenging. The remaining reduction of hydrogen is suggested to be attributable to scavenging of ionic precursors of hydrogen as suggested by Blachford and Dyne, but it is shown that these ions are not precursors also of measured gaseous hydrocarbon products. The yield of ionic precursors of hydrogen is estimated with the aid of an electron-capture mechanism suggested by effects of hydrogen iodide and iodine.

Experimental Section

Materials. Phillips Research grade cyclohexane was used from Lot No. 435 and 1078 with stated purities of 99.94 and 99.99 mole %, respectively. Chromatographic analysis using a silver nitrate- β,β' -oxydipropionitrile column showed cyclohexene present at concentrations of 0.09 mole % in Lot No. 435 and less than 0.001 mole %, the lower limit of detection, in Lot No. 1078. Samples used from both lots were successively passed through silica gel until the cyclohexene concentration was less than 0.001 mole %. Two impurities, 2,4-dimethylpentane and methylcyclopentane, each present at a concentration of ca. 0.005 mole %, were not removed by silica gel.

Phillips Research grade cyclohexane and benzene, Eastman White Label cyclohexene, and Fisher Certified reagent iodine (in cyclohexane) were dried over P_2O_5 prior to use. Phillips Research grade ethylene and propylene and Matheson hydrogen iodide and nitric oxide, the latter containing 3% nitrogen, were used as received. Attempts to remove the nitrogen impurity from nitric oxide were unsuccessful.

Apparatus and Sample Preparation. Cylindrical Pyrex radiolysis cells of ca. 15-cm. length, 7-cm. diameter, and 480-ml. volume were used. Two side arms were constructed 90° apart at one end of each cell, one of which was used for sample introduction and the other, fitted with a break-seal, for gaseous product collection. Prior to introducing the samples, the cells were pumped overnight at a pressure of ca. 5×10^{-6} mm. For 0.5 hr. prior to and for the duration of the irradiation, the samples were heated in a furnace

constructed of nichrome wire (or heating tape) wrapped around formed copper sheet with an outer covering of asbestos. Cell temperature was controlled at $100 \pm 2^\circ$ by a thermoregulator.

Cyclohexane samples and solutions were degassed by one of two methods. (1) Approximately 30-ml. lots of pure cyclohexane, after drying over P_2O_5 under vacuum, were distilled into a storage bulb and degassed by the microstill-reflux method.¹⁴ Individual samples were vacuum distilled as required into a calibrated volume for measurement and subsequently into the radiolysis cells. (2) Individual pipetted samples, dried over P_2O_5 under vacuum, were degassed by successive freeze-pump-thaw cycles at -196 and -78° and distilled into the radiolysis cells. By adjustment of the amounts of cyclohexane and additives, total pressure of the samples at 100° was maintained at ca. 100 cm.

Irradiation and Dosimetry. Samples were irradiated with γ -rays from a 2000-curie Co^{60} source. The dose rate (ca. 2×10^{19} e.v./g. hr. for cyclohexane vapor) determination was based on measuring H_2 produced from ethylene (at 1-atm. pressure and 23°) and assuming $G(H_2) = 1.28$.¹⁵ Extrapolation to the samples under study was made on the basis that energy absorption is proportional to electron density. Total dose for most runs was ca. 3×10^{19} e.v./g. In order to determine zero-dose yields by extrapolation, several samples were irradiated at doses ranging from 1.7×10^{18} to 2.1×10^{20} e.v./g.

Analysis. Hydrogen in the product gases volatile at -196° was determined from the pressure difference before and after passage through a heated palladium thimble (270°). Residual gases (ca. 5%) collected at -196° were mixed with the measured gas fraction collected at -110° by the microstill-reflux method.¹⁴ This sample was then mixed with a measured comparable amount of cyclopropane which was used as a quantitative marker for chromatographic analysis.¹⁶ The gaseous mixture was analyzed chromatographically by use of dibutyl maleate and silica gel columns. Separate duplicate samples were irradiated for chromatographic

(10) P. J. Dyne and W. M. Jenkinson, *Can. J. Chem.*, **39**, 2163 (1961).

(11) J. A. Stone and P. J. Dyne, *Radiation Res.*, **3**, 353 (1962).

(12) J. R. Nash and W. H. Hamill, *J. Phys. Chem.*, **66**, 1097 (1962).

(13) R. P. Borkowski and P. J. Ausloos, *J. Chem. Phys.*, **39**, 818 (1963).

(14) W. Van Dusen, Jr., and W. H. Hamill, *J. Am. Chem. Soc.*, **84**, 3648 (1962).

(15) R. A. Back, T. W. Woodward, and K. A. McLaughlan, *Can. J. Chem.*, **40**, 1380 (1962).

(16) K. H. Jones, W. Van Dusen, Jr., and L. M. Theard, *Radiation Res.*, **23**, 128 (1964).

analysis of liquid products. Columns used and products determined were silver nitrate- β,β' -oxydipropionitrile for cyclohexane, Apeizon for dicyclohexyl, and di-*n*-decyl phthalate for ethylcyclohexane and propylcyclohexane.

Results

Table I shows the effect of dose on the identified radiolysis products for pure cyclohexane vapor. The zero-dose yields were obtained by extrapolation. Also shown are product yields previously reported for pure cyclohexane vapor γ -radiolysis at 125°⁷ and α -radiolysis at 108°.⁴

Table I: Radiolysis Product Yields for Pure Cyclohexane Vapor

Product	G_0^a	G^b	G^c	G_0^d
H ₂	4.8	4.7 ± 0.2	5.3	8.0
CH ₄	0.36	0.36 ± 0.03	0.6	0.13
C ₂ H ₂	0.35	0.32 ± 0.04	...	0.65
C ₂ H ₄	1.7	1.35 ± 0.08	2.8	2.48
C ₂ H ₆	1.4	0.71 ± 0.14	1.9	0.28
C ₃ H ₆	0.55	0.35 ± 0.04	0.43	0.78
C ₃ H ₈	0.44	0.30 ± 0.03	2.2	0.95
C ₄ hydrocarbons	0.6	0.59 ± 0.10		0.34
Cyclohexene	1.2	1.0	2.2	0.77
Dicyclohexyl	1.0	0.8	1.0	0.5
Ethylcyclohexane		0.3		
Propylcyclohexane		0.2		

^a Zero dose. ^b Dose: ca. 3×10^{19} e.v./g. ^c Blachford and Dyne, γ -rays; dose: ca. 3×10^{19} e.v./g. ^d Ramaradhy and Freeman, α -rays; zero dose.

The hydrocarbon product yields reported for this work and that of Blachford and Dyne⁷ differ markedly, for which there seems to be no readily apparent explanation. The slightly higher temperature (125°) employed by the latter authors does not account for the difference since in the present study it was determined that an increase of temperature from 100 to 150° has no effect on gas yields. It is noteworthy that at the lower doses the yields reported for the present work would be considerably higher if they were computed on the basis of collected-gas pressure rather than by comparison with added cyclopropane. The difference of yields computed by the two methods increases with decreasing dose. For example, $G(C_2, C_3, C_4)_{tot \text{ press method}} - G(C_2, C_3, C_4)_{cyclopropane \text{ method}}$ is 2.6 and 0.8 at 0.3×10^{19} and 3×10^{19} e.v./g., respectively. Two explanations appear plausible. (1) Small amounts of cyclohexane vapor are collected at -110° as shown by chromatographic analysis. Con-

sequently, because the amount of collected vapor should be independent of dose, the amount of collected vapor relative to products should increase with decreasing total products, *i.e.*, with decreasing dose. (2) Alternatively, included in the gases collected may have been unidentified volatile products whose yields decrease with dose more markedly than the gas yields actually determined. In this connection it is pertinent that Doepker and Ausloos⁸ proposed a radiation-induced decomposition process for cyclohexane vapor leading to butyne formation. Butyne and propyne would have been difficult to determine by our analytical technique and consequently our lack of detection does not imply that they were not formed.

Figure 1 displays plots of $G(H_2)_{obsd}$, the observed molecules of hydrogen formed per 100 e.v. absorbed by the system, and $g(H_2)$, molecules of hydrogen formed from cyclohexane per 100 e.v. absorbed by cyclohexane, *vs.* electron per cent benzene. The dashed line in Figure 1 represents the expected yield of hydrogen, $G(H_2)_{expd}$, if the yields of hydrogen for each component of the mixture were unaffected by the presence of the other, and therefore it fits the relationship

$$G(H_2)_{expd} = \epsilon_{C_6H_{12}}G^0(H_2)_{C_6H_{12}} + \epsilon_{C_6H_6}G^0(H_2)_{C_6H_6} \quad (I)$$

where ϵ is electron fraction, $G^0(H_2)$ is the G value of hydrogen for the pure component, and the subscripts represent the pertinent component. The relationship between $G(H_2)_{obsd}$ and $g(H_2)$ is shown by the equation for cyclohexane-benzene mixtures

$$G(H_2)_{obsd} = \epsilon_{C_6H_{12}}g(H_2)_{C_6H_{12}} + \epsilon_{C_6H_6}g(H_2)_{C_6H_6} \quad (II)$$

It is assumed that the yield of hydrogen for benzene is unaffected by the presence of cyclohexane; *i.e.*, $g(H_2)_{C_6H_6} = G^0(H_2)_{C_6H_6}$ for all values of $\epsilon_{C_6H_6}$, and consequently the observed differences in values of $G(H_2)_{expd}$

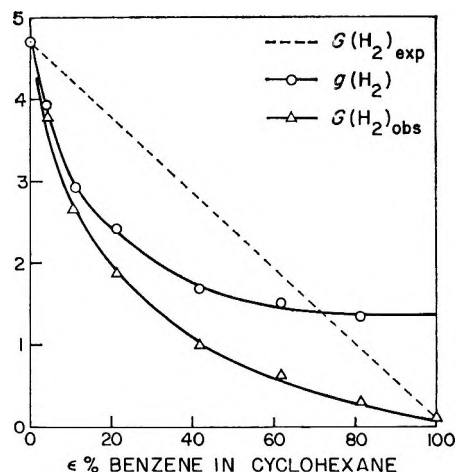


Figure 1. Effect of benzene on hydrogen yield.

and $G(\text{H}_2)_{\text{obsd}}$ are attributed to a decrease of $g(\text{H}_2)_{\text{C}_6\text{H}_{12}}$ with increasing concentration of benzene. Similar assumptions are made for other systems for which values of $g(\text{H}_2)$, representing $g(\text{H}_2)_{\text{C}_6\text{H}_{12}}$, are reported.

Figure 2 presents plots of the G values of C_2H_4 , C_3H_6 , and C_2H_2 vs. electron per cent benzene. Straight lines drawn to fit the points extrapolate to values of $G(\text{C}_2\text{H}_4)$ and $G(\text{C}_3\text{H}_6)$ for pure cyclohexane which are higher than the values actually determined at a dose of 3×10^{19} e.v./g. (Table I). Table II includes effects

Table II: Effects of Additives on Gaseous Radiolysis Product Yields for Cyclohexane Vapor

Additive	Concn., mole %	g						
		H_2	CH_4	C_2H_2	C_2H_4	C_2H_6	C_4H_6	C_2H_8
...	...	4.7	0.36	0.32	1.4	0.71	0.30	0.35
C_6H_6	4	3.9	0.34	0.30	1.6	0.10	0.10	0.50
C_6H_6	23	2.4	0.33	0.30	1.6	0.10	0.04	0.50
<i>c</i> - C_6H_{10}	4	2.5	0.29	0.28	1.5	0.11	0.12	0.44
<i>c</i> - C_6H_{10}	21	2.2	0.44	0.33	1.7	0.12	0.05	0.53
I_2	0.4	1.7	0.07	0.27	1.3	0.05	0.12	0.06
HI	1.3	7.3	0.33	0.36	1.6	0.86	0.34	0.05
NO	0.5	4.3	...	0.36	1.7	0.07	0.07	0.50
NO	9	2.9	...	0.32	1.7	0.05	0.08	0.43

of several additives which increase yields of C_2H_4 and C_3H_6 . Similar effects have been observed previously for cyclohexane liquid¹⁷ and *n*-hexane vapor.¹⁸ The increase of yields can be explained by presuming that, in the absence of additives, products are partially consumed by reaction with intermediate species such as free radicals and ions. In the presence of additives, the intermediate species may react preferentially with the additives rather than the products. Thus, the products are protected from consumption, and the net effect of the additives is an increase of product yield.

Figure 3 gives plots of $g(\text{H}_2)$ vs. low concentrations of C_2H_4 , C_3H_6 , and *c*- C_6H_{10} , and Figure 4 shows $g(\text{H}_2)$ over the full concentration range of these additives. In Figure 4 a single curve representing all the points for the latter three additives has been drawn for simplicity. Perhaps as suggested by the data points there is a real difference of additive effects at high concentration, but the magnitude of the difference is small and is considered to be insignificant for over-all interpretation. Figure 4 also shows the effect of NO on $g(\text{H}_2)$. The increase of $g(\text{H}_2)$ between 18 and 36 mole % is qualitatively similar to an observation by Ausloos, *et al.*,¹⁹ on the effect of NO on $G(\text{H}_2)$ for CH_4 - C_3H_8 mixtures. Thus, attention is called to the fact that the curve for NO in Figure 4 may indeed increase as suggested by the

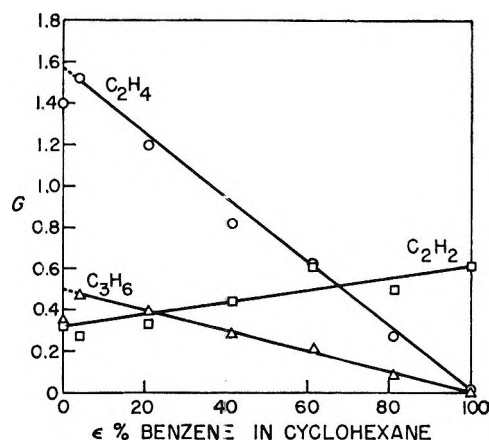


Figure 2. Effect of benzene on C_2H_4 , C_3H_6 , and C_2H_2 .

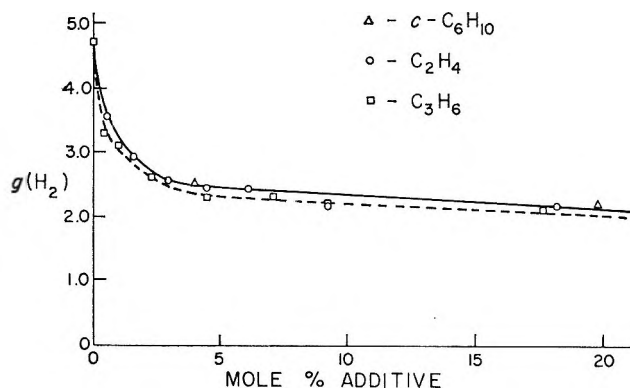


Figure 3. Effects of C_2H_4 , C_3H_6 , and *c*- C_6H_{10} on $g(\text{H}_2)$.

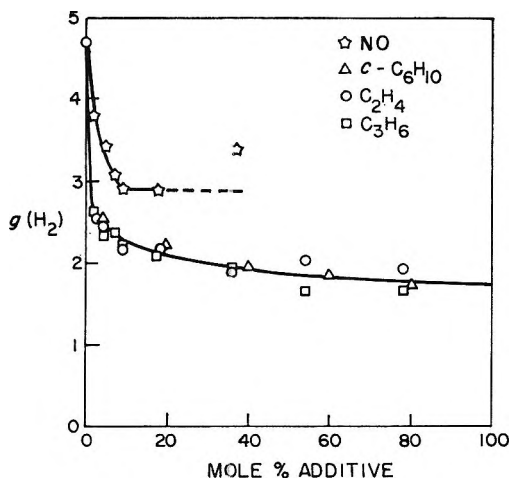


Figure 4. Effects of C_2H_4 , C_3H_6 , *c*- C_6H_{10} , and NO on $g(\text{H}_2)$.

(17) S. Sato, K. Kikuchi, and S. Shida, *J. Chem. Phys.*, **41**, 2216 (1964).

(18) H. A. Dewhurst, *J. Am. Chem. Soc.*, **83**, 1050 (1961).

(19) P. Ausloos, S. G. Lias, and R. Gorden, Jr., *J. Chem. Phys.*, **39**, 3341 (1963).

data. However, in the absence of more data in the high concentration region, the shape of the curve is uncertain. The dashed line is an extrapolation of the low concentration data. Most of the points of Figures 1, 2, and 4 represent an average of at least two independent determinations.

Figure 5 shows effects of HI and I₂ on $g(\text{H}_2)$, and Table II includes effects of these additives on the principal gaseous hydrocarbon products. No H₂ was produced in a 1.5% mixture of HI in cyclohexane prepared as were the irradiated samples and heated to 100° for 1 hr. Correction for H₂ produced from direct irradiation of HI was made on the basis that $G(\text{H}_2) = 9.2$, determined for pure HI at 1.4 cm. and 100°.

Table III reports some vapor phase radiolysis product yields for pure cyclohexene and pure benzene. For pure propylene $G(\text{H}_2) = 1.26$.

Table III: Gaseous Radiolysis Product Yields for Pure Cyclohexene and Pure Benzene

Pure vapor	G					
	H ₂	CH ₄	C ₂ H ₂	C ₂ H ₄	C ₂ H ₆	C ₃ H ₆
C ₆ H ₆	0.084	...	0.61	0.02
<i>c</i> -C ₆ H ₁₀	1.2	0.27	0.45	1.4	0.04	0.13

Discussion

The zero-dose yields reported in Table I show that products with an H:C ratio less than 2 and a total G value possibly as high as 5 have not been measured. The dose dependence of many of the products detected (Table I) suggests that secondary reactions account for the mass imbalance. Presumably, the principal unmeasured products are polymers.^{4,7}

Since the curve for $G(\text{H}_2)_{\text{obsd}}$ in Figure 1 lies below that for $G(\text{H}_2)_{\text{expd}}$, benzene inhibits the formation of hydrogen from the radiolysis of cyclohexane vapor. The extent of the effect of benzene is shown by the decrease of $g(\text{H}_2)$ from 4.7 to 1.3, the latter value being the unaffected yield of hydrogen for cyclohexane. Table II shows that benzene also decreases $g(\text{C}_2\text{H}_6)$ and $g(\text{C}_3\text{H}_8)$ but at a rate faster than it decreases $g(\text{H}_2)$. Thus, it can be concluded that the process responsible for the principal decrease of $g(\text{H}_2)$ is different from that responsible for the decrease of $g(\text{C}_2\text{H}_6)$ and $g(\text{C}_3\text{H}_8)$. Further, since benzene does not affect C₂H₄, C₂H₂, C₃H₆ (Figure 2), or CH₄ (Table II), it can be concluded that more than one precursor is involved in the formation of the gaseous products.

It might be considered that part of the decrease of hydrogen, in the presence of benzene, is attributable to protection by benzene of a cyclohexane species

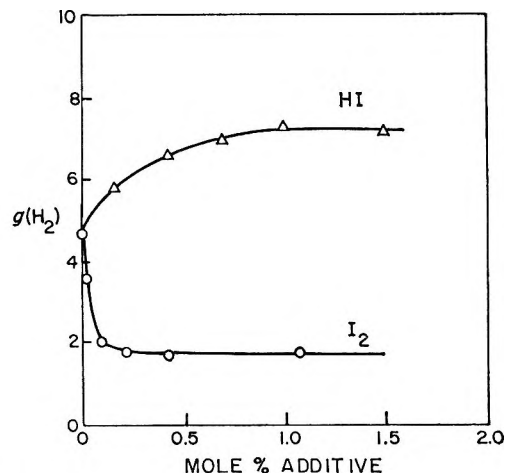
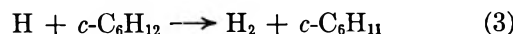
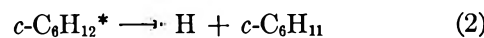
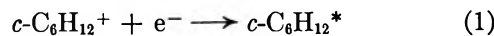
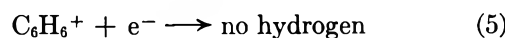
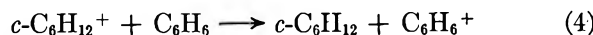


Figure 5. Effects of HI and I₂ on $g(\text{H}_2)$.

which, in the absence of benzene, yields hydrogen as its only gaseous product. For example, in pure cyclohexane vapor, neutralization of parent ions may lead to hydrogen production *via* the reactions



where $c\text{-C}_6\text{H}_{12}^*$ represents highly excited cyclohexane. In the presence of benzene, hydrogen may be decreased by the following reactions.



Ramaradhy and Freeman⁵ considered ionization transfer to be the most plausible explanation for the decrease of hydrogen by benzene, cyclohexene, and propylene in the vapor phase α -radiolysis of binary mixtures containing cyclohexane. Effects of olefins, to be further discussed, determined in the present study are inconsistent with the above ionization-transfer mechanism.

Blachford and Dyne found that benzene reduces bimolecularly produced hydrogen but does not affect unimolecularly produced hydrogen. Assuming that the decrease of hydrogen was attributable to hydrogen atom scavenging, they computed from their data the ratio of the rate constant for hydrogen atom addition to benzene to the rate constant for abstraction of H atoms from cyclohexane by H atoms. They argued that the computed ratio was unreasonably small and therefore concluded that the hydrogen atom scavenging mechanism was implausible. Alternatively,

they suggested that benzene scavenges ionic precursors (probably C₂-C₃ ion fragments) of hydrogen atoms.

The present data show that, if C₂-C₃ ion fragments are principal precursors of benzene-reduced hydrogen, these same fragments are not also precursors of measured C₂-C₃ products. This is concluded from the fact that the decrease of C₂H₆ and C₃H₈ with increasing benzene concentration is more rapid than is the major decrease of hydrogen, and C₂H₄, C₂H₂, and C₃H₆ are unaffected by benzene.

The lack of effect of benzene on C₂H₄, C₂H₂, and C₃H₆ suggests that they are not produced by free-radical or fragment-ion precursors because benzene reacts with both species.²⁰ NO reacts with free radicals but apparently does not react readily with fragment ions.²⁰ Thus, the reduction of C₂H₆ and C₃H₈ by NO (Table II), and presumably also by benzene, cyclohexene, and iodine, very likely is attributable to scavenging of C₂H₅ and C₃H₇ radicals.

The observed dependence of $g(\text{H}_2)$ on the concentration of olefins suggests that they reduce $g(\text{H}_2)$ by at least two processes, one of which is more prominent at low additive concentration. Figure 3 shows that C₂H₄, C₃H₆, and *c*-C₆H₁₀ reduce $g(\text{H}_2)$ relatively rapidly at low concentration and more gradually, but persistently, at higher concentration. Figure 4 shows that $g(\text{H}_2)$ continues to decrease over most of the additive concentration range. These results are inconsistent with a single process being responsible for the decrease of hydrogen over the full additive concentration range. If the low concentration effect were solely operative throughout, $g(\text{H}_2)$ would be expected to reach a constant high concentration limiting value considerably higher than that observed in Figure 4.

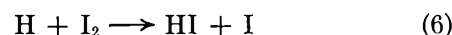
The similarity of the decrease of hydrogen as a function of C₂H₄, C₃H₆, or *c*-C₆H₁₀ concentration appears unattributable to charge transfer from ground-state cyclohexane ions to the additives because the ionization potentials favor charge transfer only to C₃H₆ and *c*-C₆H₁₀. That is, the ionization potential of cyclohexane is greater than those of C₃H₆ and *c*-C₆H₁₀ and less than that of C₂H₄.²¹ It appears also unlikely then that benzene reduces hydrogen by charge transfer although the ionization potential of cyclohexane is greater than that of benzene.

It is suggested that the decrease of H₂ by benzene and the olefins is attributable principally to scavenging of H atoms at low concentration and additional scavenging of fragment-ion precursors of hydrogen atoms at high concentration. The latter mechanism, similar to that proposed by Blachford and Dyne to explain all the depression of hydrogen by benzene, is based on the suggestion by Lias and Ausloos²⁰ of the occurrence

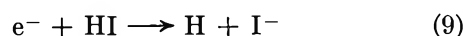
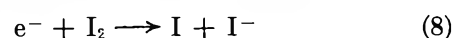
of radiation-induced fragment-ion addition reactions with olefins and benzene in propane. It should be noted that, if fragment-ion precursors of hydrogen atoms are scavenged principally at high additive concentration, the hydrogen atoms normally produced by the unscavenged ions must be non-scavengable and perhaps are hot H atoms. If the atoms were scavengable, the scavenging of their ionic precursors would not decrease the concentration-dependent rate of hydrogen decrease, and the minimum over-all rate of decrease of hydrogen would be that expected for exclusive hydrogen atom scavenging. In other words, if in the presence of olefins the faster low concentration effect is attributed principally to hydrogen atom scavenging, the slower high concentration effect cannot be attributed to scavenging of precursors of the scavengable hydrogen atoms.

NO is not so effective in reducing $g(\text{H}_2)$ as are the olefins (Figure 4). However, interpretation of the difference is complicated by the likelihood that some reaction involving NO produces hydrogen,¹⁹ which tends to increase the hydrogen yield at high NO concentration.

As components of radiolysis systems, I₂ and HI may scavenge H atoms

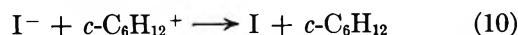


and/or dissociatively capture thermal electrons.^{12,22}



Considering that the fate of H atoms in pure cyclohexane is formation of H₂ via reaction 3, H atom scavenging by I₂ reduces $g(\text{H}_2)$ while H atom scavenging by HI does not affect $g(\text{H}_2)$.

Electron capture by I₂, reaction 8, may reduce the yield of hydrogen if, for example, in pure cyclohexane radiolysis hydrogen is produced by reactions 1, 2, and 3. In the presence of I₂, neutralization of positive ions following reaction 8 probably occurs via



where it is unlikely that the *c*-C₆H₁₂ species decomposes.¹² Thus, the hydrogen yield may be depressed by quenching reaction 2. Of course, in cyclohexane-vapor radiolysis, ions other than *c*-C₆H₁₂⁺ are formed,

(20) S. G. Lias and P. Ausloos *J. Chem. Phys.*, **37**, 877 (1962).

(21) F. H. Field and J. L. Franklin, "Electron Impact Phenomena," Academic Press Inc., New York, N. Y., 1957, pp. 108, 109.

(22) D. C. Frost and C. A. McDowell, *J. Chem. Phys.*, **29**, 503 (1958).

and these ions also may produce hydrogen upon neutralization.

Although electron capture by HI also can be expected to quench reaction 2, the loss of hydrogen may be equaled or exceeded by attendant hydrogen formation *via* reactions 9 and 7. It is suggested that the increase of hydrogen shown in Figure 5 arises from such hydrogen formation *via* reactions 9 and 7 with greater efficiency than normally occurs *via* reactions 1 and 2 and other neutralization-induced decompositions, as suggested by Nash and Hamill¹² for liquid cyclohexane. In other words, it is suggested that in pure cyclohexane all ion neutralizations do not produce hydrogen. Recent results on the effects of additives on gaseous hydrogen chloride²³ and propane²⁴ radiolyses have been explained on the basis of electron capture.

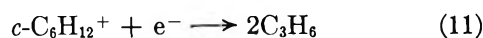
Assuming the proposed electron-capture mechanism for the effect of HI, the yield of hydrogen resultant from neutralization reactions can be estimated by comparing the yield of electrons with the increase of hydrogen. The G value of electrons can be estimated by assuming that W , energy absorbed per ion pair produced, is *ca.* 24 e.v. as found for many hydrocarbons²⁵: thus, $G(e^-) = 100/W \simeq 4.2$. Figure 5 shows that the increase of $g(H_2)$ by HI is 2.7, which is interpreted to equal the G value of electrons which do not yield hydrogen through neutralization in pure cyclohexane, assuming that each hydrogen-producing neutralization is responsible for formation of one molecule of hydrogen. Conversely, the G value of electrons which yield hydrogen is 4.2 - 2.7, or 1.5.

The decrease of $g(H_2)$ by I_2 *via* electron capture can be estimated to be equal to 1.5, the G value of electrons which yield hydrogen. Since the total decrease of $g(H_2)$ by I_2 is 3.0, an additional decrease of 1.5 is attributable to some other process, presumably hydrogen atom scavenging.

It appears then that the decrease of hydrogen by iodine and, as suggested above, also by the olefins and benzene is attributable to two processes, one of which is hydrogen atom scavenging. The other process apparently involves suppression of ion-neutralization decomposition reactions with the distinction that iodine reacts with the hydrogen-producing ionic species by neutralization following electron capture and the olefins and benzene react by addition. The extent of hydrogen decrease by the two processes in the presence of the olefins and benzene may be approximately equal as suggested for iodine. However, Figures 3 and 4 only indicate that both processes are important, and the complexity of the decrease of $g(H_2)$ by benzene

is apparently masked by the fact that the processes responsible for the decrease occur with comparable rates.

Table II shows that I_2 and HI reduce C_3H_6 markedly, while the other additives increase C_3H_6 slightly. The latter effect is presumed to be attributable to protection of C_3H_6 from consumption by a bimolecular dose-dependent process. It appears that the decrease of C_3H_6 is attributable to electron capture by I_2 and HI since this process is highly probable for these additives and improbable for the others. Thus, neutralization of cyclohexane molecule ions may produce C_3H_6



and, following electron capture by I_2 and HI, substituted neutralization *via* reaction 10 presumably does not produce C_3H_6 . Accordingly, the near lack of effect of I_2 and HI on the yield of C_2H_4 supports the suggestion of Doepker and Ausloos⁸ that C_2H_4 is produced by decomposition of neutral excited cyclohexane.

It appears that, in general, the determination of the effect of HI on the radiolysis of gaseous hydrocarbons may be quite helpful in elucidating the mechanism of formation of various products. The present study of the effect of HI suggests that the importance of neutralization processes in the formation of hydrogen and propylene can be estimated. In this regard, the approach may compare well with the electric field method.²⁶ In the latter case it is assumed that neutralization of positive ions at a negative electrode is non-dissociative, and it appears that neutralization of positive ions by I^- also is nondissociative. HI is interesting also in that it converts free radicals to stable products by addition of an H atom to the free radical. Therefore, free radicals that abstract hydrogen atoms in the pure hydrocarbon do likewise by reaction with HI. In this connection note that HI does not affect C_2H_6 and C_3H_8 (Table II).

Acknowledgments. The helpful assistance contributed by Drs. K. H. Jones and W. Van Dusen, Jr., through experimental work and discussions, is gratefully acknowledged. The experimental assistance of J. Schmidt, D. R. Begeal, and L. L. Stephenson is also gratefully acknowledged.

(23) R. A. Lee, R. S. Davidow, and D. A. Armstrong, *Can. J. Chem.*, **42**, 1906 (1964).

(24) G. R. A. Johnson and J. M. Warman, *Nature*, **203**, 74 (1964).

(25) G. G. Meisels, *J. Chem. Phys.*, **41**, 51 (1964).

(26) H. Essex, *J. Phys. Chem.*, **58**, 42 (1954).

The Outer Coordination Sphere. I. Nuclear Magnetic Resonance Relaxation Time Effects Produced by Paramagnetic Ions with Nonlabile Inner Coordination Spheres¹

by Thomas R. Stengle and Cooper H. Langford

Chemistry Departments, University of Massachusetts, Amherst, Massachusetts, and Amherst College, Amherst, Massachusetts (Received February 26, 1965)

The effects of various paramagnetic Cr(III) complexes with well-defined, nonlabile inner coordination spheres on the transverse relaxation times of F^{19} n.m.r. signals from F^- and PF_6^- have been determined in aqueous solution. The effects of the paramagnetic ions on nuclei in the second coordination sphere are seen to be substantial. The chemical evidence (concentration dependence, structure dependence, etc.) suggests that a consistent interpretation of the effects may be given in terms of relative outer-sphere coordinating tendencies. The interpretation emphasizes the importance of the interaction between inner-sphere ligands and solvent molecules.

Introduction

The composition of the solvation sphere of a complex ion has been the subject of some study in the past. Despite a number of investigations, a controversy still exists as to whether an ion such as tris(ethylenediamine)chromium(III) in aqueous solution will have its first solvation sphere composed completely of water molecules, or whether an anion may enter this "second coordination sphere" and form an "outer-sphere" complex. In recent work on inorganic reaction mechanisms, the second coordination sphere has come under increasing scrutiny. For example Tobe and Watts,² Schmidt and Taube,³ and Langford and Johnson⁴ have discussed ligand interchange reactions between the first and second coordination spheres of Co(III) complexes in a way that assumed that outer-sphere complexes were well-defined entities in solution. However, the status of such entities is by no means clear, especially with respect to aqueous solutions. There is need for experimental data derived from short-range interactions between a complex with a well-defined (nonlabile) inner coordination sphere and ligands (anions) in solution.

The best extant experiments⁵⁻⁷ study outer-sphere complexing by observing modifications of the ultra-

violet spectrum of the complex that are dependent upon anion concentration, but even this technique has led to some serious disagreements. Evans and Nancollas⁸ derived outer-sphere association constants of 74 and 46 for the hexaamminecobalt(III) ion with chloride and bromide in good agreement with predictions from Bjerrum's⁹ theory, whereas King, *et al.*,¹⁰ studied the same systems over a wider range of halide concentration (and incidentally a wide range of perchlorate concentration which should not be regarded as innocuous) and concluded that the outer-sphere association constant was less than 0.2, so small that it seemed that the ions could not desolvate each other

(1) Presented in part at the 145th National Meeting of the American Chemical Society, New York, N. Y., Sept. 1963.

(2) M. L. Tobe and D. W. Watts, *J. Chem. Soc.*, 4614 (1962).

(3) W. Schmidt and H. Taube, *Inorg. Chem.*, **2**, 698 (1963).

(4) C. H. Langford and M. P. Johnson, *J. Am. Chem. Soc.*, **86**, 229 (1964).

(5) H. Taube and F. A. Posey, *ibid.*, **75**, 1463 (1953).

(6) F. A. Posey and H. Taube, *ibid.*, **78**, 15 (1956).

(7) N. Fogel, J. Tai, and J. Yarbrough, *ibid.*, **84**, 1145 (1962).

(8) M. G. Evans and G. H. Nancollas, *Trans. Faraday Soc.*, **49**, 363 (1953).

(9) N. Bjerrum, *Kgl. Danske Videnskab. Selskab*, **7**, No. 9 (1926).

(10) E. L. King, J. H. Espenson, and R. E. Visco, *J. Phys. Chem.*, **63**, 755 (1959).

to form an outer-sphere complex. This discrepancy with the results of Evans and Nancollas⁸ is discussed in detail by King, *et al.*¹⁰

Recently Alei¹¹ studied the association between hexaquo chromium(III) ion and perchlorate ion using an n.m.r. technique. The effect of the paramagnetic ion on the chemical shift of O¹⁷ nuclei in enriched water was measured as a function of chromium and ClO₄⁻ concentration. From these data it was concluded that the perchlorate ion does enter the second coordination sphere of Cr(H₂O)₆³⁺ and that the ratio of ClO₄⁻ to water in the second sphere is of the same order of magnitude as in the bulk solution. The "equilibrium constant" for the association cannot be calculated from this datum alone, but it would appear that its value is small, probably less than unity.

In this work a new method of studying outer-sphere association is proposed. This technique is based on the effect of a paramagnetic ion on the relaxation time of nearby nuclei. This interaction is short ranged and leads to a significant reduction in the relaxation time of nuclei which are quite close to the paramagnetic center. In this work we studied the association between a nonlabile Cr(III) complex and a fluorine-containing anion. In a typical experiment, the spin-spin relaxation time of the F¹⁹ nucleus was determined in a 0.25 M solution of KPF₆, and this was compared with the value obtained when the solution was also made 0.1 M in a Cr(III) complex. The addition of the paramagnetic complex resulted in a large reduction of the spin-spin relaxation time of the F¹⁹ signal (as evidenced by a broadening of the n.m.r. line). Since the interaction of the paramagnetic ion with the F¹⁹ nucleus is short ranged, most, but not all, of the effect must arise from those PF₆⁻ ions which are in the second coordination sphere of the Cr(III) complex ion. To a rough approximation, the magnitude of the line broadening is proportional to the fraction of the PF₆⁻ ions which are in association with the complex ion. Although there is no way of determining the value of the proportionality constant *a priori*, a great deal of useful information can be obtained from a study of the trends of outer-sphere association with changes in concentration, temperature, and the nature of both the cation and anion.

Although all the details of the mechanism of the relaxation are not yet clear, the important study of Bloembergen and Morgan¹² seems to justify the following assumptions: (1) the observed relaxation rate is the average over all different nuclear environments weighted for the probability that the nucleus is in the given environment; (2) the decrease of the relaxation time results predominantly from those F¹⁹-containing

anions which are actually in "contact" with (*i.e.*, in the second coordination sphere of) the paramagnetic ions; and (3) in the relaxation mechanism of an F¹⁹ nucleus in the second coordination sphere of a Cr(III) complex, the spin-exchange interaction is only of secondary importance when compared with the dipolar interaction.

Assumption 1 is valid if the exchange of the F¹⁹ nuclei is rapid between the various environments when compared with the reciprocal of the difference of the Larmor frequencies for the environments and the relaxation time of the F¹⁹ nucleus in the paramagnetic environment. These are the conditions given by eq. 10(d) of ref. 13. Such lability is certainly expected for outer-sphere interactions, and the assumption is confirmed by the temperature dependence of the relaxation times. For a dipole-dipole mechanism in the fast-exchange case, one expects the relaxation time of a fluorine nucleus to decrease with decreasing temperature according to the temperature dependence of the correlation time. For Cr(III) ions, the diffusion correlation time predominates¹⁴ which would lead to an activation energy of 2 or 3 kcal. mole⁻¹ for the relaxation process. The experimental temperature dependence of the relaxation time is governed by the heat of association of the second-sphere complex as well as by the activation energy of the relaxation process. The experimental values of 2.5 and 5.0 kcal. mole⁻¹ for the two systems studied are in agreement with this analysis and lead to heats of association between zero and -2.5 kcal. mole⁻¹.

The solution of the Bloch equations with chemical exchange has been discussed by McConnell¹⁵ and by Swift and Connick.¹³ In the fast-exchange case, the observed relaxation time, T_2 , is given by eq. 1

$$\frac{1}{T_2} = \frac{p_A}{T_{2A}} + \frac{p_B}{T_{2B}} \quad (1)$$

where p_A is the probability that the nucleus is in environment A, T_{2A} is the relaxation time in environment A, and p_B and T_{2B} refer to the same quantities in environment B. Taking A to be the bulk solution (diamagnetic environment) and B to be the second coordination sphere (paramagnetic environment), we can determine the probability of finding the F¹⁹-containing anion in the second coordination sphere of the

(11) M. Alei, *Inorg. Chem.*, **3**, 44 (1964).

(12) N. Bloembergen and L. O. Morgan, *J. Chem. Phys.*, **34**, 842 (1961).

(13) T. J. Swift and R. E. Connick, *ibid.*, **37**, 307 (1962).

(14) Z. Luz and S. Meiboom, *ibid.*, **40**, 2686 (1964).

(15) H. M. McConnell, *ibid.*, **28**, 430 (1958).

paramagnetic complex if the other quantities are known. The relaxation time T_{2A} is simply the relaxation time in a solution which is free of paramagnetic ions. At the outset, T_{2B} cannot be determined. For reasonably dilute solutions, p_A is nearly unity; therefore, p_B will be proportional to the quantity $\Delta\nu - \Delta\nu_A$, where $\Delta\nu$ is the line width at half-height and is related to the relaxation time by the equation $\Delta\nu = 1/\pi T_2$.

Assumption 2 is suggested since all proposed mechanisms of interaction are short ranged. The two effects which can lead to relaxation are the nuclear magnetic dipole-electron magnetic dipole interactions and the isotropic spin-exchange mechanism.¹² It is well known that the field of a dipole falls off as r^{-3} which leads to $1/T_{2B}$ varying as r^{-6} . The spin-exchange mechanism depends on the value of the wave function of the paramagnetic electrons at the position of the F^{19} nucleus. Since the paramagnetic electrons of the Cr(III) ion are localized in t_{2g} nonbonding orbitals, the wave function will rapidly approach zero at large distances from the metal atom. This interaction is much shorter ranged than the dipolar term. It seems that interactions beyond the second sphere must be wholly dipolar in nature. In estimating that part of the quantity $\Delta\nu - \Delta\nu_A$ which is due to interactions beyond the second sphere, a geometrical factor of $4\pi r^2$ must be taken into account. This allows for the increasing number of ions which can be contained within a shell of fixed thickness as the radius increases. Therefore, interactions beyond the second sphere must be small, falling off at least as rapidly as r^{-4} . They are large enough to be observable, but it is certain that they will be much smaller than second-sphere interactions.

If T_{2B} changes in a regular fashion from one Cr(III) complex to another, it is possible to make direct comparisons of experimental data for different complexes. This will be true if the predominant mechanism of relaxation in the second sphere is dipolar; this is assumption 3. The results of several studies may be cited in support of this contention. The data of Morgan, *et al.*,¹⁶ on the proton relaxation times in aqueous solutions of Cr(III) complexes have been satisfactorily explained in terms of the size of the ion and its solvation. The spin-exchange mechanism, if present, did not vary widely from one complex to the next. More recently Morgan and Nolle¹⁷ made a detailed study of the proton resonance in aqueous solutions of $Cr(H_2O)_6^{3+}$ in an attempt to elucidate the relaxation mechanism in the *first* coordination sphere. Although their data cannot be explained in terms of a dipolar mechanism alone, it seems that this effect is responsible for a major part of the relaxation. Since

the dipolar interaction falls off less rapidly with distance than any other interaction, it is reasonable to suppose that it is the predominant interaction present in the second sphere. Finally our results show that the size of the complex ion is not the most important factor causing variations from one complex to another as would be expected if the spin-exchange mechanism were of paramount importance.

Experimental Section

Materials. Potassium hexafluorophosphate was obtained from Matheson Coleman and Bell and recrystallized from water. Sodium fluoride was prepared by neutralizing primary standard sodium carbonate with reagent grade HF. This procedure was necessary because most reagent grade fluoride salts contain enough paramagnetic impurities to cause difficulty. This is due to the extreme sensitivity of the relaxation time of F^- to the presence of small amounts of paramagnetic ions which have labile first coordination spheres.¹⁸ For example, a concentration of 10^{-6} M manganous ion is sufficient to cause appreciable broadening of the F^- line. This problem is not encountered with KPF_6 , since the PF_6^- ion has little tendency to enter a first coordination sphere.

The chromic complexes $K_3[Cr(ox)_3] \cdot 3H_2O$ and *cis*- $[Cr(en)_2Cl_2]Cl$ ¹⁹ were prepared by standard methods.²⁰ A simple and convenient synthesis of $[Cr(en)_3]Cl_3$ and $[Cr(pn)_3]Cl_3$ was developed. Hexa(urea)chromium(III) chloride was dissolved in anhydrous dimethylformamide and refluxed for 20 min. with excess ligand. First a red color developed in the solution, and finally a yellow precipitate separated. The precipitate was recrystallized from an ethanol-water mixture at room temperature. The compounds were obtained in about 25% yield, and their identities were established by analysis for chloride ion. The yields are comparable to those obtained by the standard method.²¹

N.m.r. Measurements. N.m.r. spectra were recorded on a Varian DP-56.4 spectrometer. The instrument was equipped with a thermostated probe which maintained the temperature within limits of $\pm 1^\circ$. Values of T_2 were obtained from measurements of the width at half-height of the recorded absorption lines. Care was taken to demonstrate that saturation was not oc-

(16) L. O. Morgan, A. W. Nolle, R. L. Hull, and J. Murphy, *J. Chem. Phys.*, **25**, 206 (1956).

(17) L. O. Morgan and A. W. Nolle, *ibid.*, **31**, 365 (1959).

(18) V. M. Vdovenko, L. L. Pavlova, and V. A. Shcherbakov, *Zh. Strukt. Khim.*, **3**, 707 (1962); *Chem. Abstr.*, **58**, 7528e (1963).

(19) ox = oxalato, en = ethylenediamine, pn = 1,2-diaminopropane.

(20) D. M. Yost, *Inorg. Syn.*, **1**, 37 (1939); C. L. Rollinson and J. C. Bailar, Jr., *ibid.*, **2**, 200 (1946).

(21) C. L. Rollinson and J. C. Bailar, Jr., *ibid.*, **2**, 196 (1946).

curing and affecting the line width. The accuracy of the T_2 measurements was limited by the poor signal-to-noise ratio at large line widths. In general the line widths are reliable to ± 1 c.p.s. or $\pm 10\%$, whichever is larger. In some favorable cases an accuracy of $\pm 5\%$ was achieved. An attempt was made to determine relaxation times by the spin-echo technique. This method was not sensitive enough to be of utility at the concentrations used in this study, and in general more reliable data were obtained from steady-state absorption curves.

Results

Line-width measurements were made on KPF_6 in solution with several Cr(III) complexes. The variation of the line width was observed as a function of metal ion concentration; the results are given in Figure 1. The same results for NaF solutions are shown in Figure 2. Temperature dependence data for two Cr(III) complexes in KPF_6 solution are shown in Figure 3. These data are suggestive of the temperature dependence of T_{2B} and thus support the assumption of fast exchange in the second sphere. In the slow-exchange case the temperature dependence would be that of a reaction rate constant, which would have opposite sign.¹⁵ It is not possible to determine the heat of association from the temperature-dependence data, since the temperature dependence of T_{2B} is known only approximately.

Discussion

The probability that an anion is in the second coordination sphere of a Cr(III) complex is p_B (neglecting effects beyond the second sphere). The relationship between the line width ($\Delta\nu$) and p_B may be obtained from eq. 1. In most of our experiments the concentrations are such that p_A is near unity. The quantity T_{2A} may be evaluated from $\Delta\nu_A = 1/\pi T_{2A}$, where $\Delta\nu_A$ is the line width in the absence of Cr(III) complex. Equation 1 then becomes

$$\pi(\Delta\nu - \Delta\nu_A) = p_B/T_{2B} \quad (2)$$

If we apply the law of mass action to the equilibrium between a second-sphere complex and the ions from which it is formed, we have



$$\alpha_1 = [MX]/C_m \text{ and } \beta_1 = [MX]/[M][X] \quad (3)$$

Here M represents the Cr(III) complex ion with a fixed inner coordination sphere, X the F^{19} -containing anion, and MX the first outer-sphere complex. Following the

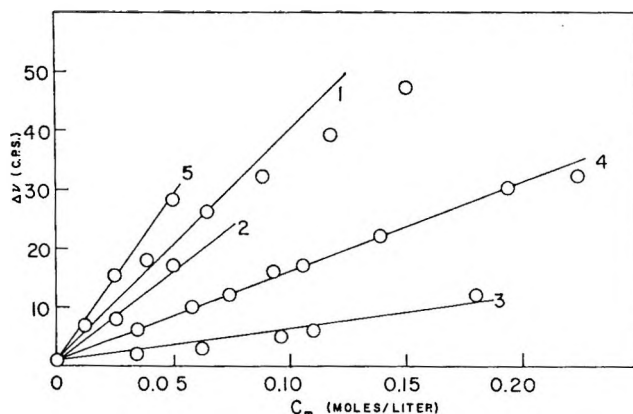


Figure 1. Variation of line width in 0.25 M KPF_6 solution with Cr(III) complex concentration: 1, $Cr(en)_3Cl_3$; 2, $[Cr(en)_2Cl_2]Cl$; 3, $K_3Cr(ox)_3$; 4, $Cr(H_2O)_6(NO_3)_3$; 5, $Cr(pn)_3Cl_3$.

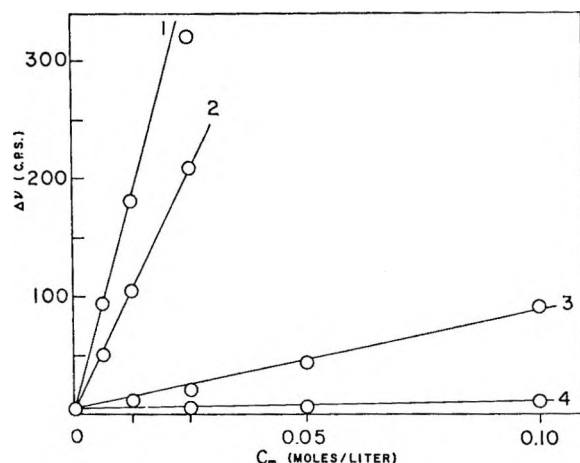


Figure 2. Variation of line width in saturated (ca. 1 M) NaF solution: 1, $Cr(pn)_3Cl_3$; 2, $Cr(en)_3Cl_3$; 3, $[Cr(en)_2Cl_2]Cl$; 4, $K_3Cr(ox)_3$.

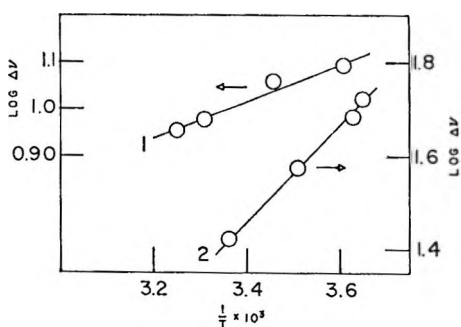


Figure 3. Temperature dependence of line width in 0.25 M KPF_6 solution: 1, 0.05 M $K_3Cr(ox)_3$; 2, 0.05 M $Cr(en)_3Cl_3$.

usual notation, α_1 is the degree of monocomplex formation, and β_1 is the formation constant for this complex. The concentrations of the species in 3 are de-

noted by bracketing, and C_m is the analytical concentration of the Cr(III) complex. The definitions of p_B and α_1 lead to

$$p_B = [MX]/C_x \text{ and } p_B = \alpha_1 C_m / C_x \quad (4)$$

where C_x is the analytical concentration of the F^{19} -containing anion. This treatment predicts that linearity is to be expected in the plots in Figures 1 and 2 at low values of C_m . The deviation from linearity for some complexes at high C_m indicates substantial complexing. In such cases we no longer have $[X] \approx C_x$, which is a necessary condition that α_1 be constant.

Assuming for the present that, for a given anion, T_{2B} is the same for a series of Cr(III) ions, the quantity $(\Delta\nu - \Delta\nu_A)$ is proportional to α_1 . Therefore the relative slopes in Figure 1 provide a measure of the relative values of α_1 for the PF_6^- complexes. Figure 2 yields the ordering of α_1 values for F^- outer-sphere complexes. For both anions, the order of decreasing complexation is: $Cr(pn)_3^{3+} > Cr(en)_3^{3+} > Cr(en)_2Cl_2^+ > Cr(ox)_3^{3-}$. The interesting ion $Cr(H_2O)_6^{3+}$, which lies below $Cr(en)_2Cl_2^+$ for complexation with PF_6^- , was necessarily omitted from the F^- measurements because of solubility limitations.

If we remove the assumption that T_{2B} is the same for all of the Cr(III) complex ions, we can no longer obtain quantitative data on the variation of the α_1 values. However, some important qualitative information will result if the T_{2B} values can be shown to vary in a regular manner with the size of the complex ion. The two factors which must be considered are the strength of the interaction between the paramagnetic electron and the F^{19} nucleus and the correlation time for this interaction. The magnitude of the interaction will depend on the inverse sixth power of the distance between the interacting centers. This will lead to a rapid decrease of the relaxation rate, $1/T_{2B}$, with increasing radius of the Cr(III) ion. The tumbling correlation time²² will depend on the size of the ion in such a way as to increase the relaxation rate with increasing size. For a sphere turning in a viscous medium, it can be shown¹² that the relaxation rate will vary directly with the third power of the radius. Hence the magnitude of the dipolar interaction will be the predominant factor in determining the dependence of $1/T_{2B}$ on ion size. The relaxation rate will be smaller for larger ions.

Our results show an increase in the F^{19} line width as the size of the Cr(III) complex increases. This is the opposite of what would be expected on the basis of the change of T_{2B} with ion size, and *can only be explained in terms of ion association*. The relative values of the slopes in Figures 1 and 2 will place a limit

on the relative values of α_1 . For example, in Figure 1 the slope of the $Cr(en)_3^{3+}$ line is three times larger than the slope of the $Cr(H_2O)_6^{3+}$ line. Hence we can say that α_1 for $Cr(en)_3^{3+}$ must be *at least* three times the value for $Cr(H_2O)_6^{3+}$.

The ratio of the values of $\Delta\nu - \Delta\nu_A$ for a given complex at two C_x values (C_m constant) gives the p_B ratio with the unknown quantity T_{2B} canceled. Assuming various β_1 values, the p_B ratios may be calculated, and the calculated ratios may be compared with experiment to determine the approximate value of β_1 . Unfortunately, the present experimental requirement of large C_x (to observe the resonance) limits such experiments to β_1 values between 1 and 10. In some cases, misleading values may be obtained when higher complexing interferes with the analysis in terms of monocomplex formation. Moreover, activity effects are expected to be important. Very approximate values of β_1 were obtained as follows: $Cr(ox)_3^{3-}$ with PF_6^- , $\beta_1 = 0$; $Cr(en)_3^{3+}$ with PF_6^- , $\beta_1 = 1$; $Cr(en)_2Cl_2^+$ with F^- , $\beta_1 = 3$; $Cr(en)_3^{3+}$ with F^- , $\beta_1 > 10$. These values seem reasonable in the light of the prior literature.^{5-7,11,23}

We shall attempt to give an over-all evaluation of the n.m.r. method. For a series of complexes of very similar electronic structure, it provides a simple way to determine relative degrees of outer-sphere complexing. If the association is weak, an approximate value of the first outer-sphere association constant is obtained. The value cannot be obtained precisely,²⁴ but what is more important is that the n.m.r. method does appear to detect genuine second-sphere association because of its "short-range" character. Although the results of the measurements on the $Cr(ox)_3^{3-}$ systems (in which no ion association is likely to take place) suggest some broadening due to "third-sphere" effects, it is small, approximately independent of the source of F^{19} , and leads to a β_1 value of zero.

Using only relative degrees of outer-sphere association obtained from the data in Figure 1 and 2, it is possible to comment on the factors which influence second-sphere complexing. As expected, electrostatic forces are quite important; Figures 4 and 5 present

(22) If the correlation time for the interaction is determined by the electron spin relaxation time, $1/T_{2B}$ will depend on factors other than the size of the Cr(III) ion. However, the temperature-dependence data of Luz and Meiboom¹⁴ and our data for the $Cr(ox)_3^{3-}-PF_6^-$ system (in which it is likely that no ion pairs are formed) indicate an activation energy for the relaxation process of 2.5 kcal. mole⁻¹, which is consistent with a tumbling and not an electron spin relaxation mechanism.

(23) R. G. Pearson and F. Basolo, *J. Am. Chem. Soc.*, **78**, 4878 (1956).

(24) It is quite possible that thermodynamic constants for weak ion associations of this type cannot be precisely defined.

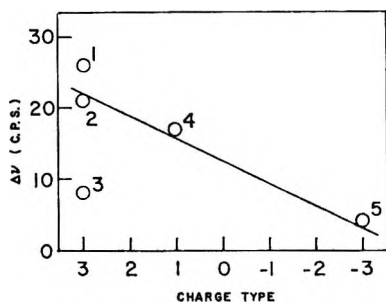


Figure 4. Variation of line width in 0.25 M KPF_6 solution with charge type of Cr(III) complex, $C_m = 0.05 M$: 1, $Cr(pn)_3Cl_3$; 2, $Cr(en)_3Cl_3$; 3, $Cr(H_2O)_6(NO_3)_3$; 4, $[Cr(en)_2Cl_2]Cl$; 5, $K_3Cr(ox)_3$.

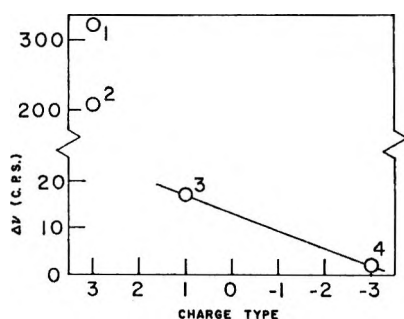


Figure 5. Variation of line width in saturated (ca. 1 M) NaF solution with charge type of Cr(III) complex, $C_m = 0.025 M$: 1, $Cr(pn)_3Cl_3$; 2, $Cr(en)_3Cl_3$; 3, $[Cr(en)_2Cl_2]Cl$; 4, $K_3Cr(ox)_3$.

line broadening as a function of the charge on the Cr(III) complex. Generally, the degree of association increases with increasing positive charge on the Cr(III) complex as a simple electrostatic model would predict. However, the nature of the ligands in the first coordination sphere also influences the degree of second-sphere association. *Despite its high positive charge, $Cr(H_2O)_6^{3+}$ shows only a small tendency to associate with PF_6^- .*

The possibility that this effect arises from a lowering of the charge due to hydrolysis can be dismissed because the line broadening does not increase in more acid solutions.

The anomalous behavior of the hexaquo chromium(III) ion is easily explained. It is able to form strong hydrogen bonds with second-sphere water molecules and these must be broken for association to occur. This viewpoint provides a clue to the other major anomaly revealed by Figures 1 and 2, *i.e.*, the *increasing* association of the hexamine ions as the radius *increases*. This behavior is shown in the ions $Cr(en)_3^{3+}$ and $Cr(pn)_3^{3+}$; the latter has the larger radius, and also the greater tendency to associate with anions. Although simple electrostatic considerations suggest that increasing ionic radius would lead to lower association, it is clear that increasing radius, especially in the form of added organic groups, reduces solvation by water. Thus as the water molecules of the second sphere become easier to replace, the association increases. The process is easily seen from the point of view of coordination chemistry. Association requires removal of one second-sphere "ligand" and its replacement by another, a process which does depend on the details of the structure of the first coordination sphere. Note that it is probably not necessary to postulate any covalent bonding to the second sphere, it is simply necessary to use considerations of electrostatics and hydrogen bonding with sufficient regard for microstructure.

Acknowledgments. This investigation was supported by the Directorate of Chemical Sciences, Air Force Office of Scientific Research Grant No. 212-63, and in its early stage by a grant from the Research Corporation. The authors are indebted to Mr. James D. McNeil for his help in the preparation of some of the compounds.

Mathematical Analysis of Multicomponent Free-Diffusion Experiments

by J. L. Duda and J. S. Vrentas

*Process Fundamentals Research Laboratory, The Dow Chemical Company, Midland, Michigan
(Received March 1, 1965)*

An exact procedure is developed which permits the calculation of the $(N - 1)^2$ independent diffusion coefficients of an N -component system from appropriate free-diffusion experiments. In this development, the coefficients are considered to be arbitrary functions of concentration, and the effect of volume changes due to mixing of the diffusing species is included. It is shown that the number of experiments necessary for the determination of the diffusion coefficients at several concentrations can be minimized by the use of this new procedure. In order to realize this economy in experiments it is necessary to obtain accurate concentration and concentration gradient distribution data over large concentration ranges in multicomponent systems. The special case of no volume change on mixing is also considered.

Introduction

In recent years, there has been increasing interest in the measurement of diffusion coefficients in multicomponent systems. The majority of such studies has been concerned with the analysis of free-diffusion experiments employing ternary liquid systems.¹ Free-diffusion experiments utilizing *in situ* methods of measuring concentration or concentration gradient distributions possess distinct advantages over other methods for the study of multicomponent diffusion.² Consequently, in what follows we have chosen to restrict our analysis of diffusion experiments to those of the free-diffusion type.

The interpretation of any multicomponent diffusion experiment is greatly complicated by the fact that interactions between the individual species must be included in any comprehensive analysis. In an N -component system, there are thus $(N - 1)^2$ independent diffusion coefficients that must be determined for complete description of the diffusion process. In general, the data from one free-diffusion experiment can be used to generate only $N - 1$ equations³ for the $(N - 1)^2$ coefficients. Consequently, in the general case where the diffusion coefficients are functions of composition, it is necessary to perform $N - 1$ independent experiments which have a common point of composition in their diffusion fields if all $(N - 1)^2$ diffusion coefficients at this common composition point are to be evaluated. For m compositions, it is evident that $m(N - 1)$ experiments

generating $m(N - 1)^2$ equations are needed to determine the $m(N - 1)^2$ different values of the diffusion coefficients.

For a ternary system, it follows that two experiments which have a common composition point in their diffusion fields are needed to evaluate the four independent coefficients at this point. The common procedure previously has been to conduct two experiments with the same mean concentration but with different terminal compositions. In practice, the terminal compositions of these two experiments are set very close to the mean composition so that the diffusion coefficients can be considered constant over the concentration range of interest and so that any volume change on mixing can be essentially eliminated.⁴ An added benefit of performing experiments over small concentration ranges when the common interferometric methods are employed is that the refractive index at any point in the free-dif-

(1) Typical studies which give references to previous work: G. Reinfelds and L. J. Gosting, *J. Phys. Chem.*, **68**, 2464 (1964); P. J. Dunlop and L. J. Gosting, *ibid.*, **68**, 3874 (1964).

(2) Reviews which discuss various methods of measuring diffusion coefficients: L. J. Gosting, *Advan. Protein Chem.*, **11**, 429 (1956); A. L. Geddes in "Physical Methods of Organic Chemistry," Vol. I, A. Weissberger, Ed., Interscience Publishers, Inc., New York, N. Y., 1949.

(3) These are simply the $N - 1$ species continuity equations.

(4) J. G. Kirkwood, R. L. Baldwin, P. J. Dunlop, L. J. Gosting, and G. Kegeles, *J. Chem. Phys.*, **33**, 1505 (1960), have shown that volume change on mixing effects tend to vanish as the terminal composition differences become small.

fusion field can be assumed to be a linear function of the concentrations at this point. Since most experimental data have been collected over small concentration ranges, the methods which have been developed for the analysis of ternary free-diffusion experiments are specifically for the case of constant diffusion coefficients and no volume change on mixing.^{5,6} These procedures require a minimum of two experiments for the evaluation of the complete set of four independent diffusion coefficients at each composition point in the three-component system.

The required number of experiments could be significantly reduced, however, if the individual experiments were conducted over large concentration ranges and if these experiments were chosen with some degree of discretion. The key to this experimental economy is choosing the terminal compositions of a given experiment such that its diffusion path intersects the diffusion paths of as many of the other experiments as possible.

For the sake of illustration, we consider diffusion in a ternary system of components A, B, and C whose composition at any point in a free-diffusion field can be represented as a point on a triangular diagram such as shown in Figure 1. If a solution of composition represented by point K on this diagram is brought into contact with the composition represented by point L in a free-diffusion cell, the compositions in the resulting diffusion field will lie on a line connecting these terminal points. In general, this line formed from the locus of compositions within the free-diffusion field will not be straight and for illustrative purposes has been arbitrarily drawn as shown. Similarly, the other lines in Figure 1 represent the diffusion paths of other free-diffusion experiments with different terminal compositions. In principle, if the concentration and concentration gradient distributions are known as functions of time for each of these experiments, then the complete set of independent diffusion coefficients can be determined at each of the compositions represented by the points of intersection of these concentration profiles. In general, one cannot expect a diffusion path to intersect another diffusion path more than once. Therefore, if we have m diffusion paths generated from m independent experiments and if each of these paths intersects all of the other $m - 1$ paths once, there will be a total of $m(m - 1)/2$ distinct intersection points.

In summary then for a ternary system, it is possible to determine the diffusion coefficients at $m/2$ compositions with m experiments (where m must be an even number here) by the conventional method whereas it is, in principle, possible to evaluate coefficients at $m(m - 1)/2$ compositions by the new procedure. It should

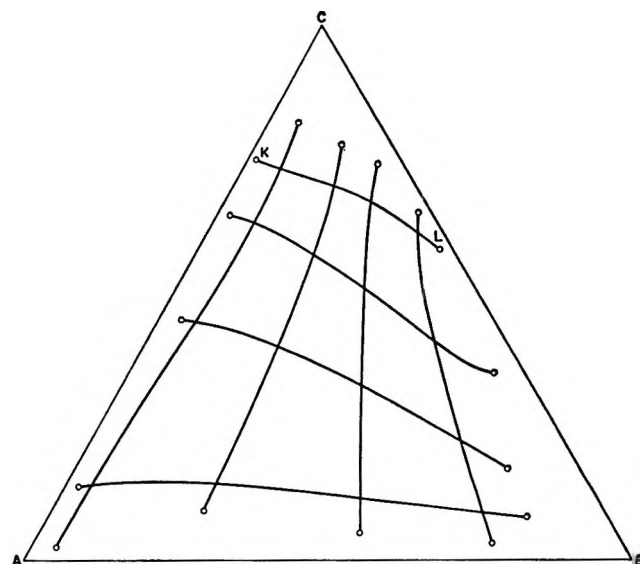


Figure 1. A typical diagram showing the intersections of several free-diffusion paths in a ternary system.

be pointed out that $m(m - 1)/2$ is the maximum number of distinct intersections if all the diffusion paths cross all the other diffusion paths. Figure 1 shows how eight experiments on a ternary system can be designed to give 16 intersections and, ultimately, the diffusion coefficients at 16 compositions. This number is less than the predicted maximum value of 28 but is certainly a great improvement over the four sets of coefficients that could be obtained from eight conventional-type experiments. The eight experiments represented in Figure 1 have been chosen to cover most of the ternary diagram as well as to ensure the intersection of diffusion paths, and, consequently, the number of intersections is less than optimal.

The extension of this economy of experiments to systems of four or more components is not straightforward since we must first guarantee that $N - 1$ experimental diffusion paths intersect at the same composition point⁷ before planning experiments to maximize the number of points of intersection. This is largely an experimental problem that can perhaps be overcome.

Before the aforementioned economy in experiments can be realized, there are two other obstacles that must be overcome. First, it is necessary to develop methods of accurately measuring concentration or concentration gradient distributions over large concentration ranges in free-diffusion cells. Accuracy of these measured

(5) H. Fujita and L. J. Gosting, *J. Am. Chem. Soc.*, **78**, 1099 (1956).

(6) H. Fujita and L. J. Gosting, *J. Phys. Chem.*, **64**, 1256 (1960).

(7) For example, for a four-component system, this requires that three concentration curves in three-dimensional space intersect at the same composition point.

quantities is especially important here because, in part, point values of the concentration profiles are employed rather than integrated values as in the conventional methods. One difficulty of obtaining data over large concentration ranges in multicomponent systems is the uncertainty in deducing concentration distributions from refractive index distributions. In addition, care must be taken to avoid convective mixing resulting from adverse density gradients which can develop in multicomponent free-diffusion processes.⁸ Secondly, methods of analyzing such data must be developed. The purpose of this paper is to develop a method of analyzing multicomponent free-diffusion experiments which will include the effects of variable diffusion coefficients and the effect of volume changes during mixing of the diffusing species.⁹ This development will be based on the premise that accurate concentration and concentration gradient distribution data are available. It is hoped that this development will serve as an incentive for the experimentalists to perfect methods of obtaining such data.

The following analysis for the general case will be developed in part in matrix notation for a system of N components. The special case of variable diffusion coefficients with no volume change on mixing will also be considered.

Formulation of General Case

Development of Basic Equations. To effect a detailed analysis of data from a free-diffusion cell, we must consider the conservation laws which describe the diffusion process in a continuum. If we limit our development to an isothermal system of N nonreacting components, the equations of change which mathematically describe the physical behavior of the system¹⁰ are the total continuity equation

$$\frac{\partial \rho}{\partial t} + (\rho v^i)_{,i} = 0 \quad (1)$$

the $N - 1$ species continuity equations

$$\frac{\partial \rho_I}{\partial t} + (\rho_I v^i)_{,i} + (j_I^i)_{,i} = 0 \quad (2)$$

and the three equations of motion

$$\rho \frac{\partial v^i}{\partial t} + \rho v^j v^i_{,j} + \left(\sum_{I=1}^N \rho_I W_I^i W_I^j \right)_{,j} = \sum_{I=1}^N \rho_I F_I^i + \sum_{I=1}^N T_I^{ij} \quad (3)$$

Here, v^i and j_I^i denote components of the mass-average velocity¹¹ and the mass diffusion flux of component I relative to the mass average velocity, respectively. Fur-

thermore, by restricting the analysis to purely viscous, nonpolar fluids, we can write the thermal equation of state in the form

$$\rho = \rho(\rho_1, \rho_2, \dots, \rho_{N-1}, p) \quad (4)$$

A complete analysis of any isothermal diffusion process necessarily requires the inclusion of all of the above equations. However, in certain flow fields it is possible to effect great simplifications by uncoupling the equations of motion from the species continuity equations. We shall now establish that free diffusion is one class of flows for which such simplifications are possible.

For a one-dimensional free-diffusion process, there is one-directional motion with all variables changing in that direction only. Furthermore, free-diffusion cells are usually constructed so that the flows are best described relative to rectangular Cartesian coordinate axes and so that the effects of external fields can be neglected. Consequently, eq. 1 and 2 can be expressed as

$$\frac{\partial \rho}{\partial t} + \frac{\partial(\rho v)}{\partial x} = 0 \quad (5)$$

$$\frac{\partial \rho_I}{\partial t} + \frac{\partial(\rho_I v)}{\partial x} + \frac{\partial j_I}{\partial x} = 0 \quad (6)$$

Now, introduction of the mass fraction

$$\omega_I = \frac{\rho_I}{\rho} \quad (7)$$

into eq. 6 and utilization of eq. 5 give the following modified form of the species continuity equations

$$\rho \frac{\partial \omega_I}{\partial t} + \rho v \frac{\partial \omega_I}{\partial x} + \frac{\partial j_I}{\partial x} = 0 \quad (8)$$

In addition, eq. 5 can also be written as

$$\frac{\partial v}{\partial x} = -\frac{1}{\rho} \frac{\partial \rho}{\partial t} - \frac{v}{\rho} \frac{\partial \rho}{\partial x} \quad (9)$$

Also, for a free-diffusion process the pressure variations throughout the system will be small, and, to a high degree of accuracy, we can assume that the total density

(8) Some aspects of gravitational stability in three-component systems are discussed by R. P. Wendt, *J. Phys. Chem.*, **66**, 1740 (1962).

(9) It has been shown elsewhere (J. L. Duda and J. S. Vrentas, to be published in *Ind. Eng. Chem. Fundamentals*) that volume change on mixing effects must be taken into account if accurate values of diffusion coefficients are to be determined for binary systems.

(10) C. Truesdell and R. A. Toupin in "Handbuch der Physik," Band III/1, S. Flügge, Ed., Springer-Verlag, Berlin, 1960.

(11) R. B. Bird, W. E. Stewart, and E. N. Lightfoot, "Transport Phenomena," John Wiley and Sons, Inc., New York, N. Y., 1960, p. 497 ff.

of the system is affected negligibly by the pressure. Consequently, we can rewrite eq. 4 as

$$\rho = \rho(\omega_1, \omega_2, \dots, \omega_{N-1}) \quad (10)$$

from which we deduce that

$$\frac{\partial \rho}{\partial t} = \sum_{I=1}^{N-1} \left(\frac{\partial \rho}{\partial \omega_I} \right)_{\omega_J} \frac{\partial \omega_I}{\partial t} \quad (11)$$

$$\frac{\partial \rho}{\partial x} = \sum_{I=1}^{N-1} \left(\frac{\partial \rho}{\partial \omega_I} \right)_{\omega_J} \frac{\partial \omega_I}{\partial x} \quad (12)$$

Finally, if each of the species continuity equations represented by eq. 8 is multiplied by $(\partial \rho / \partial \omega_I)_{\omega_J}$ and the resulting equations are summed over $N - 1$ components, there results

$$\rho \sum_{I=1}^{N-1} \left(\frac{\partial \rho}{\partial \omega_I} \right)_{\omega_J} \frac{\partial \omega_I}{\partial t} + \rho v \sum_{I=1}^{N-1} \left(\frac{\partial \rho}{\partial \omega_I} \right)_{\omega_J} \frac{\partial \omega_I}{\partial x} + \sum_{I=1}^{N-1} \left(\frac{\partial \rho}{\partial \omega_I} \right)_{\omega} \frac{\partial j_I}{\partial x} = 0 \quad (13)$$

Substitution of eq. 11, 12, and 13 into eq. 9 gives the expression for the velocity gradient anywhere in the free-diffusion field

$$\frac{\partial v}{\partial x} = \frac{1}{\rho^2} \sum_{I=1}^{N-1} \left(\frac{\partial \rho}{\partial \omega_I} \right)_{\omega_J} \frac{\partial j_I}{\partial x} \quad (14)$$

It is evident from eq. 8, 10, and 14 that, if the velocity is specified at one point in the diffusion field, it is possible to investigate the diffusion process independently of the equations of motion. We have thus essentially uncoupled the species continuity equations from the momentum equations.

For complete specification of eq. 8 and 14, we must, of course, substitute proper expressions for the mass diffusion fluxes of each of the components in the system. If we assume that the fluids we are considering are isotropic, it can be shown from nonequilibrium thermodynamics¹² that the proper linear constitutive equation for the mass diffusion flux of component I relative to the mass-average velocity can be expressed as

$$j_I = - \sum_{J=1}^N L_{IJ} \frac{\partial \mu_J}{\partial x} \quad (15)$$

where μ_J is the specific chemical potential of component J and the L_{IJ} terms are the usual phenomenological coefficients. Now, since

$$\mu_J = \mu_J(\omega_1, \omega_2, \dots, \omega_{N-1}, p) \quad (16)$$

at constant temperature we can equivalently write eq. 15 as

$$j_I = - \rho \sum_{K=1}^{N-1} D_{IK} \frac{\partial \omega_K}{\partial x} \quad (17)$$

where

$$D_{IK} = \sum_{J=1}^N \frac{L_{IJ}}{\rho} \left(\frac{\partial \mu_J}{\partial \omega_K} \right)_{\omega_S, p} \quad (18)$$

and where, in general

$$D_{IK} = D_{IK}(\omega_1, \omega_2, \dots, \omega_{N-1}) \quad (19)$$

In the above development, we have neglected the effect of the pressure gradient on the diffusion flux.

Finally, we establish the boundary conditions which represent the physical behavior of a free-diffusion cell. First of all, the following set of boundary conditions is valid for each species I

$$\omega_I(0, x) = \omega_{I0} \quad x < 0 \quad (20a)$$

$$\omega_I(t, -\infty) = \omega_{I0} \quad (20b)$$

$$\omega_I(0, x) = \omega_{I\infty} \quad x > 0 \quad (20c)$$

$$\omega_I(t, \infty) = \omega_{I\infty} \quad (20d)$$

In addition, diffusion cells are usually constructed or can easily be modified so that the fluid is constrained at one of the infinite boundaries. Consequently, we can set the velocity there equal to zero, and the appropriate boundary condition becomes, for example

$$v(t, -\infty) = 0 \quad (21)$$

It should be pointed out that a very complex problem results if neither of the infinite boundaries is constrained.

Solution for the D_{IK} . We proceed now to solve eq. 8, 10, 14, 17, 20, and 21 for the $(N - 1)^2$ diffusion coefficients D_{IK} in terms of quantities which can be obtained experimentally from a free-diffusion cell. It is possible to simplify the problem considerably by converting the partial differential equations to ordinary differential equations by introduction of the familiar Boltzmann transformation

$$\eta = \frac{x}{2t^{1/2}} \quad (22)$$

Application of eq. 22 gives

$$-2\eta\rho \frac{d\omega_I}{d\eta} + 2\rho v\sqrt{t} \frac{d\omega_I}{d\eta} - \frac{d}{d\eta} \left(\rho \sum_{K=1}^{N-1} D_{IK} \frac{d\omega_K}{d\eta} \right) = 0 \quad (23)$$

for eq. 8 and 17

$$\frac{d(v\sqrt{t})}{d\eta} = - \frac{1}{2\rho^2} \sum_{I=1}^{N-1} \left(\frac{\partial \rho}{\partial \omega_I} \right)_{\omega_J} \frac{d}{d\eta} \left(\rho \sum_{K=1}^{N-1} D_{IK} \frac{d\omega_K}{d\eta} \right) \quad (24)$$

(12) S. R. de Groot and P. Mazur, "Non-Equilibrium Thermodynamics," North-Holland Publishing Co., Amsterdam, 1962, p. 33 ff.

for eq. 14 and 17, and

$$\omega_I(-\infty) = \omega_{I0} \tag{25a}$$

$$\omega_I(\infty) = \omega_{I\infty} \tag{25b}$$

$$v\sqrt{t}(-\infty) = 0 \tag{25c}$$

for the boundary conditions. Integration of eq. 24 using eq. 25c and substitution of the resulting expression into eq. 23 yield

$$-2\eta\rho \frac{d\omega_I}{d\eta} = \frac{d}{d\eta} \left(\rho \sum_{K=1}^{N-1} D_{IK} \frac{d\omega_K}{d\eta} \right) + \rho \frac{d\omega_I}{d\eta} \sum_{J=1}^{N-1} \int_0^{\xi_J} \frac{1}{\rho^2} \left(\frac{\partial \rho}{\partial \omega_J} \right)_{\omega_R} d\xi_J \tag{26}$$

where

$$\xi_J = \rho \sum_{K=1}^{N-1} D_{JK} \frac{d\omega_K}{d\eta} \tag{27}$$

and where use has been made of the fact that all gradients vanish at the infinite limit.

Equation 26 represents a set of $N - 1$ coupled Volterra integro-differential equations which are to be solved for the variables of interest, the $N - 1$ ξ_I .¹³ Division of eq. 26 by $\rho d\omega_I/d\eta$ and differentiation with respect to η lead to

$$-2 = \frac{1}{\rho} \frac{d}{d\eta} \left(\frac{d\xi_I}{d\eta} / \frac{d\omega_I}{d\eta} \right) - \frac{1}{\rho^2} \frac{d\rho}{d\eta} \left(\frac{d\xi_I}{d\eta} / \frac{d\omega_I}{d\eta} \right) + \frac{1}{\rho^2} \sum_{J=1}^{N-1} \left(\frac{\partial \rho}{\partial \omega_J} \right)_{\omega_R} \frac{d\xi_J}{d\eta} \tag{28}$$

However, from eq. 10 we can write

$$\frac{d\rho}{d\eta} = \sum_{J=1}^{N-1} \left(\frac{\partial \rho}{\partial \omega_J} \right)_{\omega_R} \frac{d\omega_J}{d\eta} \tag{29}$$

and, consequently, eq. 28 can be converted to

$$-2\rho = \frac{d\alpha_I}{d\eta} - \frac{1}{\rho} \left[\sum_{J=1}^{N-1} \left(\frac{\partial \rho}{\partial \omega_J} \right)_{\omega_R} \frac{d\omega_J}{d\eta} \right] \alpha_I + \frac{1}{\rho} \sum_{J=1}^{N-1} \left(\frac{\partial \rho}{\partial \omega_J} \right)_{\omega_R} \frac{d\omega_J}{d\eta} \alpha_J \tag{30}$$

where

$$\alpha_I = \frac{d\xi_I/d\omega_I}{d\eta/d\eta} \tag{31}$$

If we now subtract from eq. 30 the equivalent equation for component K , we discover that

$$\frac{d(\alpha_I - \alpha_K)}{d\eta} = \frac{1}{\rho} \left[\sum_{J=1}^{N-1} \left(\frac{\partial \rho}{\partial \omega_J} \right)_{\omega_R} \frac{d\omega_J}{d\eta} \right] (\alpha_I - \alpha_K) \tag{32}$$

From eq. 26 it is evident that

$$-2 \lim_{\eta \rightarrow -\infty} (\eta\rho) = \lim_{\eta \rightarrow -\infty} \alpha_I \tag{33}$$

and, since we can infer an equivalent expression for α_K , it follows then that

$$\lim_{\eta \rightarrow -\infty} (\alpha_I - \alpha_K) = 0 \tag{34}$$

Utilization of this boundary condition in the above first-order differential equation leads to the immediate conclusion that eq. 32 can be satisfied only if

$$\alpha_I - \alpha_K = 0 \tag{35}$$

everywhere in the diffusion field. Thus, we conclude that

$$\alpha_1 = \alpha_2 = \dots = \alpha_{N-1} \tag{36}$$

and eq. 30 can therefore be shown to reduce to

$$\frac{d\alpha_I}{d\eta} = -2\rho \tag{37}$$

It remains now only to solve each differential equation of this set separately for the $N - 1$ ξ_I .

Integration of eq. 37 from $\eta = -\infty$ to any point in the diffusion field gives

$$\alpha_I - \lim_{\eta \rightarrow -\infty} \alpha_I = - \int_{-\infty}^{\eta} 2\rho d\eta \tag{38}$$

which upon integration by parts becomes

$$\frac{d\xi_I}{d\eta} / \frac{d\omega_I}{d\eta} - \lim_{\eta \rightarrow -\infty} \left(\frac{d\xi_I}{d\eta} / \frac{d\omega_I}{d\eta} \right) = -2\rho\eta + \lim_{\eta \rightarrow -\infty} (2\rho\eta) + \int_{\rho_0}^{\rho} 2\eta d\rho \tag{39}$$

Substitution of eq. 33 into eq. 39 and further integration¹⁴ yield

$$\xi_I = - \int_{\omega_{I0}}^{\omega_I} 2\rho\eta d\omega_I + \int_{\omega_{I0}}^{\omega_I} \int_{\rho_0}^{\rho} 2\eta d\rho d\omega_I \tag{40}$$

If the double integral in this expression is integrated by parts, we obtain the desired result

$$\rho \sum_{K=1}^{N-1} D_{IK} \frac{d\omega_K}{d\eta} = - \int_{\rho_{I0}}^{\rho_I} 2\eta d\rho_I + \omega_I \int_{\rho_0}^{\rho} 2\eta d\rho \tag{41}$$

We shall now proceed to the final stage of the development, the derivation of explicit expressions for the $(N - 1)^2$ diffusion coefficients at one composition from $(N - 1)^2$ equations of the type represented by eq. 41. As mentioned previously, since each free-diffusion experi-

(13) Once the ξ_I are known, we can then determine the D_{IK} since the diffusion coefficients appear only in the ξ_I variable.

(14) Note here that $\xi_I(-\infty) = 0$ because all gradients are zero at $\eta = -\infty$.

ment necessarily yields only $N - 1$ equations similar in form to eq. 41, we must conduct $N - 1$ such experiments (possessing a common composition point) if we are to generate the $(N - 1)^2$ required independent equations. For each component, the $N - 1$ equations of the form of eq. 41 derived from the $N - 1$ experiments can be expressed compactly in matrix notation. For example, for component I we can write

$$\{B\}_I = [T]\{D\}_I \quad (42)$$

where $\{B\}_I$ and $\{D\}_I$ are $(N - 1) \times 1$ column matrices defined by

$$\{B\}_I = \begin{Bmatrix} \left(-\frac{1}{\rho} \int_{\rho_{10}}^{\rho_I} 2\eta d\rho_I + \frac{\omega_I}{\rho} \int_{\rho_0}^{\rho} 2\eta d\rho\right)_\alpha \\ \left(-\frac{1}{\rho} \int_{\rho_{10}}^{\rho_I} 2\eta d\rho_I + \frac{\omega_I}{\rho} \int_{\rho_0}^{\rho} 2\eta d\rho\right)_\beta \\ \vdots \\ \left(-\frac{1}{\rho} \int_{\rho_{10}}^{\rho_I} 2\eta d\rho_I + \frac{\omega_I}{\rho} \int_{\rho_0}^{\rho} 2\eta d\rho\right)_{N-1} \end{Bmatrix} \quad (43)$$

$$\{D\}_I = \begin{Bmatrix} D_{I1} \\ D_{I2} \\ \vdots \\ D_{IN-1} \end{Bmatrix} \quad (44)$$

and where the $(N - 1) \times (N - 1)$ square matrix $[T]$ is given by

$$[T] = \begin{bmatrix} \left(\frac{d\omega_1}{d\eta}\right)_\alpha & \left(\frac{d\omega_2}{d\eta}\right)_\alpha & \cdots & \left(\frac{d\omega_{N-1}}{d\eta}\right)_\alpha \\ \left(\frac{d\omega_1}{d\eta}\right)_\beta & \left(\frac{d\omega_2}{d\eta}\right)_\beta & \cdots & \left(\frac{d\omega_{N-1}}{d\eta}\right)_\beta \\ \dots & \dots & \dots & \dots \\ \left(\frac{d\omega_1}{d\eta}\right)_{N-1} & \left(\frac{d\omega_2}{d\eta}\right)_{N-1} & \cdots & \left(\frac{d\omega_{N-1}}{d\eta}\right)_{N-1} \end{bmatrix} \quad (45)$$

In the above equations, a Greek letter subscript denotes the number of the experiment. There exists, of course, an equation analogous to eq. 42 for each of the $N - 1$ components. By combining these $N - 1$ matrix equations, we arrive at the matrix equation

$$\{B\} = [T^*]\{D\} \quad (46)$$

Here, $\{B\}$ is an $(N - 1)^2 \times 1$ column matrix with submatrices defined by eq. 43 as elements. $\{D\}$ is an $(N - 1)^2 \times 1$ column matrix with submatrices defined by eq. 44 as elements, and $[T^*]$ is the $(N - 1)^2 \times (N - 1)^2$ square matrix defined by

$$[T^*] = \begin{bmatrix} [T] & 0 & \cdots & 0 \\ 0 & [T] & \cdots & 0 \\ \dots & \dots & \dots & \dots \\ 0 & 0 & \cdots & [T] \end{bmatrix} \quad (47)$$

Premultiplication of eq. 46 by $[T^*]^{-1}$ gives an explicit expression for the column of diffusion coefficients

$$\{D\} = [T^*]^{-1}\{B\} \quad (48)$$

where the inverse of $[T^*]$ is simply

$$[T^*]^{-1} = \begin{bmatrix} [T]^{-1} & 0 & \cdots & 0 \\ 0 & [T]^{-1} & \cdots & 0 \\ \dots & \dots & \dots & \dots \\ 0 & 0 & \cdots & [T]^{-1} \end{bmatrix} \quad (49)$$

The diagonal form of $[T^*]$ allows us to solve the set of linear equations by inverting one $(N - 1) \times (N - 1)$ matrix rather than an $(N - 1)^2 \times (N - 1)^2$ matrix.

Equation 48 is the final desired result. From eq. 43, 44, 45, and 49, it is clear that eq. 48 can be used to determine the values of all of the diffusion coefficients at one composition from mass fraction distribution data¹⁵ (for each component and for $N - 1$ experiments) and from the multicomponent density-mass fraction relationship. The former information can, of course, be obtained from free-diffusion experiments whereas the density-composition data must be obtained from an entirely independent experiment.

Binary and Ternary Systems. We now deduce expressions for two- and three-component systems from the general results derived above. For a binary system we need consider only eq. 41 which for component one reduces to

$$\rho D \frac{d\omega_1}{d\eta} = - \int_{\rho_{10}}^{\rho_I} 2\eta d\rho_1 + \omega_1 \int_{\rho_0}^{\rho} 2\eta d\rho \quad (50)$$

This equation was derived previously elsewhere.⁹ For a three-component system eq. 48 produces the following results after inversion of the matrix $[T]$

$$D_{11} = \left[I_1 \left(\frac{d\omega_2}{d\eta} \right)_\beta - I_2 \left(\frac{d\omega_2}{d\eta} \right)_\alpha \right] / |T| \quad (51)$$

$$D_{12} = \left[-I_1 \left(\frac{d\omega_1}{d\eta} \right)_\beta + I_2 \left(\frac{d\omega_1}{d\eta} \right)_\alpha \right] / |T| \quad (52)$$

$$D_{21} = \left[I_3 \left(\frac{d\omega_2}{d\eta} \right)_\beta - I_4 \left(\frac{d\omega_2}{d\eta} \right)_\alpha \right] / |T| \quad (53)$$

$$D_{22} = \left[-I_3 \left(\frac{d\omega_1}{d\eta} \right)_\beta + I_4 \left(\frac{d\omega_1}{d\eta} \right)_\alpha \right] / |T| \quad (54)$$

$$|T| = \left(\frac{d\omega_1}{d\eta} \right)_\alpha \left(\frac{d\omega_2}{d\eta} \right)_\beta - \left(\frac{d\omega_2}{d\eta} \right)_\alpha \left(\frac{d\omega_1}{d\eta} \right)_\beta \quad (55)$$

$$I_1 = \left(-\frac{1}{\rho} \int_{\rho_{10}}^{\rho_I} 2\eta d\rho_1 + \frac{\omega_1}{\rho} \int_{\rho_0}^{\rho} 2\eta d\rho \right)_\alpha \quad (56)$$

(15) All variables, gradients of variables, and integrals must, of course, be evaluated at the intersection composition.

$$I_2 = \left(-\frac{1}{\rho} \int_{\rho_{10}}^{\rho_1} 2\eta d\rho_1 + \frac{\omega_1}{\rho} \int_{\rho_0}^{\rho} 2\eta d\rho \right) \quad (57)$$

The quantities I_3 and I_4 are defined similarly for component two.

Finally, it should be noted that completely equivalent expressions can, of course, be obtained if the velocity at the positive infinity boundary is set equal to zero. However, integration of the experimental data must always begin at the infinite boundary at which the velocity vanishes.

Special Case of No Volume Change on Mixing

In this section, we obtain expressions for the determination of diffusion coefficients from experiments for which volume change on mixing effects are completely negligible but the concentration dependence of the diffusion coefficients is not. We first derive explicit relationships between the diffusion coefficients relative to the mass-fixed frame of reference (the D_{IK} introduced above) and the diffusion coefficients based on the volume-fixed frame of reference (these will be denoted by \bar{D}_{IK}). The latter set of coefficients is the one most often measured by the experimentalist since it can be determined for systems which exhibit no volume change on mixing without the need for auxiliary data. We shall then develop a procedure for determining the \bar{D}_{IK} for the special case outlined above. Finally, we shall derive an alternate form of eq. 41 which illustrates the correction terms that must be included to describe the effects of significant volume changes on mixing.

Relationships between the \bar{D}_{IK} and the D_{IK} . The velocity of each component in the mixture relative to stationary coordinate axes can be expressed as

$$\rho_I v_I = \rho_I \bar{v} + j_I = \rho_I \bar{v} + \bar{j}_I \quad (58)$$

where \bar{v} is the volume-average velocity¹¹ and \bar{j}_I is the mass diffusion flux of component I relative to the volume-average velocity. Multiplication of eq. 58 by the partial specific volume \hat{V}_I and summation over all components give

$$v - \bar{v} = -\sum_{J=1}^N j_J \hat{V}_J \quad (59)$$

where we have utilized the well-known identities

$$\sum_{I=1}^N \hat{V}_I \rho_I = 1 \quad (60)$$

$$\sum_{I=1}^N \hat{V}_I \bar{j}_I = 0 \quad (61)$$

Substitution of eq. 59 into eq. 58 yields the relationship between the two types of diffusion fluxes

$$\bar{j}_I = j_I - \rho_I \sum_{J=1}^N j_J \hat{V}_J \quad (62)$$

In addition, since

$$\sum_{I=1}^N j_I = 0 \quad (63)$$

we can modify eq. 62 to give the result

$$\bar{j}_I = j_I - \rho_I \left[\sum_{J=1}^{N-1} j_J (\hat{V}_J - \hat{V}_N) \right] \quad (64)$$

Now, eq. 17 can equivalently be written as

$$j_I = -\sum_{K=1}^{N-1} D_{IK} \left[\frac{\partial \rho_K}{\partial x} - \frac{\rho_K}{\rho} \sum_{S=1}^{N-1} \left(\frac{\partial \rho}{\partial \rho_S} \right)_{\rho_R, p, T} \frac{\partial \rho_S}{\partial x} \right] \quad (65)$$

where we concern ourselves only with the ordinary diffusion contribution to the mass flux. Furthermore, it can be shown that

$$\left(\frac{\partial \rho}{\partial \rho_S} \right)_{\rho_R, p, T} = -\frac{\hat{V}_S - \hat{V}_N}{\hat{V}_N} \quad (66)$$

Substitution of eq. 65 and 66 into eq. 64 gives after some rearrangement

$$\bar{j}_I = -\sum_{S=1}^{N-1} \bar{D}_{IS} \frac{\partial \rho_S}{\partial x} \quad (67)$$

where

$$\begin{aligned} \bar{D}_{IS} = & D_{IS} - \sum_{J=1}^{N-1} \rho_I (\hat{V}_J - \hat{V}_N) D_{JS} + \\ & \left(\frac{\hat{V}_S - \hat{V}_N}{\hat{V}_N} \right) \sum_{J=1}^{N-1} \left[\omega_J D_{IJ} - \sum_{K=1}^{N-1} \rho_I \omega_K (\hat{V}_J - \hat{V}_N) D_{JK} \right] \end{aligned} \quad (68)$$

In an analogous manner, it is possible to obtain the inverse relationship

$$\begin{aligned} D_{IK} = & \bar{D}_{IK} + \omega_I \sum_{J=1}^{N-1} \bar{D}_{JK} \left(\frac{\hat{V}_J - \hat{V}_N}{\hat{V}_N} \right) + \\ & \rho (\hat{V}_N - \hat{V}_K) \sum_{S=1}^{N-1} \left[\omega_S \bar{D}_{IS} + \sum_{J=1}^{N-1} \omega_S \omega_I \bar{D}_{JS} \frac{\hat{V}_J - \hat{V}_N}{\hat{V}_N} \right] \end{aligned} \quad (69)$$

Equations 68 and 69 permit relatively simple calculation of the one type of diffusion coefficient from knowledge of the other type. These two sets of diffusion coefficients are perhaps the most widely used in the analysis of mass-transfer phenomena.

Solution for the \bar{D}_{IK} . When examining the special case of no volume change during mixing, it is helpful to cast the species continuity equations into the following form

$$\frac{\partial \rho_I}{\partial t} + \frac{\partial(\rho_I \bar{v})}{\partial x} + \frac{\partial \bar{j}_I}{\partial x} = 0 \quad (70)$$

Furthermore, it is well known that, when the partial specific volumes are constant, the volume-average velocity vanishes identically everywhere in the diffusion field of a free-diffusion cell. Consequently, substitution of eq. 67 and application of eq. 22 convert eq. 70 to

$$-2\eta \frac{d\rho_I}{d\eta} = \sum_{K=1}^{N-1} \frac{d}{d\eta} \left(\bar{D}_{IK} \frac{d\rho_K}{d\eta} \right) \quad (71)$$

with boundary conditions

$$\rho_I(-\infty) = \rho_{I0} \quad (72a)$$

$$\rho_I(\infty) = \rho_{I\infty} \quad (72b)$$

and where, in general

$$\bar{D}_{IK} = \bar{D}_{IK}(\rho_1, \rho_2, \dots, \rho_{N-1}) \quad (73)$$

Integration of eq. 71 from $\eta = -\infty$ to $\eta = \eta$ leads to the equation

$$-\int_{\rho_{I0}}^{\rho_I} 2\eta d\rho_I = \sum_{K=1}^{N-1} \bar{D}_{IK} \frac{d\rho_K}{d\eta} \quad (74)$$

since all gradients are zero at the negative infinity boundary.

As before, it is possible to generate $(N-1)^2$ equations of the form of eq. 74 by performing $N-1$ independent experiments. Solution for the \bar{D}_{IK} proceeds now just as for the general case described above. Consequently, for component I we can write analogously to eq. 42

$$\{\bar{B}\}_I = [\bar{T}]\{\bar{D}\}_I \quad (75)$$

where $\{\bar{D}\}_I$ represents a column matrix of \bar{D}_{IK} similar to eq. 44, $[\bar{T}]$ is a square matrix defined the same as $[T]$ but with component densities ρ_I replacing mass fractions ω_I , and $\{\bar{B}\}_I$ is defined as

$$\{\bar{B}\}_I = \left\{ \begin{array}{c} \left(-\int_{\rho_{I0}}^{\rho_I} 2\eta d\rho_I \right)_\alpha \\ \left(-\int_{\rho_{I0}}^{\rho_I} 2\eta d\rho_I \right)_\beta \\ \vdots \\ \left(-\int_{\rho_{I0}}^{\rho_I} 2\eta d\rho_I \right)_{N-1} \end{array} \right\} \quad (76)$$

As in the previous development, we derive the expression

$$\{\bar{D}\} = [\bar{T}^*]^{-1}\{\bar{B}\} \quad (77)$$

The definitions of the barred matrices follow immediately from the definitions of the unbarred matrices

given previously. From eq. 77 it is possible to determine the column vector of \bar{D}_{IK} from free-diffusion data only. For a ternary mixture, the equations for the four diffusion coefficients are similar to eq. 51-55 with ρ_I replacing ω_I wherever it appears and with I_1 and I_2 given by

$$I_1 = \left(-\int_{\rho_{I0}}^{\rho_I} 2\eta d\rho_I \right)_\alpha \quad (78)$$

$$I_2 = \left(-\int_{\rho_{I0}}^{\rho_I} 2\eta d\rho_I \right)_\beta \quad (79)$$

Alternate Form of Eq. 41. In the final part of this section, an alternate form of eq. 41 which explicitly illustrates the influence of the volume change on mixing on the determination of the diffusion coefficients will be derived. We start by transforming the variables in eq. 17 and 67 through utilization of eq. 22, thus obtaining

$$2j_I \sqrt{t} = -\rho \sum_{K=1}^{N-1} \bar{D}_{IK} \frac{d\omega_K}{d\eta} \quad (80)$$

$$2\bar{j}_I \sqrt{t} = -\sum_{K=1}^{N-1} \bar{D}_{IK} \frac{d\rho_K}{d\eta} \quad (81)$$

Substitution of eq. 80 into eq. 41 produces

$$-2\sqrt{t} j_I = -\int_{\rho_{I0}}^{\rho_I} 2\eta d\rho_I + \omega_I \int_{\rho_0}^{\rho} 2\eta d\rho \quad (82)$$

and multiplication of eq. 82 by $(\hat{V}_I - \hat{V}_N)$ and summation over $N-1$ of the components yield

$$-\sum_{I=1}^{N-1} 2\sqrt{t} j_I (\hat{V}_I - \hat{V}_N) = -\sum_{I=1}^{N-1} (\hat{V}_I - \hat{V}_N) \int_{\rho_{I0}}^{\rho_I} 2\eta d\rho_I + (1/\rho - \hat{V}_N) \int_{\rho_0}^{\rho} 2\eta d\rho \quad (83)$$

Finally, substitution of eq. 64, 81, and 83 into eq. 82 gives the result

$$\sum_{K=1}^{N-1} \bar{D}_{IK} \frac{d\rho_K}{d\eta} = -\int_{\rho_{I0}}^{\rho_I} 2\eta d\rho_I + \rho_I \sum_{J=1}^{N-1} (\hat{V}_J - \hat{V}_N) \int_{\rho_{J0}}^{\rho_J} 2\eta d\rho_J + \hat{V}_N \rho_I \int_{\rho_0}^{\rho} 2\eta d\rho \quad (84)$$

Now, remembering that the partial specific volumes are constant for the case of no volume change on mixing and applying eq. 66, we are able to reduce eq. 84 to eq. 74. Therefore, it is clear that eq. 84 is composed of the same terms as the corresponding equation for no volume change on mixing plus two additive integral correction terms which express the importance of any volume change on mixing. This equation more directly exhibits the nature and magnitude of the ef-

fects of significant volume changes on the diffusion process, and it furthermore yields values of \bar{D}_{IK} rather than D_{IK} . A matrix analysis based on eq. 84 analogous to that stemming from eq. 41 could easily be for-

mulated. One distinct disadvantage in using eq. 84 is the appearance of partial specific volumes in the terms of the equation, thus necessitating differentiation of the multicomponent density-mass fraction data.

Oxidation and Chemiluminescence of Tetrakis(dimethylamino)ethylene. I.

Reversible Reactions of Oxygen with Tetrakis(dimethylamino)ethylene

and *n*-Decane

by Carl A. Heller and Aaron N. Fletcher

Research Department, U. S. Naval Ordnance Test Station, China Lake, California (Received March 1, 1965)

The solubility and heat of solution of oxygen in *n*-decane and tetrakis(dimethylamino)-ethylene (TMAE) have been measured and found to be almost equal. The spectrally measurable interaction species, TMAE-O₂ and *n*-C₁₀H₂₂-O₂, are shown to have very low ΔH of formation (-1.2 and -0.4 kcal.). Thus, in nonpolar media the good electron donor TMAE and poor electron donor *n*-decane react similarly with oxygen.

Introduction

This paper will describe studies of a weak charge-transfer contact pair¹ or complex² between oxygen and both tetrakis(dimethylamino)ethylene (TMAE) and *n*-decane. This type of complex has been observed by absorption spectrometry for several hydrocarbons which have been shown to form 1:1 pairs.³⁻⁵ TMAE has been shown to form stable complexes with a number of electron acceptors.⁶ It can also be oxidized to form both a cation radical and a dication.⁷

Since our chemiluminescent studies involve *n*-decane solutions of TMAE and oxygen we have studied the solubilities and interaction species of oxygen with both molecules. The ΔH values found appear to be the first reported for such species.

Experimental Section

Oxygen Uptake Apparatus. The pressure drop was used to measure oxygen uptake in a 10-ml. erlen-

meyer flask. In operation the liquid was degassed by freezing and pumping. Oxygen was let into the flask with the stirrer off, initial pressure zeroed quickly, and the stirrer started. With the stirrer off, the solution rate was very slow so little error arose from the initial short delay. The final pressure, pressure change, and known volume gave the amount dissolved. The pressure change was measured with a Pace transducer and a recorder. The oxygen was in 1-l. flasks in an air bath, and the sample was immersed in a stirred bath slightly above the liquid level.

- (1) R. S. Mulliken, *J. chim. phys.*, **61**, 20 (1964).
- (2) S. Carter, J. N. Murrell, and E. J. Rasch, *J. Chem. Soc.*, 2048 (1965).
- (3) D. F. Evans, *ibid.*, 345 (1953).
- (4) A. U. Munck and J. F. Scott, *Nature*, **177**, 578 (1958).
- (5) D. F. Evans, *J. Chem. Soc.*, 1987 (1961).
- (6) N. Wiberg and J. W. Buckler, *Chem. Ber.*, **97**, 618 (1964).
- (7) N. Kuwata and D. H. Geske, *J. Am. Chem. Soc.*, **86**, 2101 (1964).

Spectrophotometric Study. The apparatus consists of two constant temperature liquid reservoirs connected by vacuum-jacketed tubing and includes spectrophotometric flow cells. The gas system above the reservoirs is used to produce a reciprocating flow of the liquid between the reservoirs or to bubble gas through the liquid phase.

A Beckman DK-2 spectrophotometer is used to monitor the absorbance of the liquid in the cells which can be placed in series or filled separately. Temperature control in the sample cell is $\pm 0.2^\circ$ during flow. Absorbances as low as 0.001 can be measured.

Material. The *n*-decane was stirred overnight with 30% fuming sulfuric acid and washed with concentrated sulfuric acid, water, and a dilute sodium hydroxide solution. After drying over activated alumina, the *n*-decane was distilled from sodium under an atmosphere of 700 torr of purified argon.

TMAE was obtained from E. I. du Pont de Nemours and Co., Wilmington, Del. It was purified by filtering through a bed of Al_2O_3 (Alcoa F-1, 4-8 mesh). This gave a material which was pure by a gas chromatographic analysis. The purified TMAE was stored under nitrogen or argon. The uncorrected melting point was -4° .

Water and similar compounds increase the irreversible reaction of TMAE with oxygen.^{7,8} All apparatus and operations were handled so as to minimize impurities including air. However, after long storage TMAE would often show a precipitate of tetramethyloxamide. Therefore, it was repurified about once a month.

During runs on the solubility there was always a slow irreversible reaction as indicated by the production of light. In the spectral runs tetramethyloxamide eventually precipitated and halted the work. The base line was determined after each run with oxygen for the work with both TMAE and decane. The rate of the irreversible reaction increased with temperature and limited studies with TMAE to 30° and lower.

The problems mentioned limited the reproducibility of data to that shown in the next section.

Results

Solubility. Table I shows the results obtained for oxygen solubility in *n*-decane and TMAE. The results reported here can be compared with a value of 0.0127 for oxygen in *n*-heptane at 25° .⁹ The solubility was taken at a series of pressures from 100 to 700 torr. It obeyed Henry's law for both *n*-decane and TMAE so best straight lines were drawn for each temperature. For these the slope, k , was obtained.

Table I: Solubility of Oxygen^a

$T, ^\circ\text{C.}$	k for <i>n</i> -decane, mmole l. ⁻¹ torr ⁻¹	k for TMAE, mmole l. ⁻¹ torr ⁻¹
0	0.0154	0.0151
24	0.0137	0.013 \pm 0.001
ΔH	-0.8 kcal.	-0.8 kcal.

^a $S = kP_{\text{O}_2}$ mmole/l.

There was a problem in measuring the solubilities in TMAE at room temperature (24°). Figure 1 shows a typical pressure trace. Instead of a pressure plateau, we obtained a slope due to the irreversible reaction of O_2 with TMAE. We measured the pressure drop at two points which should give minimum and maximum solubility possibilities. The k at 24° represents a best line drawn through the values of the mean.

A few runs were made at 0° with $10^{-3} M$ 1-octanol in the TMAE to learn whether this affected the solubility. These runs looked like those at 24° with "pure" TMAE, and we took maximum and minimum values which naturally include larger errors. The mean values showed no significant difference from those taken without 1-octanol.

In all the runs with TMAE the brown coloration appeared and deepened as the O_2 dissolved. There was no perceptible lag. If the stirrer was turned off and O_2 pumped away, the brown remained for several

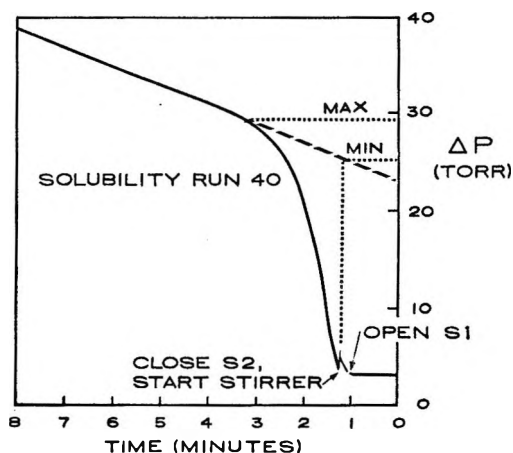


Figure 1. Solubility of O_2 in TMAE at 24° . Speedomax record showing method of obtaining maximum and minimum values of solubility.

(8) H. E. Winberg, J. R. Downing, and D. D. Coffman, *J. Am. Chem. Soc.*, **87**, 2054 (1965).

(9) J. H. Hildebrand and R. L. Scott, "Regular Solutions," Prentice-Hall, Inc., Englewood Cliffs, N. J., 1962.

minutes; if the stirrer was on, the brown disappeared rapidly.

Spectra. In Figures 2 and 3 we show spectra of the type used in our measurements. The solvent in all cases is *n*-decane.

Figure 2 shows in curve B the shoulder which is used to measure the *n*-decane-oxygen interaction species. Curve C shows the absorption of TMAE in *n*-decane. We find a peak at 221 $m\mu$ as opposed to 240 $m\mu$ reported elsewhere.⁸

Figure 3 shows similar curves for TMAE-oxygen systems. Curve A indicates the shoulder of the TMAE

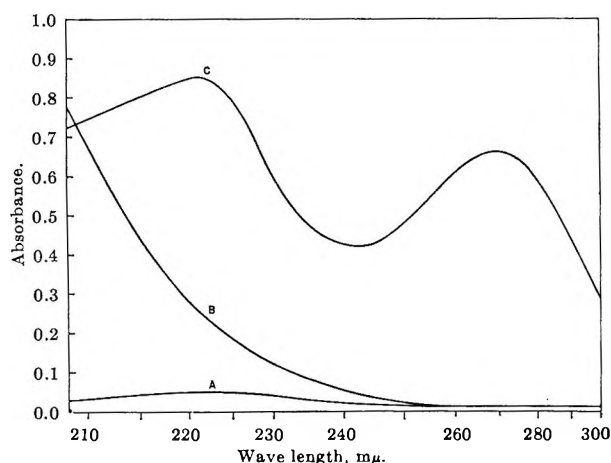


Figure 2. (A) Base line: *n*-decane vs. *n*-decane; (B) *n*-decane + 400 torr of O₂ vs. *n*-decane; (C) [TMAE], $0.65 \times 10^{-4} M$, vs. *n*-decane. All at 30°.

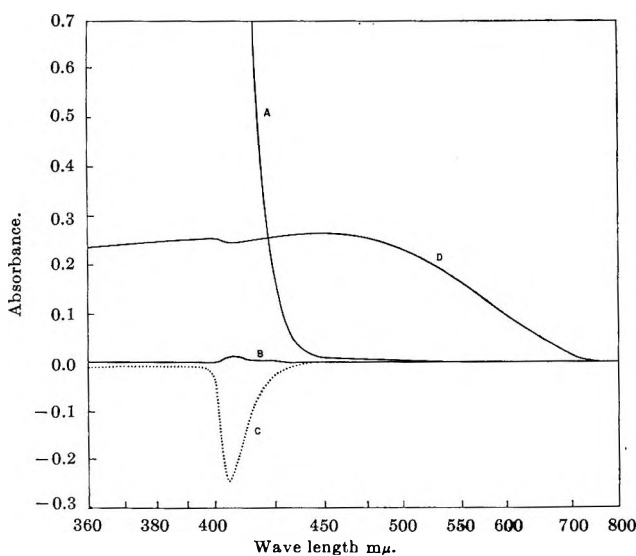


Figure 3. (A) [TMAE], 0.4 *M*, vs. *n*-decane, both 30°; (B) base line: [TMAE], 0.4 *M*, vs. [TMAE], 0.4 *M*, both 30°; (C) [TMAE], 0.4 *M*, 20°, vs. [TMAE], 0.4 *M*, 30°; (D) [TMAE], 0.4 *M*, + 1400 torr of O₂ vs. [TMAE], 0.4 *M*, both 30°.

absorption. The base line B is obtained with the spectrophotometer slits less than fully open so that curves C and D are not artifacts although less resolution is obtained below 400 $m\mu$.

Curve D is due to the difference in the molar absorptivity of TMAE and the interaction species. The absorbance of the interaction species results in the brown coloration which follows the addition or removal of oxygen with no perceptible lag.

The monocation, TMAE⁺, absorption can be seen in curve C as a narrow negative peak. The monocation is formed by the reaction⁷: TMAE²⁺ + TMAE = 2TMAE⁺. The equilibrium is shifted to form more monocation at higher temperatures. Once again, the spectrum is due to a difference between molar absorptivities. The peak at 405 $m\mu$ is shifted from that found in acetonitrile at 385 $m\mu$.⁷

Spectrophotometric Results. The *n*-decane plus oxygen interaction was measured at 220, 225, and 230 $m\mu$. The absorbance change from oxygen-free *n*-decane was taken as the absorbance of the complex. The equilibrium quotient is first order in oxygen pressure. The *n*-decane concentration was not varied, but Evans' work³ has shown that these interactions are first order in hydrocarbon. Table II shows how the quotient changed with temperature and the calculated ΔH . The variation with wave length is probably due to a change of the extinction coefficient due to a bathochromic shift of the whole band.¹⁰

Table II: Variation of p*Q* with Temperature for *n*-Decane^a

<i>T</i> , °C.	220 $m\mu$	225 $m\mu$	230 $m\mu$
0	3.840	4.076	4.312
10	3.861	4.092	4.323
20	3.866	4.106	4.334
30	3.886	4.115	4.344
40	3.894	4.123	4.350
50	3.898	4.125	4.346
60	3.923	4.134	4.355
ΔH	-0.52 kcal.	-0.39 kcal.	-0.29 kcal.

$${}^a pQ = -\log \frac{\text{absorbance}}{[n\text{-decane}]P_{O_2}}$$

TMAE plus oxygen interaction was measured only at 450 $m\mu$ and again by subtracting the decane and any slight TMAE absorbance. In this work the TMAE

(10) H. H. Willard, L. L. Merritt, Jr., and J. A. Dean, "Instrumental Methods of Analysis," 3rd Ed., D. Van Nostrand Co., Inc., New York, N. Y., 1958, p. 7.

concentration was varied with *n*-decane as the solvent. Table III shows that the interaction is first order in both species.

Table III: Negative Log [Equilibrium Quotient] at 0° for TMAE^a

[TMAE], <i>M</i>	<i>P</i> _{O₂} , torr	Absorbance at 450 mμ	p <i>Q</i>
0.0219	1200	0.0123	3.329
0.0865	1200	0.051	3.313
0.128	100	0.0056	3.356
0.128	300	0.0146	3.421
0.128	500	0.0301	3.328
0.128	700	0.0410	3.338
0.128	900	0.0540	3.329
0.128	1100	0.0675	3.320
0.128	1300	0.0804	3.317
0.210	1200	0.112	3.353
0.401	1200	0.230	3.320
			3.339 ± 0.006

$${}^a \text{p}Q = -\log \frac{\text{absorbance}}{[\text{TMAE}]P_{\text{O}_2}}$$

Table IV shows the change of the quotient with temperature and the calculated ΔH with estimated σ .¹¹

Table IV: Variation of Average Equilibrium Quotient with Temperature for TMAE

<i>T</i> , °C.	p <i>Q</i>
0	3.34
5	3.38
10	3.35
15	3.38
20	3.42
25	3.43
30	3.43

$$-\Delta H = 1.2 \pm 0.2 \text{ kcal. mole}^{-1}$$

We attempted to measure the actual concentration of the complex by measuring the decrease in TMAE absorbance as the complex formed. No decrease could be seen, as might be expected if not much complex is formed and its spectra is similar to TMAE in the ultraviolet region. The other method for measuring the actual amount of the complex involves monitoring the free oxygen *vs.* complexed oxygen. Experimental methods all measure total, not free, oxygen by equilibrium with a second phase. The Benesi-Hildebrand equations¹² or a modification² is not applicable to our present data. A technique for adding a

known constant amount of gas would have to be developed to use these equations. Also, an inert solvent would have to be found since hydrocarbons form complexes with O₂.

Thus, we cannot calculate a concentration equilibrium constant nor the free energy of complex formation. Since O₂ and argon show similar solubilities in hydrocarbons,⁹ the amount of complexing of O₂ must be small. The similarity of O₂ solubility in *n*-decane and TMAE indicates a similar weak complex for the latter.

Discussion

From a kinetic point of view one wants to know whether the spectrally observed species can be considered a real intermediate; that is, does it have a lifetime longer than a normal collision? The contact pair formulation¹ visualizes only short lifetimes with no potential well. The experimental basis of this has been questioned,² and it appears possible that even weak interactions indicate that a complex is formed. That is to say, there will be no extinction coefficient unless there is a real complex in a potential well with an equilibrium constant and a lifetime long compared with collision time. Under these circumstances, the complex can be considered an intermediate for subsequent reactions, which is of importance in the consideration of third-order reactions. These need not be termolecular, but rather the result of a 1:1 complex reacting with a third molecule.

In alkane oxidation Denisov¹³ has measured initiation kinetics which are first order in oxygen and second order in alkane. This could be due to a reaction between the alkane-oxygen complex and an alkane molecule to form free radicals.

The evidence from our measurements is that there is a slight negative enthalpy for both interaction species. For TMAE-O₂ it amounts to a few hundred calories even if we subtract the enthalpy of solution of oxygen from the measured enthalpy of formation of the peak at 450 mμ. Although the negative enthalpy does not prove there is a free energy well, it makes it appear more probable.

If the complex is an intermediate and the equilibrium is rapid compared to subsequent reactions, the ΔH will enter the observed activation energy.

The effect of traces of water⁸ in increasing the irreversible oxidation of TMAE can be understood in terms of the donor-acceptor theories of Mulliken,¹

(11) A. M. Mood, "Introduction to the Theory of Statistics," McGraw-Hill Book Co., Inc., New York, N. Y., 1950, p. 291.

(12) H. A. Benesi and J. H. Hildebrand, *J. Am. Chem. Soc.*, **71**, 2703 (1949).

(13) E. E. Denisov, *Kinetika i Kataliz*, **4**, 53 (1963).

who points out that the change from a weak complex to an ion pair is assisted by a polar environment or by formation of a complex ion. Thus, water could be expected to react with the TMAE-O₂ complex to give ion pairs. This irreversible reaction will be the subject of the next paper in this series.

Acknowledgment. The reversible brown coloration due to the TMAE-O₂ interaction species was first

noted by Charles M. Drew of this laboratory. Discussions with Drs. R. H. Knipe, P. Hammond, and W. Urry have been very helpful. Results by H. E. Winberg, J. R. Downing, D. D. Coffman, and J. P. Paris of Du Pont on TMAE were made available to us before their publication. This research was supported in part by the Advanced Research Projects Agency, Chemistry Office, Order No. 205-62-AM5.

The Dynamics of Cryosorption Pumping

by S. H. Bauer and Peter Jeffers

Department of Chemistry, Cornell University, Ithaca, New York (Received March 2, 1965)

A technique has been developed for the rapid injection of gas samples into a low pressure system (Knudsen regime) and for faithfully recording the consequent changes in pressure. The experimental procedure may be used for measurement of initial rates of adsorption on a millisecond time scale and in this investigation was used for dynamically testing the speed of cryosorption pumping of air, argon, and hydrogen by activated charcoal (temperature: liquid nitrogen). The utility of cryosorption pumping has been demonstrated for the rapid removal of bursts of gas as well as for obtaining and holding pressures down to 10⁻⁶ to 10⁻⁷ mm. The initial pumping rate is limited by a "geometric" sticking coefficient, which depends on the gas. After about 10 msec. the pumping rate declines and appears to be limited by the rate of diffusion of molecules into the cracks and pores of the large area adsorbent.

Introduction

Dynamic measurements were made of the speed of pumping by activated charcoal cooled to liquid nitrogen temperature. This study was undertaken to evaluate cryosorption for three applications.¹⁻⁵ The first, as a means of rapidly removing the gas injected as a burst in dump tanks which comprise the transition section from a shock tube to the ion source of a time-of-flight mass spectrometer. The second application is the development of a very rapid pump to maintain a local low pressure within an electron diffraction apparatus during the injection of gaseous samples. The third is the maintenance of pressures in the 10⁻⁷-mm. range in the arc chamber of an analytical mass spectrometer during continued arcing.

To make these measurements it was necessary to devise methods for rapid gas injection in the Knudsen flow regime and for following rapid pressure changes at submicron levels. For the former we used a miniature shock tube and for the latter a d.c.-operated ionization gauge and a dual-trace oscilloscope for recording con-

(1) N. M. Kuluva and E. L. Knuth, *Transactions of the Ninth Symposium of the American Vacuum Society*, 1962, pp. 237-242.

(2) M. Manes and R. J. Grant, *Transactions of the Tenth Symposium of the American Vacuum Society*, 1963, pp. 122-127.

(3) L. O. Mullen and M. J. Hiza, *Symposium on Molecular Properties at Cryogenic Temperatures*, 56th Meeting of the American Institute of Chemical Engineers, Preprint 45A, 1963.

(4) L. O. Mullen and R. B. Jacobs, *Transactions of the Ninth Symposium of the American Vacuum Society*, 1962, pp. 220-226.

(5) D. W. Breck, *J. Chem. Educ.*, **41**, 678 (1964); on zeolite.

currently the total electron emission and the positive ion current.

Apparatus and Procedure

Pittsburgh Activated Carbon Co. charcoal types BPL 12 × 30 and FCB 12 × 30 were tested, with Celanese water base emulsion polymer CL-303 as a binder. Although zeolite would have proved equally effective and merits investigation, for our application charcoal is preferred since the latter releases adsorbed water when warmed to room temperature so that no additional heating is essential. The supporting surface was a $5.08 \times 27.94 \times 0.16$ cm. sheet of copper, bent into a spiral. Serpentine copper tubing (0.32-cm. i.d.) was soldered to the strip to provide direct cooling by the liquid nitrogen. The CL-303 binder was diluted so that it consisted of 10% solids and was then mixed 1:1, proportioned by weight, with activated charcoal. The paste was rapidly applied to the pumping panel to a thickness of about 3 mm. Forty grams of charcoal was thus spread onto the panel, which was cured at 120° for 2 hr. The geometric area (charcoal covered and liquid nitrogen cooled) is approximately 140 cm.²; the estimated surface area is 4×10^4 m.². In this study we did not ascertain the possible loss in surface area of the charcoal due to local covering by the emulsion polymer.

The tests were made with the arrangement sketched in Figure 1. The ion gauge was an NRC Type 507 (glass mantle cut off); slowly varying pressures were read with a control circuit, NRC Equipment Corp. Type 710B. For the measurement of rapid changes the battery-powered circuit shown in Figure 2 was used; oscilloscope deflections were calibrated against the NRC control. The pressure response was found to be linear in the region of interest. It proved essential to record concurrently the grid current and the positive ion current since the magnitude of the latter is directly proportional to the product of the molecular density and the electron flux. The filament emission was found to change appreciably during a gas burst. The power supplies in the NRC control unit are not adequately filtered, and the circuit contains a feedback loop which regulates the emission, but response to regulations is limited to 60 c.p.s., which is too slow for the tests described.

Diaphragms for the "shock tube" were of cellophane. The plunger was in the shape of a pointed "X," 2-cm. in diameter; the diaphragms were cut cleanly into seven or eight radial petals. The high pressure chamber had a volume of 5 ml. and was filled to pressures which ranged from 1 mm. to 38 cm. Since expansion to 6.2 l. occurred, the final expected pressures

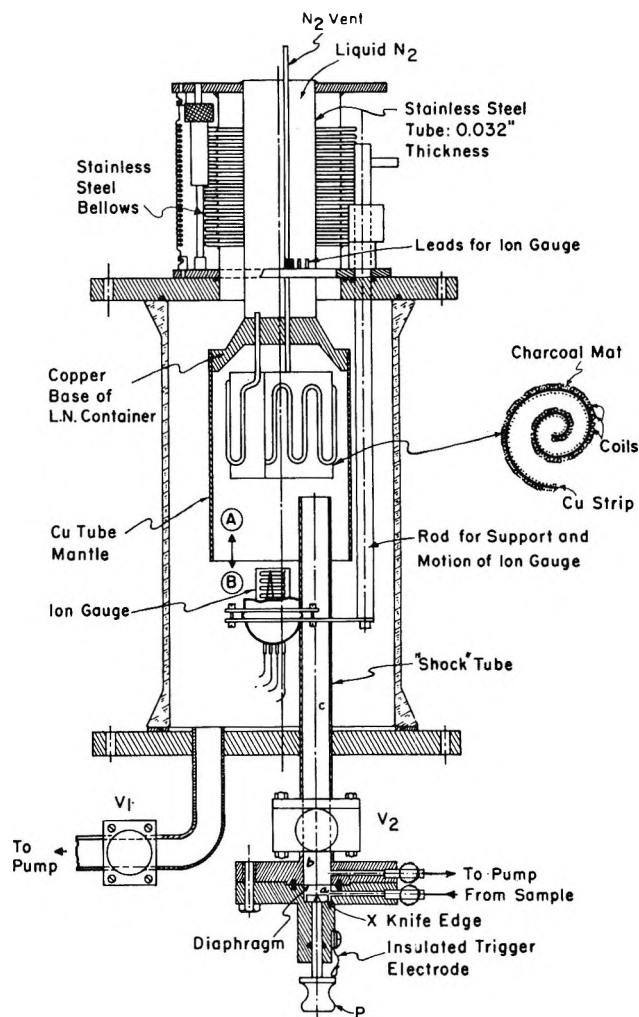


Figure 1. Apparatus for testing cryopumping rate. The bellows and spiral strip support was designed for insertion above the injection nozzle in an electron diffraction apparatus. The bellows and three spacing screws are needed to permit accurate positioning of the Cu tube mantle with respect to the electron beam. The mantle also serves as a radiation shield. For rapid gas injection region *a* is filled with sample to a pressure between 0.1 and 38 cm. With valve V_2 open, regions *b* and *c* are at the low pressure of the large vessel. The diaphragm is burst by hitting plunger *P*. V_2 is closed for replacing the diaphragm and recharging the "high pressure" chamber.

(for no pumping) ranged from 10^{-1} to 10^{-3} mm. The ion gauge was supported on a solid sliding rod and could be placed within the copper tube mantle which enclosed the charcoal-coated pumping surface (the top of the ion collector was within 2 cm. of the bottom of the spiral, position A), or it could be situated 15 cm. from the copper spiral (position B) as indicated on Figure 1.

Results

With the system newly assembled and valve V_1

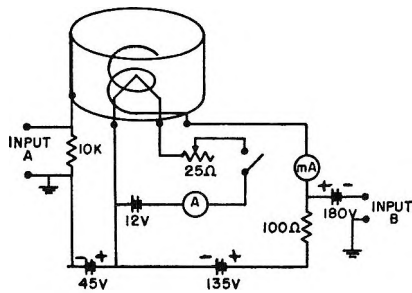


Figure 2. Circuit for ion gauge, for the measurement of rapid pressure changes. A Tektronix 535 oscilloscope with Type CA dual-trace plug-in unit was used.

open to the diffusion pump and the charcoal at room temperature, the ion gauge read 2×10^{-4} mm. On closing V_1 a leak rate of $0.3 \mu/\text{min.}$ was observed. When liquid nitrogen was poured into the container, the pressure fell to 2×10^{-6} mm. in 20 min. (V_1 closed) and was steady for several hours. A small leak was found and repaired; this reduced the leak rate to $0.1 \mu/\text{min.}$ Upon cooling the panel from room temperature with liquid nitrogen, the pressure fell from 10^{-4} to 5.6×10^{-6} mm. in 4 min. and to 4×10^{-7} mm. in 20 min. The lowest observed pressure (V_1 closed) was 1.4×10^{-7} mm. and could be held for up to 4 hr.

Preliminary tests with rapid gas injection were made using the NRC control circuit. These tests indicated that the gas was being injected and adsorbed very rapidly. In fact, the response time of the meter was the limiting factor. The observed maximum deflections of the meter needle suggested that the ionization gauge was sensing less than 25% of the injected air; the rest was adsorbed during the response time of the instrument.

Figure 3 shows typical oscilloscope traces recorded with the battery-powered circuit. The top and bottom straight lines are the zeroes for grid and plate currents, respectively. The vertical amplifiers were set so that 1 division represents a pressure of 9×10^{-6} mm., while 1.35 divisions equal 5-ma. grid current. The finite rise time noted on the pressure trace is limited by the opening time of the diaphragm and the rate of flow of the injected gas through tube c and the test vessel. The ion current traces were corrected for changes in electron emission, and reduced to pressure curves such as those shown in Figure 4. Note the difference between the pressures recorded with the gauge inside and outside the copper mantle. These typical differences are limited to the first 10 msec. and imply that a significant amount of cryopumping takes place during the time required for the gas to spread from the point of

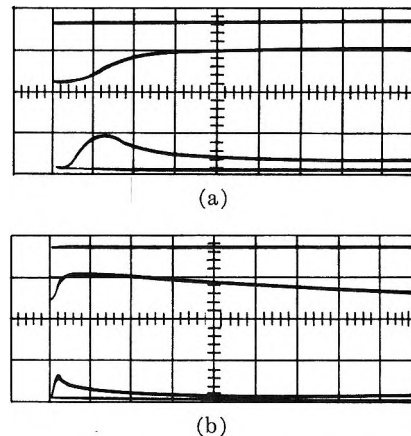


Figure 3. (a) Injection of 1 mm. of air onto BPL charcoal. Lower trace is of the ion current and the upper trace is of the grid current. Sweep speed, 10 msec./division. (b) Injection of 0.5 mm. under conditions similar to 3(a). Time scale, 100 msec./division. Grid current returned slowly to its initial level after most of the injected gas had been removed.

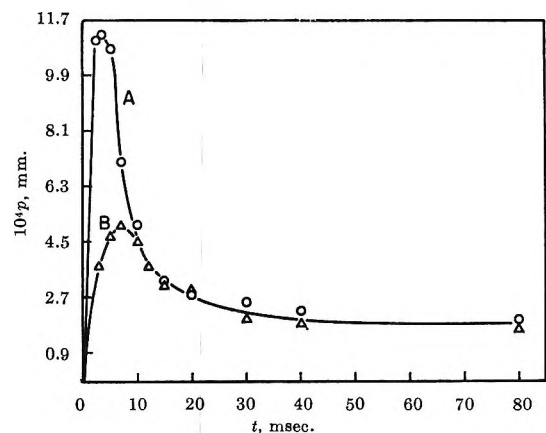


Figure 4. Ion current traces corrected for electron emission. Air (1.5 mm.) was injected into an initial pressure of 7×10^{-7} mm. For no pumping the expected pressure was 1.25×10^{-3} mm. Curves A and B refer to the ion gauge position inside and outside the copper mantle, respectively.

injection throughout the vessel. To ascertain the efficiency of pumping for large bursts, a sample of air at 38 cm. was injected; the initial pressure was 7×10^{-7} mm. Although the expected pressure for no pumping was 0.31 mm., the pressures observed in 10 sec., 5 min., and 15 min. were 3×10^{-4} , 2×10^{-5} , and 6×10^{-6} mm. The injected air would give a monolayer coverage of about 9.8 m.². Since the charcoal is quoted as having a surface area of 1100 m.²/g., the apparently efficient handling of a comparatively large volume is to be expected. Additional results are summarized in Table I.

Table I

Sample ^a	$P(\text{initial})$	$P(\text{no pumping})$	$P_{\text{max}}(\text{obsd.})$	$P(\text{final})$	Type of carbon
2 mm. of air	1×10^{-6}	1.7×10^{-3}	6.6×10^{-4}	4×10^{-5} (80 msec.)	FCB
1 mm. of H ₂	3.5×10^{-7}	8.3×10^{-4}	8.3×10^{-4}	7×10^{-7} (2 min.)	FCB
2 mm. of Ar	9×10^{-7}	1.7×10^{-3}	9.9×10^{-4}	6.8×10^{-5} (80 msec.)	FCB
2 mm. of air	6×10^{-7}	1.7×10^{-3}	5.4×10^{-4}	1×10^{-6} (15 sec.)	BPL
2 mm. of air	2×10^{-6}	1.7×10^{-3}	7.2×10^{-4}	3×10^{-6} (15 sec.)	BPL
1 cm. of air	7×10^{-7}	8.3×10^{-3}	1.4×10^{-3}	6×10^{-6} (15 sec.)	BPL
10 cm. of air	6×10^{-8}	8.3×10^{-2}	8.2×10^{-3}	6×10^{-5} (15 sec.)	BPL
				1×10^{-5} (3 min.)	
19 cm. of air	7×10^{-6}	1.6×10^{-1}	1.4×10^{-2}	2×10^{-4} (15 sec.)	BPL
				2×10^{-6} (3 min.)	
3.5 mm. of Ar	6×10^{-7}	3×10^{-3}	2.7×10^{-3}	3×10^{-6} (15 sec.)	BPL

^a $V_0 = 5 \text{ cm.}^3$.

Analysis of Data

No attempt was made to develop a quantitative theory for the observed pressure patterns; clearly it will prove difficult to formulate equations for the finite gas flow rates at these low pressures in a complex geometry. Nevertheless, a semiquantitative analysis led to interesting conclusions. The instantaneous injection rate was assumed to depend on the moles of gas (m_i) which remained in the driver section (a)

$$\frac{dm_i}{dt} = \beta(m_0 - m_i) = m_0\beta e^{-\beta t} \quad (1)$$

β is a constant characteristic of the gas and the geometry of the broken diaphragm, which proved to be unexpectedly reproducible. The pumping rate was assumed to be the kinetic theory collision rate, based on the geometric area (A) of the pumping panel and an accommodation coefficient (α)

$$\frac{dm_p}{dt} = \frac{\alpha A \bar{c}}{4 RT} p(t) \quad (2)$$

where \bar{c} is the mean molecular speed and $p(t)$ is the instantaneous pressure within the copper mantle. The net change in pressure follows the equation

$$dp/dt + \gamma p = \xi e^{-\beta t} \quad (3)$$

$$\gamma = \frac{\alpha A}{4V} \bar{c}; \quad \xi = p_0 V_0 \beta / V$$

p_0 and V_0 are the pressure and volume, respectively, of the high pressure chamber (a) of the shock tube, and V is the volume of the complete system. This equation is readily solved provided neither α nor \bar{c} are functions of the time.

$$p(t) = \frac{p_0 V_0}{V} (1 - \gamma/\beta)^{-1} \exp(-\gamma t) [1 - e^{-(\beta-\gamma)t}] \quad (4)$$

Recordings of the pressure transients for the case of *no cooling* gave the following values for β (deduced from the time required to reach 0.9 of the final pressure): air and argon, $\beta \approx 355 \text{ sec.}^{-1}$; hydrogen, $\beta \approx 570 \text{ sec.}^{-1}$. These relative magnitudes are expected from the corresponding sound speeds at room temperature. Values of γ and hence of α were then deduced from the time at the peak pressures, recorded when the panel was cooled.

$$t_{\text{max}} = (\beta - \gamma)^{-1} \ln(\beta/\gamma)$$

Typical magnitudes are listed in Table II. Past the maximum, for $t > 2/(\beta - \gamma)$, it follows from eq. 4 that the moles adsorbed (n) are logarithmically de-

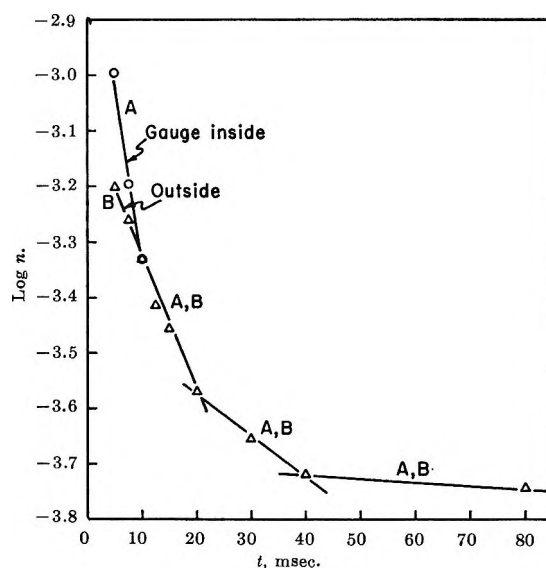


Figure 5. $\text{Log } n$ vs. t for injection of 1.5 mm. of air onto FCB charcoal (pressure data given in Figure 4 for gauge positions A and B). Discrete linear portions were drawn to emphasize the inferred presence of different stages in the redistribution process.

pendent on the time; the slope of a plot of $\log n$ vs. t should be $(\alpha/2.303)(\bar{c}A/4V)$. Figure 5 is such a replot of the pressure curves shown in Figure 4. Since A/V is a constant, the different regimes to which attention is directed by the straight line portions indicate several regimes in $\alpha\bar{c}$. Owing to cooling of the injected gas from room temperature to about 77°K. by collision with the cryopanel, $\bar{c} = (8RT/\pi M)^{1/2}$ should decrease with time. However, the maximum expected decline is $(77/300)^{1/2} \approx 0.5$, whereas the product $\alpha\bar{c}$ changed by a much larger factor. These

experiments therefore demonstrate that α decreases with the amount of gas adsorbed.

At the first break (15 msec.) the amount of gas adsorbed corresponds to monolayer coverage of the *geometric* area of the cryopumping panel. However, the total gas injected was insufficient to cover the available area with a monolayer. Hence, we conclude that the high initial pumping rate was limited by diffusion of the initially adsorbed gas molecules to the internal adsorption sites. From these measurements it appears that the time required for statistical redistribution onto the total available surface is of the order of 1 min. (It may be of the order of seconds, but this could not be established without extensive revision of the experimental arrangement.) Thereafter, a second injection, without allowing the panel to warm up, produces the same pressure-time pattern.

Acknowledgments. This work was supported by a grant from NASA (NsG-116161), to whom grateful acknowledgment is made. We appreciate the kindness of the Pittsburgh Activated Carbon Co. for providing us with samples of the activated carbons and with directions for the preparation of the mixture applied to the copper panel.

Table II

Injection	t_{\max} , sec.	γ	$\alpha(\text{initial})$
1.5 mm. of air, gauge inside	0.003	135	0.51
1.5 mm. of air, gauge outside	0.007	40	0.15
2 mm. of air, gauge outside	0.0065	50	0.19
3.5 mm. of Ar, gauge outside, FCB carbon ^a	0.010	10	0.045
1 mm. of H ₂ , FCB carbon ^a	0.016	0.1	10^{-4}

^a FCB activated carbon is impregnated with iron and copper oxides for removing hydrogen by *chemisorption* at liquid nitrogen temperatures.

The Reduced Thermodynamic Functions for the Significant Structure

Theory of Simple Liquids

by Teresa S. Ree, Taikyue Ree, Henry Eyring, and Richard Perkins

Department of Chemistry, University of Utah, Salt Lake City, Utah (Received March 17, 1965)

The Einstein characteristic temperature, sublimation energy, and solid molar volume at the melting point introduced in the partition function of the significant structure theory of liquids are calculated theoretically by using the 6-12 Lennard-Jones potential. The thermodynamic properties such as the vapor pressure, density, excess entropy, excess energy, and critical point data for simple liquids were calculated. It is found that the present theory agrees with the experiment better than any other model theories.

I. Introduction

There are two main approaches to the formulation of the theory of liquids: the method of the radial distribution function and the use of model structures of liquids. The theories based on the radial distribution function are the most fundamental; however, for the sake of mathematical expediency, this approach usually assumes the rigid-sphere potential. At present the most promising of such are the scaled particle theory¹ and the Percus-Yevick theory.² The theories based on the model have the advantage of intuitive appeal and produce numerical results more easily.³⁻⁵

Among the model theories, the most successful one appears to be the significant structure theory of liquids.⁵ According to the theory, the fluid is assumed to consist of a quasi-lattice in which highly mobile holes of molecular size move from site to site. If V_s and V are the molar volumes of the solid and fluid phases, respectively, and a random distribution of holes and molecules is assumed, the number of holes present in the fluid is given by $N(V - V_s)/V_s$, N being Avogadro's number. Such a hole is assumed to confer gaslike properties on neighboring molecules which jump into it. Thus, there will be effectively $N(V - V_s)/V$ molecules with gaslike degrees of freedom and effectively NV_s/V molecules with solidlike degrees of freedom. Further, these holes provide for a solidlike molecule a positional degeneracy equal to the available neighboring positions, n_h , multiplied by a Boltzmann-type probability factor involving the necessary

energy ϵ_0 to exclude competing molecules from the available positions.

Thus, the partition function of liquids, f , is given by

$$f = [f_s(1 + n_h e^{-\epsilon_0/kT})]^{NV_s/V} f_g^{N(V - V_s)/V} \quad (1)$$

where f_s and f_g are the partition functions for the solidlike and gaslike degrees of freedoms, respectively, and

$$n_h = n(V - V_s)/V_s \quad (2)$$

$$\epsilon_0 = \frac{aE_s V_s}{(V - V_s)} \quad (3)$$

where E_s is the sublimation energy, and n and a are proportionality constants. The gaslike degrees of freedom are represented by a perfect gas partition function because

(1) H. L. Frisch, *Advan. Chem. Phys.*, **6**, 229 (1964).

(2) (a) J. K. Percus and G. J. Yevick, *Phys. Rev.*, **110**, 1 (1958); (b) E. Thiele, *J. Chem. Phys.*, **39**, 474 (1963).

(3) (a) J. A. Barker, "Lattice Theories of the Liquid State," The Macmillan Co., New York, N. Y., 1963; (b) H. S. Chung and J. S. Dahler, *J. Chem. Phys.*, **40**, 2868 (1964).

(4) J. E. Lennard-Jones and A. F. Devonshire, *Proc. Roy. Soc. (London)*, **A163**, 53 (1937).

(5) (a) H. Eyring and T. Ree, *Proc. Natl. Acad. Sci. U. S.*, **47**, 526 (1961); (b) H. Eyring and R. P. Marchi, *J. Chem. Educ.*, **40**, 562 (1963); (c) T. S. Ree, T. Ree, and H. Eyring, *Proc. Natl. Acad. Sci. U. S.*, **48**, 501 (1962).

$$f_g^{N(V-V_s)/V} = \left[\frac{(2\pi mkT)^{3/2}}{h^3} (V - V_s) J(T) \right]^{N(V-V_s)/V} \times \left[\frac{N(V - V_s)}{V} \right]^{-1} \\ = \left[\frac{(2\pi mkT)^{3/2}}{h^3} \frac{eV}{N} J(T) \right]^{N(V-V_s)/V} \quad (4)$$

where the Stirling approximation has been applied to the factorial term, $J(T)$ is the partition function for the rotational and vibrational degrees of freedom of the molecule, and the other notation has the usual significance. If we use the Einstein oscillator function for the partition function, f_s , we have for the solidlike degrees of freedom the equation

$$f_s = \frac{e^{E_s/RT}}{(1 - e^{-\theta/T})^3} J(T) \quad (5)$$

where θ is the Einstein characteristic temperature. Henderson⁶ and Ree, Ree, and Eyring⁷ have also calculated f_s using the Lennard-Jones and Devonshire (hereafter abbreviated as LJ-D) cell theory.⁴ This gives

$$f_s = \frac{(2\pi mkT)^{3/2}}{h^3} v_f \left[\exp\left(-\frac{Z\psi(r)}{2kT}\right) \right] J(T) \quad (6)$$

where v_f is the free volume, Z is the number of nearest neighbors, and $\psi(r)$ is the interaction potential between two molecules separated a distance r . From eq. 1 with eq. 2 to 6, one can calculate various thermodynamic quantities of liquids such as the molar volumes and the vapor pressures at various temperatures, the specific heats, the expansion coefficients, the compressibilities, the surface tensions, and the second virial coefficients for dense gases. The calculated results for various liquids^{5,7-10} including the systems of rigid spheres⁶ and rigid disks¹¹ are very satisfactory, and the significant structure theory agrees better with experiment than other theories.^{11,12} The significant structure theory is also applicable to the calculation of viscosities,¹³ diffusion coefficients,¹³ and thermal conductivities.¹⁴ Again the results are in very good agreement with experiment.

From the above equations, one notes that the partition function of significant structure theory includes the quantities, E_s , V_s , θ , n , and a , characteristic of a substance. Naturally, one inquires whether the thermodynamic functions derived from this theory are reducible since reducibility is experimentally true for simple liquids. In this paper, we calculate θ , E_s , V_s , n , and a theoretically, and the result is used to obtain various reduced thermodynamic properties of simple liquids. The agreement between the present

theory and experiment is much better than the cell theory⁴ or the tunnel theory.³

II. Theory

(1) *Evaluation of n and a .* As already mentioned fluidized holes in a liquid confer gaslike properties on neighboring molecules, *i.e.*, the holes by their motion simulate gaslike molecules. They also make an additional separate contribution to thermodynamic properties by introducing degeneracy for the solidlike molecules with respect to position; *i.e.*, the degeneracy factor g is given by $g = 1 + n_h \exp(-\epsilon_0/kT)$ (*cf.* eq. 1), where unity in the sum g indicates the most stable equilibrium position, and n_h and ϵ_0 are expressed by eq. 2 and 3, respectively. We now consider the degeneracy effect in more detail.

The quantity n_h , the number of positions available for a solidlike molecule, near the melting point where it is appropriate to assume a latticelike structure, is represented by the number of holes around a molecule, *i.e.*

n_h (at melting point) =

$$Z \frac{V_m - V_s}{V_m} + Z \frac{V_s}{V_m} \frac{V_m - V_s}{V_s} = n \frac{V_m - V_s}{V_s} \quad (7a)$$

Hence

$$n = Z(V_s/V_m) \quad (7b)$$

where V_m is the volume of the liquid at the melting point. For simple liquids, there is about 12% expansion on melting. Thus, one obtains $n = Z(V_s/V_m) = 12(1/1.12) = 10.7$, where Z has been assumed to be 12. The theoretical value 10.7 for n agrees very well with the n value 10.8 obtained for argon, where n is a constant at all volume and temperatures. The form of n_h , given in eq. 2, is necessary if the calculated second virial coefficient is to come out correctly.^{5c} From the definition of n (*cf.* eq. 7b), n is to be understood as the number of nearest neighbors to a solid molecule. Next, we calculate the proportionality constant a by considering the value which ϵ_0 must have

(6) D. Henderson, *J. Chem. Phys.*, **39**, 1857 (1963).

(7) T. S. Ree, T. Ree, and H. Eyring, *ibid.*, **41**, 524 (1964).

(8) D. Henderson, H. Eyring, and D. Felix, *J. Phys. Chem.*, **66**, 1128 (1962).

(9) T. R. Thomson, H. Eyring, and T. Ree, *ibid.*, **67**, 2701 (1963).

(10) R. P. Marchi and H. Eyring, *ibid.*, **68**, 221 (1964).

(11) Y. L. Wang, T. Ree, T. S. Ree, and H. Eyring, *J. Chem. Phys.*, **42**, 1926 (1965).

(12) T. S. Ree, T. Ree, and H. Eyring, *J. Phys. Chem.*, **68**, 1163 (1964).

(13) T. S. Ree, T. Ree, and H. Eyring, *ibid.*, **68**, 3262 (1964).

(14) S. H. Lin, H. Eyring, and W. J. Davis, *ibid.*, **68**, 3017 (1964).

near the melting point where a lattice structure can again be assumed.

The average solid molecule has a kinetic energy $(3/2)kT$. Now, if a molecule is to pre-empt, in addition to its original position, a neighboring position, it must possess additional kinetic energy equal to or in excess of that with which all the other $(n - 1)$ neighboring molecules would confer on this position. We can say this because kinetic energy density measures the pressure. If an average molecule divides its time equally between two neighboring positions, this will cut its energy density in two. Since a molecule will be moving $1/Z$ th of its time in the direction of any neighbor, the average kinetic energy of $(n - 1)$ ordinary molecules will provide a vacancy with the kinetic energy $(1/2)(3/2)kT(n - 1)/Z$, and this is the value which ϵ_0 must take near the melting point, *i.e.*

$$\epsilon_0 = \frac{aE_s V_s}{V - V_s} = \frac{1}{2} \left(\frac{3}{2} kT \right) \frac{n - 1}{Z} \quad (8)$$

Since the entropy of melting per molecule of simple liquids is very close to $(3/2)k$ and since the energy of melting E_m is due to the potential energy arising from the introduction of holes into the solid with no change in kinetic energy, we have $E_m = (V_m - V_s)E_s/V_m$. Accordingly, we can write approximately that

$$\frac{aE_s V_s}{V_m - V_s} = \frac{1}{2} E_m \frac{n - 1}{Z} = \frac{1}{2} \frac{(V_m - V_s)E_s}{V_m} \frac{n - 1}{Z} \quad (9a)$$

or

$$a = \frac{1}{2} \frac{n - 1}{Z} \frac{(V_m - V_s)^2}{V_m V_s} \quad (9b)$$

This gives for argon $a = 0.0052$, which is to be compared with the best empirical value 0.00534.

(2) *Theoretical Evaluations of E_s , θ , and V_s .* We assume that the molecules in the solid state are hexagonally close packed and that the interaction potential $\psi(r)$ between two molecules is given by the 6-12 Lennard-Jones potential, *i.e.*

$$\psi(r) = 4\epsilon \left[\left(\frac{\sigma}{r} \right)^{12} - \left(\frac{\sigma}{r} \right)^6 \right] \quad (10)$$

where σ and ϵ are the distance and energy characteristic of the system and are listed by Hirschfelder, *et al.*,^{15a} for various liquids. By using eq. 10, the sublimation energy E_s is written as^{4,16}

$$E_s = \frac{Z}{2} N \epsilon \left[2.4090 \left(\frac{V_s}{N \sigma^3} \right)^{-2} - 1.0109 \left(\frac{V_s}{N \sigma^3} \right)^{-4} \right] \quad (11)$$

where the effect of non-nearest neighbors has also been taken into account.

At the nearest neighbor distance a' for the solid, the interaction energy $\psi(r)$ given by eq. 10 attains its minimum value. Thus, we have the relation: $a' = 2^{1/6}\sigma$. For hexagonal close packing, V_s is represented by $N a'^3 / \sqrt{2}$. Consequently, the following relation holds

$$V_s = \frac{N a'^3}{\sqrt{2}} = N \sigma^3 \quad (12)$$

Next we consider the Einstein characteristic temperature θ which may be written as

$$\theta = \frac{h\nu}{k} = \frac{h}{k} \frac{1}{2\pi} \left(\frac{k_r}{m} \right)^{1/2} \quad (13)$$

where a simple harmonic oscillator has been assumed. The force constant k_r can be calculated by using the approximate relation¹⁷

$$k_r \frac{r^2}{2} \simeq Z [\Psi(r) - \Psi(a')] \quad (14)$$

where $\Psi(r)$ and $\Psi(a')$ are the averaged potentials obtained from eq. 10. Hence¹⁷

$$k_r = 2Z \epsilon \left[22.106 \left(\frac{N \sigma^3}{V_s} \right)^4 - 10.559 \left(\frac{N \sigma^3}{V_s} \right)^2 \right] \times \frac{1}{2^{1/3} \sigma^2} \left(\frac{N \sigma^3}{V_s} \right)^{2/3} \quad (15)$$

Introducing eq. 15 with eq. 12 into eq. 13, one obtains

$$\theta = \frac{h}{k} \frac{1}{2\pi} \left(\frac{23.094 Z \epsilon}{2^{1/3} m \sigma^2} \right)^{1/2} \quad (16)$$

(3) *The Reduced Partition Function.* In this paper, we shall not use eq. 6 for f_s . Although the LJ-D function yields a reduced function, it introduces the free volume v_t , which is not an analytic function and can only be found from the values tabulated by Wentorf, *et al.*,¹⁶ for a limited range of temperatures. Further, the values of $\partial^2 v_t / \partial T^2$ are not available from the tabulated values although they are necessary for calculating heat capacities.

By applying an approximation to the Einstein partition function, eq. 5 may be written as

(15) J. O. Hirschfelder, C. F. Curtiss, and R. B. Bird, "Molecular Theory of Gases and Liquids," John Wiley and Sons, Inc., New York, N. Y., 1964, (a) pp. 1110-1113 and 1212-1215; (b) Chapter 6.

(16) R. H. Wentorf, R. J. Beuhler, J. O. Hirschfelder, and C. F. Curtiss, *J. Chem. Phys.*, **18**, 1484 (1950).

(17) I. Prigogine, "The Molecular Theory of Solutions," North-Holland Publishing Co., Amsterdam, 1957, p. 130.

$$f_s = e^{E_s/RT} \left(\frac{T}{\theta}\right)^3 J(T) \quad (17)$$

The substitutions of eq. 2, 3, 4, and 17 into eq. 1 yields the equation

$$f = \left\{ e^{E_s/RT} \left(\frac{T}{\theta}\right)^3 J(T) \left[1 + n \frac{V - V_s}{V_s} \times \exp\left(\frac{-aE_s V_s}{(V - V_s)RT}\right) \right]^{NV_s/V} \times \left[\frac{(2\pi mkT)^{3/2} eV}{h^3 N} J(T) \right]^{N(V - V_s)/V} \right\} \quad (18)$$

Making use of eq. 11, 12, and 16, eq. 18 is transformed into

$$f = \left[\frac{(2\pi mkT)^{3/2} eV}{h^3 N} J(T) \right]^N \frac{e^{8.388/T^*} (T^*)^{3/2}}{eV^* (35.01)} \times \left[1 + 10.7(V^* - 1) \exp\left(\frac{-0.0436}{T^*(V^* - 1)}\right) \right]^{N/V^*} \quad (19)$$

where the values $n = 10.7$ and $a = 0.0052$ have been used; T^* and V^* are the reduced temperature and volume, respectively, and are given by the equations

$$T^* = kT/\epsilon \quad V^* = V/N\sigma^3 \quad (20)$$

III. Calculations

The Helmholtz free energy written in terms of the partition function is

$$A = -kT \ln f \quad (21)$$

If the Helmholtz free energies are calculated using eq. 21 and 19 and are then plotted against V^* , one obtains a curve with two minima, one corresponding to the solid phase and one corresponding to the liquid phase, as shown by the isotherm in Figure 1. Since the slope gives the pressure, the common tangent to the curve at the two points corresponding to the liquid and gaseous phases gives the vapor pressure when these phases are in equilibrium and the tangential point near the minimum corresponding to the liquid phase yields the liquid volume while tangent point at the larger volume indicates the volume of the vapor (*cf.* Figure 1). The melting temperature is the temperature at which the slope of the common tangent between the solid and liquid minima is $P^* = P\sigma^3/\epsilon = \sigma^3/\epsilon$; *i.e.*, $P = 1$. We calculate the normal melting temperature and the liquid melting volume for argon, and in Table I the results are compared with the argon experimental data along with the results from other theories^{3a} at $T^* = 0.70$.

In Figures 2, 3, and 4, we compare the reduced experimental vapor pressure (P^*) and the volume (V^*)

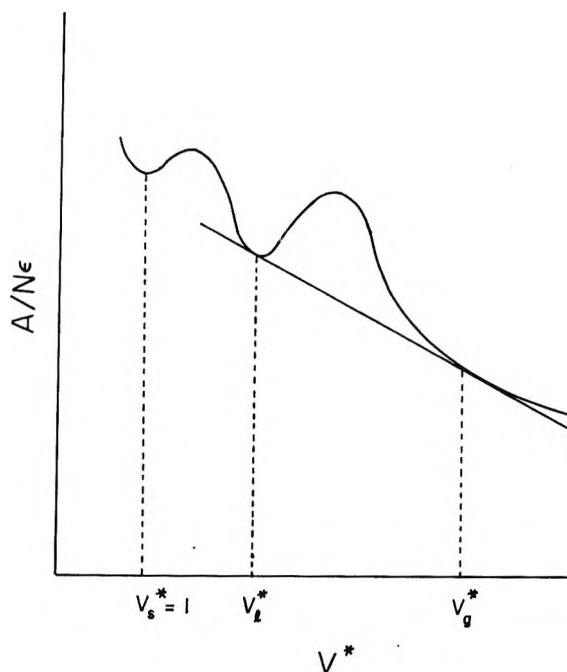


Figure 1. Schematic diagram of the reduced Helmholtz free energy, $A/N\epsilon$, plotted against reduced volume V^* at a constant reduced temperature T^* . Here, V_s^* , V_l^* , and V_g^* are reduced volumes of the solid, liquid, and gas, respectively.

Table I: Theoretical and Experimental Properties at the Melting Point

	Melting temp., T^*	Reduced vol., V^*	Reduced excess entropy, S^E/Nk	Reduced excess energy, $E^E/N\epsilon$
Significant structure theory	0.711	1.159	-3.89	-6.19
Tunnel theory		1.184	-4.8	-5.9
Liquid argon	0.701	1.178	-3.64	-5.96
LJ-D theory		1.037	-5.51	-7.32
Solid argon	0.701	1.035	-5.53	-7.14

for the simple liquids such as Ne,^{18,19} Ar,²⁰ N₂,^{19,21} and CH₄,^{20,21} with the theoretical values calculated from our theory using the procedure just mentioned. The agreement between our theory and the experiment is very good and is better than the values from the cell and tunnel theories.

(18) E. A. Washburn, Editor-in-Chief, "International Critical Tables," McGraw-Hill Book Co., Inc., New York, N. Y., 1926.

(19) C. D. Hodgman, Editor-in-Chief, "Handbook of Chemistry and Physics," 41st Ed., Chemical Rubber Publishing Co., Cleveland, Ohio, 1959-1960.

(20) F. Din, Ed., "Thermodynamics Functions of Gases," Butterworths Scientific Publications, London, 1961-1962.

(21) Landolt-Börnstein, "Physikalisch-Chemische Tabellen I," Springer-Verlag, Berlin, 1923.

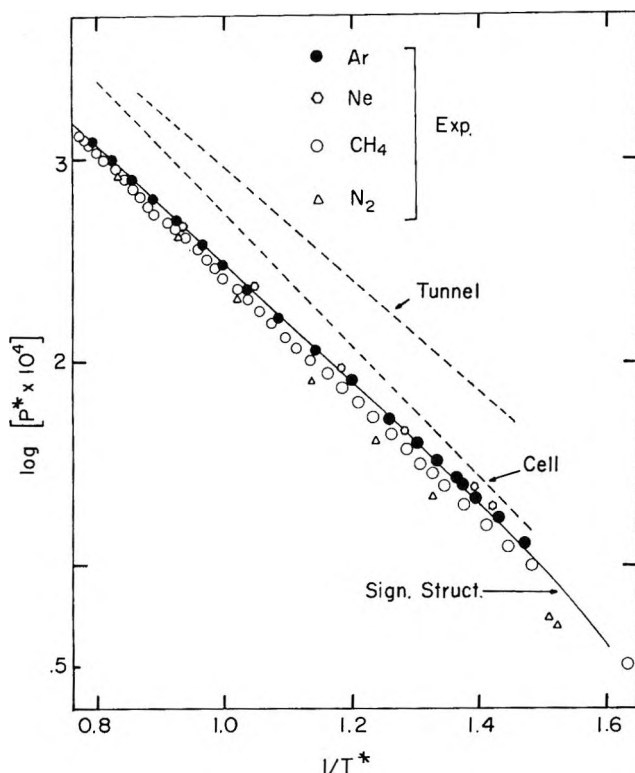


Figure 2. Logarithm of the reduced vapor pressure, P^* , vs. $1/T^*$ for simple liquids. The experimental values^{19,20} have been reduced by using ϵ/k and $N\sigma^3$ listed in Table III. The significant structure theory (full curve) is compared with the cell theory and the tunnel theory (broken curves).

The critical constants are obtained by using the conditions $(\partial P/\partial V)_T = 0$ and $(\partial^2 P/\partial V^2)_T = 0$. In Table II, we compare the critical constant for the present theory and the experimental data for the simple liquids²² along with the data for other model theories such as Barker's tunnel theory^{3a} and the LJ-D theory.²² The agreement between the experiment and the present theory is far better than for any of the other theories. The tunnel theory values are in slightly worse agreement than the LJ-D values. This is almost certainly due to the approximation of treating the motion in the tunnels as strictly one dimensional.

Table II: Experimental and Theoretical Critical Constant

	T_c^*	P_c^*	V_c^*	$\left(\frac{PV}{RT}\right)_c$
Mean values for Ne, Ar, N ₂ , CH ₄	1.277	0.121	3.09	0.292
Significant structure theory	1.306	0.141	3.36	0.362
Tunnel theory	1.07	0.37	1.8	0.6
LJ-D theory	1.30	0.434	1.77	0.591

Entropy, S , and internal energy, E , are derived from the partition function as

$$S = \left[\frac{\partial(kT \ln f)}{\partial T} \right]_V \quad (22)$$

$$E = kT^2 \left[\frac{\partial}{\partial T} \ln f \right]_V \quad (23)$$

The excess of a property is defined as the difference between the real liquid property and the ideal gas property; hence, the excess reduced entropy, S^E/Nk , and the excess reduced energy, $E^E/N\epsilon$, for the significant liquid structure theory is derived from eq. 22 and 23 by using eq. 19 as

$$\begin{aligned} \frac{S^E}{Nk} = & \frac{1}{V^*} \ln \left\{ 1 + 10.7(V^* - 1) \times \right. \\ & \left. \exp \left[\frac{-0.0436}{T^*(V^* - 1)} \right] \right\} + \\ & \frac{0.4665}{T^*V^*} \exp \left[\frac{-0.0436}{T^*(V^* - 1)} \right] \\ & \frac{1.5}{V^*} \ln \left(\frac{T^*}{35.01} \right) + \frac{0.5}{V^*} - \frac{\ln V^*}{V^*} \quad (24) \end{aligned}$$

$$\begin{aligned} \frac{E^E}{N\epsilon} = & -\frac{8.388}{V^*} + \frac{1.5T^*}{V^*} + \\ & \frac{0.4665}{V^*} \exp \left[\frac{-0.0436}{T^*(V^* - 1)} \right] \\ & \frac{1}{1 + 10.7(V^* - 1) \exp \left[\frac{-0.0436}{T^*(V^* - 1)} \right]} \quad (25) \end{aligned}$$

In columns 4 and 5 of Table I, we compare the calculated reduced excess entropy and excess energy at the melting temperature with the corresponding experimental quantities for the liquid and solid argon.^{3a} Included for comparison are the values calculated from the LJ-D theory^{3a} and the tunnel theory.^{3a} The tunnel theory values of $E^E/N\epsilon$ and S^E/Nk are less accurate because their calculations involve the numerical differentiation of f with respect to temperature. The comparison between the calculated values from the LJ-D theory and the experimental value for solid argon is in accord with the fact that the LJ-D theory is a superheated solid theory rather than a liquid theory. Had the experimental values of T^* and V^* been used for the present theory, the agreement of

(22) T. L. Hill, "Statistical Mechanics," McGraw-Hill Book Co., Inc., New York, N. Y., 1956, p. 389.

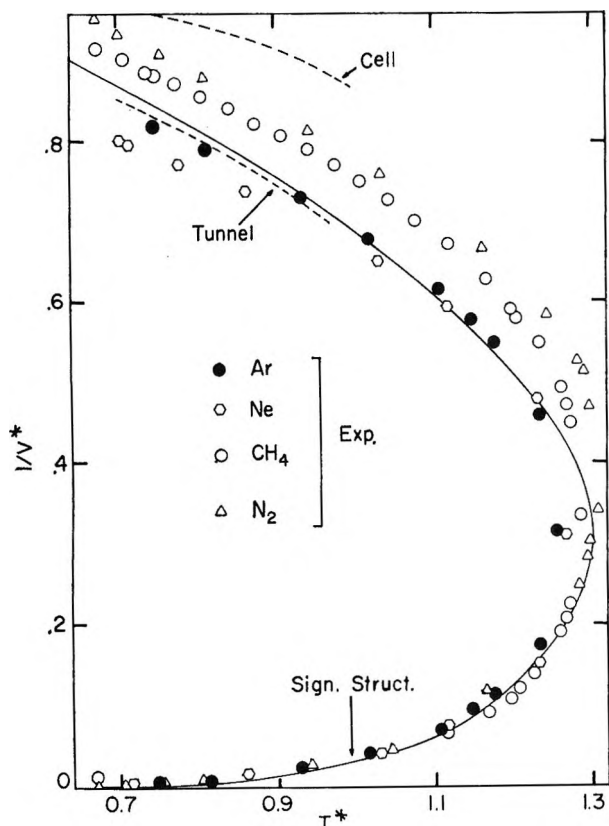


Figure 3. Reduced density vs. T^* . The experimental values^{18,20,21} have been reduced by using ϵ/k and $N\sigma^3$ listed in Table III. The significant structure theory (full curve) is compared with the cell theory and the tunnel theory (broken curves).

$E^E/N\epsilon$ and S^E/Nk with experiment would have been better.

IV. Discussion

Previously, V_s , the molar solid volume at the melting point, as well as θ , the Einstein temperature, and E_s , the sublimation energy, were obtained either from the available experimental data or by fitting the entropy calculated from the partition function, eq. 18, to the available solid entropy data with the triple point condition; *i.e.*, $F_l = F_g = F_s$, where F is the Gibbs free energy and the subscripts represent the liquid, gas, and solid, respectively.²³ Equation 18 with the parameters so obtained was successfully applied to calculate the thermodynamic properties of liquids for the melting temperatures through the critical points.^{5,7-12,23}

In Table III, we make a comparison of the values of E_s , V_s , and θ , calculated from eq. 11, 12, and 16, respectively, with those previously determined.²³ In column 2 are listed the values¹⁵ of ϵ/k used for calcu-

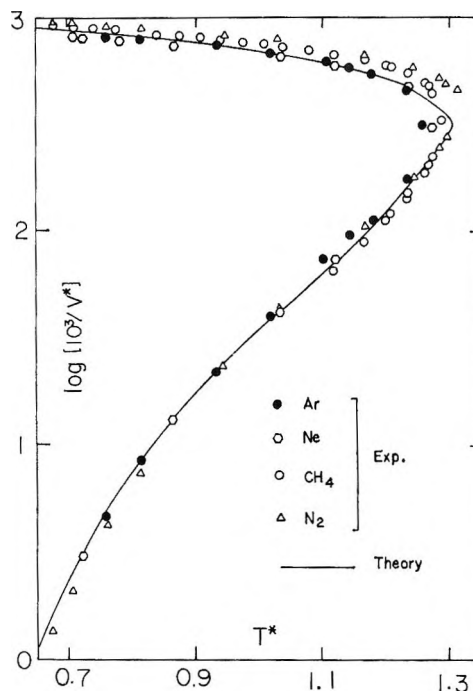


Figure 4. Logarithm of $1/V^*$ vs. T^* . This figure shows the lower portion of the curve of Figure 3 in an enlarged way. The full curve was calculated from the present theory.

lating θ and E_s . In column 3 we list¹⁵ $N\sigma^3$ in order to compare with the experimental V_s ,^{20,24,25} listed in column 4. Thus, eq. 12 is verified. The θ -values in column 5 are calculated from eq. 16. The θ -values used previously are listed in column 6; the first three values of θ are the experimental values^{24,26} while the last value was obtained by fitting the solid entropy data.²³ It is very interesting to note that the agreement between the theoretical and experimental values is very close. The E_s values in column 7 are calculated using eq. 11 and 12. The first three values of E_s ,^{27,28} in the last column were obtained experimentally by applying the Clausius-Clapeyron equation to the sublimation vapor pressure, while the last value²³ was obtained by fitting the triple point condition with the θ listed in column 6. The greater deviation between the theoretical and experimental values of E_s for Ne is

(23) E. J. Fuller, T. Ree, and H. Eyring, *Proc. Natl. Acad. Sci. U. S. A.*, **45**, 1594 (1959).

(24) K. Clusius, *Z. physik. Chem.*, **B31**, 459 (1936).

(25) K. Clusius and K. Wiegand, *ibid.*, **B46**, 1 (1940).

(26) W. F. Giaque and J. O. Clayton, *J. Am. Chem. Soc.*, **55**, 4882 (1933).

(27) H. Eyring, J. Walter, and A. E. Stearn, "Surface Chemistry, Publication No. 21," F. R. Moulton, Ed., American Association for the Advancement of Science, Washington, D. C., 1943, pp. 88-97.

(28) J. Walter and H. Eyring, *J. Chem. Phys.*, **9**, 393 (1941).

Table III: Comparison between the Theoretical and Experimental Values for V_s , θ , and E_s

	ϵ/k	$N\sigma^3$	V_s , exptl.	θ , theoret.	θ , exptl.	E_s , theoret.	E_s , exptl.
Ne	34.9 ^a	12.94 ^a	13.94 ^b	48.87	44.7 ^b	581.4	447.4 ^p
Ar	119.8 ^a	23.79 ^a	24.98 ^b	52.57	60.0 ^b	1996	1889 ^h
N ₂	95.9 ^a	30.75 ^a	29.65 ^c	51.55	51.0 ^e	1598	1508 ^h
CH ₄	148.1 ^a	33.26 ^a	30.94 ^d	82.37	75.33 ^f	2468	2200 ^f

^a See ref. 15. ^b See ref. 24. ^c See ref. 20. ^d See ref. 25. ^e See ref. 26. ^f See ref. 23. ^g See ref. 27. ^h See ref. 28.

probably due to quantum effect,^{15b} which should have been considered in eq. 11; *i.e.*, the zero point energy should have been included.

In the above calculations of the reduced properties, we used the values $n = 10.7$ and $a = 0.0052$, which were calculated from eq. 7b and 9b, respectively, by assuming $V/V_s = 1.12$ at the melting point. These values of n and a were very close to the best values for calculating the experimental properties of argon as mentioned previously. We also found that the theo-

retical values of n and a agree very well with the best values for other simple liquids, such as nitrogen and methane, which expand about 12% on melting. The fact that n and a should have closely the same values for different substances is a natural consequence of eq. 7b and 9b.

Acknowledgments. The authors express appreciation to the National Science Foundation for financial support under Grant Gp-415 of this research and to Joan Ree for the calculations she made for this paper.

Voltage Transients of Freshly Produced Noble Metal Electrode Surfaces

by R. S. Perkins, R. C. Livingston,¹ T. N. Andersen, and H. Eyring

Rate Processes Institute, University of Utah, Salt Lake City, Utah (Received May 11, 1965)

The faces of Pt, Pd, Au, Cu, and Ag electrodes were scraped off in N₂-saturated solutions of varying ion types, ion concentrations, and pH. The accompanying potential transients show peak potentials which vary with anion type and concentration in a manner qualitatively similar to the variance of zero charge potential (z.c.p.) or electrocapillary maximum of mercury in the same solutions. The peak potentials, however, are also more negative in solutions of higher pH. The mechanism of establishing the peak potentials is discussed, as well as the relationship of these potentials to zero charge potentials. In the case of all metals studied, reactions spontaneously drive the potential positive from the z.c.p.

Introduction

In a previous communication² we introduced a method for determining zero charge potentials (z.c.p.) of solid electrodes. The method consists of generating a completely new electrode surface by rapidly scraping or cutting off the existent surface (with its charge and double layer) and measuring the accompanying open-circuit transient.³ If certain criteria are satisfied, the resulting potential transient peak, V_{pk} , is the zero charge potential. These criteria are: (1) that adsorption must approach equilibrium before appreciable reaction occurs to change the electrode charge⁴; (2) that the experimental scraping and recording times must be sufficiently rapid to separate the adsorption and reaction processes; and (3) that a sufficient number of scrapes be performed that charge redistribution from the departing metal shaving onto the fresh surface be negligible.

In the present paper, the method is applied to several systems in order to determine to what extent the above criteria are experimentally satisfied.

Criterion 1 can best be satisfied by dealing with noble metals in nondilute simple ionic solutions. From such solutions the time for specific adsorption of ions would be expected to be less than 10⁻⁵ sec. (as it is onto mercury)^{5,6} provided that the adsorption is of the nonhomopolar type (as evidence indicates is the case for Hg),⁷ and providing the metal electrodes do not contain deep pores. By studying noble metal electrodes the reaction should be limited to solvent reduction or oxidation which are slow compared to

many metal dissolution reactions. Criterion 3 can be determined experimentally by comparing the size of transients for different numbers of successive scrapes of the electrode. Whether criterion 2 is satisfied in a given experiment cannot be simply determined, but rather all evidence for the separation of adsorption and charge-transfer reactions must be considered. Such a separation is apparently feasible for some systems as evidenced by results of the dip method.⁴ In the present case, the peak potential should reach a limit with increase in the rate at which fresh metal surface is exposed. This condition does not alone satisfy criterion 2 since a very fast reaction may be over in a time too short for us to measure. To eliminate the possibility that such fast reactions are occurring, other evidence such as V_{pk} trends with variation of ion types, ion concentrations, pH, and electrode composition must be considered. This paper considers the

(1) Summer N.S.F. Undergraduate Research Fellow, 1964.

(2) T. N. Andersen, R. S. Perkins, and H. Eyring, *J. Am. Chem. Soc.*, **86**, 4496 (1964).

(3) The present method has little relationship to the Billiter scrape method [J. Billiter, *Trans. Am. Electrochem. Soc.*, **57**, 351 (1930); *Z. Elektrochem.*, **14**, 624 (1908)].

(4) The "dip" method [B. Jakuszewski and Z. Kozłowski, *Roczniki Chem.*, **36**, 1873 (1962)] utilizes the separation of double-layer formation and Faradaic processes but involves the uncertainty of the prepip environment of the electrode and hence differs from the present method.

(5) V. I. Melik-Gaikazyan and P. I. Dolin, *Dokl. Akad. Nauk SSSR*, **64**, 409 (1949).

(6) V. I. Melik-Gaikazyan and P. I. Dolin, *Tr. Inst. Fiz. Khim., Akad. Nauk SSSR*, No. 1, 115 (1950).

(7) T. N. Andersen and J. O'M. Bockris, *Electrochim. Acta*, **9**, 347 (1964).

above-mentioned effects on V_{pk} , as well as the rate of the transient decay at the same potential, relevant to the judging of the suitability of the present method for determining z.c.p. values. Comparisons of V_{pk} values with z.c.p. values obtained by independent methods is also made.

Experimental Section

Apparatus and Material. The Pyrex electrolytic cell is shown in Figure 1. The test electrode was inserted into the solution through the side of the center compartment of the cell. This electrode consisted of a length of metal wire tightly fitted in a cylindrical Teflon tube in such a way that only the face of one end of the wire was exposed to the solution. The wire-containing tube was inserted into the cell through another Teflon connection. The reference electrode used throughout the work was a saturated calomel electrode connected to compartment 2 of the test cell by an agar-KCl salt bridge.

Extending into the solution through a Teflon stopper and a mercury seal was an alumina rod attached to a variable speed motor capable of 17,000 r.p.m. The end of the alumina rod was shaped into a cutting form which was used to remove the entire surface of the electrode, thus exposing a new surface.

Another cell, similar in design to that described above, was also used for hand scraping of the electrodes and differed in appearance from the above cell only in the manner of sealing. Hand or manual scraping was accomplished by vertical motion of an alumina or Pyrex rod (with identical results in either case). This system was kept gas tight with an inflated inverted polyethylene bag covering the top of the cell and attached securely to the scraper. The hand-scraping device was more convenient and faster to use than the powered scraper, and when comparison of the peak potential values obtained from the two types of scraping showed that they were in close agreement, the hand scraper was used to complete studies of anion and concentration effects.

Potential measurements were made with an Offner Type P dynograph assembly containing a Type 9405 cathode follower coupler which provides 10^9 ohms input impedance. This instrument amplified the voltage output and recorded it on a strip chart recorder. The maximum chart speed was 100 mm./sec., and the full scale balance time of the needle did not exceed 0.005 sec. The internal input impedance of the dynograph was high enough to not influence the results as was shown by comparing the results with those obtained by feeding the input first through a Keithley Model 610A electrometer, of 10^{14} ohms internal im-

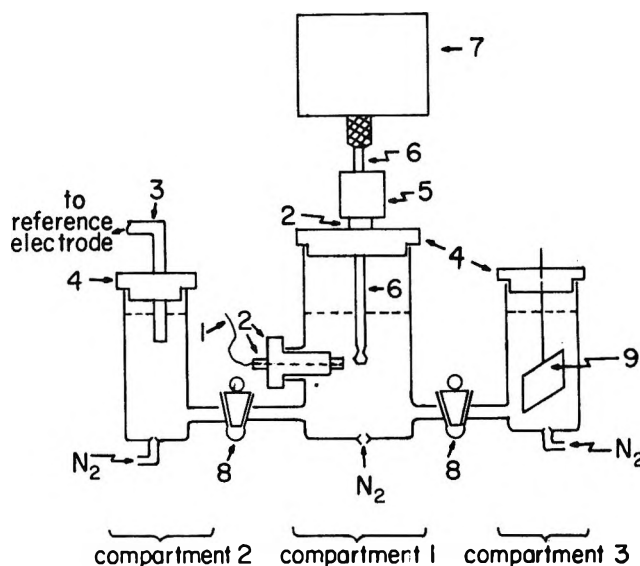


Figure 1. Schematic diagram of electrolytic cell: (1) electrode; (2) Teflon tubing and connections; (3) salt bridge; (4) Teflon stoppers; (5) mercury seal; (6) aluminum oxide scraping rod; (7) variable speed motor; (8) mercury seal stopcock (no grease); and (9) auxiliary electrode.

pedance. The response time of the dynograph was fast enough to follow the potential as was shown by comparing transients recorded on it to those recorded on an oscilloscope.

The test electrodes used were wires of 0.020-in. diameter (supplied by A. D. Mackay Co.) and of the following minimum purities: Cu, Ag, and Au, 99.95%; Pt and Pd, 99.99%. The solutions used were prepared with reagent grade chemicals and water twice distilled from a basic permanganate solution.⁸ Experiments were run with prepurified (99.997%) nitrogen bubbling through the cell. The peak potentials in solutions open to the atmosphere were 0 to 50 mv. more positive than those in N_2 -saturated solutions, indicating that O_2 leakage in the latter case could be neglected.

Procedure. After cleaning and assembling the cell, the powdered scraper was begun rotating at some arbitrary speed, and the electrode was moved against it. The electrode was scraped approximately 20 or 30 times before being withdrawn. The above procedure was repeated four to five times, and then the scraper was set at a higher speed. Repetition of this procedure usually initially produced a larger voltage transient, but the size of the transient, or the value of V_{pk} , soon became constant with increase in scraping speed. A typical result is shown in Figure 2 in which the time scale is the order of several seconds.

(8) This degree of purity has been found sufficient to give satisfactory zero charge potentials in the case of the streaming mercury electrode.

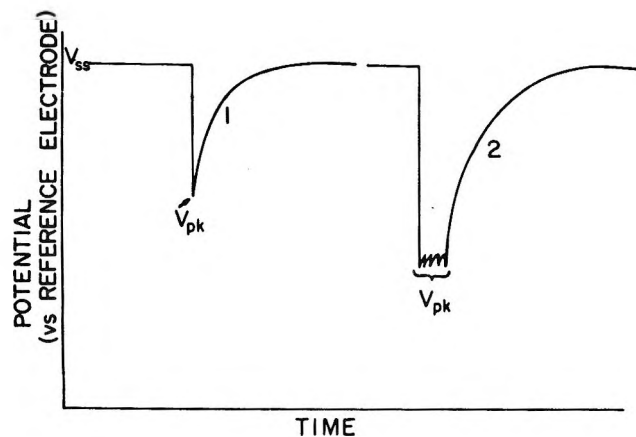


Figure 2. Appearance of experimental data as obtained. Curve 1 is for a single scrape and curve 2 for multiple scrapes.

In the case of manual scraping, one pass over the metal produced a smaller transient than did many successive scrapes. Since it was considered that this was due to incomplete removal of the old surface or incomplete removal of the charge, due to charge redistribution, the more reproducible "many-scrape" V_{pk} was the peak potential which was recorded.

The peak potential, V_{pk} , was independent of the pre-scrape potential, V'_{ss} , as shown by varying the latter, in several experiments, from the stable steady-state potential to values several hundred millivolts negative of the peak potential. Such experiments were executed by cathodically polarizing the electrode to the desired pre-scrape potential, whereupon the polarization was stopped and the electrode was scraped while its potential decayed. A marked difference in the natural decay rate and the scrape-induced potential shift from these negative pre-scrape potentials was noted for most systems.

The net rate, $\Sigma i_{cath} - \Sigma i_{anod}$, at which Faradaic reactions occur at V_{pk} , and hence add charge to the electrode, can be measured as follows. Under open circuit conditions and at all decay potentials

$$i_{ext} = 0 = \frac{dq_{dL}}{dt} + \Sigma i_{cath} - \Sigma i_{anod} \quad (1)$$

where dq_{dL}/dt is the rate of change of charge on the electrode, and Σi_{cath} and Σi_{anod} are the summations of the currents produced by all cathodic and anodic reactions, respectively. If the electrode is potentiostatted at V_{pk} by passing through it external current i_{pk} (under steady-state conditions), then $dq_{dL}/dt = 0$ and

$$i_{pk} = \Sigma i_{cath} - \Sigma i_{anod} = \left(\frac{dq}{dt} \right)_{V=V_{pk}} \quad (2)$$

i_{pk} values were obtained in many of the experiments in order to estimate the error in the electrode charge caused by the finite scraping time and also in order to estimate the order of net reaction rate which the scraping process can "outrun."

Experimental Results

The peak potentials, steady-state potentials, i_{pk} , and comparison of manually and power-scraped peaks are given in Tables I through V. The z.c.p. and amount of specific adsorption for mercury in corresponding solutions given in Table VI were determined by Grahame and co-workers⁹⁻¹² and by Wroblowa, Kovac, and Bockris.¹³ The reproducibility of V_{pk} values as determined from repetitive experiments (i.e., different solutions, days, etc.) is given in the results as a \pm value following the V_{pk} value. Detailed comparison between manual and power scraping is made later. Junction potentials were omitted since they were smaller than the experimental deviation. The potentials are recorded relative to a normal hydrogen electrode with the potential of the saturated calomel electrode being taken as +0.242 v. (European sign convention). The potentiostat experiments (i_{pk}) were run in the manually operated cell. After the tables are also given qualitative observations concerning the transient decays, which are relevant to the explanation of the data in the tables.

Table I: Experimental Results for Gold [Potentials in volts vs. N.h.e. and i_{pk} in amp. cm.⁻² (Geometrical Area)]

Solution	V_{ss}	V_{pk} (manual scraper)	i_{pk}
0.1 N KF	+0.17 ± 0.17	-0.06 ± 0.02	2.5 × 10 ⁻⁶
1.0 N KF	+0.17 ± 0.17	-0.06 ± 0.02	
0.1 N K ₂ SO ₄	+0.17 ± 0.17	-0.06 ± 0.02	3.5 × 10 ⁻⁶
0.01 N KCl	+0.17 ± 0.17	-0.05 ± 0.02	7.5 × 10 ⁻⁶
0.1 N KCl	+0.17 ± 0.17	-0.11 ± 0.02 ^a	1.0 × 10 ⁻⁶
1.0 N KCl	+0.17 ± 0.17	-0.19 ± 0.02	2.2 × 10 ⁻⁶
0.1 N KClO ₄	+0.17 ± 0.17	-0.18 ± 0.02	
0.1 N KNO ₃	+0.17 ± 0.17	-0.04 ± 0.02	
0.1 N KBr	+0.17 ± 0.17	-0.26 ± 0.02	3.0 × 10 ⁻⁶
0.1 N KSCN	+0.17 ± 0.17	-0.44 ± 0.02	
0.1 N KI	+0.17 ± 0.17	-0.47 ± 0.02	1.5 × 10 ⁻⁶
0.1 N K ₂ SO ₄ (pH 12)	+0.20	-0.09 ± 0.02 ^a	
0.1 N K ₂ SO ₄ (pH 3)	+0.41	+0.14 ± 0.02	

^a Potential also measured with power scraper.

(9) D. C. Grahame and B. A. Soderberg, *J. Chem. Phys.*, **22**, 449 (1954).

(10) D. C. Grahame, *J. Am. Chem. Soc.*, **80**, 4201 (1958).

(11) D. C. Grahame, *J. Electrochem. Soc.*, **98**, 343 (1951).

(12) D. C. Grahame, E. M. Coffin, J. I. Cummings, and M. A. Poth, *J. Am. Chem. Soc.*, **74**, 1207 (1952).

(13) H. Wroblowa, Z. Kovac, and J. O'M. Bockris, unpublished.

Table II: Experimental Results for Copper [V_{ss} and V_{pk} vs. N.h.e. (in volts) and i_{pk} in amp. cm.⁻² (Geometrical Area)]

Solution	V_{ss}	V_{pk} (power scraper)	V_{pk} (manual scraper)	i_{pk}
0.1 N KF	-0.12 ± 0.07	-0.50 ± 0.02	-0.30	1.0 × 10 ⁻³ (at -0.64 v.)
0.1 N KCl	-0.12 ± 0.07	-0.64 ± 0.02	-0.36	
0.1 N KBr	-0.12 ± 0.07	-0.70 ^a	-0.49	
0.1 N KI	-0.12 ± 0.07	-0.71 ^a		
0.1 N KCl (pH 2.3)	+0.06	-0.36 ^a		

^a V_{pk} had not leveled out at maximum scraping speed.

Table III: Experimental Results for Platinum (Potentials Are Given in volts vs. N.h.e. and i_{pk} in amp. cm.⁻²)

Solution	V_{ss}	V_{pk} (power scraper)	V_{pk} (manual scraper)	i_{pk}
0.1 N KF	+0.34 ± 0.10		-0.19 ± 0.05	5 × 10 ⁻⁵
1.0 N KF	+0.34 ± 0.10		-0.19 ± 0.05	
0.1 N K ₂ SO ₄	+0.34 ± 0.10		-0.16 ± 0.03	5 × 10 ⁻⁵
0.1 N KCl	+0.34 ± 0.10	-0.06 ± 0.02	-0.17 ± 0.05	1.1 × 10 ⁻⁴
1.0 N KCl	+0.34 ± 0.10		-0.21	4.7 × 10 ⁻⁴
0.1 N KClO ₄	+0.34 ± 0.10		-0.23	
0.1 N KBr	+0.34 ± 0.10		-0.26 ± 0.05	
0.1 N KSCN	+0.34 ± 0.10		-0.43	
0.1 N KI	+0.34 ± 0.10		-0.43 ± 0.03	3.0 × 10 ⁻⁴
0.1 N KCl (pH 11.5)	+0.27	-0.40 ± 0.02	-0.40 ± 0.02	
0.1 N KCl (pH 2.7)	+0.60	+0.05 ± 0.02		
0.1 N K ₂ SO ₄ (pH 2.3)	+0.48	+0.13	-0.04	5 × 10 ⁻⁵

Table IV: Experimental Results for Palladium (Potentials Are Given in volts vs. N.h.e. and i_{pk} in amp. cm.⁻²)

Solution	V_{ss}	V_{pk} (manual scraper)	i_{pk}
0.1 N KF	+0.35 ± 0.12	-0.18 ± 0.05	2.0 × 10 ⁻⁵
1.0 N KF	+0.35 ± 0.12	-0.18 ± 0.05	
0.1 N K ₂ SO ₄	+0.35 ± 0.12	-0.16 ± 0.05	
0.01 N KCl	+0.35 ± 0.12	-0.14 ± 0.05	
0.1 N KCl	+0.35 ± 0.12	-0.16 ± 0.05	
1.0 N KCl	+0.35 ± 0.12	-0.21 ± 0.05	2.5 × 10 ⁻⁵
0.1 N KClO ₄	+0.35 ± 0.12	-0.21 ± 0.05	
0.1 N KBr	+0.35 ± 0.12	-0.23 ± 0.05	
0.1 N KSCN	+0.35 ± 0.12	-0.33 ± 0.05	
0.1 N KI	+0.35 ± 0.12	-0.33 ± 0.05	
0.1 N K ₂ SO ₄ (pH 12)	+0.35 ± 0.12	-0.41 ± 0.02 ^a	

^a Value also obtained with power scraper.

Table VI: Zero Charge Potentials for Mercury

Solution	Z.c.p. (volts vs. N.h.e.)	Amount of anion specifically adsorbed in μcoulombs cm. ⁻²
0.1 N KF	-0.19	0.0
1.0 N KF	-0.19	0.0
0.1 N K ₂ SO ₄	-0.20	0.1
0.1 N KCl	-0.23	2.7
1.0 N KCl	-0.28	7.3
0.1 N KNO ₃	-0.24	2.3
0.1 N KClO ₄	-0.24	3.7
0.1 N KBr	-0.30	5.2
0.1 N KSCN	-0.35	9.6
0.1 N KI	-0.45	11.1
0.1 N KOH	-0.19	0.3
0.1 N HCl	-0.28	3.0

Table V: Experimental Results for Silver (Potentials Are Given in volts vs. N.h.e.)

Solution	V_{ss}	V_{pk} (power scraper)
0.1 N KCl	+0.28	-0.82 ± 0.02

Decay Data. A. General. The transient decays lasted from about a second up to several minutes.

Limited work indicates that vigorous stirring facilitates a faster decay rate for all metals studied. Decay rates in general paralleled the i_{pk} values, *i.e.*, the decay rate (as studied by means of the manual-scraping assembly) increased in the order: Au < Pd, Pt < Cu, as did i_{pk} . With the manual scraper, the decay was much more rapid following a single scrape (at the same potential) than it was after multiple successive scrapes.

B. Gold and Copper. The decay rate increased with a decrease in pH and increased slightly with an increase in anion adsorption (interpreting the varying values of V_{pk} as a measure of adsorbability).

C. Platinum and Palladium. Decay rates for these metals were very nonreproducible, but within the experimental uncertainty no trends in decay rates as a function of solution were observed.

Discussion

Comparison of Results with Manual and Power Scraper. Before the experimental results are discussed in relationship to the meaning of V_{pk} , the difference in V_{pk} values between the power and manual scraping must be considered. Both methods produce identical results for Au and for Pt and Pd in basic solutions; a more negative V_{pk} is produced with the power scraper for Cu and with the manual scraper for Pt in neutral and slightly acidic solutions. Two effects are responsible for these differences: (1) because of the rapid H_3O^+ reduction, the local pH at an electrode is increased, and the effect is more pronounced for the manual scraping assembly since it does not effect mass transfer of solution to and from the electrode as rapidly as the mechanical scraper; and (2) the manual scraper operates more slowly than the mechanical one and hence cannot "outrun" the cathodic reactions when the latter are rapid. In the case of copper, the results indicate the latter effect is dominant. In the case of Pt and Pd, both methods of scraping remove the charge from the electrode so that the pH effect is the dominant one. At pH 12, for Pt and Pd, there is no mass-transfer problem since the solution is self-buffered, and thus there is no difference in V_{pk} between the two scraping methods. In the case of gold, H_3O^+ reduction is slow enough that neither of the effects 1 or 2 is significant. Although the trends in V_{pk} for manual scraping are qualitatively correct (*cf.* the results on Cu for both methods), the absolute values obtained with the mechanical scraper must be considered the more reliable.

Interpretation of V_{pk} . The following experimental facts are in accord with V_{pk} values being the zero charge potential: (a) V_{pk} is independent of V'_{ss} ; (b) V_{pk} comes to a limiting value with increased scraping speed; (c) V_{pk} increasingly becomes more negative with anion variation in the order F^- , $SO_4^{2-} < Cl^- < ClO_4^- < Br^- < SCN^- < I^-$ (compare Table VI with Tables I-IV); (d) there is a greater difference between V_{pk} for 0.1 N KCl and 1.0 N KCl than between V_{pk} for 0.1 N KF and 1.0 N KF (compare Table VI with Tables I, III, and IV); (e) in a given solution (0.1 N KCl), V_{pk} is more negative for metals with lower work functions,^{14,15} *i.e.*, $V_{pk}^{Pt} > V_{pk}^{Au} > z.c.p.^{Hg} > V_{pk}^{Cu}$.

Ag does not fit this trend if one uses its "usually accepted" work function.

The pH dependence of V_{pk} cannot be explained with the theory that V_{pk} is the z.c.p. If the following model is assumed, all of the experimental facts can be explained, however.

Scraping removes the metal charge and double layer which results in the metal achieving its z.c.p., but immediate discharge of nearby H_3O^+ and H_2O drives the potential positive before V_{pk} is measured. Immediately following this the reduction rate decreases rapidly since the rate-controlling step changes from rapid discharge onto an empty surface to the slower H-atom desorption (electrochemical or recombination) and slow mass transfer of H_3O^+ to the surface. These latter processes control the observed transient decay and i_{pk} . V_{pk} is recorded between the rapid discharge reaction and the slower (desorption- and mass transfer-controlled) reduction, and faster scraping outruns the latter process (except in cases such as Cu in KI where V_{pk} did not level out with an increase in scraping speeds). It follows from this model that the peak potential in acidic solutions is positive of that in basic solutions because of the additional H_3O^+ and H_2O reduction occurring in the initial prerecorded time, and the z.c.p. is at least as negative as V_{pk} in basic solution.

Discussion of Z.c.p. Values Obtained by Other Investigators. Kheifets and Krasikov¹⁶ have done extensive capacitance measurements on a series of metals. Their z.c.p. results for Pt are in excellent agreement with our V_{pk} in neutral and basic solutions and show the same general trend with pH. Our peak potential in acid solution corresponds quite closely to other reported values of z.c.p. for Pt.¹⁷⁻²⁴ The reported potentials (+0.1 to 0.3 v.) were usually measured in

(14) P. Ruetschi and P. Delahay, *J. Chem. Phys.*, **23**, 697 (1955).

(15) B. Jakuszewski, *Bull. Acad. Polon. Sci., Ser. Sci. Chim.*, **9**, No. 1, 11 (1961).

(16) V. L. Kheifets and B. S. Krasikov, *Zh. Fiz. Khim.*, **31**, 1992 (1957).

(17) T. N. Voropaeva, B. V. Deryagin, and B. N. Kabanov, *Izv. Akad. Nauk SSSR, Otd. Khim. Nauk*, No. 2, 257 (1963).

(18) L. Young, Ph.D. Dissertation, Cambridge University, 1949.

(19) A. N. Frumkin, A. W. Gorodetskaya, B. Kabanov, and N. Nekrassov, *Physik. Z. Sowjetunion*, **1**, 225 (1932).

(20) T. Voropajeva, B. Derjaguin, and B. Kabanov, *Dokl. Akad. Nauk SSSR*, **128**, 981 (1959).

(21) N. Balashova and A. N. Frumkin, *ibid.*, **20**, 449 (1938).

(22) N. A. Balashova, *ibid.*, **103**, 639 (1955).

(23) A. Frumkin and B. Kabanov, *Physik. Z. Sowjetunion*, **5**, 418 (1934).

(24) E. K. Wenstrom, V. I. Lichtman, and P. A. Rehbinder, *Dokl. Akad. Nauk SSSR*, **107**, 105 (1956).

acidic solutions containing salts which are not strongly adsorbed on mercury.

Two z.c.p. values have been given for Au in the literature. A recent determination by the method of double-layer repulsion gives a value of 0.05 v. in very dilute Cl^- and NO_3^- solutions.¹⁷ A value of 0.2–0.3 v. has been obtained by the adsorption-shift method²⁵ and by the capacity method in HClO_4 solutions.^{26,27} The present experimental transient peaks, V_{pk} , in acid solution (about +0.1 v. for solutions of slightly adsorbing ions) are in better agreement with the above values^{25–27} than is the V_{pk} in basic solutions.

A variety of values has been given for the z.c.p. of silver. These are well reviewed by Leikis.²⁸ The values fall roughly into two classes. One class consists of values that are in the vicinity of the normal hydrogen electrode potential. The other class consists of two values: -0.6 v., the result of electrocapillary measurements on molten silver,²⁹ and -0.7 v., found by capacity measurements²⁸ in dilute sulfate solutions. Leikis performed a detailed study of concentration, anion, and organic adsorbant effects, and Frumkin³⁰ considers Leikis' values to be correct. The present V_{pk} values agree quite well with the latter two values.

Z.c.p. values reported for Cu in the literature are quite inconsistent. A review of these has been given by Bockris, Green, and Swinkels³¹ who consider the z.c.p. of Cu to be -0.2 v. with an uncertainty of $+0.2$ and -0.1 v.; this value is positive of the present V_{pk} values except in acidic solutions.

Summary

From the present experiments, our proposed model predicts z.c.p. values near the peak voltage, V_{pk} , in

basic solutions. The V_{pk} values in acid solutions more nearly agree with results and interpretations of other investigators. This difference requires further consideration. In addition to the H_3O^+ and water reduction reactions occurring at z.c.p., reactions such as $\text{M} + 2\text{OH}^- \rightarrow \text{M}(\text{OH})_2 + 2e^-$ should become more important in basic solution and should shift the peak potential in the negative direction. Even in neutral solutions, due to the H_3O^+ reduction producing a more basic solution near the electrode, this result may still be observed. Also, OH^- adsorption may be important in neutral solutions since its local concentration is high. A detailed pH study of the scrape transients, which would show leveling out of V_{pk} with pH if it existed, would be valuable in testing such considerations. Also, it would be valuable to study metals exhibiting high hydrogen overvoltage since for them H_3O^+ and H_2O reduction reactions would be negligibly slow at the z.c.p., as is the case with mercury.

Acknowledgment. The authors gratefully acknowledge financial support from the Atomic Energy Commission under Contract No. AT(11-1)1144. R. C. L. wishes to thank the National Science Foundation for a summer undergraduate research fellowship.

(25) M. Green and H. Dahms, *J. Electrochem. Soc.*, **110**, 466 (1963).

(26) G. M. Schmid and N. Hackerman, *ibid.*, **109**, 243 (1962).

(27) G. M. Schmid and N. Hackerman, *ibid.*, **110**, 440 (1963).

(28) D. I. Leikis, *Dokl. Akad. Nauk SSSR*, **135**, 429 (1960).

(29) S. Karpachev and A. Stromberg, *J. Phys. Chem. USSR*, **18**, 47 (1944).

(30) A. N. Frumkin, *J. Electrochem. Soc.*, **107**, 461 (1960).

(31) J. O'M. Bockris, M. Green, and D. A. J. Swinkels, *ibid.*, **111**, 743 (1963).

Electrosorption of Ethylene on Platinum as a Function of Potential, Concentration, and Temperature

by E. Gileadi, B. T. Rubin, and J. O'M. Bockris

Electrochemistry Laboratory, University of Pennsylvania, Philadelphia, Pennsylvania 19104
(Received March 19, 1965)

A radiotracer method was employed to study the electrosorption of ethylene from 1 *N* sulfuric acid on Pt-plated gold electrodes. The dependence of the partial surface coverage θ on concentration, temperature, and potential was determined. The coverage reached a saturation value when the bulk concentration of ethylene exceeded 2×10^{-8} mole/ml. Peak adsorption occurs at 0.40 v. vs. n.h.e. at high coverage, shifting toward 0.46 v. as the coverage approaches zero. The equilibrium constant for adsorption is independent of temperature within experimental error in the range of 30–70°. The energetics of adsorption are consistent with a model in which four water molecules are replaced by each ethylene molecule adsorbed. Mobile adsorption is indicated at low and intermediate values of the coverage and a net positive entropy of adsorption is observed. The kinetics of adsorption is controlled by mass transfer. Good agreement between the equilibrium constants calculated from measurements of the rate of adsorption and from steady-state measurements is obtained.

Introduction

The interpretation of kinetic parameters observed in the study of electrode reactions cannot be made without an understanding of the properties of the interface, the extent of adsorption of reactants, products, and stable or unstable intermediates, as a function of concentration in the bulk of the solution and the electrical field across the interface, as well as a knowledge of the nature of the forces between the surface atoms and the adsorbent and the lateral interactions between the adsorbent molecules on the surface.

The mercury–electrolyte interface has been studied extensively and a relatively large amount of data concerning the adsorption behavior of various compounds at this interface is available. Gas phase adsorption of H₂, O₂, N₂, and hydrocarbons on metals and semiconductor catalysts has been extensively studied.^{1,2} Little is known, however, about adsorption from solution onto solid metal electrodes and only a few^{3,4} measurements of adsorption of simple hydrocarbons on solid electrodes have so far been reported.

A method of determining the extent of adsorption from solution onto solid metal electrodes has been

developed in this laboratory^{5,6} and has been applied, following slight modifications, to the adsorption of ethylene on Pt electrodes from 1 *N* H₂SO₄ solution.

Experimental Section

1. *Electrodes.* A thin gold foil (about 2×10^4 Å thick) plated with platinum served as the working electrode. The gold foil was first cleaned in acetone and rinsed with distilled water. An anodic pulse was applied for 20 sec., the electrode was left on open circuit for about 20 min., and then a cathodic pulse was applied for 30 sec. at 0.08 amp. cm.⁻² in 1 *N* H₂SO₄. Subsequently it was transferred to a new solution and polarized in the cathodic direction for an addi-

(1) D. O. Hayward and B. M. T. Trapnell, "Chemisorption," Butterworth and Co. Ltd., London, 1964.

(2) G. C. Bond, "Catalysis by Metals," Academic Press Inc., London, 1962.

(3) L. W. Niedrach, *J. Electrochem. Soc.*, **111**, 1309 (1964).

(4) S. B. Brummer, Second Interim Technical Report, Contract No. DA44-009 AMC 410(T), prepared by Tyco Laboratories, Inc., for U. S. Army Engineering Research and Development Laboratories, Fort Belvoir, Va.

(5) E. Blomgren and J. O'M. Bockris, *Nature*, **186**, 305 (1960).

(6) H. Dahms, M. Green, and J. Weber, *ibid.*, **196**, 1310 (1962).

tional 30 sec. at the same current density. A platinizing solution (120 ml.) containing 3 g. of chloroplatinic acid/100 ml. was used, and the platinum was deposited at 5 ma./cm.² for 3.5 min. giving rise to about 10³ atomic layer (or an average thickness of 2.5×10^3 Å.). The resulting platinum surface was activated by pulsing anodically for 3 sec. and cathodically for 7 sec., five to seven times, at a current density of 0.08 amp./cm.², ending with 30 sec. of cathodic polarization.

The working electrode was mounted over the window of a thin mica end-window proportional counter. A palladium tube inserted into the cell through a side arm (see Figure 1) served as a nongassing counter electrode, and the potential of the working electrode was set and controlled with respect to a mercury-mercurous sulfate reference electrode by means of an electronic potentiostat.

2. *The Cell. a. Temperature Control.* The newly designed cell (Figure 1) permits accurate internal temperature control to about $\pm 0.01^\circ$. Temperature regulation is achieved by means of an alternating current bridge circuit. One leg of the bridge consists of a temperature-sensing thermistor probe (inserted into the cell) and the other leg is a variable resistance. The temperature controller (Yellow Springs Instruments Model 71) provides power to a nichrome wire coil enclosed within the cell to maintain constant temperature. Direct contact with the solution is avoided by housing the nichrome coil in a short glass tube.

b. *Addition and Removal of Ethylene.* To allow introduction of the ethylene solution into a closed system without loss due to its high volatility, one of the radial arms of the cell was adapted at its terminus with a self-sealing septum. The septum was separated from the solution in the cell by means of a Teflon-clad glass stopcock (Figure 1). Special platinum needle syringes were employed such that quantities ranging from 0.05 to 20 ml. of liquid could be injected into and withdrawn from the cell.

3. *Electrical Circuit.* A Wenking potentiostat Type 61R was used to maintain the potential of the test electrode in the region where no steady-state Faradaic reaction occurs. The potential was measured on a Keithly 610A electrometer and the current was recorded on an Esterline Angus Model AW graphic ammeter.

For capacitance measurements, a Trygon Model HR40-750 power supply was used together with a transistorized constant-current device (galvanostat) described elsewhere.⁷ Potentiostatic control was maintained with the potentiostat and galvanostat connected in the circuit (the constant current is taken up by the potentiostat and does not affect the electrode). Switch-

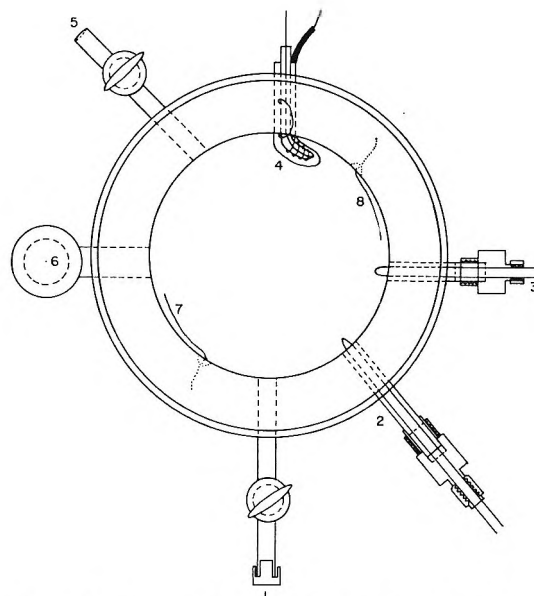


Figure 1. Adsorption cell: 1, sample outlet; 2, thermistor temperature probe; 3, palladium counter electrode; 4, heater; 5, nitrogen inlet; 6, reference electrode; 7, platinum wire; and 8, platinum wire.

ing over to galvanostatic control is affected by opening a single fast switch (Western Electric Type 275 B, mercury-wetted relay). A flat platinum gauze served as a counter electrode in these determinations to ensure a uniform current distribution on the test electrode.

The potential-time relationship during the galvanostatic transient was recorded on a Type 543 differential-input Tektronix oscilloscope triggered externally from the counter electrode, and the trace was photographically recorded with a Model C12 Polaroid camera.

4. *Procedure. a. Adsorption Measurements.* The test electrode was prepared as discussed above and introduced into the cell which had been previously filled with 1 N H₂SO₄. Two platinum wires situated along the bottom rim of the cell were used for pre-electrolysis, which was carried out for 15 hr. at an apparent current density of 0.025 ma./cm.², with purified nitrogen bubbling through the cell.⁸ The test electrode potential was then set at 0.50 v. vs. n.h.e. for 1 hr. to eliminate any hydrogen which may have adsorbed on the surface or absorbed near the surface. A measured amount of a saturated ethylene solution was introduced into the cell through the rubber septum and the potential was set quickly to the desired value.

(7) J. O'M. Bockris, H. Wroblowa, E. Gileadi, and B. J. Piersma, *Trans. Faraday Soc.*, in press.

(8) This step was eliminated in subsequent experiments after it was ascertained that it had no effect on the final results. The current density for pre-electrolysis was chosen about twice the maximum current density observed during adsorption measurements.

b. Solution Preparation. Active ethylene (1,2- C^{14} -ethylene, specific activity about 1 mc./mmole) was introduced under a pressure of 1 atm. into a mixing chamber containing 1 *N* sulfuric acid. After equilibrium had been reached, the excess volume in the mixing chamber was displaced by mercury at *P* of 1 atm. The solution thus obtained was used as the stock solution, from which small amounts were introduced into the cell, which was completely filled with liquid.

c. Determination of Surface Concentration. The surface concentration of ethylene is proportional to the net count rate obtained by subtracting the environmental and solution background from the total count rate. The time usually required for adsorption equilibrium to be reached, as observed by a steady count rate, depended strongly on temperature. At 30° about 30–60 min. was usually required. During measurement of surface concentration as a function of potential, readings were taken with increasing and decreasing anodic potentials to check the reversibility of adsorption. Adsorption isotherms were obtained by setting the potential at a fixed value and adding small amounts of ethylene solution after adsorption equilibrium had been reached.

d. Determination of the Bulk Concentration of Ethylene. Small samples (0.1–0.3 ml.) of solution were withdrawn from the cell after adsorption equilibrium had been reached and the concentration of ethylene was measured in a liquid scintillation counter (Baird Atomic Model F-7). The scintillation liquid consisted of 75% dioxane, 11.85% anisole, 12% 1,2-dimethoxy-methane, 0.05% PPO, and 1.1% POPOP. The internal standard (C^{14} -toluene) was added before addition of the sample, to minimize loss of ethylene by evaporation. The concentration of the stock solution was measured in a similar way. An additional check on the concentrations was made by comparing the directly measured concentration with that calculated from the concentration of the stock solution and the ratio of dilution. In the most dilute solutions only the latter method was available and the concentrations in the bulk were obtained after due allowance for the amount of ethylene adsorbed on the surface had been made.

e. Capacity Measurements. For capacity measurements the test electrode was prepared as described above. The electrode was activated by anodic and cathodic pulsing and then set to 0.50 v. *vs.* n.h.e. The capacity was measured (by the galvanostatic-charging method) at different times after activation, until its variation with time was negligible. The average of the last few values was then used to compute the roughness factor of the electrode.

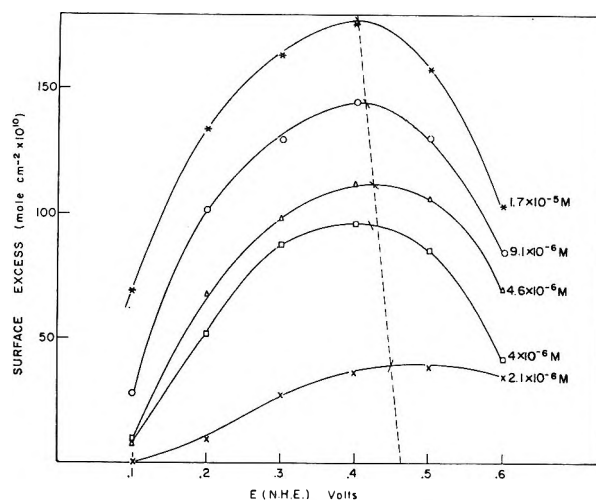


Figure 2. Variation of adsorption with potential at 30°.

Results

1. Variation of Surface Concentration with Potential. The variation of surface concentration of ethylene with potential at five different bulk concentrations is shown in Figure 2. The potential range available for measurement is limited on the cathodic side by hydrogen evolution and on the anodic side by rapid consumption of ethylene due to its electrooxidation. In the range where measurements were taken, the current passing to maintain potentiostatic control was of the order of 2–20 μ a./cm.² of apparent surface area, corresponding to about 10^{-8} – 10^{-7} amp./cm.² of real surface area.

At relatively high bulk concentrations a maximum in coverage occurs at 0.40 v. (n.h.e.) and the value of the potential of maximum adsorption, extrapolated to zero coverage, is about 0.46 v. (n.h.e.). The maximum surface concentration Γ_m is taken as 6×10^{-10} mole of ethylene/cm.² of real surface area, assuming that each molecule occupies four sites on the most dense (1.1.1) crystal plane of platinum. The values of surface concentration in Figure 2 are per apparent square centimeters and indicate a high roughness factor, in agreement with direct double-layer capacitance measurements (see below).

2. Reversibility of Adsorption. Preliminary experiments showed that the surface concentrations of ethylene change irreversibly with potential. The procedure, described above, in which the electrode potential was maintained at 0.50 v. *vs.* n.h.e. with nitrogen bubbling before ethylene was introduced into the solution, was intended to ionize all the hydrogen formed on or just below the surface of the platinum electrode so that catalytic hydrogenation of ethylene on the surface could not occur. In order to obtain reversible

Γ - V results, however, it was found necessary (in addition to the above treatment of the working electrode) to charge up the Pd counter electrode with hydrogen (by prolonged cathodic polarization outside the cell). It is possible that the electrode thus treated either does not adsorb ethylene, or adsorbs it reversibly without causing dehydrogenation and does not therefore cause changes in the concentration of ethylene in solution. It should be noted in this connection that while direct measurement of the ethylene concentration in the bulk revealed no changes in irreversible runs, the liquid scintillation method of determining this concentration is only sensitive to C^{14} and would not detect a chemical change, *e.g.*, formation of ethane or acetylene from ethylene.

3. *Roughness Factor Determination.* The roughness factor was determined by measurement of the ionic double-layer capacitance at 0.50 v. (n.h.e.) in 1 N H_2SO_4 solution with nitrogen bubbling through the solution. A value of 18 $\mu f./cm.^2$ of real surface area was assumed⁹ and the roughness factor was obtained by dividing the capacity measured per square centimeter of apparent surface area by this figure. The capacity of a freshly activated electrode was found to change rapidly with time in the first 30–60 min. and more slowly afterward. The capacity of each electrode was measured before every run, until its variation with time had become negligible (less than 10% variation per hour). Values of roughness factor in the range of $R = 50$ –100 were obtained on different electrodes at different times.

4. *Adsorption Isotherms.* The variation of the partial coverage with concentration at 0.40 v. *vs.* n.h.e. and 30° is shown in Figure 3. Figure 4 shows the effect of temperature on the adsorption isotherm. The variation of the extent of adsorption with temperature is within experimental error of the points at one temperature, pointing to a small value for the standard heat of adsorption (see below).

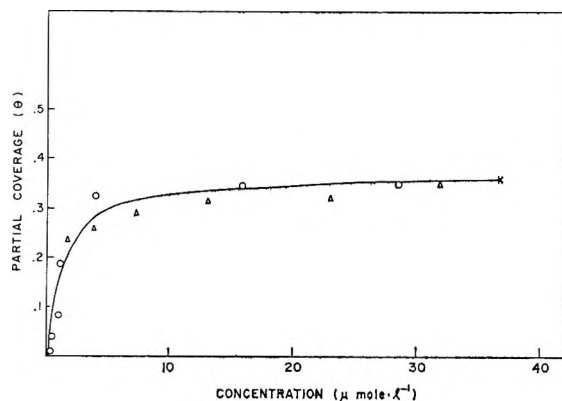


Figure 3. Adsorption isotherm at 30° and 0.4 v. *vs.* n.h.e.

Adsorption isotherms measured at several potentials are shown in Figure 5. The form of the isotherm is not substantially affected by the electrode–solution potential difference. The coverage θ reached its saturation value at 0.40 v. *vs.* n.h.e. faster than at the other potentials measured (*cf.* Figure 2), but saturation behavior was observed in all cases when the bulk concentration of ethylene exceeded about $2 \times 10^{-5} M$.

Two general features common to isotherms taken under all above conditions are (a) a rapid change of θ from essentially zero to a saturation value over a small concentration change of ethylene in solution, and (b) a saturation value of θ of the order of 0.35–0.45 calculated on the basis of surface area determination by the double-layer capacity method, as discussed above.

The data presented in Figures 3–5 were normalized, for the purpose of comparison, to have a maximum surface coverage of $\theta_{max} = 0.4$. The significance of this value of θ_{max} and the values of the coverage to be used in evaluating the isotherm parameters will be discussed below.

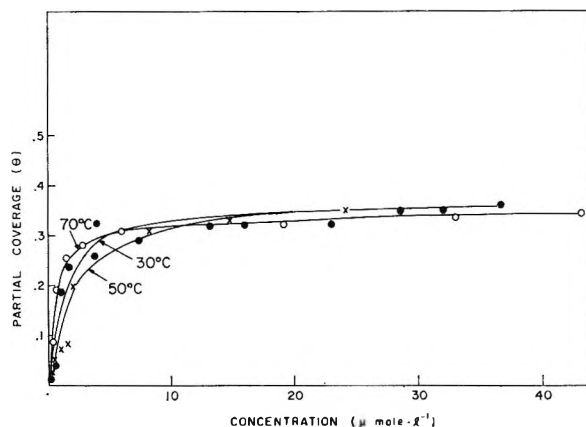


Figure 4. Adsorption isotherms at three temperatures; $E = 0.4$ v. *vs.* n.h.e.

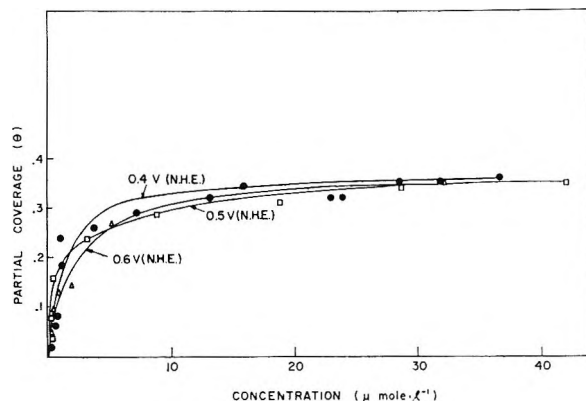


Figure 5. Adsorption isotherms at three potentials at 30°.

5. *Time Effects.* Figures 6a, b, and c show typical plots of net count rate (proportional to the surface concentration) vs. time for 70, 30, and 6°, respectively, obtained in gently stirred solutions. The time taken to reach adsorption equilibrium depends on temperature. At 70°, only about 15 to 20 min. was required while at 6° the system was still far from equilibrium after 1 hr. The same data are plotted in Figures 7a, b, and c as the net count rate vs. the square root of time. A linear relationship between the surface concentration and $t^{1/2}$ is observed in the range where Γ is not too close to its equilibrium value corresponding to a given bulk concentration.

Discussion

1. *The Potential of Zero Charge on Pt.* Major difficulties are encountered in attempting to determine the potential of zero charge on solid metal electrodes. The methods most commonly employed are based on differential capacity measurements in dilute electrolyte in the absence of specifically adsorbed ions,^{9,10} methods based on measurement of the coefficient of friction of metals,^{11,12} or methods in which new metal surface is bared in solution and the current required to charge the newly formed double-layer capacitor is measured. The potential of zero charge (p.z.c.) corresponds to that value of the potential at which this charging current is zero.¹³ The differences between the electronic work function of metals have been correlated to the difference in their p.z.c. values.^{14,15} Results obtained by different methods are widely discrepant as are those obtained by different investigators using the same method. A new method based on the measurement of the adsorbability of neutral organic molecules and its variation with the concentration of the supporting electrolyte has recently been developed.¹⁶ It has been employed in conjunction with other methods in a systematic study¹⁷ of the potential of zero charge under identical, high purity conditions.

Kheifets and Krasikov¹⁸ have used the capacitance method to measure the variation of the p.z.c. on Pt and a number of other metals with pH. No pH dependence was found on metals such as Ag, Cu, Hg, and Zn, while on Pt, Pd, Ni, Fe, and Co the p.z.c. changed in the anodic direction with decreasing pH. In the case of Pt a nonlinear relationship between the p.z.c. and pH was found by these authors, who reported values of 0.30 and 0.50 v. vs. n.h.e. at pH values of 3 and 2, respectively. Recent measurements of the p.z.c. of Pt in this laboratory¹⁷ gave a value of 0.48 v. vs. n.h.e. at pH 3 with an average variation of 58 mv./pH unit between pH 12 and 3. Further support

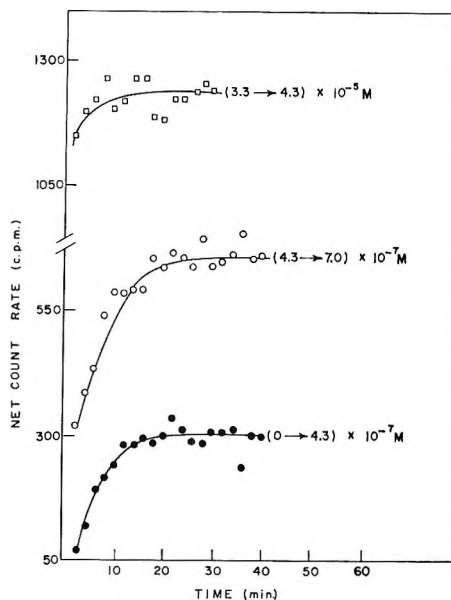


Figure 6a. Variation of adsorption with time for specified initial and final concentrations ($C_1 \rightarrow C_2$ in moles/liter) at 70°; $E = 0.4$ v. vs. n.h.e.

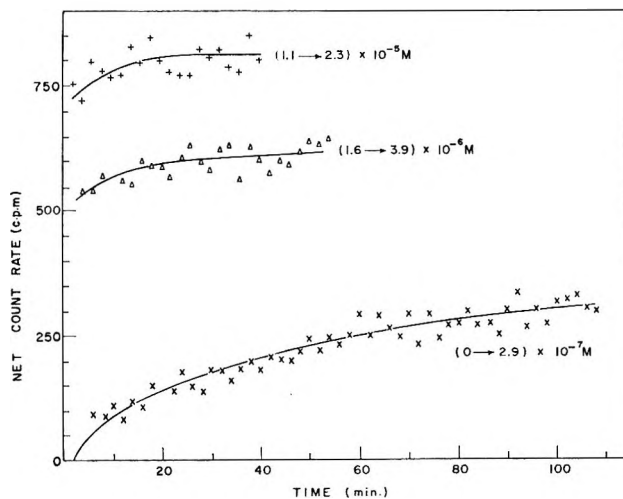


Figure 6b. Adsorption vs. time as in Figure 6a at 30°. $E = 0.4$ v. vs. n.h.e.

- (10) T. Borisova, B. Ershler, and A. N. Frumkin, *J. Phys. Chem. USSR*, **22**, 925 (1948).
 (11) (a) L. Young, Ph.D. Thesis, Cambridge University, 1949; (b) J. O'M. Bockris and R. Farry-Jones, *Nature*, **171**, 930 (1953).
 (12) D. N. Staicopoulos, *J. Electrochem. Soc.*, **108**, 900 (1961).
 (13) B. Jakaszewski and Z. Kozlowski, *Roczniki Chem.*, **36**, 1873 (1962).
 (14) R. M. Vasenin, *Zh. Fiz. Khim.*, **22**, 878 (1953); **28**, 1672 (1954).
 (15) V. M. Novakovskii, E. A. Ukshe, and A. I. Levin, *ibid.*, **29**, 1847 (1955).
 (16) H. Dahms and M. Green, *J. Electrochem. Soc.*, **110**, 466 (1963).
 (17) J. O'M. Bockris, S. D. Argade, and E. Gileadi, to be published.
 (18) V. L. Kheifets and B. S. Krasikov, *Zh. Fiz. Khim.*, **31**, 1992 (1952).

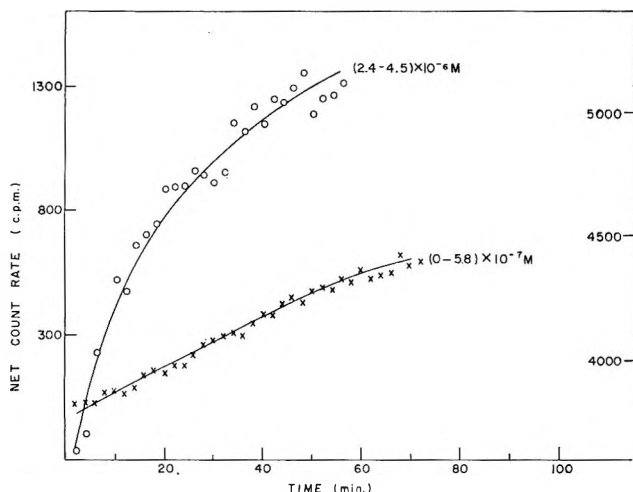


Figure 6c. Adsorption vs. time as in Figure 6a at 6° (lower concentration left-hand scale). $E = 0.4$ v. vs. n.h.e.

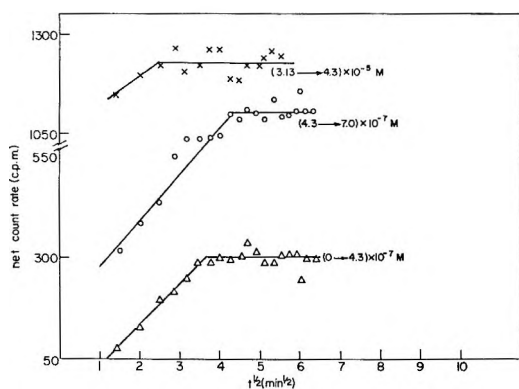


Figure 7a. Variation of adsorption with the square root of time for specified initial and final concentrations ($C_1 \rightarrow C_2$ in moles/liter) at 70°; $E = 0.4$ v. vs. n.h.e.

for a similar pH dependence of the potential of zero charge is found in the apparently anomalous pH effects observed in the anodic oxidation of ethylene¹⁹ and in studies of the oxygen evolution reaction.^{20,21} In these systems all the kinetic evidence is in favor of a mechanism involving water discharge as the rate-determining step. The value of the parameter $d \log i_0/dpH = 0$ can only be explained on the basis of this mechanism if a variation of ca. 60 mv./pH unit for the potential of zero charge is assumed.¹⁹ A relationship between the p.z.c. and the potential of maximum adsorption for uncharged organic molecules is known experimentally²²⁻²⁴ and has been interpreted theoretically.²⁵ Thus maximum adsorption is expected to occur when the metal has a small negative charge (about 2-3 $\mu\text{coulombs/cm}^2$ on mercury) and the p.z.c. is some 50-250 mv. anodic to the potential of maximum adsorption.²⁶

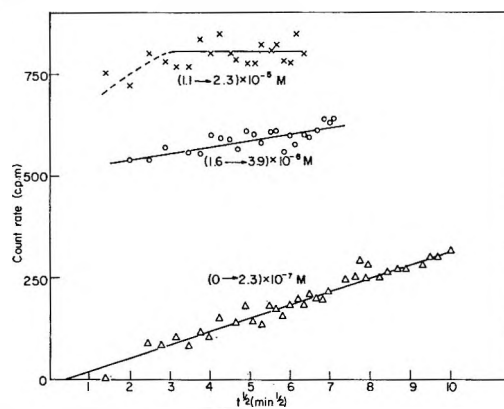


Figure 7b. Adsorption vs. $t^{1/2}$ as in Figure 7a at 30°. $E = 0.4$ v. vs. n.h.e.

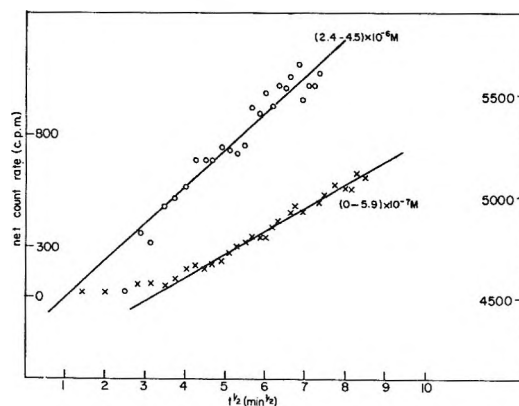


Figure 7c. Adsorption vs. $t^{1/2}$ as in Figure 7a at 6° (lower concentration left-hand scale). $E = 0.4$ v. vs. n.h.e.

Extrapolation of the results of Bockris, *et al.*,¹⁷ to a pH value of 0.5 corresponding to 1 N H_2SO_4 gives a value of 0.63 v. vs. n.h.e. The potential of maximum adsorption (extrapolated to zero coverage) for ethylene on Pt in 1 N sulfuric acid (see Figure 2) is 0.46 mv., which is consistent with a value of 0.51 to 0.71 v. vs. n.h.e. for the p.z.c. in this system. The

(19) H. Wroblowa, B. J. Piersma, and J. O'M. Bockris, *J. Electroanal. Chem.*, **6**, 401 (1963).

(20) J. McDonald and B. E. Conway, *Proc. Roy. Soc. (London)*, **A269**, 419 (1962).

(21) K. J. Vetter and D. Berndt, *Z. Elektrochem.*, **62**, 378 (1958).

(22) E. Blomgren, J. O'M. Bockris, and C. Jesch, *J. Phys. Chem.*, **65**, 2000 (1961).

(23) J. O'M. Bockris and D. A. J. Swinkels, *J. Electrochem. Soc.*, **111**, 736 (1964).

(24) J. O'M. Bockris, D. A. J. Swinkels, and M. Green, *ibid.*, **111**, 743 (1964).

(25) J. O'M. Bockris, M. A. V. Devanathan, and K. Müller, *Proc. Roy. Soc. (London)*, **A274**, 55 (1963).

(26) Aromatic compounds may behave differently due to a specific π -electron interaction with the positively charged surface at potentials anodic to the p.z.c.

data of Kheifets and Krasikov¹⁸ cannot be extrapolated to lower pH values since the p.z.c. changes rapidly in this region according to their result (0.2 v. in going from pH 3 to 2) and unreasonably high values would be predicted for a pH value of 0.5.

Previously a value of 0.3 v. was reported for the p.z.c. of Pt in acid solutions.²³ This, however, was based on methods where high purity conditions could not be generally attained and maintained during the experiment. In particular, atmospheric oxygen could not be eliminated in most cases. Furthermore, the pH dependence of the p.z.c. on Pt was not realized in some of these measurements.

It is thus suggested, on the basis of the above evidence, that a new value of 0.5 to 0.6 v. *vs.* n.h.e. be adopted for the p.z.c. of Pt in 1 *N* sulfuric acid, with a probable variation of about 60 mv./pH unit.

2. *The Maximum Coverage.* The plots of surface coverage θ *vs.* the concentration of ethylene in the bulk of the solution (Figures 3-5) show a saturation behavior typical of monolayer adsorption. However, the value of the limiting coverage, based on determination of the roughness factor from double-layer capacity measurements, is in the range of $\theta_{\max} = 0.35-0.45$. Similar behavior, *i.e.*, partial coverage values approaching a limit substantially less than unity, has been observed previously^{23,27} and the possible causes will be discussed briefly below.

(i) It may be argued that the value of 18 $\mu\text{f./cm.}^2$ of real surface area, chosen as the basis of the calculation of roughness factor, cannot be justified. The measurement is made at a potential of 0.5 v. *vs.* n.h.e. *i.e.*, very near and possibly slightly cathodic to the potential of zero charge. In the corresponding region on mercury, rather higher values of the capacity are observed. Measurement of the capacity of our electrode *vs.* potential showed no variation in the range of 0.4 to 0.8 v. *vs.* n.h.e., and the same results were obtained in the presence of C_2H_4 as in its absence.⁷ Such behavior is found on mercury when an organic compound is strongly adsorbed, and the value of the capacitance there is in the range of 5-15 $\mu\text{f./cm.}^2$ depending on the nature and concentration of the organic substance. In addition, measurements of the capacity of bright platinum electrodes under identical conditions gave values of 30 $\mu\text{f./cm.}^2$. Assuming a roughness factor of 1.5 for bright Pt, this would suggest a value of 20 $\mu\text{f./cm.}^2$ of real surface area, close to the value of 18 $\mu\text{f./cm.}^2$ used in our calculation.

In conclusion, the roughness factors obtained in our measurements probably represent the lower limit of acceptable values, and the value of $\theta_{\max} = 0.35-0.45$ is an upper limit for θ_{\max} . Had we assumed

strong organic adsorption on the electrode and a low value of the capacity, an even lower value of θ_{\max} would result.

(ii) The low value of the limiting coverage is often claimed to be due to inactive sites or small crevices on the surface. The argument is that the capacitance method measures the full surface area of the electrode while a fraction of the sites may be unavailable for adsorption, either due to a different degree of affinity of the surface atoms for adsorbent (inactive sites) or due to some of the sites being inside small crevices inaccessible for the larger organic molecules. In either case one is only concerned with the available part of the surface. The limiting coverage which corresponds to adsorption on practically all the *available* sites may then be defined as $\theta = 1.0$.

The effect of inactive sites is expected to be larger the larger the adsorbing molecule. Thus, if the fraction of active sites is α and they are randomly distributed on the surface, the fraction of the surface which can be covered by a molecule which requires n active sites is $\theta_{\max} = \alpha^n$. However, in this case when the surface is saturated with respect to an adsorbent having a given value of n , active sites will still be available on the surface for another species which adsorbs on a smaller number of sites.

(iii) A special case of inactive sites would be when sites of different nature exist on the surface. This may be regarded as either a kinetic effect, *i.e.*, that the energy of activation on some of the sites is small while on others it is quite high,⁷ or a thermodynamic effect caused by the standard free energies of adsorption being substantially different on different sites. Ample evidence for the kinetic effect is found in gas phase adsorption studies¹ where an initial amount of gas is often adsorbed very rapidly, followed by very slow adsorption, with rate constants several orders of magnitude smaller. Substantially different energies of adsorption may be encountered if, *e.g.*, adsorption occurs first on grain boundaries and then on the rest of the surface. On an oxide or hydrated oxide, *e.g.*, NiOOH, two or three types of sites could be defined corresponding to different chemical entities on the surface. Whatever the cause for the low values of the limiting coverage, one is justified in defining $\theta_{\max} = 1.00$, as long as it is established experimentally (*cf.* Figures 3-5) that a limiting saturation coverage is reached. Physically, this means that the conclusions reached regarding the adsorption behavior apply only to that part of the surface upon which adsorption occurs during the time and in the concentration range studied.

(27) H. Wroblowa and M. Green, *Electrochim. Acta*, **8**, 679 (1963).

3. *Nature of the Adsorption Isotherm.* For a species taking up n sites on the surface a Langmuir-like adsorption isotherm of the form

$$\frac{\theta}{(1 - \theta)^n} = Kc \quad (1)$$

may be applied as a first approximation.^{19,28} Using the data in Figures 3-5, a constant value of K is calculated over most of the coverage and concentration range if n is taken as unity. A linear plot of $\theta/(1 - \theta)$ vs. c going through the origin (Figure 8) and a linear plot of c/θ vs. c (Figure 9) with a slope of unity confirm that a value of $n = 1$ applies for this system. This is rather surprising in view of the large size of the ethylene molecule which is believed¹⁹ (cf. below) to occupy four sites on the Pt surface. The observed behavior is probably due to a high degree of mobility of the adsorbed molecules on the surface. It may be noted that at high concentrations of ethylene where $\theta \doteq 1$ a value of $n = 4$ was found from the dependence of the rate of electrooxidation of ethylene on its partial pressure.^{7,19} Thus, when the surface becomes almost completely covered with adsorbed molecules, lateral motion is hindered and a behavior characteristic of localized adsorption is observed.

The equilibrium constant for adsorption was calculated from the slope of the plot in Figure 8 and from the intercept in Figure 9. The results are given in Table I for three temperatures.

Table I

Temp., °C.	$10^8 K$, cm. ³ /mole		
	c/θ vs. c	$\theta/(1 - \theta)$ vs. c	Average
30	6.7	8.0	7.4
50	4.6	5.4	5.0
70	10	8.3	9.2

Good agreement is found between the values of K obtained by the two methods. From the average values of K at 30 and 50° a value of $\Delta H^\circ = -3.7$ kcal./mole is obtained, where the standard state is chosen as a 1 M solution of ethylene and $\theta = 0.5$. However, from the values of K at 30 and 70°, we find $\Delta H^\circ = +1.2$ kcal./mole. We thus conclude that

$$\Delta H^\circ \doteq 0.0 \pm 4 \text{ kcal./mole}$$

and the value of the equilibrium constant is

$$K = (7.5 \pm 2.5) \times 10^8 \text{ cm.}^3/\text{mole}$$

4. *Energetics of Ethylene Adsorption.* The adsorp-

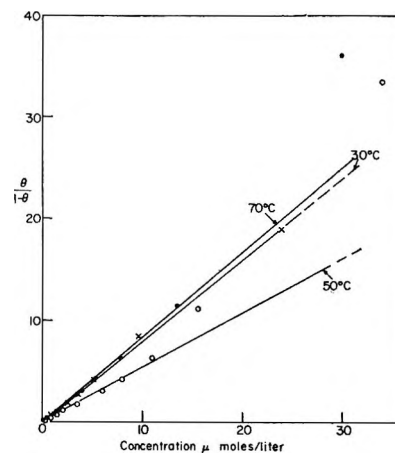


Figure 8. A plot of $\theta/(1 - \theta)$ vs. concentration in moles/liter at 30, 50, and 70°.

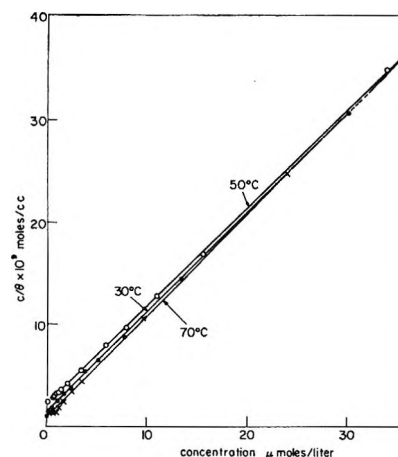
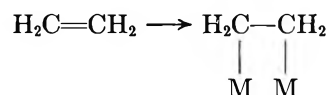


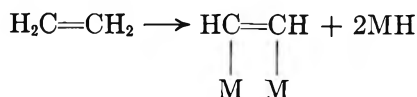
Figure 9. A plot of c/θ in moles/cc. vs. concentration in moles/liter at 30, 50, and 70°.

tion of ethylene and other hydrocarbons from the gas phase on transition metal elements has been rather extensively studied.^{1,2} Saturated hydrocarbons usually undergo dehydrogenation upon adsorption from the gas phase while with larger olefinic compounds a coupled dehydrogenation-hydrogenation process (*i.e.*, disproportionation) takes place. For ethylene two modes of adsorption have been considered. In associative adsorption the double bond is opened and the orbitals are released to form bonds with the metal. Alternatively,

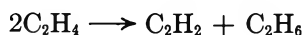


hydrogen may be split off with the double bond remaining intact (dissociative adsorption). The hy-

(28) A. R. Miller, *Proc. Cambridge Phil. Soc.*, **35**, 293 (1939).

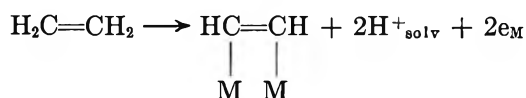


drogen atoms formed in this process may interact with other ethylene molecules to form ethane. The overall process may then be represented by



Evidence for both associative and dissociative adsorption in the gas phase has been reported, although associative adsorption is favored on the basis of energetic consideration.

In electrosorption the process of dissociative adsorption is better represented as

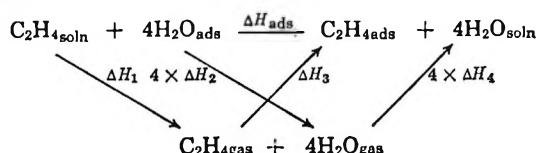


in the potential region where hydrocarbon oxidation occurs. Thus, the energies of ionization and solvation of hydrogen and a proton, respectively, as well as the electronic work function of the metal have to be considered. Taking all these factors into account, the associative mode of adsorption is found more stable by about 60 kcal./mole than dissociative adsorption.¹⁹

Further support for associative adsorption of ethylene is obtained from comparison of the kinetics of anodic oxidation of ethylene and acetylene. The species left on the surface in dissociative adsorption is an acetylene molecule adsorbed. Thus, dissociative adsorption would lead to the same kinetic behavior for ethylene and acetylene, which is not found experimentally.²⁹

The heat of adsorption of ethylene on various metals (as well as that of CO_2 and H_2) from the gas phase was found to depend on the position of the metal in the periodic table.^{1,2} No data are available for Pt but a value of -58 kcal./mole obtained on Ni may be taken as a good approximation. The low value of the heat of adsorption from solution must be interpreted in terms of the replacement of water molecules from the surface^{23,25} and, to a smaller extent, the energy of solvation of ethylene.

The adsorption of ethylene from solution can be represented by the following thermodynamic cycle. The



numerical values for the ΔH terms are $\Delta H_1 \doteq 4$ kcal./

mole, $\Delta H_2 = 22.6$ kcal./mole, $\Delta H_3 = -58$ kcal./mole, and $\Delta H_4 = -9.6$ kcal./mole.

The value of ΔH_2 was calculated as the sum of the dispersion energy and the image force interaction.²⁴

Summing up, one obtains

$$\Delta H_{\text{ads}} = -2.0 \text{ kcal./mole}$$

in excellent agreement with the observed value.

5. *Entropy of Adsorption.* With the standard heat of adsorption of ethylene from solution taken as zero one finds

$$\Delta G^\circ_{\text{ads}} = -T\Delta S^\circ_{\text{ads}} \quad (2)$$

and hence

$$\Delta S^\circ_{\text{ads}} = 2.3R \log K \quad (3)$$

It is convenient here to choose a standard state of unit activity of ethylene. This corresponds to a concentration of 4×10^{-6} mole/ml. With this standard state the equilibrium constant becomes

$$K = (3 \pm 1) \times 10^3$$

and hence

$$\Delta S^\circ_{\text{ads}} = 16 \pm 1 \text{ e.u.}$$

It is noted that a positive entropy of adsorption is measured here, in contrast to negative values of the entropy usually observed in adsorption from the gas phase. This behavior is well understood when one remembers that electrosorption is a replacement reaction. When a molecule is adsorbed from the gas phase it loses at least one and often three degrees of freedom of translation, in addition to loss of rotational degrees of freedom. Hence a decrease in entropy is usually observed for adsorption processes. In electrosorption of ethylene, four water molecules are desorbed per ethylene molecule adsorbed and the net increase in the number of degrees of freedom of the system gives rise to a positive entropy of adsorption. A similar effect has been observed in the adsorption of polynuclear aromatic derivatives.³⁰

6. *The Coverage-Potential Relationship.* The coverage-potential relationship for various concentrations of ethylene at 30° is shown in Figure 2. The decrease of coverage with increasing anodic and cathodic potential is explained in terms of the "competition with water" model discussed elsewhere.²⁵ The symmetrical shape of the curves indicates essentially no effect of the elec-

(29) J. W. Johnson, H. Wroblowa, and J. O'M. Bockris, *J. Electrochem. Soc.*, 111, 864 (1964).

(30) B. E. Conway and R. G. B. Barradas, *J. Electroanal. Chem.*, 6, 314 (1963).

tric field on the interaction between the adsorbed ethylene molecule and the surface metal atoms.

A small shift in the potential of maximum adsorption V_{\max} in the cathodic direction with increasing coverage is observed. Since q_{\max}^m , the charge on the metal at V_{\max} , is constant,^{23,24} we may write

$$q_{\max}^m = K(V_{\max} - V_{pzc}) \quad (4)$$

where K is the integral capacity and V_{pzc} is the potential of zero charge. The differential capacity measured on Pt in 1 *N* sulfuric acid is independent of potential in the range of 0.3–0.8 v. vs. n.h.e.⁷ and is not changed by the addition of ethylene.^{7,31}

Since q_{\max}^m and K in eq. 4 are constant, the quantity $\Delta V = V_{\max} - V_{pzc}$ must also be constant. Thus the potential of maximum adsorption measured on the rational potential scale³² is independent of coverage in this system. The apparent shift of V_{\max} measured against a constant reference electrode is attributed to a shift in the potential of zero charge, also found for a number of uncharged organic substances on mercury.²²

The variation of the apparent standard free energy of adsorption $\Delta G_{\text{ads}}^\circ$ with potential is shown in Figure 10. A nearly parabolic plot of $\Delta G_{\text{ads}}^\circ$ vs. V is obtained with an average variation of $\partial \Delta G_{\text{ads}}^\circ / \partial V \doteq 7$ kcal./mole on either side of the maximum.

7. Adsorption Kinetics. When adsorption studies are carried out from very dilute solutions (as in the present case) mass transport may become a limiting factor in determining the rate of adsorption. The kinetics of the adsorption process under diffusion limiting conditions have been worked out by Delahay and Tractenberg³³ and by Blomgren, Bockris, and Jesch²² for the case of a linear adsorption isotherm, and more recently by Reinmuth³⁴ for the full Langmuir isotherm. In essence all these calculations are based on the assumption that adsorption equilibrium is maintained at all times between particles adsorbed on the surface and those at the outer Helmholtz layer (considered for the purpose of the diffusion calculation as the plane where $x = 0$). Application of the condition of continuity then requires that the flux at this plane ($x = 0$) be equal to the rate of adsorption.

$$J(t) = d\Gamma_t/dt \quad (5)$$

Solving the diffusion equation for the case when the linear adsorption isotherm is applicable^{22,32} and at short times such that $\theta_t < \theta_{\text{equil}}$ where θ_t is the time-dependent value of θ and θ_{equil} is its equilibrium value under a given set of conditions, one obtains

$$\theta_t = \frac{2D^{1/2}\theta_{\text{equil}}}{\pi^{1/2}K\Gamma_{\max}} \sqrt{t} \quad (6)$$

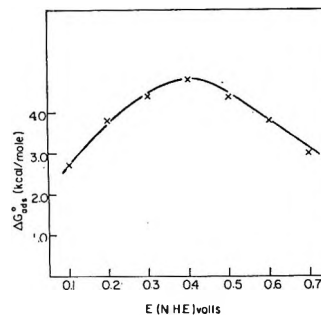


Figure 10. The variation of the standard apparent free energy of adsorption, $\Delta G_{\text{ads}}^\circ$, with potential. A solution saturated with respect to ethylene at 1 atm. was taken as the standard state.

where K is the equilibrium constant for adsorption and Γ_{\max} is the maximum surface concentration.

The results obtained in these measurements (*cf.* Figures 6 and 7) show a distinct linear relationship between θ_t and \sqrt{t} in agreement with eq. 6. This implies that the assumptions used in deriving eq. 6 are applicable in the case of ethylene adsorption from dilute aqueous solutions studied here. Thus the most important conclusion reached at this point is that the rate of adsorption of ethylene from dilute solutions (10^{-5} – 10^{-7} *M*) is diffusion controlled.

From eq. 6 a transition time τ may be defined as the time (extrapolated) corresponding to $\theta_t/\theta_{\text{equil}} = 1$. The transition time²² is given by

$$\tau = \frac{\pi \Gamma_{\max}^2 K^2}{4D} \quad (7)$$

Since the diffusion coefficient D is known or can be estimated fairly accurately for most compounds in aqueous solutions, the equilibrium constant can be calculated from eq. 7. Alternatively, eq. 6 may be differentiated to give

$$\frac{d\theta_t}{d(t^{1/2})} = \frac{2D^{1/2}\theta_{\text{equil}}}{\pi^{1/2}K\Gamma_{\max}} \quad (8)$$

Thus K may be obtained from the slope of the plot of θ_t vs. $t^{1/2}$.

The values of the equilibrium constant obtained from eq. 7 and 8 at two temperatures are shown in Table II, where the average value obtained from the

(31) "Basic Studies of Sorption of Organic Fuels During Oxidation at Electrodes," Final Report M64-341, prepared by American Oil Research and Development for U. S. Army Research Office, Durham, N. C.

(32) D. C. Grahame, *Quart. Rev. (London)*, **41**, 441 (1947).

(33) P. Delahay and I. Tractenberg, *J. Am. Chem. Soc.*, **79**, 2355 (1957).

(34) W. H. Reinmuth, *Anal. Chem.*, **65**, 473 (1961).

isotherms (Table I) is also given for comparison. The agreement between the two last columns of Table II is very good considering the different types of experiments compared and lends further support for the fact that the rate of adsorption is diffusion controlled in

Table II

Temp., °C.	10 ⁸ K, cm. ³ /mole			Av. from isotherm
	Eq. 7	Eq. 8	Av.	
30	9.7	9.5	9.6	7.4
70	10.0	5.8	7.9	9.2

this case. The average of all ten determinations from Tables I and II (assuming that they represent a sample from a single distribution) gives a value of

$$K = (7.8 \pm 2.0) \times 10^8 \text{ cm.}^3/\text{mole}$$

which is not significantly different from the value of $(7.5 \pm 2.5) \times 10^8 \text{ cm.}^3/\text{mole}$ estimated from the equilibrium data above.

In the calculations leading to Table II values of the diffusion coefficients of $D_{30} = 6 \times 10^{-6} \text{ cm.}^2/\text{sec.}$ and $D_{70} = 1.5 \times 10^{-5} \text{ cm.}^2/\text{sec.}$ were used. The ratio of D_{70}/D_{30} was obtained assuming an energy of activation for diffusion of 5 kcal./mole. For the maximum surface coverage $\Gamma_{\text{max}} = 2.2 \times 10^{-10} \text{ mole/cm.}^2$ was used. This is based on a value of $6.0 \times 10^{-10} \text{ mole/cm.}^2$ calculated on the assumption that each ethylene molecule occupies four sites on the (1.1.1) plane of platinum, and the value of $\theta_{\text{max}} = 0.37$ obtained experimentally.

Conclusion

The potential, concentration, and temperature dependence of the adsorption of ethylene on a platinized gold electrode have been investigated. The familiar "bell-shaped" potential-coverage relationship was observed with the peak potential at 0.46 v. (extrapolated to $\theta = 0$). The peak potential shifts slightly in the cathodic direction with increasing coverage, due to a similar shift in the potential of zero charge.

The equilibrium constant for adsorption is essentially independent of temperature in the range of 30–70°. This leads to $\Delta H_{\text{ads}} \doteq 0$, as compared to a heat of adsorption of -58 kcal./mole in the gas phase. The difference is explained quantitatively by considering adsorption as a replacement reaction. Four water molecules are assumed replaced by each ethylene molecule.

A positive standard entropy of adsorption is observed which is also consistent with the water displacement mechanism. Finally, the rate of adsorption is shown to be diffusion controlled. The equilibrium constant obtained from diffusion measurements is in excellent agreement with the one obtained from the isotherm.

Acknowledgments. Financial support for this work by United Aircraft Corporation (Pratt and Whitney Aircraft Division) under Contract No. 63-29 and by the U. S. Army Engineer Research and Development Laboratory under Contract No. DA44-009-AMC-469(7) is gratefully acknowledged. The authors also wish to thank Dr. A. K. N. Reddy for helpful discussion.

Electron Density Shifts during Chemical Bond Formation¹

by P. R. Smith and J. W. Richardson

Department of Chemistry, Purdue University, Lafayette, Indiana (Received March 23, 1966)

Indications of electronic charge density and the character of charge density relocations during bond formation may be obtained from the increasingly accurate molecular wave functions becoming available. A series of first-row diatomic molecules has been studied. Most had been computed using at least two approaches: (a) molecular orbitals (MO's) approximated by valence-shell, free-atom atomic orbitals only and (b) similar MO's, but with additional provision (of one sort or another) for orbital contraction or "clustering" in Ruedenberg's recent terminology. The following observations and conclusions are drawn as to what happens during a hypothetical experiment in which two atoms are placed, undisturbed, at their normal bond distance and *then* allowed to interact to form a molecule. (1) The major result of s-p hybridization alone is to move electron density out of the internuclear region into those regions identified with lone-pair electrons. (2) Electron density in the internuclear region is found to increase *only* as a result of the orbital contraction allowed in the better wave functions. No support for "bent bonding" in multiply bonded molecules like N₂ is found in these considerations. Since diatomic molecules are somewhat unique, only cautious generalizations to polyatomic molecules may be made at this time.

Introduction

The way in which electronic charge density is located in molecules has not received the attention it would seem to deserve. Although the nuclear geometry of most molecules is known, where the electrons are in the molecule is open to much debate. A knowledge of the total molecular charge density is of utmost importance if an accurate quantitative understanding of molecular events, including chemical reactions is to be gained. Even though accurate theoretical predictions of molecular properties for complex molecules will not be obtained for some time to come, many concepts which are useful in discussing their properties may be critically evaluated within the framework of small molecules.

Relocation of electronic charge density has always been presumed to be an important adjunct, if not cause, of chemical bond formation. The transfer of electron density into the internuclear region of the H₂ molecule is a long recognized phenomena even though the reasons for it are still the subject of considerable discussion.² With scant additional illustration, the same sort of phenomena has been assumed to occur in larger molecules. The present discussion considers that effect

in a series of second-row diatomic molecules, for which reasonably accurate molecular orbital (MO) wave functions have been computed. From these wave functions, and from those of the free atoms involved, it is possible to determine the redistribution of electronic charge predicted by each MO calculation. For several molecules, wave functions in successive degrees of refinement are considered.

It has long been held by most chemists that, in addition to "exchange" effects, a chemical bond forms as a result of electronic charge density flow out into the internuclear region where the potential energy is lower. Recently, Ruedenberg^{2a} has suggested that the main potential energy lowering occurs by a contraction or clustering of valence electron density about the nuclei. The concomitant and necessary (from the standpoint

(1) (a) From the thesis submitted by P. R. Smith to the Department of Chemistry, Purdue University, in partial fulfillment of the requirements for the Ph.D. degree. Supported by a contract with the Advanced Research Projects Administration. (b) Presented in part at the 145th National Meeting of the American Chemical Society, Division of Physical Chemistry, New York, N. Y., Sept. 8-13, 1963.

(2) See, for example, (a) K. Ruedenberg, *Rev. Mod. Phys.*, **34**, 326 (1962); (b) R. O. Miller and P. G. Lykos, *J. Chem. Phys.*, **37**, 993 (1962), and references cited therein.

of the virial theorem) increase in kinetic energy is partially offset by the effects of delocalization.

One may gain insight into the question of what happens when an atom unites with another atom to form a molecule by examining the changes which the electronic charge densities undergo in such a process as bond formation. To obtain a measure of this change one can construct a molecule which would result if the two atoms making up the molecule were united without perturbing each other. Clearly, this can be done by simply superposing the electronic charge densities of the constituent atoms.

One can then characterize a chemical bond by the function

$$\delta\rho(R) = \rho_M(R) - \rho_A(R)$$

where $\rho_M(R)$ is the total electronic charge density of the molecule, M, at some point in space, R ; $\rho_A(R)$ is the electronic charge density (at the same point) which would occur if the two constituent atoms were superposed at the molecular equilibrium distance. Thus, $\delta\rho(R)$ is positive in regions of the molecule where charge density has accumulated and negative where charge density has left. Because net charge is conserved, the integral of $\delta\rho(R)$ over all space is zero. This function has been computed for several molecules by Roux, Daudel, and co-workers,^{3a,b} and further by Rosenfeld,^{3c} for example, discussed abstractly by Ruedenberg, and considered more quantitatively in a study of N_2 by Richardson and Smith.^{3d}

The construction of a proper molecular wave function still provides a somewhat formidable problem and one which will remain for some time to come. At best, one is faced with using wave functions which have been constructed with the purpose of optimizing certain molecular parameters, such as the criterion of minimization of the total molecular energy in the SCF-LCAO-MO procedures, which may not be entirely appropriate for our needs. However, this is not to suggest that, in making use of such approximate functions, a reasonably accurate picture may not be obtained.

In this study two general types of computed wave functions are distinguished: (a) those in which free-atom atomic orbitals (AO's) are used and preserved in constructing the LCAO approximation and (b) improved functions tending toward the molecular Hartree-Fock limit, in which effects like clustering may be detected. The improvements may be merely altering the effective nuclear charges of the free-atom AO's or may be in using a larger set of functions in the LCAO approximation. An alternate way of describing these improved functions is that they include

hybridization of 3s, 3p, 3d, 4s, etc., with the valence-shell AO's.

Such improvements do make significant changes (usually for the better) in computed molecular properties. By no means, though, should these MO functions be regarded above suspicion. Nonetheless, it is felt that significant conclusions can be drawn from them.

Specifically, the following wave functions were used for the molecules discussed: for the N_2 molecule, the Scherr SCF-MO wave function,⁴ which uses a minimal set of Slater-type orbitals (STO's) with the free-atom orbital exponents (ζ 's) fixed by Slater's rules, and the "double- ζ " SCF-MO's of Richardson,⁵ in which the basis set was expanded by doubling the number of second quantum STO's included; for the CO molecule, Ransil's SCF-MO wave function,⁶ which uses a minimal set of STO's with fixed free atom ζ 's, and the improved SCF-MO wave function of Lefebvre-Brion, *et al.*,⁷ which uses an extended set of basis functions with fixed orbital exponents; for the CN^- molecule, an SCF-MO wave function which utilizes a minimal set of STO's, for which the ζ 's have been fixed by Slater's rule by considering the extra electron to be placed on the nitrogen nucleus, and a 2- ζ SCF-MO wave function of a similar type as that used by N_2 ⁸; for the BF molecule, only one wave function of type a which uses a minimal set of STO's with free-atom orbital exponents⁶; for the Li_2 molecule, Ransil's minimal SCF-MO wave function,⁶ and a 2- ζ SCF-MO wave function⁹ of the type used for N_2 and CN^- ; and for the LiF molecule, a type a function as determined by Ransil,⁶ and an improved SCF-MO wave function¹⁰ which uses an extended basis set of STO's for which the ζ 's have been optimized.

It should be remarked that, in evaluating $\delta\rho(R)$ for various improved molecular wave functions, there arises a necessity to adopt a convention for the construction of the superposed atomic density, $\rho_A(R)$. The convention adopted for this study was to use wave

(3) (a) M. Roux, M. Cornille, and L. Burnelle, *J. Chem. Phys.*, **37**, 933 (1962); (b) S. Bratoz, R. Daudel, M. Roux, and M. Allavena, *Rev. Mod. Phys.*, **32**, 412 (1960); (c) J. L. J. Rosenfeld, *Acta Chem. Scand.*, **18**, 1719 (1964); (d) J. W. Richardson and P. R. Smith, to be published.

(4) C. W. Scherr, *J. Chem. Phys.*, **23**, 569 (1955).

(5) J. W. Richardson, *ibid.*, **35**, 1829 (1961).

(6) B. J. Ransil, *Rev. Mod. Phys.*, **32**, 245 (1960).

(7) H. Lefebvre-Brion, C. Moser, and R. K. Nesbet, *J. Chem. Phys.*, **35**, 1702 (1961).

(8) We are indebted to Professor C. C. J. Roothaan and co-workers at the Laboratory of Molecular Structure and Spectra, The University of Chicago, for the use of their heteropolar SCF package in computing the wave functions for CN^- .

(9) J. W. Richardson, unpublished results.

(10) A. D. McLean, *J. Chem. Phys.*, **39**, 2653 (1963).

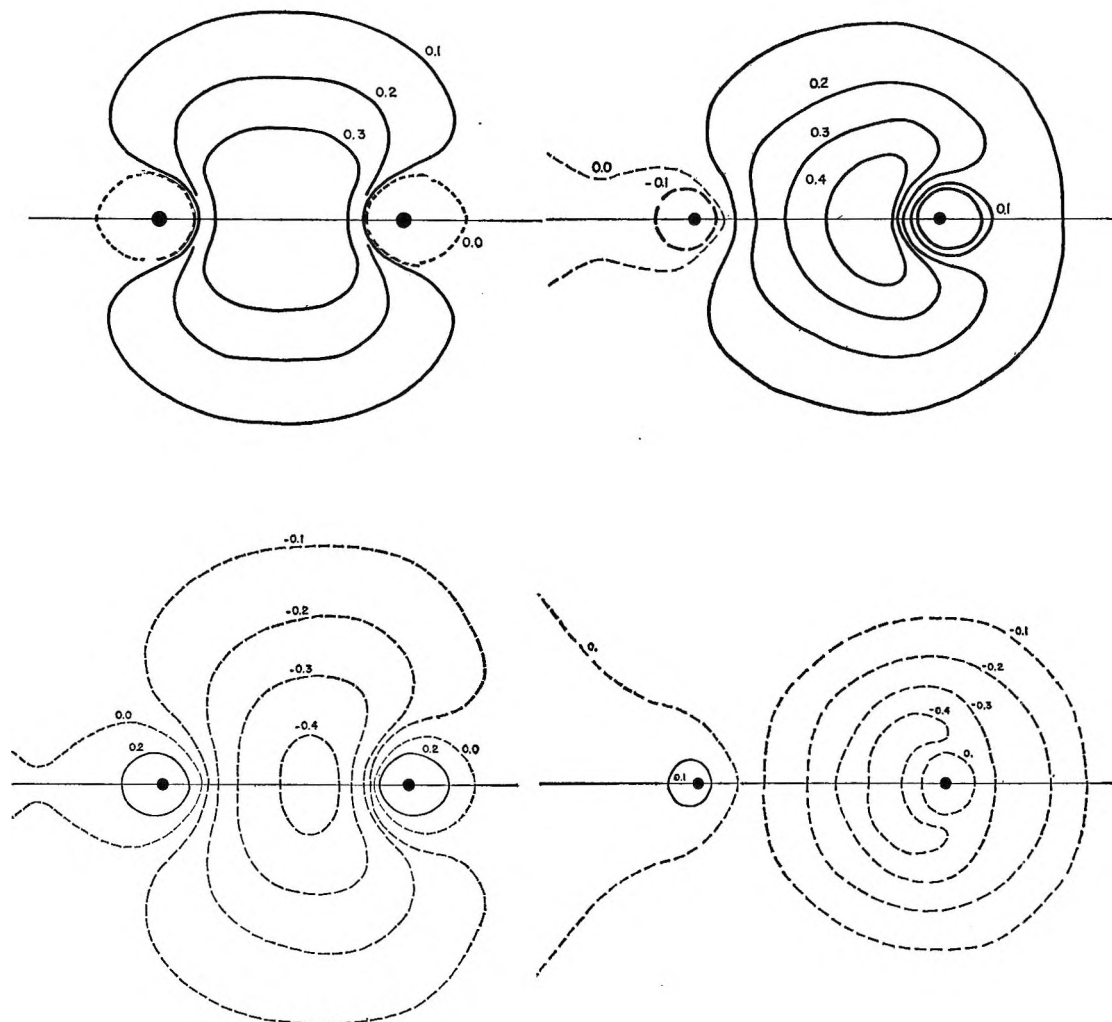


Figure 1. Contour diagrams of the $2\sigma_g(3\sigma)$ MO's of N_2 , CO, CN^- , and BF: upper left, $2\sigma_g$ MO of N_2 ; upper right, 3σ MO of CO; lower left, 3σ MO of CN^- ; lower right, 3σ MO of BF.

functions for the atoms with the same degree of improvement as the wave function used for the molecule. Thus, $\delta\rho(R)$ for type a functions is obtained by the densities of the atoms being constructed from free-atom AO's, and $\delta\rho(R)$ for type b functions uses atomic wave functions which approach the Hartree-Fock limit. While this convention is arbitrary, it does eliminate artificial discrepancies arising near the nuclei when different orbital exponents are used for the $1s$ AO's, also perhaps to a lesser extent, in regions far from the nucleus.

Both types of wave functions are considered for N_2 , CN^- , Li_2 , LiF , and CO. Some results from type a functions are presented for the BF molecule.

Method

The total molecular electronic charge density is equal to the diagonal of the first-order density matrix. For

a single determinantal wave function constructed from n doubly occupied MO's, the electron density per unit volume at the point R is

$$\rho = 2 \sum_{i=1}^n \rho_i(R) = 2 \sum_{i=1}^n |\varphi_i(R)|^2$$

where $\rho_i(R)$ is the volume density of the MO, $\varphi_i(R)$, which has the form

$$\varphi_i(R) = \sum_{j=1}^m \chi_j(R) C_{ji}$$

Here the $\chi_j(R)$ terms ($j = 1, 2, 3, \dots, m$) are non-orthogonal Slater-type orbitals (STO's) with appropriate orbital exponents, and the C_{ji} 's are linear variational coefficients.

The charge densities for the noninteracting constituent atoms were constructed by utilization of real

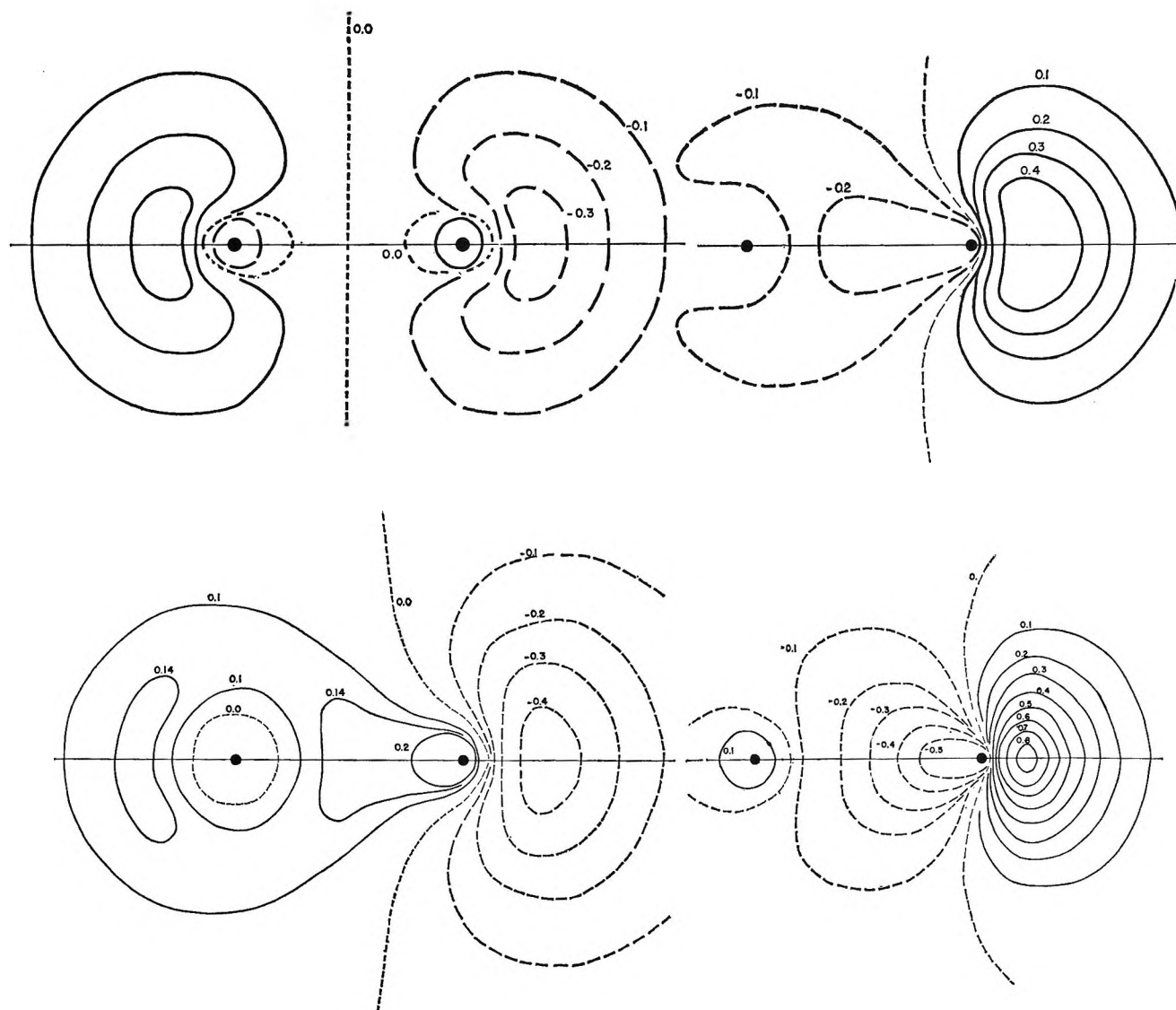


Figure 2. Contour diagrams of the $2\sigma_u(4\sigma)$ MO's of N_2 , CO, CN^- , and BF: upper left, $2\sigma_u$ MO of N_2 ; upper right, 4σ MO of CO; lower left, 4σ MO of CN^- ; lower right, 4σ MO of BF.

Slater atomic orbitals. In all cases the $2s$ STO was made orthogonal to the $1s$ AO by the equation

$$2s = \frac{1}{\sqrt{1 - S_{12}^2}} [2s^* - S_{12}(1s)]$$

where

$$S_{12} = \int (1s)(2s^*) dv$$

Since diatomic molecules possess a unique axis of cylindrical symmetry characteristic of their point group $C_{\infty v}$ or $D_{\infty h}$, the interesting two-dimensional projection of the three-dimensional wave function and charge density is the half-plane containing the internuclear axis, in this case the $x-z$ plane. In this case,

z was taken as the axis directed along the internuclear axis with the positive sense being taken from each nucleus toward the center of the σ -bond.

For molecules discussed below, the wave function, molecular charge densities, and difference densities were evaluated at a series of points over a range of $3R$ (R here represents the equilibrium internuclear distance) along the z axis. In all cases considered, this range was adequate for the contours of useful interest. The increments along the x and z axes were variable, but generally it was found that intervals of $0.1R$ provided a fine enough grid, except in regions near the nuclei. To gain uniformity for purposes of comparison, the computed grid was the same for each molecule.¹¹

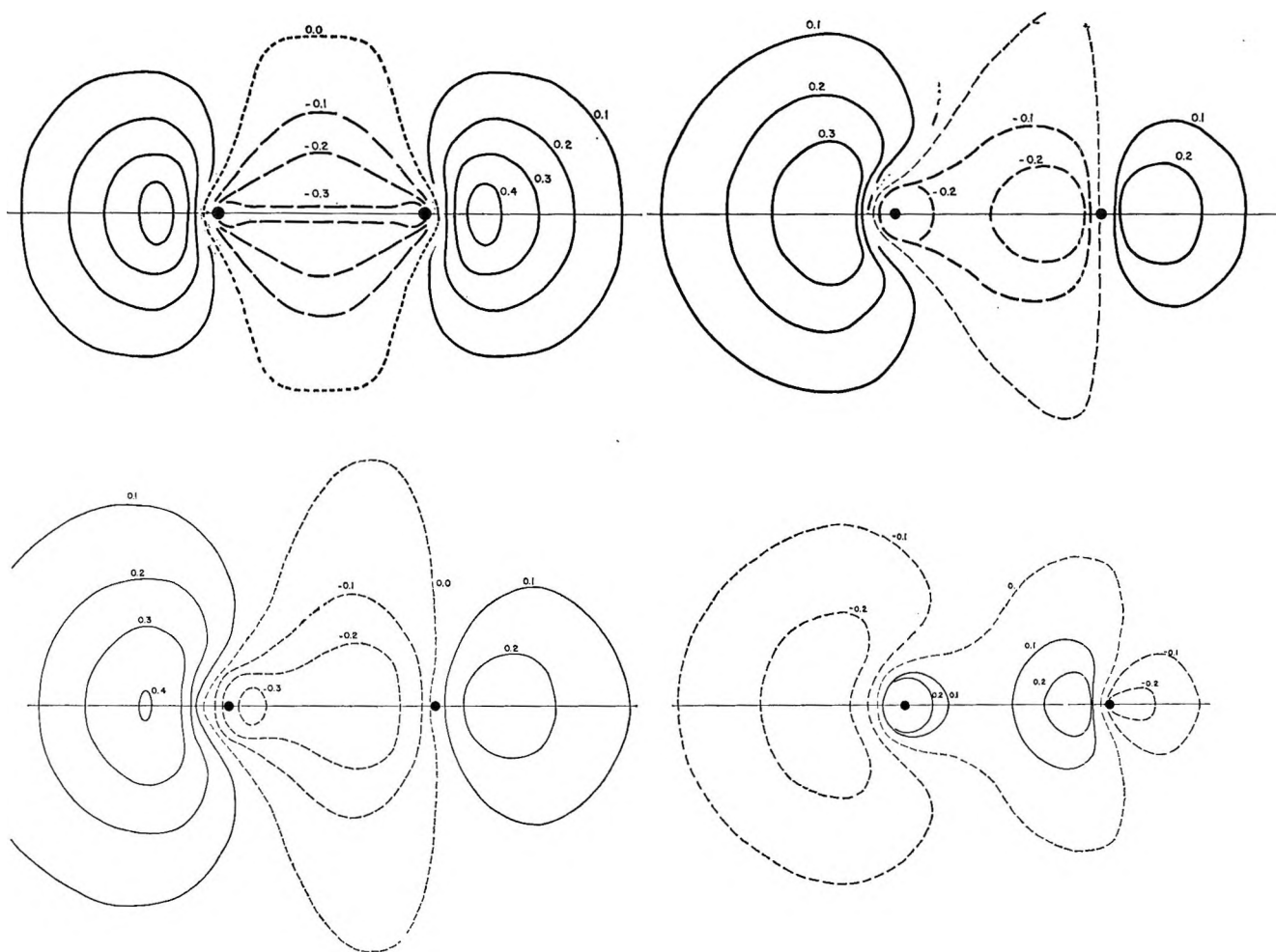


Figure 3. Contour diagrams of the $3\sigma_g(5\sigma)$ MO's of N_2 , CO, CN^- , and BF: upper left, $3\sigma_g$ MO of N_2 ; upper right, 5σ MO of CO; lower left, 5σ MO of CN^- ; lower right, 5σ MO of BF.

Comparisons of the Shapes of the MO's

Comparisons of the two-dimensional contour diagrams of the three-dimensional occupied MO's for the isoelectromers N_2 , CO, CN^- , and BF are presented in Figures 1-4. Since the inner-shell MO's, 1σ and 2σ MO's in the heteropolar cases and $1\sigma_g$ and $1\sigma_u$ MO's in the homopolar cases, are not significantly different from free-atom $1s$ AO's, contour drawings of only the valence-shell MO's are presented. It should be mentioned that, although the character of the $\delta\rho(R)$ function, for any given molecule, is seen to vary considerably with improvement of the approximate wave functions (see discussion below), only minor variations occur in the shapes of the MO's as the basis set is improved.

The often discussed relationship of the MO's to united-atom AO's is most clearly evident from these contour diagrams. Except for minor details it is seen that $3\sigma(2\sigma_g)$ correlates with $2s$. This is especially

noticeable in the heteropolar cases CO and BF which are essentially $2s_O$ and $2s_F$ in character. The $5\sigma(3\sigma_g)$ correlates with $3d\sigma$; and $1\pi(1\pi_u)$ with $2p\pi$. Here again, for the heteropolar BF molecule it is seen that the 1π MO resembles an almost undistorted $2p\pi$ AO centered on the fluorine center. Because of its similarities to the $1\pi(1\pi_u)$, the $4\sigma(2\sigma_u)$ would seem to correlate with $2p\sigma$ (this is especially noticeable in the homopolar N_2). However, this is the property of $2\sigma(1\sigma_u)$, with $4\sigma(2\sigma_g)$ passing into $3p\sigma$.

From these drawings it appears that one might attach significance to these MO's and re-establish a description of how the electrons are situated in these molecules. Thus, for the case of N_2 , the $2\sigma_g$ could be described as a "buried" pair of electrons¹² which represent the majority

(11) All calculations of wave functions, charge densities, and difference functions, upon which the figures are based, were computed from a Fortran program written for the Purdue University IBM 7090.

(12) I. Langmuir, *J. Am. Chem. Soc.*, **41**, 868 (1919).

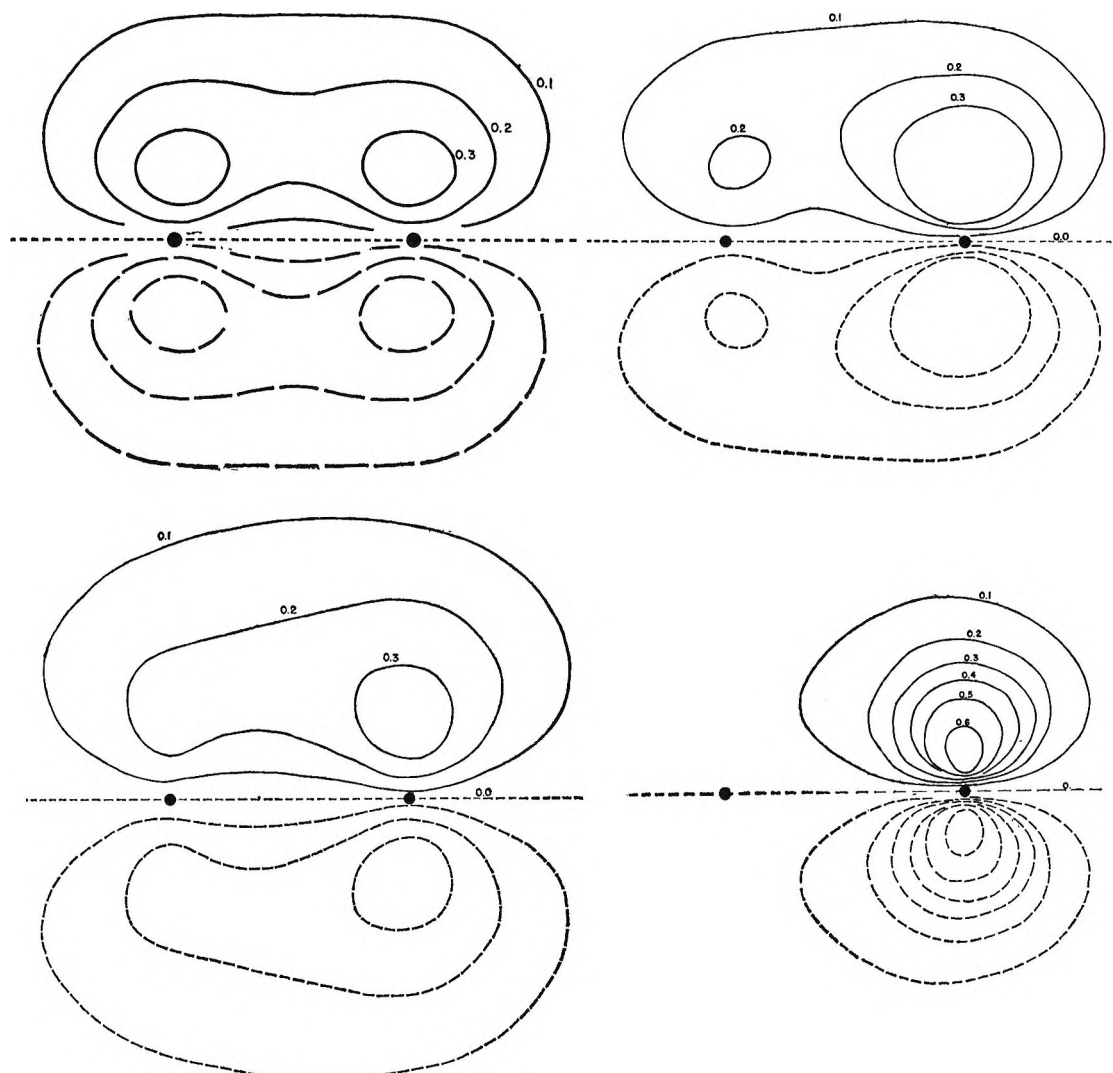


Figure 4. Contour diagrams of the $1\pi_u(1\pi)$ MO's of N_2 , CO, CN^- , and BF: upper left, $1\pi_u$ MO of N_2 ; upper right, 1π MO of CO; lower left, 1π MO of CN^- ; lower right, 1π MO of BF.

of the σ -bonding in the molecule. In a similar fashion, the $2\sigma_u$ and $3\sigma_g$ each contribute half of the nonbonding lone-pair electrons, with $1\pi_u$ describing the π -bonding. It is more difficult to attach significance to the individual MO's of the heteropolar cases, but what appears is a general loss in π -bonding as the 1π MO becomes polarized toward the more electronegative centers. There is still evidence of what could be called the lone-pair electrons even though the character of the 4σ and 5σ MO's is seen to change somewhat.

Comparison of the shape of the MO's with the results of corresponding population analyses¹³ is extremely interesting. Thus, for example, one finds that the overall shapes of the MO's in N_2 in passing from the type a function of the type b function remain virtually unchanged. While there exists a uniformity in the MO's

of the two wave functions the overlap populations change quite radically. For the $2\sigma_u$ MO in N_2 there is a drastic change in the overlap population from a reasonable -0.37 to the disastrous -2.05 , for the Scherr and $2-\zeta$ approximations, respectively. This very negative value for the $2-\zeta$ approximation causes even the *total* overlap population to become negative.

A few words of caution are pertinent at this point. First, yet to be clearly established is the extent to which these observations may be extended to polyatomic molecules. Second, it is not clearly established that a one-electron picture of a molecule (upon which this paper is based) is sufficiently accurate to describe adequately the phenomenon of chemical binding. The

(13) R. S. Mulliken, *J. Chem. Phys.*, **23**, 1833 (1955).

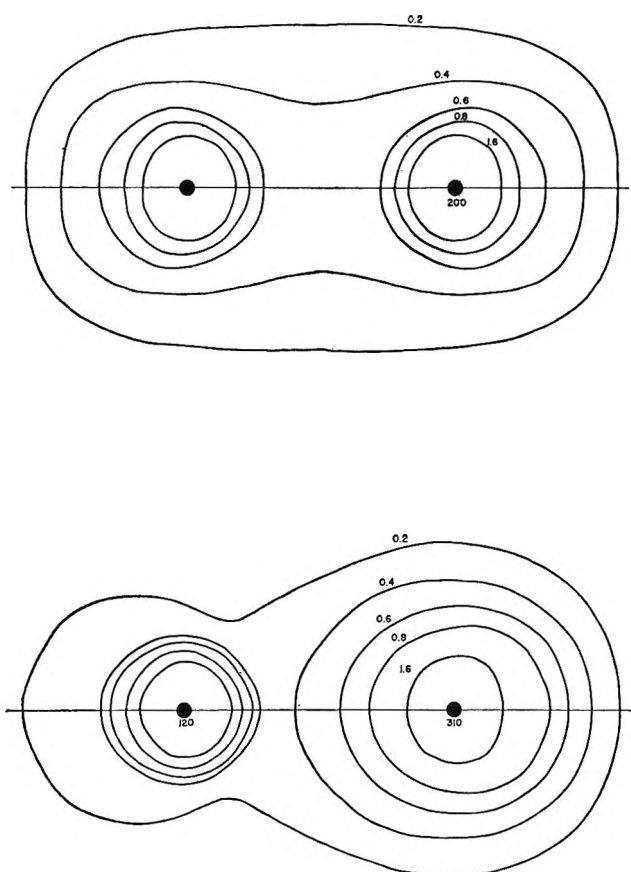


Figure 5. The two-dimensional cross section of the total electronic charge density of N_2 and CO. The numbers correspond to the density in electrons per cubic atomic unit: upper, $\rho_M(R)$ for N_2 ; lower, $\rho_M(R)$ for CO.

picture given here is about the best generally available now; furthermore, large changes would be necessary to alter many of the effects observed. Thus, it is doubtful that inclusion of electron correlation into the wave functions would alter the character of $\delta\rho(R)$ obtained from the more flexible wave functions of type b.

Molecular Charge Distributions

The three-dimensional total molecular charge densities in a plane passing through the internuclear axis are given in Figures 5 and 6 for N_2 , CO, CN^- , BF, and LiF. It will be noticed that these functions are very smooth despite the occurrence of nodes in each of the occupied MO's. In each of the molecules the contours of high density nearest the nuclei are nearly concentric circles. This is to be expected since in this region the dominant contributors to the total density are the inner-shell MO's which resemble the free-atom 1s AO's. It is evident that the N_2 contours take on an oval appearance as the density decreases while the CO and

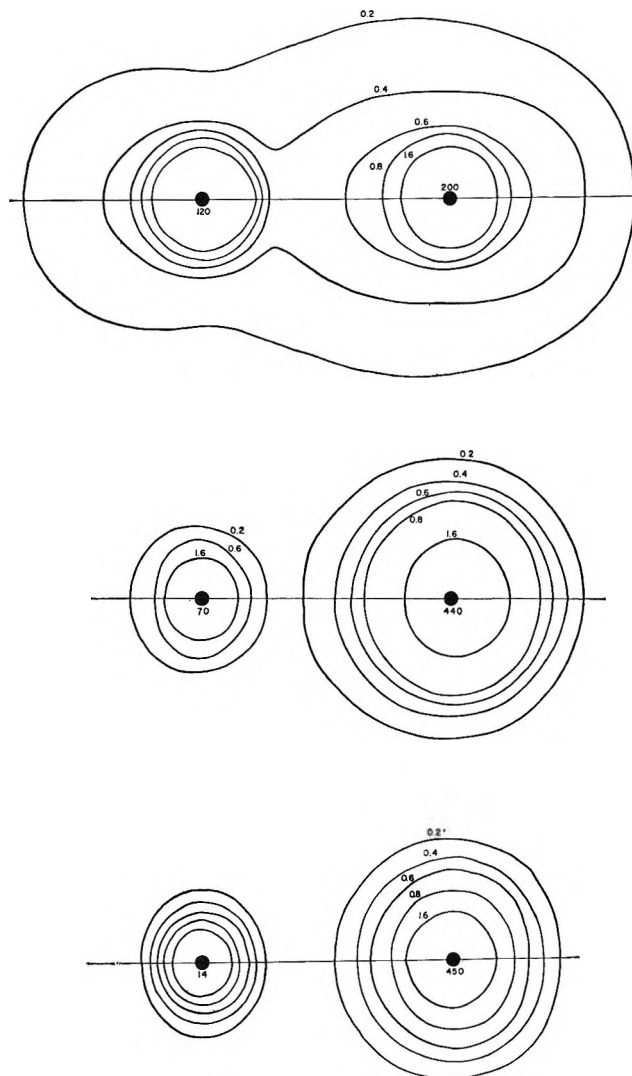


Figure 6. The two-dimensional cross section of the total electronic charge density of CN^- , BF, and LiF. The numbers correspond to the density in electrons per cubic atomic unit: upper, $\rho_M(R)$ for CN^- ; middle, $\rho_M(R)$ for BF; lower, $\rho_M(R)$ for LiF.

CN^- contours resemble an ellipsoid with a pileup of electron density near the heavier, more electronegative centers, O and N, respectively. The character of the functions for BF and LiF is evident from considerations of the differences in the nuclear charge of the lighter boron and lithium with that of the fluorine.

It is pertinent to point out that total molecular charge densities computed from wave functions with varying degrees of sophistication consistently display contour maps which are virtually indistinguishable. This similarity, however, is superficial; indeed, striking variations are observed when one characterizes these charge densities with the function, $\delta\rho(R)$.

Density Difference Maps

In the discussion that follows, the density difference function, $\delta\rho(R)$, is compared for the isoelectronic series N_2 , CO, CN^- , and BF for both types a and b SCF-MO wave functions. Additional $\delta\rho(R)$ contour drawings are presented for the molecules Li_2 and LiF.

The N_2 Molecule. As will be noted in Figure 7 there is an increase in charge density at the ends of the molecule. N_2 possesses nonbonding electrons, and this behavior is due to the s - $p\sigma$ hybridization moving lone-pair electrons away from the bonding electrons. The improved type b wave function for N_2 shows the results of a more flexible wave function accommodating orbital contraction which serves to move charge into the region between the nuclei and restore the usual chemical picture. It is pertinent to point out here that, in consideration of successive improvements to the N_2 wave function which approach the molecular Hartree-Fock limit, this character is always observed; indeed, the charge density buildup between the nuclei is seen to increase even more.^{3c}

The CO Molecule. CO has the ground-state electronic configuration

$$1\sigma^2 2\sigma^2 3\sigma^2 4\sigma^2 1\pi^4 5\sigma^2$$

Wave functions of types a and b were considered for the study of this system. A question arises in defining $\delta\rho(R)$ in this case; neither the free carbon atom nor the free oxygen atom possesses a spherically symmetric atomic electronic density, and, hence, some ambiguity is introduced in the construction of $\rho_A(R)$. Although various definitions were employed for the construction of $\rho_A(R)$, the essential character of $\delta\rho(R)$ remained unchanged. For the purposes of the discussion presented here, $\rho_A(R)$ will be defined such that the 2p electrons are averaged over all orientations in space, thus reintroducing spherical symmetry to the atoms. One then finds for the carbon atom density

$$\rho_{\text{carbon}} = 2(1s)^2 + 2(2s)^2 + 2(\bar{p}_{2pC})$$

where

$$\bar{p}_{2p} = \frac{\zeta^5}{3\pi} r^2 e^{-2\zeta r}$$

and for the oxygen atom density

$$\rho_{\text{oxygen}} = 2(1s)^2 + 2(2s)^2 + 4(\bar{p}_{2pO})$$

with

$$\rho_A(R) = \rho_{\text{carbon}}(R) + \rho_{\text{oxygen}}(R)$$

The difference function $\delta\rho(R)$, computed for wave functions of types a and b, are given in Figure 8. The most conspicuous feature of these plots is that for

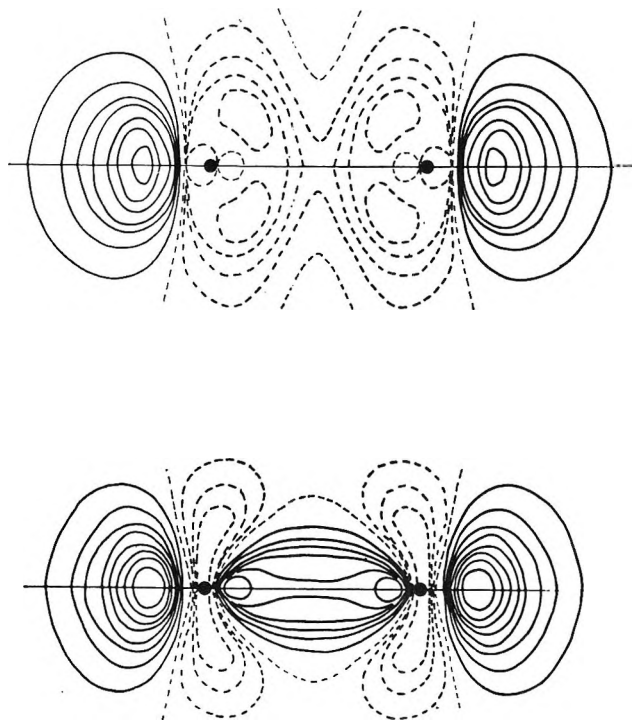


Figure 7. The two-dimensional cross section of the difference density function, $\delta\rho(R)$, for type a and b approximations for N_2 . The lightly dashed line is the zero contour; solid lines are positive, and heavy dashed lines are negative contours. Contours are drawn at intervals of 0.02 electron/cubic atomic unit: upper, $\delta\rho(R)$ for N_2 using the Scherr approximation; lower, $\delta\rho(R)$ for N_2 using 2- ζ approximation.

both approximations to the wave function there is exhibited an increase in charge density at the ends of the molecule. For a molecule such as CO, which possesses nonbonding valence-shell electrons, this behavior can be ascribed to s - $p\sigma$ hybridization moving lone-pair electrons away from the bonding electrons. It will be noted that in the type a wave function there is a noticeable decrease in charge density in the inter-nuclear region while for the type b wave function there is substantial increase of charge density between the nuclei. This change in character of $\delta\rho(R)$ in passing to type b functions can be easily explained if one realizes that in the type a function the use of free-atom orbitals has resulted in an inflexible wave function which is incapable of allowing for adequate promotion of the atoms into their valence state. It will also be noted that for both approximations to the wave functions there is a decrease in density in the immediate vicinity of the nuclei. While it is true that the approximate wave functions used in this study exhibit their poorest behavior in these regions, the behavior that is revealed is a decrease in 2s electron density as a result of 2s

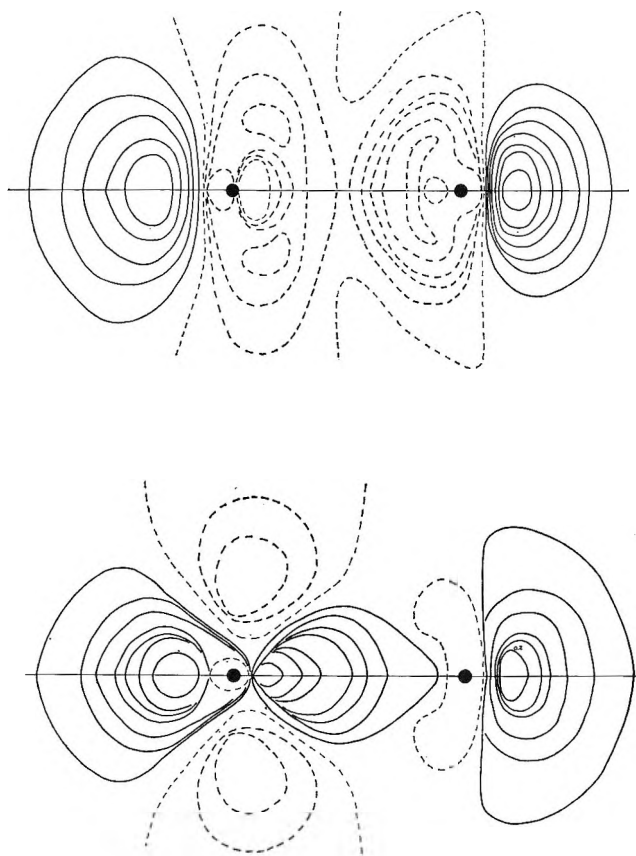


Figure 8. The two-dimensional cross section of the difference density function, $\delta\rho(R)$, for type a and b approximations for CO. The lightly dashed line is the zero contour; solid lines are positive, and heavy dashed lines are negative contours. Contours are drawn at intervals of 0.02 electron/cubic atomic unit, unless otherwise indicated: upper, $\delta\rho(R)$ for CO using type a approximation (see text); lower, $\delta\rho(R)$ for CO using type b approximation (see text).

promotion to $2p\sigma$ character. In addition, clustering serves to move charge into the internuclear region by orbital contraction of the second-quantum AO's which have their maxima in regions other than those at the nuclei.

The CN⁻ Molecule Ion. The ground-state electronic configuration for CN⁻ is

$$1\sigma^2 2\sigma^2 3\sigma^2 4\sigma^2 1\pi^4 5\sigma^2$$

Two distinct wave functions of type a were considered for this molecule ion: one in which the free-atom orbital exponents are determined by assigning the negative charge in the ion to the carbon nucleus and the second in which the negative charge is assigned to the nitrogen nucleus and the free-atom orbital exponents determined. The improved type b wave function used for this molecule consisted of seven STO's centered on each of the nuclei. This basis set was the 2- ζ type

in which the 1s ζ 's were assigned the best-atom values,¹⁴ and the doubled valence-shell STO ζ 's were assigned the value $\pm 25\%$ of the best-atom value.

Both wave functions of type a were examined and only very minor differences observed in the individual MO contours and total charge densities. For the purpose of this discussion we have selected the type a function obtained by placing the negative charge at the nitrogen nucleus.

As in CO, the construction of $\rho_A(R)$ for CN⁻ is somewhat arbitrary. Here again, the 2p electrons of the carbon were averaged over all orientations in space. In addition, the "extra electron" was divided equally between the carbon and nitrogen nuclei giving

$$\rho_{\text{carbon}} = 2(1s)^2 + 2(2s)^2 + (5/2)\bar{p}_{2pC}$$

and

$$\rho_{\text{nitrogen}} = 2(1s)^2 + 2(2s)^2 + (7/2)\bar{p}_{2pN}$$

Presented in Figure 9 are plots for $\delta\rho(R)$ using types a and b functions. The dominant effect in the type a function is the pileup of charge at the ends of the molecule and the decrease in charge between the nuclei. This, as in the case of CO and N₂, is clearly the effect of the displacement of the non- (and anti-) bonding electrons away from the bond side of the atom. By way of emphasis, if the atomic densities of C⁻ and N⁰, of C⁰ and N⁻, or even of C⁰ and N⁰ are subtracted from type a CN⁻ (giving, in this last case one might say, the distribution of the excess negative charge in the ion), there is still, in all three cases, a region of electron deficiency found between the nuclei. In passing to a higher level of approximation, in which clustering by one means or another is allowed for, it is evident that density has moved into the internuclear region *via* orbital contraction. Note that this effect is also observed in N₂ and CO and is due to the contraction of the second-quantum AO's which have their maxima in regions out from the nuclei.

The BF Molecule. As will be noted in Figure 10, the $\delta\rho(R)$ plot follows the same pattern as the previously discussed molecules. For the type a function for BF there remains the charge relocation resulting in an increase at the ends of the molecule and a decrease in density in the internuclear region. The deficiency of charge density in regions near the nuclei still persists. Here again, what is observed is the effect of s-p σ hybridization moving the nonbonding electrons away and apart from the bonding electrons. Unfortunately, for BF, an improved wave function

(14) C. C. J. Roothaan, Laboratory of Molecule Structure and Spectra, University of Chicago, Technical Report, 1955, p. 24.

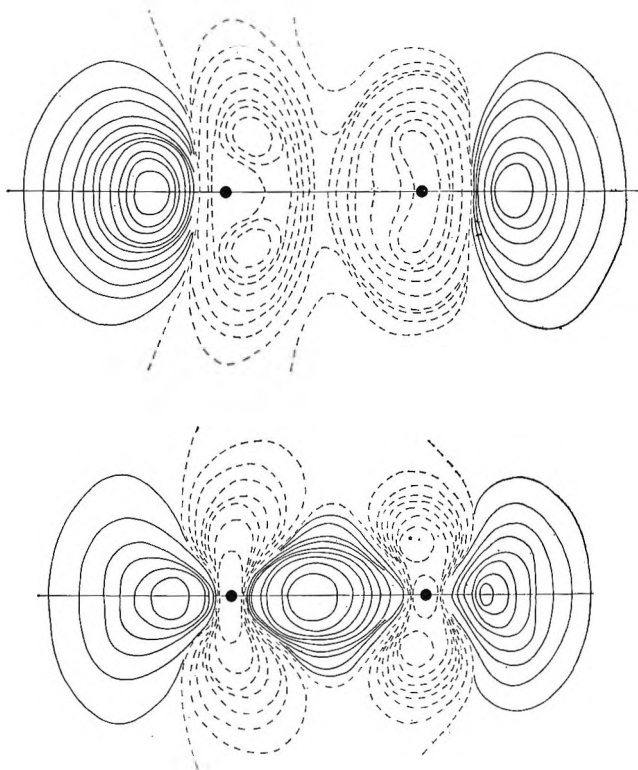


Figure 9. The two-dimensional cross section of the difference density function, $\delta\rho(R)$, for type a and b approximations for CN^- . The lightly dashed line is the zero contour; solid lines are positive, and heavy dashed lines are negative contours. Contours are drawn at intervals of 0.02 electron/cubic atomic unit: upper, $\delta\rho(R)$ for CN^- using type a approximation (see text); lower, $\delta\rho(R)$ for CN^- using type b approximation (see text).

of type b was not available at the time this work was completed; however, we have no doubt that a similar trend would be observed if a more flexible wave function was used.

The Li_2 and LiF Molecules. The ground-state electronic configuration for Li_2 is

$$1\sigma_g^2 1\sigma_u^2 2\sigma_g^2$$

The $\delta\rho(R)$ plots for type a and b approximations were in this instance nearly identical. As is seen in Figure 10, the function, $\delta\rho(R)$, for the type a function for Li_2 lacks one essential feature that the previous plots of $\delta\rho(R)$ possessed, namely, an accumulation of charge density at the ends of the molecule. Clearly, this is attributable to the lack of valence-shell non- (anti-) bonding electrons in the Li_2 molecule. Still observed, however, is the increase in charge density in the internuclear region accompanied by a decrease in density in the immediate vicinity of the nuclei. At the level of approximation of type a wave functions, only 2s-

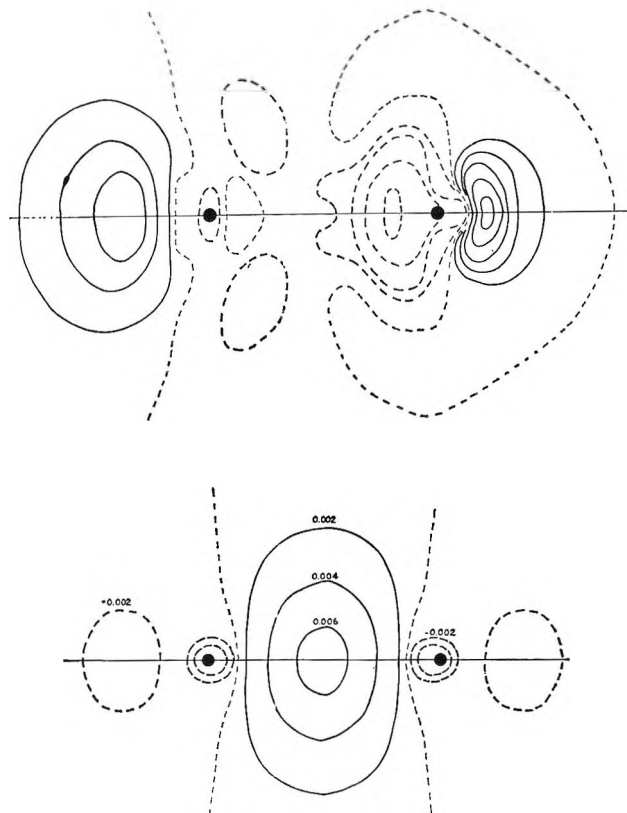


Figure 10. The two-dimensional cross section of the difference density function, $\delta\rho(R)$, for BF and Li_2 . The lightly dashed lines are the zero contours; solid lines are positive, and the heavy dashed lines are negative contours. Contours are drawn at intervals of 0.02 electron/cubic atomic unit, unless otherwise indicated: upper, $\delta\rho(R)$ for BF using type a approximation; lower, $\delta\rho(R)$ for Li_2 using type b approximation.

$2p\sigma$ hybridization is allowed for, but, even so, promotion of s to $p\sigma$ character moves more charge into this region than the other atom brings up and contributes to ρ_A . There is observed an even greater buildup of charge density in the internuclear region when the wave function is improved, accompanied by the loss of density at the ends of the molecule.

LiF has the ground-state electronic configuration

$$1\sigma^2 2\sigma^2 3\sigma^2 4\sigma^2 1\pi^4$$

The character of the $\delta\rho(R)$ function in this instance is quite different than those which have been considered previously. Figure 11 presents $\delta\rho(R)$ plots for LiF in which the atomic densities have been constructed, first by an averaging of the fluorine 2p electrons as described before and second by superposition of the densities of the Li^+ and F^- ions. Consistent in both diagrams is the decrease in density at the nuclei and an increase in density near the lithium nucleus.

The picture obtained for the ionic situation is compatible with the accepted chemical picture of such a process; namely, the negative fluorine atom has given up electron density which moves into the internuclear region, in this instance nearer the lithium atom. It should be noted that the positive regions of $\delta\rho(R)$ are quite diffuse, thus explaining the absence of any positive contours on the diagram. When the neutral atoms are referred to, what is observed is the movement of the antibonding valence electrons away and apart from the bonding electrons, resulting in an increase in electronic charge density at the extremities of the molecule though mostly, of course, at the fluorine end. Orbital contraction and *s* promotion to *p* σ character are especially noticeable in the vicinity of the fluorine nucleus. This is evidenced by the accumulation of density in the bond region near the fluorine nucleus and at the extremities of the molecule in the region of the fluorine nucleus. There is also an apparent deficiency of π_F density, as if it has been displaced nearer to the lithium nucleus.

Conclusions and Remarks

The most prominent feature, displayed by all the molecules possessing nonbonding valence-shell electrons, is the increase in charge density at the ends of the molecule. This behavior cannot be inferred, of course, from H_2 but is quite reasonable from other considerations. At distances up to 1 Å. beyond the nuclei there may be increases of as much as 15–20% in the electron density. Clearly, as Mulliken has earlier suggested, an important function of *s*–*p* σ hybridization is to move lone-pair electrons apart and away from the bonding electrons. These increases are most pronounced where the most hybridization is expected, namely, in N_2 and at the carbon atoms of CO and CN^- .

Most striking among the observations made from type a LCAO wave functions (*i.e.*, with free-atom AO's) is that $\delta\rho(R)$ is generally found to be *negative* between the nuclei. In other words, at this level of approximation wherein only *2s*–*2p* σ hybridization is allowed, the charge density on the bond side of an atom is increased by less than that brought up by the other atom. The dominant effect here is the displacement of non-(anti-) bonding electrons from the bond side of the atom. It is worth mentioning that, although there is computed a net *decrease* in the internuclear charge density, in all cases the Mulliken total overlap population¹⁵ is positive.

However, in passing to the type b calculation, where clustering by one means or another is allowed for, the internuclear situation is rather different. Now $\delta\rho(R)$

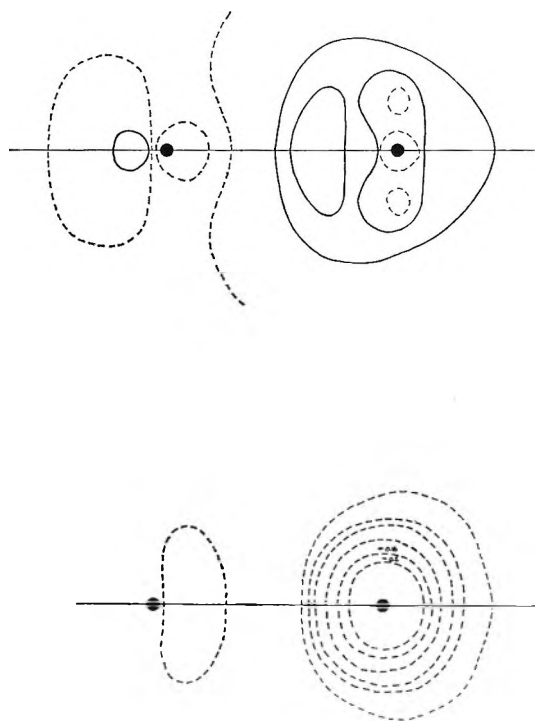


Figure 11. The two-dimensional cross section of the difference density function, $\delta\rho(R)$, for LiF using type b approximations. The lightly dashed lines are zero contours; solid lines are positive, and heavy dashed lines are negative contours. Contours are drawn at intervals of 0.02 electron/cubic atomic unit, unless otherwise indicated: upper, $\delta\rho(R)$ for LiF using type b approximation, constructed by using atomic densities (see text for discussion); lower, $\delta\rho(R)$ for LiF using type b approximation, constructed by using "ionic" densities (see text for discussion).

is quite positive between the nuclei (and becomes even more positive in the lone-pair regions). The annular triple bond in N_2 from a type a wave function is no longer seen.

In the immediate vicinity of the nuclei in the molecules there is observed in all cases a *decrease* in density. It is certainly true that the approximate wave functions were not designed to reveal changes in these regions. However, in addition, despite "clustering," *2s* electron density is decreased through promotion to *2p* σ character. It would appear that, in addition to lone-pair rearrangements *via* *2s*–*2p* σ hybridization, the clustering, or orbital contraction, actually serves to bring the charge into the bond region and restores the usual chemical picture.

Acknowledgments. The authors wish to express their gratitude to Professor C. C. J. Roothaan and

(15) R. S. Mulliken, *J. Chem. Phys.*, **23**, 1833 (1955).

members of his research group for the use of their heteropolar SCF computer package in obtaining

the CN^- wave functions. Mr. M. Putt is also thanked for his assistance with the drawings.

On the Nature of Valence-Shell Molecular Orbitals¹

by Dean W. Robinson

Department of Chemistry, The Johns Hopkins University, Baltimore, Maryland 21218
(Received March 26, 1965)

Most probable assignments of the known electronic states of the diatomic molecules of the Li-Ne period have been reviewed, previous assignments being used where possible, and used to construct simple quantitative diagrams representing orbital energies below ionization. Considerable regularity is apparent in orbital heights of similar molecules and several unknown ionization potentials and orbital energies may be predicted by interpolation from these charts. Assignment of measured bond distances to configurations permits assessment of relative bonding power of the valence shell orbitals as a function of bond polarity.

Introduction

As electronic states of diatomic molecules have been discovered and reviewed, attempts have usually been made, where possible, to understand their origins in terms of molecular orbital electron configurations. The most completely understood molecule is nitrogen for which Mulliken has published a comprehensive table of known and predicted states with their assignments.^{2a} Of no other molecules have the spectra been as completely studied and definitive assignments made. However, Mulliken's early papers^{2b-d} on this subject established a foundation for the understanding of spectra of most of the diatomic molecules containing elements from the lithium row of the periodic chart. Since that time, many new states and new molecules have been discovered, but there does not seem to have been an attempt to survey a set of similar molecules and correlate empirically but quantitatively the properties of their electronic states in terms of regularly varying properties of the intravalence shell molecular orbitals. The pointing out of regularities can on the one hand enhance understanding of the energy and bonding effects of these orbitals in isoelectronic se-

quences and other such sets, and on the other hand aid in the assignment of currently unassigned states and states yet to be found.

Although serious voids exist in the knowledge of the spectra of many molecules, it is shown in this paper that a rather surprising degree of regularity can be found, at least when lithium-neon period diatomic molecules and ions are examined.

Neutral Molecules Differing by One Nuclear Charge Unit. In Figure 1 are shown neutral molecules from B_2 through F_2 differing by one unit of nuclear charge. The top of the chart represents an ionized state. Wherever possible, horizontal lines are placed at distances below the ionized state proportional to the energy necessary to ionize from the orbital labeling the line. The figure differs from Mulliken's^{2d} Figures 43 and 44 in that it is simplified by omission of any r -dependence which, over the relatively small range of

(1) Supported by the National Science Foundation.

(2) (a) R. S. Mulliken, Proceedings of the Conference on Aeronomy, Cambridge, Mass., June 1956, Pergamon Press, Ltd., London, 1957, p. 169; (b) R. S. Mulliken, *Rev. Mod. Phys.*, 2, 60 (1930); (c) *ibid.*, 3, 89 (1931); (d) *ibid.*, 4, 1 (1932).

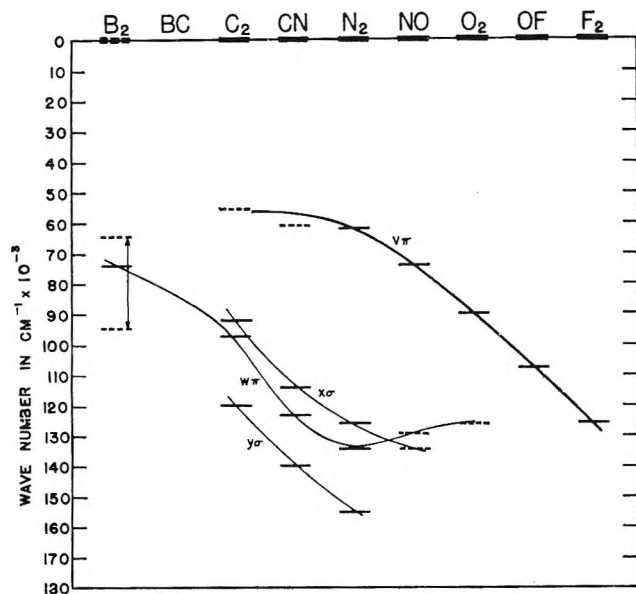


Figure 1. Variation of the difference between ionization and orbital energies with nuclear charge. Heavy lines under formulas indicate known or well-estimated ionization potentials. Horizontal lines at various heights give the orbital energies below ionization. Dotted lines denote uncertainty of probably more than ± 3000 cm^{-1} . Vertical tie lines denote knowledge of orbital separation but complete ambiguity regarding energy below ionization.

r encompassed, is absorbed in the smooth curves connecting the orbital energies. The diagram is, as are all observations in this paper, strictly determined from experiment, and its value, if any, lies only in providing interpolative facility and physical acquaintanceship.

The means of estimating the energy heights shown in Figure 1 are described briefly in this section. As will be seen, much of the interpretation is not new. As the molecule C_2 is very well understood, as discussed by Ballik and Ramsay,³ it provides a convenient place to start. The lowest ionization potential is at $96,800 \text{ cm}^{-1}$.⁴ Using the Mulliken notation for the L-shell molecular orbitals, the ground-state configuration is $\text{KK}(z\sigma_g)^2(y\sigma_u)^2(w\pi_u)^4$. Ionization must then be from the $w\pi$ -orbital, fixing its position at $96,800 \text{ cm}^{-1}$ below the limit. Referring again to Ballik and Ramsay,³ it is seen that the center of the configuration $(y\sigma_u)^2(w\pi_u)^3(x\sigma_g)$ lies near 4600 cm^{-1} above $(y\sigma_u)^2(w\pi_u)^4$; thus the height of $x\sigma_g$ is 4600 cm^{-1} above $w\pi_u$ and is so placed in Figure 1. The position of $y\sigma_u$ is fixed from the average of the states $d^1 \Sigma_u^+$ and $A''^3 \Sigma_u^+$ of the configuration $(y\sigma)(w\pi)^4(x\sigma)$ which is at about $28,000 \text{ cm}^{-1}$. The orbital $y\sigma_u$ must be about this far below $x\sigma$. These latter two numbers are consistent with Mulliken's estimates⁵ of 0 and 3 e.v., respectively.

As a test of the justification for estimating orbital energies to this precision, the center of gravity of the configuration $(y\sigma)(w\pi)^3(x\sigma)^2$ is provided. The sum of 4600 and 28,000 is $32,600 \text{ cm}^{-1}$, to be compared with $31,300 \text{ cm}^{-1}$ from experiment.

The relative position of $v\pi$ cannot be found with certainty. One of the ten states arising from the configuration $(y\sigma)^2(w\pi)^2(x\sigma)(v\pi)$ is probably $B^3 \Pi_g$.³ This is perhaps a few thousand wave numbers below the center of gravity of this configuration which would place $v\pi$ somewhere near $42,000 \text{ cm}^{-1}$ above $w\pi$. This uncertainty is shown in Figure 1.

The fact that state $e^1 \Sigma_g^+$ combines with $(y\sigma_u)^2(w\pi_u)^3(x\sigma_g)$, $b^1 \Pi_u$ ⁶ suggests various configurations using $v\pi$ and $u\sigma$ differing from this by a one-electron transition. None of these is consistent with Σ_g^+ symmetry and a smaller bond distance than $b^1 \Pi_u$. Either this is a Rydberg state, unlikely considering the bond length, or it is the one member of the configuration $(z\sigma)^2(w\pi)^4(x\sigma)^2$ which from Figure 1 would be expected at $52,000 \text{ cm}^{-1}$, but is observed at $55,000 \text{ cm}^{-1}$. The latter is almost certainly the correct assignment.

Nitrogen is next considered; it is easy to deduce the relative orbital heights from Mulliken's complete assignment.^{2a} These are put into Figure 1 relative to $x\sigma$ from which the first electron ionizes at $125,700 \text{ cm}^{-1}$.⁴ The $x\sigma-v\pi$ separation of $64,100 \text{ cm}^{-1}$ is derived from the average height of $(y\sigma)^2(w\pi)^4(x\sigma)-(v\pi)$, $B^3 \Pi_g$ and $a^1 \Pi_g$, above $(y\sigma)^2(w\pi)^4(x\sigma)^2$, $X^1 \Sigma_g^+$. The $w\pi-v\pi$ separation was estimated from the center of gravity of the six states of the configuration $(y\sigma)^2(w\pi)^3(x\sigma)^2(v\pi)$, two of which were estimated by Mulliken^{2a} and three more involving uncertainty in assignment or position.^{2a} The approximate result is $72,000 \text{ cm}^{-1}$ which yields a separation of $x\sigma-w\pi$ of 8000 cm^{-1} . Ignoring the uncertainty in this number and the fact that Rydberg series limits should give orbital separations of the resulting ions rather than molecules, whose bond distances and electron correlation effects are different, comparison of the Worley's⁷ and Worley-Jenkins'⁸ Rydberg series limits should lead to a value for the $x\sigma-w\pi$ separation. The result is 9000 cm^{-1} whose agreement with 8000 is encouraging. It might be mentioned here that the same quantity obtained from a transition in N_2^+ is 9000 cm^{-1} (see below).

The $x\sigma-y\sigma$ separation in N_2 may be estimated from

- (3) E. A. Ballik and D. A. Ramsay, *Astrophys. J.*, **137**, 84 (1963).
- (4) P. G. Wilkinson, *ibid.*, **138**, 778 (1963).
- (5) R. S. Mulliken, *Phys. Rev.*, **56**, 778 (1939).
- (6) H. Freymark, *Ann. Physik*, **8**, 221 (1951).
- (7) R. E. Worley, *Phys. Rev.*, **89**, 863 (1953).
- (8) R. E. Worley, *ibid.*, **64**, 207 (1943).

the two states of the configuration, $(y\sigma)(w\pi)^4(x\sigma)^2(v\pi)$, the ${}^1\Pi_u$ of which has been estimated by Mulliken,^{2a} but not observed. An approximate value of 29,000 cm^{-1} is obtained. This might be compared with 25,500 obtained from Hopfield's⁹ and Worley-Jenkins'⁸ Rydberg series limits, but this figure, again, really applies to the $x\sigma$ - $y\sigma$ separation in N_2^+ which from other data (see below) is the same, 25,500 cm^{-1} . These orbital heights are indicated in Figure 1.

Between C_2 and N_2 is found CN, the first ionization potential of which is between 112,000 and 117,000 cm^{-1} .⁴ In agreement with the assignments of Mulliken^{2b-d} and Douglas and Routly¹⁰ that the three lowest known states arise from the three unsplit configurations $(y\sigma)^2(w\pi)^4(x\sigma)$, X ${}^2\Sigma^+$; $(y\sigma)^2(w\pi)^3(x\sigma)^2$, A ${}^2\Pi_i$; and $(y\sigma)(w\pi)^4(x\sigma)^2$, B ${}^2\Sigma^+$; the orbital, $x\sigma$, has been placed at 114,000 cm^{-1} . The heights of $w\pi$ and $y\sigma$ are then readily found from these configurations. The height of $v\pi$ is not so easily determined. Carroll¹¹ has suggested that the states E ${}^2\Sigma$ and J ${}^2\Delta$ belong to the nine-state configuration $(y\sigma)^2(w\pi)^3(x\sigma)(v\pi)$ as must also the state F ${}^2\Delta_r$, as proposed by Douglas and Routly.¹⁰ These assignments seem reasonable but do not provide support for a very definite estimate of $v\pi$. Their average height, 62,000, is probably a poor estimate of the configuration center, none of the three quartet states having been found, but this figure has been used in Figure 1 to fix approximately the $v\pi$ height, shown by a dotted bar. Douglas and Routly¹⁰ point out the difficulties attending the assignment of the state D ${}^2\Pi_i$ to the configuration $(y\sigma)^2(w\pi)^4(v\pi)$. The great bond distance and low vibrational frequency are more consistent with the assignment of this state to $(y\sigma)^2(w\pi)^2(x\sigma)^2(v\pi)$ which might combine by a one-electron jump with A ${}^2\Pi_i$; however, not with X ${}^2\Sigma^+$. Furthermore, the $T_0 = 53,900 \text{ cm}^{-1}$ ¹⁰ is inconsistent with this assignment and Figure 1. There seems to be no alternative to assignment to the configuration $(y\sigma)^2(w\pi)^3(x\sigma)(u\sigma)$, indicating that $u\sigma$ here is more strongly antibonding than $v\pi$ and lies very close to it, probably around 1 e.v. below it. It should be pointed out that this low energy of $u\sigma$ is inconsistent with the much higher energy of this orbital implied by Mulliken's^{2a} assignments in nitrogen. It is difficult to assign the state H ${}^2\Pi_r$ ¹⁰ to any configuration other than $(y\sigma)(w\pi)^4(x\sigma)(v\pi)$ but its $T_0 = 61,000 \text{ cm}^{-1}$ seems too low for this if $v\pi$ in Figure 1 is nearly correct.

On the low atomic number side of the C_2 , CN, N_2 sequence are found B_2 and BC. The latter has not been observed; the former was first and last reported in emission by Douglas and Herzberg¹² in 1940. The only band system reported was assigned as ${}^3\Sigma_u^-$

${}^3\Sigma_g^-$ which fits, as they point out, the expected ground-state configuration, $(y\sigma)^2(w\pi)^2$. The upper state most probably¹² is one of the seven members of the configuration, $(y\sigma)(w\pi)^2(x\sigma)$. There is a certain amount of ambiguity due to the manifold states of these configurations. However, a separation of $x\sigma$ - $y\sigma$ amounting to 30,000 cm^{-1} is probably good to within 5000 cm^{-1} . Thus these σ -orbitals are tied together, but their height below ionization is not known. In fact, the first ionization would involve loss of an electron from $w\pi$ leaving the σ -orbitals still floating. The separation of these orbitals has been sketched into Figure 1, an attempt having been made to indicate that their height is unknown.

The height of $w\pi$ can be guessed from a guessed ionization potential. The latter is probably about 74,000 cm^{-1} , considering that the atomic ionization potential of boron is 67,000 cm^{-1} ,¹³ and that ionization in the molecule occurs from the orbital $w\pi$.¹⁴ This height has been indicated in Figure 1.

Turning attention now to the higher atomic-number molecules, it is difficult to find transitions in which the lower energy MO's figure, due to the fact that they are filled; Rydberg transitions predominate. In the molecule NO there is no question of assignment of all of the known states to the Rydberg or non-Rydberg categories.¹⁵ The first ionization potential of 74,000 cm^{-1} ⁴ is due to electron loss from $v\pi$; thus the height of this orbital is definite. The $w\pi$ - $v\pi$ separation can be guessed from the fact that two Π states of the five-state configuration $(y\sigma)^2(w\pi)^3(x\sigma)^2(v\pi)^2$ may well be identifiable with P ${}^2\Pi_i$ and B ${}^2\Pi_r$.^{15a} The center of gravity of the five states cannot be estimated with any certainty; its height is simply taken to be the average of P ${}^2\Pi_i$ and B ${}^2\Pi_r$. This guess allows $w\pi$ to be fixed at near 55,000 cm^{-1} below $v\pi$.

Estimating the height of $x\sigma$ in NO is also risky. Referring again to Miescher,^{15a} the state G ${}^2\Sigma^-$ is probably a member of the configuration $(y\sigma)^2(w\pi)^4(x\sigma)(v\pi)^2$ along with three others, one of which may be B' ${}^2\Delta_i$. If the average of these is taken as the center

(9) J. J. Hopfield, *Phys. Rev.*, **36**, 789 (1930).

(10) A. E. Douglas and P. M. Routly, *Astrophys. J. Suppl.*, **1**, 295 (1955).

(11) P. K. Carroll, *Can. J. Phys.*, **34**, 83 (1956).

(12) A. E. Douglas and G. Herzberg, *Can. J. Res.*, **18A**, 165 (1940).

(13) G. Herzberg, "Atomic Spectra and Atomic Structure," Dover Publications, New York, N. Y., 1944, p. 200.

(14) R. S. Mulliken, *Phys. Rev.*, **46**, 549 (1934).

(15) Representative are: (a) E. Miescher, Technical Reports of May 1962 and 1963, University of Basel, Switzerland; (b) K. P. Huber, *Helv. Phys. Acta*, **34**, 929 (1961); (c) K. P. Huber, M. Huber, and E. Miescher, *Phys. Letters*, **3**, 315 (1963).

of the configuration, then $x\sigma$ should lie $61,000 \text{ cm.}^{-1}$ below $v\pi$. Nothing can be said about $y\sigma$.

In the case of O_2 , ionization is again from $v\pi$, but the lowest energy configuration $(y\sigma)^2(v\pi)^4(x\sigma)^2(v\pi)^2$ is split into $X^3\Sigma_g^-$, $b^1\Sigma_g^+$, and $a^1\Delta_g$. The center of gravity of these states is 7000 cm.^{-1} above $X^3\Sigma_g^-$; this and the reported ionization energy⁴ were used to place $v\pi$ at $90,000 \text{ cm.}^{-1}$. Mulliken^{2b-d} has strongly stated the case and theoretical reasons for $x\sigma$ dropping below $w\pi$ for molecules to the right of NO. The lowest excited configuration is therefore probably $(y\sigma)^2(x\sigma)^2(w\pi)^3(v\pi)^3$; $^1\Sigma_u^+$, $^1\Sigma_u^-$, $^1\Delta_u$, $^3\Sigma_u^+$, $^3\Sigma_u^-$, $^3\Delta_u$. As Herzberg has observed,¹⁷ the $^3\Sigma_u^-$ and $^3\Sigma_u^+$ are certainly the upper states of the Schumann-Runge bands and a second ultraviolet band system reported by him.¹⁷ He has also suggested that two more of his observed states belong to this same configuration, identifying them with $^1\Sigma_u^-$ and $^3\Delta_u$. Consideration of the rather similar bond distances supports this assignment. The average of these four out of the six states belonging to the configuration gives $35,000 \text{ cm.}^{-1}$ as an estimated center of gravity. It is a low estimate containing a preponderance of triplet states and perhaps should be raised a volt or so for this reason. When taken in conjunction with the center of gravity 7000 cm.^{-1} of the lowest configuration, the $v\pi-w\pi$ separation amounts to about $36,000 \text{ cm.}^{-1}$. This is dashed into Figure 1. From O_2 spectra alone, nothing can be said about $x\sigma$ or $y\sigma$.

With the molecules OF and F_2 , only $v\pi$ from which the first electron ionizes has been shown. No spectrum of OF has been reported but its ionization energy has been determined by electron impact.¹⁸ A good spectroscopic ionization energy¹⁹ has been reported for fluorine. The orbitals $v\pi$ for both of these molecules have thus been drawn in Figure 1 at the appropriate heights.

Isoelectronic Sequences. Attention is turned next to isoelectronic sequences of neutral molecules. Figure 2 consists of a presentation similar to Figure 1, and again serious gaps in experimental information are apparent. Happily, the sets which are best understood show the most regularity so there is some hope that the regularity is meaningful even though it has not been conclusively demonstrated.

The most complete isoelectronic set is the 14-electron set N_2 , CO, BF. The theoretical work of Lefebvre-Brion and Moser²⁰ shows which of the known states of CO are non-Rydberg states, and these have been used to make what is believed to be an unambiguous assignment leading to the energies shown of orbitals below the ionized state. Assignment of the only two known non-Rydberg states of BF²¹ likewise fixes the heights of $v\pi$ and $x\sigma$. The trends are almost as ex-

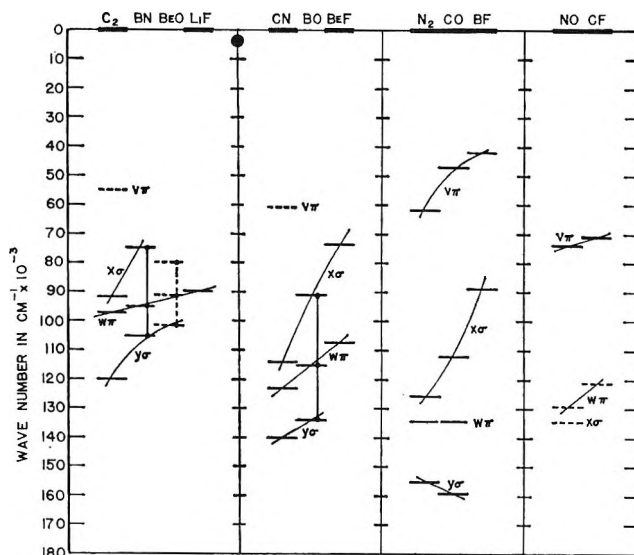


Figure 2. Variation of the difference between ionization and orbital energies with polarity in isoelectronic sequences. Heavy lines under formulas indicate known or well-estimated ionization potentials. Horizontal lines at various heights give the orbital energies below ionization. Dotted lines denote uncertainty of probably more than $\pm 3000 \text{ cm.}^{-1}$. Vertical tie lines denote knowledge of orbital separation but complete ambiguity regarding energy below ionization.

pected, considering the changing nature of the molecular orbitals with increasing separation of charge. Ransil's calculations²² show that $v\pi$ and $x\sigma$ tend to become lone pairs on the more electropositive atom, while $w\pi$ and $y\sigma$ tend toward lone pairs on the more electronegative atom. Thus, $v\pi$ and $x\sigma$ should increase in energy relative to $w\pi$ and $y\sigma$ which might be expected to become deeper.

Turning to the CN, BO, BeF sequence and considering first BeF, the $A^2\Pi_i$ state belongs to the configuration $(y\sigma)^2(w\pi)^3(x\sigma)^2$ and so the $w\pi-x\sigma$ separation is $33,000 \text{ cm.}^{-1}$.^{23,24} Using Price's estimate²⁵ of the

(16) G. Herzberg, "Molecular Spectra and Molecular Structure. I," 2nd Ed., D. Van Nostrand Co., Inc., Princeton, N. J., 1950, p. 560.

(17) G. Herzberg, *Can. J. Phys.*, **31**, 657 (1953).

(18) V. H. Dibeler, R. M. Reese, and J. L. Franklin, *J. Chem. Phys.*, **27**, 1296 (1957).

(19) R. P. Iczkowski and J. L. Margrave, *ibid.*, **30**, 403 (1959).

(20) H. Lefebvre-Brion and C. Moser, *ibid.*, **35**, 1702 (1961).

(21) D. W. Robinson, *J. Mol. Spectry.*, **11**, 275 (1963).

(22) B. J. Ransil, *Rev. Mod. Phys.*, **32**, 239, 245 (1960).

(23) Mulliken²⁴ has suggested that this state is mixed with a $^2\Pi$ state of the configuration $\dots 2p\pi^4 3d\pi$ (to use the united atom notation) but this circumstance does not affect rough estimates of the energy of the $\dots 2p\pi^3 3s\sigma^2$ configuration with which this discussion is concerned.

(24) R. S. Mulliken, *Phys. Rev.*, **38**, 836 (1931).

(25) W. C. Price, T. R. Passmore, and D. M. Roessler, *Discussions Faraday Soc.*, **35**, 201 (1963).

ionization potential of this molecule, the heights of the two orbitals have been indicated in Figure 2. The states A $^2\Pi$ and B $^2\Sigma$ of BO²⁶ are unquestionably assignable^{2b-d} to the configurations $(y\sigma)^2(w\pi)^3(x\sigma)^2$ and $(y\sigma)(w\pi)^4(x\sigma)^2$, respectively, providing measures of the $w\pi-x\sigma$ and $y\sigma-x\sigma$ separations. Since the ionization potential of BO is not known, the set of three orbitals relative to those of CN and BeF in Figure 2 is not fixed in height. They have simply been drawn in at a height which seems reasonable by comparison with the CN, BeF analogs. A value of about 90,000 cm.⁻¹ is thus predicted for the first ionization potential of BO. There is a suggestion here that $y\sigma$ as well as $w\pi$ are creeping up in energy even though the electronegativities of their hosts are increasing. It must be borne in mind, however, that these energies are relative to ionized states of different molecules, so that all that can be said is that $y\sigma$ drops faster than $w\pi$ in the 14-electron sequence, about the same as $w\pi$ in the 13-electron sequence, and not as fast as $w\pi$ in the 12-electron sequence C₂, BN, BeO, and LiF.

These 12-electron molecules are not well understood. Only one band system of BN has been fully measured and analyzed.¹⁸ The assignment to $(y\sigma)(w\pi)^3(y\sigma)^2$ and $(y\sigma)^2(w\pi)^3(x\sigma)$ is clear by the strong analogy to the Swan bands of C₂, but the singlet-triplet splittings of these configurations could vary over a wide range. Another band system involving transitions between singlet states has not been completely analyzed,²⁷ but is probably assignable to the configurations $(y\sigma)^2(w\pi)^3(x\sigma)$ and $(y\sigma)^2(w\pi)^4$. Assuming not unreasonable splittings between singlet and triplet states of the same configuration, the relative orbital heights are shown in Figure 2. If these are nearly correct relative to each other, the ground state must be a singlet as is the case for C₂.³ Since the ionization potential is unknown for BN, the heights have been drawn so as to interpolate $w\pi$ between its counterparts in C₂ and LiF. The latter was again taken from Price,²⁵ but nothing else is known about the electronic states of this molecule. BeO is an enigma. No strong triplet bands were observed²⁸ as they were in C₂ and BN. Ignoring configuration splitting and making what seem to be the most reasonable assignments of X $^1\Sigma$ to $(y\sigma)^2(w\pi)^4$, A $^1\Pi$ to $(y\sigma)^2(w\pi)^3(x\sigma)$, and B $^2\Sigma$ to $(y\sigma)(w\pi)^4(x\sigma)$, one produces the relative orbital spacings shown dotted in Figure 2. Their collective height relative to the adjacent molecules was adjusted by the interpolated height of $w\pi$. It is obvious that BeO does not fit; at present no better assignment can be suggested.

On the right of Figure 2 the ionization potential of CF has been taken from Price.²⁵ The state A $^2\Sigma^+$ must be Rydberg,²⁹ since the bond distance is decreased

below the ground-state value. The other known state B $^2\Pi$, is probably part of the configuration $(y\sigma)^2(w\pi)^3(x\sigma)^2(v\pi)^2$. Taking it as the center of gravity of this configuration, a radical approximation, places $v\pi$ in the vicinity of 50,000 cm.⁻¹ above $w\pi$. This is indicated in Figure 2.

Molecules and Their Ions. In Figure 3 are diagrammed in the same way as with the previous figures, the separations between the ionized states and the molecular orbitals of the five molecules whose ions have been spectroscopically observed, O₂, NO, N₂, CO, and CN. Wherever knowledge permits, the orbitals of the ions have also been added, but not referred to the doubly ionized state, as this would vitiate comparison. In-

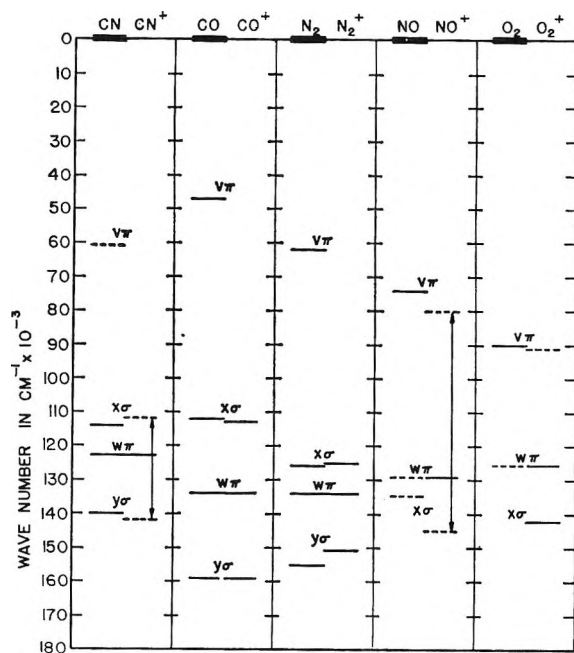


Figure 3. Comparison of orbital energy separations of molecules with their ions. Heavy lines under formulas indicate known or well-estimated ionization potentials. Horizontal lines at various heights give the orbital energies below ionization. Dotted lines denote uncertainty of probably more than ± 3000 cm.⁻¹. Vertical tie lines denote knowledge of orbital separation but complete ambiguity regarding energy below ionization. In all cases the orbitals of the ions are relative only, having been adjusted for coincidence of the $w\pi$ -orbital of the two species, ion and corresponding molecule.

(26) Yu. Ya. Kuz'yakov, V. M. Tetevskiy, and L. N. Tunitsky, *Opt. Spectry.* (USSR) (English Transl.), **9**, 84 (1960); A. A. Mal'tsev, D. I. Kataev, and V. M. Tatevskii, *ibid.*, **9**, 376 (1960).

(27) A. E. Douglas and G. Herzberg, *Can. J. Res.*, **18A**, 179 (1940).

(28) A. Lagerqvist, *Arkiv Fysik*, **7**, 473 (1954).

(29) B. A. Thrush and J. J. Zwolenik, *Trans. Faraday Soc.*, **59**, 582 (1963).

stead, the $w\pi$ -orbital of the ions has been aligned with the same orbital of the molecules. The best understood cases, as with previous examples, demonstrate the most extraordinarily nice behavior.

NO^+ is isoelectronic with N_2 . The state $A\ ^1\Pi$ is readily assignable³⁰ to the configuration $(y\sigma)^2(x\sigma)(w\pi)^4(v\pi)$ as discussed by Huber^{15b} where the order of orbitals $(x\sigma)(w\pi)$ now reflects the most probable order of increasing energies for this ion. The $73,000\text{ cm.}^{-1}$ excitation, reduced by an amount due to singlet-triplet splitting equal to the average of that in the N_2 and CO analogous cases, fixes $v\pi$ at $66,500\text{ cm.}^{-1}$ above $x\sigma$. The $x\sigma-v\pi$ separation may also be computed from the limits of Rydberg series of NO , the one ending in $X\ ^1\Sigma^+$ of NO^+ and the γ -series ending in $A\ ^1\Pi$.^{15b} Substantially the same figure results. The height of $w\pi$ in NO^+ can only roughly be estimated. Adopting Huber's^{15b} assignments of the α and β Rydberg series limits of NO , one finds the relative heights of a $^3\Sigma^+$ and one other state, both from the six-state configuration $(y\sigma)^2(x\sigma)^2(w\pi)^3(v\pi)$. Averaging these produces a figure of $48,500\text{ cm.}^{-1}$ for $v\pi$ above $w\pi$. When this is added to Figure 3 (dotted), it suggests that the $48,000\text{ cm.}^{-1}$ may be low. If the β series limit were a triplet state, this would be the natural result.

For N_2^+ , besides the ground state $X\ ^2\Sigma_g^+$, two states $B\ ^2\Sigma_u^+$ ¹⁶ and $A\ ^2\Pi$ ³¹ have been observed and measured in emission. The ground configuration is $(y\sigma)^2(w\pi)^4(x\sigma)$; the $B\ ^2\Sigma_u^+$ state can only belong to $(y\sigma)(w\pi)^4(x\sigma)^2$; and the $A\ ^2\Pi$ state must correspond to $(y\sigma)^2(w\pi)^3(x\sigma)^2$. Thus, the $y\sigma-x\sigma$ and $w\pi-x\sigma$ separations are established with comforting certainty. These are shown in Figure 3 to agree well with the orbitals of N_2 .

As with N_2^+ , the isoelectronic CO^+ has yielded its lowest $A\ ^2\Pi$ state in the well-known Comet-tail bands as well as the lowest excited $B\ ^2\Sigma$ state.³² These are assignable as in N_2^+ to give the $y\sigma-x\sigma$ and $w\pi-x\sigma$ separations. Agreement with CO is perfect.

The ion CN^+ is isoelectronic with C_2 . Like BeO , but unlike C_2 and BN , no triplet bands were seen³³; the known spectrum shows only two singlet-singlet band systems. From bond-distance considerations the state $f\ ^1\Sigma$ most likely belongs to the configuration, $(y\sigma)(w\pi)^4(x\sigma)$, which permits an estimate of the $y\sigma-x\sigma$ separation to be made. In order to make this estimate, a singlet-triplet splitting for this configuration was assumed the same as that in C_2 .³ Unfortunately, an estimate of the $y\sigma-x\sigma$ separation is not sufficient to permit adding these heights to Figure 3 since their relation to $w\pi$ is unknown. No unambiguous assignment of the other state, believed to be $^1\Sigma$, can be made which would relieve this dilemma. These or-

bitals have been drawn in to show their comparison in separation with those of CN . Arrows signify the complete uncertainty in their position with respect to $w\pi$.

Finally, O_2^+ is considered. The excited states $A\ ^2\Pi_u$ and a $^4\Pi_u$ ¹⁶ almost assuredly stem from the five-state configuration, $(y\sigma)^2(x\sigma)^2(w\pi)^3(v\pi)^2$. Taking the average of these for the center of gravity of that configuration yields a $w\pi-v\pi$ separation of $35,000\text{ cm.}^{-1}$. The short bond distance of state $c\ ^4\Sigma_u^-$ suggests a Rydberg state, but state $b\ ^4\Sigma_g^-$ may be a member of the four-state configuration $(x\sigma)(w\pi)^4(v\pi)^2$. The center of gravity of this configuration cannot be estimated very accurately from one of four possible states but this quartet is the lowest, perhaps something like $10,000\text{ cm.}^{-1}$ below the center. If this were the case, then $x\sigma$ would lie $50,000$ to $55,000\text{ cm.}^{-1}$ below $v\pi$ as indicated in Figure 3. Since $b\ ^4\Sigma_g^-$ and a $^4\Pi_u$ have the same multiplicity, their difference in energy should represent rather closely the difference in ionization energy of $x\sigma$ and $w\pi$,³⁴ $17,000\text{ cm.}^{-1}$. Since orbital heights of molecules and their ions may be seen in Figure 3 to agree nicely, the $x\sigma$ curve of Figure 1 could with some confidence be extrapolated to the right.

Bonding Effectiveness of the Four Orbitals, $y\sigma$, $w\pi$, $x\sigma$, $v\pi$. The previous sections illustrate that reasonable assignments of the known electronic states of the second-row diatomic molecules lead to ionization potential-orbital separations which vary in a strikingly regular way. The regularity, on the other hand, tends to verify the assignments, many of which have been given before in the literature. Using these assignments, further interesting comparisons can be made bearing on the bonding effectiveness of the molecular orbitals in question as measured by their ability to decrease or increase the bond distance as they become occupied.

Table I is a collection of bond distances measured for some low-energy configuration of sets of isoelectronic molecules. The encircled numbers are the numbers of electrons.

The first column lists the approximate configurations preceded by an identifying number in parentheses. The second column indicates the states that may arise from these configurations. The remaining columns list bond distances in Ångstroms and are headed by the molecules to which the distances refer, and in parentheses the electronegativity differences between the atoms in the molecule—a rough measure of bond

(30) E. Miescher, *Helv. Phys. Acta*, 29, 135 (1956).

(31) A. E. Douglas, *Astrophys. J.*, 117, 380 (1953).

(32) K. N. Rao, *ibid.*, 111, 50, 306 (1950).

(33) A. E. Douglas and P. M. Routly, *ibid.*, 119, 303 (1954).

(34) The author is indebted to a referee for mentioning this.

Table I: Configurations, Possible States, and Measured Bond Distances (in Å.) for Second Row Diatomic Molecules^a

Configuration	States (12)	C ₂ (0)	CN ⁺ (0.5)	BN (1.0)	BO ⁺ (1.5)	BeO (2.0)	BeF ⁺ (2.5)	LiF (3.0)
(1) (yσ) ² (wπ) ⁴	¹ Σ ⁺	1.24	1.17			1.33		1.53
(2) (yσ) ² (wπ) ³ (xσ)	^{1,3} Π _i	1.32		1.28		1.46		
(3) (yσ)(wπ) ⁴ (xσ)	^{1,3} Σ ⁺	1.24	1.17			1.36		
(4) (yσ) ² (wπ) ² (xσ)(wπ)	¹ Π(3), ¹ Φ, ³ Π _r (2)	1.54						
	³ Π _i (2), ³ Φ _r , ⁵ Π _r							
(5) (yσ)(wπ) ³ (xσ) ²	^{1,3} Π _i	1.27		1.33				
	(13)	N ₂ ⁺ (0)	CN (0.5)	CO ⁺ (1.0)	BO (1.5)	BF ⁺ (2.0)	BeF (2.5)	
(1) (yσ) ² (wπ) ⁴ (xσ)	² Σ ⁺	1.12	1.17	1.12	1.20	1.22	1.36	
(2) (yσ) ² (wπ) ³ (xσ) ²	² Π _i	1.19	1.24	1.25	1.35		1.39	
(3) (yσ)(wπ) ⁴ (xσ) ²	² Σ ⁺	1.08	1.15	1.17	1.30			
	(14)	N ₂ (0)	NO ⁺ (0.5)	CO (1.0)	CF ⁺ (1.5)	BF (2.0)		
(1) (yσ) ² (wπ) ⁴ (xσ) ²	¹ Σ ⁺	1.09	1.07	1.13		1.26		
(2) (yσ) ² (wπ) ⁴ (xσ)(vπ)	^{1,3} Π _r	1.21	1.20	1.24		1.31		
(3) (yσ) ² (wπ) ³ (xσ) ² (vπ)	^{1,3} Σ [±] , ^{1,3} Δ	1.27		1.40				
(4) (yσ)(wπ) ⁴ (xσ) ² (vπ)	^{1,3} Π _r	1.15						
	(15)	O ₂ ⁺ (0)	NO (0.5)	NF ⁺ (1.0)	CF (1.5)			
(1) (yσ) ² (wπ) ⁴ (xσ) ² (vπ)	² Π _r	1.13	1.15		1.27			
(2) (yσ) ² (wπ) ³ (xσ) ² (vπ) ²	² Π _{i,r} , ² Π, ² Φ _i , ⁴ Π _i	1.41	1.42					
	(16)	O ₂ (0)	OF ⁺ (0.5)	NF (1.0)				
(1) (yσ) ² (wπ) ⁴ (xσ) ² (vπ) ²	¹ Σ ⁺ , ³ Σ ⁻ , ¹ Δ	1.21						

^a A secondary source of these data for C₂, CN, CN⁺, N₂, N₂⁺, CO, CO⁺, NO, NO⁺, O₂, and O₂⁺ is L. Wallace, *Astrophys. J. Suppl.*, **68**, 165 (1962). For the molecules BN, BO, BF, BeF, LiF, CF, and BeO, see text.

polarity. Many bond lengths are missing, and in some cases several have been averaged where more than one state in the configuration has been observed. As is generally known, different states of the same configuration have similar bond distances and for the purposes of this discussion more precision is not required.

In comparing bond distances in isoelectronic molecules, some correction must be made for charge. The method adopted here of simply investigating the effect on bond distance of adding an electron always results in comparison of a charged with an uncharged species. The ions, other things being equal, are expected and observed to have shorter bond lengths than uncharged molecules due to the contraction of the orbitals by the excess nuclear charge. In order to correct for this small effect, the following rough and empirical method was used. In Table II is presented the effect on bond distance of adding one electron to the xσ-orbital in a 12-electron molecule to produce a 13-electron molecule (indicated by the encircled numerals);

Table II: Bond-Length Increase (%) on Addition of One Electron to the xσ-Orbital

	(1) → (1)	Corrected for 4% shortening in ions	
(12) → (13)	C ₂ → N ₂ ⁺	-9.7	-5.7
	CN ⁺ → CN	0.0	-4.0
	BeO → BF ⁺	-8.3	-4.3
	(2) → (2)		
	C ₂ → N ₂ ⁺	-9.8	-5.8
	BN → CO ⁺	-2.3	1.7
	(3) → (3)		
	C ₂ → N ₂ ⁺	-12.9	-8.9
	CN ⁺ → CN	-1.7	-5.7
	(1) → (1)		
(13) → (14)	N ₂ ⁺ → N ₂	-2.7	-6.7
	CN → NO ⁺	-8.5	-4.5
	CO ⁺ → CO	0.9	-3.1
	BF ⁺ → BF	3.3	-0.7

this is done with as many configurations (labeled by numbers in parentheses referring to Table I) as possible. In the first column of per cent bond distance increase no regularity is seen, but if these percentages are corrected by about 4% for ionic shortening the second column of percentages is obtained. This approximate value of 4% is clearly suggested by the values in the uncorrected per cent column and this is the sole origin of the correction. Of course, the percentage decrease in a bond distance due essentially to the addition of a proton should be, if it is at all constant, a certain fraction of the bond distance. However, since bond distances vary only between narrow limits, and the correction probably is not constant even when properly separated from other effects, the 4% was adopted as an additive correction to all percentage bond increases. Thus in Tables II, III, V, and VIII, the columns of corrected percentages have arisen by addition or subtraction of 4% from the uncorrected values according as the addition of an electron produces or destroys a positive ion.³⁵

Examining, then, the corrected percentage increases in Table II, the apparent effect of addition of one electron to the $x\sigma$ -orbital is a decrease in bond distance in most cases. This is to be expected since it is generally considered to be a bonding orbital; however, the bonding ability decreases as the electronegativity difference or polarity increases, as can be seen in any of the iso-electronic sequences.

As shown in Table III, the result of adding one electron to $y\sigma$ is also in general a decrease in bond distance. This is perhaps surprising in view of the fact that at least for homonuclear molecules $y\sigma$ is antibonding. Relative to $x\sigma$, the orbital $y\sigma$ is less effective in shortening bonds in the cases of homonuclear molecules but becomes more effective than $x\sigma$ with sufficient electronegativity difference. Thus using bond shortening as a measure of bonding character it must be concluded that both $x\sigma$ and $y\sigma$ are bonding orbitals. For homonuclear molecules $x\sigma$ is more strongly bonding than $y\sigma$, but as the electronegativity difference between the atoms increases, $y\sigma$ becomes more strongly bonding and $x\sigma$ more weakly bonding. The orbital $y\sigma$ actually is considerably more strongly bonding than $x\sigma$ in several polar molecules. This observation is more clearly apparent when the effect of transfer of one electron from $y\sigma$ to $x\sigma$ is examined. Table IV depicts this for as many molecules as data permit. Here, no uncertain correction for ionic charge effects must be made as they were in Tables II and III.

As is well known by diatomic spectroscopists,³⁶ but not generally appreciated among chemists, $w\pi$ is a more effectively bonding orbital than $x\sigma$.³⁷ In Table

Table III: Bond-Length Increase on Addition of One Electron to the $y\sigma$ -Orbital

	(3) → (1)	Cor.	(5) → (2)	Cor.		
⑫ → ⑬	$C_2 \rightarrow N_2^+$	-9.7	-5.7	$C_2 \rightarrow N_2^+$	-6.3	-2.3
	$CN^+ \rightarrow CN$	0.0	-4.0	$BN \rightarrow CO^+$	-6.0	-2.0
	$BeO \rightarrow BF^+$	-10.3	-6.3			
	(3) → (1)					
⑬ → ⑭	$N_2^+ \rightarrow N_2$	0.9	-3.1			
	$CN \rightarrow NO^+$	-7.0	-3.0			
	$CO^+ \rightarrow CO$	-3.4	-7.4			
	(4) → (1)					
⑭ → ⑮	$N_2 \rightarrow O_2^+$	-1.7	2.3			

Table IV: Bond-Length Increase on Transferral of One Electron from $y\sigma$ to $x\sigma$

	(1) → (3)		(2) → (5)	
⑫	C_2	0.0	C_2	-3.8
	CN^+	0.0	BN	3.9
	BeO	2.3		
	(1) → (3)			
⑬	N_2^+	-3.6		
	CN	-1.7		
	CO^+	1.8		
	BO	8.3		
	(2) → (4)			
⑭	N_2	-5.0		

(35) In cases where two different nuclear species are involved, it is rather surprising that wild deviations from the trends do not appear. For example, in Table II, ⑬ → ⑭, omission of $CN \rightarrow NO^+$ establishes a uniform trend, -6.7, -3.1, -0.7, into which the case of $CN \rightarrow NO^+$ fits. In fact, the reader may object to the inclusion in these tables of species differing in nuclear kind, one type being $XY \rightarrow YZ^+$ and the second type being $X_2 \rightarrow Y_2^+$, but this objection may be relieved by examining more closely the nature of the empirical correction. In both types there is no change in electronegativity difference but there is an increase by two in the number of protons. In the nonobjectionable cases, $Y_2^+ \rightarrow Y_2$ and $XZ^+ \rightarrow XZ$, there is no increase in the number of protons. Since the "proton-increase" type always involves charge change of zero → plus (-4% correction) and the "proton-constant" type is always accompanied by a charge change of plus → zero (+4% correction) it is impossible to separate the proton effect on bond distance from the electron effect. For example, it could well be that the proton increase causes a 4% shrinkage and the charge increase produces a 2% shrinkage. Then a charge decrease would produce a 2% expansion. In considering the proton effect in applying corrections, in order to maintain monotonic trends, it is only necessary (1) that twice the electron correction in the zero → plus case plus the proton correction add up to approximately 8%, and (2) that the electron effects differ only in sign in the two types of cases. The effect of a 4% to 2% proton to electron correction, as in the example above, would be that all of the "corrected" bond length increases would have been increased by +2, or in Table II, ⑬ → ⑭, the numbers become -4.7, -2.5, -1.1, +1.3. So the sign of a negative value near zero in the Tables II, III, V, and VIII should not be taken too seriously.

(36) R. S. Mulliken, *J. Phys. Chem.*, 56, 295 (1952).

V is presented, as in Tables II and III, the percentage bond increase on addition of one electron to the $w\pi$ -orbital. In every case there is a considerable contraction and this shrinkage is independent of polarity. The bonding ability of $w\pi$ relative to $x\sigma$ is demonstrated in Table VI, which depicts the result of transferring an electron out of $w\pi$ into $x\sigma$. It is evident that in every case the bond suffers, even with O_2 , where the longer bond distance sends $w\pi$ above $x\sigma$ in energy and would be expected to exhibit a debilitated strength. It was seen above that the bonding capability of $x\sigma$ decreases as polarity increases. The increase in bond length accompanying $w\pi \rightarrow x\sigma$ transfer should thus be rendered greater as bond polarity increases. Data are not complete enough to verify this and BeF provides an exception to this expectation.²⁸

Table V: Bond-Length Increase on Addition of One Electron to the $w\pi$ -Orbital

	(2) → (1)	Cor.	(5) → (3)	Cor.
⑫ → ⑬	$C_2 \rightarrow N_2^+$	-15.1	-11.1	$C_2 \rightarrow N_2^+$ -15.0
	$BN \rightarrow CO^+$	-10.9	-6.9	$BN \rightarrow CO^+$ -12.0
	$BeO \rightarrow BF^+$	-16.4	-12.4	
	(2) → (1)			
⑬ → ⑭	$N_2^+ \rightarrow N_2$	-8.4	-12.4	
	$CN \rightarrow NO^+$	-13.7	-9.7	
	$CO^+ \rightarrow CO$	-9.6	-13.6	
	(3) → (1)			
⑭ → ⑮	$N_2 \rightarrow O_2^+$	-11.0	-7.0	
	(2) → (1)			
⑮ → ⑯	$O_2^+ \rightarrow O_2$	-14.1	-18.1	

Table VI: Bond-Length Increase on Transferral of One Electron from $w\pi$ to $x\sigma$

	(1) → (2)			
⑫	C_2	6.5		
	BeO	9.8		
	(1) → (2)			
⑬	N_2^+	6.3	CO^+	11.6
	CN	6.0	BO	12.5
			BeF	2.2
	(2) → (3)			
⑭	N_2	5.0	CO	12.9

Transfer of an electron from $y\sigma \rightarrow w\pi$ should shorten the bond, and since $y\sigma$ becomes more strongly binding with electronegativity difference, the shortening should decrease as polarity increases. In Table VII avail-

able data are set down. The prediction is verified for the 13-electron molecules; the questionable BeO provides, as usual, some trouble. Clearly, the data are insufficient to say very much about trends in polarity; however, $w\pi$ certainly has much more bond shortening ability than either $x\sigma$ or $y\sigma$.

Table VII: Bond-Length Increase on Transferral of One Electron from $y\sigma$ to $w\pi$

	(2) → (3)		(2) → (3)
⑫	C_2	-6.1	
	BeO	-6.8	
	(2) → (3)		(2) → (3)
⑬	N_2^+	-9.2	CO^+ -6.4
	CN	-7.3	BO -3.7
	(3) → (4)		
⑭	N_2	-9.4	

The experimental evidence for the behavior of molecules on population of $v\pi$ is good and Table VIII presents this. As is generally felt, $v\pi$ is strongly antibonding, and Table VIII supports this feeling. There seems as with $w\pi$ to be no apparent trends with respect to changing polarity in isoelectronic sequences. Underlined values as well as doubly underlined values refer to the same process in the same molecule but with different configurations. These numbers should be the same. Considering the approximate nature of this whole discussion, agreement is quite satisfactory.

In Table IX are presented the effects of transferring an electron into $v\pi$ out of $x\sigma$, $y\sigma$, and $w\pi$. Naturally, the $x\sigma \rightarrow v\pi$ transfer produces a lengthening which decreases with increasing polarity due to the waning strength of $x\sigma$ in bonding. The one available $y\sigma \rightarrow v\pi$ transfer is bond-lengthening as expected from the foregoing. The $w\pi \rightarrow v\pi$ transfer is bond-lengthening and much more effectively so than the other two. This is a transfer from a strongly bonding orbital to a strongly antibonding one.

Discussion

It appears that more quantitative regularity can be found than was anticipated; however, exceptions are not at all discouraging. What is encouraging is that the best-known molecules provide the best examples of trends.

(37) This has been discussed theoretically in terms of overlap integrals as a bonding criterion by R. S. Mulliken, *J. Am. Chem. Soc.*, **72**, 4493 (1950).

Table VIII: Bond-Length Increase on Addition of One Electron to the $v\pi$ -Orbital

	(1) → (2)		Cor.	(2) → (3)		Cor.	(3) → (4)		Cor.
⑬ → ⑭	$N_2^+ \rightarrow N_2$	8.0	<u>4.0</u>	$N_2^+ \rightarrow N_2$	6.7	<u>2.7</u>	$N_2^+ \rightarrow N_2$	6.5	<u>2.5</u>
	$CN \rightarrow NO^+$	2.6	<u>6.6</u>	$CO^+ \rightarrow CO$	12.0	<u>8.0</u>			
	$CO^+ \rightarrow CO$	10.7	<u>6.7</u>						
	$BF^+ \rightarrow BF$	7.4	<u>3.4</u>						
	(1) → (1)			(3) → (2)					
⑭ → ⑮	$N_2 \rightarrow O_2^+$	3.7	7.7	$N_2 \rightarrow O_2^+$	11.0	15.0			
	$NO^+ \rightarrow NO$	7.5	3.5						
	(1) → (1)								
⑮ → ⑯	$O_2^+ \rightarrow O_2$	7.1	3.1						

Table IX: Bond-Length Increase on Several One-Electron Transfers Involving the $v\pi$ -Orbital

Effect of $x\sigma \rightarrow v\pi$ transfer		
	(1) → (2)	
⑭	N_2	11.0
	NO^+	12.1
	CO	9.7
	BF	4.0
Effect of $w\sigma \rightarrow v\pi$ transfer		
	(1) → (4)	
⑭	N_2	5.5
Effect of $w\pi \rightarrow v\pi$ transfer		
	(1) → (3)	
⑭	N_2	16.5
	CO	23.9
	(1) → (2)	
⑮	O_2^+	24.8
	NO	23.5

In Figure 1, curves have been drawn through orbitals having the same label, not to imply functional dependence of energy on anything, but simply to clarify the figure. All curves slope downward similarly to the analogous trend of atomic orbital energies with increasing nuclear charge. In Figure 2 the sequences involve transfer of a proton from one atom to the other with no change in number of electrons. It seems clear that the orbitals fan out in energy. On an absolute basis, not relative to ionization potentials, this fanning out would be a manifestation of $y\sigma$ and $w\pi$ tending to become nonbonding on the atom with higher nuclear charge, while $x\sigma$ and $v\pi$ tend to localize on the atom with the lower nuclear charge²² and increase in energy. It might be predicted from this, for example, that the

ground state of BN is most likely to be a singlet state unless the singlet-triplet splitting of the configuration $\sigma^2\pi^3\sigma$ is considerably greater in the case of BN than in C_2 . Within 1 e.v., the ionization potentials of BN and BO are probably 11.8 and 11.2 e.v., respectively; those of B_2 and BC are approximately 9.2 and 9.7 e.v., respectively. The comparisons of molecules with their ions in Figure 3 is striking. This correspondence has been assumed in the literature in deducing orbital energies for molecules from those of their ions and *vice versa*; however, here they have been deduced quite separately.

The effect on bond distance of increasing polarity of isoelectronic sequences of molecules in analogous configurations is seen in Table III. In concordance with expectation, increasing electronegativity difference increases the bond lengths. The effect of this can only be to move charge density in the valence shell out of the bonding region, with very little change in inner shell (K-shell) dimension. Of course, there are exceptions, but the general trend is obvious.

Tables II through IX illustrate the bond-length effect on population of the four orbitals, $y\sigma$, $w\pi$, $x\sigma$, and $v\pi$. The results are summarized as follows. Addition of an electron to $x\sigma$ decreases the bond length, this decrease becoming less as the polarity of the molecule becomes greater. Addition of one electron to $y\sigma$ also decreases the bond length in most cases, the decrease becoming greater as the polarity of the molecule becomes greater. $x\sigma$ is more effectively bonding than $y\sigma$ for nearly homonuclear molecules, but $y\sigma$ is a more effective bond-shortening orbital than $x\sigma$ in polar molecules. In all cases addition of an electron to $w\pi$ decreases the bond distance by a factor greater than that for $x\sigma$ or $y\sigma$, and this percentage decrease is seemingly not smoothly dependent on polarity. The orbital $v\pi$ increases bond distances, when populated, by percentages somewhat less than $w\pi$'s, decreases,

and again is not smoothly dependent on electronegativity difference.

Conclusion

Although Mulliken^{2b-d} 35 years ago published curves (his Figures 43 and 44) exhibiting relative orbital energies, these cannot be used for quantitative prediction of excitation energies in first-row diatomic molecules. The curves given in this paper, if the future is

kind enough to substantiate them, can be so used. In fact, they are perhaps good to within 5000 cm.^{-1} or so, since the reverse process of deriving them from excitation energies could largely be followed with that accuracy. Although much of the material herein contained has been discussed before, its collection and presentation in this way reveals some remarkable regularities that hopefully will be instructive and useful.

The P - T - x Phase Diagram of the System Zinc-Tellurium¹

by F. A. Kröger

Department of Electrical Engineering, University of Southern California, Los Angeles, California
(Received March 29, 1965)

Combination of the results of thermodynamic and phase diagram studies with those of a physicochemical investigation of the semiconductor properties of ZnTe makes it possible to construct the pressure-temperature-composition (P - T - x) phase diagram of the system Zn-Te.

Introduction

The system Zn-Te contains one compound, ZnTe, which fuses at 1295° .² The liquidus curves determined by Carides, *et al.*,² plotted as T^{-1} vs. composition in atom fractions (x), are shown in Figure 1(b).

The heat and entropy of formation of ZnTe from solid zinc and tellurium at 660°K. have been determined by an electrochemical method³: $\Delta H = -28.2$ kcal./mole; $\Delta S = -2.85$ kcal./deg.⁻¹ mole⁻¹.

Evaporation studies by Korneeva, *et al.*,⁴ as corrected for dissociation by Pashinkin,⁵ give for the vapor pressure (corresponding to the minimum pressure of the compound) in atmospheres

$$\log \left(\frac{P_{\min}}{\text{atm.}} \right) = - \frac{10.627}{T} \text{ deg.} + 6.698 \quad (1)$$

In formulating this equation we have followed the system of equations of quantities advocated by Guggenheim.⁶ Finally, Thomas and Sadowski⁷ have deter-

mined the concentrations of free holes in ZnTe in equilibrium with zinc vapor at 650 - 900° . Assuming the holes to originate by double ionization of zinc vacancies (V_{Zn}), as indicated by the pressure dependence and by Hall effect data on quenched samples, their results are represented by eq. 2.

(1) This work was supported by the Joint Services Electronics Program (U. S. Army, U. S. Navy, U. S. Air Force) under Contract AF-AFOSR-496-65.

(2) J. Carides and A. G. Fischer, *Solid State Commun.*, **2**, 217 (1964).

(3) J. H. McAteer and H. Seltz, *J. Am. Chem. Soc.*, **58**, 2081 (1936); O. Kubaschewski and E. L. Evans, "Metallurgical Thermochemistry," Pergamon Press, London and New York, 1951, p. 280.

(4) I. V. Korneeva, A. V. Belyaev, and A. V. Novoselova, *Zh. Neorgan. Khim.*, **5**, 3 (1960).

(5) A. S. Pashinkin, *ibid.*, **7**, 2632 (1962).

(6) E. A. Guggenheim, "Thermodynamics," North Holland Publishing Co., Amsterdam, 1959, p. 1.

(7) D. G. Thomas and E. A. Sadowski, *J. Phys. Chem. Solids*, **25**, 395 (1964).

$$[V_{Zn}^{''}] = 1.02 \left(\frac{p_{Zn}}{\text{atm.}} \right)^{-1/3} \exp(-1.31eV/kT) \quad (2)$$

Here $V_{Zn}^{''}$ indicates a doubly ionized zinc vacancy, *i.e.*, a place in the crystal where a zinc atom has been removed and two electrons added (= two holes removed); the two primes indicate the double negative effective charge. The square brackets indicate concentrations expressed in site fractions, *i.e.*, the number of zinc vacancies divided by the total number of zinc sites. In the following we shall combine these data to con-

struct the (P - T - x) phase diagram of the system Zn-Te.^{8,9}

Construction of the P - T and T - x Projections of the P - T - x Phase Diagram. As is seen from the melting diagram, the system has two degenerate eutectic points, the triple points T_{Zn} and T_{Te} of Zn and Te almost coinciding with the quadruple points Q_1 and Q_2 of ZnTe in equilibrium with vapor, liquid, and solid Zn or Te. As shown by Lorenz,¹⁰ the vapor pressure of the constituents of a compound at its three-phase line solid compound-liquid-gas follows fairly exactly Raoult's law, at least as long as x of the majority component of the liquid phase is not too different from 1. Making use of this, one can construct large sections of the P - T projection, starting from the liquidus curves and the vapor pressure data (or the corresponding thermodynamic data) for the pure constituents.¹¹ Figure 1(a) shows this for ZnTe, using a $\log P \therefore 1/T$ plot. At low temperatures the three-phase line coincides almost with the vapor lines of pure Zn and Te: here the vapor over ZnTe(s) + L is almost pure Zn or Te (Te_2). Only at higher temperatures do the lines deviate, giving rise to two pressure maxima similar to those found in the system Cd-Te.⁸ The point M is the melting point of ZnTe where the compositions of the solid and the liquid phase are almost identical. Note that at this point $(x_{Zn})_G \approx 0.9$. Point U, the upper sublimation point, is the point where the sublimation line (= $P_{min} \therefore 1/T$) touches the three-phase line.

The sublimation line may be calculated from the standard enthalpy and entropy of formation of ZnTe, using an estimated specific heat for ZnTe

$$C_p = 10 + 3 \times 10^{-3}T \text{ cal. deg.}^{-1} \text{ mole}^{-1}$$

and the thermodynamic data for Zn and Te¹¹

$$P_{min} = (p_{Zn} + p_{Te_2})_{min} = \left(\frac{K_{evap}}{0.385} \right)^{2/3} \text{ atm.} \quad (3)$$

with

$$K_{evap} = p_{Zn} p_{Te_2}^{1/2} \text{ atm.}^{3/2} \quad (4)$$

This gives the dashed line in Figure 1(a); since this line intersects the vapor pressure line of Te below the temperature of fusion of ZnTe, it cannot be correct. No such discrepancy exists for the directly observed

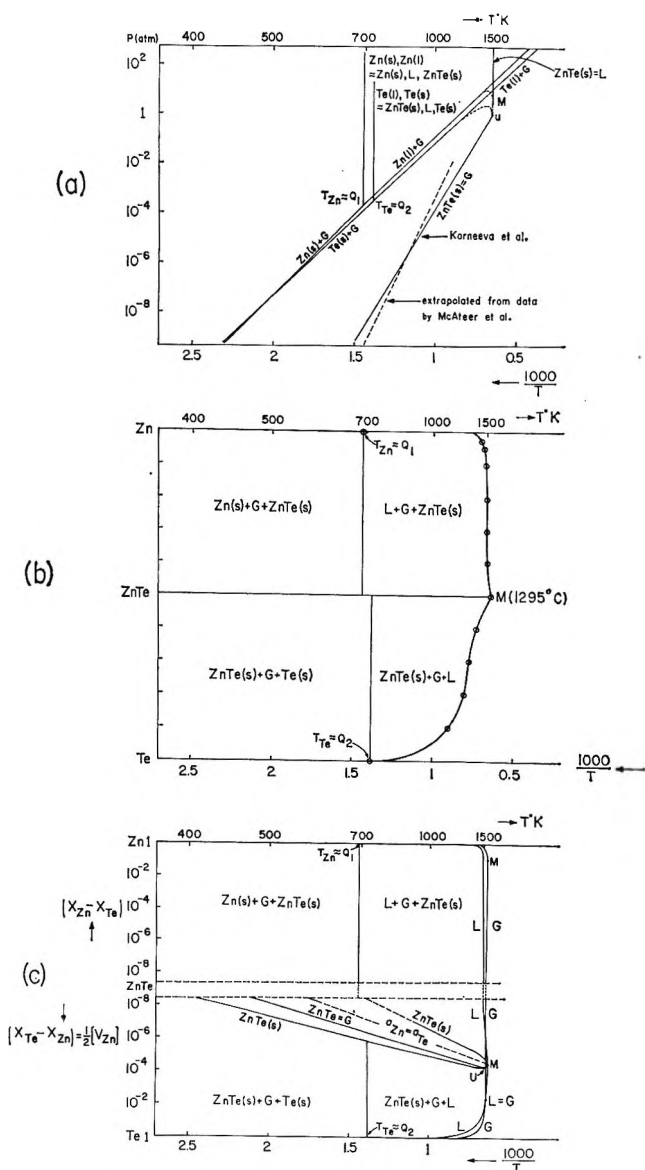


Figure 1. Two-phase lines and projections of three-phase blades for the system Zn-Te: (a) P - T projection; (b) x - $1/T$ projection with a conventional x scale; (c) Δx - $1/T$ projection, with a logarithmic scale for Δx .

(8) See F. A. Kröger, "The Chemistry of Imperfect Crystals," North Holland Publishing Co., Amsterdam, Interscience Publishers, Inc., New York, N. Y., 1964, p. 101 ff.

(9) L. J. Vieland, *Acta Met.*, 11, 137 (1963).

(10) M. R. Lorenz, *J. Phys. Chem. Solids*, 23, 939 (1962).

(11) D. R. Stull and G. C. Sinke, "Thermodynamic Properties of the Elements," *Advances in Chemistry Series*, No. 18, American Chemical Society, Washington, D. C., 1956.

pressure values^{4,5} (solid line in Figure 1(a)). Using the latter data in (3) we find

$$K_{\text{evap}} = 4.3 \times 10^9 \exp(-3.16eV/kT) \text{ atm.}^{1/2} \quad (5)$$

The pressure of zinc over a zinc source with activity a_{Zn} is¹¹

$$p_{\text{Zn}} = 1.8 \times 10^5 a_{\text{Zn}} \exp(-1.22eV/kT) \text{ atm.} \quad (6)$$

Similarly, the tellurium (Te_2) pressure over a tellurium source of activity a_{Te} is¹¹

$$p_{\text{Te}_2}^{1/2} = 2.06 \times 10^2 a_{\text{Te}} \exp(-0.57eV/kT) \text{ atm.}^{1/2} \quad (7)$$

Combining (4), (5), and (7), we find for the zinc pressure over ZnTe in equilibrium with a tellurium source of given activity

$$(p_{\text{Zn}})_{\text{ZnTe}, a_{\text{Zn}}} = 2.08 \times 10^7 a_{\text{Te}}^{-1} \exp(-0.59eV/kT) \text{ atm.} \quad (8)$$

Substituting (6) and (8) into (2) we find expressions for the concentration of V_{Zn}'' and thus the deviation from stoichiometry at the phase boundaries as an atom fraction

$$\Delta x = x_{\text{Te}} - x_{\text{Zn}} \approx [V_{\text{Zn}}''] / ([\text{ZnZn}] + [\text{TeTe}]) \approx 1/2 [V_{\text{Zn}}'']$$

$$\Delta x = 9.0 \times 10^{-3} a_{\text{Zn}}^{-1/2} \exp(-0.903eV/kT) \quad (9)$$

$$\Delta x = 1.86 \times 10^{-3} a_{\text{Te}}^{1/2} \exp(-0.447eV/kT) \quad (10)$$

Since we know $P_{\text{min}} = (p_{\text{Zn}} + p_{\text{Te}_2})_{\text{min}} = 3/2(p_{\text{Zn}})_{\text{min}}$, we can also find an expression for Δx at P_{min} ; *i.e.*, Δx in freely evaporating ZnTe

$$\Delta x(P_{\text{min}}) = 3.43 \times 10^{-3} \exp(-0.61eV/kT) \quad (11)$$

Expressions 9, 10, and 11 have been used to construct Figure 1(c). The point M has been identified with the point of the three-phase line where $a_{\text{Zn}} = a_{\text{Te}}$, *i.e.*, the point of intersection of the liquidus with the line $\Delta x(a_{\text{Zn}} = a_{\text{Te}})$. The latter was found by substituting into (2)

$$a_{\text{Zn}} = a_{\text{Te}} = (a_{\text{Zn}} a_{\text{Te}})^{1/2} = 10.8 \exp(-0.685eV/kT) \quad (12)$$

obtained from (4), (5), (6), and (7).

The phase boundaries show a discontinuity at the quadruple points, the ZnTe field widening slightly below these points. Point U lies at a slightly larger value of Δx than M—consistent with the larger value for p_{Te_2} , indicated by Figure 1(a). The data determining the phase boundary have been determined down to 650° .⁷ The dashed part indicated in Figure 1(c) for temperatures $< 650^\circ$ is an extrapolation which will be valid if there is no major change in the type of dominant charged imperfections in this range. If this is true, ZnTe can only exist with an excess of Te and is invariably a p-type semiconductor. If there is a change in the type of dominant charged imperfections, however, and such a change is to be expected sooner or later, the phase boundary will cross over to the zinc excess side. The question is, does it occur at a temperature high enough to make possible the establishment of thermodynamic equilibrium in a reasonable time. In any case, attempts to obtain ZnTe with a stoichiometric excess of zinc and showing n-type conduction should be carried out at the lowest temperature at which diffusion still occurs, using the highest possible zinc activity.

A Study of the Radical Termination Mechanisms in the Radiolysis of Crystalline Choline Chloride¹

by Margaret A. Smith and Richard M. Lemmon

Lawrence Radiation Laboratory, University of California, Berkeley, California (Received April 2, 1965)

A search was made for the termination mechanism in the radical-induced decomposition of irradiated crystalline choline chloride. It appears that the chain propagating radical, $\text{CH}_3\dot{\text{C}}\text{HOH}$ or $\cdot\text{CH}_2\text{CH}_2\text{OH}$, terminates by reaction with another radical [possibly $(\text{CH}_3)_3\dot{\text{N}}\cdot$] that propagates into its vicinity. Other possible radical termination mechanisms, such as dimerization to a butanediol or disproportionation to ethanol and acetaldehyde, appear to play only negligible roles.

Crystalline choline chloride, $[(\text{CH}_3)_3\text{NCH}_2\text{CH}_2\text{OH}]^+\text{Cl}^-$, is of considerable interest to radiation chemists because of its extraordinarily high decomposition G value. Under certain conditions of irradiation, it decomposes by a chain reaction that gives $G(-M)$ values as high as 55,000.² The anomalous radiation sensitivity is shown only by the crystalline form; in solution, the compound exhibits normal radiation stability.³ The main radiolysis products are trimethylamine and acetaldehyde.⁴

Electron spin resonance studies of the irradiated crystals have shown the appearance of a free radical with a postulated structure approximating $\cdot\text{CH}_2\text{-CH}_2\text{OH} \leftrightarrow \text{CH}_2\text{CH}_2\dot{\text{O}}\text{H}$.² This structure appears to be stabilized by hydrogen bonding and by crystal cage effects. Kinetic studies indicate that the e.s.r.-observed radical acts to initiate, rather than to propagate, the chain reaction.²

In the present work a study was made of the fate of the observed free radical among the possible dimerization products, 1,4-butanediol and 2,3-butanediol, and the disproportionation product, ethanol. The results of this work give greater weight to the previously postulated radical termination mechanism² (reaction with a different radical, such as $(\text{CH}_3)_3\dot{\text{N}}\cdot$, that propagates into the vicinity).

Experimental Section

Compounds Used. Two different ¹⁴C-labeled choline chlorides were used in this work. The first, $[(\text{CH}_3)_3\text{NCH}_2^{14}\text{CH}_2\text{OH}]^+\text{Cl}^-$, was prepared in this laboratory

from commercially available ethyl bromoacetate-1-¹⁴C (the procedure was described previously⁵). The second, $[(\text{CH}_3)_3\text{N}^{14}\text{CH}_2^{14}\text{CH}_2\text{OH}]^+\text{Cl}^-$, was prepared from the labeled bromide that was obtained from Nuclear Research Chemicals, Inc., Orlando, Fla. In the cases of both labeled choline chlorides we had evidence [(1) preparation of the chloride from either the bromide or iodide shortly before use, (2) paper chromatography] that the compounds were radiopure.

The 2,3-butanediol, used as a carrier in the search for the labeled compound, was obtained from L. Light and Co., Colnbrook, England. The 1,4-butanediol was obtained from Eastman Organic Chemicals. The trimethylsilyl ether derivatives of both diols were prepared by the procedure of Sweeley, *et al.*⁶

In the thin layer chromatographic purification of the ethanol carrier, the ethanol was converted to phenylurethan by reaction with phenyl isocyanate according to standard procedures.⁷

Irradiations. The ¹⁴C-labeled crystalline choline chloride was irradiated either by Co^{60} γ -rays or by an

(1) The work described in this paper was sponsored by the U. S. Atomic Energy Commission.

(2) R. O. Lindblom, R. M. Lemmon, and M. Calvin, *J. Am. Chem. Soc.*, **83**, 2484 (1961).

(3) R. M. Lemmon, *et al.*, *ibid.*, **80**, 2730 (1958).

(4) B. M. Tolbert, *et al.*, *ibid.*, **75**, 1867 (1953).

(5) R. M. Lemmon and M. A. Smith, *ibid.*, **85**, 1395 (1963).

(6) C. C. Sweeley, *et al.*, *ibid.*, **85**, 2497 (1963).

(7) S. M. McElvain, "The Characterization of Organic Compounds," The Macmillan Co., New York, N. Y., 1953, pp. 199, 200.

electron beam from a linear accelerator. In all cases the sample temperature was kept between 25 and 35°. At a given dose rate and total dose, there seems to be little difference between the effects of γ -rays and electron beams on the decomposition of choline chloride.³ The choice of the radiation used was merely one of convenience.

The choline chloride samples were all given a total radiation dose of approximately 50 Mrads. After the irradiation the crystals were allowed to stand for about 20 hr. at room temperature. Under these conditions the choline chloride reaches approximately 12% decomposition.² However, with the short times of irradiation and storage used in the present work, the $G(-M)$ value drops to 15-20, and the "chain length" is back essentially to unity.

Ethanol Determinations. Both gas-liquid partition chromatography (g.l.p.c.) and thin layer chromatography (t.l.c.) of the phenylurethan derivative were used to determine the radioactivity in the ethanol. The g.l.p.c. was carried out on commercial instruments (Wilkens Instrument Co. Models 90 and 350A). These instruments were equipped with flow-through gas proportional counters that permitted monitoring any radioactivity in a g.l.p.c. peak. More accurate measurements of the total activity in a trapped g.l.p.c. peak were made by liquid scintillation counting.

A typical experiment using g.l.p.c. was as follows. A sample of freshly prepared choline chloride (4.79 μ c.) was irradiated with an electron beam (total dose 5×10^7 rads, delivered over about 1 hr.). The sample was dissolved in 500 μ l. of ethanol carrier, and the ethanol was then removed by vacuum transfer. A 200- μ l. aliquot of the ethanol was chromatographed on a Castorwax column (5 ft., 0.25 in., 20% on 60-80 mesh firebrick, 35°, 15 cc. of He/min.) in four 50- μ l. injections. The chromatographed ethanol samples were combined, an aliquot was withdrawn for radioactivity assay, and the remainder was rechromatographed on β -cyanoethyl ether (5 ft., 0.25 in., 20% on 60-80 mesh firebrick, 70°, 15 cc. of He/min.). Again, an aliquot was withdrawn for radioactivity assay and, on the remainder, a third g.l.p.c. purification was carried out on a Carbowax column (5 ft., 0.25 in., 5% on Fluoropak, 80°, 20 cc. of He/min.).

Further determinations of the radiopurity of the ethanol (after it was added as a carrier to irradiated choline chloride) were made by means of thin layer chromatography of the phenylurethan derivative.⁷ The t.l.c. plates were coated with Al_2O_3 (aluminum oxide G from Research Specialties Co., Richmond, Calif.) that contained 0.5% (by wt.) each of zinc silicate and zinc sulfide. When this mixture is used the entire

t.l.c. plate fluoresces under ultraviolet light except in the areas where ultraviolet-absorbing compounds are located.⁸ Preliminary experiments showed that negligible amounts of ultraviolet-absorbing material were removed from this Al_2O_3 -phosphor mixture when it was slurried in acetone or ethanol; consequently, the amount of urethan eluted from the t.l.c. chromatograms could be determined spectrophotometrically (ϵ 1.67×10^4 at 237 $m\mu$). Acetone (2%) in hexane and 7.5% chloroform in hexane were found to be good developing solvents. The best results were obtained when the chromatograms were run at approximately 4°.

A typical experiment using t.l.c. was as follows. An irradiated (5×10^7 rads) choline chloride-1,2-¹⁴C sample (25 mg. containing 2.85 μ c.) was dissolved in 500 μ l. of methanol and 50 μ l. of ethanol. The methanol was removed by g.l.p.c. (in 50- μ l. amounts) on a 5-ft., 0.25-in. column of 20% Castorwax on 60-80 mesh firebrick, at room temperature, with a helium flow rate of 37 cc./min. The combined ethanol fractions were then transferred on a vacuum line into a flask containing 300 μ l. of phenyl isocyanate (Aldrich Chemical Co., Milwaukee, Wis.); usually the reaction mixture was allowed to stand overnight. The excess phenyl isocyanate was removed by evaporation, the resultant crystalline solid was dissolved in 10 ml. of acetone, and 200 μ l. of this solution was streaked on each of five Al_2O_3 t.l.c. plates (20 \times 20 cm.). After the one-dimensional development of the plates with 2% acetone in hexane, the phenylurethan streak from each plate was eluted with absolute ethanol and the eluates were combined. The phenylurethan was then rechromatographed using 7.5% chloroform in hexane as the solvent; a third chromatography was accomplished by a return to the original 2% acetone in hexane system.

Diol Derivative Purifications. Initial attempts to purify the 2,3-butanediol by g.l.p.c. were unsuccessful because of thermal destruction at the high temperatures needed to move the diol through the column. The phenyl isocyanate derivative was also prepared,⁷ but suitable solvents for its chromatographic purification (paper and t.l.c.) were not found. We finally prepared trimethylsilyl ether derivatives of the diols and obtained satisfactory g.l.p.c. purifications of these compounds.

After preparation of the trimethylsilyl ethers by the method of Sweeley,⁶ the ethers were initially purified by g.l.p.c. on a 10-ft., 0.25-in. column of 20% Apiezon L on 60-80 mesh firebrick, at 130°, with a helium flow rate of 30 cc./min. In the case of the ether from the 2,3-diol we obtained a split peak; the ether from

(8) J. W. Sease, *J. Am. Chem. Soc.*, **70**, 3630 (1948).

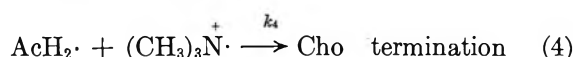
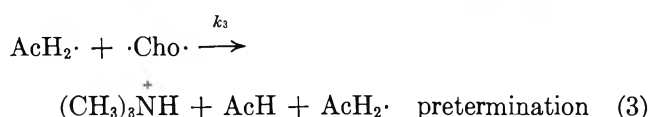
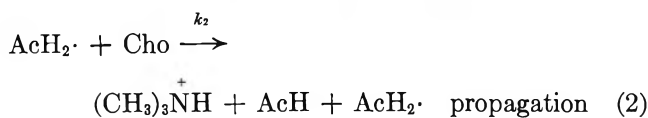
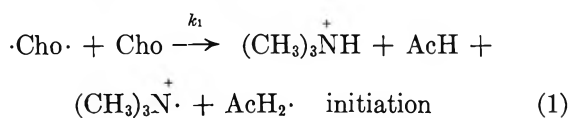
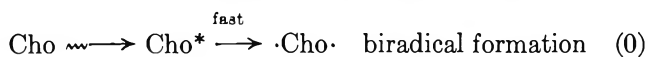
the 1,4-diol gave a single, unsplit peak. Mass spectra (taken on a CEC Model 130 mass spectrometer) of the two split peaks from the 2,3-diol were essentially identical, and we concluded that we had separated the DL- from the *meso* compound. Practically identical mass spectra have been reported for a number of aliphatic diastereomers.⁹ In later work the Apiezon columns were discarded in favor of poly-*m*-phenyl ether and SF-96 (see below).

A typical experiment in the search for labeled 2,3-diol was as follows. Irradiated choline chloride-1,2-¹⁴C (40 mg.), containing 8.63 μ c., was dissolved in 500 μ l. of 2,3-butanediol. The diol was removed from the choline by distillation in a small molecular still. It was dissolved in 600 μ l. of pyridine and to this solution were added 800 μ l. of hexamethyldisilazane (K and K Laboratories, Plainview, N. Y.) and 400 μ l. of trimethylchlorosilane (California Biochemical Corp., Los Angeles, Calif.). The solution was extracted three times with water and dried over MgSO₄, and the product was chromatographed (in 50- μ l. quantities) on the two g.l.p.c. columns: (1) 10-ft., 0.25-in. column of 15% SF-96 on 60-80 mesh firebrick, at 140°, He flow of 15 cc./min.; (2) 10-ft., 0.25-in. column of 15% poly-*m*-phenyl ether on Fluoropak, at 150°, He flow of 15 cc./min.

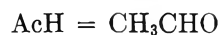
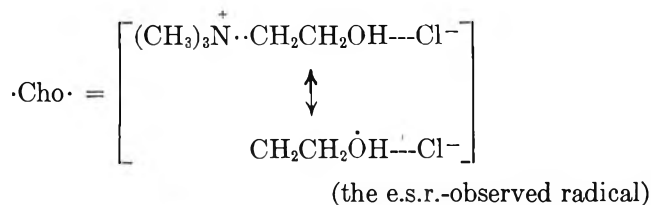
The procedures used to prepare and purify the trimethylsilyl ether from the 1,4-diol were the same as for the 2,3-diol with but one exception: SF-96 was used on a Fluoropak support instead of on firebrick.

Results and Discussion

In determining how much radioactivity we would expect to find in the diols or in the ethanol we assume that the previously postulated decomposition model² (below) is correct, at least through reaction 3.

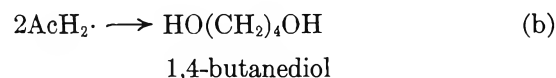
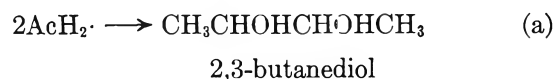


where



The chain propagating radical, AcH₂·, is written in two ways because previous work⁶ has shown that the five hydrogen atoms of the ethanol moiety have considerable mobility during the radiolysis. (It should be emphasized that this is a crystalline-state, chain-mechanism radiolysis. The hydrogen atom mobility is not typical of aqueous-solution radiolyses.)

However, the chain termination mechanism might be, not reaction 4, but one of the following.



Under the irradiation conditions used in the present work we would get about 12% decomposition of the choline chloride with a minimum (approaching unity)

Table I: Activity Appearing in 2,3- and 1,4-Butanediol from Irradiated Choline-1,2-¹⁴C Chloride^a

Expt. no. ^b	Choline chloride irradiated, μ c.	Carrier diol added, mmoles	Sp. act., d.p.m./mmole Expected ^c	Found	% of expected activity
1	8.63	5.81	200,000	49	<0.1
2	7.29	5.81	167,000	0	0
3	10.93	5.66	257,000	13	<0.01
4	1.33	5.66	31,000	12	<0.1

^a Both diols were isolated as the trimethylsilyl ethers; the derivatives were purified on g.l.p.c. columns of (1) SF-96 and (2) poly-*m*-phenyl ether. ^b Experiments 1 and 2 were done with carrier 2,3-butanediol; experiments 3 and 4 were done with the 1,4-diol. ^c Assuming one diol is produced for every four cholines destroyed (*i.e.*, a chain length of unity).

(9) K. Biemann, "Mass Spectrometry—Organic Chemical Applications," McGraw-Hill Book Co., Inc., New York, N. Y., 1962, p. 144.

chain length.² Consequently, we have maximized the chances for reactions a, b, or c to occur.

Assuming a chain length of unity, the production of two $\text{AcH}_2\cdot$ radicals requires the decomposition of four cholines. The activity appearing in a resultant diol could, if this were the only radical termination product, be as high as one-half the activity of the decomposed choline. Similarly, if reaction c represented the fate of the free radical, the resultant ethanol would have one-fourth the activity of the decomposed choline. In Tables I and II the one-half and one-fourth figures are used to calculate the specific activity expected in the diols and ethanol, respectively.

The results of this work show that neither 1,4- nor 2,3-butanediol are detectable products of the choline radiolysis. If they are formed at all, their yields from crystalline choline chloride are below 0.1%. Ethanol is also, at most, only a minor product and can account for the ultimate fate of not more than about 3% of the radical chain-terminating events. It appears that most of the radicals (about 95%) terminate by reaction with another radical that propagates into the vicinity. Previous work has suggested² that this radical may be $(\text{CH}_3)_3\dot{\text{N}}\cdot$ (reaction 4), and the present

Table II: Activity Appearing in Ethanol from Irradiated Choline-1,2-¹⁴C Chloride

Expt. no.	Choline chloride irradiated, μc .	Carrier EtOH added, mmoles	Purification method	Sp. act., $\mu\text{c}/\text{mmole}$		% of expected activity
				Expected ^a	Found	
1	2.85	0.85	T.l.c. ^b	0.10	0.0028	2.8
2	2.85	0.85	T.l.c. ^c	0.10	0.0025	2.5
3	2.85	0.85	T.l.c. ^d	0.10	0.0030	3.0
4	4.79	8.52	G.l.p.c. ^e	0.017	5.6×10^{-4}	3.3
5	4.79	8.52	G.l.p.c. ^f	0.017	5.5×10^{-4}	3.2
6	4.79	8.52	G.l.p.c. ^g	0.017	5.6×10^{-4}	3.3

^a Assuming one ethanol is produced for every four cholines destroyed (*i.e.*, a chain length of unity). ^b One solvent system used: 2% acetone in hexane. ^c Two successive solvents used: (1) 2% acetone in hexane, (2) 7.5% CHCl_3 in hexane. ^d Three successive solvents used: (1) 2% acetone in hexane, (2) 7.5% CHCl_3 in hexane, (3) 2% acetone in hexane. ^e Castorwax column. ^f Two successive g.l.p.c. purifications: (1) Castorwax, (2) β -cyanoethyl ether. ^g Three successive g.l.p.c. purifications: (1) Castorwax, (2) β -cyanoethyl ether, (3) Carbowax.

work, by eliminating other possibilities, adds support to that suggestion.

Definitive Test of the Onsager Reciprocal Relations in Isothermal Ternary Diffusion of Water–Sodium Chloride–Potassium Chloride¹

by Donald G. Miller

Lawrence Radiation Laboratory, University of California, Livermore, California (Received April 5, 1965)

The Onsager reciprocal relations for ternary diffusion in the system H₂O–NaCl–KCl (system I) are verified experimentally by a rigorous test.

An absolute test of the Onsager reciprocal relations (ORR) in isothermal ternary diffusion requires the four diffusion coefficients D_{ij} , partial molal volumes \bar{V}_i , and activity coefficient data at the same composition. Such experimental data existed or were measured for the systems H₂O–NaCl–KCl (one composition),² H₂O–glycine–KCl (six compositions),³ and H₂O–Na₂SO₄–H₂SO₄ (four compositions),⁴ and the ORR were found to be satisfied within the estimated experimental error.

Diffusion coefficients were available for the systems: I, H₂O–NaCl–KCl (four compositions); II, H₂O–LiCl–KCl (one composition); III, H₂O–LiCl–NaCl (one composition); IV, H₂O–raffinose–KCl (two compositions); and V, H₂O–raffinose–urea (one composition) in 1958 when this author gave the first preliminary test of the ORR⁵ (the details were presented in 1959⁶). However, because thermodynamic data did not exist in the appropriate concentration ranges, it was necessary to estimate the activity coefficient derivatives. Dunlop and Gosting,⁷ in giving a similar test for system I only, also estimated activity coefficients but in a different way.

Since then, more accurate thermodynamic data for system I⁸ have become available, which now extend over the whole concentration range where diffusion coefficients exist. Moreover, considerably improved methods for computing the D_{ij} from the raw data have been worked out by Fujita and Gosting,⁹ who recomputed the D_{ij} for system I.

The ORR can now be given a *definitive* test for system I at all five compositions, using the previously unavailable activity data⁸ and the best values of D_{ij} .⁹ This new test is desirable to eliminate completely any

possibility that compensating errors in estimated activity derivatives were responsible for the previous good verification of the ORR.

The results are given in Tables I, II, and III, which may be considered as a collection of the best available data for system I. The notation is that of ref. 3, and calculations were made using equations of ref. 3, 6, and 7. In particular, the $d \ln \gamma_i/dm_j$ were obtained using eq. 19 of ref. 7. The values of $d \ln \gamma_i^0/dm$ were re-determined from existing data¹⁰ using better differentiation techniques than previously. Table I contains the concentration, volumetric, and diffusion data given in mole units, and Table II contains the thermodynamic data in mole units. Table III contains a standard test form for the ORR in terms of the experimentally determined $(D_{ij})_V$ (eq. 29 of ref. 3), as well as the probable experimental error. This test form is better than the difference of the L_{ij} because a common denominator contributing to the uncertainty of each L_{ij} is not present. For comparison, the old test is also given.^{5,11}

(1) This work was performed under the auspices of the U. S. Atomic Energy Commission.

(2) P. J. Dunlop, *J. Phys. Chem.*, **63**, 612 (1959).

(3) L. A. Woolf, D. G. Miller, and L. J. Gosting, *J. Am. Chem. Soc.*, **84**, 317 (1962).

(4) R. P. Wendt, *J. Phys. Chem.*, **66**, 1279 (1962).

(5) D. G. Miller, *ibid.*, **62**, 767 (1958); **63**, 2089 (1959).

(6) D. G. Miller, *ibid.*, **63**, 570 (1959); **63**, 2089 (1959).

(7) P. J. Dunlop and L. J. Gosting, *ibid.*, **63**, 86 (1959).

(8) R. A. Robinson, *ibid.*, **65**, 662 (1961).

(9) H. Fujita and L. J. Gosting, *ibid.*, **64**, 1256 (1960).

(10) R. A. Robinson and R. H. Stokes, "Electrolyte Solutions," 2nd Ed., Butterworth and Co. Ltd., London, 1959, Appendixes 8.3 and 8.10.

Table I: Diffusion Data at 25°^{a-c}

	IA	IB	IC	ID	IE
c_0	54.706	54.443	54.300	54.633	51.140
c_1	0.2500	0.5000	0.2500	0.5000	1.5000
c_2	0.2500	0.2500	0.5000	0.5000	1.5000
d	1.018830	1.028717	1.030165	1.039957	1.120786
\bar{V}_0	18.062	18.057	18.058	18.050	17.961
\bar{V}_1	18.69	19.14	19.12	19.52	21.96
\bar{V}_2	28.87	29.38	29.36	29.90	32.34
m_1	0.2537	0.5098	0.2556	0.5136	1.6282
m_2	0.2537	0.2549	0.5110	0.5136	1.6282
$(D_{11})_V \times 10^6$	1.3729	1.4176	1.3555	1.3865	1.3971
$(D_{12})_V \times 10^6$	-0.0024	-0.0060	0.0008	-0.0021	0.1000
$(D_{21})_V \times 10^6$	0.1422	0.0919	0.1907	0.1570	0.3198
$(D_{22})_V \times 10^6$	1.8224	1.8170	1.8360	1.8314	1.8021
$(D_{11})_0 \times 10^6$	1.3804	1.4328	1.3635	1.4028	1.4641
$(D_{12})_0 \times 10^6$	0.0109	0.0211	0.0145	0.0260	0.1988
$(D_{21})_0 \times 10^6$	0.1497	0.0995	0.2068	0.1733	0.3868
$(D_{22})_0 \times 10^6$	1.8357	1.8305	1.8635	1.8594	1.9009

^a Units: c_i , moles/l.; d , g./ml.; \bar{V}_i , ml./mole; m_i in moles/kg. of solvent; D_{ij} in cm.²/sec. for a mole description. ^b Data for system I obtained or calculated from data in ref. 9. Molecular weights in g./mole: H₂O, 18.02; NaCl, 53.454; KCl, 74.557. ^c More figures are reported than are significant to avoid round-off errors.

Table II: Thermodynamic Data at 25°^{a-c}

	IA	IB	IC	ID	IE
$d \log \gamma_1^0/dm$	-0.06129	-0.02762	-0.02745	-0.01144	0.03761
$d \log \gamma_2^0/dm$	-0.09449	-0.05908	-0.05895	-0.04145	0.00480
ϕ_1^0	0.9210	0.9277	0.9278	0.9365	1.0625
ϕ_2^0	0.8988	0.8970	0.8970	0.8975	0.9437
$d \ln \gamma_1/dm_1$	-0.13588	-0.06136	-0.05881	-0.02376	0.08257
$d \ln \gamma_1/dm_2$	-0.19314	-0.11695	-0.11382	-0.07702	0.03136
$d \ln \gamma_2/dm_1$	-0.19314	-0.11695	-0.11382	-0.07702	0.03136
$d \ln \gamma_2/dm_2$	-0.22335	-0.14170	-0.13852	-0.09917	0.01131
μ_{11}/RT	5.759	3.245	5.249	2.989	1.236
μ_{12}/RT	1.662	1.151	1.156	0.900	0.485
μ_{21}/RT	1.642	1.130	1.136	0.878	0.452
μ_{22}/RT	5.599	5.098	3.104	2.852	1.100
$(L_{11})_V \times 10^8 RT$	0.260	0.472	0.280	0.509	1.289
$(L_{12})_V \times 10^8 RT$	-0.0784	-0.110	-0.105	-0.165	-0.505
$(L_{21})_V \times 10^8 RT$	-0.0766	-0.109	-0.104	-0.159	-0.482
$(L_{22})_V \times 10^8 RT$	0.345	0.378	0.620	0.681	1.743
$(L_{11})_0 \times 10^8 RT$	0.261	0.478	0.281	0.514	1.334
$(L_{12})_0 \times 10^8 RT$	-0.0756	-0.104	-0.100	-0.153	-0.407
$(L_{21})_0 \times 10^8 RT$	-0.0737	-0.102	-0.0984	-0.147	-0.381
$(L_{22})_0 \times 10^8 RT$	0.350	0.382	0.637	0.698	1.896

^a Units: L_{ij}/RT have the units moles/cm. sec. ^b $\log \gamma_i^0$ and ϕ_i^0 for system I are from ref. 10. ^c More figures are reported than are significant to avoid round-off errors.

Examination of Table III for all five compositions of system I shows that the condition for the validity of the ORR (eq. 29 of ref. 3) is satisfied very closely, and well within the experimental error.^{12,13} We conclude therefore that the ORR are definitely verified for system I at all

compositions studied. Thus the ORR have been verified for all three systems for which complete experimental

(11) D. G. Miller, *Chem. Rev.*, **60**, 15 (1960), contains a summary of the 1959 results as well as the results for system IE.

Table III: Test of the Onsager Reciprocal Relations^{a,b}

	IA	IB	IC	ID	IE	II	III	IVA	IVB	V
(10 ⁸ /RT)LHS	3.077	2.137	2.193	1.711	1.106	3.615	3.435	1.522	1.548	0.416
(10 ⁸ /RT)RHS	3.132	2.156	2.218	1.757	1.135	3.756	3.639	1.524	1.239	0.325
Difference	-0.06	-0.02	-0.02	-0.05	-0.03	-0.14	-0.20	0.00	0.31	0.09
Old difference	-0.12	-0.03	-0.05	-0.04	-0.04	-0.07	-0.21	0.00	0.39	0.09
Probable error	0.12	0.08	0.07	0.05	0.06	0.17	0.20	0.27	0.21	0.10

^a RHS and LHS refer to the right-hand and left-hand sides of eq. 29 of ref. 3 (originally given in ref. 5). Difference is (10⁸/RT) · (LHS - RHS). ^b The probable experimental errors and old differences are from ref. 11 (all but IE are in ref. 6).

data exist (H₂O-NaCl-KCl, H₂O-glycine-KCl, and H₂O-Na₂SO₄-H₂SO₄).

Systems II, III, IV, and V cannot be given a definitive test until experimental activity data become available. However, Dunlop¹⁴ has recently given experimental \bar{V}_i and has recomputed the D_{ij} by the new method.⁹ These new data together with new estimates of $d \ln \gamma_i / dm_j$ for systems II and III¹⁵ have been used to compute the ORR test form. The entries in Tables I and II have been omitted here¹⁷ because no definitive test was possible, but the test form is included in Table III. The results are that little is changed from the previous test⁶ except (1) agreement for II is not as good as before but is still within the experimental error, and (2) there is substantial improvement for system IVB, but the difference is still outside the original estimated experimental error (which may be too low).

Acknowledgment. The author is indebted to Mr. Joseph Brady of the Computation Division of Lawrence Radiation Laboratory for aid in the calculations.

(12) The differences are slightly smaller than those using the improved D_{ij} ⁹ with the Dunlop-Gosting approximation.⁷

(13) It is a curious but undoubtedly fortuitous fact that L_{12} is greater than L_{21} when 1 refers to the ion most hydrated and of smallest size in these two-electrolyte systems.

(14) P. J. Dunlop, *J. Phys. Chem.*, **68**, 3062 (1964).

(15) The Dunlop-Gosting approximation⁷ was used with the appropriate data,¹⁶ hopefully because this approximation was closest to the experimental data for system I. There are some reservations about it, however, because Harned's α_i change so rapidly with concentration at low concentrations.

(16) R. A. Robinson and C. K. Lim, *Trans. Faraday Soc.*, **49**, 1144 (1953).

(17) They are available in D. G. Miller, UCRL-12462, March 1965

Reactivity and Surface Composition. Anodic Methanol Oxidation on Platinum-Gold Alloys

by M. W. Breiter

General Electric Research Laboratory, Schenectady, New York (Received April 5, 1965)

The anodic oxidation of methanol in 0.5 M H₂SO₄ was studied on heterogeneous platinum-gold alloys whose surface composition is known from voltammetric current-potential curves measured in the absence of methanol. Periodic current-potential curves were taken potentiostatically in the potential range between hydrogen and oxygen evolution with 30 mv./sec. at methanol bulk concentrations between 0.004 and 1 M. The ohmic and capacitive component of the impedance was determined by voltammetry with superimposed alternating voltage. The rate of methanol oxidation which was characterized by different kinetic parameters depends in the same way upon the bulk composition of the alloys as the amount of the platinum-rich phase on the surface. As a first approximation the rate is proportional to the amount of the platinum-rich phase on the surface. Methanol oxidation occurs only on this phase. The results on the inhibition of methanol oxidation by oxygen layers lead to the same conclusion. There is no direct correlation between the reactivity and the d-band character of the platinum-gold alloys. Different mechanisms of the anodic oxidation of methanol on platinum or the platinum-rich phase are evaluated critically.

Introduction

It is known that systematic changes of the reactivity of a catalyst may be produced by alloying it with increasing amounts of another metal whose catalytic properties differ from that of the catalyst. If the influence of transport processes is negligible, the reactivity may be expressed by the rate constant of the rate-determining step of the same net reaction on the alloys or by equivalent kinetic parameters. Similar statements apply to electrochemical reactions in which the electrode affects the state of the reactants and intermediates.¹ Usually it is assumed in the interpretation of kinetic data of the above type that the surface composition is equal to that of the bulk for each of the alloys. Indirect evidence like self-consistency of the results or independence of the reactivity of extended pretreatment have been reported in support of this assumption since its experimental verification is difficult in most cases. To avoid these uncertainties it appeared desirable to the author to study an electrochemical reaction on a set of alloys for which the surface composition may be determined in an independent way.

Experimental results on the anodic methanol oxidation in acidic solutions will be reported and discussed for heterogeneous platinum-gold alloys in this communication. These alloys are composed² of a platinum-rich phase α_1 and a gold-rich phase α_2 . It was found that the phase α_1 behaves like platinum with respect to the electrochemical formation and removal of the oxygen layer³ and of the layer of adsorbed hydrogen atoms⁴ while the phase α_2 has the electrochemical properties of gold. These conclusions were derived from the following results. Voltammetric current-potential curves may be constructed³ in a first approximation according to the equation

$$I(U) = a'I_{Pt}(U) + b'I_{Au}(U) \quad (1)$$

from the respective curves on smooth platinum and gold in acidic solution. The parameter a' agrees⁴ well with another parameter c' for a given alloy.

(1) R. Parsons, *Surface Sci.*, **2**, 418 (1964).

(2) See A. S. Darling, *Platinum Metals Rev.*, **6**, 60, 106 (1962).

(3) M. W. Breiter, *J. Phys. Chem.*, **69**, 901 (1965).

(4) M. W. Breiter, *Trans. Faraday Soc.*, **61**, 749 (1964).

$$c' = {}_sQ_{\text{H}}/{}_sQ_{\text{H,Pl}} \quad (2)$$

Here I designates the current density, U the potential, a' and b' are constants⁴ determined by a least-square fit. ${}_sQ_{\text{H}}$ is the total amount of adsorbed hydrogen atoms on each of the alloys in millicoulombs per square centimeter, ${}_sQ_{\text{H,Pl}}$ that on platinum as obtained by the integration of $I-U$ curves in the so-called⁵ hydrogen region. The parameters a' (or c') and b' represent a relative measure^{3,4} of the amount of the phase α_1 and α_2 , respectively, on the surface. It is a relative measure since the roughness factors are included in a' and b' . This allows the kinetic data on methanol oxidation to be correlated to those on the surface composition. Methanol oxidation was chosen as a suitable reaction for several reasons. As on platinum,^{6,7} the influence of transport processes is negligible at the foot and in the rising portion of the first wave during the anodic sweep in acidic solutions. Kinetic data are analyzed in this region. The rate of methanol oxidation on gold is much smaller⁸ than that on platinum. The anodic methanol oxidation is inhibited by oxygen layers on platinum metals.⁶⁻⁸ Since the formation (or reduction) of the oxygen layers on the phases α_1 and α_2 , respectively, occurs in the same potential ranges on all the alloys, the inhibiting effect of the oxygen layers on methanol oxidation may be expected to be the same. Different mechanisms⁶⁻¹⁵ have been suggested for the anodic oxidation of methanol on platinum. Earlier work is reviewed extensively in these papers. A critical evaluation of the recent mechanisms will be given under consideration of the new results in this paper.

Experimental Section

The electrodes were prepared as described³ from the supply of platinum-gold alloys delivered in form of wires by the Sigmund Cohn Corp., New York, N. Y. The gold content of the alloys studied was 5, 10, 20-70 atom %. The measurements were carried out at 30° in a Pyrex vessel of conventional design in quiescent solutions. The solutions were made from A.R. sulfuric acid, double-distilled water, and A.R. methanol. Molecular oxygen was removed by stirring the solutions extensively with purified helium before the actual measurements. The electrode potential U was measured against a hydrogen electrode in the same solution as the test electrode. The current density I and the capacitive component $1/\omega C_s$ of the interfacial impedance in a series circuit were computed on the basis of the geometric surface area of the electrodes.

The assembly for the measurements of voltammetric $I-U$ curves and of the ohmic and capacitive component

of the impedance by voltammetry with superimposed alternating voltage was described previously.¹⁶ The sweep rate was 30 mv./sec., and the frequency for the impedance measurements was 1000 c.p.s. The measurements were always carried out on all the alloy electrodes in the same solution (0.5 M H_2SO_4 + X M CH_3OH ; $X = 0, 0.004, 0.01, 0.1, 1$). The procedure was the same for every electrode: cleaning in hot chromic acid solution, thorough rinsing in double-distilled water, insertion in the solution, and removing of traces of molecular oxygen from the solution by He stirring with the electrode at open circuit. The recording of the $I-U$ curves and of the $1/\omega C_s-U$ curves was started after the 20th cycle. It takes about 15 cycles before the curves approach a shape which changes only slightly with the number of subsequent cycles. The initial behavior is attributed as in the previous studies^{3,4} in 1 N H_2SO_4 to the removal of impurities from the surface by the intermediate formation of the oxygen layers. The $I-U$ curves and $1/\omega C_s-U$ curves were recorded on the Varian F80 X-Y recorder if a large resolution was required. Otherwise they were photographed from the screen of the Tektronix oscilloscope 502.

Results

Different experimental curves are put together as an example for the measurements on the 30 atom % Au alloy in Figure 1. The curves are reproductions of the original traces. Solid lines represent anodic sweeps; dashed lines correspond to cathodic sweeps. Curves a and b were recorded in the absence of methanol, curves a' and b' in 0.5 M H_2SO_4 + 0.1 M CH_3OH . Curve a exhibits the three regions which are characteristic⁹ for platinum: hydrogen region (0 to 0.4 v.), double-layer region (0.4 to 0.6 v.), and region of the oxygen layer (0.6 to 1.5 v.). The reduction waves of the oxygen layers on the phases α_1 and α_2

(5) A. Slygin and A. Frumkin, *Acta Physicochim. URSS*, **3**, 791 (1935).

(6) M. W. Breiter and S. Gilman, *J. Electrochem. Soc.*, **109**, 1099 (1962); **110**, 449 (1963).

(7) M. W. Breiter, *ibid.*, **110**, 1005 (1963).

(8) M. W. Breiter, *Electrochim. Acta*, **8**, 973 (1963).

(9) R. P. Buck and L. R. Griffith, *J. Electrochem. Soc.*, **109**, 1005 (1962).

(10) W. Vielstich, *Z. Instrumentenk.*, **71**, 29 (1963).

(11) J. Giner, *Electrochim. Acta*, **9**, 63 (1964).

(12) S. Gilman, *J. Phys. Chem.*, **68**, 70 (1964).

(13) V. S. Bagotzky and Yu. B. Vasilyev, *Electrochim. Acta*, **9**, 869 (1964).

(14) J. E. Oxley, G. K. Johnson, and B. T. Buzalski, *ibid.*, **9**, 897 (1964).

(15) C. Liang and T. C. Franklin, *ibid.*, **9**, 517 (1964).

(16) M. W. Breiter, *J. Electroanal. Chem.*, **7**, 38 (1964).

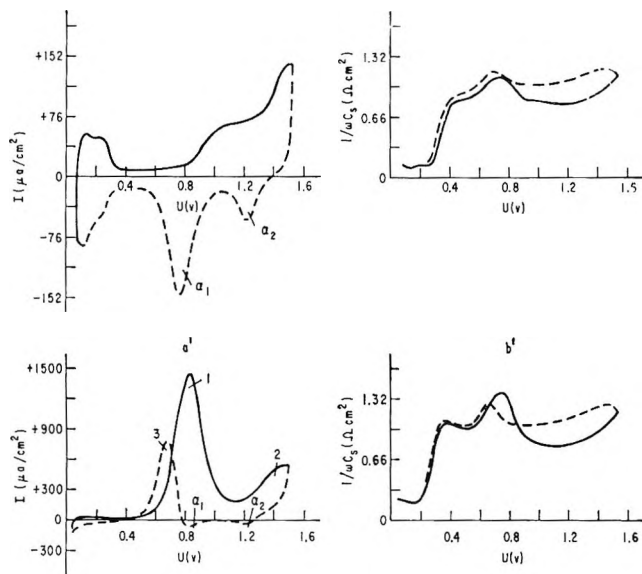


Figure 1. Periodic current-potential curves (a and a') and capacitive component-potential curves (b and b') at 1000 c.p.s. on the 30 atom % Au alloy at 30 mv./sec.: a and b in 0.5 M H_2SO_4 ; a' and b' in 0.5 M H_2SO_4 + 0.1 M CH_3OH .

are marked. As to be expected on the basis of the common supply the I - U curve of each of the alloys coincided in the oxygen region with the previous³ curve of the same alloy. Thus the parameters a' , b' , c' of the preceding communications^{3,4} may be used here to characterize the surface composition.

The $1/\omega C_s$ - U curve b reflects as on platinum¹⁶ the same regions as the I - U curve a. The capacitive component has small values in the hydrogen region because of the large pseudo-capacity¹⁷ of adsorbed H atoms. The transition from the double-layer region to the potential region of the oxygen layer is less steep in curve b than on platinum.¹⁶ This is attributed to the presence of the α_2 phase. The influence of the α_2 phase on the shape of $1/\omega C_s$ - U curves is better discernible at gold contents above 50 atom %. A relatively large amount of the α_2 phase is required since the double-layer capacities of the two phases are in parallel and since the capacity of the phase α_2 is smaller than that of the phase α_1 . The R_s - U curve which is not shown does not yield any additional information. Since the impedance is largely capacitive here, the $1/\omega C_s$ - U curves give more detailed information in general than the R_s - U curves.

Curve a' exhibits the methanol oxidation waves 1 and 2 during the anodic sweep and wave 3 during the cathodic sweep. It looks very similar to the curve on platinum.⁶ As on platinum^{6,13} the peak current densities of the three waves are considerably smaller than are computed⁶ for a diffusion-controlled process at

${}_0C_M \geq 0.01$ M under the present conditions. Thus the influence of transport processes is negligible. The comparison of curve a' with curve a shows that the rising portion of wave 1 below 0.7 v. is in the potential region of negligible oxygen coverage. The formation of the oxygen layer on the phase α_2 starts at about 0.75 v. during the anodic sweep. Thus the peak of wave 1 is attributed as on platinum^{6,13} to the inhibiting effect of the oxygen layer, here on the phase α_2 . Wave 2 is located in the potential region of large oxygen coverages and will not be discussed in detail for this reason. The two reduction waves of the oxygen layers on the phases α_1 and α_2 are just recognizable in curve a' . A methanol oxidation wave does not exist between 1.10 and 0.9 v. during the cathodic sweep although the phase α_2 is free of its oxygen layer. Wave 3 appears when part of the oxygen layer on the phase α_1 has been reduced. Based on the analysis of the effect of the oxygen layers on methanol oxidation, it is concluded that methanol oxidation occurs at a noticeable rate only on the platinum-rich phase of the alloys. This conclusion will be confirmed subsequently by the strong evidence from the correlation between the rate of methanol oxidation and the composition of the alloys.

Evidence for the adsorption of methanol on the alloy with 30 atom % Au is presented by curve b' (see also Figure 2, curve b). The pseudo-capacity in the hydrogen region is smaller in curve b' than in curve b because methanol molecules occupy partly the sites for hydrogen adsorption. Methanol molecules are adsorbed in the double-layer region since the capacity is smaller in the presence than in the absence of methanol. This makes the double-layer region look broader in curve b' than curve b. The formation of the oxygen layer starts at about 0.75 v. during the anodic sweep as indicated by the rapid increase of the capacity between 0.75 and 0.85 v. in curves b and b' . The values of $1/\omega C_s$ do not differ much for curves b and b' in the potential region of the oxygen layer. Methanol adsorption is negligible there. These results correspond to those on platinum⁶ which were obtained by different techniques.

The rate I_M of methanol oxidation at ${}_0C_M = 1$ M is plotted as a function of potential in the rising portion of wave 1 for different alloys in Figure 3. I_M is practically equal to the current density at gold contents below 30 atom %; otherwise

$$I_M(U) = I(U) - I_R \quad (3)$$

The residual current density I_R was determined as the minimal value of the current density between 0.2 and

(17) P. Dolin and B. Ershler, *Acta Physicochim. URSS*, 8, 747 (1940).

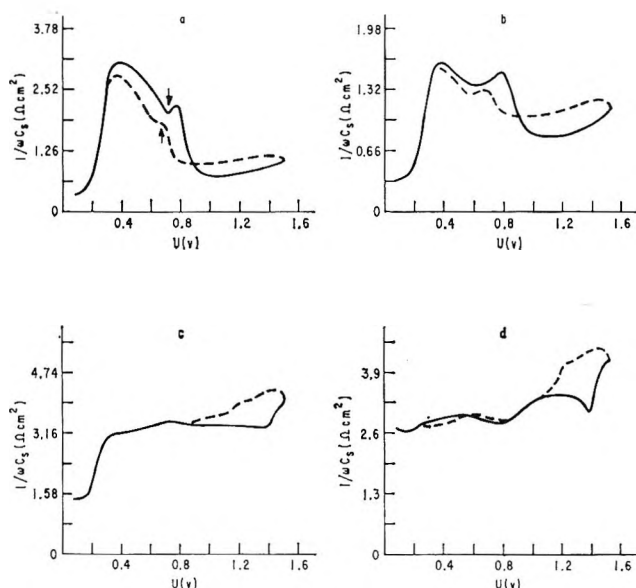


Figure 2. Capacitive component-potential curves in 0.5 M $\text{H}_2\text{SO}_4 + 1 \text{ M CH}_3\text{OH}$ on different alloys: curve a, 10 atom % Au; curve b, 30 atom % Au; curve c, 50 atom % Au; curve d, 70 atom % Au.

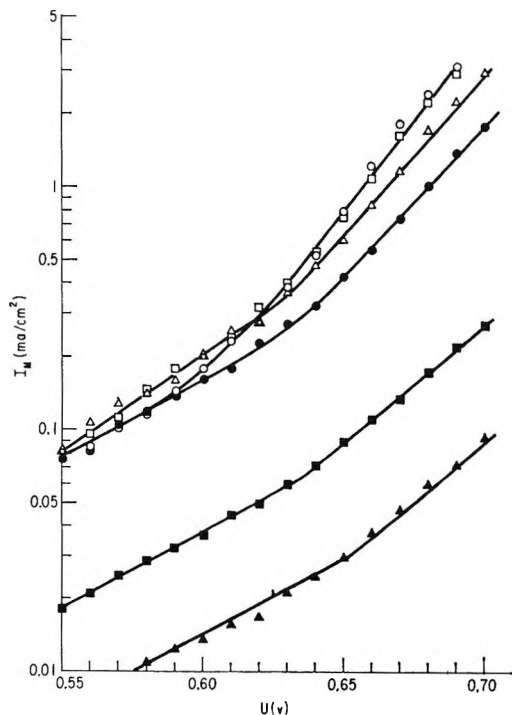


Figure 3. Tafel plots of the rate of methanol oxidation in 0.5 M $\text{H}_2\text{SO}_4 + 1 \text{ M CH}_3\text{OH}$ on different alloys in the rising portion of wave 1: O, 5 atom % Au; □, 10 atom % Au; Δ, 20 atom % Au; ●, 30 atom % Au; ■, 40 atom % Au; ▲, 50 atom % Au.

0.5 v. during the anodic sweep. The semilogarithmic plots show the existence of two different Tafel regions

for each of the alloys. The rate I_M does not differ much at a given potential for the alloys with gold contents up to 20 atom %. Then it decreases rapidly with the gold content above 30 atom %. Similar plots are obtained at the other methanol bulk concentrations. However, they are less reliable in the lower Tafel region since the corrective term I_R becomes larger with decreasing ${}_0C_M$.

Conclusions on the mechanism of methanol oxidation have been derived^{6,13} from the rising portion of wave 1 for $U > 0.65$ v. The results in Figure 3 establish that the mechanism at low potentials ($U < 0.65$ v.) is different from that at potentials above 0.65 v. At $U > 0.65$ v. the slope b of the Tafel line

$$U = a + b \log I \quad (4)$$

is 68 mv. ($\alpha_n = 0.85$) for the alloys with 5 and 10 atom % Au, 82 mv. ($\alpha_n = 0.71$) for the 30 atom % Au alloy, and 106 mv. ($\alpha_n = 0.55$) for the 40 and 50 atom % Au alloys, where

$$\alpha_n = \frac{2.3RT}{bF} \quad (4a)$$

The b values of the alloys with gold contents between 5 and 30 atom % Au are close to the value of 86 mv. ($\alpha_n = 0.67$) found⁶ on platinum. In the Tafel region below 0.65 v. the b value increases from 143 mv. ($\alpha_n = 0.4$) for the alloys with 10 and 20 atom % Au to 161 mv. ($\alpha_n = 0.36$) for the alloys with 40 and 50 atom % Au. The small decrease of θ_M with potential below 0.7 v. was neglected in the determination of the b values. This appears justified by the results on platinum⁶ at ${}_0C_M = 1 \text{ M}$.

The change of the shape of the $1/\omega C_s - U$ curves with increasing gold content (10, 30, 50, 70 atom %) is illustrated at ${}_0C_M = 1 \text{ M}$ in Figure 2. Curve a on the 10 atom % Au alloy is very similar to the curve on platinum.⁸ Hydrogen adsorption has been largely replaced by adsorption of methanol. A considerable decrease of the double-layer capacity results from methanol adsorption in the double-layer region. During the anodic sweep the beginning of the formation of the oxygen layer is paralleled by the removal of the adsorbed methanol molecules. During the cathodic sweep methanol adsorption starts after the oxygen layer has been largely reduced. Small humps which are marked by arrows in curve a appear in the curves of the 5 and 10 atom % Au alloys as on platinum⁸ at ${}_0C_M \geq 0.1 \text{ M}$. They are characteristic for the removal or the formation of an adsorbed layer of organic species as on mercury.¹⁸ These humps are not detectable any more

(18) A. N. Frumkin and V. I. Melik-Gaikazyan, *Dokl. Akad. Nauk SSSR*, 77, 855 (1951).

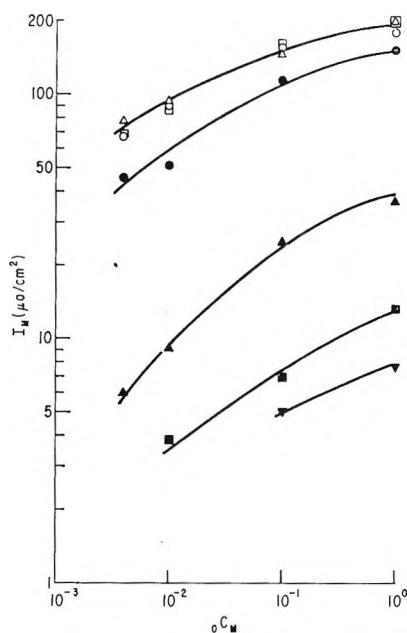


Figure 4. Rate of methanol oxidation at 0.6 v. during the anodic sweep as a function of the bulk concentration of methanol: O, 5 atom % Au; □, 10 atom % Au; Δ, 20 atom % Au; ●, 30 atom % Au; ▲, 40 atom % Au; ■, 50 atom % Au; ▼, 70 atom % Au.

at gold contents above 10 atom % at $oC_M \leq 1 M$. The transition from the double-layer region to the region of the oxygen layer becomes less pronounced with increasing gold content and is not discernible above 40 atom % Au any longer. It is concluded from the small variation of the capacity between 0.4 and 1.0 v. during the anodic and cathodic sweep on the alloys with gold contents above 40 atom % that methanol adsorption on the phase α_2 is negligibly small. This is in agreement with previous results⁸ on gold.

The rate I_M of methanol oxidation at 0.6 v. during the anodic sweep is plotted as a function of the methanol bulk concentration for different alloys in Figure 4. I_M was determined according to eq. 3. The corrective term I_R is very small at $oC_M \geq 0.01 M$ for the alloys with gold contents below 30 atom %. The above potential is located in the lower Tafel region of Figure 3. The shape of the upper three curves in Figure 4 is similar to that of adsorption isotherms. I_M does not increase much with oC_M and tends toward a limiting value which is nearly reached at $oC_M = 1 M$. Similar results are obtained at other potentials in the lower Tafel region. It is concluded that I_M represents the rate of oxidation of adsorbed molecules. The variation of I_M with the composition of the alloys is also illustrated by Figure 4. The alloys with 5, 10, and 20 atom % Au possess nearly the same reactivity. Above

20 atom % Au the rate \bar{I}_M decreases rapidly with the gold content.

It was found that the peak currents I_P of the waves 1 and 3 depended in a characteristic way upon the gold content. As on platinum,⁶ these peak currents decrease slightly with stirring on the platinum-rich alloys, indicating the influence of the diffusion of formic acid which is formed as an intermediate from the oxidation of CH_3OH to CO_2 . The peak currents are plotted in Figure 5 for $oC_M = 1 M$ and $oC_M = 0.01 M$ as a func-

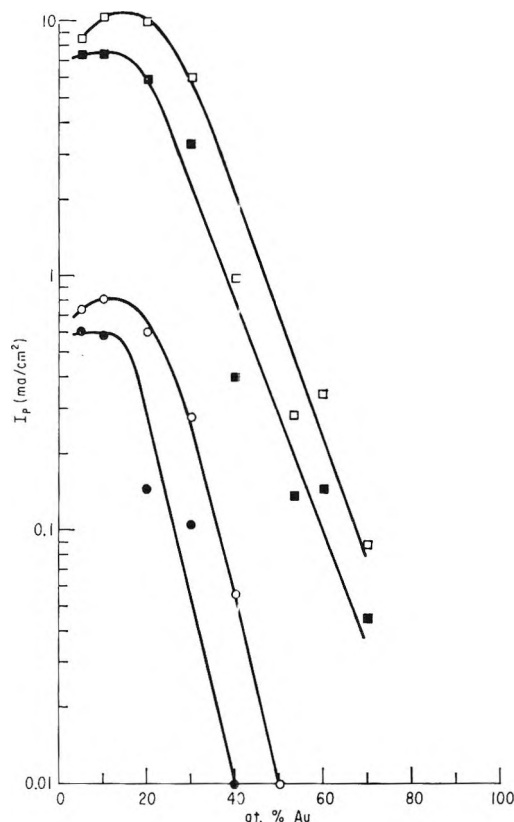


Figure 5. Rate of methanol oxidation at the peaks of waves 1 and 3 as a function of bulk composition of the alloys: □, wave 1, 1 M CH_3OH ; ○, wave 1, 0.01 M CH_3OH ; ■, wave 3, 1 M CH_3OH ; ●, wave 3, 0.01 M CH_3OH .

tion of the bulk composition of the alloys. The curves in Figure 5 have a parabolic shape. The variation of I_P with increasing gold content is small up to 20 atom %. Above this value the peak currents decrease rapidly with the gold content. It was demonstrated for platinum⁶ that the methanol coverage is negligibly small at the peak potentials during the respective sweeps. The same conclusion was derived here from the $1/\omega C_s-U$ curves for the platinum-gold alloys. Thus I_P is representative of the inhibited rate of methanol oxidation on a surface with a small oxygen coverage.

Discussion

Reactivity and Surface Composition. The parameters a' and c' which are a measure for the amount of the platinum-rich phase on the surface are plotted in Figure 6 as a function of the bulk composition of the alloys. The resulting curve 1 has a parabolic shape. The increase of a' and c' between 0 and 20 atom % Au was attributed³ to an increase of the roughness factor of the phase α_1 . This increase overcompensates the decrease of a' which is due to the gradual replacement of the phase α_1 . Above 20 atom % Au the phase α_1 is rapidly replaced by the phase α_2 with increasing gold content. The results in Figures 4 and 5 were used to obtain curve 2. The ratio $I_M/I_{M,\max}$ was computed at $0C_M = 0.1 M$ for different compositions from the data in Figure 4 with $I_{M,\max} = 150 \mu\text{a./cm.}^2$. From the data in Figure 5 the ratio $I_P/I_{P,\max}$ was determined for wave 1 as a function of composition at $0C_M = 1 M$ with $I_{P,\max} = 10 \text{ ma./cm.}^2$. Then the different scales of the ordinate for the curves 1 and 2 were normalized as shown in Figure 5.

The shape of curve 2 in Figure 6 is very similar to that of curve 1. The specific reactivities I_M and I_P depend in nearly the same way upon the bulk composition as the amount of the platinum-rich phase on the surface. In a first approximation I_M and I_P are proportional to the amount of the phase α_1 on the surface. This is direct evidence that methanol oxidation occurs at a noticeable rate only on the phase α_1 . Since each of these two rates is proportional to the product of a rate constant and the electrochemically active part of the geometric surface area, it is concluded that the respective rate constant remains nearly independent of the amount of the phase α_2 on the surface. However, there exist systematic deviations from this rule at gold contents above 40 atom % as the comparison between curve 1 and 2 shows. These deviations are paralleled by the increase of the b values found from results in Figure 3.

The fact that $I_M/I_{M,\max}$ and $I_P/I_{P,\max}$ depend in the same way upon the bulk composition implies that the inhibition of methanol oxidation at the peak of wave 1 by the oxygen layer on the phase α_1 is nearly the same for all the alloys. A similar statement holds for the inhibition at the peak of wave 3 according to the results in Figure 5.

In recent years variations in the reactivity of the same electrochemical reaction have been correlated¹⁹ to the change of the d-band character of alloys. Usually the d-band character on the surface is assumed equal to that of the bulk. It may be easily checked if such a correlation exists between the specific reactivities I_M and I_P of methanol oxidation and the d-band

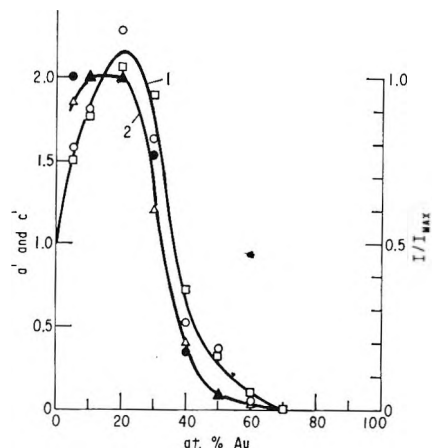


Figure 6. Parameters a' and c' , measuring the amount of the platinum-rich phase on the surface, and ratio I/I_{\max} as functions of bulk composition: curve 1: \square , a' ; \circ , c' ; curve 2: \triangle , $I_P/I_{P,\max}$ for wave 1 at $1 M$ CH_3OH ; \bullet , $I_M/I_{M,\max}$ for $0.6 v.$ at $1 M$ CH_3OH .

character of the bulk of platinum-gold alloys. The d-band character was computed^{20,21} under the assumption that the d band of platinum is gradually filled with increasing gold content. The filling of the d band is achieved^{20,21} between 30 and 40 atom % Au for homogeneous alloys. It occurs²⁰ at even smaller gold contents for heterogeneous alloys. Figure 6 demonstrates that the reactivities decrease more slowly with gold content than it should be if the decrease were controlled by the d-band character. The present system exemplifies the oversimplification on which correlations between reactivity and d-band character are based. In most cases the d-band character on the surface will not be equal to that of the bulk and there is no reliable method to determine the d-band character of the surface.

Mechanism of Methanol Oxidation in the Upper Tafel Region. It was demonstrated in the preceding section that the platinum-rich phase has the electrochemical properties of platinum with respect to methanol oxidation in acidic solution. Therefore, the conclusions for platinum which were derived^{6,7} for the first time with consideration of the coverage θ_M under working conditions apply also to platinum-gold alloys. Both the

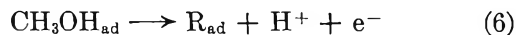


adsorption step and the subsequent discharge step (6)

(19) M. Oikawa, *Bull. Chem. Soc. Japan*, **28**, 626 (1955); S. Schuldiner and J. P. Hoare, *J. Phys. Chem.*, **61**, 705 (1957); H. H. Uhlig, *Z. Elektrochem.*, **62**, 626, 700 (1958).

(20) K. A. Lapteva, I. R. Borissova, and M. G. Slinko, *Zh. Fiz. Khim.*, **30**, 61 (1956).

(21) R. J. Weiss and K. J. Tauber, *Phys. Chem. Solids*, **7**, 249 (1958).



were established as rate-determining steps at ${}_0C_M \geq 0.01 M$ in $1 N \text{HClO}_4$ in the rising portion of wave 1 between about 0.68 and 0.78 v. during the anodic sweep and in the falling portion of wave 3 between about 0.7 and 0.6 v. during the cathodic sweep. The results do not allow the specification of the configuration of the radical R beyond its net composition CH_3O . Similarly the single steps of eq. 6 are not known. It should be pointed out that the mechanism predicts satisfactorily the pH dependence observed^{9,13} experimentally since the potential U , measured against a hydrogen electrode in the same solution as the test electrode, differs in a first approximation only by a constant from η , the overvoltage of methanol oxidation, at methanol bulk concentrations between 0.01 and $1 M$.

Mechanism of Methanol Oxidation in the Lower

Tafel Region. In general it is difficult to elucidate the mechanism of the anodic oxidation of fuels at low potentials. The current densities are small there. Side reactions whose contributions do not matter at larger oxidation rates have to be considered. The subsequent conclusions on methanol oxidation in the lower Tafel region are tentative. The α_n values of the lower Tafel region in Figure 3 and the results in Figure 4 suggest that a reaction of the type 6 is rate-determining. The existence of two Tafel regions may be attributed to different heats of adsorption of the species ($\text{CH}_3\text{OH}_{\text{ad}}$ or R_{ad}) of reaction 6 in the respective regions. The exchange current densities which are obtained by extrapolation of the Tafel lines, for instance to $U = 0$, are larger in the lower Tafel region than in the upper one. Loosely bonded methanol molecules⁷ are oxidized in the lower Tafel region. This may lead to a different configuration of R.

The Gel Melting Point as a Measure of the Tacticity of Poly(methyl methacrylate)

by Charles F. Ryan and Paul C. Fleischer, Jr.

Research Division, Rohm & Haas Company, Bristol, Pennsylvania (Received April 5, 1965)

When solutions of isotactic and syndiotactic polymers in dimethylformamide are mixed, a thermally reversible gel is formed. Melting points of these gels formed in dimethylformamide from various syndiotactic poly(methyl methacrylate) samples and a standard sample of isotactic poly(methyl methacrylate) correlate well with X-ray observations, infrared J values, and n.m.r. measurements made on the syndiotactic polymer. Comparison of gel melting point and n.m.r. results leads us to believe that the gel melting point measures some relative weighted average sequence length of syndiotactic placements in the polymer. The gel melting points of isotactic whole polymers, as measured against a standard syndiotactic polymer, indicate that the isotactic sequence length is quite long. Data obtained on isotactic polymer fractions indicate that 8 to 10 monomer units are required for gel formation. This result is in excellent agreement with the kinetic studies of Glusker, *et al.* The relative tactic sequence lengths of the syndiotactic and isotactic placements contained within type III poly(methyl methacrylate) were estimated from gel melting point measurements. Such measurements have indicated that in certain polymers the lengths of both the syndiotactic and isotactic sequences of the polymer are very short.

Introduction

The preparation of several different crystallizable forms of stereoregular poly(methyl methacrylate) has been described in the literature.¹⁻⁸ These species have been characterized through their different X-ray diffraction patterns,^{1-5,7} infrared spectra,^{1,3-8} far-ultraviolet spectra,⁹ densities,¹ glass temperatures,^{1,5,8,10} dielectric loss curves,^{5,11-13} mechanical properties,¹⁴ and both broad-band⁵ and high-resolution^{15,16} n.m.r. spectra. Differences in rates of hydrolysis have been demonstrated also.¹⁷

Certain of these measurements have given direct information on the structure of these polymers. The X-ray diffraction studies of Stroupe and Hughes² identify the type-II polymer of Fox, *et al.*¹ (apparently identical with the Miller, *et al.*, α polymer⁴), as isotactic, and Miller, *et al.*,⁴ agree with this conclusion. Independent confirmation of this steric arrangement was provided by high-resolution n.m.r. spectra,¹⁵ and this method has also indicated that the Fox type-I polymer is syndiotactic. The Fox type-III polymer (apparently

identical with the Miller, *et al.*, β polymer⁴ and the Kawasaki, *et al.*, F polymer⁷) appears, from hydrolysis rate studies¹⁷ and high-resolution n.m.r. measurements¹⁵

- (1) T. G. Fox, B. S. Garrett, W. E. Goode, S. Gratch, J. F. Kincaid, A. Spell, and J. D. Stroupe, *J. Am. Chem. Soc.*, **80**, 1768 (1958).
- (2) J. D. Stroupe and R. E. Hughes, *ibid.*, **80**, 2341 (1958).
- (3) T. G. Fox, W. E. Goode, S. Gratch, C. M. Huggett, J. F. Kincaid, A. Spell, and J. D. Stroupe, *J. Polymer Sci.*, **31**, 173 (1958).
- (4) R. G. J. Miller, B. Mills, P. A. Small, A. Turner-Jones, and D. G. M. Wood, *Chem. Ind. (London)*, 1323 (1958).
- (5) A. A. Korotkov, S. P. Mitsengendler, V. N. Krasulina, and L. A. Volkova, *Vysokomolekul. Soedin.*, **1**, 1319 (1959).
- (6) U. Bauman, H. Schreiber, and K. Tessmar, *Makromol. Chem.*, **36**, 81 (1959).
- (7) A. Kawasaki, J. Furukawa, T. Tsuruta, S. Inoue, and K. Ito, *ibid.*, **36**, 260 (1960).
- (8) W. E. Goode, F. H. Owens, R. P. Fellmann, W. H. Snyder, and J. E. Moore, *J. Polymer Sci.*, **56**, 317 (1960).
- (9) M. D'Alagni, P. DeSantis, A. H. Liquori, and M. Savino, *ibid.*, **B2**, 925 (1964).
- (10) J. A. Shetter, *ibid.*, **B1**, 209 (1963).
- (11) H. A. Pohl, R. Bacskai, and W. P. Purcell, *J. Phys. Chem.*, **64**, 1701 (1960).
- (12) N. S. Steck, *SPE Trans.*, **4**, 1 (1964).

to be composed of blocks of relatively high proportions of relatively long isotactic and syndiotactic sequences. Although most of its properties are intermediate between those of types I and II polymer, its crystalline X-ray diffraction pattern is not a combination of those of type I and type II, but rather is entirely distinct from either of these. Presumably the type-III pattern arises from some specific aggregation of the isotactic and syndiotactic blocks, since the same pattern is observed with mixtures of type-I and type-II polymers.¹

The tacticity of the monomer units in the three crystallizable forms of poly(methyl methacrylate), is, therefore, known. With any single molecule of an isotactic or syndiotactic polymer, however, there need not be a total predominance of one type of linkage over any other. Accordingly, a molecule of polymer identified as syndiotactic by X-ray diffraction may have portions which contain isotactic (*ddd* or *lll*), syndiotactic (*ddl* or *ldl*), or heterotactic (*lld*, *ddl*, *dll*, or *ldd*) sequences,¹⁵ but only the syndiotactic sequences would be long enough to crystallize. For a complete description of this chain it is necessary to specify (a) the fraction of the total number of monomer-to-monomer linkages which is present as each of the two types of linkages, (b) the average length of sequences of each of the three types, (c) the distribution of lengths of each of these types of regular sequences, and (d) the probability of the occurrence of such sequences.

For a, an absolute method is available in high-resolution n.m.r. measurements, and data thus obtained may be used to calibrate more readily available empirical parameters such as those derived from quantitative infrared measurements.⁸ For b, a number-average sequence length can be determined from n.m.r.,^{15,16} but for c, no general method is known except that in the special case of sequence probabilities determined by Bernoullian statistics ($\rho = 1$) the n.m.r. measurement suffices to establish c and d as well. In a preliminary communication¹⁸ we reported a further method of measurement which is specific to poly(methyl methacrylate), and which we believe is responsive to b or perhaps to a combination of b and c. A detailed description of this work is given here.

Briefly, it has been found that the gel which is formed when isotactic and syndiotactic poly(methyl methacrylate) are mixed together, in all except very good solvents for poly(methyl methacrylate), can be melted over a narrow temperature range. The melting points which are thus measured can be correlated with reaction variables in the preparation of the syndiotactic polymer, and thereby with the tacticity of the syndiotactic polymer.

Experimental Section

Measurement of Gel Melting Points. In a small, screw-cap glass vial 0.2 ml. of a 5 wt. % solution of a syndiotactic polymer in dimethylformamide was mixed with an equal volume of a 5 wt. % solution of an isotactic polymer in the same solvent. The vial was capped, heated in boiling water for about 5 min. to melt the gel, and shaken to ensure complete mixing. A portion of this melted gel was then drawn into a standard 1-ml. volumetric transfer pipet to a height of 7–8 cm., the liquid was held in the pipet, the pipet was inserted into a tight-fitting test tube, and the assembly was then lowered into a Dry Ice–acetone bath for 5 min. to attain complete gel formation. Once the gel is formed it will remain in the pipet tip without support until melted, and the melting point measurement is, therefore, done with the top of the pipet open.

The pipet and tube assembly was warmed to room temperature and suspended in an unsilvered dewar flask containing a mineral oil bath. The bath was stirred and heated at the rate of about 0.5°/min., and the temperature was measured. The lower end of the melting point range was taken as that temperature at which the first drop of melted gel falling from the tip of the pipet was followed quickly by a continuous flow of melted gel. The upper end of the range was the temperature at which the gel had emptied to within 2–3 cm. of the bottom of the pipet. The melting point is taken as the midpoint of this temperature range. For most of the gels studied, the melting point range was within 0.5° with a reproducibility of $\pm 0.5^\circ$.

This method equates the melting point with the temperature at which a sudden sharp drop occurs in the viscosity of the gel. An alternative measurement would be to determine the temperature at which the cloudy gel passes over into a clear solution. This can be done by visual inspection, or, more accurately, by measuring the transmission of light through the gel as its temperature is raised. For this measurement the gel was prepared in a 1-cm. Corex cell and the per cent transmission of light at 450 μ m was measured in a Beckman DK-1 spectrophotometer with a heated cell compartment. A typical curve of per cent transmission vs. temperature is shown in Figure 1. The temperature at which this curve levels off was taken as the gel melt-

(13) G. P. Mikhaelov and T. I. Borisova, *Vysokomolekul. Soedin.*, **2**, 619 (1960).

(14) W. A. Gall and N. G. McCrum, *J. Polymer Sci.*, **50**, 489 (1961).

(15) F. A. Bovey and G. V. D. Tiers, *ibid.*, **44**, 173 (1960).

(16) T. G. Fox and H. W. Schnecko, *Polymer*, **3**, 575 (1962).

(17) F. J. Glavis, *J. Polymer Sci.*, **36**, 547 (1959).

(18) W. H. Watanabe, C. F. Ryan, P. C. Fleischer, Jr., and B. S. Garrett, *J. Phys. Chem.*, **65**, 836 (1961).

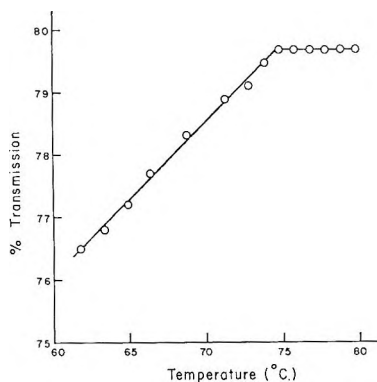


Figure 1. Transmission vs. temperature for a gel consisting of a syndiotactic polymer and a standard isotactic polymer.

ing point. The same relative order of melting points was found for a series of gels by this technique as by the pipet flow method, although the transmission measurements gave melting points uniformly about 2° higher than the flow method. Since the flow method is much simpler and more rapid, it was adopted as the standard method of measurement in this work.

Gel Melting Point of Syndiotactic (Type I) Polymers. Differences in the gel melting point of syndiotactic polymers were determined from gels made with each syndiotactic polymer and a standard isotactic polymer.

Two different standard isotactic polymers were used during the course of this work. Standard isotactic polymer no. 44 (listed in Table V) was prepared in toluene using phenylmagnesium bromide as initiator. After swelling in 4-heptanone, this polymer was found to be crystalline by X-ray observation. The viscosity-average molecular weight for this polymer ($\bar{M}_v = 1.29 \times 10^5$), as well as for all other isotactic polymers, was determined in chloroform at 25° from the equation described by Goode, *et al.*⁸ Number-average molecular weights for all poly(methyl methacrylate) samples were determined from osmotic pressure measurements.¹⁹ Standard isotactic polymer no. 60 was prepared in toluene at -60° using fluorenyllithium as initiator. This polymer was found to have the following properties: X-ray, crystalline after swelling in 4-heptanone; $\bar{M}_v = 5.50 \times 10^5$; $\bar{M}_n = 3.0 \times 10^4$.

Gel Melting Point of Isotactic (Type II) Polymers. The technique used to determine the gel melting point of syndiotactic polymers can in principle be inverted, and by using a standard syndiotactic polymer the gel melting point of isotactic polymers can be determined. For these measurements two different standard syndiotactic polymers were used.

Standard syndiotactic polymer no. 35 (listed in Table IV) was prepared by initiation with sodamide in liquid ammonia-dimethyl ether at -88° . The viscosity-

average molecular weight, determined from the equations reported by Goode, *et al.*,¹⁹ and other physical characterizations of this polymer are as follows: $\bar{M}_v = 19.0 \times 10^5$; $\bar{M}_n = 1.38 \times 10^5$; X-ray, crystalline after swelling in 4-heptanone; the gel melting point against standard isotactic polymer no. 44 was 97.7° .

Standard syndiotactic polymer no. 33 was prepared using sodamide in liquid ammonia: $\bar{M}_v = 0.92 \times 10^5$; $\bar{M}_n = 0.52 \times 10^5$; X-ray, crystalline after swelling in 4-heptanone; the gel melting point against standard isotactic polymer no. 44 was 79.5° .

Gel Melting Point of Syndiotactic-Isotactic (Type III) Polymers. Three separate gel melting point measurements were made on most type-III polymers. The first was made on the type-III polymer alone. The second was made on gels formed from the type-III polymer and a standard isotactic polymer; the third was made on gels formed from the type-III polymer and a standard syndiotactic polymer. Viscosity-average molecular weight measurements of type-III polymers were made in chloroform using the relationship reported earlier.⁸

Factors Which Influence the Reproducibility of the Gel Melting Point. The reproducibility and sharpness with which the syndiotactic-isotactic gels melt are affected by (1) the total polymer concentration in the gel and (2) the ratio of syndiotactic polymer to isotactic polymer in the gel.

1. *Total Polymer Concentration.* The effect of total polymer concentration on the melting point of gels prepared in dimethylformamide from equal weights of syndiotactic polymers of varying molecular weight and standard isotactic polymer no. 60 is illustrated by the data in Table I. At less than 5 wt. %, gels formed from the lower molecular weight syndiotactic polymers were too loose, and uneven melting occurred. At concentrations greater than 5 wt. %, gels formed with the highest molecular weight syndiotactic polymer gave, on melting, solutions which were too viscous to permit reproducible melting points. Reproducibility and sharpness of the melting point to within $\pm 0.5^\circ$ were not affected seriously over the entire molecular weight range of syndiotactic polymers at the 5% concentration level, and this concentration was, therefore, fixed as optimum for all subsequent measurements. The gel melting point is affected by the interaction of polymer concentration and molecular weight. It appears that the dependence of the gel melting point on polymer concentration becomes stronger as the molecular weight of the syndiotactic polymer is lowered.

(19) W. E. Goode, W. H. Snyder, and R. C. Fettes, *J. Polymer Sci.*, **42**, 367 (1960).

Table I: Gel Melting Points ($^{\circ}\text{C}.$) as a Function of Total Polymer Concentration

Syndiotactic polymer No.	$\bar{M}_v \times 10^{-5}$	Total polymer concentration, wt. %				
		1.0	3.0	5.0	7.0	9.0
7	31.50	60.9	62.0	<i>a</i>	<i>a</i>	<i>a</i>
6	25.10	55.6	61.4	60.1	<i>a</i>	<i>a</i>
5	16.10	50.5	61.0	60.6	<i>a</i>	<i>a</i>
4	2.18	<i>b</i>	57.4	60.3	61.9	<i>a</i>
3	0.42	<i>b</i>	46.7-55.5	60.8	61.7	62.5
2	0.17	<i>b</i>	42.0-52.6	58.5	61.3	62.5
1	0.10	<i>b</i>	41.4-43.6	57.0	59.6	58.6

^a Gel too viscous for accurate measurement. ^b Gel too loose for accurate measurement.

2. The Ratio of Syndiotactic to Isotactic Polymer.

This ratio has no serious effects on the reproducibility or sharpness of the melting point, provided the ratio is held within certain limits. Figure 2 defines these limits for gels prepared at 5 wt. % concentration in toluene from standard isotactic polymer no. 60 and a syndiotactic polymer shown to be crystalline by X-ray measurement after solvent treatment. Gels having the same melting point are produced when the syndiotactic component of the gel is varied from about 40 to 80 wt. %. Results almost identical with these were obtained when dimethylformamide was used instead of toluene.

The range in gel composition which produces the same melting point narrows, however, when syndiotactic polymers of different molecular weight are used. The melting point plateau constructed from the data in Table II for intermediate molecular weight syndio-

Table II: Gel Melting Points ($^{\circ}\text{C}.$) as a Function of Syndiotactic Polymer Content

Syndiotactic polymer No.	$\bar{M}_v \times 10^{-5}$	Syndiotactic polymer in gel, wt. %						
		10	20	35	50	65	80	90
6	25.1	54.9	60.4	62.3	60.1	<i>b</i>	<i>b</i>	<i>b</i>
4	2.18	47.9	55.9	52.9	60.3	60.4	60.3	38.7
3	0.42	41.5	48.9	56.6	60.8	58.5	46.3	<27

^a Gels made in dimethylformamide, 5 wt. % total polymer.

^b Gel too viscous for accurate measurement.

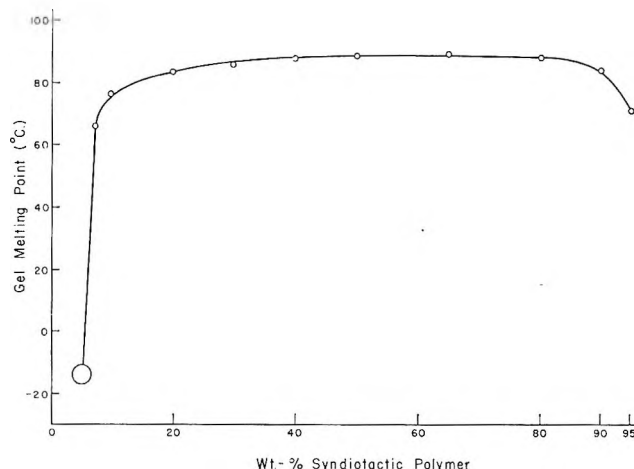


Figure 2. Gel melting point vs. gel composition using syndiotactic polymer no. 11 and standard isotactic polymer no. 60.

dropped on either side. The effect of molecular weight here is similar to that described upon the concentration chosen, *i.e.*, the dependence of the gel melting point on the proportions of standard and syndiotactic polymer becomes stronger as the molecular weight of the syndiotactic polymer is lowered. These data indicate that the effect of molecular weight on the melting point is minimized when equal amounts of syndiotactic and isotactic polymer are used.

The above data fix as the optimum conditions for measurement a 1:1 ratio by weight of syndiotactic to isotactic polymer and a total polymer concentration of 5 wt. % in dimethylformamide; reproducibility under these circumstances is excellent.

3. Minor Factors. For all of the syndiotactic polymers employed, the gel melting point against standard isotactic polymer no. 60 was insensitive to change in (a) the rate of heating of the gel, between 0.2 and 0.9 $^{\circ}$ /min.; (b) the age of the gel, at room temperature, up to about 40 hr., and (c) the water content of the dimethylformamide, from 0.12 to 0.88 wt. %. Although syneresis occurs if the gels are left for more than 40 hr., no irreversible changes occur in the polymers when this happens. In one instance a gel with a melting point of 94.1 $^{\circ}$ was left at room temperature for 28 days. During this time extensive syneresis took place. This gel was melted and cooled and a melting point was again taken; the same value was obtained.

Preparation of Poly(methyl methacrylate) Samples. Freshly distilled regular production grade Rohm & Haas Co. uninhibited methyl methacrylate was used without further purification. All other chemicals used were reagent grade or recrystallized material. Free-radical polymerizations were carried out under conditions whereby the reactants were freed from oxygen

tactic polymer is similar to that in Figure 2. The highest molecular weight polymer may have a plateau, but measurements at the high syndiotactic polymer content were not considered reliable because of the high viscosity of the melted gel. Melting points of the lowest molecular weight sample peaked at 50 wt. % but

by repeated freeze-thaw cycling on a high-vacuum line and then sealed in Pyrex ampoules. Except where indicated, all polymers were isolated and purified by precipitation from petroleum ether (b.p. 30–78°).

Syndiotactic Polymers. High-Temperature Preparations. Polymers of moderate syndiotactic content were prepared in bulk at 210, 180, 140, and $60 \pm 0.1^\circ$ using either di-*t*-butyl hydroperoxide (D-*t*-BHP) or azobisisobutyronitrile (AIBN) as the initiator. Molecular weight was varied by use of *n*-butyl mercaptan (*n*-BM). A reaction time of 4 hr. was allowed for each polymerization conducted at 60° and 0.5–1.5 hr. for each polymerization conducted at temperatures higher than 60°. Data for these preparations are presented in Table III.

Table III: Preparation of Syndiotactic Poly(methyl methacrylate) at High Temperatures

Sample no.	Polym. temp., °C.	D- <i>t</i> -BHP, %	[<i>n</i> -BM] × 10 ² , <i>M</i>	% Conversion	\bar{M}_v × 10 ⁻⁶	\bar{M}_v/\bar{M}_n
A	210	0.05	0	25.2	2.60	
B	180	0.05	0	35.0	0.93	2.5
C	140	0.05	0	94.6	...	
		[AIBN] × 10 ⁴ , <i>M</i>				
1	60	3.16	25.4	9.6	0.10	
2	60	3.39	12.6	10.2	0.17	
3	60	3.11	5.0	10.1	0.42	
4	60	3.18	1.1	9.9	2.18	1.9
5	60	3.30	0.17	9.7	16.30	
6	60	3.18	0.04	10.4	25.10	
7	60	4.50	0.0	10.3	31.50	

Low-Temperature Preparations. Free-radical polymers of moderate-to-high syndiotactic content were prepared in bulk at 0, –30, and –50° using benzoin as photoinitiator and a 100-w. ultraviolet light source.²⁰ Molecular weight of the polymers was varied by changes in benzoin concentration. Data for these preparations are listed in Table IV. Also listed in the table are anionic polymers prepared in liquid ammonia using sodamide as initiator at temperatures ranging from –33 to –88°.

Isotactic Polymers. The isotactic polymers used in this study were prepared at various temperatures using either Grignard reagents or fluorenyllithium, as indicated in Table V. All polymers were broad in molecular weight distribution.

Type-III Polymers. The type-III polymers were prepared over a broad temperature range using a

Table IV: Preparation of Syndiotactic Poly(methyl methacrylate) at Low Temperatures

Sample no.	Polym. temp., °C.	G. of benzoin/100 g. of monomer	Irradiation time, hr.	% Conversion	$\bar{M}_v \times 10^{-5}$
Free-radical polymers					
8	0	0.6270	2.0	6.4	0.34
9	0	0.1751	2.25	8.8	1.05
10	0	0.0250	6.25	17.1	2.30
11	0	0.0090	6.25	9.7	5.75
12	0	0.0025	6.25	5.9	8.30
13	0	0.0011	6.25	4.7	11.50
14	–30	0.2500	2.75	12.5	0.70
15	–30	0.1252	2.75	9.1	1.25
16	–30	0.0250	3.50	5.4	2.50
17	–30	0.0125	3.50	3.9	4.10
18	–30	0.0025	4.25	1.7	10.50
19	–30	0.0005	11.0	1.1	19.00
20	–50	0.3330	5.0	10.5	0.89
21	–50	0.2240	5.0	9.9	1.10
22	–50	0.1332	5.0	8.8	1.55 ^a
23	–50	0.0135	6.0	3.9	4.30
24	–50	0.0270	5.75	5.5	5.70
25	–50	0.0025	6.0	2.1	8.00
26	–50	0.0013	5.0	1.9	11.50
27	–50	0.0005	5.0	1.4	31.00
Anionic polymers					
28	–33			97–99	0.37
29	–44			97–99	0.44
30	–54			97–99	0.50
31	–64			97–99	0.53
32	–70			97–99	0.97
33	–70			97–99	0.92 ^b
34	–74			97–99	0.48
35 ^c	–88			78	19.00 ^d

^a $\bar{M}_v/\bar{M}_n = 3.4$. ^b $\bar{M}_v/\bar{M}_n = 1.8$. ^c Reaction mixture contained dimethyl ether. ^d $\bar{M}_v/\bar{M}_n = 13.8$.

variety of initiators and solvents. Polymerization details are listed in Table VI.

Characterization. X-Ray Diffraction Measurements. The methods used for X-ray diffraction characterization are described by Stroupe and Hughes.²

Infrared Measurements. The infrared *J* values were determined by the method described by Goode, *et al.*⁸

N.m.r. Measurements. Chloroform solutions of the polymers (either 5 or 10 wt. %) were examined at 25° using a Varian HR-60 instrument. The fractions of triads were determined from the spectra by first defining

(20) The ultraviolet light source was a Hanovia Inspectorite, supplied by Meseroll and Co. (No. SC-5041), equipped with a 100-w. CH-4 high-pressure mercury arc and a No. 5874 Corning filter, transmitting 65% at 3600 Å. The lamp was mounted so that the surface of the filter was 6 in. from the ampoule containing the reaction mixture.

Table V: Preparation of Isotactic Poly(methyl methacrylate)

Sample no.	Polym. temp., °C.	Initiator	Solvent	$\bar{M}_v \times 10^{-5}$	$\bar{M}_n \times 10^{-5}$
36	0	PhMg-MgBr ₂	Toluene	0.36	...
37	0	sec-BuMgBr	Methyl methacrylate	0.44	...
38	0	PhMgI etherate	Toluene	...	0.14
39	0	PhMgBr	Toluene	3.13	...
40	0	Grignard from 4-bromobiphenyl	Toluene	3.47	...
41	0	sec-BuMgBr	Toluene	5.20	...
42	0	Ph ₂ N _g -BF ₃	Toluene	7.00	...
43	0	PhMgBr	Toluene	7.40	...
44	3	PhMgBr	Toluene	1.29	...
45	2	di-BuMg-MgBr ₂	Toluene	0.64	0.16
46	2	Fluorenyllithium	Diethyl ether	0.76	...
47	-40	Fluorenyllithium	Benzene	1.70	...
48	-50	Fluorenyllithium	Diethyl ether	1.11	0.13
49	-50	Fluorenyllithium	Diethyl ether	1.94	0.40
50	-50	Fluorenyllithium	Diethyl ether	2.77	0.45
51	-60	Fluorenyllithium	Diethyl ether	1.42	0.11
52	-60	Fluorenyllithium	90% toluene-10% Et ₂ O	1.50	0.13
53	-60	Fluorenyllithium	Diethyl ether	1.64	...
54	-60	Fluorenyllithium	Benzene	1.82	...
55	-60	Fluorenyllithium	90% toluene-10% Et ₂ O	2.0	0.19
56	-60	Fluorenyllithium	90% toluene-10% Et ₂ O	2.25	0.27
57	-60	Fluorenyllithium	90% toluene-10% Et ₂ O	2.30	0.28
58	-60	Fluorenyllithium	90% toluene-10% Et ₂ O	2.70	0.26
59	-60	Fluorenyllithium	Diisobutyl ether	3.48	...
60	-60	Fluorenyllithium	Toluene	5.50	0.30
61	-70	sec-BuMgBr	...	0.13	...
62	-70	Fluorenyllithium	...	5.20	...

the shapes of the peaks using the reflection technique, and then by measuring the area under each peak with the aid of a planimeter.

Results

Syndiotactic Poly(methyl methacrylate). The value of the gel melting point is affected by the molecular weight of the polymers contained in the gel. This was found from the use of two standard isotactic polymers (no. 44 and 60) and measuring with each standard the gel melting points of several sets of syndiotactic polymers, each set being prepared at a given temperature and containing within it a range of molecular weights. The syndiotactic polymers used for this study were those listed in Tables III and IV. The gel melting point data are given in Table VII.

Within each set of syndiotactic polymers there is first a rise in gel melting point at low molecular weight, and then a leveling-off to a nearly constant value. The plateau is reached for the 60° polymers at \bar{M}_v of about 40,000, for the 0° polymers at about 200,000, for the -30° polymers at about 400,000, and for the -50° polymers a very slow rise is noted up to the highest

molecular weight measured. Thus, the molecular weight above which the melting point becomes independent of molecular weight of the syndiotactic polymer is a function of the preparation temperature of the syndiotactic polymer.

Although small differences in melting point arise from the use of two different standard isotactic polymers, it is clear that the molecular weight dependence is quite similar in each case, and with each standard the relative values of the melting points remain the same. If the melting points obtained with standard no. 44 ($\bar{M}_v = 1.29 \times 10^5$) are plotted against those obtained with standard no. 60 ($\bar{M}_v = 5.50 \times 10^5$), there is a linear relationship for polymers with gel melting points greater than 75° and for these it is possible to convert quantitatively from one standard to the other.

X-Ray Measurements. Evidence that the gel melting point measures some aspect of syndiotacticity in poly(methyl methacrylate) comes from X-ray observations (Table VIII). Here there is good qualitative agreement between these measurements; polymers that are not crystallizable by solvent treatment have relatively low gel melting points (less than about 75°), whereas those polymers classified by X-ray⁸ as crystal-

Table VI: Preparation of Type-III Poly(methyl methacrylate)

Sample no.	Polym. temp., °C.	Initiator	Solvent	$\bar{M}_v \times 10^{-5}$
63	1-5	Fluorenyllithium	Dioxane-toluene	0.67
64	1-5	(<i>n</i> -Bu) ₂ Mg	Toluene	...
65	0	Pb ₂ Mg-LiBr	Toluene	0.42
66	0	Fluorenyllithium	Dioxane-toluene	0.56
67	0	<i>n</i> -BuMgCl	Toluene	0.87
68	-20	Fluorenyllithium	Dioxane-toluene	0.90
69	-40	Fluorenyllithium	Dioxane-toluene	0.53
70	-40	Fluorenyllithium	Dioxane-toluene	1.75
71	-60	Fluorenyllithium	Dioxane-toluene	0.75
72	-60	Fluorenyllithium	Dioxane-toluene	1.05
73	-60	Fluorenyllithium	Dioxane-toluene	2.00
74	-60	Fluorenyllithium	Dioxane-toluene	2.22
75	-60	Fluorenyllithium	Dioxane-toluene	4.00
76	-60	Fluorenyllithium	Toluene	...
77	-60	Fluorenyllithium	Diethyl ether	...
78	-70	PhMgBr	Toluene	0.44
79	-70	PhMgBr	Toluene	0.53
80	-70	<i>n</i> -BuMgCl	Toluene	0.97
81	-70	<i>n</i> -BuMgCl	Toluene	1.75
82	-70	Pb ₂ Mg-LiBr	Toluene	1.98
83	-70	PhMgBr	Toluene	2.55
84	-70	Pb ₂ Mg-EF ₃	Toluene	6.40
85	-70	Pb ₂ Mg-BuOH	Toluene	...
86	-78	Naphthalenesodium	Tetrahydrofuran (THF)	1.2
87	-78	<i>n</i> -BuLi	THF	2.3
88	-78	Naphthalenesodium	THF	2.8
89	-78	Naphthalenelithium	THF	3.4
90	-78	Naphthalenepotassium	THF	6.7
91	-78	Stilbenesodium	THF	...
92	-78	Fluorenyllithium	THF	...
93	-78	Diisobutylmagnesium	THF	...
94	-78	Naphthalenesodium	2% THF in toluene	...
95	-78	Naphthalenesodium	5% THF in toluene	...
96	-78	Naphthalenesodium	10% THF in toluene	...
97	-78	Naphthalenesodium	20% THF in toluene	...

line syndiotactic polymers have relatively high gel melting points (greater than about 75°).

The data in Table VIII serve to emphasize that the gel melting point shows no discontinuity between crystallizable and noncrystallizable poly(methyl methacrylate). This suggests that the gel melting point considers both the crystallizable and noncrystallizable content of a polymer. It was found that the gel melting point (82.8°) of the 4-heptanone-soluble polymer isolated from a crystallizable syndiotactic polymer was almost as high as that of the whole polymer (gel melting point 84.8°) and only slightly below that of the 4-heptanone-insoluble portion of the polymer (gel melting point 89.5°). (Molecular weight data and n.m.r. data were not obtained on the 4-heptanone-soluble and 4-heptanone-insoluble portions of this polymer. Therefore, it is not known whether the 4-heptanone treatment caused fractionation of the polymer, and, if so, whether fractionation was on the basis of molecular weight, tacticity, or both.) In order to test this possibility further, 25 wt. % of a syndiotactic polymer (no. A, Table VII, gel melting point 37.1°), which under ordi-

Table VII: Gel Melting Points of Syndiotactic Poly(methyl methacrylate)

No.	Syndiotactic polymer $\bar{M}_v \times 10^{-5}$	Gel m.p., ^a °C. (±0.5°)	
		Against std. isotactic polymer no. 44	Against std. isotactic polymer no. 60
Polymer prepared at 210°			
A	2.60	37.1	...
Polymer prepared at 180°			
B	0.93	38.5	...
Polymer prepared at 140°			
C	...	43.5	...
Polymer prepared at 60°			
1	0.10	58.6	56.7
2	0.17	58.7	59.7
3	0.42	60.7	62.0
4	2.18	60.2	62.7
5	16.10	60.6	65.1
6	25.10	60.0	65.4
7	31.50	Too viscous for accurate measurement	
Polymer prepared at 0°			
8	0.34	74.2	75.3
9	1.05	74.8	77.2
10	2.30	76.0	78.0
11	5.75	75.2	78.5
12	8.30	75.7	80.0
13	11.50	76.5	79.5
Polymer prepared at -30°			
14	0.70	82.0	84.9
15	1.25	85.0	87.0
16	2.50	85.6	87.7
17	4.10	86.7	88.0
18	10.50	88.2	89.1
19	19.00	87.5	88.6
Polymer prepared at -50°			
20	0.89	89.0	88.6
21	1.10	88.9	89.8
22	1.55	90.5	91.5
23	4.30	92.1	93.0
24	5.70	91.5	92.0
25	8.00	92.7	93.3
26	11.50	95.0	95.4
27	31.00	96.0	96.5

^a Gels made in dimethylformamide.

nary solvent treatment is incapable of crystallizing, was added to a crystallizable syndiotactic polymer (no. 27, Table VII, gel melting point 96°). (Here the total polymer concentration and the total syndiotactic polymer content of the gel were held constant at 5 and 50%, respectively.) The resulting melting point was lowered only slightly (92.8°) below that of the crystallizable syndiotactic polymer (no. 27). These results indicate that the gel melting point is not linearly de-

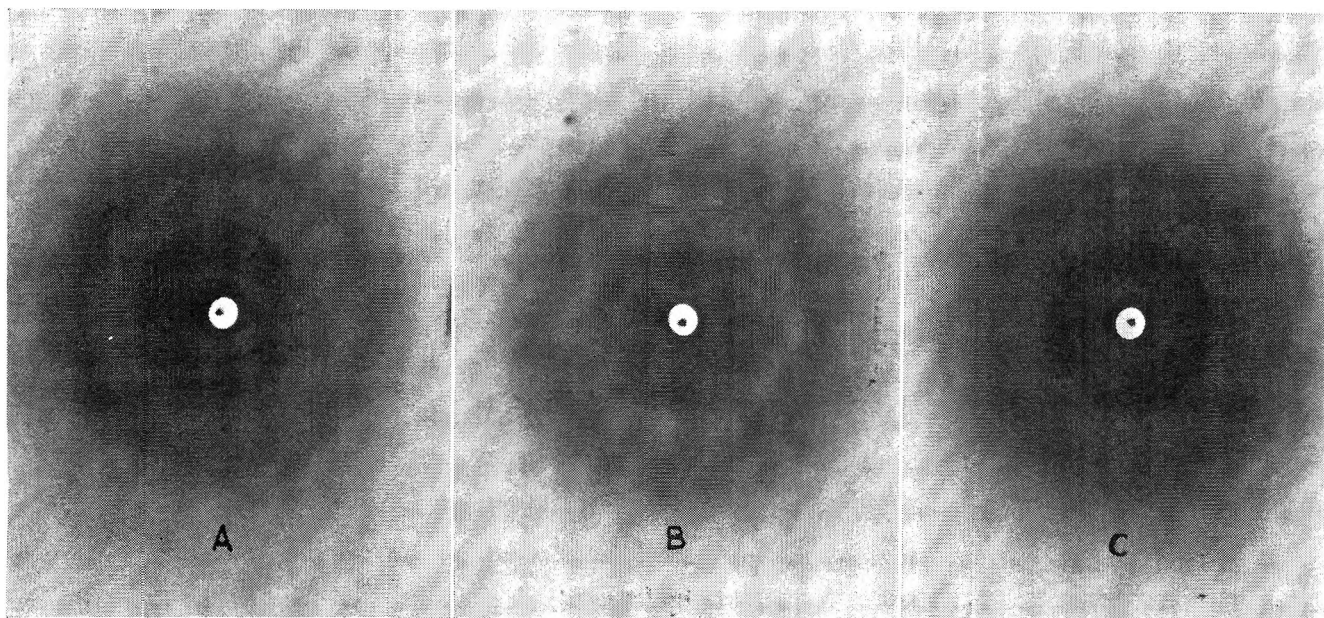


Figure 3. X-Ray diffraction pattern of syndiotactic-isotactic gel: A, unmelted gel at 25°; B, melted gel at 110°; C, melted gel after cooling to 25°.

Table VIII: Correlation between Gel Melting Point and X-Ray Measurement

Syndiotactic polymer no.	X-Ray ^a	Gel m.p. (°C.) against std. isotactic polymer no. 44
2	Noncrystalline	58.7
4	Noncrystalline	60.2
28	Noncrystalline	72.1
8	Noncrystalline	74.2
31	Crystalline	77.3
33	Crystalline	79.5
34	Crystalline	83.5
16	Crystalline	85.6
18	Crystalline	88.2
22	Crystalline	90.5
27	Crystalline	96.0

^a After swelling in 4-heptanone to develop crystallinity in the insoluble fraction of the polymer.¹

pendent on the concentration of long syndiotactic sequences.

It is known that intimate mixtures of syndiotactic and isotactic poly(methyl methacrylate) crystallize to give the same X-ray diffraction pattern as that obtained with type-III poly(methyl methacrylate).¹ Recently, Dr. H. S. Yanai of these laboratories has performed semiquantitative X-ray measurements of a gel consisting of syndiotactic polymer no. 33 and standard isotactic polymer no. 44. When the gel was present to the extent of 5 wt. % in dimethylformamide no evidence

for crystallinity was observed. When, however, the gel content in dimethylformamide was increased to 20 wt. %, the X-ray diffraction pattern for type-III crystalline material was indeed observed at 25° (Figure 3A). When the same gel was heated (110°) above its melting point, X-ray examination at 110° showed the gel to be amorphous (Figure 3B). Again, when the same gel was allowed to cool to 25°, X-ray measurements showed it to be crystalline (Figure 3C). These data provide direct evidence that the formation and melting of this gel involves a crystallization of segments in poly(methyl methacrylate) chains, which (*vide supra*) might not be capable of crystallizing in the absence of polymer of the opposite configuration.

Infrared Measurements. Changes in gel melting points of syndiotactic poly(methyl methacrylate) samples may be correlated with changes in their infrared *J* values, an arbitrary parameter which measures differences in the infrared absorption spectra among the different stereoregular forms of poly(methyl methacrylate).³ The data listed in Table IX show that the *J* value increases as the gel melting point increases. The good correlation found between these measurements again provides evidence that the gel melting point does indeed measure some aspect of the syndiotacticity of poly(methyl methacrylate).

The range in gel melting points for the polymers listed in Table IX is from 37.1 to 95.0°, while the range of *J* values is from 78 to 115. It follows from this that the gel melting point measurement provides a more

Table IX: Correlation between Gel Melting Point and J Value

Syndiotactic polymer no.	J value (± 3)	Gel m.p. ($^{\circ}\text{C.}$) against std. isotactic polymer no. 44
A	78	37.1
B	79	38.5
6	95	60.0
3	96	60.2
11	100	75.2
8	101	74.2
28	101	72.1
30	103	75.9
31	103	77.3
14	104	82.0
19	104	87.5
34	105	83.5
20	115	89.0
26	115	95.0

sensitive tool than the J value from measuring differences among syndiotactic poly(methyl methacrylate) specimens.

N.m.r. Measurements. It is known that n.m.r. spectra provide a quantitative measure of the fractions of triads of syndiotactic (s), isotactic (i), and heterotactic (h) configurations in a polymer chain, and such data have been used¹⁵ to determine whether a single probability for syndiotactic or isotactic addition describes the set of triads obtained. Analyses such as those of Miller²¹ and of Coleman and Fox²² have also been applied²³ to n.m.r. data to provide an estimate of average tactic sequence length.

The n.m.r. data giving the fraction of s , i , and h triads in a polymer have been handled by Coleman and Fox^{22a} to give $p[\text{S}] = (s + h/2)$ = the probability that a placement selected at random is syndiotactic; $p[\text{I}] = (i + h/2)$ = the probability that a placement selected at random is isotactic; $\mu[\text{S}] = (2s + h)/h$ = the number average length of closed syndiotactic sequences; $\mu[\text{I}] = (2i + h)/h$ = the number-average length of closed isotactic sequences; and $\rho = \mu[\text{I}]p[\text{S}]$ = the persistence ratio, a measure of the deviation of sequence distributions from those predicted by random statistics.

The n.m.r. spectra of several of the syndiotactic polymers used in this study were obtained in chloroform at room temperature. Unfortunately, the resolution of the n.m.r. spectra obtained here was limited, and difficulty was experienced in the assignment of the areas to the three absorption peaks. Hence, the n.m.r. results listed in Table X are considered as semiquantitative data only, and the values of $\rho > 1$ do not imply that the free-radical polymers deviate from Bernoullian trial

Table X: Correlation of Gel Melting Point with N.m.r. Data

Syndiotactic polymer no.	s	h	i	$\mu[\text{S}]$	$p[\text{S}]$	ρ	Gel m.p. ($^{\circ}\text{C.}$) against std. isotactic polymer no. 44
A	0.45	0.41	0.14	3.20	0.66	1.11	37.1
B	0.46	0.33	0.21	3.79	0.63	1.43	38.5
6	0.64	0.26	0.10	5.92	0.77	1.36	60.0
3	0.63	0.23	0.14	6.48	0.75	1.67	60.7
28 ^a	0.83	0.12	0.05	14.85	0.89	1.63	72.1
29 ^a	0.88	0.10	0.02	18.6	0.93	1.30	74.1
8	0.77	0.17	0.06	10.1	0.85	1.45	74.2
11	0.85	0.13	0.02	14.1	0.92	1.21	75.2
14	0.85	0.13	0.02	14.1	0.92	1.21	82.0
32 ^a	0.96	0.04	0.00	49.0	0.98	0.98	85.7
19	0.71	0.22	0.07	7.45	0.82	1.34	87.5
20	0.80	0.17	0.03	10.4	0.88	1.19	89.0
26	0.78	0.14	0.08	12.15	0.85	1.82	95.0

^a Prepared anionically in liquid ammonia.

statistics ($\rho = 1$). We consider the high values of ρ to be unreasonable owing to the limitations in the n.m.r. measurements cited above.

However, the data in Table X can be used in a qualitative sense and, when taken collectively, show a tendency for increasing gel melting points to be accompanied by increases in the fraction of polymer which is syndiotactic. Within the limitations on the quantitative validity of the data noted above, we find samples which contain essentially the same fractions of s , i , and h in triads (Table X, no. 8 and 26) may vary in gel melting point by as much as 21° . The data also indicate that a polymer prepared anionically (no. 32) which is quite rich in syndiotactic content can have a gel melting point (85.7°) similar to a polymer prepared free radically (no. 19, gel melting point 87.5°) which contains considerably less syndiotactic polymer. It is expected that the gel melting point of polymer no. 32 would be somewhat higher than 85.7° if its molecular weight ($\bar{M}_v = 0.97 \times 10^6$) were as high as polymer no. 19 ($\bar{M}_v = 1.9 \times 10^6$).

Correlation of Gel Melting Point with Polymerization Temperature. Both n.m.r.^{15,16} and infrared spectroscopy³ have established that with poly(methyl methacrylate) the fraction of syndiotactic placements increases with decreasing polymerization temperature.

(21) R. L. Miller, *SPE Trans.*, **3**, 123 (1963).

(22) (a) B. D. Coleman and T. G. Fox, *J. Chem. Phys.*, **38**, 1065 (1963); (b) B. D. Coleman and T. G. Fox, *J. Polymer Sci.*, **C4**, 345 (1963).

(23) D. L. Glusker, R. A. Galluccio, and R. A. Evans, *J. Am. Chem. Soc.*, **86**, 187 (1964).

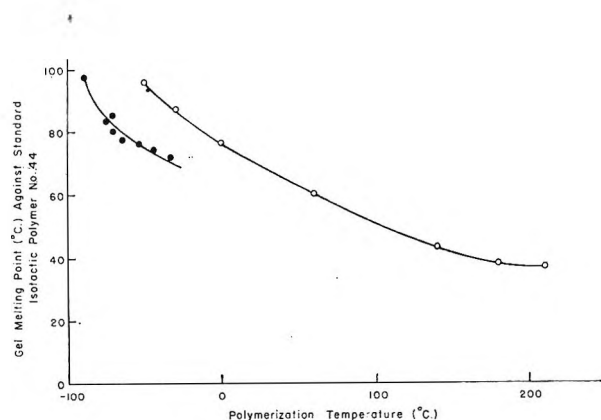


Figure 4. Gel melting point of syndiotactic polymers as a function of their preparation temperature: O, polymers prepared free radically; ●, polymers prepared anionically in liquid ammonia.

Gel melting point measurements of syndiotactic poly(methyl methacrylate) show the same general increase with decreasing polymerization temperature.

The general trend of increasing melting points with decreasing polymerization temperature is represented graphically in Figure 4. For polymers prepared free radically, the melting point varies from 37.1 to 95.0° for samples prepared at 210 and -50° , respectively. As already reported by Graham, *et al.*,²⁴ significant differences in gel melting point are found for the polymers prepared at the higher temperatures (*i.e.*, 140–210°); hence even at these temperatures some preference for syndiotactic placement apparently still exists in these polymers. The ordering is still increasing rapidly with decreasing temperature even at a polymerization temperature of -50° , the freezing point of methyl methacrylate monomer.

Similar data are shown for syndiotactic polymers prepared anionically in liquid ammonia. For these polymers, the gel melting point varies from 72.1 to 97.7° for samples prepared at -33° and -88° , respectively. It would appear from examination of Figure 4 that at any given temperature of polymerization the gel melting point of a free-radical syndiotactic polymer is greater than that of a liquid-ammonia syndiotactic polymer. This difference could be due to the difference in molecular weight between the free-radical polymers and the liquid-ammonia polymers. A direct comparison of gel melting points for free-radical and liquid-ammonia polymers prepared at the same temperature and possessing the same molecular weight is not available. The best comparisons that can be made are between (1) a free-radical polymer (gel melting point 84.9°) prepared at -30° ($\bar{M}_v = 70,000$) and a liquid ammonia polymer (gel melting point 72.1°) prepared at -33° ($\bar{M}_v = 37,000$), and (2) a free-radical polymer (gel melting

point 88.6°) prepared at -50° ($\bar{M}_v = 89,000$) and a liquid-ammonia polymer (gel melting point 75.9°) prepared at -54° ($\bar{M}_v = 50,000$).

Isotactic Poly(methyl methacrylate). Gel melting points were measured for Grignard-initiated isotactic polymers, fluorenyllithium-initiated isotactic polymers, and fractions of some fluorenyllithium polymers. These measurements were made against two different standard syndiotactic polymers.

Gel Melting Points against Standard Syndiotactic Polymer No. 35. Standard polymer no. 35 was high in molecular weight ($\bar{M}_v = 1,900,000$), and had a very broad molecular weight distribution ($\bar{M}_v/\bar{M}_n = 13.8$). Against this standard the gel melting points of all the isotactic polymers with \bar{M}_v greater than 40,000 are essentially constant and identical with each other (Table XI). The lack of change in melting point is consistent

Table XI: Gel Melting Points of Isotactic Polymers against Standard Syndiotactic Polymer No. 35

Isotactic polymer no.	Initiator	$\bar{M}_v \times 10^{-5}$	$\bar{M}_n \times 10^{-5}$	J value	Gel m.p. (°C.) against std. syndiotactic polymer no. 35
62-2 ^a	Fluorenyllithium	25.2	5.10		103.9
43	Grignard	7.4		28	97.7
42	Grignard	7.0		31	100.5
60	Fluorenyllithium	5.5		33	99.1
62	Fluorenyllithium	5.2		29	98.6
59	Fluorenyllithium	3.48			97.6
40	Grignard	3.47			100.2
39	Grignard	3.13		34	100
50	Fluorenyllithium	2.77	0.45	33	98.1
49	Fluorenyllithium	1.94	0.40	32	97.1
54	Fluorenyllithium	1.82		30	99.9
47	Fluorenyllithium	1.70		30	97.2
53	Fluorenyllithium	1.64	0.13		99.9
44	Grignard	1.29		34	97.7
51	Fluorenyllithium	1.42	0.11		99.0
62-7 ^a	Fluorenyllithium	1.2	0.72		98.7
48	Fluorenyllithium	1.11	0.13		99.0
46	Fluorenyllithium	0.76			94.6
45	Grignard	0.64	0.16	33	99.2
37	Grignard	0.44			100.2
62-11 ^a	Fluorenyllithium	0.39	0.26		96.0
36	Grignard	0.36		30	96.4
62-12 ^a	Fluorenyllithium	0.30	0.20		93.9
62-13 ^a	Fluorenyllithium	0.22	0.15		93.3
61	Grignard	0.13			92.0

^a Fractions obtained from fluorenyllithium polymer no. 62 by precipitation from benzene-hexane mixtures.

(24) R. K. Graham, D. L. Dunkelberger, and J. R. Panchak, *J. Polymer Sci.*, 59, 843 (1962).

with J values and X-ray analyses. Above this molecular weight insignificant changes occur in J value, and all of the isotactic polymers are crystalline by X-ray analysis after solvent swelling. At \bar{M}_v less than 40,000, the gel melting point falls off slowly as the molecular weight is decreased to $\bar{M}_v = 13,000$. The good fit of all points in a plot of gel melting point vs. \bar{M}_v to a single curve is good indication that the gel melting point-molecular weight dependence is the same for all of these isotactic polymers. Any differences in the isotactic polymers caused by change of initiator (Grignard vs. fluorenyllithium), or by the change in molecular weight distribution (fluorenyllithium whole polymers vs. fluorenyllithium fractions), or by change in any other reaction variable appear to be relatively unimportant and do not affect the melting point-molecular weight relationship.

The dependence of the gel melting point on the molecular weight of isotactic polymers using standard syndiotactic polymer no. 35 was extended below $\bar{M}_v = 13,000$. This was accomplished with a series of isotactic polymer (F) fractions (Table XII) obtained by Glusker, *et al.*,²⁵ from the countercurrent extraction of a methyl methacrylate-fluorenyllithium reaction mixture.

Table XII: Gel Melting Points of Isotactic Polymer Fractions

Fraction no.	Initiator	\bar{M}_n	Gel m.p. (°C.) against std. syndiotactic polymer no. 35
F-1	Fluorenyllithium	19,700	94.7
F-2	Fluorenyllithium	8,380	85.9
F-3	Fluorenyllithium	2,530	80.0
F-4	Fluorenyllithium	1,120	75.0
F-5	Fluorenyllithium	968	57.5
G-1	Grignard	928	57.3
G-2	Grignard	880	< -78
F-6	Fluorenyllithium	711	< -78

The gel melting points of two (G) fractions recovered from the ether-soluble portion of an isotactic polymer prepared with Grignard initiator were measured also. Gels from the F fractions melted at gradually decreasing temperatures as \bar{M}_n was reduced. At $\bar{M}_n = 800$ –900, the melting point fell very sharply and reached a value of < -78°. A similar drop also occurred in the same \bar{M}_n range for the G fractions.

Glusker, *et al.*,²³ in considering these same data, have suggested that (1) polymers below a certain molecular weight tend to be more random than those above that molecular weight, or (2) that a certain number of isotactic or syndiotactic placements in sequence are re-

quired to allow a molecular conformation which can contribute to gel formation. They concluded that the latter possibility was the more probable.

Gel Melting Points against Standard Syndiotactic Polymer No. 33. It was shown earlier with syndiotactic polymers that only small differences in melting point occurred from the use of two different isotactic polymers. This is not the case when the gel melting points of isotactic polymers are measured against two different standard syndiotactic polymers.

Against the high molecular weight ($\bar{M}_v = 1,900,000$), broadly distributed ($\bar{M}_v/\bar{M}_n = 13.8$) syndiotactic

Table XIII: Gel Melting Points of Isotactic Polymers against Standard Syndiotactic Polymer No. 33

Polymer no.	$\bar{M}_v \times 10^{-5}$	$\bar{M}_n \times 10^{-5}$	J value	Gel m.p. (°C.) against std. syndiotactic polymer no. 33
Fluorenyllithium polymers				
62-2 ^a	25.2	5.10		84.9
62-3 ^a	13.6	3.23		
60	5.50		33	81.9
59	3.48			
50	2.77	0.45	33	75.0
58	2.70	0.26		79.3
57	2.30	0.28		78.5
56	2.25	0.27		79.3
62-5 + 6 ^a	2.2	1.33		
55	2.0	0.19		78.7
49	1.94	0.40	32	71.6
54	1.82		30	75.1
47	1.70		30	72.0
53	1.64	0.13		74.3
52	1.50	0.16		77.3
51	1.42	0.11		71.2
62-7 ^a	1.2	0.72		73.0
48	1.11	0.13		67.7
62-8 ^a	0.9	0.57		
46	0.76			60.6
62-9 ^a	0.74	0.43		62.2
62-11 ^a	0.39	0.26		53.5
62-12 ^a	0.30	0.20		46.6
62-13 ^a	0.22	0.15		40.5
Grignard polymers				
43	7.40		28	83.0
42	7.00		31	84.0
39	3.13		34	82.4
44	1.29		34	79.6
45	0.64	0.16	33	81.5
37	0.44			-10
36	0.36		30	43.5
61	0.13			-78

^a Fractions obtained from fluorenyllithium polymer no. 62 by precipitation from benzene-hexane mixtures.

(25) D. L. Glusker, E. Stiles, and B. Yoncoskie, *J. Polymer Sci.*, **49**, 297 (1961).

standard (no. 35), gel melting points of isotactic polymers were found to be essentially independent of molecular weight, as long as $\bar{M}_v > 40,000$ (see Table XI). On the other hand, the gel melting points of isotactic polymers against standard syndiotactic polymer no. 33 ($\bar{M}_v = 92,000$, $\bar{M}_v/\bar{M}_n = 1.8$) varied considerably with changes in molecular weight (Table XIII). In addition, the gel melting points of two of the low molecular weight isotactic samples (no. 37 and 61) were anomalously low. Other than the possibility that these samples were contaminated, there is no apparent explanation for these low melting point values.

The gel melting point-molecular weight relationship plotted in Figure 5 for isotactic polymers against standard syndiotactic polymer no. 33 shows considerable scatter. However, these data do serve to indicate that the gel melting point of isotactic polymers against this standard does not become independent of molecular weight until $\bar{M}_v > 300,000$ is reached.

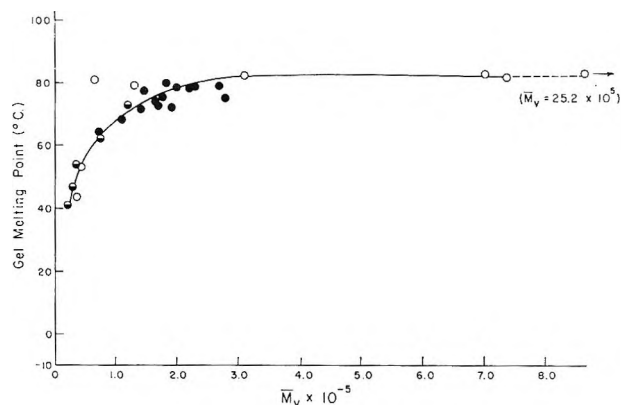


Figure 5. The gel melting point of isotactic polymers against standard syndiotactic polymer no. 33 as a function of the molecular weight of the isotactic polymer: O, Grignard-initiated isotactic whole polymers; ●, fluorenyllithium-initiated isotactic whole polymers; ◐, fluorenyllithium-initiated isotactic polymer fractions.

N.m.r. Measurements. The semiquantitative data listed in Table XIV for some of the isotactic polymers indicate that the isotactic content varies from 69 to 92%. For two of the samples (no. 47 and 60) the fraction of isotactic triads is nearly the same ($i = 0.92$ and $i = 0.85$). The gel melting point of these polymers against standard syndiotactic polymer no. 35 are also nearly the same (97.2 and 99.1°). However, the gel melting points of these same polymers against standard syndiotactic polymer no. 33 are quite different (72 and 81.9°), and the polymer with the lower value of $i = 0.85$ has the higher gel melting point. It is possible that with this standard the gel melting point is more

Table XIV: Correlation between Gel Melting Point and N.m.r. Data

Polymer no.	s	h	i	μ [I]	μ [S]	p[I]	ρ	Gel m.p. (°C.) against std. syndiotactic polymer	
								No. 35	No. 33
44	0.04	0.13	0.83	13.8	1.62	0.90	1.52	97.7	79.6
62	0.10	0.13	0.77	12.8	2.54	0.84	2.17	98.6	
46	0.15	0.16	0.69	9.62	2.87	0.77	2.22	94.6	60.6
51	0.03	0.17	0.80	10.4	1.35	0.89	1.25	99.0	71.2
47	0.02	0.06	0.92	31.7	1.67	0.95	1.58	97.2	72.0
60	0.02	0.13	0.85	14.1	1.31	0.92	1.27	99.1	81.9

sensitive than n.m.r. in detecting differences in the tacticity of isotactic polymers. This could occur if the gel melting point measured a weighted-average sequence length rather than the simple number-average obtained from n.m.r. An alternate explanation is that the difference in gel melting point between isotactic samples no. 47 and 60 against standard syndiotactic polymer no. 33 is due solely to a difference in molecular weight. It has been established from the data listed in Table VII that the melting point of syndiotactic polymers *vs.* a standard isotactic polymer is dependent on the molecular weight of the syndiotactic polymer. Figure 6 shows this dependence for syndiotactic polymers of different molecular weight prepared free radically at -30° . Here the molecular weight of the syndiotactic polymer must be greater than $\bar{M}_v = 400,000$ before the gel melting point reaches the plateau region shown by the curve in Figure 6. Standard syndiotactic polymer no. 33 has $\bar{M}_v = 92,000$ and is therefore not high enough in molecular weight to reach this plateau. Of the two isotactic polymers under discussion, no. 60 ($\bar{M}_v = 550,000$) is sufficiently high in molecular weight to be on the plateau of the curve constructed in Figure 5, where syndiotactic polymer no. 33 was employed as the standard; the other isotactic polymer (no. 47) has $\bar{M}_v = 170,000$ and therefore might be expected to have a lower gel melting point against this standard. In order to settle this point, one would need to compare polymers of the same molecular weight but which contain different isotactic contents.

Type-III Poly(methyl methacrylate). Type-III poly(methyl methacrylate) is reported to contain relatively high concentrations of relatively long blocks of both syndiotactic and isotactic sequences.^{15,17} This material alone, like mixtures of syndiotactic and isotactic polymer, forms gel in dimethylformamide. Melting point measurements on type-III materials were made by adding the appropriate amount of a type-III polymer

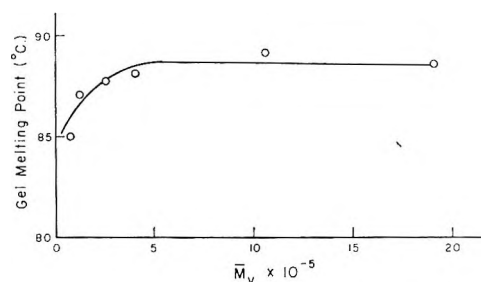


Figure 6. The gel melting point of syndiotactic polymers prepared at -30° against standard isotactic polymer no. 60 vs. the molecular weight of the syndiotactic polymer.

to dimethylformamide solvent and then heating the mixture to effect a clear solution, which gelled upon cooling to -78° . Melting points were then determined in the usual manner.

Such measurements were made on a variety of type-III polymers. The results are listed in Table XV.

Table XV: Gel Melting Points of Type-III Polymers Alone in Dimethylformamide

Polymer no.	$\bar{M}_v \times 10^{-5}$	J value	Gel m.p. ($^\circ\text{C}.$) alone
84	6.40	40	73.8
63	0.67	41	<25
83	2.55	42	68.6
79	0.53	45	<-78
66	0.56	45	<25
68	0.90	45	<25
70	1.75	47	40.3
82	0.44	48	<-78
71	0.75	52	38.6
72	1.05	52	34.7
82	1.98	53	69.5
75	4.00	53	79.6
67	0.87	56	45.0
73	2.00	60	57.7
81	1.75	63	87.6
74	2.20	63	79.7
64	...	64	72.4
85	...	69	86.1
78	0.42	73	25.0
80	0.97	91	100.4

Here, the polymers are listed in order of increasing J values. In general, the gel melting point does not increase uniformly with increasing J value. For example, two of the type-III polymers (no. 81 and 74) have the same J value, yet the gel melting points are different. This difference in melting point is probably not due to molecular weight: polymer no. 74, which has the higher molecular weight, has the lower gel melting point. Polymers with the same J value have

gel melting points which in some cases increase with an increase in molecular weight while in some other cases decrease with an increase in molecular weight. It appears, therefore, that the lack of correlation between the gel melting point of type-III polymers alone and J value is not due to molecular weight variations within the series of type-III polymers.

Gel Melting Point of Type-III Polymer against Standard Isotactic Polymers. Two standard isotactic polymers (no. 44 and 60) were added to type-III polymer no. 83 (Table XVI) in such manner that the

Table XVI: The Effect of Added Isotactic Polymer on the Gel Melting Point of Type-III Polymer No. 83

—Added isotactic polymer— No.	$\bar{M}_v \times 10^{-5}$	mixtures Gel m.p., $^\circ\text{C}.$		
		0 Wt. % of added polymer in type-III	25	50
Standard no. 44	1.29	68.9	65.6	58.9
Standard no. 60	5.50	68.9	67.7	66.6

total polymer concentration was kept constant at 5 wt. %. In each case the melting point of the type-III polymer was lowered, but only to a minor extent. The melting points of the isotactic-type-III polymer mixtures are slightly dependent on the isotactic polymer added. Isotactic polymer of low molecular weight (standard no. 44) has a greater effect on the gel melting point than does isotactic polymer of high molecular weight (standard no. 60). This molecular weight dependence was observed previously when standard isotactic polymers were added to syndiotactic polymers (Table VII).

Gel Melting Point of Type-III Polymer against Standard Syndiotactic Polymers. A variety of syndiotactic polymers, already classified in terms of their gel melting point against standard isotactic polymer no. 44, was added in varying amounts to type-III polymer no. 83. The replacement of some type-III polymer no. 83 by these syndiotactic polymers, such that the total polymer concentration was kept constant at 5 wt. %, affected the melting point in the manner shown in Table XVII.

The addition of these syndiotactic polymers causes a change in the gel melting point and the J value over that of the type-III polymer alone. The addition of the high molecular weight standard syndiotactic polymer (no. 35) raises the melting point to the 95 – 100° range. A similar melting point range is observed when this same standard is added to a variety of type-III polymers (Table XVIII). The data in Table

Table XVII: The Effect of Added Syndiotactic Polymer on the Gel Melting Point and J Value of Type-III Polymer No. 83

No.	Added syndiotactic polymer		% of added polymer in type-III mixtures							
	$\bar{M}_v \times 10^{-5}$	Gel m.p. ($^{\circ}\text{C}$) vs. std. isotactic polymer no. 44	0	J	25	J	40	J	60	J
			Gel m.p., $^{\circ}\text{C}$.		Gel m.p., $^{\circ}\text{C}$.		Gel m.p., $^{\circ}\text{C}$.		Gel m.p., $^{\circ}\text{C}$.	
Std. no. 35	19.00	97.7	68.6	42	96.0	61	98.0		100.1	88
Std. no. 33	0.92	79.5	68.6	42	76.9	61	78.3		79.0	81
28	0.37	72.1	68.6	42	72.0	60	73.2		74.2	80
4	2.18	60.2	68.6	42	66.4	59	65.2		63.3	77

XVIII are similar to those in Table XI where gel melting points are recorded for a variety of isotactic polymers against standard syndiotactic polymer no. 35. It would appear from this that changes in melting point are not observed for either isotactic polymers of type-III polymers against this standard. The lack of change in J values for the isotactic polymers of Table XI is consistent with the narrow gel melting point range of these polymers. However, the J values listed in Table XVIII for the type-III polymers varies from 41 to 63; this is not consistent with the narrow melting point range of these polymers. Here, it is suspected that the isotactic content of these type-III polymers is different, yet the melting points are essentially the same. A possible interpretation of these data is that although the isotactic content of these polymers is different, the isotactic sequence lengths of each type-III polymer is sufficiently great that differences cannot be determined accurately. Such an interpretation is consistent with the observation that these type-III polymers behave as isotactic polymers. Under this condition it would be predicted that the gel melting points listed in Table XVII for each added syndiotactic polymer should be close to the gel melting point of each syndiotactic polymer against a standard isotactic polymer. This prediction appears to be valid. For each added syndiotactic polymer in Table XVII, the gel melting point of all mixtures is nearly the same, and these are similar to the gel melting point of the syndiotactic polymer against standard isotactic polymer no. 44. Hence the melting points obtained from mixtures of syndiotactic polymer and type-III polymer represent the gel melting point of the added syndiotactic polymer.

An attempt was made to determine the relative isotacticity and syndiotacticity of a variety of polymers ranging in J value from 35 to 115. Gel melting points were measured on each polymer (a) alone, (b) after displacement with 50 wt. % of a standard isotactic polymer, and (c) after displacement with 50 wt. % of a standard syndiotactic polymer. The results are listed in Table XIX. The gel melting points alone of all of these samples are low; therefore, none of these

Table XVIII: The Effect of Added Syndiotactic Polymer on the Gel Melting Point and J Value of Various Type-III Polymers

Type-III polymer	$\bar{M}_v \times 10^{-5}$	J value	Gel m.p. ($^{\circ}\text{C}$) of mixtures containing 50 wt. % type-III polymers and std. syndiotactic polymer no. 35
No. 63	0.67	41	93.7
71	0.75	52	99.2
68	0.90	45	95.4
70	1.75	47	96.1
74	2.20	63	96.1

Table XIX: The Gel Melting Point of Polymers Alone and in the Presence of Added Isotactic and Syndiotactic Polymers

Polymer	$\bar{M}_v \times 10^{-5}$	J value	Gel m.p., $^{\circ}\text{C}$.		
			Alone	Vs. std. isotactic polymer no. 44	Vs. std. syndio- tactic polymer no. 33
89	3.4	115	< -78	91.0	< -78
92	...	107	< -78	87.4	< -78
86	1.2	89	< -78	58.4	< -78
87	2.3	88	< -20	67.1	< -78
90	6.7	71	6.1	10.0	< -78
88	2.8	68	< -20	25.0	< -78
97	...	60	< -20	0	11.6
96	...	49	< -20	-20	44.5
95	...	42	< -20	< -20	79.6
94	...	38	< -20	< -20	83.2
76	...	35	0 to -20	-20 to -78	80.8

samples can be considered a type-III polymer. In these samples either (a) the syndiotacticity is high and the isotacticity is low (or *vice versa*), or (b) the polymers must contain mostly heterotactic sequences. The gel melting points of these polymers against standard isotactic polymer no. 44 decrease as the J value decreases. Hence, the syndiotacticity of these

polymers decreases as the J value decreases. On the other hand, the gel melting points against standard syndiotactic polymer no. 33 remain low until a J value of 60 is reached. At this point, the gel melting point increases as the J value decreases below 60, and at $J = 42$ it reaches a maximum value at about 80° . Further decreases in J value below 42 do not affect the value of the gel melting point significantly. This limiting gel melting point value of 80° was observed previously using standard syndiotactic polymer no. 33 when gel melting points were determined for isotactic polymers (Table XIII) and for type-III polymer no. 83 (Table XVII).

It could be concluded from these data that the relative syndiotactic sequence length of polymers can be determined from gel melting point measurements. The gel melting point measurement also permits determination of the relative isotactic sequence length of polymers, providing the isotacticity is not too high. Finally, such measurements give information on the relative syndiotactic and isotactic contents of a given polymer. For example, polymer no. 97 (Table XIX) apparently is composed of very short sequences of both isotactic and syndiotactic polymer and is therefore considered more nearly atactic than any other polymer listed in Table XIX.

Discussion

Syndiotactic-Isotactic Gel Formation. The results of this study indicate that the gel melting point is probably a true first-order transition. Melting occurs at the same temperature at which the cloudy gel changes to a clear solution. The melting point is sharp and reproducible and is essentially independent of the method of preparation of the gel or its age, short of syneresis.

Direct evidence that the formation and melting of this gel involves crystalline segments has been obtained from X-ray diffraction studies. The type-III X-ray diffraction patterns of these gels disappear at very near the melting points of the gels and reappear on cooling the same gels below their melting point.

The closest well-characterized system analogous to the gel formation in the literature is that of gelatin in water. It has been shown that the melting of gelatin is accompanied by liberation of heat²⁶ and a clearly defined increase in specific volume.²⁷ Moreover, light-scattering measurements give evidence for cross-linked aggregates in gelatin solutions when the concentration is too low for gelation, and indicate that gelation occurs as these aggregates increase in size.²⁸ Boedtger and Doty²⁸ and Flory²⁹ have, therefore, identified the gelation of gelatin as cross-link formation

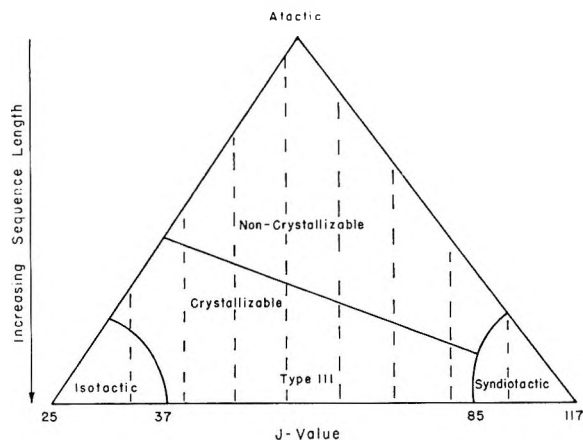


Figure 7. Schematic diagram indicating the insensitivity of the J value to sequence length for isotactic, syndiotactic, and type-III polymer.

by crystallization. No such definitive experiments have been performed for the syndiotactic-isotactic gels, but it is suggestive that light-scattering studies of a dilute solution containing both syndiotactic and isotactic polymer have also given evidence for aggregate formation.³⁰ In view of the above observations, it should be at least a good working hypothesis to postulate that the syndiotactic-isotactic gelation also occurs by crystallite formation.

The Significance of the Gel Melting Point. It has been proposed by Dr. A. Spell of these laboratories that the J value gives information concerning the syndiotactic and isotactic content of poly(methyl methacrylate) but is insensitive to the tactic sequence length, *i.e.*, the infrared measurement furnishes only a single moment of one-sequence distribution. He represents this using the schematic triangular diagram shown in Figure 7. The regions outlined represent very roughly the parameters for which polymers may be crystallized as either isotactic, syndiotactic, or type III. The vertical dashed lines represent lines of constant J value, and tactic sequence length increases in going from noncrystallizable poly(methyl methacrylate) to crystallizable poly(methyl methacrylate), as indicated in Figure 7.

Crystallizable isotactic polymers will not form gels by themselves in dimethylformamide, but must be

(26) L. W. J. Holleman, H. G. Bungenburg de Jong, and R. S. T. Modderman, *Kolloidchem. Beih.*, **40**, 211 (1934).

(27) P. J. Flory and R. R. Garrett, *J. Am. Chem. Soc.*, **80**, 4836 (1958).

(28) H. Boedtger and P. Doty, *J. Phys. Chem.*, **58**, 968 (1954).

(29) P. J. Flory, "Principles of Polymer Chemistry," Cornell University Press, Ithaca, N. Y., 1953.

(30) S. Krause, Rohm & Haas Co., unpublished results.

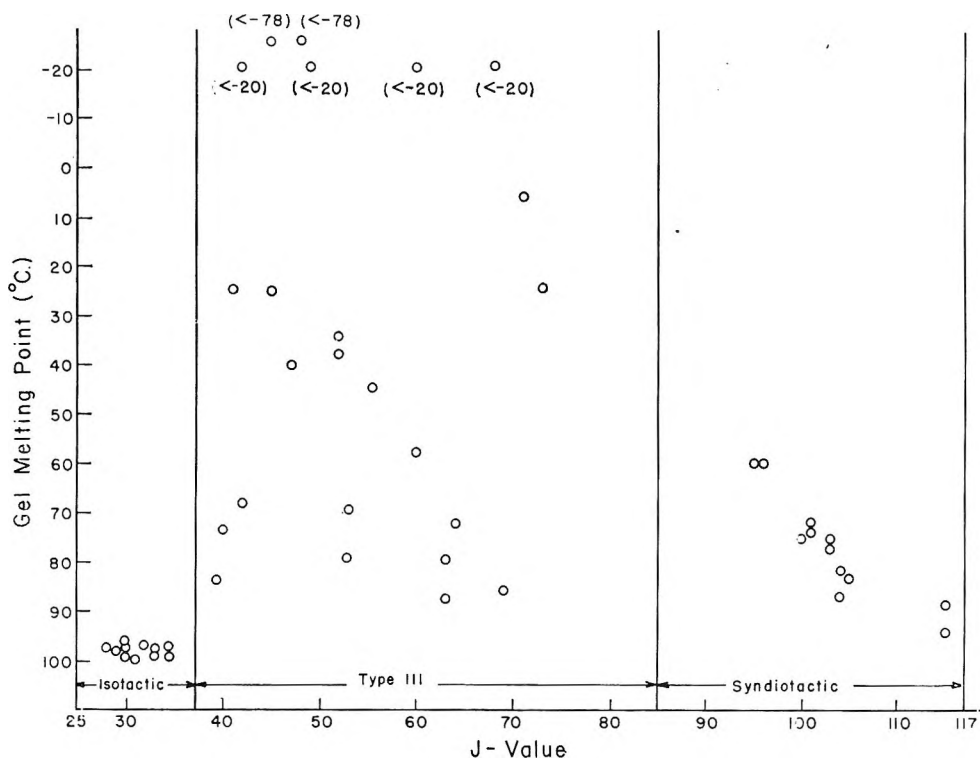


Figure 8. The gel melting point of isotactic, syndiotactic, and type-III polymer as a function of J value.

first mixed with a syndiotactic polymer. Gel melting points thus obtained on a series of isotactic polymers ranging in J value from 28 to 34 are plotted in Figure 8 in a manner similar to the schematic diagram of Figure 7, except that sequence length has been replaced with gel melting point. The gel melting points of all of the isotactic polymers are essentially the same, and differences in sequence length, as indicated from gel melting points, cannot be determined.

Crystallizable syndiotactic polymers will not form gels by themselves in dimethylformamide but must first be mixed with an isotactic polymer. Gel melting points thus obtained on a series of syndiotactic polymers ranging in J value from 95 to 115 are plotted in Figure 8 also. Gel melting points increase as the J value increases. It is believed that the polymers with the higher gel melting points contain the longer tactic sequences, since Gornick³¹ concludes for partially tactic systems that in a polymer chain containing blocks of crystallizable sequences the equilibrium melting point will be dependent primarily on the lengths of the crystallizable blocks, and only secondarily on the concentration of the blocks within the chain. It is important to observe that syndiotactic polymers with the same J value vary only slightly in gel melting point. This is predicted from the schematic in Figure 7,

since within the syndiotactic region the sequence length is not expected to vary over a broad range.

Crystallizable type-III polymers gel by themselves in dimethylformamide. According to the schematic of Figure 7 the tactic sequence length distribution of type-III polymers should vary considerably. The gel melting points of type-III polymers (Figure 8) vary from 87 to $<-78^\circ$. Moreover, a tremendous variation in gel melting point is observed among polymers with the same J value. It is on the basis of these data that we conclude that the gel melting point measures relative differences in the tactic sequence length distribution of poly(methyl methacrylate). It is also quite possible that the gel melting point is not proportional to a simple number-average length, but rather to a weighted-average length, in which the longer regular sequences are more heavily weighted than the shorter sequences. Indications that this may be true come from the lack of consistency between gel melting point data and n.m.r. results.

This work represents an extensive rather than an intensive study of a thermally reversible gelation not due to hydrogen bonding. While this is indeed

(31) F. Gornick, Ph.D. Thesis, University of Pennsylvania, June 1959.

interesting, we have used this phenomenon only as a tool and have tried to indicate in some way the factors influencing the gel melting point. No attempt was made to elucidate the nature of the forces governing the gelation. Very recently, Liquori, *et al.*,³² have proposed a structural model for the syndiotactic-isotactic interaction which provides an explanation for the gelation phenomenon. Their proposal provides also an explanation for the dependence of the gel melting point upon the molecular weight of the syndiotactic component contained in the gel.

Acknowledgments. The authors are indebted to Dr. W. H. Watanabe for directing this work, to Drs.

D. L. Glusker and C. L. Levesque for their encouragement and enthusiasm during this work, and to Mr. J. Gormley and all of our other colleagues at Rohm & Haas who supplied us with polymer samples. We acknowledge the support of Dr. H. S. Yanai who provided X-ray information, Dr. A. Spell for *J*-value measurements, and Dr. K. S. McCallum for n.m.r. results. In particular we wish to thank Dr. Glusker for encouraging the writing of this paper. Without his assistance this paper would not have been submitted for publication.

(32) A. M. Liquori, G. Anzuino, V. M. Coiro, M. D'Alagni, P. Desantis, and M. Savino, *Nature*, **206**, 358 (1965).

Kinetics of Ion Exchange in the Phosphonic Resin Bio-Rex 63

by C. Heitner-Wirguin and V. Urbach

Department of Inorganic and Analytical Chemistry, Hebrew University, Jerusalem, Israel
(Received April 5, 1965)

The exchange of the cations Ca, Cu, UO₂, and Th on the phosphonate resin Bio-Rex 63 was studied. The slow step which determines the rate of exchange of copper and calcium ions is diffusion through the resin particles, while for uranyl and thorium the chemical reaction seems to be the rate-determining step, probably because of the formation of inert complexes with the phosphonic resin. Diffusion coefficients, rate constants, and activation energies for the various cations were calculated.

Introduction

Interest in chelating resins has grown in the last few years because of their possible specific analytical uses. The rate of exchange on this type of resin is generally slower than on normal cation exchangers, and the kinetics of some of these exchangers has therefore already been studied in further detail. Generally, in ion-exchange reactions the rate of exchange is controlled either by diffusion through the resin bead (in concentrated solutions), or by diffusion through the film surrounding the particle (in dilute solutions). Boyd, *et al.*,¹ also developed equations for exchange kinetics where the slow step was the chemical reaction,

but this case is practically not encountered. Helfferich² observes that the chemical reaction could be the slow step in ion exchange on chelating resins. Up to now only the exchange kinetics of the chelating resin Bio-Chelex 100 (containing the iminodiacetic group) were studied under various experimental conditions. Turse and Rieman³ studied the rate of exchange of a series of cations under the limited bath conditions using the

(1) G. E. Boyd, L. L. Myers, Jr., and A. W. Adamson, *J. Am. Chem. Soc.*, **69**, 2836 (1947).

(2) F. Helfferich, "Ion Exchange," McGraw-Hill Book Co., Inc., New York, N. Y., 1962.

(3) R. Turse and W. Rieman, III, *J. Phys. Chem.*, **65**, 1821 (1961).

equations of Kressman and Kitchener.⁴ They concluded from this study that the slow step is particle diffusion for cations giving no chelates with the iminodiacetic group and chemical reactions for cations which chelate with the functional group. In our laboratory, a study⁵ of the rate of exchange of the cations calcium, strontium, and magnesium was made using the same resin, but in the hydrogen form. For all these cations the exchange reaction was found to be controlled by particle diffusion. Schwarz, *et al.*,⁶ made self-exchange measurements using Na²², Co⁶⁰, and Zn⁶⁶ with the same resin. Their results also indicate that the slow step in the self-exchange process is the particle diffusion mechanism. In a more recent report, Varon and Rieman⁷ revised their previous results and also concluded that the slow step in all cases studied was the diffusion through the particle bead. They explained their previous error by the fact that there were some inaccuracies in the capacity determinations due to hydrolysis of the sodium resin form by excessive washings. In some further work done in our laboratory, a careful kinetic study⁸ was effected on the sorption of copper on the sodium form of the iminodiacetic resin and here also the rate of exchange was found to be diffusion-controlled. Although in all the studies on this resin a small concentration effect was observed, it is well established that the ion exchange on the iminodiacetic resin is controlled by particle diffusion.

In the present paper, the characteristics of the phosphonic resin Bio-Rex 63 are studied. From the literature,⁹ it is known that cations which chelate with phosphate in solution, *e.g.*, UO₂ and Th, are very strongly sorbed on this resin. A comparative kinetic study was therefore effected, taking calcium and copper as non-chelatable ions, and uranyl and thorium as ions chelated by phosphate. This resin was used by Kennedy, *et al.*,⁹ for analytical separations, and the selectivity order for a series of cations was determined. Persoz and Rosset¹⁰ have recently studied the equilibria exchange properties of this resin and its selectivity toward cations.

Experimental Section

The resin used was Bio-Rex 63 produced by Bio-Rad Laboratories (*i.e.*, purified Duolite 63). The resin is of the styrene type (6% D.V.B.) and contains the phosphonic group $\text{RP}(=\text{O})(\text{OH})_2$.

The resin was washed with distilled water until the effluent was colorless, then washed with two column volumes of 2 N HCl. After washing the resin free of HCl, the exchanger was brought back to the sodium form by treating it with four column volumes of 1–1.5 N NaOH and water washing. This cycle was repeated twice, then the exchanger was air-dried, sieved, and

separated into various mesh sizes and stored in well-stoppered bottles.

Determination of the Capacity of the Exchanger. A 0.5-mg. portion of the hydrogen form of the resin was stirred with 50 ml. of 0.1 N NaOH until equilibrium was attained (no further changes occurred in the pH of the solution). The supernatant solution was filtered off and the free hydroxide titrated by 0.1 N HCl. The capacity found was 6.06 ± 0.07 mequiv./g.

Titration curves of the resin were constructed by Persoz and Rosset¹⁰ and also by us. These experiments show clearly that the Bio-Rex 63 is a weak acid. (The pK value given by Duolite for this resin is 4–4.8, while the carboxylic resin has a value of 4–6.) The aqueous solution in which the sodium form of the resin was immersed has a pH value of 10–11.

Since the phosphonic acid is weak, no exchange reactions can be realized in the hydrogen form with cations such as Fe³⁺, Cr³⁺, Al³⁺, UO₂²⁺, and Th⁴⁺. This fact limits markedly the uses of the resin since at pH values higher than 4 most of these cations hydrolyze.

The capacity of the sodium form of the resin toward the cation uranyl and thorium was determined under the same conditions as for the sodium ions. The capacities found were (a) UO₂²⁺ 6.04 ± 0.02 mequiv./g., and (b) Th⁴⁺ 5.98 ± 0.05 mequiv./g. These cations are very strongly sorbed, but their elutions from the resin need further study.

Kinetic Measurements. The limited bath⁴ technique method was used. Solutions (50–100 ml.) which were 0.003–0.02 M in the cation studied in 1 M neutral salt were taken for each measurement. The solutions were vigorously stirred. In most cases, the concentration of the cations was kept equivalent to the resin capacity. The solutions were brought to the desired temperature in thermostats which could be regulated to $\pm 0.1^\circ$, and the weighed amount of exchanger was then added (generally 0.1 g.). At measured time intervals, the resin was rapidly separated from the solution, and the content of cation was determined. This procedure was repeated at each time interval with new fractions of resin and solutions.

The radius of the resin particles was determined in two different ways: (a) microscopically; the diameters

(4) T. R. E. Kressman and J. A. Kitchener, *Discussions Faraday Soc.*, **4**, 90 (1949).

(5) C. Heitner-Wirguin and G. Markovits, *J. Phys. Chem.*, **67**, 2263 (1963).

(6) A. Schwarz, J. A. Marinsky, and K. S. Spiegler, *ibid.*, **68**, 918 (1964).

(7) A. Varon and W. Rieman, III, *ibid.*, **68**, 2716 (1964).

(8) C. Heitner-Wirguin and N. Liebling, unpublished results.

(9) J. Kennedy and R. V. Davies, *Chem. Ind. (London)*, 378 (1956).

(10) J. Persoz and R. Rosset, *Bull. soc. chim. France*, 2197 (1964).

of 100 particles swollen in the appropriate solutions were measured and the average value was calculated; (b) the method used by Kressman and Kitchener⁴; determining the specific density of 500 swollen particles (in similar solutions to those used in the kinetic measurements) and calculating from it the mean value of the radius.

Analytical Methods Used. 1. Uranyl was determined colorimetrically by peroxide.¹¹ 2. Thorium was determined by EDTA titration using xylenol orange as indicator.¹² 3. Copper was determined by thio-sulfate titration.¹² 4. Calcium was determined by EDTA titration¹² or colorimetrically using glyoxal bis-(2-hydroxyanil).¹³

Results

The limited bath method was used for the kinetic measurements and the equations developed by Kressman and Kitchener⁴ for the first-order reaction, and those by Frost and Pearson¹⁴ for the second-order reaction. For the first case, *i.e.*, particle diffusion, the equations are

$$F = \frac{Q_t}{Q_\infty} = \frac{6}{r} \frac{Q_0}{Q_0 - Q_\infty} \sqrt{\frac{Dt}{\pi}} \quad (1)$$

where F is the extent of exchange, Q_t is the amount of exchange in time t , Q_∞ is the amount of exchange at equilibrium, Q_0 is the amount of resin and of solute taken in each experiment (all the Q values are taken in milliequivalents), r is the radius of the resin particle in centimeters, and D is the diffusion coefficient in square centimeters per second.

From this equation it can be seen that a plot of F vs. \sqrt{t} should be a straight line if the rate of exchange is controlled by particle diffusion. From the slope (S) of this line, the diffusion coefficient of the ion examined can be evaluated.

$$S = \frac{6}{r} \frac{Q_0}{Q_0 - Q_\infty} \sqrt{\frac{D}{\pi}} \quad (2)$$

For the second-order reaction, *i.e.*, the chemical reaction, the equations used are

$$Z = \frac{Q_t(Q_0 - 2Q_\infty) + Q_0Q_\infty}{Q_0(Q_\infty - Q_t)} \quad (3)$$

If the rate of exchange is controlled by the chemical reaction, a plot of $\log Z$ vs. t should be linear, and from its slope, S , the rate constant k can be determined

$$S = 2kQ_0(Q_0 - Q_\infty)/2.30Q_\infty \quad (4)$$

Both equations given here are valid only in the cases of equivalent concentrations of cations in solutions with the exchangeable cations on the resin.

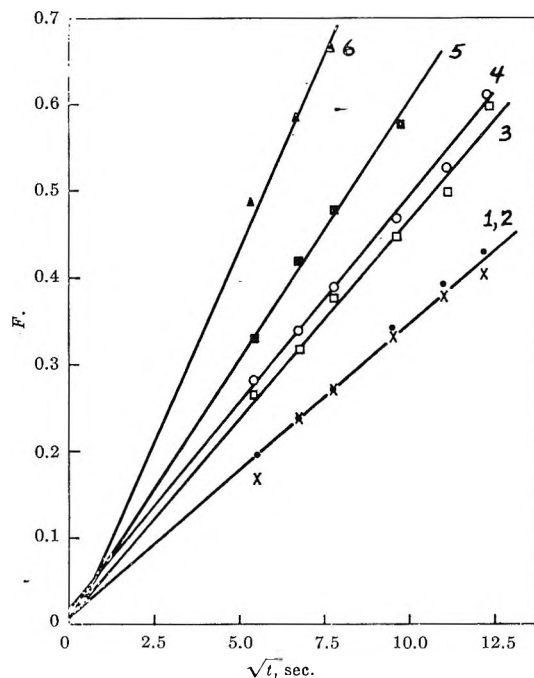


Figure 1. Plots of F vs. \sqrt{t} for CaCl_2 solutions in $0.1 M$ NaCl : 1 and 2, 0.01 and $0.02 M$ CaCl_2 , $r = 0.0175$ cm., 29° ; 3, $0.02 M$ CaCl_2 , $r = 0.0131$ cm., 29° ; 4, $0.01 M$ CaCl_2 , $r = 0.0131$ cm., 29° ; 5, $0.02 M$ CaCl_2 , $r = 0.0175$ cm., 39° ; 6, $0.02 M$ CaCl_2 , $r = 0.0131$ cm., 39° .

The exchange of calcium ions in the solution for sodium of the exchanger was studied, particularly the dependence of the rate of exchange on the particle size, concentration of the solution, and temperature. It can be seen from these graphs that the rate of exchange decreases markedly with increase in particle size and increases steeply with rising temperature. A very small concentration effect can be observed, *i.e.*, a decrease in the rate of exchange with an increase in concentration. This effect was also previously observed in diffusion-controlled reactions.^{3,5,6}

Figure 1 shows that all the plots of F vs. \sqrt{t} are linear, and this leads to the conclusion that the slow step for the exchange of calcium on the phosphonated resin is diffusion through the particle.

Similar plots for the exchange of copper ions were obtained and it can be concluded that the rate of exchange depends on the particle size, and practically not on the concentration of copper ions in solution.

(11) N. H. Furman, "Standard Methods of Chemical Analysis," Vol. I, D. Van Nostrand Co., Inc., Princeton, N. J., 1962, p. 1199.

(12) A. Vogel, "Quantitative Inorganic Analysis," Longmans, Green and Co., London, 1961, pp. 358, 442.

(13) A. Glasner and S. Skurnik, *Israel J. Chem.*, 2, 363 (1965).

(14) A. A. Frost and R. G. Pearson, "Kinetics and Mechanism," John Wiley and Sons, Inc., New York, N. Y., 1953, p. 174.

From the experiments with calcium and copper, the respective diffusion coefficients have been evaluated, taking into consideration that the equation is valid only for the experiments with equivalent amounts of exchangeable ions in solutions to those of the exchanger. In order to obtain this validity, very dilute solutions must be used. For the exchange of calcium ions a suitable colorimetric method¹³ was used, which gave accurate determinations of the dilute solutions used, while no appropriate method for copper was found. However, it was possible to infer the correct value of D from solutions containing higher ion concentrations. A plot of D (calculated at higher concentrations of the solution) vs. the concentration of the cation in solution gives a straight line from which the desired value of D (at the equivalent concentration point) can be extrapolated. This approach was used for the evaluation of D for the exchange of copper ions (Table I). From the values of D at two temperatures the activation energies were calculated.

Table I: Diffusion Data for the Exchange of Calcium and Copper on Bio-Rex 63

Exchange reaction	T , °C.	$D \times 10^8$ cm. ² sec. ⁻¹	E_a , kcal./mole
Ca ²⁺ /Na ⁺	29	0.705	21
Ca ²⁺ /Na ⁺	39	2.25	
Cu ²⁺ /Na ⁺	29	1.24	
Cu ²⁺ /Na ⁺	39		15 ^a

^a Evaluated from a different series of experiments.

Figure 2 shows the rate of sorption of UO₂ with resin of two different particle sizes and at two temperatures. From this figure it can be seen that the rate of exchange is not dependent on the size of the particles, and that there is an increase of rate with rising temperature. From Table II it is clearly seen that an increase in UO₂ concentration increases the rate of exchange appreciably.

Table II: Influence of UO₂ Concentration in the Solution on the Rate of Exchange

UO ₂ , mequiv./g. sorbed from solutions	0.003 M	t , min.					
		2	6	10	14	20	30
0.003 M	0.5	0.71	0.81	0.87	0.99	...	2.00
0.006 M	0.56	0.76	0.90	1.00	1.16	1.38	2.00

Figure 3 shows the linearity of the plots of $\log Z$ against t for two temperatures and two mesh sizes of

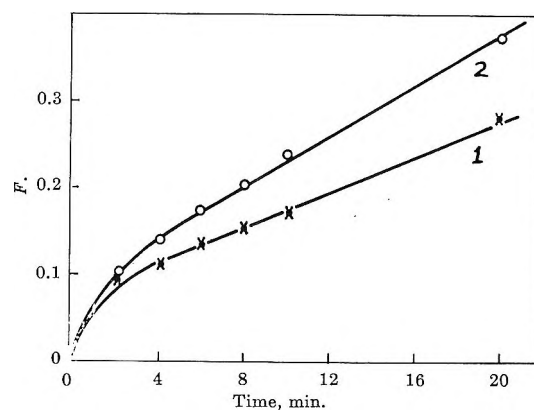


Figure 2. Rate of exchange adsorption of uranyl ion on Bio-Rex 63 from 0.003 M UO₂(NO₃)₂ and 1 M NaCl solutions: 1, $r = 0.0088$ and 0.0150 cm., 29°; 2, $r = 0.0088$ and 0.0150 cm., 39°.

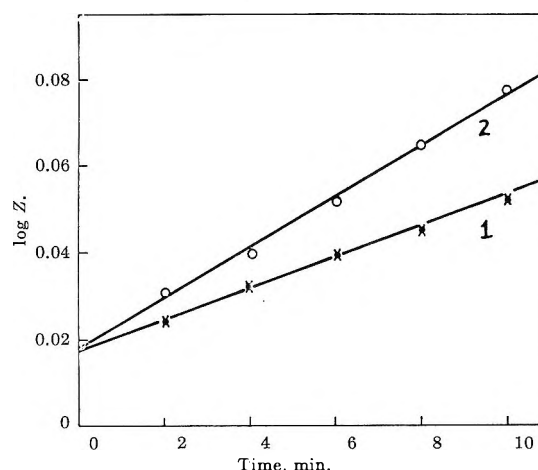


Figure 3. Plots of $\log Z$ vs. t for 0.003 M UO₂(NO₃)₂ solutions in 1 M NaCl on Bio-Rex 63: 1, $r = 0.0088$ and 0.0150 cm., 29°; 2, $r = 0.0088$ and 0.0150 cm., 39°.

resin, and from these slopes the rate constant k and the activation energy were calculated (Table III). Very similar results were obtained for the exchange of thorium; *i.e.*, the rate is dependent on the concentration of thorium in solution and independent of the size of the particles (Figure 4). Some of the measurements were made at different stirring rates, but without affecting the rate of exchange. From these experiments it can be assumed that the chemical reaction is the slow step which controls the exchange of uranyl and thorium on the phosphonated resin.

Discussion

The kinetics of exchange of four cations on the phosphonated resin Bio-Rex 63 were studied, and two different types of reactions were found. In the case of

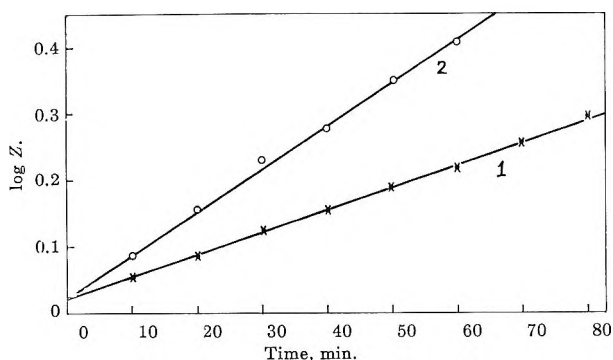


Figure 4. Plots of $\log Z$ vs. t for $0.01 M$ $\text{Th}(\text{NO}_3)_4$ solutions in $1 M$ NaCl on Bio-Rex 63: 1, $r = 0.0170$ and 0.0115 cm., 29° ; 2, $r = 0.0170$ and 0.0115 cm., 39° .

Table III: Rate Constants and Activation Energies for UO_2 and Th

Ion	T , $^\circ\text{C}$.	$k \times 10^3$	E_a , kcal./mole
UO_2^{2+}	29	3.18	10
UO_2^{2+}	39	5.37	
Th^{4+}	29	35	11
Th^{4+}	39	63	

calcium and copper, the rate of exchange increases with decrease of the particle size of the resin, and increases considerably with an increase in temperature. An increase in concentration of the solution decreases the rate of exchange slightly.⁵ In these cases the exchange reaction proceeds very quickly, the half-time of reached equilibrium being of the order of 30–100 sec. according the resin particle size used. It may therefore be concluded that the exchange of copper and calcium on a phosphonated resin is diffusion-controlled, as is the case of a regular cation exchanger. From the literature it is also known that these ions form no complex with the monomeric phosphate group.

The results obtained for the exchange of uranyl and thorium ions on the phosphonated resin are surprising. The exchange reactions proceed very slowly, and half-time of equilibrium is attained in 40–50 min. The rate of exchange is independent of the particle size of the resin (particles of radius 0.0878–0.169 cm. were used, and practically no changes in swelling were observed during the experiments). A particularly careful study of the particle sizes and their shrinking was made. Uniformity of particle sizes was attained by sieving the samples through standardized sieves and taking frac-

tions within a limit of 8–10 mesh. Although the particale shrinkage in the uranyl and thorium form is somewhat greater than in the copper or calcium form, exact measurements showed it to be no more than 5% (for the same mesh size of the resin the radius of the copper form was 0.0123 ± 0.0006 cm., while for the thorium form the measured radius was 0.0117 ± 0.0008). This difference in shrinking cannot be responsible for the different behavior of the two kinds of cations. Increased concentration of the solution considerably raises the rate of exchange; the contrary effect was observed in the case of copper and calcium. A rise in temperature increases the rate of exchange, but the increase is much smaller than in the case of the two uncomplexed cations. Changes in the rate of stirring do not affect the rate of exchange. It must be concluded from these experiments that the slow step in these reactions is the chemical reaction, and not the diffusion through the resin beads.

This conclusion seems somewhat unusual since until now no exchange reactions have been known where the chemical reaction is the slow step. Even strongly chelating ions, such as copper, exchange on the chelating resin Bio-Chelex 100 (iminodiacetic group) by a diffusion-controlled mechanism.

It may be assumed from these experiments that the complex formed by copper with the iminodiacetic group is labile, while the complexes formed by uranyl and thorium with the phosphonic group are inert, and therefore the chemical reaction is the slow step. It is also due to the inertness of these complexes that once these ions are sorbed it is very difficult to elute them, while copper is easily eluted from the iminodiacetic resin.

The different temperature effect in the two types of exchange kinetics calls for further explanation. This difference can be seen directly from Figures 1 and 2, or from the calculated values of the activation energies (Tables I and III). It can be assumed that the activation energies for chemically controlled exchange reactions should be higher than for diffusion-controlled reactions. In this case, the activation energies calculated for uranyl and thorium, which are in the range of 10 kcal./mole, are acceptable.

The activation energies for copper and calcium are very high, and are of the same order of magnitude as those found for similar ions on Bio-Chelex 100 in the hydrogen form. No explanation can be given until further data are available.

A Gas Phase Electron Diffraction Investigation of Iron Pentacarbonyl

by M. I. Davis

Department of Chemistry, University of Texas, Austin, Texas

and H. P. Hanson

Department of Physics, University of Texas, Austin, Texas (Received April 7, 1965)

The molecular structure of iron pentacarbonyl has been studied by the gas phase electron diffraction method. The conformation was found to be that of a trigonal bipyramid in agreement with several earlier investigations. The axial Fe-C bonds were found to be shorter than the trigonal by 0.045 Å., the values being $r(\text{axial}) = 1.797 \text{ \AA.}$ and $r(\text{trigonal}) = 1.842 \text{ \AA.}$ The mean value of the C=O bond lengths was found to be $1.136 \pm 0.003 \text{ \AA.}$ It was found that the existence of shorter axial bonds is corroborated by the results of both X-ray crystallographic and vibrational spectroscopic studies. Considerations of the possible bonding situations in the molecule seem to be consistent with the existence of shorter axial Fe-C bonds.

Introduction

A great deal of interest has been shown, over a period of years, in the chemistry of the metal carbonyls. From the results of a wide variety of investigations,¹ a reasonably coherent concept has been developed of the bonding in these compounds.

The general bonding picture may be discussed within the framework of ligand field theory. This approach is relatively straightforward in the instances where the carbonyls are all symmetrically equivalent (*e.g.*, $\text{Ni}(\text{CO})_4$, $\text{Cr}(\text{CO})_6$) but becomes more involved when they are not (*e.g.*, $\text{Fe}(\text{CO})_5$).

It is well established that iron pentacarbonyl exists in a trigonal bipyramid configuration. This much could be ascertained from the original electron diffraction study² and has since been verified by an X-ray crystallographic investigation³ and by consideration of the numbers of infrared and Raman active fundamental modes of vibration.⁴

One of the more intriguing aspects of the structures of trigonal bipyramid molecules is the comparison of the axial and trigonal bond lengths. In both PCl_5 and SbCl_5 , the axial bonds are reported to be significantly longer than the trigonal.⁵ In neither the original electron diffraction study² nor the more recent X-ray investigation³ was any distinction made between the axial and trigonal bond lengths. In each instance

only mean values for the Fe-C and C=O bond lengths were given.

It has been the principal purpose of the investigation to determine what difference, if any, can be discerned between the two types of bond lengths.

It has proved fruitful to compare the results of the electron diffraction investigation with the atomic coordinates as found by X-ray crystallography and with certain spectroscopic information.

In conjunction with the publication of the results of the vibrational spectroscopic studies, Edgell⁴ has examined the bonding from a symmetry standpoint. It is interesting to take up this approach in the light of the measured bond lengths.

Experimental Section

This investigation was carried out with the recently completed electron diffraction unit of the University of Texas. A brief description of the equipment has been given in another paper.⁶

(1) E. W. Abel, *Quart. Rev.* (London), **17**, 133 (1963).

(2) R. V. G. Ewens and M. Lister, *Trans. Faraday Soc.*, **35**, 681 (1939).

(3) A. W. Hanson, *Acta Cryst.*, **15**, 930 (1962).

(4) W. F. Edgell, W. E. Wilson, and R. Summitt, *Spectrochim. Acta*, **19**, 863 (1963).

(5) L. E. Sutton, Ed., "Tables of Interatomic Distances," Special Publication No. 11, The Chemical Society, London, 1958.

Intensity data were collected photographically at distances of 25, 50, and 100 cm. from the scattering center. No reliable interference pattern could be discerned beyond $s = 42 \text{ \AA}^{-1}$.

Preliminary Data Handling

The transmissions were measured at intervals of $\Delta s = 0.25 \text{ \AA}^{-1}$ from traces of the microphotometric records. They were converted first to optical densities and then by means of a correction formula⁷ to electron intensities

Corrections were applied to take into account the sectoring of the beam and the use of flat plates. For convenience of handling, the intensities were multiplied by s^4 .

Theoretical Outline⁸

The theoretical expressions which are employed in the analysis of data are given in eq. 1-3

$$I_{\text{ex}}(s) = Ks^4(B(s) + M(s)) \quad (1)$$

where s is the scattering parameter $= 4\pi \sin(\theta/2)\lambda^{-1}$, θ is the angle of scattering, λ is the deBroglie wave length, K is the product of a number of experimental and natural physical constants. $M(s)$, the molecular scattering intensities, vary in an undulating fashion with s . $B(s)$, the atomic scattering intensities, provide a relatively smooth background to $M(s)$. $B(s)$ is given theoretically by eq. 2.

$$B_c(s) = \sum n_i [(Z_i - F_i(s))^2 + S_i(s)] \quad (2)$$

$F_i(s)$ and $S_i(s)$ are, respectively, the atomic and inelastic scattering factors of the element with atomic number Z_i ; n_i atoms of this element occur in the molecule.

$$M(s) = \sum 2n_{ij} (Z_i - F_i(s))(Z_j - F_j(s)) \cos(\eta_i(s) - \eta_j(s)) \exp(-l_{ij}^2 s^2 / 2) (sr_{ij})^{-1} \sin(sr_{ij}) \quad (3)$$

n_{ij} is the number of symmetrically equivalent atom pairs of the type ij , with a mean vibrational amplitude of l_{ij} and an internuclear distance r_{ij} . The $\eta_i(s)$ terms are the atomic phase shifts for the element i .

The r_{ij} values obtained from the use of eq. 3 are related to the mean internuclear distances r_g by the approximate relationship given in eq. 4.

$$r_{ij} = r_g - l_{ij}^2 / r_{ij} \quad (4)$$

The relationship between r_g and the equilibrium internuclear distance r_e has been investigated by a number of people⁹ and can be given approximately by eq. 5

$$r_g = r_e + 3al_{ij}^2 / 2 \quad (5)$$

a being the Morse potential constant.

Further Data Handling

Two further steps were carried out in the treatment of the data previous to any attempts at structure determination. A two-parameter adjustment was made to normalize the background of the experimental curve with that of its theoretical counterpart. The atomic and molecular scattering contributions were separated by a least-squares numerical technique. The mathematical nature of these two steps has been described in a previous publication.⁶

Structure Determination

A radial distribution curve was calculated from the experimental molecular scattering intensities by means of eq. 6.

$$\sigma(r)/r = \sum_s M(s) s Z_{\text{Fe}} Z_{\text{O}} / (Z_{\text{Fe}} - F_{\text{Fe}}(s)) \times (Z_{\text{O}} - F_{\text{O}}(s)) \exp(-ks^2) \sin(sr) \Delta s \quad (6)$$

The damping factor k is introduced to compensate for the existence of an upper limit of s at which intensities are measured.

The positions and sizes of the major peaks in the radial distribution curve left no doubt as to the correctness of the trigonal bipyramid model.

Despite the large number of distances which are dependent upon a relatively small number of independent dimensional parameters, the radial distribution curve was not simple to analyze. Not only is it impossible to separate the axial and trigonal contributions to the C=O, Fe-C, and Fe-O peaks, but many of the other contributions occur at closely similar distances. It was, however, fairly obvious from the positions of a number of the minor peaks, that there does exist a difference between the axial and trigonal bond lengths.

Although it was possible to obtain, from the radial distribution curve, good values for the mean Fe-C and C=O bond lengths, it was not feasible to proceed with any analysis, involving the distinction between the axial and trigonal bonds, by that particular method. It was evident that an analytical procedure, involving the intensity curves directly, was required to achieve that distinction.

Three distinct methods were employed to refine the structural parameters of the basis of the intensity curves. One of these was the matrix least-squares method, described by Hedberg.¹⁰ The other two methods involved continuous adjustment of the struc-

(6) M. I. Davis and H. P. Hanson, in press.

(7) J. Karle and I. L. Karle, *J. Chem. Phys.*, **18**, 957 (1950).

(8) See ref. 6 for a more detailed presentation.

(9) See, e.g., L. S. Bartell, *J. Chem. Phys.*, **23**, 1219 (1955).

(10) K. Hedberg and M. Iwasaki, *Acta Cryst.*, **17**, 529 (1964).

tural parameters in the direction leading to improving compatibility between the theoretical and experimental molecular scattering curves. The two methods differed inasmuch as while one entailed simultaneous adjustment of all parameters, the other involved cyclic variation of each parameter in turn. More than one method was used to avoid the danger of finding false minima.

As stated, the complete structure of iron pentacarbonyl can be described in terms of four independent parameters. It was not feasible in the first instance to analyze the intensity curve without using the mean Fe-C and Fe-O interatomic distances as two of the parameters. The other two were chosen to be the two axial bond lengths. It was assumed that the trigonal bond lengths could be calculated in a simple fashion from the axial and mean values. The Fe-C and Fe-O scattering contributions were still handled in terms of equal axial and trigonal bonds. The remaining contributions, where appropriate, were calculated on the basis of the two bond types being different.

It rapidly became evident that the axial Fe-C bonds are at least 0.04 Å. shorter than the trigonal. With a difference of this magnitude, a fair amount of error is introduced into the analysis of both the Fe-C and Fe-O scattering contributions. Consequently, with a reasonable idea as to the lengths of the two Fe-C bonds, it was possible to change to another more realistic coordinate system.

The new system involved the use of three independent parameters. Two of these were the two Fe-C bond distances, the other being the mean C=O bond length. It was recognized that the difference between the axial and trigonal C=O bond lengths is sufficiently small that no meaningful results can be obtained by allowing for any distinction.

With the adoption of this system, an appreciable improvement was noted in the correlation between the theoretical and experimental molecular scattering curves.

Results

The results of the study of the radial distribution curve, together with those of the various intensity curve analyses, are given in Table I.

The structural parameters, obtained from this investigation are given in Table II, together with the limits of tolerance. These limits are based largely upon the results of an error matrix calculation of the type described by Hedberg.¹⁰ The values quoted have been made slightly larger than those calculated, in order to take into account the uncertainty involved in measuring the deBroglie wave length.

Table I: Comparison of the Results of Four Methods of Structure Refinement^a

	Bond lengths, Å.			
	RD	A	B	C
C=O (mean)	1.139	1.134	1.134	1.135
Fe-C (axial)		1.802	1.796	1.795
Fe-C (trig.)	1.827	1.839	1.841	1.840
(mean)				
	Vibrational amplitudes, Å.			
	A	B	C	
C=O (mean)	0.037	0.036	0.034	
Fe-C (axial)	0.041 ^b	0.039	0.046	
Fe-C (trig.)	0.059 ^b	0.062	0.059	

^a RD is radial distribution curve analysis. Intensity curve analyses: A, Hedberg method; B, simultaneous continuous adjustment of parameters; C, individual continuous adjustment of parameters. ^b Assumed.

Table II: The Molecular Structure of Iron Pentacarbonyl

	r_e , Å.
C=O	1.136 ± 0.003
Fe-C (axial)	1.797 ± 0.015
Fe-C (trig.)	1.842 ± 0.015
Configuration: trigonal bipyramid	

The radial distribution curve is shown in Figure 1, together with its theoretical counterpart. The theoretical curve was obtained by Fourier inversion of the molecular scattering curve, rather than by the more usual procedure of summation of gaussian curves. This explains why the theoretical curve is slightly negative at low s .

The experimental and theoretical molecular scattering curves are shown in Figure 2. The over-all correlation between the two curves would seem to be reasonable.

Comparison with the Results of an X-Ray Study. The electron diffraction investigation shows quite clearly that the axial Fe-C bonds are shorter than the trigonal.

The results are available of a recent X-ray crystallographic study.³ In presenting those results, the author has not seen fit to distinguish between the lengths of the two bond types. It was possible, however, using the published atomic coordinates, to calculate the bond lengths of the molecule in the crystalline state. The values, obtained from that calculation, are given in Table III. While it might be expected that there exist small differences between the internuclear

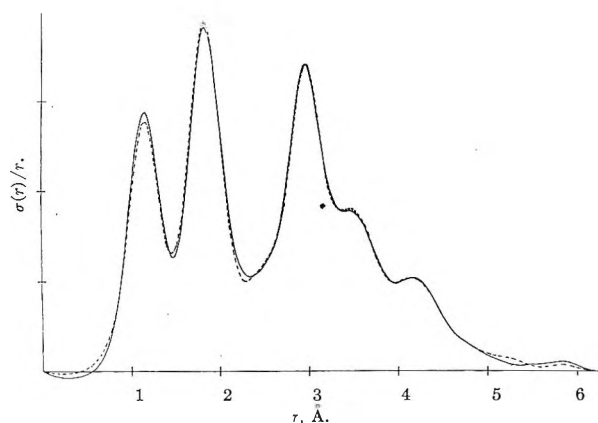


Figure 1. Radial distribution curve of iron pentacarbonyl. The broken line is the theoretical version. Damping factor, $k = 0.01$.

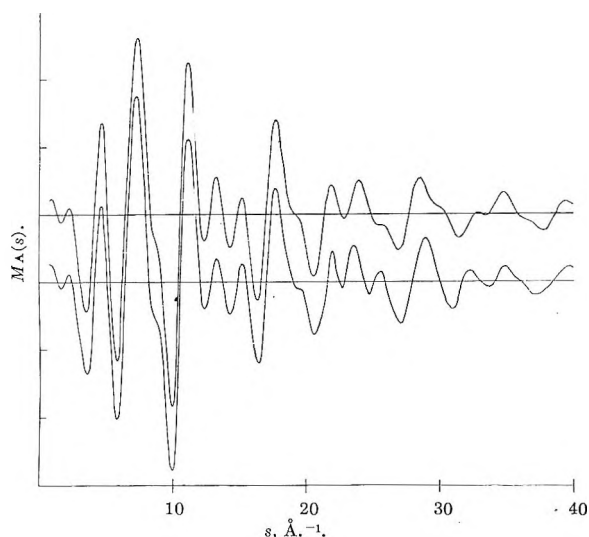


Figure 2. Molecular scattering curves for iron pentacarbonyl. The lower curve is the experimental version; the upper is theoretical.

distances of a molecule depending upon the state of aggregation (and, consequently, exact coincidence between the electron diffraction and X-ray values is not to be anticipated) the results of this calculation of the solid-state bond lengths may be taken to corroborate the finding of shorter axial bonds.

Comparison with Spectroscopic Findings. Several studies have been made of the vibrational spectra of $\text{Fe}(\text{CO})_5$. The most recent and comprehensive of these is that of Edgell and co-workers.⁴ From this investigation, it has proved to be possible to ascertain the symmetry species of the modes associated with specific fundamental frequency values. In certain instances it was also possible to state that, because of the symmetry requirements, certain of the vibrational modes involve the motion of either the trigonal

Table III: Fe-C Bond Lengths Calculated from Crystal Atomic Coordinates^a

Bond type	r (Fe-C), Å.
Axial	1.785
	1.807
Trigonal	1.827
	1.827
	1.837

^a See ref. 3.

carbon and oxygen atoms alone or, alternatively, only the axial. Furthermore, it can be deduced from the magnitude of their frequencies that certain of the modes are strongly dominated by one particular type of bond or angle variation.

Although frequency values can be misleading in predicting structural properties from them, it is interesting to note that there are certain features of this spectroscopic study which are compatible with the findings of the diffraction investigation.

The asymmetric stretching frequencies (ν_6 and ν_{10}) for modes belonging to the symmetry species A_2'' and E' are found to be 2014 and 2034 cm^{-1} , respectively.¹¹ The A_2'' mode (ν_6) is strongly dominated by asymmetric stretching of the axial $\text{C}=\text{O}$ bonds while the E' mode (ν_{10}) is dominated by that of the trigonal $\text{C}=\text{O}$ bonds. The lower frequency of the axial bond stretching could indicate that they are weaker than the trigonal. If one accepts the hypothesis that the sum of the bond orders ($N_{\text{CO}} + N_{\text{FeC}}$) is a constant,¹² it follows that the axial Fe-C bonds would be the stronger of the two.

Fe-C stretching frequencies are of the order of 400 cm^{-1} . $\nu_8(A_2'')$ and $\nu_{13}(E')$ have been assigned values of 474 and 431 cm^{-1} , respectively.⁴ It is argued that these modes are associated with asymmetric stretching of the Fe-C bonds, the former involving only the axial bonds and the latter, the trigonal. Here, the relative magnitudes indicate, as above, that the axial Fe-C bond is the stronger.

That the axial Fe-C bond should be the stronger is consistent with the electron diffraction finding that it is shorter than the trigonal.

Discussion

The conclusion that must be drawn from the foregoing electron diffraction results, coupled with spectro-

(11) The authors of ref. 4 present two conflicting versions as to the assignments of A_2'' and E' .

(12) H. Stammreich, K. Kawai, O. Sala, and P. Krumholtz, *J. Chem. Phys.*, 35, 2168 (1961).

scopic and X-ray evidence, is that the axial Fe-C bonds in iron pentacarbonyl are shorter than the trigonal. It is desirable to establish whether or not this state of affairs might be predicted from bonding considerations. It should at least be possible to determine if it is consistent with current bonding theories.

The simplest picture of the formation of metal carbonyl bonds is one in which σ M-C bonds are produced by donation of the carbon lone pairs into the vacant orbitals of the metal.¹³ There is also predicted to be some back donation from the metal into the antibonding C=O orbitals to offset any unfavorable charge distribution.

This description does not differentiate between the axial and trigonal bonds, nor does it allow for any π -bonding between the iron and the bonding π (C=O) orbitals.

A discussion of the bonding situation, in terms of symmetry arguments has been presented by Edgell, *et al.*⁴ It is this sort of approach that must be adopted to achieve the required ends.

The symmetry species of the various sets of equivalent carbonyl molecular orbitals are given in Table IV, together with the iron orbitals available for bond formation.

Table IV

MO (CO)	No. of bonds	Symmetry	Available Fe orbitals
σ (C lone pair)	5	$2a_1' + a_2'' + e'$	a_1' 4s3d _{z²} a_2'' 4p _z e' 4p _x 4p _y 3d _{xy} 3d _{x²-y²}
π Axial	4	$e' + e''$	e' 4p _x 4p _y 3d _{x²-y²} e'' 3d _{xz} 3d _{yz}
π Planar trigonal	3	$a_2' + e'$	a_2' None e' 4p _x 4p _y 3d _{xy} 3d _{x²-y²}
π Nonplanar trigonal	3	$a_2'' + e''$	a_2'' 4p _z e'' 3d _{xz} 3d _{yz}
σ (C-O)	5		
(O lone pair)	(5)		

Each of the Fe orbitals may participate in only one strongly bonding interaction. It is convenient to treat the orbitals in terms of their symmetry species.

For the a_1' case, both the 3d_{z²} and 4s orbitals are involved in σ -bonding.

There are no Fe a_2' orbitals; consequently, the C=O m.o. of that symmetry will be nonbonding.

In the a_2'' case the 4p_z orbital is suitable for bonding with either the σ_a or π_t' (C=O) orbitals. The (C=O) σ orbital is the carbon lone pair. It is predicted to be strongly directed away from the carbon¹⁴ and is there-

fore well suited for the formation of a strong Fe-C bond. It would follow that the 4p_z orbital can only have a weak π -interaction.

The e'' iron orbitals can form bonds with either the π_a or the π_t (C=O) orbitals. In the latter case the directional properties of the iron orbitals are only suitable for strong bonding when hybridized with an orbital of a'' symmetry. Since only the 4p_z is available and since it is involved in strong σ -bonding, the chances for any appreciable bonding interaction with the π_t orbitals are small. No such restriction is placed upon the interaction with the π_a . It is therefore probable that the most stable orbital of this symmetry will be one with appreciable 3d (Fe)- π_a (C=O) overlap. Next in order of stability would be an orbital of predominantly π_t (C=O) character. The third orbital here would require some antibonding, either Fe-C or C=O. It is quite probable that there is some mixing of π_a and π_a^* .

The five Fe(CO)₅ molecular orbitals might be represented approximately by

$$e_1'' = (3d + \pi_a)/2$$

$$e_2'' = \pi_t$$

$$e_3'' = (3d - \pi_a + \sqrt{2}\pi_a^*)/2$$

$$e_4'' = \pi_t^*$$

$$e_5'' = (3d - \pi_a - \sqrt{2}\pi_a^*)/2$$

This would give a net partial double bond character to the axial Fe-C bonds.

The most stable of the e' orbitals will presumably be that involving the formation of σ_t -bonds. Edgell⁴ predicts the existence of two strong e' bonding interactions while Eyring, *et al.*,¹⁵ produce arguments suggesting that only weakish interactions can accompany the strong σ -bonding.

Since there are no a_2' Fe orbitals, it is impossible to form those hybrids with the appropriate directional properties to give strong bonding with the π_t^* (C=O) orbitals.

There are no such restrictions on bonding with the π_a orbitals. Again it is necessary that electrons be placed in an orbital with some antibonding. The possibility of mixing π_a and π_a^* also exists here.

The seven orbitals that seem to be most likely are

(13) See, *e.g.*, A. F. Wells, "Structural Inorganic Chemistry," 3rd Ed., Oxford University Press, Oxford, 1962, p. 747.

(14) C. A. Coulson, "Valence," 2nd Ed., Oxford University Press, Oxford, 1961, p. 222.

(15) H. Eyring, J. Walter, and G. E. Kimball, "Quantum Chemistry," John Wiley and Sons, Inc., New York, N. Y., 1944, p. 230.

$$e_1' = (e'(\text{Fe}) + \sigma_t)/2$$

$$e_2' = (e'(\text{Fe}) + \pi_a)/2$$

$$e_3' = \pi_t^*$$

$$e_4' = (e'(\text{Fe}) - \pi_a + \sqrt{2}\pi_a^*)/2$$

$$e_5' = \pi_t^*$$

$$e_6' = (e'(\text{Fe}) - \pi_a - \sqrt{2}\pi_a^*)/2$$

$$e_7' = (e'(\text{Fe}) - \sigma_t)/2$$

This again gives a net partial double-bond character to the axial Fe-C bonds.

This sort of consideration, even though it involves a certain measure of speculation, would seem to indicate quite strongly that the situation for axial Fe-C double bonding is more favorable than that for the trigonal. This is, of course, consistent with the finding that the axial bonds are significantly shorter.

Conclusions

Molecules of iron pentacarbonyl exist in the tri-

gonal bipyramid configuration. This had been demonstrated by several independent investigations,²⁻⁴ and no other interpretation can be placed upon the data of this present study.

The most significant finding of this investigation is that the axial Fe-C bonds are of the order of 0.04 Å. shorter than the trigonal. This is, to a large extent, corroborated by the re-examination of the results of previous X-ray³ and vibrational spectra⁴ studies. There is also some degree of substantiation obtainable from a consideration of the probable bonding situation in the molecule.

Acknowledgments. This investigation was sponsored by the Robert A. Welch Foundation of Houston, Texas. The equipment was built with financial assistance from the Graduate School of the University of Texas. Much credit for the construction goes to Dr. D. M. Cowan. Our gratitude is extended to the staff of the Computation Center of the University of Texas and also to Mr. Bobby Turman for technical assistance.

Esin and Markov Effect for Adsorbed Organic Ions and Molecules

by R. G. Barradas, P. G. Hamilton,

Lash Miller Chemical Laboratories, Department of Chemistry, University of Toronto, Toronto 5, Ontario, Canada

and B. E. Conway

Department of Chemistry, University of Ottawa, Ottawa 2, Ontario, Canada (Received April 8, 1965)

Electrochemical adsorption of piperidine, pyridine, morpholine, dioxane, furfurylamine, tetrahydrofurfurylamine, N-methylfurfurylamine, N-methyltetrahydrofurfurylamine, *n*-propyl alcohol, allyl alcohol, and propargyl alcohol have been investigated at $25 \pm 1^\circ$ in 1 *N* aqueous potassium chloride solutions at the mercury electrode by means of an improved Lippmann electrocapillarometer. Electrocapillary measurements were carried out for three aromatic and heterocyclic amines, which could be converted by protonation to the corresponding cations in aqueous hydrochloric acid solutions. The first objective was to verify experimentally, from a general thermodynamic standpoint suggested by Parsons, the quantitative validity of the Esin and Markov effect for specifically adsorbed *organic* cations. This effect is concerned with the linear relation of the potential of the electrocapillary maximum, measured with respect to a given reference electrode, to the logarithm of the activity of ionic additives present in the solution. A second but more important aim has been to develop a theoretical extension of Parsons' treatment to explain the possible existence of an analogous Esin and Markov effect for the specific adsorption of neutral organic molecules. Agreement and limitations in the comparison of theoretical predictions and experimental results are discussed in terms of orientation effects, electronic and molecular structure, and the dependence of the Esin and Markov coefficient on the electrode surface charge.

Introduction

The Esin and Markov effect refers to the experimental observation made by these authors¹ that the potential of zero charge (p.z.c.) on mercury varies linearly with the logarithm of activity (a_A) of surface-active anions. This subject has been examined by various workers²⁻⁵ and the thermodynamic treatment by Parsons⁶ is of special interest to the present work, since we are concerned with the correlation of the theoretical predictions of Parsons with our electrocapillary results for specifically adsorbed *organic* cations. In addition, we shall examine whether there is a comparable Esin and Markov effect for the specific adsorption of neutral organic molecules, a subject which has hitherto not been investigated. The Esin and Markov co-

efficient $\partial E/\partial \ln a_A$ is an important quantity for development of rate equations for adsorption of neutral substances at a metal-electrolyte interface⁷ where there is very little information known except for a few cases

(1) O. A. Esin and B. F. Markov, *Acta Physicochim. URSS*, **10**, 353 (1939).

(2) D. C. Grahame, *Ann. Rev. Phys. Chem.*, **6**, 337 (1955).

(3) D. C. Grahame, Technical Report No. 1, Office of Naval Research, Washington, D. C., June 13, 1957.

(4) O. A. Esin and V. M. Shikov, *Russ. J. Phys. Chem.*, **17**, 236 (1943).

(5) B. V. Ershler, *ibid.*, **20**, 679 (1946).

(6) R. Parsons, *Proc. Intern. Congr. Surface Activity*, 2nd, London, **38** (1957).

(7) P. Delahay and D. M. Mohliner, *J. Am. Chem. Soc.*, **84**, 4247 (1962).

of purely diffusion-controlled processes (*cf.* ref. 8 and the literature cited therein).

Experimental Section

The method and experimental details for electrocapillary measurements have been described previously.⁹ More recently, improvement in instrumental design of the electrocapillarometer assembly in the form of a very sensitive pressure-regulating device led to better precision and accuracy of results,¹⁰ and the electrocapillary data used in the present paper were obtained from measurements on the modified apparatus.^{10,11} The following neutral substances were investigated in 1.0 *N* aqueous KCl solutions at $25 \pm 1^\circ$: piperidine, pyridine, morpholine, dioxane, *n*-propyl alcohol, allyl alcohol, propargyl alcohol, furfurylamine, tetrahydrofurfurylamine, N-methylfurfurylamine, and N-methyltetrahydrofurfurylamine. For the adsorption of organic ions, aniline, furfurylamine, and tetrahydrofurfurylamine were examined in 1.0 *N* aqueous HCl solutions. As in previous papers, the activities of the organic compounds in neutral KCl solutions were assumed to be equal to their concentrations,^{9,10,12,13} but for the ionized aminium bases the activity coefficients were based on those for sodium toluenesulfonate.^{12,14}

The electrocapillary curves for various concentrations of the six-membered heterocyclic compounds and the aliphatic alcohols in KCl base electrolyte solutions have been reported previously,¹⁰ but the ones for the neutral five-membered heterocyclic amines and the ionized bases have not yet been published. The furfurylamines and their conjugate ions constitute a newly available class of corrosion inhibitors (Miles Chemical Co., Elkhart, Ind.), whose adsorption on mercury has been determined by electrocapillary¹¹ and capacitance methods.¹⁵ A detailed analysis of the results from the two complementary methods will be compared later in terms of their general adsorption effects and corrosion-inhibitory properties.¹⁶

The potential of zero charge for all the neutral organic molecules shifts progressively to more anodic values with increasing concentration of the additives and the greatest shifts were observed for the saturated compounds. Conversely, the smallest shift in the p.z.c. was noted for substances such as propargyl alcohol and furfurylamine. The electrocapillary curves for the organic ions were much more symmetrical than the ones for the neutral molecules. In general, the shifts in the p.z.c. and the extents of surface-tension depression were less for corresponding concentrations of the additives in HCl base electrolyte solutions.

Discussion

Theoretical Background for Specifically Adsorbed Ions. The following equation has been derived by Parsons⁶ for inorganic ion systems (the original symbols and significance are retained).

$$(\partial E_{\pm} / \partial \ln a_{\pm})_{q_M} = - (\kappa T / z_{\mp} e) (\partial q_{\mp} / \partial q_M) a_{\pm} \quad (1)$$

In applying this equation to our work where specifically adsorbed *organic* cations (derived by reaction of the base with excess HCl) are involved, we must rewrite eq. 1 in the following form

$$(\partial E_{\text{cal}} / \partial \ln a_{+})_{q_M} = - RT/F (\partial q_{\text{specific}} / \partial q_M) a_{+} \quad (2)$$

where q_{specific} now represents q_{+} , the adsorbed charge due to the cation, and a_{+} is the "activity of the cation"; a_{+} has been assumed to be equivalent to a_{S} , *i.e.*, a_{\pm} for the organic salt at an ionic strength determined mainly by the excess HCl, since chloride ion activity in the base electrolyte will be almost invariant in the solutions studied. E_{-} is written as E_{cal} and refers to the electrode potential measured with respect to that of the calomel reference electrode.

The experimental electrocapillary data for anilinium, furfurylaminium, and tetrahydrofurfurylaminium ions have been used to examine the applicability of eq. 2. Values of q_{specific} , which were assumed¹⁷ to equal $F\Gamma_A$ (where F is the Faraday and Γ_A represents the surface excess of the adsorbed species,^{9,12} and under the present conditions these species are almost entirely the protonated form of the organic molecule^{12b}) were plotted against q_M , and both charge terms were computed at constant activity of the organic electrolyte for each of the above-mentioned ions. These plots are shown in Figure 1 and the slopes were then evaluated. Correspondingly, the values of E_{cal} and $RT/F \ln a_{+}$ (assuming $a_{\pm} \approx a_{+}$) at a chosen constant value of q_M (at the p.z.c.) have been plotted for the three

(8) R. G. Barradas and F. M. Kimmerle, *J. Electroanal. Chem.*, in press.

(9) B. E. Conway and R. G. Barradas, *Electrochim. Acta*, **5**, 319 (1961).

(10) R. G. Barradas and P. G. Hamilton, *Can. J. Chem.*, in press.

(11) P. G. Hamilton, M.A. Thesis, University of Toronto, 1964.

(12) (a) R. G. Barradas and B. E. Conway, *Electrochim. Acta*, **5**, 349 (1961); (b) *J. Electroanal. Chem.*, **6**, 314 (1963).

(13) E. Blomgren and J. O'M. Bockris, *J. Phys. Chem.*, **63**, 1475 (1959).

(14) R. A. Robinson, *J. Am. Chem. Soc.*, **57**, 1165 (1935).

(15) E. M. L. Valeriotte, M.A. Thesis, University of Toronto, 1964.

(16) R. G. Barradas, P. G. Hamilton, and E. M. L. Valeriotte: (a) Abstract, Corrosion Inhibitor Symposium, Electrochemical Society Meeting, Buffalo, N. Y., 1965; (b) *J. Electrochem. Soc.*, in course of preparation.

(17) This is justified since the principal nonspecifically adsorbed charge in the diffuse layer will be associated with H^{+} and Cl^{-} ions.

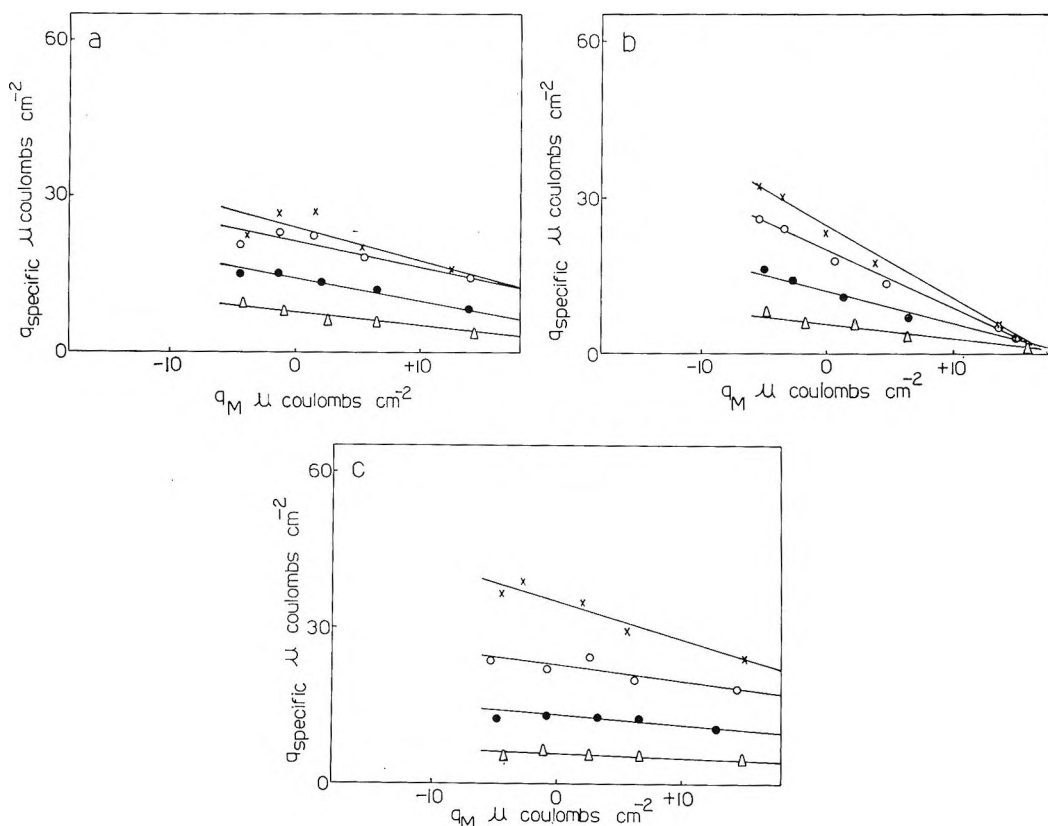


Figure 1. Plots of specific charge due to the adsorbed cations against the charge on the electrode at constant activities. (a) Furfurylamine; activities: \times , $3.15 \times 10^{-1} M$; \circ , $2.04 \times 10^{-1} M$; \bullet , $7.60 \times 10^{-2} M$; and Δ , $2.73 \times 10^{-2} M$. (b) Tetrahydrofurfurylamine; activities: \times , $3.15 \times 10^{-1} M$; \circ , $2.04 \times 10^{-1} M$; \bullet , $7.60 \times 10^{-2} M$; and Δ , $2.73 \times 10^{-2} M$. (c) Aniline; activities: \times , $2.63 \times 10^{-1} M$; \circ , $0.75 \times 10^{-1} M$; \bullet , $2.99 \times 10^{-2} M$; and Δ , $1.07 \times 10^{-2} M$.

organic ions, and the slopes have been evaluated. For convenience, the results of these derived calculations are summarized in Table I. It is noteworthy that

within the limits of the experimental errors the average values of $(\partial q_{\text{specific}}/\partial q_M)_{a_+}$ are in reasonably satisfactory agreement with those of $[\partial E_{\text{cal}}/(RT/F \partial \ln a_+)]_{q_M}$ as required theoretically.

Table I: Test of Eq. 2 for the Esin and Markov Effect Due to Organic Cations

System	a_+, M	$(\partial q_{\text{specific}}/\partial q_M)_{a_+}$	$-(\partial E_{\text{cal}}/RT/F \partial \ln a_+)_{q_M}$
Furfurylamine in 1 N HCl	2.73×10^{-2}	-0.2	-0.4
	7.60×10^{-2}	-0.4	
	2.04×10^{-1}	-0.5	
	3.15×10^{-1}	-0.6	
	Av.	-0.4	
Tetrahydrofurfurylamine in 1 N HCl	2.73×10^{-2}	-0.3	-0.8
	7.60×10^{-2}	-0.6	
	2.04×10^{-1}	-1.1	
	3.15×10^{-1}	-1.4	
	Av.	-0.9	
Aniline in 1 N HCl	1.07×10^{-2}	-0.1	-0.2
	2.99×10^{-2}	-0.2	
	0.75×10^{-1}	-0.3	
	2.63×10^{-1}	-0.7	
	Av.	-0.3	

Thermodynamic Analysis for Neutral Molecules. A comparable new thermodynamical equation for un-ionized molecules, equivalent to that deduced by Parsons for ions, is required for describing the "Esin and Markov" behavior of neutral molecules.

$$(\partial E_{\text{cal}}/\partial \ln a_A)_{q_M} = -RT(\partial \Gamma_A/\partial q_M)_{a_A} \quad (3)$$

where a_A is the activity of the neutral molecule and will be assumed to be equal to the concentration C_A as stated previously.^{9,10,12,13} By an equivalent procedure to that described for the organic ions, we can test eq. 3 by plotting (i) E_{cal} vs. $RT \ln a_A$ at constant q_M (e.g., at the p.z.c.) and (ii) Γ_A vs. q_M at constant a_A for the neutral substances investigated. The slopes of both sets of curves have been evaluated and are compared in Tables II-IV. The comparison of the evaluated slopes shows that they are generally not in good agreement with one another, and the comparison

Table II: Test of Eq. 3 for the Esin and Markov Effect Due to Neutral Six-Membered Heterocyclic Compounds

System	a_A, M	$10^6(\partial\Gamma_A/\partial q_M)_{a_A}$	$-10^6(\partial E_{cal}/RT \partial \ln a_A)_{q_M}$
Piperidine in 1 N KCl	3.0×10^{-2}	-2.1	
	1.0×10^{-1}	-1.9	-1.5
	3.0×10^{-1}	-1.9	
	1.0	-1.8	
	Av.	-1.9	
Pyridine in 1 N KCl	3.0×10^{-2}	-1.0	
	1.0×10^{-1}	-1.9	-2.4
	3.0×10^{-1}	-1.6	
	1.0	-0.9	
	Av.	-1.4	
Dioxane in 1 N KCl	1.0×10^{-1}	-0.7	
	3.0×10^{-1}	-1.0	
	1.0	-2.0	-2.7
	2.0	-3.3	
	Av.	-1.8	
Morpholine in 1 N KCl	1.0×10^{-1}	-0.8	
	3.0×10^{-1}	-1.4	
	5.0×10^{-1}	-1.4	-1.7
	1.0	-1.4	
	Av.	-1.3	

Table III: Test of Eq. 3 for the Esin and Markov Effect Due to Neutral Aliphatic Alcohols

System	a_A, M	$10^6(\partial\Gamma_A/\partial q_M)_{a_A}$	$-10^6(\partial E_{cal}/RT \partial \ln a_A)_{q_M}$
<i>n</i> -Propyl alcohol in 1 N KCl	1.0×10^{-1}	-1.1	
	3.0×10^{-1}	-2.3	
	5.0×10^{-1}	-2.7	-3.7
	1.0	-3.5	
	Av.	-2.4	
Allyl alcohol in 1 N KCl	1.0×10^{-1}	-0.6	
	3.0×10^{-1}	-1.5	
	5.0×10^{-1}	-2.1	-2.2
	1.0	-2.8	
	Av.	-1.8	
Propargyl alcohol in 1 N KCl	1.0×10^{-1}	-0.2	
	3.0×10^{-1}	-0.6	
	5.0×10^{-1}	-1.3	-0.7
	1.0	-1.6	
	Av.	-0.9	

is less satisfactory than for the case of organic ions. From Tables III and IV it will be noted that the agreement between $(\partial\Gamma_A/\partial q_M)_{a_A}$ and $-(\partial E_{cal}/RT \partial \ln a_A)_{q_M}$ is better for the unsaturated compounds than for their corresponding saturated analogs. In general, the two derivatives are in better agreement at the higher concentrations. From the tabulated data, it is seen that $(\partial\Gamma/\partial q_M)_{a_A}$, which should be a constant

Table IV: Test of Eq. 3 for the Esin and Markov Effect Due to Neutral Five-Membered Heterocyclic Compounds

System	a_A, M	$10^6(\partial\Gamma_A/\partial q_M)_{a_A}$	$-10^6(\partial E_{cal}/RT \partial \ln a_A)_{q_M}$
Furfurylamine in 1 N KCl	1.0×10^{-2}	-0.5	
	3.0×10^{-2}	-1.1	-1.9
	1.0×10^{-1}	-1.5	
	3.0×10^{-1}	-1.6	
	Av.	-1.2	
Tetrahydrofurfurylamine in 1 N KCl	1.0×10^{-2}	-0.5	
	3.0×10^{-2}	-0.9	
	1.0×10^{-1}	-1.3	-2.1
	3.0×10^{-1}	-1.3	
	Av.	-1.3	
N-Methylfurfurylamine in 1 N KCl	1.0×10^{-2}	-1.1	
	3.0×10^{-2}	-1.4	
	1.0×10^{-1}	-1.5	
	3.0×10^{-1}	-1.4	
	Av.	-1.4	-1.8
N-Methyltetrahydrofurfurylamine in 1 N KCl	1.0×10^{-2}	-1.0	
	3.0×10^{-2}	-1.3	
	1.0×10^{-1}	-1.1	-1.9
	3.0×10^{-1}	-1.3	
	Av.	-1.2	

quantity for varying concentrations of the organic additive, in fact tends to increase with increasing adsorbate concentration. It is suggested that this variation arises from orientation of the molecules of the adsorbate in the surface layer at high coverages when the additives are present at high concentrations, as we have argued from other points of view previously.^{9,12a}

Changes in the Potential of Zero Charge with $(\Gamma_A)_{pzc}$ and $\log C_A$. For the compounds listed in Tables II and III, the variation of ΔE_{pzc} with $(\Gamma_A)_{pzc}$ and with $\log C_A$ have been previously reported.¹⁰ Similar plots for the ionic species and the neutral furfurylamines are shown in Figures 2 and 3, respectively, which confirm our earlier contention^{9,10,12} that "π-excessive" substances¹⁸ show the smallest shifts in ΔE_{pzc} while the "π-deficient" hydrogenated derivatives show the opposite behavior. For the latter compounds, noticeable breaks are observed at certain critical $(\Gamma_A)_{pzc}$ and C_A values. We have previously attributed the sharp changes in $d\Delta E_{pzc}/d(\Gamma_A)_{pzc}$ and $d\Delta E_{pzc}/d \log C_A$ to sudden orientation effects.^{9,10,12} For the saturated six-membered heterocyclic compounds, we have demonstrated that it is not possible to discern orientation effects with increasing surface coverage or

(18) A. Albert, "Heterocyclic Chemistry," Athlone Press, London, 1959.

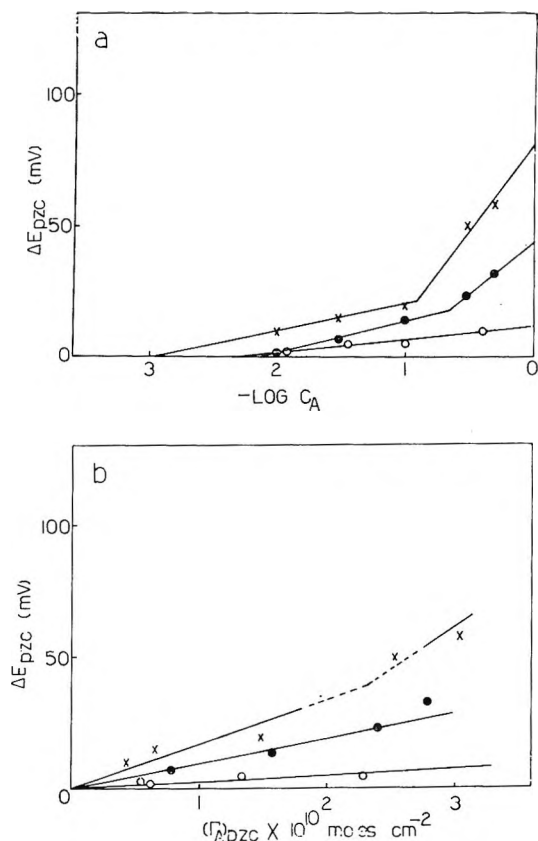


Figure 2. (a) Shifts of the potential of zero charge with additive concentrations in 1 N HCl. (b) Shifts of the potential of zero charge against surface excess at the p.z.c. in 1 N HCl. ●, furfurylamine; X, tetrahydrofurfurylamine; and O, aniline.

C_A because of the similarity of the projected molecular areas of the four possible orientational configurations (see Figure 4) involving the upright or inverted forms of either of the two conformational isomers for each of these substances¹⁰; also, the interconversion rate between the isomeric forms will generally be large unless field effects stabilize one form, e.g., that with the higher dipole moment.

The change in ΔE_{pzc} with $(\Gamma_A)_{pzc}$ is a more dependable indication for discerning orientation effects than the plots of ΔE_{pzc} against $\log C_A$. It has been suggested by other workers^{19,20} that the following electrostatic formula of Helmholtz can account for the variation of ΔE_{pzc} with $(\Gamma_A)_{pzc}$.

$$\Delta E_{pzc} = 4\pi N\mu(\Gamma_A)_{pzc}/\epsilon \quad (4)$$

where μ here represents the dipole moment, ϵ the dielectric constant of the organic substance, and N is Avogadro's number. Equation 4 may be used to give indirect support for the orientation effects involved with the organic molecules investigated and also to add

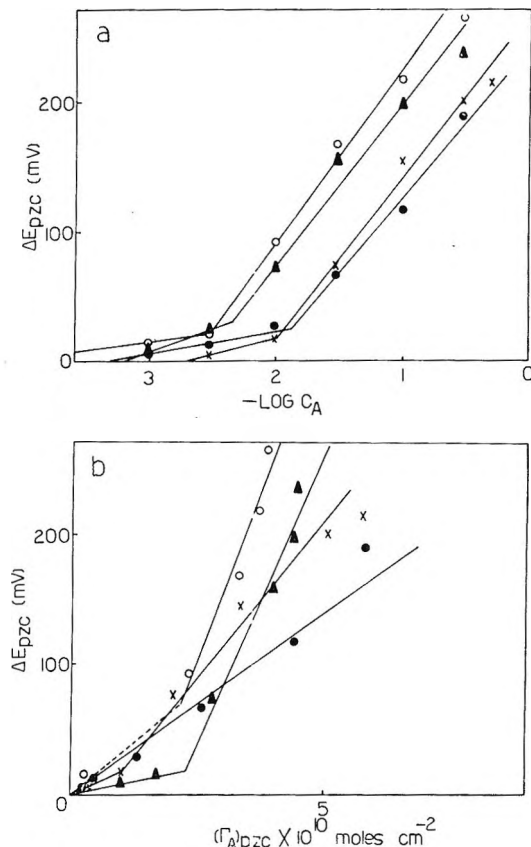


Figure 3. (a) Shifts of the potential of zero charge with additive concentrations in 1 N KCl. (b) Shifts of the potential of zero charge against surface excess at the p.z.c. in 1 N KCl. ●, furfurylamine; X, tetrahydrofurfurylamine; ▲, N-methylfurfurylamine; and O, N-methyltetrahydrofurfurylamine.

substance to our discussion of the Esin and Markov behavior. A test of eq. 4 has been made by evaluation of the slopes of ΔE_{pzc} with $(\Gamma_A)_{pzc}$ from the plots reported and are compared with $4\pi N\mu/\epsilon$ in Table V for a representative selection of compounds, the μ and ϵ values of which are available.

It has been shown that the effective μ for orientated films will be greater²¹⁻²³ than for unorientated films and this is borne out in the results of the calculations reported in Table V for pyridine, *n*-propyl alcohol, and allyl alcohol. Pyridine will tend to orient²⁴ from a planar to a perpendicular position of adsorption,

(19) F. W. Schapink, M. Ondeman, K. W. Len, and J. W. Helle, *Trans. Faraday Soc.*, **56**, 415 (1960).

(20) J. H. Schulman and E. K. Rideal, *Proc. Roy. Soc. (London)*, **A130**, 259, 270, 284 (1930); cf. A. N. Frumkin, *Ergeb. Exakt. Naturwiss.*, **7**, 258 (1928).

(21) J. S. Mitchell, *Trans. Faraday Soc.*, **31**, 980 (1935).

(22) M. Gerowicz, A. N. Frumkin, and D. Vargin, *J. Chem. Phys.*, **6**, 906 (1938).

(23) M. Gerowicz and A. N. Frumkin, *ibid.*, **4**, 624 (1936).

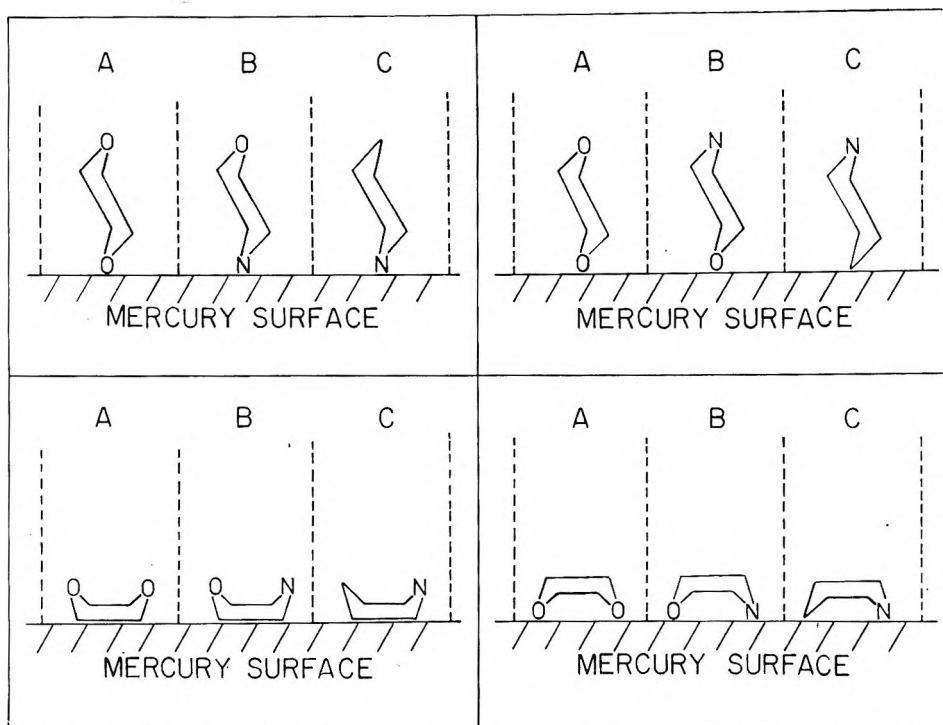


Figure 4. Schematic representation of the four possible positions involving the upright or inverted boat and chair conformations of the adsorbed molecule at the mercury–electrolyte interface: A, dioxane; B, morpholine; and C, piperidine.

Table V: Test of Eq. 4 for the Change of E_{pzc} with Respect to $(\Gamma_A)_{pzc}$

Substance	$10^{-6} d(\Delta E_{pzc}) / d(\Gamma_A)_{pzc}$	$4\pi N\mu / \epsilon \times 10^{-6}$
Dioxane	1.19	1.52
Pyridine	1.82	1.35
<i>n</i> -Propyl alcohol	3.3	0.56
Allyl alcohol	(a) 0.53	0.57
	(b) 1.10	
Propargyl alcohol	0.43	0.57

presumably with the polar group pointing towards and hydrogen bonded with the solvent as surface coverage increases,^{9,10,26} and $d(\Delta E_{pzc})/d(\Gamma_A)_{pzc}$ would be equal to $4\pi N\mu/\epsilon$ if μ increased by approximately 30% of its actual value¹⁸ of 2.2 D. (We assume that the dielectric constant of 12.3 for pyridine²⁷ remains unchanged after orientation; however, it is more probable that the ratio of μ/ϵ changes through variation in both terms.) The same change of planar to perpendicular orientation has been postulated for *n*-propyl alcohol¹⁰ and numerical agreement between the values in the second and third columns of Table V may be obtained with the fairly reasonable supposition that μ increases from 1.65²⁸ to 3.30 D. with a corresponding decrease

in ϵ from about 22²⁸ to *ca.* 7. For allyl alcohol two values of $d(\Delta E_{pzc})/d(\Gamma_A)_{pzc}$ are reported as a and b (Table V), and these slopes were evaluated over two equivalent ranges of $(\Gamma_A)_{pzc}$ since the change in slope occurs approximately at the middle region of the range of $(\Gamma_A)_{pzc}$ values plotted. We note that excellent agreement with $4\pi N\mu/\epsilon$ is obtained for slope a when $\mu = 1.63$ D.²⁹ and $\epsilon = 21.6$,³⁰ but after the onset of orientation, agreement with slope b would be obtained if μ increased from 1.63 to 3.26 D. (again we note that μ may be less than 3.26 D. after orientation, but with a corresponding decrease in ϵ). If we assume that μ and ϵ for propargyl alcohol are similar to the values

(24) As pyridine (and other neutral molecules) enter the double layer, water molecules become displaced.^{9,12} This would cause a change of surface potential even if the pyridine molecules were not oriented, since water molecules may have been oriented to an extent dependent on rational potential (*cf.* ref. 25).

(25) J. O'M. Bockris, M. A. V. Devanathan, and K. Müller, *Proc. Roy. Soc. (London)*, **A274**, 55 (1963).

(26) L. Gierst, D. Bermann, and P. Corbusier, *Ric. Sci., Suppl.*, **4**, 75 (1959).

(27) R. Parsons, "Handbook of Electrochemical Constants," Butterworth and Co. (Publishers) Ltd., London, 1959.

(28) B. E. Conway, "Electrochemical Data," Elsevier Publishing Co., London, 1952.

(29) L. G. Wesson, "Tables of Electric Dipole Moments," Massachusetts Institute of Technology, Cambridge, Mass., 1948.

(30) A. Weissberger, "Techniques of Organic Chemistry," Vol. VII, 2nd Ed., Interscience Publishers, Inc., New York, N. Y., 1955.

for allyl alcohol, then approximate agreement between the figures in the second and third columns of Table V is again observed.

The numerical values of $d(\Delta E_{pzc})/d(\Gamma_A)_{pzc}$ and $4\pi N\mu/\epsilon$ are reversed in magnitude for dioxane in comparison with the data for other molecules listed in Table V. Agreement between the two quantities can be obtained if $\epsilon = 2.2^{28}$ is increased to 2.7 or if μ ($= 0.45$ D.²⁸) is taken as 0.36 D. The latter suggestion is not unreasonable since the value of $\mu = 0.45$ D.²⁸ has been cited from a paper originating in 1923, and may possibly be in error.³¹ The calculations according to eq. 4 seem to indicate that there is no confirmation of orientation effects from the dipole moment and/or dielectric constant considerations for saturated heterocyclic compounds which exhibit conformational isomerism. The only valid conclusion that may be inferred from the applicability of the value of $\mu \approx 0.4$ D. is that it gives weight to our previous hypothesis that dioxane molecules may adsorb in the boat conformation on mercury.¹⁰ It may be noted, however, that even in the chair form the electric field, being inhomogeneous, will interact with the dioxane



molecule since one C—C end of the molecule will probably be in a higher field than the other. The field will also modify the equilibrium constant for the boat-chair equilibrium as we have implied in the earlier discussion.

Dependence of the Esin and Markov Coefficients upon Charge on the Electrode. The thermodynamic treatment for the Esin and Markov effect for inorganic ions according to Parsons⁶ is only applicable in an approximate manner for organic ions since simple inorganic ions like I^- , Cl^- , etc., do not affect the mean di-

electric constant or thickness of the inner Helmholtz layer to any great extent. Parsons has predicted that larger ions (*e.g.*, organic cations or anions) may behave like neutral molecules at the interface.³² Our experimental observations are shown in Table V and, with regard to the variation of $(\partial q_{\text{specific}}/\partial q_M)_{a+}$ with increasing activity, confirm the theoretical expectancy. For neutral molecules, the greater discrepancy between $(\partial \Gamma_A/\partial q_M)_{a_A}$ and $-(\partial E_{\text{cal}}/RT \partial \ln a_A)_{q_M}$ is probably due to the uncertainty in the dependence of the latter term on q_M .^{7,32} Γ_A is largest for neutral substances when q_M tends to a minimum, and decreases as the charge on the electrode increases anodically or cathodically with respect to the p.z.c. Furthermore, the lack of constancy in $(\partial q_{\text{specific}}/\partial q_M)_{a+}$ and $(\partial \Gamma_A/\partial q_M)_{a_A}$ for different a_+ and a_A values, respectively, may be associated with orientation effects at high surface coverages or corresponding additive concentrations. In considering the above-mentioned reasons, we conclude that the theoretical requirements of eq. 2 and 3 can provide only approximate estimates of the Esin and Markov behavior for organic species, although it is to be noted that theory and experiment agree better for organic cations and for molecules with π -orbital systems.

Acknowledgments. We are grateful to the University of Toronto for financial support of this work, and to the National Research Council of Canada for research grants at both the University of Toronto and at the University of Ottawa. P. G. H. acknowledges the award of two Province of Ontario Government Fellowships for 1963–1965.

(31) S. Walker in "Physical Methods in Heterocyclic Chemistry," Vol. I, A. R. Katritzky, Ed., Academic Press Inc., New York, N. Y., 1963, p. 198.

(32) R. Parsons, *Trans. Faraday Soc.*, **55**, 999 (1959).

Nuclear Magnetic Resonance Study of Aluminum Alkyls

by Kermit C. Ramey, James F. O'Brien, Ichiro Hasegawa, and Alfred E. Borchert

*The Atlantic Refining Company, Research and Development Department, Glenolden, Pennsylvania
(Received April 12, 1965)*

The temperature dependence of the n.m.r. spectra of a number of aluminum alkyl dimers has been studied in an attempt to elucidate the mechanism by which the alkyl groups are transferred from the bridging to the terminal positions. The data are consistent with a process involving rupture of one Al-C bond which then re-forms with a different alkyl group in the bridging position. For $(\text{Al}(\text{CH}_3)_3)_2$ the free energy ΔF^* , enthalpy ΔH^* , and entropy ΔS^* of the above process were found to be 11.0 ± 0.2 kcal./mole, 15.6 ± 0.2 kcal./mole, and 20 e.u., respectively.

Introduction

The detailed molecular structures of aluminum alkyls and their complexes are of considerable interest and importance, particularly in the field of stereospecific polymerization. Most of these compounds occupy an interesting position in the field of structural chemistry, not only because of their dimeric form but also because of the equilibration of the alkyl groups within the dimer. The aluminum alkyls have been studied extensively by means of X-ray¹ and electron diffraction^{2,3} as well as by Raman and infrared spectroscopy.⁴⁻⁶ Nevertheless, the detailed nature of the equilibrium and the mechanism for interconversion of mixed aluminum alkyls remain somewhat uncertain. A few n.m.r. studies have been reported,⁷⁻¹³ but most of these have been concerned with the correlation of the electronegativity of the central metal atom with the chemical shift of the attached group. Muller and Prichard⁷ reported on the temperature dependence of the n.m.r. spectrum of $(\text{Al}(\text{CH}_3)_3)_2$. They observed only one resonance at room temperature rather than the two expected for the bridging and terminal groups. This indicated that the two species either were magnetically equivalent or were involved in a rapid exchange process.¹⁴ By lowering the temperature to -75° , they were able to confirm the latter process since the spectrum exhibited two resonances with an area ratio of 2:1. The authors⁷ postulated that the monomer $\text{Al}(\text{CH}_3)_3$ was probably not formed as an intermediate but that the process was probably intramolecular. They suggested two possible mechanisms: (1) the

breaking of one Al-C bond or (2) the deformation of the molecule in which no bonds are broken, leading to a structure having four methyl groups at the corners of a square. Furthermore, they state that the Arrhenius activation energy is between 6 and 14 kcal./mole as based on some preliminary data. The present study was undertaken because of the lack of n.m.r. data on aluminum alkyls and the uncertainties that exist concerning the mechanism of exchange.

Experimental Section

The n.m.r. spectra were obtained on solutions containing approximately 10 mole % dimer in cyclopentane

- (1) P. H. Lewis and R. E. Rundle, *J. Chem. Phys.*, **21**, 986 (1953).
- (2) K. J. Palmer and N. Elliott, *J. Am. Chem. Soc.*, **60**, 1852 (1938).
- (3) L. O. Brockway and N. R. Davidson, *ibid.*, **63**, 3287 (1941).
- (4) C. P. Van der Kelen and M. A. Herman, *Bull. soc. chim. Belges*, **65**, 362 (1956).
- (5) E. G. Hoffmann, *Z. Elektrochem.*, **64**, 616 (1960).
- (6) E. G. Hoffmann and G. Schomburg, *ibid.*, **61**, 1101 (1957).
- (7) N. Muller and D. E. Prichard, *J. Am. Chem. Soc.*, **82**, 248 (1960).
- (8) Y. Sakurada, M. L. Huggins, and W. R. Anderson, *J. Phys. Chem.*, **68**, 1934 (1964).
- (9) O. Yamamoto, *Bull. Chem. Soc. Japan*, **36**, 1463 (1963).
- (10) B. P. Dailey and J. N. Shoolery, *J. Am. Chem. Soc.*, **77**, 3977 (1955).
- (11) P. T. Narasimhan and M. T. Rogers, *ibid.*, **82**, 34 (1960).
- (12) S. Brownstein, B. C. Smith, G. Erlich, and A. W. Laubengayer, *ibid.*, **82**, 1000 (1960).
- (13) C. R. McCoy and A. L. Allred, *ibid.*, **84**, 912 (1962).
- (14) J. A. Pople, W. G. Schneider, and H. J. Bernstein, "High Resolution Nuclear Magnetic Resonance," McGraw-Hill Book Co., Inc., New York, N. Y., 1959, p. 218.

and on the pure liquid alkyl whenever possible, both with and without tetramethylsilane (TMS) which interfered with the terminal methyl resonance in most cases. A Varian A-60 spectrometer, equipped with a variable temperature probe and accessories, was used. The chemical shifts are reported in τ units. The aluminum alkyls were obtained from the Ethyl Corp. and Texas Alkyls, Inc., and were used without further purification. All samples were prepared in an inert atmosphere.

Interpretive Techniques

The use of high resolution n.m.r. to obtain kinetic information on the rates of reactions, particularly conformational isomerization, has been established.¹⁴⁻¹⁶ The simplest procedure involves the measurement of the width ($W^{1/2}$) of the resonances at one-half peak height. For slow exchange this width is related to the average time (τ_{eA}) that the molecule spends in a particular configuration by $1/\tau_{eA} = \pi W^{1/2}$ cor., where $W^{1/2}$ cor. is equal to the full line width at one-half height minus the corresponding quantity for cyclopentane at the same temperature. In most cases the line width of the solvent was about 0.5 c.p.s. and did not exceed 1.0 c.p.s. in any case. The quantity τ_e is defined¹³ as

$$\tau_e = \frac{\tau_{eA}\tau_{eB}}{\tau_{eA} + \tau_{eB}} \quad (1)$$

and for $(Al(CH_3)_3)_2$ τ_{eA} refers to the average time that a particular methyl group spends in the bridging position and τ_{eB} the corresponding time for the terminal position. τ_{eA} was taken as one-half τ_{eB} since there are twice as many methyl groups in the terminal position. For fast exchange τ_e may be approximated by the relationship¹⁴

$$1/\tau_e = \frac{\pi\nu^2}{2W^{1/2} \text{ cor.}} \quad (2)$$

where ν is the relative chemical shift in the absence of exchange. In both cases the rate of exchange (k) is related to τ_e by $k = 2/\tau_e$.

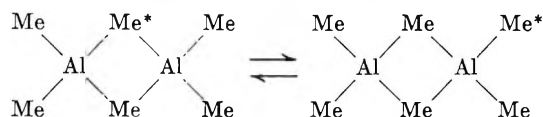
A more elaborate method for calculating τ_e involves a comparison of the calculated and experimental line shapes.^{15,16} Although this method allows values of τ_e to be determined for the intermediate temperatures, the accuracy of the values for this range is somewhat limited. Neglecting the contribution of the transverse relaxation to the line width, the line shape function $g(\nu)$ becomes

$$g(\nu) = \frac{1/4 K \tau_e (\nu_a - \nu_b)^2 (1 - (P_a - P_b)^2)}{4\pi^2 \tau_e^2 [(\nu - \nu_b)(\nu_a - \nu)]^2 + [1/2(\nu_a - \nu_b)(1 + P_a - P_b) - (\nu - \nu_b)]^2} \quad (3)$$

For $(Al(CH_3)_3)_2$, P_a and P_b are the fractional populations of bridging and terminal methyl groups, respectively, and ν_a and ν_b are their corresponding resonant frequencies. The calculations were carried out with an IBM 704 computer using a Fortran II card deck. P_a and P_b were taken as $1/3$ and $2/3$, respectively, and the zero point was set at 1.0 p.p.m. upfield from TMS. On this scale ν_a and ν_b are +90 and +21 c.p.s., respectively.

Results and Discussion

The temperature dependence of the n.m.r. spectrum of $(Al(CH_3)_3)_2$ in cyclopentane is shown in Figure 1. The spectra show a sharp singlet at room temperature which has a chemical shift of τ 10.30 and two resonances at -60° , with chemical shifts of τ 9.50 and 10.65 in agreement with the results of Muller and Prichard.⁷ The exchange process may be represented as



In Table I are listed the widths of the various resonances and the calculated values of τ_e and k , as ob-

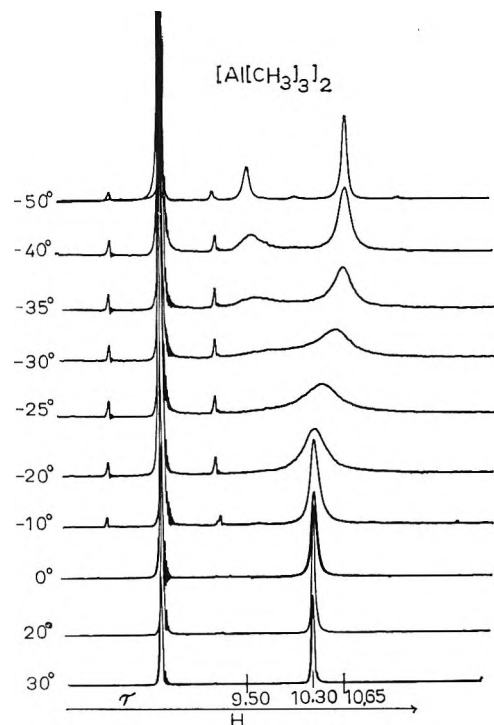
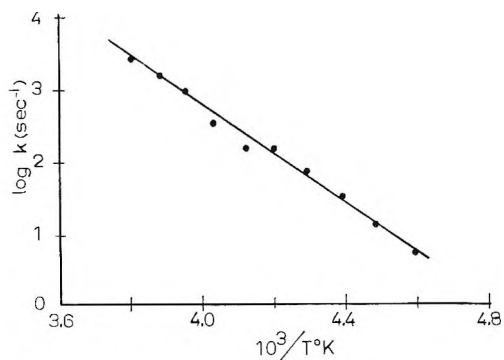


Figure 1. The temperature dependence of the n.m.r. spectrum of $(Al(CH_3)_3)_2$ in solution in cyclopentane.

(15) H. S. Gutowsky and C. H. Holm, *J. Chem. Phys.*, **25**, 1228 (1956).

(16) F. A. Bovey, E. W. Anderson, F. P. Hood, and R. L. Kornegay, *ibid.*, **40**, 3099 (1964).

Figure 2. Plot of $\log k$ (sec.⁻¹) vs. $1/T^\circ\text{K}$.**Table I:** Rate of Exchange (k) of Bridging and Terminal Methyl Groups in $(\text{Al}(\text{CH}_3)_2)_2$ at Various Temperatures

Temp., °C.	—Cor. line width, c.p.s. ^a — Bridging Averaged Terminal	τ_a	k , sec. ⁻¹
-55	1.7	1.0	1.30×10^{-1}
-50	4.0	2.0	5.32×10^{-2}
-45	9.8	5.4	2.17×10^{-2}
-40	17.8	10.0	1.00×10^{-2}
-35			4.74×10^{-3}
-30			4.74×10^{-3}
-25			2.11×10^{-3}
-20	10.1		7.50×10^{-4}
-15	6.3		4.51×10^{-4}
-10	4.0		2.82×10^{-4}

^a Line width at half-height minus the line width of cyclopentane at the same temperature.

tained by a comparison of the experimental and calculated line shapes and widths, for temperatures ranging from -10 to -55° . A plot of $\log k$ vs. $1/T^\circ\text{K}$. is shown in Figure 2. The variation of the k values for the intermediate temperatures is expected since it is rather difficult to obtain a good fit of the experimental and calculated spectra. Equations 4-6 were used to calculate ΔF_T^* , the free energy of activation, ΔH_T^* , the enthalpy, and ΔS^* , the entropy of activation

$$\Delta H_T^* = R \left[\frac{\partial \ln k}{\partial (1/T)} \right]_p - RT \quad (4)$$

$$\Delta F_T^* = 2.303RT(10.319 + \log T - \log k) \quad (5)$$

$$\Delta S^* = (\Delta H_T^* - \Delta F_T^*)/T \quad (6)$$

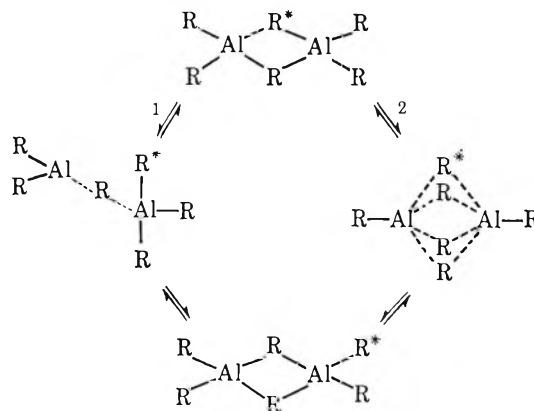
The following values were calculated from the above equations

$$\Delta H_{223}^* = 15.6 \text{ kcal./mole}$$

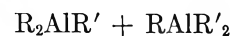
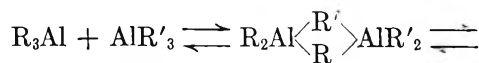
$$\Delta F_{223}^* = 11.0 \text{ kcal./mole}$$

$$\Delta S^* = 20 \text{ e.u.}$$

Since the heat of dissociation of the dimer to the monomer is reported to be 20.2 kcal./mole, at 100 to 150° in the gaseous phase,¹⁷ the above data are not sufficient to differentiate between the two processes by which the molecules seem most likely to rearrange methyl groups. According to Muller and Prichard⁷ the two processes are: (1) the breaking of one Al-C bond which may reform with a different methyl group in the bridging position and (2) a deformation of the molecule in which no bonds are broken, leading to a structure having four methyl groups in the bridging position. These processes are depicted below



Mixed Aluminum Alkyls. Ziegler¹⁸ has discussed the interconversion of mixed aluminum alkyls in some detail. He postulated the following reaction to account for the rapid exchange of alkyl groups.



In an attempt to elucidate the mechanism of exchange of alkyl groups in aluminum alkyl dimers, the temperature dependence of the n.m.r. spectra of a number of mixed aluminum alkyls were studied. $\text{Al}(\text{CH}_2\text{CH}(\text{CH}_3)_2)_3$ which has been reported to be monomeric in solution in C_6H_6 ¹⁹ was chosen as one of the constituents. The n.m.r. spectrum of this compound in solution in cyclopentane is essentially temperature independent over the range of temperatures studied ($+50$ to -75°) in agreement with the above results. The spectrum consists of three resonances with chemical shifts of τ 8.13, 9.05, and 9.60, corresponding to the CH, CH_3 , and CH_2 protons, respectively.

(17) A. W. Laubengayer and W. F. Gilliam, *J. Am. Chem. Soc.*, **63**, 477 (1941).

(18) H. Zeiss, "Organometallic Chemistry," Reinhold Publishing Corp., New York, N. Y., 1960, p. 208.

(19) E. G. Hoffman, *Ann. Chem.*, 629 (1960).

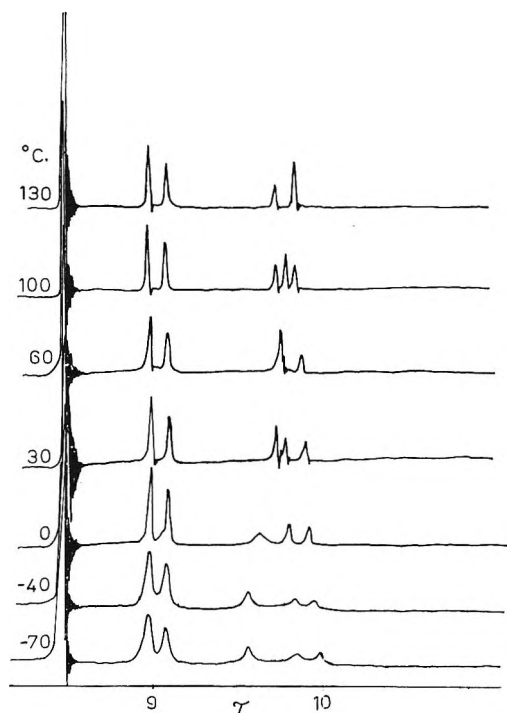
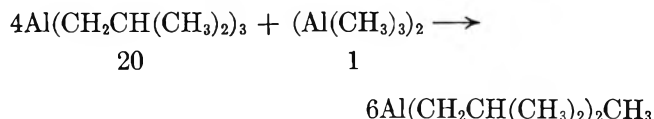


Figure 3. The temperature dependence of the n.m.r. spectrum of the system consisting of a 20:1 molar ratio of $\text{Al}(\text{CH}_2\text{CH}(\text{CH}_3)_2)_3$ to $(\text{Al}(\text{CH}_3)_3)_2$ in solution in cyclopentane.

The temperature dependence of the n.m.r. spectrum of a mixture of $\text{Al}(\text{CH}_2\text{CH}(\text{CH}_3)_2)_3$ and $(\text{Al}(\text{CH}_3)_3)_2$ (20:1 molar ratio) is shown in Figure 3. Cryoscopic measurements¹⁹ indicate the formation of a mixed alkyl wherein the newly formed molecules are able to associate *via* the CH_3 bridge-forming dimers.



Therefore the system under consideration consists of the monomer $\text{Al}(\text{CH}_2\text{CH}(\text{CH}_3)_2)_3$ and the dimer $(\text{AlR}_2\text{CH}_3)_2$. Surprisingly enough, the high temperature spectrum exhibits only one resonance for the methyl groups and only three resonances for the isobutyl groups. This indicates that the isobutyl groups of the monomer and dimer are either magnetically equivalent or that they are involved in a rapid exchange process. A plot of the chemical shifts of the CH_3 resonance and of the CH_2 resonance of the isobutyl groups for the above system in cyclopentane and of the CH_2 resonance of the monomer $\text{Al}(\text{CH}_2\text{CH}(\text{CH}_3)_2)_3$ in cyclopentane *vs.* temperature is shown in Figure 4. The data indicate that (1) the alkyl groups are involved in an exchange process which seems to cease at about -40° and (2)

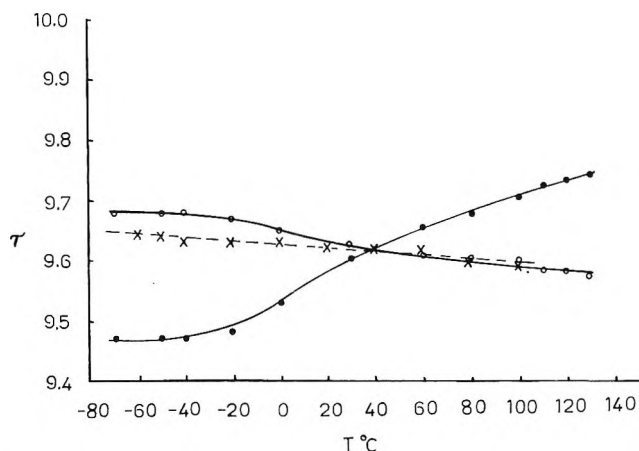
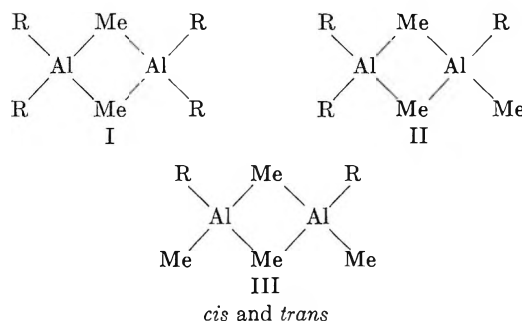


Figure 4. The temperature dependence of the chemical shifts of the methyl protons (O) and the methylene protons (●) for the system consisting of a 20:1 molar ratio of $\text{Al}(\text{CH}_2\text{CH}(\text{CH}_3)_2)_3$ to $(\text{Al}(\text{CH}_3)_3)_2$ in solution in cyclopentane and the methylene protons (×) of $\text{Al}(\text{CH}_2\text{CH}(\text{CH}_3)_2)_3$ in solution in cyclopentane.

the resonance of the isobutyl groups of the monomer and dimer overlap over the range of temperatures studied. Furthermore, the data seem to indicate that the transition state involves the breaking of at least one Al-C bond. The second process involving four bridging alkyl groups at the corners of a square seems to be ruled out on the basis of steric effects since it seems unlikely that two isobutyl groups could participate in such a structure.

The temperature dependence of the n.m.r. spectrum of a mixture of aluminum alkyls consisting of 3 moles of $\text{Al}(\text{CH}_2\text{CH}(\text{CH}_3)_2)_3$ and 0.5 mole of $(\text{Al}(\text{CH}_3)_3)_2$ is shown in Figure 5. In this case the reaction products are probably AlR_2CH_3 and $\text{AlR}(\text{CH}_3)_2$.¹⁹ These molecules are expected to associate *via* the CH_3 bridge-forming I, II, and III



Again, the high temperature n.m.r. spectrum exhibits only one methyl resonance and only three resonances for the isobutyl groups which indicates that the alkyl groups are involved in an exchange process. The low temperature spectrum exhibits two methyl resonances

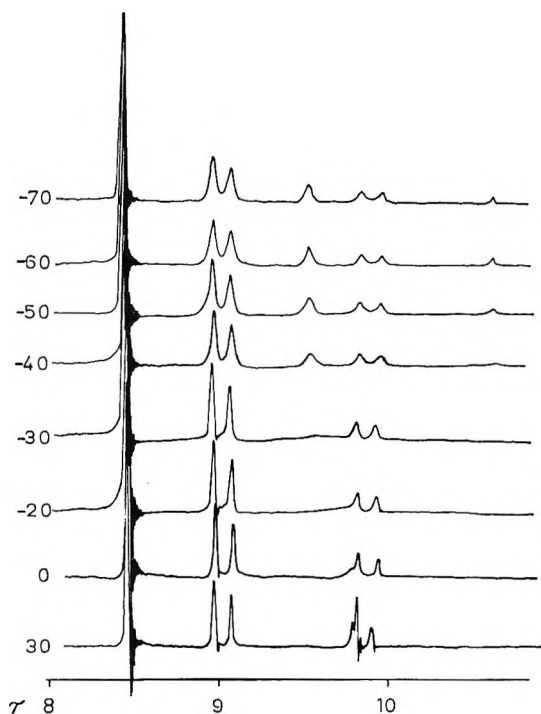


Figure 5. The temperature dependence of the n.m.r. spectrum of the system consisting of a 3:1 molar ratio of $\text{Al}(\text{CH}_2\text{CH}(\text{CH}_3)_2)_3$ to $\text{Al}(\text{CH}_3)_3$ in solution in cyclopentane.

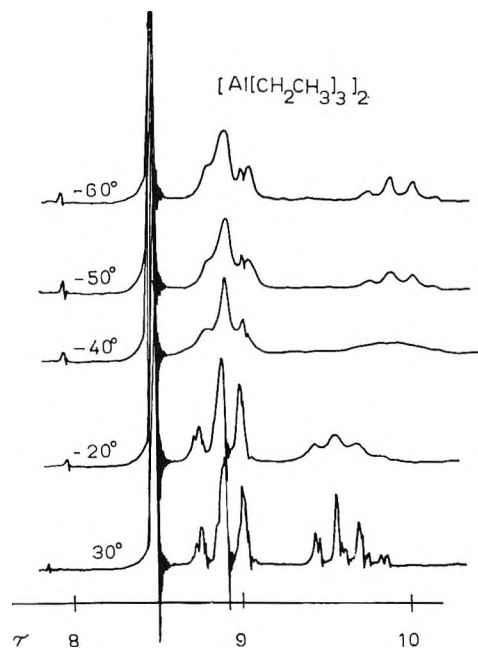
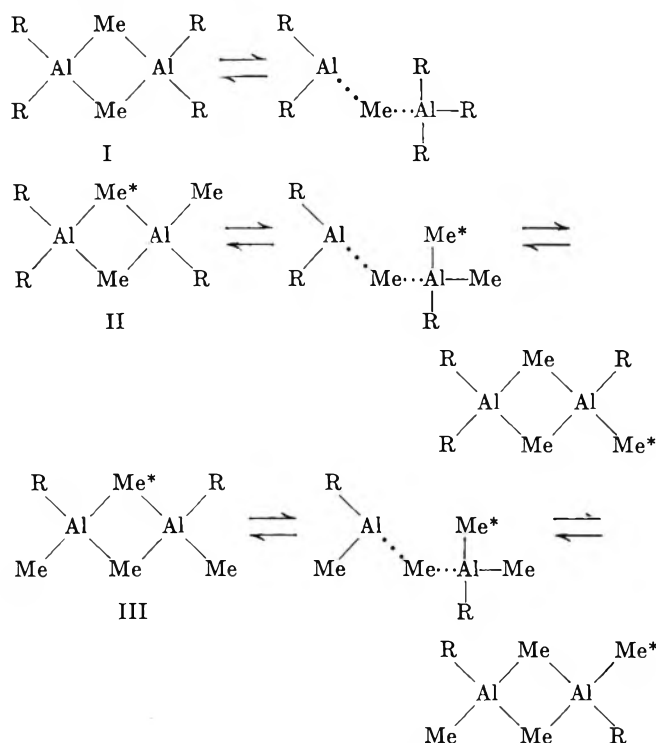


Figure 6. The temperature dependence of the n.m.r. spectrum of $(\text{Al}(\text{CH}_2\text{CH}_3)_3)_2$ in solution in cyclopentane.

with chemical shifts of τ 9.55 and 10.65. The most likely explanation involves the breaking of at least one Al-C bond as depicted



Aluminum Triethyl. The temperature dependence of the n.m.r. spectrum of $(\text{Al}(\text{CH}_2\text{CH}_3)_3)_2$ in solution in cyclopentane is shown in Figure 6. The room temperature spectrum consists of two resonances which indicates that the ethyl groups are involved in a rapid exchange process. As the temperature is decreased, the methylene resonance broadens and finally emerges as two resonances with chemical shifts of τ 8.92 and 9.92, corresponding to the bridging and terminal methylene groups, respectively. The bridging methylene resonance is obscured by the methyl resonance. However, the integral of the low temperature spectrum yields the expected area ratio for the above assignment.

A similar n.m.r. study of $(\text{Al}(\text{CH}_2\text{CH}_3)_3)_2$ in solution in toluene appeared shortly after the completion of our work.²⁰ Although there are slight differences in the chemical shifts of the various groups, this is probably due to the solvent, and the results do confirm the dimeric structure of aluminum triethyl.

Other Aluminum Alkyl Dimers. The temperature dependence of the n.m.r. spectra of $(\text{Al}(n\text{-C}_3\text{H}_7)_3)_2$ and $(\text{Al}(n\text{-C}_4\text{H}_9)_3)_2$ are quite similar to that for the other aluminum alkyl dimers. The spectra of $(\text{Al}(n\text{-C}_3\text{H}_7)_3)_2$ are illustrated in Figure 7. Cryoscopic measurements²¹⁻²³ indicate that the higher homologs of this series

(20) O. Yamamoto, *Bull. Chem. Soc. Japan*, **37**, 1125 (1964).

(21) K. Pitzer and H. Gutowsky, *J. Am. Chem. Soc.*, **68**, 2204 (1946).

(22) K. Ziegler, Special Publication No. 13, The Chemical Society, London, 1959.

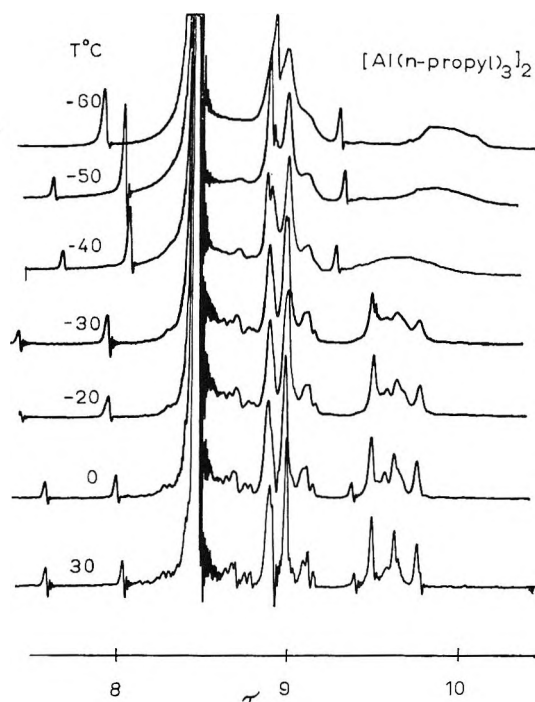
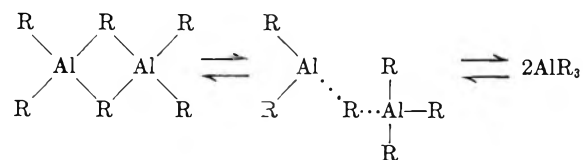


Figure 7. The temperature dependence of the n.m.r. spectrum of $(Al(n-C_3H_7)_3)_2$ in solution in cyclopentane.

are not 100% associated to the dimeric form and that there is a small percentage of monomer present. These results are not inconsistent with the n.m.r. spectra since the spectra only indicate that the alkyl groups are involved in an exchange process which could involve one or more equilibria. The following process is postulated on the basis of the n.m.r. and cryoscopic measurements.



The chemical shifts of the alkyl groups in the bridging, terminal, and averaged positions are summarized in Table II.

Table II: Chemical Shifts of Aluminum Alkyls (τ Units)

Compd.	Temp., °C.			
	30		-50	
			Bridging	Terminal
$(Al(CH_3)_3)_2$	10.27		9.50	10.65
$(Al(CH_2CH_3)_3)_2$	8.89	9.61	8.92	9.92
	b	a		
$(Al(CH_2CH_2CH_3)_3)_2$	8.55	9.00	9.63	9.05
	c	b	a	c
$(Al(CH_2CH_2CH_2CH_3)_3)_2^a$	8.57	9.03	9.58	8.92
	c	a	b	c

^a Run in toluene.

Acknowledgment. The assistance of several members of the staff of this laboratory, particularly Mr. Donald Harrison of the computer section and Dr. N. D. Field for much helpful discussion, is gratefully appreciated.

(23) G. W. Coates and F. Glockling, *J. Chem. Soc.*, 22 (1954).

The Adsorption and Oxidation of Hydrocarbons on Noble Metal

Electrodes. I. Propane Adsorption on Smooth Platinum Electrodes

by S. B. Brummer, J. I. Ford, and M. J. Turner

Tyco Laboratories, Inc., Waltham, Massachusetts (Received April 12, 1965)

The adsorption of propane on smooth Pt electrodes was studied in 13 *M* phosphoric acid solutions at 80 and 110° as a function of time (1 msec. to 10 min.) and potential (0.1 to 0.7 v. vs. Pt, H₂/H⁺ in the same solution, r.h.e.). Quantitative measurements of the adsorbate were made by anodic and cathodic galvanostatic pulses in conjunction with rapidly applied controlled potential techniques to ensure a reproducible electrode surface at each potential of interest. Anodic charging curves yield the charge, $Q_{\text{ads}}^{\text{C}_3\text{H}_8}$, required to oxidize the adsorbed material on the electrode. At 80°, the anodic curves indicate that at 0.2, 0.3, and 0.4 v., the rate of adsorption is initially limited by diffusion of propane in the solution. However, at longer times (~20, 10, and 3 sec., respectively), the adsorption rate declines and the concentration of the adsorbate appears to reach a constant value which varies with potential. The steady-state coverage by adsorbed material at 80°, as determined after 2 min. of adsorption, shows a maximum of ~550 $\mu\text{coulombs/real cm.}^2$ at ~0.2 v. The extent of adsorption declines rapidly at more cathodic potentials and becomes essentially zero at ~0.1 v. At potentials anodic to 0.2 v., the adsorbate concentration decreases approximately linearly with increase in potential and approaches zero at ~0.6 v. At 110°, the amount of adsorption is similar to that at 80°, but the maximum is displaced to a higher potential (~0.22 v.). Cathodic galvanostatic pulses indicate the extent to which the electrode is covered with irreversibly adsorbed material. They show, as before, that adsorption is initially limited by solution diffusion but, at all potentials, this diffusional limitation persists to much longer times of adsorption than is indicated by the anodic pulses. The kinetics of adsorption show that the adsorbate occupies three sites per molecule of adsorbed propane for potentials ≥ 0.3 v. and only one site at 0.2 v. The coverage-potential isotherm is also much different from that obtained from anodic measurements, indicating a considerably wider potential range of high adsorption, with the maximum at higher potentials. The disagreement between the results of the anodic and cathodic measurements is resolved by considering that, while the propane is adsorbed as such, at first, it then undergoes partial oxidation on the electrode and thus the anodic charge is less than expected. The postulated partial oxidation results in a residue whose ultimate oxidation at high potentials involves about two electrons for every Pt surface atom which it covers. It is suggested that the oxidation of this residue is the rate-limiting step in the over-all conversion of propane to carbon dioxide. The sequence of reactions corresponding to the chemisorption process is discussed and possible reasons for the observed variation of the mode of attachment with potential are presented.

I. Introduction

The work reported here is part of a study of the basic mechanisms of oxidation of saturated hydrocarbon in a fuel cell. This follows reports that fuel cells

can be operated with saturated hydrocarbons in concentrated H₃PO₄ electrolytes at elevated temperatures.¹ Studies of the adsorption of a typical fuel,² propane, on smooth Pt, from concentrated H₃PO₄

solution have been initiated, and results for this system at 80 and 110° are reported in this paper. An important finding is that anodic stripping, perhaps the simplest and most direct method of investigating the adsorption of the propane, yields a detailed, quantitative characterization of the adsorbate. However, the experimental results are unusual in some respects, and show that even this direct approach must be used with considerable caution in a complex system of this kind.

Anodic stripping is carried out most conveniently either galvanostatically³⁻⁸ or with an anodic linear potential sweep.^{9,10} The former method readily provides the required electrical charge data for oxidation of the adsorbed species, but the latter gives better resolution between different electrode processes. Both techniques should give the same total anodic charge for a given system and are to be preferred to other methods, *e.g.*, estimation of θ from the double-layer capacity¹¹ or, as will become apparent from the present results, to what is seemingly a more direct measurement of adsorption by radio tracers.^{12,13} This is because of the much more detailed information about the adsorbate which can be obtained with the stripping methods. The present paper gives results for propane adsorption obtained by the anodic galvanostatic method. This technique, used in conjunction with cathodic galvanostatic charging curves and with pretreatment of the electrode at controlled potentials, yields a detailed description of the adsorption process.

II. Experimental Section

Some of the experimental techniques have been described previously,⁵⁻⁷ but a number of modifications are necessary for work in H₃PO₄.

The *electrochemical cell* was similar to that described previously⁵ but was constructed of Vycor glass instead of Pyrex, since Pyrex is slowly attacked by concentrated H₃PO₄ at elevated temperatures.¹⁴

The *working electrode* was a wire of thermocouple grade Pt of ~0.1-cm.² geometric area. It was found that the electrode tends to roughen appreciably in the acid at elevated temperatures, and that this is mitigated by flaming it to red heat either in an alcohol flame or in an oxidizing natural gas flame. The electrode area as measured by cathodic H-atom deposition (see below) was reproducible to better than 5% after flaming, even if the electrode had become rough in the preceding experiment. After flaming, the electrodes were washed with H₂SO₄ cleaning mixture, triple-distilled water, and the H₃PO₄ solution. The electrodes were anodized before each measurement as described below.

The *Reference Electrode*. The reversible hydrogen

electrode is somewhat unreliable in concentrated H₃PO₄ and tends to drift.¹⁵ We have also found erratic behavior and believe that it is due to the presence of a small concentration of an impurity couple which tends to raise the potential. There may also be some material in the acid which poisons platinized Pt for the H₂ reaction. Giner¹⁵ has described a cathodically polarized electrode which is reliable in concentrated H₃PO₄. The potential of this electrode is referred to the reversible H₂ electrode in the same solution in separate experiments. We have, in general, used this technique, although in some cases we were able to reactivate the platinized platinum electrode by alternate O₂ and H₂ evolution terminating on the cathodic cycle. All of our measurements are referred to the reversible hydrogen electrode (r.h.e.) either directly or indirectly.

Phosphoric Acid. It was found that H₃PO₄ (ACS grade from Baker or 85% Food grade from Monsanto) contains material which adsorbs rapidly on Pt and inhibits the deposition of H atoms. It is believed this is a lower-valent phosphorous compound since it has been observed, both in this laboratory and elsewhere, that at more elevated temperatures (130°) a substantial steady-state, anodic current is found in the absence of hydrocarbon (N₂-saturated solution). These currents are eliminated by refluxing with H₂O₂¹⁶; it is also found that the inhibition of hydrogen adsorption by these impurities is largely eliminated after treatment with H₂O₂.

The solutions used in this study were prepared from 85% H₃PO₄ (14.6 M), which was refluxed overnight with 10% v./v. of a 30% solution of H₂O₂ (Baker Analyzed, stabilized with 0.05% Na₄P₂O₇). Then a

(1) W. T. Grubb and L. W. Niedrach, *J. Electrochem. Soc.*, **110**, 1086 (1963).

(2) W. T. Grubb and C. J. Michalske, *ibid.*, **111**, 1015 (1964).

(3) T. O. Pavela, *Ann. acad. sci. Fennicae, Ser. A. II.*, **59** (1954).

(4) M. W. Breiter, *Electrochim. Acta*, **8**, 447, 457 (1963).

(5) S. B. Brummer and A. C. Makrides, *J. Phys. Chem.*, **68**, 1448 (1964).

(6) S. B. Brummer, *ibid.*, **69**, 562 (1965).

(7) S. B. Brummer and J. I. Ford, *ibid.*, **69**, 1355 (1965).

(8) T. B. Warner and S. Schuldiner, *J. Electrochem. Soc.*, **111**, 992 (1964).

(9) S. Gilman, *J. Phys. Chem.*, **66**, 2657 (1962); **67**, 78 (1963).

(10) S. Gilman, Report by General Electric Co., to U. S. Army Engineer Research and Development Laboratories, Fort Belvoir, Va., on Contract DA-009-ENG-479T (Dec. 1964).

(11) A. N. Frumkin, *Z. Physik*, **35**, 792 (1926).

(12) M. Green and H. Dahms, *J. Electrochem. Soc.*, **110**, 466 (1963).

(13) J. O'M. Bockris and D. A. J. Swinkels, *ibid.*, **111**, 736 (1964).

(14) P. V. Popat and A. Kuchar, *cf. ref. 10* (report dated Dec. 1963).

(15) J. Giner, *J. Electrochem. Soc.*, **111**, 376 (1964).

(16) J. E. Oxley, private communication.

volume of water equivalent to the original volume of H_2O_2 was distilled off. On cooling, a similar volume of triple-distilled H_2O was added to make the final concentration of the solution 13 *M* in H_3PO_4 . The H-atom charge was diminished by only $\sim 8\%$ after 2 min. at 0.4 v. vs. r.h.e. at 80° in acid treated in this way whereas in the original H_3PO_4 it is diminished by more than 60% after only 60 sec. More specific details of the behavior of Pt electrodes in H_3PO_4 before and after such treatment will be presented elsewhere.

Gases. H_2 and N_2 were "pre-purified" grade and were passed through cold traps and water presaturators, at the same water vapor pressure as the test solution, prior to passage through the cell. Propane (Matheson) was of instrument grade (99.5% min.) and was pre-saturated with water vapor before bubbling through the solution.

Electrode Area. Results are quoted in terms of "real area" unless specifically stated to the contrary. One square centimeter of real area is defined in terms of the maximum cathodic galvanostatic charge for depositing H atoms on a clean electrode prior to H_2 evolution, in 1 *N* HClO_4 at 40° . It is assumed that this quantity, after correction for double-layer effects, $Q_{\text{H}}^{40^\circ}$, is 210 $\mu\text{coulombs/cm}^2$.¹⁷

A clean electrode is defined as one which has recently undergone anodization. Potentiostatic anodization at 1.35 v. vs. r.h.e. for 1 min. (last 30 sec. without stirring) removes impurities and forms a passive layer of oxide. This oxide layer was then reduced at 0.1 v. for 10–100 msec. and the potential was raised to 0.5 v. for 10 msec. to desorb H atoms deposited at 0.1 v. A cathodic galvanostatic current of ~ 100 ma./ cm^2 was then applied to measure $Q_{\text{H}}^{40^\circ}$. A similar technique was used for H_3PO_4 at all temperatures and Q_{H}^t ($t \equiv ^\circ\text{C}.$) was found to be almost independent of temperature ($\pm 2\%$), in the range of measurements reported in this paper, and within 10% of the above value for 1 *N* HClO_4 . Thus, the measurements are based on $Q_{\text{H}}^t = 210 \mu\text{coulombs/cm}^2$.

As has been indicated, the electrode tends to roughen in concentrated H_3PO_4 at elevated temperatures (about 1–2% per day for a flamed electrode, but occasionally, and erratically, rather more). This represents a serious source of error in estimating surface concentrations of the adsorbate. This error was eliminated by monitoring the area continually by measuring Q_{H}^t . Fortunately (see below) this is possible even in the presence of propane.

Potential Sequences. The electrode potential was manipulated in rapid sequence so as to bring the electrode surface to a specified condition prior to a measurement. As indicated above, this involved the

formation and subsequent reduction of a passive oxide film, and the first part of the above procedure (1.35 v. for 60 sec. followed by 10–100 msec. at 0.1 v.) was used in all our measurements. The improvement in reproducibility of the electrochemical behavior of Pt after anodization is well known.^{9,10,18} This kind of anodic pretreatment is particularly successful in removing complex adsorbed species rapidly and in allowing further studies on a cleaned electrode; this allows rationalization of very complex kinetic data.^{5,9} After cleaning, the electrode potential is moved to the potential of interest, E , where it is held for time τ_E . Then an anodic or cathodic galvanostatic pulse is applied to determine the surface concentration of adsorbate at time τ_E . The methods of achieving these potential-time sequences are described elsewhere.¹⁹

Temperature control was achieved by placing the cell in a circulated-air oven (uniformity $\pm 0.5^\circ$). Most of the reported experiments were carried out at 80° , but some data for 110° are also presented.

III. Results and Discussion

Anodic Charging Curves. Typical anodic charging curves taken after adsorption of propane (1 atm. less the vapor pressure of the acid) for 2 min. at 0.3 v. in 13 *M* H_3PO_4 at 80° are shown in Figure 1. These do not differ appreciably in shape from curves taken with N_2 (Figure 2), save that the charge passed is considerably larger. Referring to Figure 1, we can identify three main regions in these curves: the region of rapidly rising potential from 0.3 to ~ 1.0 v. (0.8–1.1 v. depending on the current density, i_a); the region from ~ 1.0 to ~ 1.8 v. (1.7–2.0 v. dependent on i_a), where the potential rises rather less steeply and in which a considerable quantity of charge is passed, ($Q_{\text{anodic}}^{\text{total}}$) $_{\text{C}_3\text{H}_8}$; and finally, a high potential plateau which corresponds mainly to O_2 evolution. It is the middle region which is of most interest, since part of the charge passed in this region undoubtedly corresponds to the oxidation of propane previously adsorbed at the lower potential, $Q_{\text{ads}}^{\text{C}_3\text{H}_8}$. Other processes which can take place in this region are oxidation of the electrode and O_2 evolution, contributing a charge $Q_{\text{electrode}}$; oxidation of propane which diffuses up to the electrode during the transient, $Q_{\text{diff}}^{\text{C}_3\text{H}_8}$; and charging of the double layer, Q_{dl} . Thus

(17) This estimate is by no means completely arbitrary and there is reason to suppose that it is in fact quite realistic. It is discussed in some detail in ref. 6.

(18) F. G. Will and C. A. Knorr, *Z. Elektrochem.*, **64**, 782 (1960).

(19) S. B. Brummer, Report by Tyco Laboratories, Inc., to U. S. Army Engineer Research and Development Laboratories, Fort Belvoir, Va., on Contract DA-44-009-AMC-410(T) (April 1965).

$$(Q_{\text{anodic}}^{\text{total}})_{\text{C}_3\text{H}_8} = Q_{\text{ads}}^{\text{C}_3\text{H}_8} + Q_{\text{electrode}} + Q_{\text{diff}}^{\text{C}_3\text{H}_8} + Q_{\text{d1}} \quad (1)$$

It is also possible that some of the originally adsorbed propane is desorbed rather than oxidized.

Q_{d1} is fairly small, particularly as the method of subtracting $Q_{\text{electrode}}$ (see below) largely removes even this small contribution, and it will consequently be ignored.

$Q_{\text{diff}}^{\text{C}_3\text{H}_8}$ was shown to be negligible or zero in the following way: the potential sequence shown in Figure 1 was employed, under propane, save that $\tau_{0.3 \text{ v}}$ was only 10 msec. rather than 2 min. This does not allow sufficient time for any appreciable quantity of propane to adsorb. $(Q_{\text{anodic}}^{\text{total}})_{\text{C}_3\text{H}_8}$ was measured with current densities from 1 to 300 ma./cm.², and was the same within experimental error at each current density as previously determined under N₂. Evidently, C₃H₈ must be adsorbed before it can be oxidized at these temperatures.

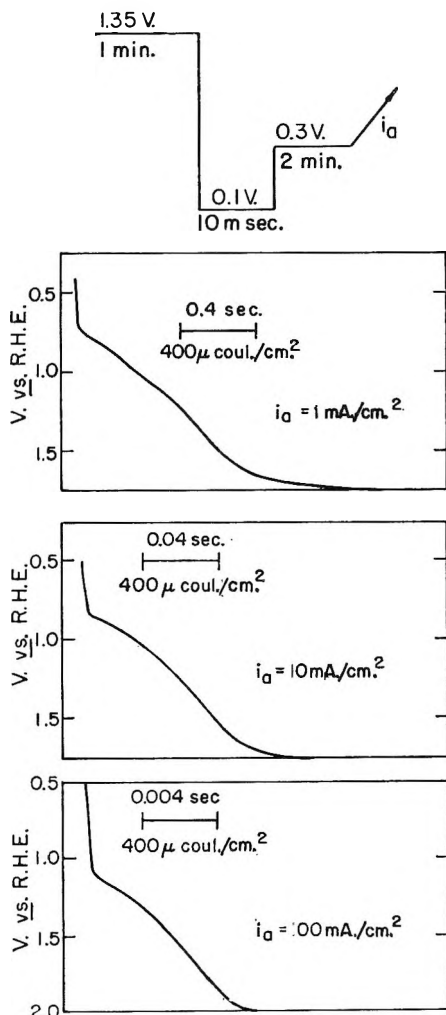


Figure 1. Typical anodic charging curves taken after 2 min. of adsorption of C₃H₈ at 0.3 v. at 80°.

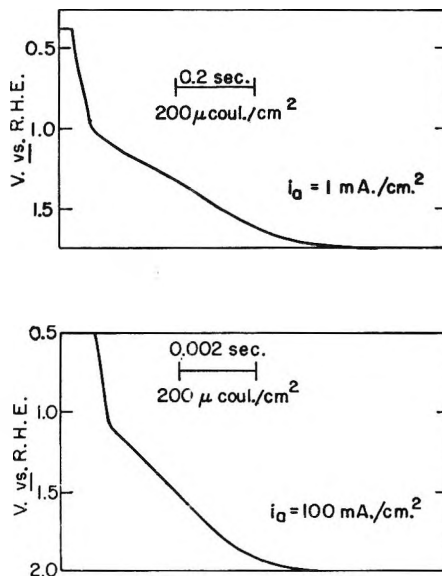


Figure 2. Typical anodic charging curves taken after 10 msec. at 0.3 v., under N₂, at 80°.

In Figure 3, the data at 80° for 2 min. of adsorption at 0.3 v. are shown. Also shown are the anodic charges made at only 10 msec. of adsorption where θ is zero as $Q_{\text{anodic}}^{\text{total}} = (Q_{\text{anodic}}^{\text{total}})_{\text{N}_2}$, the anodic galvanostatic charge determined under N₂. The difference between these charges is independent of the current density over a wide range of current density (1–300 ma./cm.²) both at 80° (Figure 3) and at 110° (Figure 4). In a previous investigation of CO adsorption,⁷ an essentially similar effect of the nondependence on i_a of, in that case $(Q_{\text{anodic}}^{\text{total}})_{\text{CO}}$ was shown to be due to the cancellation of two independent effects (equivalent to $Q_{\text{diff}}^{\text{CO}}$ and $Q_{\text{electrode}}$), but this cannot be the case here, for $Q_{\text{diff}}^{\text{C}_3\text{H}_8}$ is zero. The most reasonable assumption is that $Q_{\text{electrode}} + Q_{\text{d1}}$ is equal to $(Q_{\text{anodic}}^{\text{total}})_{\text{N}_2}$ and that, therefore

$$(Q_{\text{anodic}}^{\text{total}})_{\text{C}_3\text{H}_8} - (Q_{\text{anodic}}^{\text{total}})_{\text{N}_2} = Q_{\text{ads}}^{\text{C}_3\text{H}_8} \quad (2)$$

The possibility of significant desorption of some C₃H₈, without oxidation, during the anodic charging curve must then be ruled out.

The above result is in contrast to reported data for ethane adsorption.¹⁰ There, it is found that $(Q_{\text{anodic}}^{\text{total}})_{\text{C}_2\text{H}_6}$ minus the N₂ charge is not independent of the rate of measurement, except at low rates.

Adsorption Kinetics and Steady-State Adsorption from Anodic Charging Curves. The variation of $Q_{\text{ads}}^{\text{C}_3\text{H}_8}$ with the time of adsorption, τ_{ads} , at a number of potentials, at 80°, is shown in Figure 5; the measurements were made at 50 ma./cm.². It is seen that $Q_{\text{ads}}^{\text{C}_3\text{H}_8}$ increases with $\tau_{\text{ads}}^{1/2}$ for short times of adsorption, independently of potential. At longer adsorption

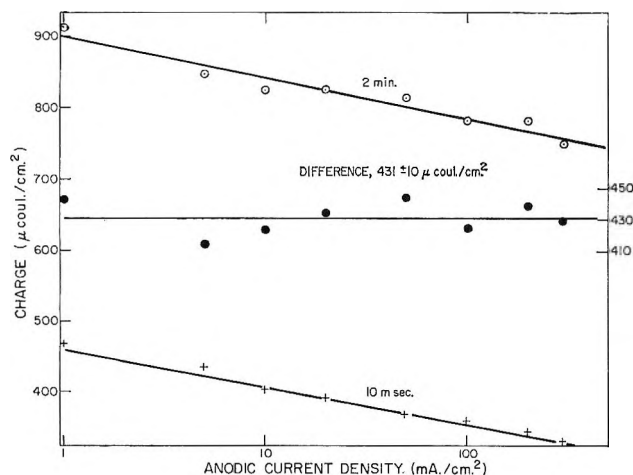


Figure 3. Adsorption of C_3H_8 at 0.3 v. and 80° :
 \circ , $(Q_{\text{anodic}}^{\text{total}})_{C_3H_8}$ for 2 min.; $+$, $(Q_{\text{anodic}}^{\text{total}})_{C_3H_8}$ for 10 msec.;
 \bullet , difference, equal to $Q_{\text{ads}}^{C_3H_8}$.

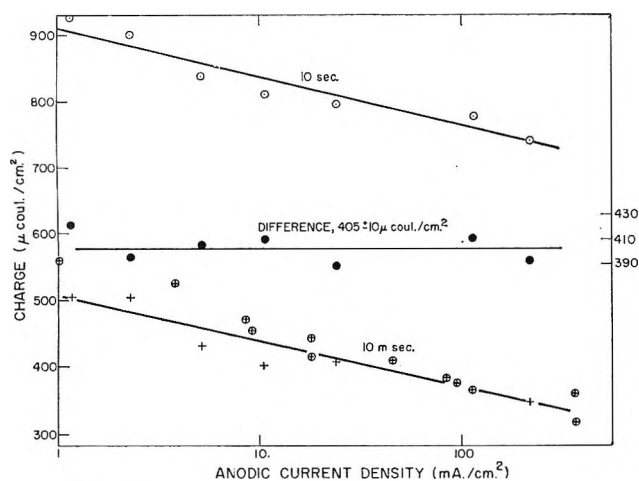


Figure 4. Adsorption of C_3H_8 at 0.3 v. and 110° :
 \circ , $(Q_{\text{anodic}}^{\text{total}})_{C_3H_8}$ for 10 sec.; $+$, $(Q_{\text{anodic}}^{\text{total}})_{N_2}$ for 10 msec.; \oplus ,
 $(Q_{\text{anodic}}^{\text{total}})_{C_3H_8}$ for 10 sec. minus $(Q_{\text{anodic}}^{\text{total}})_{C_3H_8}$ for 10 msec.

times, however, $Q_{\text{ads}}^{C_3H_8}$ is less than expected from the linear $Q-\tau^{1/2}$ relation and becomes potential dependent.

The linear $Q-\tau^{1/2}$ plot, independent of potential at short τ , suggests that the adsorption rate is initially limited by diffusion in the solution. For semi-infinite linear diffusion, Q would be given by²⁰

$$Q_{\text{ads}}^{C_3H_8} = 2nF \left(\frac{D^{C_3H_8}}{\pi} \right)^{1/2} C^{C_3H_8} \tau_{\text{ads}}^{1/2} \quad (3)$$

Here, $Q_{\text{ads}}^{C_3H_8}$ should be in coulombs/geometric cm^2 , n is the number of electrons released in the oxidation of the adsorbate (which for the oxidation of C_3H_8 to CO_2 would be 20), $D^{C_3H_8}$ and $C^{C_3H_8}$ are the diffusion

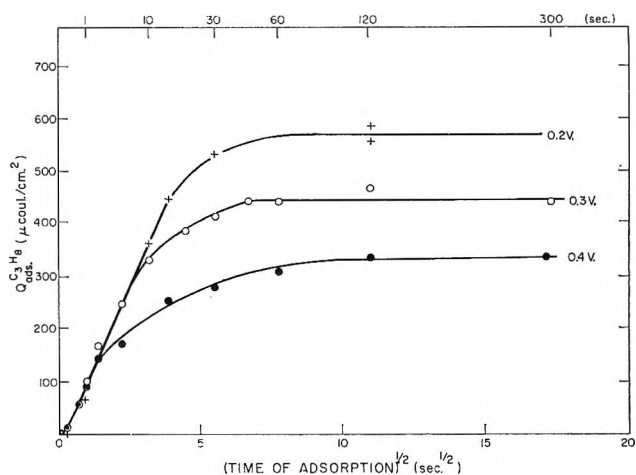


Figure 5. Adsorption of C_3H_8 at 80° as a function of time of adsorption at various potentials.

coefficient and concentration (in moles/ cm^3) of propane. The initial slope from Figure 5 is

$$\frac{dQ_{\text{ads}}^{C_3H_8}}{d\tau_{\text{ads}}^{1/2}} = 1.2 \times 10^{-4} \text{ coulomb/sec.}^{1/2}/\text{cm.}^2 \quad (4)$$

Since 1 geometric cm^2 , under the conditions of this experiment, was equivalent to 3.0 real cm^2 , this gives

$$\frac{dQ_{\text{ads}}^{C_3H_8}}{d\tau_{\text{ads}}^{1/2}} = 3.6 \times 10^{-4} \text{ coulomb/sec.}^{1/2}/\text{geometric cm.}^2 \quad (5)$$

Then, taking $C^{C_3H_8}$ as 1.6×10^{-7} mole/ cm^3 ,¹⁰ we find for the diffusion constant 1.07×10^{-6} cm^2/sec . Using the Walden rule, and taking into account the viscosity of 13 M H_3PO_4 at 80° , we estimate a value of a 6.6×10^{-6} cm^2/sec . at 25° in water. This value is to be compared, for example, with $\sim 0.9 \times 10^{-5}$ cm^2/sec . for 1-propanol,²¹ a molecule similar in size to propane. This agreement provides additional justification for the conclusion that propane adsorbs, initially at least, at a rate which is limited by diffusion in solution.²²

This observation of a *diffusionally-limited adsorption rate* of propane, coupled with other observations in this laboratory that the *over-all, steady-state oxidation of propane to CO_2 is not limited by diffusion* clearly indicates that the *rate-limiting step* in the operation of a

(20) H. A. Laitinen and I. M. Kolthoff, *J. Am. Chem. Soc.*, **61**, 3344 (1939).

(21) "Chemical Engineers' Handbook," McGraw-Hill Book Co., Inc., New York, N. Y., 1950, p. 540.

(22) This agreement can be improved if (see later) n is taken as 17 (three-site adsorption model). Then, $D^{C_3H_8}$ is 1.47×10^{-6} cm^2/sec . at 80° in 13 M H_3PO_4 and 9.3×10^{-6} cm^2/sec . in water at 25° .

hydrocarbon anode is not the initial adsorption of the fuel. At least, this is the case for a clean Pt electrode.

As indicated above, the adsorption rate becomes less than the limiting diffusional rate after a few seconds of adsorption. This effect is significant after about 3 sec. at 0.4 v., after about 10 sec. at 0.3 v., and after about 20–30 sec. at 0.2 v. After about 60 sec. at any potential, $Q_{\text{ads}}^{\text{C}_3\text{H}_8}$ becomes almost constant (at rather long times, ~ 10 min., at 110°, $Q_{\text{ads}}^{\text{C}_3\text{H}_8}$ appears to fall somewhat; this will be discussed elsewhere), clearly indicating that the adsorption of propane is reaching a steady-state concentration. The variation of $Q_{\text{ads}}^{\text{C}_3\text{H}_8}$ (taken at 50 ma./cm.² after 2 min. of adsorption) with potential, at 80 and 110°, is shown in Figure 6. The over-all effect is that the adsorption is about zero at 0.1 v., rises very rapidly to a peak at ~ 0.2 v., and then declines gradually as the potential is increased, becoming about zero by about 0.7 v. The effect of temperature is small, but the tentative finding is that increase of temperature shifts the maximum of adsorption of propane to somewhat higher potentials.

Adsorption Kinetics and Steady-State Adsorption from Cathodic Charging Curves. The data presented in the previous two sections indicate that anodic galvanostatic measurements of propane adsorption provide a reasonable measure of $Q_{\text{ads}}^{\text{C}_3\text{H}_8}$ as a function of τ_{ads} and E . In order to confirm this and, also, to obtain additional information about the stoichiometry (number of Pt sites occupied per adsorbed molecule) cathodic charging experiments were undertaken.

The potential-time sequence in cathodic measurements was first to oxidize and reduce the electrode as usual, and then to jump to the potential of interest, E , for time τ_E , variable from 1 msec. to 10 min. Then, for $E \geq 0.45$ v., a cathodic galvanostatic pulse of ~ 50 ma./cm.² was applied. For $E < 0.45$ v., a short intermediate potential step (5 msec. at 0.5 v.) was interposed before this pulse to remove any residual adsorbed H atoms at the lower potentials. This step at 0.5 v. was shown not to influence the previous adsorbed material by a comparison of $Q_{\text{ads}}^{\text{C}_3\text{H}_8}$, with and without it.

A cathodic pulse deposits H atoms, as in the measurement of the electrode's area. From the charge corresponding to this process one can estimate the fraction of the maximum number of H atoms which can be adsorbed onto the electrode after a certain quantity of propane adsorption has occurred, $\theta_{\text{H}}^{80^\circ}$. A general discussion of the use of H-atom deposition in adsorption studies on Pt has been presented earlier.⁵⁻⁷

The variation of $\theta_{\text{H}}^{80^\circ}$ under propane in 13 M H₃PO₄, as a function of τ_{ads} and the potential of adsorption,

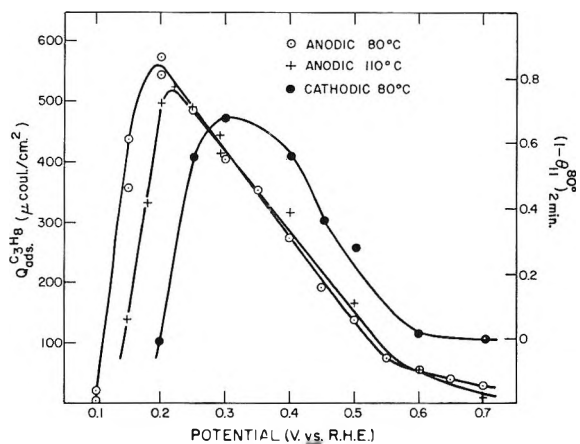


Figure 6. Adsorption of C₃H₈ as a function of potential, after 2 min. of adsorption.

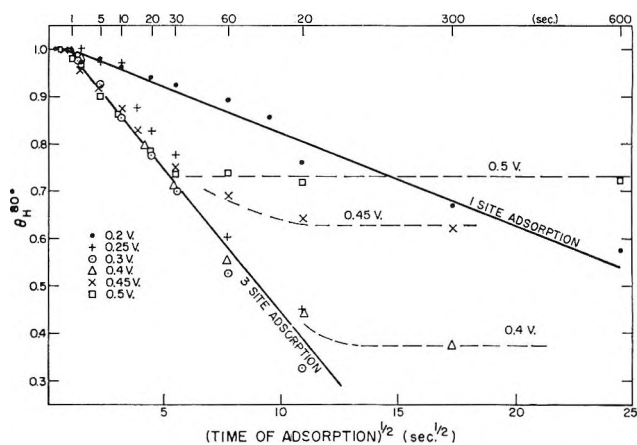


Figure 7. Adsorption of C₃H₈ at 80° as a function of time of adsorption at various potentials. Adsorption was determined with cathodic charging curves.

is shown in Figure 7. Propane is a sufficiently complex molecule that its mode of adsorption cannot be assigned *a priori*. Thus, the adsorbed material could occupy one, two, three, or even more Pt atoms on the surface. In order to discuss these possibilities, we will calculate the limiting diffusion-controlled adsorption rate, using eq. 3 and the above value of $D^{\text{C}_3\text{H}_8}$, on the basis of various modes of attachment. Thus, the amount of adsorption is 2.6×10^{13} molecules/real cm.²/sec.^{1/2}. (The electrode used in this part of the study had an average roughness factor of 3.5, and this is included in the calculation.) Then, since the basis of the present measurements in terms of real area is 1.3×10^{15} Pt atoms/cm.² (see, for example, ref. 6), this corresponds to 0.020 $\theta_{\text{H}}^{80^\circ}$ /sec.^{1/2}, if the adsorption of a propane molecule involves only one Pt surface atom (one-site adsorption), and 0.060 $\theta_{\text{H}}^{80^\circ}$ /sec.^{1/2} for three-site adsorption.

The data at 0.3 v. follow the slope of the three-site adsorption line (Figure 7), but appear to originate at $\tau_{\text{ads}} \simeq 0.5$ sec. At 0.4, 0.45, and 0.5 v., the data fit the same three-site adsorption line as the 0.3-v. data but θ_{H}^t tends to a limiting value of 0.37, 0.62, and 0.72, respectively. The 0.4-v. data depart from the three-site line for $\tau_{\text{ads}} \sim 100$ sec., but at 0.45 and 0.5 v. this departure occurs sooner, at ~ 40 sec. The data at 0.2 v. fit the slope of the one-site adsorption line, but appear to originate at $\tau_{\text{ads}} \simeq 1$ sec. The data at 0.25 v. bridge the two diffusionally limited adsorption models. Thus, for $1 < \tau_{\text{ads}} < 10$ sec., they follow one-site adsorption but from ~ 15 to 120 sec. they follow the three site line.

We can see that much of the description of the adsorption from the anodic charging curves, in terms of initial rate limitation by diffusion, is substantiated in these measurements. However, there are a number of important differences between the results of the anodic and cathodic data. Comparing Figure 7 with Figure 5, we see that whereas for anodic charging the data depart from the $\tau_{\text{ads}}^{1/2}$ relation at $\sim 20, 10,$ and 3 sec. at 0.2, 0.3, and 0.4 v., respectively, the cathodic data do not depart from the $\tau_{\text{ads}}^{1/2}$ relation at 0.2 v. up to 600 sec.; nor, at 0.3 v., do they deviate from the $\theta_{\text{H}}^t - \tau_{\text{ads}}^{1/2}$ relation up to 120 sec. and, at 0.4 v., the amount of adsorption becomes less than dependent on $\tau_{\text{ads}}^{1/2}$ between 120 and 300 sec. Also, if we equate $(1 - \theta_{\text{H}}^t)_{2 \text{ min}}$ to $\theta_{2 \text{ min}}$, we find a different adsorption-potential relation (Figure 6). Thus, while the two methods agree very well over a part of the range of τ_{ads} and E , there is a striking and a very significant difference between the results of the two methods in other regions.

Before attempting to analyze this difference, we will consider whether the θ_{H}^t values could be in error for one or more of the following reasons: (a) some of the more loosely adsorbed material could be desorbed during the measurement; (b) some additional propane could be adsorbed during the measurement, (c) some of the adsorbate could be reduced during the measurement. (a) and (c) would lead to unusually high values of θ_{H}^t , but (b) would lead to low values of θ_{H}^t .

The fact that the lines in Figure 7 do not go through the origin suggests that, for $0.3 \leq E \leq 0.5$ v., some of the adsorbed material is desorbed (perhaps reduced and desorbed) during the measurement of θ_{H}^t . It is unlikely that the material which is desorbed is singly bonded propane for it is found that singly bonded material (1–600 sec. at 0.2 v.) is not desorbed during the measurement of θ_{H}^t . In addition, a similar effect for the $\theta_{\text{H}}^t - \tau_{\text{ads}}^{1/2}$ lines is found at 0.2 v., where all of the

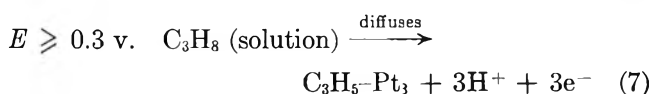
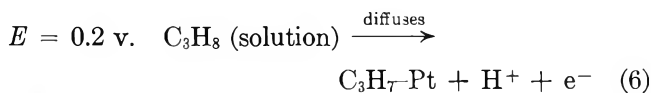
adsorbate is singly bound, as at the higher potentials. It is most likely, then, that the material which is desorbed is physically, and probably reversibly, adsorbed propane which is, perhaps, a prerequisite of the chemisorption. Since the effect of this material is evidently only to shift the θ_{H}^t vs. $\tau_{\text{ads}}^{1/2}$ lines rather than to curve them, it must be concluded that the amount of this material essentially does not change during the progress of the chemisorption. In addition, since the departure from the origin of the lines in Figure 7 is quite small, it may be concluded that this material is present only in small amounts. That some of this material, at least, is not detected with the anodic pulses is seen from a close examination of the curve of Figure 5 close to the origin. We see that here, too, there is a small deviation from the $\tau_{\text{ads}}^{1/2}$ relation, and it is in the correct sense.

With reference to (b) above, the amount of propane adsorption which could occur during the measurement can be calculated from eq. 3, and is insignificant. Concerning (c), it is known that it is possible to reduce the products of hydrocarbon adsorption on Pt.²³ However, this hydrogenation occurs only slowly. With the large current densities used here, we expect to reach H₂ evolution in < 4 msec. and very little hydrogenation would occur. The striking demonstration of a large quantity of singly bonded material at 0.2 v., which should be the easiest to reduce and which evidently is not reduced under the conditions of the experiment, clearly rules out any significant error from this. Thus, we can confidently conclude that the θ_{H}^t measurements cannot be significantly in error for adsorption times in excess of ~ 1 sec.

Reconciliation of the anodic and cathodic data can be made on the basis of the thesis that while *cathodic charging detects the number of Pt surface sites which are occupied by the adsorbate, anodic charging involves not only the amount of material adsorbed, but also the average charge required to oxidize it.* Thus, to take an extreme example, if the adsorbate were a monolayer of CO₂, the anodic charging method would describe the electrode as clean, but the same quantity of CO would give ~ 390 $\mu\text{coulombs/cm}^2$.⁷ A monolayer of singly bonded propane, as such, would give ~ 4200 $\mu\text{coulombs/cm}^2$ for conversion to CO₂ during the anodic measurement. The argument is, then, that propane is adsorbed as such, probably dissociatively and, since any H atoms so produced are in excess of the equilibrium H-atom concentration at the potential of adsorption, they are expected to be oxidized. Then,

(23) L. W. Niedrach, *J. Electrochem. Soc.*, 111, 1309 (1964).

we may expect that the adsorbed propane is effectively partially oxidized, *viz.*



It is assumed that this adsorbed propane is then gradually oxidized while still occupying the same number of sites. During the anodic transient, singly bonded and triply bonded propane can both be oxidized all the way to CO_2 , since the $Q_{\text{ads}}^{\text{C}_3\text{H}_8}$ vs. $\tau_{\text{ads}}^{1/2}$ line appears to have the same slope at each potential (Figure 5). (Equations 6 and 7 suggest that we should perhaps have selected $n = 19$ for the 0.2-v. data and $n = 17$ for the 0.3- and 0.4-v. data in eq. 3, but it is beyond the precision of the data to discriminate this difference.)

We can follow this postulated change in the composition of the adsorbate by plotting θ_{H}^t against $Q_{\text{ads}}^{\text{C}_3\text{H}_8}$ at each potential. This is shown in Figure 8 for the data at 0.2, 0.3, and 0.4 v. at 80° . The arrows indicate the limit of the linear region in the $Q_{\text{ads}}^{\text{C}_3\text{H}_8}$ vs. $\tau_{\text{ads}}^{1/2}$ data (Figure 5), and the θ_{H}^t region to the left of this (*i.e.*, at lower adsorption) is suggested as the region where only reactions 6 and 7 are taking place (and, also, the above-mentioned physical adsorption). The line through the 0.2-v. data was biased to pass through the $Q_{\text{ads}}^{\text{C}_3\text{H}_8}$ value of $85 \mu\text{coulombs/cm}^2$ for $\theta_{\text{H}}^t = 1$. This corresponds to the extrapolation of the θ_{H}^t vs. $\tau_{\text{ads}}^{1/2}$ line of Figure 7 to zero τ_{ads} , and assumes that all of the charge corresponding to the oxidation of the physically adsorbed material is, in fact, found during the anodic transient. The fact that the $Q_{\text{ads}}^{\text{C}_3\text{H}_8}$ vs. $\tau_{\text{ads}}^{1/2}$ data do not, as mentioned, quite go through the origin means that this is not actually true, but the error is less than $20 \mu\text{coulombs/cm}^2$ (Figure 5). However, the increase of $Q_{\text{ads}}^{\text{C}_3\text{H}_8}$ at $\theta_{\text{H}}^t \simeq 1$ clearly shows that a considerable part of the physically adsorbed propane is found during the anodic oxidation of the adsorbate.

Then, at 0.2 v., for θ_{H}^t from 1 to ~ 0.92 (τ_{ads} 1 to ~ 30 sec.), the region where only reaction 6 is supposed to occur, $Q_{\text{ads}}^{\text{C}_3\text{H}_8}$ vs. θ_{H}^t is linear and the slope, $[\Delta Q_{\text{ads}}^{\text{C}_3\text{H}_8} / 210 \times 10^{-6} (1 - \theta_{\text{H}}^t)]$, is about 25. This quantity, e , yields the number of electrons involved in the oxidation of the material associated with each Pt surface atom. The expectation for the residue of eq. 6 is 19 and the observed value is in reasonable agreement with this, considering the short range of θ_{H}^t which is accessible for experiment. The linear region at 0.3 v.

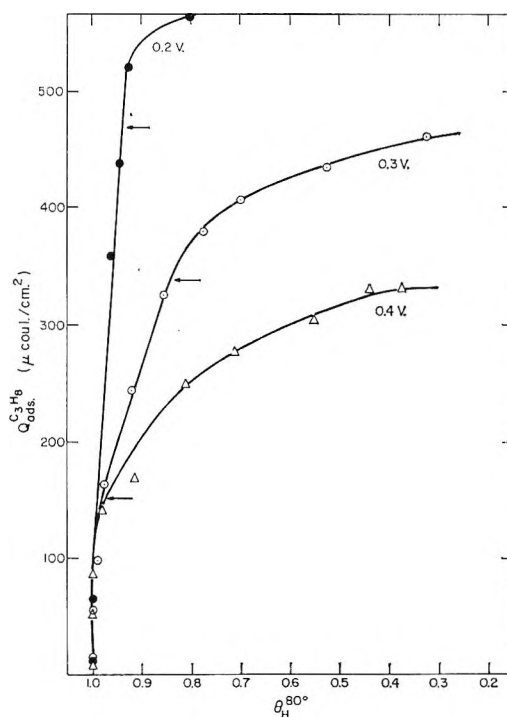


Figure 8. Comparison of anodic and cathodic charging data at 80° .

yields a slope of 6.2 compared with 5.67 predicted from eq. 7. The range in θ_{H}^t at 0.4 v., before the degradation of the adsorbate sets in, is too short to allow any estimate of e for the adsorbate at this potential. These slopes provide a verification of the three-site and one-site initial adsorption models which is independent of eq. 3 and the need to assume, there, that $n = 20$, *i.e.*, the complete oxidation of the adsorbed material to CO_2 . Taken together with the other data, however, a convincing and self-consistent demonstration of the way in which propane is adsorbed on Pt may be made.

In the region beyond the arrows in Figure 8, the value of e falls, as expected if some of the adsorbed material is partially oxidized while fresh adsorption is still continuing. The value of e in this region represents the difference between these two processes. The higher anodic charges found at the lower potentials of adsorption (Figure 5) and the observation that the departures from the linearity of the $Q_{\text{ads}}^{\text{C}_3\text{H}_8}$ vs. $\tau_{\text{ads}}^{1/2}$ data occur after shorter times of adsorption, and with smaller quantities of adsorbate, at the higher potentials, supports this explanation of the striking discrepancies between the anodic and the cathodic charging curve data.

The material chemisorbed at 0.2 v., on one site, is evidently oxidized further, but without the need, in so

doing, to occupy more than one site on the surface. There is no indication that reaction 6 is followed by reaction 7 at 0.2 v., at least at 80°.

The over-all picture of the adsorption process, as suggested by the cathodic charging curve data is, then, that at all potentials some physically adsorbed precursor is involved in the adsorption. Also, at 0.2 v., each chemisorbed C_3H_8 covers one Pt surface atom, but from 0.3 to 0.5 v., three sites are involved. At 0.25 v., the initial chemisorption appears to be on one site, but this material reverts to three-site attachments and all subsequently chemisorbed material is triply bonded. The rate of accumulation of covered Pt atoms is governed by the diffusion of propane in solution. Ultimately, at each potential, a limiting surface coverage is found (the data at 0.25 and 0.3 v. at 80° do not extend to sufficiently long times to show this) which is not necessarily unity.

The Final State of Adsorbed Propane. The limiting value of $Q_{ads}^{C_3H_8}$ divided by the limiting value of $(1 - \theta_H) 210 \times 10^{-6}$ at the same potential gives the limiting number of electrons involved in the oxidation of the material adsorbed on each covered Pt surface atom. This is shown as a function of the potential of adsorption in Figure 9. The values at 0.2, 0.25, and 0.3 v. at 80° are undoubtedly too high (*cf.* Figure 7) since the θ_H values have not leveled off at the maximum time of adsorption (10, 2, and 2 min., respectively). Above 0.3 v., however, the steady-state condition is found and, evidently, the degraded propane ultimately involves about two electrons for its conversion to CO_2 , for every Pt surface atom that it covers. The data in Figure 9 for 110° were taken for $\tau_{ads} = 10$ min. and, except for $E \leq 0.25$ v., the θ_H values had become constant in this instance. The agreement with the measurements at 80° is striking and, as before, the residue on the electrode releases about two electrons in its ultimate oxidation to CO_2 . Since no steady-state current is observed at these potentials at either 80 or 110°, it must be assumed that the product is not converted to CO_2 at these potentials and it is very likely that the surface oxidation of this species is the rate-limiting step in the conversion of propane to CO_2 .

The accumulation of products which inhibit the kinetics of organic anodic processes was noted earlier for the oxidation of $HCOOH$.⁵⁻⁷ Giner²⁴ has suggested that this product is the same for a diverse range of organic compounds and also the same as a product which he found on Pt in CO_2 saturated solution which he called "reduced CO_2 ."²⁵ Some evidence has been presented that this product is CO ,²⁶ but other evidence²⁷ suggests that, while the difference is small, the poisoning species is not CO . The present observation of

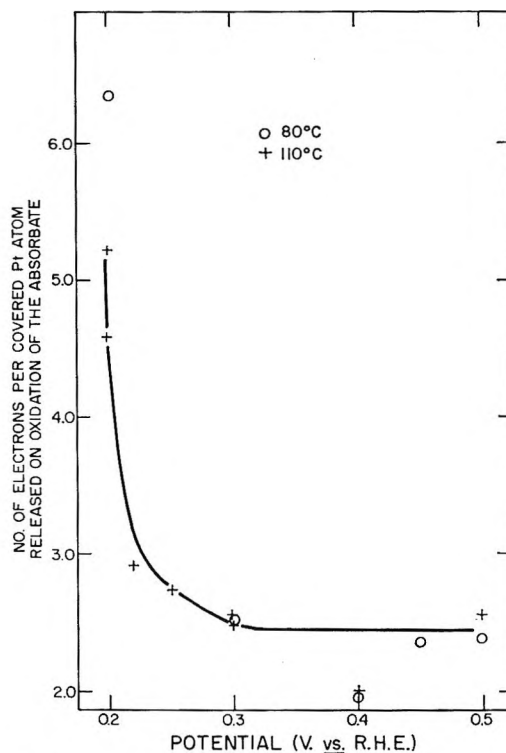
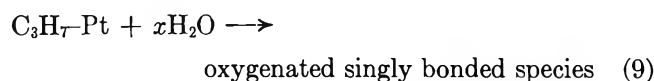
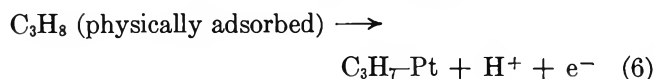
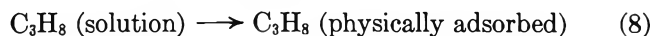


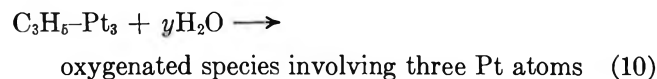
Figure 9. Final stoichiometry of adsorbed C_3H_8 .

two electrons involved in the oxidation of each ad-species would give possible credence to a CO species, but the shape of the anodic charging curves alone is strong evidence that this is not so (*cf.* Figure 1 and *ref.* 7).

Progress of Adsorption of Propane. At 0.2 v., the following scheme is suggested



At 0.3 v., reaction 8 is followed by reaction 7, and then by



The reactions yielding carbon, *viz.*

(24) J. Giner, paper presented at C.I.T.C.E. Meeting in London, Sept. 1964.

(25) J. Giner, *Electrochim. Acta*, **8**, 857 (1963); **9**, 63 (1964).

(26) D. R. Rhodes and E. F. Steigemann, *J. Electrochem. Soc.*, **112**, 16 (1965).

(27) S. B. Brummer, *J. Phys. Chem.*, **69**, 1363 (1965).



or the similar reactions yielding a partly hydrogenated species, *viz.*



which also lead to a product whose ultimate oxidation involves about two electrons, are not possible since they involve too many Pt atoms per adsorbed propane molecule. At 0.25 v., (8) is followed by (6) and, presumably when the singly bonded product of (6) reaches a certain concentration it can be oxidized to the triply bonded product *via* reaction 7. Then it follows reaction 10.

The persistence of a diffusionally limited rate of adsorption over long ranges of θ (Figure 7) implies that the product of reaction 8, which is the precursor of the chemisorbed species, is relatively long-lived near the surface and is mobile.²⁸

In order to account for the persistence of the singly bonded species at 0.2 v., it is tempting to consider that the initial adsorption occurs *via* a primary carbon atom of the propane, since this would be relatively unlikely to yield a three-site adsorbate. Similarly, the adsorption at 0.3 v. and above might be assumed as occurring *via* the secondary carbon atom. This agrees with the well-known fact that electrophilic substitution occurs more readily at the secondary carbon atom. An alternative explanation is to assume that initial chemisorption always occurs *via* the more reactive secondary carbon atom, but that further adsorption requires the presence of a deep-energy Pt surface site. At 0.2 v., most of these sites would still be covered with H atoms, which the C_3H_8 could not, perhaps, readily displace. At 0.3 v., however, al-

most all of the required deep energy wells are free and the progress from one-point to three-point attachment can proceed. At 0.25 v., the adsorption of propane on one site is assumed to change the heat of adsorption of the residual H atoms just enough to allow three-site adsorption to commence which, in turn, accelerates the displacement of the remainder of the adsorbed H.

IV. Summary and Conclusions

Although the results are incomplete in some respects, the following important conclusions may be drawn. (1) Propane is chemisorbed on Pt from 13 M H_3PO_4 solution at a rate which is limited by diffusion in solution. (2) The amount of this adsorbate under a given condition may be estimated by anodic stripping but, used alone, anodic stripping is misleading. (3) Adsorption at low potentials involves one surface Pt atom per adsorbed molecule, but at higher potentials three sites are used. (4) The adsorbate is oxidized, while remaining adsorbed on the electrode, to a partially oxygenated residue whose further oxidation at higher potentials involves about two electrons per surface Pt atom which it covers. (5) The rate-limiting step in the over-all electrochemical conversion of propane to CO_2 is probably the oxidation of this residue.

Acknowledgments. The authors wish to thank Dr. A. C. Makrides for a number of helpful discussions. This work was supported by U. S. Army Engineer Research and Development Laboratories, Fort Belvoir, Va., under Contract No. DA-44-009-AMC-410(T).

(28) D. O. Hayward and B. M. W. Trapnell, "Chemisorption," Butterworth Inc., Washington, D. C., 1964, p. 90.

Rare Gas Sensitized Radiolysis of Methane

by Vincenzo Aquilanti

Laboratorio di Chimica delle Radiazioni e Chimica Nucleare del C.N.E.N., Istituto di Chimica Generale e Inorganica, Università di Roma, Rome, Italy (Received April 13, 1965)

This paper reports the results of a systematic investigation of the xenon-, krypton-, and argon-sensitized radiolysis of methane and of CH₄-CD₄ mixtures in the gas phase. The results are interpreted in terms of nonionic mechanisms for xenon sensitization and of ionic processes for krypton and argon sensitization.

Introduction

Although the radiolysis of methane has been investigated by several authors,^{1,2} some major questions remain unanswered. In particular, the relative roles of ions and free radicals in the mechanism of formation of hydrogen and higher hydrocarbons is not clear.

Following previous studies from this laboratory of charge-exchange processes between rare gas ions and methane³ and ion-molecule reactions in methane,⁴ it was thought of interest to investigate systematically the radiolysis of mixtures of rare gases and methane. If the rare gas (Xe, Kr, or Ar) is in large excess, practically all the radiation is absorbed by it, and the energy is then transferred to the methane by different mechanisms, depending on the nature of the rare gas itself. It should therefore be possible to obtain evidence about some of the reaction paths which occur in the radiolysis of pure methane, *i.e.*, nonionic processes in xenon-sensitized experiments, and the reactions of particular ions in the radiolysis sensitized by krypton or argon.

The ionic nature of Kr-sensitized and Ar-sensitized radiolysis was first proposed by Meisels, Hamill, and Williams⁵; a few experiments are reported by Ausloos and Lias,^{2b} but only with free-radical scavengers and at relatively low concentrations of rare gases. Other studies⁶ were made at very high conversions, and it is difficult to establish a correlation between the elementary processes and the over-all observed behavior.

Present experiments include studies of the general features of sensitized radiolysis in pure methane and in the presence of small amounts of NO, O₂, and hydrocarbons, and the isotopic spectrum of hydrogen produced in the radiolysis of mixtures containing a rare gas, methane, and methane-*d*₄.

Experimental Section

All the hydrocarbons used in the present study were Phillips research grade. Methane was purified by collecting the vapor at -196°; this procedure produced a purity better than 99.95%. The rare gases, obtained from Air Liquide Co., were used without further purification. Matheson NO was purified by bulb-to-bulb distillations. Methane-*d*₄ was obtained by Merck Sharp and Dohme of Canada, and contained 4.5% CH₃D₃. The gaseous mixtures were prepared manometrically and their composition was checked by mass spectrometry and gas chromatography.

The cells used were cylindrical Pyrex vessels (about 73 cc.), and the base, which was directly exposed to radiation, consisted of an aluminium plate sealed to the Pyrex with Araldite 121B. The source of radiation was a Machlett EG-60 X-ray tube, operated at 50 kv., with tungsten as anticathode; plate currents to the tube were adjusted in the 5-30-ma. range. The dose rate was measured with a ferrous sulfate dosimeter, taking into

(1) For a review, see S. C. Lind, "Radiation Chemistry of Gases," Reinhold Publishing Corp., New York, N. Y., 1961; F. Williams, *Quart. Rev. (London)*, **17**, 101 (1963).

(2) More recent papers include: (a) J. Maurin, *J. chim. phys.*, **59**, 15 (1962); (b) P. Ausloos, *et al.*, *J. Chem. Phys.*, **38**, 2207 (1963); **39**, 3341 (1963); **40**, 1854 (1964); (c) L. W. Sieck and R. H. Johnsen, *J. Phys. Chem.*, **67**, 2281 (1963); (d) R. W. Hummel, *Discussions Faraday Soc.*, **36**, 75 (1963); (e) F. Fayard, *J. chim. phys.*, **60**, 651 (1963); (f) W. P. Hauser, *J. Phys. Chem.*, **68**, 1576 (1964).

(3) A. Galli, A. Giardini-Guidoni, and G. G. Volpi, *Nuovo Cimento*, **31**, 1145 (1964).

(4) G. A. W. Derwish, A. Galli, A. Giardini-Guidoni, and G. G. Volpi, *J. Chem. Phys.*, **40**, 5 (1964).

(5) G. G. Meisels, W. H. Hamill, and R. R. Williams, Jr., *J. Phys. Chem.*, **61**, 1456 (1957).

(6) (a) R. W. Hummel, *Nature*, **192**, 1178 (1961); (b) K. Yang, U. S. Patent 898,015 (1962); (c) R. Cipollini, A. Guarino, and G. Perez, *Gazz. chim. ital.*, **95**, 43 (1965).

account the absorption coefficients of the various gases in the X-ray spectral range and the geometrical conditions of irradiation. Under typical radiolysis conditions (rare gas pressure 100 mm., plate current 15 ma.), the absorbed dose rates were calculated to be: xenon, 7.6×10^{17} e.v./min.; krypton, 6.3×10^{17} e.v./min.; argon, 8.5×10^{16} e.v./min. However, these values are not expected to be very accurate, and since similar uncertainties affect the absolute G values, the yields of the products are referred to methane conversion.

After irradiation, the samples were analyzed by mass spectrometry for methane conversion, inorganic gas partial pressures, and isotopic ratios. C_1 - C_5 hydrocarbons were measured by gas chromatography, using two columns in series (15-m. dimethylsulfolane on Celite, plus 1-m. dinonyl phthalate on Celite),⁷ nitrogen as carrier gas, and a hydrogen-flame ionization detector. Calibrations were made by means of mixtures of known composition.

Results and Discussion

General. The radiolysis of mixtures of CH_4 and rare gases was studied by measuring the methane conversion and the distribution of the main products at different irradiation times. Experiments at different mixture compositions (methane from 3 to 7%), different total pressures (from 50 to 200 mm.), and different dose rates (plate currents from 5 to 30 ma.) were also carried out. However, both the methane conversion and the product distribution were found to depend only on the total dose absorbed.

In all cases, methane conversion (up to about 20%) was found to be a linear function of the total absorbed dose. The $G(-CH_4)$ values shown in Table I were calculated from the slopes of the straight lines so obtained. The hydrogen yields were also found to be proportional to the absorbed doses and are reported in Table I as ratios $G(H_2)/G(-CH_4)$.

Table I: Conversion Rates and Hydrogen Yields in the Rare Gas Sensitized Radiolysis of Methane

Rare gas	$G(-CH_4)$	$G(H_2)/G(-CH_4)$	$G(H_2)/G(-CH_4)^a$
Xenon	6	1.00	0.50
Krypton	7	0.75	0.46
Argon	22	0.72	0.52

^a With added NO.

Ethane, propane, iso- and *n*-butane are the main hydrocarbons produced in the radiolyses. Only traces (<0.01% of the initial methane) of pentanes and un-

saturated hydrocarbons were found, but for the argon-sensitized experiments ethylene was rather more abundant: at 3% conversion, it amounted to 0.05% of the initial methane. In the experiments where NO was added to the gaseous mixtures (as much as 30% of the initial methane), no change in conversion rate was observed; however, the hydrogen yields decreased (Table I) and no gaseous hydrocarbons were found, apart from ethylene in the experiments with krypton and argon.

Figures 1, 2, and 3, which report typical results for the production of C_2H_6 , C_3H_8 , *i*- C_4H_{10} , and *n*- C_4H_{10} , show that all hydrocarbon yields decrease with increasing methane conversion. A study of the yields at low conversion is therefore necessary if one wishes to investigate the initial processes.

Figure 4 gives the ratio C_3H_8/C_2H_6 obtained at the lowest conversion values allowed by present analytical methods. This ratio is constant for the krypton and argon mixtures, but shows a marked initial increase when xenon is used as sensitizer. Therefore, in the latter case propane is a typical secondary product.

In Figure 5, the ratios HD/D_2 , obtained in the radiolysis of rare gas- CH_4 - CD_4 mixtures, are plotted against conversion. This ratio extrapolates towards zero at zero conversion for the xenon experiments, while for krypton and argon it seems to maintain a finite value. Therefore it appears that in these latter systems HD is a primary radiolysis product, namely, that hydrogen atoms are initially produced; conversely, in xenon-sensitized radiolysis hydrogen is mainly produced by a process of molecular detachment. Figure 5 also shows that the exchange reactions leading to HD formation are strongly inhibited in the presence of NO. These results, together with the observation (Table I) that NO decreases hydrogen yields, seem to indicate that, besides primary processes leading to the formation of H_2 , more hydrogen is produced during the radiolysis *via* the products themselves; this latter source of hydrogen is inhibited by NO because of its effect in decreasing the yield of hydrocarbons. It seems altogether unjustifiable to identify the yields obtained in the presence of NO as "molecular yields" (as suggested by several authors^{1b,8}) because NO should not act as a scavenger of hydrogen atoms, but as a catalyzer in their recombination.⁹

Xenon-Sensitized Radiolysis. In their lower state $^2P_{3/2}$, Xe^+ ions do not transfer their charge to methane,

(7) E. M. Fredericks and F. R. Brooks, *Anal. Chem.*, **28**, 297 (1956).

(8) L. M. Dorfman and M. C. Sauer, Jr., *J. Chem. Phys.*, **32**, 1886 (1960).

(9) H. M. Smallwood, *J. Am. Chem. Soc.*, **51**, 1985 (1929).

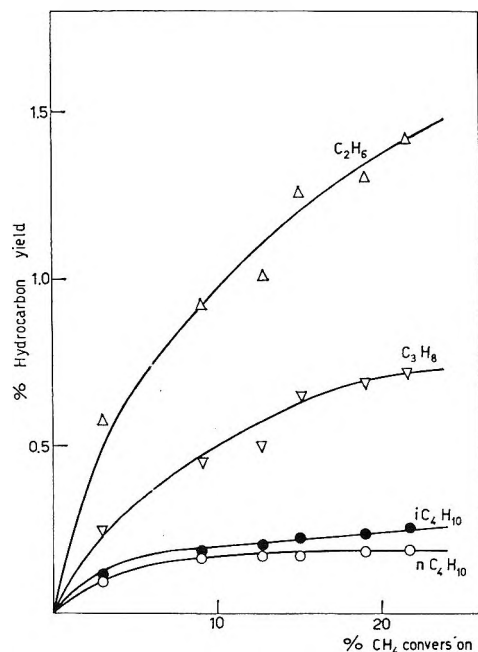


Figure 1. Hydrocarbon yields (per cent of the initial methane) in the xenon-sensitized radiolysis (mixture, Xe with 6.4% CH₄; total pressure, 100 mm.).

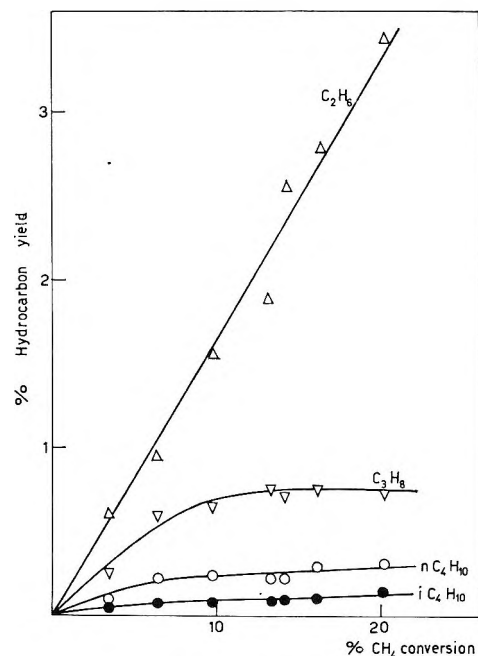


Figure 3. Hydrocarbon yields (per cent of the initial methane) in the argon-sensitized radiolysis (mixture, Ar with 5.8% CH₄; total pressure, 100 mm.).

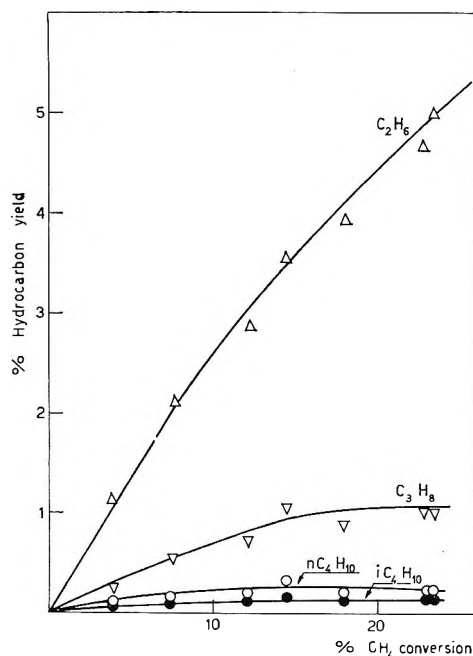


Figure 2. Hydrocarbon yields (per cent of the initial methane) in the krypton-sensitized radiolysis (mixture, Kr with 5.8% CH₄; total pressure, 100 mm.).

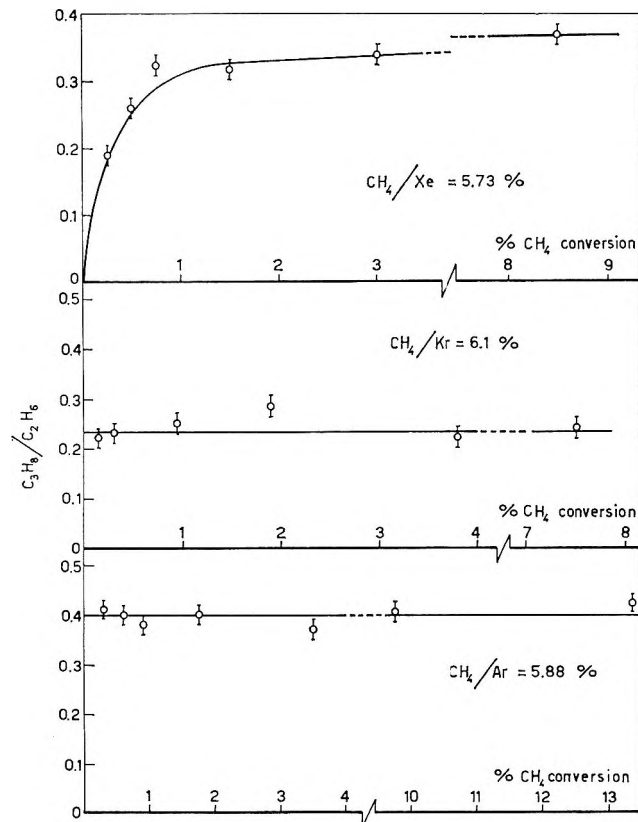
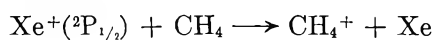


Figure 4. Ratio C₃H₈/C₂H₆ in low-conversion sensitized radiolysis.

and according to mass spectrometric measurements,^{3,10} the process



(10) F. H. Field and J. L. Franklin, *J. Am. Chem. Soc.*, **83**, 4509 (1961).

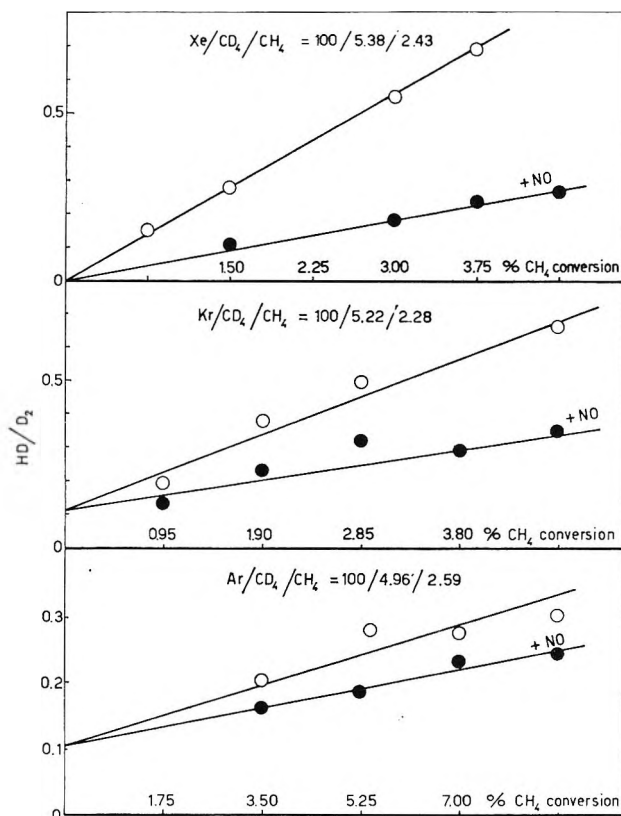
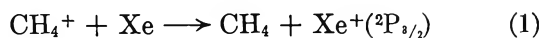
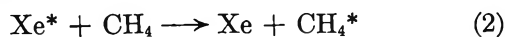


Figure 5. Ratio HD/D₂ in sensitized radiolysis of CH₄-CD₄ mixtures.

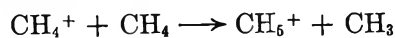
when [CH₄] ≪ [Xe], should be counterbalanced by



Therefore, it seems reasonable to assume that the xenon sensitization is mainly due to a process of excitation transfer (2).

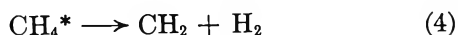
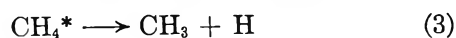


When the ratio [CH₄]/[Xe] is increased, ionic processes can become operative, because the reaction



may compete with (1) and methane may be directly ionized by secondary electrons. This effect, which will result in an increase of $G(-\text{CH}_4)$, is confirmed by the results in Table II.

After reaction 2, two possible reaction paths for CH₄* are (3) and (4). While (3) is most important in methane



pyrolysis¹¹ and in the Hg-sensitized photolysis,¹² reac-

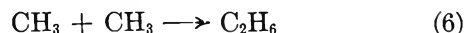
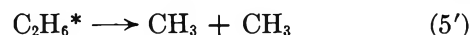
Table II: Conversion Rates and Hydrogen Yields in the Radiolysis of Xe-CH₄ Mixtures

Mixture composition ^a CH ₄ /Xe	$G(-\text{CH}_4)^b$	$G(\text{H}_2)/G(-\text{CH}_4)$
0.033	5.8	1.04
0.064	5.9	1.00
1.00	10	0.71
2.13	15	0.77
2.78	16	0.73
11.8	20	0.68

^a Total pressure, 100 mm. ^b Calculated assuming energy absorption only in xenon. (As ascertained in separate experiments, the contribution of direct absorption in pure methane may be neglected.)

tion 4 is the main decomposition mode of methane in the vacuum ultraviolet photolysis.¹³ An examination of the excited states of xenon shows that process 2 should be similar to vacuum ultraviolet photolysis; in fact, the radiolysis of mixtures Xe-CH₄-CD₄ clearly demonstrate (Figure 5) that in this system hydrogen is produced in molecular form.

Methylene radicals react further with methane to give ethane *via* the formation of methyl radicals. Several



authors¹⁴ have previously suggested that the insertion reaction (5) is followed by decomposition into methyl ions (5'); in our system, the reaction sequence 5-6 was proved to occur by the experiments carried out in the presence of NO. NO is not a scavenger of methylene radicals¹⁵ and therefore does not change the conversion rate, but it inhibits reaction 6 and, therefore, the formation of hydrocarbons.

The interesting result, obtained at low conversions (Figure 4), namely, that ethane is practically the only hydrocarbon produced primarily, suggests that reactions 4, 5, and 6 might be sufficient to explain the initial processes of the xenon-sensitized radiolysis.

(11) E. W. R. Steacie, "Atomic and Free Radical Processes," Reinhold Publishing Corp., New York, N. Y., 1961.

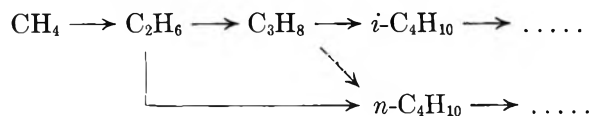
(12) R. A. Back and D. Van Der Auwera, *Can. J. Chem.*, **40**, 2339 (1962).

(13) (a) B. H. Mahan and R. Mandal, *J. Chem. Phys.*, **37**, 207 (1962); (b) E. M. Magee, *ibid.*, **39**, 855 (1963).

(14) See, e.g., J. A. Bell and G. B. Kistiakowsky, *J. Am. Chem. Soc.*, **84**, 3417 (1962).

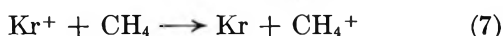
(15) M. Burton, T. W. Davis, A. Gordon, and H. A. Taylor, *ibid.*, **63**, 1956 (1941).

As the radiolysis goes on, hydrocarbons are formed with an ever increasing number of carbon atoms; however, the yields of the measured ones (C_2H_6 , C_3H_8 , $i-C_4H_{10}$, $n-C_4H_{10}$) decrease at higher conversions and account only for one-third of the carbon atoms produced by the decomposition of methane (Figure 1). In order to clarify the mechanism of product formation, we have radiolyzed Xe- CH_4 mixtures at low conversions, with added hydrocarbons, NO, and O_2 (Table III). Because the addition of C_2H_6 and C_3H_8 increases, respectively, C_3H_8 and $n-C_4H_{10}$, and $i-C_4H_{10}$, the carbon-chain lengthening seems to proceed by the scheme¹⁶



where at every step hydrogen is formed. On the other hand, many of these processes may take place from right to left also, until a sort of radiolytic equilibrium is attained and the yields are reduced to zero. This is shown by the fact that the ratio $G(C_3H_8)/G(C_2H_6)$ becomes constant and equal to 0.35 at conversions greater than 3%; if in addition ethane or propane are added, this ratio will approach the same value of 0.35 rather quickly (Figure 6). The formation of ethane from propane is also observed (Table III) in scavenged experiments and, since it occurs through ionic processes in Xe-sensitized radiolysis of propane,¹⁷ can be attributed to $Xe^+(^2P_{3/2})$ ions, which, according to the present mechanism, do not react with methane. In addition, the fast disappearance of the added C_2H_4 and C_2H_2 (probably to give polymers) (Table III) may be explained on the same basis, and this may be the fate of unsaturated hydrocarbons (if produced during the radiolysis). Indeed, all the complicated behavior which follows the ethane formation seems to be due to an efficient $Xe^+(^2P_{3/2})$ sensitized radiolysis of the products themselves.

Krypton-Sensitized and Argon-Sensitized Radiolysis. It has been well established^{3,18} that the following charge-exchange processes (7-10) occur between krypton and argon ions and methane. Therefore, in the con-



ditions of sensitized radiolysis, the krypton and argon ions formed by ionizing radiation will produce³ CH_4^+ and $(CH_3^+ + H)$ in the ratio 1:0.7 for Kr sensitization, and $(CH_3^+ + H)$ and $(CH_2^+ + H_2)$ in the ratio 1:0.25

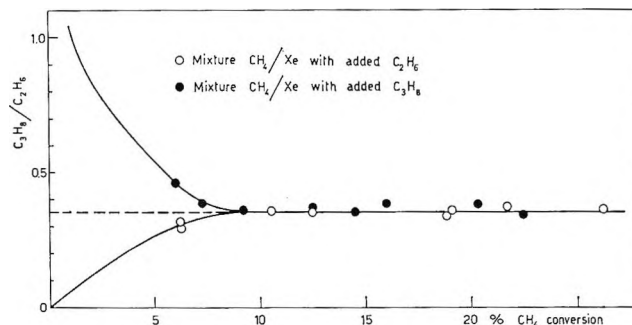
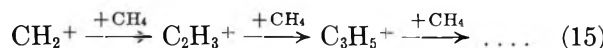


Figure 6. Effect of added C_2H_6 and C_3H_8 on the ratio C_3H_8/C_2H_6 in the Xe-sensitized radiolysis. (Added $C_2H_6 = 1.53\%$ of CH_4 ; added $C_3H_8 = 1.19\%$ of CH_4 .)

for Ar sensitization. The formation of atomic hydrogen, expected from processes 8 and 9, may explain the observation (Figure 5) that HD appears as a primary molecular product in the radiolysis of Kr (or Ar)- CH_4 - CD_4 mixtures. The ions CH_4^+ , CH_3^+ , and CH_2^+ cannot be directly neutralized, because their reactivity with methane is very high; their reactions have been cleared up fairly well through recent mass spectrometric investigations.^{4,19} Besides the already known ones (11 and 12) other fast reactions (13 and 14) have been ob-



served.⁴ Rather than (14), CH_2^+ ions may give polymeric ions at a high rate.¹⁹ This reaction sequence (15)



leads to the formation of products with a high molecular weight *via* the conversion of several methane molecules for every primary formed CH_2^+ ion. This explains two features of argon-sensitized radiolysis: the high value of $G(-CH_4)$ and the material balance, which is very poor even at fairly low conversions, as can be ascertained from Figure 3. A comparison with Figure 2 shows that this is not the case for krypton sensitization, where no CH_2^+ ions are present.

Reactions 11-14 produce molecular hydrogen, methyl radicals, and CH_5^+ and $C_2H_5^+$ ions; since there is no

(16) G. J. Mains and A. S. Newton [*J. Phys. Chem.*, **64**, 212 (1961)] propose a similar scheme for Hg-sensitized radiolysis and photolysis.

(17) J. H. Futrell and T. O. Tiernan, [*J. Chem. Phys.*, **37**, 1694 (1962)].

(18) F. H. Field, H. N. Head, and J. L. Franklin, [*J. Am. Chem. Soc.*, **84**, 1118 (1962)].

(19) (a) S. Wexler and N. Jesse, *ibid.*, **84**, 3425 (1962); (b) F. H. Field, J. L. Franklin, and M. S. B. Munson, *ibid.*, **85**, 3575 (1963).

reliable information about the fate of these ions (which seem to be unreactive with methane^{4,19}), no detailed mechanism for the observed product distribution can be given at present. However, some information can be obtained by considering the results already quoted, together with those presented in Tables IV and V.

Table III: Effect of Additives on Hydrocarbon Yields in Xenon-Sensitized Radiolysis^a

Added gas	Added gas concentration ^b	Hydrocarbon yields ^b				
		C ₂ H ₆	C ₂ H ₄	C ₃ H ₈	<i>i</i> -C ₄ H ₁₀	<i>n</i> -C ₄ H ₁₀
None	...	0.57	...	0.26	0.10	0.10
C ₂ H ₆	3.75	2.73	...	0.55	0.11	0.16
C ₃ H ₈	2.08	0.74	...	1.36	0.27	0.13
NO	15
O ₂	5
C ₂ H ₆ + NO	3.4 + 8	2.54	0.1	0.03	0.03	0.03
C ₃ H ₈ + NO	7 + 8	0.35	0.27	2.40	(C ₃ H ₈ = 0.12)	
C ₃ H ₈ + O ₂	5.4 + 4	0.70	...	2.44	0.15	0.10
C ₂ H ₄	2.25	0.60	...	0.32	0.11	0.12
C ₂ H ₂	5	0.45	0.02	0.12	0.04	0.03

(C₂H₂ = 0.00)

^a Mixture, Xe with 5% CH₄; total pressure, 100 mm.; absorbed dose corresponding to 3% conversion. ^b Per cent of the initial methane. For the added gases, the "yields" given in the table are the amounts of added gases found after irradiation.

Table IV: Effect of Additives on Hydrocarbon Yields in Krypton-Sensitized Radiolysis^a

Added gas	Added gas concentration ^b	Hydrocarbon yields ^b				
		C ₂ H ₆	C ₂ H ₄	C ₃ H ₈	<i>i</i> -C ₄ H ₁₀	<i>n</i> -C ₄ H ₁₀
None	...	1.18	...	0.25	0.05	0.07
C ₂ H ₆	4.7	5.3	...	0.41	0.06	0.11
C ₃ H ₈	5.0	1.99	0.04	2.9	0.15	0.09
NO	11	...	0.20
O ₂	7	...	0.03
C ₂ H ₆ + NO	5 + 9.1	4.17	0.30
C ₃ H ₈ + NO	5.2 + 9.1	0.74	0.33	4.3	(C ₃ H ₈ = 0.17)	
C ₃ H ₈ + O ₂	6 + 9.7	0.71	0.17	3.9	(C ₃ H ₈ = 0.04)	
C ₂ H ₄	3.57	1.19	0.38	0.82	0.09	0.33
C ₂ H ₂	5	0.90	0.07	0.28	0.05	0.04

(C₂H₂ = 0.3)

^a Mixture, Kr with 6% CH₄; total pressure, 100 mm.; absorbed dose corresponding to 3.8% conversion. ^b Per cent of the initial methane. For the added gases, the "yields" given in the table are the amounts of added gases found after irradiation.

It appears from Figure 4 that in these systems ethane and propane are simultaneous radiolytic products (in contrast with Xe sensitization). On the other hand, a higher yield of ethane is produced with krypton than with argon (Figures 2 and 3); this suggests that the

Table V: Effect of Additives on Hydrocarbon Yields in Argon-Sensitized Radiolysis^a

Added gas	Added gas concentration ^b	Hydrocarbon yields ^b				
		C ₂ H ₆	C ₂ H ₄	C ₃ H ₈	<i>i</i> -C ₄ H ₁₀	<i>n</i> -C ₄ H ₁₀
None	...	0.65	0.05	0.20	0.05	0.09
C ₂ H ₆	7	7.10	...	0.37	0.05	0.21
C ₃ H ₈	6.7	1.60	...	5.39	0.14	0.07
NO	9	...	0.18
O ₂	5	...	0.10
C ₂ H ₆ + NO	4.5 + 10	3.81	0.52
C ₃ H ₈ + NO	5.5 + 10	0.60	0.18	4.43	(C ₃ H ₈ = 0.10)	
C ₃ H ₈ + O ₂	4.7 + 2.4	0.52	0.09	3.36
C ₂ H ₄	3.6	0.77	0.60	0.51	0.07	0.53
C ₂ H ₂	5	0.26	0.14	0.13	(C ₂ H ₂ = 2)	

^a Mixture, Ar with 6% CH₄; total pressure, 100 mm.; absorbed dose corresponding to 3.5% conversion. ^b Per cent of the initial methane. For the added gases, the "yields" given in the table are the amounts of added gases found after irradiation.

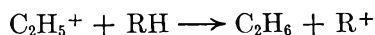
CH₅⁺ ions, which are prevalent in Kr sensitization *via* (7) and (11) and almost absent in Ar sensitization (they arise only *via* (13)), give mainly ethane through neutralization to molecular hydrogen and methyl radicals; these latter, together with those formed from (11) and (13), will eventually dimerize to ethane. Accordingly, the observed primary yield of propane comes mainly from ethyl ions,²⁰ presumably *via* ethyl radical, whose presence in pure methane radiolysis is known.²¹ In our experiments this is supported by the yield of *n*-C₄H₁₀, dimerization product, which is higher than for xenon sensitization (Figures 2 and 3). However, a direct neutralization of ethyl ions to ethyl radicals seems unfavorable energetically; probably, ethyl ions are neutralized by decomposition to ethylene and atomic hydrogen and the rather fast reaction H + C₂H₄ → C₂H₅ should then follow. If ethyl radicals are produced by this mechanism, in our conversion range propane could still behave as a primary product. The yield and role of ethylene in methane radiolysis has been much debated,^{2b-f} because the quantitative measurements of initial yields may be strongly affected by impurities of oxygen (see also Tables IV and V). We note (Tables IV and V) that if ethylene is added to Kr (or Ar)-CH₄ mixtures, there is an increase in C₃H₈ and *n*-C₄H₁₀, and also in the argon experiments trace concentrations of ethylene were observed. Scavengers enhance ethylene yields

(20) The C₂H₇⁺ ion, previously suggested in this connection,⁶ has not been found to be of importance in high-pressure mass spectroscopic studies of methane carried out in this laboratory.

(21) L. H. Gevantman and R. R. Williams, *J. Phys. Chem.*, **56**, 569 (1952).

although this could be due to reactions in which the scavengers themselves participate.

Finally, CH_5^+ and C_2H_5^+ ions may react with the products of radiolysis; however, of the several reactions proposed,^{2b} only those of the type



are confirmed by mass spectrometric studies.²² The occurrence of these reactions explains the increase of ethane yield when propane is added both in unscavenged and in scavenged experiments (Tables IV and V), and further supports the effectiveness of ionic processes in krypton-sensitized and argon-sensitized radiolysis.

Acknowledgments. The author wishes to thank Professor G. G. Volpi for suggesting this research and for his continuous advice and aid. Thanks are also due to Dr. Anna Giardini-Guidoni who participated in the early stages, and to Mr. E. Luzzatti, who helped in the experimental work. A fellowship from the Consiglio Nazionale delle Ricerche is gratefully acknowledged.

(22) (a) E. Patterson and E. Lindholm, *Arkiv Fysik*, **24**, 49 (1962); (b) G. A. W. Derwish, A. Galli, A. Giardini-Guidoni, and G. G. Volpi, *J. Chem. Phys.*, **41**, 2998 (1964).

Anion Exchange in Concentrated Solutions¹

by C. H. Jensen² and R. M. Diamond

Lawrence Radiation Laboratory, University of California, Berkeley, California (Received April 15, 1966)

The resin selectivity of tracer halide ions has been discussed as a function of the nature of the anion, of the resin-group cation, and of the macroelectrolyte. In dilute solution, interactions between ions and water and between the anions and resin-group ions are dominant, but with concentrated solutions, anion-cation interactions play an important role. Experimental confirmation of the ideas presented was obtained with Dowex 1 and Dowex 4 resins, containing a quaternary ammonium and a tertiary amine group, respectively, and employing KOH, LiCl, and tetramethylammonium chloride (NMe_4Cl) solutions as the eluting agent.

Introduction

In a recent pair of papers the dilute-solution elution orders of the alkali³ and alkaline earth⁴ metal cations have been explained as a competition between the water molecules and resin-group anions for solvating the cations. In going to concentrated external solutions, the effect of the aqueous anion must also be included, and the decrease in water activity in such solutions makes the interactions of the cations with both the aqueous anion and resin anion increasingly important. Depending upon the relative strength of these interactions, the elution order may invert with concentrated electrolyte solutions, and the conditions necessary for

such selectivity reversals are consistent with the type of model suggested.

It seemed of interest to extend these considerations to the case of anion-exchange resins. A corresponding model for the dilute-solution exchange of anions has already been presented⁵ which, however, makes use of an

(1) This work was supported by the U. S. Atomic Energy Commission.

(2) Summer Visitor, 1962, N.S.F. High School Teachers Research Participation Program.

(3) D. C. Whitney and R. M. Diamond, *Inorg. Chem.*, **2**, 1284 (1963).

(4) D. C. Whitney and R. M. Diamond, *J. Inorg. Nucl. Chem.*, **27**, 219 (1965).

additional feature for large monovalent ions such as ClO_4^- , AuCl_4^- , FeCl_4^- , ReO_4^- , etc. (and NMe_4^+ , NEt_4^+ , etc., in cation exchange). Such large, lowly charged ions do not coordinate the neighboring water molecules into a first hydration shell and are squeezed by the hydrogen-bonded water structure out into the less structured (less hydrogen-bonded) resin phase. If the resin group itself is also a large, lowly charged, and relatively hydrophobic ion, *e.g.*, the quaternary ammonium ion of a strong-base resin, the residual water structure in the resin phase pushes the two oppositely charged ions together to associate as a water-structure-enforced ion pair.⁶ The result for the large ions is the dilute-solution elution order observed, *i.e.*, $\text{Br}^- < \text{I}^- < \text{ClO}_4^-$.

However, more important to the present discussion is whether such considerations can explain the elution behavior of the halide (and other) anions with a change in the nature of the resin group and in the presence of concentrated external solutions. If so, this might lead to the systematic tailoring of conditions to yield desired types of behavior, as, for example, an inverted selectivity sequence for the halide ions.

Experimental Section

Reagents. The anion-exchange resins used were Dowex 1-X8, a strong-base resin with a polystyrene matrix, and Dowex 4, a tertiary amine resin derived from the condensation of epichlorohydrin and ammonia. The capacity and water uptake of the Dowex 1 were 3.46 mequiv. and 0.72 g., respectively, per g. of dry Cl-form resin, and the corresponding figures for the Dowex 4 were 2.99 mequiv. and 0.89 g. per g. of dry Cl-form resin. The solutions of KOH, LiCl, and $\text{N}(\text{CH}_3)_4\text{Cl}$ (NMe_4Cl) were prepared by volumetric dilution with conductivity water of analyzed stock solutions of reagent grade materials. The ^{18}F tracer was prepared at the Lawrence Radiation Laboratory HILAC from reagent grade Li_2SO_4 by the nuclear reaction, $^{16}\text{O}(\alpha, d)^{18}\text{F}$. The $^{36,38}\text{Cl}$ and ^{82}Br were prepared by neutron irradiation of reagent grade LiCl and LiBr at the Livermore reactor. The ^{131}I tracer (carrier free in Na_2SO_3) was purchased from Oak Ridge National Laboratory. The ^{22}Na (carrier free) was purchased from Nuclear Science and Engineering Corp., Pittsburgh, Pa.

Procedure. Batch measurements were made with the I^- tracer by placing weighed samples (0.0150–0.1000 g.) of resin and 10.0 or 20.0 ml. of solution of known tracer content into 30-ml. polyethylene screw-cap bottles and shaking for at least 8 hr. Two 2.00-ml. aliquots of solution were then removed through fritted-glass filters and γ -counted using a well-type

$\text{NaI}(\text{Tl})$ scintillation counter with single-channel analysis. Two 2.00-ml. samples of the stock solution were also counted to give the initial tracer activity. After correction for background, the distribution coefficient was calculated in the usual way.³ Column elution measurements were made for the Br^- , Cl^- , and F^- tracers; several polyethylene columns were used. The resulting elution volumes were converted to distribution coefficients by means of a proportionality factor determined for each column by calibrating them with I^- against the batch measurements with I^- tracer. The free column volume was determined for each column using the tracer ^{22}Na , and this volume was subtracted from the peak elution volumes of the halide ions before they were converted to D values. A polyethylene thimble was placed at the top of each column to prevent floating of the resin in concentrated solutions and to keep the total volume of the column a constant. All experimental work was done at room temperature, $23 \pm 2^\circ$.

Results

The results are recorded as log-log plots of D vs. aqueous salt molarity in Figures 1–4. Figure 1 is for the halide tracers vs. KOH on Dowex 1; Figure 2 has the tracers vs. LiCl on Dowex 1; Figure 3 has the tracers vs. LiCl on Dowex 4; and Figure 4 is for the tracers vs. NMe_4Cl on Dowex 4.

Discussion

The equation for the exchange of a halide tracer ion, A^- , with a univalent macroion, B^- , on an anion-exchange resin can be written



where charge and ion hydration have been omitted for simplicity, and the superscript bar denotes the resin phase. Choosing the standard state to be the same in both phases and, in particular, to be the usual hypothetical state of unit activity with the properties of the infinitely dilute solution leads in the usual way to the expression

$$1 = \frac{(\bar{\text{A}})(\text{B})}{(\text{A})(\bar{\text{B}})} = \frac{[\bar{\text{A}}][\text{B}]}{[\text{A}][\bar{\text{B}}]} \frac{\bar{\gamma}_{\text{A}}\gamma_{\text{B}}}{\gamma_{\text{A}}\bar{\gamma}_{\text{B}}} = \bar{K}_{\text{A/B}}\Gamma_{\text{A/B}} \quad (2)$$

When this is combined with the definition of the distribution coefficient

$$D \equiv \frac{[\bar{\text{A}}]}{[\text{A}]} \quad (3)$$

(5) B. Chu, D. C. Whitney, and R. M. Diamond, *J. Inorg. Nucl. Chem.*, **24**, 1405 (1962).

(6) R. M. Diamond, *J. Phys. Chem.*, **67**, 2513 (1963).

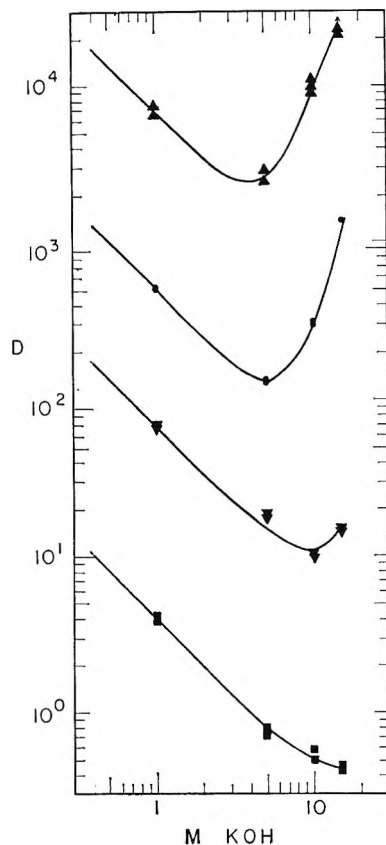


Figure 1. Plot of $\log D$ vs. \log KOH molarity with Dowex 1 resin for tracer F^- , \blacksquare ; Cl^- , \blacktriangledown ; Br^- , \bullet ; I^- , \blacktriangle .

we obtain

$$D = \frac{[B]\bar{\gamma}_B\gamma_A}{[B]\bar{\gamma}_A\gamma_B} \quad (4)$$

For dilute solutions, where resin invasion is negligible and the activity coefficient ratios are essentially constant, eq. 4 reduces to the well-known form, $D \propto [B]^{-1}$. As can be seen in Figures 1-4, this is obeyed in dilute solution for all of the tracers with the types of resins and eluting solutions studied.

Furthermore, the elution order is the same in all cases, $F^- < Cl^- < Br^- < I^-$. We believe this sequence is due mainly to the better hydration available to the (crystallographically) smaller halide ion in the dilute external phase over that possible in the concentrated resin phase solution and not due to electrostatic ion pairing with the large quaternary ammonium resin group.⁵ For example, the extraction order of the halides by tertiary ammonium ions in organic solvents (the so-called "liquid exchangers") is the same,⁷ $F^- < Cl^- < Br^- < I^-$, and yet here there is infrared and n.m.r. evidence⁸ that the halides are ion paired to the ammonium cation in the inverse order, $Cl^- >$

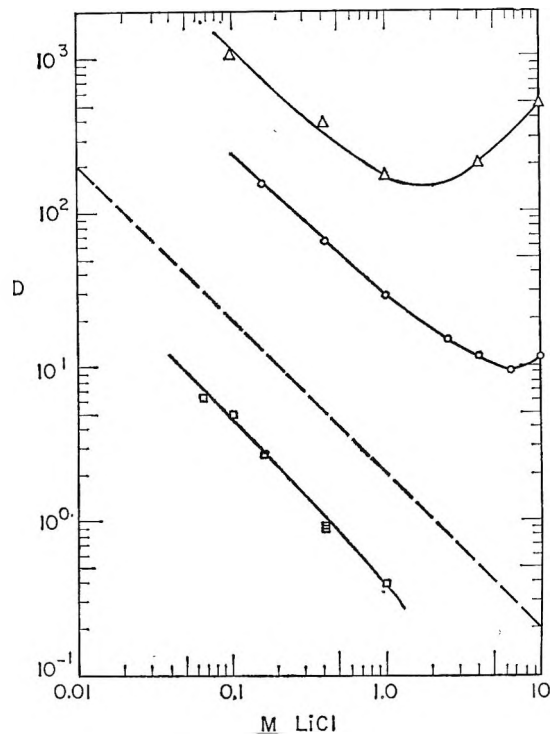


Figure 2. Plot of $\log D$ vs. \log LiCl molarity with Dowex 1 resin for tracer F^- , \square ; Br^- , \circ ; I^- , \triangle . Dashed line is "ideal" slope of -1 .

$Br^- > I^-$. It is obviously necessary to account for the order of extraction in a different way than by ion-pairing explanations.

We further feel that some recent thermodynamic measurements on ion-exchange reactions are in agreement with, although they certainly do not prove, this viewpoint. In particular, the sign of the free energy change for the exchange of Cl^- by Br^- on Dowex 1-X10 has been shown to be determined by the enthalpy change⁹; both ΔH and $T\Delta S$ are negative but the former is the larger quantity. This is what would be expected if the reaction involved an increase in the hydration of the (ions in the) system. That is, there is an enthalpy decrease due to the additional hydration and a smaller decrease in $T\Delta S$ due to the increased ordering of the water molecules around the ion, just as in the much more energetic hydration of bare, gaseous ions. The same changes in ΔH and $T\Delta S$ have also been found in the exchanges of the alkali cations on a strong-acid sulfonic resin,¹⁰ where again

(7) A. S. Wilson and N. A. Wogman, *J. Phys. Chem.*, **66**, 1552(1962).

(8) (a) W. Keder, A. Wilson, and L. Burger, Hanford Laboratory Report HW-SA 2959, April 1963; (b) W. Keder and A. Wilson, *Nucl. Sci. Eng.*, **17**, 287 (1963).

(9) K. A. Kraus, R. J. Raridon, and D. L. Holcomb, *J. Chromatog.*, **3**, 178 (1960).

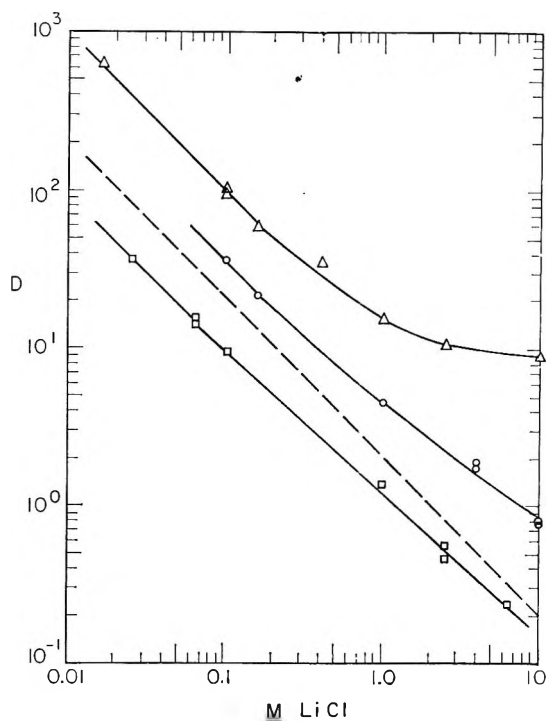


Figure 3. Plot of $\log D$ vs. \log LiCl molarity with Dowex 4 resin for tracer F^- , \square ; Br^- , \circ ; I^- , \triangle . Dashed line is "ideal" slope of -1 .

we believe changes in ion hydration mainly determine the selectivity order rather than resin-group ion pairing. However, this is not the case for the Cs^+Li^+ exchange on a weak-acid carboxylate resin where bonding to the resin group does determine the (inverse) selectivity order,¹¹ $Li^+ > Cs^+$. In this exchange the binding of Li^+ to the carboxylate group lowers the unfavorable enthalpy change enough so that the entropy increase of releasing some water of hydration of the lithium ion can dominate ΔF , as is observed.

However, it can be seen that the degree of separation of the halide tracers varies with the nature of the macroanion and of the resin group. Figures 1 and 2 compare the use of OH^- and Cl^- as eluents with the Dowex 1 resin. The 1750-fold increase in D from F^- to I^- with OH^- as the macroanion is compressed to a 250-fold increase when Cl^- is the macroanion. This type of behavior was earlier noticed in the cation-exchange case when substituting the more tightly held Cs^+ for Li^+ as the macrocation in the ion exchange of alkali metal tracers with Dowex 50.³

A more dramatic compression of the halide separation factors occurs if a tertiary amine rather than a quaternary ammonium ion is used as the resin group. An obvious result is that the selectivity for OH^- is increased enormously, but halide exchange is also affected. Dowex 4 is such a weak-base resin and, so, in slightly

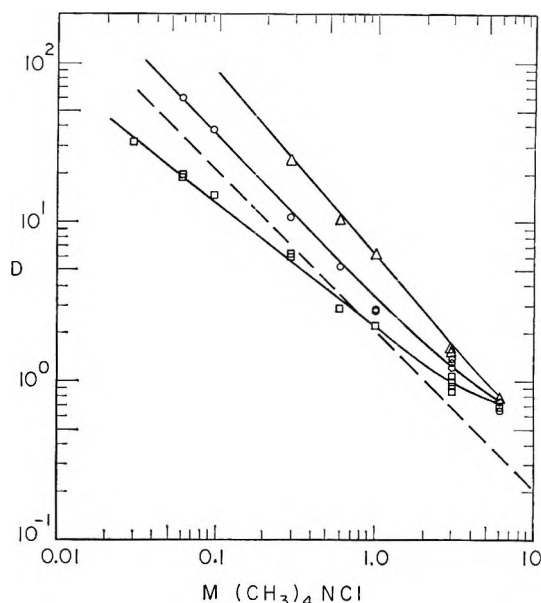


Figure 4. Plot of $\log D$ vs. \log NMe_4Cl molarity with Dowex 4 resin for tracer F^- , \square ; Br^- , \circ ; I^- , \triangle . Dashed line is "ideal" slope of -1 .

acid solutions has R_3NH^+ as the exchange group. The resulting ammonium ion is still a large ion, but it has a special site, the hydrogen, which probably carries much of the ion charge and which can hydrogen bond to water and to other bases. That is, it has the possibility of (hydrogen) bonding, even though weakly, to small basic anions such as F^- , and so making the resin phase more attractive to such ions than is the case with strong-base resins. Furthermore, the tertiary ammonium ions cannot participate in water-structure-enforced ion pairing as well as can the quaternary ion, thereby decreasing its attraction for large ions like I^- . For both reasons, the halide elution sequence should be compressed over that with a quaternary ammonium resin, and Figures 3 and 4 show only a 10-fold spread in D from F^- to I^- with Dowex 4 and eluting solutions of LiCl or NMe_4Cl below a few hundredths molar in concentration compared to the 250-fold range in D with Dowex 1.

That this compression of the halide separation is due to the presence of the hydrogen on the ammonium group and not to the fact that Dowex 4 has a different lattice structure than Dowex 1 (polystyrene structure) was shown by the similar behavior observed with Dowex 3, a polystyrene-base resin containing a mixture of primary, secondary, and tertiary amine groups; the

(10) G. E. Boyd, F. Vaslow, and S. Lindenbaum, *J. Phys. Chem.*, **68**, 590 (1964).

(11) S. Lindenbaum and G. E. Boyd, private communication, Feb. 1965.

ratio of the distribution coefficients of tracer Br^- to tracer F^- with LiCl as the macroelectrolyte is 5.5, compared to 50 with the quaternary ammonium resin, Dowex 1. The differences in the exchange capacity and cross linking of these resins certainly influence their behavior, as has been amply shown in other anion resin systems (*cf.* ref. 12 and 13), but the similar compression of the selectivity of the two quite different amine resins with respect to the selectivity of the quaternary ammonium resin leads us to believe that it is the amine group itself which is responsible. A conclusion, then, for dilute solution exchange, is that the largest separation factors will be obtained using a quaternary ammonium resin with a not too strongly held macroanion.

As can be seen in Figures 1-4, all of the tracers deviate from the mass-action slope of -1 as the external salt solution concentration is increased. These deviations indicate a breakdown in the dilute solution assumptions made in the derivation of eq. 4. One effect is the entrance of nonexchange electrolyte into the resin phase at high external solution concentration. This resin invasion electrolyte acts, to a first approximation, as additional cationic sites for the anions (increase of $[\bar{B}]$ in eq. 4) and, so, contributes to a gradual increase above the ideal mass-action line of slope -1 for all the tracer anions, but with some leveling of the selectivity. More important, however, are the increasingly stronger interactions of the anions with the aqueous cations and with the resin groups as the amount of water available to hydrate each ion decreases. That is, as the external aqueous phase concentration is increased, ion hydration gradually tends to become replaced by solvation (complexing) by the aqueous phase macrocation and by the resin group. With the halide anions and simple cations such as the alkali metal ions, these interactions are not chemical complex-ion formation, but more transient types of electrostatic association. Two such types, a temporary contact ion pairing of the bare ions and an association through one, or more, polarized water molecules (localized hydrolysis), have been discussed in an earlier paper on cation exchange.³ The strength of such electrostatic associations depends upon the crystallographic size of the ions, decreasing from $\text{Li} > \text{Na} > \text{K} > \text{Rb} > \text{Cs}$ and from $\text{F} > \text{Cl} > \text{Br} > \text{I}$. It should be remembered that the very different type of water-structure-enforced ion pairing has precisely the opposite behavior, becoming more important the larger the ion and occurring noticeably only with ions as large as NMe_4^+ (possibly Cs^+) and I^- (Br^-).

If, as the aqueous phase concentration increases, the interactions of the tracer anion of interest with the

resin group are stronger than those with the aqueous phase macrocation, the anion will increasingly prefer the resin phase, and, conversely, if the aqueous phase cation interactions are the stronger, the anion will go preferentially into that phase. However, in an ion-exchange reaction it must be remembered that both anions are competing for the best solvating medium; the exchange goes in such a direction as to provide the most favorable situation, the lowest free energy, for the system as a whole, and this will usually be determined by the smallest ion, that which needs solvation the most.

With these considerations in mind, we can take up the experimental results in concentrated salt solutions. Figure 1 shows the behavior of tracer F^- , Cl^- , Br^- , and I^- on a quaternary ammonium resin with KOH as the macroelectrolyte. Only the small F^- can compete with the OH^- for solvation by water in the concentrated KOH solutions, and so the larger halide ions are pushed into the resin phase in the exchange, and the more so, the larger the halide ion and the lower the water activity. This leads to an increasingly greater separation of the halides in concentrated solution over that in dilute KOH and, together with the effect of the resin invasion electrolyte, results in an increase in the value of D above the mass-action line for all the tracer ions.

With LiCl as the eluting agent, one has a more strongly complexing cation (Li^+ instead of K^+), as well as the already mentioned effect of a more tightly held macroanion (Cl^- for OH^-). As the external solution concentration increases, the aqueous phase remains the more favorable one for solvating the anions, for with decreasing water activity, anion hydration tends to be replaced by complexing with the lithium ion. Fluoride is complexed more strongly than Cl^- , and enough so that it is held in the aqueous phase more strongly relative to Cl^- in concentrated LiCl than in dilute solution; the curve for F^- tracer shows a slight negative deviation from the mass-action slope of -1 in concentrated solutions (Figure 2). Furthermore, the dilute solution selectivity order $\text{F} < \text{Cl} < \text{Br} < \text{I}$ is greatly enhanced in concentrated LiCl solutions, as the larger halides are pushed out of the aqueous phase into the resin in order to permit the smaller anions to achieve their solvation by complexing with the Li^+ in the concentrated external solution.

(12) S. Lindenbaum, C. F. Jumper, and G. E. Boyd, *J. Phys. Chem.*, **63**, 1924 (1959).

(13) (a) R. H. Herber, K. Tonguc, and J. W. Irvine, *J. Am. Chem. Soc.*, **77**, 5840 (1955); (b) J. Aveston, D. A. Everest, and R. A. Wells, *J. Chem. Soc.*, 231 (1958); (c) B. Chu, Ph.D. Thesis, Cornell University, 1959; (d) Y. Marcus and D. Maydan, *J. Phys. Chem.*, **67**, 983 (1963).

However, it should be possible to greatly change this selectivity order by changing the nature of the resin group and of the macrocation. Obviously, as already mentioned for the dilute solution case, the replacement of the quaternary ammonium cation of the strong-base resin with a group capable of (hydrogen) bonding to the (smaller) anions would more nearly equalize the distribution coefficients of the halide ions. This effect should be even more significant in concentrated solutions, where the anion-cation interactions become more important relative to anion-water solvation, than in dilute solution. A comparison of the results given in Figure 2 for the quaternary ammonium ion resin and in Figure 3 for the tertiary amine resin shows indeed this result; the 250-fold range in distribution coefficients from F^- to I^- for Dowex 1 in dilute solution is increased 80 times in going to 10 M LiCl, while the 10-fold spread of D values with Dowex 4 in dilute solution only increases by a factor of ~ 5 at 10 M LiCl. Furthermore, the ability of the R_3NH^+ resin group to hydrogen bond to the small electronegative anions means that even F^- can obtain solvation in the resin phase comparable to that available in the aqueous phase (from the Li^+) and, so, yields a small positive deviation from the ideal mass-action curve in concentrated LiCl.

By going to a still better complexing resin group or

to a more poorly complexing macrocation, a reversal in the elution order of the halides should be possible in concentrated solution. The latter approach was tried, substituting tetramethylammonium chloride for lithium chloride and using Dowex 4 resin. Now, as the water activity falls, the tertiary amine resin group can provide stronger interactions for the smaller anions than does the macrocation in the aqueous phase although, unfortunately, the water activity does not fall as rapidly with NMe_4Cl concentration as with LiCl. As can be seen in Figure 4, the distribution curves for F^- , Br^- , and I^- tracers, instead of diverging at higher macroelectrolyte concentrations as in the three previous cases, come together at 6 M NMe_4Cl . (It should be noted that the differences in the behavior of all the distribution curves from those with LiCl solutions extend down to concentrations as low as 0.05 M .) Although no region of inverted selectivity order was actually observed, the behavior found certainly supports the ideas presented, and somewhat more forcing conditions would appear capable of yielding such an inverted sequence.

Acknowledgments. The authors would like to thank Mr. J. Bucher and Dr. D. C. Whitney for help with some of the experiments and Dr. R. Wheaton of the Dow Chemical Co., Midland, Mich., for the sample of Dowex 4 resin before it was commercially available.

Properties of Partially Localized Adsorbed Monolayers¹

by William A. Steele

Department of Chemistry, Whitmore Laboratory, Pennsylvania State University, University Park, Pennsylvania
(Received April 19, 1965)

The properties of monolayers adsorbed on uniform surfaces with small but nonzero potential barriers to translation parallel to the surface are calculated. The pair interaction potential between adsorbed molecules is represented by a hard sphere repulsion plus a weak attraction at distances larger than the hard sphere radius. It is shown that the chemical potential of the monolayer is equal to the chemical potential of a hard sphere system plus perturbation terms. The hard sphere chemical potential is calculated from two-dimensional hard sphere equations of state; the perturbation terms are expressed as power series in the density, and the first two terms are computed. The theoretical isotherms obtained in this way are compared with experimental data for argon adsorbed on a P-33 graphitized carbon black, and it is shown that the effect of the potential barriers to translation is very small for this system and that the data are in good agreement with the form of the theory obtained in the limit of vanishingly small potential barriers.

1. Introduction

Recent reports^{2,3} of extensive measurements of physical adsorption on solid adsorbents having quite uniform surfaces has led to renewed interest in the theory of two-dimensional systems of interacting molecules. In particular, data obtained in studies of the properties of rare gases adsorbed on P-33 graphitized carbon black have been subjected to detailed analyses.²⁻⁵ The theories used in these treatments have been based upon the assumption that the monolayer could be treated as a completely mobile two-dimensional phase, and differ from one another only in the approximations used to obtain the two-dimensional equation of state or partition function which serves as the basis for the theoretical isotherm. (In the context of this paper, a completely mobile monolayer is one in which the potential barriers to translation in the plane parallel to the adsorbent surface are negligibly small compared to kT .) Calculations reported include theories based on two-dimensional versions of: the virial equation of state (second virial coefficient only)⁶; the van der Waals equation of state^{2a}; the Lennard-Jones-Devonshire cell theory⁵; and the Eyring significant structures theory.⁴ The present paper has a dual purpose: to consider the problem of a two-dimensional system in which the potential barriers to translation are finite but small (a "partially localized" film); and to derive

yet another approximate partition function for a two-dimensional system and to obtain a theoretical isotherm equation from this partition function. This calculation is based upon the use of an approximate potential energy function for pairwise interaction of adsorbed molecules which consists of a hard sphere repulsion plus a weak attractive interaction. The techniques required for computing the properties of such systems in three dimensions (and in the absence of barriers to translation) are well known⁷⁻⁹ and their adaptation to the adsorption problem is straightforward. The theoretical equations obtained will

(1) This work was supported by a grant from the National Science Foundation.

(2) (a) S. Ross and J. P. Olivier, "On Physical Adsorption," Interscience Publishers, Inc., New York, N. Y., 1964; (b) several reviews of this work are to be found in "The Solid-Gas Interface," E. A. Flood, Ed., Marcel Dekker, Inc., New York, N. Y., 1965.

(3) D. M. Young and A. D. Crowell, "Physical Adsorption of Gases," Butterworth and Co., Ltd., London, 1962.

(4) J. J. McAlpin and R. A. Pierotti, *J. Chem. Phys.*, **41**, 68 (1964).

(5) E. L. Pace, *ibid.*, **27**, 1341 (1957); "Proceedings of the Fourth Conference on Carbon," Pergamon Press, New York, N. Y., 1960, p. 35.

(6) J. R. Sams, G. Constabaris, and G. D. Halsey, Jr., *J. Chem. Phys.*, **36**, 1334 (1962).

(7) E. B. Smith and B. J. Alder, *ibid.*, **30**, 1190 (1959).

(8) R. Zwanzig, *ibid.*, **22**, 1420 (1954).

(9) B. W. Davis, *J. Phys. Chem.*, **68**, 3860 (1964).

be compared with experimental data for argon adsorbed on P-33 graphitized carbon black as well as with other theories.

2. General Theory

At the relatively low temperatures of conventional physical adsorption experiments, the molecules adsorbed in a monolayer are most probably in the neighborhood of the position of the minimum in the gas surface potential energy $u_s(\mathbf{r})$. In the region of the minimum, this function can be represented by

$$u_s(\mathbf{r}) = \epsilon^{(s)} + \epsilon_r(\boldsymbol{\tau}) + \frac{1}{2}k_z(z - z_m)^2 \quad (2.1)$$

where z is the perpendicular distance between the adsorbed atom and the surface; z_m is the position of the minimum energy; k_z is the force constant for vibration perpendicular to the surface; $\boldsymbol{\tau}$ is a two-dimensional vector in a plane parallel to the surface; $\epsilon^{(s)}$ is the minimum potential energy at the point where $\boldsymbol{\tau} = 0$; and $\epsilon_r(\boldsymbol{\tau})$ is the variation in the depth of the minimum as the adsorbed atom is displaced parallel to the surface at fixed $z = z_m$. If it is assumed that the adsorbed molecules obey classical statistical mechanics, the use of eq. 2.1 for $u_s(\mathbf{r})$ leads to a general expression for the monolayer adsorption isotherm which can be written^{10,11}

$$(\mu - \mu_{id})/kT = \Delta\mu/kT = -(\partial \ln Z_N^{(2D)}/\partial N) \quad (2.2)$$

Here, μ is the chemical potential per molecule in the adsorbed phase and μ_{id} is the chemical potential of a molecule in an ideal two-dimensional gas on the same adsorbent. The two-dimensional configurational integral $Z_N^{(2D)}$ for N molecules on a uniform surface is the key quantity in this statistical treatment of monolayer adsorption and is formally defined as

$$Z_N^{(2D)} = \int P_0^{(N)}(\boldsymbol{\tau}_1 \cdots \boldsymbol{\tau}_N) \times \exp\left[-\sum_{1 \leq i < j \leq N} u(\tau_{ij})/kT\right] d\boldsymbol{\tau}_1 \cdots d\boldsymbol{\tau}_N \quad (2.3)$$

where $u(\tau_{ij})$ is the effective interaction energy between adsorbed molecules i and j which are separated by a distance τ_{ij} , and $P_0^{(N)}(\boldsymbol{\tau}_1 \cdots \boldsymbol{\tau}_N)$ is the probability of finding N noninteracting molecules at points $\boldsymbol{\tau}_1 \cdots \boldsymbol{\tau}_N$ on the surface and is thus

$$P_0^{(N)}(\boldsymbol{\tau}_1 \cdots \boldsymbol{\tau}_N) = \frac{\exp\left[-\sum_{i=1}^N \epsilon_r(\boldsymbol{\tau}_i)/kT\right]}{\int \cdots \int \exp\left[-\sum_{i=1}^N \epsilon_r(\boldsymbol{\tau}_i)/kT\right] d\boldsymbol{\tau}_1 \cdots d\boldsymbol{\tau}_N} \quad (2.4)$$

The adsorption isotherm can now be obtained from the chemical potential by writing

$$\Delta\mu/kT = \ln(p/p_{id}) \quad (2.5)$$

where p_{id} is the pressure of a two-dimensional ideal gas on the surface

$$p_{id} = NkT/Z_1^{(s)} \quad (2.6)$$

$Z_1^{(s)}$ is the configurational integral for an isolated adsorbed atom. The computation of this quantity has been discussed elsewhere^{2a,10,11}; for the purposes of the present work, it is necessary only to realize that the constant $kT/Z_1^{(s)}$ can be calculated from the low coverage limiting slopes of the experimental isotherms.

Equations 2.3 and 2.4 can be made to describe a completely mobile monolayer on a uniform surface as defined in section 1 by setting $\epsilon_r(\boldsymbol{\tau}) = 0$. If the two-dimensional configurational integrals for such systems are denoted by $Z_N^{(2D)}$, it is easy to show that

$$Z_N^{(2D)} = A^{-N} \int \cdots \int \exp\left[-\sum_{1 \leq i < j \leq N} u(\tau_{ij})/kT\right] d\boldsymbol{\tau}_1 \cdots d\boldsymbol{\tau}_N \quad (2.7)$$

where A is the area of the adsorbent. However, in spite of the great utility of such expressions, they do describe a highly idealized and, in general, unrealistic situation and we thus wish to estimate the effect of nonzero $\epsilon_r(\boldsymbol{\tau})$ upon $Z_N^{(2D)}$. In the case where these functions are not too large compared to kT , it is convenient to expand the exponentials in eq. 2.4 to obtain

$$P_0^{(N)}(\boldsymbol{\tau}_1 \cdots \boldsymbol{\tau}_N) = A^{-N} \left[1 - (1/kT) \sum_{i=1}^N \int \epsilon_r(\boldsymbol{\tau}_i) d\boldsymbol{\tau}_i + \frac{1}{2}(1/kT)^2 \sum_{i,j} \int \int \epsilon_r(\boldsymbol{\tau}_i) \epsilon_r(\boldsymbol{\tau}_j) d\boldsymbol{\tau}_i d\boldsymbol{\tau}_j + \cdots \right] \quad (2.8)$$

When eq. 2.8 is substituted into 2.3, one can make use of the fact that the integrand in $Z_N^{(2D)}$ depends only upon the relative separations τ_{ij} and not upon the absolute position of any particular molecule, to obtain a result which can be written

$$Z_N^{(2D)} = Z_N^{(2D)} \left\{ 1 + \frac{1}{2}(N/AkT)^2 \int \int \epsilon_r(\boldsymbol{\tau}_1) \epsilon_r(\boldsymbol{\tau}_2) (g_0(\tau) - 1) d\boldsymbol{\tau}_1 d\boldsymbol{\tau}_2 + \cdots \right\} \quad (2.9)$$

where $g_0(\tau)$ is the correlation function for molecules 1 and 2 separated by a distance τ in a completely mobile two-dimensional system. The formal definition of this function is obtained from a straightforward modification of the expression for the three-dimensional pair correlation function¹² and is

(10) W. A. Steele, *Advances in Chemistry Series*, No. 33, American Chemical Society, Washington, D. C., 1961, p. 269.

(11) W. A. Steele and M. Ross, *J. Chem. Phys.*, 33, 464 (1960).

(12) T. L. Hill, "Introduction to Statistical Thermodynamics," Addison-Wesley Publishers, Reading, Mass., 1960, eq. 17.29.

$$g_0(\tau) = (A^2/Z_N^{(2D)}) \times \int \cdots \int \exp\left[-\sum_{1 \leq i < j \leq N} u(\tau_{ij})/kT\right] d\tau_3 \cdots d\tau_N \quad (2.10)$$

If the term in eq. 2.9 due to the presence of the potential barriers to translation parallel to the surface is small, the logarithm of the configurational integral can be written

$$\ln Z_N^{(2D)} = \ln Z_N^{(2D)} + 1/2(N/AkT)^2 \times \iint \epsilon_r(\tau_1)\epsilon_r(\tau_2)(g_0(\tau) - 1)d\tau_1 d\tau_2 + \cdots \quad (2.11)$$

Although eq. 2.11 shows schematically how the presence of finite $\epsilon_r(\tau)$ will affect the properties of an otherwise perfectly mobile monolayer, a detailed evaluation of the importance of the perturbation term necessitates the introduction of approximations to $Z_N^{(2D)}$ and to $g_0(\tau)$. The approximations used in this paper are based on the following pair interaction potential function

$$u(\tau) = u_{hs}(\tau) + u_p(\tau) \quad (2.12)$$

where

$$u_{hs}(\tau) = +\infty, \tau \leq \sigma \\ = 0, \tau > \sigma \quad (2.13)$$

$$u_p(\tau) = 0, \tau \leq \sigma \\ = 4\epsilon((\sigma/\tau)^{12} - (\sigma/\tau)^6), \tau > \sigma \quad (2.14)$$

In this way, $u(\tau)$ is given by the interaction between a pair of hard spheres of diameter σ plus an attractive energy at distances greater than σ . If it is assumed that the attractive part of the potential (which is given by eq. 2.14) is not large compared to kT , it is convenient to write

$$\exp[-u(\tau)/kT] = \exp[-u_{hs}(\tau)/kT] \times \{1 - u_p(\tau)/kT + \cdots\} \quad (2.15)$$

When eq. 2.15 is substituted into 2.7, $Z_N^{(2D)}$ becomes

$$Z_N^{(2D)} = Z_N^{(hs)} [1 - (N^2/2AkT) \int g_{hs}(\tau) u_p(\tau) d\tau + \cdots] \quad (2.16)$$

or approximately

$$\ln Z_N^{(2D)} = \ln Z_N^{(hs)} - (N^2/2AkT) \int g_{hs}(\tau) u_p(\tau) d\tau + \cdots \quad (2.17)$$

where $Z_N^{(hs)}$ is the two-dimensional configurational integral for a completely mobile hard sphere fluid and $g_{hs}(\tau)$ is the pair correlation function for this system. If eq. 2.15 is also substituted into 2.10, one finds that $g_0(\tau)$ is equal to $g_{hs}(\tau)$ plus perturbation terms of order ϵ/kT . In the evaluation of the first perturbation term to $\ln Z_N^{(2D)}$, one can thus set

$$g_0(\tau) = g_{hs}(\tau) \quad (2.18)$$

Unfortunately, even the hard sphere pair correlation function is not accurately known for two-dimensional systems at high density and it will be necessary to introduce approximations for this function and for its derivatives with respect to N which are needed to compute the partial molal thermodynamic properties of the system.

The final equation for the chemical potential of the adsorbed film can now be written as

$$\Delta\mu = \Delta\mu_{hs} + I_s + I_1 \quad (2.19)$$

where

$$I_s = 1/2(1/A^2kT) \iint \{\partial/\partial N [N^2(g_{hs}(\tau) - 1)]\} \times \epsilon_r(\tau_1)\epsilon_r(\tau_2) d\tau_1 d\tau_2 \quad (2.20)$$

$$I_1 = -1/2(1/A) \int \{\partial/\partial N [N^2 g_{hs}(\tau)]\} u_p(\tau) d\tau \quad (2.21)$$

and $\Delta\mu_{hs}$ is the difference in chemical potential between the two-dimensional hard sphere fluid and an ideal two-dimensional gas, and I_s and I_1 are the leading terms in the perturbation expansions for the effects of potential barriers to translation and attractive lateral interactions, respectively.

3. Chemical Potential of Hard Spheres in Two Dimensions

The equation of state of hard spheres, in two dimensions as well as three, has been the subject of extensive investigation.¹³⁻¹⁷ The chemical potential of a two dimensional system with spreading pressure Φ can readily be calculated from

$$\Delta\mu_{hs}/kT = \int_0^x \frac{d}{dx} (\Phi^* - x) \frac{dx}{x} \quad (3.1)$$

where

$$\Phi^* = \pi\sigma^2\Phi/4kT \quad (3.2)$$

and x is a reduced surface density $N\pi\sigma^2/4A$. Several curves of $\Delta\mu_{hs}/kT$ vs. x are shown in Figure 1. These were obtained from the following expressions.

Virial Expansion

$$\Phi^* - x = \sum_{n \geq 2} B_n x^n \quad (3.3)$$

(13) B. W. Davis, Ph.D. Thesis, University of California, Riverside, Calif., 1964.

(14) J. P. Stebbins and G. D. Halsey, Jr., *J. Phys. Chem.*, **68**, 3863 (1960).

(15) (a) H. L. Frisch, *Advan. Chem. Phys.*, **6**, 229 (1964); (b) H. L. Frisch and J. L. Lebowitz, "The Equilibrium Theory of Classical Fluids," W. A. Benjamin, Inc., New York, N. Y., 1964.

(16) F. H. Ree and W. G. Hoover, *J. Chem. Phys.*, **40**, 939 (1964).

(17) B. J. Alder and T. E. Wainwright, *Phys. Rev.*, **127**, 359 (1962)

$$\Delta\mu_{hs}/kT = \sum_{n \geq 2} (n/(n-1))B_n x^{n-1} \quad (3.4)$$

with¹⁶ $B_2 = 2$, $B_3 = 3.128$, $B_4 = 4.262$, $B_5 = 5.340$, $B_6 = 6.374$.

Analytic Approximation to Monte Carlo Results^{16,17}

$$\Phi^* - x = -[x/(1-hx)]^2 [2-ax+bx^2] \quad (3.5)$$

$$\Delta\mu_{hs}/kT = (2h^{-1} - ah^{-2} + bh^{-3})(1-hx)^{-2} + (ah^{-2} - 2bh^{-3})[(1-hx)^{-1} - \ln(1-h)] - 2bh^{-3}(1-hx) - 2h^{-1} + 3bh^{-2} \quad (3.6)$$

with $a = 0.786812$, $b = 0.056304$, $h = 0.978702$.

Volmer Equation^{14,15}

$$\Phi^* - x = 2x^2/(1-2x) \quad (3.7)$$

$$\Delta\mu_{hs}/kT = 2x/(1-2x) - \ln(1-2x) \quad (3.8)$$

*Scaled Particle Theory*¹⁵

$$\Phi^* - x = (2x^2 - x^3)/(1-x)^2 \quad (3.9)$$

$$\Delta\mu_{hs}/kT = x(3-2x)/(1-x)^2 - \ln(1-x) \quad (3.10)$$

The value of x for a triangular close-packed array of spheres is 0.9069; however, it will be shown that multilayer formation begins in real systems at monolayer densities which are considerably smaller than the close-packed value of x ; *i.e.*, the effective monolayer density is smaller than the close-packed density.

The scaled-particle theory is based upon a calcula-

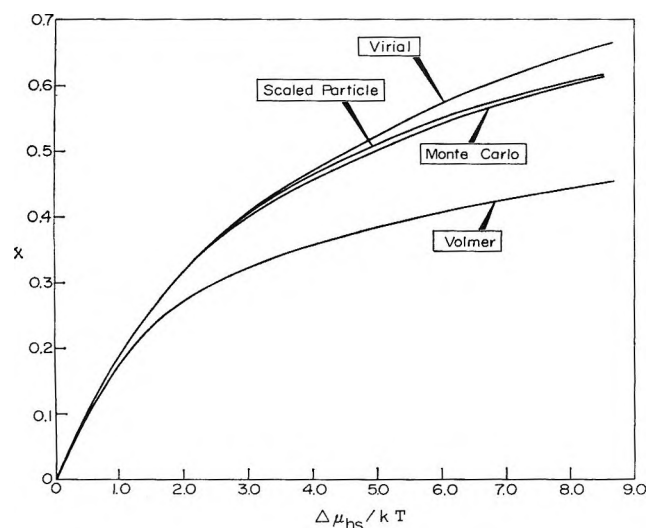


Figure 1. The difference between the chemical potential of a two-dimensional system of hard spheres and an ideal two-dimensional gas divided by kT is plotted as a function of the reduced density x . The curve denoted "Monte Carlo" was obtained from machine computations^{16,17} and is presumably very near to the exact result. The other curves were calculated from several approximate equations of state which are explicitly given in section 3.

tion of the density of hard spheres on the surface of a cavity of arbitrary size in the fluid. Since the virial equation gives the pressure of such a system in terms of this density in the limit of infinite radius (fluid in contact with a planar interface), an equation of state is obtained by calculating this density for finite values of the radius and extrapolating the equations found in this way. Although this computation involves considerable intuitive reasoning, it has been found that the expressions obtained are exact for the one-dimensional case; that they are in excellent agreement with the three-dimensional equation of state which results from machine calculations; and that they are identical with the three-dimensional equation of state obtained from the analytic solution of the Percus-Yevick equation for the pair correlation function.^{15b} (This agreement is particularly striking in view of the fact that the derivations of the two theories apparently have no points in common.) The curves shown in Figure 1 indicate that the scaled particle results are also in good agreement with the machine computations for the chemical potential of the two-dimensional hard sphere system. We will thus utilize eq. 3.9 and 3.10 in the calculation of the adsorption isotherm.

4. Pair Correlation Function for Hard Spheres in Two Dimensions

It is well known that values of the pair correlation function of hard sphere molecules in contact can be calculated directly from the equation of state for the system.¹⁸ In two dimensions, one has

$$g_{hs}(\sigma) = (\Phi^* - x)/2x^2 \quad (4.1)$$

Thus, one can use the equations of state of section 3 to obtain $g_{hs}(\tau)$ at arbitrary density, but only for a single separation distance. In order to calculate $g_{hs}(\tau)$ at other distances, we expand it in powers of the reduced density x . When the general equation for $g(r)$ as a power series in the density¹⁸ is adapted to the two-dimensional case, one finds that

$$g_0(\tau_{12}) = \exp[-u(\tau_{12})/kT] \{ 1 + (N/A) \times \int f_{13} f_{23} d\tau_3 + \dots \} \quad (4.2)$$

with

$$f_{ij} = \exp[-u(\tau_{ij})/kT] - 1 \quad (4.3)$$

In the case of hard sphere molecules, eq. 4.2 gives rise to a $g_{hs}(\tau)$ which has the following properties

$$g_{hs}(\tau^*) = 0 \quad \tau^* < 1 \quad (4.4)$$

$$= 1 + (2N\sigma^2/A)f(\tau^*) \quad 1 < \tau^* < 2 \quad (4.5)$$

$$= 1 \quad \tau^* > 2 \quad (4.6)$$

where only the terms linear in the density have been retained, and $\tau^* = \tau/\sigma$. $f(\tau^*)$ can be computed from eq. 4.2 by shifting to bipolar coordinates¹⁹ and remembering that

$$\begin{aligned} f_{13}f_{23} &= 1 & \tau_{13}^* \text{ and } \tau_{23}^* \leq 1 \\ &= 0 & \tau_{13}^* \text{ or } \tau_{23}^* > 1 \end{aligned} \quad (4.7)$$

for hard spheres. $f(\tau^*)$ can thus be written

$$f(\tau^*) = 4 \int_{\tau^*}^1 d\tau_{23}^* \int_{\tau - \tau_{23}^*}^{\tau_{23}^*} d\tau_{13}^* (\tau_{13}^* \tau_{23}^* / y^* \tau^*) \quad (4.8)$$

where $\tau_{23}^* = \tau_{23}/\sigma$, $\tau_{13}^* = \tau_{13}/\sigma$, and y^* is the altitude of a triangle having τ^* as a base and τ_{23}^* , τ_{13}^* as sides

$$(2y^* \tau^*)^2 = 4(\tau_{13}^* \tau^*)^2 - (\tau_{13}^{*2} + \tau_{23}^{*2} - \tau^{*2})^2 \quad (4.9)$$

When new variables $u = \tau_{13}^{*2}$, $v = \tau_{23}^{*2}$, and $w = \tau^{*2}$ are introduced, eq. 4.8 becomes

$$f(\tau^*) = 2 \int_{w/4}^1 dv \int_{(\sqrt{w} - \sqrt{v})^2}^v du (4wu - (u - v + w)^2)^{-1/2} \quad (4.10)$$

Equation 4.10 can be integrated to give an equation for $g_{hs}(\tau^*)$ correct to terms linear in the density which can be written

$$g_{hs}(\tau^*) = d(\tau^*) + (N\sigma^2/A)f(\tau^*) \quad (4.11)$$

where

$$\begin{aligned} d(\tau^*) &= 0 & \tau^* \leq 1 \\ &= 1 & \tau^* > 1 \end{aligned} \quad (4.12)$$

$$\begin{aligned} f(\tau^*) &= 0 & 2 < \tau^* < 1 \\ &= \pi - 2 \sin^{-1}(\tau^*/2) - \\ & & \tau^*(4 - \tau^{*2})^{1/2}/2, & 2 > \tau^* > 1 \end{aligned} \quad (4.13)$$

Equation 4.11 turns out to give surprisingly accurate results when used in eq. 2.21 to evaluate the mean lateral interaction energy, at least at the densities of interest in real monolayer adsorption systems. When eq. 4.11 is substituted into eq. 2.20 and 2.21, one obtains

$$\begin{aligned} I_s &= (1/A^2kT) \times \\ & \left\{ -N\sigma^4 \int_0^1 \int_{A/\sigma^2} \epsilon_r(\tau_1^*) \epsilon_r(\tau_1^* - \tau^*) d\tau_1^* d\tau^* + \right. \\ & \left. (3N^2\sigma^4/2A) \int_1^2 \int_{A/\sigma^2} f(\tau^*) \epsilon_r(\tau_1^*) \epsilon_r(\tau_1^* - \tau^*) d\tau_1^* d\tau^* \right\} \end{aligned} \quad (4.14)$$

$$\begin{aligned} I_1 &= (1/A) \left\{ N\sigma^2 \int_1^\infty u_p(\tau^*) d\tau^* + \right. \\ & \left. (3N^2\sigma^4/2A) \int_1^2 f(\tau^*) u_p(\tau^*) d\tau^* \right\} \end{aligned} \quad (4.15)$$

5. Evaluation of Perturbation Terms

Equation 4.15 for I_1 is readily evaluated if it is assumed that $u_p(\tau^*)$ is given by eq. 2.14. After performing a numerical integration for the term involving $f(\tau^*)$, one finds that

$$I_1 = -\epsilon(4.80x + 5.76x^2) \quad (5.1)$$

Since this computation is based on the first two terms in the series expansion of $g_{hs}(\tau^*)$ in powers of the density, it might be thought to become quite inaccurate at densities corresponding to the completion of the monolayer. An estimate of the probable error involved can be made by using the known characteristics of $g_{hs}(\tau^*)$ at high densities. Since $u_p(\tau^*)$ is large only in the region near $\tau^* = 1.12$, it is evident that knowledge of the behavior of $g(\tau^*)$ at τ^* between 1.0 and ~ 1.4 is adequate to obtain a rough value of I_1 . If one compares the true value of $g_{hs}(\tau^* = 1)$ which can be obtained from the equation of state with the predictions of eq. 4.11, it is found that the true $g_{hs}(1)$ increases more rapidly with density than the approximate function. One can write

$$(g_{hs}(1) - 1)_{\text{true}} = (\Phi^* - x - 2x^2)/2x^2 \quad (5.2)$$

$$= 1/2(B_3x + B_4x^2 + B_5x^3 + \dots) \quad (5.3)$$

if the virial expansion is inserted for Φ^* , whereas the approximation of eq. 4.11 gives

$$(g_{hs}(1) - 1)_{\text{approx}} = 1/2B_3x \quad (5.4)$$

Suppose we now introduce a scaled $g_{hs}(\tau^*) - 1$ which has the same functional dependence on τ^* at all densities, but a density-dependent scale factor which ensures that $g_{hs}(\tau^*)$ has the correct value at $\tau^* = 1$

$$\begin{aligned} (g_{hs}(\tau^*) - 1)_{\text{scaled}} &= (g_{hs}(\tau^*) - 1)_{\text{approx}} \times \\ & (1 + (B_4/B_3)x + B_5/B_3x^2 + \dots), \quad 1.5 > \tau^* > 1 \end{aligned} \quad (5.5)$$

where

$$(g_{hs}(\tau^*) - 1)_{\text{approx}} = (4x/\pi)f(\tau^*) \quad (5.6)$$

In terms of this scaled correlation function, I_1 becomes

(18) T. L. Hill, "Statistical Mechanics," McGraw-Hill Book Co., Inc., New York, N. Y., 1956, Chapter 6.

(19) See ref. 12, p. 336.

$$(I_1)_{\text{scaled}} = -\epsilon[4.80x + 5.76x^2(1 + 4B_4x/3 + 5B_5x^2/4 + \dots)] \quad (5.7)$$

A Monte Carlo calculation²⁰ of the true $g_{\text{hs}}(\tau^*)$ for a relatively dense system is plotted in Figure 2, together with the scaled $g_{\text{hs}}(\tau^*)$ and that obtained from eq. 4.11. Although the true and the scaled pair correlation functions agree at $\tau^* = 1$, it is evident that the true correlation function decreases more rapidly with τ^* than does the scaled. Thus, it seems probable that the I_1 calculated from eq. 5.7 will generally be larger than the true values, whereas those calculated from eq. 5.1 using the approximate $g_{\text{hs}}(\tau^*)$ will ordinarily be smaller than the true values. Curves of I_1/ϵ vs. x are shown in Figure 3 for the approximate and the

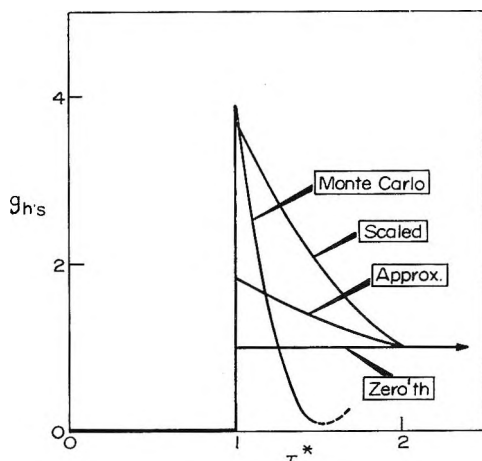


Figure 2. The pair correlation function for a two-dimensional system of hard spheres at a reduced density of 0.545 is plotted as a function of the reduced distance $\tau^* = \tau/\sigma$. The curve denoted "Monte Carlo" was obtained from machine computations,²⁰ and the other curves show the various approximations to g_{hs} which are discussed in section 5.

scaled pair correlation function, together with the linear plot obtained from the zeroth approximation to $g_{\text{hs}}(\tau^*)$ which is

$$g_{\text{hs}}(\tau^*) = 1 \quad \tau^* > 1 \quad (5.8)$$

The curves in Figure 3 indicate that the values of I calculated from the approximate pair correlation function are probably reasonably accurate at least for $x < 0.5$.

In order to compute I_s , it is of course necessary to introduce a specific expression for $\epsilon_r(\tau_i)$. If the variations in $\epsilon_r(\tau_i)/kT$ are not too large, the detailed form of this function is not too important. It is convenient to represent it by a sinusoidal function of x_i and y_i , the coordinates in the plane of τ_i . We thus write

$$\epsilon_r(\tau_i) = (E/2) \{ \cos(2\pi x_i/a) + \cos(2\pi y_i/a) \} \quad (5.9)$$

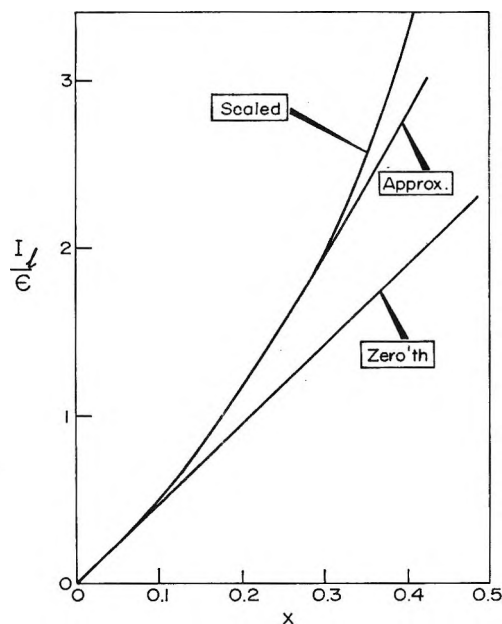


Figure 3. The integral I_1/ϵ is shown as a function of density. I_1 is defined in eq. 2.21, and the curves shown were calculated using the different assumptions concerning the density dependence of $g_{\text{hs}}(\tau^*)$, which are discussed in section 5.

In this way, the height of the potential barrier to motion in the x or y direction is E and the distance between successive maxima in the energy is a . (Note that only the τ dependent part of $\epsilon_r(\tau)$ need be considered in this computation, since any constant contributions can be canceled in the original eq. 2.4 for $P_0^{(N)}(\tau_1 \dots \tau_N)$.) If eq. 5.9 is substituted into eq. 4.14, it can be shown that

$$I_s = (E^2/8kT) \left\{ - (N/A) \int_0^{2\pi} \int_0^1 [\cos(2\pi x_{12}/a) + \cos(2\pi y_{12}/a)] \tau^* d\tau^* d\alpha + \right. \\ \left. (3/2) [N\sigma/A]^2 \int_0^{2\pi} \int_1^2 f(\tau^*) [\cos(2\pi x_{12}/a) + \cos(2\pi y_{12}/a)] \tau^* d\tau^* d\alpha \right\} \quad (5.10)$$

where $x_{12} = \tau \cos \alpha$, $y_{12} = \tau \sin \alpha$. After integrating over α , one has

$$I_s = (\pi E^2/2kT) \left\{ - (N/A) \int_0^1 J_0(2\pi\tau/a) \tau^* d\tau^* + \right. \\ \left. (3/2) (N\sigma/A)^2 \int_1^2 f(\tau^*) J_0(2\pi\tau/a) \tau^* d\tau^* \right\} \quad (5.11)$$

where J_0 is the Bessel function of order zero. Equation 5.11 can be further reduced to

(20) M. Metropolis, A. W. Rosenbluth, M. N. Rosenbluth, A. H. Teller, and E. Teller, *J. Chem. Phys.*, **21**, 1087 (1953).

$$I_s = (2E^2/kT)(xW(\zeta) + 3x^2V(\zeta)) \quad (5.12)$$

where $\zeta = 2\pi\sigma/a$ and

$$W(\zeta) = -\zeta^{-1}J_1(\zeta) \quad (5.13)$$

$$V(\zeta) = (2/\pi) \int_1^2 J_0(\zeta\tau^*)f(\tau^*)\tau^*d\tau^* \quad (5.14)$$

The quadrature in eq. 5.14 was performed numerically, and the resulting values of $V(\zeta)$ are plotted in Figure 4, together with $W(\zeta)$.

6. Theoretical Isotherm

The results obtained in sections 4 and 5 can now be collected to give an isotherm equation. It is assumed that an adequate representation of $\Delta\mu_{hs}/kT$ can be obtained from the scaled particle theory, and that I_1 and I_s are given by eq. 5.1 and 5.12, respectively. One thus has

$$\ln(p/p_{id}) = x(3 - 2x)/(1 - x)^2 - \ln(1 - x) - (\epsilon/kT)(4.80x + 5.76x^2) + 2(E/kT)^2(xW(\zeta) + 3x^2V(\zeta)) \quad (6.1)$$

Of course, this expression includes only the leading terms in the expansion of $\ln Z_N^{(2D)}$ in powers of $1/kT$ and might be expected to be limited to situations with relatively small values of ϵ/kT , E/kT . However, an inspection of the first few coefficients of the higher powers of $1/kT$ shows that they involve differences; although the individual terms in the coefficients may be large, the differences can be quite small. Furthermore, the analogous treatment of the three-dimensional

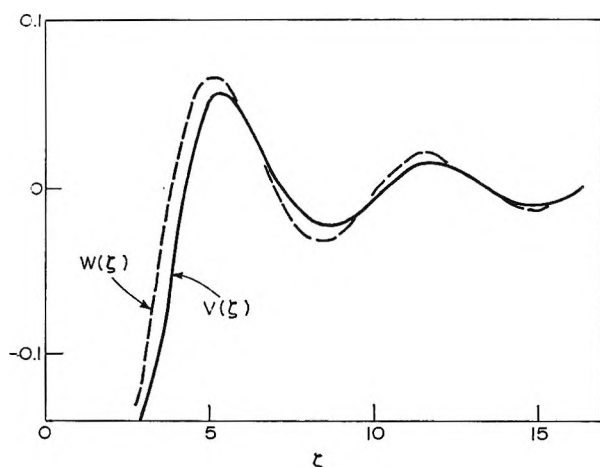


Figure 4. The component functions of the integral I_s (defined in eq. 2.20) are shown here as a function of $\zeta = 2\pi\sigma/a$, where a is the site dimension and σ the size of the adsorbed atoms. The relation between the functions plotted and I_s is given in eq. 5.12. At larger values of ζ , these curves continue as decaying sine-like functions.

problem was found to be in good agreement with experiment even at relatively low temperatures.⁷ We will therefore assume that eq. 6.1 is a useful isotherm even when ϵ/kT , E/kT are not small. The isotherm equation can be split into energy and entropy terms. $\bar{E}_1(x)$ is defined to be the partial molal lateral interaction energy at reduced density x

$$-\bar{E}_1(x) = q_{st}(x) - q_{st}(0) \quad (6.2)$$

Equation 6.1 leads to an explicit expression for $\bar{E}_1(x)$

$$-\bar{E}_1 = L[\epsilon(4.80x - 5.76x^2) - 4E(E/kT)(xW(\zeta) + 3x^2V(\zeta))] \quad (6.3)$$

where L is Avagadro's number.

The partial molal entropy due to lateral interactions is $S - \bar{S}_{id}$, where S , \bar{S}_{id} are the partial molal entropies of the real adsorbed film and of the adsorbed ideal two-dimensional gas, respectively. If this quantity is denoted by $\Delta\bar{S}(x)$, one has

$$\Delta\bar{S}(x)/R = -x(3 - 2x)/(1 - x)^2 + \ln(1 - x) + 2(E/kT)(xW(\zeta) + 3x^2V(\zeta)) \quad (6.4)$$

In the case of the completely mobile monolayer where E is zero, eq. 6.1 reduces to a particularly simple form. $\Delta\bar{S}(x)/R$ is equal to $\Delta\mu_{hs}/kT$ and is independent of temperature; \bar{E}_1 is also independent of temperature; and the isotherm equation can be written

$$\ln p_{red} = x(3 - 2x)/(1 - x)^2 + \ln(x/(1 - x)) - (\epsilon/kT)(4.80x + 5.76x^2) \quad (6.5)$$

where the reduced pressure is

$$p_{red} = p(4AkT/\pi\sigma^2Z_1^{(s)}) \quad (6.6)$$

Several isotherms calculated from eq. 6.5 are shown in Figure 5. It is evident that this equation gives condensation in two dimensions with critical parameters which are listed in Table I, together with the predic-

Table I: Two-Dimensional Critical Parameters

	kT_{cr}/ϵ	x_{cr}
Statistical van der Waals ²¹	0.15	0.17
Significant structures ⁴	0.65	0.23
Devonshire cell theory ²²	0.69	0.51
This work ($E/kT = 0$)	0.65	0.28

tions of other isotherms which have been derived for completely mobile monolayers. Since Smith and Alder obtained $T_{cr}/k\epsilon = 1.40$ for the analogous three-dimensional theory,⁷ one finds that $T_{cr}^{(2D)}/T_{cr}^{(3D)} = 0.53$ for this approach, in reasonable agreement with

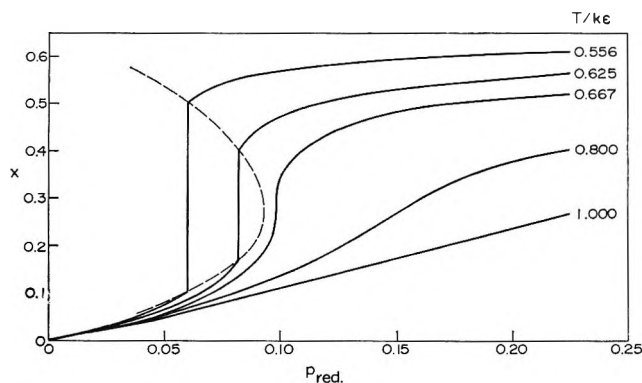


Figure 5. Theoretical isotherms for the reduced density of the adsorbed layer as a function of the reduced pressure were calculated from eq. 6.5 and 6.6 for a number of reduced temperatures. The values of kT/ϵ used are shown at the right of the curves. The vertical risers across the condensation region were obtained by applying the method of equal areas to the actual isotherms, and the dotted curve shows the coexistence line along the boundary of the two-phase region.

other estimates of this ratio.^{4,21,22} At first glance, the value of x_{cr} obtained in this work seems to be rather small, since it is less than one-third of the close packed monolayer density. However, from Figure 5 it is apparent that the pressure required to obtain reduced densities in excess of 0.5 is quite large at $T_{cr}^{(2D)}$; it is reasonable to suppose that multilayer formation will occur at these pressures, thus giving rise to a practical limit of the reduced monolayer density which is ~ 0.5 (at $T_{cr}^{(2D)}$). In this way, the critical density would turn out to have the more reasonable value of roughly one-half the monolayer density.

Even though the reduced critical temperatures and densities shown in Table I vary considerably from one model to another, it can be demonstrated that the various isotherm equations are quite similar in form if they are plotted in a corresponding states form which utilizes the critical data as reducing parameters; *i.e.*, if one plots

$$p_{red} = f(x/x_{cr}, T/T_{cr}) \quad (6.7)$$

Furthermore, if the constants in the two-dimensional van der Waals equation are calculated from the empirical constants in the three-dimensional van der Waals equation rather than from the statistical model, the critical constants are in reasonable agreement with experiment, with the significant structures theory, and with the present work. However, it must be emphasized that all of these theories, together with corresponding states theorems of the form of eq. 6.7, are valid only when the effects of the potential barriers to translation parallel to the surface are negligibly

small. Because these barriers give rise to terms in the isotherm which are dependent upon two parameters (ζ and E), it is difficult to make generalizations about their effects on the properties of the system. If the adsorbed atoms are the same size as the atoms of the solid, one expects ζ to be ~ 6 ; in this case, the coefficient of $(E/kT)^2$ in eq. 6.1 is small and positive. Consequently, both the lateral interaction energy and the entropy will be reduced in magnitude and the adsorbed phase will appear to be more nearly ideal when the effects of the barriers are included. Note, however, that the signs of $W(\zeta)$ and $V(\zeta)$ change with changing ζ and that one can obtain effects which make the system appear less ideal for other values of the relative sizes of the adsorbed and solid molecules.

7. Comparison with Experiment

Computations of the potential energy of interaction of an argon atom and a graphite surface indicate that the barrier to surface translation is probably quite small in this system.³ Therefore, some of the data for the adsorption of argon on a graphitized P-33 carbon black^{6,23,24} were analyzed in terms of the theory presented here. It was found most convenient to use the tabulated isotherms of Constabaris, Sams, and Halsey²³ at $T = 110.0, 120.2, 130.1,$ and 140.6°K. , together with the heats of adsorption²⁴ at $\sim 125^\circ\text{K.}$ Henry's law constants were obtained from the published result for 140.6°K. ,⁶ and were calculated at other temperatures using the point at 140.6° and the experimental $q_{st}(0)$. The constants obtained in this way are tabulated in Table II. Partial molal interaction energies

Table II: Henry's Law Constants for Argon on P-33

$T, ^\circ\text{K.}$	$kT/Z_1^{(s)}, \text{ atm./cc. (STP)}$
140.607	287.6
130.138	566.6
120.257	1197
109.956	3014

for this system are plotted in Figure 6 as a function of the coverage; from these results and the Henry's law constants, the partial molal entropy difference can readily be calculated

$$\Delta\bar{S}/R = -\ln(p/p_{id}) + \bar{E}_1/RT \quad (7.1)$$

(21) See ref. 12, p. 289.

(22) A. F. Devonshire, *Proc. Roy. Soc. (London)*, **A163**, 132 (1937).

(23) G. Constabaris, J. R. Sams, Jr., and G. D. Halsey, Jr., *J. Chem. Phys.*, **37**, 915 (1962).

(24) J. R. Sams, Jr., G. Constabaris, and G. D. Halsey, Jr., *J. Phys. Chem.*, **66**, 2154 (1962).

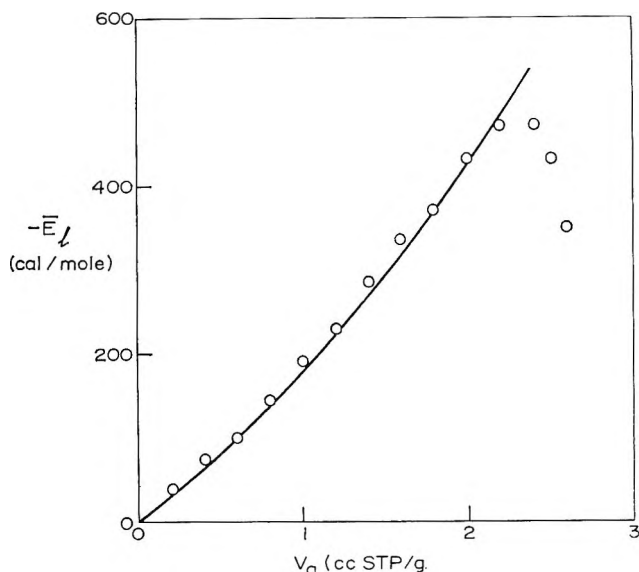


Figure 6. The partial molal lateral interaction energies E_1 calculated from the data for argon adsorbed on P-33 at coverage intervals of 0.2 are shown as open circles. The curve is calculated from the theoretical expression (eq. 6.3) with $E/kT = 0$, $\epsilon/k = 108^\circ$, and $x = 0.149V_a$.

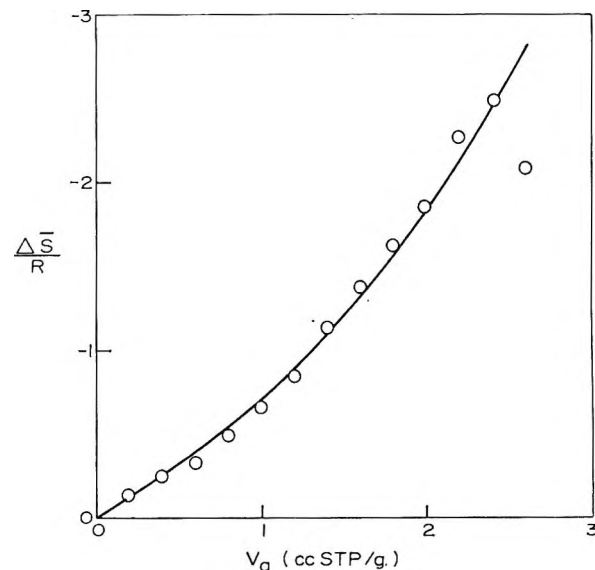


Figure 7. The open circles show the differences between the experimental partial molal entropies for argon on P-33 and those of the ideal two-dimensional gas. These points were calculated from eq. 7.1 at coverage intervals of 0.2, and include data for temperatures from 110 to 140°K. The curve is calculated from the theoretical expression eq. 6.4 with $E/kT = 0$ and $x = 0.149V_a$.

Values of $\Delta S/R$ are plotted against coverage in Figure 7. The results shown were calculated from isotherms covering a 30° range of temperature, and it was found that $\Delta S/R$ was independent of temperature to within ± 0.01 at all coverages considered. This indicates that the effects of potential barriers to translation are negligible in this system, since the theoretical $\Delta S/R$ is temperature independent in eq. 6.4 only if the term in E/kT vanishes. (The \bar{E}_1 must also be temperature independent in this case; however, it is more difficult to determine a temperature dependence in the energies than in the entropies.) In fact, the effects of the potential barriers upon the isotherm can be estimated from the computed interaction energies of an argon atom with a graphite surface.³ The calculated barrier heights are roughly 50 cal./mole, and the distance between minima is 2.4 Å. If one approximates the hexagonal sites on the graphite surface by the square array used in section 5, one obtains $E/kT \simeq 0.2$, $\zeta \simeq 9$ for the system under consideration. When these values are substituted into eq. 6.1, the anticipated result is confirmed: the presence of these barriers does not appreciably affect the isotherm.

The curve in Figure 7 shows the theoretical entropy obtained by neglecting the term in E/kT in eq. 6.4. The coverage scale was adjusted to give the best fit between theory and experiment and corresponds to setting $x = 0.149 V_a$. The curve in Figure 6 shows the

energy obtained from eq. 6.3 with negligible E/kT and was fitted to the data using the coverage scale of Figure 7 and $\epsilon/k = 108^\circ\text{K}$. Although the free space ϵ/k is 124° for argon, it has been pointed out^{4,6} that this value should be reduced by $\sim 18\%$ for the adsorbed atoms. Thus, the assumed value of ϵ/k is in reasonable agreement with expectations. If one takes $\sigma = 3.40$ Å. for argon, the coverage scale factor corresponds to a specific area of 16.2 m.²/g. for this adsorbent. Other estimates of the area of this material are in general somewhat smaller than this value. For instance, the measured step heights of a number of low temperature isotherms give 14 m.²/g.,²⁵ and the high temperature virial coefficient data give rise to areas ranging from 8 to 17 m.²/g., depending upon the assumptions made in the analysis.^{6,26} It should be noted that Alder and Smith⁷ found it necessary to use a σ for argon which became smaller than 3.40 Å. at high temperatures if they wished to maintain agreement between theory and experiment. The introduction of such a smaller value for σ would of course give rise to a smaller value for the area.

(25) C. F. Prenzlow and G. D. Halsey, Jr., *J. Phys. Chem.*, **61**, 1158 (1957).

(26) J. R. Sams, Jr., G. Constabaris, and G. D. Halsey, Jr., *ibid.*, **64**, 1689 (1960).

Vaporization Catalysis. The Decomposition of Gallium Nitride¹

by Richard C. Schoonmaker, Albert Buhl, and James Lemley

Department of Chemistry, Oberlin College, Oberlin, Ohio (Received April 19, 1965)

The vaporization of gallium nitride has been studied by weight loss and torsion effusion techniques. In the temperature range around 900° the nitride vaporizes by decomposition to gallium and nitrogen. The results suggest that the vaporization coefficient for the decomposition is much less than unity. The rate of vaporization of gallium nitride is shown to be markedly enhanced in the presence of metallic gallium or indium, and it is concluded that these metals serve as catalysts for the vaporization of gallium nitride.

Introduction

It has been suggested² that crystalline gallium nitride, GaN, vaporizes to form gaseous, heteronuclear species, (GaN)_n(g), in a temperature range around 1000°. In general, nitrides vaporize by decomposition; and, in particular, the nitrides of the first two elements of group III in the periodic table have been shown to undergo decomposition during vaporization.^{3,4} The present work was initiated to investigate both thermodynamic and kinetic aspects of the vaporization of gallium nitride.

Experimental Section

Conventional weight loss effusion and torsion effusion measurements were made with samples of pure gallium nitride and mixtures of gallium nitride with either gallium or indium. A mass spectrometer was utilized to confirm assumptions concerning the identity of the vaporizing species. The apparatus^{5,6} and a general discussion of the torsion effusion technique^{5,7} have been previously described. High density graphite effusion cells were employed in all runs. During several weight loss measurements, a temperature gradient was established so that the lid was 25–50° cooler than the body of the effusion cell. In the torsion effusion measurements the cell was suspended from a fine tungsten wire of 0.0051 cm. diameter. Four torsion effusion cells were used. Three of them were of a conventional, double-orifice type,^{5,7} with significant differences only in the effective orifice area. Geometrical factors for these cells are listed in Table I. The fourth cell will be designated as a differential torque cell. It contains four sample chambers (A₁, A₂, B₁, B₂) and four orifices (A₁', A₂', B₁', B₂') which are arranged so that effusion

from the A set of orifices produces a torque couple which acts in opposition to a torque couple produced by effusion from the B set. Geometrical factors for the differential torque cell are listed in Table II.

Table I: Geometrical Factors for Conventional Torsion Effusion Cells^a

	Cell					
	1		2		3	
	Left	Right	Left	Right	Left	Right
<i>d</i> , cm.	0.230	0.230	0.121	0.121	0.080	0.082
<i>g</i> , cm.	0.940	0.920	0.900	0.870	0.895	0.900
<i>L</i> , cm.	0.155	0.125	0.065	0.070	0.050	0.053
<i>f</i>	0.669	0.717	0.720	0.704	0.686	0.679
($\bar{W}a/A$) _{av}	0.036		0.010		0.0045	

^a \bar{d} , average orifice diameter; *g*, torque arm; *L*, minimum thickness of orifice; *f*, Searcy-Freeman factor [R. Freeman and A. W. Searcy, *J. Chem. Phys.*, **22**, 762 (1954)]; *W*, Clausing factor [S. Dushman, "Scientific Foundation of Vacuum Technique," John Wiley and Sons, Inc., New York, N. Y., 1948]; \bar{a} , average orifice area; *A*, cross-sectional area of sample chamber.

(1) Work supported by a grant from the U. S. Army Research Office (Durham).

(2) (a) W. Johnson, J. Parsons, and M. Crew, *J. Phys. Chem.*, **36**, 2651 (1932); (b) R. Sime and J. Margrave, *ibid.*, **60**, 810 (1956).

(3) P. Schissel and W. Williams, *Bull. Am. Phys. Soc.*, **4**, 139 (1959).

(4) D. L. Hildenbrand and W. F. Hall, "Condensation and Evaporation of Solids," Gordon and Breach Publishing Co., New York, N. Y., 1965.

(5) P. K. Lee and R. C. Schoonmaker, "Condensation and Evaporation of Solids," Gordon and Breach Publishing Co., New York, N. Y., 1965, p. 379.

(6) R. C. Schoonmaker and R. F. Porter, *J. Chem. Phys.*, **28**, 454 (1958).

Table II: Differential Torque Cell Geometrical Factors

	\bar{a} , cm.	q , cm.	L , cm.	f
A ₁ '	0.134	0.870	0.069	0.726
A ₂ '	0.132	0.872	0.073	0.711
B ₁ '	0.134	0.901	0.068	0.733
B ₂ '	0.136	0.900	0.073	0.711

Pure, finely powdered gallium nitride was synthesized by a previously described technique.⁸ Approximately 75 runs were made in weight loss and torsion effusion studies with samples of pure GaN and mixtures of GaN with either liquid gallium or indium.

Theoretical Section

The pressure, P_K , in a conventional torsion effusion cell may be calculated from^{6,7}

$$P_K = 2\tau\theta / \sum_{i=1}^2 a_i q_i f_i = k\theta \quad (1)$$

where τ is the torsion constant of the fine wire from which the cell is suspended, θ is the angular deflection through which the cell twists, and a_i , q_i , and f_i are, respectively, cross-sectional area, moment arm, and Searcy-Freeman factors⁹ for the orifices. It should be noted that it is unnecessary to make any assumptions concerning the nature of the effusing species in order to calculate the pressure in the cell. For purposes of analysis the differential torsion effusion cell may be considered to be equivalent to two conventional cells which are suspended from the same torsion wire and which generate opposed torques. Samples in wells A₁ and A₂ provide an A torque couple which acts in opposition to a B couple which results from samples in the B set of wells. Equations 2 and 3, which are analogous to (1), are applicable to the A and B torque couples, respectively, where θ_+ is the angular deflection of the torque

$$P_{K(A)} = 2\tau\theta_+ / \sum_{i=1}^2 a_{A_i} q_{A_i} f_{A_i} = k_A \theta_+ \quad (2)$$

$$P_{K(B)} = 2\tau\theta_- / \sum_{i=1}^2 a_{B_i} q_{B_i} f_{B_i} = k_B \theta_- \quad (3)$$

cell in a direction arbitrarily designated as positive with respect to the null point and θ_- is the angular deflection of the cell in the direction opposite to θ_+ . Equations 2 and 3 may be combined to provide an expression for the difference in pressures between the A and B sets of sample chambers.

$$P_{K(A)} - P_{K(B)} = k_A \theta_+ - k_B \theta_- \quad (4)$$

If the differential torque cell is designed so that $k_A \simeq k_B = k$ then

$$P_{K(A)} - P_{K(B)} \simeq k(\theta_+ - \theta_-) = k\theta_m \quad (5)$$

where θ_m is the net angular deflection of the cell. When identical samples are placed in all four chambers, there should be no deflection of the differential torque cell despite appreciable rates of effusion from the orifices. However, if samples having different pressures at a given temperature are placed in the A and B sets of sample wells, the difference in pressure should result in a deflection of the cell.

Results

During the first phase of this study, weight loss effusion measurements were made over the temperature range 875–1000° on finely divided samples of pure, crystalline gallium nitride and on mixtures of the nitride with gallium metal. At the lower temperatures in the range, no change in weight was observed for previously outgassed graphite cells which contained pure GaN and which were heated for approximately 90 min. Weight losses were measured over the entire range of temperature with mixtures of gallium metal and the nitride. However, there was considerable scatter in the data, and they were not reproducible. At temperatures in the upper part of the range, rates of effusion with pure GaN samples were both temperature and time dependent. As expected, the effusion rate increased with increasing temperature. However, another curious result was observed. In successive runs at the same temperature with the same sample of initially pure, crystalline gallium nitride the rate of effusion, calculated from weight loss, increased from one run to the next. This trend of increasing effusion rate with time at constant temperature was characteristic of the vaporization of gallium nitride and was reproducible with several different samples of initially pure nitride. In runs with initially pure GaN, when a temperature gradient was established between the bottom of the effusion cell and the lid, which contained the orifice, a layer of liquid gallium deposited on the interior surface of the lid. In all runs, except those with very large effusion orifices, a black residue of finely divided gallium covered the surface of the initially pale yellow nitride. Photomicrographs of the residue showed that it consisted of small globular particles which were a few microns in diameter.

In a mass spectrometric analysis of the vapors which effused from a graphite effusion cell containing a mixture of liquid gallium and gallium nitride in the tem-

(7) A. W. Searcy and R. Freeman, *J. Am. Chem. Soc.*, **76**, 5229 (1954).

(8) R. C. Schoonmaker and C. Burton, *Inorg. Syn.*, **7**, 16 (1963).

(9) R. Freeman and A. W. Searcy, *J. Chem. Phys.*, **22**, 762 (1954).

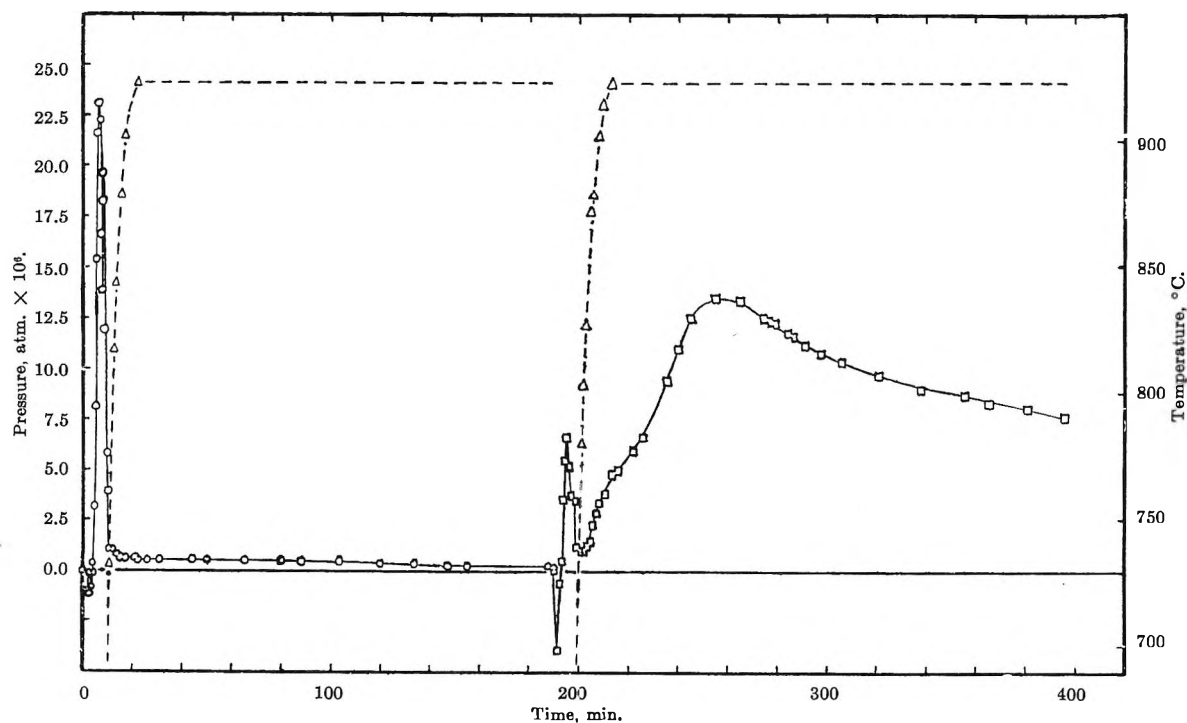


Figure 1. Pressure and temperature vs. time for cell 4. B set of sample wells: empty. A set: pure GaN during 0–180 min. and GaN plus Ga during 180–400 min.

perature range around 800° only gaseous nitrogen was detected although a careful search was conducted for species containing gallium. Since nitrogen behaves as a noncondensable gas under the conditions of operation of the mass spectrometer, it was not possible to cover a wide temperature range, and quantitative measurements were difficult to make. However, if the intensity of ion peaks representing other effusing species is placed at the limit of detection, they would probably be at least two orders of magnitude less abundant than nitrogen. The appearance of the residue after effusion runs, together with the evidence from nonisothermal effusion and mass spectrometric studies, strongly suggests that in the temperature range and under the conditions of this investigation the vaporization of gallium nitride occurs primarily through decomposition to gallium and nitrogen.



The apparent increase in a rate process with time at constant temperature is suggestive of an autocatalytic effect. Brewer and Kane¹⁰ have previously reported the phenomenon of vaporization catalysis. In order to test a hypothesis concerning catalysis in the vaporization of gallium nitride, it seemed desirable to use a technique, such as torsion effusion, with which the decomposition pressure could be continuously monitored.

Approximately 50 runs were made with conventional and differential torque cells in which sample wells were loaded with pure, crystalline GaN, GaN(c) in direct contact with gallium or indium metal, and GaN(c) in the same chamber in which was placed a small uncovered graphite container filled with gallium metal. Selected results are shown in Figures 1 and 2. Without exception, the results of runs not shown confirm the reported behavior. Figure 1 shows the results of a run consisting of two parts in which the differential torque cell was used as a conventional cell. Samples of pure GaN were placed in the A set of sample wells, and the B set was empty during the initial 3 hr. at 916°. Deflections during the first 15 min. were due to outgassing as the temperature increased. In Figure 1 cell temperature is represented by the dotted line and pressure by the solid line. It is apparent from the figure that little or no decomposition of the sample of pure, crystalline GaN occurred at 916°. This conclusion was confirmed by examination of the samples which, after 3 hr. at 916°, were identical in appearance with the initial pale yellow charges. In the second part of the run extending from 180 to 400 min., small, open graphite containers with charges of liquid gallium were placed in the A set of sample wells with the

(10) L. Brewer and J. S. Kane, *J. Phys. Chem.*, **59**, 105 (1955).

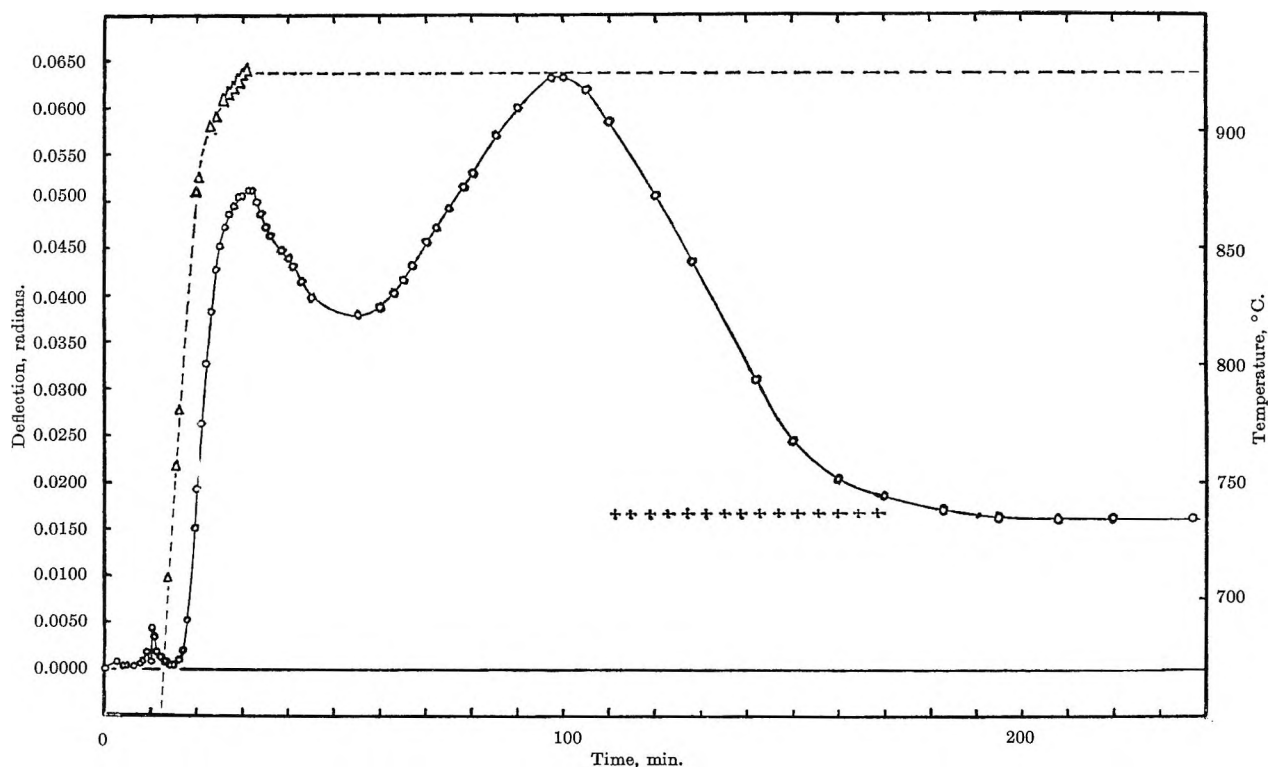


Figure 2. Differential torque cell deflection and temperature *vs.* time. A sample wells: pure GaN. B sample wells: GaN in direct contact with In(l).

previously undecomposed sample of GaN from the first part of the run. The cell was reheated to 916° , and the results are shown in the second part of Figure 1. Clearly, the sample of GaN began to decompose as evidenced by the increasing pressure in the torque cell. The vapor pressure of gallium is small^{11,12} compared to the measured pressures. It should be noted that there was an induction period of approximately 50 min. during which the decomposition pressure, which is proportional to cell deflection, slowly increased toward a peak from which it slowly decreased at constant temperature. Similar behavior was noted in other runs where balls of liquid gallium were placed directly in contact with the nitride surface. However, the length of the induction period is considerably reduced when there is initial direct contact between the liquid metal and the nitride. At the conclusion of the run shown in Figure 1 the surface of the crystalline GaN was covered by a finely divided black residue of gallium metal. The only place where the yellow gallium nitride surface remained unchanged was where it was covered by the base of the graphite container. From this result it is concluded that liquid gallium did not penetrate the graphite container and that the black surface residue above the crystalline GaN consisted of liquid which had distilled through the vapor phase

onto the GaN surface. It is clear that the presence of liquid gallium markedly enhances the rate of decomposition of the crystalline nitride. It is hypothesized that the liquid metal may participate in the vaporization process by dissolving GaN and breaking up the rigid crystalline structure after which the nitrogen atoms may diffuse through the liquid and form molecular nitrogen which may migrate to the liquid-gas interface where vaporization occurs. Thus, the liquid metal would act as a vaporization catalyst. A relatively long induction period might be expected for the type of experiment which has been described since the gallium must pass through the gas phase and build up a layer on the crystal surface before catalytic activity can be observed. The shorter induction period which is observed when there is initial direct contact between liquid gallium and the nitride is consistent with the proposed mechanism. In all runs the torque cell deflection, or pressure, reached a maximum and then declined. The decline may have been due either to depletion of the sample or to increasing thickness of the surface layer of gallium with consequent onset of a

(11) C. N. Cochran and L. M. Foster, *J. Electrochem. Soc.*, **109**, 144 (1962).

(12) Z. Munir and W. W. Searcy, *ibid.*, **111**, 1170 (1964).

diffusion-controlling migration of nitrogen through the liquid.

In the vaporization of GaN it is difficult to achieve saturation pressures in effusion cells even when the decomposition of gallium nitride occurs in the presence of liquid gallium. Conventional effusion cells 1, 2, and 3, which were identical except for orifice dimensions (see Table I), were loaded with mixtures of liquid gallium and gallium nitride and heated to 916°. With effective orifice areas in the approximate ratios 1:2:8 the measured steady-state pressures were in the ratios 1:0.5:0.17. Thus, the equilibrium decomposition pressure may be very much larger than the highest pressures measured in this investigation.

In order to test further the hypotheses concerning vaporization catalysis, runs were made with a differential torque cell in which the B set of sample wells was loaded with pure gallium nitride while the A set, which generates a torque which acts in opposition to that from the B set, was loaded with gallium nitride and the previously described graphite vessels which contained liquid gallium. The run was conducted in two parts, and in the first part (0-350 min.) the cell deflected in the positive direction indicating that the rate of effusion from the A set of sample wells (Ga + GaN) exceeded that from the B set (pure GaN). At the conclusion of the first part of the run, examination of the samples revealed that the pure GaN in the B set of wells remained unchanged from its initial pale yellow appearance while the nitride residue in the sample wells with gallium metal was black and appeared to be almost completely decomposed. In part two of the run the containers of gallium metal were shifted from the A to the B set of sample wells, and the nitride residue in the A set was stirred. The cell was remounted and heated again to 916°. In the initial stages of part two of the run, which began at 350 min., gallium metal was being distilled onto the nitride surface in the B set of sample wells, and during this induction period the gallium was not expected to be effective in catalyzing the decomposition. However, by 425 min. the cell had undergone significant deflection in the negative direction, and the effusion rate from the B set of orifices clearly exceeded that from the A set indicating that the previously undecomposed GaN was decomposing in the presence of gallium metal and that the GaN in the A wells which had partially decomposed in the first part of the run was subsequently expended. Similar differential torque experiments have been made with liquid gallium placed in direct contact with the crystalline nitride. In all cases it was apparent that the rate of decomposition of

gallium nitride was markedly enhanced by the presence of gallium metal.

The effectiveness of catalysis by direct initial contact between metallic gallium and nitride compared to that by distillation of the metal from a container onto the nitride surface was investigated by placing a mixture of liquid gallium and nitride in the A set of differential torque cell sample wells and pure GaN and containers of gallium in the B set. The initial peak deflection at a time of approximately 60 min. was in the positive direction which would be expected if the effusion rate from the A set of orifices exceeded that from the B set. However, at a later time the rate of effusion from the B set exceeded that from the A set as indicated by a negative cell deflection. These results demonstrate that the length of the induction period is smaller when gallium metal is in direct contact with the crystalline nitride than when the metal is physically separated from the nitride and must pass through the vapor phase and condense on the surface of the nitride before catalytic action can commence.

Finally, it was thought that if the hypothesis concerning a catalytic mechanism for vaporization was correct, then other liquid metals which could dissolve GaN might also be effective as catalysts. Phase equilibria in the systems Ga-GaP,¹³ In-InP,¹⁴ Ga-GaAs,¹⁵ and Ga-GaSb¹⁵ have been investigated, and in all cases the phase diagram is of the simple eutectic type with limited solubility of the compound in the liquid metal. Although phase data are not available for the In-GaN system, it seemed reasonable to assume that gallium nitride might have limited solubility in liquid indium with the result that the liquid metal could act as a vaporization catalyst for GaN. The reported heat of formation of InN¹⁶ is small, and a reaction between GaN and In is not expected. The predicted catalysis by indium of the vaporization of GaN was tested by placing pure GaN in the B set of sample wells of the differential torque cell and a mixture of GaN and indium pellets in the A set. The results are shown in Figure 2. At the conclusion of the run, the gallium nitride in the B set of chambers was unchanged while that in the A set appeared to be completely decomposed. The crosses in Figure 2 represent cell deflections in a separate experiment in which pure indium was placed in the A set of chambers and

(13) M. Rubenstein, *J. Electrochem. Soc.*, Elec. Div. Enlarged A Abstracts, Vol. II.

(14) M. Shafer and K. Weiser, *J. Phys. Chem.*, **61**, 1424 (1957).

(15) E. Wright and L. Willey, "Gallium Binary Phase Diagrams," Alcoa Research Laboratories Technical Paper No. 16, Aluminum Company of America, Pittsburgh, Pa.

(16) H. Hahn and R. Juza, *Z. anorg. allgem. Chem.*, **244**, 111 (1940).

the B set was empty. It is clear from the results that indium is an effective catalyst for the vaporization of gallium nitride.

Discussion

The results of these experiments suggest that the coefficient for vaporization of gallium nitride in the temperature range around 900° is much less than unity. Low vaporization coefficients appear to be characteristic of vaporization processes involving metallic nitrides. Searcy¹⁷ has estimated a coefficient for congruent vaporization of GaN of the order 10^{-6} , and he has suggested that the enthalpy of activation for vaporization is approximately 125 kcal./mole, which is unusually large. With such a small vaporization coefficient, it is not possible for us to measure the equilibrium decomposition pressure of GaN by the effusion technique. Equilibrium decomposition pressures may be measured in a high-temperature static system if a suitable material can be found which can be fabricated into an appropriate pressure-sensing element and which is unreactive toward hot liquid and gaseous gallium.

Perhaps the most interesting result of the present work has been the demonstration of vaporization catalysis by the liquid metals gallium and indium. The reason for the low vaporization coefficient and a possible mechanism for the catalytic activity is suggested by examination of the structure of crystalline GaN. The very rigid wurtzite lattice¹⁸ may be viewed as a hexagonal closest-packed arrangement of gallium atoms with nitrogen atoms in tetrahedral positions. The crystal involves covalent bonds between each nitrogen atom and its four nearest gallium neighbors. In order for vaporization to occur by decomposition directly from the solid, very strong covalent bonds must be broken and nitrogen atoms must diffuse over the crystal surface. Such a process might well be expected to have a high activation energy with consequent low vaporization rate. A nonreactant liquid which can dissolve GaN may act as a catalyst for the vaporization

process by providing an alternate path of lower activation energy. The liquid may participate in the vaporization by disrupting the rigid crystal structure during the solution process after which nitrogen atoms may migrate relatively freely through the liquid to form nitrogen molecules which can diffuse through the liquid and escape into the vapor phase. The results of the present study suggest that liquid gallium or indium may be effective catalysts for the vaporization of other nitrides, such as AlN, which are known to have low vaporization coefficients.

The vaporization of GaN may be compared to that of GaP which has been reported recently.⁵ The phosphide and nitride of gallium have similar crystal structures, and both vaporize by decomposition to Ga(l) and $X_2(g)$. In a torsion effusion study it was demonstrated that the decomposition pressure of GaP was not strongly dependent upon orifice area, and it was concluded that saturation pressures of $P_2(g)$ were attained. It seems clear that the vaporization coefficient for GaN is much smaller than that for GaP. The difference in the magnitudes for the vaporization coefficients may be a direct reflection of the difference in Ga-X bond strengths in the two crystals.¹⁹

Acknowledgment. We wish to express our appreciation to Professor R. F. Porter for generously providing the opportunity to make the mass spectrometric measurements and to colleagues at the Gordon Research Conference on High Temperature Chemistry (1962) for stimulating discussions related to this work.

(17) A. W. Searcy, "High Temperature Technology," Butterworth and Co. Ltd., London, 1964.

(18) H. Hahn and R. Juza, *Z. anorg. allgem. Chem.*, **239**, 232 (1938).

(19) NOTE ADDED IN PROOF. Z. A. Munir and A. W. Searcy [*J. Chem. Phys.*, **42**, 4223 (1965)] have recently reported an enthalpy of activation at 1400°K. of 29 kcal. for $2\text{GaN}(s) \rightarrow 2\text{Ga}(l) + \text{N}_2(g)$, which is about 8 kcal. smaller than the equilibrium enthalpy of reaction. However, for $2\text{GaN}(s) \rightarrow 2\text{Ga}(g) + \text{N}_2(g)$ they report that the experimental enthalpy of activation exceeds the equilibrium enthalpy of reaction by about 46 kcal.

Potential Curves and Bond Strength of PO

by Ran B. Singh and D. K. Rai^{1a}

Department of Spectroscopy, Banaras Hindu University, Varanasi-5, India (Received April 23, 1965)

Potential energy curves for P–O interactions corresponding to the X $^2\Pi$, A $^2\Sigma^+$, and B $^2\Sigma^+$ states of PO have been calculated by the Rydberg–Klein–Rees method as modified by Vanderslice, *et al.* The ground-state dissociation energy has been estimated.

Introduction

The spectra of the PO molecule have been studied to a small extent as compared to the closely analogous molecule NO. Since the work of Dressler,^{1b} however, a number of workers have directed their attention toward PO. These studies include the rotational analysis of the A–X system by Rao² and the B–X system by Singh,³ the discovery of the visible bands by Durga and Rao,⁴ and the recent discovery of a number of new band systems in the far ultraviolet by Santaram and Rao.⁵ This paper deals with the experimental potential energy curves of the electronic states for which sufficient spectroscopic data are available.

Santaram and Rao,⁶ from a qualitative analysis of the various spectroscopic data, have suggested a value 6.8 e.v. for the dissociation energy of PO. This value was in disagreement with the values suggested by Dressler^{1b} (5.4 e.v.), Ghosh and Ball⁷ (7.4 e.v.), and Herzberg⁸ (6.2 e.v.). An attempt has been made to clarify this situation.

Method, Results, and Discussion

The Rydberg–Klein–Rees method,^{9–11} as modified by Vanderslice, *et al.*,¹² for constructing the potential energy curves of diatomic molecules is a semiclassical method and utilizes spectroscopic data to determine the values of the bond length corresponding to the classical turning points in the vibrational motion of the molecule. Spectroscopic data for PO were taken from Ghosh and Ball,⁷ Dressler,^{1b} Rao,² and Singh.³ The results of the calculations are given in Table I.

Recently,¹³ experimental potential energy curves have been used to estimate the dissociation energies by a comparison with the results obtained from an empirical function. This method is quite reliable if the experimental curves are known over a large range of energy. The three-parameter Lippincott function,

which fits¹⁴ to a good extent the RKR curves for a large number of diatomic molecules, has been used for the estimation of ground-state dissociation energy. It is found that a value of D_0 about 5.4 e.v. gives the best fit to the RKR curve in the known range. The results are given in Table II.

The vibrational levels of B $^2\Sigma^+$ state, as shown by Dressler,^{1b} converge very rapidly to a limit 55,000 cm.^{-1} above the ground state. The E state shows a predissociation at about the same height and this may be caused by the B state. Kanak Durga and Rao,⁴ in their study of the visible band systems of PO, reported that vibrational levels in D and D' states above $v = 0$ level (at about 49,000 cm.^{-1}) are predissociated. If the absence of the levels with $v > 0$ in D state is correctly ascribed to predissociation, the values 6.8 and 7.4 e.v. for the D_0 (PO) are ruled out. The above argument, however, does not rule out unambiguously D_0 (PO) \sim 6.2 e.v. as given by Herzberg.⁸

(1) (a) Quantum Chemistry Group, Uppsala University, Uppsala, Sweden; (b) K. Dressler, *Helv. Phys. Acta.*, **28**, 563 (1955).

(2) K. S. Rao, *Can. J. Phys.*, **36**, 1526 (1958).

(3) N. L. Singh, *ibid.*, **37**, 136 (1959).

(4) K. K. Durga and P. T. Rao, *Indian J. Phys.*, **32**, 223 (1958).

(5) C. V. V. S. N. K. Santaram and P. T. Rao, *Z. Physik*, **168**, 553 (1962).

(6) C. V. V. S. N. K. Santaram and P. T. Rao, *Indian J. Phys.*, **37**, 14 (1963).

(7) P. N. Ghosh and G. N. Ball, *Z. Physik*, **71**, 362 (1931).

(8) G. Herzberg, "Spectra of Diatomic Molecules," D. Van Nostrand Co. Inc., New York, N. Y., 1950.

(9) R. Rydberg, *Z. Physik*, **73**, 376 (1931); **80**, 514 (1933).

(10) O. Klein, *ibid.*, **76**, 226 (1932).

(11) A. L. G. Rees, *Proc. Phys. Soc. (London)*, **59**, 998 (1947).

(12) J. T. Vanderslice, E. A. Mason, W. G. Maisch, and E. R. Lippincott, *J. Mol. Spectry.*, **3**, 17 (1959); **5**, 83 (1960).

(13) D. Steele, *Spectrochim. Acta.*, **19**, 411 (1963).

(14) D. Steele, J. T. Vanderslice, and E. R. Lippincott, *Rev. Mod. Phys.*, **34**, 239 (1962).

Table I: RKR curves for the PO molecule

State	T_e , cm. ⁻¹	U , cm. ⁻¹	r_{\min} , Å.	r_{\max} , Å.	$T_e + U$ cm. ⁻¹
X $^2\Pi$	0 ^a	615.1	1.427	1.529	615.1
		1834.9	1.394	1.572	1834.9
		3041.4	1.373	1.604	3041.4
		4234.6	1.357	1.631	4232.6
		5415.1	1.344	1.656	5415.1
		6582.6	1.332	1.679	6582.6
		7737.1	1.322	1.700	7737.1
		8878.6	1.313	1.721	8878.6
		10007.1	1.305	1.742	10007.1
		B $^2\Sigma^+$	30731.8	579.6	1.414
1716.8	1.382			1.566	32448.6
2826.6	1.362			1.602	33558.4
3909.0	1.346			1.633	34640.8
4961.3	1.333			1.662	35693.1
5988.3	1.322			1.690	36720.1
6985.5	1.312			1.717	37717.3
7953.8	1.303			1.744	38685.6
8893.3	1.295			1.769	39625.1
A $^2\Sigma^+$	40406.8			693.8	1.386
		2071.7	1.355	1.522	42478.5
		3436.8	1.335	1.552	43843.6
		4783.3	1.320	1.577	45190.1
		6116.3	1.307	1.600	46523.1
		7432.1	1.296	1.622	47838.9

^a The mean of $^2\Pi_{1/2}$ and $^2\Pi_{3/2}$ has been taken as the zero of the energy scale. ^b According to Rao,² both the states have the same symmetry, and are presumably Σ^+ .

The upper state of the γ system which is a $^2\Sigma^+$ state is perturbed² in its $v = 0$ level at two values of J . These perturbations are homogeneous in character; *i.e.*, they are caused by a Σ state. The B $^2\Sigma^+$ state cannot be the perturbing state because the near equality of rotational constants for A and B states make it unlikely that the rotational energies of these can come into coincidence at two values of J . Now, the ground-state atoms can lead to the following six states $^2\Pi$, $^2\Sigma$, $^4\Sigma$, $^4\Pi$, $^6\Sigma$, and $^6\Pi$ of which $^2\Pi$ is the ground state. If the B state is identified with the $^2\Sigma$ state arising from

Table II: Calculations for the Ground State of the PO Molecule Using the Lippincott Function (Three-Parameter Form)^a

r , Å.	$D_e =$ 44375.7 (cm. ⁻¹)	$D_0 = 44861.7$ (cm. ⁻¹)	$D_0 = 50023.5$ (cm. ⁻¹)	R.K.R.V. (cm. ⁻¹)
1.742	9936.3	10045.1	11200.9	10007.1
1.721	8808.9	8905.4	9930.1	8878.6
1.700	7668.1	7752.1	8644.0	7737.1
1.679	6517.6	6589.0	7347.2	6582.6
1.656	5357.0	5415.7	6038.8	5415.1
1.631	4190.8	4236.7	4724.4	4234.6
1.604	2964.3	2996.8	3341.6	3041.4
1.572	1809.4	1829.2	2039.7	1834.9
1.529	608.6	615.2	686.0	615.1
1.427	608.2	614.9	685.6	615.1
1.394	1820.3	1840.2	2052.0	1834.9
1.373	3019.2	3052.3	3403.5	3041.4
1.357	4188.5	4234.4	4721.6	4234.6
1.344	5351.6	5410.2	6032.7	5415.1
1.332	6500.8	6572.0	7328.2	6582.6
1.322	7625.5	7709.0	8596.0	7737.1
1.313	8750.5	8846.4	9864.3	8878.6
1.305	9860.3	9968.3	11115.2	10007.1

^a The $D_0 \sim 6.8$ and 7.4 e.v. were also used for calculations, but the results are not reported here as they deviate greatly from the RKR values.

these products, a simple quantum mechanical argument¹⁵ may be used to calculate the curves for $^4\Sigma$ and $^4\Pi$. It is found that these curves do not cut the A state at the appropriate height. Thus it seems more likely that the B state dissociates into 2D (P) + 3P (O) which leads to $D_0 \sim 5.4$ e.v. and there is some lower state of the type $^2\Sigma$ or $^4\Sigma$ arising from normal atoms which is causing the observed perturbations.

Acknowledgment. The authors are grateful to Professor N. L. Singh for his interest in this work. R. B. S. wishes to thank C.S.I.R. (India) for financial assistance.

(15) J. T. Vanderslice, E. A. Mason, and W. G. Maisch, *J. Chem. Phys.*, **31**, 738 (1959).

Infrared Spectroscopic Investigations of Zeolites and Adsorbed Molecules.

I. Structural OH Groups¹

by C. L. Angell and Paul C. Schaffer

Union Carbide Research Institute, Tarrytown, New York (Received April 23 1965)

The infrared spectra of mono- and divalent cations containing X- and Y-type zeolites show several bands in the OH stretching region which cannot be removed even at 585° although their number and size depend on the activation (dehydration) technique. The band at 3744 cm.⁻¹ has the same frequency and intensity in all samples and does not interact with adsorbed molecules. Its assignment to crystal surface groups, occluded impurities, or defective sites is discussed. The bands at 3640 and 3540 cm.⁻¹ are assigned to cation deficiency OH groups, the latter being due to association. Changes in these bands on the addition of water, benzene, ammonia, trimethylamine, hydrogen chloride, and hydrogen cyanide are discussed.

Introduction

The crystal structures of synthetic zeolites have recently been reviewed by Breck.² The theoretical structure of X- and Y-type zeolites does not include any OH groups; still, several authors³⁻⁶ have reported bands in the OH stretching region in the infrared spectra and have given a number of different, often inconsistent, interpretations for them. Bertsch and Habgood⁵ reported that all of the OH bands found were due to adsorbed water, each molecule of which was both attached to the exchangeable cations and hydrogen-bonded to the surface oxygens. Carter, Lucchesi, and Yates⁶ assigned the three OH bands in the 3- μ region to surface hydroxyl groups, the band at 3750 cm.⁻¹ to Si-OH groups, the band at 3700 cm.⁻¹ to Al-OH groups, and the band around 3650 cm.⁻¹ to some OH groups which were influenced by the exchangeable cations. In the present work, further evidence is presented on this controversial issue. The availability of special materials was a factor contributing to the significance of this work. (1) All previous authors have used material of normal particle size such that the light scattering in the 3- μ region is very considerable, causing serious loss in transmission and forcing their instruments considerably beyond their normal performance. In the present work special trouble was taken to obtain an especially fine-grained material. With this material, trans-

mission losses were very much reduced, and normal resolution of the infrared spectrometers used was achieved. (2) A much larger variety of cation-exchanged samples was available, including a series of Y zeolites with different degrees of cation deficiency.

Several OH bands were found in the 3- μ region. Some of these bands varied with the zeolitic cation, and some bands were related to the cation deficiency. Deuterium-exchange experiments were carried out also, and the effects of a variety of adsorbed molecules on the OH bands were observed.

Experimental Section

Materials. The Y-type zeolite samples were prepared from one original specially fine-grained sodium Y sample with a silicon/aluminum ratio of 2.35. (This sample was found to be 98% Y zeolite by X-

(1) The major portion of this work was presented at the 49th Annual Meeting of the Optical Society of America, New York, N. Y., Oct. 6-9, 1964.

(2) D. W. Breck, *J. Chem. Educ.*, **41**, 678 (1964).

(3) (a) J. A. Rabo, P. E. Pickert, D. N. Stamires, and J. E. Boyle, *Actes Congr. Intern. Catalyse, 2e Paris, 1960*, 2055 (1961); (b) H. A. Szymanski, D. N. Stamires, and G. R. Lynch, *J. Opt. Soc. Am.*, **50**, 1323 (1960).

(4) S. P. Zhdanov, A. V. Kiselev, V. I. Lygin, and T. I. Titova, *Dokl. Akad. Nauk SSSR*, **150**, 584 (1963).

(5) L. Bertsch and H. W. Habgood, *J. Phys. Chem.*, **67**, 1621 (1963).

(6) J. L. Carter, P. J. Lucchesi, and D. J. C. Yates, *ibid.*, **68**, 1385 (1964).

ray examination.) All the other Y-zeolite samples were prepared from this by cation exchange (the decationized samples by NH_4 exchange, see ref. 3); during the exchange special care was taken to keep the pH of the solutions above 4.0 to avoid partial decomposition. Each sample was analyzed by wet chemical methods for Al_2O_3 , SiO_2 , Na_2O , and metal oxide. The samples were also subjected to an X-ray examination, and, in most cases, the intensity and sharpness of the lines indicated that the samples had retained a very high degree of crystallinity during the cation exchange. A few samples showed weakened lines or increased background, but this was to be expected because of absorption or fluorescence by the particular cations present. The small-particle-size sodium Y, obtained from the Linde Division, had a size range, estimated from electron micrographs, from 0.04 to 1.2 μ , with an average of 0.4 to 0.8 μ . Unfortunately, it is not the average particle size that counts for the scattering since even small amounts of larger particles can cause serious scattering. Therefore, the material was further fractionated by suspending it in water and shaking ultrasonically for about 3 hr. The fraction, about 0.1 of the original sample, that stayed in suspension after 24 hr. of settling was collected by centrifugation. The particle size of this fraction was not measured directly, but comparison of the infrared spectrum in the 3- μ region with the spectra of materials of known particle size indicated a size less than 0.1 μ . (A number of samples of X and Y zeolites of varying particle size was made available from the Linde Division (Union Carbide Corp., Tonawanda, N. Y.); the transmission in the 2-3.5- μ region seems to be inversely proportional to the average particle size.) This treatment was successful: the resulting materials gave very good transmission in the 2-3.5- μ region. Sodium X and calcium X samples were available in extremely small particle size (<0.05 μ) form and were not subjected to further separation. The chemical analyses of these samples are given in Table I.

All the infrared samples were pressed into self-supporting disks of 0.5-in. diameter under a pressure of not more than 10,000 p.s.i. The disks weighed 20 ± 1 mg., giving a density of 16 ± 1 mg./cm.². All-glass vacuum cells of a new design were used.

For this design two considerations were of primary importance: (1) the gas path length must be as short as possible since considerable gas pressure is often present during the taking of the spectra; (2) the cell must be easy to construct and be reasonably inexpensive, so that many cells can be in operation at the same time.

Table I: Analyses of Samples Used

	Na_2O	Metal oxide	Al_2O_3	SiO_2
Decat. YI	0.14	0.54 MgO	1.00	4.68
Decat. YII	0.16	...	1.00	4.74
NaY			1.00	4.70
LiY ^a	0.45	0.47 Li ₂ O	1.00	4.84
MgY	0.27	0.72 MgO	1.00	4.74
CaY	0.16	0.77 CaO	1.00	4.80
MnY	0.26	0.63 MnO	1.00	4.70
CoY	0.30	0.66 CoO	1.00	4.84
NiY	0.27	0.66 NiO	1.00	4.80
ZnY	0.28	0.66 ZnO	1.00	4.80
AgY	0.01	0.95 Ag ₂ O	1.00	4.96
CdY	0.28	0.67 CdO	1.00	4.74
NaX	0.94	...	1.00	2.70
CaX	0.03	0.98 CaO	1.00	2.70
Error:	± 0.02	± 0.02	± 0.03	± 0.05

^a Not small particle size material.

The final version of the all-glass cell is illustrated in Figure 1. The samples are placed in magnetic stainless steel holders and rest on the flat bottom of the cell. In this position the cell can be evacuated (10^{-6} torr) or filled with gas and the sample treated at any temperature from liquid N_2 temperature to nearly the softening point of glass. After treatment, the sample

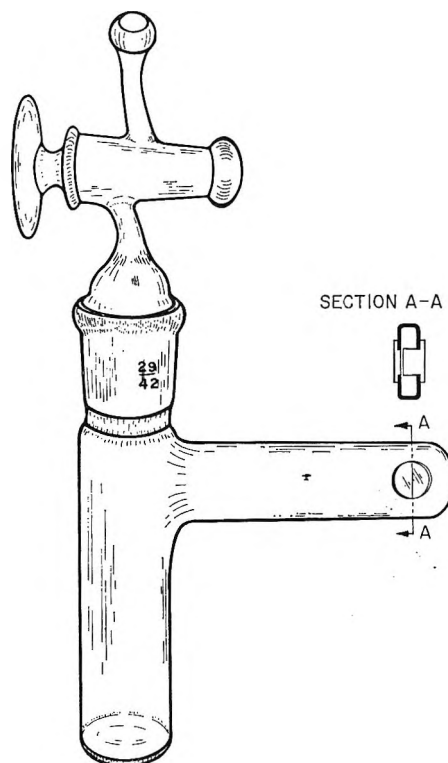


Figure 1. Glass vacuum cell.

is allowed to return to room temperature, then transferred with the help of an external magnet to the side arm. The cell is rotated 90° and placed in the beam of an infrared spectrometer.

The side arm is constructed from a flat rectangular glass tube (2.54 × 0.635 cm., internal⁷), through which 1.43-cm. holes are drilled, and 1.91-cm. sodium chloride disks are glued on the outside with Pliobond. The gas path length is only about 8 mm., but in many experiments involving physical adsorption even this path length is too much. By the use of suitably shaped sodium chloride windows (outer diameter 1.91 cm., inner diameter 1.27 cm.⁸) this distance can be decreased to 1 mm. One of the mushroom-shaped windows is flush with the inside of the glass, so that the sample holder can smoothly slide into position along the inner surface of the tube, while the other window extends 6 mm. into the tube leaving a gap of 1 mm. between the two windows.

The illustrated cell is very easy to construct and costs about \$35 (without windows). This way it is possible to have many cells in operation, making it easy to have a number of long experiments running concurrently.

Attempts were made to construct cells in which the actual spectra could be taken at temperatures higher or lower than room temperatures, but no satisfactory design based on the flat glass tube and its 8-mm. path length was found.

Spectrometers. Survey runs were made on a Perkin-Elmer Model 21 spectrometer and a Beckman IR-10 grating spectrometer, and high-resolution runs in the 3- μ region were made on a Perkin-Elmer Model 112 spectrometer equipped with a lithium fluoride prism. With the small particle size materials slit widths of 0.045 to 0.100 mm. could be used in the 3800 to 3000-cm.⁻¹ region corresponding to a spectral resolution of 2.0 to 4.0 cm.⁻¹. Some additional runs were obtained on the same spectrometer converted to grating operation (slit width: 0.15 to 0.25 mm. in the 3800 to 3000-cm.⁻¹ region), but these showed no difference either in position or shape of bands compared with the prism instrument.

Sample Activation. Several activation techniques were used: vacuum activation, air activation, and flash activation.

Vacuum Activation. The sample was evacuated at room temperature overnight (final pressure $\sim 5 \times 10^{-5}$ torr), heated up to 500° over a period of about 4 hr. while pumping, kept at this temperature under vacuum for 3 hr. (final pressure $\sim 5 \times 10^{-6}$ torr), and then allowed to cool under vacuum.

Air Activation. The sample was gradually heated in

air (no air circulation was thought to be necessary, the samples were so small) up to 500° over a period of 2 hr., kept at this temperature for about 3 hr., evacuated at the same temperature (final pressure $\sim 5 \times 10^{-6}$ torr), and then allowed to cool under vacuum.

Flash Activation. The sample was evacuated at room temperature very briefly (pressure about 10^{-3} torr), heated to 500° in less than 10 min., kept at this temperature under vacuum for about 3 hr. (final pressure $\sim 5 \times 10^{-6}$ torr), and then allowed to cool under vacuum.

Results

All the samples examined showed several bands in the OH stretching region. These bands are illustrated in Figures 2 and 3 and their frequencies are summarized in Table II. The OH band at 3745 cm.⁻¹ always had the same frequency, shape, and intensity within experimental error, even for decationized Y. All these bands remained unchanged when the activation temperature was raised as high as 585° although the rather sharp band at 3640 cm.⁻¹ was of variable strength on samples taken from the same batch of the same zeolite but activated on different occasions. Variation in activation technique was suspected, and it was found that for CaY, MgY, CoY, and NiY very much smaller 3640-cm.⁻¹ bands resulted from flash activation than from the (prolonged) vacuum activation; see Figure 4. The differences between spectra from various activation techniques were complicated: the bands around 3690 and 3600 cm.⁻¹, which were always quite small, decreased or disappeared at the higher temperatures of activation, or with flash activation, except for the 3690-cm.⁻¹ band of MgY, SrY, and ZnY, which was not removed even on flash activation or on activation at the higher temperatures, and the 3595-cm.⁻¹ band of CoY which actually appeared on flash activation. The 3640-cm.⁻¹ band also showed a small variation with cation, the frequency being reproducible to within two wave numbers, so that the indicated differences are real. The band at 3540 cm.⁻¹ was always broad compared to the 3640-cm.⁻¹ band (half-width 85 and 25 cm.⁻¹, respectively, in the decationized series).

All the OH groups can be exchanged to OD groups by exposing the fully activated sample to the full vapor pressure of heavy water at room temperature, then evacuating and reactivating the sample under vacuum at 500°. However, when about 2% of heavy water was adsorbed on a MgY zeolite sample, there was no decrease of the 3745-cm.⁻¹ band while the 3643-cm.⁻¹

(7) Available from Fischer and Porter Co., Warminster, Pa.

(8) Manufactured on special order by the Harshaw Co., Cleveland, Ohio.

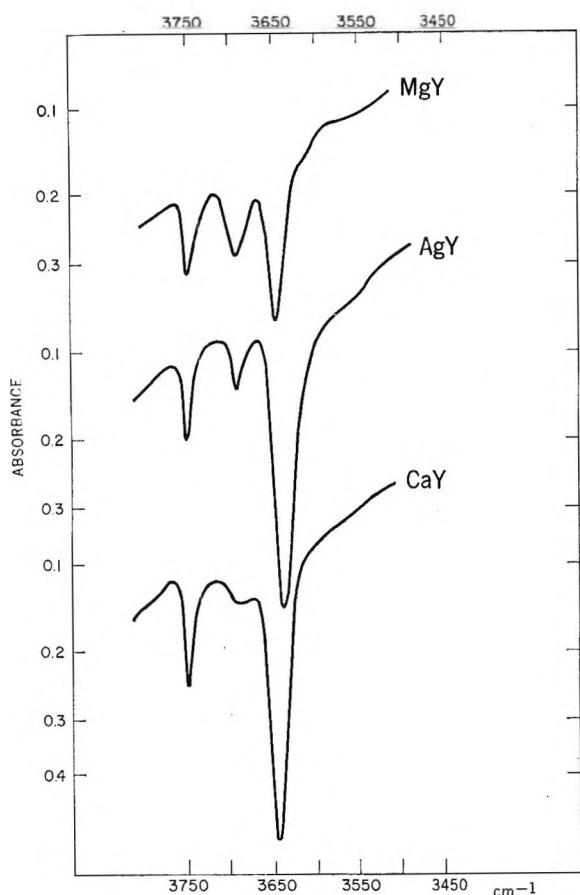


Figure 2. Infrared spectra of vacuum-activated MgY, AgY, and CaY zeolites in the OH stretching region.

Table II: OH Frequencies on Zeolites

Type of zeolite	—OH bands, cm. ⁻¹			OD bands, cm. ⁻¹			Water bending, cm. ⁻¹
Decat. Y	3744	3636	3544	2758	2686	2617	
NaY	3748		3652				1645
LiY ^a	3744						
MgY	3745	3688	3643	3540	2762	2686	2616
CaY	3746		3645		2762	2690	
SrY ^a	3746	3691					
BaY ^a	3744		3647				
MnY	3748		3644	3545		2685	2616
CoY	3748		3646	3540			
NiY	3746	3682	3643	3544			
ZnY	3744	3675	3642	3542			
AgY	3745		3634	3550	2762		2610
NaX	3744						
CaX	3744						

^a Not small particle size material.

band was nearly completely removed by deuterium exchange. For corresponding bands the ratio of OH frequency to OD frequency (also shown in Table II) is equal to 1.355 ± 0.002 , very close to the value 1.37 expected for completely free OH groups.

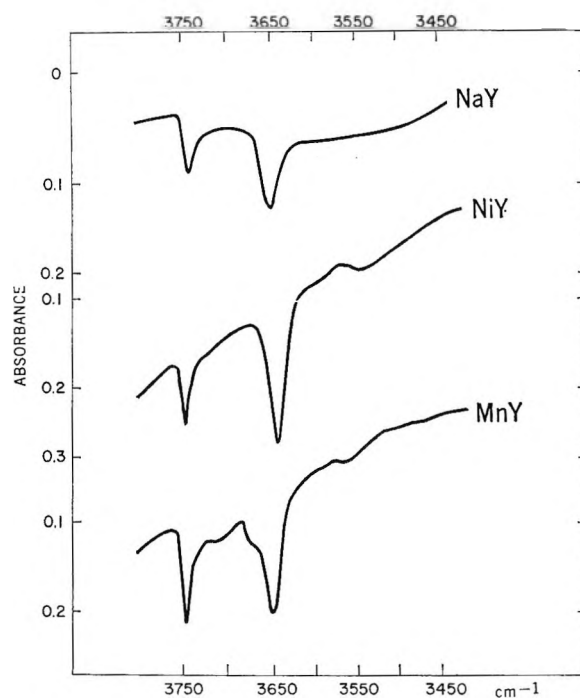


Figure 3. Infrared spectra of vacuum-activated NaY, NiY, and MnY zeolites in the OH stretching region.

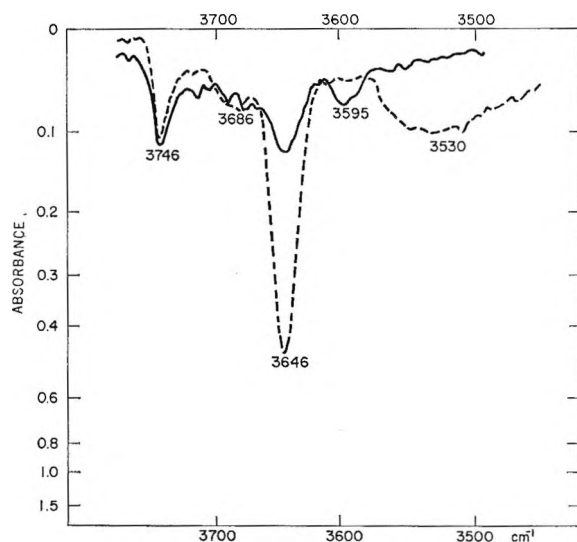


Figure 4. Spectrum of CoY zeolite: —, flash activated; - - -, vacuum activated.

Stepwise addition of small amounts (up to 2 wt. %) of water to the divalent cation containing Y zeolites causes a broad, gradual increase of the band at 3540 cm.⁻¹ but no change at all in the band at 3640 cm.⁻¹ (see Figure 5). The added water evidently is not adsorbed to the OH group responsible for the 3640-cm.⁻¹ band. On reactivation the broad increment to the 3540-cm.⁻¹ band is completely removed and the original

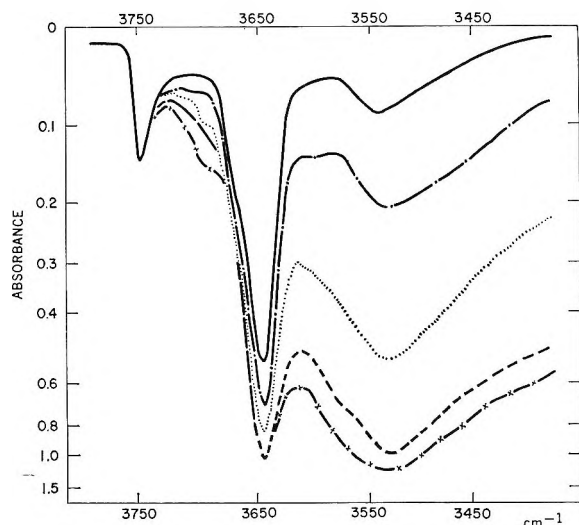


Figure 5. Water addition to vacuum-activated CoY zeolite: —, 0.3% water; - - - -, 0.6% water; ·····, 0.9% water; — · — ·, 1.2% water; -x-x-x, 1.5% water.

spectrum recreated, without any net change. The difference between the broad band caused by added water and the band appearing at the same frequency in the decationized zeolites will be discussed later. On adding larger amounts of water the broad band completely blanks out the whole OH region. Adding heavy water to an already deuterium-exchanged sample gives analogous results: the broad 2616-cm.⁻¹ band increases, but the sharp 2685-cm.⁻¹ band does not.

Our results on water adsorption significantly extend those of Bertsch and Habgood.⁵ Their observations (and assignments), on NaX, were that a sharp band at 3690 cm.⁻¹ (the free OH of a water molecule attached to a cation), a broad band at 3400 cm.⁻¹ (the other OH of the same molecule hydrogen bonded to a surface oxygen atom), and a band at about 1645 cm.⁻¹ (H₂O bending) appeared and increased simultaneously on the addition of water. We have repeated this experiment on NaX (which before the addition of water showed only the 3745-cm.⁻¹ band) and NaY and found the same results, *i.e.*, the growth of both the 3690- and the 3400-cm.⁻¹ bands; however, addition of water to CaX did not cause the appearance of a band at 3690-cm.⁻¹, but only the appearance of a broad band at about 3480 cm.⁻¹.

The water bending frequency around 1630 cm.⁻¹ is also definitely observable on adding water. In all our studies of activated zeolites this band was absent, indicating that no water was present and that the bands observed must have been due to surface OH groups instead. The water bending frequency around 1630 cm.⁻¹ definitely depends on the nature of the cations

(see Table II), but we could not correlate the shifts with any cationic property.

When benzene was added to samples of NiY or MgY, the 3640-cm.⁻¹ band disappeared, and a very broad band appeared at 3310 cm.⁻¹. Various authors⁹ have used such a shift with benzene to identify SiOH bands, the shift with silica being 120 cm.⁻¹. The present shift is much larger, indicating that the OH group at 3640 cm.⁻¹ is probably not of the simple SiOH silica type. The 3744-cm.⁻¹ band is invariant to benzene both in position and size, and the same invariance is observed with ammonia, trimethylamine, and hydrogen cyanide. In every case, the 3640-cm.⁻¹ band is shifted to lower frequency and broadened (hydrogen bonding), but the 3744-cm.⁻¹ band is left completely unchanged.

Decationized samples show two prominent bands, at 3640 and 3540 cm.⁻¹, of intensity depending on the amount of decationization (Figure 6). In the 84% cation-deficient material these bands become so big that their position cannot be exactly located. Since these two bands appear as small bands in the spectra of all the zeolites, it is reasonable to try to associate them with the existing cation deficiency. (See table of analyses.) However, it was not possible to correlate quantitatively the intensity of these bands in various samples to the amount of cation deficiency indicated by the chemical analysis. On the other hand, these bands do depend on the mode of activation, being considerably weaker with flash activation than with the normal activation by more prolonged heating at intermediate temperatures. This effect has been observed in CoY, NiY, MgY, ZnY, and CaY (see Figure 4).

When hydrogen chloride is added to fully dehydrated MgY zeolite, a reaction occurs and OH bands appear at 3643 and 3533 cm.⁻¹ which are apparently the same as in the case of the decationized samples. However, no increase in intensity of the 3744-cm.⁻¹ band was noticed. Attempts to follow the rate of this reaction quantitatively by following the growth of the 3640-cm.⁻¹ band were unsuccessful because the band reaches its full height within 20 sec. of exposure to the hydrogen chloride. Similarly, on adding DCl to a MgY zeolite, bands appeared at 2684 and 2605 cm.⁻¹. The formation of these bands on the addition of hydrogen chloride is additional proof that these bands are due not to the stretching vibration of water but rather to surface OH groups: both the hydrogen chloride and the zeolite are completely dry before the reaction takes place. No band at 1630 cm.⁻¹ appears

(9) (a) M. R. Basila, *J. Chem. Phys.*, **35**, 1151 (1961); (b) G. A. Galkin, A. V. Kiselev, and V. I. Lygin, *Trans. Faraday Soc.*, **60**, 431 (1964).

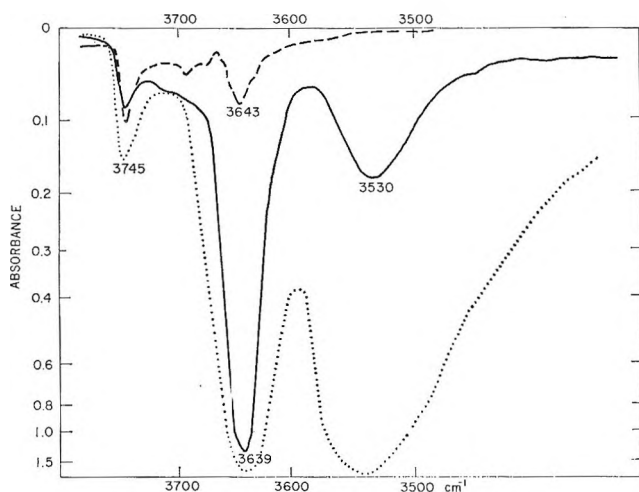


Figure 6. Air-activated decationized Y zeolites: ----, 7% decationized; —, 32% decationized; ·····, 84% decationized.

when the hydrogen chloride reaction occurs, indicating that no water is formed in the reaction. A similar reaction occurs between hydrogen cyanide and some, but not all, cation-exchange Y zeolites.

Discussion

The 3745-Cm.⁻¹ Band. The frequency of the Si-OH stretching vibration in silica is 3749 cm.⁻¹,¹⁰ in agreement with our ubiquitous, invariant band. There is little doubt, therefore, that this band is due to an Si-OH stretching vibration. However, it is interesting to note the wide variation in size of all the other OH bands between various cation-containing zeolite samples and differently activated samples while this particular band is always exactly the same size, including the decationized zeolite samples. In a previous discussion¹¹ this band was ascribed to the Si-OH groups that must terminate the external surfaces of the small, finite crystals. However, in view of the fact that this band does not change on the adsorption of various molecules which would be expected to hydrogen bond with OH groups, such a proposition seems difficult to maintain. It is not easy to see why these external OH groups should not interact with adsorbed molecules just as easily as OH groups on the zeolitic surface do. Is the band then due to some small amount of silica-type impurity? If the impurity is in the form of particles outside the zeolite structure, then it seems that such OH groups should interact with molecules that usually cause shifts of the Si-OH frequency in silica—but they do not. It seems rather that the band must be due to OH groups so placed as to accept no adsorbed (hydrogen-bonded) molecules at all, even the quite small molecule water. On treatment with heavy water, the

3744-cm.⁻¹ band also is replaced by the OD band at 2762 cm.⁻¹. Under our conditions of deuterium exchange, the samples are saturated with heavy water, and it is considered that only proton or deuterium mobility is necessary for the exchange; actual water molecules need not penetrate to the OH position. On the other hand, in the experiment where 2% heavy water did not cause deuterium exchange of this OH group, the small number of water molecules present (about two per cavity) is apparently quite tightly bound, so that no proton migration is possible. Also, the inaccessibility of the OH groups to all other adsorbed molecules seems to indicate that they are in a position where these molecules cannot get to them. It could be suggested that these OH groups are inside the sodalite baskets or in the so-called site I cation positions. However, it is difficult on this basis to see why the 3745-cm.⁻¹ band should be so constant in intensity. Since exchange of cations, in aqueous solution, occurs for all sites, the eventual proportion of H⁺ ions in site I (which would give rise to our insensitive OH groups) would vary according to the treatment during cation exchange, just as the total amount of cation deficiency changes from sample to sample. However, considering possible imperfections in the zeolite structure, it is possible that a proton in a defective site I² could not be exchanged by cations. Such defects, however, would have to be a constant part of the structure to account for the unchanging size of the 3744-cm.⁻¹ band in samples from various sources.

It is also possible that siliceous material of some kind is occluded inside the zeolite structure, filling parts of the main pore system or perhaps even as single Si(OH)₄ molecules occupying sodalite baskets. In either case, deuterium migration could lead to exchange of the hydrogens. However, again, despite the fairly standardized technique of zeolite preparation, it is not clear that the amount of such occluded impurity would be as constant in various samples as the observed intensity of the 3744-cm.⁻¹ band.

The 3640-cm.⁻¹ Band. There seems to be very little doubt left that the band at 3640 cm.⁻¹ from the decationized forms of zeolites is due to OH groups formed from proton attack on surface oxygens. The mechanism of this reaction in the case of NH₄-exchanged zeolites has been discussed by Rabo, *et al.*, and Szymanski, *et al.*,³ who describe a mechanism in which first the ammonia is removed from the NH₄⁺ ions and then the remaining protons attack some of the surface

(10) R. S. McDonald, *J. Phys. Chem.*, **62**, 1168 (1958).

(11) C. L. Angell and P. C. Schaffer, *J. Opt. Soc. Am.*, **54**, 1391 (1964).

oxygen atoms to form hydroxyl groups, most likely on silicon atoms, while converting the aluminum atoms of the structure to a threefold coordination. Analogous reaction must occur in the case of the cation-deficient forms when removal of water from the H_3O^+ ion leaves a bare proton. According to this, the 3640-cm^{-1} band would be ascribed to vibrations of an Si-OH group close to a three-coordinated aluminum atom. This explains the frequency being different from the silica Si-OH vibration and the shift with benzene (330 cm^{-1}) being so much larger than the shift of silica Si-OH with benzene (120 cm^{-1}). The existence of Al-OH groups giving rise to a band in the same position, however, cannot be ruled out completely since a number of alumina minerals, like kaolinite, have Al-OH stretching vibrations in this region.¹² The fact that this band shows a slight dependence on the cations present seems to indicate an interaction between the OH groups on the structural framework with the cations. However, the variation is so small (20 cm^{-1}) that this interaction can only be described as very weak.

The 3540-cm^{-1} Band. In the decationized series this broad band always seems to be associated with the 3640-cm^{-1} band. We suggest that this is a band due to interaction between two neighboring OH groups, presumably through hydrogen bonding. Such an interaction would result in the lowering of the OH frequency and in the broadness of the band. The relation of these two bands is similar to the association of hydroxyl-containing molecules in solution, where at low concentration only the monomer band appears but on increasing the concentration the associated band increases much faster than the monomer band. However, in the zeolites the OH groups are in fixed positions; therefore, there must be a sufficient number of OH groups present so that neighboring OH groups would get close enough for interaction before the 3540-cm^{-1} band can appear. For the various cationic zeolites with their small amounts of cation deficiency, however, the ratio of these two bands is quite variable.

The Band around 3690 cm^{-1} . This band, which occurs in the spectra of a number of zeolite samples, is most likely an Al-OH stretching frequency and is presumed to be the same band as observed on some X zeolites by Carter, *et al.*⁶ However, the appearance of a strong band in this position in an NiY sample that has been heated with its own water in a closed system at 500° is not understood. Undoubtedly, we are dealing with a kind of hydrolysis, but further experiments are needed to establish the nature of the reaction.

The Addition of Water. It is interesting to observe that on the addition of *small* amounts of water (up to

2%) the broad band appearing at 3540 cm^{-1} does not seem to influence the band at 3640 cm^{-1} . (Whether small amounts of benzene, ammonia, trimethylamine, and hydrogen cyanide would behave similarly has not been investigated. In all these cases, large excesses of the adsorbents were used; it was only with water (and heavy water) that the adsorbent was added gradually in small amounts.) This indicates that the water is not attached (hydrogen bonded) to the OH groups but must be adsorbed at some other site. This conclusion is confirmed by results of CO adsorption¹³ where it is shown that the first amounts of water definitely go to the cations displacing the CO adsorbed there. In most of our divalent cation-containing zeolites the exchange is about 66%, which means that there are 19 divalent and 19 monovalent cations per unit cell; so it is possible that the 2% water (about 16 molecules per unit cell) could all be adsorbed on the cations even though cations in site I would not be expected to be available to the water molecules.

The suggestion that the 3540-cm^{-1} band is due to isolated water molecules attached to the cations raises two questions: Why is the band so broad? Why aren't there two OH stretching vibrations, asymmetric and symmetric? We would like to suggest that the water molecule is attached not only through the oxygen atom to a cation but also through both of the hydrogen atoms to adjacent surface oxygens. This would account for the broadening of the bands and the fact that the two vibrations cannot be observed as two separate bands. The different spectral behavior of water on NaX (KX and LiX⁵), on NaY, and on our series of Y zeolites (all containing divalent cations) cannot be explained without further experiments.

Both the broad band ascribed to associated cation deficiency OH groups and the band appearing on the addition of water are in the same position (3540 cm^{-1}), but they are quite clearly due to different entities. They have very different widths (3540 cm^{-1} , cation-deficiency band: half-width $\sim 85\text{ cm}^{-1}$; adsorbed-water band: half-width $\sim 200\text{ cm}^{-1}$), and, of course, the first is quite stable even at 580° while the second is removed on evacuation at around 500° .

Variation of the 3640-cm^{-1} Band with Activation Technique. It has been noted that on flash activation of the same sample this band was smaller than on normal prolonged activation. A small amount of cation deficiency is present in each of the samples, and on flash activation these cation deficiencies are

(12) J. M. Serratosa, A. Hidalgo, and J. M. Vinas, *Nature*, **195**, 486 (1962).

(13) C. L. Angell and P. C. Schaffer, to be published.

turned into OH groups giving rise to the typical de-cationized bands. On the other hand, it is suggested that on slow removal of water the zeolite sample is exposed to water vapor at an elevated temperature, referred to by Peri¹⁴ as "self-steaming": at high temperatures the water apparently attacks the zeolite structure and forms more hydroxyls than there were present originally. Differences between samples activated by vacuum and flash methods have also been observed in adsorption studies carried out at Linde and so interpreted.¹⁵ There it was observed that different adsorption capacity could be obtained on flash activation

as compared to normal activation; the effect was again attributed to hydrolysis due to exposure of the zeolite to water vapor at elevated temperatures.

Acknowledgments. The authors wish to express their sincere thanks to Drs. Verner Schomaker and Jule Rabo for many helpful discussions and constructive criticism and to Dr. Edith Flanigen for many of the zeolite samples.

(14) J. B. Peri, *J. Phys. Chem.*, **69**, 211 (1965).

(15) Dr. R. Neddenriep, private communication.

The Heat Capacity of Potassium Hexabromorhenate(IV) from 7 to 300°K. Manifestation of Thermal History Behavior. Antiferromagnetic Anomaly near 15°K. Entropy and Free Energy Functions¹

by R. H. Busey, R. B. Bevan, Jr., and R. A. Gilbert

Chemistry Division, Oak Ridge National Laboratory, Oak Ridge, Tennessee (Received April 26, 1965)

Low-temperature heat capacity data on K_2ReBr_6 are presented and the thermodynamic functions are tabulated. A typical λ -transition with a heat capacity maximum at 15.25°K. was observed, which represents the transition from a paramagnetic state to an ordered antiferromagnetic state below this temperature. An unusual, spontaneous heat evolution at approximately 150°K. accompanied by the occurrence of a small heat capacity anomaly with a maximum at approximately 214°K. was observed to be dependent upon the thermal history of the sample, both phenomena essentially disappearing after a sufficient number of coolings to 150°K. In addition to the heat capacity anomaly associated with the magnetic transition at 15.25°K., an anomalous heat capacity above 200°K. with heat capacity maxima at 226 and 246°K. was observed. Evidence is presented that these transitions are the result of changes from the K_2PtCl_6 -type cubic crystal structure at room temperature to a lower symmetry structure at lower temperatures. The thermodynamic functions at 298.15°K. (gibbs mole⁻¹) are: $C_p^\circ = 54.24$, $S^\circ = 108.74$, $(H^\circ - H^\circ_0)/T = 44.63$, and $-(F^\circ - H^\circ_0)/T = 64.11$.

Introduction

The unusual low-temperature heat capacity observed for K_2ReCl_6 ² prompted the measurements reported here on K_2ReBr_6 . In addition to the heat capacity anomaly which arises from the transition from a paramagnetic state to an ordered antiferromagnetic state below 11.9°K., the heat capacity of K_2ReCl_6 exhibits three λ -type transitions with maxima at 76.05, 103.4, and 110.9°K. It has been suggested² that these transitions may represent successive distortions of the face-centered cubic structure and/or distortions of the octahedral $ReCl_6^{2-}$ ion. It was considered to be of interest to determine if K_2ReBr_6 shows similar behavior. Three measurements also provide values of the entropy and free energy functions which are desired in connection with the study of the chemistry of technetium and rhenium being carried out at this laboratory. The results presented here do indeed show that the heat capacity of K_2ReBr_6 is anomalous above 200°K.

Both of the complex salts undergo a transition to an ordered, antiferromagnetic state at low temperatures,³ and at room temperature both have a face-centered

cubic structure⁴⁻⁶ of the K_2PtCl_6 type. No previous heat capacity data on K_2ReBr_6 have been reported.

Experimental Section

Potassium Hexabromorhenate Samples. The measurements reported were made on a sample of K_2ReBr_6 (sample I) prepared by reduction of $KReO_4$ in concentrated hydrobromic acid (48% HBr) by $CrBr_2$ according to the procedure given by Meloche and Martin.⁷ Gravimetric analyses gave 64.44 \pm 0.06% Br and 10.40 \pm 0.04% K; theoretical values are 64.46 and 10.51%, respectively. In order to determine the

(1) Research sponsored by the U. S. Atomic Energy Commission under contract with the Union Carbide Corporation.

(2) R. H. Busey, H. H. Dearman, and R. B. Bevan, Jr., *J. Phys. Chem.*, **66**, 82 (1962).

(3) R. H. Busey and E. Sonder, *J. Chem. Phys.*, **36**, 93 (1962).

(4) B. Aminoff, *Z. Krist.*, **94**, 246 (1936).

(5) D. H. Templeton and C. H. Dauben, *J. Am. Chem. Soc.*, **73**, 4492 (1951).

(6) J. Dalziel, N. S. Gill, R. S. Nyholm, and R. D. Peacock, *J. Chem. Soc.*, 4012 (1958).

(7) V. W. Meloche and R. Martin, *J. Am. Chem. Soc.*, **78**, 5955 (1956).

reproducibility of the heat capacity results in the anomalous region (200°K. and above), this first sample was recrystallized from 48% HBr and measurements were repeated over the temperature range 200 to 300°K. These results (sample II) were higher on an average by 1.5% from those of sample I. Based upon the experience with duplicate results² on two preparations of K_2ReCl_6 where good reproducibility was obtained, it was decided to discontinue measurements on this second sample and make an entirely new preparation. The third sample (sample III) was prepared by reduction of $KReO_4$ by the hydrobromic acid (48%) itself in the presence of an equivalent amount of KBr. The first product of this procedure gave crystals which contained a white material which was presumably unreduced $KReO_4$. This product was resubjected to reduction by redissolving the sample in 48% hydrobromic acid and saturating the solution with hydrogen bromide. After standing for a period of 3 weeks, a first batch of K_2ReBr_6 crystals (~0.5 mm.) was removed. A second batch of crystals was obtained following concentration of the mother liquor with a heat lamp. Both batches of crystals were washed with 48% hydrobromic acid, combined, and dried in an oven at 105° for 2 hr. An odor of hydrogen bromide was observed when the desiccator in which the sample was stored was opened; consequently, the sample was reheated to 50° under high vacuum for 6 hr. and again stored in a desiccator charged with P_2O_5 . No further evidence of HBr was detected. These crystals were identical in appearance with sample I ($CrBr_2$ preparation). Gravimetric analyses gave $64.33 \pm 0.06\%$ Br and $10.22 \pm 0.04\%$ K. This sample likewise gave results differing from sample I in the anomalous region. Measurements were made on this sample, however, over the whole temperature range in order to check other phenomena observed on sample I. Results on this third sample will be discussed below.

The weight of sample I introduced into the calorimeter was 136.778 g. (*in vacuo*⁸), which represents 0.18387 mole based upon 743.86 as the molecular weight.⁹ One atmosphere pressure of helium was added to aid rapid thermal equilibrium.

Apparatus and Temperature Scale. The cryostat is similar to that described by Westrum, Hatcher, and Osborne,¹⁰ and later modified by Osborne and Westrum¹¹ except for the following details. An evacuated metal dewar is employed in place of the outer radiation shield. The radiation shields are fastened to their respective refrigerant tanks by machined threaded joints, which are greased with Apiezon N to improve heat transfer. The upper and lower tanks (each of 1-l. capacity) and their radiation shields

are 2-mm. copper, nickel-plated and polished on the outer surfaces. The helium economizer is a helix 9 cm. in diameter having 18 turns of 6-mm. o.d. copper tubing.

The adiabatic shield is made of 1-mm. gold-plated copper in the form of two hemispherical sections at the top and bottom, and a cylindrical center section. The end sections are held in thermal contact with the center section by screws. Each section is provided with appropriate differential thermocouples and heater. All lead wires (B. and S. No. 36 Teflon-covered copper) entering the cryostat are thermally anchored with G.E. 7031 adhesive to the components in the following order: upper tank, helium economizer (18 turns), lower tank, floating ring (approximately four turns), and adiabatic shield (three turns in a spiral groove on the outside of the center section of the shield).

The calorimeter is of copper, gold-plated and polished on the exterior surface. The top and bottom are spun copper hemispheres of 38-mm. diameter. The top is provided with a filling port of thin-wall Inconel tubing which may be closed by soldering a small copper cap. A small hole in the latter permits evacuation and introduction of helium exchange gas and is readily closed by a small amount of solder. The bottom of the calorimeter has a tubular copper re-entrant well which receives the heater tube and platinum resistance thermometer. The copper heater tube is wound bifilarly with 200 ohms of B. and S. No. 40 double silk-covered Advance wire, cemented in place with G.E. 7031 adhesive. The capsule-type platinum resistance thermometer (25.5 ohms at 0°) fits snugly inside the heater tube. Good thermal contact between thermometer, heater, and re-entrant well is established with a weighed amount of Apiezon N grease. Eight copper vanes soldered to the re-entrant well and side of the calorimeter are spaced radially about the former to facilitate heat transfer within the calorimeter. The differential thermocouple between the calorimeter and adiabatic shield is attached with a small copper nut to a bolt soldered to the side of the calorimeter. Provision for cooling the calorimeter and adiabatic shield is described adequately elsewhere.^{10,11} The calorimeter, including heater and thermometer, weighs 57 g. and has a capacity of 65 ml.

The temperature scale is that given by a Leeds and

(8) The density of K_2ReBr_6 was determined to be 4.14 g./ml. at 25°. The density from crystallographic data is 4.34 g./ml.

(9) A. E. Cameron and E. Wichers, *J. Am. Chem. Soc.*, **84**, 4175 (1962).

(10) E. F. Westrum, Jr., J. B. Hatcher, and D. W. Osborne, *J. Chem. Phys.*, **21**, 419 (1953).

(11) D. W. Osborne and E. F. Westrum, Jr., *ibid.*, **21**, 1884 (1953).

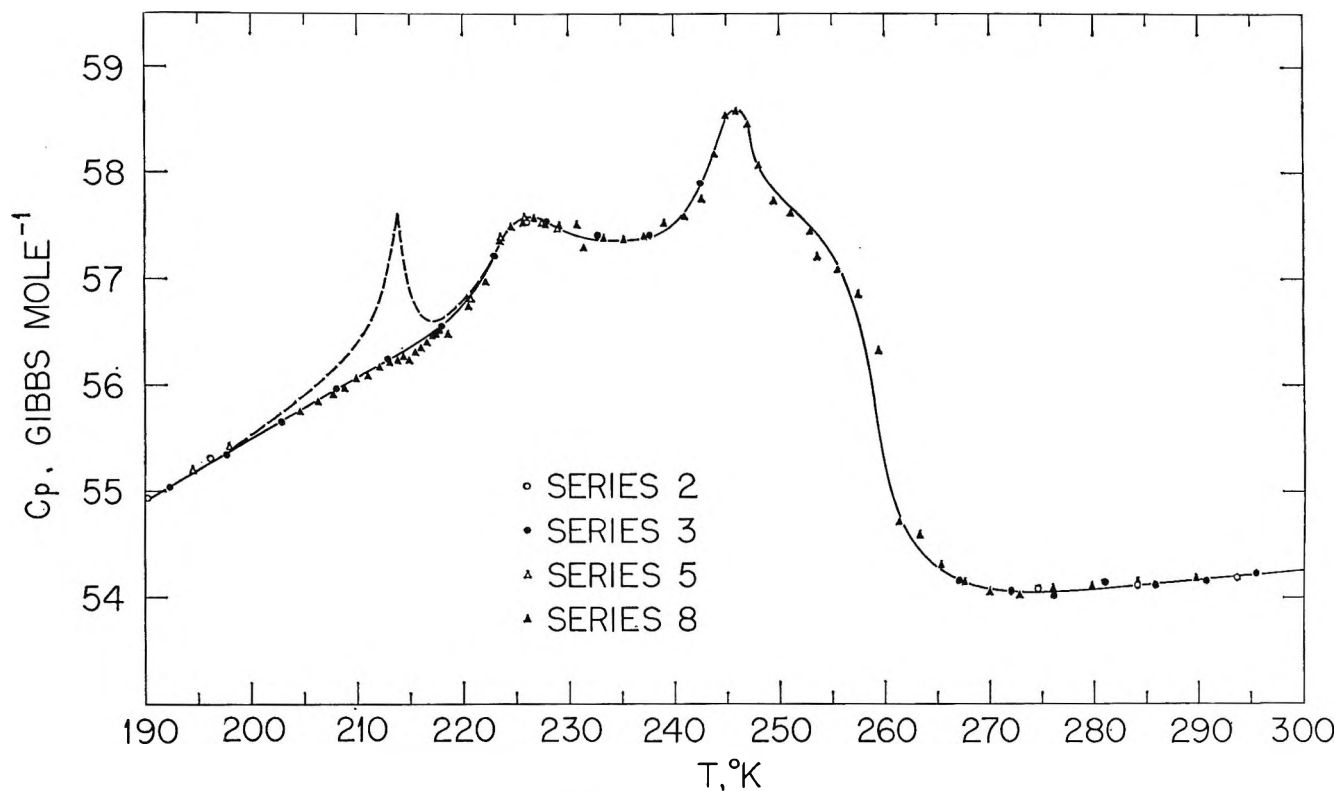


Figure 1. Anomalous behavior of the heat capacity of K_2ReBr_6 above $200^\circ K$, which arises from crystal structure changes from a K_2PtCl_6 -type cubic structure above approximately $270^\circ K$, to a lower symmetry crystal structure below the anomalous region. The size of the anomaly with a maximum at approximately $214^\circ K$ (dotted curve) depends upon the thermal history of the sample and disappears after a sufficient number of coolings to low temperatures. See text for explanation of series.

Table III: Excess Heat Content in 205 to $220^\circ K$. Region

Series	T_1	T_2	ΔH_{meas} , cal. mole $^{-1}$	$\int C_p dT$, cal. mole $^{-1}$	Δ (excess)
2	198.913	204.623	318.05	317.48	0.57
2	204.623	210.811	347.48	346.20	1.28
2	210.811	216.921	347.52	344.01	3.51
2	216.920	223.001	345.44	345.33	0.11
Total excess heat content					5.47
$\Delta H(\text{excess})$ at $T < 199$					0.12
					5.59
5	199.616	203.028	189.81	189.61	0.20
5	203.028	206.756	208.15	207.96	0.19
5	205.869	209.237	188.69	188.40	0.29
5	209.237	212.584	188.48	187.88	0.60
5	212.584	215.896	188.61	186.54	2.07
5	215.896	219.212	187.92	187.48	0.44
Total excess heat content					3.79

Difficulty was experienced in cooling the calorimeter to the lowest temperatures in series 4, which covered the temperature interval from 25 to $132^\circ K$. Following this series, the calorimeter was warmed to $151.5^\circ K$, where again spontaneous evolution of heat was ob-

served. The sample was allowed to stand at this temperature overnight to allow the heat evolution to go to completion. No further heat evolution was detectable the following morning. Series 5 measurements covering the temperature interval 152 to $229^\circ K$, were then made, which again exhibited the small anomaly at approximately 214° but reduced in size compared with measurements of series 2 (see Table III).

Between series 5 and 6, the sample was cooled to 100° , then warmed to $150^\circ K$, where spontaneous heat evolution was again observed, although much reduced in amount. Series 6 measurements revealed the heat capacity anomaly around $15^\circ K$. (Figure 2). Following this series, the sample was allowed to warm to room temperature.

A study of the rate of spontaneous heat evolution vs. the temperature was made by cooling the sample to 78° , then warming to $120^\circ K$, and observing the rate of heat evolution at several temperatures over the range 120 to $160^\circ K$. The total heat evolution was found to be reduced substantially compared to its first detection in the series 2 measurements, but the experiment showed that the maximum rate of heat evolution occurs at

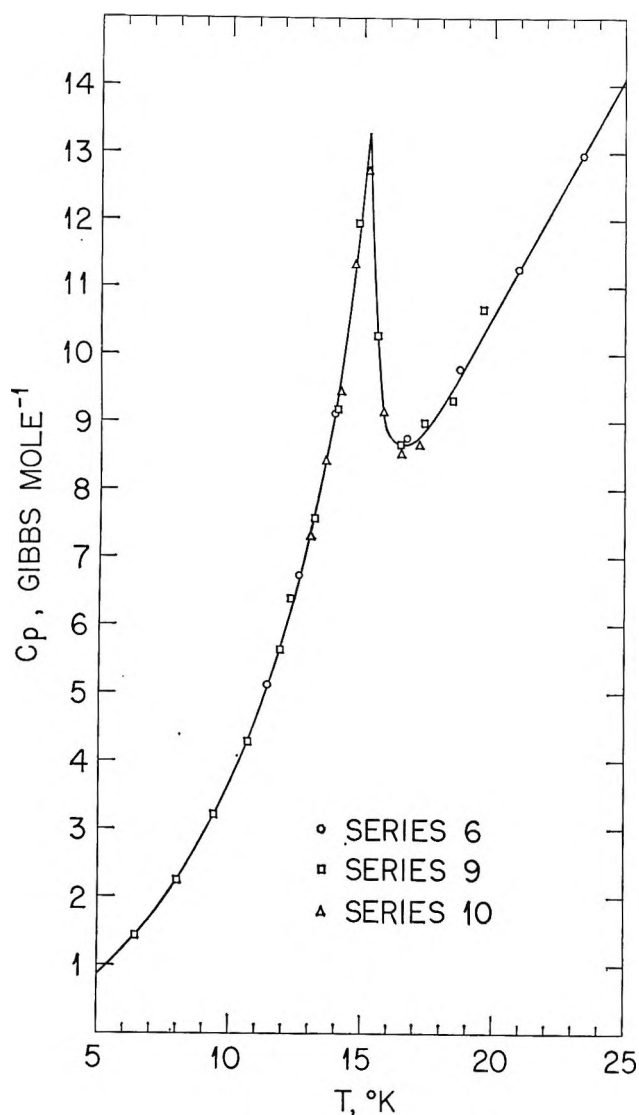


Figure 2. Cooperative transition of K_2ReBr_8 with heat capacity maximum at 15.25°K. The transition is from an ordered, antiferromagnetic state below 15.25°K. to the paramagnetic state above this temperature. See text for explanation of series.

148–149°K. The rate drops to zero approximately 10° to either side of this temperature. (Additional measurements on this effect were made on sample III and are discussed below.) The sample was allowed to stand overnight at 160°, cooled to 118°K. the next morning, and series 7 measurements were made over the temperature range 124 to 158°K. in which no heat evolution occurred.

The measurements of series 8 consisting of small temperature rise determinations were made to characterize the detail shape of the heat capacity curve above 200°K. Series 9 and 10 do the same for the anomaly around 15°K. Results of these measurements are pre-

sented graphically in Figures 1 and 2. Virtually no heat evolution was observed when the sample was warmed to 150°K. following the series 10 measurements; in addition, a series of heat capacity measurements from 190 to 225°K., which are not tabulated, yielded results only 0.2–0.3% above the solid smooth curve of Figure 1, indicating the anomaly around 214° had essentially disappeared.

The smooth heat capacity curve for the temperature region above 200°K. shown in Figure 1 was established by adjusting slightly a preliminary curve, drawn through the small temperature rise determinations, to make the final curve agree with the more accurate normal temperature rise determinations of series 2 and 3. The latter determinations are given in Table II, in which columns 2 and 3 give the temperature interval covered by a determination made in the series given in column 1, column 4 gives the measured heat content over this interval, and column 5 gives the heat content for the same interval obtained by integration of the smooth curve. The agreement, columns 6 and 7, is satisfactory. Also given in Table II is a single heat content measurement made in series 6, which spans the maximum in the heat capacity anomaly shown in Figure 2.

Reference has been made above (series 2, 3, and 5) to a heat capacity anomaly centered at approximately 214°K. which decreased with subsequent coolings to low temperatures. A study of the thermal history of the sample clearly demonstrated that this anomaly was related to the spontaneous heat evolution phenomenon observed around 150°K. The anomaly was observed only when the sample had been cooled to approximately 150°K. and held at this temperature to allow heat evolution to occur. Both the heat evolution and the 214°K. anomaly were reduced in magnitude with subsequent coolings. The dotted portion of the curve in Figure 1 agrees with the observed heat content for the temperature interval 198.913 to 223.001°K. (series 2 measurements given in Table III) to 0.05%, but only approximates the shape of the anomaly which was estimated from the measurements of both series 2 and 5 and results on sample III.

The excess heat content associated with this anomaly is given in Table III in which column 4 gives the observed heat content over the temperature interval given in columns 2 and 3, and column 5 gives the heat content for the same interval obtained by integration of the solid curve. The excess heat content for the intervals and their sum is given in the last column. Thus the excess heat absorption was 5.6 cal. mole⁻¹ in series 2 (in which series the spontaneous heat evolution at 150°K. was not quite completed) and 3.8 cal.

mole⁻¹ in series 5. Since the series 2 measurements followed the second cooling to 150° and series 5 followed the third such cooling, the excess heat following the first cooling to this temperature in series 1 measurements could have been 7 to 10 cal. mole⁻¹. The maximum entropy associated with this anomaly was thus <0.05 gibbs mole⁻¹ and dropped to an insignificant amount after several coolings to 150°K.

Visual examination of the sample after completion of the measurements showed no change in particle size or color, nor was there any evidence of chemical attack in the calorimeter. Other materials measured have not shown this behavior, and there is no reason to suspect the calorimetric apparatus.

Results on Sample III. No detailed heat capacity results are tabulated for sample III. Analytical results indicated its purity to be inferior to that of sample I, and the observed differences in the thermodynamic properties of the two samples are attributed to this. Agreement between the heat capacities of the two samples was obtained below 20°, but at 40°, sample III gave results 0.5% lower than sample I, and at 200°K. the difference had increased to 2%. Above 200°K. both samples exhibited a rise to a maximum heat capacity around 250° followed by a rather abrupt drop giving a minimum at approximately 275°K., but the two heat capacity curves in this region differed in details. Details of the heat capacity in this region are presumably much influenced by sample purity.

Being forewarned by the results on sample I of the likely spontaneous evolution of heat near 150°K., it was possible to obtain a good measurement of the total heat evolved on the first cooling of sample III to this temperature. The sample was cooled rapidly through the region of 150° (0.65° min.⁻¹) to liquid nitrogen temperatures, then warmed to 140° at which temperature no spontaneous heat evolution was detected. The sample was then heated to 148.6°K., at which temperature there is maximum rate of spontaneous heat evolution. The rate of heat evolution *vs.* time was derived from the rate of temperature rise of the calorimeter under adiabatic control. The measurements were made over a 2-hr. period, at the end of which time the heat evolution had become insignificant. The result was 4.0 ± 0.3 cal. mole⁻¹ for the total heat spontaneously evolved, a result which includes a correction for the heat evolved in cooling through the 150°K. region before warming back up to this temperature.

Heat capacity measurements in the 200 to 220°K. temperature interval following the above spontaneous heat evolution showed the 214°K. anomaly. The

Table IV: Thermodynamic Properties of K₂ReBr₆ (gibbs mole⁻¹)

T_{av} , °K.	C_p°	S°	$H^\circ - H^\circ_0$	$F^\circ - H^\circ_0$
			T	T
5	0.82	0.308	0.230	0.078
10	3.68	1.630	1.150	0.480
12.5	6.51	2.726	1.914	0.812
15	12.34	4.342	3.087	1.255
15.25	13.40	4.554	3.247	1.307
16	8.81	5.040	3.574	1.466
17	8.71	5.566	3.875	1.691
20	10.59	7.117	4.728	2.389
25	14.07	9.854	6.318	3.536
30	17.56	12.716	7.889	4.827
35	20.96	15.680	9.515	6.165
40	24.05	18.684	11.142	7.542
45	26.90	21.684	12.736	8.948
50	29.56	24.658	14.288	10.370
60	34.17	30.467	17.228	13.239
70	37.98	36.031	19.930	16.101
80	41.11	41.313	22.388	18.925
90	43.66	46.309	24.616	21.693
100	45.64	51.014	26.622	24.392
110	47.33	55.445	28.429	27.016
120	48.78	59.627	30.066	29.561
130	50.04	63.581	31.554	32.027
140	51.17	67.331	32.915	34.416
150	52.11	70.894	34.165	36.729
160	52.88	74.283	35.301	38.982
170	53.60	77.511	36.366	41.145
180	54.29	80.594	37.343	43.251
190	54.91	83.546	38.252	45.294
200	55.50	86.378	39.099	47.279
210	56.14	89.100	39.894	49.206
220	56.76	91.722	40.644	51.078
225	57.54	93.006	41.010	51.996
230	57.43	94.270	41.369	52.901
235	57.36	95.504	41.710	53.794
240	57.52	96.712	42.037	54.675
245	58.53	97.907	42.362	55.545
246	58.58	98.145	42.428	55.717
250	57.79	99.084	42.680	56.404
255	57.24	100.22	42.97	57.25
260	55.23	101.32	43.23	58.09
265	54.27	102.36	43.44	58.92
270	54.08	103.37	43.64	59.73
273.15	54.05	104.00	43.76	60.24
280	54.08	105.34	44.02	61.32
290	54.17	107.24	44.36	62.87
298.15	54.24	108.74	44.63	64.11
300	54.27	109.08	44.69	64.38
310	54.37	110.86	45.00	65.85

excess heat content associated with this anomaly, calculated in the manner described above for sample I, was 11.40 cal. mole⁻¹. Following a second cooling and spontaneous heat evolution near 150°, this excess heat content was reduced to 8.40 cal. mole⁻¹.

After completion of the heat capacity studies, an experiment was made to determine if any visible color change occurs when K_2ReBr_6 is cooled to low temperatures. A sample was observed to undergo a color change from a reddish purple (color at room temperature) to an orange color over the temperature interval 150 to 130°K. The color change was reversible and readily observed.

Thermodynamic Properties of K_2ReBr_6 . Smoothed values of the thermodynamic properties obtained from large scale graphs are given in Table IV. Because of the cooperative transition with a heat capacity maximum at 15.25°K., extrapolation of the heat capacity to 0°K. utilizing the Debye T^3 law is more uncertain than usual. The estimated entropy at 7°K. is 0.742 ± 0.07 gibbs mole⁻¹. The smoothed heat capacities are believed to be accurate to 5% below 15°, to 1% at 25°, and to 0.2% above 40° except in the anomalous region above 200°K. where the values may be in error by 2%. The entropy at 298.15°K. should be accurate to 0.5%, *i.e.*, 108.74 ± 0.50 gibbs mole⁻¹. The values of entropy and free energy given in Table IV do not include the contributions from nuclear spin or isotope mixing and are therefore the conventional ones to be used in calculations of chemical equilibria.

Discussion

Antiferromagnetic Anomaly at 15.25°K. The magnetic susceptibility *vs.* temperature data³ of K_2ReBr_6 clearly demonstrate that the typical cooperative transition with a heat capacity maximum at 15.25°K. (Figure 2) is a transition from a paramagnetic state to an ordered antiferromagnetic state below this temperature. The magnetic entropy of K_2ReBr_6 at high temperatures is $R \ln 4 = 2.75$ gibbs mole⁻¹ corresponding to three unpaired spins. The magnetic entropy has most certainly reached this value below 100°K., which leads to the conclusion that the anomalous behavior of the heat capacity above 200°K. is not magnetic in origin.

Dependence of the Heat Capacity on Thermal History, the 214°K. Anomaly. Morfee and Staveley¹⁴ have observed a dependence of the heat capacity of certain ammonium and alkali hexahalostannates on their thermal history.¹⁵ Repeated cooling of these salts to low temperatures resulted in a lowering of the heat capacity in the temperature region above approximately 150°K., the lowering amounting to about 4% at room temperature for K_2SnCl_6 . After a sufficient number of coolings to low temperatures, constant heat capacity results were obtained. It may be estimated from their data^{15,16} that the repeated coolings resulted in an entropy decrease between the initial and final

results of approximately 1.0 gibbs mole⁻¹ in the case of K_2SnCl_6 , or about 1% in the entropy at room temperature. By contrast, the corresponding decrease observed for K_2ReBr_6 is only ~ 0.05 gibbs mole⁻¹, after the ultimate disappearance of the 214°K. anomaly which covers a temperature range of only 20°. Heat capacity results outside this rather narrow temperature region appeared to be independent of the thermal history. The experimental data presented above clearly demonstrate that this transition is exceedingly sluggish on cooling, the excess heat associated with the transition not appearing until the sample has been cooled approximately 65° below the transition region. Equilibrium is rapid, however, in warming through the transition region.

Considerable detail has been given on this anomalous behavior of K_2ReBr_6 because of its uniqueness. It may be that the phenomenon described arises because a low concentration of a metastable crystalline phase (which exhibits a transition in the region of 214°K.) is formed when the compound is crystallized from hydrobromic acid solution. As will be discussed below, the remaining anomalous behavior, which persists above 200°K. after repeated coolings, represents a change (or changes) in the crystal structure of the compound from that stable at room temperature. It is this crystal structure change which could provide the mechanism by which this metastable phase could be "annealed out" of the sample. In cooling through the region 270 to 150°K., the ions in the crystals undergo movements or shifts to the configuration stable at lower temperatures, and these movements could anneal the sample, provided a sufficient number of coolings were made, in much the same way as thermal motion of the atoms at higher temperatures anneals a material.

Morfee and Staveley¹⁴ suggest that the thermal history behavior exhibited by certain hexahalostannate salts may arise because the crystals are formed with a higher concentration of defects (Frenkel) than they eventually possess when equilibrium has been achieved. Such defects, they point out, should affect the heat capacity through an enhanced ($C_p - C_v$) term and by altering the vibrational energy levels of certain of the octahedral ions which are perturbed by neighboring

(14) R. G. S. Morfee and L. A. K. Staveley, *Nature*, **180**, 1246 (1957).

(15) D. H. Parkinson, F. E. Simon, and F. H. Spedding (*Proc. Roy. Soc. (London)*, **A207**, 137 (1951)) have also observed a dependence of the heat capacity of Ce metal on its thermal history. The phenomena observed, which are attributed to a transition of the 4f electron to a 5d state, cannot be related to those observed in K_2ReBr_6 and the hexahalostannates if the $4f \rightleftharpoons 5d$ transition explanation is correct since the tin in the complexes has no 4f electrons and in the Re^{+4} the 4f shell is filled.

(16) R. G. S. Morfee, L. A. K. Staveley, S. T. Walters, and D. L. Wigley, *J. Phys. Chem. Solids*, **13**, 132 (1960).

defects. It should be pointed out, however, that the latter effect of the defects must be quite small as shown by the following considerations. In the face-centered cubic structure (O_h^6 -Fm3m) stable at room temperature for these salts, the octahedral ions are in O_h site symmetry.¹⁷ The introduction of Frenkel defects (assumed to be cation interstitials and cation vacancies) will result in a lowering of the site symmetry of those octahedral ions surrounding the interstitials or vacancies from O_h to some lower symmetry. The lower site symmetry will cause the degeneracy of certain of the normal modes of vibration of the octahedral ions to be partially or completely removed depending on the new site symmetry. An estimate of the magnitude of this splitting, which is of the order of a few per cent¹⁸ (0–10%), may be obtained from the observed spectra of polyatomic anions in various salts where the same ion is in different site symmetries. Using the fundamental vibrations of $\text{SnCl}_6^{2-}(\text{aq})$ ¹⁹ as an approximation of the energy levels of the ion in O_h site symmetry, it may be calculated that a symmetrical split of the energy levels (the most common case) gives an insignificant alteration in the vibrational entropy, and that a 10% maximum asymmetrical split gives ~ 0.1 gibbs mole⁻¹ change if at most a few per cent of the ions are assumed to be perturbed by defects.

It is possible to visualize how interstitial cation defects in crystals of K_2ReBr_6 could be located in a potential well with a single minimum below $\sim 214^\circ\text{K}$. and with double or triple minima above this temperature, giving rise to a cooperative transition. The development of a degeneracy for the position of a defect cation could result from the structural changes (see below) which occur over this temperature region. The ultimate disappearance of the anomaly could result from the defects being annealed out in the manner described above in the discussion of the "metastable phase." That the 214°K . anomaly is due to cation defects appears to be unlikely, however, because of the estimated relatively high concentration of defects that would be required. If the anomaly is assumed to be a cooperative transition with an entropy of $R \ln n$, then any reasonable value of n gives the concentration of the defects to be 2 to 3%, calculated from the observed 0.05 gibbs mole⁻¹ excess entropy. Although very little is known about defects in salts of this type, such concentrations seem to be much too great. The disappearance of such a high concentration of defects based upon the disappearance of the 214°K . anomaly would also be expected to be accompanied by a significant change in the heat capacity outside this anomalous region, a result which is not observed.

Anomalous Behavior of the Heat Capacity above 200°K.

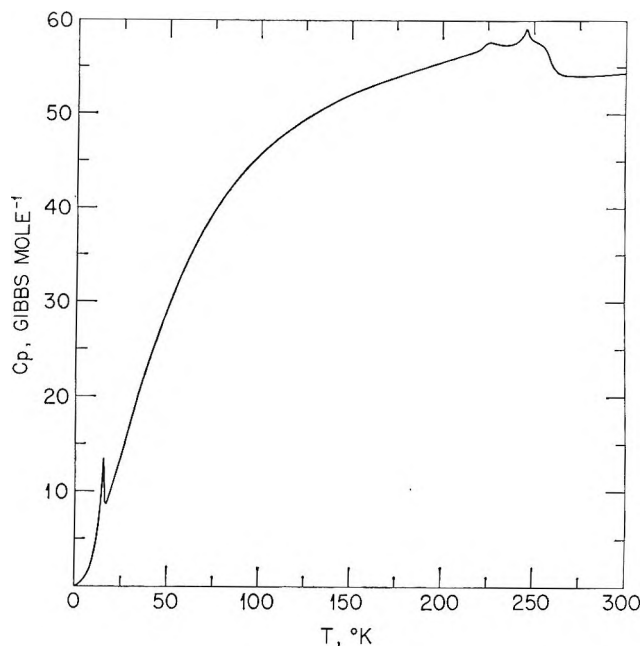


Figure 3. Heat capacity of K_2ReBr_6 showing the anomalies in relation to the remainder of the heat capacity curve.

Examination of the heat capacity curve for K_2ReBr_6 given in Figure 3 reveals that the transitions with heat capacity maxima at 226 and 246°K . could have their beginning around 100°K . as is shown by an attempt to join smoothly the heat capacity above 270° with that at lower temperatures. However, such a procedure for estimating the entropy of a transition, or the temperature interval which the transition covers, has an implicit assumption that the heat capacity of the crystals above the anomalous region is a simple extrapolation of the heat capacity below the transition. Although this may be a good assumption for magnetic or electronic excitation (Schottky transition) anomalies, it may not be so for a transition arising from a structural change. The anomalous behavior of the heat capacity of K_2ReBr_6 above 200°K . and that shown by certain of the hexahalostannate salts do arise from structural changes as shown below. In the absence of any knowledge of the transition entropies involved, the heat capacity data on K_2ReBr_6 , K_2SnCl_6 , and $(\text{NH}_4)_2\text{SnBr}_6$ are not inconsistent with the hypothesis that the

(17) "International Tables for X-Ray Crystallography," Vol. I, Kynoch Press, Birmingham, England, 1952, p. 338.

(18) See, e.g., R. S. Krishnan, *Proc. Indian Acad. Sci.*, **23A**, 288 (1946); F. A. Miller and C. H. Wilkins, *Anal. Chem.*, **24**, 1253 (1952); R. H. Busey and O. L. Keller, Jr., *J. Chem. Phys.*, **41**, 215 (1964); M. Hass and G. B. B. M. Sutherland, *Proc. Roy. Soc. (London)*, **A236**, 427 (1956).

(19) J. Hiraiishi, I. Nakagawa, and T. Shimanouchi, *Spectrochim. Acta*, **20**, 819 (1964).

heat capacity of the lower symmetry crystal phase exceeds that of the cubic phase, both extrapolated to the anomalous region.

Evidence, in addition to the existence of two maxima, that the heat capacity above 200° represents multiple transitions is furnished by the pure quadrupole resonance work of Ikeda, Nakamura, and Kubo.²⁰ They state that the resonance frequency measurements of ⁷⁹Br in K₂ReBr₆ carried out between room and Dry Ice temperatures revealed the existence of three transition points at about 269, 257, and 246°K. At room temperature, a single resonance line for ⁷⁹Br was observed, indicating that all the bromines in the unit cell of the crystal are crystallographically equivalent in conformity with the observed cubic structure. Below 270°K. more than a single resonance line appears showing that a reduction in the symmetry of the crystal has occurred giving rise to two or more nonequivalent bromine atoms in the unit cell of the crystal. These data together with the heat capacity data show unequivocally that the crystal structure of K₂ReBr₆ changes from the K₂PtCl₆-type cubic structure above ~270°K. to a less symmetrical structure below this temperature.

Nakamura, Kubo, and co-workers²¹ have observed the pure quadrupole resonance of halogens in many A₂MX₆ octahedral complexes from room temperature to liquid nitrogen temperatures, with the main objective being to make a quantitative estimation of the covalent character of M-X bonds in these complexes. Of the 35 octahedral complexes examined, over one-fourth of them were observed to undergo at least one transition below room temperature; two salts, K₂-SeBr₆ and Rb₂TeI₆, in addition to K₂ReCl₆²² and K₂-ReBr₆, gave evidence of multiple transitions. These data show that the thermal behavior exhibited by K₂ReCl₆, K₂ReBr₆, and certain hexahalostannates is not uncommon among complex salts containing large octahedral anions. The transitions exhibited by these compounds are most likely displacive transitions in the sense defined by Buerger.²³

An interesting correlation for crystals containing octahedral anions and univalent cations has recently been made by Brown.²⁴ The correlation is between the crystal structure and the radius ratio, the latter being defined as the ratio of the cation radius to the radius of the cavity (formed by twelve halogens from four octahedral anions in the K₂PtCl₆-type cubic structure) in which the cation resides. It is assumed that if the cation is very much smaller than the cavity into which it fits, the anions will reorient themselves in such a way as to reduce the effective size of the cavity and thus lock the cation in place. From observations of the

crystal structure behavior of many such crystals, Brown gives the following correlations: (1) crystals with a radius ratio of less than about 0.89 are distorted from the cubic structure at room temperature; (2) crystals with radius ratios between about 0.89 and 0.98 are cubic at room temperature but distort at lower temperatures; (3) crystals with radius ratios >0.98 would not be expected to distort at any temperature. From the crystal structure data⁵ on K₂ReBr₆, the radius ratio is computed to be 0.91. Thus the crystal would be expected from the above correlations to distort from the cubic structure at a temperature a little below room temperature, which is observed. Similarly for K₂ReCl₆, the radius ratio is computed to be 0.97 which suggests that the crystal should distort from the cubic structure at a lower temperature than the K₂ReBr₆, as indeed it does at ~110°K.²

The deductions from the radius ratios computed for the six hexahalostannates, whose thermal properties were observed by Morfee, *et al.*,¹⁶ agree with the heat capacity results in that K₂SnCl₆, (NH₄)₂SnBr₆, and Rb₂SnBr₆ should exhibit transitions below room temperature (distort), and Rb₂SnCl₆, (NH₄)₂SnCl₆, and K₂SnBr₆²⁵ should not. The anomalies in the heat capacities of the first three salts most likely result from structural changes. Nakamura, *et al.*,²⁶ have observed the pure quadrupole resonance spectra of K₂SnBr₆ and (NH₄)₂SnBr₆. K₂SnBr₆ shows three resonance lines at all temperatures consistent with the tetragonal structure,²⁵ but the data on (NH₄)₂SnBr₆ relative to a structural change are inconclusive in that a single line was observed at room and Dry Ice temperatures, but no resonance line was observed at liquid nitrogen temperatures. Similar data on K₂SnCl₆ and Rb₂-SnCl₆ might confirm that the heat capacity anomalies observed are structural changes.

(20) R. Ikeda, D. Nakamura, and M. Kubo, *Bull. Chem. Soc. Japan*, **36**, 1056 (1963).

(21) D. Nakamura and M. Kubo, *J. Phys. Chem.*, **68**, 2986 (1964), and references quoted therein to their previous work.

(22) Recent neutron diffraction measurements on K₂ReCl₆ by H. G. Smith of this laboratory (*Acta Cryst.*, **16**, A187 (1963)) confirm a change in the space group from O_h⁵-Fm3m at room temperature to a space group of lower symmetry, although still cubic, below 77°K. Anomalies in the thermal expansion were observed accompanying the heat capacity anomalies.

(23) M. J. Buerger, "Phase Transformations in Solids," R. Smoluchowski, Ed., John Wiley and Sons, Inc., New York, N. Y., 1951, Chapter 6.

(24) I. D. Brown, *Can. J. Chem.*, **42**, 2758 (1964).

(25) K₂SnBr₆ is tetragonal at room temperature and becomes cubic at 400°K. (E. E. Galloni, M. R. DeBenyacar, and M. J. DeAbeledo, *Z. Krist.*, **117**, 407 (1962)).

(26) D. Nakamura, K. Ito, and M. Kubo, *Inorg. Chem.*, **1**, 592 (1962).

Acknowledgment. We wish to thank Dr. J. G. Spencer for assisting with some of the measurements

and Mr. D. E. LaValle for preparation of the samples of K_2ReBr_6 .

Temperature Dependence of the Viscoelastic Behavior of Polystyrene

by Donald J. Plazek

Mellon Institute, Pittsburgh, Pennsylvania 15213 (Received April 26, 1965)

The creep and recovery behavior of a narrow molecular weight distribution polystyrene sample was measured from 97.0 to 160°. Measurements were carried out on this 46,900 molecular weight sample in a creep apparatus that employs a magnetically levitated rotor in which constant torques are induced by means of a drag cup motor. Creep compliances measured extend from 10^{-10} to above 10^{-4} cm.²/dyne. Simple superposition of the results to obtain a reduced master curve was not possible because the viscous flow contributing to the total measured compliance had a different temperature dependence from that of the recoverable compliance. The recoverable compliance results by themselves were reducible. The temperature dependences obtained were analyzed in terms of free volume parameters.

Introduction

In 1941, Leaderman made the observation that the creep compliance curves obtained on a polymeric material at different temperatures had the same shape and differed only in their positions on the logarithmic time scale.^{1a} Tobolsky and Andrews in 1945 were the first to make use of this time-temperature superposition principle in constructing "master" curves over an enhanced time scale range with their stress relaxation data introducing at the same time the required rubber-like vertical or amplitude shift for amorphous polymers.^{1b} The underlying assumptions for the successful application of reduced variables to linear viscoelastic phenomena were further developed by Ferry in 1950.^{1c} Since then many reduced "master" curves for polymeric materials have appeared in the literature. In some of these cases, it will be shown that the application of simple reduction principles was not appropriate although it appeared successful. In a number of other studies²⁻⁵ it was found that simple reduction failed, but with the exception of the methacrylate polymers^{2,3} the viscoelastic response of amorphous polymers and their

solutions have apparently proved to be reducible. The "master" curves have importance because the complete characterization of the time-dependent behavior requires description over the entire time scale. In practice, the reduced curves come the closest to fulfilling this requirement. In addition, the temperature dependence of the viscoelastic mechanisms is a by-product of the determination of such curves. For simple temperature reduction to be possible, all of the contributing viscoelastic mechanisms must have the same temperature dependence.

In the study reported here, the creep behavior of an anionically polymerized sample of polystyrene was

(1) (a) H. Leaderman, *Textile Res. J.*, **11**, 171 (1941); (b) A. V. Tobolsky and R. D. Andrews, *J. Chem. Phys.*, **13**, 3 (1945); (c) J. D. Ferry, *J. Am. Chem. Soc.*, **72**, 3746 (1950).

(2) J. D. Ferry, W. C. Child, Jr., R. Zand, D. M. Stern, M. L. Williams, and R. F. Landel, *J. Colloid Sci.*, **12**, 53 (1957).

(3) J. W. Berge, P. R. Saunder, and J. D. Ferry, *ibid.*, **14**, 135 (1959).

(4) E. Catsiff, J. Offenbach, and A. V. Tobolsky, *ibid.*, **11**, 48 (1956).

(5) H. Nakayasu, H. Markovitz, and D. J. Plazek, *Trans. Soc. Rheol.*, **5**, 261 (1961).

extensively measured at temperatures from 97°, one degree below its conventional glass temperature, T_g , to 160°.

Experimental Section

Materials. The polystyrene studied was prepared⁶ by anionic means *in vacuo* with butyllithium as the catalyst.⁷ The resulting whole polymer was subsequently fractionated⁶ by means of the conventional cocervation technique with methyl ethyl ketone as the solvent and methyl alcohol as the nonsolvent. From the fractionation results a ratio of weight-to-number-average molecular weight, \bar{M}_w/\bar{M}_n , was calculated to be 1.047. Three of the fractionation cuts with intrinsic viscosities that appeared to be within 0.5% of one another were mixed in solution and freeze dried from benzene. The three fractions represented that part from 25–64% of the whole sample. The Flory temperature intrinsic viscosity, $[\eta]_f$, for the combination was determined⁸ in cyclohexane at 34.5° to be 0.184. It is believed that \bar{M}_w/\bar{M}_n for the combined central fractions is about 1.01.

A molecular weight of 46,900 was calculated from $[\eta]_f$ using the expression⁹ $[\eta]_f = 8.5 \times 10^{-4} M^{0.5}$. The relation $[\eta]_f = 0.44 [\eta]_{\text{benzene}}^{0.667}$ was used to obtain the corresponding intrinsic viscosity in benzene at 30° so that a molecular weight of 45,300 could be obtained from the Ewart and Tingey relation¹⁰ for comparison with earlier characterization measurements in the literature.

Reagent grade cyclohexane was dried overnight over calcium sulfate, filtered, and distilled under N_2 through a packed column designed to 80 theoretical plates at total reflux. The central fraction which distilled at a constant temperature and had been stored in a dark bottle under N_2 was used in the intrinsic viscosity determination.

Method. Torsional creep and creep recovery measurements were made with an instrument that contained a magnetically suspended rotor. The electronic feedback circuit employed to achieve stable suspension was developed by Dr. Victor MacCosham.¹¹ Constant torques were induced in the rotor by means of a drag cup motor, and angles reflecting the torsional deformation in the cylindrical samples were monitored with a light lever and a Beckman photopen recorder modified to obtain a range of chart speeds from 30 to 960 in./hr. Temperatures were held constant to within 0.05° with a silicone oil bath (Dow Corning 550). Cylindrically shaped samples, 0.64 cm. in diameter and about 0.64 cm. high, were prepared in a vacuum mold at about 150°.

Samples that were measured were visible at all times

through a pair of mutually perpendicular flat glass windows in the sample housing of the instrument and corresponding windows in the stainless steel thermostat. Sample heights were measured optically to within a few microns with a Gaertner traveling microscope equipped with a relay lens system to yield 50 power at a working distance of 19 cm. Sample coefficients, j/h , where j is the second moment of the cross-sectional area and h is the height of the right circular cylinder, were calculated from the expression $m^2/2\pi\rho^2h^3$, where m is the mass of the sample and ρ is

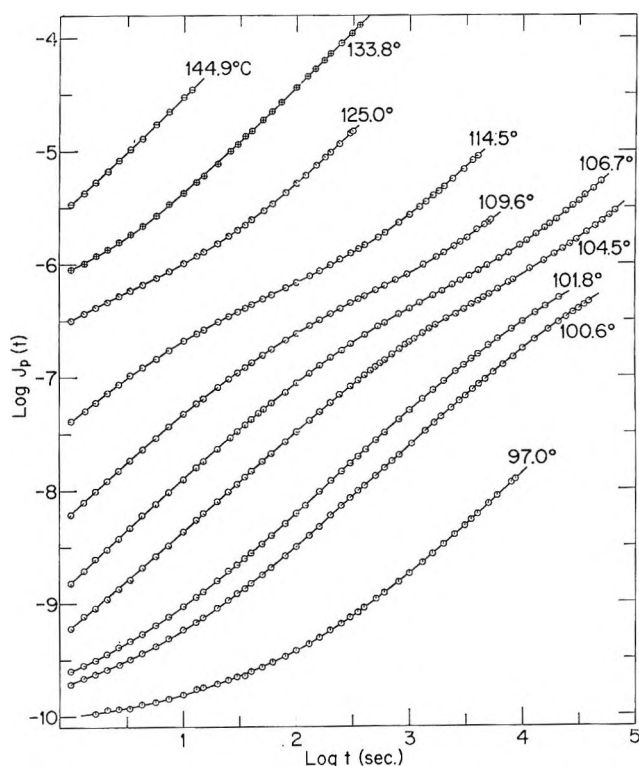


Figure 1. The creep compliance $J_p(t)$, cm.²/dyne, of polystyrene, $M_w = 46,900$, plotted logarithmically against the time, sec. Temperatures of measurement are indicated. Subscript p indicates amplitude adjustment for the temperature dependence of the rubberlike nature of the response.

(6) This sample was prepared and purified by Timothy Altares, Jr. Its fractionation was carried out by Marguerite Fulton.

(7) (a) D. J. Worsfold and S. Bywater, *Can. J. Chem.*, **38**, 1894 (1960); (b) F. Wenger and S.-P. S. Yen, *Makromol. Chem.*, **43**, 1 (1961).

(8) This measurement was made by Elizabeth Frommell.

(9) T. Altares, Jr., D. P. Wymann, and V. R. Allen, *J. Polymer Sci.*, **A2**, 4533 (1964).

(10) R. H. Ewart and H. C. Tingey, paper presented at the 111th National Meeting of the American Chemical Society, Atlantic City, N. J., 1947.

(11) V. J. MacCosham, "Conference on the Ultracentrifuge," Academic Press Inc., New York, N. Y., 1963, p. 249.

its density (g./cm.³) at the temperature of measurement. Creep compliances, $J(t)$, cm.²/dyne, were computed from $j\alpha/h\tau$. The angle of twist, α , is measured, and the applied torque, τ , dyne-cm., is known from a previous calibration. Densities were calculated using $1/\rho = 0.767 + 5.5 \times 10^{-4}T + 643 \times 10^{-4} T/M$, T is in °K.¹²

Results and Analysis

The creep compliance results obtained are logarithmically plotted as a function of the logarithm of the time, t in seconds, in Figure 1 as $J_p(t) = (T\rho/T_0\rho_0)J(t)$, cm.² dyne, where ρ is the density at the temperature, $T^\circ\text{K}$., of measurement and ρ_0 is the density at the reference temperature, T_0 , 373.2°K. The vertical adjustment $T\rho/T_0\rho_0$ takes into account the temperature dependence of rubberlike nature of the response. Measurements were made from 97.0 to 160.0°. At 160° the response was experimentally entirely viscous in nature and therefore is not shown in this compliance plot. Most of the curves are composites of two or three runs. Besides two separate installations, *in situ* manipulations of the sample shape along with the use of torques which varied from 75 to 3,450 dynes/cm. were necessary to measure accurately the millionfold change in compliance. At compliances less than 10^{-8} cm.²/dyne the sample had to be drawn into a longer thin cylinder (diameter ≈ 0.2 cm., height ≈ 2 cm.). Sample drawing was carried out at 145° where most of the deformation was viscous. The sample was allowed to relax at the high temperature for about 0.5 hr. to eliminate orientation in the sample. Upon removal of the drawn-out sample from the instrument at room temperature, inspection in a polarizing microscope revealed no perceptible birefringence and hence negligible orientation in the central highly elongated section. A trace of birefringence at the ends of the sample was probably caused by the cooling to room temperature with the sample adhering to the stainless steel sample surfaces. Since the diameters of the drawn-out samples were not uniform, an empirical sample coefficient had to be determined by measuring and matching the level of compliance to a previously determined curve.

It can be seen in Figure 1 that the creep compliance of this 46,900 molecular weight polystyrene has been measured from that of glassy hardness, 10^{-10} cm.²/dyne, at 97.0° to that of a very viscous liquid at 145° and above. The conventional glass temperature, T_g , at this molecular weight is 97.7°,¹³ so that at 97.0° we can be confident that our period of thermostating, about 10 hr. before the start of the determination, ensured that the sample was at its equilibrium volume.

To make meaningful investigations at any temperature below a material's T_g , one must take pains to ascertain the volume of the sample at the time of measurement or at least record its thermal history.

Viscosities can be determined in four different ways. (1) After apparent steady-state flow is reached, the viscosity, η , can be calculated from the velocity of deformation. (2) Following a reasonably long creep run, the difference between the early parts of the creep and recovery portions of the run can be shown to be a measure of the viscous deformation through the application of Boltzmann superposition. (3) Determination can be made of the amount of permanent deformation produced during a creep run by waiting for complete recovery. An increase in temperature to speed the recovery is necessary if the creep run was longer than a few minutes or the recovery time becomes excessively long. (4) Ninomiya has shown¹⁴ that a plot of $(J(t)/t)(d \log J(t)/d \log t)$ vs. $1/t$ yields a relatively linear extrapolation to the intercept. This intercept is the limiting value of $dJ(t)/dt$ at infinite time, which is the reciprocal of the viscosity.

All four methods were used in obtaining the viscosities listed in Table I. According to the reduction principles,^{1c} if all of the contributing mechanisms have the same temperature dependence, all of the creep data should fall onto a single curve when $\log J_p(t)$ is plotted as a function of $\log [t\eta(T_0)/\eta_p(T)]$, where $\eta_p(T) = \eta(T)T_0\rho_0/T\rho$. ($a_T = \eta_p(T)/\eta(T_0) = \dot{J}_p(t)_{T_0}/\dot{J}_p(t)_T$ where $J_p(t)_{T_0} = J_p(t)_T$; dot denotes time derivative.)

Table I: Temperature Dependences^a

Graph symbols	$T^\circ\text{C}$.	$\log \eta_p$	$\log a_T, [\eta_p]$	$\log a_T, [J_p(t)-t/\eta_p]$	$T\rho/T_0\rho_0$
○	97.0	(12.353)	(0.81)	1.13	0.994
	100.0	(11.540)	0	0	1.000
⊙	100.6	(11.39)	(-0.15)	-0.22	1.001
⊖	101.8	(11.10)	(-0.44)	-0.585	1.004
⊙	104.5	10.503	-1.04	-1.385	1.010
⊙	106.7	10.039	-1.50	-1.96	1.014
⊙	109.5	9.474	-2.07	-2.58	1.020
⊙	114.5	8.680	-2.86	-3.49	1.031
⊙	125.0	7.345	-4.195	-4.87	1.052
⊙	133.8	6.435	-5.105	-5.67	1.070
⊖	144.9	5.523	-5.98	(-6.41)	1.093
	160.0	4.556	-6.98	(-7.13)	1.123

^a Quantities in parentheses have been calculated using equations given in text.

(12) T. G. Fox and S. Loshaek, *J. Polymer Sci.*, **15**, 371 (1955).

(13) T. G. Fox and P. J. Flory, *ibid.*, **14**, 315 (1954).

(14) K. Ninomiya, *J. Phys. Chem.*, **67**, 1152 (1963).

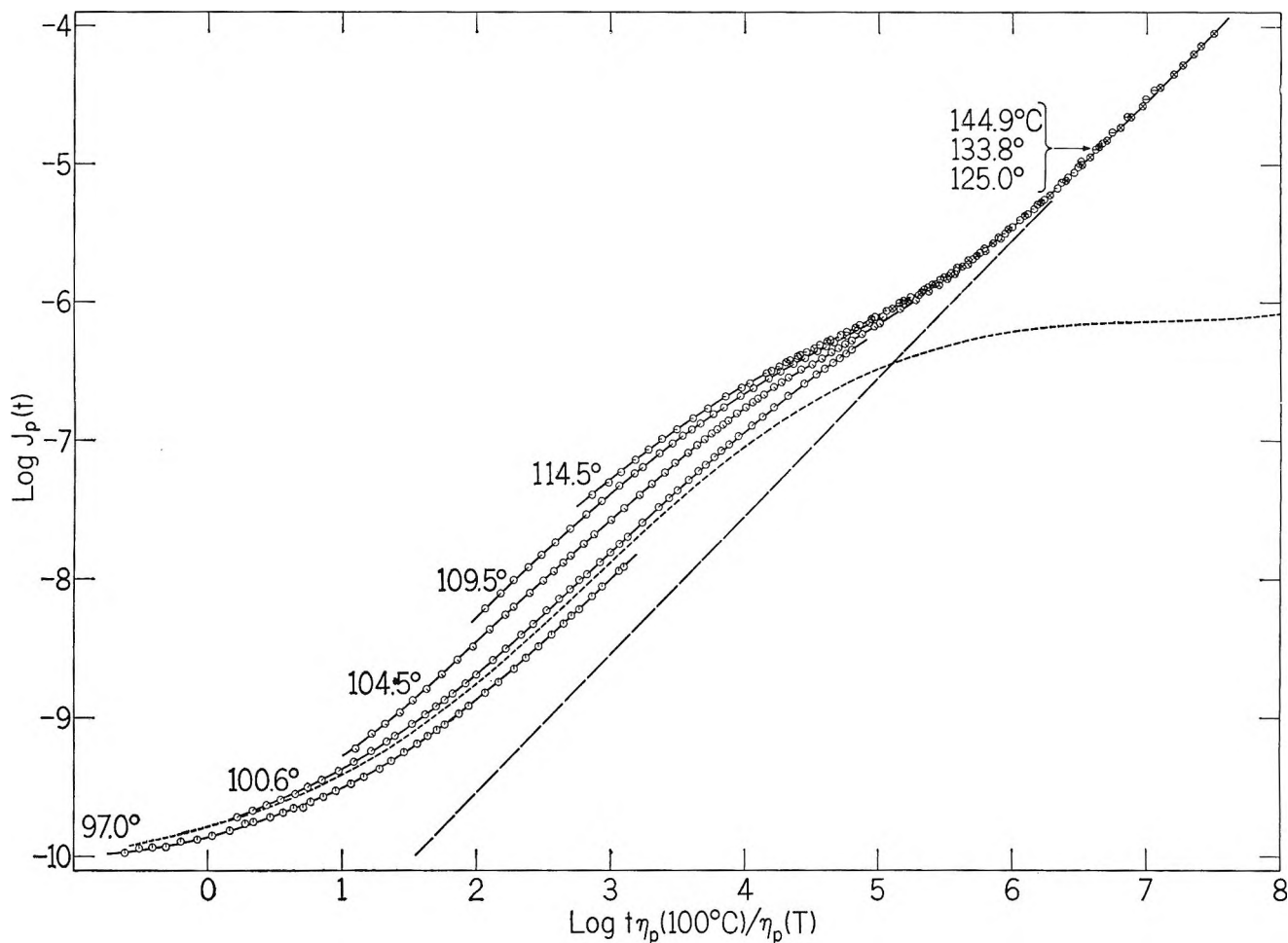


Figure 2. Logarithmic plot of creep compliance, $J_p(t)$ against reduced time scale t/a_T , $a_T = \eta_p(T)/\eta_p(T_0)$, $T_0 = 100^\circ$. Failure of temperature reduction is indicated. Long-dashed line is the 100° t/η contribution. Short-dashed line is the reduced recoverable compliance curve.

Figure 2 illustrates clearly that a single curve is not obtained when such an attempt is made to reduce the data to 100° . The data have merged at the long time, high temperature end, where they must because here $J(t)$ is largely determined by the viscous contribution, t/η . In the region of the glasslike to rubberlike or primary transition, the separation of curves is pressing toward an order of magnitude. The 100° viscous deformation is represented by the long dashed line.

According to current phenomenological theories of linear viscoelasticity, creep compliance for a linear amorphous polymer is described as

$$J(t) = J_g + J_e\psi(t) + t/\eta \quad (1)$$

where J_g , the glassy compliance, is a constant in the neighborhood of 10^{-10} cm.²/dyne and represents the instantaneous contribution to the deformation by the bending and stretching of molecular bonds; J_e , a

constant, is the steady-state or long-time-limiting recoverable compliance; $\psi(t)$ is a normalized retarded elasticity function, which is zero at $t = 0$, describing the form of the time-dependent recoverable deformation.

The logarithmic recoverable compliance curves, $\log(J_p(t) - t/\eta_p)$, shown in Figure 3 as functions of $\log t$ have been obtained directly from recovery measurements following fairly long creep runs or indirectly by subtracting the viscous contributions, t/η , from the measured creep compliance results.

Reliable shift factors, a_T , from 97.0 through 133.8° were obtained and are given in Table I. Utilizing these temperature shift factors, which were obtained only from the retarded elastic behavior, the curves from Figure 3 were reduced to 100° . The resulting curve is shown in Figure 4. It is clear that superposition has been achieved and that the retarded elastic

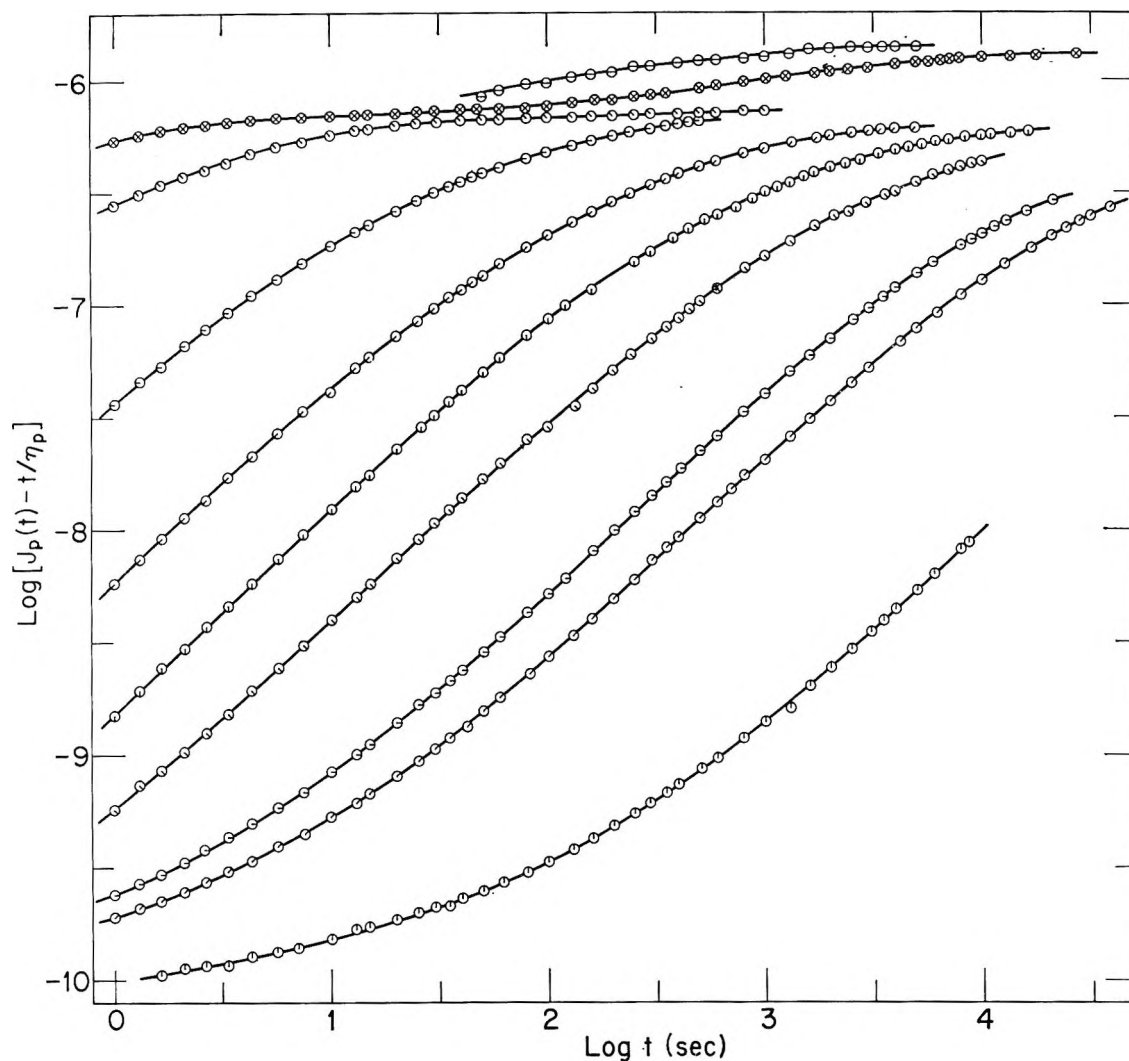


Figure 3. The logarithm of the recoverable compliance, $J_p(t) - t/\eta_p$, shown as a function of logarithmic time. Pips indicate temperature of measurement; identified in Table I.

behavior has a different temperature dependence from the viscous flow.

This "master" curve describes the behavior of the recoverable compliance at 100° , extending from a level of glassy hardness, through the primary, glasslike to rubberlike transition to a smaller second transition in the usual "plateau" region. Whereas the primary transition in this bulk material reflects the retarded configurational adjustments of the individual polymer chain backbones to the applied stress,^{15,16} the plateau existing in the neighborhood of 10^{-6} cm.²/dyne has been attributed to the existence of an entanglement network.¹⁷ The final increase seen, starting at about 10^8 sec. on the reduced time scale, has been attributed to the slipping of the chain entanglements. However, on the basis of the response exhibited by poly(dimethyl)siloxane¹⁸ and polyvinyl acetate¹⁹ (both of which

exhibit at least two transitions, beyond the rubberlike plateau), it is certain that even a complete qualitative picture for this region is lacking. It is likely that the apparent reduction of the second transition seen here is spurious and that more accurate measurements would reveal a temperature behavior different from that of the primary transition and of flow.

In addition, we wish to point out for the theorist's consideration that experimentally the compliances,

(15) (a) P. E. Rouse, Jr., *J. Chem. Phys.*, **21**, 1272 (1953); (b) F. Bueche, *ibid.*, **22**, 603 (1954).

(16) J. D. Ferry, R. F. Landel, and M. L. Williams, *J. Appl. Phys.*, **26**, 359 (1955).

(17) F. Bueche, *ibid.*, **26**, 738 (1955).

(18) D. J. Plazek, W. Dannhauser, and J. D. Ferry, *J. Colloid Sci.*, **16**, 101 (1961).

(19) Author's unpublished results.

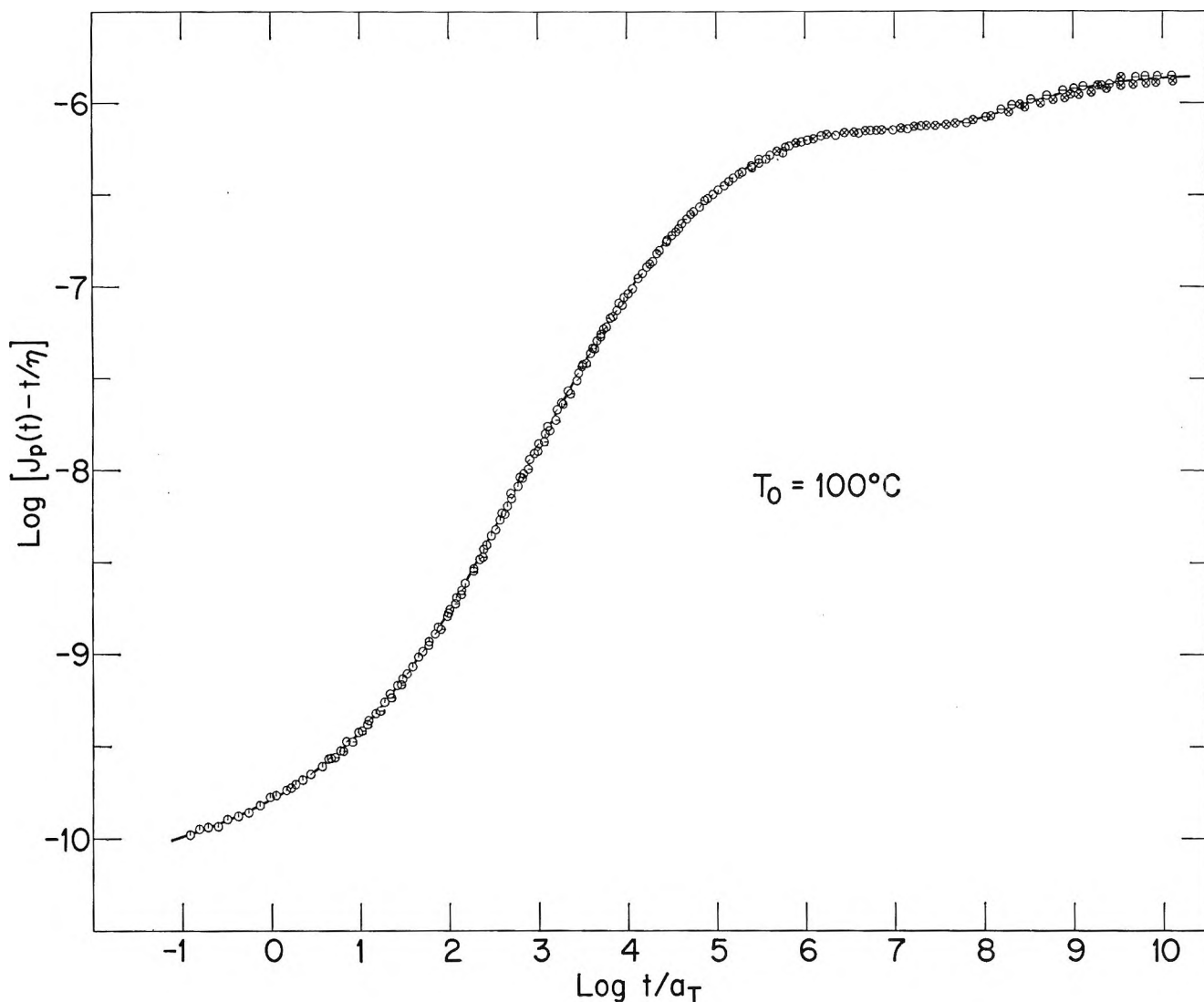


Figure 4. Logarithmic plot of recoverable compliance, $J_p(t) - t/\eta$, against reduced time, t/a_T , reduced to 100° .

creep and dynamic, appear to be composed of contributions from transitions or groups of molecular mechanisms in an additive manner; *i.e.*, the groups of mechanisms contribute to the *strain* additively. Separation of such contributions is therefore possible. If, within a group of molecular mechanisms, the temperature dependence is the same, reduction will be possible. Subsequent recombination will then yield a master curve which should be an accurate description of the sample behavior at the temperature of reduction over an enhanced time scale. For this kind of behavior dynamic rigidity and stress relaxation data cannot be properly reduced since a simple decomposition is not possible.

The somewhat more elaborate formula proposed by Ferry, Grandine, and Fitzgerald²⁰ for the amplitude

temperature shift (which allows for a different temperature dependence of the glassy mechanism) was not necessary because all of the data taken in the glassy region were measured at temperatures not far from the temperature of reduction. Part of the reduced recoverable compliance curve is also shown in Figure 2 as a short-dashed line.

Temperature Dependence Analysis. The shift factors, a_T , representing the temperature dependences of the viscous flow and the recoverable compliance are shown in Figure 5. With a temperature near T_g as the reference (here $T_0 = 100^\circ$), the temperature dependence of the recoverable compliance in the primary

(20) J. D. Ferry, L. D. Grandine, and E. R. Fitzgerald, *J. Appl. Phys.*, **24**, 911 (1953).

transition region is more severe than that of the viscous deformation. A similar trend was noticed in the early work on polyisobutylene.²⁰ The dynamic compliance measurements being reduced at the time covered only the primary softening transition and for the high molecular weight sample had no measurable contribution from viscous deformation. The reduction was therefore successful and valid. Subsequent discrepancies reported in the literature have either been ignored or have been subjected to different rationales than that presented here.

Equations having the Williams, Landel, and Ferry, WLF, form²¹

$$\log a_T = \frac{-C_1(T - T_0)}{C_1 + T - T_0} \quad (2)$$

were fitted to the two sets of data. The objective and sensitive plot of $-(T - T_0)/\log a_T$ vs. $T - T_0$, shown in Figure 6, was used to determine the constants. For viscous flow with $T_0 = 100^\circ$, $C_1 = 12.7$ and $C_2 = 49.8$; with $T_0 = T_g$, $C_1 = 13.3$ and $C_2 = 47.5$. For the transition recoverable compliance with $T_0 = 100^\circ$, $C_1 = 10.7$ and $C_2 = 29.9$; with $T_0 = T_g$, $C_1 = 11.6$ and $C_2 = 27.6$.

From the above constants, free volume parameters were calculated. The interpretation of the constants assumed is in essence the same as that of Williams.²² The principal difference from the original WLF analysis²¹ is that here the constant B from the Doolittle equation,²³ $\eta = Ae^{B/f}$, is not assumed equal to unity. Here A is a constant and $f = (v - v_0)/v_0$ is the relative free volume and v and v_0 are the total and occupied specific volumes. The thermal expansion coefficient of f , α_f , is assumed equal to $(1/v_0)dv/dT$ and not $\alpha_1 - \alpha_g$, where α_g is the expansion coefficient of the glass and is equated to α_0 , the expansion coefficient of v_0 . (The derivative here is that of the liquid just above T_g , and $(1/v_0)dv/dT \simeq \alpha_1$, the expansion coefficient of the liquid.) Since α_0 has been found to be much smaller than α_g in the neighborhood of T_g ,²⁴ it appears that equating α_0 to zero should be a more realistic assumption. Substitution of $f = f_g + (1/v_0)dv/dT(T - T_g)$, where f_g is the relative free volume at T_g , into the expression

$$\log a_T = \frac{B}{2.303} \left[\frac{1}{f} - \frac{1}{f_g} \right]$$

leads to

$$\log a_T = - \frac{\frac{B}{2.303 f_g} (T - T_g)}{\frac{v_0 f_g}{dv/dT} + T - T_g} \quad (3)$$

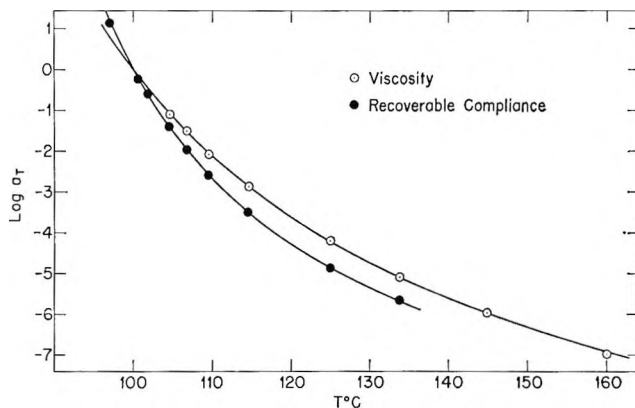


Figure 5. Temperature dependences illustrated as $\log a_T$ vs. temperature: open circles from viscosity; filled points from recoverable compliance in primary transition region.

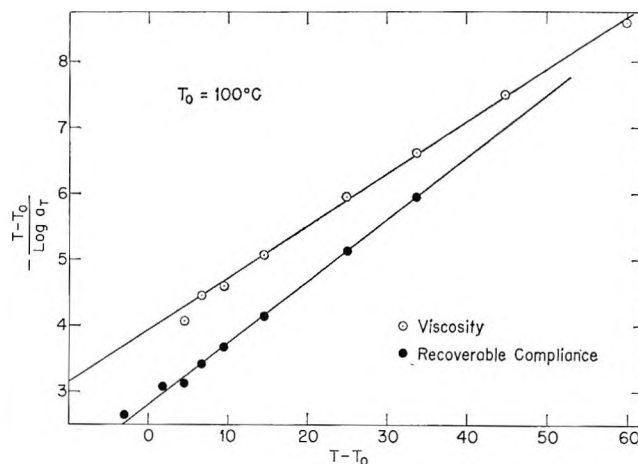


Figure 6. Linear form, $-(T - T_0)/\log a_T$ vs. $T - T_0$, of temperature dependences shown, from which characterizing constants are obtained.

where it can be seen that $C_1 = B/2.303f_g$ and $C_2 = v_0 f_g / (dv/dT)$. Assuming that the free volume is zero on the extrapolation of the specific volume line of the liquid at a temperature $T_\infty = T_g - C_2$, the occupied volume, v_0 , can be calculated from $v_0 = v_g - C_2 dv/dT$. Using a specific volume at the glass temperature of $v_g = 0.971 \text{ cm}^3/\text{g}$. and setting $dv/dT = 5.5 \times 10^{-4} \text{ cm}^3/\text{g. deg.}$,¹² the effective occupied volume for viscous flow is $0.945 \text{ cm}^3/\text{g}$. and for the recoverable compliance is $0.956 \text{ cm}^3/\text{g}$. The values for B and f_g for viscous flow are 0.85 and 0.028, respectively, and for the recoverable compliance, 0.43 and 0.016, re-

(21) M. L. Williams, R. F. Landel, and J. D. Ferry, *J. Am. Chem. Soc.*, **77**, 3701 (1955).

(22) M. L. Williams, *J. Appl. Phys.*, **29**, 1395 (1958).

(23) A. K. Doolittle, *ibid.*, **23**, 236 (1952).

(24) D. J. Plazek and J. H. Magill, to be published.

spectively. The agreement with Williams' values²² of $f_g = 0.029$ and $B = 0.91$ derived from the polystyrene viscosity data of Fox and Flory²⁵ is gratifying since the results presented here were measured nearer to T_g , and the viscosities reached much higher values.

The surprising conclusion that the effective relative free volume for viscous flow is appreciably larger than that for the recoverable compliance mechanisms may suggest that viscous flow in polymers involves more motion parallel to the chain backbone than do retarded elastic conformational changes. The postulates of slipping entanglements¹⁷ and normal mode motions¹⁵ would seem to be in accord with this possibility.

One can alternatively ask why the occupied volume should appear smaller for the viscous or nonrecoverable deformation than for the recoverable deformation. A possible explanation for this phenomenon resides in the long time span required to accomplish a given nonrecoverable deformation compared to that for the same amount of recoverable deformation. Thus, the probability for a density rarefaction at a given point during the period of deformation may be expected to be greater in the nonrecoverable flow than in recoverable deformation, giving rise to an apparently smaller effective occupied volume for viscous flow. The decrease in f_g for viscous flow found with decreasing molecular weight by Williams²² conforms to this hypothesis.

The constant B has been interpreted by Cohen and

Turnbull²⁶ as being within a factor of 2 of the critical volume necessary for a diffusional displacement. In spite of the larger B value found for the viscous flow, the severity of the temperature dependence near T_g is greater for the recoverable compliance. The 1% difference in the occupied volumes dominates the response in this temperature region. At higher temperatures the effect of the differences in B becomes the dominating factor, and in Figure 5 it can be seen that the slopes of the curves have become equal in the neighborhood of 130°. At still higher temperatures the slope of the viscosity-derived curve should be the larger.

Acknowledgments. This work was supported in part by the Office of Naval Research, Contract No. Nonr 2693(00), and the development of the principal instrument used in this investigation was supported by the National Aeronautics and Space Administration under Research Grant NsG 147-61. The author wishes to thank V. Michael O'Rourke for his help with the measurements and Franklin L. Miller for his assistance with the calculations. Helpful criticisms made by Dr. Guy C. Berry are also gratefully acknowledged.

(25) T. G. Fox and P. J. Flory, *J. Am. Chem. Soc.*, **70**, 2384 (1948); *J. Appl. Phys.*, **21**, 581 (1950); *J. Phys. Chem.*, **55**, 221 (1951); *J. Polymer Sci.*, **14**, 315 (1954).

(26) M. H. Cohen and D. Turnbull, *J. Chem. Phys.*, **31**, 1164 (1959)

Spectroscopy of Titanium, Zirconium, and Hafnium Oxides in Neon and Argon Matrices at 4 and 20°K.

by William Weltner, Jr., and Donald McLeod, Jr.

Union Carbide Research Institute, Tarrytown, New York 10592 (Received April 27, 1965)

TiO (and perhaps TiO₂), ZrO, and HfO, prepared by vaporization of the solid oxides at ~2500°K., have been trapped in neon and argon matrices at 4 and 20°K. The ¹⁸O-substituted molecules were also prepared by passing ¹⁸O₂ over the corresponding heated metal. The electronic spectra of these molecules indicate that ZrO and probably HfO have a ¹Σ⁺ ground state as opposed to the known ³Δ_r ground state of TiO. For TiO, the α and γ triplet-triplet gas transitions are observed, as expected. Only one other transition appears, at 6124 Å., corresponding to Coeur's γ' system or to one of Rosen's tentatively assigned systems. The triplet systems of ZrO are not observed, but the singlet A bands in the gas, assigned here as ¹Σ⁺ ← X¹Σ⁺, appear strongly in the matrices. The spectrum of HfO is discussed in relation to that of ZrO, and the energy levels of the three oxides assigned to configurations of a simple molecular orbital scheme. The infrared spectra of TiO, ZrO, and HfO in neon matrices yield ground state frequencies of 1005, 975, and 974 cm.⁻¹, respectively; the gas values are 999.2, 969.7, and 967.6 (?) cm.⁻¹.

Introduction

TiO and ZrO are observed strongly in the spectra of classes M and S stars. Because of this, these molecules have been studied rather thoroughly, and it has been found that TiO has a triplet ground state, most probably ³Δ_r.¹ In this case Phillips showed by intensity measurements of TiO bands at several temperatures in a King furnace that the ¹Δ level was ~580 cm.⁻¹ higher.² The ground state of ZrO has not been definitely established, but it is generally assumed also to be ³Δ_r since this is the lower state of several prominent emission systems. HfO spectra have been measured, but very little analysis has been carried out.

Our recent work on TaO in solid neon at 4°K. has helped to establish a ²Δ_r ground state for that molecule.³ One can reason from the molecular configuration leading to such a state that the removal of one electron should yield a ¹Σ⁺ ground state for HfO. Since the ground state of NbO is ²Δ (and we assume it is also regular) one would also predict a ¹Σ⁺ ground state for ZrO, contrary to the current view. Hence a comparison of the absorption spectra of TiO, ZrO, and HfO at 4°K. is of value since it could be expected to resolve the discrepancy and give us more faith in our

understanding of the electronic structure of these transition metal molecules.⁴

Our purpose here has been to compare the matrix spectra of these three molecules with each other and with gas emission spectra, where known. The results of this comparison are that ZrO has a singlet ground state, and HfO probably does also. The spectra obtained further confirm the belief that neon matrix observations correlate well with gas data.

Experimental Section

The apparatus and procedure are described in previous publications.⁵ The induction-heated furnace was used throughout this work with the sample contained in thick-walled tungsten Knudsen cells (0.16-cm. effu-

- (1) U. Uhler, Dissertation, University of Stockholm, Sweden, 1954.
- (2) J. G. Phillips, *Astrophys. J.*, **115**, 567 (1952).
- (3) W. Weltner, Jr., and D. McLeod, Jr., *J. Chem. Phys.*, **42**, 882 (1965).
- (4) A preliminary note concerning this research was recently published: W. Weltner, Jr., and D. McLeod, Jr., *Nature*, **206**, 87 (1965).
- (5) W. Weltner, Jr., and J. R. W. Warn, *J. Chem. Phys.*, **37**, 292 (1962); W. Weltner, Jr., P. N. Walsh, and C. L. Angell, *ibid.*, **40**, 1299 (1964); W. Weltner, Jr., and D. McLeod, Jr., *ibid.*, **40**, 1305 (1964).

sion hole). Solid Ti^{16}O_2 (Fisher reagent grade), Zr^{16}O_2 (Fisher reagent grade), and Hf^{16}O_2 (Wah Chang Corp.; Zr, 260 p.p.m.; other elements <50 p.p.m.) were vaporized at temperatures of about 2300, 2600, and 2700°K., respectively. Mass spectrometric studies^{6,7} of TiO_2 and ZrO_2 were referred to in order to establish the proper vaporization temperature and identify the expected molecular species. Assuming every molecule passing into the dewar region is trapped in the matrix, one calculates⁵ that the M/A ratios should be near 20,000. One can only suppose that this is the case for HfO since it has not been investigated mass spectrometrically. Tungsten oxide species did not usually appear and when they did they were easily identified from earlier matrix spectra obtained in these laboratories. However, as described in the section on the infrared spectra of TiO_2 species, many strong infrared bands were observed when solid TiO_2 was vaporized.

Samples were also vaporized which were prepared by passing $^{16}\text{O}_2$ or $^{18}\text{O}_2$ over pure titanium (E. H. Sargent Co.), zirconium (greatest impurity 0.06–0.6% Fe), or hafnium (Carborundum Co.; Zr, 3%; Ti, 215 p.p.m.; other elements <50 p.p.m.). The $^{18}\text{O}_2$ (98% enriched) was obtained from Yeda Research and Development Co., Rehovoth, Israel. After preparation the oxides were placed in tungsten Knudsen cells previously outgassed at 2700°K.

The spectroscopic equipment is the same as that previously used. Only in the measurement of the infrared emission of TiO matrices was an innovation introduced. A plano-convex KBr lens (diameter 5.0 cm., focal length 7.6 cm.) obtained from Harshaw Co. was used to focus the fluorescent infrared light on the slit of the Perkin-Elmer 112 spectrometer. A 150-w. xenon high pressure lamp, with an infrared absorbing filter, was used for excitation.

Observations

I. TiO. The rather thorough studies of the emission spectra of gaseous TiO have been summarized by Pearse and Gaydon⁸ and by Gatterer, Junkes, Salpeter, and Rosen.⁹ The observed transitions are shown in Figure 1. Phillips analyzed much of the spectrum and revised the previous work on the β , γ , and δ systems.¹⁰ The triplet-triplet assignments were later again revised by Uhler¹ who showed that their lower state is a $^3\Delta_r$ level. Phillips also proved the $^3\Delta_r$ to be the ground state² and, as mentioned earlier, found that the $^1\Delta$ state was higher in energy by about 581 cm^{-1} . (This number is determined to within perhaps a few hundred cm^{-1} .) Another singlet system in the infrared has been analyzed by Petterson.¹¹ Three systems have

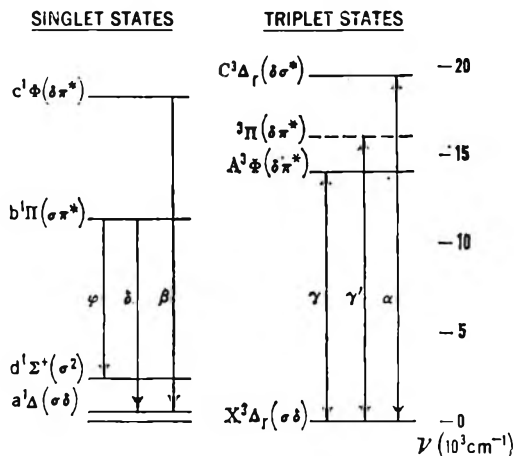


Figure 1. Energy levels and observed transitions of TiO . Arrow heads indicate whether transitions were observed in emission or absorption or both. For assignment of $^3\Pi$ state, see the discussion in the text.

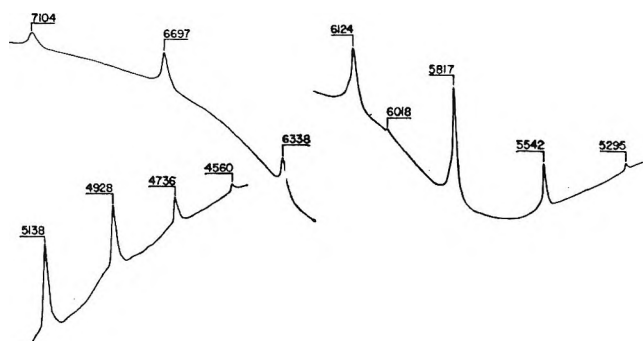


Figure 2. Absorption spectrum of Ti^{16}O in a neon matrix at 4°K. Wave lengths are in Å.

been tentatively proposed by Rosen and Lemaitre^{9,12}; two of these involve reassignments of Coheur's observation of a γ' triplet system.¹³

The matrix spectra exhibit the α , γ , and γ' systems, as expected if TiO has a $^3\Delta_r$ ground state. Perhaps the most important thing that these spectra of TiO estab-

(6) J. Berkowitz, W. A. Chupka, and M. G. Inghram, *J. Phys. Chem.*, **61**, 1569 (1957).

(7) W. A. Chupka, J. Berkowitz, and M. G. Inghram, *J. Chem. Phys.*, **26**, 1207 (1957).

(8) R. W. B. Pearse and A. G. Gaydon, "The Identification of Molecular Spectra," 3rd Ed., John Wiley and Sons, Inc., New York, N. Y., 1963.

(9) A. Gatterer, J. Junkes, E. W. Salpeter, and B. Rosen, "Molecular Spectra of Metallic Oxides," Vatican Press, Vatican City, 1957.

(10) J. G. Phillips, *Astrophys. J.*, **111**, 314 (1950); **114**, 152 (1951).

(11) A. V. Petterson and B. Lindgren, *Arkiv Fysik*, **22**, 491 (1962).

(12) B. Rosen, 4th International Meeting on Molecular Spectroscopy, Bologna, 1959, Vol. 2, Pergamon Press, Inc., New York, N. Y., 1962, p. 533.

(13) F. P. Coheur, *Bull. Soc. Roy. Sci. Liege*, **12**, 98 (1943).

Table I: Absorption Bands of TiO in a Neon Matrix at 4°K.

Gas band system	ν'	Ti ¹⁶ O			Ti ¹⁸ O			ν^{18}/ν^{16} ^a
		λ , Å.	ν , cm. ⁻¹	$\Delta G'_{\nu+1/2}$, cm. ⁻¹	λ , Å.	ν , cm. ⁻¹	$\Delta G'_{\nu+1/2}$, cm. ⁻¹	
γ	0	7104	14,073		7100	14,081		0.956
	1	6697	14,928	855	6710.5	14,898	817	0.956
	2	6337.5	15,775	847	6364.5	15,708	810	0.961
	3	6018	16,612	837	6054.5	16,512	804	
γ^b	0	6124	16,325		6120	16,335		0.950
	1	5816.5	17,188	863	5827.5	17,155	820	0.957
	2	5541.5	18,041	853	5563	17,971	816	0.963
	3	5294.5	18,882	841	5323	18,781	810	
α	0	5137.5	19,459		5137	19,461		0.960
	1	4927.5	20,289	830	4935	20,258	797	0.954
	2	4735.5	21,111	822	4751	21,042	784	0.961
	3	4560	21,924	813	4581	21,823	781	0.971
	4	4398.5	22,729	805	4422.5	22,605	782	

^a Theoretical ratio = 0.9574. ^b This is Coheur's γ' system,¹³ possibly reassigned by Rosen and Lemaitre.^{9,12}

lish is that there are only these three triplet-triplet transitions in the visible region.

Electronic Absorption Spectra. The bands observed in the absorption spectrum (between 8900 and 3100 Å.) of Ti¹⁶O trapped in a neon matrix at 4°K. are shown in Figure 2; the band positions and vibrational frequencies are given in Table I. The corresponding data on Ti¹⁸O are also included in the table along with the ratio of $\nu(^{18}\text{O})/\nu(^{16}\text{O})$, which should lie near the theoretical value of 0.9574. The bands are broad enough in the matrix that the peaks are probably not established to better than ± 0.5 Å., and this accounts for the variation in the observed ratio in Table I. Although the (0,0) bands at 7104 and 6124 Å. are the largest bands in each of these two progressions, they do not appear as such in Figure 2 because of the variation in energy of the tungsten light source in that region.

The data for Ti¹⁶O in an argon matrix at 20°K. are given in Table II. The bands are considerably broader in this matrix (particularly the α system), and their peak positions are therefore harder to establish than in neon. However, it does appear that the potential curves in the upper electronic states in the first two transitions in the table exhibit less anharmonicity in an argon than in a neon environment. Also, the electronic levels shift by about 300–400 cm.⁻¹ to lower energies in argon, and $\Delta G'_{1/2}$ values are lowered by as much as 20 cm.⁻¹.

A comparison of the neon and argon data is given in Table III along with that of the corresponding band systems in the gas emission spectra. The identification of the neon matrix systems with those in the gas is straightforward for the well-known γ and α triplet-

Table II: Absorption Bands of Ti¹⁶O in an Argon Matrix at 20°K.

Gas band system	ν'	λ , Å.	ν , cm. ⁻¹	$\Delta G'_{\nu+1/2}$, cm. ⁻¹
γ	0	7253	13,783	
	1	6839	14,618	835
	2	6470	15,451	833
	3	6142.5	16,276	825
γ^a	0	6254.5	15,984	
	1	5941	16,827	843
	2	5657	17,672	845
	3	5400.5	18,511	839
α	0	5241.5	19,073	
	1	5023.5	19,901	828
	2	4825	20,719	818
	3	4645	21,522	803
	4	4478	22,325	803

^a See footnote b of Table I.

triplet transitions. The remaining system at 6124 Å. (16,325 cm.⁻¹) may be identified with any one of the three systems proposed by Rosen and Lemaitre¹² since they begin at about (I) 6215, (II) 6174, and (III) 6149 Å. The upper state $\Delta G'_{1/2}$ values in these three cases are all about 864 cm.⁻¹ which again allows no definite choice to be made since they all agree with the neon matrix value. System II seems to be the most logical choice since it is a triplet system and its gas-matrix shift agrees best with the α and γ bands. The important thing is that only one system is observed in neon, which indicates that there is only one triplet-triplet transition to the ground state among the three

proposed gas systems of Rosen and Lemaître or perhaps that there are not really three separate systems occurring in that region. We are thereby identifying it with the orange-red triplet system observed by Coheur¹³ with an exploding wire source and designated by him as γ' .

Table III: Comparison of Gas Transitions of Ti¹⁶O with Neon and Argon Matrix Values

Gas band system ^a	Gas		Neon		Argon	
	λ , Å.	$\Delta G^{1/2}$, cm. ⁻¹	λ , Å.	$\Delta G^{1/2}$, cm. ⁻¹	λ , Å.	$\Delta G^{1/2}$, cm. ⁻¹
γ [A ³ Φ_2 -X ³ Δ_1]	7130.4	859.8	7104	855	7253	835
γ' [³ Π_0 -X ³ Δ_1] ^b	6174	862.2	6124	863	6254.5	843
α [C ³ Δ_1 -X ³ Δ_1]	5167.36	829.8	5137.5	830	5241.5	828

^a See ref. 8 and 9. ^b See footnote b of Table I. The upper state has here been designated as ³ Π ; see Discussion.

Although a band attributed to TiO₂ was observed in the infrared spectra (see below) of neon matrices, no electronic spectrum of this molecule was observed.

Emission Spectra. The emission from TiO matrices excited by light at 4900 to 5150 Å. was relatively weak compared to the extensive TaO signals under comparable conditions.³ Several short progressions were detected, one with a lower state frequency of 956 cm.⁻¹ which may be the ³ Δ level, but generally they could not be satisfactorily analyzed.

It seemed possible that TiO was undergoing radiationless transitions to a lower state and perhaps even to the very low lying d¹ Σ^+ or a¹ Δ which are supposed to lie about (1708 + 581) and 581 cm.⁻¹ above the X³ Δ level, respectively. An attempt was therefore made to measure emission in the infrared, as indicated in the Experimental Section, and a large band was found at 3590 cm.⁻¹ in a neon matrix and at 3710 cm.⁻¹ in argon. However, when Ti¹⁸O was irradiated, the neon band appeared to shift to 3730 cm.⁻¹. No other bands, particularly at longer wave lengths down to 300 cm.⁻¹, could be found. The lifetime of the emission was not extremely long, *i.e.*, not seconds or longer.

Efforts were made to eliminate the possibility that the band was produced by reflection from the light source, and a recent failure in this laboratory to find infrared emission from an argon matrix of ScO under the same conditions indicates that the emission is derived from the trapped species. Further work is needed to identify the source of this anomalous emission.

Infrared Spectra (TiO and TiO₂). Ti¹⁶O in a neon matrix at 4°K. yields one strong infrared band at 1005 cm.⁻¹ which drops to 963.5 cm.⁻¹ when ¹⁸O is

substituted (observed $\nu^{18}/\nu^{16} = 0.959$, theory = 0.9574). This agrees well enough with the corresponding frequency observed in the gas for Ti¹⁶O in the X³ Δ , state, ν 999.2 cm.⁻¹. In general, only this one band appeared when vaporization took place at 1950° and when the sample was prepared by passing oxygen over titanium in a tungsten cell.

At higher temperatures (2050–2200°), or if solid TiO₂ reagent was vaporized at 2000°, another band appears at 940 cm.⁻¹ in neon although in the latter case it was surrounded by bands of the various tungsten oxide molecules.¹⁴ This band is attributed to the asymmetric stretching frequency of the TiO₂ molecule, which is presumably nearly linear since the symmetric stretching frequency was not observed. For a linear symmetric TiO₂ molecule, this frequency yields $k_1 = 4.99 \times 10^5$ dynes/cm. as the Ti–O stretching force constant if the interaction force constant, k_{12} , is neglected. This may be compared with the force constant in the TiO diatomic molecule, which is 7.181×10^5 dynes/cm. If this latter value were used in a valence bond approximation, as done by Berkowitz, *et al.*,⁶ one would find ν_3 1129 cm.⁻¹. Either the bond in the triatomic molecule is considerably weaker than in TiO or k_{12} is large and positive. This is in line with what was found³ for TaO₂ although in that case the molecule is more definitely bent.

II. ZrO. One may again be referred to well-known summaries^{8,9} for the extensive work done on the gaseous emission spectra of this molecule. Three triplet systems, the α , β , and γ , are observed, as well as the tentative δ and ϕ systems and another tentative system at about 5900 Å. proposed by Lemaître and Rosen.^{9,12} Two singlet systems have been definitely identified, the A and B bands,^{15,16} and it is significant that Åkerlind¹⁷ has shown that their transitions do not involve a common upper or a common lower state. Another singlet system at 6498.9 Å. has been proposed by Lemaître and Rosen⁹ with the suggestion that it involves the same lower state as the B bands, but the matrix results indicate that may be in error. The ³ Δ state of ZrO has usually been assumed to be the ground state. All of the known transitions of ZrO are shown in Figure 3.

A note has recently been published⁴ presenting evidence that ZrO has a ¹ Σ^+ ground electronic state. This is derived from matrix spectra at 4°K. which will be presented here in more detail.

(14) W. Weltner, Jr., and D. McLeod, Jr., work to be published.

(15) M. Afaf, *Proc. Phys. Soc. (London)*, **A63**, 674 (1950).

(16) U. Uhler and L. Åkerlind, *Arkiv Fysik*, **10**, 431 (1956).

(17) L. Åkerlind, *ibid.*, **11**, 395 (1957).

Table IV: Absorption Bands of ZrO in a Neon Matrix at 4°K.

Gas band system ^a	ν'	Zr ¹⁶ O			Zr ¹⁸ O			ν^{18}/ν^{16b}
		λ , Å.	ν , cm. ⁻¹	$\Delta G'_{\nu+1/2}$, cm. ⁻¹	λ , Å.	ν , cm. ⁻¹	$\Delta G'_{\nu+1/2}$, cm. ⁻¹	
2 ^c	0	6446	15,509	854	6443.4	15,515	812	0.951
	1	6109.5	16,363	845	6123	16,327	804	0.951
	2	5809.5	17,208	842	5836	17,131	792	0.941
	3	5538.5	18,050	834	?5578	17,924		
	4	5294	18,884		?5267.5			
?	0	5872	17,025	872	5870	17,032	831	0.953
	1	5586	17,897	867	5597	17,863	832	0.960
	2	5328	18,764		5348	18,695	816	
	3				?5124	19,511		
?	0	5154	19,397	836	5156.5	19,388	792	0.947
	1	4941	20,233	823	4954	20,180	783	0.951
	2	4748	21,056		4769	20,963		
A	0	3660	27,315	838	3658	27,329	800	0.955
	1	3551	28,153	824	3554	28,129	790	0.959
	2	3450	28,977	816	3457	28,919	780	0.956
	3	3355.5	29,793	817	3366	29,699		
	4	?3266	30,610					

^a See ref. 8 and 9. ^b Theoretical ratio = 0.9515. ^c This is system number 2 at 6498.9 Å, tentatively proposed by Lemaitre and Rosen.⁹

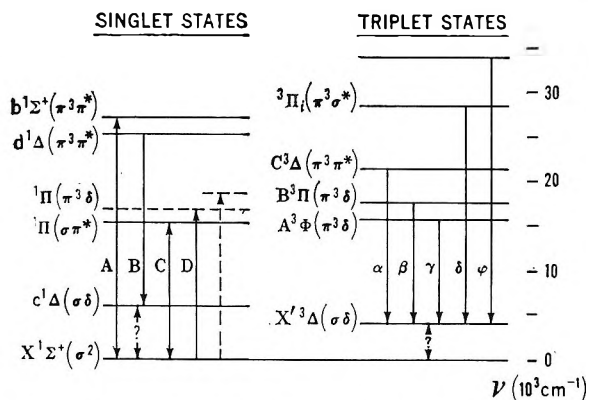


Figure 3. Energy levels and observed transitions of ZrO. Arrow heads indicate whether transitions were observed in emission or absorption or both. See text for discussion of C and D bands and the assignment of their upper states.

Electronic Absorption Spectra. Figure 4 shows for Zr¹⁸O in neon at 4°K. three strong band systems at 6444, 5870, and 3658 Å., and the (0,0) band of a weak system at 5157 Å. (The ¹⁸O spectra were recorded in a form more easily used for illustration; that is the reason for presenting them in Figure 4.) Table IV gives the Zr¹⁶O and Zr¹⁸O band positions, the derived vibrational frequencies, and $\nu(^{18}\text{O})/\nu(^{16}\text{O})$ ratios. The theoretical value of this ratio is 0.9515, and, in view of the widths of the bands (~ 63 cm.⁻¹), the agreement with column nine is considered satisfactory. Contrary

to the impression given by Figure 4, the (0,0) bands are the strongest in each progression.

The data for Zr¹⁶O in argon at 4 or 20°K. are given in Table V. The electronic levels are lowered by 130 to 500 cm.⁻¹ in going from neon to argon, and the vibrational frequencies generally drop by about 20 to 30 cm.⁻¹ in argon. The change in the vibrational frequency in the longest wave length system is, however, anomalous since it increases by 20 cm.⁻¹ in the argon environment.

The bands in argon at 4°K. are narrowed in the wings and peaked up in the center as compared to those measured at 20°K. The change is relatively small:

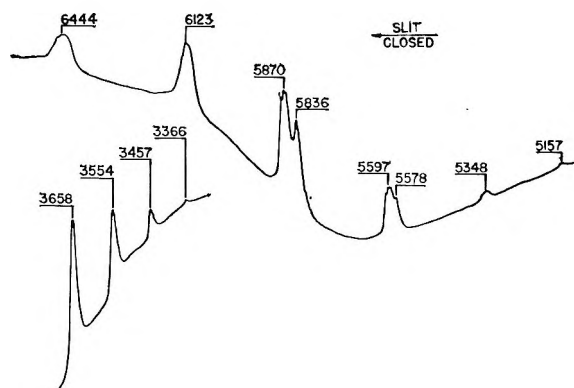


Figure 4. Absorption spectrum of Zr¹⁸O in a neon matrix at 4°K. Wave lengths are in Å.

for a band width of about 150 cm.^{-1} at half-peak height, the wings move out at 20°K. by roughly 20 cm.^{-1} on each side at the base of the band. Returning the temperature to 20°K. reproduced the former spectrum exactly.

This effect may be due to increasing rotation of the molecule in the matrix or perhaps to the expansion of the solid argon at the higher temperature. The order of magnitude of the band broadening is about what one might expect for a rotating ZrO molecule for a 4 to 20°K. temperature change. (The band width of the gas molecule would be about 4 cm.^{-1} at 4°K. , and its base

Table V: Absorption Bands of Zr^{16}O in an Argon Matrix at 4 or 20°K.

Gas band system ^a	ν'	$\lambda, \text{ \AA.}$	$\nu, \text{ cm.}^{-1}$	$\Delta G'_{\nu+1/2}, \text{ cm.}^{-1}$
2 ^b	0	6633	15,072	
	1	6270	15,945	873
	2	5947	16,811	866
	3	5659	17,666	855
	4	5406	18,493	827
?	0	6024	16,596	
	1	5729	17,450	854
	2	5461	18,307	857
?	0	5302	18,856	
	1	5084	19,664	808
A	0	3678	27,181	
	1	3572	27,988	807
	2	3470	28,794	806
Other weak bands				
		4849	20,617	
		4630	21,592	
		3778	26,462	
		3754	26,631	
		3722	26,860	

^a See ref. 8 and 9. ^b See footnote c of Table IV.

against rotation in HfO and therefore also in ZrO. It seems most likely that the observed small temperature effect is associated with the matrix perturbations and not with the intrinsic molecular properties of the trapped molecule.

A comparison of neon and argon data with their most likely counterparts in the observed gas emission spectra is given in Table VI. The identification of the neon matrix system at 3660 \AA. with the A bands in the gas appears to be quite definite, not only because of the proximity of the electronic transitions and upper state $\Delta G'_{1/2}$ values but, perhaps most decisively, because of the infrared matrix results to be related below. The neon system at 6446 \AA. is identifiable with the proposed 6498.9-\AA. singlet system of Rosen and Lemaitre,⁹ but in this case there is a disagreement between our infrared data and the ground state vibrational frequency derived from Rosen's assignment. Only the (0,0), (1,0), and (0,1) transitions were observed, and we believe the (0,1) may be incorrectly assigned since an alternative can be found which yields agreement with the matrix results. This will be considered more fully in the Discussion.

Table VI: Comparison of Gas Transitions of Zr^{16}O with Neon and Argon Matrix Values

Band system ^a	Gas		Neon		Argon	
	$\lambda, \text{ \AA.}$	$\Delta G'_{1/2}, \text{ cm.}^{-1}$	$\lambda, \text{ \AA.}$	$\Delta G'_{1/2}, \text{ cm.}^{-1}$	$\lambda, \text{ \AA.}$	$\Delta G'_{1/2}, \text{ cm.}^{-1}$
2	6498.9 ^b	852.9	6446	854	6633	873
?	(5926.4) ^c	(832.7) ^c	5872	872	6024	854
?	(5187.3) ^c	(835.5) ^c	5154	836	5302	808
A($^1\Sigma-^1\Sigma$)	3682.0	837.3	3660	838	3678	807

^a See ref. 8 and 9. ^b Note that the lower state of this gas transition is in doubt (see text). ^c These are the gas systems nearest the observed neon matrix systems. The 5926.4 \AA. system is a tentatively proposed triplet system of Lemaitre and Rosen.⁹ The 5187.3 \AA. system is the singlet B system of Afaf¹⁶ and Åkerlind.¹⁷

would increase from about 10 to 20 cm.^{-1} when going from 4 to 20°K.) The only other similar molecules for which the band shape has been studied in argon at 4 and 20°K. are HfO and WO. In WO, the resolution of structure in its somewhat narrower bands was poorer at 20° , but the characteristic weakening and broadening of the wings of the bands was not observed.¹⁴ HfO exhibits the same behavior as ZrO, as will be mentioned below. The WO molecule probably has about the same interatomic distance as ZrO and a considerably smaller one than HfO if one can judge from the trend of r_e values in TiO, ZrO, TaO, and NbO. Hence, the observations indicating that WO is not rotating argue

Emission. When Zr^{18}O in neon at 4°K. is irradiated with light at $\sim 3600 \text{ \AA.}$, two systems of bands are observed in emission as shown in Table VII. The bands are quite strong, and their positions and vibrational intervals correlate with what might be expected for the A bands, corresponding to what we now call the $b^1\Sigma^+ \rightarrow X^1\Sigma^+$ transition, and the β bands, corresponding to the $B^3\Pi_0 \rightarrow X'^3\Delta_1$ transition. The theoretical ratio of 0.9515 allows one to calculate from Table VII the lower state frequencies for Zr^{16}O of 963 and 931 cm.^{-1} which are in approximate agreement with frequencies expected for the $X^1\Sigma^+$ and $X'^3\Delta$ states, re-

spectively. The 963-cm.^{-1} value deviates from the 975-cm.^{-1} value expected for a ground-state frequency, but the value of $\text{cm.}^{-1}/\text{\AA.}$ is quite large near 3800 \AA. , and the band width makes it difficult to establish the peak positions. It appears to be close enough to warrant our assignment to the A system. The (0,0) band of the β system, although unobservable in matrix absorption spectra, may then be placed at 5455 \AA. from the neon emission spectrum.

Table VII: Emission Spectrum of Zr^{18}O in a Neon Matrix at 4°K. (Excitation $\sim 3600\text{ \AA.}$)

Assignment ^a	(v',v'')	$\lambda, \text{\AA.}$	$\nu, \text{cm.}^{-1}$	$\Delta\nu, \text{cm.}^{-1}$
	(0,1)	3799	26,315	916
A [$b^1\Sigma^+-X^1\Sigma^+$]	(0,2)	3936	25,399	908
	(0,3)	4082	24,491	902
	(0,4)	4238	23,589	
	(0,0)	5455	18,327	886
β [$B^3\Pi_0-X^3\Delta_1$]	(0,1)	5732	17,441	865
	(0,2)	6031	16,576	859
	(0,3)	6361	15,717	

^a See Figure 3.

Infrared Spectra. One strong band at 975 cm.^{-1} is observed in the infrared spectrum of Zr^{16}O in neon matrices at 4°K. This band appears at 927 cm.^{-1} for Zr^{18}O in neon. The ratio of frequencies is in excellent agreement with the theoretical ratio of 0.9515.

In argon, the results were similar to those of Linevsky¹⁸ in that a large number of bands was observed. A band occurring at 965 cm.^{-1} is probably Zr^{16}O , but other unidentified bands appeared at 887, 880, 822, 816, and 794 cm.^{-1} . Linevsky attributed his bands at 819 and 884 cm.^{-1} to the ZrO_2 molecule. Here, as in the case of HfO (see below), our observed frequency of the diatomic molecule in argon is larger by about 5 cm.^{-1} than that measured by Linevsky. Unfortunately, Zr^{13}O was not trapped in argon, which might have helped to clear up the assignment of the numerous bands.

III. HfO. Bands of HfO were found in the gas spectrum of hafnium by Meggers¹⁹ and King.²⁰ Shaw and Ketcham²¹ observed about 100 bands in an arc-flame source in the region of 6350 to 3330 \AA. and grouped them into two systems and a poorly developed third one. Only an abstract has been published, but they believe that triplet electronic levels are involved. Krishnamurty²² believes the lower state is $^3\Pi$ although few details are given. Gatterer, Junkes, Salpeter, and Rosen,⁹ in their recent compilation, give a pro-

visional vibrational analysis of a spectrum measured by Junkes. Nine sequences between 6500 and 3200 \AA. are analyzed, and from their assignment the vibrational frequencies shown in Table VIII may be derived. As might be expected, the spectra of HfO in a neon matrix at 4°K. in the infrared and visible regions resemble those of ZrO .

Table VIII: Provisional Electronic Transitions and Vibrational Frequencies of HfO in the Gas as Derived from Gatterer, *et al.*⁹

Band system	(0,0) transitions		$\Delta G^{1/2}, \text{cm.}^{-1}$	$\Delta G''^{1/2}, \text{cm.}^{-1}$
	$\lambda, \text{\AA.}$	$\nu, \text{cm.}^{-1}$		
A	6021.1	16,603.7	902.4?	963.2? ^a
B	5698.1	17,545.2	897.1	964.1 ^b
	5703.6	17,527.9		
C	5074.7	19,700.1	841.6	913.6
	5079.2	19,682.7	843.8	919.1
D	4252.0	23,511.7	870.5	967.1 ^c
	4253.5	23,503.4	866.3	
E	3970.1	25,181.2	853.8	
	3972.8	25,164.0	864.9	
F	3654.3	27,357.2	842.7	967.6
G	3327.9	30,040.3	852.2	
H	4707.0	21,239.0		
	4703.1	21,256.6		
J	4412.2	22,658.1		
	4408.8	22,675.5		

^a (0,1) transition is doubtful; $\Delta G^{1/2}$, also doubtful since derived from (1,1) and (0,1). ^b Only one (1,0) and (0,1) transition given; most reasonable ΔG values obtained from (0,0) shown. ^c Only one (0,1) transition given.

Electronic Absorption Spectra. The three main systems of Hf^{18}O in a neon matrix at 4°K. are shown in Figure 5, and the positions of all of the observed bands for Hf^{16}O and Hf^{18}O are given in Table IX. No bands were found between 8800 and 5910 \AA. , and the region below 3100 \AA. was not examined. Figure 5 shows the ^{18}O spectrum because some band overlapping occurring in the ^{16}O spectrum in the 4196 - and 3912-\AA. systems is less marked in the ^{18}O spectrum. Not shown are three weaker bands at 5910 , 5598 , and 5342 \AA. and a weaker progression of bands beginning at 3326 \AA. , decreasing in intensity toward the ultraviolet region.

(18) M. J. Linevsky, Proceedings of the First Meeting of the Interagency Chemical Rocket Propulsion Group on Thermochemistry, New York, N. Y., 1963, Vol. 1, Chemical Propulsion Information Agency, Silver Spring, Md., 1964, p. 11.

(19) W. F. Meggers, *J. Res. Natl. Bur. Std.*, **1**, 151 (1928).

(20) A. S. King, *Astrophys. J.*, **70**, 105 (1929).

(21) R. W. Shaw and H. C. Ketcham, *Phys. Rev.*, **45**, 753 (1934).

(22) S. G. Krishnamurty, *Proc. Phys. Soc. (London)*, **A64**, 852 (1951).

Table IX: Absorption Bands of HfO in a Neon Matrix at 4°K.

Band system ^a	v'	Hf ¹⁶ O			Hf ¹⁸ O			ν^{18}/ν^{16b}
		λ , Å.	ν , cm. ⁻¹	$\Delta G'_{v+1/2}$, cm. ⁻¹	λ , Å.	ν , cm. ⁻¹	$\Delta G'_{v+1/2}$, cm. ⁻¹	
A	0	5910	16,916		5910	16,916		
B	0	5601	17,849		5598	17,850		
	1	5331	18,755	906	5342	18,714	855	0.944
D	0	4195.5	23,829		4196.5	23,825		
	1	4049	24,691	862	4057.5	24,639	816	0.947
	2	~3916	25,529	838	3928.5	25,448	809	0.965
	3	3790.5	26,375	846	3808.5	26,250	802	0.948
	4	3673.5	27,215	840	3698.5	27,030	780	0.929
E	5	~3566	28,035	820				
	0	3912.5	25,553		3912.5	25,555		
	1	3783	26,427	874	3790	26,378	825	0.944
	2	3663.5	27,289	862	3677	27,188	810	0.940
	3				3570.5	27,999	811	
F	0	3642.5	27,447		3643.5	27,438		
	1	3534.5	28,285	838	3541	28,235	795	0.949
	2	3433.5	29,117	832	3445.5	29,019	786	0.945
	3	3339	29,941	824	3354	29,807	788	0.956
G	0	3322	30,090		3326	30,058		
	1	3230	30,951	861	3238.5	30,870	812	0.943
	2	~3144	31,777	826				

^a As in gas, see Table VIII. ^b Theoretical value = 0.9476.

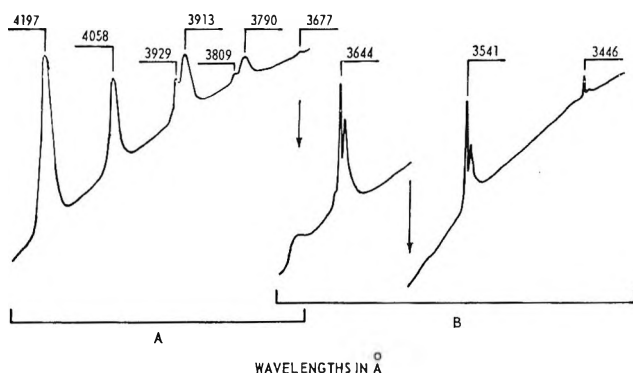


Figure 5. Absorption spectrum of Hf¹⁸O in a neon matrix at 4°K. The arrows indicate where the amplifier gain was increased so as to display the weaker bands more strongly.

A vibrational analysis of the observed progressions is given in Table IX for Hf¹⁶O and Hf¹⁸O. The calculated ratio of $\nu(^{18}\text{O})/\nu(^{16}\text{O})$ should be in approximate agreement with the theoretical value of 0.9476. The matching of gas and neon matrix systems is attempted in Table X.

One notes in Figure 5 that the F system bands, with (0,0) at 3643 Å. (see Table IX), have a distinctly different shape from the others. The G system, which is not shown there, and also the 5910-, 5601-, and 5331-Å. bands have the broader, rounded shape of the other systems.

Table X: Comparison of Gas and Neon Matrix Data on Hf¹⁶O

Band system ^a	Neon		Gas ^a	
	(0,0) transition λ , Å.	$\Delta G'_{1/2}$, cm. ⁻¹	(0,0) transition λ , Å.	$\Delta G'_{1/2}$, cm. ⁻¹
A	5910		6021	902.4?
B	5601	906?	5700	897.1
D	4196	862	4253	870.5-866.3
E	3912	874	3971	864.9-853.8
F	3642	838	3654.3	842.7
G	3322	861	3327.9	852.2

^a From Table VIII.

The three extraneous bands are puzzling. Although they are all relatively weak, the 5601-Å. band is by far the strongest and the 5331-Å. band the weakest among the three. They are broad enough so that their exact positions are difficult to specify, but the lack of isotopic shift in the 5910- and 5600-Å. bands is certain and indicates that there are at least two systems involved. The 5331-Å. band has then been assigned as the (1,0) band of the B system since it does show an isotopic shift. The argon spectrum at 4°K. (see Table XI) gives further evidence on this assignment. The 5601-Å. neon band has now become two, and, although Hf¹⁸O has not been measured in argon, it is likely from the lack of any effect on the 5601-Å. band in neon that

there are two (0,0) bands at that wave length. Hence, it is believed that there are three weak overlapping systems in this spectral region, one at 5910 Å. and two near 5600 Å. (The possibility that any of these bands arises from Hf atoms was eliminated by measuring the spectrum of the atoms trapped in neon.)

Table XI: Absorption Spectrum of Hf¹⁸O in an Argon Matrix at 4 and 20°K.

Band system	Intensity	ν'	λ , Å.	ν , cm. ⁻¹	$\Delta G''_{\nu+1/2}$, cm. ⁻¹
A	vw	0	5959 ^a	16,776	891
			5942	16,826	
		1	5643 ^b	17,717	
B	vw	0	5649	17,697	838
		?	0	5589	
D	vs	0	4240	23,578	848
		1	4095	24,416	
		2	3957	25,264	
		3	3831	26,095	
E	m	0	3920	25,502	830
		1	3797	26,332	
F	s	0	3689	27,099	833
		1	3579	27,932	
		2	3477	28,756	
G	w?	0	3365	29,708	824

^a This band only appears at 4°K. ^b This is a weak spike which appears on the top of the 5649-Å. band at 4°K.

The temperature effect in argon matrices when proceeding from 20 to 4°K. was generally as described for ZrO: a slight narrowing and peaking up of the bands. Only in the long wave length region was a striking change observed at 4°K. in that a new band appears next to the 5942-Å. band; both of these bands are much sharper than the 20°K. band centered at 5942 Å. As in ZrO, the change in the band appearance was completely reversible, and the discussion in that section indicates why it is likely that the temperature effect is not related to rotation of the molecules in the matrix.

Emission Spectra. When a neon matrix of Hf¹⁶O or Hf¹⁸O is irradiated by mercury light at 3650 Å., a series of strong emission bands appears with a maximum at about 4460 Å., as illustrated in Figure 6 for Hf¹⁸O. Each band exhibits structure on its high frequency side consisting of a series of peaks (five in the largest band at 4450 Å.), which are separated by 90–100 cm.⁻¹. The vibrational spacing between the largest peaks is given in Table XII for Hf¹⁸O and Hf¹⁶O, and, as can be seen, the isotopic shift is generally in accord with the theoretical value of 0.9476.

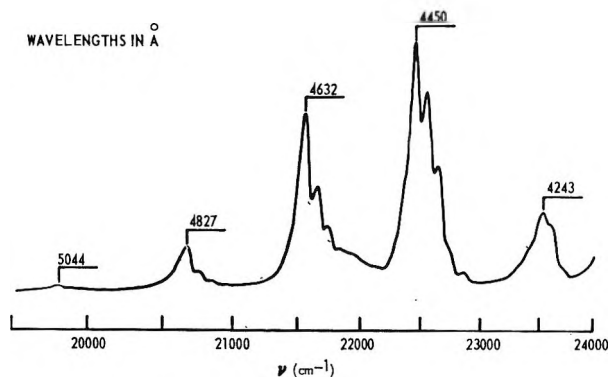


Figure 6. Emission spectrum of Hf¹⁸O in a neon matrix at 4°K. (Excitation is at ~3650 Å.)

Table XII: Fluorescence of HfO in Neon Matrices at 4°K. (Excitation 3650 Å.)

ν	Hf ¹⁶ O			Hf ¹⁸ O			ν^{18}/ν^{16}
	λ , Å.	ν , cm. ⁻¹	$\Delta G''_{\nu+1/2}$, cm. ⁻¹	λ , Å.	ν , cm. ⁻¹	$\Delta G''_{\nu+1/2}$, cm. ⁻¹	
0	4469	22,373		4243	23,564		
0	4469	22,373		4450	22,466	881	0.948
1	4662	21,444	929	4632	21,585	885	0.949
2	4874	20,511	933	4827	20,700	880	0.961
3	5102	19,595	916	5044	19,820		
4	5349	18,690	905				
In argon at 20°K.							
0	4321	23,136	959				
1	4508	22,177	947				
2	4709	21,230	943				
3	~4928	20,287					

The Hf¹⁶O bands have the same characteristic structure as in Figure 6, with the same spacing between the peaks on each band, but the most intense peak now occurs at 4469 Å. rather than at 4450 Å. as in Hf¹⁸O. Hence, this intense band, presumably the (0,0) transition, shifts by about 100 cm.⁻¹ to higher frequency in the heavier molecule. There is no band at shorter wave lengths (such as the 4243-Å. band in Figure 6) which can qualify for the (0,0) band and so correct this anomaly. This remains unexplained; however, it may be suggestive that the shift is of the same size as the spacing of the substructure of the bands. One must assume that the emission is occurring predominantly from (or to) different sublevels in the upper state (or lower state) when ¹⁸O is substituted. This substructure is presumably a matrix effect.

An interesting feature of this emission is the lack of agreement between the lower state vibrational frequency of HfO obtained here (929 cm.⁻¹) and that value found in the infrared (974 cm.⁻¹). This and the

fact that the system is not observed in absorption suggest that a triplet-triplet transition is occurring here; *i.e.*, the lower state is not the ground state. The vibrational frequency in the lowest ${}^3\Delta$ state²³ of ZrO is 931 cm^{-1} , and the infrared frequencies for ZrO and HfO are almost the same. Then, this could be the neon matrix equivalent of the proposed J system of HfO in Table VIII, which would be assigned to the triplet manifold.

In argon, when excitation occurs at $\sim 3600\text{ \AA}$, Hf¹⁶O exhibits a fluorescence beginning at 4321 \AA , which is probably to be identified with the D system seen in absorption at 4240 \AA . The vibrational frequency intervals given in Table XII are about what is to be expected of Hf¹⁶O in its ground state in an argon matrix. The $\Delta G''_{1/2}$ value of 960 cm^{-1} agrees well enough with the infrared frequency of 967 cm^{-1} (see the next section) in view of the breadth of the visible bands and consequent uncertainties in choosing their peaks.

Infrared Spectra. The infrared spectrum of Hf¹⁶O has been previously determined by Linevsky¹⁸ in argon, krypton, and xenon matrices at 4°K . Only one strong band was observed in each case, and the frequencies found were 960 , 959 , and 952 cm^{-1} , respectively. The argon measurement was repeated here, and the band was found to lie at 967 cm^{-1} . This places it more in line with the krypton and xenon results and also with our neon matrix work.

Both Hf¹⁶O and Hf¹⁸O were trapped here in neon matrices at 4°K . The observed spectrum in the ¹⁶O case is shown in Figure 7, indicating that there is a strong band at 974 cm^{-1} and a weak one at 945 cm^{-1} . The spectrum of Hf¹⁸O appears exactly the same, but the bands are shifted to 923 and 896 cm^{-1} , respectively. The ν^{18}/ν^{16} ratio is 0.948 for both the strong and the weak band as compared to a theoretical value of 0.9476 . In view of the results of Linevsky in the other rare gases, it seems likely that the weak band observed arises from multiple sites^{24a} or aggregation of trapped molecules^{24b} in neon. Unfortunately, mass spectrometry has not been carried out on the vapor over solid HfO₂ so that one cannot make a definite statement about the presence of other molecules such as HfO₂.

Discussion

The group of molecules considered here contains transition metals having two d electrons in the atomic state. Although it is certainly clear that these molecules are not completely ionic, it is convenient to begin a discussion of their electronic properties by considering the crystal field model^{25,26} as we did with TaO.³ In a cylindrically symmetrical electric field occurring in a

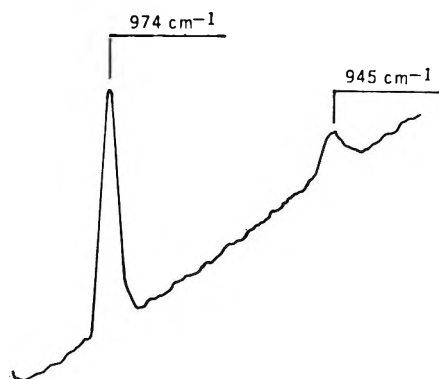


Figure 7. Infrared spectrum of Hf¹⁶O in a neon matrix at 4°K .

diatomic molecule, the d orbitals of M^{2+} are split into orbitals of symmetry δ , π , and σ , in order of increasing energy. One then predicts, as Berg and Sinanoglu²⁵ did for TiO, that the two electrons will go into the δ orbitals, yielding a δ^2 configuration (over closed shells) and a ${}^3\Sigma^-$ lower state. This is, of course, not the case, and it has been shown by Carlson and Moser²⁷ and by Carlson and Nesbet²⁸ that the ${}^3\Sigma^-$ state is in fact a state of high energy because of the relatively large repulsion energy of two δ electrons. Because of the more favorable energy, one of these electrons is excited to the closely lying σ level, the π level having been lowered below the δ by bonding with the oxygen orbitals. Then the configuration $\delta\sigma$ is obtained, resulting in a ${}^3\Delta_r$ ground state for TiO and low-lying ${}^1\Delta(\sigma\delta)$ and ${}^1\Sigma^+(\sigma^2)$ states, as observed. A crude MO scheme for TiO, based upon the ligand-field approach but with levels arranged in such a way as to yield the correct ground state, is given in Figure 8.

Such an energy level scheme is more useful for prediction of the electronic properties of transition metal oxides within the same period than within the same group because of the much greater changes in atomic number when going down the periodic table. For that reason it is more relevant to consider the properties of NbO and TaO when one desires to predict the properties of ZrO and HfO. It is well known²⁹ that the second

(23) F. Lowater, *Proc. Phys. Soc. (London)*, **44**, 51 (1932).

(24) (a) C. K. Jen, V. A. Bowers, E. L. Cochran, and S. N. Foner, *Phys. Rev.*, **126**, 1749 (1962); K. B. Harvey and J. F. Ogilvie, *Can. J. Chem.*, **40**, 85 (1962); (b) G. C. Pimentel and S. W. Charles, *Pure Appl. Chem.*, **7**, 111 (1963); K. B. Harvey, H. F. Shurvell, and J. R. Henderson, *Can. J. Chem.*, **42**, 911 (1964).

(25) R. A. Berg and O. Sinanoglu, *J. Chem. Phys.*, **32**, 1082 (1960).

(26) J. T. Hougen, G. E. Leroi, and T. C. James, *ibid.*, **34**, 1670 (1961); C. K. Jørgensen, *Mol. Phys.*, **7**, 417 (1964).

(27) K. D. Carlson and C. Moser, *J. Phys. Chem.*, **67**, 2644 (1963).

(28) K. D. Carlson and R. K. Nesbet, *J. Chem. Phys.*, **41**, 1051 (1964).

(29) F. A. Cotton and G. Wilkinson, "Advanced Inorganic Chemistry," Interscience Publishers, Inc., New York, N. Y., 1962, p. 760 ff.

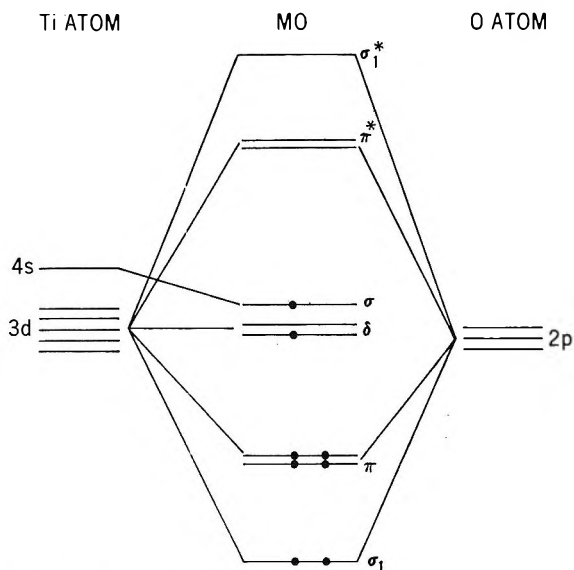


Figure 8. Molecular orbitals of TiO.

and third-period transition metals resemble each other more closely in their properties, essentially because of the filling of the 4f shell between these periods, than either one of them resembles the first-period metals. It is also expected that the "crystal-field" splitting will be larger and the interelectronic repulsion less important in these heavier oxides.

The ground state of TaO is ${}^2\Delta_r$ (see the MO scheme of ref. 3) and it has been found that NbO also has a ${}^2\Delta$ ground state³⁰ although it has not been established whether it is regular or not. We will assume that it is also regular. Then the removal of one electron from the $\sigma^2\delta$ configuration leading to this ground state³ yields a σ^2 configuration or a ${}^1\Sigma^+$ lowest state for ZrO and HfO. Now the situation is the reverse of that in TiO since the excitation of one electron to form the $\sigma\delta$ configuration leads to the low-lying energy levels ${}^1\Delta$ and ${}^3\Delta_r$ in the transition metal oxides of the second and third period. Hence, theoretically it is expected, based upon the TaO result, that ZrO and HfO should have singlet ground states and that these will be ${}^1\Sigma^+$ rather than ${}^1\Delta$.

With the above considerations in mind, one can now consider the matrix results and the excited states which best explain the observed transitions.

TiO. The agreement between the triplet transitions observed in the gas and the neon matrix systems, as shown in Table III, indicates that TiO is being trapped in the $X^3\Delta$ level at 4°K. and presumably in the lowest multiplet of that level, *i.e.*, ${}^3\Delta_1$. This is confirmed by the good agreement between the ground-state vibrational frequencies measured in the gas and in the neon matrix, 999 and 1005 cm.^{-1} , respectively.

The observation of another triplet-triplet transition at 6124 Å. (16325 cm.^{-1}) in neon is partially in accord with Rosen's analysis¹² but indicates that only one triplet level lies between the $A^3\Phi$ and $C^3\Delta_r$ states, these being the upper levels of the γ and α systems. Table XIII gives the single-electron excited states expected from a ${}^3\Delta_r(\sigma\delta)$ molecule on the basis of Figure 8, approximately in the order of increasing energy. Since there is only one configuration leading to a ${}^3\Phi$ and one leading to a ${}^3\Delta_r$ excited state among those listed, the observed matrix triplet level must be ${}^3\Pi$, derived from either the $\delta\pi^*$ or $\sigma\pi^*$ configurations. The position of the $b^1\Pi$ level (see Figure 1) below the $A^3\Phi$ indicates that it is $\sigma\pi^*$ so that the ${}^3\Pi$ level is most probably $\delta\pi^*$, with the $\sigma\pi^*$ lying considerably lower. The ${}^3\Sigma^-(\delta^2)$ state is considered as lying very high from the work of Carlson, Moser, and Nesbet.^{27,28}

Table XIII: Excited States of TiO, ZrO, and HfO

Configuration	Excited states
	TiO [ground state ${}^3\Delta_r(\delta\sigma)$]
$\delta\sigma$	${}^1\Delta$ low lying
σ^2	${}^1\Sigma^+$ low lying
$\sigma\pi^*$	${}^3\Pi$, ${}^1\Pi$
$\delta\pi^*$	${}^3\Phi$, ${}^1\Phi$, ${}^3\Pi$, ${}^1\Pi$
$\delta\sigma^*$	${}^3\Delta_r$, ${}^1\Delta$
$\sigma\sigma^*$	${}^3\Sigma^+$, ${}^1\Sigma^+$,
δ^2	${}^3\Sigma^-$, ${}^1\Sigma^+$, ${}^1\Pi$
	ZrO and HfO [ground states ${}^1\Sigma^+(\pi^4\sigma^2)$]
$\pi^4\sigma\delta$	${}^3\Delta_r$, ${}^1\Delta$ low lying
$\pi^4\sigma\pi^*$	${}^3\Pi_r$, ${}^1\Pi$
$\pi^4\sigma\sigma^*$	${}^3\Sigma^+$, ${}^1\Sigma^+$
$\pi^3\sigma^2\delta$	${}^3\Phi$, ${}^1\Phi$, ${}^3\Pi$, ${}^1\Pi$
$\pi^3\sigma^2\pi^*$	${}^3\Delta$, ${}^1\Delta$, ${}^3\Sigma^+$, ${}^1\Sigma^+$, ${}^3\Sigma^-$, ${}^1\Sigma^-$
$\pi^3\sigma^2\sigma^*$	${}^3\Pi_i$, ${}^1\Pi$

ZrO. From the experimental observations in matrices, there is clear evidence that ZrO has a singlet and not a triplet ground state. This evidence may be summarized by the following three points.

(1) The A system in the gas at 3682 Å., identified as a singlet-singlet system, is observed at 3660 Å. in neon (see Table VI).

(2) No transition in the matrix at 4°K. can be identified with a triplet-triplet emission system in the gas. On the other hand, no band systems appear in the matrix near 4640 Å. where the α triplet bands appear strongly in the gas. (Comparison can be made with the TiO matrix spectra where strong triplet-triplet transitions appear.)

(30) U. Uhler, *Arkiv. Fysik*, **8**, 265 (1954).

(3) There is a correspondence between the observed infrared vibrational frequency of $Zr^{16}O$ in a neon matrix (ν 975 cm^{-1}) and that in the lower state of the A gas system (ν 969.7 cm^{-1}) rather than that in the lowest ${}^3\Delta$ state (ν 931 cm^{-1}). (Note that other matrix infrared frequencies are in good agreement with gas values; for example, for TaO and TiO, neon matrix values are 1020 and 1005 cm^{-1} , respectively; gas values are 1021.7 and 999.2 cm^{-1} .)

All of the presently known energy levels of ZrO are contained in Figure 3, along with the most probable configurations from which they arise. The configurations given in Table XIII are derived from the simple MO scheme of TaO given previously,³ but with one electron removed from the δ orbital.

The A bands have been identified as either a ${}^1\Sigma^+ \leftarrow {}^1\Delta$ or a ${}^1\Delta \leftarrow {}^1\Delta$ transition, and we have chosen the former, and $X^1\Sigma^+$, for the reasons given earlier. From Table XIII, it is clear that the upper ${}^1\Sigma$ level of this transition must be derived from the $(\pi^3\sigma^2\pi^*)$ configuration since the identification of the A, B, and C triplet levels is quite definite (see Figure 3).

The other three observed matrix systems at 6446, 5872, and 5154 Å. (see Table VI) can now be considered. The strong 6446-Å. (15,509- cm^{-1}) bands correspond very well in wave length and $\Delta G'_{1/2}$ with the 6498.9-Å. (15,383.0- cm^{-1}) singlet system in the gas, tentatively proposed by Lemaître and Rosen,⁹ but the $\Delta G''_{1/2}$ derived from their assignment is 938.8 cm^{-1} which is not in agreement with our infrared value of 975 cm^{-1} . However, if their (0,1) band assignment is incorrect and it is instead assigned to an unidentified band at 6936.8 Å. (14,411.9 cm^{-1}) rather than at 6921.3 Å. (14,444.2 cm^{-1}), $\Delta G''_{1/2}$ now becomes 971.1 cm^{-1} . It remains to be seen whether the rotational structure of the gas band at 6936.8 Å. is in accord with this new assignment. Since the 6446-Å. system, designated as the C bands in Figure 3, lies at longer wave lengths than the other two systems, its upper state has been chosen as ${}^1\Pi(\sigma\pi^*)$ (see Table XIII). It seems likely that the ${}^3\Pi_r(\sigma\pi^*) \leftarrow X^3\Delta(\sigma\delta)$ transition lies in the near-infrared region.

The strong 5872-Å. (17,025.3- cm^{-1}) progression is apparently a new singlet system overlapping a proposed triplet system in the gas¹² so that a more complete analysis of that region of the gaseous spectrum is needed. It can be assigned to either ${}^1\Sigma^+(\sigma\sigma^*) \leftarrow X^1\Sigma^+(\pi^4\sigma^2)$ or to ${}^1\Pi(\pi^3\delta) \leftarrow X^1\Sigma^+(\pi^4\sigma^2)$. The latter has been chosen, as indicated by the D bands in Figure 3, because the approximate positions of triplet levels derived from the $\pi^3\delta$ configuration are known, but the assignment is very uncertain.

The weak 5154-Å. (19,397- cm^{-1}) system may be a

new singlet system which overlaps the B bands in the gas, or it may be a forbidden triplet-singlet transition. The B bands are now assigned to a ${}^1\Delta \leftarrow {}^1\Delta$ transition originating at the $c^1\Delta$ level. The close correspondence between the position of the 5154-Å. system and its $\Delta G'_{1/2}$ with the B bands (see Table VI) also suggests that some ZrO molecules in the matrix could be undergoing transitions from this low-lying excited $c^1\Delta$ state. It is possible, although, we feel, unlikely, that some molecules could be trapped in that state during the preparation of the matrix³¹; that possibility is not eliminated by our experiments. However, it is clear that the $c^1\Delta$ state is not so low-lying that it is being thermally populated at 4°K. The evidence for this is that the intensity of the 5302 Å. system in argon, the counterpart of the 5154-Å. system in neon, is unaffected by changing the temperature from 4 to 20°K.

The 5154-Å. system could then be assigned as the remaining ${}^1\Sigma^+(\sigma\sigma^*) \leftarrow X^1\Sigma^+(\sigma^2)$ transition. The other possibility, which is similar to our assignment of the 4804.5-Å. system in TaO, is that the 5154-Å. bands in neon are a forbidden triplet-singlet transition. The most likely assignment would be $B^3\Pi(\pi^3) \leftarrow X^1\Sigma^+(\sigma^2)$ since the upper state vibrational frequencies would approximately match (836 vs. 838.8 cm^{-1}). If this is true, then it would place the $X^3\Delta$ level about 1650 cm^{-1} above the ground state.

HfO. The resemblance of HfO to ZrO is confirmed by the closeness of the vibrational frequency of the former, 974 cm^{-1} , to that of ZrO, 975 cm^{-1} , in a neon matrix. This also appears to carry over to the electronic spectra if, in making the assignments, we can assume that the $\Delta G'_{1/2}$ values in the two molecules in their various electronic states continued to correspond closely. Then by this criterion and by intensity, the matching of the stronger matrix systems can be made and is shown in Table XIV. The A bands of ZrO at 3660 Å. shift very little in going to the HfO spectrum, whereas the other two systems shift by about 8000 cm^{-1} toward the ultraviolet region.

HfO should exhibit larger splittings of the d orbitals from a ligand-field point of view than ZrO, which can lead to the two observed shifts toward the ultraviolet region in the spectrum. The σ and δ orbitals will lie further apart in HfO, and an increase in the energy of the $\sigma\pi^* \leftarrow \sigma^2$ and $\pi^3\delta \leftarrow \pi^4$ transitions can result, as observed. (This implies also that the ${}^1\Delta(\sigma\delta)$ and ${}^3\Delta(\sigma\delta)$ states, although unobserved, will lie higher in HfO than in ZrO). The facts that the 3600-Å. bands

(31) There is evidence that C_2 is trapped in an excited electronic state: G. W. Robinson and M. McCarty, Jr., *J. Am. Chem. Soc.*, **82**, 1859 (1960), footnote 10; W. Weltner, Jr., P. N. Walsh, and C. L. Angell, *J. Chem. Phys.*, **40**, 1299 (1964).

Table XIV: Matching of the Strong Band Systems of ZrO and HfO in Neon Matrices

Assignment	ZrO			HfO		
	λ , Å.	ν , cm. ⁻¹	$\Delta G'_{1/2}$, cm. ⁻¹	λ , Å.	ν , cm. ⁻¹	$\Delta G'_{1/2}$, cm. ⁻¹
${}^1\Sigma^+(\pi^3\pi^*) \leftarrow X^1\Sigma^+$	3660	27,315	838	3642.5	27,447	838
${}^1\Pi(\pi^3\delta) \leftarrow X^1\Sigma^+$	5872	17,025	872	3912.5	25,553	874
${}^1\Pi(\sigma\pi^*) \leftarrow X^1\Sigma^+$	6446	15,509	854	4195.5	23,829	862

lie at about the same frequency in the two molecules and that they are surely the ${}^1\Sigma^+(\pi^3\pi^*) \leftarrow {}^1\Sigma^+(\pi^4)$ transition indicate that the $\pi^* \leftrightarrow \pi$ spacing is the same in HfO as in ZrO.

There then remain three weak systems to be accounted for. The 3322-Å. system is the strongest among them and exhibits a progression of vibrational transitions which resembles that of the strong spectral bands. It is probably a transition to the ${}^1\Sigma^+(\sigma\sigma^*)$ or ${}^1\Pi(\pi^3\sigma^*)$ level. Its identification with the weak 5154-Å. system in ZrO is difficult because of the different $\Delta G'_{1/2}$ values in the two systems. The other bands at 5910 and 5600 Å. do not have counterparts in the ZrO spectrum, but they do appear in the gas at 6021 and 5700 Å. It is presumed that they are forbidden transitions to lower triplet states made more "allowed" in the heavier molecule.

A Small Angle X-Ray Scattering Study of the Colloidal Nature of Petroleum

by C. W. Dwiggin, Jr.

Bureau of Mines, Bartlesville Petroleum Research Center, U. S. Department of the Interior, Bartlesville, Oklahoma
(Received April 28, 1965)

The colloids occurring in petroleum were investigated using small angle X-ray scattering. When necessary, scattering curves were corrected for finite collimation slits using convolution methods. Radii of gyration were determined for several whole crude oils, for crude oils diluted with solvents, and for a crude oil at different temperatures. In addition, the Hosemann and the Shull and Roess methods, the Fourier inversion method, and other methods were applied to selected crude oils. Results are compared with ultracentrifuge and other studies of petroleum and petroleum asphalts and asphaltenes. In general, the colloids of petroleum can have different average radii of gyration and probably exhibit some polydispersity. No large temperature effect was detected. However, the colloid size can be changed greatly by some solvents while the size is changed only slightly by other solvents. The small angle X-ray scattering method shows considerable promise for allowing an understanding of the mechanism of colloid growth and precipitation of colloidal material from petroleum.

Introduction

It is well known that petroleum contains colloidal material. The precipitation of asphaltic materials from petroleum by low molecular weight aliphatic hydrocarbons is one indication of this fact. Asphaltic-rich materials and asphaltenes separated from petroleum have been the subject of extensive investigation in

recent years. Ultracentrifuge studies probably have given some of the most reliable results. However, the study of asphalts and asphaltenes does not necessarily provide a true picture of the colloidal material *as it exists in whole crude petroleum*. Recent ultracentrifuge studies¹ have indicated that the molecular weight of separated asphaltene colloids dissolved in various

solvents is quite sensitive to changes in chemical and physical conditions. This fact produces considerable doubt as to whether asphaltenes or asphaltic-enriched materials can give a true indication of the colloidal material in petroleum, although such studies are extremely valuable in understanding the colloidal nature of asphaltic materials.

Ultracentrifuge and other research concerning whole crude oil²⁻⁶ has indicated that crude petroleum does contain colloids, that the size of the colloids can be estimated, and that at least some polydispersity is likely. The ultracentrifuge studies of petroleum and asphaltic materials also suggest that a spheroidal model, not departing too greatly from spherical, probably is satisfactory for describing petroleum colloids in many cases. All of this information is useful, but more information concerning petroleum colloids is needed to understand the mechanism of precipitation of petroleum colloids and changes in their size under various conditions. The colloids of petroleum are thought to have an important effect on the viscosity of petroleum⁴ and other important physical properties that are of great importance in understanding the behavior of petroleum in underground reservoirs.

Although there are several methods for studying colloids, there are difficulties in applying many of the methods to petroleum. The more exact ultracentrifuge studies of petroleum are plagued with several difficulties such as defining the partial specific volume and concentration of the petroleum colloids and recording changes in refractive indices or absorption of light in highly absorbing samples. Light scattering studies seem to be nearly hopeless because of the high absorption of light, fluorescence of many crude oils, and traces of dust in some samples. Small angle X-ray scattering also presents some difficulties including low intensities of scatter. However, certain parameters such as radii of gyration often can be obtained with considerable confidence, and information concerning polydispersity and shape of the particles often can be obtained or estimated. Furthermore, small angle X-ray scattering sees the particle as a whole, including possible internal solvation, while the more exact ultracentrifuge methods allow determination of the weight average anhydrous molecular weight.⁷ Thus, small angle X-ray scattering studies should throw considerable light on the nature of petroleum colloids, allow determination of different parameters, and often involve different assumptions when assumptions are necessary. In combination with ultracentrifuge studies and other studies, this should allow a much better understanding of petroleum colloids.

Because the studies were expected to be difficult,

it was decided to try several methods of data treatment of proved value. The use of all available methods was not possible. However, it was decided to determine radii of gyration for several samples and to determine the more difficult, and often less accurate, parameters for a limited number of samples most suitable for experimental investigation.

Experimental Section

The general experimental principles of small angle X-ray scattering have been described in detail.^{8,9} Thus, this discussion is limited to specification of the particular experimental arrangements and problems encountered in this investigation.

The samples studied scattered radiation only weakly. Thus, particular attention was required to reduce parasitic scattering, to obtain sufficient resolution, and to be able to make corrections for finite collimation slits when necessary. Because the colloids were not expected to fit a simple, monodisperse model, generalized slit-smearing corrections appeared necessary. The generalized slit height correction is made with the most confidence when the equipment is arranged so that the slits are of effective infinite height for the problem at hand. This requirement has been discussed in detail,⁹ and it is important that it is considered in arranging the instrument. The following conditions were selected as the best compromise for these studies with the equipment available.

The instrument was a highly modified Norelco¹⁰ diffractometer. Usually this instrument uses para-focusing geometry. For this study a high intensity

(1) M. Wales and M. van der Waarden, "Molecular Weights of Asphaltenes by Ultracentrifugation," Symposium on Asphalt: Composition, Chemistry, and Physics, Division of Petroleum Chemistry, American Chemical Society, Philadelphia, Pa., April 5-10, 1964. See preprints, Division of Petroleum Chemistry, American Chemical Society, 19, No. 2, April 1964, pp. B21-B26.

(2) C. W. Dwiggin and H. N. Dunning, *J. Phys. Chem.*, **64**, 377 (1960).

(3) I. A. Eldib, H. N. Dunning, and R. J. Bolen, *J. Chem. Eng. Data*, **5**, 550 (1960).

(4) P. B. Lorenz, R. J. Bolen, H. N. Dunning, and I. A. Eldib, *J. Colloid Sci.*, **16**, 493 (1961).

(5) B. P. Ray, P. A. Witherspoon, and R. J. Grim, *J. Phys. Chem.*, **61**, 1296 (1957).

(6) P. A. Witherspoon, *Illinois State Geol. Surv. Rept. Invest.*, **206**, 1 (1958).

(7) H. K. Schachman, "Ultracentrifugation in Biochemistry," Academic Press, New York, N. Y., 1959, pp. 210-214.

(8) W. W. Beeman, P. Kaesberg, J. W. Anderegg, and M. B. Webb, "Handbuch der Physik," Vol. 32, Goettingen, Heidelberg, Springer-Verlag, Berlin, 1957, pp. 321-442.

(9) A. Guinier, G. Fournet, and K. L. Yudowitch, "Small-Angle Scattering of X-Rays," Translated by C. B. Walker, John Wiley and Sons, Inc., New York, N. Y., 1955.

(10) Trade names are used for information only, and endorsement by the Bureau of Mines is not implied.

copper target X-ray tube which was operated at 35 kv. and 45 ma. was used. The line focus of this tube was viewed at a take-off angle of approximately 4° . In effect, the line focus of the tube acts as the first collimator. A 0.25° divergence slit was used in the same position as in the parafocusing arrangement to minimize radiation scattered from the X-ray tube. The second collimator slit was a 0.0025-cm. slit located 14.5 cm. from the focus of the X-ray tube. This was followed by a 0.0102-cm. scatter slit separated from the second collimator slit by 5 cm. Sample cells were placed in contact with this scatter slit. A 0.0076-cm. receiving slit was located 14.5 cm. from the sample center. This was followed by the usual scatter slit of the parafocusing instrument, in this case 0.25° . A scatter shield was located about halfway between the sample and receiving slits. Furthermore, a holder for absorption filters could be inserted between the sample and the receiving slit. The usual Ni $K\beta$ filter was used. The temperature of the room should be controlled to within 1° during alignment and experiments.

A proportional counter was used when low peak to background ratios became a problem, while a scintillation counter was used at other times. Adequate monochromatization resulted using both counters with narrow pulse height analyzer window settings. When adjusted properly, the calculated and measured mass absorption coefficients for a known sample at 1.54 Å. should agree. For measuring some of the lowest intensities, a high-voltage battery was used to supply the counters, and batteries were used for the preamplifier plate and filament supplies. The high degree of collimation makes studies down to $0.08^\circ 2\theta$ possible for samples that produce strong small angle scattering. This allows studies of very weak scattering down to angles of $0.18^\circ 2\theta$ without large background corrections.

Sample cell windows were 0.00064-cm. Mylar film. The thickness of the samples was adjusted to approximately the theoretical ideal with the aid of absorption measurements.⁹

Background intensity measurements were made for all experiments. Methods used were similar to those reported in the literature.¹¹ Each scattering experiment required determination of a small angle scattering curve, a measurement of absorption coefficient, a measurement of background produced by the counter, and a measurement of the background curve. Only in this way could reliable and repeatable results be obtained. A minimum of two and usually more complete experiments were necessary for each sample to ensure reliable results.

Interpretation of Data

Correction of Experimental Curves. Although experimental curves often need not be corrected for finite slit size for Guinier analysis of radii of gyration, other methods of data treatment often require such corrections. The general methods based on convolution analysis using numerical Fourier transforms were used. The method used for slit width correction was based on the integral equation^{8,9}

$$g(h) = \int i_{1.0}(x) g_1(h - x) dx \quad (1)$$

Thus, Fourier cosine transforms for the relative observed intensity of scatter curve and the $i_{1.0}(x)$ curve can be obtained. This allows solution for the Fourier transform of the intensity curve unsmearred for slit width. Taking the inverse transform gives $g_1(h)$, the desired function.⁹ This correction was small for the experimental conditions used and could be neglected for many of the samples.

The correction for slit height is much more important. Experimental conditions were selected so the beam was effectively of infinite height for the samples studied. The equation that applies in this case is^{8,9}

$$-I(h) = \frac{1}{\pi c} \int_0^\infty \frac{g_1'(\sqrt{h^2 + u^2}) du}{\sqrt{h^2 + u^2}} \quad (2)$$

These slit height and width corrections are time-consuming, and use of a digital computer is necessary if several curves are to be corrected in a reasonable time.

In this work all curves were corrected for finite slits when the data were to be used for purposes other than Guinier analysis. The uncorrected curves proved sufficient for Guinier analysis.

Guinier Analysis. Guinier analysis of all of the samples was made using the usual $\log I$ vs. h^2 curves. When there was difficulty in determining the slope at $h^2 = 0$, slopes taken at various values of h^2 were extrapolated.^{8,9} For colloids exhibiting polydispersity, the radius of gyration determined is weighted toward the larger-sized particles. Details are available in the literature.^{8,9}

Determination of Average Radii of Gyration. Because the Guinier radius of gyration is weighted toward larger particles, it often is desirable to calculate the average radius of gyration. Two of the most frequently used methods are those of Hosemann and of Shull and Roess.^{8,9,12-14} Both assume that the mass distribution function of the particles can be approximated by

(11) G. W. Brady, *J. Chem. Phys.*, **32**, 45 (1960).

(12) R. Hosemann, *Ergeb. Exakt. Naturw.*, **24**, 142 (1951).

(13) L. C. Roess and C. G. Shull, *J. Appl. Phys.*, **18**, 308 (1947).

(14) C. G. Shull and L. C. Roess, *ibid.*, **18**, 295 (1947).

a Maxwellian distribution with two parameters determined from experiment. Although there has been considerable controversy over the relative merits of these two methods,⁸ both gave nearly equivalent results for these studies.

Calculation of R_{0m} from Maxwellian Parameters. As a necessary but not sufficient condition for the validity of \bar{R}_0 , the Maxwellian parameters determined using the Hosemann or the Shull and Roess method should allow calculation of R_{0m} in good agreement with the value obtained using the Guinier method. Using equations for intensity of scatter and the Maxwellian distribution,^{8,9,12-14} and using the two Maxwellian parameters that can be determined from experiment, substitutions and integrations show that the following equation applies

$$R_{0m} = r_0 \sqrt{\frac{\Gamma\left(\frac{n+6}{2}\right)}{\Gamma\left(\frac{n+4}{2}\right)}} \quad (3)$$

Fourier Inversion of Experimental Data. Fourier inversion of the corrected experimental scattering curve gives the characteristic function $\gamma(R)$. The meaning of the characteristic function is discussed in detail in the literature.^{8,9} The first derivative of the normalized characteristic function often allows calculation of the average surface to volume ratio for the particle.^{8,9} If the particles are roughly spherical, it is necessary that the particle radius calculated from the surface to volume ratio be close to the average radius of the particle and give a radius of gyration in good agreement with the radius of gyration calculated from the Hosemann or Shull and Roess methods.

Results

Table I lists radii of gyration for a variety of crude oils. Tables II and III illustrate the effect on radii of gyration on dilution of crude oils with various solvents. Table IV illustrates the temperature effect upon radii of gyration of colloids in a crude oil. Table V gives more detailed parameters calculated for two crude oils. The temperature for all determinations was 27° unless otherwise noted in the tables. The units of length used are Ångströms.

Discussion of Results

A typical Guinier plot for determining R_{0m} is shown in Figure 1. The data for Table I illustrate that the observed Guinier radii of gyration can differ significantly for different crude oils. The petroleum colloids are thought to consist largely of asphaltic-rich materials. The inability to obtain appreciable

Table I: Guinier Radii of Gyration of Colloids in Crude Oils

Oil	Location	R_{0m}
Lagunillas	Venezuela	34
Santa Maria	California	32
Tia Juana	Venezuela	40
Bartlesville	Oklahoma	40
Bachaquero	Venezuela	31
Texas Wilcox	Texas	^a
Rhodes	Kansas	~69

^a Insufficient intensity for accurate determination.

Table II: Guinier Radii of Gyration of Lagunillas Colloids in *cis*-Decahydronaphthalene Solutions

Wt. fraction of oil	R_{0m}
1	34.1
0.7332	33.5
0.4615	34.5
0.2750	33.6
0 ^a	33.9

^a Extrapolated to zero concentration.

Table III: Guinier Radii of Gyration of Lagunillas Colloids in Mineral Oil Solutions

Wt. fraction of crude oil	R_{0m}
1	34
0.8207	38
0.4423	55
0.2212	43 ^a

^a Accuracy doubtful because of low intensity.

Table IV: Temperature Dependence of Guinier Radii of Gyration of Lagunillas Colloids

Temp., °C.	R_{0m}
27	34
37	38
50	34
62	37
73	37
28 ^a	35

^a After cooling from 73°.

scattering intensity for an asphaltic-poor crude oil (Texas Wilcox) and the available ultracentrifuge evidence concerning colloids in crude oils³⁻⁶ strongly

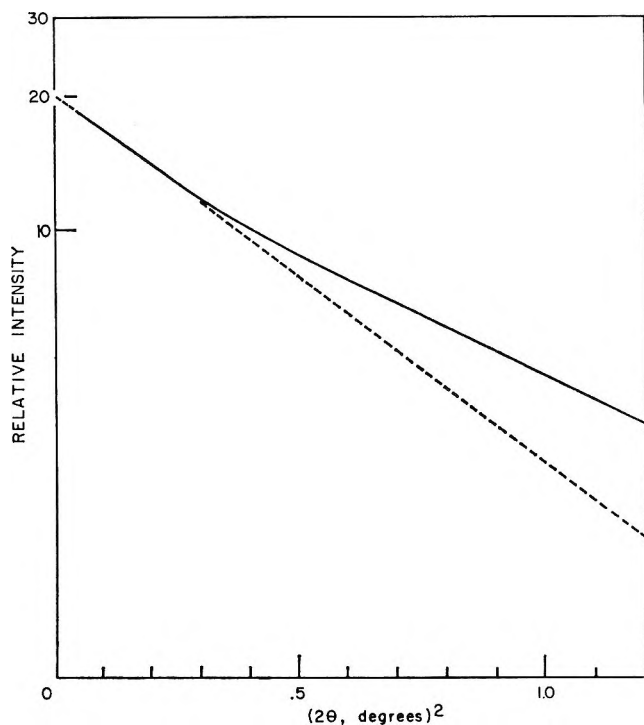


Figure 1. Guinier plot for Lagunillas petroleum.

Table V: Detailed Parameters for Lagunillas and Tia Juana Colloids

Parameter	Lagunillas	Tia Juana
\bar{R}_0 , Shull and Roess	26	30
\bar{R}_0 , Hosemann	26	27
n , Shull and Roess	3.80	5.49
τ_0 , Shull and Roess	17.32	17.32
S/V , from $\gamma(R)$	0.0917	0.0833
\bar{R}_0 , from S/V	25	28
R_{0m} , from n and τ_0	34	38
Assuming monodisperse prolate ellipsoid		
a	68	80
b	24	28
S/V , from a and b	0.1021	0.0891
ν	2.79	2.91

suggest that the colloids being seen are largely of an asphaltic nature. It could be argued that suspended materials such as clays, wax crystals, or water were being seen. Much of this material can be separated easily, using an ultracentrifuge, before much asphaltic material is separated.² Briefly ultracentrifuged samples gave scattering curves that were not significantly different from those of untreated crude oils although water, wax crystals, and minute traces of inorganic materials were separated from some of the samples on ultracentrifugation. Thus, these large particles are not significantly increasing scatter intensities at the

angles for which intensities were recorded. This adds further evidence that the colloids being seen by X-ray scattering are the same as the asphaltic-rich colloids seen in ultracentrifuge experiments. Furthermore, it is known that asphaltenes produce small angle X-ray scattering.¹⁵ Thus, at least for the samples studied, any other possible particles present in the petroleum were either of too large particle size, had an electronic density too close to that of the solvent, or were present in insufficient concentration to produce significant small angle X-ray scattering in the angular range observed.

The fact that the scattering curves were identical, within experimental error, for repeated experiments using the same sample indicates that radiation damage effects or other changes with time are not causing errors.

In very concentrated solutions, the observed radii of gyration often can be low because of interparticle interference effects. Polydispersity often, but not always, reduces these effects.⁸ The data in Table II for diluted Lagunillas samples, as well as the close agreement when using the methods of Hosemann and of Shull and Roess, strongly suggest that interference effects are not important in these studies. The same effect was observed with Santa Maria oil diluted with *cis*-decahydronaphthalene. The Lagunillas and Santa Maria oils are highly asphaltic oils that should show interference effects if present for any of the oils. Thus, based on the above arguments, the radii of gyration given in Table I should be reasonably good determinations of the true radii of gyration of the colloids in the oils studied.

The data of Table III indicate that the size of the petroleum colloids can be significantly increased up to a point on dilution with mineral oil. The last row of the table suggests that the colloid size begins to decrease on high dilution. Although this decrease on high dilution appears significant ($R_{0m} = 43 \pm 2.6$), intensities of scatter were low, and any possible sources of error in accuracy would tend to be magnified. The mineral oil represents a high molecular weight aliphatic substance. It is known that low molecular weight aliphatic compounds, for example pentane, cause precipitation of asphaltic materials and that the yield of asphalt is increased up to a point but begins to become less on very great dilution. Thus, it appears possible that the same effect is being observed on dilution with mineral oil, except the magnitude of the effect is small and only an increase in colloid size results on moderate dilution rather than precipitation of the colloids.

(15) C. Alexanian and M. Louis, *Compt. rend.*, 231, 1233 (1950).

The data of Table IV illustrate the temperature effect on colloid size over a wide range of temperatures. These data are not as precise as the other data because of experimental difficulties at elevated temperatures with the equipment used. If a temperature effect is present, it is small and results in only slightly increased colloidal size with increased temperature. Recent studies of asphaltenes separated from petroleum and suspended in various solvents have shown a large temperature effect on colloid molecular weight (and size), the molecular weight being roughly inversely proportional to temperature.¹ However, if the best straight line is fitted to the data of Table IV using least squares, the slope for R_{0m} vs. temperature is 0.0531 with a standard deviation of 0.045. Although X-ray small angle scattering and ultracentrifuge methods of particle size determination are based on somewhat different principles, as previously discussed, the simplest explanation for the fact that the temperature dependence of petroleum colloids is different, within reasonable statistical certainty, using the two methods is that the colloidal materials present in petroleum are somewhat different from asphaltenes separated from petroleum and suspended in solvents.

Parameters for two petroleum samples that were studied in more detail are given in Table V. It is interesting to note that the average radii of gyration determined by the Hosemann method and by the Shull and Roess method are in reasonably good agreement. Such is often not the case when appreciable interference effects exist.⁸ The Maxwellian parameters should not be interpreted as giving the true distribution of particle sizes. As has been shown, assuming a Maxwellian, Gaussian, or square distribution gives values of \bar{R}_0 that are usually in good agreement.^{8,9,12,13} Thus, \bar{R}_0 is determined with reasonable confidence, but the shape of the distribution is not.

A typical $\gamma(R)$ curve is shown in Figure 2. The S/V ratios determined from the $\gamma(R)$ curves are average values for polydisperse systems. However, it is interesting to note that average radii of gyration calculated from S/V , assuming a spherical colloid, give results in reasonable agreement with those using the Hosemann and the Shull and Roess methods.

It also is of interest that the R_{0m} values calculated from the \bar{R}_0 values using the method previously described give reasonable agreement with the R_{0m} values calculated using the Guinier method.

As has been pointed out,^{8,9} the small angle X-ray data alone often are insufficient to fix the particle shape. The data at hand could be fitted well to a prolate ellipsoid model, and the parameters for the ellipsoids also are given in Table V. A graphical

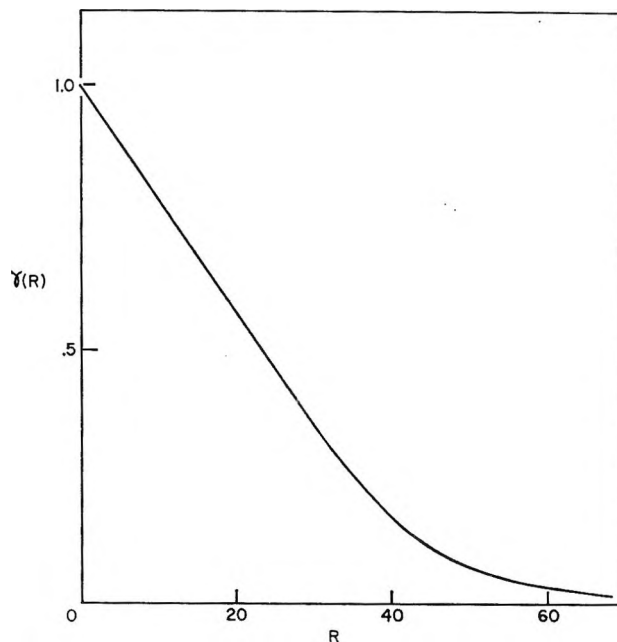


Figure 2. Characteristic function plot for Lagunillas petroleum.

method⁸ using plots of $\log I$ vs. $\log hR_{0m}$ was used to determine the axial ratios of the ellipsoids. The length of the axes then could be calculated using the axial ratio and the definition of R_{0m} in terms of lengths of axes of an ellipsoid. A monodisperse ellipsoidal model is unlikely, based on previously mentioned ultracentrifuge and other work. The distribution of spheres and the monodisperse ellipsoid represent two possible extreme cases, with available evidence pointing to a true state of affairs close to the distribution of spheres. The S/V ratios calculated from the ellipsoidal models are higher than those calculated from the $\gamma(R)$ curves. This is more, but not very strong, evidence that the monodisperse ellipsoid model is not likely. The ellipsoid can describe a wide variety of shapes ranging from rods to flat plates fairly well. Thus, other models of the colloid shape seem very remote.

It appears too early to attempt to relate the chemical composition of the crude oils studied to the colloidal properties in detail. Such relations probably are rather complex. Elemental analyses for several of the oils studied are available.^{16,17}

Nomenclature

h	$(4\pi \sin \theta)/\lambda \cong [2\pi(2\theta)]/\lambda$
2θ	Scattering angle, radians = 2(Bragg angle, radians)
λ	Wave length, Å.

(16) C. W. Dwiggin and H. N. Dunning, *Anal. Chem.*, **32**, 1137 (1960).

(17) C. W. Dwiggin, *ibid.*, **33**, 67 (1961).

$\Gamma(z)$	The Γ -function of an arbitrary quantity, z		
$I(h)$	The relative intensity of scatter as a function of h , corrected for finite collimation slit height and width	r_0	A Maxwellian distribution parameter determined from experimental data using the Hosemann or the Shull and Roess method as further defined in ref. 9
$s(h)$	Experimentally determined relative intensity of scatter as a function of h , using finite collimation slits	n	Another Maxwellian distribution parameter determined from experimental data using the Hosemann or Shull and Roess method as further defined in ref. 9
$s_1(h)$	Relative intensity of scatter as a function of h , corrected for finite collimation slit width	S/V	The average surface to volume ratio of a particle with the unit of length being Ångstroms
$i_{1,0}(x)$	$i_1(x)/\int i_1(x)dx$ = fraction of the total power of the real direct beam striking the plane of observation between the abscissas, x and $x + dx$ as further defined in ref. 9	$\gamma(R)$	The characteristic function of small angle X-ray scattering as a function of R as further defined in ref. 9
u	A variable of integration without physical significance	R	Radius of a spherical particle or the length of the two identical semi-axes of an ellipsoid
Q'	The first derivative of an arbitrary function Q	c	A constant
R_0	Radius of gyration of a particle based on electron density as further defined in ref. 9	a	Semimajor axis of a prolate ellipsoid
R_{0m}	Weighted average radius of gyration as determined by the Guinier method as further defined in ref. 9	b	Seminor axis of a prolate ellipsoid
\bar{R}_0	Average radius of gyration as determined by the Hose-	v	Axial ratio of an ellipsoid

Ionization Potentials of Aromatic Amines

by P. G. Farrell and J. Newton

Department of Chemistry, Sir John Cass College, Aldgate, London, E.C.3, England
(Received April, 28, 1965)

The charge-transfer spectra of complexes formed by tetracyanoethylene with substituted anilines have been used to determine values for the ionization potentials of the amines. The results are discussed in terms of the electronic effects of the substituent groups.

Introduction

Direct measurements of the ionization potentials (I_D) of aromatic molecules have been made for relatively few substances only. Watanabe¹ has measured ionization potentials for a range of substituted benzenes and for some aromatic hydrocarbons by a photoionization method, and Wacks and Dibeler² used an electron-impact method to obtain values for a few aromatic hydrocarbons. This latter method has also been used by other workers to measure ionization potentials of substituted benzenes.³ For alternant hydrocarbons the ionization potential (the energy required to remove an electron from the uppermost filled molecular orbital) is simply related to the energy of the electronic transition from this orbital into the lowest

unfilled orbital as was shown by Matsen.⁴ Using his relationship, or the modified form proposed by Kuroda,⁵ one can obtain ionization potentials for alternant aromatic hydrocarbons from their electronic spectra.

An alternative method for obtaining ionization potential values is from the measurement of the charge-transfer spectra of aromatic molecules with an electron acceptor. To a first approximation, it has been shown

- (1) K. Watanabe, *J. Chem. Phys.*, **26**, 542 (1957).
- (2) M. E. Wacks and V. H. Dibeler, *ibid.*, **31**, 1557 (1959).
- (3) J. D. Morrison and A. J. C. Nicholson, *ibid.*, **20**, 1021 (1952); F. H. Field and J. L. Franklin, *ibid.*, **22**, 1895 (1954).
- (4) F. A. Matsen, *ibid.*, **24**, 602 (1956).
- (5) H. Kuroda, *Nature*, **201**, 1214 (1964).

that the energy of the charge-transfer transition may be expressed as

$$h\nu_{CT} = aI_D + b \quad (1)$$

where a and b are constants for a given acceptor, b containing terms such as the electron affinity of the acceptor, coulombic interaction terms between the non-bond and dative states, and any solvent effects.⁶ These latter are assumed constant for a series of similar donors with a given acceptor in the same solvent. Thus, from the long wave length, charge-transfer absorption maximum of an electron donor with a given acceptor the ionization potential of the donor may be calculated if the constants a and b for the system are known.

A number of expressions for predicting ionization potentials from charge-transfer data have been proposed⁶⁻⁸ but these have mainly been based upon the ionization potential values of aromatic hydrocarbons, either measured directly or obtained from their electronic spectrum. In order to obtain an expression more applicable to the prediction of values for substituted benzenes, we have measured the charge-transfer spectra with tetracyanoethylene (TCNE) as acceptor of most of the substituted benzenes whose ionization potentials have been measured by Watanabe. TCNE was chosen as acceptor because the charge-transfer bands occur in general in the visible region and are well removed from bands arising from electronic transitions within either the donor or the acceptor molecules themselves. Values of a and b have been obtained from the linear relationship of eq. 1 and used to predict I_D values for a series of substituted anilines.

Experimental Section

Materials. Tetracyanoethylene, obtained commercially, was sublimed three times at 125° (4 mm.), m.p. 197–199° (sealed tube), lit.⁹ 198–200°.

All amines were either prepared in this laboratory or obtained commercially and purified according to the literature.

Solvents. Chloroform was washed four times with an equal volume of distilled water, dried over calcium chloride, and distilled under nitrogen. Diethyl ether and carbon tetrachloride were purified according to Vogel.¹⁰ All other solvents were of Spectroscopic grade and used without any further purification.

Measurements. The charge-transfer absorption spectra were measured using a Beckman DK2 recording spectrometer fitted with a constant temperature cell housing thermostated at 24 ± 0.2°. In general, the optical density due to the charge-transfer complex was observed to decrease slowly with time.

The rate of decay was minimized, however, by ensuring that the aniline-TCNE concentration ratio was low.

Solutions of the complexes were prepared in 10-mm. stoppered silica cells immediately before use. These solutions were prepared from stock solutions of TCNE in the various solvents, and the amine concentration was adjusted to give between 45 and 75% absorption for the complex. Each spectrum was run three times.

Results and Discussion

Effect of Solvent. The effect of changing the solvent on the spectra of substituted aniline-TCNE complexes was investigated in order to determine the most suitable solvent in which to measure the spectra. Table I gives the wave lengths of maximum absorption for the long wave length bands of a number of amines in various solvents, the values in chloroform being close to those in other chlorinated solvents (carbon tetrachloride, methylene dichloride). Although measurements for use in calculating ionization potentials should ideally be made in a solvent in which the interaction between the solvent and the solutes is at a minimum (*e.g.*, isooctane, *n*-hexane), the extremely low solubility of TCNE in these solvents and the broad charge-transfer bands obtained with low optical densities make accurate measurement of the wave lengths impossible. Diethyl ether and chloroform are suitable solvents for TCNE, but in the former there is evidence of hydrogen bonding with primary and secondary amines¹¹ (see Table I). As any interaction between the electron donors and

Table I: Values (in $m\mu$) for the Position of the Long Wave Length Absorption Band of a Number of Anilines in Various Solvents at 24 ± 0.2°

Aniline	Solvent		
	Isooctane	Diethyl ether	Chloroform
Aniline	287	290.2	287.5
NMe	293.5	296	296
NEt	294	296	296.2
N- <i>n</i> -Pr	294.5	296.5	297
NMe ₂	297	297.7	301
NEt ₂	302	302.5	307.5
N- <i>n</i> -Pr ₂	302.7	303	308
N- <i>n</i> -Bu ₂	303	303	308

(6) H. McConnell, J. S. Ham, and J. R. Platt, *J. Chem. Phys.*, **21**, 66 (1953); R. Foster, *Tetrahedron*, **10**, 96 (1960).

(7) G. Briegleb, *Angew. Chem. Intern. Ed. Engl.*, **3**, 617 (1964).

(8) E. M. Voigt and C. Reid, *J. Am. Chem. Soc.*, **86**, 3930 (1964).

(9) T. L. Cairns, *et al.*, *ibid.*, **80**, 2775 (1958).

(10) A. I. Vogel, "A Textbook of Practical Organic Chemistry," Longmans, Green and Co., London, 1951, pp. 173–175.

(11) S. Nagakura and H. Baba, *J. Am. Chem. Soc.*, **74**, 5693 (1952).

chloroform should be of the same type and probably similar in magnitude (assuming zero solvent-donor interaction in isooctane), this solvent was used in the present work.

Evaluation of a and b. Values of $h\nu_{CT}$ for the TCNE charge-transfer complexes of the aromatic donors used to calculate a and b in eq. 1 are given in Table II, together with the ionization potentials of the donors. Analysis of the data by a least-squares method, assuming the error to be in the measurement of $h\nu_{CT}$, gives a and b the values shown in eq. 2

$$h\nu_{CT} = 0.82I_D - 4.28 \text{ e.v.} \quad (2)$$

This expression may be compared with that obtained from a more restricted series of substituted benzenes ($8.2 \text{ e.v.} < I_D < 9.25 \text{ e.v.}$) by Voigt and Reid.⁸ Using their decomposition method, they found $a = 0.83$ and $b = -4.42$.

Table II: Charge-Transfer Energies of Substituted Benzene-TCNE Complexes in Chloroform Solution at $24 \pm 0.2^\circ$ together with the Ionization Potentials of the Donors

Substituted benzene	$h\nu_{CT}$, e.v.	I_D , e.v. ^a
Toluene	2.992	8.82
Isopropylbenzene	2.949	8.69
<i>n</i> -Butylbenzene	2.956	8.69
<i>o</i> -Xylene	2.809	8.56
<i>m</i> -Xylene	2.803	8.56
<i>p</i> -Xylene	2.636	8.445
Mesitylene	2.636	8.39
Chlorobenzene	3.217	9.07
Bromobenzene	3.073	8.98
<i>p</i> -Chlorotoluene	2.759	8.69
<i>o</i> -Bromotoluene	2.970	8.78
Anisole	2.420	8.20
Aniline	2.097	7.70

^a See ref. 1.

Table III: Ionization Potentials of Some Substituted Benzenes from the Charge-Transfer Energies of Their TCNE Complexes in Chloroform at $24 \pm 0.2^\circ$

Substituent	$h\nu_{CT}$, e.v.	I_D , e.v. ^a	I_D , e.v. ^b
NH ₂	2.097	7.76	7.70 ^c
NHMe	1.946	7.58	7.6 ^d
NHEt	1.931	7.56	7.5 ^d
NH- <i>n</i> -Pr	1.916	7.54	7.5 ^d
NH- <i>n</i> -Bu	1.910	7.53	7.5 ^d
NMe ₂	1.839	7.44	7.3 ^d
NEtMe	1.774	7.37	
NEt ₂	1.469	6.99	7.15 ^d
N- <i>n</i> -Pr ₂	1.444	6.96	7.15 ^d
N- <i>n</i> -Bu ₂	1.435	6.95	7.15 ^d
NMe ₂ - <i>o</i> -Me	1.774	7.37	
NMe ₂ - <i>m</i> -Me	1.761	7.35	
NMe ₂ - <i>p</i> -Me	1.749	7.33	
NEt ₂ - <i>p</i> -Me	1.419	6.93	
NMe ₂ - <i>p</i> -Et	1.786	7.38	
NMe ₂ - <i>p</i> - <i>i</i> Pr	1.813	7.41	
NMe ₂ - <i>p</i> - <i>t</i> Bu	1.831	7.43	
NMe ₂ - <i>p</i> -F	1.881	7.50	
NMe ₂ - <i>p</i> -Cl	1.786	7.38	
NMe ₂ - <i>p</i> -Br	1.749	7.33	
NMe ₂ - <i>p</i> -I	1.713	7.29	
NEt ₂ - <i>p</i> -Br	1.444	6.96	
NMe ₂ -2,6-Me ₂	1.655	7.22	
NMe ₂ -2,4-Me ₂	1.612	7.17	
NMe ₂ -3,5-Me ₂	1.682	7.25	

^a Calculated from eq. 2; error less than ± 0.1 e.v. ^b Values obtained by other workers. ^c K. Watanabe and J. R. Mottl, *J. Chem. Phys.*, **26**, 1773 (1957). ^d G. Briegleb and J. Czekalla, *Z. Elektrochem.*, **63**, 6 (1959).

cordance with the leveling-off of the inductive effects of the substituents. A similar trend is observed in the dialkyl series, but our value for N,N-dimethylaniline is appreciably higher than that obtained by other workers (see Table III). Replacement of methyl by ethyl groups has a large effect upon the ionization potential in both the dialkylanilines and their *para*-substituted analogs. This difference was noted by Foster and Hammick¹² in their investigation of *s*-trinitrobenzene complexes and has been observed with other electron acceptors.¹³

This sudden drop in ionization potential is accompanied by a considerable change in reactivity. The rate of reaction of N,N-diethyl- and higher N,N-dialkylanilines with TCNE is considerably faster than that of N,N-dimethylaniline, and furthermore there is a substantial amount of 1,1,2,3,3-pentacyanopropenide

Values for the ionization potentials of the donors in Table II, recalculated from eq. 2, show that the average difference between the experimental and the calculated values is ± 0.06 e.v. This agreement is far closer than one could expect considering the different types of substituted benzenes used but does indicate that the method has some value.

Ionization Potentials. I_D values for a wide range of aromatic amines obtained from eq. 2 are given in Table III, together with those of other workers where available.

In the monoalkylaniline series I_D rapidly approaches a minimum value as one ascends the series, in ac-

(12) R. Foster and D. Ll. Hammick, *J. Chem. Soc.*, 2685 (1954).

(13) R. Beukers and A. Szent-Gyorgyi, *Rec. trav. chim.*, **81**, 255 (1962).

ion produced in these faster reactions.¹⁴ In the similar reaction with tricyanovinyl chloride, Rappoport and co-workers¹⁵ noted a large difference between the rate of reaction with N,N-dimethylaniline and that with higher N,N-dialkylanilines, this difference being in accordance with the part of the basicity of the amines resulting from the inductive effects of the alkyl groups.¹⁵ Other workers have also observed marked differences in the behavior of N,N-dimethylaniline and N,N-diethylaniline. Bell and Ramsden¹⁶ were unable to measure the rate of bromination of N,N-diethylaniline owing to its greater complexing power with bromine, and Price and Belanger¹⁷ found that the rate of saponification of alkyl *p*-dialkylaminobenzoates decreased markedly on going from *p*-N,N-dimethylamino to *p*-N,N-diethylamino as substituent but varied little to *p*-N,N-di-*n*-propylamino. The small variation on substitution by *n*-alkyl groups higher than ethyl may be due to the leveling-off of electronic effects or to bulk effects and the possibility of steric interactions. $h\nu_{CT}$ for N-methyl-N-ethylaniline lies closer to that for N,N-dimethylaniline than to that for N,N-diethylaniline supporting the premise that this greater electron-releasing power is peculiar to the diethylamino group in this environment. Further work is in progress in an attempt to shed further light on this problem.

The dependence of the ionization potential on the electronic structure of the aromatic molecule is also illustrated in Table III. N,N-dialkylated anilines have been used to exclude any possibility of substitu-

tion on the nitrogen atom, but the results for the nitrogen-unsubstituted compounds follow a similar pattern.¹⁸ These are consistent with accepted theories of substituent effects in an aromatic nucleus and to a small degree reflect any steric factors although these latter have a more pronounced effect upon the equilibrium constant and extinction coefficient for the complex than upon the charge-transfer energy. Substitution in the aniline ring by a methyl group shifts the charge-transfer maximum to longer wave lengths, the shift being small in the case of N,N-dimethyl-*m*-toluidine. Further methyl substitution shifts the absorption maximum to still longer wave lengths in accordance with the position of substitution and thus decreases the ionization potential. Halogen substitution in the *para* position leads to an increase in I_D as the electronegativity of the halogen increases, whereas the I_D values for the *p*-alkyl-substituted analogs follow the Baker-Nathan order.¹⁹

Acknowledgments. We thank the Department of Scientific and Industrial Research for financial support to J. N.

-
- (14) P. G. Farrell and J. Newton, *Tetrahedron Letters*, 189 (1964).
(15) Z. Rappoport, P. Greenzaid, and A. Horowitz, *J. Chem. Soc.*, 1334 (1964).
(16) R. P. Bell and E. Ramsden, *ibid.*, 161 (1958).
(17) C. C. Price and W. J. Belanger, *J. Am. Chem. Soc.*, **76**, 2682 (1954).
(18) P. G. Farrell and J. Newton, unpublished results.
(19) J. W. Baker and W. S. Nathan, *J. Chem. Soc.*, 1844 (1935).

A Proposed Model for Electron Injection into Some Organic Semiconductors in the Dark

by M. E. Green

Department of Chemistry, Middle East Technical University, Ankara, Turkey (Received April 30, 1965)

A model of a rectifying contact, proposed by Bardeen in 1947, is adapted to account for the electrical behavior in the dark of organic semiconductors. The voltage and temperature dependence of the resistance of naphthalene and anthracene are calculated.

1. Introduction

Organic semiconductors have been the objects of considerable research, both experimental and theoretical. However, the experimental results on such thoroughly studied materials as naphthalene and anthracene show only moderately good reproducibility. The theoretical interpretation of the electronic conductivity has been even more puzzling.

It has been clear for some time that these materials are not intrinsic semiconductors, in spite of the fact that they share one important experimental characteristic with them—namely, the resistance decreases exponentially with temperature. One can write

$$\rho = \rho_0 \exp(+E_{\text{act}}/kT) \quad (1)$$

where ρ is resistivity, k is the Boltzmann constant, T the absolute temperature, and E_{act} a measured activation energy. For an intrinsic semiconductor, $E_{\text{act}} = E_G/2$, where E_G is the energy gap. For naphthalene, one expects an energy gap of 5 to 6 e.v.¹ Measured values fall far short of this; usually E_{act} is less than 1 e.v., giving an apparent E_G less than 2 e.v.² The voltage dependence of the resistivity has also been investigated^{2a,3} but not explained. It is also approximately exponentially decreasing, with voltage, and is independent of the temperature to the limits of experimental error.

It is difficult to account for both of these results by invoking "impurity effects"; it is especially difficult to explain the voltage dependence in these terms.

Some important points concerning the electrical behavior of these materials do seem well established. The mobilities have been measured and found to agree with theoretical expectations. In addition, the photo-

conductivity of anthracene is a well-established phenomenon, and it has been known for some time that most of this photoconductivity comes from the surface.⁴ Even more interesting is the fact that it is possible to inject large quantities of carriers into anthracene in the dark, provided sufficient energy is supplied chemically.⁵ With all of this evidence in hand, it seems most reasonable to look to the surface as a possible source of charge carriers in the dark under ordinary conditions as well. Kepler has already made this point, in general terms.⁶ In the next section, we will see that it is possible to find a barrier which is physically justified and can account for the experimental data.

II. Model for a Surface Barrier

Physically, we expect naphthalene or anthracene to behave as a very narrow band semiconductor,⁷ so that the carriers, if they are to be injected through a surface barrier, must find themselves in a fairly well-defined energy level. (Since it is somewhat easier to visualize the injection of electrons, we will consider only this.

(1) (a) L. E. Lyons, *J. Chem. Soc.*, 5001 (1957); (b) Abstracts, Organic Crystal Symposium, Ottawa, 1962, p. 42.

(2) (a) N. V. Riehl, *Zh. Fiz. Khim.*, 29, 959 (1955); (b) J. A. Bornmann, *J. Chem. Phys.*, 36, 1691 (1962).

(3) For anthracene, apparently similar results were found for the voltage dependence. It is difficult to be sure, from the presentation of the data on a small graph [H. Mette and H. Pick, *Z. Physik.*, 134, 566 (1953)].

(4) D. M. J. Compton, W. G. Schneider, and T. C. Waddington, *J. Chem. Phys.*, 27, 160 (1957).

(5) (a) M. Pope, H. P. Kallman, A. Chen, and P. Gordon, *ibid.*, 36, 2482 (1962); (b) H. P. Kallmann and M. Pope, *ibid.*, 36, 2486 (1962).

(6) R. G. Kepler, *Org. Semicond. Proc. Inter-Ind. Conf.*, Chicago, 1961, 1 (1962).

(7) O. H. LeBlanc, *J. Chem. Phys.*, 35, 1275 (1961).

The same model can be directly applied in the case of holes as well. For dark conductivity, the question of which carrier predominates is still not clear.) Furthermore, the organic crystal can be expected to have surface states, caused possibly by impurities or irregularities. We should expect Tamm states, arising simply from the termination of the lattice, to be present in any case. For our purposes, the actual origin of the surface states is not important.

The electrodes that have been used in measurements of naphthalene conductivity have themselves varied. Simplest to consider is a metal electrode. However, this may itself be covered with an oxide layer, causing it to behave more like a semiconductor than a metal. For the purposes of this discussion, a semiconductor electrode will be considered, and, later, some experiments will be suggested to give a more precise test of the model, particularly in respect of the effect of the nature of the electrode.

An energy level diagram for a rectifying metal-semiconductor contact proposed by Bardeen in 1947⁸ gives a satisfactory fit to the data. Bardeen's model can be applied here, with the dirty metal or a semiconductor taking the place of the metal in the picture of the rectifying contact, provided that the electrode has its Fermi level near to its conduction band. Otherwise, the picture would require some modification. In this paper, only the case in which the condition is fulfilled will be discussed in detail.⁹

From now on, the symbols we use will be those defined in Figure 1. Our treatment depends on two points: (1) the upper part of the barrier can be tunneled through; and (2) the lower part of the barrier, below the conduction band of the organic crystal, is essentially infinitely thick. The electron must first acquire sufficient energy to reach the conduction band before it can begin to tunnel (at the energy of the conduction band).

In terms of the quantities defined in Figure 1, we then have

$$E_{\text{act}} = \zeta + \phi_0 \tag{2}$$

(ζ will presumably be determined by the electrode Fermi level.) Next, we must calculate the probability of the electron tunnelling through the remainder of barrier. The transmission probability is given by¹⁰

$$K \cong \exp \left\{ -2 \int_0^a \left[\frac{2m}{\hbar^2} (U(x) - E) \right]^{1/2} dx \right\} \tag{3}$$

where a is the thickness of the barrier, $U(x)$ is the potential energy, E is the kinetic energy, m is the mass of the electron, and \hbar is Planck's constant divided by 2π .

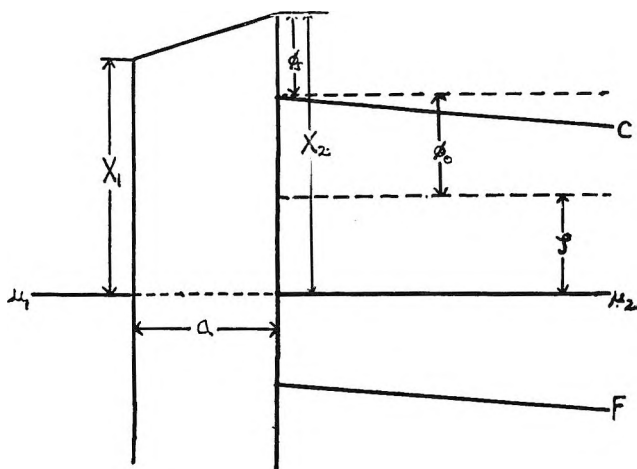


Figure 1. Energy level diagram (following Figure 3 of ref. 8) for contact, illustrating notation used in text: μ_1 and μ_2 are the Fermi levels, X_1 and X_2 the work functions. The organic semiconductor conduction band is labeled C, the top of its valence band F. The barrier width is a . ϕ_0 is the potential energy rise at the surface due to the surface charges. ϕ_a is the work required to remove an electron from the conduction band to just outside the semiconductor surface. ζ , in this discussion, is the energy required to go from the Fermi level to the conduction band, if the charge on the surface states makes $\phi_0 = 0$.

For $U(x) - E$, let us take $A + Zx$, where $A = X_1 - E_{\text{act}}$, and $Z = (X_1 - X_2)/a$. Then

$$K \cong \exp \left\{ -2 \left(\frac{2m}{\hbar^2} \right)^{1/2} \int_0^a (A + Zx)^{1/2} dx \right\}$$

and

$$\ln K \cong -2 \left(\frac{2m}{\hbar^2} \right)^{1/2} \frac{2}{3Z} [(A + Za)^{3/2} - A^{3/2}] \tag{4}$$

Next, suppose we add a field $E = -eVx$, V being the applied voltage and e the electronic charge. Going through the same procedure

$$\ln K \cong -2 \left(\frac{2m}{\hbar^2} \right)^{1/2} \frac{2}{3(Z - eV)} \times \{ [A + (Z - eV)a]^{3/2} - A^{3/2} \} \tag{4a}$$

While it is not at first clear from this that $\ln K$ will give a linear dependence on V , we can safely assume that $eV < Z$, and expand both terms in which eV appears. If

(8) J. Bardeen, *Phys. Rev.*, **71**, 717 (1949).

(9) One other modification in the original model is, in principle, needed here: the space charge layer may extend through an appreciable fraction of the crystal, because of the low charge density, so that the curvature of the bands near the surface may be inappreciable. However, this will not change our argument in any case.

(10) N. F. Mott, "Elements of Wave Mechanics," Cambridge University Press, Cambridge, 1952, p. 35.

we do so, two first-order terms appear in eV , and, combining them

$$\ln K \approx -2 \left(\frac{2m}{\hbar^2} \right)^{1/2} \left\{ \frac{2}{3Z} [(A + Za)^{3/2} - A^{3/2}] - \left[\frac{ea}{Z} (A + Za)^{1/2} - \frac{2e}{3Z^2} [(A + Za)^{3/2} - A^{3/2}] \right] V \right\} \quad (4b)$$

so that

$$\frac{d \ln K}{dV} = -2 \left(\frac{2m}{\hbar^2} \right)^{1/2} \left\{ \frac{ea}{Z} (A + Za)^{1/2} - \frac{2e}{3Z^2} [(A + Za)^{3/2} - A^{3/2}] \right\} \quad (5)$$

We are now faced with the task of choosing reasonable parameters and comparing with experiment. We have three parameters which we apparently can vary within fairly wide limits, A , Za , and a . However, $A - E_{\text{act}}$ is the work function of the electrode, and $A + Za + E_{\text{act}}$ is the work function of the sample. For naphthalene, the work function ought to be 6 e.v., or a bit less,¹ while for most electrodes one might pick a value about 1 e.v. smaller. a should correspond to several molecular diameters, and may well be of the order of 10–20 Å. Our choice of values for the parameters is thus fairly well circumscribed, in spite of first appearances. Picking values within the range available to us, say $A = 3$ e.v., $a = 15$ Å., $Za = 1.5$ e.v., we would find $K \approx 10^{-12}$, $d \ln K/dV \approx 8 \times 10^{-7}$ (v./cm.)⁻¹. The experimental value for $d \ln K/dV \approx 3 \times 10^{-4}$, or more than two orders of magnitude larger. To compare $\ln K$ with experiment, we must try to find the actual current which our model would predict. The number of electrons flowing through the barrier is given by

$$n = n_0 k_b \quad (6)$$

where n_0 is the number of electrons available in the electrode and k_b is a rate constant given, in the thermodynamic representation, by

$$k_b = (kT/h) K \exp(S_{\text{act}}/k) \exp(-E_{\text{act}}/kT) \quad (7)$$

where k , t , and h have their usual significance, S_{act} is an entropy of activation, and E_{act} is the activation energy. S_{act} cannot be very large. The entropy of an electron in a metal or degenerate semiconductor at ordinary temperatures is very small.¹¹ If the electron behaved like a free particle, its entropy would be $3k/2$. It is apparent that $\exp(S_{\text{act}}/k)$ is of the order of unity. The best value of E_{act} to choose is about 0.75 e.v.² Then, at room temperature, $k_b \approx 10^{-12}$ and, if $n_0 \approx 10^{14}$, $n \approx 10^2$ e/sec., for a 1-v./cm. field. Since experimental

resistivities at room temperature are about 10^{16} to 10^{17} ohm-cm. meaning an electron current of 10^2 to 10^3 e/sec., agreement is certainly satisfactory here. In fact, of course, both the experimental and theoretical values can vary,¹² the theoretical ones by choosing different values of the parameters.

The discrepancy in the slope of the voltage dependence seems more serious, since with no reasonable choice of parameters can agreement with experiment be achieved. Indeed, eq. 5 is not very sensitive at all to the parameters chosen. We may achieve some variation by choosing a somewhat more realistic barrier shape, in which the walls are not perfectly vertical. The major cause of the difficulty does not seem hard to locate, however. We have assumed that the voltage drop across the barrier layer is simply given by eVx , as though there were no extra voltage drop across the surface region. If, however, the voltage drop is written as $ceVx$, where c is a constant, then the measured value of $d \ln K/dV$ would be c times our previously calculated value. If the barrier is, in fact, to act as a high-resistance layer, c must be greater than 1. In order for our calculation to agree with experiment, $c \approx 10^2$ is needed, which is not unreasonable. A value much higher than 10^2 would in fact be unreasonable, since at high fields $ceVx$ would become greater than Za , and the approximation would break down. If $d \ln K/dV$ is to continue to be linear to about 10^6 v./cm., then, with $a \approx 10^{-7}$ and $Za \approx 1$ e.v., the maximum value for $c \approx 10^2$. With c being of this order, it should be possible to observe deviations from eq. 5 above about 10^6 v./cm. Thus, the most important features of the electrical behavior of compounds such as naphthalene and anthracene can be reproduced by this simple model of a surface barrier. However, the evidence is more nearly suggestive than conclusive at this point, and further experimental tests are clearly needed before the model can be considered as established. It is one of the purposes of this note to suggest such experiments.

III. Possible Experimental Tests of this Model

One test has already been suggested, that is, a search for deviations from linearity of the $\ln \rho$ - V curve, at high fields. These deviations should follow eq. 4a and thus provide a quantitative test of the model.

Other tests are possible which depend on the choice of electrodes, electrode parameters being involved in eq. 4, 5, and 6. To begin with, eq. 6 shows a direct depend-

(11) E. A. Moelwyn-Hughes, "Physical Chemistry," 2nd Ed., The MacMillan Co., New York, N. Y., 1961, p. 652.

(12) Y. Okamoto, F. T. Huang, A. Gordon, W. Brenner, and B. Rubin, *Org. Semicond. Proc. Inter-Ind. Conf., Chicago, 1961*, 100 (1962).

ence of total current on the number of carriers available in the electrode. If the same type of semiconductor is used as electrode, on the same crystal of naphthalene, in replicate runs, with only the doping of the electrode varied, it should be possible to have the barrier thickness approximately constant, and thus see the effect of varying n_0 . If, on the other hand, the electrode is simply a low resistance in series with the organic crystal, then no effect at all should be detectable. A relatively small variation in Fermi level should suffice for this test. More critical tests of the model are possible, however.

By using asymmetric electrodes, that is different electrodes on the two sides of the sample—for example, on one side n-type silicon with the Fermi level close to the conduction band, on the other p-type silicon with the Fermi level much farther away from the conduction band—it would be possible to find the sign of the charge carriers if the model is correct, since E_{act} would presumably differ for the directions of current flow if one carrier predominated in both cases.

Another experiment would involve the use of a "good" electrode, which would make contact to the sample through a much smaller barrier layer. Although it might not be easy to find such an electrode, perhaps this experiment has already been done, by the use of liquid naphthalene. This has a conductivity about three orders of magnitude higher than the solid,² despite probably a lower mobility (if Le Blanc's data¹³ on pyrene are generally true), and a constant energy gap.² As a corollary to this behavior, we should then expect a weaker voltage dependence. However, the liquid may not prove relevant to this model at all, since Silver¹⁴ has shown that the conductivity of liquid insulators usually can be accounted for by a different model.

Finally, the naphthalene or other organic semiconductor can itself have its surface somewhat varied, most importantly in respect of the charge on the surface. The work of Belyaev, *et al.*,¹⁵ indicates that charges as high as $10^{10}/\text{cm}^2$ may be expected. Changing the charge must affect E_{act} and the voltage dependence both. $E_{\text{act}} = \zeta + \phi_0$ for negative carriers, and, as the surface

charge becomes more negative, ϕ_0 will increase, causing E_{act} to increase. The reverse effect will, of course, occur for positive carriers, where $E_{\text{act}} = E_{\text{Fermi}} - E_{\text{val band}} = \mu_2 - F$ in Figure 1.

These experiments should suffice to indicate clearly whether or not the model proposed here is valid. We should note here that the model discussed above does *not* apply in the case of electrolyte electrodes which must behave considerably differently. Therefore, the results predicted here are entirely different from those found and discussed by Pope and Kallmann.⁵ Furthermore, this model does not apply to phthalocyanine, for which the evidence is all in favor of its being a bulk semiconductor: in particular, the voltage dependence of the current is completely different.¹⁶

IV. Conclusions

In this paper, we have discussed a model which may account for the electrical behavior of naphthalene and anthracene in contact with metal or semiconductor electrodes in terms of the picture of a rectifying contacted presented by Bardeen. It has been necessary to modify the picture slightly to account for the low density of charge carriers in these materials.

From this picture, we have been able to calculate the voltage and temperature dependence of the resistance of naphthalene and anthracene, and found (1) how the small value for the energy of activation arises; and (2) that the voltage dependence should be exponential. Comparing calculated values, based on reasonable estimates of the parameters involved, we found agreement with the size of the total current, but found that it was necessary to postulate a higher than proportional voltage drop across the barrier layer.

Further experimental tests of the model were proposed.

(13) O. H. Le Blanc, *J. Chem. Phys.*, **37**, 916 (1962).

(14) M. Silver, *ibid.*, **42**, 1011 (1965).

(15) L. M. Belyaev, G. S. Belikova, V. M. Fridkin, and I. S. Zheludov, *Kristallografiya*, **3**, 762 (1958).

(16) G. H. Heilmeyer and G. Warfield, *ibid.*, **38**, 163 (1963).

The Thermodynamics of the Scandium-Hydrogen System^{1,2}

by M. L. Lieberman and P. G. Wahlbeck

Department of Chemistry, Illinois Institute of Technology, Chicago 16, Illinois (Received May 3, 1965)

Isothermal equilibrium hydrogen pressure measurements were made as a function of composition for the scandium-hydrogen system in the temperature range 600.9 to 1052.6° and up to a hydrogen pressure of 1 atm. These data indicate the existence of two solid solution ranges; the first extends to about $\text{ScH}_{0.55}$, and the second can be described as a scandium hydride phase deficient in hydrogen with respect to ScH_2 . The solubility boundaries defining the immiscibility interval between these two solid solution phases were evaluated; for this two-phase region the hydrogen pressures were found to obey $\log P$ (mm.) = $-[(10,477 \pm 93)/T] + (10.409 \pm 0.087)$. The relative partial molal and integral thermodynamic properties were calculated. Marked changes with composition of the relative partial molal enthalpy and entropy of hydrogen were noted in the first solid solution region.

Introduction

Recently, great interest has been shown in the metal-hydrogen systems because there is a need for stable metal hydrides, *i.e.*, hydrides which exhibit low equilibrium hydrogen pressures. Of the transition and rare earth metal-hydrogen systems investigated, it appears that the yttrium-hydrogen system³ exhibits the greatest stability.

Only limited data have been available for the scandium-hydrogen system. McGuire and Kempter⁴ reported measurements which they believed to be valid temperature-pressure data for the two-condensed-phase region between a solid solution of hydrogen in scandium and an apparently hydrogen-deficient dihydride phase. They reported a maximum hydrogen composition at room temperature corresponding to $\text{ScH}_{2.027}$. Beck⁵ reported temperature-pressure-composition data for the scandium-hydrogen system. Warf and Hardcastle⁶ reported inability to prepare a scandium trihydride phase under conditions of 400° and 40 atm. whereas trihydride phases of yttrium³ and of several of the rare earth metals⁷ have been prepared under less stringent conditions.

The purposes of this work were the determination of thermodynamic data and the establishment of the phase diagram for the scandium-hydrogen system.

Experimental Section

Apparatus. A Sieverts apparatus modified so that equilibrium hydrogen pressures between 10^{-4} mm.

and 1 atm. could be measured was used to obtain pressure-temperature-composition data. The apparatus has been described elsewhere.¹⁻³

Materials. The scandium used in this research was prepared from Sc_2O_3 obtained from the American Scandium Corp. by reduction at the Ames Laboratory of Iowa State University. An analysis of the metal performed by the Ames Laboratory showed the following impurities: O, 1805 p.p.m.; N, 80 p.p.m.; H, 15 p.p.m.; Y, 0.03%; Er, <0.01%; Tm, <0.01%; Yb, <0.004%; Lu, <0.01%; Si, 80 p.p.m.; Ca, 320 p.p.m.; Fe, 180 p.p.m.; and Ta, 1000 p.p.m. The metal was work-hardened to the extent that it could be trimmed on a cleaned lathe to produce fine turnings. The turnings were cleaned by rinsing at least three

(1) Based on a thesis by M. L. Lieberman submitted to the Illinois Institute of Technology in partial fulfillment of the requirements for the Ph.D. degree, June 1965.

(2) Presented before the Physical Chemistry Division at the 148th National Meeting of the American Chemical Society, Chicago, Ill., Sept. 1964.

(3) L. N. Yannopoulos, R. K. Edwards, and P. G. Wahlbeck, *J. Phys. Chem.*, **69**, 2510 (1965).

(4) J. C. McGuire and C. P. Kempter, *J. Chem. Phys.*, **33**, 1584 (1960).

(5) R. L. Beck, Denver Research Institute Report No. LAR-10, 1960.

(6) J. C. Warf and K. Hardcastle, Office of Naval Research Reports 1 and 2, Contract No. 228 (15), Project No. NR-052-390.

(7) R. N. R. Mulford and C. E. Holley, Jr., *J. Phys. Chem.*, **59**, 1222 (1955).

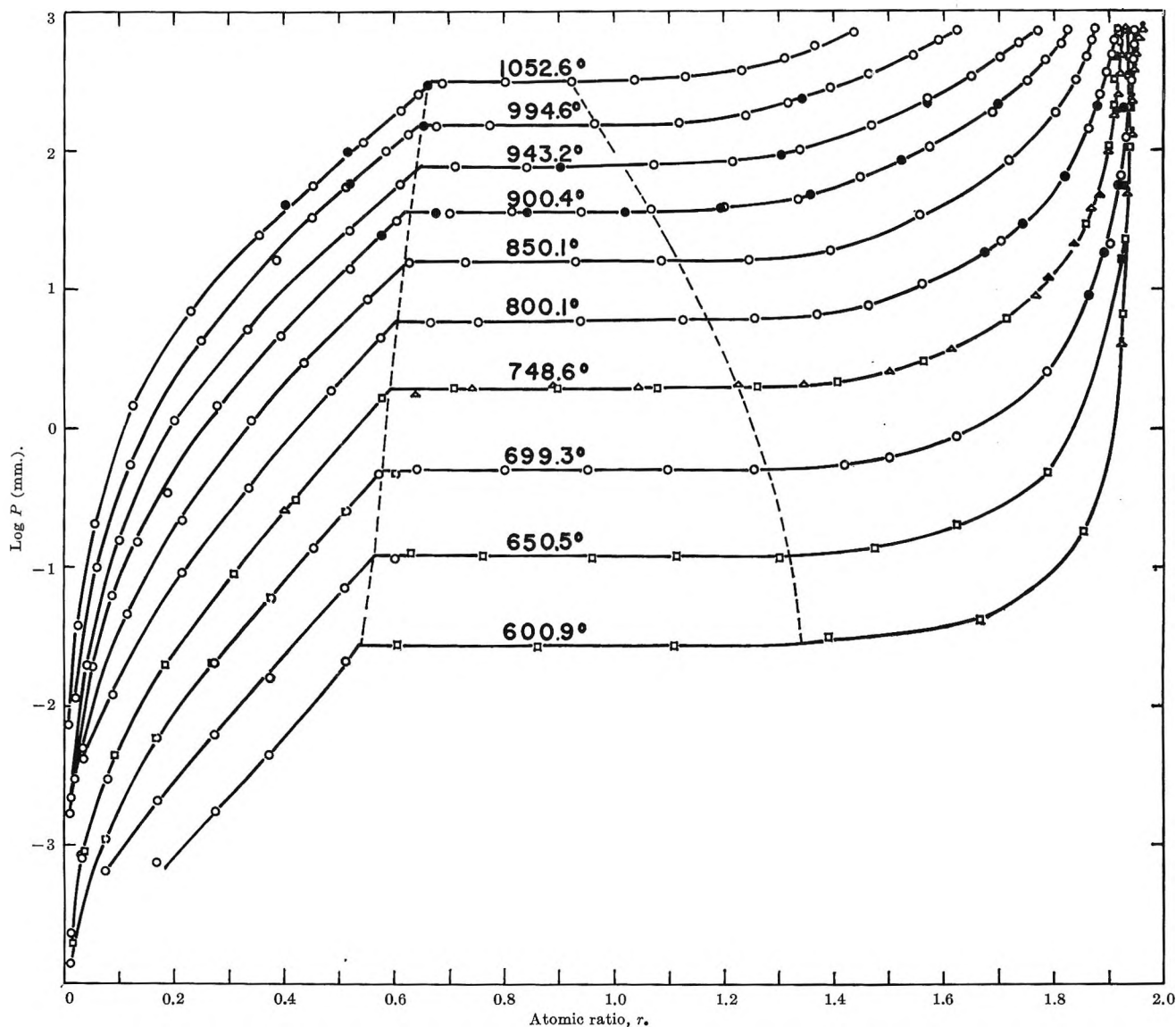


Figure 1. Experimental isotherms for the scandium-hydrogen system: open symbols, absorption points; solid symbols, desorption points.

times with reagent grade acetone and dried under vacuum.

Gases were obtained from the Matheson Co. Ultra pure grade hydrogen had a reported analysis of less than 10 p.p.m. total impurities. Helium, used in calibrating the apparatus, had a reported purity of 99.99%. Both gases were further purified before use as described elsewhere.¹⁻³

Crucibles. Crucibles for containing scandium were fabricated from swaged molybdenum rod. Degassing of crucibles was performed by heating to about 1400° until the vacuum was at least 10^{-5} mm. Absorption of hydrogen by empty crucibles was measured between 700 and 900° at about 0.5 atm. of hydrogen and found

to be no more than 5×10^{-4} atomic ratio unit. Since the crucibles weighed about 25 g., this implied a possible error no larger than 0.025 atomic ratio unit at high hydride composition if one assumed that all hydrogen was absorbed by the scandium. No interaction between molybdenum and scandium was observed.

Procedure. A typical run was made in the following manner. A sample of 0.4 to 0.5 g. of cleaned scandium turnings was placed in a degassed molybdenum crucible. The crucible containing the sample was placed in a quartz cell and was degassed in an auxiliary furnace at 900° until a vacuum of at least 10^{-5} mm. was attained. While still hot, the quartz cell containing the crucible with the degassed sample was trans-

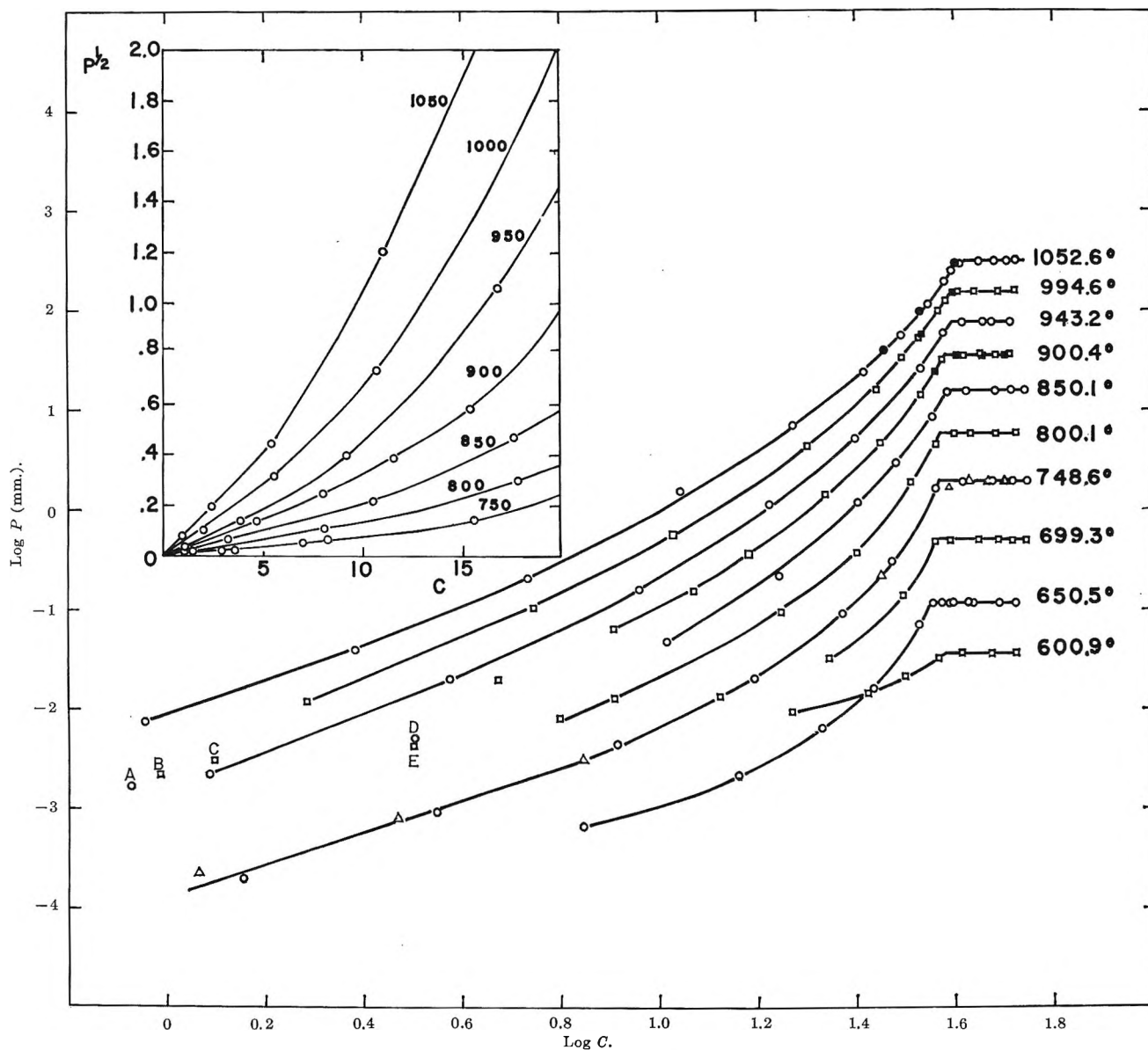


Figure 2. Experimental isotherms for the scandium-hydrogen system: open symbols, absorption points; solid symbols, desorption points. Identification of lettered points: A, isotherm at 850.1°; B, 800.1°; C, 900.4°; D, 850.1°; E, 800.1°. Inserted drawing: approximate temperatures are indicated on the isotherms.

ferred to the main furnace, the temperature of which was set and controlled. The transfer was accomplished without admitting air to the sample.

After the quartz cell containing the sample was attached to the Sieverts apparatus, a calibration of the effective volume of the system was performed by admitting a known number of moles of helium gas which was assumed to be nonreactive with scandium. After the calibration was completed, the quartz cell was re-evacuated.

A known number of moles of hydrogen gas was admitted to the quartz cell. After equilibrium had been

established, the hydrogen pressure was measured. The amount of hydrogen absorbed by the scandium was calculated from the difference between the amount of hydrogen added to the quartz cell and the amount of hydrogen remaining in the gas phase as determined by the hydrogen pressure measurement and volume calibration. Measurements were continued with successive additions of hydrogen until the hydrogen pressure reached 1 atm. Desorption points were obtained to establish the reversible nature of the hydrogenation reaction. Thus, one obtained pressure-composition-temperature data for the scandium-

hydrogen system. After all measurements for an isotherm were completed, the sample in the quartz cell was degassed so that it could be used for another isotherm.

Results

The experimental data are presented in Figure 1 in the form of pressure-composition isotherms for the temperature range of 600.9 to 1052.6°. From the shapes of the isotherms, it is ascertained that there exist two single-condensed-phase regions separated by a two-condensed-phase region. The boundaries of these regions are indicated by dashed lines in Figure 1, and the uncertainty in these boundaries is estimated to be no larger than ± 0.05 H/Sc atomic ratio unit.

In the scandium solid solution region, Sieverts' law was examined for validity; *i.e.*, $P^{1/2} = KC$, where P is the equilibrium hydrogen pressure, C is the hydrogen gram-atom per cent, and K is a constant dependent on temperature. One may examine the data for Sieverts' law validity by plotting $\log P$ vs. $\log C$ which should give a straight line of slope 2 or by plotting $P^{1/2}$ vs. C which should give a straight line. Both methods are represented in Figure 2 with data from several isotherms. Several of the isotherms are constructed from data of more than one run; *e.g.*, the isotherm at 748.6° is constructed from three separate runs at 748.6°. Data for dilute solutions at low pressures have large errors associated with them and must be considered to have a large uncertainty. In the logarithmic plot, the data of the 1052.6, 994.6, 943.2, and 748.6° isotherms yield lines which are highly linear for dilute solutions and have slopes approaching 2 if the first point of each isotherm is discarded. In the nonlogarithmic plot, the isothermal data for dilute solutions give straight lines which pass through the origin. It is to be noted that Sieverts' law represents the experimental data to higher hydrogen concentrations as the temperature is lowered; the straight line fits the data to approximately 12 atomic % at 748.6° but only approximately 6 atomic % at 1052.6°. At an H/Sc atomic ratio of 0.1 unit ($C = 9.1$), the isotherms up to a temperature of 900° obey Sieverts' law; *i.e.*, there are more than half of the isotherms for which Sieverts' law adequately describes the data. Consequently, in the following treatment Sieverts' law is taken to be valid from zero to 0.10 H/Sc atomic ratio unit.

For the two-condensed-phase region, for which the equilibrium hydrogen pressure depends only on temperature, the data were fitted by least-squares analysis to the expression $\log P$ (mm.) = $-[(10477 \pm 93)/T] +$

(10.409 ± 0.087) , where the indicated uncertainties are probable errors.

In the second single-condensed-phase region, a limiting composition of $\text{ScH}_{1.96}$ was obtained at 600.9°; this composition suggested that this region should be identified as a hydrogen-deficient dihydride.

In an attempt to prepare a trihydride phase a scandium sample that had been hydrogenated at 748.6° to an atomic ratio of 1.91 was slowly cooled to about 120°. With this change in temperature the pressure decreased from 730 to 660 mm. which corresponds to a final composition of 2.02 atomic ratio units. It was concluded that a trihydride phase had not formed. These results are in agreement with those of Warf and Hardcastle⁶ and McGuire and Kempter.⁴

It was found that a scandium sample could be reused reproducibly for four isotherms which showed that there was not a large accumulation of impurities during each run.

Desorption points obtained after completing absorption points of an isotherm agreed well with the absorption points as is shown on Figure 1. Since no hysteresis effect was observed, it was concluded that the absorption process is reversible for the scandium-hydrogen system.

The thermodynamic data are presented in Table I. The procedure for the calculation of the thermodynamic data from the experimental data has been reported elsewhere.^{1,2} Ideal behavior has been assumed for hydrogen gas. The quantities $(\bar{H}_H - 1/2H_{H_2}^\Delta)$ and $(\bar{S}_H - 1/2S_{H_2}^\Delta)$ represent the relative partial molal properties of hydrogen per gram-atom of hydrogen in the solid solution where \bar{H} represents the partial molal enthalpy, H^Δ represents the molar enthalpy for the pure substance, and entropy symbols are defined similarly. The integral properties ΔH_f° and ΔS_f° represent the standard enthalpy and entropy of formation of 1 g.-atom of solution formed from solid scandium and gaseous diatomic hydrogen at a pressure of 1 atm.; these integral properties were obtained by graphical integration of the $(\bar{H}_H - 1/2H_{H_2}^\Delta)$ and $(\bar{S}_H - 1/2S_{H_2}^\Delta)$ values by means of the equation

$$\Delta H_f^\circ = \frac{1}{1+r} \int_0^r (\bar{H}_H - 1/2H_{H_2}^\Delta) dr$$

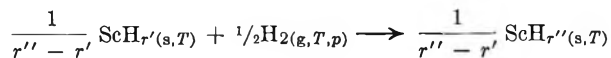
and a similar equation for ΔS_f° , where r represents the atomic ratio. The integration in the dilute solution region was performed by using conclusions drawn from Sieverts' law which was considered to be valid from zero to 0.10 (H/Sc) atomic ratio unit. Sieverts' law implies that $(\bar{H}_H - 1/2H_{H_2}^\Delta)$ is constant in the composition range of its validity and also that the integral entropy is given by the equation

$$\Delta S_f^\circ = \frac{1}{1+r} [r(\bar{S}_H - \frac{1}{2}S_{H_2}^\Delta) + R \ln(1+r)]$$

Table I: Thermodynamic Properties for the Scandium-Hydrogen System

Atomic ratio, g.-atom of H/g.-atom of Sc	$-(\bar{H}_H - \frac{1}{2}H_{H_2}^\Delta),^a$ cal./g.-atom of H	$-(\bar{S}_H - \frac{1}{2}S_{H_2}^\Delta),^a$ cal./°K. g.-atom of H	$-\Delta H_f^\circ,^a$ cal./g. atom	$-\Delta S_f^\circ,^a$ cal./°K. g.-atom
0	21,595 ^b	$-\infty$	0	0
0.10	21,595 ± 271	9.357 ± 0.240	1,960	0.678
0.15	22,022 ± 307	10.694 ± 0.279	2,823	1.077
0.20	22,698 ± 263	12.004 ± 0.239	3,632	1.518
0.25	22,773 ± 165	12.707 ± 0.150	4,391	1.937
0.30	23,055 ± 159	13.541 ± 0.145	5,105	2.394
0.35	22,863 ± 130	13.919 ± 0.118	5,767	2.811
0.40	22,750 ± 148	14.316 ± 0.135	6,377	3.214
0.45	22,484 ± 229	14.571 ± 0.208	6,935	3.592
0.50	22,096 ± 255	14.678 ± 0.232	7,447	3.961
0.55	21,728 ± 286	14.802 ± 0.260	7,914	4.287
(0.65-1.15) ^c	23,999 ± 212	17.388 ± 0.199
1.15	24,089 ± 188	17.479 ± 0.176	12,303	7.937
1.20	24,297 ± 164	17.697 ± 0.153	12,573	8.155
1.25	24,546 ± 132	17.956 ± 0.123	12,836	8.369
1.30	24,884 ± 105	18.314 ± 0.098	13,094	8.582
1.35	25,379 ± 78	18.840 ± 0.073	13,349	8.794
1.40	25,788 ± 93	19.318 ± 0.088	13,603	8.986
1.45	26,240 ± 91	19.851 ± 0.085	13,855	9.223
1.50	26,794 ± 93	20.511 ± 0.089	14,108	9.442
1.55	27,126 ± 83	20.971 ± 0.079	14,358	9.662
1.60	27,619 ± 72	21.639 ± 0.069	14,610	9.886
1.65	28,082 ± 86	22.320 ± 0.084	14,859	10.113
1.70	28,345 ± 94	22.843 ± 0.092	15,105	10.344
1.75	28,714 ± 162	23.533 ± 0.156	15,348	10.576
1.80	29,586 ± 164	24.867 ± 0.163	15,594	10.818
1.85	30,232 ± 146	26.220 ± 0.148	15,844	11.073

^a No temperature dependence of the thermodynamic data was found within the experimental error. ^b Graphically extrapolated value in the infinite dilution range. ^c Two-phase region composition limits at 850°. It is to be noted that the relative partial molal properties for the two-phase region correspond to the enthalpy and entropy changes for the reaction



where r' and r'' are the H/Sc atomic ratios of the two-phase boundaries.

Discussion

The scandium-hydrogen system yields temperature-pressure-composition and thermodynamic data which are very similar to those of the yttrium-hydrogen system³ and rare earth metal-hydrogen systems. Therefore, the scandium-hydrogen system belongs to the class of systems which exhibits intermetallic-type hydrides.

Scandium hydrides were found to be less stable toward the liberation of hydrogen gas than are yttrium hydrides.³ It thus appears that the yttrium hydrides are the most stable of the transition and rare earth metal hydrides.

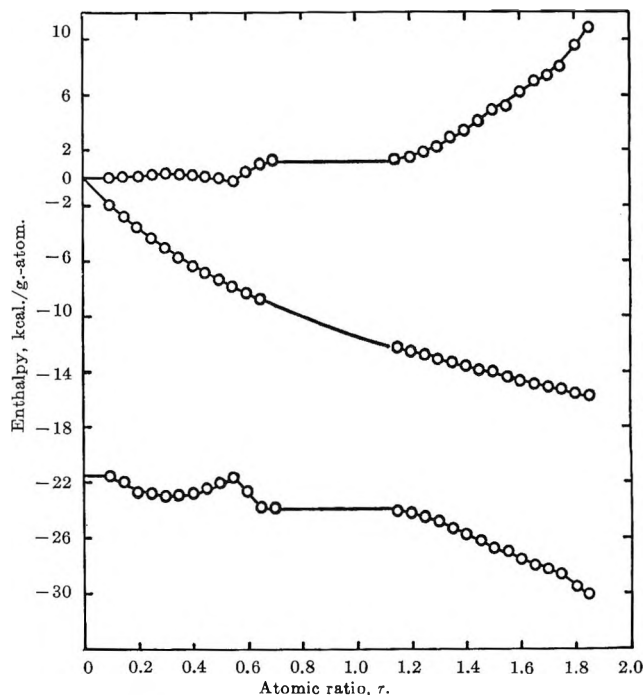


Figure 3. Enthalpy data for the scandium-hydrogen system: upper curve, $\bar{H}_{Sc} - H_{Sc}^\Delta$; middle curve, ΔH_f° ; lower curve, $\bar{H}_H - \frac{1}{2}H_{H_2}^\Delta$.

The thermodynamic data of Table I and the relative partial molal properties of the metal are plotted in Figures 3 and 4. It is to be noted that the relative partial molal properties undergo marked changes for compositions in the metal solid solution phase region. However, the integral properties vary smoothly with composition. In the case of the yttrium-hydrogen³ system there is a small tendency toward a similar effect. The same effect in relative partial molal properties was again observed in the scandium-yttrium-hydrogen system.¹ From pressure-temperature-composition data of Hall, Martin, and Rees⁸ for the zirconium-hydrogen system, similar changes in the relative partial molal properties were observed. An explanation is offered for these observations based on the statistical mechanical theory of Rees.⁹ He assumed that the entrance of a hydrogen atom into an interstitial site transforms other nearby sites, perhaps crystallographically equivalent, into sites which have a higher energy associated with them. Hydrogen atoms preferentially enter low energy sites first if there is a significant difference in the energy of the sites. Low energy sites correspond to small values of relative partial molal enthalpy of hydrogen. It is possible that,

(8) M. N. A. Hall, S. L. H. Martin, and A. L. G. Rees, *Trans. Faraday Soc.*, **41**, 306 (1945).

(9) A. L. G. Rees, *ibid.*, **50**, 335 (1954).

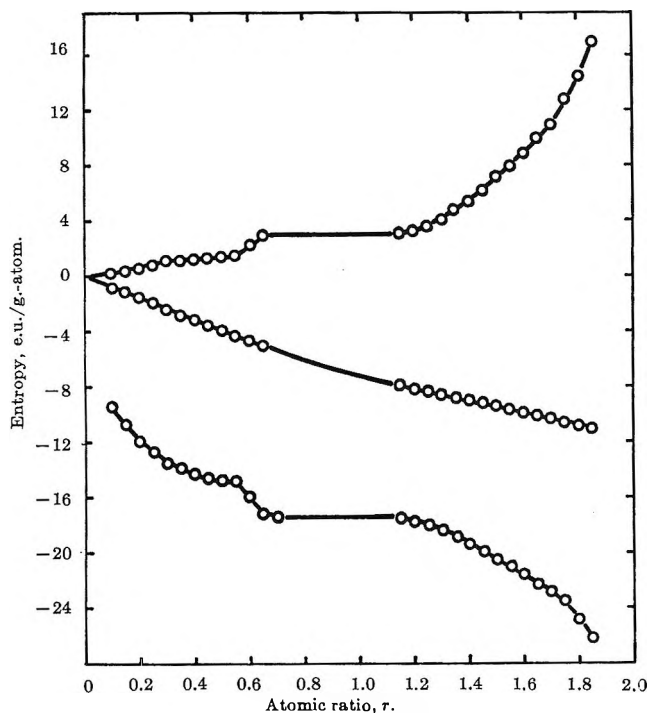


Figure 4. Entropy data for the scandium-hydrogen system: upper curve, $\bar{S}_{Sc} = S_{Sc}^{\Delta}$; middle curve, ΔS_f° ; lower curve, $\bar{S}_H - \frac{1}{2}S_{H_2}^{\Delta}$.

as the low energy or low enthalpy sites become occupied, a highly ordered state is produced which has a lower entropy associated with it. As more hydrogen is added to the metal, there is an increase in enthalpy since the hydrogen atoms must occupy sites of higher energy, and there is an increase in entropy since there is an increase in the number of ways of putting the hydrogen atoms in the sites. At the composition of the minimum in the enthalpy curve of about 0.3 atomic ratio unit, it is noted in the isotherms of Figure 1 that there is a change from a curve to a straight line representing the data. Similar changes in properties are observed in the case of surface adsorption of argon on rutile as found by Drain and Morrison.¹⁰ A decrease in partial molal entropy is associated with the completion of a monolayer of adsorbed gas with all monolayer sites occupied. The beginning of a second layer with high energy sites gives an increase in partial molal enthalpy and entropy.

Unsuccessful attempts were made to fit the pressure-temperature-composition data to the statistical mechanical equations derived by Lacher¹¹ and Rees.⁹ It is possible that Rees' statistical model is valid for the scandium-hydrogen system, but the necessary assumptions made to simplify the equations make it

impossible to apply the equations directly to this system.

McGuire and Kemper⁴ reported some pressure-temperature measurements on the scandium-hydrogen system. Without composition data they made the assumption that some of their data were applicable to the two-condensed-phase region. Superimposing their pressure-temperature data on Figure 1, one may see that the composition of their condensed phase was not in the two-condensed-phase region nor was it constant. Thus, one cannot attach any significance to their ΔH (note *c* of Table I) of -8.3 kcal. (g.-atom of H)⁻¹.

Beck⁵ obtained pressure-temperature-composition data for the temperature range 800 to 1100°. At 800°, the pressure which he reported for the two-condensed-phase region is 5.8 mm. which corresponds well with the value 5.75 mm. of this investigation. At higher temperatures, however, his pressures are progressively lower than those of this work; *e.g.*, at 1100° Beck reported a pressure of 400 mm. whereas at 1052.6° this study found a pressure of 410 mm. Beck found that ΔH (note *c* of Table I) was -20.7 kcal. (g.-atom of H)⁻¹ whereas the value from this investigation is -24.0 kcal. (g.-atom of H)⁻¹. Jones, *et al.*,¹² have compared their pressure-temperature data for the two-condensed-phase regions of the Dy-H and Er-H systems with the comparable data of Beck,⁵ and Sturdy and Mulford's¹³ data for the two-condensed-phase region of the Gd-H system with Beck's data.⁵ For these three systems, as for the scandium-hydrogen system, it was found that Beck's pressure measurements were in agreement with those of other workers at the lowest temperatures. In all cases, however, Beck's data gave rise to less negative values of ΔH which suggests that an error was present in Beck's measurements that became increasingly serious as the temperature increased.

The inability to form a trihydride phase is in agreement with the unsuccessful attempts by McGuire and Kemper⁴ and Warf and Hardcastle.⁶

Acknowledgment. The authors gratefully acknowledge the financial support of this work by the A.E.C. under Contract No. AT (11-1)-1029.

(10) L. E. Drain and J. A. Morrison, *Trans. Faraday Soc.*, **48**, 840 (1952).

(11) J. R. Lacher, *Proc. Roy. Soc. (London)*, **A161**, 525 (1937).

(12) P. M. S. Jones, J. Southall, and K. Goodhead, Atomic Weapons Research Establishment Report No. 0-22/64.

(13) G. E. Sturdy and R. N. R. Mulford, *J. Am. Chem. Soc.*, **78**, 1083 (1956).

Dissociation of Phosphoric Acid Solutions at 25^o

by K. L. Elmore, J. D. Hatfield, R. L. Dunn, and A. D. Jones

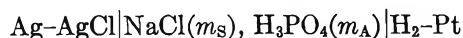
Division of Chemical Development, Tennessee Valley Authority, Wilson Dam, Alabama (Received May 3, 1965)

Degrees of dissociation of phosphoric acid solutions, calculated from the vapor pressure, conductance, and pH of the solutions, pass through a minimum at 1 *m* acid as the concentration is increased. This phenomenon is attributed to the presence in the acid of a species more acidic than the monomer H₃PO₄; the more acid species is assumed to be the dimer H₆P₂O₈ which ionizes to yield H₆P₂O₈⁻. On the basis of this model, an expression is derived that expresses the degree of dissociation of phosphoric acids in the concentration range 0.1 to 10 *m* as a function of the concentration and the pH.

Knowledge of the thermodynamics and kinetics of phosphate systems is essential to an understanding of the reactions involved in the manufacture of phosphatic fertilizers, the equilibration of fertilizers with soil systems, and the utilization of soil phosphates by growing plants. One application of such knowledge would be in studies of the kinetics of the reaction of phosphoric acid with rock phosphate in the preparation of phosphate fertilizers. Complete understanding of this reaction requires knowledge of the degree of ionization of phosphoric acid over the concentration range from dilute to concentrated solutions.

Attempts were made to determine the degree of ionization of phosphoric acid at concentrations up to 90% H₃PO₄ from vapor pressure,² conductance,³ and pH (measured with the saturated salt bridge)⁴ data on 0.1 to 10 *m* phosphoric acid solutions at 25°. Unpublished TVA data obtained from measurements of pH in cells without liquid junction were used also.

For the cells without liquid junction



the e.m.f. is given as

$$E = 0.2224 - 0.059136 \log a_{\text{H}}a_{\text{Cl}} \quad (1)$$

where $a_{\text{H}}a_{\text{Cl}} = \alpha m_A \gamma_{\text{H}} m_S \gamma_{\text{Cl}}$, m_S is the concentration, m , of NaCl, m_A is the concentration, m , of H₃PO₄, μ is the ionic strength = $\alpha m_A + m_S$.

It was assumed that the mean ion activity coefficient, $\gamma_{\pm} = \sqrt{\gamma_{\text{H}}\gamma_{\text{Cl}}}$, in dilute phosphoric acid solutions was equal to that in hydrochloric acid solutions^{5,6} of the same ionic strength. This assumption undoubtedly is

erroneous in phosphoric acid solutions of high ionic strengths, but it apparently is satisfactory for solutions not greater than 1 *m* phosphoric acid, as shown in Figure 1.

The degree of ionization α was calculated by reiteration and smoothed by the method of least squares. The pH was calculated as $\text{pH} = -\log(\alpha m_A \gamma_{\pm})$. In 0.1 *m* H₃PO₄ containing 0.0002 *m* NaCl, α was determined to be 0.2948, which agrees acceptably with 0.2896 as determined in this paper.

The cell with the saturated salt bridge was



and the pH was calculated directly from the equation

$$-\log a_{\text{H}} = \text{pH} = (E - 0.2442)/0.059156 \quad (2)$$

Since the diffusion coefficient of phosphoric acid solutions over the concentration range 1 to 10 *m* does not change greatly,⁷ the liquid junction of these cells was assumed to be constant. The cell constant, $E^{\circ} = 0.2442$, was determined in a 0.1 *m* HCl standard solu-

(1) Presented in part before the Division of Physical Chemistry at the 145th National Meeting of the American Chemical Society, New York, N. Y., Sept. 8-13, 1963 (Abstracts, p. 34T).

(2) K. L. Elmore, C. M. Mason, and J. H. Christensen, *J. Am. Chem. Soc.*, **68**, 2528 (1946).

(3) C. M. Mason and J. B. Culvern, *ibid.*, **71**, 2387 (1949).

(4) A. J. Smith and E. O. Huffman, *Chem. Eng. Data Ser.*, **1**, 99 (1956).

(5) H. S. Harned and R. W. Ehlers, *J. Am. Chem. Soc.*, **55**, 2179 (1933).

(6) G. Åkerlöf and J. W. Teare, *ibid.*, **59**, 1855 (1937).

(7) O. W. Edwards and E. O. Huffman, *J. Phys. Chem.*, **63**, 1831 (1959).

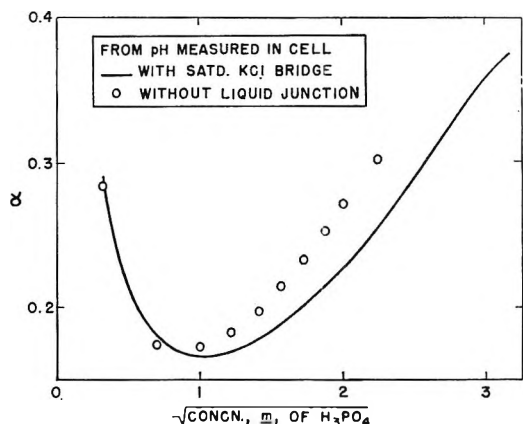


Figure 1. Dissociation of phosphoric acid.

tion which has a pH close to that of a 1 *m* H₃PO₄ solution. This value was also checked with other standard buffer solutions.

The measured values of the conductance of H₃PO₄ solutions³ do not agree with the theoretical model of Fuoss⁸ for simply associated 1-1 electrolytes in the dilute range. The anomalies can be explained, however, if it is assumed that the acid contains additional species such as the triple ion H₅P₂O₈⁻ and the dimeric acid H₆P₂O₈. Bassett⁹ also has concluded that the system P₂O₆-H₂O contains a dimeric orthophosphate species, and Selvaratnam and Spiro¹⁰ explain the properties of phosphoric acid on the basis of the existence of the triple ion H₅P₂O₈⁻.

The method of Wooster,¹¹ slightly modified and made more rigorous, was used with the conductance data to evaluate the parameters of the triple ion for concentrations up to 1 *M* by the equation

$$c\Lambda = \Lambda_0 \frac{b}{f_{\pm}} \left(\frac{K_1 CX}{1 + K_0 CX} \right)^{1/2} (1 + K_0 CX) \quad (3)$$

where $X = 1 - \Lambda/\Lambda_0$, $n = \lambda_0/\Lambda_0$, C = moles per liter of total phosphorus, Λ = equivalent conductance, Λ_0 = limiting conductance of the ions H⁺ and H₂PO₄⁻, λ_0 = limiting conductance of the ions H⁺ and H₅P₂O₈⁻, f_{\pm} = mean activity coefficient of all ions, from Debye's limiting law, b = mobility coefficient of ions, from Onsager's limiting law, $K_1 = a_{\text{H}^+} a_{\text{H}_2\text{PO}_4^-} / a_{\text{H}_3\text{PO}_4}$, and $K_0 = a_{\text{H}_5\text{P}_2\text{O}_8^-} / a_{\text{H}_3\text{PO}_4} a_{\text{H}_2\text{PO}_4^-}$.

The mobility coefficient was tested also in the equation

$$\Lambda = b(\gamma\Lambda_0 + \gamma_3\lambda_0) \quad (4)$$

where γ is the mole ratio H₂PO₄⁻/total P and γ_3 is the mole ratio H₅P₂O₈⁻/total P. According to the electroneutrality equation H⁺ = γC + $\gamma_3 C$ or

$$\text{H}^+ = \text{H}_2\text{PO}_4^- + \text{H}_5\text{P}_2\text{O}_8^- \quad (5)$$

The constants K_1 and K_0 are defined as

$$\text{H}_3\text{PO}_4 \rightleftharpoons \text{H}^+ + \text{H}_2\text{PO}_4^-; K_1 = \frac{C^2 \gamma (\gamma + \gamma_3) f_{\pm}^2}{(1 - \gamma - 2\gamma_3) C} \quad (6)$$

$$\text{H}_3\text{PO}_4 + \text{H}_2\text{PO}_4^- \rightleftharpoons \text{H}_5\text{P}_2\text{O}_8^-; K_0 = \frac{C \gamma_3}{C \gamma (1 - \gamma - 2\gamma_3) C} \quad (7)$$

in which the activity coefficient of the undissociated monomeric acid is assumed to be unity.

In eq. 3, the equivalent conductance is expressed in terms of four parameters (Λ_0 , K_1 , K_0 , and n or λ_0/Λ_0) and three variables (b , f_{\pm} , and X). Isovariance contours of $\Sigma(C\Lambda_{\text{obsd}} - C\Lambda_{\text{calcd}})^2$ are defined by the equation

$$0.13797\Lambda_0 + 4518.4K_1 - 12.915k + 87.185n = 161.326 \pm \sqrt{\frac{\Sigma(r)^2 - 0.01153}{0.4834}} \quad (8)$$

where $k = 1/K_0$ and $r = C\Lambda_{\text{obsd}} - C\Lambda_{\text{calcd}}$, which was derived from a study of the effects of the four parameters on the variance surface by use of the central composite design¹² and by reduction of the empirical surface to canonical form.¹³

The limiting equivalent conductance, $\Lambda_0 = 382.88$, was determined independently from the conductance of the ions H⁺ and H₂PO₄⁻ as calculated from published conductances of HCl,¹⁴ NaCl,¹⁵ and Na₂HPO₄,³ and K_1 was taken as 0.007107, as reported by Bates.¹⁶ Setting $\Sigma(r)^2 = 0.01153$, eq. 8 then becomes

$$87.185n - 12.915k = 76.3876 \quad (9)$$

for which many pairs of values of n and k will give equally good fits to the conductance data.

The limiting conductance of H₂PO₄⁻ is 33.01 mhos, and it is expected that that of H₅P₂O₈⁻ is between 25 and 33 mhos, so that n is between 0.98 and 1.00. The

(8) R. M. Fuoss, *J. Am. Chem. Soc.*, **80**, 3163 (1958); **81**, 2659 (1959).

(9) H. Bassett, *J. Chem. Soc.*, 2949 (1958).

(10) M. Selvaratnam and M. Spiro, *Trans. Faraday Soc.*, **61**, 360 (1965).

(11) C. B. Wooster, *J. Am. Chem. Soc.*, **59**, 377 (1937).

(12) G. E. P. Box and K. B. Wilson, *J. Roy. Statistical Soc.*, **B13**, 1 (1951).

(13) G. E. P. Box in "Design and Analysis of Industrial Experiments," O. L. Davis, Ed., Hafner Publishing Co., New York, N. Y., 1954, Chapter 11.

(14) R. H. Stokes, *J. Phys. Chem.*, **65**, 1242 (1961).

(15) T. Shedlovsky, A. S. Brown, and D. A. MacInnes, *Trans. Electrochem. Soc.*, **66**, 165 (1934).

(16) R. G. Bates, *J. Res. Natl. Bur. Std.*, **47**, 127 (1951).

value of K_0 is then between 1.2 and 1.4; the value of 1.263 was selected because it is near the middle of this range, and, as will be shown in this paper, it is consistent with the properties of phosphoric acid. When $K_0 = 1.263$, the limiting conductance of $\text{H}_5\text{P}_2\text{O}_8^-$ is 30.50 mhos.

The pH data from cells without liquid junction indicated that the apparent degree of ionization, α , of phosphoric acid passes through a minimum at 1 *m* acid and then increases with increasing concentration (Figure 1). This observation leads to the hypothesis that an acid stronger than H_3PO_4 is present in the system; the stronger acid is assumed to be the dimer $\text{H}_6\text{P}_2\text{O}_8$ which yields the triple ion $\text{H}_5\text{P}_2\text{O}_8^-$ on ionization.

Evidence for the existence of the dimer $\text{H}_6\text{P}_2\text{O}_8$ and the triple ion $\text{H}_5\text{P}_2\text{O}_8^-$ is presented in Figures 2 and 3. In Figure 2, the units on the ordinate ($d \ln a_u / d \ln a_H - 1$, in which a_u is the activity of undissociated H_3PO_4 , were obtained by differentiation of the logarithmic form of the expression for K_1 ; the units are numerically the same as $d \ln a_{\text{H}_3\text{PO}_4} / d \ln a_H$, but those in the figure are more readily obtained from measurable quantities. The units on the abscissa result from the following mathematical operations that were made in attempts to determine reasonable values for α .

The equation

$$a_H = \alpha m \gamma_H \quad (10)$$

in which m is the concentration, molality, of total phosphorus (here considered entirely monomeric), contains two known quantities (for each concentration of acid), a_H (as determined by eq. 2) and m , and two unknown but interdependent quantities, α and γ_H . Equation 10 may be written

$$(a_H / \gamma_H) - \alpha m = 0 \quad (11)$$

Adding $m - a_H$ to both sides of eq. 11 and collecting terms gives

$$m(1 - \alpha) - a_H(1 - 1/\gamma_H) = m - a_H \quad (12)$$

which may be considered the equation of the straight line AP in Figure 4 in the system with coordinates $1 - \alpha$ and $1 - 1/\gamma_H$. When $1 - \alpha = 1$, $1 - 1/\gamma_H = 1$, and the line must pass through P.

The area of triangle AOP is $(m - a_H)/2a_H$; the reciprocal of this area, $2a_H/(m - a_H)$, which is a function of the activity coefficient of the hydrogen ion, is the unit on the abscissa in Figure 2. The marked change in the direction of the curve in Figure 2 is taken to indicate the presence of the stronger acid species. The concentration, 2.1 *m*, of acid at which this change occurs is that of the acid in which a saturated solution of $\text{Ca}(\text{H}_2\text{PO}_4)_2$ is the invariant-point solution at 25° with which

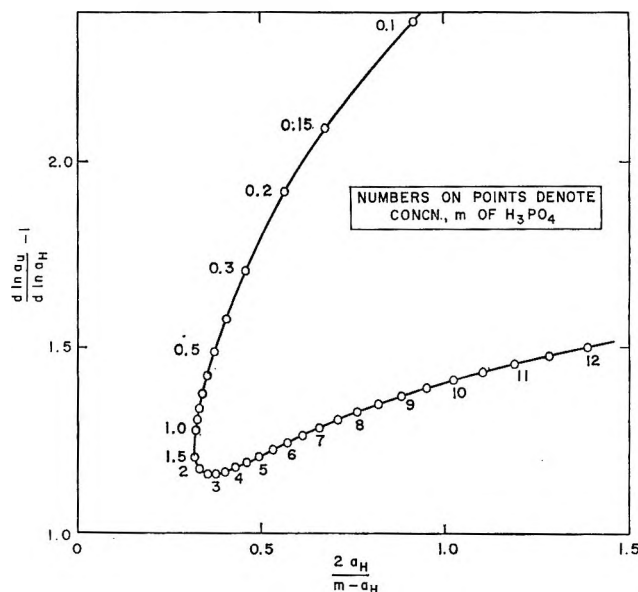


Figure 2. Relation between $d \ln a_{\text{H}_3\text{PO}_4} / d \ln a_H$ and activity coefficient of H^+ in phosphoric acid solutions.

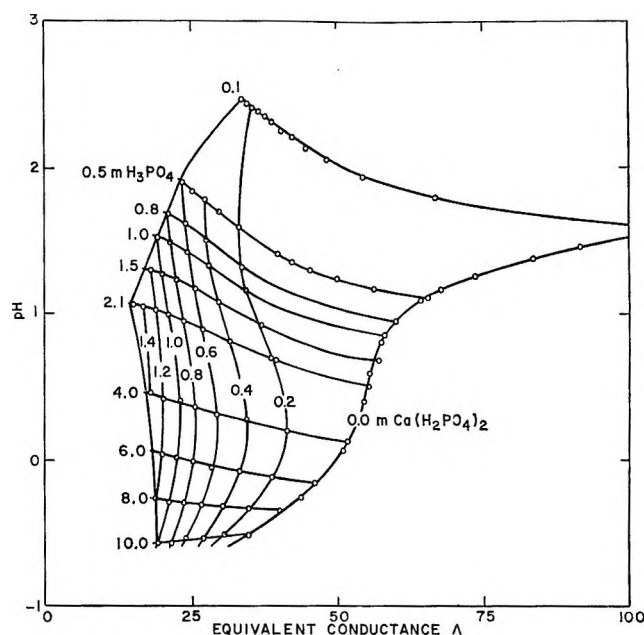
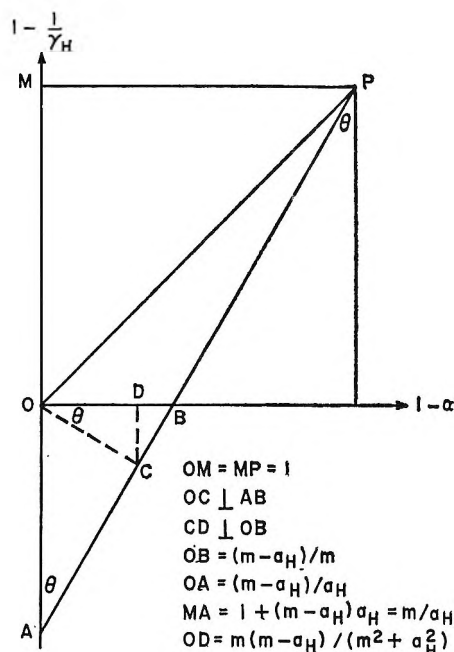


Figure 3. Relation between equivalent conductance and pH in the system $\text{CaO}-\text{P}_2\text{O}_5-\text{H}_2\text{O}$.

both $\text{Ca}(\text{H}_2\text{PO}_4)_2 \cdot \text{H}_2\text{O}$ and CaHPO_4 are in equilibrium.¹⁷

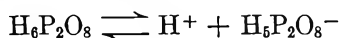
The significance of 2.1 *m* acid is shown also in Figure 3 in which is plotted pH vs. equivalent conductance, Λ , for solutions in the system $\text{CaO}-\text{P}_2\text{O}_5-\text{H}_2\text{O}$.⁴ The S curve at the right of the figure is for acid solutions containing no calcium; the curve has the same shape as that of the titration of a strong acid with a base. Since

(17) K. L. Elmore and T. D. Farr, *Ind. Eng. Chem.*, 32, 580 (1940).

Figure 4. Plot of the definition of α_H .

equivalent conductance is proportional to the concentration of the ionized species, the H^+ concentration along this curve is decreased (and the pH is increased) by dilution, rather than by neutralization; the inflection point is at 2.1 m acid, and the pH of this acid is 0.52.

If the assumption that the acid contains the strong acid species $H_6P_2O_8$ is valid, it may then be assumed that the inflection of the acid curve is at the point at which the ratio of activities $c_{H_6P_2O_8^-}/a_{H_6P_2O_8}$ is unity and at which $pH = pK = 0.52$. Then



$$K_4 = (H^+)(H_5P_2O_8^-)/(H_6P_2O_8) = \text{antilog } -0.52 = 0.3 \quad (13)$$

The diagram in Figure 4 is useful in arriving at reasonable estimates of α for each concentration of acid. Although eq. 12 is taken as the equation of a line, it is apparent that there is a different line AP for each concentration of acid and that only one point on this line will satisfy eq. 8 for this concentration. Values of α for acid concentrations up to 1 m were available from pH data measured in cells without liquid junction and from conductance data^{3,4}; the values of α determined by these methods agreed within 2%. When values of α and the corresponding values of γ_H were plotted in Figure 4, each point was close to C, which, for each concentration, is the intersection with AP of a line through the origin perpendicular to AP. In Figure 4,

the value of $1 - \alpha$ at C is $m(m - \alpha_H)/(m^2 + \alpha_H^2)$ from which

$$\alpha = \frac{c_H}{m} \frac{1 + \frac{\alpha_H}{m}}{1 + \left(\frac{\alpha_H}{m}\right)^2} \quad (14)$$

Equation 14 fits the data for acid concentrations below 1 m so well that it appeared that it might also fit the data for more concentrated acid solutions. Values of α for phosphoric acid solutions then were calculated through use of a modification of the equation of Van Rysselberghe and Eisenberg,¹⁸ and the results were checked against those obtained from eq. 14.

By definition

$$K_1 = \frac{a_H a_{H_2PO_4^-}}{a_{H_3PO_4}} \quad (15)$$

and

$$K_0 = \frac{a_{H_6P_2O_8^-}}{a_{H_3PO_4} a_{H_2PO_4^-}} \quad (16)$$

and by the electroneutrality equation

$$[H^+] = [H_2PO_4^-] + [H_5P_2O_8^-] \quad (5)$$

or

$$[H^+] = \frac{a_{H_2PO_4^-}}{f_{H_2PO_4^-}} + \frac{a_{H_5P_2O_8^-}}{f_{H_5P_2O_8^-}} \quad (17)$$

Since λ_0 is nearly equal to Λ_0 , it is assumed that

$$f_{H_2PO_4^-} = f_{H_5P_2O_8^-} = f_-$$

It then follows that

$$[H^+]f_- = a_{H_2PO_4^-} + a_{H_5P_2O_8^-} \quad (17a)$$

However, since

$$a_{H_2PO_4^-} = \frac{K_1 a_{H_3PO_4}}{a_H} \quad (15)$$

and

$$a_{H_5P_2O_8^-} = \frac{K_1 K_0 a_{H_3PO_4}^2}{a_H} \quad (16a)$$

then

$$[H^+]f_- = \frac{K_1 a_{H_3PO_4}}{a_H} + \frac{K_1 K_0 a_{H_3PO_4}^2}{a_H} \quad (17b)$$

but

$$a_H = [H^+]f_H$$

(18) P. Van Rysselberghe and S. Eisenberg, *J. Am. Chem. Soc.*, **61**, 3030 (1939); **62**, 451 (1940).

Hence

$$[H^+]^2 f_{Hf-} = K_1 a_{H_3PO_4} [1 + K_0 a_{H_3PO_4}] \quad (18)$$

and

$$f_{Hf-} = \frac{K_1 a_{H_3PO_4} [1 + K_0 a_{H_3PO_4}]}{[H^+]^2} \quad (19)$$

When concentrations are expressed in moles per liter and

$$[H^+] = \alpha C \quad (20)$$

eq. 19 becomes

$$f_{Hf-} = \frac{K_1 a_{H_3PO_4} [1 + K_0 a_{H_3PO_4}]}{[\alpha C]^2} \quad (21)$$

or

$$\log f_{Hf-} = \log K_1 a_{H_3PO_4} + \log [1 + K_0 a_{H_3PO_4}] - 2 \log \alpha C \quad (22)$$

The value of $\log f_{\pm}$ for strong electrolytes has been expressed by Van Rysselberghe and Eisenberg¹⁸ as

$$\log f_{\pm} = \frac{-0.5091\sqrt{C}}{1 + 0.3286a\sqrt{C}} + 2.20626 \times 10^{-3}a^3C + 2.62692 \times 10^{-6}a^6C^2 \quad (23)$$

in which a is the distance of closest approach, Å., of the ions. By definition $f_{Hf-} = f_{\pm}^2$. On substituting αC for weak electrolytes for C of strong electrolytes, eq. 23 becomes

$$\log f_{Hf-} = -\frac{1.0182\sqrt{\alpha C}}{1 + 0.3286a\sqrt{\alpha C}} + 4.41252 \times 10^{-3}a^3(\alpha C) + 5.25384 \times 10^{-6}a^6(\alpha C)^2 \quad (24)$$

Equating the right-hand terms of eq. 22 and 24 and inserting the value 4.25 for a yields, for the model of phosphoric acid containing both $H_2PO_4^-$ and the triple ion $H_5P_2O_8^-$, the equation

$$\log K_1 a_u + \log (1 + K_0 a_u) = \frac{-1.0182\sqrt{\alpha C}}{1 + 1.39655\sqrt{\alpha C}} + 2 \log \alpha C + 0.3387298\alpha C + 0.030961(\alpha C)^2 \quad (25)$$

where $a_u = a_{H_3PO_4}$, the activity of the undissociated monomer acid.

The degree of ionization α (expressed as $\alpha = m_H/m$, in which m_H is the molality of H^+ and m is the molality of total P, here assumed to be entirely monomeric) calculated from conductance data for concentrations up to 1 m H_3PO_4 is approximately equal to α calculated from eq. 14 when a_H is computed from the pH ($pH = -\log a_H$) measured in cells with the saturated KCl bridge.⁴

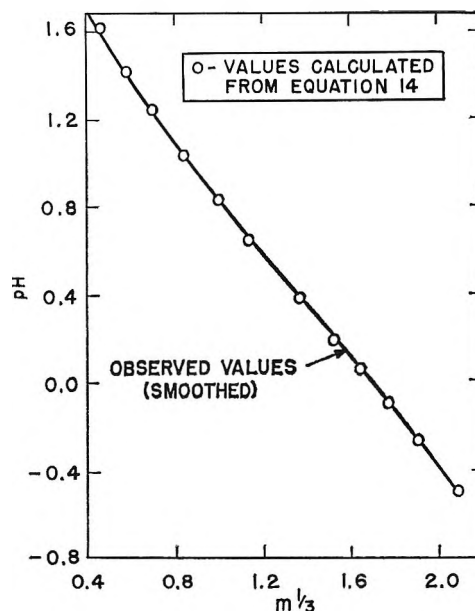


Figure 5. pH of phosphoric acid solutions at 25°.

Table I: pH of Phosphoric Acid Solutions at 25°

Concn. of H_3PO_4 Molality, m	Molarity, C	Activity of un- dissocd. H_3PO_4 , a_u	α , calcd. from eq. 25	pH		Diff.
				Obsd. (smoothed)	Calcd. from eq. 14	
0.1000	0.0993	0.0769	0.28963	1.589	1.608	0.019
0.2000	0.1977	0.1605	0.22547	1.391	1.407	0.016
0.3000	0.2951	0.2493	0.19990	1.269	1.279	0.010
0.4000	0.3917	0.3417	0.18616	1.179	1.183	0.004
0.5000	0.4875	0.4373	0.17787	1.105	1.104	-0.001
0.6000	0.5823	0.5360	0.17263	1.042	1.037	-0.005
0.7000	0.6763	0.6377	0.16927	0.986	0.977	-0.009
0.8000	0.7694	0.7425	0.16718	0.936	0.924	-0.012
0.9000	0.8617	0.8504	0.16598	0.890	0.876	-0.014
1.0000	0.9532	0.9615	0.16543	0.847	0.832	-0.015
1.5000	1.3983	1.5690	0.16853	0.670	0.648	-0.022
2.0000	1.8239	2.2750	0.17671	0.528	0.504	-0.024
2.5000	2.2313	3.0960	0.18732	0.407	0.384	-0.023
3.0000	2.6211	4.0510	0.19937	0.301	0.280	-0.021
3.5000	2.9950	5.1650	0.21240	0.207	0.188	-0.019
4.0000	3.3534	6.4610	0.22600	0.121	0.105	-0.016
4.5000	3.6958	7.9680	0.24004	0.043	0.030	-0.013
5.0000	4.0260	9.7210	0.25419	-0.030	-0.039	-0.009
5.5000	4.3431	11.7600	0.26844	-0.096	-0.102	-0.006
6.0000	4.6469	14.1200	0.28260	-0.159	-0.160	-0.001
6.5000	4.9416	16.8600	0.29650	-0.217	-0.214	0.003
7.0000	5.2207	20.0300	0.31042	-0.271	-0.265	0.006
7.5000	5.4936	23.7100	0.32391	-0.322	-0.312	0.010
8.0000	5.7605	27.9600	0.33683	-0.370	-0.356	0.014
9.0000	6.2411	37.7900	0.35990	-0.457	-0.434	0.023
10.0000	6.7074	48.9700	0.37553	-0.516	-0.497	0.019
				Std. dev.		0.015
				Probable error		0.010

When values of α , calculated from eq. 25 with values of a_u obtained from vapor pressure data,² are substituted in eq. 14 (with conversion of concentration from molarity to molality), the values of a_H convert to values

of pH that agree with a probable error of ± 0.01 unit with the measured values for acid concentrations in the range 0.1 to 10 m H_3PO_4 . The density data of Christensen and Reed¹⁹ were used in the conversion of the concentration units.

Equation 14 has been tested only with phosphoric acid solutions, and with these it gives highly consistent results. The equation is based on the assumption that there are no appreciable liquid-junction effects in the pH measurements, and its applicability to phosphoric

acid solutions indicates that it may be used to calculate the degree of ionization of other weak acids.

The agreement between the observed pH data and those calculated from eq. 14 is shown in Figure 5 and Table I.

By assuming that the activity coefficients of the two negative ions are equal and that similarly the activity coefficients of both the monomeric and dimeric unionized acids are equal and making suitable substitutions in the total phosphorus and electroneutrality equations containing the ionization constants K_1 , K_0 , and K_4 , we can calculate the concentration of each of the species in each concentration of acid whenever $[\alpha m]$ or $[H^+]$ is known from eq. 14.

The following equations have been derived by the above procedure and the results of the calculations are shown in Table II.

Table II: Calculated Distribution of Species in Phosphoric Acid Solutions

Concn. of H_3PO_4 , m	Activity of undissoc. H_3PO_4 , a_u	Degree of dissociation, α	Concn., m				
			H^+	$H_2PO_4^-$	$H_6P_2O_8^{2-}$	H_3PO_3	$H_5P_2O_8$
0.1	0.077	0.2896	0.0290	0.0264	0.0026	0.0682	0.0002
0.2	0.161	0.2255	0.0451	0.0375	0.0076	0.1459	0.0007
0.3	0.249	0.1999	0.0600	0.0456	0.0144	0.2223	0.0017
0.4	0.342	0.1862	0.0745	0.0520	0.0224	0.2969	0.0031
0.5	0.437	0.1779	0.0889	0.0573	0.0316	0.3696	0.0049
0.6	0.536	0.1726	0.1036	0.0618	0.0418	0.4402	0.0072
0.7	0.638	0.1693	0.1185	0.0656	0.0529	0.5089	0.0099
0.8	0.743	0.1672	0.1337	0.0690	0.0647	0.5755	0.0130
0.9	0.850	0.1660	0.1494	0.0720	0.0774	0.6401	0.0166
1.0	0.962	0.1654	0.1654	0.0747	0.0907	0.7026	0.0206
1.5	1.569	0.1685	0.2528	0.0848	0.1680	0.9849	0.0471
2.0	2.275	0.1767	0.3534	0.0912	0.2622	1.2157	0.0844
2.5	3.096	0.1873	0.4683	0.0954	0.3729	1.3952	0.1318
3.0	4.051	0.1994	0.5981	0.0978	0.5003	1.5247	0.1884
3.5	5.165	0.2124	0.7434	0.0988	0.6446	1.6059	0.2530
4.0	6.461	0.2260	0.9040	0.0987	0.8053	1.6430	0.3238
4.5	7.968	0.2400	1.0802	0.0976	0.9825	1.6400	0.3986
5.0	9.721	0.2542	1.2710	0.0957	1.1752	1.6031	0.4754
5.5	11.76	0.2684	1.4764	0.0931	1.3833	1.5373	0.5515
6.0	14.12	0.2826	1.6956	0.0900	1.6056	1.4498	0.6245
6.5	16.86	0.2965	1.9273	0.0864	1.8408	1.3467	0.6926
7.0	20.03	0.3104	2.1729	0.0826	2.0903	1.2316	0.7526
7.5	23.71	0.3239	2.4293	0.0785	2.3508	1.1117	0.8041
8.0	27.96	0.3368	2.6946	0.0742	2.6204	0.9923	0.8463
9.0	37.79	0.3599	3.2391	0.0665	3.1726	0.7830	0.9026
10.0	48.97	0.3755	3.7553	0.0598	3.6955	0.6393	0.9549

$$[H_2PO_4^-] = \frac{[H^+]}{1 + K_0 a_u} \quad (26)$$

$$[H_5P_2O_8^-] = \frac{K_0 a_u}{1 + K_0 a_u} [H^+] \quad (27)$$

$$[H_3PO_4] = \frac{m - \frac{1 + 2K_0 a_u}{1 + K_0 a_u} [H^+]}{1 + \frac{2K_1 K_0}{K_4} a_u} \quad (28)$$

$$[H_6P_2O_8] = \frac{K_1 K_0}{K_4} a_u \left[\frac{m - \frac{2K_0 a_u}{1 + K_0 a_u} [H^+]}{1 + \frac{2K_1 K_0}{K_4} a_u} \right] = \frac{K_1 K_0}{K_4} a_u [H_3PO_4] \quad (29)$$

(19) J. H. Christensen and R. B. Reed, *Ind. Eng. Chem.*, **47**, 1277 (1955).

Catalytic Deuterium-Exchange Reactions With Organics. XX. A π -Complex Mechanism for the Isomerization and Isotope Exchange of *cis*- and *trans*-Stilbenes on Platinum Catalysts

by J. L. Garnett and W. A. Sollich-Baumgartner

Department of Physical Chemistry, The University of New South Wales, Kensington, New South Wales, Australia (Received May 3, 1965)

The results of isomerization and exchange reactions with *cis*- and *trans*-stilbenes provide further evidence for the predominant participation in both reactions of the dissociative π -complex substitution mechanism recently proposed for isotope exchange between aromatic compounds and heavy water in the presence of transition metal catalysts. Consistent with this π -complex exchange mechanism, it is found that the isomerization mechanism in the presence of deuterium oxide does not depend on atomic hydrogen derived from the dissociative chemisorption of water. The well-known catalytic effect of hydrogen gas in isomerization is attributed to the removal of toxic by-products by hydrogenation. The present π -complex theory also provides a satisfactory explanation for the observed differences in the vinyl exchange rates of *cis*- and *trans*-stilbenes and for the effective absence of disproportionation reactions.

Introduction

The role of π complexes in catalysis has been the subject of a series of recent investigations.¹⁻⁷ Extensive data from the platinum-catalyzed exchange of organic compounds with heavy water have resulted in two new mechanisms being proposed for catalysis, namely the dissociative (eq. I, II, and III) and associative (eq. I and IV) π -complex substitution mechanisms. These new concepts have been extended to other group VIII transition metal catalysts such as palladium, rhodium, ruthenium, iridium, and nickel.⁸

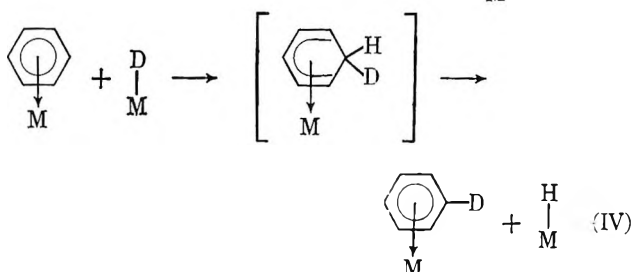
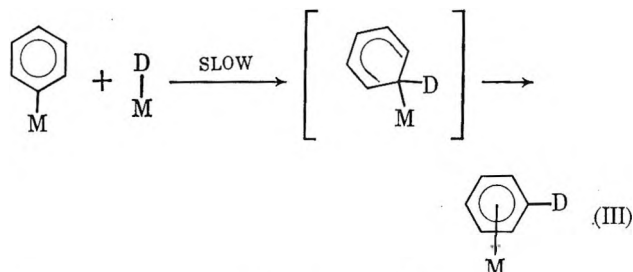
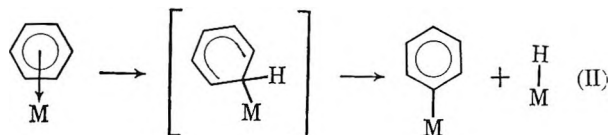
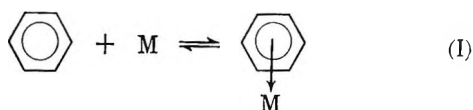
Data from benzene randomization reactions⁴ indicate that exchange involving heavy water as the source of isotope proceeds predominantly, if not exclusively, by the dissociative process. It is the purpose of the present paper to clarify further the relative importance of the dissociative and associative π -complex mechanisms using the platinum-catalyzed isomerization and exchange properties of the *cis*- and *trans*-stilbenes in the presence and absence of heavy water.

In the dissociative π -complex substitution mechanism (eq. I-III) the π -bonded aromatic (eq. I) under-

goes a substitution reaction with a metal radical (active site). During this step (eq. II) the molecule rotates through 90° to form a carbon-metal σ -bond. While σ bonded, the molecule undergoes a further, rate-controlling (isotope effect $k_D/k_T = 1.7^4$) substitution reaction (eq. III) at the carbon-metal bond with a chemisorbed deuterium atom and returns to the π -bonded state.

In the associative π -complex substitution mechanism (eq. I and IV) a π -complexed (flatly adsorbed) molecule undergoes a substitution reaction with a chemisorbed

- (1) J. L. Garnett and W. A. Sollich, *Australian J. Chem.*, **14**, 441 (1961).
- (2) J. L. Garnett and W. A. Sollich, *ibid.*, **15**, 56 (1962).
- (3) J. L. Garnett and W. A. Sollich, *J. Catalysis*, **2**, 350 (1963).
- (4) J. L. Garnett and W. A. Sollich-Baumgartner, *J. Phys. Chem.*, **68**, 3177 (1964).
- (5) E. Crawford and C. Kemball, *Trans. Faraday Soc.*, **58**, 2452 (1962).
- (6) G. C. Bond, "Catalysis by Metals," Academic Press, Inc., New York, N. Y., 1962, p. 313.
- (7) J. J. Rooney, *J. Catalysis*, **2**, 53 (1963).
- (8) J. L. Garnett and W. A. Sollich, *Australian J. Chem.*, **18**, 1003 (1965).

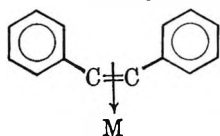


deuterium atom originating from the dissociative chemisorption of water.

The important distinguishing feature of the dissociative and associative exchange mechanisms is the fact that the latter mechanism cannot operate in the absence of a dissociatively adsorbed reagent such as water or hydrogen gas. Exchange reactions between an aromatic and its deuterated analog are therefore precluded by this mechanism; however, such a reaction may occur readily by the dissociative mechanism.

cis-Stilbene exhibits several unique features for the present work, the most important being the strong steric hindrance of the two aromatic rings which turns the conjugational plane of the vinyl double bond out of alignment with those of the two rings; *i.e.*, electron delocalization is largely restricted to each ring. By contrast, *trans*-stilbene is planar and electron delocalization occurs throughout the whole molecule.

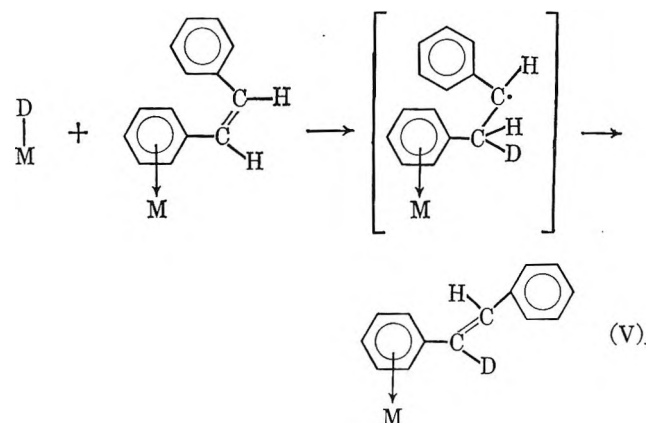
The rotation of the conjugational plane of the vinyl group relative to the ring in *cis*-stilbene is important in π -complex substitution mechanisms since the steric hindrance exerted by the rings seriously restricts π -complex adsorption *via* the vinyl double bond, *viz.*



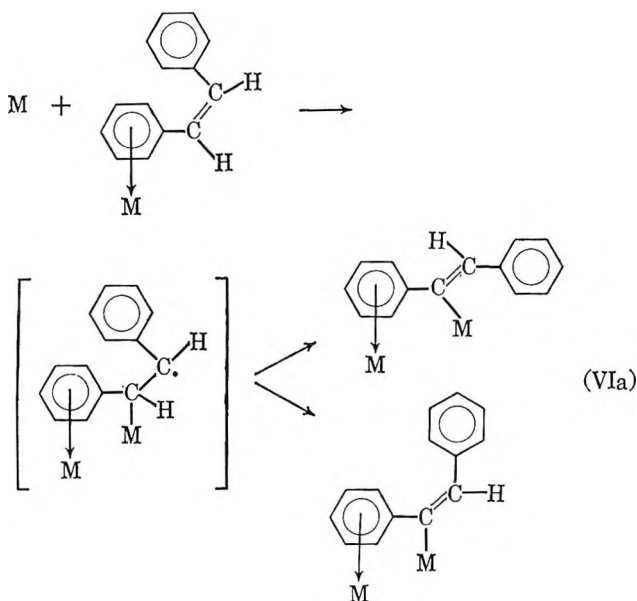
cis-Stilbene can, however, be π bonded *via* one of the aromatic rings, especially when assisted by a slight rotation about the C-C "single" bond which decreases the steric hindrance exerted by the vinyl hydrogen atom in contact with the catalyst surface. This slight rotation also places the vinyl hydrogen atoms in a suitable position for a substitution reaction with the result that only a small ring rotation is necessary for dissociative chemisorption instead of the usual rotation through 90° .

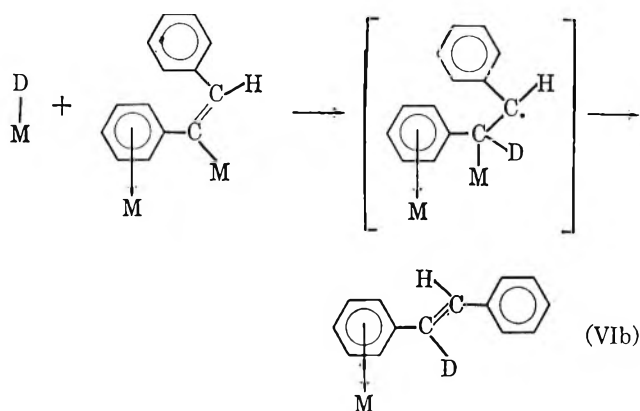
The associative and dissociative π -complex substitution mechanisms for *cis*-stilbene isomerization may be summarized by eq. V and VI, respectively.

Isomerization by the Associative π -Complex Substitution Mechanism



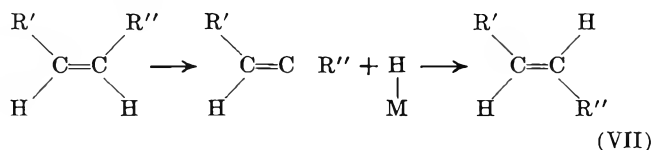
Isomerization by the Dissociative π -Complex Substitution Mechanism



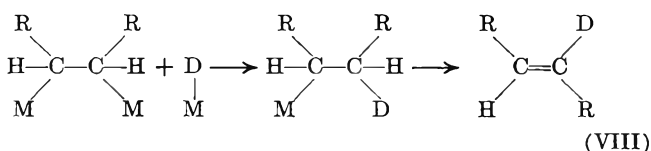


The important difference between the associative and dissociative mechanisms is the fact that the latter can operate without a second dissociatively adsorbed substance; *i.e.*, chemisorbed hydrogen is not necessary for reaction VIa, and for reaction VIb it may be obtained from the dissociative chemisorption of other *cis*-stilbene molecules.

An additional feature of the present system is the opportunity to compare the π -complex isomerization mechanisms with classical associative⁹ and dissociative¹⁰ isomerization mechanisms. *cis-trans* isomerization reactions require the opening of the vinyl double bond and provide therefore a means for distinguishing between the classical associative and dissociative isomerization mechanisms. The classical dissociative mechanism of Farkas and Farkas does not involve the opening of the double bond (eq. VII) and consequently cannot account for isomerization reactions in the case where substituents, R' and R'' (eq. VII), do not undergo bond rupture on catalyst surfaces. In the experience of the present authors, this was found to be invariably the case when a carbon-carbon bond was involved.



On the other hand, the classical associative mechanism of Horiuti and Polanyi can only occur in the presence of chemisorbed hydrogen atoms (eq. VIII), *i.e.*, in the presence of a dissociatively adsorbed substance such as water or hydrogen gas.



The importance of adsorbed hydrogen in isomerization has been established¹¹; however, its function is still in

doubt in view of Beeck's finding^{12,13} that hydrogen removes the toxic coatings of degradation products formed in a side reaction. Water, in spite of dissociative chemisorption, does not possess this activating effect; consequently, the possibility of equal isomerization rates in the presence and absence of water could be explained by the dissociative π -complex substitution mechanism.

Experimental Section

Exchange reactions were performed for 168 hr. at 145° with hydrogen-activated prerduced platinum catalysts,¹⁴ maintaining a constant organic:catalyst ratio. First-order rate constants were calculated from

$$k_N = \frac{-2.3}{t} \log \left(\frac{x - x_\infty}{100 - x_\infty} \right) \quad (1)$$

where x and x_∞ represent the percentage of *cis* isomer at time t and at equilibrium, respectively. Under present conditions $x_\infty < 1\%$.¹⁵

The deuterium content in the vinyl group and the amount of *trans* isomer formed were determined from the infrared absorption band at 965 cm^{-1} caused by the out-of-plane bending vibrations of two *trans*-situated vinyl hydrogens; the corresponding *cis* band occurs at 770 cm^{-1} .¹⁶ Cyclohexane does not interfere with the band at 965 cm^{-1} and was consequently used as solvent in the spectroscopic *trans* isomer determination. A calibration graph was constructed for this purpose by measuring the optical density of solutions (at 965 cm^{-1}) containing different concentrations of pure *trans*-stilbene. The per cent conversion is then readily calculated from optical density measurements and accurately known concentrations of *nondeuterated cis-trans* reaction products. Since deuterated products yield different spectra, these cannot be analyzed by the optical procedure and a less accurate crystallization technique was employed. Fortunately, sufficiently large quantities of *trans* isomers were formed so that crystallization losses did not seriously affect the result. The deuterated product (56% deuterated *trans* isomer) was then used in the determination of the orienta-

(9) J. Horiuti and M. Polanyi, *Trans. Faraday Soc.*, **30**, 1164 (1934).

(10) A. Farkas and L. Farkas, *Nature*, **132**, 894 (1933).

(11) T. I. Taylor and V. H. Dibeler, *J. Phys. Chem.*, **55**, 1036 (1951).

(12) O. Beeck, *Rev. Mod. Phys.*, **17**, 61 (1945).

(13) O. Beeck, *Discussions Faraday Soc.*, **8**, 118 (1950).

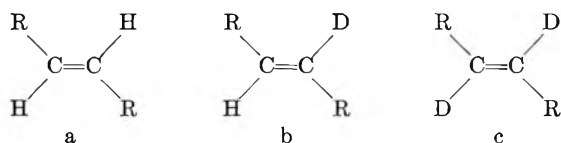
(14) J. L. Garnett and W. A. Sollich, *J. Catalysis*, **2**, 339 (1963).

(15) D. J. Cram and G. S. Hammond, "Organic Chemistry," McGraw-Hill Book Co., Inc., New York, N. Y., 1959, p. 122.

(16) L. J. Bellamy, "The Infrared Spectra of Complex Molecules," Methuen and Co. Ltd., London, 1954, p. 45.

tion effect by the method of "apparent *trans* isomer content."

This method is based on the fact that of the three possible reaction products, a, b, and c, only a exhibits an absorption band at 965 cm^{-1} .



The percentage of a in the deuterated product is then given by the apparent *trans* isomer content (p) as determined by the previously outlined optical procedure. Substituting this value (p) into eq. 2 giving the statistical deuterium distribution for normal, mono-, and dideuterated vinyl hydrogens (*i.e.*, $m = 0, 1$, and 2), one is able to calculate the average vinyl deuterium content (Q).

$$p = \frac{2!}{(2-m)!m!} (1-Q)^m Q^{2-m} \quad (2)$$

The deuterium content in the ring is then obtained from the mass spectrometrically determined average deuterium content of the stilbene molecule. First-order exchange rate constants can then be calculated for the two types of hydrogen atoms from eq. 3, D_t and D_∞ being the deuterium contents in both ring and vinyl hydrogens at time t and equilibrium, respectively.

$$k_E = \frac{-2.3}{t} \log \left(\frac{D_\infty - D_t}{D_\infty} \right) \quad (3)$$

Results and Discussion

Isomerization experiments were performed to ascertain whether *cis*-stilbene isomerization is drastically affected by the absence of hydrogen-donating substances such as water. Deuterium oxide was also included in some reactions to obtain information about the reaction mechanism from possible isotope effects or characteristic deuterium distributions within the molecule. With respect to the latter, it is of particular interest to establish whether vinyl hydrogens exchange at different rates from those in the ring, and whether *trans*-stilbene exhibits different orientation effects. In view of the occurrence of thermal isomerization and the possible catalysis of this reaction by water,^{17,18} it was necessary to perform "blank" runs (run 1, Table I).

Results in Table I show that thermal isomerization in the presence of water is approximately $1/20$ as fast as isomerization in the presence of platinum catalysts. More important, however, catalytic isomerization rates are not significantly increased by water. Consequently, isomerization as well as exchange appear to

Table I: *cis*-Stilbene Isomerization

Run	Reagents	Quantities, g.	Catalyst, g.	Reaction Time, hr.	Temp., °C.	Conversion, %	$k_I \times 10^3, \text{hr}^{-1}$
1	<i>cis</i> -Stilbene H ₂ O	0.57	0	168	145	3.0	0.2
		1.54					
2	<i>cis</i> -Stilbene	0.57	0.156	168	145	45.1	3.6
		1.54					
3	<i>cis</i> -Stilbene H ₂ O	0.57	0.158	168	145	46.5	3.8
		1.54					
4	<i>cis</i> -Stilbene D ₂ O	1.17	0.323	168	145	50.4	4.2
		3.13					

^a k_I = normalized *cis-trans* isomerization rate constant.

proceed exclusively *via* the dissociative π -complex substitution mechanism.

Isomerization is accompanied by appreciable exchange; the average deuterium content in the *trans* isomer formed in run 4 from *cis*-stilbene was found to be 56.0%. Table II contains the deuterium distributions in the ring and vinyl hydrogens as calculated by the apparent *trans* isomer content. These results were compared to an exchange reaction performed under different reaction conditions with *trans*-stilbene. Only the *ratio* of vinyl to ring exchange rates and not the absolute value of the exchange rates of the different stilbene isomers can therefore be used for comparison.

The results show that the vinyl hydrogens in *trans*-stilbene exchange at a very much slower rate than those of the ring, while the converse occurs with *cis*-stilbene. It must, however, be emphasized that the deuterium analysis of run 4 was not performed on the actual *cis* isomer, but on the isomerized product, *viz.*, *trans*-stilbene. Since vinyl exchange is retarded once the *trans* isomer is formed, it follows that the vinyl exchange rate in *cis*-stilbene must be greater than that quoted ($11.4 \times 10^{-3} \text{ hr}^{-1}$). The fact that vinyl hydrogen exchange is faster than isomerization may largely be the result of steric hindrance to ring rotation on the catalyst surface. Incomplete localization of the radical electron and the slow rotation of the heavy phenyl group in the transition state may also contribute significantly to this effect.

The difference in the vinyl hydrogen exchange rates in *cis*- and *trans*-stilbenes may be due to several factors. Molecular scale models show that vinyl hydrogens in *trans*-stilbene are sterically hindered in σ -bonded chemisorption. This impediment can only be overcome if the

(17) L. Crombie, *Quart. Rev.* (London), 6, 106 (1952).

(18) C. M. Wyman, *Chem. Rev.*, 55, 625 (1955).

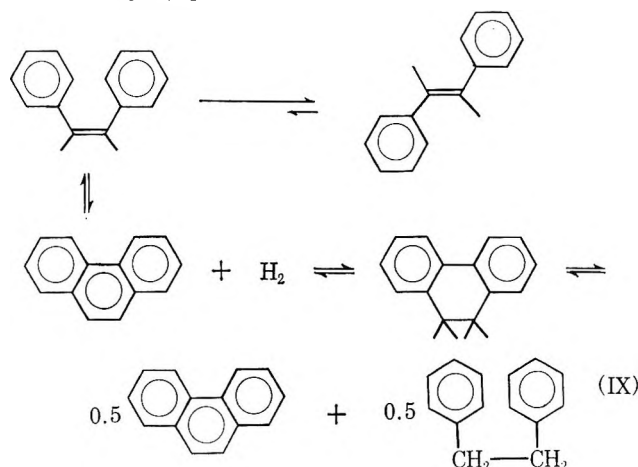
Table II: Deuterium Distribution and Exchange Rates of *cis*- and *trans*-Stilbenes

Source of <i>trans</i> -stilbene	Apparent <i>trans</i> isomer content, %	Average deuterium content, ^a %	Vinyl hydrogen distribution, %			Deuterium content, ^b %		Rate constants (hr. ⁻¹ × 10 ³) ^c		
			2H	HD	2D	Vinyl	Ring	I	VE	RE
<i>cis</i> -Stilbene isomerization	10.2	56.0	10.2	43.4	46.4	68.1	53.6	4.2	11.4	6.6
<i>trans</i> -Stilbene exchange	82.0	22.0	82	17.1	0.9	9.5	25.5	...	6.2	24.4

^a Average deuterium content determined mass spectrometrically. ^b Values calculated from "apparent *trans* isomer content." ^c Rate constants: I = isomerization; VE = deuterium exchange in vinyl group; RE = deuterium exchange in ring.

vinyl group twists out of the conjugational plane; steric repulsion between *ortho* aromatic hydrogens tends to assist this process. However, on the whole, the molecule exists in a planar configuration. Steric repulsion of the rings prevents a planar configuration in *cis*-stilbene, with the result that the vinyl hydrogens are readily accessible for σ -bonded chemisorption. Another consequence of nonplanarity is the greater π -electron localization in the vinyl double bond which should also increase the reaction rate.¹⁹

Besides formation of the *trans* isomer there exists also the possibility that *cis*-stilbene forms phenanthrene and dibenzyl (eq. IX).



No traces of aliphatic C-H stretching bands were found in the infrared spectra of the reaction products, indicating that disproportionation is relatively unimportant. This result is readily explained by stereochemical considerations. For disproportionation to occur, *cis*-stilbene would have to undergo simultaneous σ -bonded chemisorption in the *ortho* position of the two rings. This is prevented by steric factors, since only one ring at a time can adopt a suitable position for such bonding, the other having to assume a position of least steric hindrance which is unfavorable for σ bonding in the *ortho* position. However, once *trans*-stilbene is formed, phenanthrene formation by ring closure is prevented by molecular geometry.

Acknowledgment. The authors thank the Australian Institute of Nuclear Science and Engineering (Mr. E. A. Palmer) for assistance with the purchase of the heavy water, the New South Wales State Cancer Council for the use of their facilities, and Commander J. Mason for instrumentation advice. Acknowledgment is also made to the donors of The Petroleum Research Fund, administered by the American Chemical Society, for support of this research.

(19) C. A. Coulson, *Research* (London), 4, 307 (1951).

Heats of Formation of Solid Solutions in the Systems (Na–Ag)Cl and (Na–Ag)Br

by O. J. Kleppa and S. V. Meschel

Department of Chemistry and Institute for the Study of Metals, The University of Chicago, Chicago, Illinois 60637 (Received May 3, 1965)

The heats of formation of solid solutions in the systems (Na–Ag)Cl and (Na–Ag)Br have been determined by high-temperature solution calorimetry at 350° with pure liquid silver nitrate as the solvent. The molar enthalpies of formation, ΔH^M , may be represented analytically by the expressions

$$\text{(Na–Ag)Cl: } \Delta H^M = X(1 - X)(2.50 + 0.41X) \text{ kcal./mole}$$

$$\text{(Na–Ag)Br: } \Delta H^M = X(1 - X)(1.91 + 0.72X) \text{ kcal./mole}$$

Here X represents the mole fraction of the sodium halide. The results are compared with data for the liquid mixtures. In each case the solid solutions have larger positive enthalpies of formation than the liquid solutions, the chlorides are more endothermic than the bromides, and the bromide system has a larger energetic asymmetry than the corresponding chloride system. Both for the solid and liquid mixtures the enthalpies of formation are believed to arise mainly from the van der Waals–London interaction between second nearest neighbor cations.

Introduction

In the past two decades there have been a number of calorimetric studies of the heats of formation (or mixing) of the solid solutions formed among the alkali halides. Through these studies, which are due to different investigators, it has been established that the molar enthalpies of formation of the solid solutions, ΔH^M , characteristically depend on composition through expressions of the type

$$\Delta H^M = X(1 - X)\lambda$$

Here X and $1 - X$ are the mole fractions of the two components, while for a given system the *interaction parameter*, λ , is a constant or varies relatively little with composition. If we compare the values of λ for different mixed cation systems, we find that this quantity appears to depend linearly on the square of the parameter $\delta = (d_1 - d_2)/(d_1 + d_2)$. Here d_1 and d_2 are the characteristic interionic distances of the two pure salts. This empirical relationship is illustrated in Figure 1, in which we plot the experimental values of λ evaluated

at $X = 0.5$ vs. δ^2 . The data apply for the four mixed alkali cation systems for which heat data have been reported. Note that all points fall close to a single straight line. This has a slope of about 1400 kcal./mole.

Beginning with the work of Tobolsky¹ several attempts have been made to provide a theoretical explanation for the dependence of the enthalpy of mixing on δ^2 . Most extensively these investigations have been carried out by members of the Finnish school and notably by Wasastjerna,² Hovi,³ and Hietala.⁴

While there have been many investigations, both theoretical and experimental, of the solid solutions formed by the alkali halides, much less attention has been given to solutions which involve the highly polarizing ions Ag^+ and Tl^+ . For example, no calorimetric

(1) A. V. Tobolsky, *J. Chem. Phys.*, **10**, 187 (1942).

(2) J. A. Wasastjerna, *Soc. Sci. Fennica, Commentationes Phys. Math.*, **15**, No. 3 (1949).

(3) V. Hovi, *ibid.*, **15**, No. 12 (1950).

(4) J. Hietala, *Ann. Acad. Sci. Fennicae*, **6A**, No. 121, 122 (1963).

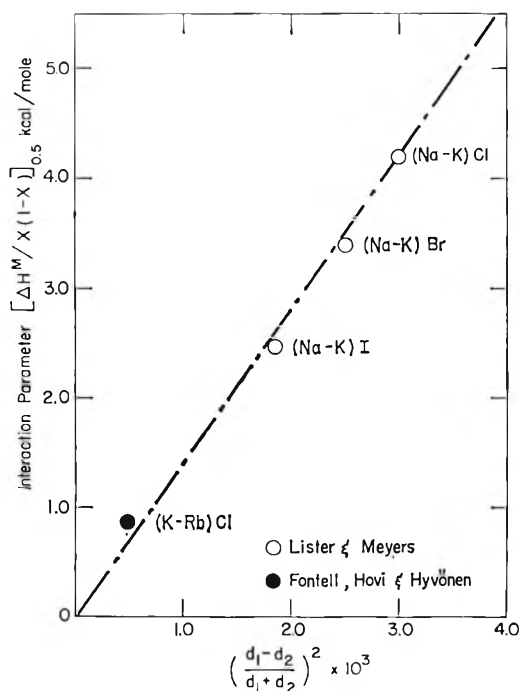


Figure 1. Plot of experimental interaction parameters $[\Delta H^M/X(1-X)]_{0.5}$ for mixed cation-common halogen ion solid solution systems. (Data from M. W. Lister and N. F. Meyers, *J. Phys. Chem.*, **62**, 145 (1958), and from N. Fontell, V. Hovi, and L. Hyvonen, *Ann. Acad. Sci. Fennicae*, **65** (1949).)

data are available for the silver halide-alkali halide systems. On the other hand, some e.m.f. data for the solid silver chloride-sodium chloride system have been reported by Wachter⁵ and by Panish and co-workers.⁶ Recently, we have initiated a thermochemical investigation of this class of solid solution systems. In the present paper we report data on the enthalpies of formation for the systems (Na-Ag)Cl and (Na-Ag)Br. The reported equilibrium phase diagrams for these systems are shown in Figure 2.^{7,8}

These phase diagrams indicate that the systems both have a complete range of solid solubility at elevated temperatures. For (Na-Ag)Cl the recent work of Stokes and Li⁸ indicates the existence of a miscibility gap with a critical temperature near 175°. In the case of (Na-Ag)Br the literature gives no information regarding any miscibility gap. Nevertheless, in view of the similarity of the two systems, a miscibility gap at room temperature may be inferred. This is supported by the new enthalpy data reported in the present work. However, since the positive enthalpies of formation for the bromide solutions (see below) are about 20% smaller than those for the corresponding chlorides, a critical temperature somewhat below 175° is predicted.

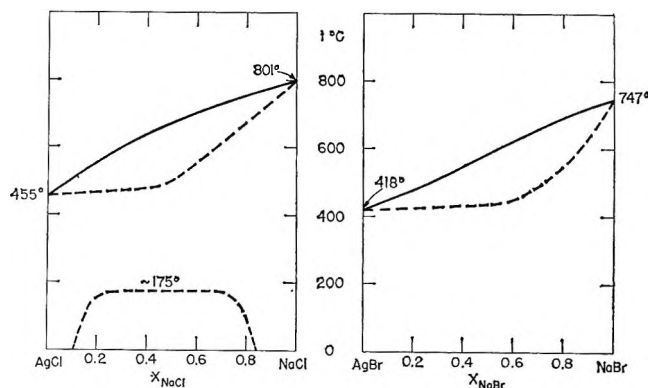


Figure 2. Equilibrium phase diagrams for silver chloride-sodium chloride and silver bromide-sodium bromide systems taken from ref. 7 and 8.

Experimental Section and Chemicals

The silver halides dissolve only with difficulty in most room temperature calorimetric solvents. Therefore, the present investigation was based on the use of high-temperature solution calorimetry, and pure liquid silver nitrate was selected as a suitable solvent. This salt melts at 202° and is an effective solvent for the sodium and silver halides. In the present work, all measurements were carried out at $350 \pm 1^\circ$, in a calorimeter which has been described elsewhere.⁹

Calorimetric calibrations were by the gold-drop method. This method has been described in earlier work from this laboratory.⁹ It is based on the heat content data for pure gold given by Kelley.¹⁰ There is a small, reproducible error of about 0.5% associated with the use of this calibration method in liquid silver nitrate, owing to the deposition of trace amounts of silver on the surface of the gold.¹¹ This error is not considered to be significant compared to other uncertainties associated with the present work.

The two sodium salts were Baker Analyzed reagents, while the silver halides were purchased from Goldsmith Brothers as analytical grade reagents. The silver nitrate used was obtained from Fisher. The solid solution samples were prepared from finely ground master mixtures of the two components. Each sample,

(5) A. Wachter, *J. Am. Chem. Soc.*, **54**, 919 (1932).

(6) M. B. Panish, F. F. Blankenship, W. R. Grimes, and R. F. Newton, *J. Phys. Chem.*, **62**, 1325 (1958).

(7) S. F. Zencuzny, *Z. anorg. allgem. Chem.*, **153**, 52 (1926).

(8) R. J. Stokes and C. H. Li, *Acta Met.*, **10**, 535 (1962).

(9) O. J. Kleppa, *J. Phys. Chem.*, **64**, 1937 (1960).

(10) K. K. Kelley, U. S. Department of the Interior, Bureau of Mines, Bulletin No. 584, U. S. Government Printing Office, Washington, D. C., 1960.

(11) O. J. Kleppa, R. B. Clarke, and L. S. Hersh, *J. Chem. Phys.*, **35**, 175 (1961).

Table I: Molar Enthalpies of Formation (ΔH^M) for Solid Solutions in the System NaCl-AgCl at 350°

Size of sample, g.	Mole fraction, X_{NaCl}	$n_1 + n_2$, mmoles	ΔH_1 , ^a cal.	ΔH_2 , ^{b,c} cal.	ΔH_3 , ^{b,c} cal.	ΔH^M , ^c kcal./mole
0.5000	0.85	7.04	2.83	-53.94(7) ± 0.5	-53.59(3) ± 0.4	0.35 ± 0.09
0.5000	0.75	6.28	4.21	-42.34(7) ± 0.3	-41.77(4) ± 0.4	0.58 ± 0.08
0.5000	0.60	5.41	5.81	-29.31(6) ± 0.2	-26.93(5) ± 0.2	0.63 ± 0.05
0.5000	0.50	4.98	6.72	-22.34(4) ± 0.1	-18.86(4) ± 0.1	0.65 ± 0.03
1.0000	0.35	8.80	15.79	-27.53(5) ± 0.3	-16.84(4) ± 0.3	0.58 ± 0.05
1.0000	0.15	7.72	18.17	-10.36(3) ± 0.1	+5.15(4) ± 0.1	0.34 ± 0.02

^a Values calculated from eq. 5a. ^b Numbers in parentheses represent number of experiments. ^c All stated limits of error are standard deviations.

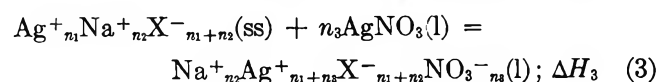
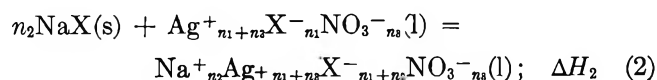
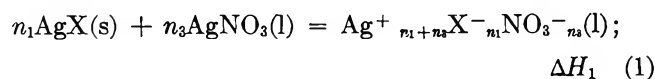
Table II: Molar Enthalpies of Formation (ΔH^M) for Solid Solutions in the System NaBr-AgBr at 350°^a

Size of sample, g.	Mole fraction, X_{NaBr}	$n_1 + n_2$, mmoles	ΔH_1 , ^b cal.	ΔH_2 , ^c cal.	ΔH_3 , ^c cal.	ΔH^M , kcal./mole
0.5000	0.87	4.39	0.86	-58.14(3) ± 0.3	-58.55(3) ± 0.1	0.29 ± 0.07
0.5000	0.77	4.09	1.44	-48.72(3) ± 0.2	-49.01(3) ± 0.3	0.42 ± 0.09
0.5000	0.70	3.92	1.81	-42.20(3) ± 0.25	-42.42(4) ± 0.3	0.52 ± 0.09
0.5000	0.65	3.77	2.03	-37.44(4) ± 0.35	-37.68(4) ± 0.2	0.60 ± 0.10
0.5000	0.50	3.46	2.68	-25.43(3) ± 0.1	-24.50(4) ± 0.15	0.51 ± 0.05
1.0000	0.45	6.72	5.99	-45.26(3) ± 0.2	-42.69(3) ± 0.2	0.51 ± 0.04
1.0000	0.27	6.08	7.33	-24.07(2) ± 0.15	-19.48(2) ± 0.15	0.45 ± 0.03
1.0000	0.27	6.08	7.33	-24.80(2) ± 0.02 ^d	-20.24(2) ± 0.1 ^d	0.46 ± 0.02

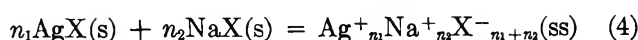
^a All stated limits of error are standard deviations. ^b Values calculated from eq. 5b. ^c Numbers in parentheses represent number of experiments. ^d Experiments involved a different batch of silver nitrate.

in an amount slightly larger than that required for the solution experiment, was melted down separately in a small Vycor test tube in air, thoroughly mixed in the liquid state, and quenched by immersing the container in a salt-ice-water bath. Then the sample was removed from the test tube and ground in a mortar. With few exceptions all samples were 500 mg. in weight and were kept in the calorimeter overnight at 350° in order to obtain a complete anneal. The solvent was 10.00 g. of pure silver nitrate.

The enthalpy of formation of the solid solutions was calculated from three separate measurements as



Clearly, we have from (1) + (2) - (3)



and the molar enthalpy of formation is simply

$$\Delta H^M = (\Delta H_1 + \Delta H_2 - \Delta H_3)/(n_1 + n_2) \quad (5)$$

For each composition we carried out two to seven separate measurements of ΔH^M , from which the average values were calculated. Among the measured enthalpies ΔH_1 usually was relatively small and endothermic, except at low NaCl concentrations, while ΔH_2 and ΔH_3 were large and exothermic. Therefore, it was of overriding importance to achieve high precision in the measurement of ΔH_2 and ΔH_3 . On the whole, we were able to measure these quantities with a precision of about 0.5%. Even so, the reported values of ΔH^M are associated with uncertainties of the order of 5 to 7%.

Results

We give in Tables I and II a summary of all the experimental data obtained in the course of the present investigation. From left to right the columns in these tables give:

(1) Sample size. Most solid solution samples weighed precisely 0.5000 ± 0.0001 g. while a smaller number weighed 1.0000 ± 0.0001 g.

(2) Mole fraction of sodium halide in the solid solution sample.

(3) Total millimoles in the solid solution sample. The product of (2) and (3) gives the number of moles of sodium halide in the sample (n_2).

(4) ΔH_1 , the heat of reaction according to eq. 1. In the course of the present work the heats of solution of solid silver chloride and silver bromide in pure liquid silver nitrate were determined over a range of compositions at 350°. The following equations were obtained through a least-squares analysis of the data

$$\Delta H_1(\text{AgCl}) = n_1(2.65 + 1.21n_2/(n_1 + n_3)) \text{ kcal.} \quad (5a)$$

and

$$\Delta H_1(\text{AgBr}) = n_1(1.49 + 2.27n_2/(n_1 + n_3)) \text{ kcal.} \quad (5b)$$

In these expressions n_1 is the number of moles of silver halide while n_3 is 58.86 millimoles throughout, corresponding to 10.00 g. of silver nitrate. The values of ΔH_1 given in Tables I and II were calculated from these expressions. In a previous investigation the present authors have made related measurements at 234°. There is reasonable agreement between the two sets of data, indicating only a modest temperature dependence of the heats of solution.

(5) ΔH_2 , the enthalpy change associated with the process given by eq. 2.

(6) ΔH_3 , the enthalpy change for the process given by eq. 3.

The numbers in columns 5 and 6 represent the averages of from two to seven separate experiments along with the appropriate standard deviations.

(7) ΔH^M , the molar enthalpy of formation of the considered solid solution, calculated according to eq. 5. The values of ΔH^M for the two solid solution systems are plotted against mole fraction in Figures 3 and 4 and exhibit the expected parabolic dependence on mole fraction. A further illustration of this is included in the figures, which contain also plots of the interaction parameter, $\lambda = \Delta H^M/X(1 - X)$ vs. X . A linear dependence of λ on X is indicated. Subjecting the experimental values of λ to a least-squares analysis, giving equal weight to each point, we obtained empirical expressions for the molar enthalpies of formation of the two solid solutions

$$(\text{Ag-Na})\text{Cl: } \Delta H^M = X(1 - X)(2.50 + 0.41X) \text{ kcal./mole} \quad (6a)$$

$$(\text{Ag-Na})\text{Br: } \Delta H^M = X(1 - X)(1.91 + 0.72X) \text{ kcal./mole} \quad (6b)$$

In these expressions X represents the mole fraction of sodium halide. The standard deviation of the experi-

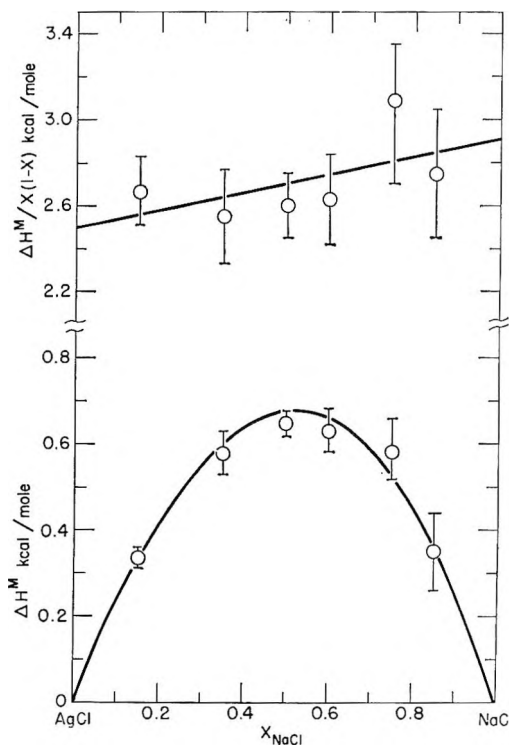


Figure 3. Experimental molar enthalpies of formation, ΔH^M , and interaction parameters, $\Delta H^M/X(1 - X)$, for silver chloride-sodium chloride solid solutions.

mental points from these expressions are 0.13 kcal./mole (5%) for (Ag-Na)Cl and 0.17 kcal./mole (7%) for (Ag-Na)Br.

Discussion

We noted by way of introduction that the enthalpies of formation of simple ionic solid solutions to a first approximation are related to the interionic distances in the two solution partners through an empirical expression of the type

$$\Delta H^M = X(1 - X)A\delta^2 \quad (7)$$

If this expression is applied to the considered systems, we obtain values of $\Delta H^M_{0.5}$ of 0.02 kcal./mole for (Na-Ag)Cl and 0.09 kcal./mole for (Na-Ag)Br. These numbers should be compared to our experimental values which may be derived from eq. 6a and 6b above and are 0.67 ± 0.03 and 0.57 ± 0.04 kcal./mole, respectively. From this it will be apparent that the enthalpies of formation in the considered systems cannot be explained along this line. In fact, the small difference in size between the silver and sodium ions can give rise only to a small fraction of the over-all positive enthalpies of formation.

(12) O. J. Kleppa and S. V. Meschel, *J. Phys. Chem.*, 67, 668 (1963).

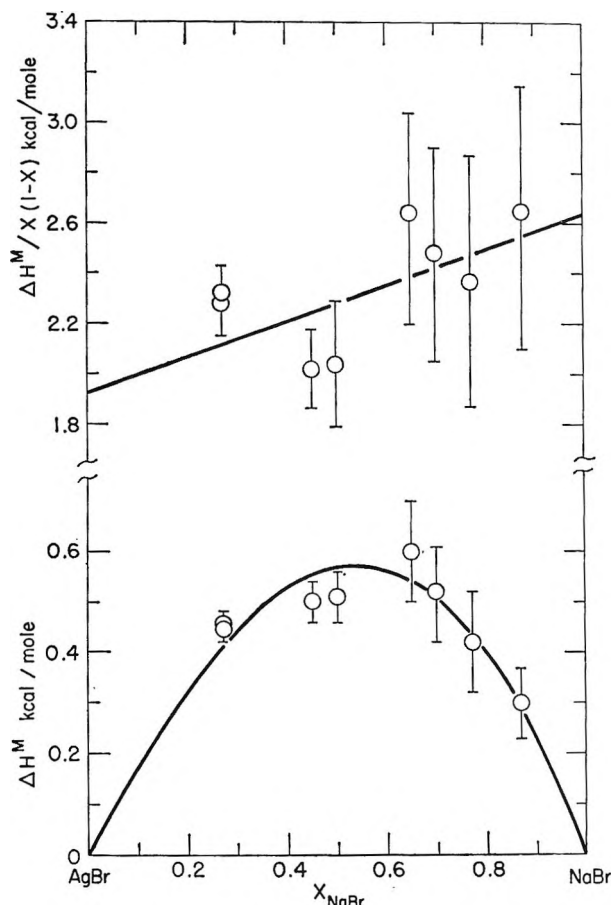


Figure 4. Experimental enthalpies of formation, ΔH , and interaction parameters, $\Delta H^M/X(1-X)$, for silver bromide-sodium bromide solid solutions.

The nature of the forces acting between the ions in the silver halides has for a long time been the subject of considerable interest. While the early theoretical work of Mayer^{13,14} seemed to indicate that covalency did not play a very important role in these salts, the recent calculations of Ladd and Lee¹⁵ point in a different direction. The latter authors find significant discrepancies between the experimental lattice energies and the best theoretical values calculated from ionic and dispersion interactions. These discrepancies are attributed to covalent bonding and amount to about 15 kcal./mole (7%) for silver chloride and about 18 kcal./mole (8.5%) for silver bromide. We note that the covalent contributions to bonding are somewhat larger for silver bromide than for silver chloride. This is consistent with the recent n.m.r. chemical shift data of Hafner and Nachtrieb¹⁶ for thallium halides, for which salts the chemical shifts indicate increasing covalency in the sequence $F^- < Cl^- < Br^- < I^-$. A similar situation may be expected to exist in the silver halides.

We note also that the lattice parameter difference is somewhat larger for the bromides than for the chlorides. In spite of this, we actually find that the experimental values of ΔH^M are smaller. These observations would seem to rule out the covalent bonding contribution between cation and anion as the principal source of the mixing enthalpies.

We propose instead that in the main the mixing enthalpies arise from the van der Waals-London dispersion interaction between the cations. For certain mixtures of fused salts this possibility has been considered by Lumsden¹⁷ and independently by Blander.¹⁸ In the present discussion we shall adopt an analogous approach.

The predominant term in the van der Waals-London interaction energy between the two cations i and j is the dipole-dipole term

$$U_{ij} = -C_{ij}/d_{ij}^6 \quad (8)$$

In this expression d_{ij} is the cation-cation distance while C_{ij} is given by the London approximation formula

$$C_{ij} = (3/2)\alpha_i\alpha_j I_i I_j / (I_i + I_j) \quad (9)$$

Here α is the polarizability of the cation, while I is set equal to 0.75–0.85 times the ionization potential of the cation.^{13,14} Owing to the short-range character of the dispersion forces, the principal effect will arise from second nearest neighbor cations. In this second nearest neighbor approximation¹⁷ we obtain the following expression for the van der Waals-London contribution to the interaction parameter, λ_{London}

$$\lambda_{\text{London}} = 6N[C_{\text{NaNa}}/d_{\text{NaNa}}^6 + C_{\text{AgAg}}/d_{\text{AgAg}}^6 - 2C_{\text{AgNa}}/d_{\text{AgNa}}^6] \quad (10)$$

where N is Avogadro's number. In calculating λ_{London} we accepted the values of I quoted by Blander¹⁸; however, we have performed the evaluations on the basis of two sets of data for α , namely, the early values of Pauling¹⁹ and the recently compiled values of Tessman, Kahn, and Shockley.²⁰ The values of d_{ij} were obtained from lattice parameter data quoted by

(13) J. E. Mayer, *J. Chem. Phys.*, **1**, 270 (1933).

(14) J. E. Mayer, *ibid.*, **1**, 327 (1933).

(15) M. F. C. Ladd and W. H. Lee in "Progress in Solid State Chemistry," Vol. I, I. H. Reiss, Ed., The Macmillan Co., New York, N. Y., 1964, p. 51.

(16) S. Hafner and N. H. Nachtrieb, *J. Chem. Phys.*, **40**, 2891 (1964).

(17) J. Lumsden, *Discussions Faraday Soc.*, **32**, 138 (1961).

(18) M. Blander in "Molten Salt Chemistry," M. Blander, Ed., Interscience Publishers, Inc., New York, N. Y., 1964, pp. 161, 162.

(19) L. Pauling, *Proc. Roy. Soc. (London)*, **A114**, 181 (1927).

(20) J. R. Tessman, A. H. Kahn, and W. Shockley, *Phys. Rev.*, **92**, 890 (1953).

Table III: Calculated and Observed Enthalpies of Formation in (Na-Ag)Cl and (Na-Ag)Br Solid Solutions

System	$\Delta H_{0.5}^M$, kcal./mole					
	Ionic contribution, $Q_{0.5} = (A/4)\delta^2$	Dispersion contribution (eq. 11), $(1/4)\lambda_{\text{London}}$		$Q_{0.5} + (1/4)\lambda_{\text{London}}$		Obsd. (eq. 6)
		α (Pauling)	α (Tessman)	α (Pauling)	α (Tessman)	
(NaAg)Cl	+0.02	+0.36	+0.58	+0.38	+0.60	+0.67 \pm 0.03
(NaAg)Br	+0.09	+0.29	+0.47	+0.38	+0.56	+0.57 \pm 0.04

Wyckoff,²¹ and Vegard's law was assumed for the solid solutions. For the (Na-Ag)Cl system this is consistent with the observations of LeBlanc and Quenstadt,²² confirmed by Stokes and Li.⁸ If cation-cation interactions between more distant neighbors are taken into account, the values of λ_{London} are increased somewhat, in the considered sodium chloride structure by 20% (see, e.g., Mayer¹³)

$$\lambda_{\text{London}} = 7.2N[C_{\text{NaNa}}/d_{\text{NaNa}}^6 + C_{\text{AgAg}}/d_{\text{AgAg}}^6 - 2C_{\text{AgNa}}/d_{\text{AgNa}}^6] \quad (11)$$

The values calculated from eq. 11 are summarized in Table III. In this table we have included also the earlier mentioned estimates of the "ionic" contributions, ($Q_{0.5}$) calculated from eq. 7. The sum of $Q_{0.5} + 1/4 \lambda_{\text{London}}$ represents calculated values of the enthalpy of formation at the 50-50 composition. These may now be compared to our experimental results. Table III shows that, irrespective of our choice of α , there is agreement to better than a factor of 2 between the calculated and the experimental data. If we adopt the α values of Tessman, *et al.*,²⁰ the agreement is remarkably good. In fact, it certainly is better than one might expect from the rather approximate character of the London dispersion energy formula.

Finally, we want briefly to compare our new enthalpy data for the solid solution with corresponding values for the liquid systems (Na-Ag)Cl and (Na-Ag)Br. These data were reported recently by Hersh, *et al.*^{23,24} The comparison is presented in Table IV. For each solid and liquid system the available enthalpies of formation have been expressed empirically by relations of the form

$$\Delta H^M = X(1 - X)(a + bX)$$

In each case X represents the mole fraction of alkali halide. The experimental values of a , b , and $\Delta H_{0.5}^M$ are given in Table IV. It will be recognized that there is extensive analogy among the four sets of data; for example, all values of a and b are positive. Also, for each system the value of a (solid solution) is larger than a (liquid solution), while, on the other hand, the value of b (liquid solution) is larger than b (solid solu-

Table IV: Enthalpies of Formation (in kcal./mole) for Solid and Liquid Solutions in the Systems (Ag-Na)Cl and (Ag-Na)Br^a

System	a	b	$\Delta H_{0.5}^M$	Temp., °C.	Re- marks
(Ag-Na)Cl, sol. soln.	2.50	0.41	0.67	350	
(Ag-Na)Cl, liq. soln.	0.92	0.62	0.31	660	Ref. 23
(Ag-Na)Br, sol. soln.	1.91	0.72	0.57	350	
(Ag-Na)Br, liq. soln.	0.30	1.08	0.21	705	Ref. 24

^a $\Delta H^M = X(1 - X)(a + bX)$; X = mole fraction of sodium halide.

tion). Note that the values of $\Delta H_{0.5}^M$ for the solid solutions are 2 to 2.5 times as large as for the corresponding liquid mixtures.

Hersh and co-workers^{23,24} have argued that the observed enthalpies of mixing in the considered liquid systems may also in large measure be due to the dispersion energy between second nearest neighbor cations. For this purpose they have carried out calculations somewhat similar to those given above. At first sight, it appears surprising that the second nearest neighbor dispersion interaction should give rise to much larger positive values of ΔH^M in the solid than in the liquid mixtures. However, this apparent inconsistency may perhaps be explained as follows.

The X-ray investigations of liquid alkali halides by Levy and Danford²⁵ indicate that through the process of fusion the number of second nearest neighbor ions usually is reduced compared to that in the solid state. At the same time, the cation-cation (and anion-anion) separation is somewhat increased, presumably owing to the Coulomb repulsion. While X-ray data have not been reported for the silver halides, a similar situation may be expected to apply. It is known

(21) R. W. G. Wyckoff in "Crystal Structures," Vol. I, Interscience Publishers, Inc., New York, N. Y., 1960.

(22) M. LeBlanc and J. Quenstadt, *Z. physik. Chem. (Leipzig)*, **A150**, 321 (1930).

(23) L. S. Hersh and O. J. Kleppa, *J. Chem. Phys.*, **42**, 1309 (1965).

(24) L. S. Hersh, A. Navrotsky, and O. J. Kleppa, *ibid.*, **42**, 3752 (1965).

(25) H. A. Levy and M. D. Danford, *ref. 18*, p. 118.

that the silver bromide-sodium bromide liquid system has a small positive excess volume.²⁴ This may similarly be expected to give rise to a somewhat increased cation-cation separation in the mixture. In view of the d^{-6} dependence of the dispersion energy on interionic distance, these several effects may possibly account for the observed differences.

Finally, we want to compare our enthalpy data for the silver chloride-alkali chloride solid solutions with excess free energies derived from the e.m.f. investigation of Panish, *et al.*⁸ The work of Panish shows a great deal of experimental scatter. To a first approximation we shall assume that the partial excess free energies of silver chloride depend on composition through a relation of the type

$$\Delta\bar{G}_{\text{AgCl}}^E = B(1 - X_{\text{AgCl}})^2$$

Interpolating the results for 300 and 400°, we find a value of B of 2.2 kcal./mole. The corresponding value of the integral excess free energy at the 50-50

composition is 0.55 kcal./mole, *i.e.*, slightly smaller than $\Delta H_{0.5}^M$ (0.67 kcal./mole). This indicates that the considered solid solutions have small positive excess entropies. At the 50-50 composition the excess entropy amounts to about 0.2 cal./deg. mole. It is difficult to assess the experimental uncertainty in this value since it is based on two separate investigations. However, it is of interest to note that both the positive sign and the order of magnitude are consistent with the results previously reported by McCoy and Wallace²⁶ for the KCl-KBr solid solution system.

Acknowledgments. This work has been supported by the National Science Foundation and by the U. S. Army Research Office. The authors also wish to acknowledge general support of the Institute for the Study of Metals provided by the Advanced Research Projects Agency.

(26) W. H. McCoy and W. E. Wallace, *J. Am. Chem. Soc.*, **78**, 5995 (1956).

Diffusional Processes in Knudsen Cells

by N. A. Gokcen

*Chemical Thermodynamics Section, Laboratories Division, Aerospace Corporation, El Segundo, California
(Received May 4, 1965)*

The volume and surface diffusions in Knudsen cells have been analyzed and their erroneous effects on vapor pressure measurements have been discussed. It is found conclusively that the volume diffusion may be large in some cases. A useful equation has been derived from the relationships of Motzfeldt and of Winterbottom and Hirth, leading to a simple graphical method capable of showing measurably large contributions of surface diffusion to effusion. It is shown that in favorable cases the Knudsen cells may be used for obtaining reasonable values of the root mean square of surface diffusion distance, E^{-1} . Suggestions have been made to minimize the diffusional errors and to make calculational corrections in the absence of data on E .

Introduction

Measurements of equilibrium vapor pressures with Knudsen cells require the elimination of numerous sources of experimental errors (see, for example, Carlson¹). The errors from diffusional processes, however, have been generally ignored because it is usually assumed that a choice of appropriate cell materials would eliminate them. The volume diffusion in graphite cells has been observed and evaluated by Fujishiro and Gokcen² and the surface diffusion through the cell orifice has been critically examined and elegantly formulated by Winterbottom and Hirth.³ The latter formulation³ has been verified experimentally by Boyer and Meadowcroft⁴ for Ag(l) in Mo cells.

The purpose of this paper is (a) to show that in some cases the volume diffusion may be large, (b) to derive useful equations from the relationships of Motzfeldt⁵ and of Winterbottom and Hirth which lead to simple graphical methods capable of showing contributions from surface diffusion, and (c) to show that in favorable cases the Knudsen cells may be used for obtaining reasonable values of the root-mean-square diffusion distance. Suggestions have been made to minimize or eliminate the diffusional errors and to make calculational corrections.

Volume Diffusion

A number of investigators have used a refractory nonmetallic crucible with an attached metallic lid which is easy to drill and grind in order to obtain a knife-edge

orifice of desired dimensions. Since the coefficients of expansion of the two cell components are not the same, this procedure should be avoided whenever possible in order to eliminate unexpected leakage through the lid joint. The cell should therefore be made of one single material whenever possible. The vapor pressure of silver has been determined by this method but we shall take the cell as constructed entirely of nickel.⁴ Silver and nickel are immiscible in the solid and the liquid states but there is an estimated solid solubility of roughly 1 to 3% by weight of silver in solid nickel⁶ at 1300°K. We shall adopt a value of 2% silver by weight. The diffusivity, D , of silver in nickel is not known but it may be estimated as 10^{-10} cm.²/sec., which is about the same as that of copper in nickel or gold in nickel. The flux J_D of silver in grams per square centimeter through a cell wall is given by Fick's first law

$$J_D = -D \frac{\partial c}{\partial x} \quad (1)$$

(1) K. D. Carlson, "Molecular and Viscous Effusion of Saturated Vapors," Argonne National Laboratory, ANL-6156, Argonne, Ill., 1960.

(2) S. Fujishiro and N. A. Gokcen, *J. Phys. Chem.*, **65**, 161 (1961).

(3) W. L. Winterbottom and J. P. Hirth, *J. Chem. Phys.*, **37**, 784 (1962).

(4) A. J. Boyer and T. R. Meadowcroft, *Trans. AIME*, **233**, 388 (1965).

(5) K. Motzfeldt, *J. Phys. Chem.*, **59**, 139 (1955).

(6) M. Hansen and K. Ankerko, "Constitution of Binary Alloys," McGraw-Hill Book Co., Inc., New York, N. Y., 1958.

where c is the concentration in grams per cubic centimeter and $\partial c/\partial x$ is the concentration gradient. Assuming that (a) the steady-state diffusion prevails and $\partial c/\partial x \approx \Delta c/\Delta x$, (b) the wall thickness is 0.02 cm., or $\Delta x = 0.02$, and (c) the concentration of silver on the surface of the Knudsen cell is zero, then the concentration gradient is $\Delta c/\Delta x = -9 \text{ g./cm.}^4$. The amount of silver lost per second through the entire cell wall is the surface area, A , times J_D . The value of A for an average size cell is about 10 cm.^2 ; hence, the loss of Ag is $0.9 \times 10^{-8} \text{ g./sec.}$

The rate of weight loss, W in grams per second by effusion through a knife-edge orifice is obtained from

$$P \text{ (dynes/cm.}^2\text{)} = 2.2856 \times 10^4 \frac{W}{a} \sqrt{\frac{T}{M}} \quad (2)$$

Substitution of $a = 10^{-4} \text{ cm.}^2$ for an unusually small but not uncommon⁴ orifice, $T = 1300^\circ \text{K.}$, $M = 107.9$, and $P = 12.52 \text{ dynes/cm.}^2$ from the equilibrium data yields $W = 1.58 \times 10^{-8} \text{ g./sec.}$ It is therefore seen that the volume diffusion may be large in exceptional cases. The foregoing results may be in error by a factor of more than 10 because (a) D cannot be estimated accurately by comparison with D for other systems, (b) the solubility of silver in nickel is not known with a sufficient degree of accuracy, and (c) $\partial c/\partial x$ may be much smaller than the assumed value because the concentration on the surface may be large and c vs. x may not be linear. Increasing both the wall thickness and the orifice dimension within limits and selecting nondissolving crucible materials would minimize or entirely eliminate the volume diffusion. However, in the case when the cell material itself is one of the reactants or the products, as graphite cells containing dissociating carbides,² the choice of another material is not possible. Fujishiro and Gokcen² showed that in the cells made of the densest graphite available at that time, a substantial loss of weight occurred by diffusion through graphite and possibly through a small number of connected pores, as measured by means of cells without orifice. Fortunately, it is possible to eliminate this error entirely by using a torsion effusion cell symmetrical in shape with respect to the axis of suspension.

The loss of diffusion generally increases faster than the increase in pressure inside a given cell with increasing temperature because the activation energy for diffusion is generally greater than the standard free energy for vaporization but not necessarily for dissociation,² and the solubility of a sparingly soluble substance usually increases exponentially with temperature and thus sets up a greater concentration gradient.

Surface Diffusion

Equations. Fick's law for surface diffusion is

$$J_s = -D_s \frac{\partial n}{\partial x} \quad (3)$$

where J_s is the flux in molecules per second per centimeter of length perpendicular to the direction of diffusion, D_s is the surface diffusivity in square centimeters per second, and n is the surface concentration of diffusing substance in molecules per square centimeter. When an effusing gas is adsorbed on the inner surface of a cell, it tends to diffuse out through the orifice and reach the external surface where it is desorbed under a high vacuum. This process may contribute considerably to the observed weight loss in Knudsen cells. The use of a torsion cell in this case cannot eliminate the error.

Winterbottom and Hirth³ derived a number of useful equations by solving eq. 3 for n and J_s in terms of measurable quantities by using the prevailing boundary conditions for Ni and Mo cells containing Ag. They also obtained an expression for the ratio of surface diffusion current, W_s in grams per second to the effusion current W_{eff} , i.e., $\beta = W_s/W_{\text{eff}}$, in terms of the usual quantities encountered in surface diffusion phenomena. By using their eq. 14, 21, and 27, we derive the useful relationship

$$\beta = \frac{n'2K_1(ER)}{\gamma n_e ERK_0(ER)} \quad (4)$$

In this equation, n' is the surface concentration of the effusing substance at the top of the circular cylindrical orifice where the gas leaves the cell; n_e is the same quantity at the bottom or inner part of the orifice, hence the equilibrium value of n with Ag; γ is the transmission coefficient which closely approaches the Clausing⁷ factor with decreasing ratio of the length of the cylindrical orifice, L , to its radius, R ; $1/E$ is the root mean square of diffusion distance; and K_1 and K_0 are the modified Bessel functions of the second kind of first and zeroth order, respectively, both being functions of the variable ER . The quantity E is given by

$$E^2 D_s = \nu \exp(-\Delta G^\circ_{\text{des}}/kT) \quad (5)$$

where ν is the frequency factor and $\Delta G^\circ_{\text{des}}$ is the free energy of desorption. The values of the quantities in eq. 5 for Ag(g) adsorbed on Mo cells are $2 \times 10^9 < \nu < 4 \times 10^{11}$, $\Delta G^\circ_{\text{des}} = 2.2 \pm 0.2 \text{ e.v.}$, and $D_s = 10^{-4} \text{ cm.}^2/\text{sec.}$ as obtained by Goeler and Peacock.^{3,8} The value of D_s varies somewhat with temperature but the

(7) P. Clausing, *Ann. Physik*, 12, 961 (1932).

(8) E. Von Goeler and R. M. Peacock, *J. Chem. Phys.*, 39, 169 (1963).

activation energy for D_s is probably small, and therefore, in view of the uncertainties involved in other quantities in eq. 5, the assumption that D_s is constant³ is reasonable. The values of E computed by taking $\nu = 10^{10}$ sec.⁻¹ and by substituting the preceding quantities in eq. 5 are 29, 540, and 1100 cm.⁻¹ at 1000, 1300, and 1400°K., respectively.

We shall now take advantage of a very useful property⁹ of the ratio K_1/K_0 in eq. 4. This ratio is close to unity when ER is in excess of 2, corresponding to $\beta \approx 1$; *i.e.*, the surface diffusion current is about equal to the effusion current. In the experiments of Boyer and Meadowcroft,⁴ ER ranged from about 4 to 10 for the cells with knife-edged Mo lids at their lowest temperature.

Computations from the appropriate equations of Winterbottom and Hirth show that $n'/(γn_e)$ is very nearly equal to unity for L/R about 0.2 and smaller. For a knife-edge orifice ($L/R = 0$) this ratio is identically unity. Therefore, eq. 4 assumes the remarkably simple form

$$\beta = \frac{2}{ER} \equiv \frac{B}{R} \quad (6)$$

For large values of β , *e.g.*, $\beta = 5$ corresponding to $ER = 0.65$, eq. 4 may still be expressed by eq. 6 for a five-fold range in ER , with an accuracy of better than 15%, but an appropriate numerical coefficient is necessary to relate B to E in $B = 2/E$. We shall limit our discussion to the range where eq. 6 is valid, keeping in mind that extending the range of ER to lower values requires simple appropriate adjustments in B .

The pressure prevailing in the cell decreases with increasing R according to a useful equation derived by Motzfeldt⁵

$$\frac{1}{P_{\text{obsd}}} = \frac{1}{P_{\text{eq}}} + \frac{\pi R^2 \gamma}{\alpha A P_{\text{eq}}} \quad (7)$$

where P_{obsd} and P_{eq} are the observed and the equilibrium pressures, respectively, α is the accommodation coefficient, and A is the surface area of vaporizing phase inside the cell. Although the degree of precision of this equation has been questioned¹ in view of the assumptions used in its derivation, the significant aspects of its usefulness for our purposes are as follows: (1) a plot of $1/P_{\text{obsd}}$ vs. R^2 is linear, and the intercept is $1/P_{\text{eq}}$, and (2) the slope is a positive quantity, rather small for large values of α and P_{eq} .

The total observed rate of weight loss, W , from a cell, after correction for volume diffusion when necessary as obtained from a cell whose orifice may be sealed after evacuation, consists of the sum of the effusion loss, W_{eff} and the surface diffusion loss, W_s . The quantity from

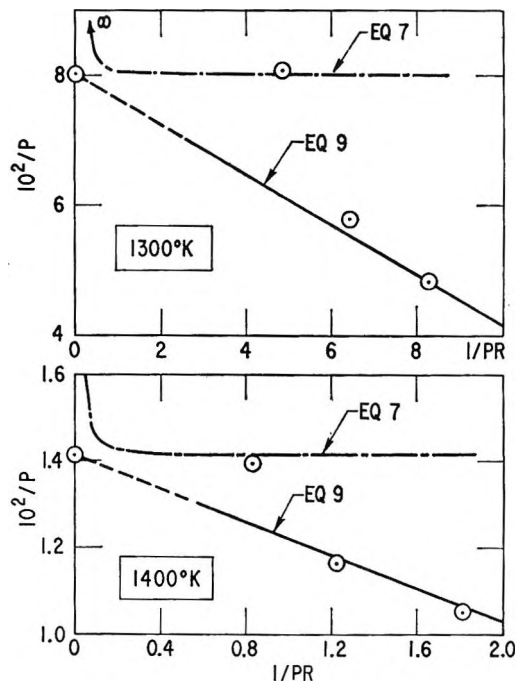


Figure 1. Plots of $10^2/P_{\text{obsd}}$ in cm.²/dyne vs. $1/(P_{\text{obsd}}R)$ in cm./dyne. All lines are calculated, and points \odot represent data⁴ for solid lines, except two points¹⁰ corresponding to P_{eq} or $1/(P_{\text{obsd}}R) = 0$.

which P_{obsd} is computed by means of eq. 2 is therefore $W - W_s$, or since $\beta = B/R = W_s/W_{\text{eff}}$, then

$$W_{\text{eff}} = \frac{WR}{B + R}$$

Substitution of this quantity in eq. 2 and then in eq. 7 gives the important relationship

$$\frac{1}{P_{\text{obsd}}} = \frac{1}{P_{\text{eq}}} + \frac{\pi R^2 \gamma}{\alpha A P_{\text{eq}}} - \frac{B}{P_{\text{obsd}}R} \quad (8)$$

where P_{obsd} is calculated by using W in eq. 2. We shall next deal with the experiments in which γ is kept constant or the knife-edge orifices in which $\gamma = 1$, while R is varied from one measurement to another in order to reduce the number of independent variables.

Applications. Equation 8 shows that while in the absence of surface diffusion, *i.e.*, when $B = 0$, a plot of $1/P_{\text{obsd}}$ vs. R^2 is linear with a positive slope, this is not true when the surface diffusion is present. As a matter of fact, for $\alpha \approx 1$, $A = 3$ cm.² for Ag in Mo cells with $R = 0.05$ cm., the second term is smaller than the absolute value of the third term by 1500 times at 1000°K. and 15 times at 1400°K. We may argue this point in a more rigorous manner that we are interested

(9) E. Jahnke and F. Emde, "Tables of Functions," Dover Publications, New York, N. Y., 1945, p. 236.

in measurably large values of β , such as $\beta \geq 0.1$, for this, P_{obsd} is not greatly different from P_{eq} and therefore the second term is only one-tenth to one-thousandth as large as the third term for the orifice radii from 0.1 to 0.01 cm., respectively. Consequently, the second term in eq. 8 may be ignored so that

$$\frac{1}{P_{\text{obsd}}} = \frac{1}{P_{\text{eq}}} - \frac{B}{P_{\text{obsd}}R} \quad (9)$$

A plot of $1/P_{\text{obsd}}$ vs. $1/(P_{\text{obsd}}R)$ is a straight line whose slope is $-B$. The solid lines in Figure 1 show eq. 9 corresponding to Ag in molybdenum cells. The broken portions of the straight lines are where R is so large that even the requirement that R be only one-twentieth as large as the mean free path is not met; however, they must intercept at $1/P_{\text{eq}}$ and $1/R = 0$ where P_{eq} was obtained from McCabe and Birchenall.¹⁰ The experimental data of Boyer and Meadowcroft⁴ are represented by the appropriate points. The agreement is fair and the discrepancy may possibly be attributed to the errors in optical temperature measurements and possible leakage at the lid joint in the cell. The upper lines represent eq. 7 on the same coordinates and show that the slope is zero; *i.e.*, there is no surface diffusion.

It is evident that in the absence of any data on E , appropriate experiments may be carried out and the results may be plotted as shown in Figure 1 to obtain B

from which fair values of E can be computed. For this purpose, it is essential to use small enough orifices and low enough temperatures so that β may be measurably large.

The existence of surface diffusion is readily detected in a plot of $1/P_{\text{obsd}}$ vs. R^2 . It would show that $1/P_{\text{obsd}}$ always remains below $1/P_{\text{eq}}$, and the relationship is not linear.

The surface diffusion can be minimized or eliminated by using different cell materials if this is experimentally permissible. For a given cell, the best that can be done is to carry out the measurements at high enough temperatures so that the effusion contribution is greater than the diffusional contribution, or the slopes of the solid lines in Figure 1 are small and therefore the resulting corrections constitute a small fraction of the observed pressure. In the absence of experimental data on E , even two points with each cell material are adequate to compute B from which P_{eq} can be obtained and compared with similar sets of data for other cell materials in order to obtain consistent values of P_{eq} for a given vaporizing substance.

(10) C. L. McCabe and C. E. Birchenall, *Trans. AIME*, 197, 707 (1953); their data are in complete agreement with P. Grievson, G. W. Hooper, and C. B. Alcock in "Physical Chemistry of Process Metallurgy," G. R. St. Pierre, Ed., Interscience Publishers, Inc., New York, N. Y., 1961.

The Solubility of Hydrogen in Liquid Sodium¹

by D. W. McClure and G. D. Halsey, Jr.

Department of Chemistry, University of Washington, Seattle, Washington 98105 (Received May 5, 1965)

The solubility of gaseous hydrogen in molten sodium has been determined over the temperature range 260–350°, in the region where concentration varies as the square root of the pressure, up to the concentration where there is separation of a hydride phase. The heat of solution is small, -2 ± 2 kcal./mole of H₂. Similar results for deuterium are reported.

Introduction

In the region of low concentration, the solubility of a diatomic gas in a metal should vary as the square root of the pressure if the gas dissociates upon solution. The isotherms of all such gas-metal systems should display the general characteristic of a constant pressure three-phase region preceded by a two-phase region where concentration varies as $P^{1/2}$. Inasmuch as the constant pressure plateau usually extends over most of the composition range, it is not surprising that there are very few accurate data available for the $P^{1/2}$ region.

The simplest group of metals from a theoretical viewpoint is the alkali metals. Since these elements form ionic hydrides with reasonable dissociation pressures, it seemed logical to choose this class of systems for an experimental treatment. The system sodium-hydrogen was chosen because it exhibited the most convenient over-all characteristics, particularly with respect to dissociation pressures at low temperatures.

Existing experimental work²⁻⁵ on the sodium hydride system has covered extensively the concentration range between 10 and 90% NaH, and temperature to a maximum of 600°. This concentration interval corresponds to the region of constant pressure. It was decided to study the solubility of H₂ in sodium in the $P^{1/2}$ region of the isotherm, namely at low concentrations.

Experimental Section

The functional parts of the apparatus (Figure 1) include a cell, furnace, gas-transfer system, and a pressure measuring unit.

Manometer System. Manometer G in conjunction with the short leg was used for the actual pressure measurements in the system. The manometer was constructed of 30-mm. Pyrex tubing and mounted on a

240-lb. concrete block to reduce vibration. The light source consisted of a weak diffuse lamp and was capable of giving a sharp reproducible meniscus when viewed through the cathetometer.

The short leg F consisted of a 30-mm. Pyrex tube with a 12-mm. neck in which was fixed a small pointer. To facilitate precise short leg settings, a mercury injector H consisting of a pressure plate working on a length of 0.95-cm. vacuum tubing was constructed.

The cathetometer was a fixed-scale Gaertner, capable of being read to 0.005 cm. The over-all cathetometer error was taken to be ± 0.01 cm. All pressure measurements were corrected for temperature and the gravitational constant.

Gas-Transfer System. The technique of gas transfer involved the use of a gas buret, B, a constant temperature bath, and manometer A. The buret jacket was thermostated to $\pm 0.05^\circ$. Manometer A was constructed of 22-mm. Pyrex tubing and backlighted with two fluorescent tubes.

The pressure in the gas buret was measured with an accuracy of one part in 700 for hydrogen transfer and better than one part in 1000 for the dead space measurements.

Reagents. Assayed reagent grade helium and hydrogen were purchased from Air Reduction Sales Co. Only 1-l. bulbs which had no impurities on a mass spec-

(1) This research partially supported by the Air Force Office of Scientific Research, and based on a thesis submitted to the University of Washington in partial fulfillment of the requirements for the Ph.D. degree by D. W. McClure.

(2) M. D. Banus, J. J. McSharry, and E. A. Sullivan, *J. Am. Chem. Soc.*, **77**, 2007 (1955).

(3) A. Herold, *Compt. rend.*, **228**, 686 (1949).

(4) F. G. Keyes, *J. Am. Chem. Soc.*, **34**, 779 (1912).

(5) D. D. Williams, J. A. Grand, and R. R. Miller, *J. Phys. Chem.*, **61**, 379 (1957).

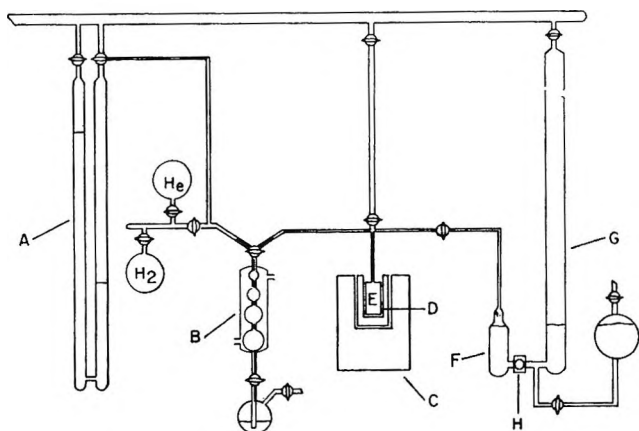


Figure 1. Apparatus for determination of solubility of H_2 in molten sodium: A and F, G, manometers; B, gas buret; C, D, E, furnace and cell assembly; H, mercury injector.

trometric level, as assayed by the company, were used in this work.

The reagent grade sodium was purchased from Baker and Adamson in 1-lb. blocks with a stated analysis of 99.996% purity. To exclude the possibility of dissolved gases, the liquid sodium was outgassed for a period of 12 hr. at the temperature of the run prior to the initial transfer of hydrogen. This outgassing period seemed entirely adequate. With the cell closed off to the vacuum system, there was no measurable change in pressure over a period of 6 hr.

The deuterium used was purchased from the General Dynamics Corp. with a stated analysis of 99.5% or better purity.

Temperature Measurements. Cell temperatures were measured with chromel-alumel thermocouples calibrated against a platinum-rhodium standard. The over-all accuracy was $\pm 1.0^\circ$.

Temperature measurements of the gas buret, manometers, and dead space were made using mercury-in-glass thermometers calibrated against a platinum resistance thermometer. The accuracy was taken to be $\pm 0.1^\circ$.

Furnace and Control. The furnace used was a 7-amp. Cooley CS-1 rated at 440 w. and modified to include a bottom heater.

In order to reduce small temperature fluctuations, a 1.25-cm. walled aluminum block was placed between the cell and the furnace elements. The temperature control unit consisted of a sensing element, phototubes, potentiometer, and a thyrotron relay circuit. The basic design of the phototube circuit was similar to that of Yanko, *et al.*,⁶ but modified for greater sensitivity. Throughout the entire course of a run the over-all con-

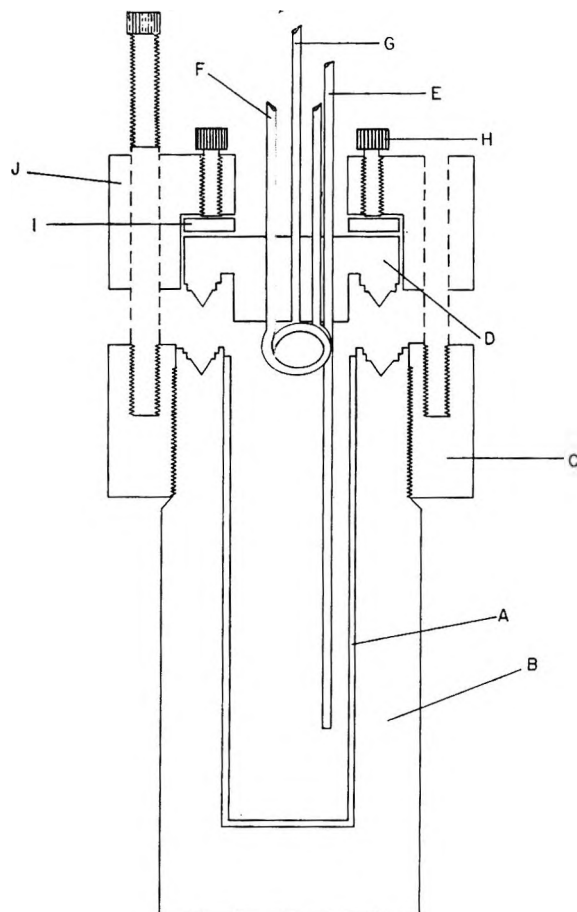


Figure 2. Cell for liquid sodium and hydrogen solutions: A, liner; B, cell; E, thermocouple tube; F, cooling tubes; G, entry tube; C, D, H, I, J, top assembly.

trol never allowed a deviation greater than $\pm 0.25^\circ$ from the set equilibrium temperature.

Cell. Construction of a cell (Figure 2) necessitated the use of materials having two characteristics: a high resistance to sodium corrosion and a low permeability to hydrogen. The liner, A, was made of molybdenum, which has a very low coefficient of permeability to hydrogen and is completely resistant to attack by sodium below 1000° . The cell body, B, was made from 2S purity aluminum. This grade aluminum has excellent retention characteristics to hydrogen and in fact shows the lowest permeability of any metal except zinc. The cell top D was constructed of Type 347 stainless steel. It was the principal site for hydrogen loss by permeation. The thermocouple tube E enabled one to measure directly the temperature of the liquid phase, as it was immersed to a depth of about 2.5 cm. in the liquid sodium.

(6) J. A. Yanko, A. E. Drake, and F. Hovorka, *Trans. Electrochem. Soc.*, **89**, 357 (1946).

The condenser coil F was necessary to stop diffusion of sodium vapor up the inlet tube during the outgassing period. Nitrogen gas at approximately 1 cm. pressure was circulated through the coil prior to the initial transfer of hydrogen and then shut off once the run actually commenced.

The gasket assembly is similar to that of other workers.⁷ The gasket was punched from pure 0.01-in. annealed silver sheet.

Dead Space Measurement. The total dead space of the system is divided into three quasi-isothermal regions: the external section which includes the short leg and all tubing available to the gas phase but external to the cell and stem, the stem itself, and the cell. All external tubing, including that leading to the cell is of 1-mm. i.d. The general procedure for dead space measurement involves the expansion of a known quantity of helium into the system and the measurement of the resulting pressure. The volume of the region of interest is then calculated from the gas law.

Corrections for the meniscus covolume were included in the external dead space. Inasmuch as it was impossible to determine a unique value for the coefficient of thermal expansion of the cell, it was necessary to measure the cell dead space as a function of temperature. It was found that the cell volume varied as a linear function of the temperature in the range between 25 and 400°. The over-all dead space error was 4 parts per 1000.

Cell Calibration. At temperatures exceeding 200° the permeation of hydrogen through the cell top became important. Consequently, it was necessary to calibrate the cell for this effect.

Randall and Salmon⁸ have measured the permeability of Type 347 stainless steel to hydrogen and tritium. The rate of permeation, R , in cm.³ (STP)/hr. for negligible back pressure is described by the relation

$$R = \frac{\gamma AP}{1 + \beta d \sqrt{P}} \quad (1)$$

and valid in the range $0 \leq P \leq 34$ cm., where γ and β are functions of temperature, P is the pressure in cm., A is the diffuser area in cm.², and d is the diffuser thickness in millimeters. The quantities α and γ were taken from ref. 8. In order that eq. 1 can be used, it is necessary to determine A and d , which depend on the exact geometry of the cell top. These constants were difficult to determine accurately from purely geometrical considerations, so instead an empirical equation of the form of eq. 1 was fitted to data obtained with the cell, empty of sodium, and filled with hydrogen at the temperatures of the actual sodium runs. With these factors, correc-

tions were made for the loss of hydrogen and deuterium by permeation. The permeation constants found for H₂ were also used for D₂ since no independent values for α and γ existed in the literature. This was considered justified since the solubility of D₂ in Type 347 stainless steel differs by only a few per cent from that of H₂,⁹ and also because the measured fall-off in pressure with time did not differ within experimental error from that of hydrogen.

Sodium-Transfer Technique. An approximately 5-g. sample of sodium was weighed and transferred under a blanket of purified and dried isopentane (IP). It was initially cleaned with a solution of 100% ethanol and acetone (20 to 1), washed in three baths of cooled IP and finally transferred into a tared vial of IP. The weight of the sodium is then found by difference. The sodium is finally transferred to the cell and the IP removed at -40° by pumping. The maximum error in weighing was approximately 1 part in 500.

Run Procedure. After the introduction of the sodium and removal of the isopentane, the cell, at room temperature, was outgassed to below 10⁻⁵ mm. Fifteen hours prior to the initial transfer of hydrogen, the furnace was turned on along with the N₂ for the condenser, and pumping was continued.

Then approximately 10⁻⁶ mole of hydrogen was introduced into the cell. The time of the transfer was noted with an accuracy of ±0.1 min. The pressure was then measured as a function of time, with equilibrium being established usually within 15 min. for the P^{1/2} region. Much longer equilibrium periods were noted for the constant-pressure region, in agreement with the similar observations by others.^{2,4}

To ensure equilibrium, the final pressure was taken 1 hr. after the initial transfer. The time along with meniscus height and all necessary temperatures were recorded. Additional aliquots of hydrogen were then added at 1-hr. intervals.

Data Reduction. The measured pressure is actually the sum of the hydrogen pressure and the vapor pressure of sodium at the cell temperature. Consequently, it is necessary to correct the measured pressure for P_{Na}. The vapor pressure of sodium was taken from the work of Ditchburn and Gilmour,¹⁰ with an estimated accuracy of 5%. The total amount of hydrogen or deuterium introduced was corrected for permeation. Then the quantities present in the various dead-space

(7) Von H. Hintenberger, *Z. Naturforsch.*, **6a**, 459 (1951).

(8) D. K. Randall and O. N. Salmon, KAPL Report No. 904 (1953).

(9) N. J. Hawkins, USAEC-KAPL Report No. 868 (1953).

(10) R. W. Ditchburn and J. C. Gilmour, *Rev. Mod. Phys.*, **13**, 310 (1941).

volumes of the apparatus were calculated, with corrections for gas imperfection, and since the cell dead space varied as a function of the sodium volume, it was necessary to correct the density of sodium as a function of temperature. The density of sodium was taken from Sittig¹¹ with an estimated accuracy of ± 0.0020 g./cm.³. The second virial coefficients for H₂ were taken from the work of Michels, *et al.*¹²

Results

The corrected experimental data were fitted by least squaring to a parabolic equation of the form

$$P = Ax^2 + B \quad (2)$$

where x is the molar ratio of H₂ to sodium. It was found that the zero intercept varied from 0.005 to 0.07 cm., depending on the temperature of the run.

Although the exact value for the zero intercept is difficult to calculate, the magnitude of this quantity is easily explained qualitatively on the basis of thermal transpiration, complicated by diffusion pumping by sodium vapor. If the effect of the sodium vapor pumping is neglected, an approximate thermal transpiration correction can be made.¹³ The result is of the order of 0.01 cm. In addition, an experimental demonstration of the effect, using an inert gas, was thought desirable. A sample of 2.5 g. of sodium was transferred to the cell in the usual way, and a measured quantity of helium sufficient to give a helium pressure in the cell of approximately 0.05 cm. was introduced. The discrepancy between the gas law pressure and the pressure observed was 0.034 ± 0.020 cm. at 300°.

It is felt that this result is in harmony with the experimental values of the intercept B . Therefore, the parabolic equation (2) was adjusted to zero intercept.

On the basis of eq. 2 we obtain the results in Table I. The hydrogen results at 263° are too fragmentary to allow evaluation of the constants.

Table I: Experimental Results^a

Hydrogen		Deuterium	
$A \times 10^{-8}$	$T, ^\circ\text{C.}$	$A \times 10^{-8}$	$T, ^\circ\text{C.}$
0.146	301.1	0.177	300.1
0.168	350.2	0.208	351.1

^a P is in cm. and x is in moles (H₂, D₂) per mole of Na.

The pressures, adjusted to zero intercept, are plotted against the mole ratio of H₂ or D₂ in Figures 3 and 4. The 263° isotherm for hydrogen was calculated on the basis of the heat of solution given below, and is in reasonable accord with the experimental points.

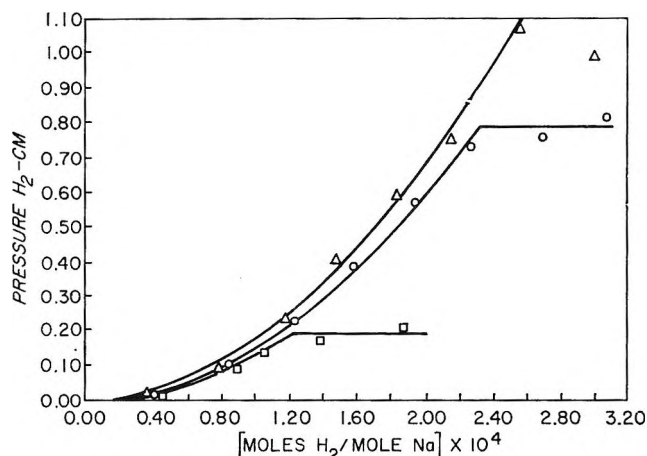


Figure 3. Pressure of H₂ adjusted to zero intercept, above sodium as a function of molar ratio H₂/Na: Δ , 350.2°; \circ , 301.1°; \square , 263.1°.

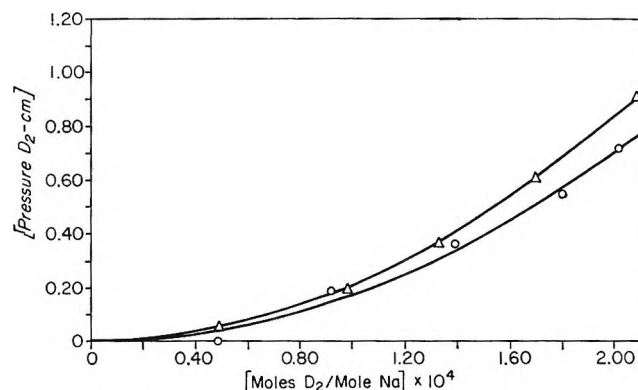


Figure 4. Pressure of D₂ adjusted to zero intercept, above sodium as a function of molar ratio D₂/Na: \circ , 300.1°; Δ , 351.1°.

The deuterium runs differed little from those of hydrogen except that equilibrium times were found to be approximately twice as long, and the pressures higher by approximately a factor of 1.2.

The heats of solution, calculated from the constants in Table I by use of the Clausius-Clapeyron equation, are

$$\Delta H = -2.0 \text{ kcal./mole of H}_2$$

and

$$\Delta H = -2.3 \text{ kcal./mole of D}_2$$

(11) M. Sittig, "Sodium, Its Manufacture, Properties and Uses," Reinhold Publishing Corp., New York, N. Y., 1956.

(12) A. Michels, W. DeGraaf, T. Wassenaar, J. H. M. Levelt, and P. Louwerse, *Physica*, 25, 25 (1959).

(13) S. Dushman, "Scientific Foundations of Vacuum Technique," John Wiley and Sons, Inc., New York, N. Y., 1962.

The experimental errors are estimated to total ± 2 kcal. These results for the isotope effect are in qualitative agreement with the results of Sollers and Crenshaw,¹⁴ who found that the dissociation pressure of NaD was approximately twice that of NaH in the constant pressure plateau region.

The shape of the curves presented here, which show a positive curvature, is in marked disagreement with the recent publication of Addison, Pulham, and Roy.¹⁵ Their curves, which cover approximately the same regions of temperature and concentration, bend over with a negative curvature, and do not appear to enter the region of ideal behavior for solution accompanied by dissociation. Curves of this shape indicate that either (a) the solution becomes progressively less ideal as the concentration is lowered, or (b) the dissolved species of hydrogen is polyatomic. Neither of these alternatives seems possible. Further work, especially at lower concentrations, is indicated to resolve the difficulty.

Behavior in the Constant Pressure Plateau. Most of the other data on the sodium-hydrogen system relate to the constant pressure region; our results are compared with others in Figure 5. Our plateau at 263° is in good agreement with the other data. At 300° our results are a little out of line with the work of Herold, but compare quite well with Addison, *et al.* Their result for the pressure of hydrogen in the plateau region at 300° (~ 0.9 cm.) is in good agreement with the present result at 301° (~ 0.8 cm.). The corresponding solubility limit is 2.5×10^{-4} compared with 2.2×10^{-4} in the present work. Finally, the last point in our 350° isotherm falls hopelessly far from the line formed by the other points, and clearly does not correspond to phase separation.

Solubility Limits for Sodium Hydride in Liquid Sodium. Our solubility limit at 300° is in reasonable agreement with the result of Addison, *et al.*, as we have pointed out above. However, if we are right in ascribing a parabolic shape to the curve of pressure *vs.* mole fraction, our results point to a possible revision in the temperature coefficient for this solubility. The pressure of H₂ in the plateau region is given by an expression of the form

$$\ln P = -\Delta H_1/RT + \text{constant} \quad (3)$$

The results of Herold³ can be fitted to an expression

$$\log P = -6100/T + \text{constant} \quad (4)$$

which corresponds to a value of ΔH_1 of about 28 kcal.

Similarly, in the parabolic range where mole fraction x depends on $P^{1/2}$, we can write for the pressure of H₂

$$P = C_2 x^2 e^{-\Delta H_2/RT} \quad (5)$$

or

$$\ln P = 2 \ln x - H_2/RT + \text{constant} \quad (6)$$

Our results for the heat of solution of H₂ (-2 kcal.) indicate that the heat of vaporization of H₂ from the solution should be $\Delta H_2 = 2$ kcal.

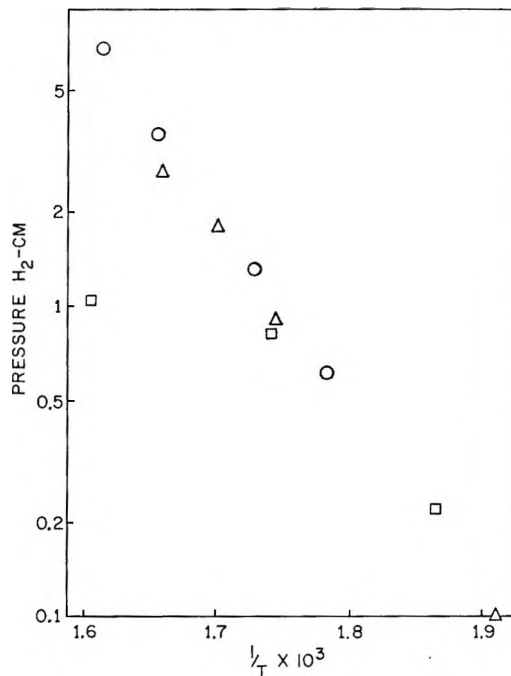


Figure 5. Pressure of H₂ over sodium in the plateau region, plotted against the reciprocal of the absolute temperature. The isolated point at 350° is apparently in the $P^{1/2}$ region: O, Herold; Δ, Addison, *et al.*; □, this work.

The solubility limit occurs when the plateau pressure equals the pressure in the parabolic region, so if we equate eq. 3 and 5, we find

$$2 \ln x = (\Delta H_2 - \Delta H_1)/RT + \text{constant} \quad (7)$$

If we insert the values of the heats, this result may be written in the form

$$\log x = -2800/T + \text{constant} \quad (8)$$

The constant can be evaluated from the solubility at any one temperature, in the units desired. However, the temperature coefficient (2800) compares poorly with the result of Addison, *et al.*, and the results of Wil-

(14) E. F. Sollers and J. L. Crenshaw, *J. Am. Chem. Soc.*, **59**, 2724 (1937).

(15) C. C. Addison, R. J. Pulham, and R. J. Roy, *J. Chem. Soc.*, 116 (1965).

liams, Grand, and Miller,¹⁶ which are reasonably self-consistent with a value of 5000 or above. On the other hand, our results appear to be consistent with the unpublished results of Thorley.¹⁶

Our calculation is of course based on the validity of eq. 5 all the way up to the solubility limit which implies ideal behavior of a monatomic hydrogen species. All of the data (Addison, *et al.*, Williams, *et al.*, and Thorley, as well as ours) are in good agreement near 300°, so if we use Addison's solubility at 300° to evaluate the constant in eq. 8, we can arrive at a definite result for the solubility

$$\log (\text{wt. } \% \text{ hydrogen}) = 2.20 - 2800/T \quad (9)$$

to compare with Addison, *et al.*

$$\log (\text{wt. } \% \text{ hydrogen}) = 6.211 - 5021/T$$

There is clearly a large discrepancy, and it is difficult to see how the coefficient could be more than half the 6100 of eq. 3, unless the solubility of hydrogen in liquid sodium was endothermic. Only further experiments can resolve the difficulty.

(16) Quoted in ref. 15.

Radiolysis of Liquid Nitrogen Tetroxide¹

by Thomas C. Castorina and Augustine O. Allen

Explosives Laboratory, Feltman Research Laboratories, Picatinny Arsenal, Dover, New Jersey 07801, and Chemistry Department, Brookhaven National Laboratory, Upton, New York 11973 (Received May 6, 1965)

Liquid N_2O_4 decomposes under γ -rays with a very small yield to N_2 , N_2O , and N_2O_5 . The N_2O_5 is stabilized against thermal decomposition by the γ -rays, which cause the products O_2 and N_2O_4 to re-form N_2O_5 in N_2O_4 solution. Detailed data are given on the kinetics of product formation and on the effects of added O_2 and NO on the course of the reactions.

The radiolytic decomposition of nitrogen dioxide gas, $\text{NO}_2 \rightleftharpoons \text{N}_2\text{O}_4$, has been studied,^{2,3} but no reports are known to us regarding the radiolysis of liquid N_2O_4 . We were informed, however, by Professor Paul Harteck that he and his co-workers had exposed the liquid to radiation in a nuclear reactor and observed no decomposition. Stability of liquid N_2O_4 (which is only 0.1% dissociated to NO_2)⁴ seemed reasonable, since breaking the N-N bond would give nothing new, while breaking the N-O bond would lead merely to N_2O_3 plus oxygen, or their chemical equivalents, which would spontaneously back-react to regenerate N_2O_4 . The liquid is a good solvent, and interesting synthetic reactions might be expected on irradiation of its solutions. We chose to study first the radiolysis of the pure liquid, and found that some decomposition does occur, though with a small yield. The γ -ray-induced

reaction has some interesting features and is the subject of this paper.

Experimental Section

Tank N_2O_4 (99% pure, Matheson Co.) was liquefied in approximately 40-cc. aliquots and sparged with oxygen purified by passage over hot CuO and through a Dry Ice trap. The N_2O_4 was distilled twice through cleaned, phosphorus pentoxide saturated glass wool and degassed two times at -78° . It was then transferred to a part of the vacuum line protected from grease by glass bead traps, and was degassed a third time at

(1) Supported in part by the U. S. Atomic Energy Commission.

(2) P. Harteck and S. Dondes, *J. Chem. Phys.*, **27**, 546 (1957).

(3) M. T. Dimitriev and L. V. Saradzhev, *Russ. J. Phys. Chem.*, **35**, 354 (1961).

(4) P. Gray and P. Rathbone, *J. Chem. Soc.*, 3550 (1958).

-78° . Only the center cut was distilled into 5-cc. Pyrex break-seals for irradiation studies. Kel-F grease (chlorotrifluoropolyethylene) which was found to be inert to NO_2 was used on all standard joints and stop-cocks. Tank nitric oxide (NO) (Matheson) was similarly purified by distillation, and was shown by mass spectrometric analysis to contain $<0.03\%$ N_2O .

For runs with added gas, tubes were prepared with two break-seals enclosing a calibrated volume of 1.5-2 cc. Gas was introduced at a known pressure into the volume by a capillary side arm, which was then sealed off. Purified N_2O_4 was then distilled into the adjacent compartment and sealed off. Smashing the break-seal then allowed gas and liquid to mix. After irradiation, the ampoule was reconnected to the vacuum line, and the second break-seal was opened, allowing gas to be withdrawn for analysis.

The cobalt-60 γ -ray sources were calibrated with the standard Fricke dosimeter and the doses are given in this paper as rads in the dosimeter solution. Values of G for N_2O_4 were calculated on the assumption that the actual energy input was proportional to the electron density of the material. The ratio of the electron density per gram of N_2O_4 to that of the dosimeter solution ($0.4 M \text{H}_2\text{SO}_4$ in H_2O) is 0.926.

After irradiation, the N_2O_4 was degassed at -196° . The gas was measured in a McLeod gauge and aliquots were analyzed either by mass spectrometry or by combustion with added hydrogen. The two methods differed by less than 1%, on the average. This gas consisted of nitrogen and oxygen only. A second degassing at -130° (2-chlorobutane mush) yielded pure nitrous oxide, as shown by mass spectrometry and gas chromatography.

Results⁵

Early runs showed the nitrogen yield to be reproducible, but the oxygen yield was variable. It soon appeared that almost all the oxygen was formed in a postirradiation reaction, which required more than 2 days for completion. Series of runs were then made in which ampoules, all given the same radiation dose, were placed in a constant-temperature bath, and opened for oxygen analysis after various periods of time. In Figure 1, the fraction of O_2 not yet evolved is plotted on a logarithmic scale against time; the resulting straight lines show the O_2 to result from first-order decomposition of a precursor. The rate constants ($\text{sec.}^{-1} \times 10^5$) were 1.03 at 20° , 1.4 at 22° , and 2.4 at 25° . An obvious candidate for the precursor is N_2O_6 , the only known higher oxide of nitrogen. The decomposition of N_2O_6 in N_2O_4 solution was reported by Eyring and Daniels⁶ to be first order with a rate con-

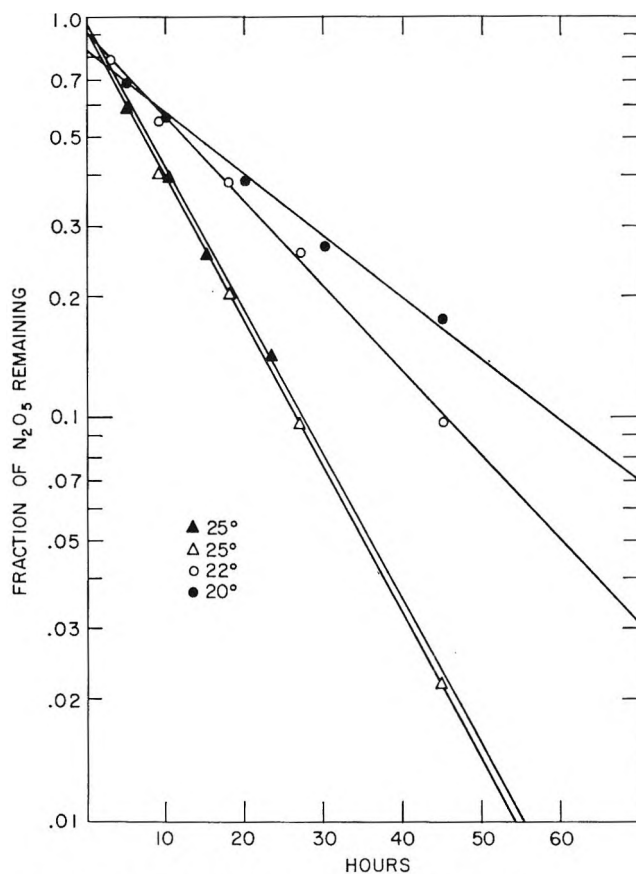


Figure 1. Decomposition of radiolytically formed N_2O_6 .

stant of 3.44×10^{-5} at 20° , or about three times the above value. However, their N_2O_6 concentration, $0.2 M$, was over 15 times the concentration in the radiolysis experiments, and Eyring's experiments in other solvents did show a small concentration effect on the rate constant. We therefore prepared dilute solutions of N_2O_6 in N_2O_4 by passing ozonized oxygen briefly through the liquid. The resulting solution was thoroughly degassed at -78° , and aliquots were poured into ampoules which were sealed off, placed in a constant-temperature bath, and removed from time to time for oxygen analysis. Solutions, ranging in concentration from 2 to 7 mM N_2O_6 , gave rate constants ($\text{sec.}^{-1} \times 10^5$) of 1.2 at 20° and 3.5 at 25° . These numbers are so close to those found for the radiolytic solutions that there can be little doubt that the radiolysis product is N_2O_6 . The differences in observed rate, which are somewhat outside the apparent experimental errors, probably show that the decompo-

(5) Some of the results are given in greater detail in Picatinny Arsenal Technical Report 3072, by T. C. Castorina (May 1963); a copy may be obtained from Armed Services Technical Information Agency, Arlington Hall Station, Arlington 12, Va.

(6) H. Eyring and F. Daniels, *J. Am. Chem. Soc.*, 52, 1472 (1930).

sition rate is more sensitive than might be expected to the presence of small amounts of foreign substances.

A great many runs were made in which the product yields were determined as a function of dose. In many runs, the samples were kept for 7 days after analysis to ensure complete decomposition of N_2O_5 . Typical results are shown in Figure 2, where the upper curve represents the yield of oxygen after complete decomposition of N_2O_5 , while the lowest curve shows the amount of oxygen present immediately after irradiation. The decomposition of N_2O_5 is markedly inhibited by γ -rays; thus after 100 hr. of radiolysis at 20° only 8% of the N_2O_5 present has decomposed to oxygen, whereas in this time in the absence of radiation, decomposition would have been practically complete.

Induction periods are seen to exist for nitrogen and N_2O_5 , but not for N_2O . To see whether these depended on time as well as radiation, the dose rate was changed by a factor of nearly 30. The quantities of product are seen in Figure 3 to depend only on the total dose, not on the dose rate. The behavior of the yields at low doses was carefully studied at the lower dose rate (Figure 4).

Other data, not given here in detail, showed that the yield of N_2 was unaffected by temperature of radiolysis (0 – 30°) and by the ratio of vapor volume to liquid volume in the irradiation ampoule (varied from 0.004 to 2.3), and that all yields were unaffected by following the oxygen sparge during the purification of N_2O_4 with a nitrogen sparge, and by irradiating with added argon gas.

Above 14 Mrads, the products increase linearly with dose. Least-squares treatment of the available data gave the results shown in Table I. The number of data points used was 33 for N_2O , 49 for N_2 , and 35 for total O_2 .

Table I: Least-Squares Treatment of Yields at High Doses^a

Product	a		b		G
	Value	Std. error	Value	Std. error	
N_2O	5.22	0.11	-4.9	3.5	0.022
N_2	11.90	0.22	-74.3	7.6	0.051
Total O_2	29.5	0.7	-133.6	23.6	0.127

^a $y = aD + b$, where $y = 10^4 \times$ cc. of product/g. of N_2O_4 , $D =$ dosimeter Mrad, $G =$ steady-state yield (molecules/100 e.v.) = 0.00431a.

The stability of N_2O_5 under γ -rays may be assumed to arise from a radiation-induced back-reaction of O_2 with the solvent to regenerate the N_2O_5 . The appear-

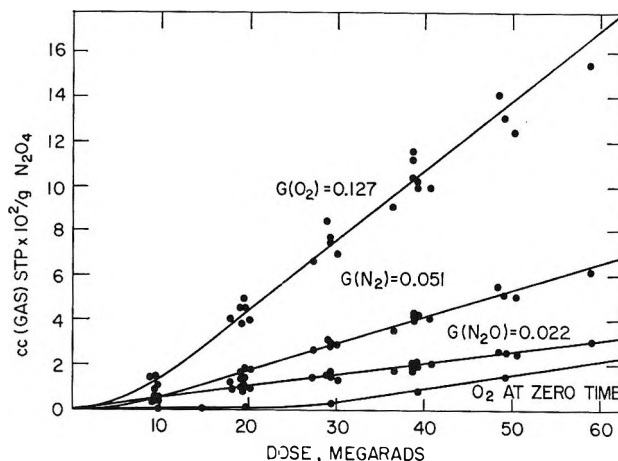


Figure 2. Product yields in radiolysis of liquid N_2O_4 at 20° : dose rate 0.41 Mrad/hr. in the dosimeter.

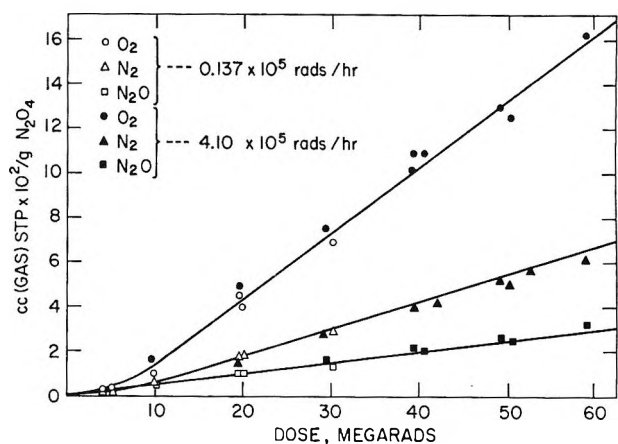


Figure 3. Radiolysis of liquid N_2O_4 at different dose rates.

ance of increasing amounts of oxygen at zero time after irradiation should then result from inability of the rate of O_2 consumption to keep pace with the increasing rate of decomposition, as N_2O_5 accumulates in solution. On this basis, the 100-e.v. yield of oxygen consumption $G(-O_2)$ may be calculated from Figure 2. At 50 Mrads, oxygen (bottom curve) is building up at a rate of 0.065×10^{-2} cc./g. Mrad \times 0.41 Mrad/hr. = 0.0267×10^{-2} cc./g. hr., while N_2O_5 is building up at a rate, given by the difference between the top and bottom curves, of 0.096×10^{-2} cc. of O_2 equiv./g. hr. The concentration of N_2O_5 is 12.0×10^{-2} cc. of O_2 equiv./g., and it is decomposing (assuming a rate constant of 1.0×10^{-5} sec.⁻¹) at a rate of 0.432×10^{-2} cc. of O_2 equiv./g. hr. The total rate of formation of N_2O_5 is the sum, 0.528×10^{-2} cc. of O_2 equiv./g. hr., or 1.29×10^{-2} cc./g. Mrad, corresponding to $G(-O_2) = 0.56$.

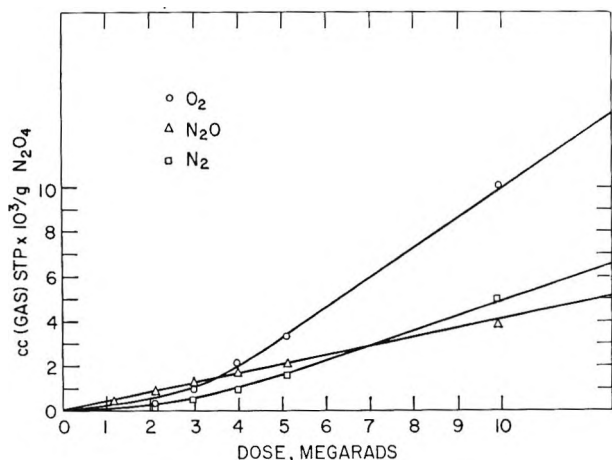


Figure 4. Product yields in radiolysis of liquid N_2O_4 at low doses: dose rate 0.0137 Mrad/hr.

To verify the above assumption, we irradiated N_2O_4 with known quantities of oxygen gas added. Immediately after irradiation, the liquids were degassed and the gases were analyzed. The samples were resealed and kept for 7 days to allow the N_2O_5 to decompose completely, then they were opened and the evolved oxygen was determined. The top curve in Figure 5 shows the oxygen formed from N_2O_5 , while the lower curves show the N_2 and N_2O found in the first analysis. The loss in oxygen during the irradiation agreed well with that expected from a material balance. The data show that the N_2O_5 builds up rapidly at first (showing that it is formed from the added O_2), then more slowly as thermal decomposition sets in.

At about 27 Mrads, N_2O_5 is seen to be still building up at a rate of 0.0325×10^{-2} cc. of O_2 equiv./g. hr., while at its concentration of 0.125 cc. of O_2 /g. it must be decomposing thermally at a rate of 0.45×10^{-2} cc. of O_2 /g. hr. The total formation rate of N_2O_5 is the sum, 0.4825×10^{-2} cc. of O_2 /g. hr., or 1.26×10^{-2} cc. of O_2 /g. Mrad, corresponding to $G(-O_2) = 0.54$, in good agreement with the previous estimate.

The data show that the formation of N_2O is unaffected by the presence of oxygen, but the induction period for N_2 formation is eliminated. The rate of N_2 formation is however reduced a little (to $G = 0.046$) by added oxygen, so the total N_2 found after 40 Mrads is about the same.

Experiments were also done with added nitric oxide, NO , to see if the role of this gas in the reaction could be evaluated. Yields of N_2 and N_2O are shown in Figure 6; they are identical with those found in the presence of oxygen. The amounts of NO present were around 0.25–0.4 cc./g. of N_2O_4 , which with respect to oxygen balance is equivalent to the amounts of N_2 and N_2O

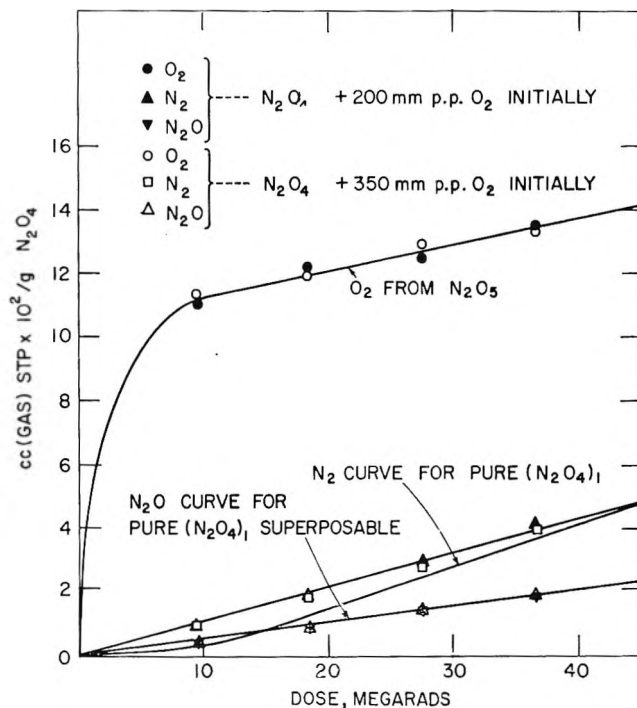


Figure 5. Effect of added oxygen on product formation in radiolysis of liquid N_2O_4 at 20° : dose rate 0.382 Mrad/hr.

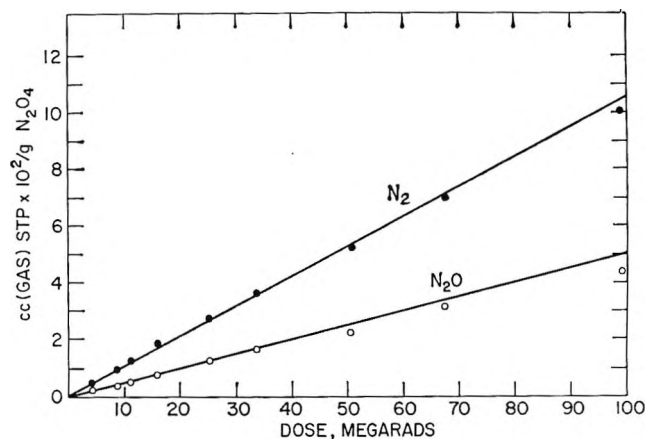


Figure 6. Formation of radiolysis products from liquid N_2O_4 with added nitric oxide.

found at doses of 50–60 Mrads. No N_2O_5 or oxygen was found at these doses or below, but at higher doses N_2O_5 (identified by its rate of thermal decomposition) was found in just those quantities expected from a material balance. The slope of the curves in Figure 6 does not change abruptly as the NO is consumed, and the only effect of the NO is, like added O_2 , to remove the induction period and slightly decrease the rate of N_2 formation.

Discussion

The amusing feature of these results is the stabilization of N_2O_5 (in N_2O_4 solution) by γ -rays. Ordinarily, we put stable materials in the radiation field, and they decompose; take them out, and the reaction stops. Now we find the reverse; N_2O_5 decomposes, but when put into the radiation field the reaction stops. This is actually an example of a familiar fact, that radiation shifts the point of equilibrium in chemical reactions and may render reversible many reactions which are ordinarily irreversible. Ordinary thermal equilibrium depends upon a balance between forward and back reaction rates; radiation must in general speed up both rates to different degrees, thereby shifting the equilibrium point.

As expected, liquid N_2O_4 is less unstable to radiation than most solvents. The small amount of decomposition which does occur proceeds in part by a complicated mechanism, as shown by the induction period for N_2 and N_2O_5 formation. Such a delay presumably results from the buildup of an intermediate which decomposes to N_2 . The amount of this decomposition depends only on total dose, not on time, so the decomposition is radiation induced and the intermediate is thermally stable at 20° for many hours, at least at the dilutions encountered here (order of $5 \times 10^{-4} M$). The ratio of the number of O and N atoms in the intermediate should be given by the ratio of the intercepts b in Table I, since these represent the amounts of O_2 and N_2 tied up in the intermediate at the steady-state condition when it is decomposing as fast as it is formed. This ratio is 1.80 ± 0.36 , suggesting that the intermediate might have the formula N_2O_3 . Addition of NO (which, in N_2O_4 solution, is in equilibrium with N_2O_3) did not increase the yield of N_2 but slightly decreased it. We conclude that the precursor of nitrogen

in this reaction must be a hitherto unknown oxide of nitrogen, perhaps an isomer of N_2O_4 or of N_2O_3 , which has escaped characterization in the literature probably because it is stable only at high dilution. Its decomposition appears to be catalyzed by the presence of either NO or O_2 .

The formation of N_2O by contrast is kinetically simple and its yield is unaffected by anything we tried. It may result directly by the loss of three O atoms from an excited state of N_2O_4 .

The consumption of oxygen to form N_2O_5 occurs with a somewhat higher yield than the decomposition reactions. We suggest that an excited N_2O_4 , which in the absence of O_2 decays without producing net chemical changes, reacts with O_2 in solution to form N_2O_5 , either directly by $N_2O_4^* + O_2 = N_2O_5 + O$, $O + N_2O_4 = N_2O_5$, or *via* NO_3 by $N_2O_4^* + O_2 = N_2O_5$, $N_2O_5 = 2NO_3$, and $2NO_3 + 2NO_2 = 2N_2O_5$.

Material balance should provide for the steady-state rates, or a values of Table I, that $a(O_2) = 2a(N_2) + 3/2a(N_2O)$. Experimentally, however, we find 29.5 ± 0.7 for the left-hand side and 31.63 ± 0.24 for the right-hand side of this equation. The discrepancy is outside of statistical error. The oxygen deficiency could result from systematic error, such as failure to extract all the oxygen from the liquid samples. We think this unlikely, since the N_2O , extracted after the O_2 and at a higher temperature, appeared pure and free of oxygen. It is possible that very small amounts of a higher oxide of nitrogen (other than N_2O_5) may also be formed in this reaction.

Acknowledgments. Initial encouragement to undertake this work was offered by Dr. Everett Johnson and the Department of Chemistry of Stevens Institute of Technology. Assistance in part of the experimental work was provided by Mr. Andrew Smetana.

Nuclear Magnetic Resonance Spectra of Phenyl- and Diphenylacetylene

by S. Castellano and J. Lorenc

Mellon Institute, Pittsburgh, Pennsylvania (Received May 10, 1965)

The high resolution proton spectra of phenyl- and diphenylacetylene at different concentrations in CCl_4 have been recorded and completely analyzed in terms of the fundamental n.m.r. parameters. A simple model is proposed which accounts semiquantitatively for the variations of the chemical shifts of the protons of phenylacetylene upon dilution in isotropic solvents. The value $\Delta\chi = -11.8 \times 10^{-6} \text{ cm}^3/\text{mole}$ has been calculated from the experimental data for the magnetic anisotropy of the acetylenic triple bond. Long-range couplings across five, six, and seven bonds have been observed and measured in the spectrum of phenylacetylene. Arguments are presented which suggest the noncoplanarity of the aromatic rings in diphenylacetylene in solution.

Introduction

The study of phenylacetylene by means of n.m.r. spectroscopy has formed the subject of several papers in the recent literature.¹⁻¹⁰ Many of these papers have been mainly concerned with the study of the effects of intermolecular interactions¹⁻³ and solvent anisotropy⁴⁻⁷ on the chemical shifts of the acetylenic proton. A systematic study of the effects of *ortho* and *para* substitution of the aromatic ring on the chemical shifts of the ethynyl proton has been reported by Cook and Danyluk.⁸ Data on the C^{13} chemical shifts of the acetylenic carbons have been published by Friedel and Retcofsky⁹ and by Frei and Bernstein.¹⁰

Notwithstanding the large number of publications related to the subject, the study of the proton spectrum of phenylacetylene has been limited only to the measurements of the chemical shift of the acetylenic proton, and no effort has been made to perform a complete analysis of the whole spectrum. It appeared likely that a detailed knowledge of the chemical shifts of the aromatic protons as well as the magnitude of the coupling constants could be useful in studies of intermolecular interactions in the neat as well as in aromatic and isotropic solvents, of the magnetic anisotropy of the acetylenic triple bond, and of the conjugative effects between the ethynyl group and the aromatic ring. On the latter two topics, further information might also be gained from a study of the related molecule, diphenylacetylene (tolane). Accordingly, we have performed a complete analysis of the proton n.m.r.

spectra of both phenylacetylene and tolane; the experimental results obtained in this study and their discussion form the subject of the present paper.

Experimental Section

Materials. The samples of phenyl- and diphenylacetylene were of commercial origin, the former from Eastman Organic Chemicals and the latter from the Orgmet Co. Purification of the samples was achieved through distillation in the case of phenylacetylene and sublimation in the case of tolane; for both samples the absence of extraneous peaks in the n.m.r. spectra was taken as a sufficient criterion of purity.

Sample Preparation and N.m.r. Spectra. Neat samples as well as solutions in CCl_4 or other solvents were degassed and sealed into 5-mm. Pyrex tubes to-

- (1) L. W. Reeves and W. G. Schneider, *Can. J. Chem.*, **35**, 251 (1957).
- (2) J. A. Pople, W. G. Schneider, and H. J. Bernstein, "High Resolution Nuclear Magnetic Resonance," McGraw-Hill Book Co., Inc., New York, N. Y., 1959, pp. 245-247.
- (3) N. Nagakawa and S. Fujiwara, *Bull. Chem. Soc. Japan*, **33**, 1634 (1960).
- (4) J. V. Hatton and R. E. Richards, *Trans. Faraday Soc.*, **56**, 315 (1960).
- (5) J. V. Hatton and R. E. Richards, *ibid.*, **57**, 28 (1961).
- (6) B. Braillon, *Compt. rend.*, **251**, 1625 (1960).
- (7) M. M. Kreevoy, H. B. Charman, and D. R. Vinard, *J. Am. Chem. Soc.*, **83**, 1978 (1961).
- (8) C. D. Cook and S. S. Danyluk, *Tetrahedron*, **19**, 177 (1963).
- (9) R. A. Friedel and H. L. Retcofsky, *J. Am. Chem. Soc.*, **85**, 1300 (1963).
- (10) K. Frei and H. J. Bernstein, *J. Chem. Phys.*, **38**, 1216 (1963).

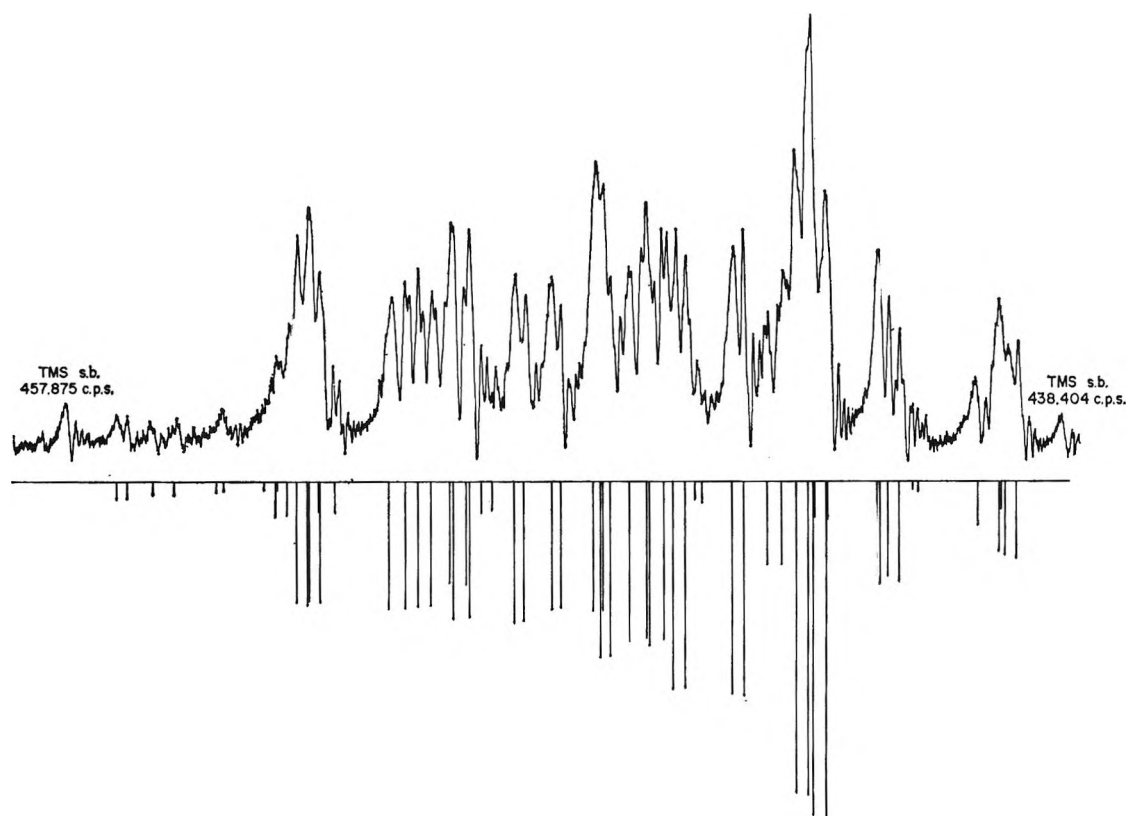


Figure 1. Experimental and calculated spectrum of phenylacetylene (*ortho* protons).

gether with 0.5–1.0% tetramethylsilane (TMS) as an internal reference. Proton spectra were obtained on the Varian A-60 spectrometer modified so that full-scale spectra with a sweep width of 25 c.p.s. could be recorded in the case of phenylacetylene; in the case of toluene full-scale spectra recorded with a sweep width of 50 c.p.s. showed well enough resolved patterns to be directly analyzed without further expansion of the scale. Calibration of the spectra was by means of the audio side-band technique. Peak positions were the average of at least six measurements, three made with increasing and three with decreasing field.

In the case of phenylacetylene, after the spectra were recorded and analyzed, the sample tubes were opened, a trace of benzene was added to the samples, and acetone-filled capillaries were introduced in the tubes; measurements of the shifts of TMS from the acetone peak furnished in this way a calibration of the spectra against an external standard. The position of the benzene peak was also measured. All spectra were recorded at 36°.

Spectral Analysis. The analysis of the spectra was performed with the aid of the Laocoon II program using a 7090 IBM computer. The main features of this program have been already reported¹¹; it is here

worthwhile to note only that it proceeds automatically by single Newton iterations from a trial spectrum, resembling the experimental one, to the best least-squares fit of the latter.

The spectrum of phenylacetylene, as a neat sample, was analyzed first. The analysis proved to be quite laborious since the long-range coupling of the acetylenic proton with all the aromatic protons complicated remarkably the pattern of the whole spectrum, and a very careful expansion of the scale was necessary in order to detect several closely spaced lines in the aromatic region. The ethynyl peak also exhibited multiplet structure but could not be resolved sufficiently to separate all the lines (theoretically 32 lines fall together in a frequency range of about 0.8 c.p.s.). Therefore, only the position of the central peak was furnished to the program as a reference for the chemical shift of the ethynyl proton. Nevertheless, the final fit showed in Figures 1 and 2 was obtained. The largest error of 0.107 c.p.s., in the fitting of the experimental data, occurred for a weak line of an unresolved

(11) S. Castellano and A. A. Bothner-By, *J. Chem. Phys.*, **41**, 3863 (1964).

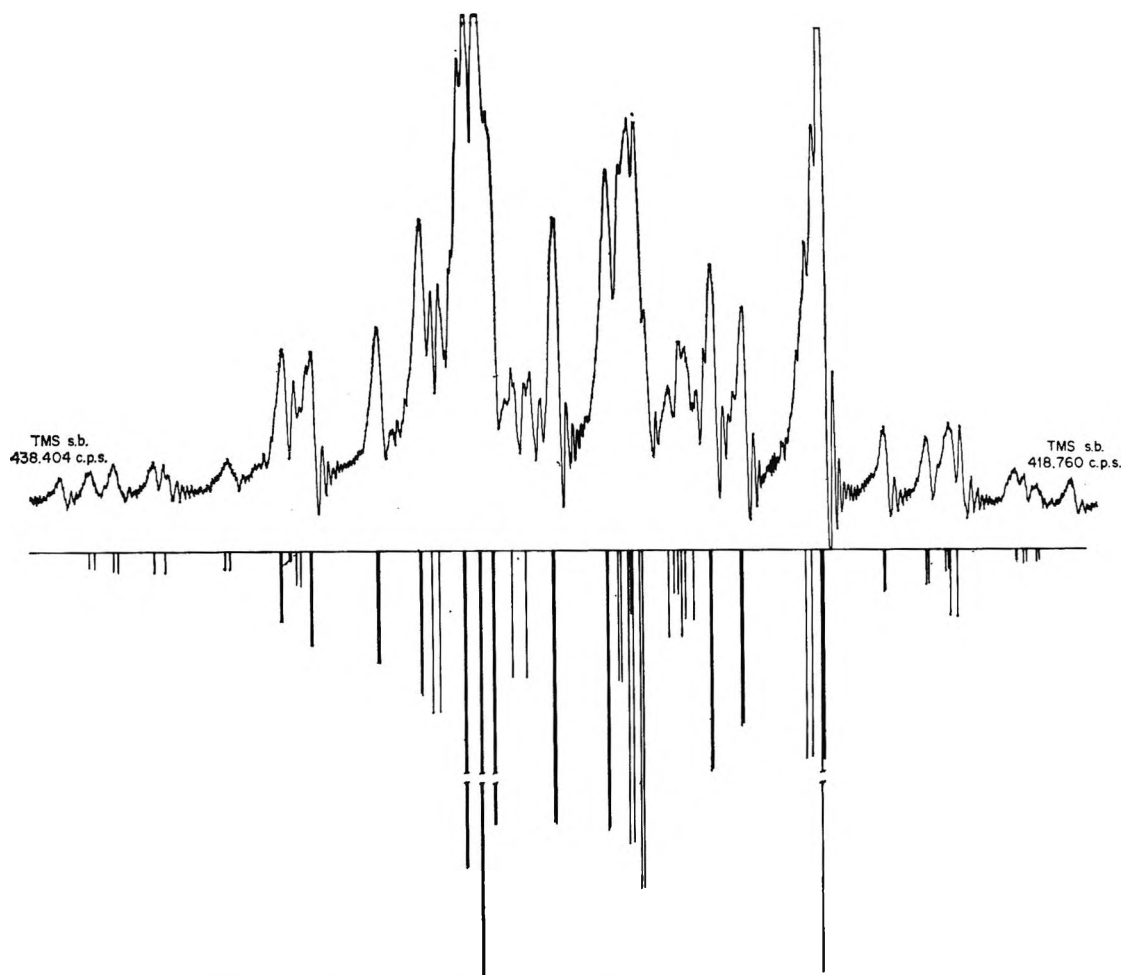
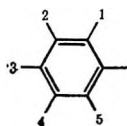


Figure 2. Experimental and calculated spectrum of phenylacetylene (*meta* and *para* protons).

doublet, and the root-mean-square error of 115 assigned lines was 0.043 c.p.s.

Upon dilution in CCl_4 (0.134 mole fraction), the pattern of the spectrum of phenylacetylene shows pronounced changes due to the variation of the relative chemical shifts of all the protons. The spectrum of this solution was analyzed following the same procedure as before. The largest error in a single line was 0.099 c.p.s., and the r.m.s. error over 124 matched lines was 0.039 c.p.s.

The parameters obtained in the analyses of the two spectra are summarized in Table I where the labeling of the protons of the phenyl ring is



The label 6 has been reserved for the ethynyl proton.

The analysis of the spectra of diphenylacetylene (0.134 and 0.065 mole fraction in CCl_4) did not offer

any particular difficulty and was carried out by the use of Laocoon II. No error larger than 0.100 c.p.s. was found in each case, and the r.m.s. errors were 0.054 c.p.s. for 49 matched lines in the first spectrum and 0.043 c.p.s. for 53 matched lines in the second. The results of these analyses are also reported in Table I where the labeling of the aromatic protons is the same as in the case of phenylacetylene. Figure 3 shows the fit of the spectrum of the more concentrated solution.

A comparison of the values of the coupling constants of the same substance determined from the spectra at two different concentrations shows very clearly that the variations are very well contained within the limits given by the computed errors. The latter were directly furnished by the program and appear to be larger, at parity of the r.m.s. error, for diphenylacetylene than for phenylacetylene. This result is a consequence of the fact that for toluene the ratio between the number of parameters and matched lines is larger than for phenylacetylene, and therefore the parameters are, in principle, less well determined than for the latter.

Table I: Spectral Parameter for Phenyl- and Diphenylacetylene^a

	Phenylacetylene		Diphenylacetylene	
	Neat	Solvent (mole fraction) CCl ₄ (0.134)	CCl ₄ (0.134)	CCl ₄ (0.065)
$W(1) = W(5)$	-447.40 ± 0.02	-445.13 ± 0.02	-447.66 ± 0.03	-447.47 ± 0.04
$W(2) = W(4)$	-427.25 ± 0.03	-433.53 ± 0.03	-433.11 ± 0.04	-435.08 ± 0.05
$W(3)$	-428.09 ± 0.04	-434.38 ± 0.03	-431.63 ± 0.06	-433.46 ± 0.07
$W(6)$	-183.44	-175.75		
$J(1,2) = J(4,5)$	7.76 ± 0.05	7.77 ± 0.04	7.80 ± 0.05	7.82 ± 0.06
$J(1,3) = J(3,5)$	1.30 ± 0.04	1.32 ± 0.04	1.27 ± 0.08	1.25 ± 0.09
$J(1,4) = J(2,5)$	0.63 ± 0.05	0.64 ± 0.04	0.62 ± 0.07	0.64 ± 0.08
$J(1,5)$	1.78 ± 0.04	1.73 ± 0.06	1.79 ± 0.08	1.78 ± 0.11
$J(2,3) = J(3,4)$	7.58 ± 0.04	7.60 ± 0.04	7.47 ± 0.07	7.53 ± 0.08
$J(2,4)$	1.45 ± 0.10	1.32 ± 0.10	1.39 ± 0.14	1.41 ± 0.17
$J(1,6) = J(5,6)$	0.27 ± 0.04	0.28 ± 0.04		
$J(2,6) = J(4,6)$	-0.11 ± 0.05	-0.11 ± 0.05		
$J(3,6)$	0.24 ± 0.08	0.22 ± 0.07		

^a All data in c.p.s. Chemical shifts measured from TMS as an internal standard; $\nu_0 = 60$ Mc.p.s.

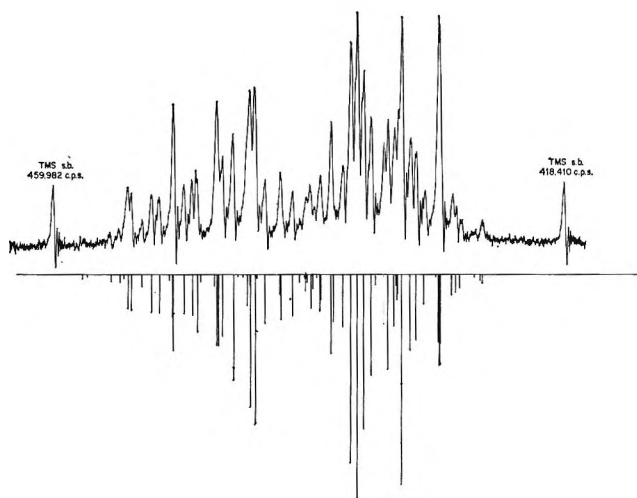


Figure 3. Experimental and calculated spectrum of diphenylacetylene.

In both cases the largest error is associated with $J(2,4)$, which is therefore the parameter toward whose variations the spectra appear to be least sensitive.¹¹

In the first column of Tables II and III are reported for both compounds the chemical shifts at infinite dilution in carbon tetrachloride. These data were obtained by a linear extrapolation from a plot of the chemical shifts *vs.* the concentration in mole fraction. Since the shifts of the *ortho* protons are very slightly sensitive to changes in the concentration, the extrapolated values for these protons may be considered to have the same accuracy as the calculated ones. For all the other protons, the linear extrapolation may introduce larger errors here estimated to be of the order of magnitude of ± 1.0 c.p.s.

Table II: Chemical Shifts (δ) of the Protons^a and Carbons^b in Phenylacetylene. Experimental (Δ_{exptl}) and Calculated (Δ_{calcd}) Deviations of the Shifts from the Corresponding Values in Benzene^c and Acetylene^d

Protons	δ	Δ_{exptl}	Δ_{calcd}	Carbons	δ	Δ_{exptl}	Δ_{calcd}
<i>ortho</i>	-444.76	-8.81	-8.81	<i>ortho</i>	61.4	-3.5	-3.5
<i>meta</i>	-434.50	+1.46	+4.74	<i>meta</i>	65.0	+0.1	+0.18
<i>para</i>	-435.35	+0.61	+4.47	<i>para</i>	65.0	+0.1	+0.14
Ethynyl	-174.57	-66.57	-66.57	C†	71.2	+6.3	+3.3
				C**	109.4
				C*	115.7

^a Present work. Values extrapolated to infinite dilution in CCl₄. Data in c.p.s. from TMS; $\nu_0 = 60$ Mc.p.s. ^b See ref. 24. Data in p.p.m. from CS₂. ^c See ref. 9, 22. $\delta_{\text{protons}} = -435.96$ c.p.s.; $\delta_{\text{carbons}} = 64.9$ p.p.m. ^d See ref. 7. $\delta_{\text{protons}} = -108.00$ c.p.s.

Table III: Experimental and Calculated Shifts of the Protons in Diphenylacetylene^a

Protons	Exptl.	Calcd.	
		Rings perpendic.	Rings parallel
<i>ortho</i>	-447.26	-447.78	-450.40
<i>meta</i>	-436.95	-433.49	-433.98
<i>para</i>	-435.85	-433.62	-433.62

^a Values extrapolated to infinite dilution in CCl₄. Data in c.p.s. from TMS; $\nu_0 = 60$ Mc.p.s.

The spectrum of phenylacetylene in deuterated benzene (15% v./v.) was not completely analyzed. The chemical shifts of the aromatic protons, reported in Table IV, were measured at the centers of the two well-separated multiplets arising from the resonance

Table IV: Chemical Shifts of the Protons of Phenylacetylene and Internal Standards Referred to Acetone as an External Reference^a

	$\delta_{\text{CCl}_4}^b$ (∞ dil.)	$\delta_{\text{C}_6\text{D}_6}^b$ (15% v./v.)	$\delta_{\text{C}_6\text{H}_6}$ (neat)	$\delta_{\text{C}_6\text{D}_6} - \delta_{\text{CCl}_4}$	$\delta_{\text{C}_6\text{H}_6} - \delta_{\text{CCl}_4}$	$\frac{\delta_{\text{C}_6\text{H}_6} - \delta_{\text{CCl}_4}}{\delta_{\text{C}_6\text{D}_6} - \delta_{\text{CCl}_4}}$
TMS	+86.31	+115.70	+115.96	+29.39	+29.65	1.009
C ₆ H ₆	-349.65	-314.82	-319.88	+34.83	+29.82	0.856
<i>ortho</i> protons	-358.45	-328.83	-331.44	+29.62	+27.01	0.912
<i>meta</i> protons	-348.19	-301.16	-311.29	+47.03	+36.90	0.785
<i>para</i> protons	-349.04	-301.16	-312.11	+47.88	+36.93	0.771
Ethynyl proton	-88.26	-51.30	-67.48	+36.96	+20.78	0.562

^a All data, corrected for the bulk susceptibility effect (see text), in c.p.s.; $\nu_0 = 60$ Mc.p.s. ^b Values accurate to within ± 1 c.p.s. (see text).

of the *ortho*, and *meta* and *para* protons, respectively. The shift of benzene was determined using the broad peak of the hydrogen-impure molecules of the solvent. All these measurements are therefore thought to be accurate only to within ± 1 c.p.s.

Discussion

Some interesting features of the sets of parameters of the spectra of phenylacetylene and toluene appear from a careful examination of the data of Table I. In an attempt to rationalize the results it is convenient, however, to discuss the chemical shifts and coupling constants separately.

Chemical Shifts. Both molecules contain two very highly magnetically anisotropic groups, namely, the benzene ring and the acetylenic triple bond.² Both of them will contribute to the chemical shifts of the aromatic and acetylenic protons both through intermolecular and intramolecular effects. A glance in Table I at the behavior of the chemical shifts of all the protons of phenylacetylene upon dilution in an inert solvent (CCl₄) shows that this is indeed the case and that in the neat sample the intermolecular effect (solvent effect) is of about the same order of magnitude as the intramolecular one. Although the two effects are very closely related and both are derived from the presence of anisotropic groups in the molecule, we shall, for clarity of exposition, keep them separated and discuss the solvent effect first.

Intermolecular Effects. The behavior of the chemical shifts of acetylenic protons in different media has been studied thoroughly by several authors.^{3-7,12} In solvents having strong proton acceptor groups, large downfield shifts of the resonance of the acetylenic proton are observed and are unequivocally attributed^{3,5,6} to the formation of hydrogen bonds by the ethynyl proton with the molecules of the solvent. Dilution of diacetylenic or conjugated acetylenic hydrocarbons in inert solvents (CCl₄, C₆H₁₂) or aromatic

hydrocarbons causes small upfield shifts of the resonance of the ethynyl proton; although these shifts have been sometimes taken^{3,12} as experimental evidence for the formation of a hydrogen bond between the acetylenic proton and the π electrons of either the acetylenic triple bond or the aromatic nucleus, a more satisfactory explanation may be found in terms of the so-called neighbor-anisotropy effect. The experimentally detected shifts are, in essence, statistically averaged quantities, over all the possible instantaneous geometrical configurations existing between one or more solvent molecules and the solute. We will call such an instantaneous configuration a juxtaposition. In the presence of strongly magnetically anisotropic groups, if some juxtapositions between solvent and solute are preferred over others, large differential shieldings may arise. Such mechanisms have been widely used in explaining the large high-field shifts observed in the resonance of the proton of any substance dissolved in aromatic hydrocarbons¹³ and is thought also to furnish a satisfactory explanation for the shifts observed upon dilution of acetylenic hydrocarbons in benzene.⁵ Circumstances which cause the acetylenic proton to spend more time above the plane of the benzene ring than the protons of the reference substance suffice to bring about the experimentally observed relative shifts. Similarly, the downfield shifts occurring in neat samples of acetylenic hydrocarbons may be explained⁶ in terms of preferred juxtapositions in which the ethynyl proton lies on an axis perpendicular to and passing through the acetylenic bond of a neighboring molecule. The magnetic anisotropy of this triple bond would cause a downfield shift of the acetylenic proton resonance.

If such a mechanism is accepted as a satisfactory

(12) N. V. Elsakov and A. A. Petrov, *Opt. Spectry.*, **16**, 77 (1964).

(13) A. A. Bothner-By and R. E. Glick, *J. Chem. Phys.*, **26**, 1647 (1957).

model for the explanation of the behavior of the acetylenic shifts in the neat liquids and in aromatic solvents, it appears *a priori* particularly interesting to test its validity also in a medium containing both the acetylenic triple bond and the aromatic nucleus, particularly if one can also follow at the same time the shifts of the protons of the aromatic ring. Phenylacetylene seems to be particularly suited for such a study; the data which have so far appeared in the literature are limited to the shifts of the acetylenic proton relative to internal standards and agree with the ones found by us and reported in Tables I and II. More valuable data, however, for any quantitative calculation are furnished by the shifts measured against an external standard. In Table IV we have reported in the first three columns the shifts of two internal standards (TMS and C_6H_6) and of all the protons of phenylacetylene in the neat liquid, CCl_4 and C_6D_6 solutions measured from the peak of acetone used as an external reference. The data were corrected for the bulk susceptibility effect^{2,14} using the accepted values for the volume susceptibilities (benzene, -0.617×10^{-6} ; CCl_4 , -0.692×10^{-6} ; $C_6H_5-C\equiv CH$, -0.655×10^{-6}) and reduced to a medium having the same volume susceptibility as carbon tetrachloride so that they could be directly compared. In the next two columns there are reported the differences between the chemical shifts in CCl_4 solution and the shifts in C_6D_6 solution and in the neat liquid; the last column of Table IV gives the ratio of these differences.

Two significant observations can be made from the behavior of the shifts of the protons of phenylacetylene in passing from a solution in CCl_4 (∞ dilution) to a solution in C_6D_6 (15% v./v.). Firstly, the shift of the acetylenic proton is not at all exceptional; it is larger than the shifts of the protons of both the internal standards, but its magnitude is largely overshadowed by the shifts occurring at the *meta* and *para* positions of the aromatic ring. It is not necessary to invoke the formation of a hydrogen bond to account for shifts of this magnitude; the magnetically anisotropic nature of the solvent suffices to furnish a reasonable explanation. This conclusion is perfectly in line with the analogous results found by Richards⁵ in the study of the solvent effect on propargyl chloride. Secondly, the largest shifts occur at the peripheral positions of the molecule. A reasonable explanation of these shifts may still be found in the tendency of the aromatic part of phenylacetylene to lie parallel to the molecules of the solvent. It must, however, be assumed that the presence of the acetylenic group creates some sort of repulsive force or steric hindrance which does not permit a complete statistical overlap of the benzene rings. The *meta* and *para* protons would lie, on the average, closer

to the axis of the solvent molecule and experience, therefore, a larger high-field shift than the protons of free benzene. In this model the *ortho* protons would concentrate in the region of space in which the induced secondary magnetic field of the solvent molecule is null or very small and would behave more or less as the protons of an isotropic molecule. Closer contact between solute and solvent would also occur at the ethynyl proton.

If the preceding model is correct, one should be able to predict the behavior of the shifts of the same protons in passing from a solution in CCl_4 (∞ dilution) to the neat liquid. In this case we may consider that the properties of the solutes—TMS, C_6H_6 , and an isolated molecule of phenylacetylene—have not been changed, whereas the structure of the solvent has been modified as compared to benzene. Because of the strong aromatic character of phenylacetylene one would expect that the protons, whose shifts were primarily determined in benzene solution by the aromatic nature of the solvent and not by preferential juxtapositions between solute and solvent, should show shifts identical with the ones observed in benzene, whereas relatively large changes should be present in the shifts of the other protons. The data of Table IV show that this is indeed the case. No appreciable changes are observed for the shifts of the protons of TMS in passing from a solution in C_6D_6 to the neat liquid, and among all the other protons the smallest changes of the shifts occur for those in the *ortho* position. For the protons of benzene, the solvent shift $\delta_{C_6H_6}^{C_6H_6} - \delta_{CCl_4}^{C_6H_6}$ (where $\delta_{C_6H_6}^{C_6H_6}$ is the shift of benzene at infinite dilution in phenylacetylene, etc.) is smaller by about 16% than the solvent shift $\delta_{C_6D_6}^{C_6H_6} - \delta_{CCl_4}^{C_6H_6}$. For the *meta* (and *para*) protons of phenylacetylene, the solvent shift $\delta_{C_6H_6}^{meta} - \delta_{CCl_4}^{meta}$ is smaller by about 23% than $\delta_{C_6D_6}^{meta} - \delta_{CCl_4}^{meta}$. In both cases, the introduction of the ethynyl group in the solvent molecule reduces the occurrence of juxtapositions with overlap of the aromatic rings and thereby decreases the net shift.

For the acetylenic proton the solvent shift, $\delta_{C_6H_6}^{C\equiv CH} - \delta_{CCl_4}^{C\equiv CH}$, is 44% smaller than $\delta_{C_6D_6}^{C\equiv CH} - \delta_{CCl_4}^{C\equiv CH}$. One may suppose that in neat phenylacetylene the presence of a high concentration of ethynyl groups will lead to a distribution of juxtapositions in which the acetylenic proton is adjacent part of the time to the aromatic and part of the time to the acetylenic groups of neighboring molecules. Since the anisotropies of these groups will produce shifts of different sign on the resonance of the acetylenic proton, the changes in the solvent shift of this proton will be larger than the ones observed for

(14) A. A. Bothner-By and R. E. Glick, *J. Chem. Phys.*, **26**, 1651 (1957).

the others. Still no formation of a strong hydrogen bond of the acetylenic proton of one molecule with the triple bond of another can be formulated; such a bond should lead to a negative value of the shift of the ethynyl proton instead of the observed positive shift.

An estimate of the downfield shift expected, if only anisotropic effects are considered and with the hypothesis that the acetylenic proton should spend all the time near the triple bond of a neighboring molecule, can be made by assuming that the contact between the proton and the π system occurs along a cylindrical surface parallel to the axis of the bond. Reasonable dimensions for this cylinder may be 4 Å. for the diameter and 1.21 Å. for the length. Considering now a magnetic dipole of magnitude -9.8×10^{-30} cm.³/molecule at each acetylenic carbon¹⁵ and directed along the axis of the bond, the calculated downfield shift, averaged over the whole surface amounts to -0.5 p.p.m. A further contribution of -0.44 p.p.m. is calculated through the tables of Bovey¹⁶ for the effect of the anisotropy of the benzene ring^{17,18} at this locus, and therefore the total averaged shielding experienced by a proton wandering along the surface amounts to -0.94 p.p.m.

If we now suppose that juxtapositions in which the ethynyl proton is adjacent to the aromatic ring give rise to the shift measured in the C₆D₆ solution and those in which it is near the acetylenic triple bond produce the above calculated shift, we may determine how these juxtapositions are partitioned in the neat liquid. The experimental shift will be the averaged mean over the two different types of juxtapositions and will be given by: $20.78 = 36.96(1.00 - \alpha) - 56.4\alpha$, from which one obtains $\alpha = 17.3\%$. This result suggests that, as far as the shift of the acetylenic proton is concerned, phenylacetylene in the neat liquid behaves for 17.3% of the time as an acetylenic hydrocarbon and for 82.7% of the time as an aromatic hydrocarbon. The behavior of the shifts of the aromatic protons seems also to support this conclusion, and, in view of the extremely simple model used in the calculations, the agreement between the experimental and calculated values is surprisingly good.

It is, however, worthwhile to mention that the same conclusions and quantitative estimate may also be reached through purely geometrical considerations. If one supposes, in fact, that the only relevant juxtapositions in determining the shift of the ethynyl proton are the ones with H directed either toward the plane of the benzene ring or toward the acetylenic triple bond and that the choice between the two is left to chance, the ratio between the two kinds of juxtapositions will be proportional to the areas on which the

contact between the acetylenic proton and the anisotropic groups may be considered effective in determining the shift. If for the aromatic ring this area is represented by the bases of a circular cylinder with a radius of 3 Å. (see ref. 13) and for the acetylenic triple bond by the lateral surface of a cylinder of radius of 2 Å. and length of 1.21 Å., one obtains the result that these areas represent, respectively, 78.8 and 21.2% of the total effective area.

If the results of the previous calculations can be accepted as proof of the validity of the model used in explaining the behavior of the shifts of the protons of phenylacetylene, further conclusions follow naturally. A specific interaction between the ethynyl proton and the electrons of the π systems of neighbor molecules is effective in determining juxtapositions with the acetylenic proton oriented toward the regions of maximum π -electron density; the shift of the ethynyl proton is, however, mainly determined by the magnetic anisotropies generally associated with these π systems, and therefore the formation of stable complexes through strong hydrogen bond has to be excluded. In the presence of different π systems a purely statistical distribution of the effective collisions seems to suffice in furnishing a reasonable semiquantitative estimate of the shifts.

This last remark may be assumed as a basis to cast doubts on some of the conclusions reported in a recent paper.¹² From the magnitudes of the dilution shifts (relative to TMS) of the ethynyl proton in a series of vinylacetylenes and diacetylenes, Elsakov and Petrov conclude that the "coordination activity" of the acetylenic proton in the first series of compounds is smaller than in the second one. On the basis of our results on phenylacetylene, we must, however, point out the possibility that, in the vinylacetylene series, collisions of the acetylenic proton with the π electron of the ethylenic group (whose magnetic properties are not well known) may cause shifts of opposite sign than the ones with the acetylenic triple bond, producing therefore an over-all upfield shift, upon dilution, smaller than the one observed with diacetylenes even at parity of the so-called "coordination activity" of the acetylenic hydrogen.

(15) Since we are considering only an averaged value of the shift, it does not matter whether the calculations are performed with the averaged value of the atomic anisotropy of the two carbons instead of with the values of the atomic anisotropy calculated for each atom separately. See the section on intramolecular effects.

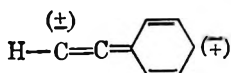
(16) C. E. Johnson, Jr., and F. A. Bovey, *J. Chem. Phys.*, **29**, 1012 (1958).

(17) The correction recently suggested by Dailey¹⁸ to the use of Bovey's tables amounts in this case to few per cent of the calculated value.

(18) B. P. Dailey, *J. Chem. Phys.*, **41**, 2304 (1964).

Intramolecular Effects. As a basis for the discussion of the intramolecular effects we shall consider the chemical shift extrapolated to infinite dilution in CCl_4 and reported in Tables II and III. The occurrence of the resonance of the acetylenic protons at high field, notwithstanding the acidic character of these hydrogens, has been thoroughly investigated and explained by Pople^{2,19} and McConnell²⁰ in terms of the large high-field shift caused by the anisotropy of the acetylenic triple bond. This shift has been theoretically estimated² to be about 10.0 p.p.m. For acetylene and nonconjugated acetylenes the proton resonance signal of the ethynyl proton occurs^{7,12,21} at τ 8.2; conjugation with an ethylenic double bond lowers the resonance to an average value^{7,12,19} of τ 7.2. The chemical shift of the ethynyl proton of phenylacetylene found in our study agrees reasonably well with the data already reported in the literature^{7,8} occurring at τ 7.09. A contribution of about 0.12 p.p.m. toward lower field is calculated¹⁵ for this shift, however, by the induced secondary field of the neighboring phenyl ring; therefore, conjugation of the acetylenic group with the benzene ring produces at the ethynyl proton the same downfield shift of about 1.0 p.p.m. as observed in conjugated vinylacetylenes.

Comparing now the chemical shifts of the aromatic protons of phenyl- and diphenylacetylene with the shift of the protons of the free benzene molecule at infinite dilution²² in CCl_4 (τ 2.754 \equiv -435.96 c.p.s. at 60 Mc.p.s.) we can detect the effects produced on the shifts of these protons upon substitution of one aromatic hydrogen by the acetylenic group. An interesting result of this comparison is that the shifts of the *meta* and *para* protons are only slightly changed by the presence of the acetylenic group. Since the neighbor anisotropy effect decreases with the cube of the distance, it should be very small at the positions of the *meta* and *para* hydrogen. The shifts of these protons should therefore be dominated by the electron density at the part of the aromatic skeleton nearer to them; the data of Tables II and III strongly suggest that no remarkable changes in the electron distribution are provoked at this part of the molecule by the introduction of the acetylenic group in the ring. In particular, from the behavior of the shift of the *para* hydrogen one must conclude that, if the two resonating structures



I

participate at all in the formation of the molecular hybrid, no significant predominance of one of them occurs,

in substantial agreement with the findings of Cook and Danyluk.⁸ The *ortho* protons are instead shifted toward lower field by 0.147 p.p.m. in phenylacetylene and by 0.188 p.p.m. in toluene. These protons are the nearest, among the aromatic ones, to the acetylenic triple bond, and, if their chemical shifts were determined only by the anisotropy of the acetylenic group, one should expect a shift toward higher field of their resonance as compared to benzene protons. If one supposes, in fact, that the effects on the shifts of the *ortho* protons due to the anisotropy of the acetylenic group can be accounted for by calculating the shifts at the *ortho* position produced by two magnetic dipoles located at the positions of the acetylenic carbons and oriented along the axis of the molecule as shown in Figure 4, from the expression which furnishes this shift

$$\Delta\sigma = \Delta\chi \left[\frac{1}{3R_1^3}(1 - 3\cos^2\theta_1) + \frac{1}{3R_2^3}(1 - 3\cos^2\theta_2) \right] \quad (1)$$

and using the following molecular parameters

$$\begin{aligned} \text{C}^*-\text{C}^{**} &= 1.21 \text{ \AA.} & \text{C}^*-\text{H} &= 1.06 \text{ \AA.} \\ \text{C}^{**}-\text{C}^\dagger &= 1.40 \text{ \AA.} & \text{C}-\text{H} &= 1.09 \text{ \AA.} \\ \text{C}^\dagger-\text{C} &= 1.39 \text{ \AA.} & \text{C}^{**}\text{C}^\dagger\text{C}, \text{C}^\dagger\text{CC} &= 120^\circ \end{aligned}$$

one gets the result that the geometrical factor in the brackets in (1) is negative; since $\Delta\chi$ is also negative the shifts of the *ortho* protons should appear at higher field than benzene. It must be pointed out that here, as well as later on, we have used Pople's suggestion¹⁹ of describing the anisotropy of the acetylenic bond in

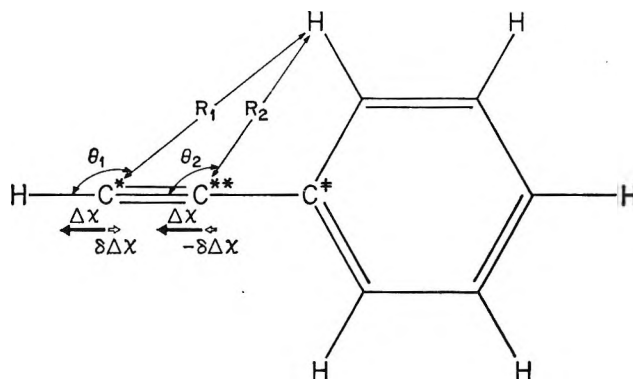


Figure 4. Dipole approximation for the magnetic anisotropies of the ethynyl carbons in phenylacetylene.

(19) J. A. Pople, *Discussions Faraday Soc.*, **34**, 7 (1962).

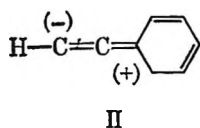
(20) H. M. McConnell, *J. Chem. Phys.*, **27**, 226 (1957).

(21) P. Jouve, *Compt. rend.*, **256**, 1497 (1963).

(22) G. V. D. Tiers, *J. Phys. Chem.*, **62**, 1151 (1958).

terms of the atomic anisotropy of the acetylenic carbons; the qualitative conclusions drawn about the shifts of the *ortho* protons, however, do not change even if the neighbor anisotropy effect is calculated in terms of a single magnetic dipole located at the center of the acetylenic triple bond. Clearly, some other mechanism, competitive with the anisotropy effect, must be invoked in order to explain the experimentally observed downfield shift of the *ortho* protons.

It is known from electric dipole moment measurements that transfer of charge from the aromatic ring to the acetylenic group occurs in phenylacetylene.²³ If this withdrawal of electron density takes place mainly from the *ortho* carbons, a downfield shift of the resonance of the *ortho* protons is to be expected. The transfer of charge is thought to occur principally by an inductive mechanism^{8,23} although contribution of resonating structures of the type



may also be effective in the process.

No conclusion, however, can be drawn on the basis of the proton shifts alone, particularly if quantitative estimates of the several effects contributing to the shifts are wanted. The shifts of the carbons of the aromatic ring should, however, provide very valuable informations in that regard. The C^{13} n.m.r. spectrum of the aromatic part of phenylacetylene (Table II) consists of a singlet at 71.2 p.p.m. toward high field from CS_2 and of two doublets, with intensity ratio 2:3, centered, respectively, at 61.4 and 65.0 p.p.m. from the same reference.²⁴ The assignment of the singlet to the resonance of the C^{\ddagger} carbon has been made by Retcofsky, but no further assignment can be made on the basis of the C^{13} n.m.r. spectrum alone. The C^{13} resonance in benzene⁹ occurs at 64.9 p.p.m. from CS_2 ; the higher-field doublet in the C^{13} n.m.r. spectrum of phenylacetylene must therefore be assigned to the carbons in the aromatic ring less affected by the presence of the acetylenic group. From the data on the proton shifts the assignment of the 65.0-p.p.m. doublet to the *meta* and *para* carbons follows straightforwardly. Consequently, the low-field doublet is assigned to the resonance of the *ortho* carbons in agreement also with the values of the shifts of the *ortho* protons.

Several papers have dealt with the correlations between the π -electron density on the aromatic carbon atoms and the chemical shifts of the protons²⁵⁻²⁷ and of the carbons.^{28,24} Fractional changes $\Delta\phi$'s in the π -

electron density at the carbon atom are correlated with changes in the chemical shifts $\Delta\sigma$'s, by linear relationships

$$\begin{aligned}\Delta\sigma_c &= K_c\Delta\phi \\ \Delta\sigma_p &= K_p\Delta\phi\end{aligned}\quad (2)$$

where the $\Delta\phi$'s are expressed in electrons per atom, the $\Delta\sigma$'s in p.p.m., and the K 's are calculated from experimental data on compounds in which the π -electron density is known. The theoretical basis for such correlations have been discussed by Richards,²⁵ Musher,³⁰ and Pople³¹; the most recent value of the K 's are^{27,29}: $K_p = 8.08$ and $K_c = 160.0$ p.p.m./electron.

Because of the qualitative agreement existing between the behavior of the chemical shifts of the aromatic protons and carbons, it is tempting to see whether a quantitative estimate of the parameters affecting these shifts is also possible. The data of Table II and the correlations (2) should, in principle, furnish sufficient information to calculate the π -electron density at the *ortho* carbons and the magnetic anisotropy of the acetylenic group. The following assumptions, which are discussed below, however, are to be made: (a) the π -electron density at the *ortho* carbons is decreased by an amount $\Delta\phi$; correspondingly, an increase of electron density $2\Delta\phi$ occurs at the terminal acetylenic carbon C^* ; (b) the atomic magnetic anisotropy $\Delta\chi = \chi_{||} - \chi_{\perp}$ of the acetylenic carbon atoms (Figure 4) is decreased by an amount $\delta\Delta\chi$ at the terminal carbon atom C^* and increased by the same amount of the other carbon C^{**} .

Before attempting any calculation, it is worthwhile to discuss the grounds on which the preceding assumptions are based. As far as the first part of assumption a is concerned, there is no doubt that it is strongly supported by all the experimental data on the shifts of the *ortho* carbons and protons. The evidences for a transfer of electron density from the aromatic ring to the acetylenic group have been previously discussed and are also supported by MO calculations.³² More contro-

(23) C. K. Ingold, "Structure and Mechanism in Organic Chemistry," Cornell University Press, Ithaca, N. Y., 1953, p. 108.

(24) H. L. Retcofsky, private communication.

(25) G. Fraenkel, R. E. Carter, A. McLachlan, and J. H. Richards, *J. Am. Chem. Soc.*, **82**, 5846 (1960).

(26) B. P. Dailey, A. Gawer, and W. C. Neikam, *Discussions Faraday Soc.*, **34**, 18 (1962).

(27) T. K. Wu and B. P. Dailey, *J. Chem. Phys.*, **41**, 2796 (1964).

(28) P. C. Lauterbur, *J. Am. Chem. Soc.*, **83**, 1838 (1961).

(29) H. Spiesscke and W. G. Schneider, *Tetrahedron Letters*, **14**, 468 (1961).

(30) J. I. Musher, *J. Chem. Phys.*, **37**, 34 (1962).

(31) M. Karplus and J. A. Pople, *ibid.*, **38**, 2803 (1963).

(32) T. L. Brown, *ibid.*, **38**, 1049 (1963).

versial may appear the assumption that all this transferred electron density is located on the terminal carbon atom; since, however, the results of the calculations do not vary sensibly by changing the electron density on the terminal carbon atom, we shall maintain here assumption a and show later on the effects provoked in the results by a variation of this charge.

On the basis of electronegativity considerations alone, an increase in the electron density in the acetylenic group should cause a high-field shift in the resonance of the ethynyl proton; the large downfield shift (-1.0 p.p.m.) observed experimentally for the resonance of this proton in passing from acetylene to conjugated acetylenes must therefore be attributed to a change in the other parameter which may affect this shift, namely, the anisotropy of the terminal carbon atom. Phenomenologically, therefore, assumption b is justified on the basis of the experimental results. From a mechanistic point of view, assumption b may be derived by assuming that the inductive effect of the benzene ring causes a distortion to occur in the π system of the acetylenic group in such a way as to increase the π -electron density at the terminal carbon C* and to decrease it at the other acetylenic carbon C**. At carbon C*, the consequent expansion of the p orbitals²⁸ decreases the paramagnetic contribution to the transverse magnetic susceptibility χ_{\perp} , with a corresponding decrease of the diamagnetic anisotropy $\Delta\chi$. At the other acetylenic carbon C** the same mechanism should cause an identical increase of the atomic anisotropy.

Contribution of the resonating structures I and II to the molecular hybrid should also be effective, by limiting the free circulation of the π electrons about the molecular axis and in reducing the diamagnetic susceptibilities χ_{\parallel} along the acetylenic triple bond. Since, however, the effects determined by the contribution of these structures are estimated to be much smaller than the inductive effect, assumption b is here retained, with the further understanding that it offers *a priori* only a simple model whose validity can only be tested by the results it furnishes.

On the basis of (a) and (b), the following three equations can be written for the variations of the shifts of the ethynyl proton and of the *ortho* protons and carbons, respectively

$$\begin{aligned} -1.000 &= 16.16\Delta\varphi - 502.526 \times 10^{-3}\delta\Delta\chi \\ -0.147 &= -8.08\Delta\varphi - 6.357 \times 10^{-3}\delta\Delta\chi - \\ &\quad 7.262 \times 10^{-3}\Delta\chi \\ -3.500 &= -160.00\Delta\varphi + 17.011 \times 10^{-3}\delta\Delta\chi - \\ &\quad 42.319 \times 10^{-3}\Delta\chi \quad (3) \end{aligned}$$

where the numerical coefficients of $\delta\Delta\chi$ and $\Delta\chi$ have been calculated through (1) and the similar expressions for the shifts at the acetylenic proton and at the *ortho* carbons. Solving the system of eq. 3 for the three unknowns, the following values are obtained: $\Delta\chi = -9.79 \times 10^{-30}$ cm.³/molecule, $\delta\Delta\chi = 2.79 \times 10^{-30}$ cm.³/molecule, $\Delta\varphi = 0.0248$ electron/atom. Before attempting any comparison of the calculated values of $\Delta\chi$ and $\Delta\varphi$ with the corresponding values reported in the literature, it is convenient to check their internal consistency by comparing the shifts calculated at other parts of the molecule with the corresponding experimental values.

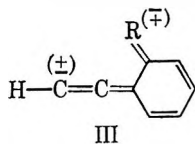
In Table II we have reported the experimental (columns 2, 5) and calculated (columns 3, 6) differences between the shifts of the protons and carbons of phenylacetylene with the corresponding shifts in benzene and acetylene. In all the cases the calculated variations are consistently in the same direction as the experimental ones. For the *meta* and *para* carbons and protons the calculated values are a little larger than the experimental ones. This result is to be expected since in the preceding calculations no removal of charge from this part of the molecule has been taken into account, whereas it is very likely that the inductive effect will also decrease the electron density at the *meta* and *para* protons.

For the acetylenic carbons, unfortunately, no direct comparison is possible since no accurate measurements of the C¹³ shifts in acetylene itself are available. The higher-field shift of the terminal carbon C* as compared with the shift of other carbon C** is, however, perfectly in line with the assumptions made; the difference between the shifts of these two carbons is 6.3 p.p.m. and, when corrected for the contribution due to the anisotropy of the benzene ring, is reduced to a value of 5.5 p.p.m., which may partially be attributed to a different contribution of the paramagnetic terms³¹ to the screening of the two carbon atoms. For the carbon C[†] a high-field shift of 3.3 p.p.m. is calculated for the neighbor anisotropy effect of the acetylenic triple bond; the experimentally observed shift is larger (6.3 p.p.m.) and reminiscent of the anomalous behavior observed by Frei and Bernstein¹⁰ in the methyl carbon of phenylmethylacetylene.

The value of $\Delta\varphi$ obtained from the solution of (3) reduces the electron density at the *ortho* carbon to the value of 0.975 electron/carbon, which seems a reasonable value in view of the large electronegativity of the acetylenic group. As a consequence of assumption a, the electron density at the terminal acetylenic carbon should be increased by 0.050 electron/atom. It must be pointed out, however, that if it is assumed that only

half of the electron density leaving the *ortho* carbons ends on the terminal carbon, the results do not change significantly. If, in fact, the coefficient of $\Delta\varphi$ in the first equation of (3) is reduced by 50%, the following values are obtained for the three variables: $\Delta\chi = -9.22 \times 10^{-30}$ cm.³/molecule, $\delta\Delta\chi = 2.38 \times 10^{-30}$ cm.³/molecule, $\Delta\varphi = 0.0251$ electron/atom. The value of the extra charge at C*, so obtained, is in better agreement with the MO calculation of Brown³²; however, at the present stage of the art of quantum mechanical calculations of electron densities, agreement of this sort can hardly be taken as a clear-cut criterion by which to choose between two hypotheses. This fact, as well as the approximate constancy of the values of all the variables, has induced us to retain the results of the first calculation as a basis for further discussion.

The main point, however, which is surely less controversial, is the further confirmation of the fact that the shift of the ethynyl proton is much more sensitive to a change in the electron distribution around the terminal carbon C* (anisotropic effect) than to the effective increase in the electron density at the same carbon (electronegativity effect). In this context, it is particularly interesting to re-examine the data of Cook and Danyluk⁸ on a study of phenylacetylenes differently substituted at the *para* and *ortho* position. For the *para* compounds the variations of the shifts of the ethynyl proton, measured from the resonance of the same proton in phenylacetylene, correlate very well with Taft's inductive σ_I and resonance σ_R parameters. From the coefficients of σ_I and σ_R in the correlation, these authors could deduce that the transfer or removal of charge from the benzene ring to or from the acetylenic group is mainly governed by the inductive effect. For the *ortho*-substituted compounds no correlation at all could be found since, always, at parity of substituent, the resonance of the ethynyl proton of the *ortho* compounds occurred at lower field than in the *para* compounds; the average value of this downfield over five different substituents was 0.25 p.p.m. Cook and Danyluk⁸ attributed this anomalous behavior to the anisotropies of the substituent groups without, however, giving any clue about the unidirectionality of the shifts. We think, instead, that a more plausible explanation can be found in the variations of the anisotropy of the acetylenic group caused by the *ortho* substitution. If one supposes, in fact, that the latter stabilizes through electrostatic or sterical effects any one of the two zwitterionic structures



a net decrease of the diamagnetic anisotropy, as previously explained, should occur at the acetylenic triple bond with consequent downfield shift of the resonance of the ethynyl proton. It is interesting to note that the largest difference between the shifts of the *ortho*- and *para*-substituted compound occurs for the NH₂ group where the formation of an internal hydrogen bond between the amino hydrogen and the π electrons of the acetylenic group⁸ may be very effective in stabilizing one of the zwitterionic structures; consistently, the smallest difference occurs for the NO₂ substituent where electrostatic repulsion between the negative charges on the oxygen atoms and the π system may reduce the stability of the ionic structures.

Finally, it is worthwhile to mention that if, in phenylacetylene itself, the contribution of the resonating structures I and II to the downfield shift observed for the ethynyl proton is of the same order of magnitude as the one found in the *ortho* compounds, the inductive effect would account for the 75% of the total shift (in good agreement with assumption b).

A review of the literature on the values of the magnetic anisotropy of the acetylenic group calculated either from theoretical quantum mechanical treatments or from experimental data has been recently made by Bothner-By and Pople.³³ The theoretical values range³³ from -1.61 to -19.4×10^{-6} cm.³/mole; the experimental ones, from³⁴ -16.5 to^{35,36} -34.0×10^{-6} cm.³/mole. Our experimental data and calculations lead to a value of -11.8×10^{-6} cm.³/mole; in view of the widely scattered range of values reported in the literature, our datum must be considered in good agreement with the value given by Reddy and Goldstein.³⁴ An even better agreement with other experimental data is found if comparison³⁷ is made with the difference of the in-plane magnetic susceptibilities of crystalline diphenylacetylene³⁸ (-13.7×10^{-6} cm.³/mole).

It may be interesting to report that with our value, the upfield shift of the ethynyl proton in acetylene, owing to the magnetic anisotropy of the triple bond, is 6.05 p.p.m.; the resonance of the acetylenic proton, corrected for the anisotropy effect, should therefore appear at τ 2.15. For completeness and warning we must, however, point out that the results of our cal-

(33) A. A. Bothner-By and J. A. Pople, *Ann. Rev. Phys. Chem.*, in press.

(34) G. S. Reddy and J. H. Goldstein, *J. Chem. Phys.*, **39**, 3509 (1963).

(35) H. Heel and W. Zeil, *Z. Elektrochem.*, **64**, 962 (1960).

(36) W. Zeil and H. Buchert, *Z. Physik. Chem. (Frankfurt)*, **38**, 47 (1963).

(37) We are indebted to Dr. J. A. Pople for having brought to our attention the possibility of such a comparison.

(38) K. Lonsdale, *Proc. Roy. Soc. (London)*, **A171**, 541 (1939).

culations are very sensitive to the variation of K_p ; the value reported by Wu and Dailey²⁷ represents an average determined from experimental data with a maximum deviation of ± 1.15 p.p.m./electron. If K_p is varied between these limits, the values of $\Delta\varphi$ and $\delta\Delta\chi$ do not change sensibly, but $\Delta\chi$ varies from -5.22 to -19.22×10^{-6} cm.³/mole. The lowest value must be discarded since it would bring the resonance of the acetylenic proton, corrected for the anisotropy effect, in a region of the spectrum at higher field than the resonance of the olefinic protons. The highest value, although better in line with Pople's calculations, should also be rejected since it would require at the *meta* and *para* protons upfield shifts about twice as large as the ones reported in Table II; larger local effects should therefore be invoked to reconcile the experimental results with the calculated ones, and that seems to be quite improbable from the general behavior of the coupling constants among the aromatic protons (see next section).

Finally, it may be interesting to know that if the value of -11.32×10^{-30} cm.³/molecule (deduced from the difference of the in-plane susceptibilities of diphenylacetylene) is substituted for $\Delta\chi$ and the equations used backward to calculate K_p , the value of 8.38 p.p.m./electron is obtained for this constant.

In the case of diphenylacetylene, unfortunately, no data are available for the C¹³ shifts of the aromatic carbons, and a comparison between the experimental and calculated shifts of only the protons is possible. For reasons of symmetry the atomic anisotropies of the acetylenic carbons must be equal; since it is impossible for lack of data to apply eq. 3 and derive new values of $\Delta\chi$ and $\Delta\varphi$, we have used for these parameters the values found in phenylacetylene and proceed backward to the calculations of the proton shifts. In diphenylacetylene the presence of the second phenyl ring contributes appreciably to the shift of the aromatic protons, particularly of those at the *ortho* position. To take into account such contributions we have calculated the shifts for the two extreme conditions, namely, the ones in which the rings are parallel and at right angles to each other; in the case of free rotation of the two rings the shift would be represented by the arithmetic mean of the preceding values. Since the tables of Johnson and Bovey do not cover the distances met in diphenylacetylene, the dipole approximation has been used. In two recent publications Dailey¹⁸ and Pople³⁹ have concluded that the contributions to the shifts of benzene, due to the ring current and calculated through Pauling's classical value of the anisotropy, are too large and have proposed smaller value for this parameter. The data reported in Table II

have been calculated with a value of the dipole equal to -70.50×10^{-30} cm.³/molecule, which is obtained from the experimental value of the anisotropy of benzene (-59.7×10^{-6} cm.³/mole) by subtracting the local contributions (-17.2×10^{-6} cm.³/mole) estimated by Pople.³⁹

For the *para* protons the shifts are independent of the relative orientation of the two rings; for the *meta* protons that is no more true, but the differences between the calculated values are too small to be significant. For both the *meta* and *para* protons the calculated shifts occur at about 2 c.p.s. at higher field than the experimental values, and the same considerations made in the case of phenylacetylene suffice to justify the results.

For the *ortho* protons the shift calculated for a perpendicular orientation of the rings is in better agreement with the experimental value although the difference between the calculated values is too small to furnish an uncontroversial conclusion.

As far as the magnetic anisotropy of the acetylenic triple bond and the model used for calculating it are concerned, the results obtained for diphenylacetylene are in satisfactory agreement both with the hypothesis made as well as with the experimental data.

Coupling Constants. A theoretical study of the mechanism of the coupling between protons in aromatic systems has been presented by McConnell.^{40,41} The conclusions of that study are that the coupling is mainly transmitted through the framework of the σ electrons with only small contributions from the π -electron system. Experimentally it has been observed^{42,43} that, in monosubstituted benzenes, the coupling constant between protons 1 and 2 is always larger than the one between protons 2 and 3. This effect seems to be quite general, and, although no correlation has until now been found between the changes in the coupling constants and the nature of the substituent, it must necessarily be assumed that, to large perturbing effects of the substituent group, must correspond large changes in the magnitude of the coupling. The magnitudes of $J(1,2)$ and $J(2,3)$ in phenylacetylene are, respectively, the smallest and the largest values which have so far appeared in the literature for the corresponding coupling constants, and their values differ by only 0.18 ± 0.05 c.p.s. A similar behavior is also present in the *meta* coupling constants $J(1,3)$ and $J(2,4)$

(39) J. A. Pople, *J. Chem. Phys.*, **41**, 2559 (1964).

(40) H. M. McConnell, *J. Mol. Spectry.*, **1**, 11 (1957).

(41) H. M. McConnell, *J. Chem. Phys.*, **30**, 126 (1959).

(42) A. A. Bothner-By, "Advances in Magnetic Resonance," in press.

(43) S. Castellano, unpublished results.

which are identical within the experimental error. It seems to us that these observations completely confirm our remarks, deduced from the behavior of the chemical shifts, about the smallness of the perturbation caused in the phenyl ring by the introduction of the acetylenic group. The value of $J(1,5)$ is decisively larger than the values of the other *meta* coupling constants in reasonable agreement with the qualitative prediction, based also on the behavior of the chemical shifts, that the main perturbation in the benzene ring is largely localized around the substituted carbon, *i.e.*, along the most plausible path for this coupling. The coupling constants between the protons of diphenylacetylene follow more or less the same behavior although larger differences are observed between the two *ortho* constants and between $J(1,3)$ and $J(2,4)$.

Our spectral analysis shows that in phenylacetylene the ethynyl proton is coupled with each of the aromatic protons⁴⁴; the coupling constant with the *meta* protons has a negative sign, and this result was directly obtained by the computer, notwithstanding the fact that, for both spectra, the sets of parameters from which the iterations were started had this coupling constant set equal to zero. This fact, as well as the impossibility of obtaining an equally good fit of the spectra by changing the sign of this coupling constant or the ones with the *ortho* and *para* protons, is taken as a proof of the correctness of the signs as reported in Table I. They are in accord with the theoretical prediction^{45,46} of the alternation of sign with the number of bonds involved in the long-range coupling (five bonds for the *ortho*, six for the *meta*, and seven for the *para* protons).

According to Karplus' theory,⁴⁶ the coupling between protons four or more carbon bonds apart in unsaturated hydrocarbons is mainly transmitted through the π -electron framework and is indicative of the degree of conjugation occurring in the molecule. The smallness of the long-range coupling constants found in phenyl-

acetylene as compared with the ones of vinylacetylene⁴⁷ seems to confirm the hypothesis made, in the previous section, about the minor role played in phenylacetylene by the resonating structures I and II.

In diphenylacetylene no coupling is observed between the protons of the two phenyl rings; if long-range couplings of the same order of magnitude of the ones observed in phenylacetylene were present, even only between the *ortho* protons of the two rings, a much more complex spectrum would have to be expected, with further splittings or at least broadening of the peaks, which could not be accounted for on the basis of an AA'BB'C calculation and which are not experimentally observed. Since the coplanarity of the two rings should, in principle, increase the contribution to the molecular hybrid of resonating structures favoring the transmission of the coupling, the experimental undetectability of the latter suggests that, at 36° and in solution, the molecule of diphenylacetylene is very likely in a nonplanar conformation.

Acknowledgments. We wish to thank Dr. J. A. Pople and Dr. A. A. Bothner-By for helpful discussions and for having furnished us with preprints of their manuscripts. We are also indebted to Dr. Bothner-By for reading the text of the present work. We acknowledge gratefully experimental assistance from Miss S. Ebersole in the purification and preparation of the samples. The computations were performed at the University of Pittsburgh Computation Center with partial support of the National Science Foundation.

(44) Long-range coupling between the acetylenic proton and fluorine in *o*- and *p*-fluorophenylacetylene had been previously reported by Cook and Danyluk.⁸

(45) M. Karplus, *J. Am. Chem. Soc.*, **82**, 4431 (1960).

(46) M. Karplus, *J. Chem. Phys.*, **33**, 1842 (1960).

(47) S. Sternhell, *Rev. Pure Appl. Chem.*, **14**, 15 (1964), and literature quoted therein.

Further Studies on the Decarboxylation of β -Resorcylic Acid in Polar Solvents

by Louis Watts Clark

Department of Chemistry, Western Carolina College, Cullowhee, North Carolina (Received May 10, 1965)

The decarboxylation of β -resorcylic acid was studied in four straight-chain aliphatic acids (hexanoic, heptanoic, octanoic, and decanoic) and in two cresols (*o*-cresol and *p*-cresol). The activation parameters for the reaction in the various solvents were calculated and compared with results previously reported for the reaction in resorcinol and in amines and glycols. The results afforded interesting insight into the decarboxylation reaction.

Brown, Hammick, and Scholefield¹ measured the rate of decarboxylation of β -resorcylic acid in resorcinol at several different temperatures between 180.45 and 207.15°.

Subsequently, kinetic studies by the present author on the decarboxylation of β -resorcylic acid in amines and glycols² strongly suggested a bimolecular mechanism for the reaction. In order to try to obtain further insight into the mechanism and energetics of this reaction, additional decarboxylation experiments with β -resorcylic acid have been carried out in this laboratory employing as solvents four straight-chain aliphatic acids and two of the cresols. The results of this investigation are reported herein.

Experimental Section

Reagents. The β -resorcylic acid used in this research assayed 99.6% pure and melted at 215° (cor.). The melting point was determined using a thermometer calibrated against one which had been calibrated by the U. S. Bureau of Standards. The solvents were highest purity chemicals. Fresh samples of each liquid were distilled at atmospheric pressure directly into the dried reaction flask immediately before the beginning of each decarboxylation experiment.

Apparatus and Technique. Details of the apparatus and technique have been described previously.³ The course of the reaction was followed by measuring the volume of CO₂ evolved at atmospheric pressure and at the temperature of a water-jacketed buret. The buret was calibrated by the U. S. Bureau of Standards at 20°. Water maintained at 20.0 ± 0.05° by means of a cooling coil and electronic relay was pumped through the water jacket during the experiment. The temperature of the oil bath was controlled to within

±0.005° using a completely transistorized temperature-control unit equipped with a sensitive thermistor probe. A thermometer which also had been calibrated by the U. S. Bureau of Standards was used to read the temperature of the oil bath. Appropriate corrections and calibrations were carefully applied to this thermometer in order to reduce errors in temperature readings to a minimum. Before the experiments the thermometer was suspended in a long glass tube and the temperature of steam at the prevailing pressure was determined. In order to be able to ascertain precisely the correct temperature of steam it is necessary to know the exact value of the barometric pressure. Furthermore, conversion of observed gas volumes to STP values requires barometric corrections. The accuracy of the barometer used in this research was ensured by completely disassembling the barometer, replacing the barometer tube with a new clean tube of larger diameter, and refilling the tube with triply distilled mercury. The height of the barometer column was then checked with a cathetometer, allowance being made for the linear expansion of the cathetometer from 0° to room temperature. Temperature, latitude, and altitude corrections were applied to all barometer readings. The steam-point correction was added to the Bureau of Standards corrections in obtaining the oil-bath temperatures.

The entraining liquid in the buret consisted of a solution of 20% sodium sulfate (by weight) and 5% sulfuric acid (by volume) (the solubility of CO₂ is

(1) B. R. Brown, D. L. Hammick, and A. J. B. Scholefield, *J. Chem. Soc.*, 778 (1950).

(2) L. W. Clark, *J. Phys. Chem.*, **67**, 2831 (1963).

(3) L. W. Clark, *ibid.*, **60**, 1150 (1956).

negligible in this solution). Using Raoult's law and data on activity coefficients, it is found that the vapor pressure of this solution at 20° is 15.96 mm. This vapor pressure must be taken into account in converting observed gas volumes to STP.

In each decarboxylation experiment a 0.2769-g. sample of β -resorcylic acid was introduced in the usual manner into the reaction flask. On complete reaction this weight of acid will produce 40.0 cc. of CO₂ at STP, calculated on the basis of the actual molar volume of CO₂ at STP, namely, 22,267 cc. About 60 g. of solvent, saturated with dry CO₂ gas, was used in each experiment.

Results

Two decarboxylation experiments were carried out in each solvent at three different temperatures over a 20° range. The decarboxylation of β -resorcylic acid gave smooth first-order kinetics in all the solvents used in this research. In each experiment the log ($V_{\infty} - V_t$) was a linear function of time over the greater part of the reaction. Rate constants were calculated from the slopes of the logarithmic plots, reproducibility between duplicate experiments being generally between 1 and 3%. Average rate constants thus obtained are shown in Table I along with data reported

by Brown and co-workers¹ for the reaction in resorcinol.

The parameters of the absolute reaction rate equation⁴

$$k = \frac{\kappa T}{h} e^{-\Delta H^*/RT} e^{\Delta S^*/R}$$

based upon the data in Table I are shown in Table II.

Table II: Activation Parameters for the Decarboxylation of β -Resorcylic Acid in Aliphatic Acids and Phenols

Solvent	ΔH^* , kcal./mole	ΔS^* , e.u./mole
Hexanoic acid	34.2	-3.53
Heptanoic acid	33.6	-5.0
Octanoic acid	32.8	-6.9
Decanoic acid	29.2	-15.4
Resorcinol ^a	28.8	-10.5
<i>p</i> -Cresol	20.94	-29.0
<i>o</i> -Cresol	18.05	-36.1

^a See ref. 1.

Discussion

The data in Table II clearly indicate a bimolecular mechanism for the decarboxylation of β -resorcylic acid in polar solvents. In the case of the aliphatic acids the enthalpy of activation as well as the entropy of activation decrease regularly with increasing chain length. Here the solvent is apparently acting as a Lewis base, the inductive effect of the alkyl residue tending to increase the electron density on the hydroxyl oxygen atom, while at the same time introducing more steric hindrance. In the case of the phenolic compounds it will be noted that the reaction in resorcinol has the highest enthalpy as well as the highest entropy of activation. The high entropy value is in accord with the greater availability of nucleophilic groups (two hydroxyl groups in the molecule), whereas the high entropy points to the greater acidity of resorcinol as compared with the cresols. The very large negative entropy of activation for the reaction in *o*-cresol is clearly a consequence of the strong steric hindrance exerted by the methyl group adjacent to the hydroxyl group. The +*I* effect of the methyl group in the *ortho* position accounts for the fact that the enthalpy of activation of the reaction is lower in *o*-cresol than it is in any of the other phenols. In

Table I: Apparent First-Order Rate Constants for the Decarboxylation of β -Resorcylic Acid in Various Solvents

Solvent	Temp., °C. (cor.)	$k \times 10^4$, sec. ⁻¹
Hexanoic acid	181.64	0.61
	191.41	1.37
	200.78	2.91
Heptanoic acid	181.64	0.52
	193.56	1.50
	201.89	2.88
Octanoic acid	181.44	0.52
	191.05	1.12
	201.02	2.45
Decanoic acid	179.92	0.34
	193.56	0.90
	201.36	1.54
<i>o</i> -Cresol	163.25	1.00
	177.23	1.96
	183.65	2.65
<i>p</i> -Cresol	166.93	1.73
	175.89	2.84
	187.11	5.15
Resorcinol ^a	180.45	5.65
	181.05	6.61
	182.25	7.41
	192.05	14.6
	207.15	36.7

^a See ref. 1.

(4) S. Glasstone, K. J. Laidler, and H. Eyring, "The Theory of Rate Processes," McGraw-Hill Book Co., Inc., New York, N. Y., 1941, p. 14.

p-cresol the entropy of activation is lower than it is in resorcinol since there is only one hydroxyl group present in *p*-cresol as compared with two in resorcinol, and it is higher than it is in *o*-cresol since very little steric hindrance would be expected from the methyl group in the *para* position as compared with the *ortho* position.

If a given reaction takes place in various solvents by the same mechanism, a plot of enthalpy of activation *vs.* entropy of activation for the reaction series will yield a straight line.⁵ The slope of the line (known as the isokinetic temperature) is the absolute temperature at which all the reactions conforming to the line have the same free energies of activation, hence equal rates.⁶ A change in type of solvent often results in the formation of a new line parallel to the original line. Leffler has attributed this discontinuous solvent effect to the existence of two potential energy minima in either the ground state or the transition state.⁵

Figure 1 is a plot of enthalpy of activation *vs.* entropy of activation for the decarboxylation of β -resorcylic acid in the various solvents shown in Table II and ref. 3. Line I connects the parameters for the reaction in acids, line II in phenols, line III in amines, and line IV in glycols. (The black circle in line II is the point calculated on the basis of the data of Brown and co-workers for the reaction in resorcinol.¹) It is evident that the four lines shown in Figure 1 are essentially parallel. The slopes of lines III and IV were shown previously to be about 418°K. or 145°. The slope of lines I and II are very nearly 422°K. or 149°. (The slight difference between these two slopes is clearly within experimental error.) The parallelism of the four lines in Figure 1 is an indication that the decarboxylation of β -resorcylic acid takes place by the same mechanism in all four homologous series.⁵

The intercept of the isokinetic temperature line on the zero (entropy of activation) axis yields the value of ΔH_0 , which is equal to ΔF_0 , the free energy of activation at the isokinetic temperature for each system.⁵ The free energy of activation at the isokinetic temperature can be substituted in the absolute reaction rate equation⁴

$$k = \frac{\kappa T}{h} e^{-\Delta F^*/RT}$$

enabling the rate of reaction at the isokinetic temperature to be calculated. Table III summarizes the results of such calculations for the four systems shown in Figure 1.

It will be seen in Table III that the free energy of activation at the isokinetic temperature for the decarboxylation of β -resorcylic acid decreases (and hence

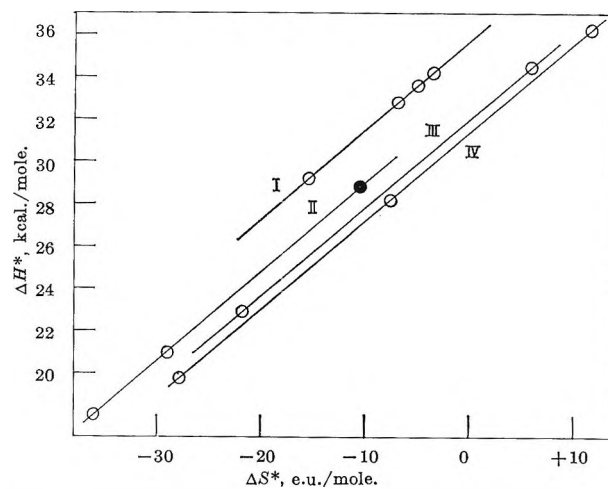


Figure 1. Enthalpy of activation *vs.* entropy of activation plot for the decarboxylation of β -resorcylic acid in polar solvents: ●, data obtained from ref. 1; O, data of Clark, this research and previous research. The solvents are: I, monocarboxylic acids; II, phenols; III, amines; and IV, glycols.

Table III: The Free Energy of Activation and Rate Constants at the Isokinetic Temperature for the Decarboxylation of β -Resorcylic Acid in Several Homologous Series

Figure 1 ref.	System	$\Delta F_{149}^{\ddagger}$, kcal./mole	$k_{149} \times 10^4$, sec. ⁻¹	Relative rate
Line I	β -Resorcylic acid in acids	35.7	0.03	1
Line II	β -Resorcylic acid in phenols	33.2	0.57	53
Line III	β -Resorcylic acid in amines	32.0	3.00	100
Line IV	β -Resorcylic acid in glycols	31.4	4.8	160

the rate of reaction increases) with increasing nucleophilicity of the functional group in the homologous series. At 149° the decarboxylation of β -resorcylic acid takes place 53 times as fast in phenols, 100 times as fast in amines, and 160 times as fast in the glycols as it does in the aliphatic acids.

The decarboxylation of malonic acid and its derivatives in the molten state and in acidic and neutral solvents has been shown to constitute a single reaction series with an isokinetic temperature of 422°K. or 149°. The decarboxylation of malonic acid in alcohols forms another reaction series having the same isokinetic temperature as the first⁸; the decarboxylation of

(5) J. E. Leffler, *J. Org. Chem.*, **20**, 1202 (1955).

(6) S. L. Friess, E. S. Lewis, and A. Weissberger, Ed., "Technique of Organic Chemistry," Vol. VIII, Part I, 2nd Ed., Interscience Publishers, Inc., New York, N. Y., 1961, p. 207.

(7) L. W. Clark, *J. Phys. Chem.*, **68**, 3048 (1964).

(8) L. W. Clark, *ibid.*, **67**, 526 (1963).

malonic acid in amines forms a third series, also having the same isokinetic temperature.⁹

Just as in the case of β -resorcylic acid (Figure 1), the parallelism of the three lines in the case of malonic acid is an indication that the decarboxylation of malonic acid takes place by the same mechanism in the three homologous series. Also, as in the case of β -resorcylic acid, the free energy of activation at the isokinetic temperature for malonic acid decreases with increasing nucleophilicity of the functional group in the homologous series.⁷⁻⁹ Furthermore, the fact that the observed isokinetic temperature for the decarboxylation of β -resorcylic acid in the various solvents is practically identical with that of malonic acid suggests that these two compounds undergo decarboxylation by the same mechanism.⁵ Malonic acid is a type of β -keto acid, whereas β -resorcylic acid is a type of β -hydroxy acid. Both types of acids are capable of forming chelate six-membered rings by intramolecular hydrogen bonding. The identity of mechanism for the decarboxylation of these two compounds is probably related to this common property.

The free energies of activation for the decarboxylation of malonic acid at the isokinetic temperature in the three homologous series have been used to calculate the rate of reaction at 149°. The results of these calculations are shown in Table IV.

It will be observed in Table IV that malonic acid at

Table IV: The Free Energy of Activation and Rate Constants at the Isokinetic Temperature for the Decarboxylation of Malonic Acid in Several Homologous Series^a

Figure 1 ref.	System	ΔF^*_{149} , kcal./ mole	$k_{149} \times 10^4$, sec. ⁻¹	Relative rate based on β -res- orcylic acid in acids = 1
Line I	Malonic acid in acids	31.0	7.84	261
Line II	Malonic acid in alcohols	29.2	66.7	2220
Line III	Malonic acid in amines	28.8	108.0	3600

^a References 7-9.

149° reacts 261 times as fast in acids, 2220 times as fast in alcohols, and 3600 times as fast in amines as does β -resorcylic acid in acids. These results show how radically the rate of a chemical reaction at a given temperature can be altered by appropriate changes in the structure of the reactant and solvent.

Acknowledgment. Acknowledgment is made to the donors of the Petroleum Research Fund, administered by the American Chemical Society, for the support of this research.

(9) L. W. Clark, *J. Phys. Chem.*, **62**, 79 (1958).

Activity Coefficients and Molal Volumes of Two Tetraethanolammonium Halides in Aqueous Solutions at 25°

by Wen-Yang Wen and Shuji Saito

Chemistry Department, Clark University, Worcester, Massachusetts (Received May 10, 1965)

Two symmetrical tetraethanolammonium halides have been employed in a study of the effect of terminal hydroxyl groups on the cationic behavior in aqueous solutions. The activity and osmotic coefficients, as well as apparent and partial molal volumes of the respective fluoride and bromide in water, were measured at 25° and compared with the corresponding tetraalkylammonium halides. The results are in agreement with the notion that the substitution of terminal methyl groups with hydroxyl groups diminishes the peculiarities of symmetrical quaternary ammonium ions in water. In other words, quaternary ammonium cations with terminal hydroxyl groups behave more normally and affect the structure of water less than the corresponding tetraalkylammonium ions.

Introduction

Studies on properties of aqueous solutions containing tetraalkylammonium salts have generally confirmed a view that some of the large symmetrical cations enhance the icelike or cagelike structure of water.¹⁻³ In contrast, the effects of tetrahydroxyalkylammonium ions on the water structure can be expected to be rather different. With a picture of water as consisting of flickering clusters of hydrogen-bonded molecules, Frank and Wen¹ inferred that the solutes containing hydrogen-bonding groups like NH₂ or OH do not alter water structure much, if at all. In this respect it will be of considerable interest to compare physical properties of tetrahydroxyalkylammonium salt solutions with those of the corresponding tetraalkylammonium salt solutions.

In this paper we are reporting the activity and osmotic coefficients as well as apparent and partial molal volumes of tetraethanolammonium fluoride and bromide in water at 25°.

Experimental Section

Materials. (1) Tetraethanolammonium bromide, (HOC₂H₄)₄NBr, was prepared by heating a mixture of triethanolamine (in excess) and 2-bromoethanol with anhydrous methanol at 115° for 22 hr. The unreacted triethanolamine in the product was precipitated as the hydrobromide, (HOC₂H₄)₃N·HBr (m.p. 185°),

by bubbling hydrogen bromide gas through the solution. Separation of the desired compound from the remaining triethanolamine hydrobromide was effected by repeated recrystallizations—five times with ethanol and twice more with ethanol-chloroform mixture. The anhydrous crystals which melt at 100–102° were very hygroscopic and were handled in a drybox. A gravimetric analysis of the bromide ion as AgBr in the compound indicated its purity to be 99.59 ± 0.02%. Density of the anhydrous crystal was found to be 1.600 g./ml. at 25°.

(2) Tetraethanolammonium fluoride, (HOC₂H₄)₄NF, was prepared by the titration of a methanol solution of the mixture of (HOC₂H₄)₄NOH and (HOC₂H₄)₃N (Matheson Coleman and Bell) with aqueous HF solution. By pH titration with a Beckman Model G pH meter, the neutralization point was determined to be pH 9.6. The resulting solution was evacuated to dryness over P₂O₅, and the white solid obtained was recrystallized several times from methanol. The same compound was also prepared by the double metathesis of (HOC₂H₄)₄NBr with Ag₂SO₄ and BaF₂. The fluoride ion content of the compound

(1) H. S. Frank and W. Y. Wen, *Discussions Faraday Soc.*, 24, 133 (1957).

(2) W. Y. Wen, Ph.D. Thesis, University of Pittsburgh, 1957, Microfilm no. 58-132.

(3) W. Y. Wen and S. Saito, *J. Phys. Chem.*, 68, 2639 (1964).

was found to be $99.0 \pm 0.5\%$ of the theoretical value by a gravimetric analysis in which the fluoride ion was precipitated as CaF_2 . The cationic analysis with $\text{NaB}(\text{C}_6\text{H}_5)_4$ gave results which are consistent with the formula $(\text{HOC}_2\text{H}_4)_4\text{NF}$ and not with $(\text{HOC}_2\text{H}_4)_3\text{N}\cdot\text{HF}$. The melting point of the former (our desired compound) is 195° while the latter is around 75° . The density of the anhydrous crystals was measured to be 1.353 g./ml. at 25° . In contrast to the bromide, the tetraethanolammonium fluoride is only very slightly hygroscopic.

(3) Reagent grade KCl was recrystallized from water and dried at 650° under nitrogen atmosphere. Doubly distilled water was used for making up the solution to be measured.

Apparatus and Measurements. (1) Activity and osmotic coefficients were determined by the gravimetric isopiestic comparison method with an apparatus similar to that employed by Owen and Cooke.⁴ Several sets of four dishes (made of gold or gold-plated silver) with dimensions of $4 \times 4 \times 1.75$ cm.³ were used on a 3.5 cm. thick copper block having a diameter of 15 cm. All contact surfaces of the dishes and the copper block have been carefully polished to render good heat conduction. KCl reference solutions (2 to 4 ml. each) were placed into two of the dishes and sample solutions in the other two dishes, all dishes equipped with covers. Four dishes of a set were tightly clamped onto the copper block and placed in a desiccator which was then evacuated and immersed in a 600-l. constant-temperature bath held at $25 \pm 0.01^\circ$. The desiccators in the bath were carefully evacuated with an aspirator in several stages over a period of 24 hr. to a pressure of 25–30 mm. The equilibrium was reached after gently rocking the unit for 3 days to 2 weeks depending on the concentrations of the solutions under measurements. The dishes were then covered before admitting air into the desiccators. The solutions in duplicate dishes were considered in equilibrium when they arrived at the same molality to within 0.1%. All weighings were done with a Sartorius single-pan balance Model 2503 having a capacity of 200 g. and a sensitivity of 0.05 mg. Our activity coefficient data are believed to be precise to within 0.5%.

(2) The density measurements were made in Weld-type pycnometers of 5 and 25 ml. capacity standardized with doubly distilled water. The process of Weissberger⁵ was followed in the measurements, all weights being reduced to weights *in vacuo*. Replicate determinations reproduced within 5×10^{-5} corresponding to a precision for the apparent molal volume of ± 0.1 ml.

Results and Discussion

A. Osmotic and Activity Coefficients. The measured molalities of the isopiestic KCl and tetraethanolammonium halide solutions are given in Table I. In this table the values of the isopiestic ratio R , defined as the ratio of the molality of KCl to the molality of the isopiestic sample solution, are also included. From the isopiestic ratio and the known osmotic coefficient of the reference salt ϕ_0 , the osmotic coefficient of the sample salt ϕ can be obtained simply by the equation

$$\phi = R\phi_0 \quad (1)$$

For measurements of concentrated solutions, several kinds of saturated salt solutions were used as the reference. ϕ of the sample salt is, in this case, given by

$$\phi = \frac{-55.51 \ln a_w}{\nu m} \quad (2)$$

Table I: Molalities of Isopiestic Solutions and Isopiestic Ratios

Reference salt ^a	(HOC ₂ -H ₄) ₄ NF	R	KCl	(HOC ₂ -H ₄) ₄ NBr	R
0.1042	0.1045	0.9971	0.1189	0.1239	0.9596
0.1800	0.1800	0.9997	0.1816	0.1934	0.9386
0.2221	0.2215	1.003	0.1887	0.2017	0.9355
0.3239	0.3216	1.007	0.2972	0.3262	0.9111
0.4535	0.4480	1.012	0.3099	0.3410	0.9088
0.6322	0.6199	1.020	0.4372	0.4935	0.8859
0.8211	0.7994	1.027	0.5328	0.6128	0.8695
0.9457	0.9168	1.032	0.5560	0.6416	0.8666
1.189	1.142	1.042	0.7017	0.8259	0.8496
1.498	1.422	1.053	0.8332	0.9962	0.8364
1.695	1.601	1.058	0.9952	1.212	0.8214
2.025	1.892	1.070	1.035	1.266	0.8181
2.248	2.082	1.080	1.360	1.707	0.7966
2.516	2.317	1.086	1.433	1.807	0.7930
2.730	2.501	1.092	1.597	2.030	0.7870
3.234	2.929	1.104	1.710	2.187	0.7821
3.264	2.955	1.105	1.919	2.472	0.7761
3.588	3.228	1.112	1.961	2.531	0.7750
4.096	3.653	1.121	2.217	2.880	0.7697
Satd. KCl	4.249		2.508	3.276	0.7654
Satd. (NH ₄) ₂ SO ₄	5.294		2.733	3.584	0.7623
Satd. NH ₄ Cl	5.981		2.862	3.760	0.7610
Satd. NaCl	6.404		3.146	4.149	0.7582
Satd. NaNO ₃	6.764		3.407	4.504	0.7566
			4.094	5.441	0.7524
			4.759	6.354	0.7490

^a KCl unless specified otherwise.

(4) B. B. Owen and T. F. Cooke, Jr., *J. Am. Chem. Soc.*, **59**, 2273 (1937).

(5) A. Weissberger, "Physical Methods of Organic Chemistry," Vol. 1, 2nd Ed., Part I, Interscience Publishers, Inc., New York, N. Y., 1949.

where a_w is the activity of water in the reference solution and ν is the number of moles of ions formed by the ionization of one mole of salt ($\nu = 2$ for 1-1 electrolytes). The mean molal activity coefficients, γ^\pm , of the salts have been calculated by the equation

$$\ln \gamma^\pm = \phi - 1 - 2 \int_0^{\sqrt{m}} [(1 - \phi)/\sqrt{m}] d\sqrt{m} \quad (3)$$

The integral in the right-hand side of eq. 3 was evaluated by plotting $1 - \phi$ against \sqrt{m} , but the calculation involves an extrapolation to infinite dilution. Since the isopiestic method cannot be employed to solutions with concentrations appreciably less than 0.1 m , the values of $1 - \phi$ at m less than 0.1 were determined by a graphical extrapolation to $1 - \phi = 0$ at $m = 0$ applying the Debye-Hückel limiting law, $1 - \phi = 0.3908 \cdot \sqrt{m}$, at 25°. In the absence of low-concentration data, this extrapolation method is likely to introduce some error, and, consequently, $\ln \gamma^\pm$ values so determined may be subject to a small constant correction when data on more dilute solutions become available, perhaps from concentration cells with transference. The osmotic and activity coefficients of the two tetraethanolammonium halides so obtained are given in Table II.

Mean molal activity coefficients of the two salts are plotted against molalities in Figure 1 for the entire concentration range studied. In Figure 2, values of

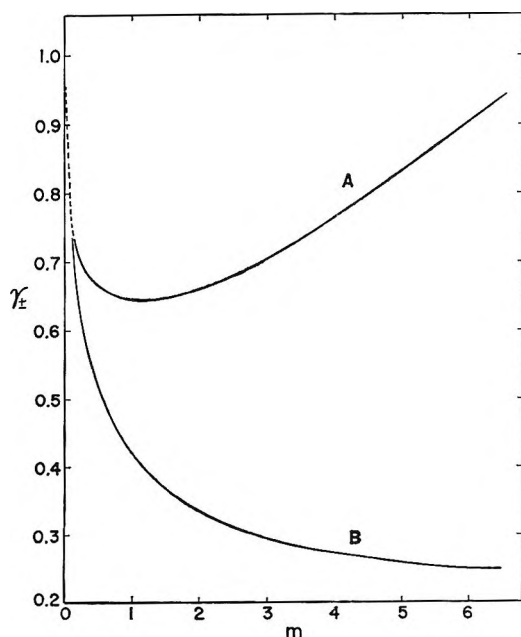


Figure 1. Mean molal activity coefficients, γ^\pm , of two tetraethanolammonium halides in aqueous solutions at various molal concentrations, m , at 25°: A, $(\text{HOC}_2\text{H}_4)_4\text{NF}$; B, $(\text{HOC}_2\text{H}_4)_4\text{NBr}$.

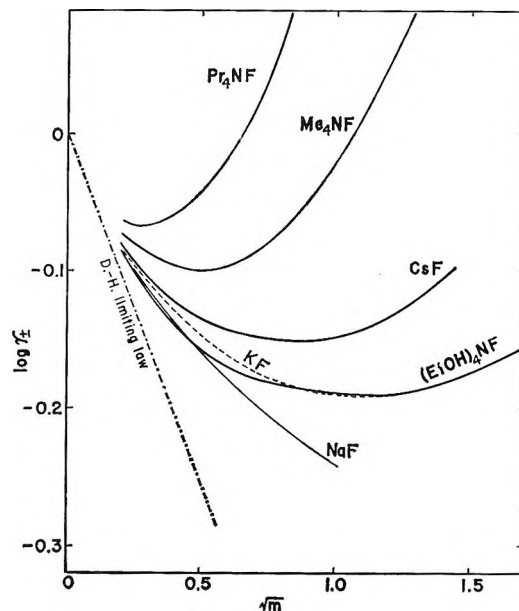


Figure 2. Plots of $\log \gamma^\pm$ vs. \sqrt{m} for $(n\text{-C}_3\text{H}_7)_4\text{NF}$, $(\text{CH}_3)_4\text{NF}$, CsF , KF , $(\text{HOC}_2\text{H}_4)_4\text{NF}$, and NaF in aqueous solutions at 25°.

Table II: Osmotic and Activity Coefficients of Tetraethanolammonium Fluoride and Bromide in Aqueous Solutions at 25°

Concn., m	$(\text{HOCH}_2\text{CH}_2)_4\text{NF}$		$(\text{HOCH}_2\text{CH}_2)_4\text{NBr}$	
	ϕ	γ^\pm	ϕ	γ^\pm
0.1	0.925	0.758	0.902	0.730
0.2	0.912	0.710	0.860	0.641
0.3	0.911	0.685	0.835	0.588
0.4	0.911	0.671	0.814	0.545
0.5	0.912	0.664	0.798	0.515
0.6	0.914	0.657	0.784	0.488
0.7	0.917	0.653	0.773	0.465
0.8	0.921	0.650	0.764	0.448
0.9	0.925	0.648	0.757	0.432
1.0	0.929	0.645	0.750	0.418
1.2	0.938	0.644	0.737	0.395
1.4	0.948	0.645	0.728	0.376
1.6	0.960	0.648	0.720	0.360
1.8	0.972	0.652	0.715	0.345
2.0	0.985	0.660	0.711	0.333
2.2	0.997	0.667	0.708	0.324
2.4	1.010	0.676	0.706	0.316
2.6	1.022	0.684	0.706	0.308
2.8	1.034	0.695	0.706	0.300
3.0	1.046	0.705	0.706	0.296
3.5	1.076	0.732	0.709	0.283
4.0	1.105	0.762	0.712	0.275
4.5	1.132	0.798	0.717	0.266
5.0	1.158	0.832	0.723	0.258
5.5	1.183	0.868	0.728	0.252
6.0	1.208	0.900	0.734	0.250
6.5	1.234	0.940	0.740	0.248

$\log \gamma^\pm$ are plotted against \sqrt{m} for $(\text{HO}C_2\text{H}_4)_4\text{NF}$ as well as some tetraalkylammonium fluorides and alkali fluorides for comparison. As can be seen from the figure, the activity coefficients of $(\text{HO}C_2\text{H}_4)_4\text{NF}$ are very different from those of either $(n\text{-C}_3\text{H}_7)_4\text{NF}$ or $(\text{C}_2\text{H}_5)_4\text{NF}$ but rather close to those of KF . This clearly demonstrates large differences which exist between quaternary ammonium ions with terminal methyl groups and those with terminal hydroxyl groups. The strikingly high activity coefficients of tetraalkylammonium fluorides in water have been attributed to the different structural effects of cations and anions upon water structure.⁶ In contrast to $(\text{C}_n\text{H}_{2n+1})_4\text{N}^+$ ions, the $(\text{HO}C_2\text{H}_4)_4\text{N}^+$ ion would be expected to affect the structure of water rather little since it should be able to enter into the flickering clusters of water and participate readily in the formation and disruption of the clusters. In this respect the structural effect of the F^- ion upon water is much closer to that of the $(\text{HO}C_2\text{H}_4)_4\text{N}^+$ ion than to that of the $(\text{C}_n\text{H}_{2n+1})_4\text{N}^+$ ions, and, therefore, $(\text{HO}C_2\text{H}_4)_4\text{NF}$ in water should be more stable and have lower free energy than the tetraalkylammonium fluorides. Incidentally, K^+ ion is believed to affect the structure of water very little,¹ and in this regard it appears similar to the $(\text{HO}C_2\text{H}_4)_4\text{N}^+$ ion although the size and type of these two ions are quite different.

In Figure 3, values of $\log \gamma^\pm$ are plotted against \sqrt{m} for $(\text{HO}C_2\text{H}_4)_4\text{NBr}$ and other bromides for a similar comparison. From Figure 3 one sees that the activity coefficients of $(\text{HO}C_2\text{H}_4)_4\text{NBr}$ are higher than those of either $(\text{C}_2\text{H}_5)_4\text{NBr}$ or $(\text{C}_3\text{H}_7)_4\text{NBr}$ but very much lower than those of KBr . Since tetraalkylammonium bromides and iodides have been known to possess abnormally low activity coefficients,^{7,8} the substitution of terminal methyl groups of these cations by hydroxyl groups should result in raising the low values. This expectation is borne out by our results, at least for the compound under discussion, though to considerably lesser extent than we expected. As mentioned above, the γ^\pm values of $(\text{HO}C_2\text{H}_4)_4\text{NBr}$ are much lower than those of KBr in distinct contrast to the case of the corresponding fluorides. Although the reasons for this observation are not yet clear, it is probably due to the "structural salting-in"⁸ of the cations by the bromide ions. At concentrations above 1.3 m the γ^\pm values of $(\text{HO}C_2\text{H}_4)_4\text{NBr}$ become smaller than those of $(\text{C}_3\text{H}_7)_4\text{NBr}$ in opposition to the situation at concentrations below 1.3 m . This may be attributed to the association of $(\text{HO}C_2\text{H}_4)_4\text{NBr}$ through hydrogen bonding of the cations. Similar inference can be drawn from the data of the molal volumes of this salt which will be discussed in the following section.

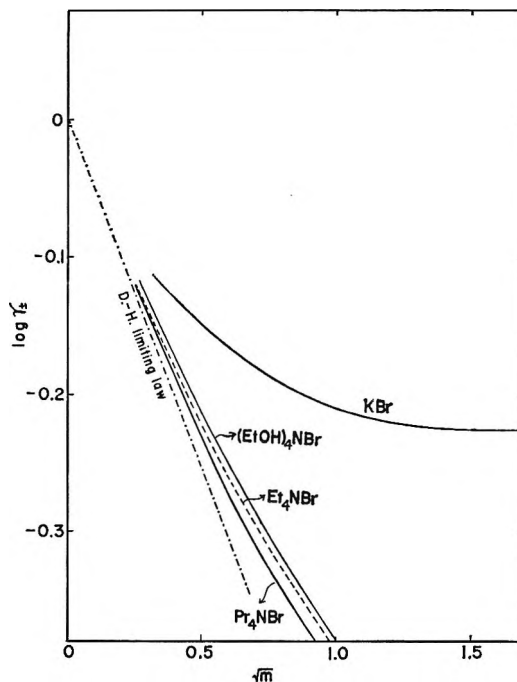


Figure 3. Plots of $\log \gamma^\pm$ vs. \sqrt{m} for KBr , $(\text{HO}C_2\text{H}_4)_4\text{NBr}$, $(\text{C}_2\text{H}_5)_4\text{NBr}$, and $(n\text{-C}_3\text{H}_7)_4\text{NBr}$ in aqueous solutions at 25° .

B. Apparent and Partial Molal Volumes. The apparent molal volumes, φ_2 , were calculated from the density data by the equation

$$\varphi_2 = \frac{1}{m} \left(\frac{1000 + mM_2}{\rho} - \frac{1000}{\rho_0} \right) \quad (4)$$

where ρ_0 is the density of pure water; M_2 , the molecular weight of the salt; ρ , the density of the solution. The partial molal volumes, \bar{V}_2 , were computed from φ_2 by the equation

$$\bar{V}_2 = \varphi_2 + \left[\frac{1000 - c\varphi_2}{2000 + c\sqrt{c} \frac{d\varphi_2}{d\sqrt{c}}} \right] \sqrt{c} \frac{d\varphi_2}{d\sqrt{c}} \quad (5)$$

where c is the molar concentration. These values for the two salts at 25° are listed in Table III. In Figures 4 and 5 the values φ_2 and \bar{V}_2 are plotted against \sqrt{c} for $(\text{HO}C_2\text{H}_4)_4\text{NF}$ and $(\text{HO}C_2\text{H}_4)_4\text{NBr}$, respectively. For both salts φ_2 seems to vary linearly with \sqrt{c} in the low concentration range (c , 0.1–0.6) following the equation

(6) W. Y. Wen, S. Saito, and C. M. Lee, Abstracts of Papers, Division of Physical Chemistry, 148th National Meeting of the American Chemical Society, Chicago, Ill., Sept. 1964, p. 35V. (Details will be published shortly.)

(7) S. Lindenbaum and G. E. Boyd, *J. Phys. Chem.*, **68**, 911 (1964).

(8) H. S. Frank, *ibid.*, **67**, 1554 (1963).

$$\varphi_2 = \varphi_2^0 + S_v \sqrt{c} \quad (6)$$

where φ_2^0 ($= \bar{V}_2^0$) is the φ_2 at infinite dilution and S_v is the limiting slope. Values of \bar{V}_2^0 obtained from these plots are 150.6 ml./mole for $(\text{HOC}_2\text{H}_4)_4\text{NF}$ and 176.9 ml./mole for $(\text{HOC}_2\text{H}_4)_4\text{NBr}$, respectively. S_v values are 3.0 for the fluoride and 1.4 for the bromide, respectively, in units of $(10 \text{ ml./mole})^{3/2}$.

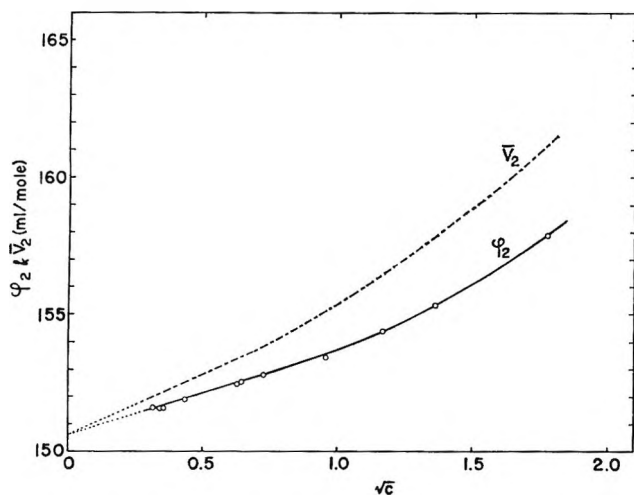


Figure 4. Apparent and partial molal volumes of $(\text{HOC}_2\text{H}_4)_4\text{NF}$ in aqueous solutions at 25° plotted against \sqrt{c} where c is the molar concentration.

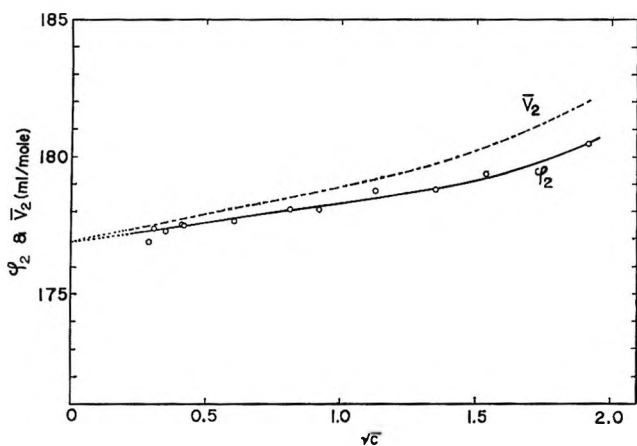


Figure 5. Apparent and partial molal volumes of $(\text{HOC}_2\text{H}_4)_4\text{NBr}$ in aqueous solutions at 25° plotted against \sqrt{c} where c is the molar concentration.

Table III: Apparent and Partial Molal Volumes of Two Tetraethanolammonium Halides in Aqueous Solutions at 25° (Unit: ml./mole)

Concn., m	$(\text{HOC}_2\text{H}_4)_4\text{NF}$		$(\text{HOC}_2\text{H}_4)_4\text{NBr}$	
	φ_2	\bar{V}_2	φ_2	\bar{V}_2
0.1	151.5	151.9	177.3	177.5
0.2	151.9	152.6	177.5	177.8
0.4	152.4	153.4	177.7	178.1
0.6	152.8	154.0	177.9	178.3
0.8	153.2	154.5	178.0	178.6
1.0	153.5	155.0	178.1	178.8
1.5	154.1	156.0	178.4	179.1
2.0	154.7	157.0	178.6	179.4
2.5	155.3	157.8	178.8	179.7
4.0	156.5	159.5	179.4	180.4
10.0	180.5	181.8

S_v would not apply to $(\text{HOC}_2\text{H}_4)_4\text{NF}$ and $(\text{HOC}_2\text{H}_4)_4\text{NBr}$. The S_v values of 3.0 and 1.4 obtained for the two salts indicate that the range of our measurements has not extended to a dilute enough region to conform to the theoretical value. It also shows that there are at least two ranges of concentration in which the plot of φ_2 vs. \sqrt{c} can be linear with different slopes. Similar remarks can be made about the S_v values of several tetraalkylammonium bromides reported by us previously.³

In view of this, the \bar{V}_2^0 values found above may be slightly in error, but not too much because of the fact that \bar{V}_2^0 for the $(\text{HOC}_2\text{H}_4)_4\text{N}^+$ ion, obtained by subtracting anionic volume, is 152.2 ml./mole from the fluoride,¹¹ which is in a reasonable agreement with a value of 151.2 ml./mole obtained from the bromide.¹¹ The values of \bar{V}_2^0 obtained by the above-mentioned procedure for $(\text{C}_2\text{H}_5)_4\text{NBr}$ and $(\text{C}_3\text{H}_7)_4\text{NBr}$ ³ are included in Table IV for comparison. S_v values for these salts in the concentration range of 0.1 to 0.6 M are also given in this table. Figure 6 gives a composite plot of \bar{V}_2^0 against \sqrt{c} for the three bromides. It is noteworthy that \bar{V}_2^0 of $(\text{HOC}_2\text{H}_4)_4\text{NBr}$ is rather small, and its S_v is positive when compared with the respective quantities of $(\text{C}_3\text{H}_7)_4\text{NBr}$. The value of \bar{V}_2^0 for $(\text{HOC}_2\text{H}_4)_4\text{N}^+$ is peculiarly small, as a matter of fact, almost as small as that for $(\text{C}_2\text{H}_5)_4\text{N}^+$. It appears as if the OH groups were occupying hardly any volume, an observation which we are not ready to interpret at present.

(9) O. Redlich and D. M. Meyer, *Chem. Rev.*, **64**, 221 (1964).

(10) L. G. Hepler, J. M. Stokes, and R. H. Stokes, *Trans. Faraday Soc.*, **61**, 20 (1965).

(11) \bar{V}_2^0 values for F^- and Br^- ions are taken as -1.6 and 25.7 ml./mole, respectively. See J. Padova, *J. Chem. Phys.*, **39**, 1552 (1963).

According to the Debye-Hückel theory, the limiting slope of apparent molal volume for any 1-1 electrolytes should be 1.868 at 25° as emphasized recently by Redlich and Meyer.⁹ Since this value of S_v has also been confirmed for $(\text{CH}_3)_4\text{NBr}$ by Hepler, Stokes, and Stokes,¹⁰ there is no reason why the same value of

Table IV: Partial Molal Volumes at Infinite Dilution and the Limiting Slopes^a at 25°

Compd.	\bar{V}_2^0 , ml./mole	S_v , (10 ml./mole) ^{3/2}
(HOC ₂ H ₄) ₄ NBr	176.9	1.4
(C ₂ H ₅) ₄ NBr ³	175.3	-3.3
(C ₃ H ₇) ₄ NBr ³	240.8	-6.0

^a Obtained from an extrapolation of experimental data on the concentration range of 0.1 to 0.6 *M*.

The positive S_v value for (HOC₂H₄)₄NBr in the indicated concentration range can be taken as a manifestation of its hydrophilic nature in contrast to the negative values for (C₂H₅)₄NBr and (*n*-C₃H₇)₄NBr which have been interpreted as indicative of their hydrophobic character.³ As far as S_v values are concerned, alkali halides also give positive values in the concentration range under discussion, but owing to its large size, the (HOC₂H₄)₄N⁺ ion should show little electrostrictive effect in contrast to the much smaller alkali metal ions. We think, therefore, that perhaps some interionic hydrogen bonds as well as hydrophobic bonds among (HOC₂H₄)₄N⁺ ions may be formed at higher concentrations and result in poorer packing with water molecules and cause the φ_2 to increase with concentration. However, since the electrostrictive effect of Br⁻ ions will also contribute to S_v , the above speculation about the cations is made plausible only in view of the low activity coefficients of this salt, particularly above 1.3 *m*. As reported above, (HOC₂H₄)₄NF has higher activity coefficients indicating relatively little association in aqueous solutions. The large value of S_v observed for the fluoride may, therefore, be taken to indicate a strong electrostrictive effect of F⁻ ions on water.¹²

In conclusion, present studies offer support to the contention that the substitution of terminal methyl groups with hydroxyl groups will diminish the peculiarities of quaternary ammonium ions in water. In other words, cations with terminal hydroxyl groups will behave more normally and affect the structure of water less than the corresponding tetraalkylammonium ions. From heat capacity measurements, Frank and Wen have found that (HOC₂H₄)₄NBr in water gives almost no extra apparent molal heat capacity,¹³ as opposed to the large excess observed for (*n*-C₄H₉)₄NBr.¹ In addition, they have found by viscosity

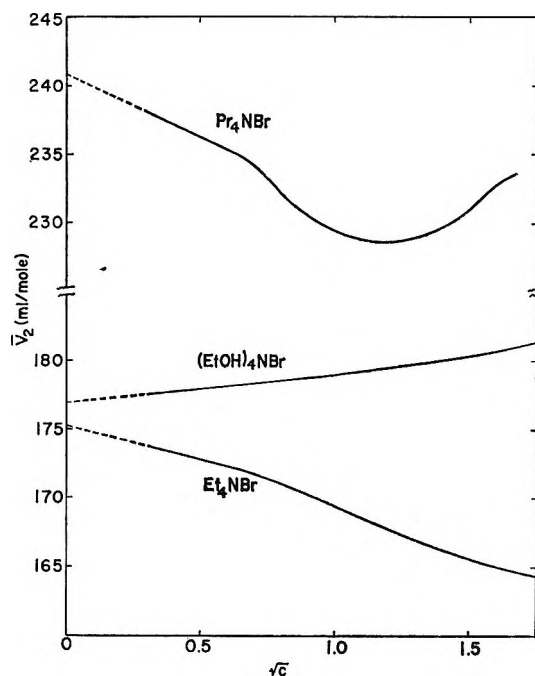


Figure 6. Partial molal volumes of (HOC₂H₄)₄NBr, (C₂H₅)₄NBr, and (*n*-C₃H₇)₄NBr in aqueous solutions at 25° plotted against \sqrt{c} where *c* is the molar concentration.

measurements that, for (HOC₂H₄)₄NBr in aqueous solutions, the *B* coefficient in the Jones-Dole equation and also dB/dT , are quite small when compared with those of (*n*-C₃H₇)₄NBr.¹³ Price and Agar observed low heats of transport for the (HOC₂H₄)₄N⁺¹⁴ and (CH₃)₃NC₂H₄OH⁺¹⁵ ions in distinct contrast to the high values of the corresponding tetraalkylammonium ions. All these results support the idea that the solutes containing hydrogen-bonding groups like OH do not alter water structure much, if at all.

Acknowledgments. We wish to thank Professor Benton B. Owen for the technical assistance at the initial stage of our isopiestic investigation. This research is supported by the U. S. Department of the Interior, Office of Saline Water, through Grant No. 14-01-0001-306 and 14-01-0001-456.

(12) S_v values for KF, KCl, KBr, and KI are 3.35, 2.33, 1.94, and 1.56, respectively, in the concentration range under discussion.

(13) H. S. Frank and W. Y. Wen, unpublished results.

(14) C. D. Price, Ph.D. Thesis, Cambridge University, 1961.

(15) J. N. Agar, *Advan. Electrochem. Electrochem. Eng.*, 3, 96 (1963).

X-Ray and Thermodynamic Studies of the Absorption of Hydrogen by Gold-Palladium Alloys

by Arnulf Maeland and Ted B. Flanagan

Department of Chemistry, University of Vermont, Burlington, Vermont (Received May 10, 1965)

At low gold contents, gold-palladium alloys form two phases upon absorption of hydrogen. Two-phase formation ceases above approximately 17 atomic % gold (25°). In the two-phase region, the enthalpy and free energy of absorption become more negative in direct proportion to the gold content. Lattice parameters of the alloys have been determined at various hydrogen contents. It is found that the rate of increase of lattice parameter with hydrogen content is independent of the gold content of the alloy. Equilibrium solubilities of hydrogen (25°, 740 mm.) have been determined as a function of gold content.

Introduction

The investigation of the absorption of hydrogen by palladium-rich alloys has been receiving renewed attention. One reason for this interest is that the method employed here has been shown to be an effective way to obtain data on these systems below 100°, where conventional gas phase techniques suffer from the problem of slow or completely inhibited rates of absorption due to surface contaminants. In the technique employed here, absorption proceeds from hydrogen-stirred aqueous solutions where it appears that the surface activity necessary for the absorption process can be maintained more readily than with conventional gas phase techniques. The course of absorption is followed by the electrode potential of the wire specimen and its resistivity.¹⁻⁴ For pure palladium the potential-time curve shows an initial decrease to 50 ± 1 mv. (25°), remains constant at this value, and then slowly falls to zero. The region of constant potential has been shown to correspond to the $\alpha \rightarrow \beta$ transformation while the potential changes before and after the plateau potential correspond to absorption of hydrogen into the α - and β -phase, respectively.^{4,5}

Using this technique, or similar techniques, data have been obtained on the platinum-palladium^{6,7} and silver-palladium⁸⁻¹¹ systems. The main interest in these palladium-rich alloys centers about how the nature of the added metal influences the absorption characteristics of palladium; more specifically, it

can be asked whether the model of absorption in which electrons from absorbed hydrogen atoms enter the partially empty d-band of palladium¹² is capable of explaining the observed behavior of palladium-rich alloys. Gold is believed to donate a 6s electron to the d-band of palladium.¹² Thus, in this ternary system both hydrogen and gold should function as donators of electrons to the d-band of palladium.

The absorption of hydrogen by the gold-palladium system has been somewhat less investigated than those mentioned above, and the available data are in disagreement in many ways. With regard to hydrogen solubility in gold-palladium alloys, Berry¹³ reported that the "equilibrium" solubility decreases uniformly with

- (1) M. Breiter, H. Kammermair, and C. A. Knorr, *Z. Elektrochem.*, **58**, 703 (1954).
- (2) S. Schuldiner and J. P. Hcare, *J. Chem. Phys.*, **23**, 1551 (1955).
- (3) T. B. Flanagan and F. A. Lewis, *ibid.*, **29**, 1417 (1959).
- (4) T. B. Flanagan and F. A. Lewis, *Trans. Faraday Soc.*, **55**, 1400, 1409 (1959).
- (5) P. C. Aben and W. G. Burgers, *ibid.*, **58**, 1989 (1962).
- (6) A. W. Carson, T. B. Flanagan, and F. A. Lewis, *ibid.*, **56**, 363, 371, 1332 (1960).
- (7) A. Maeland and T. B. Flanagan, *J. Phys. Chem.*, **68**, 1419 (1964).
- (8) F. A. Lewis and W. H. Skurter, *Naturwiss.*, **47**, 177 (1960).
- (9) F. A. Lewis, *Platinum Metals Rev.*, **5**, 21 (1961).
- (10) S. D. Axelrod and A. C. Makrides, *J. Phys. Chem.*, **68**, 2154 (1964).
- (11) A. C. Makrides, *ibid.*, **68**, 2160 (1964).
- (12) N. Mott and H. Jones, "Theory of Metals and Alloys," Clarendon Press, Oxford, 1936.
- (13) A. J. Berry, *J. Chem. Soc.*, **99**, 463 (1911).

increasing gold content to zero at ~ 75 atom % Au (room temperature). Schniedermann¹⁴ reported similar findings. Mundt,¹⁵ however, referring to room temperature experiments of F. Krüger and J. Krzoska, stated that the solubility increases with increase of gold content to a maximum and then declines rapidly. All of these results¹³⁻¹⁵ were obtained by electrolytic introduction of hydrogen and an unambiguous criterion for the establishment of equilibrium was lacking.⁶

Conflicting X-ray results have also been reported on hydrogen containing gold-palladium alloys. According to Mundt,¹⁵ the two-phase region extends at room temperature to close to 47 atom % gold.^{16a} Benard and Talbot,^{16b} on the other hand, reported that when an alloy containing 15.3 atom % gold was charged with hydrogen electrolytically, the lattice parameter varied continuously from 3.91 Å. before charging, to 4.01 Å. when fully charged. This implies single-phase behavior and is, therefore, in contradiction to Mundt's results.

More recently, Hoare and co-workers¹⁷ found that the two-phase potential for absorption was relatively unchanged from that of pure palladium at small gold contents, <12% gold, and then steadily declined to attain zero at approximately 50% gold. In contrast to the above studies on massive alloys, Tverdovsky and co-workers¹⁸ have examined the absorption of hydrogen by dispersed alloys of large surface area. Results from this technique differ from results on massive alloys.⁶

In view of the conflicting results and a desire to obtain more detailed results for comparison to theories of absorption, a reinvestigation of the absorption of hydrogen by a series of gold-palladium alloys has been undertaken.

Experimental Section

The gold-palladium alloys were employed in the form of wires 0.012 and 0.025 cm. in diameter and were obtained from Engelhard Industries, Inc. The samples were prepared from 99.99% purity gold and palladium and were melted under argon. The analysis was performed by Engelhard Industries, Inc. X-Ray patterns revealed that the alloys were face-centered cubic and showed no evidence of long-range order.

Absorption runs were performed as previously described^{6,7} except that one significant change in technique was employed. The hydrogen gas stream was diluted with helium and since the rate has been shown to be proportional to the hydrogen partial pressure,^{6,19} the rate could be slowed down as much as desired. This technique has been employed to determine thermodynamic data in the α -phase of pure palladium.²⁰

Slow absorption allowed for the establishment of more accurate and reproducible potentials and was especially useful for the determination of the potential of the two-phase region in those alloys which have such a region over only a very limited concentration range. The potentials were measured with respect to an Ag-AgCl electrode in the same dilute HCl solution. In general, even at 1 atm. of hydrogen pressure, potentials with respect to a Ag-AgCl electrode were more reliable than potentials measured with respect to a reference Pt-H₂ electrode especially during the early stages of absorption because errors, which could be traced to the reduction of the pressure of H₂, were caused by the introduction of the specimen, etc.

The reaction vessel was maintained to $\pm 0.1^\circ$ by a surrounding water bath. For the determination of heats of absorption, the temperature was varied (0-50°) and the plateau electrode potential was determined by making a separate absorption run at each temperature. The potentials determined from the Ag-AgCl electrode were converted to the standard potential by establishing the potential of Ag-AgCl vs. Pt-H₂ (1 atm.) independently at each temperature. This procedure proved more reliable than measurement of the HCl concentration and correction of concentrations to activities, although in most cases results were identical to within ± 0.1 mv. using either procedure. X-Ray studies of specimens of varying hydrogen content were made as described previously.⁷

Hydrogen content of specimens was determined by vacuum degassing or less directly from the resistance employing relationships established between R/R_0 and H/M , where R and R_0 represent the resistance of the specimen at any hydrogen content and the hydrogen-free resistance, respectively, and H/M is the atomic ratio of hydrogen to metal; these relationships were also established by vacuum degassing. A rapid

(14) J. Schniedermann, *Ann. physik*, [5]13, 761 (1932).

(15) H. Mundt, *ibid.*, [5]19, 721 (1934).

(16) (a) This is a good occasion in which to clear up some confusion which has existed in the literature for a number of years with regard to Mundt's paper (see, for example, D. P. Smith, "Hydrogen in Metals," University of Chicago Press, Chicago, Ill., 1948). There must be a mistake in the headings of columns 1 and 2 in Table I of his results; the headings should be interchanged. If column 1 is changed to read atomic per cent rather than weight per cent, and column 2 is changed to read weight per cent, the calculated lattice parameters are in close agreement with values observed elsewhere (A. Maeland and T. B. Flanagan, *Can. J. Phys.*, 42, 2364 (1964)) and the deviations from Vegard's law are small. (b) J. Benard and J. Talbot, *Compt. rend.*, 222, 493 (1946).

(17) J. P. Hoare, G. W. Castellan, and S. Schuldiner, *J. Phys. Chem.*, 62, 1141 (1958).

(18) Z. Vert and I. Tverdovsky, *Zh. Fiz. Khim.*, 28, 317 (1954); I. Tverdovsky and Z. Vert, *Dokl. Akad. Nauk SSSR*, 88, 305 (1953).

(19) R. J. Fallon and G. W. Castellan, *J. Phys. Chem.*, 64, 4 (1960).

(20) J. W. Simons and T. B. Flanagan, *ibid.*, 69, 3581 (1965).

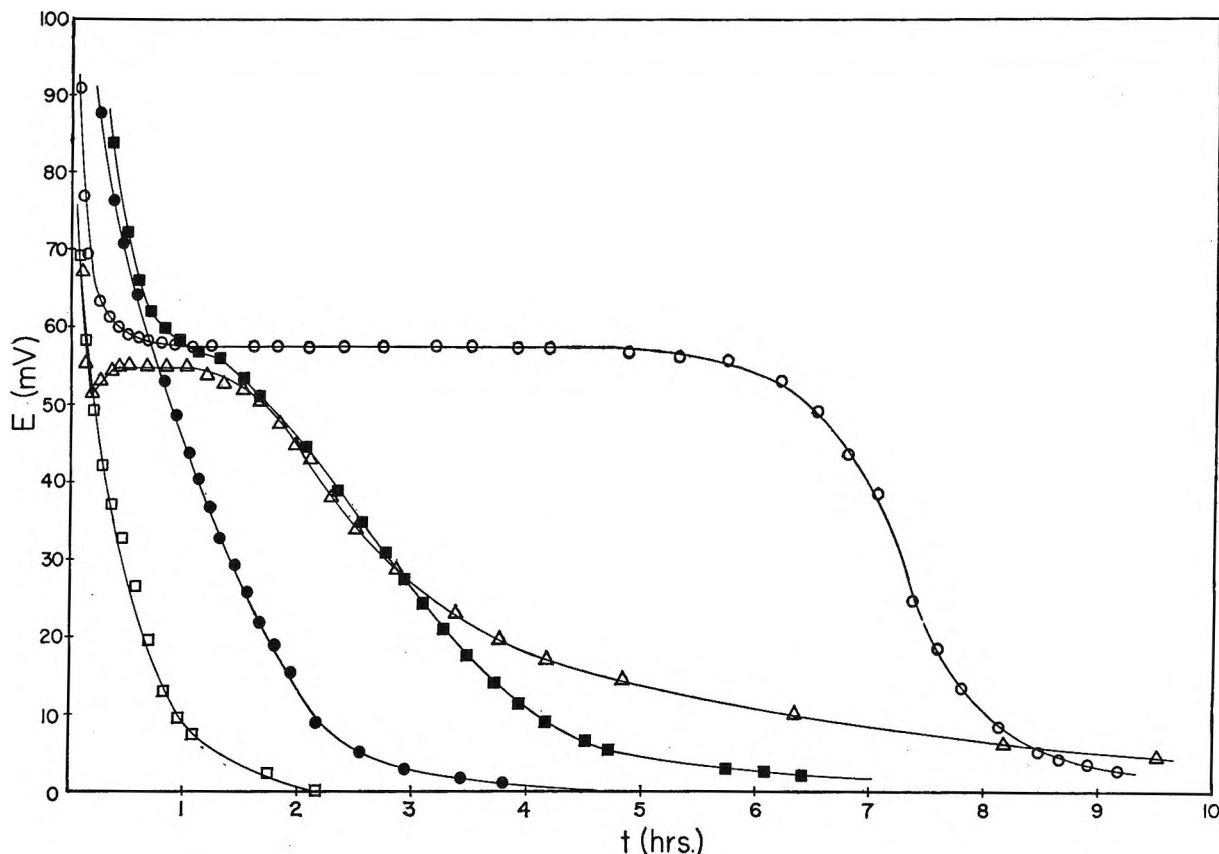


Figure 1. Potential-time curves (25°) for a series of gold-palladium alloys: \square , 35.07% Au; \bullet , 26.48% Au; \blacksquare , 18.80% Au; \circ , 15.26% Au; \triangle , 8.70% Au. Note the well-defined invariant electrode potential region for the 15.26% alloy obtained by the slow absorption technique. By contrast, the run using pure H_2 (the 8.70% alloy) shows only a limited two-phase region with respect to time.

convenient method of degassing the samples proved to be to pass a current directly through the specimens *in vacuo* until they reached a dull red color. This heating was sufficient to remove all of the hydrogen from the specimens.

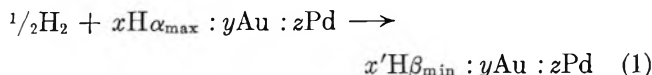
Results and Discussion

E vs. Time Plots and Thermodynamic Parameters of the Two-Phase Region. Absorption runs were made in dilute HCl solutions ($<0.04 N$) and the course of absorption was followed by changes in relative resistance, R/R_0 , and electrode potential, E , of the specimen as a function of time. A series of such runs is shown in Figure 1 (25°). The invariant electrode potential region is indicative of the coexistence of two phases. The two phases will be termed the low content, α -, and high content, β -, phase in analogy with pure palladium. The $E-t$ plots of the higher gold content alloys do not show a well-defined invariant electrode potential region, e.g., the 18.80% gold alloy (atom per cent) (Figure 1). The absence of an invariant electrode potential region was confirmed by performing

several very slow absorption runs with the 18.80% alloy and a plateau was not observed; however, the shoulder observed in the curve raised the question of whether a very small two-phase region is present which cannot be detected directly from the potential behavior, e.g., a plot of dE/dt vs. t shows a minimum at 59 mv. which is a reasonable value if two phases formed. Detailed X-ray analysis on the 0.012-cm. diameter specimen did not reveal the presence of a second phase at several H contents in the vicinity of the shoulder. It is concluded from the shape of the $E-t$ curve that it resembles an isotherm characteristic of one closely above the critical temperature. The 15.26% gold alloy exhibited two phases upon X-ray analysis. Thus these results disagree with the conclusions of Mundt¹⁵ and Benard and Talbot^{16b} although it should be pointed out that it is not surprising that the latter workers missed detecting the second phase because the region of coexistence of two phases in a 15.3% gold alloy is quite limited, i.e., $H/M = 0.09$ to 0.21 (25°).

The invariant electrode potential is a measure of the free energy change (which is closely identical with a

standard free energy change since $a_{H_2} \sim 1$) for the reaction



where x and x' represent the number of H atoms characteristic of α_{\max} and β_{\min} , respectively, and y and z represent the number of atoms of Au and Pd in the alloy under consideration. The reproducibility of the two-phase potential for a typical alloy can be seen in Figure 2; the high degree of reproducibility can be attributed to the slow absorption technique.

Results presented in terms of $\Delta\bar{G}$ are shown in Figure 3 and each determination represents the average of at least three separate determinations, some of which were performed on specimens of different diameters. It may be seen that the free energy of absorption becomes more negative in a linear manner as the alloy's gold content increases. The results of Hoare, *et al.*,¹⁷ ($30 \pm 1^\circ$) are also shown and an important discrepancy can be seen to exist between the two sets of data. The reason for the discrepancy

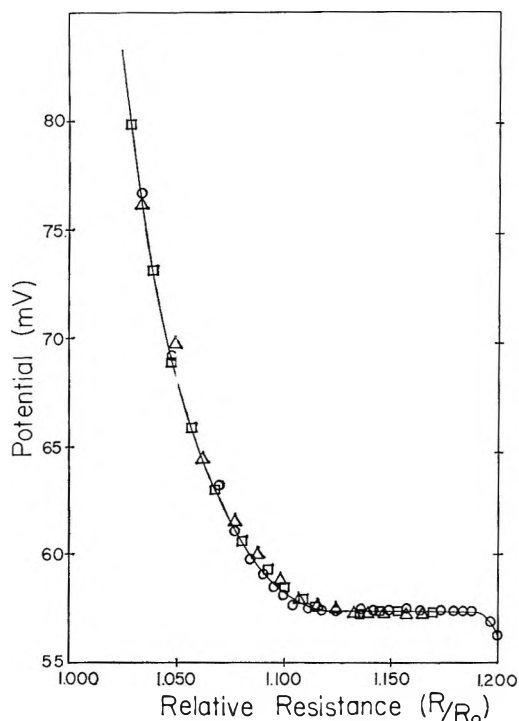


Figure 2. Electrode potentials and relative resistances for three slow absorption runs at 25° (15.26% alloy). Data are plotted with R/R_0 as the abscissa rather than time because the large range in time would make the figure unwieldy. The limiting R/R_0 values in the two-phase region correspond to $H/M = 0.09$ to 0.22 . Partial pressures of hydrogen: \circ , 0.1 atm.; \square , 0.15 atm.; \triangle , 0.2 atm.

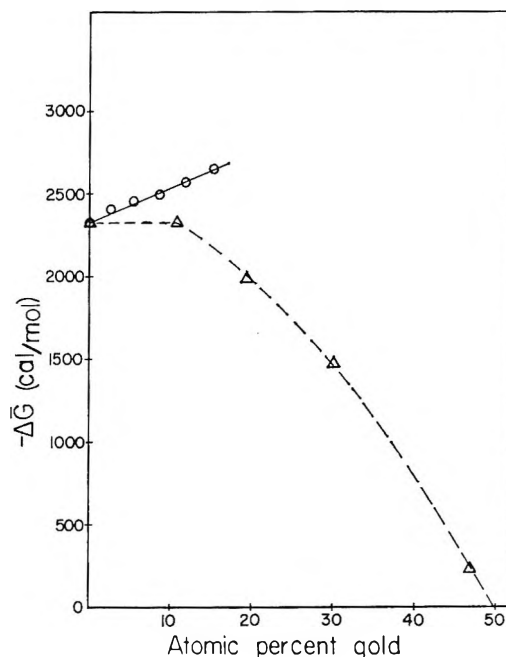


Figure 3. Free energy of absorption in the two-phase region as a function of gold content (atom per cent): \circ , present results (25°); \triangle , calculated from ref. 17 ($30 \pm 1^\circ$).

between the two sets of data is not clear; however, the present data are more consistent with other experimental results obtained here (see below). One can also argue that since there is an electronic similarity between the gold-palladium and the silver-palladium system, *i.e.*, gold and silver both donate s-electrons to the d-band of palladium,¹² the gold system, like the silver system,⁸⁻¹¹ should show an increase in negative free energy upon absorption. By contrast, the negative free energy of absorption (two-phase) decreases with platinum content in the platinum-palladium system⁶ and platinum does not donate an s-electron to the d-band of palladium.

From the variation of the two-phase potential with temperature, the corresponding enthalpy of absorption can be determined from the Gibbs-Helmholtz equation. Results are compared to values for silver in Figure 4. The increase in exothermicity is small but experimentally well established. As in the silver system, there is no evidence of a maximum in either the free energy (Figure 3) or enthalpy (Figure 4).

The entropy change upon absorption was determined from $\Delta\bar{G}$ and $\Delta\bar{H}$ and may be seen in Table I. The values of $\Delta\bar{S}$ are substantially independent of gold content, therefore the $\Delta\bar{G}$ changes can be attributed to changes in the energetics of absorption, *i.e.*, $\Delta\bar{H}$.

X-Ray Studies of Hydrogen-Containing Gold-Palladium Alloys. Lattice parameters of α_{\max} and β_{\min}

Table I: Some Properties of the H-Au-Pd System in the Two-Phase Region (25°, ~1 atm.)

Au, atom %	$-\Delta\bar{G}$, cal./mole of H ₂	$-\Delta\bar{H}$, cal./mole of H ₂	$-\Delta\bar{S}$, e.u.	$a\alpha_{\max}$, Å.	$a\beta_{\min}$, Å.	(H/M) α_{\max}	(H/M) β_{\min}
2.77	2409	9334	23.2	3.9000	4.0218	0.021	0.52 ^a
5.66	2464	9503	23.6	3.9064	4.012	0.033	0.46
8.70	2496	9634	23.9	3.9146	4.0040	0.040	0.40 ^a
11.90	2565	9832	24.4	3.9240	3.9918	0.055	0.32
15.26	2644	9832	24.1	3.8418	3.9696	0.088	0.21

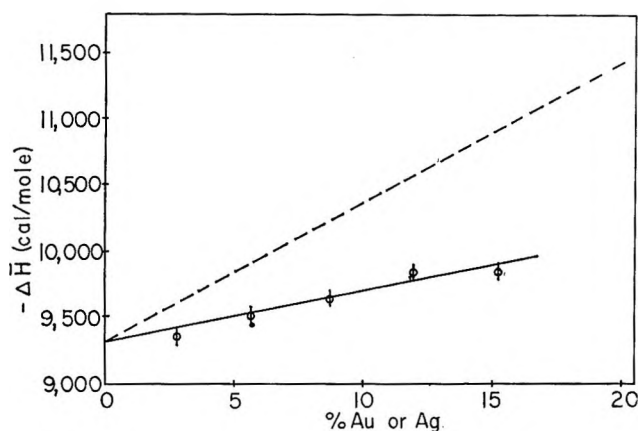
^a Estimated from Figure 6.


Figure 4. Enthalpy of absorption at 25° in the two-phase region as a function of gold content. The dotted line refers to the same quantity for the silver-palladium-hydrogen system (ref. 11).

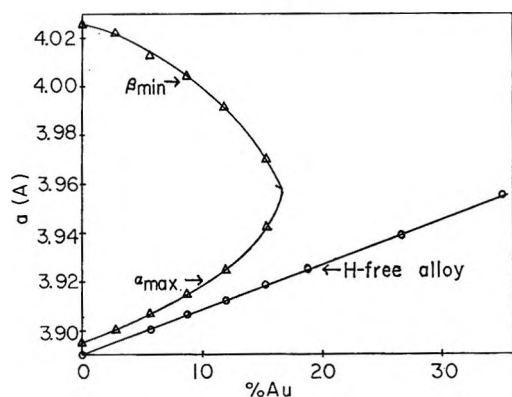


Figure 5. Lattice parameters at 25° for hydrogen-free alloys and for α - and β -phases in two-phase region.

are shown in Table I and Figure 5. The latter shows that two-phase formation (25°) ceases at gold contents >17% (25°). The closely symmetrical character of Figure 5 may be contrasted to the more asymmetric relationship obtained for the platinum-palladium system⁶; the silver-palladium system appears to resemble the gold-palladium system rather than the plati-

num system although the available results for silver-palladium disagree at the α_{\max} boundary.^{10,21}

The compositions of some of the phase boundaries were determined by the first appearance or disappearance of the second phase (see ref. 7 for details). Results are shown in Figure 6 where the β_{\min} phase boundaries were all determined by X-ray analysis. The α_{\max} boundary of the 15.26% gold alloy was directly determined by X-rays. The α_{\max} boundaries for the 11.90 and 15.26% Au alloys were found by the extrapolation of α -phase lattice constants against H content to the two-phase α_{\max} lattice parameter; the values of H/M where the extrapolated values intersect the two-phase α_{\max} parameter are taken as the composition of α_{\max} . The change of slope of the R/R_0 vs. H/M relationship in the low content region can also be associated with the phase boundary⁷; the α_{\max} boundaries for the other alloys shown in Figure 6 were determined in this way. The three different experimental approaches were used for the 15.26% alloy and the same results were obtained for α_{\max} within experimental error of each approach.

X-Ray studies of the pure α - and β -phases were also made and are shown in Figure 7 together with the two-phase values. The hydrogen contents shown in Figure 7 were determined from R/R_0 -H/M relationships established in this laboratory.

It may be seen that the lattice parameters increase approximately linearly with the H content of each alloy investigated and also for pure palladium, the values of which (in excess of β_{\min}) were determined in this research. However, there is a discontinuity observed in pure palladium at high H content, 0.58, which corresponds to the composition of β_{\min} ; however, this is believed to be coincidental because there is no corresponding discontinuity in, for example, the 15.26 or 11.90% alloys, at the β -phase boundary. Tsuchida²¹ has observed similar discontinuities in H absorption by the silver-palladium system and these were as-

(21) T. Tsuchida, *J. Phys. Soc. Japan*, **18**, 1016 (1963).

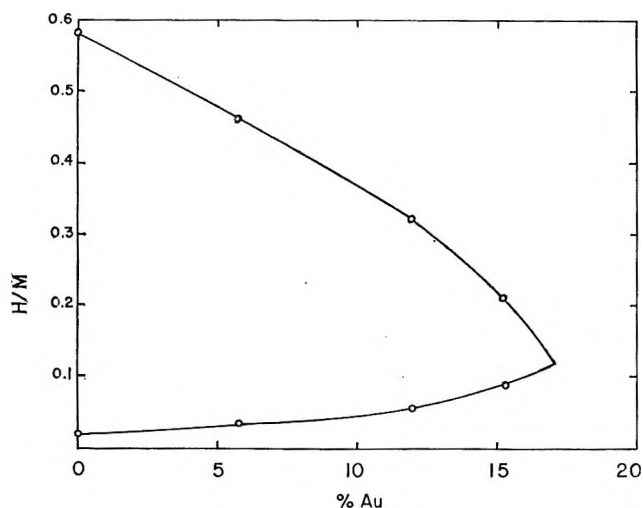


Figure 6. Phase boundaries of the hydride phases at 25° for some Au-Pd alloys.

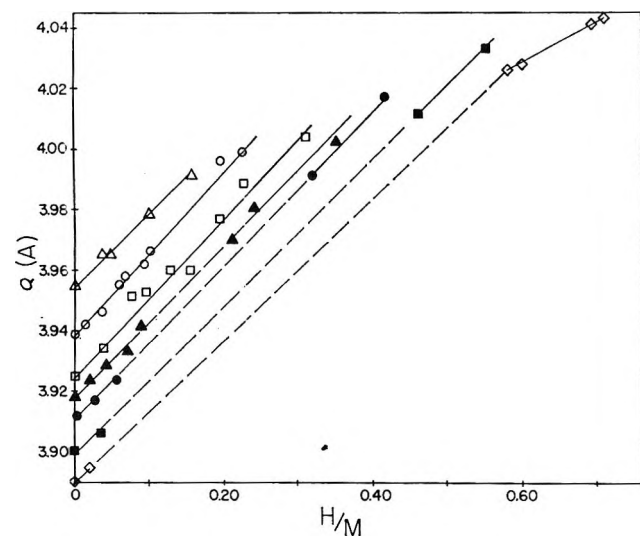


Figure 7. Lattice parameters as a function of hydrogen contents (H/M): \diamond , pure Pd; \blacksquare , 5.66% Au; \bullet , 11.90% Au; \blacktriangle , 15.26% Au; \square , 18.80% Au; \circ , 26.48% Au; \triangle , 35.37% Au.

sociated with filling of the d-band of palladium since the position of the discontinuity corresponded to the disappearance of paramagnetism. Such a decrease in slope is consistent with the greater cohesion expected when more s electrons become available.¹²

Besides showing a linear increase in lattice parameter with H content, the slopes (Figure 7) are all comparable; this indicates that the expansion is not influenced by the number of holes in the d-band (until it is full) nor by short-range interactions between hydrogen and gold atoms. This indicates, at least as

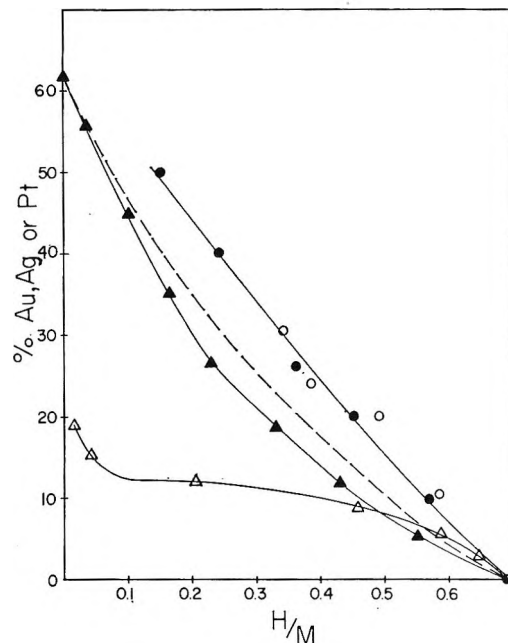


Figure 8. Equilibrium solubilities of hydrogen (25°, ~ 1 atm.) in some alloys of palladium: \triangle , Pt-Pd (ref. 6); \bullet , \circ , Ag-Pd (ref. 8 and 11); \blacktriangle , Au/Pd (740 ± 5 mm.) this work; ---, (ref. 13).

for as the lattice parameter is a criterion, that gold atoms are behaving just like palladium atoms in the lattice. This lends support to the rigid-band model.²²

Equilibrium Solubilities of Hydrogen in Gold-Palladium Alloys (25°, ~ 1 atm.). Figure 8 shows the final equilibrium solubilities of hydrogen (25°, 740 ± 5 mm.) as a function of gold content. The contents were determined by direct degassing analysis and the criterion of equilibrium is 0-mv. potential with respect to a Pt/ H_2 (1 atm.). It is seen that the solubility behavior is similar to the silver-palladium rather than the platinum-palladium system. Results are comparable, but not identical, to those obtained by Berry.¹³ There is no evidence of a maximum in solubility as suggested by Mundt.¹⁵ The large solubility in the absence of the formation of a second phase in alloys above $\sim 17\%$ gold is noteworthy.

Conclusions

The detailed hydrogen absorption behavior of the gold-palladium system has many features in common with the silver-palladium system. The differences which are appreciable in degree, but not in kind, probably have their origin in detailed differences in the band

(22) *E.g.*, F. E. Hoare, J. C. Matthews, and J. C. Walling, *Proc. Roy. Soc. (London)*, A216, 502 (1935).

structure of these alloys. A further discussion of this system will be given when research in progress on the absorption isotherms of these alloys in the α -phase are completed; these data should yield more direct information on the energetics of absorption.

Acknowledgments. Financial support by U. S. Atomic Energy Commission Contract AT(30-1)-3000 is gratefully acknowledged. We wish to thank the Engelhard Industries, Inc., for the gold-palladium alloys employed in this research.

Diffusion of Hydrogen in the α -Phase of the Palladium-Hydrogen System

by J. W. Simons and Ted B. Flanagan

Department of Chemistry, University of Vermont, Burlington, Vermont (Received May 12, 1965)

Diffusion constants for hydrogen in the low H-content α -phase of the Pd-H₂ system have been determined between 0 and 50° utilizing the technique of rapid H₂ absorption by a Pd wire specimen from an H₂-stirred aqueous solution. The electrode potential and resistivity changes of the specimen were used to determine the H concentration just beneath the surface of the wire and the total H content within the wire, respectively. An exact solution of the diffusion equation was employed to obtain values of the diffusion constant. These results, as well as the more reproducible of the higher temperature data available in the literature, are well represented by $D = 6.1 \times 10^{-3} \exp(-5990/RT)$ cm.² sec.⁻¹. Effects of nonideality, quantum mechanical tunneling, and the predictions of absolute rate theory are discussed.

Introduction

The diffusion of small interstitial atoms through a well-characterized homogeneous cubic lattice should represent a nearly experimentally ideal system for testing theories of solid-state interstitial diffusion processes. The elementary step involves the movement of an interstitial atom to an adjacent interstitial position, which on a potential energy surface is represented by passage from one minimum over a barrier to another identical minimum.

The diffusion of H atoms¹ located in octahedral interstitial positions in the face-centered cubic (f.c.c.) palladium lattice² should be among the simplest of interstitial diffusion systems, especially in the low H-content α -phase where interaction between H atoms is a minimum. The small size of an H atom should allow H-atom movement between interstitial positions to take place with a minimum of lattice perturbation and con-

sequently the approximation of representing a many-body diffusion process by a single-body process should be reasonably valid.³

The diffusion of hydrogen in palladium has been the subject of many investigations and has had a long history of irreproducibility and divergency in the results obtained by different investigators.⁴ These diverse results have been shown to be due partially to experi-

(1) For convenience *H atom* is used to describe the absorbed species, although there is a considerable amount of evidence suggesting that a more realistic description might be a proton screened by a *pile-up* of electrons from the palladium d-band.

(2) J. E. Worsham, Jr., M. K. Wilkinson, and C. B. Shull, *Phys. Chem. Solids*, **3**, 121 (1957).

(3) G. H. Vineyard, *ibid.*, **3**, 121 (1957).

(4) For a review and references prior to 1959 see W. Jost, "Diffusion in Solids, Liquids, Gases," Academic Press Inc., New York, N. Y., 1960, pp. 304-314, and R. M. Barrer, "Diffusion in and Through Solids," Cambridge University Press, London, 1951, Chapter IV.

mental conditions in which both the α -phase and the high-content β -phase were in coexistence⁵ and also due to surface contaminants that gave rise to irreproducible slow surface reactions.⁶ Davis⁶ and Katz and Gulbransen⁷ have shown that at high temperatures ($>160^\circ$) under conditions of extreme surface cleanliness reproducible α -phase diffusion constants can be obtained. Recent measurements of α -phase diffusion constants at room temperature have utilized both conventional gas phase permeation⁸ and new electrochemical permeation techniques.^{9,10}

In view of the importance of a comparison between theory and experiment for this relatively simple diffusion process and the absence of reliable data over a large temperature range, the present study of α -phase diffusion between 0 and 50° using a new method is reported.

Theory of the Method

The technique used to determine diffusion constants in the present study involved measurement of the rate of hydrogen absorption (maintained constant) by a palladium-wire specimen and determination of the concentration of dissolved hydrogen near the surface of the specimen during rapid nonequilibrium absorption experiments. The diffusion problem is well represented as radial diffusion with a constant diffusion coefficient into an infinitely long solid cylinder with zero initial concentration of diffusing material and with a constant flux of diffusing material crossing the surface of the cylinder. A general solution of the diffusion equation for these conditions has been given.¹¹ The ratio of the surface concentration to the flux at any time is given by

$$\frac{C_a}{F_0} = \frac{2t}{a} + \frac{a}{4D} - \frac{2a}{D} \sum_{n=1}^{\infty} \frac{1}{\alpha_n^2} \exp\left(-\frac{D\alpha_n^2 t}{a^2}\right) \quad (1)$$

where C_a is the surface concentration, F_0 is the flux, t is the time, D is the diffusion coefficient, a is the radius of the cylinder, and α_n terms are positive roots of the Bessel equation, $J_1(\alpha) = 0$. Curves of C_a/F_0 vs. t calculated from eq. 1 for a number of values of D are shown in Figure 1.

Experimental values of C_a/F_0 were determined for any time during an absorption experiment using the relationship

$$\frac{C_a}{F_0} = \frac{2[(R/R_0)_E - 1]}{a[d(R/R_0)/dt]} \quad (2)$$

where $(R/R_0)_E$ is the equilibrium value of the relative electrical resistivity corresponding to an actual measured value of the electrode potential, E , of the specimen and $d(R/R_0)/dt$ is the rate of increase in the actual measured

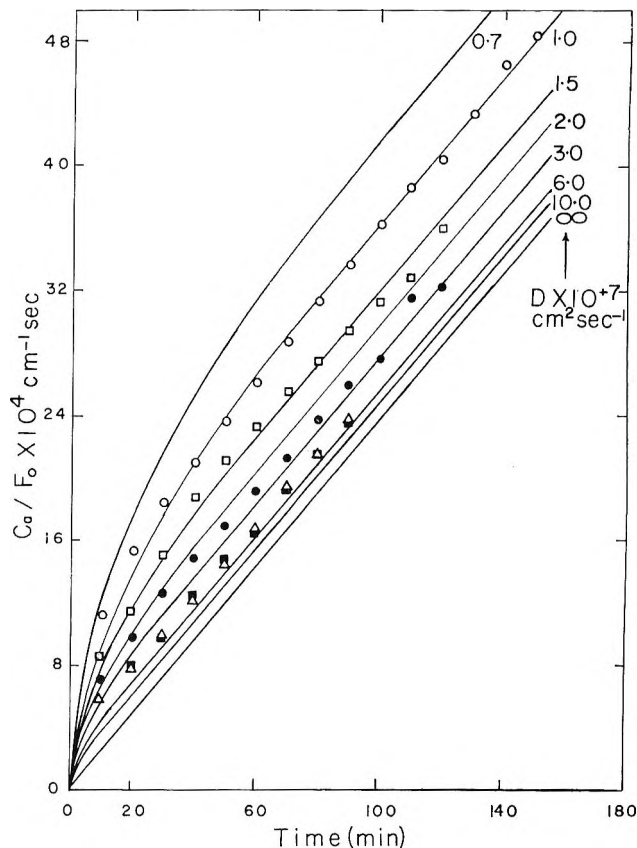


Figure 1. Theoretical curves of C_a/F_0 vs. time calculated for various values of D . Symbols represent typical experimental data: O, 0° ; □, 13° ; ●, 25° ; △, 37° ; and ■, 50° .

value of R/R_0 during a given experiment. Relationships between E and $(R/R_0)_E$ between 0 and 90° have been established in our earlier work.¹² The derivation of eq. 2 was based on the following conditions: (1) a linear relationship exists between $(R/R_0)_E$ and H content, which has been verified experimentally^{13,14}; (2)

(5) R. Ash and R. M. Barrer, *Phil. Mag.*, **4**, 1197 (1959), and references therein.

(6) W. D. Davis, Atomic Energy Commission Reports KAPL-1227 (1954) and KAPL-1375 (1955).

(7) O. M. Katz and E. A. Gulbransen, *Rev. Sci. Instr.*, **31**, 615 (1960).

(8) D. N. Jewett and A. C. Makrides, *Trans. Faraday Soc.*, **61**, 932 (1965); the authors wish to thank Dr. Makrides for a preprint of this work.

(9) M. A. V. Devanathan and Z. Stachurski, *Proc. Roy. Soc. (London)*, **A270**, 90 (1962).

(10) M. von Stackelberg and P. Ludwig, *Z. Naturforsch.*, **199**, 93 (1964).

(11) J. Crank, "Mathematics of Diffusion," Oxford University Press, London, 1956, p. 74.

(12) J. W. Simons and T. B. Flanagan, *J. Phys. Chem.*, in press.

(13) D. P. Smith, "Hydrogen in Metals," Chicago University Press, Chicago, Ill., 1948; T. B. Flanagan and F. A. Lewis, *Z. physik. Chem.*, **27**, 104 (1961); W. T. Lindsay and F. W. Pement, *J. Chem. Phys.*, **36**, 1229 (1962).

$d(R/R_0)/dt$ remains constant during an experiment, which was found to be the case; and (3) the effect of hydrogen concentration gradients, of the magnitude encountered here, on the established relationship between $(R/R_0)_E$ and the total hydrogen content is negligible. This latter assumption was verified here by calculations based on parallel path conductors for representative concentration gradients.

Experimental Section

Absorption took place from H₂-stirred dilute aqueous HCl solutions. The apparatus and procedure were similar to previous descriptions.^{12,15} A large diameter (0.1016 cm.) Pd-wire specimen was used in most experiments although a few experiments using a smaller wire (0.062 cm.) gave closely similar results. The use of a larger diameter specimen gave a wider separation of the theoretical curves in Figure 1 and also permitted nonequilibrium absorption data to be obtained over a large range of absorption rates (*ca.* sixfold). Both these factors contribute to a more accurate determination of D . Different rates of absorption were obtained by using varying compositions of hydrogen-helium mixtures at a total pressure of ~ 1 atm. It has been shown that the absorption rate from dilute HCl solutions is proportional to the partial pressure of hydrogen.^{16,17} The absorption rate was found to be constant if the hydrogen partial pressure was maintained constant and where the rate of absorption was large compared to the rate of desorption.

That β -phase hydride was not formed during an experiment was easily and unequivocally determined from the value of the electrode potential of the specimen at the end of an experiment compared to the value in the region of the coexistence of the α - and β -phases. After they were mounted, the wire specimens were washed successively in carbon tetrachloride, acetone, triply distilled water, and aqua regia, followed by several rinses with triply distilled water. Just prior to each experiment the wires were heated in air by passing a high electrical current through them until a visible green oxide layer was formed and then they were heated momentarily *in vacuo* to nearly white heat. Heating *in vacuo* removed the oxide layer. Wires prepared in this way gave reproducible results over approximately a sixfold range of absorption rates.

Results

Plots of E and R/R_0 vs. t for experiments with various partial pressures of hydrogen at 25° are shown in Figure 2. It is seen from Figure 2 that the rate, $d(R/R_0)/dt$, was constant during a given experiment and

it can be deduced from Figure 2 that the rate is proportional to the pressure of hydrogen within experimental error. It is also seen that for a given value of E the value of R/R_0 increases with decreasing rate (pressure of hydrogen), indicating as expected, a decreasing concentration gradient (small E corresponds to large surface concentration). The constancy of $d(R/R_0)/dt$ with time and its variation with the pressure of hydrogen are indirect evidence against the occurrence of slow surface reactions and indicate that irreproducibility due to slow surface reactions has been eliminated.

Values of C_a/F_0 at various times, evaluated from eq. 2 using the results in Figure 2 and previously determined $(R/R_0)_E$ vs. E relationships,¹² were found to be independent of the absorption rate and were reproducible to within $\sim 5\%$.

Results showing a similar behavior to those in Figure 2 for 25° were also obtained at 0, 13, 37, and 50°, using at least three different absorption rates in each case. The average values of C_a/F_0 at various times for each temperature are shown by the points in Figure 1. The average error in each value of C_a/F_0 is $\sim 5\%$ which introduces $\sim 20\%$ uncertainty in the D values as deduced from a comparison of the data with the theoretical curves in Figure 1.

The close correspondence between the experimental and theoretically predicted shapes of the curves in Figure 1 and the fact that they were not dependent on the rate of absorption are convincing evidence against slow surface reactions. It should be pointed out as can be seen in Figure 1 that for D values greater than approximately 4×10^{-7} cm.² sec.⁻¹ a larger uncertainty in D , than has been indicated above, results from a small uncertainty in C_a/F_0 .

An Arrhenius plot of these results is shown in Figure 3 along with some of the reportedly more reproducible of the data in the literature. The recent higher temperature results of Katz and Gulbransen⁷ and Davis⁸ virtually coincide with each other and were reported to be reproducible to within $\pm 2\%$; furthermore, since these results are not dramatically different from the other high temperature results in Figure 3, it is believed that they represent the most accurate measurements at higher temperatures.

The value of the diffusion constant at 25°, 2.5×10^{-7} cm.² sec.⁻¹, from this research is slightly less

(14) J. W. Simons and T. B. Flanagan, to be published.

(15) T. B. Flanagan and F. A. Lewis, *Trans. Faraday Soc.*, **55**, 1409 (1959).

(16) R. J. Fallon and G. W. Castellan, *J. Phys. Chem.*, **64**, 4 (1960).

(17) A. W. Carson, T. B. Flanagan, and F. A. Lewis, *Trans. Faraday Soc.*, **56**, 371 (1960).

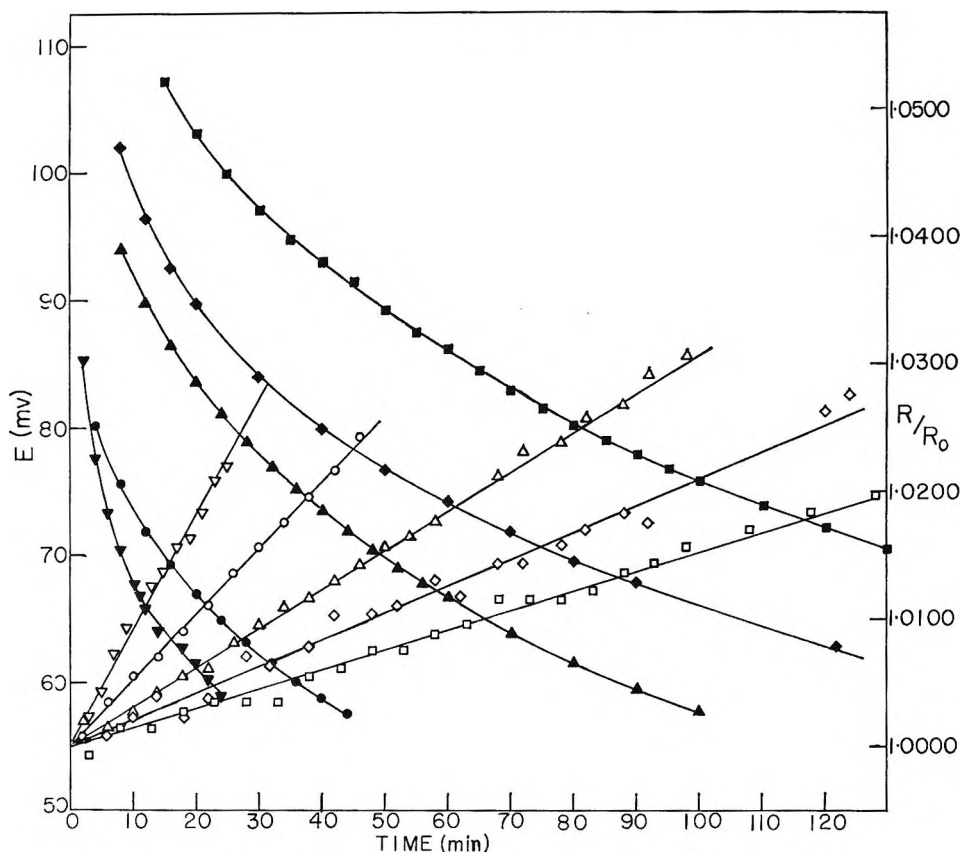


Figure 2. Plots of E and R/R_0 vs. time (25°) for five different rates of absorption, corresponding to different partial pressures of hydrogen. Solid and open symbols represent values of E and R/R_0 , respectively: ∇ , 0.76 atm. of H_2 ; \circ , 0.54 atm. of H_2 ; \triangle , 0.3 atm. of H_2 ; \diamond , 0.2 atm. of H_2 ; and \square , 0.13 atm. of H_2 .

than twice the values determined by Devanathan and Stachurski⁹ and Ludwig and von Stackelberg¹⁰ using an electrochemical technique, but the result of Makrides⁸ at 30° obtained by a conventional gas phase permeation-type experiment and recalculated here using more recent hydrogen solubility data^{12,18} is slightly larger than the present result.

It is seen from Figure 3 that the results of this study and the more reproducible of the high temperature results in the literature are well represented on a linear Arrhenius plot, for which the equation is

$$D = 6.1 \times 10^{-3} \exp(-5990/RT)$$

Discussion

In studies of diffusion of gases in metals which are based upon the rate of absorption or rate of permeation, the measured rates must reflect diffusion within the metal rather than slow reactions at the surfaces. As pointed out above, the irreproducibility encountered in past diffusion studies of the hydrogen-palladium system can be associated mainly with slow surface reactions. It should be stressed that the present tech-

nique is *not* based upon the rate of hydrogen absorption. In the present technique the rate of absorption has been demonstrated previously to depend upon the transport of hydrogen molecules up to the surface through the liquid diffusion layer.^{16,17} This slow step is a well-defined, reproducible process which is independent of the detailed nature of the surface provided only that the surface is active for absorption, *i.e.*, catalytic poisons are excluded. The rate of absorption is expected to be directly proportional to the pressure and this has been reconfirmed here (Figure 2). The constancy of rate during a run also shows that progressive poisoning does not occur.

The sequence of elementary steps occurring during absorption from solution is as follows: (a) transport up to the surface, (b) dissociation at the surface, (c) adsorption \rightarrow absorption transition, and (d) internal diffusion. (Any steps preceding these are expected to be faster than these reactions and are discussed elsewhere.¹⁶) The over-all rate of absorption is inde-

(18) E. Wicke and G. Nernst, *Z. Elektrochem.*, **68**, 224 (1964).

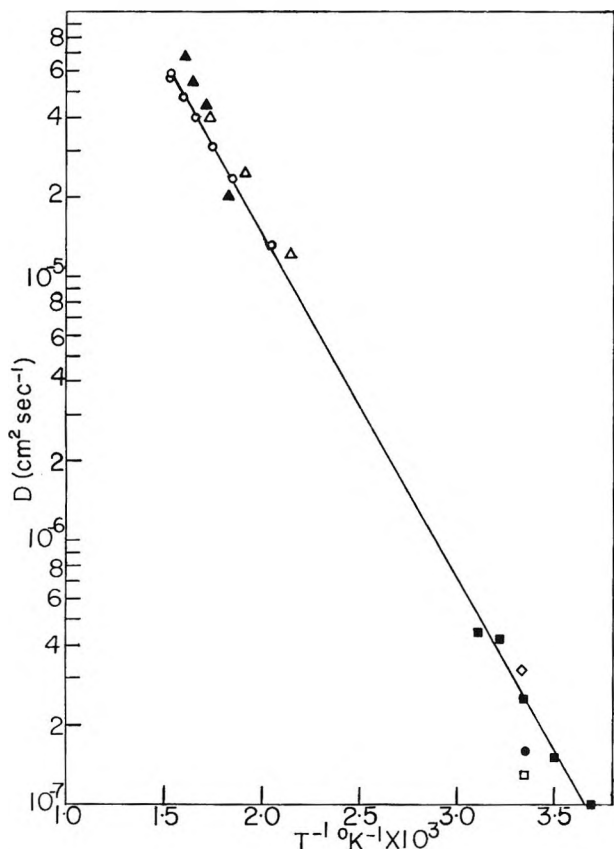


Figure 3. Arrhenius plot of D values from present research and values from the literature: ■, present research; ▲, Jost, ref. 4, p. 308; △, Jost, ref. 4, p. 310; ○, ref. 6, 7; ◇, ref. 8 as recalculated using isotherm data of ref. 12 and 18; ●, ref. 10; and □, ref. 9.

pendent of the rate of d provided, as is the case here, that step d is fast enough so that desorption can be neglected. The consequences of the possibility of step c being slower than step d should be considered. (The rate of step b relative to d is irrelevant because b does not directly influence the measured electrode potentials.) In addition, a further possibility not considered in the sequence of steps above, but which would have a similar effect as step c being slow relative to d , is that the diffusion constant of hydrogen atoms in palladium which is situated immediately adjacent to the surface is smaller than in the interior. If either of these processes, *i.e.*, step c or diffusion near the surface, is slow compared to bulk diffusion, a steady-state concentration of hydrogen atoms near the surface would be established which would be greater than expected from the value of F_0 and the bulk diffusion constant. Since this concentration (more properly, activity) determines the electrode potential, errors would result. That this is not the case in these experiments follows from the observation that the value of D obtained at

each temperature is independent of the pressure employed for the run because, for example, the larger the pressure, the larger the steady-state concentration of the potential-determining hydrogen atoms and therefore the value of D obtained would be smaller than that from runs at lower pressures (Figure 1). In addition, the values of D obtained here are larger than those in the literature, whereas if there were slow steps occurring such as described above, the values of D would be expected to be smaller (Figure 1). Finally the close correspondence between the calculated relationships (Figure 1) and the experimental data supports the absence of slow surface steps which would alter the value of C_a and consequently the experimental relationships.

Nonideality Effects. It is now generally accepted that the driving force in diffusion is not a concentration gradient but an activity or chemical potential gradient. A Ficks-law diffusion coefficient based on a concentration gradient as determined in the present study should vary with concentration as predicted by eq. 3 if the activity coefficient varies with concentration.

$$D(n) = D \frac{(d \ln a)}{(d \ln n)} = D \left\{ 1 + \frac{d \ln \gamma(n)}{d \ln n} \right\} \quad (3)$$

where a is the activity, n is the concentration (H/Pd), and $\gamma(n)$ is the concentration-dependent activity coefficient. No apparent variation of $D(n)$ within experimental error was observed in this study; thus it is of interest to examine the magnitude of the variation predicted by eq. 3. The relationship between $\gamma(n)$ and n can be derived from our previously determined isotherm equation.¹² The expression for $d \ln \gamma(n)/d \ln n$ from the isotherm equation is given by

$$\frac{d \ln \gamma(n)}{d \ln n} \cong \frac{d \ln p^{1/2}}{d \ln n} - 1 = \left[\frac{-5555}{T} + \frac{1}{1-n} \right] n \quad (4)$$

where p is the pressure of H₂ (gas) in equilibrium with absorbed hydrogen at the concentration, n . In Table I predicted values of $1 + d \ln \gamma(n)/d \ln n$ at various concentrations and temperatures relevant to this study

Table I: Predicted Values of $1 + d \ln \gamma(n)/d \ln n$

$n = \text{H/Pd}$	Temp., °K.		
	273	298	323
0	1.00	1.00	1.00
0.005	0.90	0.91	0.92
0.01	0.81	0.82	0.84
0.015	...	0.73	0.76
0.020	0.68

are shown. The maximum value of H/Pd at the surface of the wire was never allowed experimentally to increase beyond ~ 0.008 at 0° , ~ 0.010 at 25° , and ~ 0.015 at 50° . These values of the maximum surface concentration overestimate the actual concentration gradients since the maximum total average concentrations throughout the specimen were ~ 0.005 at 0° , ~ 0.007 at 25° , and ~ 0.012 at 50° . It is concluded from these considerations along with the results in Table I that the expected average decrease in the measured D values due to nonideality effects would be within the limits of experimental error.

It is similarly concluded that the high temperature results of Katz and Gulbransen were obtained under conditions in which the hydrogen content was sufficiently low for the temperatures in question that non-ideality effects on the D values would be small.

Tunneling Effects. The apparent linearity of the Arrhenius plot in Figure 3 over a relatively large temperature range suggests that quantum mechanical tunneling is unimportant. It is of interest to consider the expected contribution of quantum mechanical tunneling since rate processes which involve the motion of an H atom can exhibit a significant amount of tunneling. Initially, it can be said that the low activation energy and the appreciable distance that an H atom must move in passing over the energy barrier suggests that tunneling would be small except at very low temperatures.

An approximate expression for the tunneling correction is given by eq. 5¹⁹ where $\nu_i^2 = -E/2\pi^2 a^2 m$

$$Q_i = 1 - \frac{1}{24} \left(\frac{h\nu_i}{kT} \right)^2 \quad (5)$$

and ν_i is the imaginary frequency along the reaction coordinate for an assumed parabolic potential energy barrier, E is the height of the barrier, and a is one-half the shortest distance of passage between potential energy minima.

Setting E equal to the measured activation energy and $a = 1.38 \text{ \AA.}$ in eq. 5, a value of $Q_i = 1.1$ at 0° was calculated, which is indeed within our experimental error, and is consistent with the observed linearity of the Arrhenius plot.

Absolute Rate Theory Calculation of D . Wert and Zener have given the expression, $D = a^2 k$, for the diffusion constant of interstitial atoms by a simple jump mechanism between the octahedral interstices of a f.c.c. lattice, where a is the lattice parameter and k is the frequency of a single jump.²⁰ This expression takes into account the number of possible jump paths and the distance traveled in the direction of diffusion by a given jump.

The absolute rate theory expression for k is given by eq. 6.²¹

$$k = \kappa \frac{kT}{h} \frac{Q^*}{Q} \exp\{(E_a - E_0)/RT\} \exp(-E_a/RT) \quad (6)$$

where

$$E_a - E_0 = RT \left(1 - T \left(\frac{d \ln Q^*/Q}{dT} \right) \right)$$

Q is the partition function for an H atom in its equilibrium interstitial position, Q^* is the partition function for an H atom in the activated complex or transition state at the top of the potential energy barrier, κ is the transmission coefficient, E_a is the Arrhenius activation energy, and E_0 is the height of the potential energy barrier or critical energy.

It is assumed that the three degrees of freedom of the H atom in its equilibrium position are vibrations having equal magnitudes relative to the palladium lattice. In the transition state it is assumed that one of the vibrations becomes a translation over the barrier with no other changes relative to an H atom in its equilibrium position. The standard assumption that $\kappa = 1$ is made. For this model the Arrhenius pre-exponential factor given by eq. 6 reduces to the expression in eq. 7.

$$D_0 = a^2 \frac{kT}{h} \{1 - \exp(h\nu/kT)\} \times \exp\left\{1 - \frac{h\nu}{kT} [\exp(h\nu/kT) - 1]^{-1}\right\} \quad (7)$$

where ν is the H-atom vibrational frequency that became a translation. Using a measured value of $\nu = 1.354 \times 10^{13} \text{ sec.}^{-1}$ ²² in the high H-content β -phase, the value of $a = 3.89 \text{ \AA.}$, and the experimental value of $E_a = 5990 \text{ cal./mole}$ in eq. 7 gives $D_0 = 1.66 \times 10^{-2} \text{ cm.}^2 \text{ sec.}^{-1}$ at 0° and $1.97 \times 10^{-2} \text{ cm.}^2 \text{ sec.}^{-1}$ at 400° or an average value of 1.81×10^{-2} for the experimental temperature range. This is about the three times experimental value of $6.1 \times 10^{-3} \text{ cm.}^2 \text{ sec.}^{-1}$. This is generally considered to be satisfactory agreement for simple absolute theory calculations.

A more realistic transition-state model would allow for some tightening (higher frequency) of the two remaining vibrational motions of the H atom due to the

(19) R. P. Bell, "The Proton in Chemistry," Oxford University Press, London, 1960.

(20) C. A. Wert and C. Zener, *Phys. Rev.*, **76**, 1169 (1949).

(21) S. Glasstone, K. J. Laidler, and H. Eyring, "The Theory of Rate Processes," McGraw-Hill Book Co., Inc., New York, N. Y., 1941.

(22) J. Bergsma and J. A. Goedkoop, *Physica*, **20**, 30 (1960).

closer proximity of neighboring Pd atoms in the transition state, which would improve the agreement. The value of ν for the α -phase could be significantly different from the β -phase value used here, although α -phase isotherm data coupled with a statistical mechanical model yield a value of ν close to that used here.¹⁸

Recently, Makrides⁸ has evaluated D_0 from Zener's absolute rate theory treatment of interstitial diffusion.²³ In this somewhat different treatment to that given here, D_0 was estimated from the elastic constants of Pd metal and a measured activation energy with an assumed

simple sinusoidal potential energy function. The value obtained is slightly less than twice that calculated here.⁸

Acknowledgments. We wish to acknowledge gratefully the financial support for this research by U. S. Atomic Energy Commission Contract AT(30-1)-3000. Discussions with Mr. Arnulf Maeland have been most helpful.

(23) C. Zener in "Imperfections in Nearly Perfect Crystals," W. Shockley, Ed., John Wiley and Sons, Inc., New York, N. Y., 1952, p. 289.

Adsorption Studies on Heterogeneous Titania and Homogeneous Carbon Surfaces

by W. R. Smith and D. G. Ford

Oxides and Plastics Department, Cabot Corporation, Billerica, Massachusetts (Received May 10, 1965)

Adsorption of CO, N₂, O₂, and Ar on flame and wet process TiO₂ and on graphitized thermal carbon black have been carried out at -196°. The polarizability of the adsorbate is clearly reflected in the heats of adsorption on the oxide surface but is not evident on the uniform Sterling MTG surface. Anatase provides higher heats of adsorption and a more pronounced effect of adsorbate polarizability than rutile. The heats of adsorption on Sterling MTG evaluated by calorimetry are in good agreement with those reported by Gale and Beebe using the pulse elution technique. Adsorbate cross-sectional areas are computed from isotherm data. They are not the same on graphitized black as on TiO₂. However, they are the same on each of the titanias studied. Since the latter included rutiles and anatase of quite different origin, it would appear that the crystal form of the adsorbent is not a factor in determining the adsorbate area.

We are presently engaged in a study of the surface properties of flame process titanias. This process, which is of recent origin, involves the reaction of TiCl₄ vapor in an oxygen-rich flame with the production of TiO₂ and Cl₂. The pigment produced differs in some performance characteristics from the older wet or sulfate process titanias, and it is our opinion that this may be ascribed to the quite different environment in which the pigments had their synthesis.

The research described in the present paper provides

adsorption data on a series of titania as well as differential heats of adsorption on a flame process and sulfate process pigment. The adsorbates used in this initial study were carbon monoxide, nitrogen, oxygen, and argon. They were selected because while they have similar boiling points, they present a range of polarizability¹ from 2.0 for CO to 1.65×10^{-24} cm.³

(1) Landolt-Börnstein, "Zahlenwerte und Functionen," Vol. 1, 6th Ed., Part 3, Springer-Verlag, Berlin, 1951, p. 510.

for Ar. This should be reflected in heats of adsorption² on a polarizing oxide surface.

The flame process rutiles, in which we are chiefly interested, have a specific surface of only 7 to 8 m.²/g. Since this area is considerably lower than that of other adsorbents that we have previously employed in our calorimeter, it was decided to initiate the present research with an adsorbent of comparable low area but with a well-defined uniform surface. The graphitized carbon black Sterling MTG fills this role admirably. This adsorbent and its companion, Sterling FTG,³ have been the subject of several studies⁴ and are recognized as possessing extremely uniform or homotactic surfaces.

In addition to being a convenient adsorbent with which to evaluate the performance of our calorimeter, the heat data on Sterling MTG obtained with the four adsorbates, Ar, O₂, N₂, and CO, are of interest for comparison with data obtained on the same system by Gale and Beebe⁵ by the pulse elution technique.

Experimental Section

Adsorbents. The sample of graphitized thermal black, Sterling MTG, was prepared by heating the parent carbon black Sterling MT in an inert atmosphere to 3000 ± 200°. It was from lot D4, from which we have supplied other investigators. We found it to have an area 7.3 m.²/g. Earlier preparations have displayed areas of 6.3 m.²/g. Variation of this order can arise from different lots of the parent material used in the preparation.

Two flame process titanias were used in the present study. Rutile A was produced by reaction of TiCl₄ in an oxidizing flame and had not been surface treated after formation. Chemical analysis proved it to be better than 98% TiO₂, the remainder consisting principally of Al₂O₃. X-Ray diffraction measurements showed it to be 99.8% rutile. Electron microscope evaluation provided a surface average diameter of 1990 ± 80 Å. The B.E.T. nitrogen area was 7.8 m.²/g. Prior to use, rutile A was calcined in a muffle furnace for 30 min. at 600° and stored over Drierite before loading into the calorimeter.

TiO₂ D was produced by the flame hydrolysis of TiCl₄, and on chemical analysis was found to be about 99% TiO₂. It was a 75% rutile, 25% anatase pigment. It had an N₂ area of 31.9 m.²/g. It was used only in isotherm studies and was dried at 100° for 8 hr. and then degassed at 100° on the adsorption line.

Anatase C was used in calorimeter studies. It was a sulfate process material which analyzed about 99% TiO₂. Prior to loading in the calorimeter, it too was calcined in an open muffle furnace at 600° for 30

min. Diffraction analysis was then run, and a value of 99.8% anatase was obtained. It had an N₂ area of 9.7 m.²/g.

A second sample of wet process anatase, anatase B, was also included in the isotherm studies. Chemical analysis revealed it to be of high purity, *i.e.*, 99% TiO₂, and diffraction analysis showed it to be 99.7% anatase.

Adsorbates. The argon, oxygen, nitrogen, and carbon monoxide were Linde research grade and were used without purification other than passing through Dry Ice traps before entering the storage bulbs of the adsorption line. Helium employed was of research grade and was passed through charcoal-liquid nitrogen traps before storage. Correction factors employed for deviation of the adsorbates from ideality were: carbon monoxide, 5%; N₂, 5%; O₂, 3.17%; and argon, 8.7%. These represent the deviation at saturation pressure of the adsorbate at -196°. The deviation was assumed to be linear with respect to pressure.

Apparatus. The calorimeters employed were similar to those used in our earlier research⁶ with a few minor changes. Instead of double Pyrex arms from the calorimeter for the heater coil, and copper-constantan thermocouple leads, single 10-mm. Pyrex press seals carrying double 1-mm. i.d. Kovar tubes were employed. The copper-constantan reference junction was silver-soldered to a 10 × 60-mm. pure copper rod encased in a 12-mm. o.d. Pyrex jacket. The leads from the reference junction were led out through a double Kovar seal and silver-soldered. The Pyrex jackets of the reference junction and calorimeter were sealed to the vacuum line and helium source. The reference junction assembly was mounted close to the calorimeter jacket and level with the calorimeter junction. The heat capacity of the loaded calorimeter was about 2.6 cal./deg. All runs were made at liquid nitrogen temperature.

To ensure that the adsorbate was at bath temperature before entering the calorimeter, a 150-mm. coil of 3 × 1.5-mm. i.d. copper tubing was interposed through Kovar leads between the 1.5-mm. Pyrex capillary from the adsorption line and from the calorimeter.

(2) P. Cannon, *Advances in Chemistry Series*, No. 33, American Chemical Society, Washington, D. C., 1961, p. 130.

(3) This designation, rather than the previously used Sterling MT (3100°) or Sterling FT (2700°), seems to us to be a more convenient and more accurate designation since the temperatures of graphitization are not known to be better than ±200°.

(4) See, for example, D. Young and A. Crowell, "Physical Adsorption of Gases," Butterworth Inc., Washington, D. C., 1962, Chapter 5.

(5) R. L. Gale and R. A. Beebe, *J. Phys. Chem.*, **68**, 555 (1964).

(6) R. E. Beebe, J. Biscoe, W. R. Smith, and C. B. Wendell, *J. Am. Chem. Soc.*, **69**, 95 (1947).

A 210-mm. i.d. \times 600-mm. silvered dewar flask served as the liquid N_2 bath. In all runs the nitrogen level was maintained about 200 mm. above the top of the calorimeter. Polystyrene foam, glass wool, and aluminum foil lightly sealed the top of the dewar flask. Under these conditions thermal gradients between the two junctions during a measurement (20 min.) were negligible.

Prior to a run, the calorimeter containing approximately 10 g. of adsorbent was evacuated at 100° for several hours until a "hard" vacuum was attained. About 2 mm. of He was usually admitted to the calorimeter and reference junction jackets for thermal conductivity. The entire assembly was then immersed in the nitrogen bath. When thermal equilibrium was reached, both jackets were evacuated providing a stable base line for either an electrical calibration or an adsorption increment. About 2 ml. of adsorbate was admitted per increment. The output from the thermocouple was fed to a Liston-Becker Model 14 d.c. amplifier. It was found that most satisfactory operation was obtained by feeding only about 2.5% of the output signal to a 1-mv. range strip chart potentiometer. This was achieved by means of a potential divider across the amplifier output. With this arrangement, appropriate settings of the d.c. amplifier were selected to produce deflections of some 0.3 to 0.9 mv. on the recorder chart. These deflections, being the range normally encountered during a heat run, correspond to a 1 to 3- μ v. signal from the calorimeter thermocouple. During the course of a run, eight to ten electrical calibrations were carried out, distributed prior to, during, and at the conclusion of the adsorption increments. They usually agreed to within 3% and showed no significant trend. Accordingly, they were averaged, and the result was used to compute the heat evolved per adsorption increment.

The response of the calorimeter to an increment was of the order of 10 sec. and equilibrium was established in about 2 min. To facilitate heat exchange, about 0.3 mm. of He was admitted to the calorimeter prior to each run. The cooling curves were followed for about 20 min. The heat rise per increment was obtained by a linear extrapolation of the cooling curve back to the midpoint of the time between the start and maximum of the heat curve. This procedure did not deviate seriously from the more tedious procedure of reconstructing the curves by means of the Newton cooling coefficient.

In view of the small heat evolved per increment adsorbed, we felt it necessary to establish that the adsorbate did not carry heat to the calorimeter and that our results were not seriously affected by a heat of com-

pression. We followed Ward's procedure,⁷ substituting helium for the nitrogen he employed. In our measurements the calorimeter loaded with anatase was at -196° . Helium was admitted to the evacuated calorimeter in separate volumes sufficient to raise the pressure to about 100, 60, and 80 mm., and the corresponding heat rise was noted. The calorimeter was then cooled to the original bath temperature, and the helium was rapidly pumped out and the heat drop noted. The data are plotted in Figure 1. The heat values for the compression and expansion were in excellent agreement, and the effect was linear with pressure. The agreement indicates that heat was not carried into the calorimeter, even though the volumes of helium admitted in these experiments were in some instances over five times that of a normal adsorbate increment. Since we were seldom concerned with heats of adsorption beyond a monolayer, our equilibrium pressures were generally below 10 mm. Thus from Figure 1 the 0.005 cal. or less actually released in our calorimeter on compression from 0 to 10 mm. pressure is well within our experimental error. Consequently, we have not corrected our data for this effect. It must be borne in mind, however, that with low area materials, when equilibrium pressures of 30 or 40 mm. are encountered, the above correction may exceed 10%.

We have encountered erratic heat data with Sterling MTG as the monolayer is approached. The isotherm

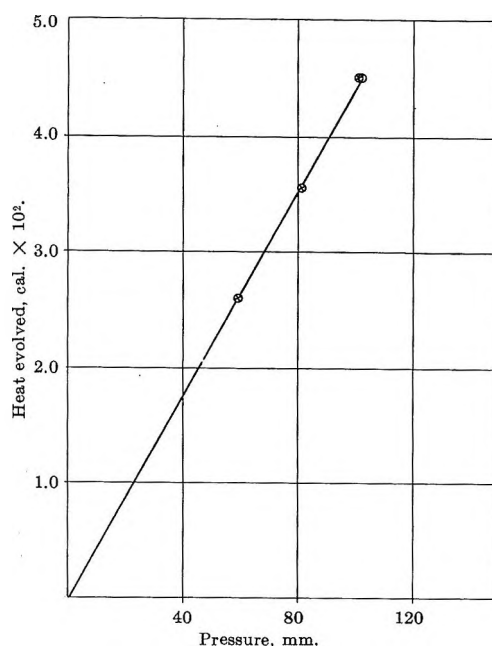


Figure 1. Expansion (O) and compression (X) of helium in calorimeter at -196° .

(7) A. F. H. Ward, *Proc. Roy. Soc. (London)*, **A133**, 506 (1931).

for this material breaks very sharply at the monolayer, and, in consequence, only a small fraction of the admitted increment is adsorbed. This results in a small deflection in the recorder with a concomitant large percentage error. Consequently, we do not claim an accuracy better than 10% for the heats approaching monolayer coverage on Sterling MTG. This could, no doubt, be corrected if one were concerned over the matter. However, in our studies these heats are generally of little interest. With the oxide surfaces, however, the change in slope of the isotherm at the monolayer is much less abrupt, and our reproducibility for the heats on titania is of the order of 5% over the entire coverage.

Results and Discussion

Studies on Sterling MTG. Isotherms for the adsorption of Ar, O₂, N₂, and CO on Sterling MTG at -196° were collected. In each instance well-defined steps at the completion of each monolayer were noted, emphasizing the extraordinary uniformity of this surface. The isotherm for argon is reproduced in Figure 2. Recent data from the argon isotherm on Sterling FTG,⁸ a higher area (12.5 m.²/g.) graphitized thermal black, are also included. We have also included data from an earlier publication⁹ as well as that published by Singleton and Halsey.¹⁰ The isotherms for these two graphitized thermal blacks coincide extremely well, suggesting that both adsorbents are identical as far as surface homogeneity is concerned. Electron micrographs of both Sterling MTG and Sterling FTG display very regular octagonal images. In the case of Sterling MTG, the side of the octagon image measures about 1000 Å. and for Sterling FTG 700 Å. Individual particles, as Graham¹¹ has observed, consist predominantly of doubly truncated polygonal bipyramids. We suggested earlier¹² that the extent of surface homogeneity may be associated with the area of the adsorbing graphite planes exposed on the surface of the graphitized black. In the present instance, *i.e.*, Sterling MTG and FTG, the degree of heterogeneity which might be introduced by the boundary of the planes appears to be of too low an order to be detected either in isotherms or heats of adsorption.

The equivalence of the two surfaces is also reflected in the data of Table II which demonstrate that the average cross-section area of the adsorbates, whether based on N₂ or Ar, is the same on both MT and FT graphitized black.

The heat curves¹³ obtained on Sterling MTG were typical of those previously encountered on uniform surfaces; that for CO adsorption is reproduced in Figure 3. The differential heats at 0.05 coverage for

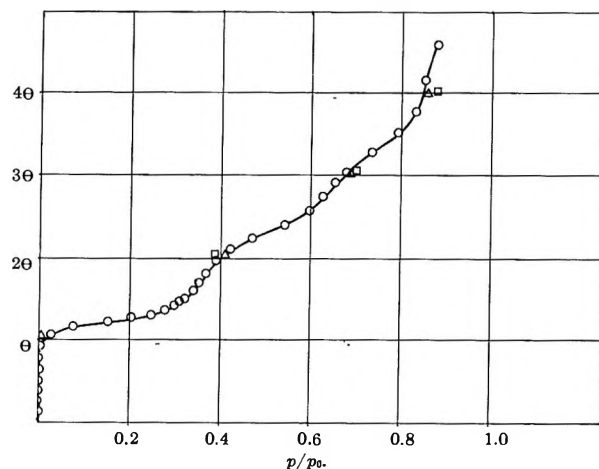


Figure 2. Adsorption of argon at -196° on Sterling MTG (O) and on Sterling FTG; data of Singleton and Halsey, ref. 10 (Δ) and from Polley, Schaeffer, and Smith, ref. 12 (□).

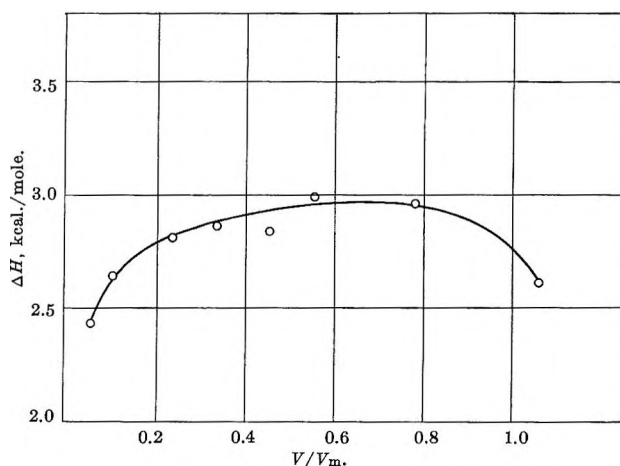


Figure 3. Differential heat of adsorption for carbon monoxide on Sterling MTG at -196°.

all four adsorbates ranged from 2.2 to 2.4 kcal./mole. A maximum of 3.0–3.2 kcal. was reached close to monolayer coverage and then fell off exceedingly rapidly. Beebe and Gale,⁵ employing the eluted pulse technique, have reported values of 2.4, 2.5, and 2.5 kcal./mole for the adsorption of N₂, O₂, and Ar, respectively, on Sterling MTG at surface coverage of the order of 0.01

(8) Sterling FTG graphitized at 2700–3000° is identical with the P-33 (2700°) carbon black used in earlier studies.

(9) M. H. Polley, W. D. Schaeffer, and W. R. Smith, *J. Phys. Chem.*, **57**, 469 (1953).

(10) J. H. Singleton and G. D. Halsey, *ibid.*, **58**, 1011 (1954).

(11) D. Graham and W. S. Kay, *J. Colloid Sci.*, **16**, 182 (1961).

(12) M. Polley, W. D. Schaeffer, and W. R. Smith, *J. Phys. Chem.*, **57**, 471 (1953).

(13) As is customary, we have plotted the heat evolved per mole of gas adsorbed in an increment as a function of V/V_m at the midpoint of the increment.

to 0.001. The present results summarized in Table I are in sufficient agreement with their values to support the chromatographic procedure, at least on homogeneous surfaces such as graphitized carbon black. Our calorimetric heats were measured at -196° , while the above authors collected the isotherms required by the pulse elution technique over a range of -131 to -84° .

Table I: Heats of Adsorption from Calorimetry and Chromatography on Sterling MTG (kcal./mole)

Adsorbate	ΔH (0.05V/V _m)	ΔH_{max} (0.8 to 1.0V/V _m)	ΔH from chromatography ^a $\theta = 0.001$ to 0.01V/V _m
CO	2.4	3.0	...
N ₂	2.4	3.1	2.4
O ₂	2.2	3.2	2.5
Ar	2.4	3.1	2.5

^a From Gale and Beebe⁵ using pulse elution.

While there may be compensating errors, the agreement of the two methods suggests that the mechanism of adsorption is unchanged over the temperature range -196 to -84° . The agreement of heat values collected at 0.001 coverage by the pulse method and at 0.050 by the calorimeter further emphasizes the remarkable homogeneity of these graphitized carbon black surfaces.

Results on Titanias. Isotherms for CO, N₂, O₂, and Ar adsorbed on each of the four titanias were evaluated at liquid nitrogen temperature. All were smooth, reversible, and type II, characteristic of a heterogeneous surface. Values of V_m derived from B.E.T. plots are summarized in Table II. The nitrogen areas and those derived from electron microscopy were in reasonable agreement. For example, rutile A had an N₂ area of 7.8 m.²/g. while that derived from the measured surface average diameter was 7.2 m.²/g. In view of the uncertainty associated with the true cross-sectional area of nitrogen and the fact that rutile particles are not spherical, we feel that the agreement is sufficient to indicate that the titanias are essentially nonporous.

The cross-sectional areas of the adsorbates derived from V_m, based first on N₂ at 16.2 Å.² and secondly on Ar at 15.0 Å.² are also presented in Table II.

It is interesting to note that the values derived from V_m, on the extremely uniform, nonpolarizing Sterling MTG and Sterling FTG surfaces, remain unchanged whether argon or nitrogen is selected as standard. This conclusion could, of course, be predicted from the

Table II

Adsorbate	Sterling MTG	Sterling FTG	Rutile A	Anatase B	Anatase C	TiO ₂ D
	N ₂ area, m. ² /g.					
	7.3	11.9	7.8	9.3	9.7	31.9
(A) V _m (B.E.T.) Values (ml.) on above Adsorbents						
CO	1.643	2.653	1.942	2.294	2.416	7.819
N ₂	1.678	2.721	1.794	2.140	2.226	7.321
O ₂	1.820	2.951	1.838	2.144	2.192	7.645
Ar	1.806	2.912	1.665	1.888	1.998	6.949
(B) Adsorbate Cross-Sectional Area (Å. ²) on above Adsorbents from V _m Assuming N ₂ = 16.2 Å. ²						
CO	16.5	16.6	15.0	15.1	14.9	15.2
N ₂	16.2	16.2	16.2	16.2	16.2	16.2
O ₂	14.9	14.9	15.8	16.2	16.5	15.5
Ar	15.0	15.1	17.5	18.4	18.0	17.1
(C) Adsorbate Cross-Sectional Areas (Å. ²) on above Adsorbents Assuming Ar = 15.0 Å. ²						
CO	16.5	16.5	12.9	12.3	12.4	13.3
N ₂	16.1	16.0	13.9	13.2	13.5	14.2
O ₂	14.9	14.8	13.6	13.2	13.7	13.6
Ar	15.0	15.0	15.0	15.0	15.0	15.0

fact that all four adsorbates had nearly identical heats of adsorption on the graphitized surface. On the other hand, when adsorbed on the polarizing TiO₂ surfaces, the computed cross-sectional areas of the adsorbates change very significantly when argon, rather than nitrogen, is selected as standard. This too might be predicted from the heat data presented below from which it is evident that the more polarizable the adsorbate, the higher is its heat of adsorption. Since the initial heats of adsorption of argon on the uniform graphite surface and on the heterogeneous oxide surface differ by only 0.6 kcal., it would appear to be a more suitable surface area standard than the other adsorbates which display larger differences in heats on the above surfaces.

It is of interest to observe that the cross-sectional areas, whether computed on the basis of N₂ or Ar, are about the same for each of the four samples of TiO₂ studied. Since both rutile and anatase configurations are included, it is evident that the crystal modification of the titania does not play a significant role in determining the covering power of the adsorbate.

Figures 4 and 5 present heat curves for the adsorption of CO, N₂, O₂, and Ar on flame process rutile A and sulfate process anatase B. They are typical of heats associated with adsorption on a heterogeneous surface. The high initial heats presumably correspond to adsorption on most active sites and thereafter fall off as less active areas are filled. The heats

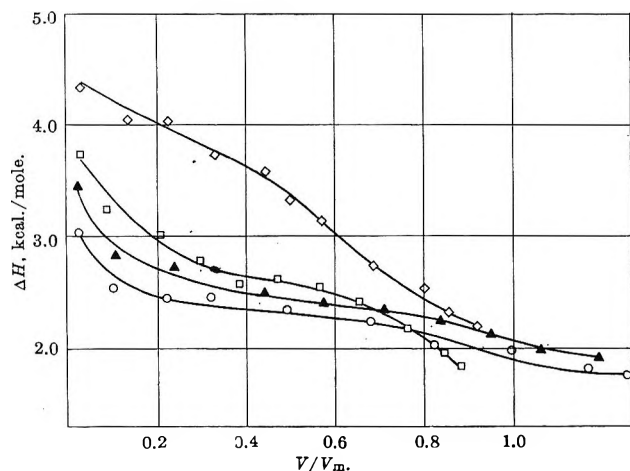


Figure 4. Differential heats of adsorption for carbon monoxide (\diamond), nitrogen (\square), oxygen (\blacktriangle), and argon (\circ) on flame process rutile A at -196° .

prior to the monolayer reflect the polarizability of the adsorbate, carbon monoxide providing the highest values and argon the lowest. This is in contrast with the adsorption on the Sterling MTG which provided nearly identical heat values for the four adsorbates. The heat curves for adsorption of carbon monoxide, nitrogen, and oxygen on anatase B are shown in Figure 5. The heats are significantly higher than those on rutile. Again the effect is most marked with carbon monoxide. Beebe and Gale,⁵ in their study on bone mineral (apatite) degassed at 500° , report an initial heat of adsorption for N_2 of 5.3 cal./mole about 1 kcal. higher than we have observed on titania. Thus in order of increasing polarity we may classify rutile, anatase, and bone mineral. In view of an earlier study⁶

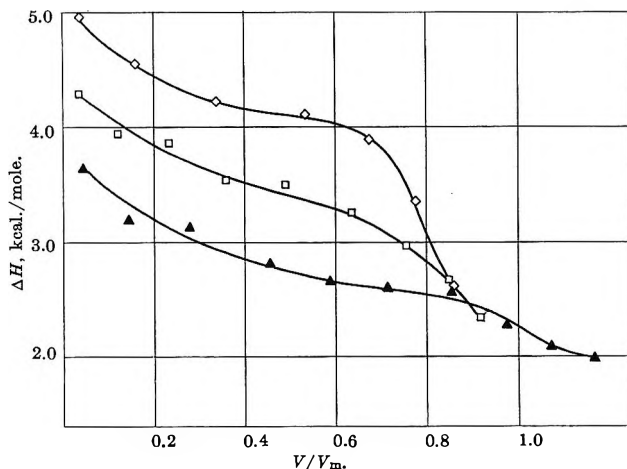


Figure 5. Differential heats of adsorption for carbon monoxide (\diamond), nitrogen (\square), and oxygen (\blacktriangle) on anatase C at -196° .

on a standard channel carbon black, Spheron 6, on which the heats of adsorption of nitrogen and oxygen were identical, one would classify it as a much less polar surface than rutile. Once again the question arises as to the extent to which their characteristics are identified with specific surface groups. It is hoped that further studies now in progress, in which the surface chemistry has been altered, will assist in answering the question.

Acknowledgments. We are pleased to thank Professor R. A. Beebe of Amherst College for many fruitful discussions and helpful suggestions. We also wish to thank our old colleague, Mr. C. B. Wendell, for his invaluable assistance and suggestions in constructing the calorimeters.

Sulfur in the Burnt Gas of Hydrogen-Oxygen Flames

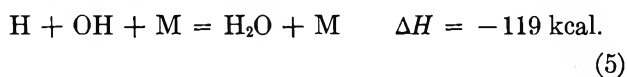
by C. P. Fenimore and G. W. Jones

General Electric Research Laboratory, Schenectady, New York (Received May 10, 1965)

In hydrogen-rich flames, a little added sulfur is found to be mostly SO_2 as predicted by the equilibrium, $\text{SO}_2 + 4\text{H}_2 = \text{H}_2\text{S} + 2\text{H}_2\text{O} + 2\text{H}$, rather than mostly H_2S as predicted by $\text{SO}_2 + 3\text{H}_2 = \text{H}_2\text{S} + 2\text{H}_2\text{O}$. The two predictions differ because $[\text{H}]$ is larger than is appropriate to the equilibrium $\text{H}_2 = 2\text{H}$. The added sulfur catalyzes the recombination of radicals at a rate consistent with the reaction cycle, $\text{H} + \text{SO}_2 + \text{M} \rightarrow \text{HSO}_2 + \text{M}$, and H (or OH) + $\text{HSO}_2 \rightarrow \text{H}_2$ (or H_2O) + SO_2 , where the constant for the first, rate-controlling, step is of the order of $k \simeq 7 \times 10^{16} \text{ cm}^6 \text{ mole}^{-2} \text{ sec}^{-1}$ (M = total flame gases). In hydrogen-lean flames where sulfur is also mostly SO_2 , the SO_3 present is not equilibrated with SO_2 , but attains a steady concentration consistent with the reaction cycle, $\text{O} + \text{SO}_2 + \text{M} \rightarrow \text{SO}_3 + \text{M}$, and O (or H) + $\text{SO}_3 \rightarrow \text{O}_2$ (or OH) + SO_2 ; this cycle catalyzes the recombination of radicals in lean gas.

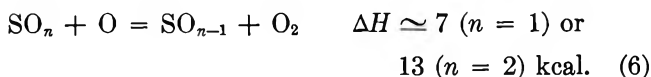
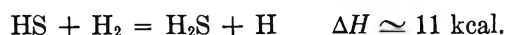
Introduction

Most readily established equilibria in flames have small energies of reaction and are maintained by processes which are bimolecular in both directions. Thus, reactions 1, 2, and 3 are easily equilibrated in hydrogen-oxygen flames, but (4) and (5) are not.¹⁻³ The easily established equilibria preserve the number of molecules,

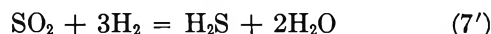
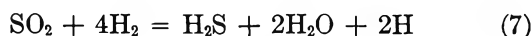


as do their linear combinations.

Equilibria with the same characteristics have been proposed for sulfur compounds. Sugden and co-workers⁴ suggested that the sulfur analogs of (1), (2), and (3) become equilibrated, and also reactions 6 with $n = 1$ and 2.



The evidence for the sulfur equilibria was admittedly scanty, and we have tried to support or disprove the suggestions. Any equilibrium among the species considered which preserves the number of molecules is a linear combination of (1), (2), (3), and the proposed sulfur equilibria; so a finding that the distribution of sulfur conforms to equilibrium 7 would support the proposals. We find that (7) is satisfied; while (7'), which is not a combination of the proposed reactions, is not satisfied.



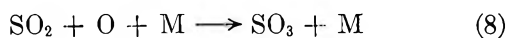
Although Sugden and co-workers did not propose equilibria involving SO_3 , one might suspect that (6) would be equilibrated for $n = 3$. It is not, nor do we find any other reaction involving SO_3 equilibrated. In fuel-lean gas, however, the observed $[\text{SO}_3]/[\text{SO}_2]$ can be interpreted as a steady-state ratio; with SO_3 formed by irreversible reaction 8 and destroyed just as fast by irreversible (9).

(1) E. M. Bulewicz, C. G. James, and T. M. Sugden, *Proc. Roy. Soc. (London)*, **A235**, 89 (1956).

(2) C. P. Fenimore and G. W. Jones, *J. Phys. Chem.*, **62**, 693 (1958).

(3) W. E. Kaskan, *Combust. Flame*, **3**, 49 (1959).

(4) T. M. Sugden, E. M. Bulewicz, and A. Demerdache, *International Symposium on Chemical Reactions in the Atmosphere*, Interscience Publishers, Inc., New York, N. Y., 1961, p. 89.



Besides maintaining a small steady-state $[\text{SO}_3]$ reactions 8 and 9 should also constitute a catalytic cycle for recombining radicals in lean gas. It has already been suggested that hydrogen-oxygen explosions are inhibited at 784°K. by added SO_2 partly because reac-



tion 8 captures free radicals.⁵ Reaction 10 was also thought to capture radicals at 784°K. and if this occurred in flames and was followed by a regeneration of SO_2 , e.g., $\text{HSO}_2 + \text{H} \text{ (or OH)} \rightarrow \text{SO}_2 + \text{H}_2 \text{ (or H}_2\text{O)}$, the recombination of radicals would be catalyzed in fuel-rich gas at the rate of (10). We find that the recombinations in flames are catalyzed at rates which are consistent with the observations at the lower temperature.

Experiments in H_2 -Rich Gas

Figure 1 shows some traverses through a flat flame on a porous burner of the type described by Kaskan.⁶ We also used his quartz-coated thermocouples and his method of correcting the readings for radiation losses. Our aim was to decide, by means of mass spectroscopic analysis of samples sucked through a quartz microprobe, if equilibrium 7 was established, its equilibrium constant being known.⁷ The mole fractions X_{H_2} and $X_{\text{H}_2\text{O}}$ were essentially constant farther than 0.5 cm. from the burner and are omitted from Figure 1.

H_2S and SO_2 were proved not to react with one another in the sampling system by adding them both to the reactants, running the mixture through the burner without igniting it, and finding the additives unchanged in samples collected in the usual way.

Other sulfur species must have been present because SO_2 and H_2S accounted for only 75% of the sulfur fed. $[\text{S}_2]$ should have been appreciable according to the proposed equilibria in the Introduction; but the only direct evidence for S_2 was its emission bands from the primary reaction zone. $[\text{HS}]$ should have been comparable to $[\text{H}_2\text{S}]$ according to the proposed equilibria, but no evidence for HS was obtained. The vessel in which burning took place was fitted with quartz windows, and the only sulfur species found by absorption of a single pass of light from a hydrogen discharge lamp was SO_2 by its bands around 2200 and 3000 Å.

Other species are irrelevant to a check of equilibrium 7 if the analyses for SO_2 and H_2S were unaffected. SO_2 was the principal sulfur species and could not have been affected very strongly, but H_2S could. For example, HS present in the flame might recombine to give

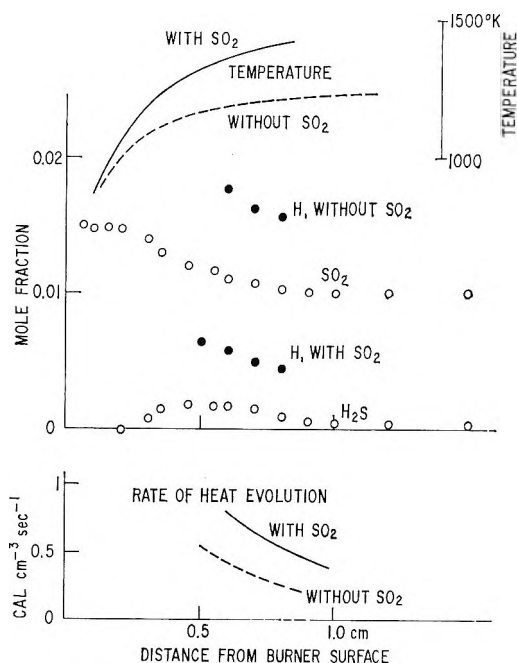


Figure 1. Traverses through a flat flame of $\text{Ar} + 1.13\text{H}_2 + 0.236\text{O}_2 + 0.033\text{SO}_2$ at 10 cm. pressure with a mass flow of $6.25 \times 10^{-3} \text{ g. cm.}^{-2} \text{ sec.}^{-1}$.

additional H_2S in the sample. On the other hand, H_2S in the flame should survive in the sample; its only likely mode of destruction would be by reaction with H atoms, and the rate of this process is known to be of the same order⁸ as the rate of $\text{H} + \text{D}_2 \rightarrow \text{HD} + \text{D}$ which is adequately quenched^{9,10} in samples probed from flames. Therefore, the measured $X_{\text{H}_2\text{S}}$ was probably an upper limit to the true fraction, and perhaps too large by a factor of two.

Hydrogen atoms were inferred from the rate of formation of HD when a little D_2O was added to the reactants.^{2,10} The formation was almost complete by the time the gas reached 0.8 cm. from the burner, so X_{H} could not be estimated farther downstream. The rate constant for reaction 3 must be known¹¹ to determine

(5) P. Webster and A. D. Walsh, 10th International Symposium on Combustion, Cambridge, England, Aug. 1964.

(6) W. E. Kaskan, 6th International Symposium on Combustion, Yale University, New Haven, Conn., Aug. 1956, Reinhold Publishing Corp., New York, N. Y., 1957, p. 134.

(7) B. J. McBride, S. HeimeI, J. H. Ehlers, and S. Gordon, NASA Report SP-3001, National Aeronautics and Space Administration, Washington, D. C., 1963.

(8) B. DeB. Darwent and R. Roberts, *Discussions Faraday Soc.*, 14, 55 (1953).

(9) C. P. Fenimore and G. W. Jones, *J. Phys. Chem.*, 63, 1154 (1959).

(10) G. Dixon-Lewis and A. Williams, 9th International Symposium on Combustion, Cornell University, Ithaca, N. Y., Aug. 1962, Academic Press Inc., New York, N. Y., 1963, p. 576.

(11) F. Kaufman and F. P. DelGreco, ref. 10, p. 659.

X_H by this method; and the constant, and therefore the X_H derived, is uncertain by a factor of about two.

Some local rates of heat release shown at the bottom of Figure 1 were calculated from the temperature traverses^{10,12} in order to estimate the rates of recombination of radicals.

If sulfur was added as H_2S rather than as SO_2 , X_{H_2S} was already small and X_{SO_2} large as far upstream as the flame could be sampled.

Observations and some calculations at two positions in each flame are given in Table I. At 0.8 cm. from the burner (as far downstream as X_H could be estimated), X_H and the local rate of heat release are listed. At 1.2 cm. (where X_{SO_2} and X_{H_2S} had leveled out), the ratio X_{H_2S}/X_{SO_2} is listed.

Table I: Observations on H_2 -Rich Flames at Two Positions

Run ^a	—0.8 cm. from burner—			Temp., °K.	—1.2 cm. from burner—		
	$10^3 X_H$ No additive	$10^3 X_H$ Sulfur added	10^{-16} k_{10}^b		X_{H_2S}/X_{SO_2} Obsd.	Calcd. by eq. 7'	$10^3 X_H$ Calcd. by eq. 7
1	15	4	8	1480	~0.04	25	1
2	7	4	6	1660	0.08	30	2
3	26	14	6	1560	0.17	120	3
4	26	9	8	1540	0.25	140	2

^a Run 1, portrayed by Figure 1; run 2, Ar + 1.18 H_2 + 0.31 O_2 + 0.030 SO_2 burnt at 10 cm. pressure; run 3, Ar + 1.50 H_2 + 0.31 O_2 + 0.030 SO_2 burnt at 5 cm. pressure; run 4, same as 3 except SO_2 replaced by 0.029 H_2S . ^b $k_{10} = \dot{h}/(104 \times 10^3 [H][SO_2][M])$ where \dot{h} in calories per cubic centimeter second is corrected for the contributions of recombinations 4 and 5.

Discussion of H_2 -Rich Gas

Because of the uncertainty in X_{H_2S} , we avoid the region where it was varying and only ask if equilibrium 7 was approached at 1.0 to 1.5 cm. from the burner where X_{H_2S} and X_{SO_2} leveled out in all four flames. If (7) was equilibrated, X_H should be calculable from X_{H_2S} , X_{SO_2} , X_{H_2O} , and the known equilibrium constant.⁷ The X_H values calculated in this way at 1.2 cm. are listed in the last column of Table I. They are smaller by a factor of 3.7 ± 1 than the measurements of X_H at 0.8 cm. which are listed in the third column.

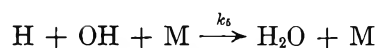
The difference can be explained away if the X_H measured at 0.8 cm. decreases as the gas flows downstream. It will be suggested below that the rate of heat evolution is approximately proportional to X_H in gases containing sulfur; and if this is so, Figure 1, which indicates a decrease in the rate of heat evolution by about a factor of 2 between 0.8 and 1.2 cm., also im-

plies a decrease in X_H by the same factor. Furthermore, the X_H calculated by equilibrium 7 at 1.2 cm. may be too small because X_{H_2S} is an upper limit. Within the uncertainties of the measurements, the X_H required to satisfy equilibrium 7 at 1.2 cm. can be reconciled with the X_H observed at 0.8 cm.

If (7') had been equilibrated at 1.2 cm., X_{H_2S}/X_{SO_2} would have been about 600 times larger than observed, as is shown by the sixth and seventh columns of Table I. It is a reasonable interpretation that the sulfur, expected to be mostly H_2S according to (7'), is in fact mostly SO_2 because the equilibrium which applies is (7).

Turning now to the recombination of radicals, which is the source of the heat evolved downstream of the primary reaction zone, we obtained semiquantitative estimates of the rates of recombination in the following way.

In the absence of sulfur, the important recombination reactions are thought¹³ to be (4) and (5)

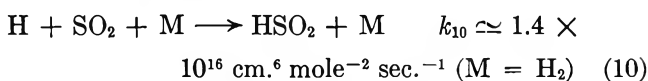


and the rate of heat evolution is therefore

$$\dot{h} \simeq 104 \times 10^3 \{k_4[H]^2[M] + k_5[H][OH][M]\} \text{ cal. cm.}^{-3} \text{ sec.}^{-1}$$

Applied to our measurements at 0.8 cm., with $[OH]$ computed from $[H]$ by equilibrium 3, and k_5/k_4 assumed to be 24,¹⁴ this mechanism gives $k_4 \simeq 0.5 \times 10^{16} \text{ cm.}^6 \text{ mole}^{-2} \text{ sec.}^{-1}$ ($[M] = \text{total gas concentration}$)—a reasonable figure.¹⁴

The heat evolution is larger in the presence of SO_2 , yet only a few per cent of it can be ascribed to (4) and (5) because $[H]$ is smaller in the presence of sulfur. It seems certain that sulfur compounds catalyze the recombination of radicals. A possible mechanism of the catalysis is suggested by Webster and Walsh,⁶ who found that hydrogen-oxygen explosions were inhibited at 784°K. by reaction 10. If (10) occurred in flames, and



was followed by a regeneration of SO_2 and formation of hydrogen molecules so that aside from the heat release due to (4) and (5)

$$\dot{h} = 104 \times 10^3 k_{10} [H][SO_2][M]$$

(12) C. P. Fenimore and G. W. Jones, ref. 5.

(13) P. J. Padley and T. M. Sugden, *Proc. Roy. Soc. (London)*, A248, 248 (1958).

(14) J. L. J. Rosenfeld and T. M. Sugden, *Combust. Flame*, 8, 44 (1964).

must be included to give the total heat release, our measurements give $k_{10} \approx 7 \times 10^{16}$ ($M = \text{total gas}$)—five times Webster and Walsh's estimate. Possibly other processes occur in flame gases and, counting their heat evolved as part of (10), we get too large a rate constant. It is not clear what process might have been overlooked, however; the reaction $\text{H} + \text{O}_2 + \text{M} \rightarrow \text{HO}_2 + \text{M}$, which is important far enough upstream even in H_2 -rich flames,¹² should have dwindled at 0.8 cm. from the burner. We can only say that the M and the temperature are not the same in flames as in the study of explosion limits, and the catalysis in flames is not inconsistent with the effect of SO_2 on explosion limits.

Experiments in H_2 -Lean Gas

Almost all the added SO_2 remained SO_2 in flames containing oxygen. The little SO_3 was collected from a sample of known size by connecting the probe through a trap cooled with liquid nitrogen to a large evacuated flask and noting the pressure of uncondensed gas. The trap was subsequently freed from SO_2 by warming it to 273°K. and passing argon through it at 0.33 atm. pressure for 20 min. Probe and trap were then washed out with water, excess BaCl_2 solution was added to the washings, and the turbidity was compared with that of known solutions of H_2SO_4 . The method was tested by adding known amounts of very dilute H_2SO_4 to the cold trap before some of the runs. The burner and probe were washed before each determination and the reproducibility of the estimates of $[\text{SO}_3]/[\text{SO}_2]$ in the flame was $\pm 15\%$, about the uncertainty in estimating very dilute H_2SO_4 by turbidity comparisons.

Radical concentrations were inferred from the rate of formation of OO^{18} when a little H_2O^{18} was added to the reactants.¹⁵ The method is based on the considerations that in lean gas, $\text{H}_2\text{O}^{18} + \text{OH} = \text{H}_2\text{O} + \text{O}^{18}\text{H}$ and $\text{O}^{18} + \text{O}_2 = \text{O} + \text{OO}^{18}$ always remained equilibrated; and the slower exchange between the H_2O -OH and the O_2 -O systems is controlled by reactions of the type of (1), $\text{H} + \text{OO}^{18} \rightleftharpoons \text{O} + \text{O}^{18}\text{H}$, with $k_1 \approx 4 \times 10^{14} e^{-18 \text{ kcal.}/RT} \text{ cm}^3 \text{ mole}^{-1} \text{ sec}^{-1}$. The reaction $\text{OH} + \text{O}^{18}\text{H} \rightleftharpoons \text{H}_2\text{O} + \text{O}^{18}$ can be allowed for in the exchange, the rate constant being known,¹¹ but it is less important.

Figure 2 shows some measurements for one mixture, and the data for all the gases are summarized in Table II. The radical concentrations, given by listing $[\text{OH}]$, also imply $[\text{O}]$ and $[\text{H}]$ by virtue of equilibrated (1), (2), and (3).

Discussion of H_2 -Lean Gases

In these gases, $[\text{O}]$ is much larger than the concentration appropriate to the equilibrium $\text{O}_2 = 2\text{O}$. For

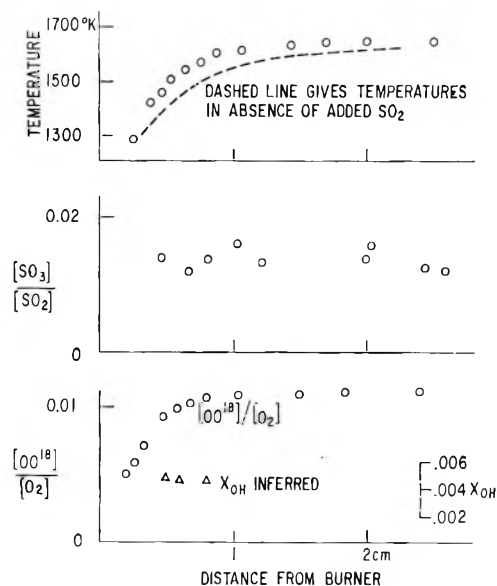


Figure 2. $\text{Ar} + 0.43\text{H}_2 + 0.43\text{O}_2 + 0.043\text{SO}_2 + 0.32\text{H}_2\text{O}$ (H_2O containing H_2O^{18}) at 10 cm. pressure with a mass flow of $7.4 \times 10^{-3} \text{ g. cm.}^{-2} \text{ sec.}^{-1}$.

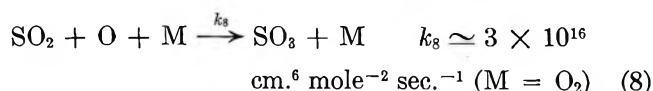
Table II: Observations on Lean Flames

Run ^a	P , cm.	Temp., °K.	$\frac{[\text{SO}_3]}{[\text{SO}_2]}$	$\frac{[\text{OH}]}{\times 10^9}$, moles cm.^{-3}	k_8/k_9^b
1	10	1600	0.014	4.7	2×10^4
2	6	1630	0.0039	3	2
3	12	1600	0.013	5.5	2.4
4	20	1600	0.016	7	1.5

^a Run 1, portrayed by Figure 2; reactants for other runs were $\text{Ar} + 0.58\text{H}_2 + 0.38\text{O}_2 + 0.040\text{SO}_2 + 0.5\text{H}_2\text{O}$ (runs 2 and 4) or $+ 0.7\text{H}_2\text{O}$ (run 3). ^b $k_8/k_9 = \frac{[\text{SO}_3]\{[\text{O}] + [\text{H}]\}}{[\text{SO}_2][\text{O}][\text{M}]}$, $[\text{M}] = \text{total gas concentration}$.

the flame portrayed by Figure 2, the ratio of $[\text{SO}_3]/[\text{SO}_2]$ expected at 1600°K. is 0.0027, if $\text{SO}_2 + 0.5\text{O}_2 = \text{SO}_3$ is equilibrated; 0.00001, if $\text{SO}_2 + \text{O}_2 = \text{SO}_3 + \text{O}$ is equilibrated; or 0.78, if $\text{SO}_2 + \text{O} + \text{M} = \text{SO}_3 + \text{M}$ is equilibrated. They are so different from the observed value of $[\text{SO}_3]/[\text{SO}_2] = 0.014$ that none of the equilibria can be satisfied.

Reaction 8 is known to be fast when O atoms from a discharge are mixed with SO_2 at 295°K.,¹⁶ and Web-



(15) C. P. Fenimore and G. W. Jones, 8th International Symposium on Combustion, Pasadena, Calif., Aug. 1960, Williams and Wilkins Co., Baltimore, Md., 1962, p. 127.

(16) F. Kaufman, *Progr. Reaction Kinetics*, 1, 30 (1961).

ster and Walsh⁵ obtained evidence that reaction 8 was an inhibiting step in their hydrogen-oxygen mixtures at 784°K. They also proposed a rate constant of the order quoted. If k_8 had the same value at 1600°K., we calculate that the [O] present 0.8 cm. from the burner in Figure 2 would oxidize 10% of the SO₂ to SO₃ by (8) while the gas flows 0.2 cm. However, no net oxidation of SO₂ was observed in this region.

The most reasonable conclusion is that SO₃ is formed by (8) but is destroyed as fast as formed by a faster reaction than the reverse of (8). An obvious choice for the process destroying SO₃ is (9), so that the steady [SO₃]/



[SO₂] ratio = $k_8[\text{O}][\text{M}]/\bar{k}_9\{[\text{O}] + [\text{H}]\}$ where \bar{k}_9 is an average rate constant for the interaction of either O or H with SO₃. The formation of HO₂ from SO₃ and OH would be endothermic by about 20 kcal., and OH is neglected as a reaction partner in the destruction of SO₃. The mechanism gives $k_8/\bar{k}_9 = 2 \times 10^4$ or \bar{k}_9 of the order of 10^{12} cm.³ mole⁻¹ sec.⁻¹ for the gas described by Figure 2—a plausible rate constant for fast bimolecular reactions in flames.

Table II shows that this interpretation also fits the other flames examined. The data are too few for a

meaningful resolution of \bar{k}_9 into separate constants for O and for H.

The other lean flames resembled Figure 2 in having a somewhat faster temperature rise in the presence than in the absence of SO₂, and this is consistent with the occurrence of reactions 8 and 9 which constitute a catalytic cycle for recombining radicals and evolving heat. In the absence of SO₂, heat is evolved in the burnt gas of hydrogen lean flames at a rate¹²

$$\dot{h} \simeq 1.1 \times 10^{22}[\text{H}][\text{O}_2][\text{H}_2\text{O}] \text{ cal. cm.}^{-3} \text{ sec.}^{-1}$$

and even when sulfur was present in the flame of Figure 2, we expect a heat release of $\dot{h} \simeq 0.6$ cal. cm.⁻³ sec.⁻¹ at 0.8 cm. from the burner from this cause. Reactions 8 and 9 should contribute an additional

$$\begin{aligned} \dot{h} &\simeq 110 \times 10^3 k_8 [\text{O}][\text{SO}_2][\text{M}] \\ &\simeq 0.2 \text{ at 0.8 cm. from the burner} \end{aligned}$$

if the k_8 quoted above is accepted. Thus, an appreciable catalysis is expected, though the contribution of (8) and (9) is not overwhelming as it would have to be to permit an estimate of k_t from the rate of heat evolution. From the temperature traverse in Figure 2, we calculate a heat release of 0.7 cal. cm.⁻³ sec.⁻¹ at 0.8 cm. from the burner, which is consistent with what is expected.

Soret Coefficients and Heats of Transport of Some Aqueous Electrolytes at 9°

by B. D. Butler and J. C. R. Turner¹

Department of Chemical Engineering, University of Cambridge, Cambridge, England (Received May 10, 1965)

Soret coefficients of seven 0.01 *M* aqueous electrolytes have been measured conductometrically at 9.35°. The heats of transport calculated from these results are considerably smaller than those at 25°, previously measured. The temperature dependence of the heat of transport appears to be much the same for all of the electrolytes investigated even though the values of the heats of transport cover a wide range.

Introduction

Conductometric methods have recently proved valuable in examining thermal diffusion (the Soret effect) in dilute aqueous electrolytes. The ratio bridge method² has been applied to a variety of solutions, mostly at 25°, and investigations of the concentration dependence of the Soret coefficients and heats of transport of several salts have also been carried out.^{3,4} These showed (i) that Soret coefficients, defined by the equation

$$s = -(\partial \ln m / \partial T)_{\text{steady state}}$$

range from about -2×10^{-3} to $+14 \times 10^{-3}$ deg.⁻¹ for the electrolytes studied, where *m* is molality and *T* is temperature, and (ii) that the variation of *s* with *m* is primarily a matter of valence type (at least in dilute solutions) and is independent of the magnitude of *s*.

Some early measurements indicated that the temperature dependence of *s* might show the same characteristic. Experiments have therefore been carried out on seven electrolytes at around 9.35° mean temperature.

Experimental Arrangements and Results

The ratio cell of Snowdon and Turner^{2b} was used, in conjunction with the thermostats and bridge network of Price.⁵ The method of measurement was not different in any important way from that described by Snowdon and Turner.^{2b} It proved rather more difficult to maintain and control the end-plate temperatures at approximately 5 and 15° than at 20 and 30°, as in earlier work.

This led to impairment of the accuracy and reproducibility of the results, as compared with the 25° results obtained earlier, but the results remain suffi-

ciently precise for some conclusions about the temperature dependence of *s* to be drawn.

The concentration of the solutions used was 0.01 *M* in all cases. The temperature difference applied across the cell was about 9.5°, and the mean temperature of the cell in the different runs varied from 9.31 to 9.42°.

To convert values of *s* to give the appropriate molar heat of transport, *Q*^{*}, it is necessary to estimate the factor $1 + (\partial \ln \gamma / \partial \ln m)_T$, in which γ is the mean ionic activity coefficient. This was done using the information of Robinson and Stokes⁶ and of Guggenheim and Stokes,⁷ making appropriate adjustment for the different temperature. For BaCl₂ the factor was estimated to be 0.878; for all the other solutions the factor lay between 0.954 and 0.958.

The results are summarized in Table I. An estimate of the reliability of the value of *Q*^{*} is given in each case. This is based on an assessment of the reproducibility, sensitivity, and convective stability. For KCl the effect is negative at this temperature. Hence, the concentration differences produced by thermal diffusion act to reduce the density gradient set up by the temperature gradient. This tends to make worse any con-

(1) Department of Chemical Engineering, The University of Texas, Austin, Texas.

(2) (a) J. N. Agar and J. C. R. Turner, *Proc. Roy. Soc. (London)*, **A255**, 307 (1960); (b) P. N. Snowdon and J. C. R. Turner, *Trans. Faraday Soc.*, **56**, 1409 (1960).

(3) P. N. Snowdon and J. C. R. Turner, *ibid.*, **56**, 1812 (1960).

(4) A. D. Payton and J. C. R. Turner, *ibid.*, **58**, 55 (1962).

(5) C. D. Price, Ph.D. Thesis, Cambridge University, 1962.

(6) R. A. Robinson and R. H. Stokes, "Electrolyte Solutions," Butterworth and Co. Ltd., London, 1955.

(7) E. A. Guggenheim and R. H. Stokes, *Trans. Faraday Soc.*, **54**, 1646 (1958).

Table I: Values of the Soret Coefficient, s , and the Molar Heat of Transport, Q^* , for 0.01 M Solutions

Sub- stance	10^3s , deg. ⁻¹	Q^* at 9.36°, cal./mole	Q^* at 25°, cal./mole ^a	$\Delta Q^*/\Delta T$, cal./mole, deg.
HCl	7.9	2405 ± 60	3062	41
BaCl ₂	3.0	1260 ± 30	2093	54
CsCl	0.43	130 ± 15	827	44
KCl	-0.65	-200 ± 50	496	44
NaCl	0.76	230 ± 60	693	29
NaF	3.5	1060 ± 60	1529	29
NaOH	13.6	4120 ± 40	4652	33

^a From ref. 2b and 4.

vectional instability^{2a}; the Soret coefficient for KCl had to be estimated by the "initial slope" method.^{2a}

Discussion

In Table I the values of Q^* at 25° refer to 25.3°,^{2b} except for the case of BaCl₂, where the mean temperature was 24.9.⁴ We can thus make an estimate of $\Delta Q^*/\Delta T$ between 9 and 25°, and these estimates are given in Table I.

BaCl₂ gives three ions in solution, and, if one multiplies its result (54) by $2/3$, the spread of these figures is remarkably small in comparison with the spread in the values of Q^* , especially when the experimental errors are considered.

Agar⁸ has defined a specific heat C_p^* by the relationship $C_p^* = T(\partial S^*/\partial T) = \partial Q^*/\partial T - Q^*/T$, and he gives some estimates of C_p^* based on values of Q^* from ref. 2a. Some of these are also given by Tyrrell.⁹ A more extensive list of values is given in a later publication by Agar.¹⁰

Usually Q^*/T amounts to only a few calories per mole per degree, and so $C_p^* \simeq \partial Q^*/\partial T$. However, with 0.01 M NaOH $Q^*/T \simeq 15$ cal./mole deg., and it would thus appear that $\partial Q^*/\partial T$ may be more closely the same for different salts than C_p^* . Our results also show that $\partial Q^*/\partial T$ does not depend very much on the temperature. Discussions of the significance of C_p^* are to be found in ref. 8-10.

Acknowledgments. The authors thank Professor R. G. W. Norrish and Dr. J. N. Agar for allowing experimental facilities in the Physical Chemistry Laboratory at Cambridge. B. D. B. also thanks the D.S.I.R. for a maintenance grant for the period within which this work was carried out.

(8) J. N. Agar in "The Structure of Electrolytic Solutions," W. J. Hamer, Ed., John Wiley and Sons, Inc., New York, N. Y., 1959, Chapter 13.

(9) H. J. V. Tyrrell, "Diffusion and Heat Flow in Liquids," Butterworth and Co. Ltd., London, 1961, Chapter 10.

(10) J. N. Agar in "Advances in Electrochemistry and Electrochemical Engineering," Vol. 3, P. Delahay, Ed., Interscience Publishers, Inc., New York, N. Y., 1963, Chapter 2.

The Mercury-Photosensitized Decomposition of Perfluoropropene¹

by Julian Heicklen and Vester Knight

Aerospace Corporation, El Segundo, California (Received May 12, 1965)

The Hg-sensitized decomposition of C_3F_6 was studied at temperatures of 210, 291, and 370° and pressures from 0.6 to 20 mm. The only products were C_2F_4 and C_4F_8-2 ; the former was more important, and in most cases the only product detected. The C_2F_4 yield falls off with increasing pressure or duration of exposure, but it rises with rising temperature. Where data exist, $\Phi(-C_3F_6)$ is similar to $\Phi(C_2F_4)$ for small conversions. However, $\Phi(-C_3F_6)$, unlike $\Phi(C_2F_4)$, does not depend on exposure time. The primary process is given by reactions a to f in the text. The activation energy for the limiting low-pressure dissociation is about 2.2 kcal./mole, which, when added to the energy of the absorbed radiation, yields a value of about 114.9 kcal./mole for the double-bond dissociation energy at absolute zero. The CF_3CF species formed combines with another radical or rearranges to C_2F_4 .

Introduction

The mercury-sensitized photolysis of C_2F_4 ² as well as its direct photolysis³ have been studied and CF_2 radicals were produced. In the Hg-sensitized experiments, an electronically excited molecule has also been postulated.^{2b} Dalby³ has examined briefly the direct photolysis of C_3F_6 , and his results suggest a split to CF_2 and CF_3CF radicals. We have examined the Hg-sensitized photolysis of C_3F_6 to see if the photochemistry is analogous to C_2F_4 and to gain more information about the reactive species produced.

Experimental Section

Hexafluoropropene from Peninsular Chem Research, Inc., was used without further purification except for degassing at -196° immediately before use. Gas chromatograms showed no impurity peaks.

The photolysis vessel was a 10-cm. long, 5-cm. diameter quartz cell. It was encased in a wire-wound aluminum furnace that overlapped each end of the cell by 2.5 cm. The ends of the furnace were covered with quartz plates to minimize convection losses. Temperature measurements were made by a thermocouple and were constant to $\pm 2^\circ$. Irradiation was from two spiral Hanovia mercury-resonance lamps, one at each end of the cell. The light passed through Corning 9-54 glasses before entering the cell, to remove unwanted radiation below 2200 Å.

At the conclusion of a run, the gases were transferred in a glass vacuum system with Teflon-Vyton stopcocks

and collected for analysis in an F & M Model 720 programmed dual-column chromatograph with a 3-m. silica gel column. The products found, C_2F_4 and C_4F_8-2 , as well as the C_3F_6 , were calibrated so that chromatogram areas could be converted to pressures.

Results

The results are listed in Table I. The absorbed intensity I_a was estimated by photolyzing mixtures of 200 mm. of C_3F_6 with either 60 or 200 mm. of oxygen at room temperature and measuring the sum of CF_2O and CF_3CFO produced. Saunders,⁴ working in this laboratory, has shown that under these conditions $\Phi(CF_2O) = \Phi(CF_3CFO) = 0.50$.

The C_3F_6 pressures listed in Table I are initial pressures at the appropriate temperatures, as obtained by direct measurement. During photolysis, C_3F_6 was depleted; for some low-pressure runs carried to extended conversions, as much as 60% of the C_3F_6 was consumed. The final C_3F_6 pressure was computed from the chromatograms; thus the C_3F_6 consumption could be estimated.

Experiments were performed for various exposures at four temperatures and several pressures. At room

(1) This work was supported by the U. S. Air Force under Contract No. AF 04(695)-469.

(2) (a) B. Atkinson, *J. Chem. Soc.*, 2684 (1952); (b) J. Heicklen, V. Knight, and S. A. Greene, *J. Chem. Phys.*, 42, 221 (1965).

(3) F. W. Dalby, *ibid.*, 41, 2297 (1964).

(4) D. Saunders, unpublished work.

Table I: Mercury-Sensitized Photolysis of C_3F_6 ($I_a = 5.4 \times 10^{-3}$ quanta/cc.-sec.)

(C_3F_6) , mm.	Exposure time, min.	$\Phi(-C_3F_6)$	$\Phi(C_2F_4)$	$\Phi(C_4F_8-2)$	(C_3F_6) , mm.	Exposure time, min.	$\Phi(-C_3F_6)$	$\Phi(C_2F_4)$	$\Phi(C_4F_8-2)$
$T = 212 \pm 4^\circ$					$T = 291 \pm 2^\circ$				
0.64	2.50	...	0.09	0 ^a	0.72	20.00	0.071	0.072	0
0.61	5.00	0.06	0.13	0	0.61	55.00	0.039	0.0145	0
0.66	7.50	0.06	0.12	0	2.24	2.50	...	0.17	0
0.66	10.00	0.07	0.090	0	2.27	5.00	...	0.14	0
2.15	5.00	...	0.10	0	2.27	7.50	...	0.10	0
2.13	10.00	...	0.066	0	2.19	10.00	...	0.12	0
2.13	15.00	...	0.060	0	2.13	15.00	...	0.077	0
2.13	20.00	...	0.050	0	2.24	21.00	...	0.070	Trace
2.36	60.00	...	0.027	0.0033	6.2	3.00	...	0.09	0
2.10	60.00	...	0.022	0.0030	6.3	6.00	...	0.08	0
6.6	5.00	...	0.05	0	6.2	9.00	...	0.085	0
6.3	10.00	...	0.034	0	6.3	12.00	...	0.074	0
6.2	20.00	...	0.035	0	6.3	15.00	...	0.062	0
6.4	30.00	...	0.037	0	6.3	50.00	...	0.031	Trace
6.0	30.00	...	0.031	0.0069	6.3	150.00	...	0.0061	0.00053
6.0	60.00	...	0.019	0.0074	20.0	5.00	...	0.050	Trace
6.2	240.00	...	0.0057	0.0042	20.0	10.00	...	0.044	Trace
20.0	15.00	...	0.024	Trace ^b	21.5	15.00	...	0.034	Trace
20.0	15.00	...	0.011	Trace	22.0	780.00	...	0.00074	0.00061
20.0	30.00	...	0.012	Trace	$T = 370 \pm 2^\circ$				
22.0	30.00	...	0.010	0.0076	0.62	2.00	0.1	0.24	0
22.0	60.00	...	0.0087	0.0064	0.64	5.00	0.14	0.24	0
19.0	90.00	...	0.0044	0.0036	0.62	7.50	0.12	0.155	0
18.5	900.00	...	0.0011	0.0019	0.67	10.00	0.15	0.140	0
20.5	930.00	...	0.00048	0.00064	0.62	10.00	0.11	0.114	0
60.0	60.00	...	0.0020	0.0045	2.11	1.00	...	0.34	0
199.0	60.00	...	Trace	0.001	2.09	2.00	...	0.29	0
$T = 291 \pm 2^\circ$					2.16	2.50	...	0.39	0
0.72	2.50	0.06	0.11	0	2.13	5.00	0.17	0.21	0
0.63	5.00	0.11	0.14	0	2.19	5.00	0.29	0.27	0
0.64	5.00	...	0.13	0	2.22	10.00	0.18	0.16	Trace
0.64	7.50	0.084	0.10	0	2.13	15.00	0.10	0.12	Trace
0.67	10.00	0.095	0.10	0	2.19	16.00	0.16	0.12	Trace
0.67	10.00	...	0.13	0	2.08	40.00	0.12	0.038	Trace
0.59	15.00	0.046	0.061	0	6.4	2.50	...	0.20	Trace
0.59	15.00	0.056	0.054	0	6.3	5.00	...	0.18	Trace
0.64	20.00	0.034	0.041	0	6.3	7.50	...	0.15	Trace
					6.4	10.00	...	0.15	Trace
					6.5	15.00	...	0.10	Trace
					6.4	15.00	...	0.11	0.025

^a The 0 means $\Phi \leq 0.10/\text{time in min.}$ ^b Trace means $\Phi \sim 0.3/\text{time in min.}$

temperature, under no conditions were products found, even for extended exposures. The only products found at the elevated temperatures were C_2F_4 and, in some cases, perfluorobutene-2. For a few runs at extended conversions, small amounts of *c*- C_3F_6 were observed, too. Presumably it is a secondary product. The C_4F_8-2 yield rarely exceeded that of C_2F_4 . It decreases in relative importance at low pressures and high temperatures. The C_2F_4 yield, and probably also the C_4F_8-2 yield, falls off with increasing pressure or dura-

tion of exposure. However, it rises with temperature. Where data exist, the quantum yield of C_3F_6 consumption $\Phi(-C_3F_6)$ is similar to $\Phi(C_2F_4)$ for small conversions. However, $\Phi(-C_3F_6)$, unlike $\Phi(C_2F_4)$, does not depend on the exposure time.

Discussion

If C_2F_4 and C_4F_8-2 are the only products, then mass-balance considerations require that

$$\Phi(-C_3F_6) = (2/3)\Phi(C_2F_4) + (4/3)\Phi(C_4F_8-2) \quad (1)$$

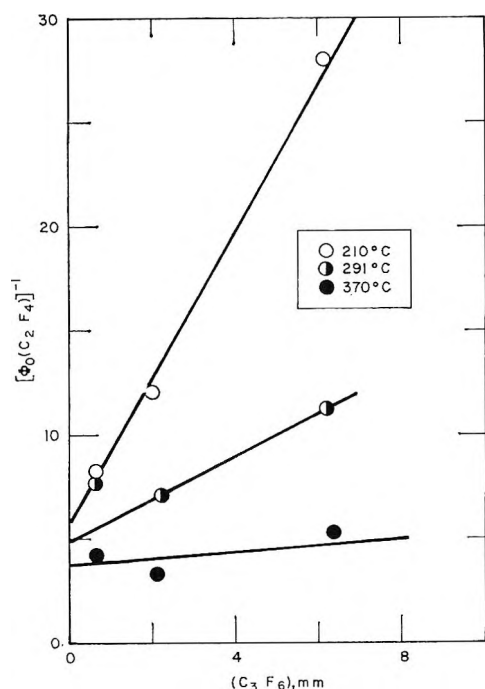


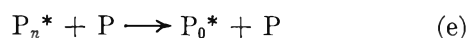
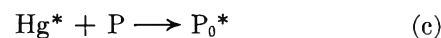
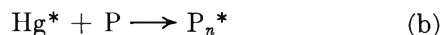
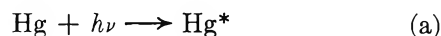
Figure 1. Plot of $[\Phi_0(C_2F_4)]^{-1}$ vs. (C_3F_6) .

For short exposures, eq. 1 is obeyed reasonably well. However, for longer exposures, both $\Phi(C_2F_4)$ and $\Phi(C_4F_8-2)$ drop markedly, whereas $\Phi(-C_3F_6)$ falls only slightly, if at all. Since $\Phi(-C_3F_6)$ is fairly constant to changing exposure times, the primary process presumably is not being inhibited. Apparently, the products are formed in such a way that they can easily disappear by polymerization. Consequently, the discussion of results will concern only the short-time limiting values of product quantum yields, $\Phi_0(C_2F_4)$ and $\Phi_0(C_4F_8-2)$.

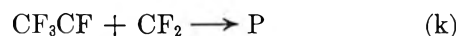
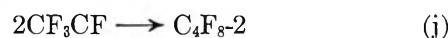
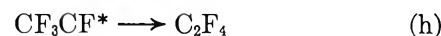
The reciprocals of $\Phi_0(C_2F_4)$ are plotted in Figure 1 vs. the C_3F_6 pressure for the three temperatures. It is apparent that the decomposition is a function of temperature and is inhibited by increasing the pressure. A temperature-dependent process can arise either from the energy distribution in the ground electronic state before excitation or from the energy distribution of the thermally equilibrated upper electronic state. For this system, the second possibility can be eliminated for two reasons. First, the results with added oxygen⁵ show that the upper electronic state is not removed by collision with C_3F_6 ; thus if the decomposition had occurred from this state, no pressure effect should have been observed. Second, the results with added oxygen show that the quantum yield of formation of the upper electronic state is at least 0.5 and probably unity. Consequently, if decomposition had occurred from the thermally equilibrated upper electronic state, $\Phi_0(C_2F_4)$ extrapolated to zero pressure should have been

greater than 0.5 and independent of temperature, contrary to extrapolated values from Figure 1.

The most likely mechanism that explains the primary process is



where P is C_3F_6 , the asterisk represents an electronically excited molecule (probably a triplet), the subscripts n and 0 refer, respectively, to vibrational levels sufficiently energetic or not sufficiently energetic to permit dissociation, and CF_3CF^x is some energetic state of CF_3CF . The amount of excess energy in CF_3CF^x should increase with temperature. We have included the possibility that CF_3CF contains some extra energy to explain the temperature and pressure dependence on the fate of the CF_3CF species. The secondary reactions that then will explain the results are



The mechanism predicts that

$$[\Phi_0(C_2F_4)]^{-1} = [\Phi_{00}(C_2F_4)]^{-1} \left[1 + \frac{k_e}{k_d} P \right] \quad (2)$$

where $\Phi_{00}(C_2F_4)$ is the low-pressure limit of $\Phi_0(C_2F_4)$. Figure 1 shows plots of $[\Phi_0(C_2F_4)]^{-1}$ vs. P for the three temperatures. The data are badly scattered owing to the difficulty in analysis at extremely short conversions. Nevertheless, reasonable straight lines could be drawn that follow a regular trend; the intercepts give $\Phi_{00}(C_2F_4)$, and the ratios of slope to intercept give k_e/k_d . Even though there is some difficulty in determining the slopes and intercepts, the conclusions are hardly affected at all. For example, if the intercepts were altered by a factor of two, the estimated dissociation energy would change by less than 1 kcal./mole. At low pressures, the only product is C_2F_4 , and eq. 1 reduces to

$$(2/3)\Phi_{00}(C_2F_4) = \phi_{00} \quad (3)$$

(5) J. Heicklen and V. Knight, *J. Phys. Chem.*, **69**, 3641 (1965).

where ϕ_{00} is the short-duration primary quantum yield of C₃F₆ consumption extrapolated to zero pressures. The approximate values obtained for ϕ_{00} and k_d/k_e are listed in Table II. Now ϕ_{00} is just k_b/k_c and is related to the distribution of energy states in the ground electronic level through the Boltzmann function

$$\phi_{00} = \exp(-E_0/RT) \quad (4)$$

where E_0 is the energy needed by the ground electronic state to form P_n* upon collision with Hg*. The approximate values of E_0 , computed at each temperature, are also listed in Table II. The value is roughly independent of temperature, as indeed it should be. If E_0 is added to the energy of the absorbed radiation (112.7

Table II: Approximate Rate Constants

Temp., °C.	ϕ_{00}	E_0 , kcal./mole	$(k_d/k_e) \times 10^4$, mole/l.
210	0.11	2.1	0.54
291	0.14	2.2	1.3
370	0.18	2.2	5.7

kcal./mole), a value of about 114.9 kcal./mole is found for the dissociation energy of the double bond in C₃F₆ at absolute zero.

Acknowledgment. The authors wish to thank Mrs. Barbara Peer for assistance with the manuscript.

The Heats of Formation and Polymerization of Carbon Suboxide

by B. D. Kybett, G. K. Johnson, C. K. Barker, and J. L. Margrave

*Departments of Chemistry, Rice University, Houston, Texas, and University of Wisconsin, Madison, Wisconsin
(Received May 12, 1965)*

The heat of formation of carbon suboxide has been determined from its heat of combustion in oxygen. The bond energies are compared with those in allene and carbon dioxide. The heat of polymerization to form the thermal polymer of C₃O₂ and the heat of hydrolysis of this polymer have also been determined.

Introduction

Marx¹ and Grauer² have reviewed the large number of investigations of the reactions and properties of carbon suboxide. There has recently been increased interest in the thermochemistry of carbon suboxide since it is a possible intermediate in the radiolysis of carbon monoxide produced in carbon dioxide-cooled reactors. Redgrove³ has stated that Diels determined its heat of combustion but this work has not been published. There is serious disagreement among estimates which have been made. The "JANAF Tables"⁴ quote $\Delta H_f^\circ(\text{g}) = -8.3$ kcal./mole. Botter⁵ calculated that $\Delta H_f^\circ(\text{g}) \geq -30$ kcal./mole from the appearance potentials of its fragment ions, and ≈ -25

kcal./mole from estimated bond energies. The old estimate,³ which has recently been quoted,⁶ is 47.4 kcal./mole. The structure of the thermal polymer has recently been investigated by X-ray diffraction and infrared, visible, and ultraviolet absorption spectroscopy.^{7,8} This paper describes determinations of the

- (1) D. Marx, Thesis, Faculté des Sciences de Paris, 1959.
- (2) R. Grauer, *Chimia (Aarau)*, **14**, 11 (1960).
- (3) H. S. Redgrove, *Chem. News*, **120**, 209 (1920).
- (4) "JANAF Interim Thermochemical Tables," D. R. Stull, Ed., The Dow Chemical Co., Midland, Mich., Dec. 31, 1960.
- (5) R. Botter, "Advances in Mass Spectrometry," Vol. II, R. M. Elliot, Ed., Pergamon Press, Oxford, 1963.
- (6) O. Glemser, "Handbook of Preparative Inorganic Chemistry," Vol. I, G. Brauer, Ed., Academic Press, New York, N. Y., 1963.

heats of formation and polymerization of carbon suboxide from heats of combustion in oxygen.

Experimental Section

A. Apparatus. A rotating bomb calorimeter built to Argonne National Laboratories design CT-3986 was used although rotation was not necessary. The bomb, Parr Instrument Co. Type 1004D, was of nickel with nickel and platinum fittings. Platinum crucibles were used for the benzoic acid calibrations and for the combustions of carbon suboxide polymer. The carbon suboxide reacted explosively, occasionally damaging the bomb fittings. A nickel alloy cup was used for these combustions, together with a 0.125-in. nickel sheet covered with platinum foil, which was mounted above the cup to prevent spattering of unreacted material. The ignition system delivered a 0.2-cal. pulse of electrical energy to the bomb by discharge of a condenser through a small platinum fuse wire to ignite a cotton thread fuse. The design was similar to that described by Coughlin, *et al.*⁹

Temperatures were measured with a 2000-ohm (at 25°) glass bead thermistor which was immersed in a few drops of silicone oil contained in the sealed metal end of a Kovar seal. This was inserted in the calorimeter in the same way as the normal platinum resistance thermometer. The thermistor formed one arm of a conventional d.c. Wheatstone bridge, used with a Leeds and Northrup galvanometer Type 2430 (5×10^{-10} amp. per scale division). With a current of 0.2 ma. through the thermistor a change of 0.1 ohm in its resistance (0.002°) corresponded to three scale divisions; the galvanometer stability allowed readings reproducible to at least 0.3 division. The normal precautions¹⁰ were taken to ensure reproducible behavior. The relationship between the resistance of the thermistor and temperature was determined by calibration against two Beckmann thermometers. The deviations from linearity of the $\ln R-T$ relation by which temperatures were expressed were smoothed graphically and used to correct subsequent readings at 10^{-4} intervals by means of a computer. The temperature rise during a combustion was calculated using the standard methods.¹¹ Calibrations with NBS benzoic acid showed that the reproducibility was better than 0.02%. The calorimeter equivalent was expressed in terms of the resistance of the thermistor and was approximately 3221 cal./deg.

B. Materials. The carbon suboxide was generously supplied by Prof. J. E. Kilpatrick. It had been prepared¹² by the dehydration of malonic acid with phosphorus pentoxide and purified by fractional distillation followed by distillation through calcium oxide,

Ascarite, and Drierite. Mass spectrometry showed that the only impurity was carbon dioxide and sharpness of melting data indicated a purity better than 99.98%. The infrared spectrum (from 400 to 4000 cm.^{-1}) taken before combustion using a Beckman IR-9 instrument, was in excellent quantitative agreement with that of Miller and Fately¹³ except for a very small absorption at 667 cm.^{-1} (CO_2), indicating that there were no hydrogen-containing impurities in the sample. The purity was taken as 99.98% with 0.02% CO_2 . Oxygen of 99.8% purity was further purified by passing over a copper wire heated to 600°, Ascarite, and Drierite.

C. Heats of Combustion. Carbon suboxide was burned as a liquid under its own vapor pressure contained in thin-walled, 1.5-cm. diameter glass bulbs. These were filled by vacuum low-temperature distillation and sealed under vacuum with the carbon suboxide at liquid N_2 temperature. When warmed to room temperature, the liquid carbon suboxide remained water clear for from 3 to 12 hr. The samples were burned after they had been at room temperature between 1 and 2 hr. and should not have contained any polymer. The combustion was vigorous and occasionally explosive. No carbon monoxide was found in the gaseous combustion products, using the test described by Shepherd,¹⁴ although some carbon was deposited on the crucible and its cover. Negligible amounts of nitric acid were formed.

The polymer was formed by sealing liquid carbon suboxide in a copper tube and keeping it at 0° for 12 hr. and room temperature for at least 12 hr. It was sealed in bags of polyester film¹⁵ inside a drybox. The polymer readily reacts with the water vapor in the air so hydrolyzed samples were prepared by exposing the polymer to the atmosphere (25°, 50% humidity) for

(7) R. N. Smith, D. A. Young, E. N. Smith, and C. C. Carter, *Inorg. Chem.*, **2**, 829 (1963).

(8) A. R. Blake, W. T. Eeles, and P. P. Jennings, *Trans. Faraday Soc.*, **60**, 691 (1964).

(9) J. L. Lacina, A. J. Enzler, and J. P. Coughlin, 18th Calorimetry Conference, Bartlesville, Okla., Oct. 1963.

(10) H. A. Skinner, J. M. Sturtevant, and S. Sunner, "Experimental Thermochemistry," Vol. II, H. A. Skinner, Ed., Interscience Publishers, New York, N. Y., 1962.

(11) J. Coops, R. S. Jessup, and K. van Nes, "Experimental Thermochemistry," F. D. Rossini, Ed., Interscience Publishers, Inc., New York, N. Y., 1956.

(12) L. A. McDougall and J. E. Kilpatrick, *J. Chem. Phys.*, **42**, 2311 (1965).

(13) F. A. Miller and W. G. Fately, *Spectrochim. Acta*, **20**, 253 (1964).

(14) M. Shepherd, *Anal. Chem.*, **19**, 77 (1947).

(15) W. D. Good and D. W. Scott, "Experimental Thermochemistry," Vol. II, H. A. Skinner, Ed., Interscience Publishers, Inc., New York, N. Y., 1962.

Table I: Heats of Combustion and Formation of Carbon Suboxide

	1	2	3	4	5	6
<i>m</i> , g.	0.18279	0.32820	1.16815	0.92815	0.94821	0.77799
ΔE_{total} , cal.	-1639.9	-2165.7	-5147.0	-4316.0	-4483.6	-3899.0
$\Delta E_{\text{benzoic acid}}$, cal.	975.7	978.1	1000.2	855.7	947.3	997.8
ΔE_{fuse} , cal.	4.9	4.4	4.2	4.3	4.8	4.7
ΔE_{carbon} , cal.	-17.6	-46.3	-21.6	-18.5	-12.2	-19.9
Washburn cor., cal.	0.3	0.3	2.1	1.6	1.4	0.9
$\Delta E_{\text{cond}}(\text{C}_3\text{O}_2)$, cal.	-0.7	-0.7	-0.2	-0.2	-0.4	-0.5
$\Delta E_c^\circ/M$, cal. g. ⁻¹	-3705.3 ^a	-3747.4	-3563.2 ^a	-3742.0	-3736.2	-3748.1
Mean $\Delta E_c^\circ/M$ for sample =	-3743.4 ± 2.8 cal./g.		$\Delta E_c^\circ/M$ for C ₃ O ₂ = -3744.1 cal./g.			
	$\Delta H_c^\circ = -253.13$ kcal./mole		$\Delta H_{\text{cond}, 298} = -5.65$ kcal./mole ^b			
	$\Delta H_{f, 298}(l) = -29.03 \pm 0.24$ kcal./mole		$\Delta H_{f, 298}(g) = -23.38 \pm 0.44$ kcal./mole			

^a Discarded; probably some polymerization had occurred. ^b Calculated from data in ref. 12.

Table II: Heats of Combustion of Carbon Suboxide Polymers

	Dry polymer				Hydrolyzed polymer		
	7	8	9	10	11	12	13
<i>m</i> , g.	0.10081	0.15082	0.26831	0.25920	0.64535	0.27926	0.14097
ΔE_{tot} , cal.	-3333.6	-3528.4	-3196.0	-3332.7	-3649.8	-3219.4	-3345.7
$\Delta E_{\text{benzoic acid}}$, cal.	1884.6	1835.7	1289.5	1380.0	1694.1	2387.0	1745.1
ΔE_{Mylar} , cal.	1101.9	1191.0	1016.1	1084.2	0.0	0.0	1173.0
ΔE_{fuse} , cal.	4.7	2.7	4.8	4.8	4.0	4.4	4.4
ΔE_{carbon} , cal.	3.8	0.0	0.0	0.0	0.0	0.0	0.0
Washburn cor., cal.	0.0	0.2	0.0	0.3	2.1	0.0	0.1
$\Delta E_c^\circ/M$, cal. g. ⁻¹	-3358.8	-3307.3	-3300.7	-3331.0	-3021.0	-2965.0	-3001.3
Mean $\Delta E_c^\circ/M =$	-3324.5 ± 13.2 cal./g.				-2995.8 ± 16.4 cal./g.		

at least 12 hr. Microcombustion analyses of the hydrolyzed polymer gave 52.16% C, 2.79% H, and 45.06% O.

Results

The results are given in Tables I and II. The sample mass was based on direct weighing and corrections for buoyancy. Corrections to standard states were made by the method of Hubbard, *et al.*¹⁶ ΔE_{cond} is a correction for the small amount of vapor present in the ampoules. The heat of formation was based on a molecular weight of 68.033, and -94.054 kcal./mole for the heat of formation of carbon dioxide. The heat of combustion of Mylar with the humidity conditions prevailing in the laboratory was -5463.5 cal./g. All energies are expressed in terms of the defined calorie equal to 4.1840 absolute joules.

Discussion

The heat of combustion of another less pure sample of C₃O₂ has also been determined. This sample was prepared by the thermal decomposition of diacetyl tartaric anhydride¹⁷ and purified by low-temperature

vacuum distillation. Infrared analyses showed a ketene impurity in a concentration of 5% by weight. A series of five combustions, with essentially the same technique but using the calorimeter at the University of Wisconsin, gave $\Delta H_{f, 298}(g) = -25.2 \pm 3.0$ kcal./mole; this uncertainty includes an added 1.5 kcal. to allow for uncertainty in the determination of the purity. This is in good agreement with the present value of -23.38 ± 0.44 kcal./mole.

Using 170.9 and 59.54 kcal./mole for the heats of atomization of carbon and oxygen, respectively,¹⁸ and the experimental standard heat of formation, the total atomization energy of C₃O₂ is 655.2 kcal./mole. The bond distances have been measured using electron diffraction by various authors^{19a,b}; the latest values^{19c} are 1.28 Å. for C=C and 1.16 Å. for C=O. The C=C

(16) W. N. Hubbard, D. W. Scott, and G. Waddington, "Experimental Thermochemistry," F. D. Rossini, Ed., Interscience Publishers, Inc., New York, N. Y., 1956.

(17) E. Ott and K. Schmidt, *Chem. Ber.*, **55**, 2126 (1922).

(18) T. L. Cottrell, "The Strengths of Chemical Bonds," Academic Press, New York, N. Y., 1958.

distance is smaller than in the ethylenes, but comparable with those in allene,²⁰ 1.309 Å., which contains a similar system of carbon atoms. The standard heat of formation of allene is 45.92 kcal./mole,²¹ which gives 675.2 kcal./mole for the total bond energy ($\Delta H_f^\circ(\text{H}) = 52.09$).¹⁸ Dewar and Schmeising²² have estimated the bond energy of a C(sp²)-H bond to be 100.9 kcal./mole, which leaves $675.2 - 4 \times 100.9 = 271.6$ kcal./mole for the energy associated with the C=C=C group. This indicates that $655.2 - 271.6 = 383.6$ kcal./mole of the bond energy in C₃O₂ is associated with the two C=O bonds. In carbon dioxide the bond length is 1.16 Å. and the bond energy 192 kcal./mole. The Dewar-Schmeising scheme has been criticized,²³ but is used here because it allots an individual term to the olefinic C-H bond.

A number of structures have been proposed for the thermal polymer of C₃O₂. Two recent investigations^{7,8} indicate that it is basically the polycyclic six-membered unsaturated lactone shown in Figure 1.

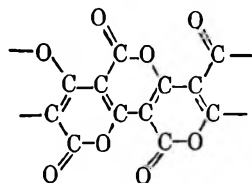
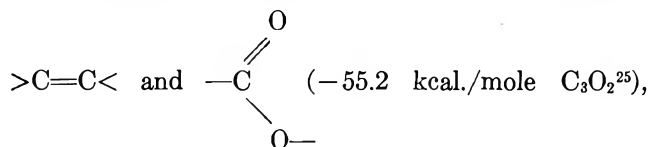


Figure 1. Structure of carbon suboxide polymer.

The chains are probably terminated by 1,2 or 2,3 addition of a C₃O₂ molecule to form five-membered terminal rings with attached ketenyl groups. The polymer formed below 100° has five to ten units in the chain. Consequently, the terminal groups will only have a small influence on the total bond energy of the polymer and will be neglected in the following discussion.

The heat of polymerization from gaseous monomer to condensed polymer is 32.6 ± 0.9 kcal./mole of C₃O₂ from the heats of combustion. There are not sufficient data on the bond energies involved to permit an accurate evaluation of this figure. An estimated heat of polymerization is 18.8 kcal., obtained from the heat of sublimation of the polymer (13.8 kcal./mole of C₃O₂ using the group increments given by Bondi²⁴), the

heat of formation of gaseous polymer considered as



and the heat of formation of carbon suboxide. Some of the differences between this and the experimental value may be due to resonance in the polymer which has been suggested by Smith, *et al.*⁷

The product of the reaction of the polymer with water is not definitely known, and depends on the degree of exposure to water and the temperature at which the polymer was originally formed. The infrared spectra suggest that the hydrolyzed polymer contains a carboxylic acid type structure.⁷ This could be due to hydrolysis of the lactone rings to give hydroxy acids. When allowance is made for the 2.79% H present in the hydrolyzed polymer which must come from reacted or adsorbed water, its heat of combustion is 3988.6 cal./g. of C₃O₂, and the heat of hydrolysis is 23 ± 2 kcal./mole of C₃O₂ ($\Delta H_f^\circ(\text{H}_2\text{O}) = 68.32$ kcal./mole). This can be compared with an estimated value of 8 kcal./mole obtained from the Bondi and Franklin group increment systems. If, however, allowance is made for the resonance energy of the dry polymer, the agreement between the experimental and estimated values is within the uncertainties involved.

Acknowledgments. This work has been supported by grants from the Robert A. Welch Foundation, the Petroleum Research Fund of the American Chemical Society, and the United States Atomic Energy Commission.

- (19) (a) H. Mackle and L. E. Sutton, *Trans. Faraday Soc.*, **47**, 937 (1951); (b) H. D. Rise, *J. Chem. Phys.*, **22**, 429 (1954); (c) R. L. Livingstone and C. N. R. Rao, *J. Am. Chem. Soc.*, **81**, 285 (1959).
 (20) C. F. Herzberg and B. P. Stoicheff, *Nature*, **175**, 79 (1955).
 (21) J. E. Kilpatrick, C. W. Beckett, E. J. Prosen, K. S. Pitzer, and F. D. Rossini, *J. Res. Natl. Bur. Std.*, **42**, 225 (1949).
 (22) M. J. S. Dewar and H. N. Schmeising, *Tetrahedron*, **5**, 166 (1959).
 (23) H. A. Skinner and G. Pilcher, *Quart. Rev. (London)*, **17**, 264 (1963).
 (24) A. Bondi, *J. Chem. Eng. Data*, **8**, 371 (1963).
 (25) J. L. Franklin, *Ind. Eng. Chem.*, **41**, 1070 (1949).

The Reduction of $\text{CuO}_{0.67}$ in Hydrogen

by A. W. Czanderna

Union Carbide Corporation, Chemicals Division, Research and Development Department, South Charleston, West Virginia (Received May 14, 1965)

The oxidation of a 500-Å copper film in oxygen and its reduction in hydrogen has been studied with gravimetric and optical techniques. The composition $\text{CuO}_{0.67}$ can be reduced to copper in hydrogen at 25° without appreciably altering the film uniformity. The data obtained were used to conclude that the reduction process is a nucleation and growth phenomenon.

Introduction

Numerous studies of the nucleation and growth of metal films and of the oxidation of metal films have been made.^{1,2} However, little is known about the effect of cyclic oxidation and reduction on the properties of films. Considerable information was accumulated during previous studies on the oxidation of evaporated copper films to $\text{CuO}_{0.67}$ ³ and on the reduction of CuO .⁴ Kinetic and optical transmission data also have been obtained during the oxidation of agglomerated copper films.⁵ It seemed desirable to study the effect of the oxidation of Cu to $\text{CuO}_{0.67}$ in oxygen and the reduction of $\text{CuO}_{0.67}$ to Cu in hydrogen on the properties of the film.

Experimental Section

A uniform copper film, 500 Å thick, was evaporated onto a Pyrex glass substrate and oxidized to $\text{CuO}_{0.67}$.³ The optical transmission of the film was measured from 400 to 800 $m\mu$ while the mass change was simultaneously monitored with a microbalance during evaporation, oxidation, and also during subsequent reduction. A detailed description of the apparatus employed has been reported.⁶ Except as noted below, the oxidation was accomplished by heating the film from room temperature to 143° in 100 torr of oxygen. The film was reduced in 100 torr of hydrogen at temperatures ranging from 25 to 125°. To permit detailed transmission studies of the film during reduction, it was found convenient to reduce the furnace temperature in one of the reduction cycles as soon as the rate of reduction became rapid. Six complete oxidation-reduction cycles were carried out on the film. After the sixth reduction, it was established that temperatures exceeding 125°

are necessary to remove the final 4% of oxygen from the film.

Results and Discussion

The mass loss during reduction of $\text{CuO}_{0.67}$ at 25° is plotted as a function of time in curve I in Figure 1. The sigmoidal shape was obtained in each reduction cycle. The shape of this curve is typical for a nucleation, growth, and depletion mechanism. In the induction period, which varied from 1 hr. at 125° to 70 hr. at 25°, the average thickness of the copper nuclei formed on the $\text{CuO}_{0.67}$ was 20–30 Å. The transition to the growth of the nuclei was extremely abrupt when nucleation was completed at temperatures of about 70° or more. This is shown by the change in the rate of mass loss at A in curve II (Figure 1). The rate of mass loss was approximately linear from a copper mole fraction of 0.2 to 0.6 at all reduction temperatures. The activation energy calculated for this mole fraction range was 12 ± 2 kcal./mole. The rate-determining step during the growth of the nuclei, suggested by the magnitude of the activation energy, could be the dissociation of a copper-oxygen-hydrogen surface complex or the diffusion of copper on a $\text{CuO}_{0.67}$ surface. The

(1) G. Haas, Ed., "Physics of Thin Films," Vol. 1, Academic Press Inc., New York, N. Y., 1963.

(2) C. A. Neugebauer, J. W. Newkirk, and D. A. Vermilyea, Ed., "Structure and Properties of Thin Films," John Wiley and Sons, Inc., New York, N. Y., 1959.

(3) H. Wieder and A. W. Czanderna, *J. Phys. Chem.*, **66**, 816 (1962).

(4) H. Wieder and A. W. Czanderna, *J. Chem. Phys.*, **35**, 2259 (1961).

(5) A. W. Czanderna and H. Wieder, unpublished.

(6) A. W. Czanderna and H. Wieder, "Vacuum Microbalance Techniques," Vol. II, Plenum Press, Inc., New York, N. Y., 1962, p. 147.

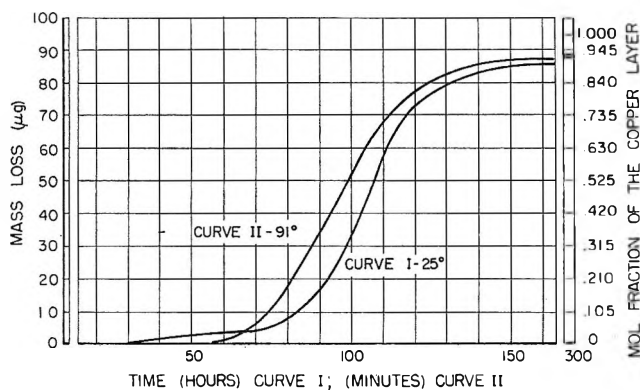


Figure 1. The reduction of $\text{CuO}_{0.67}$ in hydrogen.

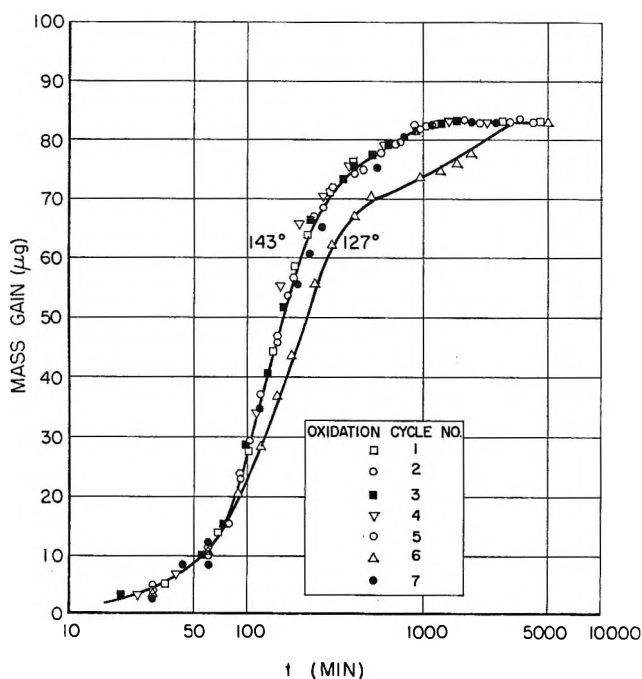


Figure 2. The reoxidation of copper films after reduction in hydrogen.

depletion tail is less gradual than has been observed for other systems.^{4,7}

The mass gain of the film during reoxidation to $\text{CuO}_{0.67}$ after each reduction cycle is shown in Figure 2. The reproducibility of the oxidation curve up to the saturation limit is within experimental error for all of these data. If important changes in the uniformity of the film had occurred, the oxidation rate would have been slower, particularly in the saturation stages and in later cycles. As can be seen, six reduction cycles produced no effect in the oxidation rate. Furthermore, the difference between the rate of the sixth oxidation, carried out at 127° , and those carried out at 143° is the same as has been observed for freshly evaporated films.⁸

The optical transmission data for $\text{CuO}_{0.67}$ obtained after each oxidation cycle and for Cu after each reduction cycle are shown in Figures 3 and 4. The data in Figure 3 are characteristic curves that have been obtained many times for $\text{CuO}_{0.67}$.⁵ The apparent shift of the absorption edge and the increased transmission at the longer wave lengths from the first cycle to the subsequent oxidation cycles probably result from annealing of the film. For example, the as-evaporated film is annealed at room temperature, while the reduced films are annealed at several different higher temperatures.

The transmission curves obtained for the reduced copper film of composition $\text{CuO}_{0.04}$ are comparable to those observed for a partially oxidized copper film.³ However, the transmission at either extreme of the wave length spectrum exhibits deviations which are characteristic of the first stages of agglomeration of a copper film.⁵ Again, nearly all changes in the trans-

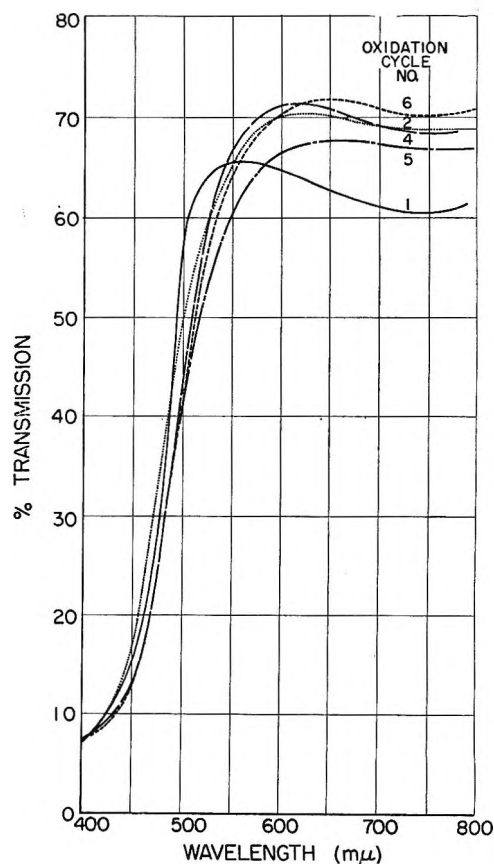


Figure 3. The effect of oxidation-reduction cycling on the optical transmission spectrum of $\text{CuO}_{0.67}$.

(7) W. D. Bond and W. E. Clark, Oak Ridge National Laboratory, Report No. ORNL-2815, March 16, 1960.

(8) A. W. Czanderna, unpublished.

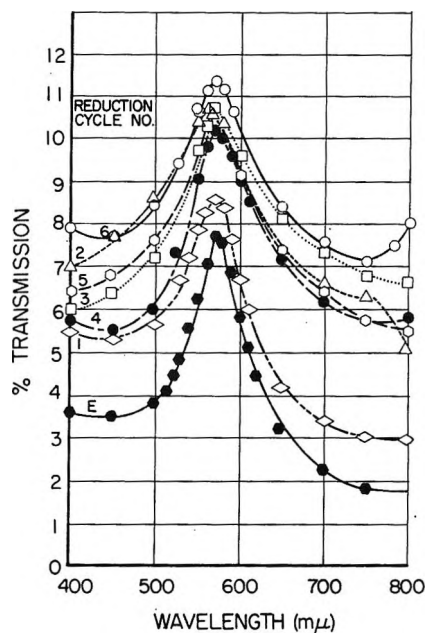


Figure 4. The effect of oxidation-reduction cycling on the optical transmission of a copper film. (E is for the evaporated film.)

mission spectrum occurred in the first two reduction cycles. Optical examination (at $2000\times$) of a similar film subjected to oxidation reduction treatment showed no "gaps" in the reduced film. If all of the increase in transmission resulted from formation of hills and trough in a continuous film, the film thickness must vary between 300 and 700 Å. to account for the transmission observed. If this were true, the thickest regions then would have a measurable effect on the rates of reoxidation⁵ which was not evident in the reoxidation curves. Hence, it seems more probable that the difference in transmission of the reduced copper film and the evaporated copper film results either from a change in the extent of annealing of the film or from the small oxygen content of the film being closer to either the substrate-oxide or the air-oxide interface.

The transmission data obtained during the sixth reduction cycle from $\text{CuO}_{0.67}$ to $\text{CuO}_{0.04}$ are shown in Figure 5. It is of interest to analyze these curves as though the reduction process consists of the formation of parallel smooth layers of copper and $\text{CuO}_{0.67}$ at all stages. The transmission of the system air-copper- $\text{CuO}_{0.67}$ -Pyrex glass could then be calculated from the mass data at each stage of the reduction from the optical constants for copper and $\text{CuO}_{0.67}$ ⁹ and the usual equation.¹⁰ The transmission, shown by the experimental curves in Figure 5, decreases much more rapidly with the formation of a very small amount of copper than is calculated. This is not unexpected be-

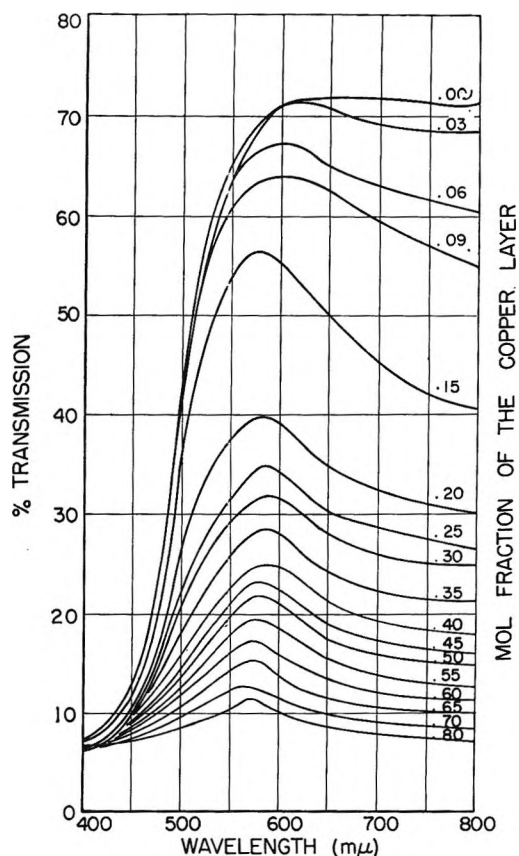


Figure 5. Optical transmission spectra obtained during the reduction of $\text{CuO}_{0.67}$. Initial temperature 85° ; final temperature 50° .

cause the long induction period indicates a nucleation and growth mechanism for the reduction. Each of the nuclei formed on the surface serves as a scattering center and therefore has different loss characteristics from the metal. The optical constants are only valid for films greater than 200 Å. thick in the case of copper and greater than 600 Å. thick for $\text{CuO}_{0.67}$. Therefore, it would not be expected that quantitatively accurate results would be obtained from these optical constants in the initiation and termination stages of the reduction process. The calculated curves follow qualitatively the shape of the experimental curves shown in Figure 5. Of greater importance is that the simplified expression (1) can be used to fit the experimental curves.

$$T = \exp[-(\alpha_1 t_1 + \alpha_2 t_2)] \quad (1)$$

Here, T is the over-all per cent transmission at any wave length, α_1 and α_2 are the absorption coefficients of

(9) H. Wieder and A. W. Czanderna, "The Optical Constants of $\text{CuO}_{0.67}$ and CuO Films," to be published.

(10) O. S. Heavens, "Optical Properties of Thin Solid Films," Butterworth and Co. Ltd., London, 1955.

copper and of $\text{CuO}_{0.67}$ at that wave length, and t_1 and t_2 are the respective thicknesses of the two species. In this formula (1), it is assumed that the entire loss in transmission through the sample may be accounted for by absorption within it. In actuality, however, there are initial effects which must be considered.⁴ Reflections at both copper interfaces and the scattering from the copper nuclei would be expected, and both of these effects might be more pronounced as the thickness of the copper layer increases. Since it would be difficult to obtain an analytical expression for these effects in a detailed treatment, an effective absorption coefficient which includes the reflection and scattering losses was calculated in terms of the simplified model of eq. 1. It was found convenient to solve for α_1 and α_2 in eq. 1 using the measured transmission and the values of t_1 and t_2 calculated from the mass data for curves corresponding to $\text{CuO}_{0.37}$ and $\text{CuO}_{0.13}$. These values of α_1 and α_2 were used with the values of t_1 and t_2 computed from the mass data to obtain transmission curves for the intermediate stages of reduction. The resultant calculated curves superimposed perfectly on all of the curves taken and shown in Figure 5. This demonstrates that no deviation from the simplified treatment exists at any stage of the reduction. This is in contrast to the reduction of CuO .⁴ Thus, after the initial copper layer is formed, any subsequent stage of the reduction of the sample can be considered as made up of parallel layers of copper and $\text{CuO}_{0.67}$. This again seems to be indicative that the uniformity of the original copper film has not been drastically altered by the cyclic oxidation and reduction treatment. It further implies that the size

of the copper nuclei must be relatively small and the number of nuclei very large.

After the seventh oxidation, the $\text{CuO}_{0.67}$ was oxidized to CuO at higher temperatures and reduced to copper in hydrogen as an additional check on the mass data. The transmission spectrum after this reduction showed severe agglomeration of the film had occurred as has been previously reported.⁴

It is interesting to compare the results obtained on the reduction of $\text{CuO}_{0.67}$ with those of CuO . Where even the mildest reduction of CuO produces severe agglomeration of the film, comparable thermal reduction of $\text{CuO}_{0.67}$ repeated several times does not produce changes in the film uniformity which are detectable with our measuring techniques. It is suspected that this may be because the crystal structures of $\text{CuO}_{0.67}$ and copper are similar, and distances between the copper in them are not drastically different. It may be possible for a large number of small nuclei to be formed by an epitaxial process on $\text{CuO}_{0.67}$ in contrast to CuO where the copper crystal structure must be formed in the nuclei during growth. It is evident from the agglomeration of the reduced CuO films which takes place that the copper nuclei formed are larger and less numerous than in $\text{CuO}_{0.67}$. It would seem very appropriate to confirm these preliminary conclusions by a study of the nucleation and growth of copper on $\text{CuO}_{0.67}$ and on CuO by selected-area electron microscopy or some other suitable technique.

Acknowledgments. The author is grateful to Drs. Harold Wieder, J. H. Block, and A. W. Smith for their helpful comments about this work.

The Lattice Energies of the Alkaline Earth Halides

by Thomas E. Brackett and Elizabeth B. Brackett

Department of Chemistry, Colgate University, Hamilton, New York (Received May 17, 1966)

The Madelung constants and lattice energies of several alkaline earth halides are calculated. The lattice energies are found to compare favorably with experimental values for all salts except magnesium bromide and iodide and calcium iodide, in which cases the large discrepancies are difficult to explain.

Introduction

The lattice energies of several groups of ionic salts have been successfully calculated. These treatments have usually been limited to salts such as the alkali halides, the alkaline earth oxides, and a few others which for the most part have simple highly symmetric structures.

Now that computational procedures for calculating the electrostatic energy of more complicated structures are relatively straightforward,¹ the alkaline earth halides provide an interesting group of compounds to study. It would be interesting to see, for example, if the calculation when applied to structures as diverse as these salts present would show fluctuations which could be correlated to structural differences. Also, it would be interesting to observe if and when the approximation breaks down when passing from salts such as BaF₂, which is almost completely ionic, to salts such as MgI₂, which is predominantly covalent.

Previous lattice energy calculations involving some of these salts have included only those exhibiting the simple fluorite structure for which the Madelung constant is well known² and the hexagonal structure for which the Madelung constant as determined by Hund³ is in error.

The electron affinities of the halides are now fairly well established. We will utilize these and other thermodynamic data to calculate the lattice energy for comparison with the results calculated from

$$\text{L.E.} = -\frac{1}{2} \sum_{ij}' \frac{e_i e_j}{r_{ij}} - B e^{-\alpha \xi} + \frac{1}{2} \sum_{ij}' \frac{c_{ij}}{r_{ij}^6}$$

based on the equation of Born and Mayer.⁴ e_i is the charge on ion i ; r_{ij} is the distance between ions i and j . B and g are constants, ξ is the cube root of the molec-

ular volume, and c_{ij} is a constant representing the van der Waals interaction between ions i and j . The terms represent the electrostatic attraction, the repulsion, and the van der Waals attraction, respectively. Two other terms ($\sum_{ij} (D_{ij}/r_{ij}^8)$ and the zero point energy) are evaluated for certain instances and found to be too small to justify their inclusion in this treatment.

The Electrostatic Attraction

The Madelung constants of MgF₂ and CaCl₂ are taken from the report of Templeton.⁵ (The value for SrBr₂ given there is calculated for an incorrect structure and is thus redone for this report.) All other Madelung constants except for the well-known fluorite structure are calculated for this report according to a method given by Wood,¹ who discusses the method and its accuracy. Considering the uncertainties in the structure determination, in addition to the uncertainty in determining the lattice sum, the over-all uncertainty in determining the value of the Madelung constant is estimated to be less than 1%, except for SrBr₂ and MgCl₂.

The structure of SrBr₂⁶ requires that n Sr²⁺ ions be statistically placed on $2n$ lattice positions. The Madelung constant for SrBr₂ was calculated by assuming the ions were equally divided between the two sites. That is, that half the ion occupied one of the $2n$ positions all the time. (The self-interaction was, of

(1) R. H. Wood, *J. Chem. Phys.*, **32**, 1690 (1960).

(2) F. Seitz, "The Modern Theory of Solids," McGraw-Hill Book Co., Inc., New York, N. Y., 1940.

(3) F. Hund, *Z. Physik*, **34**, 833 (1925).

(4) M. Born and J. E. Mayer, *ibid.*, **75**, 1 (1932).

(5) Q. C. Johnson and D. H. Templeton, *J. Chem. Phys.*, **34**, 2004 (1961).

(6) R. L. Sass, T. E. Brackett, and E. B. Brackett, *J. Phys. Chem.*, **67**, 2862 (1963).

course, not included.) The procedure was found to agree to within a few kilocalories per mole with other possible fixed arrangements. The resulting Madelung constant for SrBr₂ is somewhat less certain than that for the other salts.

The structure of MgCl₂ has one parameter, u , undetermined. Similar salts have values of u ranging from 0.250 to 0.260. The calculation for MgCl₂ is carried out for both values of u and tabulated for comparison. The comparison indicates that u is probably closer to 0.260 than to 0.250.

In connection with an over-all evaluation of the uncertainty in the electrostatic energy term, it is interesting to note the agreement of the values 526.3 and 528.8 kcal./mole for the electrostatic energy of BaCl₂. The former is calculated in this report, and the latter independently from an independent determination of the crystal structure by Sahl.⁷

Because of the large differences in crystal types it was decided to express all the results in terms of the cube root of the molecular volume, ξ . The resulting values of ξ , the Madelung constant calculated to this basis A_{ξ} , and the electrostatic energy Ae^2/ξ are presented in Table I.

It will be noted that the values A_{ξ} for the three salts of the cadmium iodide structure (MgBr₂, MgI₂, and CaI₂) differ from those originally given by Hund.³ That his values were in error was noted by Pinsker,⁸ whose results compare favorably with those in this report.

The van der Waals Attraction

The coefficients of the $1/r^6$ term may be calculated from the expression given by London

$$c_{ij} = \frac{3 I_i I_j \alpha_i \alpha_j}{2 I_i + I_j}$$

where α and I refer to the polarizabilities and ionization energies, respectively, of the ions involved. Mayer⁹ evaluated these coefficients for the alkali halide crystals using measurements of their optical properties. The ionization energies of the halides used in this work were the averages of the corresponding values calculated by Mayer for the alkali halides. The ionization energy of the positive ion was assumed to be 75% of the ionization potential (see ref. 9). The polarizabilities used were those evaluated by Tessman, Kahn, and Shockley¹⁰ from measurements of refractive index. The coefficients appear along with the sums of $1/r^6$ and the calculated van der Waals energy for each salt in Table II.

The $1/r^8$ term was investigated for some salts and was found to contribute from 4 to 6 kcal./mole. This term

Table I: Madelung Constants and Coulombic Attraction Energy

Salt	Structural type	ξ , Å.	A_{ξ}	Coulomb energy, kcal./mole	Ref. to structure
MgF ₂	Cassiterite	3.195	7.732	803.6	a
MgCl ₂	Cadmium chloride ($u = 0.26$)	4.034	7.489	616.5	b
MgCl ₂	Cadmium chloride ($u = 0.25$)	4.034	6.957	572.7	b
MgBr ₂	Cadmium hydroxide	4.285	6.878	549.0	b
MgI ₂	Cadmium hydroxide	4.674	6.852	501.4	b
CaF ₂	Fluorite	3.434	7.3306	709.0	
CaCl ₂	Cassiterite distorted	4.393	7.673	580.0	a
CaBr ₂	Cassiterite distorted	4.614	7.670	552.2	c
CaI ₂	Cadmium hydroxide	4.946	6.223	484.1	b
SrF ₂	Fluorite	3.653	7.3306	666.3	
SrCl ₂	Fluorite	4.396	7.3306	553.7	
SrBr ₂	Special structure	4.592	7.170	518.5	d
SrI ₂	Unknown				
BaF ₂	Fluorite	3.906	7.3306	623.1	
BaCl ₂ ^f	Fluorite	4.614	7.3306	527.8	e
BaCl ₂ ^g	Lead chloride	4.442	7.040	526.3	e
BaBr ₂	Lead chloride	4.668	7.037	500.6	e
BaI ₂	Lead chloride	5.020	7.022	464.5	e

^a See ref. 5. ^b R. W. G. Wyckoff, "Crystal Structures," Vol. 1, Interscience Publishers, Inc., New York, N. Y., 1963. ^c E. B. Brackett, T. E. Brackett, and R. L. Sass, *J. Inorg. Nucl. Chem.*, **25**, 1295 (1963). ^d See ref. 6. ^e E. B. Brackett, T. E. Brackett, and R. L. Sass, *J. Phys. Chem.*, **67**, 2132 (1963). ^f Cubic. ^g Orthorhombic.

did not seem to vary greatly from one salt to another, and it is believed to be unrealistic to include it in this treatment since it is probably smaller than the uncertainty in the value of the $1/r^6$ term.

The low temperature specific heat measurements on MgF₂ and CaF₂¹¹ allow one to calculate the Debye temperature from which the zero point energy may be estimated. The results for MgF₂ and CaF₂ are 2.2 and 2.1 kcal./mole, respectively. These salts should have the highest such contribution; it was decided not to include this term for any salt in this calculation.

The Repulsive Energy

In accordance with accepted procedure, we assume that the repulsive energy between two ions due to the overlap of electron clouds is of the form $e^{-\sigma r}$, or summing over all ions in the crystal

(7) K. Sahl, *Beitr. Mineral. Petrog.*, **9**, 111 (1963).

(8) Z. G. Pinsker, *Acta Physicochim. URSS*, **18**, 311 (1943).

(9) J. E. Mayer, *J. Chem. Phys.*, **1**, 270 (1933).

(10) J. R. Tessman, A. H. Kahn, and W. Shockley, *Phys. Rev.*, **92**, 890 (1953).

(11) S. S. Todd, *J. Am. Chem. Soc.*, **71**, 4115 (1949).

Table II: van der Waals Energy

Salt	$C, \text{ ergs } \text{Å}^6 \times 10^{12}$			$\frac{1}{2} \sum \frac{1}{r_{ij}^6}, \text{ Å}^{-6}$			van der Waals energy, kcal./mole
	++	--	+-	++	--	+-	
MgF ₂	2.9	6.4	3.3	0.00332	0.0244	0.0995	7.1
MgCl ₂ ($u = 0.26$)	2.9	107	12.5	0.00084	0.00630	0.02909	15.0
MgCl ₂ ($u = 0.25$)	2.9	107	12.5	0.00084	0.00590	0.02327	13.4
MgBr ₂	2.9	186	15.5	0.00108	0.00518	0.0227	19.0
MgI ₂	2.9	388	21.8	0.00067	0.00307	0.0134	21.4
CaF ₂	55.8	6.4	16.4	0.00210	0.0203	0.0501	15.4
CaCl ₂	55.8	107	64.6	0.00049	0.00388	0.0150	20.3
CaBr ₂	55.8	186	79.7	0.00036	0.00287	0.0110	20.6
CaI ₂	55.8	388	110.2	0.00042	0.00224	0.00980	28.4
SrF ₂	103	6.4	22.9	0.00148	0.0142	0.0353	15.1
SrCl ₂	103	107	88.7	0.00048	0.00458	0.0114	23.9
SrBr ₂	103	186	114	0.0043	0.00336	0.00845	25.2
SrI ₂	103	388	156				
BaF ₂	226	6.4	35	0.00098	0.00953	0.0236	16.0
BaCl ₂ ^a	226	107	135	0.00036	0.00344	0.00851	23.0
BaCl ₂ ^b	226	107	135	0.00048	0.00418	0.00928	26.0
BaBr ₂	226	186	172	0.00035	0.00309	0.00684	26.4
BaI ₂	226	388	239	0.00023	0.00200	0.00441	27.1

^a Cubic. ^b Orthorhombic.

$$E_r = \frac{1}{2} \sum'_{ij} e^{-g_{ij} r_{ij}}$$

where the indices on g express the fact that it is not necessarily independent of r . In the case of a simple highly symmetric structure, the nearest neighbors all have the same value of r (and therefore g) and furthermore constitute a major fraction of the repulsive energy. Thus

$$E_r \cong B e^{-gr}$$

where B is some constant related to the number of nearest neighbors and r is the equilibrium nearest-neighbor distance. In some cases the interaction of next nearest neighbors has been included.

In the case of more complex crystals, no simple relationship exists because, in general, numerous ions lie at different distances all fairly close to the central ion. In such cases it is still desirable to express the repulsive energy in the simple two-parameter form $E_r = B e^{-g\xi}$, where ξ should represent some sort of an average of the nearest-neighbor distances. We have chosen the cube root of the molecular volume to represent this average.

Unfortunately, the compressibility data which allow a determination of g are very scarce. In fact, only for CaF₂ has the compressibility been measured for a single crystal, and only SrF₂ and BaF₂ have been measured as powders. The approximate values of g

as determined from these experiments are 2.34, 2.15, and 2.11, respectively.^{12,13} Because of the scarcity of the independent determinations of g , it was decided to choose the single value of g which would give the best fit to all the data. The salts of magnesium bromide and iodide and calcium iodide have been left out of this determination because, as we shall see, they give totally unreasonable values. The value of g calculated in this way turned out to be 2.32, which agrees well with the measured values. B was determined by the criterion that the variation of the lattice energy with respect to ξ evaluated at the equilibrium value of ξ is zero.

The Lattice Energy from Thermodynamic Data

The lattice energy of a compound may be calculated from the equation

$$\text{L.E.} = -\Delta H_{f,298^\circ\text{K.}} + \Delta H_{s,298^\circ\text{K.}} + I_1 + I_2 + D_{(X_2)298^\circ\text{K.}} + 2E_{(X^-)} - 3\left(\frac{5}{2}RT\right) + \int_0^{298} C_p dT$$

The heats of formation, $\Delta H_{f,298^\circ\text{K.}}$, and the heats of sublimation of the alkaline earth metals, $\Delta H_{s,298^\circ\text{K.}}$, as well as the dissociation energies of the halogens, $D_{(X_2)298^\circ\text{K.}}$, were taken from the tables in Lewis, Randall, Pitzer, and Brewer.¹⁴ The ionization energies (I_1 and I_2) are

(12) P. W. Bridgman, Ed., Landolt-Börnstein Tabellen, Springer-Verlag, Berlin 1937.

(13) P. W. Bridgman, "Physics of High Pressure," The Macmillan Co., New York, N. Y., 1949.

from Moore.¹⁵ The electron affinities $E_{(X^-)}$ for F, Cl, Br, and I were taken as 80, 86, 81, and 74 kcal./mole, respectively.¹⁶ The integrated heat capacity of the solid is given in ref. 17. In many cases it is estimated, but it is a very small term. The lattice energies thus obtained are listed in Table III under L.E. (exptl.).

Table III: Calculated and Experimental Lattice Energy (kcal./mole)

Salt	Coulomb energy	van der Waals energy	Repulsion energy	L.E.	L.E. (exptl.)	Δ
MgF ₂	803.6	7.1	-114.3	696.4	702.3	5.9
MgCl ₂	616.5	15.0	-75.6	555.9	596.5	40.6
($u = 0.26$)						
MgCl ₂	572.7	13.4	-69.9	516.2	596.5	80.3
($u = 0.25$)						
MgBr ₂	549.0	19.0	-66.8	501.2	573.0	71.8
MgI ₂	501.4	21.4	-58.2	464.6	547.1	82.5
CaF ₂	709.0	15.4	-100.7	623.7	623.4	-0.3
CaCl ₂	580.0	20.3	-68.9	531.4	532.1	0.7
CaBr ₂	552.2	20.6	-63.2	509.6	509.4	-0.2
CaI ₂	484.1	28.4	-57.1	455.4	487.4	32.0
SrF ₂	666.3	15.1	-89.4	592.0	591.6	-0.4
SrCl ₂	553.7	22.3	-67.5	508.5	508.3	-0.2
SrBr ₂	518.5	23.5	-62.0	480.0	487.4	7.4
SrI ₂					463.6	
BaF ₂	623.1	16.0	-79.5	559.6	557.1	-2.5
BaCl ₂ ^a	527.8	23.0	-62.3	488.5	484.8	-3.7
BaCl ₂ ^b	526.3	26.0	-66.3	486.0	484.8	-1.2
BaBr ₂	500.6	26.4	-60.9	466.1	465.6	-0.5
BaI ₂	464.5	27.1	-53.9	437.7	441.0	3.3

^a Cubic. ^b Orthorhombic.

Results and Discussion

The three contributions to the energy and their sum, the lattice energy, appear along with the experimental value in Table III. A brief survey of this table shows general agreement to within 1% for all cases except SrBr₂, MgCl₂, and the three hexagonal salts. We feel that this agreement is surprisingly good considering the relatively crude approximation of assuming one value of g in the repulsive energy applies to all salts. As mentioned before, SrBr₂ involves exceptional difficulties

in the determination of the Madelung constant which, along with uncertainties in the structural parameters, could easily account for its discrepancy. The crystal structure of MgCl₂ is not well enough established to be certain that a real difference between calculated and experimental lattice energy exists for this case. Thus, it appears that only for MgBr₂, MgI₂, and CaI₂ does a demonstrated distinct deviation of the calculated from the experimental lattice energy exist. Since these salts are expected to be more covalent than the others, one might be tempted to give this as a sufficient reason for the difference. On the other hand, this treatment is known to work well for other salts, for example, LiI which is by some measures as covalent as MgBr₂ or CaI₂. The assumption of a considerably different repulsive energy is of no use here since even reducing it to zero will not account for the experimental lattice energy. The remainder of the calculation is completely determined by the crystal structure parameters; thus, we are left with three possibilities: (1) the approximation breaks down for these salts; (2) the values going into the experimental value of the lattice energy are in error; or (3) the crystal structure determinations are in error.

It would be interesting to do a more refined calculation when accurate compressibility data become available for these salts.

Acknowledgments. T. E. Brackett wishes to acknowledge the generous support of the Colgate Research Council, which contributed substantially to the completion of this project. We also thank Charles R. Dawson and Edward S. Macias for assistance with the machine calculations. Finally, we wish to thank Colgate University for their generosity in allowing us free time on the Colgate University computer.

(14) G. N. Lewis, M. Randall, K. S. Pitzer, and L. Brewer, "Thermodynamics," 2nd Ed., McGraw-Hill Book Co., Inc., New York, N. Y., 1961.

(15) C. E. Moore, U. S. National Bureau of Standards Circular No. 467 V, Vol. 1 and 3, U. S. Government Printing Office, Washington, D. C., 1949 and 1958.

(16) L. Brewer, UCRL Report 9952, Nov. 1961.

(17) L. Brewer, G. R. Somayajulu, and E. B. Brackett, *Chem. Rev.*, 63, 111 (1963).

Vapor Spectra and Heats of Vaporization of Some Purine and Pyrimidine Bases¹

by Leigh B. Clark, Gary G. Peschel, and Ignacio Tinoco, Jr.

Chemistry Department and Lawrence Radiation Laboratory, University of California, Berkeley, California
(Received May 18, 1965)

The vapor spectra of some purine and pyrimidine bases are presented. Vapor pressures of adenine and 9-methyladenine have been determined in order to obtain absolute intensities. Heats of vaporization are also determined from the spectral data.

Introduction

The spectra of the purine and pyrimidine bases found in nucleic acids have been extensively studied in aqueous solution where strong hydrogen bonds may occur.^{2,3} These spectra show no vibronic structure and even the number of electronic absorption bands present are not established. In less polar solvents such as acetonitrile,^{4,5} methylcyclohexane,⁵ and trimethyl phosphate³ some resolution becomes apparent. We expected that vapor phase spectra might give even better resolution, therefore we have investigated the main nucleic acid bases and their more volatile methyl derivatives. However, the vapor spectra closely resemble the solution spectra and do not show any new bands. The vapor phase studies do give the spectra of the isolated bases, and the temperature dependence of the spectra provides heats of vaporization.

Experimental Section

Adenine, cytosine, guanine, uracil, and 1,3-dimethyluracil were California Biochemical Corp. Cfp grade products. The latter two were recrystallized from water. 9-Methyladenine and 9-methylhypoxanthine were purchased from Cyclo Chemical Corp. and were recrystallized three times from water. Trimethyl phosphate was from Victor Chemical Co.; methylcyclohexane and acetonitrile were Matheson Spectrograde.

A double-windowed, quartz, 10-cm. absorption cell was covered with a layer of thin copper sheeting. Heat was supplied *via* resistance wire wound onto the cell body and insulated with asbestos. The temperature was measured by a copper-constantan thermocouple placed in contact with the cell.

Approximately 20 mg. of sample was inserted into the cell through a side arm. The cell was then evacuated (pressure $<10^{-5}$ mm.) for about 12 hr. The temperature of the cell was then slowly raised over a period of several hours until it was evident that the base itself was evaporating. The cell was allowed to cool and sealed, and the side arm was wound with heating wire so that its temperature would be a few degrees above that of the cell body.

The spectra were recorded with a Cary Model 15 spectrophotometer. An unheated double-windowed cell was used as a blank. Temperature increments of successive scans varied from 10 to 20°; spectra were recorded both upon heating and cooling to test for decomposition.

The vapor pressures of adenine and 9-methyladenine were measured by the Knudsen effusion method. The values (mm.) obtained are $5.1 \pm 0.5 \times 10^{-3}$ at 175° and 24×10^{-3} at 200° for adenine, and $0.92 \pm 0.05 \times 10^{-2}$ at 140°, $10.4 \pm 0.5 \times 10^{-2}$ at 170°, and $29.5 \pm 0.4 \times 10^{-2}$ at 185° for 9-methyladenine.

Results and Discussion

Vapor Spectra. The vapor spectra of adenine, 9-methyladenine, 9-methylhypoxanthine, uracil, and 1,3-dimethyluracil are given in Figures 1–3. These spectra are in general very similar in shape to those seen in

(1) Supported in part by Public Health Service Research Grant GM 10840 and by the U. S. Atomic Energy Commission.

(2) D. Voet, W. B. Gratzner, R. A. Cox, and P. Doty, *Biopolymers*, **1**, 193 (1963).

(3) L. B. Clark and I. Tinoco, Jr., *J. Am. Chem. Soc.*, **87**, 11 (1965).

(4) R. Haselkorn, Ph.D. Thesis, Harvard University, 1959.

(5) E. Charney and M. Gellert, *Biopolymers, Symp.*, **1**, 469 (1964).

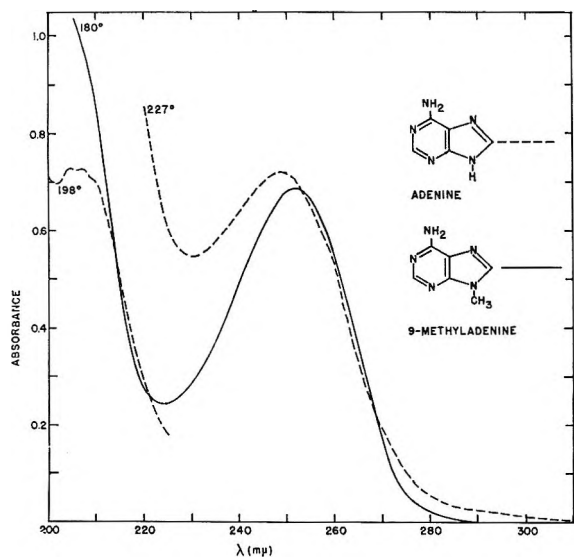


Figure 1. The vapor phase spectra of adenine and 9-methyladenine.

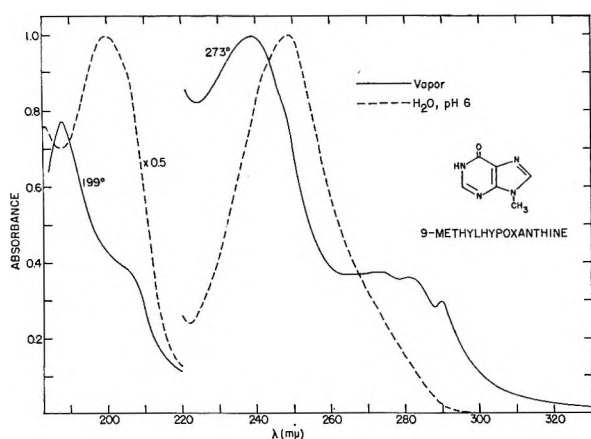


Figure 2. The spectrum of 9-methylhypoxanthine in the vapor phase and in neutral solution in water.

aqueous solution. Only in 9-methylhypoxanthine is a new band seen which is not found in the aqueous spectrum (Figure 2); however, this band is present in trimethyl phosphate solution.³ The main electronic band of each compound is shifted to the red by about 10 $m\mu$ in the aqueous solution spectrum compared with the vapor spectra. This is commonly found for $\pi-\pi^*$ transitions; it is interpreted as a greater London attraction of the solvent for the excited state than the ground state of the molecule.⁶ Table I gives the wave length maxima for these components in the vapor and in solvents of increasing polarity. The main band is seen to shift uniformly with solvent polarity (from methylcyclohexane to water).

No bands which could be attributed to $n-\pi^*$ transi-

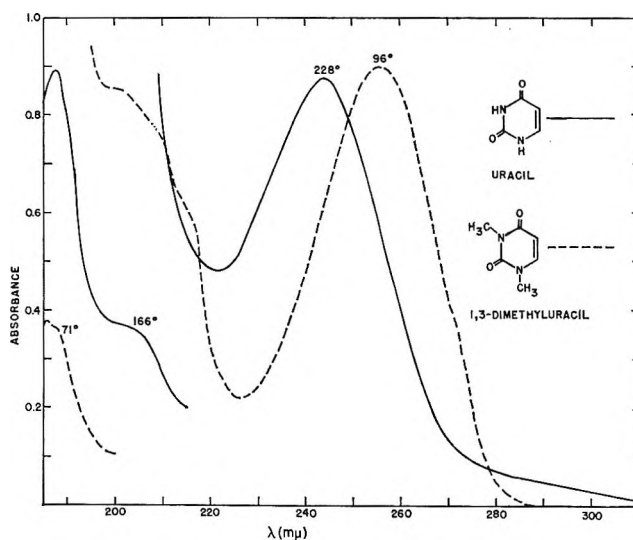


Figure 3. The vapor phase spectra of uracil and 1,3-dimethyluracil.

tions were found. These bands would be expected to shift in the opposite direction to the $\pi-\pi^*$ (the solvent prefers the ground state of the $n-\pi^*$ transition) and be easier to see in the gas phase. Their absence indicates that the $n-\pi^*$ transitions remain hidden under the $\pi-\pi^*$ transitions, or that their intensity is less than one-twentieth that of the $\pi-\pi^*$.

Extinction coefficients were obtained for adenine and 9-methyladenine from the vapor pressure data. At the maxima these are λ 249 $m\mu$ (ϵ 12×10^3 l./mole cm.) for adenine at 227° and λ 252 $m\mu$ (ϵ 7.7×10^3 l./mole cm.) for 9-methyladenine at 171°. A comparison of oscillator strengths of the gas phase and the aqueous bands shows a marked hyperchromism in solution. For adenine the oscillator strength increases from 0.24 in the gas phase to 0.28 in water, while for 9-methyladenine it increases from 0.16 to 0.28.

Cytosine, 3-methylcytosine, and guanine showed evidence of decomposition in the vapor spectra. Sharp ammonia bands as well as other unidentified bands were observed to develop with time at constant temperature. The long wave length absorption band in all three compounds, however, did not display the time dependence associated with decomposition products and therefore most probably may be attributed to the base compounds themselves. Thus, in spite of the difficulty due to decomposition, certain information may be obtained with moderate confidence.

The λ_{\max} for both cytosine and 3-methylcytosine is about 285–290 $m\mu$. Guanine shows a long wave length

(6) H. C. Longuet-Higgins and J. A. Pople, *J. Chem. Phys.*, **27**, 192 (1957).

Table I: Absorption Maxima in Solvents of Different Polarity^a

Compd.	Vapor	Methylcyclohexane	Acetonitrile	Trimethyl phosphate	H ₂ O, pH 7
Adenine	252, 207	Insol.	Insol.	260, 208	260, 207 ^b
9-Methyladenine	249, ?	258, 212	259	260, 210	260
Hypoxanthine	...?...	Insol.	269 (sh) (249, 244)	250, 196	249, 280 (sh)
9-Methylhypoxanthine	(290, 281, 273) 239, 205 (sh), 198	Insol.	270 (sh) (251, 245)	(249, 244), 198, 184	~280 (sh), 249, 200, 183
Uracil	244, 205 (sh) 187	Insol.	...?...	258, 203, 182	260, 202, ? ^b
1,3-Dimethyluracil	256, 205 (sh), 187	262, 203, 185	...?...	264, 206, 185	265, 204, 187
Cytosine	290 (s), ~260 ^c	Insol.	...?...	277, 204, 186	267, 230, 209 (sh), 196 ^b
3-Methylcytosine	290 (s), 259 ^c	Insol.	...?...	...?...	271

^a The abbreviation insol. means that a saturated solution of the compound did not give a usable spectrum in a 10-cm. cell. A shoulder is designated by sh. ^b Data from ref. 2. ^c The temperature dependence of these peaks indicated that the shoulder at 290 mμ is the absorption maximum of the compound, while the 260-mμ peak is due to decomposition.

structured band (maxima at 293 and 284 mμ) which is very similar to that found in 9-methylhypoxanthine.

Heats of Vaporization. In order to determine heats of vaporization from the spectral data one needs to measure the slope of a plot of log *p'* vs. *T*⁻¹, where *p'* is a quantity linear in the vapor pressure. Since the extinction coefficient will in general be temperature sensitive (band broadening), the optical density at constant wave length will not be a good measure of pressure changes. However, the band area or relative oscillator strength should be more nearly insensitive to temperature variations and has been used in the evaluation of

the heats of vaporization from the spectra. The product of the band area and the temperature (*B* × *T*) is proportional to the vapor pressure.

Figure 4 shows plots of log *BT* vs. *T*⁻¹ for the main band of adenine, 9-methyladenine, 9-methylhypoxanthine, uracil, and 1,3-dimethyluracil. The area of the band, *B*, is evaluated from an absorbance vs. energy plot. The slope is constant for these lines and corresponds to the heat of vaporization of the solid. For cytosine, 3-methylcytosine, and guanine only the absorbance at one wave length was used in the plots, because decomposition products obscured the low wave length part of the spectrum. A straight line was obtained for 3-methylcytosine (Figure 4), but the data for guanine and cytosine do not produce straight lines.

The heats of vaporization obtained are given in Table II. For adenine and 9-methyladenine, heats of vaporization were also calculated from the temperature dependence of the vapor pressure. The values obtained (shown in Table II in parentheses) are within 12% of

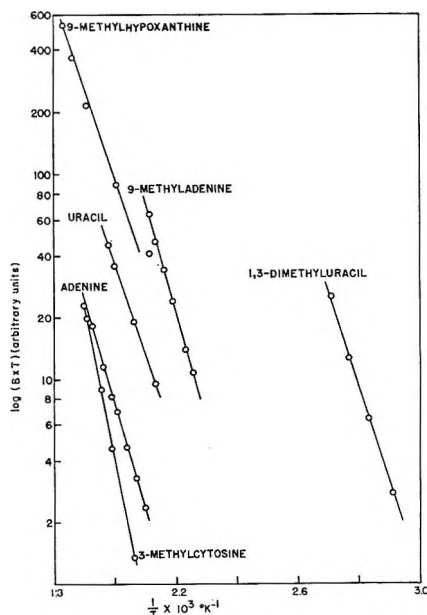


Figure 4. Heats of vaporization obtained from plots of log *p'* vs. 1/*T*. The quantity *p'*, which is proportional to pressure, is the product of the area of an absorption band and the absolute temperature (*B* × *T*).

Table II: Heats of Vaporization and Heats of Solution in Water

	ΔH_{vap} , kcal./mole	ΔH_{soln} , kcal./mole
Adenine	24 (26) ^a	8 ^b
9-Methyladenine	26 (29) ^a	6.860 ± 0.042 ^c
9-Methylhypoxanthine	20	
Uracil	20	
1,3-Dimethyluracil	22	
3-Methylcytosine	36	
1-Methylthymine	..	5.3 ± 0.030 ^c

^a The values in parentheses are calculated from the temperature dependence of the vapor pressure. ^b Data from ref. 8. ^c Data from ref. 7.

the spectral value. Heats of solution in water have been measured for 9-methyladenine and 1-methylthymine⁷; a heat of solution for adenine can also be calculated from the data of T'so, *et al.*⁸ These values (Table II) lead to a large negative ΔH (~ -20 kcal./mole) for the process: purine or pyrimidine in gas phase \rightarrow purine or pyrimidine in aqueous solution.

Knowledge of these numbers is necessary to an understanding of the forces which determine the stability of nucleic acids in solution.⁹

(7) S. J. Gill, D. B. Martin, and M. Downing, *J. Am. Chem. Soc.*, **85**, 706 (1963).

(8) P. O. P. T'so, I. S. Melvin, and A. C. Olson, *ibid.*, **85**, 1289 (1963).

(9) H. DeVoe and I. Tinoco, Jr., *J. Mol. Biol.*, **4**, 500 (1962).

Uranium Monoselenide. Heat Capacity and Thermodynamic

Properties from 5 to 350°K.^{1a}

by Yoichi Takahashi and Edgar F. Westrum, Jr.^{1b}

Department of Chemistry, University of Michigan, Ann Arbor, Michigan 48104 (Received May 20, 1965)

The low temperature heat capacity of USe was determined by adiabatic calorimetry and found to have a normal sigmoid temperature dependence except near the 160.5°K. transition from the ferromagnetic to the paramagnetic state. The heat capacity (C_p), entropy (S°), enthalpy function ($[H^\circ - H^\circ_0]/T$), and Gibbs energy function ($-[G^\circ - H^\circ_0]/T$) at 298.15°K. in cal./(g.f.m. °K.) are 13.10, 23.07, 10.39, and 12.68, respectively.

Introduction

The presence of several phases, such as USe, U₃Se₄, U₂Se₃, U₃Se₅, α -, β -, and γ -USe₂, and USe₃, has been recognized in the uranium-selenium system,² but few thermodynamic properties have been reported. Recent investigations of magnetic³ and electrical⁴ properties have shown uranium monoselenide (USe) to be of particular interest because of its ferromagnetism below 200°K. and low electrical resistivity and high thermoelectric power at room temperature. Its thermal properties are of interest also in comparison with those of other uranium compounds such as US, UC, UN, and UP, all of which also possess the NaCl structure.

Experimental Section

Preparation and Characterization of the Sample. The sample of uranium monoselenide was prepared at the Battelle Memorial Institute⁴ by allowing uranium turnings (containing 0.01 wt. % spectrographically detected

impurities) to react with the vapor of rectifier grade (99.999% pure) selenium in evacuated, sealed quartz capsules. The resulting finely divided selenide preparations were consolidated, melted, and homogenized to monoselenide under an argon atmosphere at about 2000° in a tantalum crucible. Determination of uranium and selenium gave values within $\pm 0.2\%$ of the stoichiometric ratio. Tantalum was not detected by spectrochemical analysis sensitive to 0.001%, and oxygen contamination was less than 0.1% by weight.

(1) (a) This research was supported in part by the United States Atomic Energy Commission and by the Selenium-Tellurium Development Association, Inc. (b) To whom correspondence concerning this work should be addressed.

(2) (a) R. Ferro, *Z. anorg. allgem. Chem.*, **275**, 320 (1954); (b) P. Khodadad, *Bull. soc. chim. France*, 133 (1961).

(3) W. Trzebiatowski and W. Suski, *Bull. Acad. Polon. Sci., Ser. sci. chim.*, **10**, 399 (1962).

(4) L. K. Matson, J. W. Moody, and R. C. Himes, *J. Inorg. Nucl. Chem.*, **25**, 795 (1963).

Cryostat and Calorimeter. Measurements were made in the Mark III vacuum cryostat⁵ by the quasi-adiabatic technique.⁶ The gold-plated copper calorimeter (laboratory designation W-38) used has a capacity of 13.8 cm.³ and is similar to one previously described.⁷ The heat capacity of the calorimeter-heater-thermometer assembly was determined in a separate series of measurements. Minor adjustments were applied for the differences (between these runs and those on the loaded calorimeter) in the amounts of Cerroseal (indium-tin) solder for sealing the calorimeter, Apiezon-T grease for thermal contact with the heater-thermometer assembly, and helium gas for thermal conductivity in the sample space. The mass of the calorimetric sample was 25.026 g. *in vacuo*, and its heat capacity ranged from 80% of the total at 5°K. to 32% at 350°K. Buoyancy corrections were made using the reported⁴ density of 10.91 g./cm.³. A helium pressure of 173 torr at 300°K. was used to facilitate thermal

Results and Discussion

Heat Capacities and Thermal Properties. The experimental heat capacities at the mean temperatures of the determinations are presented in Table I in chronological order. These data have been adjusted for curvature and are given in terms of the defined thermochemical calorie of 4.1840 joules, an ice point of 273.15°K., and a gram formula mass of 316.99. The data in the region of the transition are presented in Figure 1.

Table I: Heat Capacities of Uranium Monoselenide^a

T	C_p	T	C_p	T	C_p
Series I					
104.89	10.69	154.21	15.34	24.84	1.995
114.25	11.43	156.26	15.73	27.63	2.396
123.93	12.21	157.88	16.01	30.79	2.859
133.93	13.06	159.48	16.23	32.47	3.091
143.77	14.01	161.08	16.28	36.55	3.688
153.45	15.28	162.68	15.80	40.48	4.204
162.99	15.71	164.29	15.35	44.42	4.713
183.59	12.93	165.93	14.96	48.35	5.220
194.17	12.75	169.19	14.57	52.76	5.751
204.64	12.72	170.85	14.31	57.72	6.336
214.99	12.75	174.95	13.58	63.28	6.967
225.20	12.83	178.71	13.05	69.33	7.568
229.15	12.84	181.67	12.89	76.03	8.202
237.67	12.93			83.30	8.930
246.11	12.95	Series III		88.29	9.378
254.48	12.95	5.85	0.144	97.18	10.08
263.06	12.96	6.43	0.154	106.29	10.81
271.82	13.00	7.22	0.179	Series V	
280.51	13.03	8.20	0.201	158.46	16.19
289.44	13.05	9.49	0.271	159.72	16.33
298.58	13.10	11.11	0.344	160.72	16.32
307.88	13.13	12.63	0.438	161.72	16.09
317.31	13.20	13.80	0.556	163.45	15.55
326.66	13.24	14.71	0.639	165.89	15.00
336.25	13.24	Series IV		168.36	14.60
345.78	13.26	13.95	0.565	170.85	14.24
Series II		15.17	0.695	173.36	13.73
141.13	13.71	16.68	0.869	176.33	13.26
146.90	14.35	18.40	1.082	179.76	12.98
151.27	14.87	20.32	1.346	184.86	12.84
		22.44	1.651		

^a Units: cal., g.f.m., °K.

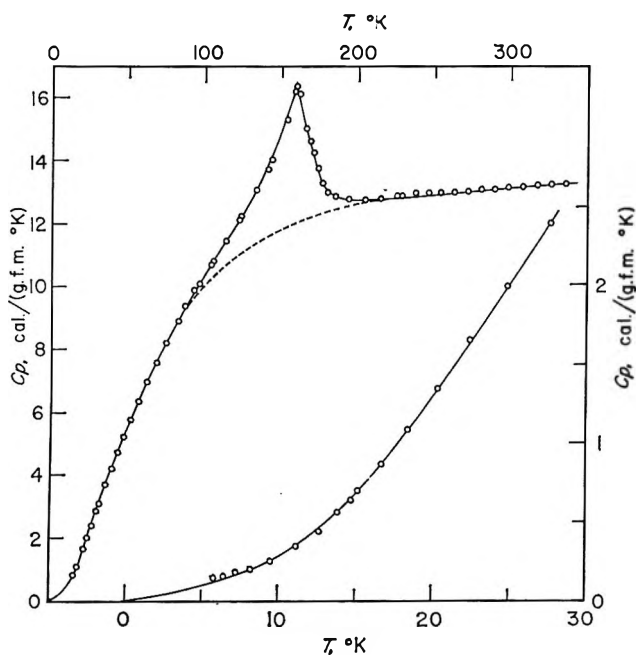


Figure 1. Heat capacity of uranium monoselenide.

equilibration in the sample space. A capsule-type, strain-free platinum resistance thermometer (laboratory designation A-3) located within the entrant well of the calorimeter was used to determine temperatures which, above the oxygen point, are believed to accord with the thermodynamic temperature scale to within 0.03°K. All measurements of mass, temperature, resistance, voltage, and time are referred to calibrations or standardizations made by the U. S. National Bureau of Standards.

The smoothed heat capacities and the thermodynamic functions derived from these data are given in Table II at selected temperatures. These values, obtained by means of a high-speed digital computer using programs

(5) E. F. Westrum, Jr., *J. Chem. Educ.*, **39**, 443 (1962).

(6) E. F. Westrum, Jr., J. B. Hatcher, and D. W. Osborne, *J. Chem. Phys.*, **21**, 419 (1953).

(7) D. W. Osborne and E. F. Westrum, Jr., *ibid.*, **21**, 1884 (1953).

Table II: Thermodynamic Properties of Uranium Monoselenide^a

T	C_p	S°	$H^\circ - H^\circ_0$	$-(G^\circ - H^\circ_0)$ T
5	0.112	0.107	0.27	0.0527
10	0.277	0.232	1.22	0.1102
15	0.674	0.409	3.47	0.1778
20	1.301	0.685	8.34	0.2681
25	2.017	1.052	16.62	0.3869
30	2.745	1.484	28.53	0.5329
35	3.457	1.961	44.04	0.7024
40	4.143	2.468	63.05	0.8911
45	4.795	2.993	85.41	1.0954
50	5.417	3.531	110.95	1.3120
60	6.592	4.624	171.1	1.773
70	7.656	5.722	242.4	2.258
80	8.642	6.809	324.0	2.760
90	9.510	7.878	414.8	3.269
100	10.314	8.922	513.9	3.783
110	11.09	9.942	621.0	4.296
120	11.88	10.940	735.8	4.809
130	12.71	11.924	858.7	5.318
140	13.61	12.898	990.2	5.825
150	14.74	13.874	1131.7	6.329
160	16.40	14.874	1286.8	6.831
170	14.28	15.803	1440.0	7.333
180	12.99	16.578	1575	7.826
190	12.74	17.271	1704	8.308
200	12.73	17.925	1831	8.770
210	12.74	18.546	1958	9.221
220	12.77	19.139	2086	9.658
230	12.82	19.708	2214	10.083
240	12.86	20.255	2342	10.496
250	12.91	20.781	2471	10.897
260	12.95	21.29	2600	11.29
270	12.99	21.78	2730	11.67
280	13.03	22.25	2860	12.04
290	13.07	22.71	2990	12.40
300	13.11	23.15	3121	12.75
325	13.21	24.20	3450	13.59
350	13.31	25.19	3782	14.38
273.15	13.00	21.93	2771	11.78
298.15	13.10	23.07	3097	12.68

^a Units: cal., g.f.m., °K.

The lowest temperature heat capacity values may be represented by an expression

$$C_v[\text{cal.}/(\text{g.f.m. } ^\circ\text{K.})] = 2.075 \times 10^{-2}T + 8.04 \times 10^{-5}T^3$$

since the values of C_p and C_v will be practically the same at these temperatures. The T^3 term represents the lattice contribution; the linear term is the electronic contribution. This equation was used to extrapolate the USe heat capacity below 5°K. The large electronic contribution is comparable to those of other isostructural uranium compounds (for example, UC⁹: 4.7×10^{-3} , US¹⁰: 4.9×10^{-3} , UN¹¹: 9.6×10^{-3}) and corresponds to the observed high electrical conductivity⁴ ($\rho \simeq 10^{-4}$ ohm-cm.) of USe at low temperatures.

The Ferromagnetic Transition. The only reported measurements of the magnetic susceptibility of USe are those of Trzebiatowski and Suski,³ who found that USe is ferromagnetic with a Curie point in the range 185 to 190°K., and a Curie-Weiss θ of 188°K. Their calculated magnetic moment from the magnetization at 0°K. was 1.31 B.M. (μ_B), whereas that calculated from the Curie-Weiss law for the paramagnetic region was 2.51 μ_B . Changes in the sense of the temperature dependency of the Hall coefficient and electrical resistivity were observed between 180 and 200°K. by Matson, *et al.*⁴

The experimental heat capacity of USe obtained by the present work is shown in Figure 1 to illustrate the features of the λ -type transition observed at 160.5°K. As described above, this anomaly is believed to be associated with ferromagnetic ordering, though the observed transition temperature is 25 to 30° lower than that obtained by magnetic and electrical measurements. It should be noted that the heat capacity "tail" of the λ -transition extends upward to about 200°K. If, as this suggests, the magnetization involves short range field dependence (instead of ordered, parallel alignment of atomic spins throughout macroscopic volumes), the transition temperatures would vary with the stoichiometry, homogenization, etc. Hence, more precise magnetic measurements on well-characterized samples are desiderata.

previously described,⁸ have been checked by comparison with large scale plots of the data. The thermodynamic functions are believed to have precision characterized by a probable error of less than 0.2% above 50°K. The entropy and Gibbs energy function have not been adjusted for nuclear spin or isotopic mixing contributions and are hence practical values for use in chemical thermodynamic calculations.

(8) B. H. Justice, Ph.D. Dissertation, University of Michigan, 1961; USAEC Report TID-12722, 1961.

(9) E. F. Westrum, Jr., E. Suits, and H. K. Lonsdale in "Advances in Thermophysical Properties at Extreme Temperatures and Pressures," S. Gratch, Ed., American Society of Mechanical Engineers, New York, N. Y., 1965, p. 156.

(10) E. F. Westrum, Jr., and F. Grønvold in "Thermodynamics of Nuclear Materials," IAEA, Vienna, 1962, p. 3.

(11) E. F. Westrum, Jr., and C. M. Barber, unpublished data.

The estimation of the entropy and enthalpy associated with the magnetic ordering process was done by utilizing a Debye function to assist in drawing a smooth curve for the lattice heat capacity contribution. This yields 154 cal./g.f.m. for the enthalpy of transition and 1.05 cal./(g.f.m. °K.) for the corresponding entropy increment. These results can be compared with the entropy increment, 1.17 cal./(g.f.m. °K.), observed in the similar magnetic transition of US^{10} at 180°K.

Acknowledgment. The authors appreciate the partial financial support of the U. S. Atomic Energy Commission and of the Selenium-Tellurium Development Association, Inc., and the cooperation of Wen-Kuei Wong and Mrs. Carolyn M. Barber in making the measurements and calculations. We thank Dr. H. L. Goering of the Chemistry and Chemical Engineering Department of Battelle Memorial Institute for his generosity in providing the calorimetric sample.

The Thermodynamic Functions above Room Temperature for Antimony and Bismuth Iodides and Their Absolute Entropies¹

by Daniel Cubicciotti and Harold Eding

Stanford Research Institute, Menlo Park, California 94025 (Received May 20, 1965)

The enthalpies of the condensed phases of SbI_3 and BiI_3 were measured from room temperature to the boiling point. The fundamental vibration frequencies for gaseous SbI_3 and BiI_3 were estimated. These, together with molecular structure data, were used to calculate their thermal functions (entropy, enthalpy, and free energy function). Literature information on vapor pressures was used to evaluate the absolute entropy for the condensed phases, and from this the thermal functions for the condensed phases were calculated.

Introduction

The vapor pressures of SbI_3 and BiI_3 have been reported in the literature; however, without information on the heat capacities of the liquid and gas, a proper thermodynamic treatment of their vaporization has not been possible. We have measured the enthalpies of the condensed phases from room temperature to the boiling points and thus obtained the heat capacities and entropies above room temperature. In the gas phase, these molecules are similar to the other trihalides of group V-A elements. By extrapolation of data from other trihalides a set of force constants was estimated which, together with structural information, was used to calculate the absolute entropies, as well as the other thermal functions, in the gas phase. The entropy of vaporization and thermal data were used

to calculate the absolute entropy of the condensed phase and, hence, the free energy functions.

Thermodynamic Functions for Gas Phases

In order to calculate the thermal functions for the gas phase, one needs to know the structure of the gaseous molecules, the fundamental vibration frequencies, and information on low-lying electronic states.² The structures of a number of the gaseous halides of arsenic, antimony, and bismuth have been determined.³ They are, in general, rather flat trigonal

(1) This work was made possible by the support of the Research Division of the U. S. Atomic Energy Commission under Contract No. AT(04-3)-106.

(2) See, for example, K. S. Pitzer and L. Brewer, revision of "Thermodynamics," by G. N. Lewis and M. Randall, McGraw-Hill Book Co., Inc., New York, N. Y., 1961, Chapter 27.

pyramids. The structural parameters for SbI_3 have been measured, and the values used in the present calculations were a Sb-I distance of 2.70 Å. and a I-Sb-I angle of 99° . No measurements on BiI_3 have been reported; however, intercomparisons of the data on the other halides with those of As and Sb allow a fairly precise estimate to be made, namely, a Bi-I distance of 2.80 Å. and a I-Bi-I angle of 100° . The moments of inertia calculated from these parameters were: for SbI_3 , 356×10^{-39} g. cm.² for the singular moment and 117×10^{-39} for the two equal ones; for BiI_3 , 389×10^{-39} for the singular and 233×10^{-39} for the two equal ones.

For the temperatures of interest in this work it was assumed that the ground electronic state was the only one of importance in establishing the thermal functions. This assumption was based on information about the electronic states of the gaseous ions⁴ Sb^{3+} , Bi^{3+} , and Xe (for I^-). The lowest excited electronic states for these are 64,400, 70,963, and 67,070 cm.⁻¹, respectively; all are too high above the ground state to be considered in these calculations.

The fundamental vibration frequencies for these gaseous molecules have not been measured; however, values for the similar molecules PCl_3 , AsCl_3 , SbCl_3 , BiCl_3 , PI_3 , and AsI_3 are available, and reasonable estimates based on them can be made. The pyramidal XY_3 molecules of this type (C_{3v}) have six fundamental modes of vibration,⁵ of which two are completely symmetrical modes (A_1) and the others are pairs of doubly degenerate modes (E).

Estimates of the fundamental vibration frequencies were made as follows. Howard and Wilson⁶ have calculated force constants for the trichlorides of P, As, Sb, and Bi. Stammreich, *et al.*,⁷ have used the same treatment for the triiodides of P and As. We have compared the force constants for these molecules and by means of a form of Badger's rule have estimated a set of force constants for the triiodides of Sb and Bi. These are given in Table I. The symbols for the force constants are consistent with the terminology of Howard and Wilson. Their vibrational analysis was used to calculate the frequencies of the various modes, which are also shown in Table I.

The molecular constants obtained above were used to calculate the thermodynamic functions for SbI_3 and BiI_3 (in the ideal gaseous standard state). The equations given by Pitzer and Brewer² were used for these calculations with a value of 1.987 cal./mole deg. for the gas constant. The results are given in Tables II and III. The accuracy of any particular value in the tables is probably about 1%, considering the nature of the estimates involved; however, for convenience in

Table I: Force Constants Estimated and Vibration Frequencies Calculated

	Force constants, mdynes/Å.			
	K	K'	H	H'
SbI_3	1.07	0.046	0.13	0.015
BiI_3	0.77	0.041	0.07	0.015

Class	Vibration frequencies, cm. ⁻¹			
	ν_1	ν_2	ν_3	ν_4
E				
SbI_3	64	75	179	188
BiI_3	45	63	131	129

Table II: Standard Thermodynamic Functions for SbI_3 in Ideal Gas State

T, °K.	$H^\circ_T - H^\circ_0$, kcal./mole	S°_T , cal./ (mole deg.)	$\frac{F^\circ_T - H^\circ_{298}}{T}$	
			cal./mole deg.	C_p° , cal./ (mole deg.)
298	4.970	95.20	95.20	19.43
400	6.965	100.96	95.98	19.63
500	8.920	105.27	97.37	19.71
600	10.905	108.97	99.08	19.76
700	12.880	111.92	100.62	19.79
800	14.830	114.61	102.29	19.81
900	16.840	116.96	103.77	19.82
1000	18.825	119.06	105.11	19.83
1250	23.785	123.47	108.42	19.84

Table III: Standard Thermodynamic Functions for BiI_3 in Ideal Gas State

T, °K.	$H^\circ_T - H^\circ_0$, kcal./mole	S°_T , cal./ (mole deg.)	$\frac{F^\circ_T - H^\circ_{298}}{T}$	
			cal./mole deg.	C_p° , cal./ (mole deg.)
298	5.210	99.77	99.77	19.65
400	7.225	105.60	100.57	19.75
500	9.200	109.96	101.98	19.79
600	11.180	113.66	103.71	19.81
700	13.160	116.67	105.32	19.83
800	15.150	119.51	107.08	19.84
900	17.135	121.99	108.74	19.84
1000	19.115	123.96	110.06	19.85
1250	24.070	128.28	113.19	19.85

(3) L. E. Sutton, Special Publication No. 11, The Chemical Society, London, 1958.

(4) C. E. Moore, National Bureau of Standards Circular 467, Vol. III, U. S. Government Printing Office, Washington, D. C., 1958.

(5) G. Herzberg, "Infrared and Raman Spectra of Polyatomic Molecules," D. Van Nostrand Co., Inc., New York, N. Y., 1945, p. 154.

(6) J. B. Howard and E. B. Wilson, Jr., *J. Chem. Phys.*, **2**, 630 (1934).

(7) H. Stammreich, R. Forneris, and Y. Tavares, *ibid.*, **25**, 580 (1956).

taking differences, a greater number of significant figures was maintained.

Thermodynamics of Vaporization

Antimony Triiodide. The vapor pressure of liquid SbI_3 has been reported by Bruner and Corbett⁸ for the range 530 to 680°K., by Sime⁹ from 510 to 620°K., and by Stull¹⁰ from 500 to 680°K. The pressures reported by Bruner and Corbett are 2–3% higher than Sime's and 5–6% higher than Stull's. The enthalpies of evaporation at the boiling point were 15.3 kcal./mole reported by Bruner and Corbett and by Stull, and 15.8 by Sime.

Bruner and Corbett measured the vapor density in the range 620 to 720°K. and found it agreed to within 0.5% of the value expected for SbI_3 molecules, indicating no important degree of dissociation or association in the gas phase. Sime measured P - V - T for a sample of SbI_3 not saturated with liquid. The gas obeyed Charles' law and so was not changing species in the vapor. The molecular weight he measured was about 15% too low. (This is presumed to have been within the experimental error of his determination.) These results are taken to indicate that over the normal liquid range SbI_3 is the predominant gaseous species.

The results of Bruner and Corbett were subjected to a Σ -plot analysis. The value 19.7 cal./mole deg. was used for the heat capacity of the gas and 34.3 for the liquid (taken from the heat content measurements below). When the vapor pressure equation of Bruner and Corbett is used to represent the pressure, the equation for Σ becomes

$$\begin{aligned}\Sigma &= -R \ln p - 14.6 \ln T \\ &= \frac{11,461}{T} + \frac{1.28 \times 10^6}{T^2} - 33.002 - 33.62 \log T\end{aligned}$$

This equation gave a straight line, in the range of the experimental data, when plotted against reciprocal of temperature. The slope of the line leads to the expression for the standard enthalpy of vaporization

$$\Delta H^\circ_T = 24,480 - 14.6T \pm 0.2 \text{ kcal./mole (530 to 680°K.)}$$

At 600°K. the enthalpy of vaporization is 15.72 kcal., and the log of the vapor pressure in atmospheres is -0.621 ; hence, the standard entropy of vaporization is 24.97 ± 0.2 e.u. The absolute entropy of the gas at 600°K. (from Table I) is 108.97; hence, that of the liquid is 84.00 e.u. From the entropy data for the condensed phase (Table IV) one finds that the absolute entropy of the crystal at 298°K. is 51.5 ± 0.2 e.u., the limits indicating a guess of the over-all errors involved.

From the data of Tables II and IV and the enthalpy expression above, the enthalpy of sublimation at 298°K. was calculated to be 24.26 ± 0.1 kcal./mole.

Table IV: Thermodynamic Functions for Condensed Phases of SbI_3

$T, ^\circ\text{K.}$	$H^\circ_T - H^\circ_{298}$, kcal./mole	S°_T , cal./ (mole deg.)	$\frac{F_T^\circ - H^\circ_{298}}{T}$, cal./(mole deg.)
298	0	51.5	51.5
400	2.49	58.7	52.5
444(s)	3.63	61.4	53.2
444(l)	9.07	73.6	53.2
500	11.02	77.7	55.7
600	14.47	84.0	59.9
700	17.87	89.3	63.8
800	21.32	93.8	67.2
900	25.78	97.9	69.3
1000	29.23	101.5	72.3

Bismuth Triiodide. The vapor pressure has been measured by a transpiration method by Cubicciotti and Keneshea¹¹ over the range 690 to 750°K. A Σ -plot treatment of these data was made using 19.8 and 36.0 cal./mole deg. for the heat capacities of the gas and liquid, respectively. The equation for Σ in this case is $\Sigma = \log p(\text{mm.}) + 8.2 \log T$. The Σ plot for BiI_3 is shown in Figure 1. The straight line drawn represents the points to within 2%, and the derived equation for the vapor pressure of BiI_3 is

$$\log p(\text{mm.}) = -\frac{6890}{T} - 8.2 \log T + 35.18$$

The enthalpy of evaporation of liquid BiI_3 is thus

$$\Delta H^\circ_T = 31.5 - 16.2T \pm 0.3 \text{ kcal./mole}$$

At 700°K., ΔH°_{700} is 20.2 kcal./mole, and, since $\log p$ is -0.873 (in atm.), ΔF°_{700} is 2.8 kcal./mole; so, ΔS°_{700} is 24.9 ± 0.3 e.u. From the enthalpies and entropies above room temperature, one finds ΔH_{298} for sublimation is 32.2 ± 0.3 kcal./mole and ΔS°_{298} is 43.9 ± 0.3 e.u. Combining the last value with the absolute entropy of the gas gives S°_{298} for $\text{BiI}_3(\text{s})$ as 55.9 ± 0.3 e.u.

(8) B. L. Bruner and J. D. Corbett, *J. Inorg. Nucl. Chem.*, **20**, 62 (1961).

(9) R. J. Sime, *J. Phys. Chem.*, **67**, 501 (1963).

(10) D. R. Stull, *Ind. Eng. Chem.*, **39**, 517 (1947).

(11) D. Cubicciotti and F. J. Keneshea, *J. Phys. Chem.*, **63**, 295 (1959).

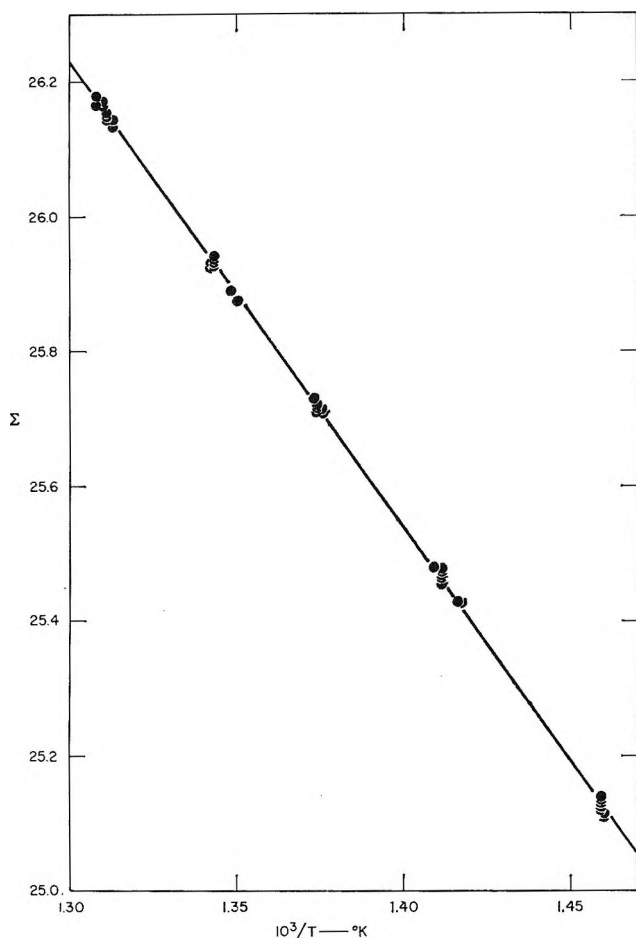


Figure 1. Σ plot of BiI_3 vaporization data.

Enthalpies of Condensed Phases

Experimental Section. The enthalpies above room temperature, up to the boiling points of these substances, were measured in the drop calorimeter described earlier.¹²

Antimony triiodide was prepared by mixing stoichiometric quantities of Baker Analyzed Reagent antimony and resublimed crystals (Mallinckrodt) of iodine. These were weighed into a dumbbell-shaped Pyrex bulb which was sealed under vacuum and then heated gently over a period of 2 or 3 days until reaction was complete as evidenced by the absence of iodine color in the vapor. The product was then distilled into one bulb of the cell; a negligible amount of black residue was left behind. The bulb, containing about 25 g. of SbI_3 , was sealed off. The weights of sample and of glass were known because the materials used were accounted for. The melting point of the sample was determined visually in an oil bath and a calibrated mercury-in-glass thermometer. The sample melted at 170.8° . A value of 170.5° is reported in N.B.S. Circular 500.

Bismuth triiodide was prepared by weighing stoichiometric amounts of bismuth (99.99+ % pure from American Smelting and Refining Co.) and resublimed iodine (Mallinckrodt) into a Pyrex glass bulb. This

Table V: Analytical Expressions for Enthalpies of Condensed Phases

	SbI_3
Solid	$H_T - H_{298}$, kcal./mole = $17.0T + 1.06 \times 10^{-2}T^2 - 6010$
	C_p , cal./(mole deg.) = $17.0 + 2.12 \times 10^{-2}T$
Fusion	$T = 444^\circ\text{K}$.
	$\Delta H = 5.44 \pm 0.05$ kcal./mole
	$\Delta S = 12.3 \pm 0.1$ e.u.
Liquid	$H_T - H_{298}$, kcal./mole = $34.3T - 6130$
	C_p , cal./(mole deg.) = 34.3
	BiI_3
Solid	$H_T - H_{298}$, kcal./mole = $9.55T + 13.15 \times 10^{-3}T^2 - \frac{0.708}{T} - 1643$
	C_p , cal./(mole deg.) = $9.55 + 26.3 \times 10^{-3}T + \frac{0.708}{T^2}$
Fusion	$T = 681.7^\circ\text{K}$.
	$\Delta H = 9.35 \pm 0.08$ kcal./mole
	$\Delta S = 13.7 \pm 0.1$ e.u.
Liquid	$H_T - H_{298}$, kcal./mole = $36.0T - 5254$
	C_p , cal./(mole deg.) = 36.0

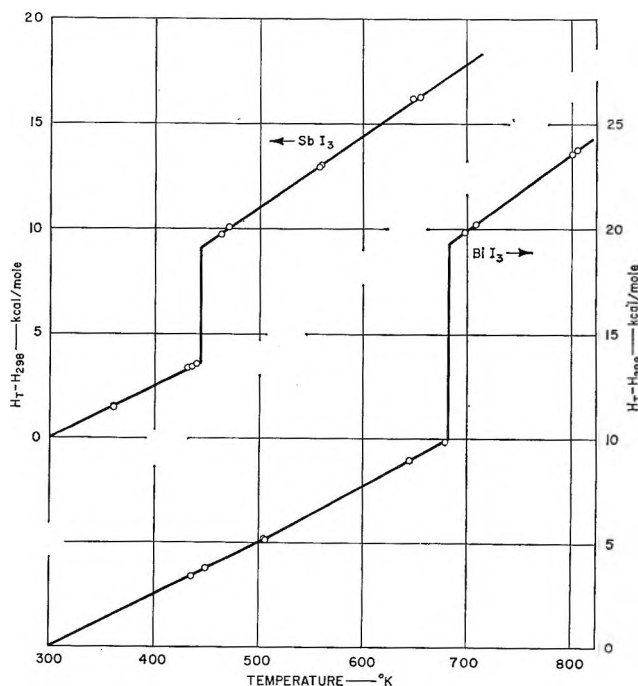


Figure 2. Enthalpies above room temperature for SbI_3 and BiI_3 .

(12) H. Eding and D. Cubicciotti, *J. Chem. Eng. Data*, 9, 524 (1964).

was evacuated and sealed off. The bulb was heated slowly over a period of several days up to the melting point and then up to the boiling point. The melting point was observed on similar samples¹³ to be 408.6° .

Results. The enthalpies measured are shown in Figure 2 as points. These values were fitted to analytical expressions such that they represented the data to better than 1%. The analytical expressions are given in Table V. The curves in Figure 2 were calculated from these expressions.

Thermodynamic Functions of Condensed Phase

The equations for the enthalpies of the condensed phases above room temperature were used to calculate the enthalpy increments and entropy increments above 298°K . These are listed in Tables IV and VI. The absolute entropies for the crystals at 298°K . calculated above were combined with the enthalpy increments to give the free energy function for the condensed phases.

Table VI: Thermodynamic Functions for Condensed Phases of BiI_3

$T, ^\circ\text{K}$.	$H^\circ_T - H^\circ_{298}$, kcal./mole	S°_T , cal./ (mole deg.)	$-\frac{F^\circ_T - H^\circ_{298}}{T}$ cal./(mole deg.)
298	0	55.9	55.9
400	2.51	63.2	56.9
500	5.00	68.7	58.7
600	7.64	73.5	60.8
681.8(s)	9.94	77.1	62.5
681.8(l)	19.29	90.8	62.5
700	19.95	91.8	63.3
800	23.55	96.6	67.2
900	27.15	100.8	70.6
1000	30.75	104.6	73.9

(13) F. E. Rosztochy and D. Cubicciotti, *J. Phys. Chem.*, **69**, 124 (1965).

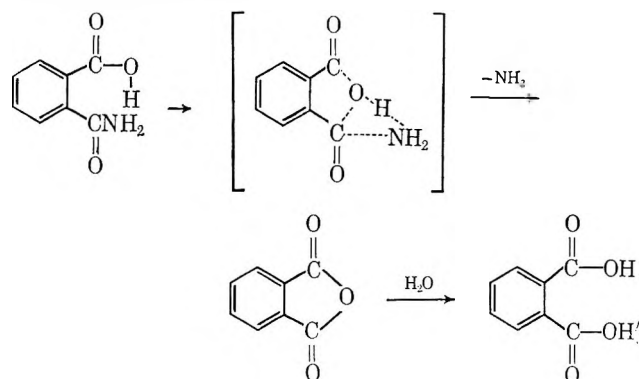
The Effect of Ethyl Substitution on the Kinetics of the Hydrolysis of Maleamic and Phthalamic Acid¹

by George Dahlgren and Nancy L. Simmerman

Department of Chemistry, University of Alaska, College, Alaska (Received May 24, 1965)

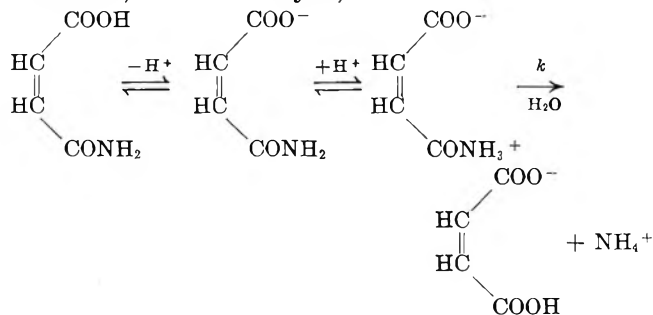
The pH-rate profiles of maleamic and phthalamic acid are similar in that they both exhibit a pH-independent portion up to a pH of slightly less than the pK of the acid function and then show a decrease with increase in pH. This pH behavior is indicative of a rate dependent on the concentration of a protonated species in solution and can be interpreted in two ways: (1) intramolecular catalysis by the carboxyl group on the carboxamide group; or (2) a "zwitterion" reaction intermediate. Other work done on phthalamic acid strongly supports the former interpretation. In both the phthalamic and maleamic acid the N-ethyl-substituted species had the smallest observed first-order rate constants (1.8×10^{-5} and 7.0×10^{-6} sec.⁻¹, respectively, at 25°). The relative rates at 25° for the unsubstituted, N-ethyl-, and N,N-diethyl-substituted derivatives are 5.0:1.0:7.8 and 4.6:1.0:7.6 for phthalamic and maleamic acids, respectively. With this similarity in rate behavior on substitution we conclude that the reactions probably occur through the same process, namely an intramolecular catalysis by the carboxyl.

Two mechanistic interpretations of kinetic data on exceptionally fast hydrolytic reactions involving a carboxamide group and a neighboring carboxylic acid group have been made. The first of these is represented by the work of Bender, *et al.*,² on the hydrolysis of phthalamic acid and suggests an intramolecular catalysis by the carboxyl group. The process is presented as a concerted electrophilic-nucleophilic reaction with the carboxyl group acting as a bifunctional catalyst, attacking the carbonyl carbon of the amide and simultaneously donating a proton to the departing ammonia molecule, *viz.*



The rate-determining step involves the simultaneous formation of the anhydride and the ejection of ammonia, followed by the rapid hydrolysis of the anhydride. Using an isotope tracer technique Bender, *et al.*,^{2b} were able to give indirect evidence for the anhydride intermediate.

The second interpretation of these reactions is represented in the work of Bruylants and Kezdy³ on the hydrolysis of maleamic acid. They interpret the kinetic data in terms of a "zwitterion" form of the amide, and acid catalysis, *viz.*



(1) This work was supported in part by Grant P-272 of the American Cancer Society. Presented in part in the Physical Chemistry Division at the 149th National Meeting of the American Chemical Society, Detroit, Mich., April 1965.

Support for this second interpretation is presented in the form of a calculation of the expected pseudo-first-order rate constant using experimental second-order constants and the ionization constant of maleamic acid. The agreement with the observed value is excellent. Additional evidence is offered in the form of a calculation of the interfunctional distances using the Bjerrum equation and rate data.

The kinetic form of these two interpretations would be identical for the two systems, and the actual reaction path (assuming it to be primarily one or the other) cannot be determined unambiguously.⁴ However, a kinetic study of the effect of substitution of ethyl groups at the reaction site should allow interesting speculation on whether or not the reactions occur through a hydrogen-bonded intermediate in a concerted process as suggested by Bender,² or through the hydrolysis of the zwitterion form as suggested by Bruylants.³ At least, a comparison of the substitution effects on the rates should show whether the reactions have similar mechanisms.

Experimental Section

Materials. *Maleamic acid* was prepared by passing anhydrous ammonia into a solution of maleic anhydride in trichloroethylene maintained at 83°. The filtered precipitate was washed with warm trichloroethylene and dried at room temperature, yielding 68% of the theoretical amount. The crude material was recrystallized from glacial acetic acid and washed with ether, m.p. 157–164° dec. (cap.), 190–191° (hot stage). *Anal.* Calcd. for C₄H₅NO₃: C, 41.8; H, 4.35; N, 12.2. Found: C, 41.3; H, 4.28; N, 12.7. Rapid recrystallization from water gave m.p. 177–178° dec. (cap.) (lit.⁵ m.p. 178–180° dec.), 197–198° (hot stage). *Anal.* Calcd. for C₄H₅NO₃·H₂O: C, 36.1; H, 5.25; N, 10.5. Found: C, 37.2; H, 5.68; N, 11.5.

In this study, only the acid-recrystallized maleamic acids were used. This appears to be the first report of the cause of the anomalous melting points reported for maleamic acid.

N-Ethylmaleamic acid was prepared by passing dry ethylamine over a solution of maleic anhydride in tetrachloroethylene at 80° until no more dissolved. The precipitate was filtered, washed with warm tetrachloroethylene, and dried at room temperature. Recrystallization from glacial acetic acid gave a product (68%), m.p. 122–124° (cap.), 127° (hot stage). *Anal.* Calcd. for C₆H₉NO₃: C, 50.4; H, 6.29; N, 9.78. Found: C, 50.4; H, 6.64; N, 9.60. Recrystallization from water gave a product, m.p. 122.5–123.5° (cap.), 125° (hot stage) (lit.⁶ m.p. 123°). *Anal.* Found: C, 50.5; H, 6.26; N, 9.34.

N,N-Diethylmaleamic acid was prepared from diethylamine and maleic anhydride in 65% yield according to the procedure of Stein and Giacomello.⁷ Recrystallization from ether–acetone gave a product of m.p. 43.3–44.4° (cap.), 47° (hot stage) (lit.⁷ m.p. 41°). *Anal.* Calcd. for C₈H₁₃NO₃: C, 56.1; H, 7.60; N, 8.18. Found: C, 55.2; H, 7.46; N, 7.94.

Fumaramic acid was prepared from methyl hydrogen fumarate and concentrated ammonium hydroxide in 87% yield by the procedure of Talley, *et al.*⁸, m.p. 216–217° (cap.), 235° (hot stage) (lit.⁸ m.p. 216.5–217.5°). *Anal.* Calcd. for C₄H₅NO₃: C, 41.8; H, 4.35; N, 12.2. Found: C, 41.6; H, 4.76; N, 11.45.

Phthalamic acid was prepared from phthalic anhydride and concentrated ammonium hydroxide in 94% yield by the procedure described by Huntress and Mulliken,⁹ m.p. 148–149° (cap.) (lit.⁹ m.p. 148–149°).

N-Ethylphthalamic acid was prepared by adding solid phthalic anhydride to a solution of ethylamine in water. After cooling, concentrated HCl was added. The precipitate was separated, washed with cold water, and dried *in vacuo*, yielding 55% of the theoretical amount, m.p. 136–137° (cap.) (lit.¹⁰ m.p. 136°).

N,N-Diethylphthalamic acid was prepared by warming an aqueous solution of phthalic anhydride and diethylamine. The solution was cooled, acidified with concentrated HCl, and allowed to stand for 24 hr. The crude acid was filtered off, washed with cold water, recrystallized from absolute ethanol, and dried *in vacuo*, giving a 36% yield of the product, m.p. 152–153° (cap.) (lit.¹¹ m.p. 153°).

Maleicdiamide was prepared from dimethyl maleate and concentrated ammonium hydroxide in 24% yield by the procedure described by Huntress and Mulliken,¹² m.p. 171–173° (cap.) (lit.¹² m.p. 181°).

(2) (a) M. L. Bender, *J. Am. Chem. Soc.*, **79**, 1258 (1957); (b) M. L. Bender, Y. L. Chow, and F. Chloupek, *ibid.*, **80**, 5380 (1958).

(3) A. Bruylants and F. Kezdy, *Record Chem. Progr. (Kresge-Hooker Sci. Lib.)*, **21**, 213 (1960).

(4) M. L. Bender, *Chem. Rev.*, **60**, 87 (1960).

(5) F. Arndt, L. Loewe, and L. Ergener, *Istanbul Univ. Fen. Fak. Mecmuasi*, **A13**, 103 (1948); *Chem. Abstr.*, **43**, 579c (1949).

(6) Y. Liwshitz, Y. Edlitz-Pfeffermann, and Y. Lipidoth, *J. Am. Chem. Soc.*, **78**, 3069 (1956).

(7) M. L. Stein and G. Giacomello, *Ric. Sci.*, **22**, 1007 (1952); *Chem. Abstr.*, **47**, 6872e (1953).

(8) E. A. Talley, T. J. Fitzpatrick, and W. L. Porter, *J. Am. Chem. Soc.*, **81**, 174 (1959).

(9) E. H. Huntress and S. P. Mulliken, "Identification of Pure Organic Compounds," John Wiley and Sons, Inc., New York, N. Y., 1941, p. 148.

(10) B. Sakurai, *Bull. Chem. Soc. Japan*, **5**, 184 (1930); *Chem. Abstr.*, **24**, 5643 (1930).

(11) N. Maxim, *Ann. chim. (Paris)*, [11] **9**, 55 (1928); *Chem. Abstr.*, **22**, 2153 (1928).

(12) Reference 9, p. 106.

N-Dimethylaminomaleamic acid and *N*-dimethylaminosuccinamic acid were provided by the Naugatuck Chemical Co. and were used without further purification.

Kinetics of Hydrolysis. The crystalline acids were dissolved in distilled water at the reaction temperature and the solution was maintained in a thermostated bath throughout the reaction. All reaction solutions were initially 0.0038 to 0.0053 *M* in the compound being studied. Within this range the observed rate constants were independent of initial concentrations. Aliquots of the reaction solution were analyzed for ammonia or amine as described below. For runs at pH 1 to 2, the pH of the reaction solution was controlled by an excess of perchloric acid. For runs between pH 3 and 5.5, MacIlvaine's citric acid–disodium hydrogen phosphate buffer mixtures were used.¹³ The pH of the initial and final reaction solution generally were identical but differed by no more than 0.1 pH unit in extreme cases. Initial reaction time, t_0 , was taken as the initial liquid–solid contact. The time required for complete solution was negligible when compared to the reaction times.

Determination of Ammonia. Ammonia was determined by nesslerization.¹⁴ Ammonia concentrations were read from a curve prepared from standard ammonium chloride solutions. Additional potassium hydroxide was added to the buffered samples, if necessary, to obtain a final nesslerized solution of pH 12.2–12.7 for maximum color development. Nesslerized solutions were read at 410 $m\mu$ on a Beckman DU spectrophotometer. The time of addition of the Nessler reagent was taken as the sampling time since the reaction was essentially stopped at this pH. No interference from the unreacted amides was observed except a deepening of color with fumaramic acid.

Determination of Ethylamine and Diethylamine. The ethylamine and diethylamine products were determined as the corresponding alkylchloramines at a pH of 8.2. Details of the analyses are described elsewhere.¹⁵

Results

The hydrolyses of maleamic, *N*-ethylmaleamic, and *N,N*-diethylmaleamic acids produce ammonia, ethylamine, and diethylamine, respectively, and maleic acid, in the form of the ionic ammonium maleates. Detection of the ammonia or amine product proved to be the most satisfactory method of following the course of the hydrolysis.¹⁶ The concentration of ammonia or amine found in an aliquot sample was subtracted from the initial amide concentration to give the concentration of unreacted amide. The observed rate constants (k_0) were obtained from standard first-order plots. In addition

to the data at 25°, additional runs were made at 0 and 50°. The values for the observed rate constants and the thermodynamic functions of activation calculated from these constants are listed in Table I.

The observed rate constants for all of the acids were found to be independent of hydrogen ion concentration in the range pH 1.5 to 3. From pH 3 to 5.5 a falloff of the rate was observed due either to the decrease in the concentration of undissociated acid as suggested by Bender² or to the decrease in the zwitterion concentration of the maleamic acid as suggested by Bruylants.³ Figure 1 shows the rate–pH profile for the three maleamic acids tested. The same dependence of the rate on the hydrogen ion concentration was observed by Bender² in the hydrolysis of phthalamic acid under similar conditions. From a consideration of the ionization constants for the acids and specifying the reactive species to be the undissociated acid or its zwitterion form, a plot of $1/k_0$ vs. $1/[H^+]$ yields an intercept of $1/k_1$, the reciprocal of the first-order rate constant, and a slope of K/k_1 , where K is the ionization constant of the acid.² Figure 2 shows these reciprocal plots for the maleamic acids and the good agreement obtained between the rate and the first-order hydrogen ion concentration dependence. The values of the first-order con-

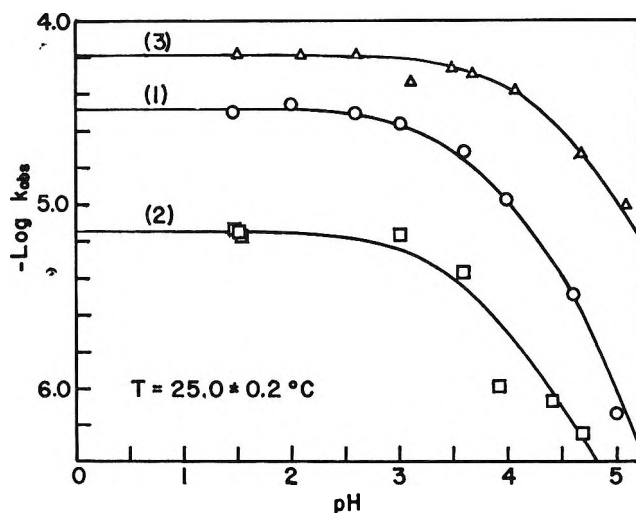


Figure 1. pH–rate profile: the hydrolysis of: (1) maleamic acid, (2) *N*-ethylmaleamic acid, and (3) *N,N*-diethylmaleamic acid at 25°. The solid line is calculated from theoretical k_1 and K values.

(13) N. A. Lange, "Handbook of Chemistry," Handbook Publishers, Inc., Sandusky, Ohio, 1952, pp. 939, 940.

(14) D. F. Boltz, Ed., "Colorimetric Determination of Nonmetals," Interscience Publishers, Inc., New York, N. Y., 1958, p. 91.

(15) G. Dahlgren, *Anal. Chem.*, **36**, 598 (1964).

(16) Conductometric titration of products was used in an earlier work: G. Dahlgren and N. L. Simmerman, *Science*, **140**, 485 (1963).

Table I: Observed First-Order Rate Constants and Thermodynamic Functions of Activation for Maleamic and Phthalamic Acids^a (pH 1.5)

Acid	$10^7 k_0$, sec. ⁻¹ (0°)	$10^6 k_0$, sec. ⁻¹ (25°)	$10^4 k_0$, sec. ⁻¹ (50°)	ΔG^\ddagger , kcal./mole (25°)	ΔH^\ddagger , kcal./mole	ΔS^\ddagger , e.u. (25°)
Maleamic	9.5	3.2	8.4	23.6 ± 0.0	21.9 ± 0.9	-5.7 ± 3.0
N-Ethylmaleamic	1.8	0.70	1.8	24.5 ± 0.0	23.6 ± 0.5	-3.0 ± 1.7
N,N-Diethylmaleamic	16	5.3	11	23.3 ± 0.0	22.3 ± 0.3	-3.3 ± 1.0
Phthalamic	...	1.8	2.3 (47°) ^b	23.9 ± 0.0	20.7 ^b	-10.4 ^c

^a The average error in k_0 was less than 3%. ^b Data from ref. 2a. ^c Calculated using $\Delta H^\ddagger = 20.7$ kcal./mole.

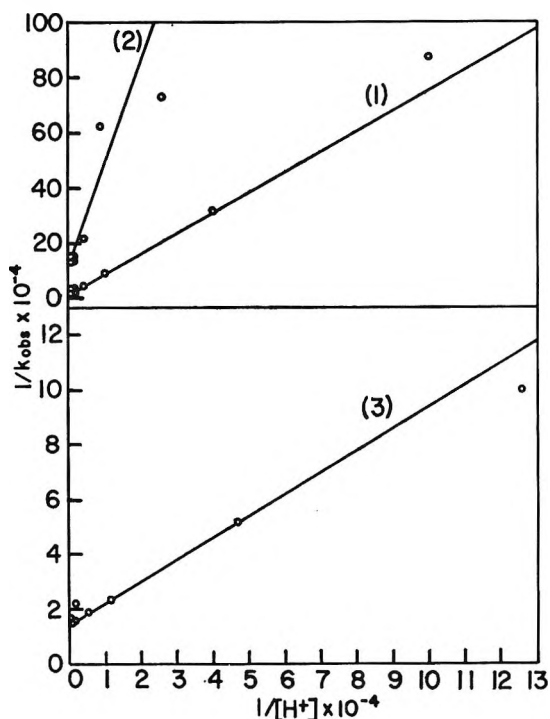


Figure 2. The hydrolysis of (1) maleamic acid, (2) N-ethylmaleamic acid, and (3) N,N-diethylmaleamic acid at 25°. The slope is K/k_1 ; the intercept is $1/k_1$.

stants and the ionization constants obtained from these plots are recorded in Table II. Additional first-order rate constants obtained at 25° in this study are listed in Table III along with available literature values. The solid lines in Figure 1 were calculated from the values of k_1 and K recorded in Table II.

Discussion

A comparison of the data on the effect of ethyl substitution on the kinetics of the hydrolysis of maleamic and phthalamic acids at 25° (Table III) shows that the two reactions are similar. The relative rates for the unsubstituted, the ethyl, and the diethyl derivatives are 4.6:1.0:7.6 and 5.0:1.0:7.8 for maleamic and phthalamic acids, respectively.

Table II: First-Order Rate Constants, Ionization Constants, and pK Values Obtained in This Work

Acid	$10^5 k_1$, sec. ⁻¹	$10^4 K$	pK	pK ^a
Maleamic (25°)	3.3	2.3	3.6	3.7
N-Ethylmaleamic (25°)	0.71	0.83	4.1	4.2
N,N-Diethylmaleamic (25°)	5.5	0.38	4.4	4.5
Maleamic (50°)	84	1.3	3.9	...
Phthalamic (47.3°) ^b	23.5	2.0	3.7	3.8
N-Ethylphthalamic	4.0
N,N-Diethylphthalamic	4.3

^a Potentiometric titration at 25°. ^b Reference 2.

Table III: Observed Rate Constants for Hydrolysis

Compd.	$10^5 k_0$, sec. ⁻¹	
	This work ^a	Lit.
Maleamic acid	3.2	4.2 ^b
N-Ethylmaleamic acid	0.70	...
N,N-Diethylmaleamic acid	5.3	...
Fumaramic acid	0.01-0.001 ^c	0.18 ^b
Phthalamic acid	1.8	2.1 ^d
N-Ethylphthalamic acid	0.36	...
N,N-Diethylphthalamic acid	2.8	...
N-Dimethylaminomaleamic acid	0.74 ^e	...
N-Dimethylaminosuccinamic acid	No reaction ^f	g
Maleic diamide	No reaction ^f	h

^a pH 1.5 and 25°. ^b Calculated from the data of Bruylants and Kezdy.³ ^c Range of values obtained; apparently small amounts of contaminant catalyze the reaction. ^d Bender.^{2a} ^e Conductometric titration method, see ref. 16. ^f No reaction detected by changes in conductance of aqueous solutions at 25° in 3 days. For clarification of expected conductance changes see ref. 16. ^g Bruylants and Kezdy³ report a value of 3.3×10^{-6} sec.⁻¹ at 65° for succinamic acid. ^h Bruylants and Kezdy³ report values of 1.2×10^{-4} and 8.4×10^{-4} sec.⁻¹ at 65° for k_1 and k_2 , respectively.

The 2-3 order of magnitude difference between the rate constants for maleamic and fumaramic acids is an indication of the catalytic effect of the *cis*-carboxyl group as compared to the *trans* form, the assumption being made that all other electronic effects are the same

in both molecules. A similar comparison between phthalamic acid and *o*-nitrobenzamide, where the substituent effect of the *o*-nitro group is similar to that for an *o*-carboxyl group, gives a factor of 10^6 in favor of phthalamic acid.^{2b} Also of interest are the hydrolysis rates, *o*-carboxybenzamide \gg benzamide $>$ *p*-carboxybenzamide.^{2b}

The effect of the substitution of a single ethyl group on the amide nitrogen of maleamic acid is approximately the same as that found for the substitution of a dimethylamino group (0.70×10^{-5} vs. 0.74×10^{-5} sec.⁻¹) which suggests similarities in the combined steric and electronic effects of the ethyl and dimethylamino groups.

In considering the effect of N-ethyl substitution on the H-bonded intermediate proposed by Bender² for reactions of this type, three effects should be taken into account: (1) the change in the basicity of the amide; (2) the change in the energy of the C-N bond; and (3) the change in the energy of the O-H bond. The basicity of the amide (and thus the ease of formation of the complex) should be in the order $-\text{NEt}_2 > -\text{NHEt} > -\text{NH}_2$, the same order expected for the ease of breaking the O-H bond. However, for the ease of breaking the C-N bond the order is reversed. The order of rates found, $-\text{NEt}_2 > -\text{NH}_2 > -\text{NHEt}$, then represents a compromise of opposing effects.

If the effect of substitution on the amide nitrogen is considered in view of the zwitterion form suggested by Bruylants,³ the expected order would involve essentially the same considerations, *i.e.*, (1) the ease of ionization of the acid, (2) the ease of protonation of the amide, and (3) the loss of the protonated amine. The observed carboxyl group ionization constants are in the order $-\text{NH}_2 > -\text{NHEt} > -\text{NEt}_2$; the ease of protonation of the amide would follow the order $-\text{NEt}_2 > -\text{NHEt} > -\text{NH}_2$, and the loss of the protonated amine the order $-\text{NH}_2 > -\text{NHEt} > -\text{NEt}_2$. Therefore, the observed order of reaction is once again a compromise of opposing effects.

Other rationalizations of the order of hydrolysis rates can be made if we consider the stereochemistry of the reaction and the suggestion of Bender¹⁷ of a transition state involving a perpendicular π -electron approach for phthalamic acid hydrolyses. The π -electrons of the nitrogen would be most accessible in the case of the unsubstituted acids. However, the increased inductive effect of two ethyl groups on the nitrogen could easily overcome any steric hindrances which they might cause, and would permit a symmetrical transition state. In the case of a single ethyl group on the nitrogen the uneven steric repulsion of the ethyl group could rotate the amide group from the favorable π -electron approach.

Morawetz and Otaki¹⁸ have investigated the rate of formation and the rate of hydrolysis of a series of aliphatic amides and have found both rates to be dependent on the type of amine involved. In the reaction of propionic acid the rate of reaction was found to be in the order $\text{CH}_3\text{NH}_2 > \text{NH}_3 > (\text{CH}_3)_2\text{NH}$ for the amide formation and the reverse order for the hydrolysis of the amide, the same amine order found for hydrolysis in this work.

Finally, it is interesting to note that the factors which slow down the hydrolysis rates of phthalamic and maleamic acids (in particular, substitution on the amide nitrogen) accelerate the formation of imides of similar structure by about the same degree. Shafer and Morawetz¹⁹ report a factor of 4 in the ratio of the second-order rate constants for imide formation for methyl N-methylphthalamate and methyl phthalamate ($12,400/3100$ l. mole⁻¹ sec.⁻¹).

Acknowledgment. The authors gratefully acknowledge the technical assistance of Mr. Donald Schell in preparing most of the compounds used in this work and the valuable comments of Dr. Sara Jane Rhoads.

(17) Reference 4, p. 60.

(18) H. Morawetz and P. S. Otaki, *J. Am. Chem. Soc.*, **85**, 463 (1963).

(19) J. A. Shafer and H. Morawetz, *J. Org. Chem.*, **28**, 1899 (1963).

The Solubility of Argon to 451 Atmospheres in Fused Sodium Nitrate at 369°

by James L. Copeland and Walter C. Zybko

Department of Chemistry, Kansas State University, Manhattan, Kansas 66504 (Received May 24, 1965)

The solubility of argon in fused sodium nitrate at 369° has been determined to a maximum saturating pressure of 451 atm. The relationship between solubility and saturating pressure is linear and thus obeys Henry's law. The experimental solubility equation is $C_d = (17.2 \times 10^{-7})P \pm 0.41 \times 10^{-4}$ mole of Ar (cm.³ of melt)⁻¹ where P is saturating pressure in atm. The Henry's law constant is given by $K = (17.2 \pm 1.7) \times 10^{-7}$ mole of Ar (cm.³ of melt)⁻¹ atm.⁻¹. The Henry's law constant in terms of the ratio of concentration of Ar in the liquid phase to its concentration in the gas phase has a value in fair agreement with simple theory. Two extreme possibilities for probable distribution of the gaseous atoms throughout the liquid salt are briefly discussed in terms of the free volume theory of liquids.

The inherent simplicity of solutions of gases in simple molten salts makes them of great interest to theoreticians concerned with structures of such melts. Solutions of noble gases constitute the simplest such systems because of the relatively weak interactions of the gaseous atoms with the ionic liquid. A relatively complicated theoretical expression for predicting Henry's law constants for such solutions has already been developed.¹ However, relatively few data are presently available to aid the theoretical situation, and most of these data are for noble gas solubilities in a few mixtures of molten fluorides.²⁻⁴ In addition, these data are for only a few atmospheres of saturating gas pressure.

The purpose of this paper is to present results of measurements of the solubility of Ar in molten NaNO₃ at 369° at relatively high pressures (up to 451 atm.) and the Henry's law constant calculated therefrom. It is shown that this constant is in fair agreement with the order of magnitude predicted by Blander, *et al.*, from their simplified theoretical treatment.³

Experimental Section

Reagent grade NaNO₃ from Baker and Adamson and from Fisher was employed. The Baker and Adamson salt was used without purification other than drying. The Fisher chemical was also dried, but exhibited traces of a residue which was insoluble in the fused salt. This residue eventually settled, and the pure molten salt was then decanted. Argon was ob-

tained from the National Cylinder Gas Co. and had a stated purity of 99.999%. It was used without further purification.

A 500-ml. capacity Inconel metal bomb, Type A243HC5 of the Parr Instrument Co., was fitted with two CONAX thermocouple glands packed with a natural magnesium silicate. Each of these glands contained a chromel-alumel thermocouple. One thermocouple junction was positioned centrally in the lower half of the bomb and the other junction was located similarly in the upper half of the system. Both junctions were protected against salt corrosion by Pyrex tubes. The accuracy of each of the thermocouples was $\pm 0.5^\circ$. The bomb was further equipped with a 0-8000 p.s.i.g. Supergauge manufactured by the U. S. Gauge Division of Ametek. The accuracy of this gauge, as quoted by the manufacturer, was ± 40 p.s.i., or slightly better than ± 3 atm.

To determine the solubility of Ar in fused NaNO₃ at a given saturating pressure, the following procedure was employed. The effective empty volume of the bomb, containing a Pyrex liner and thermocouples, was taken as the average of several measurements of the volume of water required to fill the closed bomb

(1) H. Reiss, *et al.*, *J. Chem. Phys.*, **32**, 119 (1960).

(2) W. R. Grimes, N. V. Smith, and G. M. Watson, *J. Phys. Chem.*, **62**, 862 (1958).

(3) M. Blander, W. R. Grimes, N. V. Smith, and G. M. Watson, *ibid.*, **63**, 1164 (1959).

(4) G. M. Watson, *et al.*, *J. Chem. Eng. Data*, **7**, 285 (1962).

completely through a small orifice in the bomb's head which normally accommodates the pressure gauge. This volume generally resulted as about 430 cm.³ with a maximum error of ± 1 cm.³. A correction factor of 2 cm.³ was added to this volume to account for the volume of the Bourdon tube of the pressure gauge. A sample of dry NaNO₃ of from about 350 to 450 g. was weighed into the Pyrex liner to the nearest 0.5 g. The volume of the solid salt was calculated using a density of 2.261 g. cm.⁻³.⁵ The bomb, containing the salt, was sealed and evacuated, and Ar was admitted at room temperature to some desired pressure. When pressure equilibrium was attained at room temperature, the number of moles of Ar introduced was calculated from the equilibrium pressure, temperature, and gas volume by interpolation of detailed plots of the P - \bar{V} - T data compiled by Din.⁶ The bomb was then heated in a vertical furnace to a fused NaNO₃ temperature of 369°, as indicated by the lower thermocouple within the liquid phase. At this temperature the liquid salt occupied about one-half of the bomb liner (about 200–250 cm.³ of liquid). Solution equilibrium was assumed to exist at the saturation pressure indicated and at a salt temperature of 369° when no discernible pressure change was observed for at least 24 hr., during which time the system was often agitated. The temperature of the salt was assumed to be uniform at 369° since agitation caused no perceptible change in the lower thermocouple's reading. The number of moles of gaseous Ar remaining was calculated from the new equilibrium gas pressure, volume, and temperature (indicated by the upper thermocouple located centrally in the gas phase) with the aid of the same graphs of Din's compilation. The final gas volume was the initial room temperature value corrected to the nearest 1 cm.³ for the increase in volume of the liquid NaNO₃ and its compression. A density of 1.875 g. cm.⁻³, taken from the data of Bloom, *et al.*,⁷ was used for the calculation of the volume of fused salt. Compression of the melt was found by interpolation of the data of Bockris and Richards for the isothermal compressibility coefficients of fused salts.⁸ Thermal expansions of the bomb, Pyrex liner, and thermocouples were ignored in view of their minuteness. Finally, the decrease in moles of gaseous Ar was attributed to its solubility in the melt, which was then calculated.

Results and Discussion

Figure 1 is a graph of the solubility of Ar in fused NaNO₃, at 369°, *vs.* saturating pressure to an upper value of 451 atm. Table I summarizes these data. Corrections for slightly lower gas temperatures,

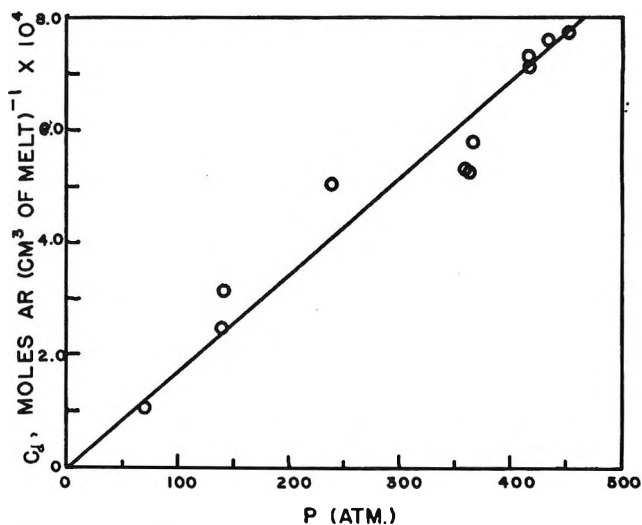


Figure 1. Solubility of argon in molten sodium nitrate at 369°, C_d , *vs.* saturating pressure of argon, P .

relative to the salt at 369°, were found not to affect the points above 200 atm. significantly and were therefore not applied thereto. Such corrections, however, were necessary for points below 200 atm. The maximum error in pressure is slightly better than ± 3

Table I: Summary of Solubility of Ar in Molten NaNO₃ at 369° *vs.* Saturating Pressure of Ar Data

Saturating pressure, P , atm.	Solubility, C_d , moles of Ar (cm. ³ of melt) ⁻¹ $\times 10^4$
70	1.10
139	2.50
140	3.16
238	5.07
359	5.35
362	5.31
366	5.81
416	7.33
417	7.16
434	7.63
451	7.78

atm. for each point. The relationship appears linear and thus obeys Henry's law. The average slope calculated from these data yields the equation for solubility, C_d

(5) "Handbook of Chemistry and Physics," 40th Ed., Chemical Rubber Publishing Co., Cleveland, Ohio, 1958–1959, p. 657.

(6) F. Din, "Thermodynamic Functions of Gases," Vol. 2, Butterworth and Co., Ltd., London, 1962, pp. 192, 193.

(7) H. Bloom, *et al.*, *Trans. Faraday Soc.*, **49**, 1458 (1953).

(8) J. O'M. Bockris and N. E. Richards, *Proc. Roy. Soc. (London)*, **A241**, 44 (1957).

$$C_d = (17.2 \times 10^{-7})P \pm 0.41 \times 10^{-4} \text{ mole of Ar} \\ (\text{cm.}^3 \text{ of melt})^{-1} \quad (1)$$

where P is the saturating pressure in atm., and the error is the probable error calculated with respect to the best straight line. The Henry's law constant is the average slope

$$K = (17.2 \pm 1.7) \times 10^{-7} \text{ mole of Ar (cm.}^3 \text{ of} \\ \text{melt})^{-1} \text{ atm.}^{-1} \quad (2)$$

where the error is the probable error of the slope. This value for K is in good agreement with the first crude results reported earlier by this laboratory.⁹ If this constant is converted to $K_c = C_d/C_g$ (where C_d and C_g denote concentrations of Ar in the liquid and gas phases, respectively), then (approximately)

$$K_c = 86 \times 10^{-3} \quad (3)$$

It is assumed that C_d is small enough to render the solution ideal, so that the activity of Ar therein may be equated to its concentration. Furthermore, ideal gas behavior is assumed for Ar at the high temperature, in spite of its pressure, so that its fugacity may be equated to pressure. The latter assumption involves errors of about 9.3% in the molar volume of Ar at the maximum employed pressure of 451 atm., and of about 2% at the lowest pressure of 70 atm., as deduced from Din's compilation.⁶

The simplified solubility model of Blander, *et al.*, equates the free energy of solution of the gas to the free energy of formation of holes the size of the gas molecules in a continuous fluid having the same surface tension as the solvent.³ Their derived relation for K_c is

$$K_c = \exp[-kA\gamma_{\text{mic}}/RT] \quad (4)$$

where A is the area of a hole created by a gas molecule, γ_{mic} is a microscopic "surface tension," R is the gas constant, T is the absolute temperature, and k is a conversion factor to obtain energy in calories. For spherical gas atoms, $kA = 18.08r^2$, where r is the atomic radius of the gas in Å. γ_{mic} is taken to be the same as that of the macroscopic fluid. For fused NaNO₃ at 369°, $\gamma = 109.7$ dynes cm.⁻¹.¹⁰ The atomic radius of Ar is taken as $r = 1.92$ Å.³ Equation 4 with these values gives a calculated K_c of 3.3×10^{-3} . Thus our experimental K_c agrees to an order of magnitude with the calculated value to about the same extent as did

some of the results of Blander, *et al.*,³ and Watson, *et al.*⁴

Two interesting extreme possibilities may exist for probable distribution of Ar atoms throughout the liquid NaNO₃. One possibility is that the gaseous atoms take up holes of their own creation in the liquid. In this case, the volume of the solution would be expected to be greater than that of the pure solvent by an amount roughly equal to the total volume of the solute particles (about 3 cm.³ for the highest solubility observed in this work at 451 atm.). Unfortunately, measurements of such possible volume changes could not be made with the present apparatus. Another extreme possibility is that the solute atoms predominantly occupy existing free volume (as holes) in the liquid. In the hole theory of fused salts, the volume increase on melting is attributed almost entirely to holes.¹¹ Thus such free volume amounts to about 4.32 cm.³ mole⁻¹ for fused NaNO₃.¹² In this case, but little volume difference would be expected between the pure solvent and solution, especially in view of the relatively weak solvent-solute interactions. A third possibility, of course, is a combination of these two cases. If the availability of liquid free volume provides for enhanced solubility to some extent, then the solubility of Ar at an equivalent temperature in LiNO₃ should be greater than in NaNO₃ by virtue of a larger free volume for the former salt (about 6.84 cm.³ mole⁻¹).¹² Similarly, the solubility should be less in KNO₃ (free volume of about 1.73 cm.³ mole⁻¹), etc. Such studies are being undertaken in this laboratory in conjunction with conductance measurements on the solutions.⁹ It is hoped that the conductance measurements will help to elucidate the mechanism of solute distribution in such liquids.

Acknowledgment. The authors gratefully acknowledge support of this work by the National Science Foundation, Grant No. GP-4274. This work has been submitted to the Graduate School of Kansas State University by W. C. Zybko in partial fulfillment of the requirements for the degree of Doctor of Philosophy.

(9) J. L. Copeland and W. C. Zybko, *J. Am. Chem. Soc.*, **86**, 4734 (1964).

(10) H. Bloom and J. O'M. Bockris, "Modern Aspects of Electrochemistry, No. 2," J. O'M. Bockris, Ed., Butterworth and Co., Ltd., London, 1959, p. 198.

(11) H. Bloom, *Discussions Faraday Soc.*, **32**, 7 (1961).

(12) H. Schinke and F. Sauerwald, *Z. anorg. allgem. Chem.*, **304**, 25 (1960).

Nonaqueous Silver Nitrate Solutions. Spectral Studies in Acetonitrile

by Colin B. Baddiel, Malcolm J. Tait, and George J. Janz

Department of Chemistry, Rensselaer Polytechnic Institute, Troy, New York (Received May 27, 1965)

The Raman, infrared, and n.m.r. spectra of solutions of silver nitrate in acetonitrile (up to 9.0 *M* AgNO₃) are reported and compared with the spectra of the pure components (silver nitrate as the fused salt). The spectral data indicate that strong solute-solvent interactions take place in these solutions; it is suggested that a complex ion of formula Ag-(CH₃CN)₂⁺ is present. In all solutions a clear splitting of the degenerate stretching vibration of the nitrate ion is observed. This splitting is also found for the molten silver nitrate and indicates the existence of strong ion-ion interactions.

Introduction

The properties of solutions of inorganic compounds in acetonitrile have been extensively studied in this laboratory over the past few years.^{1,2} Silver nitrate dissolves readily in acetonitrile and its viscosity and conductance up to a concentration of 6 *M* have been described.¹ At concentrations greater than 0.1 *M* these results indicated that increasing concentrations of ion pairs and triple-ion aggregates were present. This communication describes a Raman, infrared, and proton magnetic resonance investigation of silver nitrate in acetonitrile in the concentration range 0.2 to 9.0 *M*.

Experimental Section

Fischer certified reagent grade acetonitrile was purified by a method adopted from Coetzee.³ The acetonitrile was dried over calcium hydride for 48 hr., distilled from phosphorus pentoxide, and finally refluxed over calcium hydride to constant temperature and redistilled. The middle fraction was retained and used [b.p. 82.5° (763 mm.)]. The water content was estimated to be 0.003% by a Karl Fischer titration.

Deuterated acetonitrile, CD₃CN, was used as received from Volt Radiochemical Co. Infrared spectral analysis proved it to contain less than 1% HDO.

Reagent grade silver nitrate (m.p. 212°) was dried in a vacuum oven at 65° to constant weight. The solutions of silver nitrate in acetonitrile were prepared under N₂.

Raman measurements were made with a Hilger E-612 double-prism spectrometer, utilizing both the photoelectric and photographic methods of recording. Kodak 103a-J plates and D-19 fine-grain developer

were employed for the photographic determinations. Exposure times varied from 5 to 12 min. for the solutions, and 15 min. for the fused salt (slit width 6 cm.⁻¹; slit height 5.5 mm.). The more concentrated solutions discolored and became opaque when exposed to the exciting radiation for more than 15 min., possibly due to a photochemical decomposition of the silver salt in acetonitrile. This did not occur when the molten salt was being examined.

The transfer of molten silver nitrate to the Raman cells and the details of the high-temperature assembly within the coils of the Toronto arc have been described elsewhere.^{4,5} The spectra of the melt were taken at 250°.

For the infrared studies a Perkin-Elmer 221 double-beam grating spectrometer was used. Sodium chloride windows could not be used to contain the solutions in the infrared cells because they became opaque. Irtran-2 windows (Barnes Engineering Co., Inc., Stamford, Conn.), which contain zinc sulfide, were also attacked, but silver chloride windows proved to be inert. It was found that whereas the same frequencies were observed for the CH₃CN bands in silver nitrate solutions using either Irtran-2 or silver chloride plates,

(1) G. J. Janz, A. E. Marcinkowsky, and I. Ahmad, *J. Electrochem. Soc.*, **112**, 104 (1965).

(2) (a) G. J. Janz and S. S. Danyluk, *J. Am. Chem. Soc.*, **81**, 3846 (1959); (b) *ibid.*, **81**, 3850 (1959); (c) *ibid.*, **81**, 3854 (1959).

(3) J. F. Coetzee, G. P. Cunningham, D. K. McGuire, and G. R. Padmanabhan, *Anal. Chem.*, **34**, 1139 (1962).

(4) G. J. Janz, T. R. Kozlowski, and S. C. Wait, *J. Chem. Phys.*, **39**, 1809 (1963).

(5) G. J. Janz, Y. Mikawa, and D. W. James, *Appl. Spectry.*, **15**, 47 (1961).

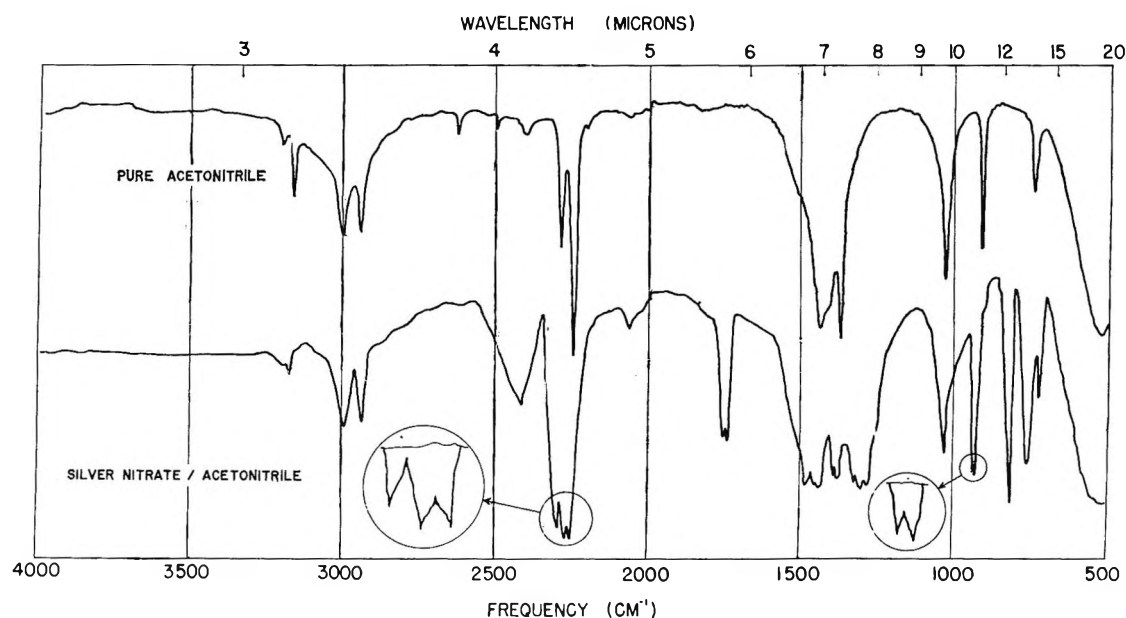


Figure 1. Infrared spectra of CH_3CN and of a solution of silver nitrate in acetonitrile of mole fraction 0.140.

Table I: CH_3CN Raman Frequencies (cm^{-1}) and Assignments for Silver Nitrate Solutions in Acetonitrile

Description	Assignment	AgNO_3 , mole fraction					
		0.00	0.017	0.091	0.20	0.32	0.38
C—C \equiv N bending	$\nu_8(e)$	378	383	394	391
C—C stretching	$\nu_4(a_1)$	918	926	925	926	925	928
CH_3 rocking	$\nu_7(e)$	Absent
CH_3 deformation	$\nu_3(a_1)$	1371	1375	1375	1373	1373	1364
CH_3 deformation	$\nu_6(e)$	1420–1450	...	1415–1450	1402–1443	1402–1449	1402–1450
C \equiv N stretching	$\nu_2(a_1)$	2252	2259	2257	2272	2270	2272
C—H stretching	$\nu_1(a_1)$	2941	2941	2941	2941	2934	2934
C—H stretching	$\nu_5(e)$	2999	3002	3001	2994	2991	2989

different frequencies were observed for the nitrate ion. Only the nitrate ion bands determined with silver chloride windows are quoted in the results. All the metal parts of the infrared cells which came in contact with the silver nitrate solutions were silver plated.

Proton resonance spectra were taken with a Varian Associates A60 high-resolution instrument. Each sample was referred to an external proton reference, tetramethylsilane, and the results were corrected for bulk susceptibility effects.

Results

The observed Raman and infrared frequencies of the silver nitrate solutions, concentration 0.2 to 9.0 M , and the frequencies of the pure components are given in Tables I–III. The vibrational assignments for the CH_3CN molecule (linear, C_{3v}), which are well estab-

Table II: CH_3CN Infrared Frequencies (cm^{-1}) and Assignments for Silver Nitrate Solutions in Acetonitrile

Assignment	AgNO_3 , mole fraction			
	0.00	0.14	0.28	0.38
Free acetonitrile				
C—C $\nu_4(a_1)$	917	922	923 (sh)	...
CH_3 $\nu_7(e)$	1047	1043	1042	1038
CH_3 $\nu_3(a_1)$	1376	1370	1370–1390	1375
CH_3 $\nu_6(e)$	1443	1420–1480	1420–1480	1420–1480
C \equiv N $\nu_2(a_1)$	2254	2255	2253	...
C—H $\nu_1(a_1)$	2944	2938	2936	2935
C—H $\nu_5(e)$	3002	2998	2996	2997
Complexed acetonitrile				
C—C $\nu_4(a_1)$...	930	929	933
C \equiv N $\nu_2(a_1)$...	2273	2272	2270

Table III: Raman and Infrared Frequencies (cm^{-1}) of the Nitrate Ion for Solutions of Silver Nitrate in Acetonitrile

Description	Assignment	AgNO ₃ , mole fraction									
		0.090	0.200	0.325	0.380	1.000	0.0100	0.140	0.280	0.375	1.000 ^a
Planar rock	$\nu_4(e')$	727	...	724	724	730	~695
NO ₂ deformation	$\nu_2(a_2'')$	Forbidden					...	823	819	816	800
NO stretch	$\nu_1(a_1')$	1040	1043	1040	1041	1043	Forbidden				1029
NO ₂ asym. stretch	$\nu_3(e')$...	1270	1275	1275	1280	1352	1309	1302	1290	1310
			1425	1423	1422	1410	1428	1425	1423	1428	1395

^a Data of J. K. Wilmschurst and S. Senderoff, *J. Chem. Phys.*, **35**, 1078 (1961).

lished,⁶⁻⁹ are listed in Tables I and II together with the Raman and infrared frequencies. It can be seen that the major changes in the CH₃CN spectrum occur in the 2250- and 920- cm^{-1} regions. This is illustrated in Figure 1, which shows the infrared traces of the pure acetonitrile and of a solution of mole fraction 0.14 in silver nitrate. The concentration dependence of the bands at 2254 and 2272 cm^{-1} is given in Figure 2.

In Table III the frequencies of the NO₃⁻ ion are listed for the fused salt and for the acetonitrile solutions. The corresponding vibrational assignments, which are given in the table, are in agreement with those made from Raman and infrared studies on solid,¹⁰ fused,^{11,12} and aqueous^{13,14} silver nitrate. Analysis of the nitrate bands in the 1410–1280 cm^{-1} range was dif-

ficult because this region is also well populated by CH₃CN bands at 1376 and 1443 cm^{-1} . Measurements were therefore made of silver nitrate solutions of the same concentrations in CD₃CN, which does not absorb in this part of the spectrum.

Proton magnetic resonance measurements yielded values of the chemical shift which were concentration dependent. This relationship is illustrated in Figure 3.

Discussion

Acetonitrile. Vibrational Spectra and Assignment. The results given in Tables I and II indicate that all of the bands observed for pure CH₃CN are still present in the silver nitrate solutions. In addition two other bands are observed in the infrared spectra at 2272 and 930 cm^{-1} . As the concentration of the solution is increased, the intensity of these two bands increases at the expense of the adjacent solvent peaks, which are the symmetrical C≡N and C—C stretching frequencies at 2254 and 920 cm^{-1} , respectively. The new bands can be assigned to the symmetrical C≡N and C—C stretching frequencies of a complex of acetonitrile with the solute. Since all the other frequencies of the acetonitrile molecules in the complex presumably coincide with those of the free solvent, then the point group symmetry of CH₃CN (C_{3v}) must be obtained in the complexed state. In the Raman measurements it was not possible, as it was in the infrared, to resolve the C≡N and C—C frequencies each into two components. However, the observed frequencies were found to in-

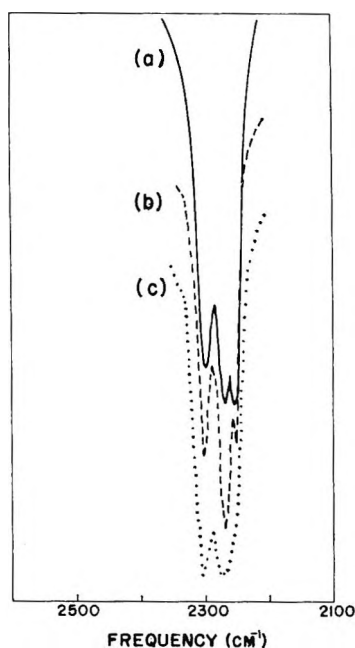


Figure 2. The concentration dependence of the C≡N stretching frequencies observed in the infrared at 2254 and 2272 cm^{-1} for a solution containing a mole fraction of AgNO₃: 0.14, —; 0.28, —; 0.38, ·····.

- (6) J. C. Evans and J. H. Bernstein, *Can. J. Chem.*, **33**, 1746 (1955).
- (7) R. M. Badger and S. H. Bauer, *J. Am. Chem. Soc.*, **59**, 303 (1937).
- (8) P. Venkateswarlu, *J. Chem. Phys.*, **19**, 293 (1951).
- (9) G. Herzberg, "Infrared and Raman Spectra of Polyatomic Molecules," D. Van Nostrand Co., Inc., New York, N. Y., 1945, p. 333.
- (10) J. R. Ferraro, *J. Mol. Spectry.*, **4**, 99 (1960).
- (11) W. Bues, *Z. physik. Chem. (Frankfurt)*, **10**, 1 (1957).
- (12) G. J. Janz and D. W. James, *J. Chem. Phys.*, **33**, 739 (1961).
- (13) R. E. Hester and R. A. Plane, *Inorg. Chem.*, **3**, 769 (1964).
- (14) H. Lee and J. K. Wilmschurst, *Australian J. Chem.*, **17**, 943 (1964).

into two bands. However, since this is the only deviation from the selection rules which was observed, it is not possible to assign a lower symmetry, such as C_{2v} , to the nitrate ion in these solutions, although a recent Raman investigation²¹ of fused silver nitrate, in which very precise intensity measurements were made, has shown that NO_3^- ions of both symmetries (D_{3h} and C_{2v}) may be present. Frequently the extent of this splitting has been used as a criterion for the magnitude of cation-anion interactions in nitrates.^{10,14} The results in Table II indicate that such interactions are present in these solutions and, since the splitting of ν_3 increases with

concentration, these interactions occur to a greater extent at higher concentrations.

Acknowledgments. We thank Dr. F. C. Nachod for use of the n.m.r. facility at Sterling Winthrop Research Institute, and for helpful discussions relative to interpretations of these results. This work was made possible, in large part, by financial support received from the U. S. Atomic Energy Commission, Division of Chemistry, Washington, D. C.

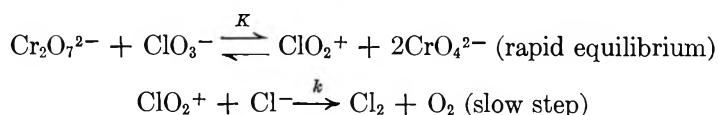
(21) G. E. Walrafen and D. Irish, *J. Chem. Phys.*, **40**, 911 (1964).

Acid-Base Reactions in Fused Salts. The Dichromate-Chlorate Reaction

by James Schlegel

Rutgers, The State University, Newark Colleges of Arts and Sciences, Newark, New Jersey
(Received July 17, 1964)

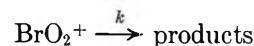
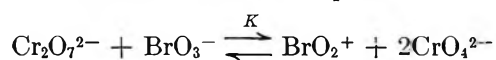
Dichromate ion reacts with chlorate ion in fused $NaNO_3$ - KNO_3 mixtures to form chlorine and oxygen. Chloride is found to catalyze the reaction. The postulated mechanism includes



Chloride was added in excess so that its concentration would remain essentially constant during the course of the reaction. Barium ion, also in excess, was added to make the reaction proceed at a measurable rate and to control the concentration of the chromate ion. Temperature and solvent effects were also determined.

Introduction

Equilibrium studies of Lewis acids and bases in fused alkali nitrates have been made in which $Cr_2O_7^{2-}$ was the acid and either NO_3^- or BrO_3^- was the base.^{1,2} It is of interest to see whether or not the other halates, ClO_3^- and IO_3^- , behave as Lewis bases in a manner similar to BrO_3^- . Bromate reacts with dichromate to form an intermediate which decomposes at a low rate



By evaluating the equilibrium constant, K , for each of the halates, the relative acidities of ClO_2^+ and IO_2^+ to BrO_2^+ in fused nitrates could be measured. No oxides of nitrogen were formed, indicating that ClO_3^-

(1) F. R. Duke and M. Iverson, *J. Am. Chem. Soc.*, **80**, 5061 (1958).

(2) F. R. Duke and J. Schlegel, *J. Phys. Chem.*, **67**, 3487 (1963).

is a sufficiently strong base that the nitrate reaction could be neglected.

Experimental Section

Materials and Apparatus. ACS reagent grade chemicals were used. All determinations were performed using a system similar to that described by Duke and Lawrence.³

Procedure. A solution of Ba^{2-} and ClO_3^- in fused $\text{NaNO}_3\text{-KNO}_3$ was purged with nitrogen for 1 hr. to allow the solution to reach the temperature of the bath and to sweep out any adsorbed water. The solution was kept at a temperature of 260° for several days and periodically checked for possible decomposition of chlorate. Analysis for the appearance of chloride and disappearance of chlorate showed that no decomposition had occurred. Dichromate was added to start the reaction.

The rate of the reaction was studied by collecting evolved chlorine in basic solution. The solution was then acidified, KI was added, and the liberated iodine was titrated with standard thiosulfate solution. The reaction was allowed to go to near completion. In all cases 1 mole of dichromate produced 1 mole of chlorine. The rate of appearance of chlorine was determined, and from this the rate of disappearance of total acid was calculated. The chlorate and barium ions were always in excess; however, their concentrations were varied from run to run to allow separation of the equilibrium constant from the rate constant. Separate runs were made to determine the amount of oxygen evolution. The evolved gases were passed through Ascarite and collected in a gas buret. Chromatographic analysis showed oxygen to be the only gas present in the gas buret along with some nitrogen which was used to purge the system before the reaction.

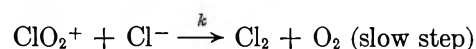
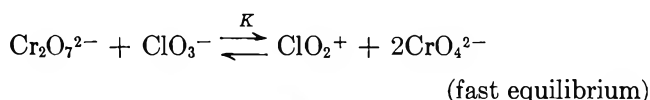
Results and Discussion

The reaction proceeds at a measurable rate when all of the reactants are in excess of dichromate. The products of the reaction are chlorine, oxygen, and chromate. Barium ion was added to control the concentration of chromate through the solubility product of barium chromate. In all runs, 1 mole of chlorine was recovered for every mole of dichromate consumed. Therefore, the rate of disappearance of total acid, $T_A = [\text{Cr}_2\text{O}_7^{2-}] + [\text{ClO}_2^+]$, may be calculated by following the rate of appearance of chlorine.

A long induction period in the absence of added Cl^- indicates a complex mechanism under these conditions. The addition of sodium chloride before the reaction caused the induction period to disappear. The order in chloride was determined by plotting the logarithm of

the pseudo rate constant *vs.* the logarithm of total chloride. The order was found to be 1 in chloride ion, which indicates the rate-determining step to be $\text{ClO}_2^+ + \text{Cl}^- \rightarrow \text{Cl}_2 + \text{O}_2$. At an initial chloride ion concentration of 0.30 *m*, chloride produced in the reaction becomes negligible, and the volume ratio of Cl_2 to O_2 is 1 to 1. This concentration is used in all subsequent runs to determine the equilibrium and rate constants.

At high chloride ion concentrations, the reactions involved are



The rate law can be written $-dT_A/dt = k[\text{ClO}_2^+] \times [\text{Cl}^-]$, where $T_A = [\text{Cr}_2\text{O}_7^{2-}] + [\text{ClO}_2^+]$. Substitute $[\text{Cr}_2\text{O}_7^{2-}] = T_A - [\text{ClO}_2^+]$ and $[\text{CrO}_4^{2-}] = K_{sp}/[\text{Ba}^{2+}]$ into the equilibrium expression to obtain

$$[\text{ClO}_2^+] = \frac{K[\text{ClO}_3^-][\text{Ba}^{2+}]^2}{K[\text{ClO}_3^-][\text{Ba}^{2+}]^2 + K_{sp}^2}$$

The rate expression will then be

$$-dT_A/dt = \frac{kK[\text{ClO}_3^-][\text{Cl}^-][\text{Ba}^{2+}]^2}{K[\text{ClO}_3^-][\text{Ba}^{2+}]^2 + K_{sp}^2} T_A$$

This equation reduces to a pseudo-first-order rate equation when the concentrations of the ions are high with respect to dichromate, $-dT_A/dt = k'T_A$. The reciprocal of the pseudo rate constant is

$$1/k' = \frac{1}{k[\text{Cl}^-]} + \frac{K_{sp}^2}{kK[\text{ClO}_3^-][\text{Cl}^-][\text{Ba}^{2+}]^2}$$

The equilibrium constant and the rate constant were separated by plotting $1/k'$ *vs.* $1/[\text{Ba}^{2+}]^2$ (Figure 1). The rate constant was obtained from the ordinate intercept, $1/k[\text{Cl}^-]$, in which the chloride ion concentration was always 0.30 *m*. Note that the abscissa intercept is equal to $-K[\text{ClO}_3^-]/K_{sp}^2$. The solubility of barium chromate in fused nitrates and its temperature dependence have been determined.² The concentration of chlorate was 0.94 *m* in all cases. Making the appropriate substitutions, the equilibrium constant can be obtained. Table I lists the values of the equilibrium constants and rate constants at several temperatures.

Lux suggested that for oxide systems an acid may be defined as any material which gains oxide ions.⁴ Flood⁵

(3) F. R. Duke and W. Lawrence, *J. Am. Chem. Soc.*, **83**, 1269 (1961).

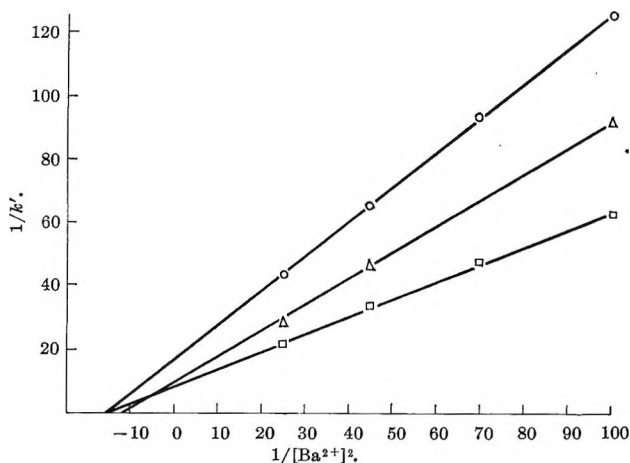


Figure 1. Variation of $1/k'$ as a function of $1/[\text{Ba}^{2+}]^2$ at 250° (O), 260° (Δ), and 270° (\square).

Table I: Equilibrium Constants and Rate Constants for the $\text{Cr}_2\text{O}_7^{2-}-\text{ClO}_3^-$ Reaction at Several Temperatures

T , °C.	k , $M^{-1} \text{ min.}^{-1}$	$K \times 10^{10}$, M
250	0.208	1.64
260	0.333	2.46
270	0.417	3.31

extended the Lux concept and pointed out that in such systems acid strengths may be compared by comparing the magnitude of equilibrium constants defined as $K = a_{\text{acid}}a_{\text{O}^{2-}}/a_{\text{base}}$. Therefore, the equilibrium constants obtained from the dichromate-halate reactions determine the relative strength of the acids, BrO_2^+ , ClO_2^+ , and IO_2^+ , in fused alkali nitrates. Table II lists the

equilibrium constants at 250° for three acid-base reactions. The strengths of the acids increase in the order BrO_2^+ , ClO_2^+ , NO_2^+ . Although the equilibrium constant for the dichromate-nitrate reaction was determined indirectly,^{6,7} its value is included as a comparison.

If no anomalies exist, one would expect the iodyl ion, IO_2^+ , to be the weakest acid. Preliminary studies of the dichromate-iodate reaction indicate that iodate is not as reactive as the other halates. This observation does not mean that the equilibrium constant for this reaction is smaller than for the other halates, making iodyl ion the strongest acid. The iodyl ion may be more stable. Experiments are now in progress to establish the relative acidity of IO_2^+ .

Table II: Equilibrium Constants for Three Acid-Base Reactions

Reaction	K , M^{-1}
$\text{Cr}_2\text{O}_7^{2-}-\text{BrO}_3^-$	3.5×10^{-8}
$\text{Cr}_2\text{O}_7^{2-}-\text{ClO}_3^-$	1.6×10^{-10}
$\text{Cr}_2\text{O}_7^{2-}-\text{NO}_3^-$	8.5×10^{-14}

Acknowledgment. The author is grateful to the Research Council of Rutgers, The State University, for support of this work.

(4) H. Lux, *Z. Elektrochem.*, **45**, 303 (1939).

(5) H. Flood and T. Forlund, *Acta Chem. Scand.*, **1**, 592 (1947).

(6) F. R. Duke and M. Iverson, *J. Phys. Chem.*, **62**, 417 (1958).

(7) F. R. Duke and S. Yamamoto, *J. Am. Chem. Soc.*, **81**, 6378 (1959).

NOTES

The Mercury-Photosensitized Oxidation of Perfluoropropene¹

by Julian Hecklen and Vester Knight

Aerospace Corporation, El Segundo, California
(Received May 12, 1965)

In the mercury-sensitized oxidation of C_2F_4 , an excited-molecule mechanism was postulated.^{2a} However, in that system CF_2 was also formed, whose presence might have influenced the results. At room temperature the Hg sensitization of C_3F_6 gives no products, even for extended exposures.^{2b} Consequently, this molecule should be ideal for studying the excited-molecule oxidation.

The experimental procedure has been described previously.^{2b} In the present study, only one resonance lamp was used rather than two. Reduced intensities were obtained by inserting Corning 9-30 glasses in the beam. Each filter transmits 42% of the radiation at 2537 Å. Matheson research grade oxygen was used without further purification. In some of the earlier runs, attempts were made to separate the CF_2O and CF_3CFO products at -160° before chromatographic analysis. This separation was not very clean and introduced additional analytic errors due to background CO_2 in both fractions. Therefore, in later runs the separation was discontinued. Conversions were as small as possible to avoid complicating side reactions. However, this meant that for many runs the background CO_2 was significant; in some cases it accounted for as much as half of that collected. Background readings were made continually throughout the course of the investigation so that the corrections could be made.

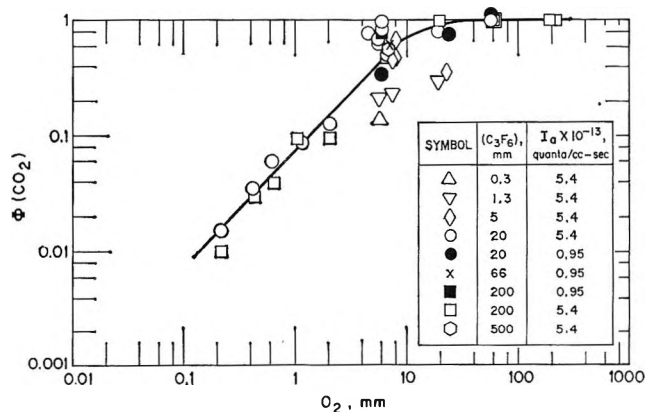
Saunders,³ working in this laboratory, has found by *in situ* infrared analysis that at room temperature the products of the Hg-sensitized photooxidation of C_3F_6 are equal amounts of CF_2O and CF_3CFO . Furthermore, he has shown that with 60 or 200 mm. of oxygen present, $\Phi(CF_2O) = \Phi(CF_3CFO) = 0.50$, and that upon chromatographic analysis the CO_2 produced is twice that expected from CF_2O alone. This information permits us to compute the absorbed intensity I_a from our data.

At room temperature, with oxygen absent, no products were found, but with oxygen present, CF_2O and CF_3CFO (whose sum is reported as $\Phi(CO_2)$) as well as a third product (called product X) were found.

The unidentified third product had a badly defined chromatographic peak with a retention time in the C_2 - C_3 region. Attempts to isolate this product for identification proved fruitless; apparently it decomposes on the column. No infrared bands were observed upon irradiation of C_3F_6 - O_2 mixtures that could be associated with this product.

The CO_2 yields of the room temperature runs are shown in Figure 1. Within the scatter, $\Phi(CO_2)$ is essentially independent of exposure time, intensity, and, at least for C_3F_6 pressures in excess of 20 mm., C_3F_6 pressure. However, it rises linearly with the oxygen pressure for oxygen pressures below about 5 mm. As the oxygen is further increased, $\Phi(CO_2)$ approaches an asymptotic limit of unity.

At 213° , C_2F_4 and C_4F_8 -2 also are found as products. In some cases, at reduced intensities, small amounts of *c*- C_3F_6 were found, too. The quantum yields of C_2F_4 and C_4F_8 -2 increase markedly with the oxygen pressure, but other trends are obscured, probably because of the dependence of the quantum yields on exposure duration.^{2b} The $\Phi(X)$ is also very markedly enhanced as the oxygen pressure is raised. $\Phi(CO_2)$ is plotted against the oxygen pressure in Figure 2. Below about 6 mm., the results are similar to those at room temperature. However, as the oxygen pressure is raised to 200 mm., $\Phi(CO_2)$ rises rapidly to as high as 1000. It is unaffected by changes in absorbed intensity or by C_3F_6 pressure except at an oxygen pres-

Figure 1. Plot of $\Phi(CO_2)$ vs. (O_2) at 24° .

(1) This work was supported under U. S. Air Force Contract No. AF 04(695)-469.

(2) (a) J. Hecklen, V. Knight, and S. A. Greene, *J. Chem. Phys.*, **42**, 221 (1965); (b) J. Hecklen and V. Knight, *J. Phys. Chem.*, **69**, 2484 (1965).

(3) D. Saunders, Aerospace Corp., unpublished work.

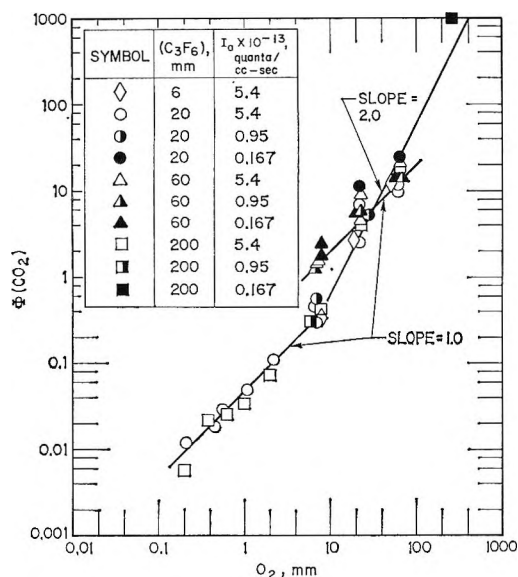
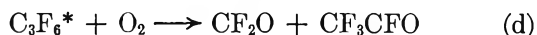
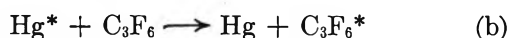
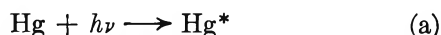


Figure 2. Plot of $\Phi(\text{CO}_2)$ vs. (O_2) at 213° .

sure of about 6 mm. For 6 mm. of oxygen, $\Phi(\text{CO}_2)$ with 60 mm. of C_3F_6 present is about four times as great as for any other C_3F_6 pressure (6, 20, 200 mm.). This result is certainly puzzling, and the 60-mm. experiment was done five times at three intensities as a check.

The results at room temperature can be explained by the mechanism



where * indicates an electronically excited molecule. The same mechanism explains the results at 213° with less than 6 mm. of O_2 present if a small percentage of C_3F_6^* is allowed to dissociate, as happens in the absence of O_2 .^{2b} Reaction c probably occurs without emission of radiation as the transition is forbidden. If reaction e accounts for all oxidation processes not leading to $\text{CF}_2\text{O} + \text{CF}_3\text{CFO}$, then $k_d = k_e$. The mechanism predicts

$$\Phi(\text{CO}_2) = \Phi(\text{CF}_2\text{O}) + \Phi(\text{CF}_3\text{CFO}) = \frac{1}{1 + k_c/k_d(\text{O}_2)} \quad (1)$$

The CO_2 yield is independent of I_a or the C_3F_6 pressure, as predicted by eq. 1. At large O_2 pressures, $\Phi(\text{CO}_2)$

should become unity, but at small O_2 pressures, eq. 1 reduces to

$$\Phi(\text{CO}_2) = \frac{k_d(\text{O}_2)}{k_c} \quad (2)$$

From Figures 1 and 2, k_d/k_c can be estimated to be 0.074 and 0.047 mm.^{-1} at 24 and 213° , respectively. Thus, k_c is about $2.4 \times 10^6 \pi \sigma^2 \text{ sec.}^{-1}$ and is independent of temperature, where $\pi \sigma^2$ is the collision cross section in square Ångströms for reaction d. Oxygen is known to quench Hg^* with a collision cross section of about 13 Å.^2 which is similar to that for N_2O .⁴ On the other hand, C_3F_6 is only about one-third as efficient as N_2O in removing Hg^* ,⁵ yet our results clearly indicate no competition between C_3F_6 and O_2 for Hg^* . Earlier work^{2a} showed no competition between O_2 and C_2F_4 for Hg^* . There are two explanations consistent with these findings: either the removal of $\text{Hg}(^3\text{P}_1)$ by O_2 produces $\text{Hg}(^3\text{P}_0)$, which then reacts with fluoroolefins in the same manner as $\text{Hg}(^3\text{P}_1)$, or the excited O_2 molecule formed by quenching Hg^* immediately transfers its energy to the fluoroolefin. For large oxygen pressures at 213° , the $\Phi(\text{CO}_2)$ goes far above unity. Clearly a long-chain mechanism is involved. In addition, $\Phi(\text{X})$ as well as $\Phi(\text{C}_2\text{F}_4)$ and $\Phi(\text{C}_4\text{F}_8-2)$ are distinctly enhanced. It is difficult to understand in detail exactly what is happening. It is hoped that further work in this laboratory will elucidate the mechanism.

Acknowledgment. The authors wish to thank Mrs. Barbara Peer for assistance with the manuscript and Professor O. P. Strausz for useful discussions.

(4) A. J. Yarwood, O. P. Strausz, and H. E. Gunning, *J. Chem. Phys.*, **41**, 1705 (1964).

(5) D. Saunders and J. Heicklen, *J. Am. Chem. Soc.*, **87**, 4062 (1965).

Normal Stresses and Dynamic Moduli in Polymer Solutions

by Kunihiro Osaki, Mikio Tamura,

Department of Industrial Chemistry, Kyoto University, Kyoto, Japan

Tadao Kotaka, and Michio Kurata

Institute for Chemical Research, Kyoto University, Takatsuki, Osaka-fu, Japan (Received February 15, 1965)

The present note is concerned with the relation between components of normal stresses in viscoelastic

fluids subjected to steady shearing motion. An attempt is made to obtain information on the relation through a comparison between normal stress and dynamic modulus data for polymer solutions. The principle for this procedure is based on the recent theory of Coleman and Noll for normal stress effects in second-order viscoelastic fluids.¹

In the Coleman and Noll theory, it is shown that the hydrodynamic behavior of the second-order viscoelastic fluids can be described in terms of three material constants (besides the density). They are the viscosity η_0 and two additional constants β and γ governing viscoelastic effects. In terms of these constants, components of stresses in the fluid subjected to a steady shearing motion with the rate of shear κ are given as second-order terms in the time scale

$$\sigma_{11} - \sigma_{22} = -2\gamma\kappa^2 \quad (1)$$

$$\sigma_{22} - \sigma_{33} = (\beta + 2\gamma)\kappa^2 \quad (2)$$

$$\sigma_{12} = \eta_0\kappa \quad (3)$$

where suffixes 1, 2, and 3 denote the directions parallel to the flow line, perpendicular to the plane of shear, and perpendicular to both 1 and 2, respectively, and the σ_{ij} terms ($i, j = 1, 2, \text{ and } 3$) denote the corresponding stress components. On the other hand, by using the same constants, the real part G' and the imaginary part G'' of the dynamic complex modulus can be given (again with second-order terms in angular frequency ω)

$$G' = -\gamma\omega^2 \quad (4)$$

$$G'' = \eta_0\omega \quad (5)$$

as was recently noted by Coleman and Markovitz.²

One would readily realize that eq. 1-5 may provide a method of evaluating the material constants separately, at least in the range of sufficiently small κ and ω . This in turn may allow us to evaluate the relative magnitude of two normal stress differences $\sigma_{11} - \sigma_{22}$ and $\sigma_{22} - \sigma_{33}$ through a comparison between steady shear flow and dynamic mechanical data. Before making such a comparison, it must be asked whether the theory is valid in general. It seems to us that there is no doubt about the generality of the theory so far as the application is restricted to within a range of sufficiently small κ and ω . Anyway, the procedure would be worthwhile to test.

In this study, measurements of the normal stresses were carried out with a parallel-plate system, and those of the dynamic moduli and steady-shear stress were carried out with a Couette-type rheometer. Details of these instruments have been reported previously.^{3,4}

Radial distribution of the pressure normal to a plate in the parallel-plate system is given as⁵

$$-\frac{\partial p}{\partial \ln r} = \sigma_{11} - \sigma_{33} + \frac{\partial(\sigma_{22} - \sigma_{33})}{\partial \ln \kappa} \quad (6)$$

where

$$\kappa = r\Omega/l \quad (7)$$

Here p is the pressure exerted normal to the fixed plate at a distance r from the axis of rotation, Ω is the angular velocity of rotation of the rotating plate, and l is the distance between two plates. From eq. 1, 2, and 6 we obtain

$$-\frac{\partial p}{\partial \ln r} = (3\beta + 4\gamma)\kappa^2 \quad (8)$$

Thus, as for the difference between $-\partial p/\partial \ln r$ as a function of κ and $2G'$ as a function of ω we obtain

$$\left(\frac{1}{\kappa^2}\right)\left(-\frac{\partial p}{\partial \ln r}\right) - \frac{2G'}{\omega^2} = 3(\beta + 2\gamma) = 3(\sigma_{22} - \sigma_{33})/\kappa^2 \quad (9)$$

if the rate of shear κ and the angular frequency ω are taken as the corresponding mechanical variables.

Systems studied in this work were (i) polystyrene (PSt) in toluene, (ii) poly(*cis*-butadiene) in xylene, (iii) cellulose trinitrate in butyl acetate, and (iv) poly(methyl methacrylate) (PMMA) in diethyl phthalate (DEP). Measurements were all carried out at $30 \pm 0.5^\circ$. Typical examples of the results are shown in Figures 1-4, in which the steady-flow properties σ_{12} and $-\partial p/\partial \ln r$ are plotted against κ , while the dynamic ones G'' and G' are plotted against ω .

In all three systems, except for the system of PMMA-DEP, coincidence between steady shear and dynamic mechanical data is fairly good, particularly in the range of small κ and ω . The good coincidence found between $-\partial p/\partial \ln r$ and $2G'$ implies that the factor $3(\beta + 2\gamma)$ is quite small in comparison with the magnitude of $|\beta|$ or $|\gamma|$ in these systems. To our surprise, the agreement between steady shear and dynamic mechanical data is seen even in the range of κ and ω

(1) B. D. Coleman and W. Noll, *Arch. Rational Mech. Anal.*, **6**, 355 (1960); *Ann. N. Y. Acad. Sci.*, **89**, 672 (1961).

(2) B. D. Coleman and H. Markovitz, *J. Appl. Phys.*, **35**, 1 (1964).

(3) M. Tamura, M. Kurata, and T. Kotaka, *Bull. Chem. Soc. Japan*, **32**, 471 (1959); T. Kotaka, M. Kurata, and M. Tamura, *J. Appl. Phys.*, **30**, 1705 (1959).

(4) T. Kotaka and K. Osaki, *Bull. Inst. Chem. Res., Kyoto Univ.*, **39**, 331 (1961).

(5) This relationship is a direct consequence of the general relation of force equilibrium in a volume element in cylindrical coordinates. See, for example, H. Markovitz, *Trans. Soc. Rheol.*, **1**, 37 (1957).

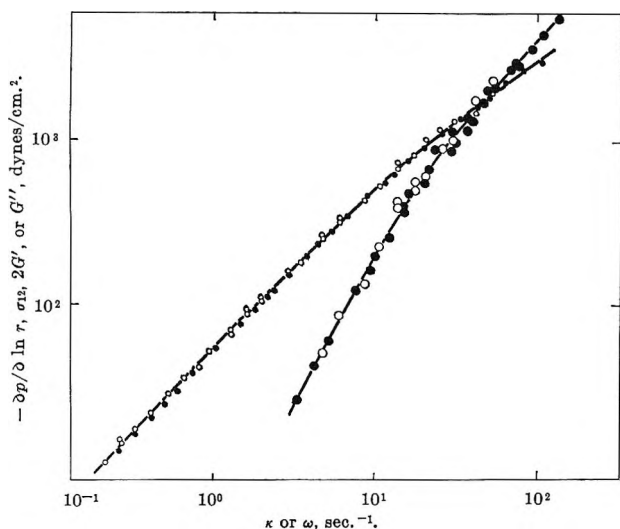


Figure 1. Comparison between steady shear and dynamic mechanical properties of a 15 wt. % solution of polystyrene in toluene at 30°: large black circles, normal stresses measured as $-\partial p/\partial \ln r$ and plotted against rate of shear κ ; small black circles, shear stresses σ_{12} plotted against κ ; large white circles, twofold storage moduli $2G'$ plotted against angular frequency ω ; small white circles, loss moduli G'' plotted against ω .

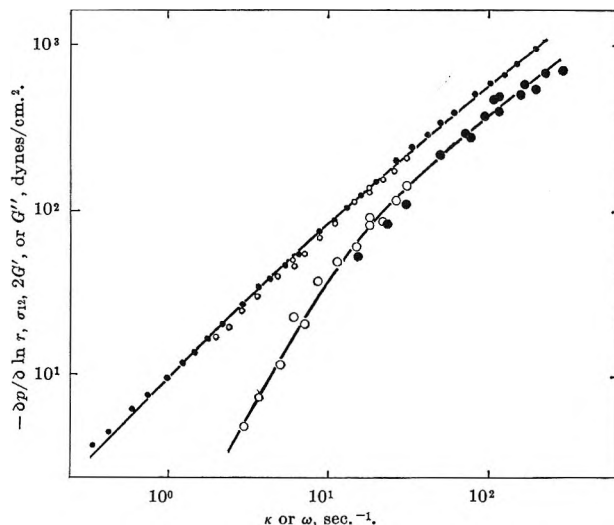


Figure 3. Comparison between steady shear and dynamic mechanical properties of a 4 wt. % solution of cellulose trinitrate in *n*-butyl acetate at 30°. Four types of circles represent normal stress, shear stress, twofold storage modulus, and loss modulus as in Figure 1.

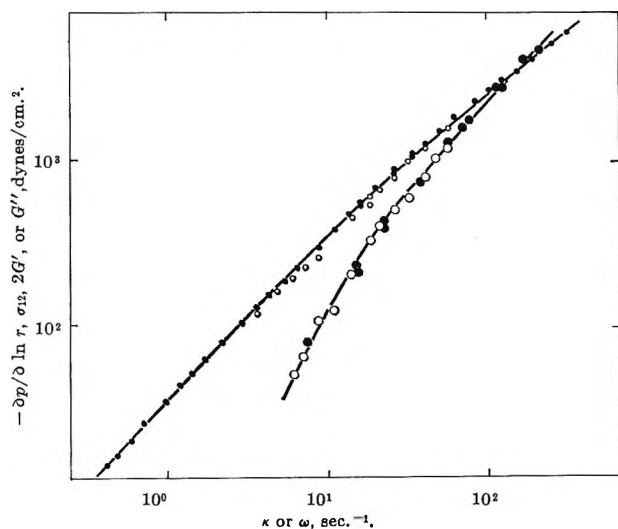


Figure 2. Comparison between steady shear and dynamic mechanical properties of a 10 wt. % solution of poly(*cis*-butadiene) in xylene at 30°. Four types of circles represent normal stress, shear stress, twofold storage modulus, and loss modulus as in Figure 1.

higher than that expected from the second-order viscoelastic theory, that is, in the range of κ where the proportionality between σ_{12} and κ is lost. This fact suggests that $3(\sigma_{22} - \sigma_{33})$ is much smaller than $\sigma_{11} - \sigma_{22}$ even in the range of rate of shear higher than the order 2.

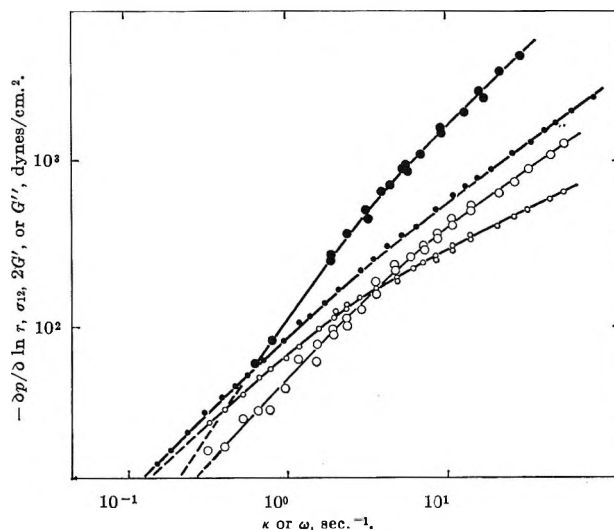


Figure 4. Comparison between steady shear and dynamic mechanical properties of a 5 wt. % solution of poly(methyl methacrylate) in diethyl phthalate at 30°. Four types of circles represent normal stress, shear stress, twofold storage modulus, and loss modulus as in Figure 1.

In the system of PMMA-DEP a considerable discrepancy can be seen between comparable variables, *i.e.*, between $-\partial p/\partial \ln r$ and $2G'$ and between σ_{12} and G'' . Furthermore, a profound deviation from the second-order viscoelastic theory is observed; that is, in the whole range of the rate of shear covered by this experiment, the slope of the curve of $\log \sigma_{12}$ vs. $\log \kappa$ and that of $\log (-\partial p/\partial \ln r)$ vs. $\log \kappa$ differ greatly

from the values of 1 and 2, respectively. Therefore, the large discrepancy between steady shear and dynamic mechanical data may not be surprising. However, closer inspection of Figure 4 reveals that the gap between the curves of $-\partial p/\partial \ln r$ and $2G'$ and that between σ_{12} and G'' become smaller and smaller as the rate of shear (or the angular frequency) is decreased. It is conceivable that they would coincide at the limit of very small rate of shear.

From the experimental results obtained above, we come to the conclusion that the value of $|\beta + 2\gamma|$ is much smaller than that of $|\beta|$ or $|\gamma|$. Therefore, from eq. 2, we conclude also that $\sigma_{22} - \sigma_{33}$ is much smaller than $\sigma_{11} - \sigma_{22}$ in their absolute values. By taking possible experimental error into account, we would say that the former is no more than 10% of the latter except for the system PMMA-DEP. At the moment, we hesitate to draw any conclusion about the observed discrepancy in the system of PMMA-DEP. It might be due to the contribution of the $\sigma_{22} - \sigma_{33}$ term in the range of higher shear rate or to the contribution of higher order terms in $\tau_{11} - \sigma_{22}$ and $2G'$ than the second order of κ and ω .

The problem of the relation between three components of the normal stresses has attracted much attention since the earliest days of research, and some controversies have been found among the results of various investigators.⁶⁻⁹ Most recent and thorough investigations on the problem were given by Markovitz¹⁰ and by Adams and Lodge.¹¹ They have drawn conclusions mostly from the comparison between the pressure distribution observed in a cone-plate (CP) system and that in a parallel-plate (PP) system. With the present notations, the difference between two pressure distributions is

$$\begin{aligned} &(-\partial p/\partial \ln r)_{PP} - (-\partial p/\partial \ln r)_{CP} = \\ &[\partial(\sigma_{22} - \sigma_{33})/\partial \ln \kappa] - (\sigma_{22} - \sigma_{33}) = (\beta + 2\gamma)\kappa^2 \quad (10) \end{aligned}$$

On the basis of the observed difference, they concluded that the value of $\sigma_{22} - \sigma_{33}$ is quite large although they did not mention specifically how large it was. Our present conclusion differs somewhat from theirs.

In principle, the use of relation 10 is a better procedure for the evaluation of $\sigma_{22} - \sigma_{33}$ because the second line of eq. 10 should be valid for any value of κ , and the method is straightforward. However, the procedure employed in this paper also has certain advantages, we believe, if its application is restricted to the range of sufficiently small rate of shear (again assuming the prediction of the second-order viscoelasticity theory is valid in general). The reasons are first, as is seen in eq. 9 and 10, the difference between $(-\partial p/\partial \ln r)_{PP}$ and $2G'$ is larger than that between

$(-\partial p/\partial \ln r)_{PP}$ and $(-\partial p/\partial \ln r)_{CP}$ by a factor of 3, and, secondly, the present method does not involve the measurement with the cone-plate system, in which the machinery set-up is much more difficult than it is in the parallel-plate system. Therefore, we would prefer our conclusion, at the moment, that $\sigma_{22} - \sigma_{33}$ is, if not zero, no larger than 10% of $\sigma_{11} - \sigma_{22}$.

(6) J. E. Roberts, *Proc. Intern. Congr. Rheology, 2nd, Oxford, 1963*, 91 (1954).

(7) H. Markovitz, *Trans. Soc. Rheol.*, **1**, 37 (1957).

(8) T. Kotaka, M. Kurata, and S. Onogi, *Progr. Theoret. Phys. (Kyoto, Suppl.)*, **10**, 101 (1959).

(9) W. Philippoff, *Trans. Soc. Rheol.*, **5**, 163 (1961).

(10) H. Markovitz, *Proc. Intern. Congr. Rheology, 4th, Providence, R. I., 1963*, in press.

(11) N. Adams and A. S. Lodge, *Proc. Roy. Soc. (London)*, **A256**, 149 (1964).

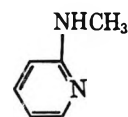
The Nuclear Magnetic Resonance Spectra of Some N-Monosubstituted Methylamines

by Morris Freifelder, Richard W. Mattoon, and Russell Kriese

Organic and Physical Chemistry Departments, Research Division, Abbott Laboratories, North Chicago, Illinois
(Received April 5, 1965)

The scarcity of information on splitting of the methyl proton signal of N-monosubstituted methylamines by the proton on nitrogen¹ prompted us to examine the n.m.r. spectra of a number of these compounds in order to group the types where splitting of the N-methyl signal is observed.

In the course of some other work the spectrum of 2-methylaminopyridine

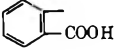
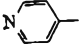
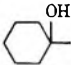


was examined.² The methyl signal was seen as a

(1) For example, only four such compounds are listed: "High Resolution NMR Spectra Catalog," Vol. 1, Varian Associates, Palo Alto, Calif., 1962; Spectrum 85, ethyl N-methylcarbamate, shows a doublet for the N-methyl protons; Spectrum 319, another N-methylcarbamate, shows a doublet; Vol. 2, 1963, Spectrum 489, N-methyl-4-nitroaniline, shows a single peak for the methyl signal; Spectrum 652, 1,4-bis(methylamino)-9,10-anthraquinone, shows a doublet, due perhaps to hydrogen bonding. In the Formula Index to "NMR Literature Data," Vol. 1, M. G. Howell, A. S. Kende, J. S. Webb, Ed., Plenum Press, New York, N. Y., 1965, only N-methylformamide and N-methyltrifluoromethylsulfonamide are reported to show doublets for the N-methyl protons.

(2) M. Freifelder, R. W. Mattoon, and Y. H. Ng, *J. Org. Chem.*, **29**, 3730 (1964).

Table I: Data for R(C=X)NHCH₃

No.	R	X	Solvent ^d	Peaks, c.p.s.		
				NH ^e	HNCH ₃	DNCH ₃
I	H ₃ C	O	A	460-500	161.5, 166	161.5
II ^a	HOCH ₂ CH ₂	O	A	347 ^f	166.5, 171.5	169.5
III	C ₆ H ₅ CH ₂	O	A	446-476	149, 154	151
IV	(H ₃ C) ₃ C	O	A	410-430	160.5, 165.5	162.5
V	C ₆ H ₁₁	O	A	440-470	161, 165.5	162
VI ^a	CH ₂ =C(CH ₃)-	O	A	450-480	164.5, 169	167
VII		O	B	<i>g, h</i>	185, 189.5	188
VIII	H ₂ C(CONHCH ₃)-	O	B	<i>g</i>	168, 172.5 ^j	169.5
IX		O	B	<i>g</i>	180, 184.5	191.5 ^o
X ^b	C ₂ H ₅ O	O	A	330-380	160.5, 165.5	163
XI	H ₂ N	O	C	346-374 ⁱ	151.5, 156	157.5
XII	H ₃ CNH	O	A	360-420	169.5, 173.5 ^k	171.5
XIII	C ₆ H ₅ CH ₂ CONH	O	B	<i>g</i>	167, 172	170
XIV	H ₂ NCONH	O	B	<i>g</i>	166.5, 171	168
XV	C ₆ H ₅ NHCONH	O	B	<i>g</i>	167.5, 172	171
XVI ^a	<i>n</i> -C ₄ H ₉ O	S	B	<i>g</i>	186, 190.5	189
XVII	(H ₃ C) ₂ N-	S	B	<i>g</i>	192, 196 ^l	195
XVIII ^a	H ₃ CNHC=S	S	B	<i>g</i>	191.5, 196.5	196
XIX ^{a,c}	<i>n</i> -C ₁₂ H ₂₅ NH	N(CH ₃)	B	<i>g</i>	191, 195 ^m	187
XX ^{a,c}	<i>t</i> -C ₈ H ₁₇ NH	NH	B	<i>g</i>	186, 190.5	188
XXI	(H ₃ C) ₂ NCH ₂ CH ₂ NH	NH	B	<i>g</i>	180.5, 184	182
XXII	(H ₃ C) ₂ NCH ₂ CH ₂ N(CH ₃)-	NH	B	<i>g</i>	<i>n</i>	185
XXIII ^c		NH	B		199.5	

^a Samples were generously supplied by Dr. Peter de Benneville of the Rohm and Haas Co., Bristol, Pa. ^b Reported in ref. 1. ^c Hydrochloride salt. ^d A = carbon tetrachloride; B = pyridine; C = deuterated dimethyl sulfoxide. ^e In most instances a broad area was seen. ^f The signal was a sharp peak for OH and NH (integration, 2). ^g The signal was lost in the solvent region. ^h No peak was observed beyond 500 to 1000 c.p.s. to indicate hydrogen bonding. ⁱ Signal for NH₂ was seen at 336 c.p.s. ^j Integration, 6H, for two methyl groups. ^k No splitting was observed in aqueous solution. ^l A sharp strong peak was also seen at 193.5 c.p.s. for N(CH₃)₂. Upon addition of D₂O, the doublet and singlet merged to a single peak. ^m In water the signal was a singlet at 199.5 c.p.s. ⁿ The area was a broad ragged one suggestive of splitting, centered at 186 c.p.s. (integration, 3). The N(CH₃)₂ signal (integration, 6) was seen at 173.5 c.p.s. (169.5 c.p.s. after D₂O); the NCH₃ signal (integration, 3) was a singlet at 204 c.p.s. (198 c.p.s. after D₂O). ^o When the spectrum was run in D₂O, the signal was a singlet at 192.5 c.p.s.

doublet ($J = 4-4.5$ c.p.s.) in carbon tetrachloride and deuteriochloroform. Addition of D₂O converted the signal to a single peak. N-Methylacetamide (I) and N-methylurea (XI) also showed splitting with J values of 4.5 and 5 c.p.s., respectively. The three compounds had a common structural relationship, adjacency of the NHCH₂ group to a carbon atom double bonded to a heteroatom [H₃CNH-C<]. This suggested examination of such compounds as were available with this structure.

The spectra of monosubstituted N-methylated aryl-, aralkyl-, and cyclic amines were also studied as well as a few N-methylsulfonamides [RSO₂NHCH₃, R = alkyl, substituted aryl, or a cyclic structure].

Experimental Section

The spectra were run on a Varian A-60 spectrometer at 60 Mc./sec. at a sweep width of 500 c.p.s. at 33° in 10-20% concentrations (weight, volume) in solvents listed in Tables I-III with tetramethylsilane as the internal standard. In general, the entire spectrum was recorded and integrated, but only those signals which have a bearing on this study are noted in the tables. The positions of other methyl signals are found in the superscripted portions of the tables. The chemical shift is given to the nearest half-cycle per second.

The compounds used in this study were either commercially available or generously supplied by colleagues

Table II: Data for $\text{RSO}_2\text{NHCH}_3^a$

No.	R	Peaks, c.p.s.	
		HNCH_3	DNCH_3
XXIV	C_6H_{11}	170.5, 175.5	173.5
XXV	$4\text{-CH}_3\text{CONHC}_6\text{H}_4$	163, 168	165
XXVI	$4\text{-CH}_3\text{OC}_6\text{H}_4$	162, 167	164
XXVII	C_6H_{11}	170.5, 175.5	173.5

^a The solvent used in this group was pyridine. The NH signal was lost in the solvent area.

Table III: Data for RNHCH_3^a

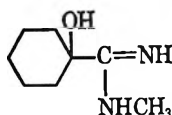
No.	R	Peaks, c.p.s.,
		HNCH_3
XXVIII	C_6H_5	159 ^b
XXIX	$2\text{-HOOCOC}_6\text{H}_4$	174 ^c
XXX	$4\text{-H}_2\text{CC}_6\text{H}_4$	132 ^d
XXXI	$4\text{-H}_2\text{C} \begin{matrix} \text{C}_6\text{H}_4 \\ \text{C}_6\text{H}_4 \end{matrix}$	167
XXXII	$\text{C}_6\text{H}_5\text{CH}_2$	139 ^e
XXXIII	$2\text{-H}_2\text{COC}_6\text{H}_4\text{CH}_2$	140
XXXIV	C_6H_{11}	141 ^f

^a The solvent used in this group was carbon tetrachloride. ^b No change in deuterated dimethyl sulfoxide solution (DM-SO). ^c Deuterated DMSO. ^d 143 c.p.s. in deuterated DMSO. ^e 137 c.p.s. in deuterated DMSO. ^f Neat; 137 c.p.s. in deuterated DMSO.

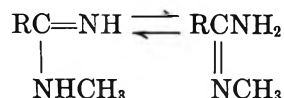
of this and other laboratories. They were generally of high purity or were purified by appropriate means. In particular, the N-methylsulfonamides (Table II) were prepared by Mr. Bruce W. Horrom, who treated the substituted sulfonyl chlorides with excess methylamine. Compound XXXIII was prepared by Dr. William B. Martin and Miss Carol Christensen by treating the substituted benzaldehyde with methylamine. After isolation and characterization of the intermediate imine, it was hydrogenated by M. F. The preparation of these compounds will be reported in greater detail at a later date by Mr. Horrom and Dr. Martin.

Results and Discussion

The amides, ureas, biurets, guanidines, thioureas, and thioamides which were examined showed splitting of the N-methyl signal when a suitable solvent was found³; see Table I, compounds I-XXII. Only one amidine (XXIII) was examined



The spectrum of the hydrochloride salt in water showed a singlet for the methyl group at 207 c.p.s. In pyridine it was still a singlet at 200 c.p.s. (We had previously reported on the failure of 2-methylamino-3,4,5,6-tetrahydropyridine, a cyclic amidine, to show splitting.²) The single signal is probably due to interchange of the tautomeric forms



or other proton transfers which occur too rapidly for the spectrometer to record the one which might give a split signal.

Among this group of compounds the spectrum of VI is worth noting. It showed that the vinyl protons $\left[\begin{matrix} \text{H} \\ > \text{C}=\text{C} < \\ \text{H} \end{matrix} \right]$ were not equivalent. One signal was a multiplet centered at 313.5 c.p.s. (integration, 1) while the other was a singlet (integration, 1) at 343 c.p.s. Also of interest among this group was the slow exchange of the proton on nitrogen with D_2O . In many instances triplets were noted in the N-methyl region after addition, the NDCH_3 singlet appearing while the doublet was slowly diminishing. In compound IX, exchange was so slow that the spectrum was run in D_2O in order to see the signal as a singlet.

When the spectra of some N-methylsulfonamides were recorded, the methyl signal was a doublet ($J = 5$ c.p.s.); see Table II. The difference in coupling constants between the compounds in Table II and those in Table I—5 c.p.s. against an average of 4.5 c.p.s.—although slight, may be significant. This difference may be due to the more acid character of the sulfonamides.⁴ Another example of the difference in coupling constants among compounds of different acidity may be seen in the work of Hedberg, who reports a J value of 5.7 c.p.s. in the splitting of the methyl signal of 2,4,6-trinitro-N-methylaniline and values of 5.5 and 5.3 c.p.s. in the spectra of the less acidic 2,6-dinitro- and 2,4-dinitro-N-methylanilines.⁵

None of the N-methylated aromatic or the more basic aralkyl- and alicyclic amines showed splitting of the methyl signal (Table III).

The lack of splitting among the last group and the doublets noted among the nonbasic types suggest that the relative acidity (or lack of basicity) of the proton

(3) In aqueous solution a single peak was observed because of exchange of the NH proton with water.

(4) Sulfonamides dissolve readily in aqueous sodium and potassium hydroxides and form salts.

(5) J. Hedberg, J. A. Weil, G. A. Janusonis, and J. K. Anderson, *J. Chem. Phys.*, 41, 1033 (1964).

on nitrogen is a potent factor in slowing down exchange so that a split signal occurs. The singlet seen in the spectrum of 4-nitro-N-methylaniline and the doublets for the N-methyl signal of the more acidic di- and trinitro-N-methylanilines⁵ may be another example of this effect.

Acknowledgments. The authors are grateful to Mrs. Ruth Stanaszek of the Chemical Physics Laboratory for running most of the spectra.

Proton Magnetic Resonance Spectra of

cis- and *trans*-¹⁵N-*n*-Butylformamide¹

by Max T. Rogers and Laurine A. LaPlanche²

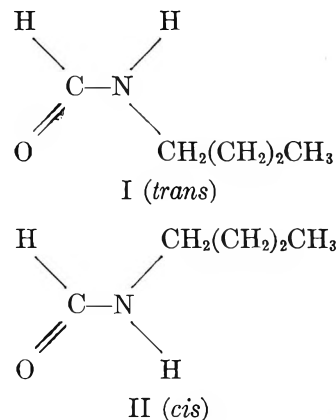
Department of Chemistry, Michigan State University,
East Lansing, Michigan 48828 (Received March 24, 1965)

It has been shown³ that the nuclear magnetic resonance (n.m.r.) spectra of the N-alkylformamides contain sets of peaks for both the *cis* and *trans* isomers and that the fraction of the latter isomer is about 82–92% in the pure liquids, with the *cis* form increasingly favored by larger substituent groups. Separate peaks due to the NH proton could not be observed, however, because of the broadening from the ¹⁴N quadrupole; also, the nuclear spin–spin couplings between nitrogen and various protons were not observable. In order to obtain these previously unobservable parameters and also to confirm our previous findings, we have prepared ¹⁵N-*n*-butylformamide and studied its n.m.r. spectrum.

Detailed studies of the n.m.r. spectra of ¹⁵N-formamide⁴ and N,N-dimethyl-¹⁵N-formamide⁵ have provided all the chemical shifts and spin–spin coupling constants (including relative signs⁶) for these molecules since ¹⁵N has nuclear spin $I = 1/2$ and no quadrupole moment; similar data were obtained for the *trans* isomer of ordinary N-methylformamide through heteronuclear spin decoupling experiments.⁷ The present experiments provide data for both the *trans* and *cis* isomers of ¹⁵N-*n*-butylformamide (I and II) and permit comparisons with previous work for the coupling constants involving nitrogen and those involving the N–H proton. Experiments with both pure liquid and hexadeuteriobenzene solutions were performed since the latter aid in analyzing the spectra.

Experimental Section

¹⁵N-*n*-Butylformamide. This was prepared from ¹⁵N-potassium phthalimide⁸ (96% ¹⁵N) by treating it



with *n*-butyl bromide to give ¹⁵N-*n*-butylphthalimide. This was treated with hydrazine hydrate in methanol to give ¹⁵N-*n*-butylamine hydrochloride⁹ which gave the free amine on treatment with aqueous sodium hydroxide. A *m*-xylene solution of the amine was added to formic acid dissolved in *m*-xylene,¹⁰ and the product ¹⁵N-*n*-butylformamide was recovered and purified in the usual way, b.p. 67° (1.5 mm.).

¹⁵N-*n*-Butylacetamide. The ¹⁵N-*n*-butylamine hydrochloride prepared as above was converted to ¹⁵N-*n*-butylacetamide by reaction with acetyl chloride, and the solvent was removed in a molecular still.¹¹

N.m.r. Spectra. These were measured using a Varian Associates A-60 n.m.r. spectrometer operating at 60.0 Mc./sec. Chemical shifts are in c.p.s. relative to internal tetramethylsilane.

Results and Discussion

The chemical shifts for the various proton groups of I and II in both pure liquid and hexadeuteriobenzene solution are given in Table I along with the nuclear spin–spin coupling constants. The lines of the *cis* isomer were assigned using the principles discussed

(1) This work was supported, in part, by Public Health Service Research Grant GM-12530 from the Division of General Medical Sciences.

(2) National Institutes of Health Predoctoral Fellow, 1961–1963.

(3) L. A. LaPlanche and M. T. Rogers, *J. Am. Chem. Soc.*, **86**, 337 (1964).

(4) B. Sunners, L. H. Piette, and W. G. Schneider, *Can. J. Chem.*, **38**, 681 (1960).

(5) A. J. R. Bourn and E. W. Randall, *J. Mol. Spectry.*, **13**, 29 (1964).

(6) E. W. Randall, private communication.

(7) E. W. Randall and J. D. Baldeschweiler, *J. Mol. Spectry.*, **8**, 365 (1962).

(8) Isomet Corp., Palisades Park, N. J.

(9) W. R. Vaughan, M. V. Andersen, Jr., H. S. Blanchard, D. I. McCane, and W. L. Meyer, *J. Org. Chem.*, **20**, 819 (1955).

(10) J. H. Robson and J. Reinhart, *J. Am. Chem. Soc.*, **77**, 498 (1955).

(11) S. M. McElvain and C. L. Stevens, *ibid.*, **69**, 2667 (1947).

Table I: Chemical Shifts and Spin-Spin Coupling Constants for the Isomers of ^{15}N -*n*-Butylformamide^{a-d}

Parameter	<i>trans</i>	<i>cis</i>
$\delta_{\text{H}(2)}$ (pure liquid)	-486.0	-470.0
$\delta_{\text{H}(2)}$ (C_6D_6 solution) ^e	-478.5	-462.4
$\delta_{\text{H}(1)}$ (pure liquid)	-487.0	-482.5
$\delta_{\text{H}(1)}$ (C_6D_6 solution) ^e	-490.5	-478.2
$\delta_{\text{CH}_2(3)}$ (pure liquid)	-194.0	-194.0
$J_{\text{H}(1)\text{H}(2)}$	(+)2.0	(+)11.6
$J_{^{15}\text{N}-\text{H}(1)}$	(-)15.0	(-)14.3
$J_{^{15}\text{N}-\text{H}(2)}$	(-)92.2	(-)89.8
$J_{\text{H}(2)-\text{H}(3)}$	(+)5.8	(+)5.8

^a Chemical shifts are in c.p.s. from tetramethylsilane; $\nu_0 = 60.0$ Mc./sec. ^b Signs of J values were not measured; probable relative signs are listed in parentheses based on the work of Randall, *et al.*^{5,6} ^c Measurements on *trans*- ^{15}N -*n*-butylacetamide give the values $J_{^{15}\text{N}-\text{H}(2)} = (-)92.0$ and $J_{\text{H}(2)-\text{H}(3)} = (+)5.5$ c.p.s. ^d Coupling constants did not change, within experimental error, in going from pure liquid to C_6D_6 solution. ^e Solutions were about 0.46 mole fraction amide.

earlier,^{3,12} along with the knowledge that in N-mono-substituted formamides the *trans-cis* isomer ratio is about 5:1.³ The N-H proton resonance for the *trans* isomer is easily seen to be a doublet ($J_{^{15}\text{N}-\text{H}} = 92.2$ c.p.s.) of triplets ($J_{^{15}\text{NH}-\text{CH}_2} = 5.8$ c.p.s.) each line of which is again a doublet from the small coupling with the formyl proton ($J_{\text{HC}-^{15}\text{NH}} = 2.0$ c.p.s.). The NH proton of the *cis* isomer gives rise to a weaker set of lines to the high field side of those for the *trans* isomer which now are a doublet ($J_{^{15}\text{N}-\text{H}} = 89.9$ c.p.s.) of quintets. The latter have intensity ratio 1:2:2:2:1 indicating that $J_{^{15}\text{NH}-\text{CH}_2} = 5.8$ c.p.s. and $J_{\text{HC}-^{15}\text{NH}} = 11.6$ c.p.s. The formyl proton for the *trans* isomer is a doublet of doublets ($J_{^{15}\text{N}-\text{CH}} = 15.0$ c.p.s., $J_{^{15}\text{NH}-\text{CH}} = 2.0$ c.p.s.) while that for the *cis* isomer is an apparent triplet due to coalescence of the inner two members of the AB part of an ABX spectrum. The derived parameters are summarized in Table I.

The coupling of ^{15}N to the formyl proton, which is 19.0 c.p.s. in formamide,⁴ has decreased to 15.0 c.p.s. in *trans*- ^{15}N -*n*-butylformamide and to 14.3 c.p.s. in the *cis* isomer. The relatively large value of the coupling across the central C-N bond [compared to a value <1.0 c.p.s. found for $J_{^{15}\text{N}-\text{CH}_2}$ in *trans*- ^{15}N -butylacetamide where the C-N bond is essentially a single bond] is usually associated with the partial double-bond character of this bond so the decrease found in going from formamide to a substituted formamide may be attributed to a decrease in the π -elec-

tron density of this bond. This, in turn, could result from greater opportunities for hydrogen bonding in formamide or from a less planar arrangement of atoms in the substituted amides. The corresponding values^{5,7} of $J_{^{15}\text{N}-\text{CH}}$ for *trans*- ^{15}N -methylformamide and N,N-dimethylformamide are 15.6 c.p.s., very close to our value for the *trans* isomer.

The coupling of ^{15}N to the bonded proton is 92.2 c.p.s. in the *trans*- ^{15}N -*n*-butylformamide and 89.8 c.p.s. in the *cis* molecule. These values are close to the 92 and 88 c.p.s. reported for the protons *trans* and *cis* to carbonyl, respectively, in ^{15}N -formamide.⁴ The chemical shift in ^{15}N -*n*-butylformamide for the N-H proton *trans* to carbonyl is 16.0 c.p.s. to low field of the proton *cis* to carbonyl compared to a corresponding chemical shift of 12.1 c.p.s. in formamide itself. Methyl groups *cis* to carbonyl oxygen also occur to higher field of the *trans* groups,¹¹ and, presumably, in both cases this is the result of long-range shielding effects from the large magnetic anisotropy of the carbonyl bond.¹³

The coupling of the formyl proton to the NH proton is large when these are *trans* across the intervening C-N bond (11.6 c.p.s.) but small when they are *cis* (2.0 c.p.s.), the values being close to those reported in other amides³⁻⁷; the coupling of the NH proton to the α -methylene protons of the butyl group (5.8 c.p.s. in both isomers) compares with the 6.0 c.p.s. found for $J_{\text{NH}-\text{CH}_2}$ in N-ethylformamide.³

Dilution with benzene is known to have a large effect on the chemical shifts of protons in the various groups of amides.^{3,12,14} In the present case the NH proton resonance moves to higher field in both isomers; the α -methylene protons of the butyl group also move to higher field, but, when the CH_2 group is *trans* to carbonyl oxygen (the *cis* isomer of ^{15}N -*n*-butylformamide), the resonance moves to higher field faster on dilution with benzene. These dilution shifts are typical of collision complexes between benzene and amides in which the planes of the molecules are parallel.¹⁴ It is difficult, however, to account on this basis for the shift to low field of the formyl proton of the *trans* isomer in benzene; this might result if the collision complex involved an interaction in which the N-H proton was along the sixfold axis of the benzene molecule, with the formyl proton near the plane of the ring and, so, in a region of paramagnetic shielding. Both types of complex may be important in the N-alkyl-amides.

(12) L. A. LaPlanche and M. T. Rogers, *J. Am. Chem. Soc.*, **85**, 3728 (1963), and earlier references quoted therein.

(13) P. T. Narasimhan and M. T. Rogers, *J. Phys. Chem.*, **63**, 1388 (1959).

(14) J. V. Hatton and R. E. Richards, *Mol. Phys.*, **5**, 139 (1962).

Infrared Band Width of the Nitrate Ion ν_2 Mode. Ionic Lifetimes and a Solvent Isotope Effect

by J. C. Evans and G. Y-S. Lo

Chemical Physics Research Laboratory, The Dow Chemical Company, Midland, Michigan 48640 (Received April 5, 1965)

Vibrational bands, both Raman and infrared, measured in the liquid and solution phases have widths which, depending on the molecule and its environment, vary considerably over a wide range. It is generally recognized that intermolecular interactions of various kinds determine the observed widths and that the natural line widths are usually relatively insignificant. Recently, however, it was demonstrated that Raman band broadening produced by shortening the lifetime of a molecular species could give information about the rate of a process with a half-time of about 10^{-11} sec.¹ Comparable infrared measurements do not appear to have been made. A preliminary investigation showed that the system studied by the Raman method,¹ the trifluoroacetate ion in aqueous trifluoroacetic acid solution, did not offer favorable bands in the infrared, and another system, the nitrate ion in aqueous nitric acid solution, was chosen for study. Here the nitrate ions are exchanging protons rapidly, the mean lifetime t_s of a nitrate ion is very short, and both the vibrational energy levels, a and b, involved in any one infrared transition of the nitrate ion have this same very short lifetime t_s . The corresponding absorption band has a natural line width γ_{ab} , which is given by the sum of the uncertainties γ_a and γ_b (in frequency units) in the two energy values. The uncertainty relation between time and energy, $\Delta t \Delta E = h$, taken with the relation between energy and frequency, $E = h\nu$, yields the relation $\gamma = 1/t_s$ for each energy level, so that $\gamma_{ab} = 2/t_s$. Thus, the natural line width of the absorption band, if it can be measured, yields directly the mean lifetime of the ion. Implicit in this discussion is the assumption that the lifetimes of the vibrational energy levels of the nitrate ion under normal conditions, e.g., in a salt solution where the proton exchange reaction does not occur, are relatively long. This seems to be well founded since lifetimes for excited vibrational energy levels of the order of 10^{-4} sec. have been reported; the natural line width then contributes negligibly to the observed band width. If all the processes, other than the reduction of the ionic lifetime, which contribute to vibrational line broadening are unaffected by the difference in

environment between the neutral salt solution and the acid solution, then the band width increase observed in the acid solution spectra can be attributed entirely to the natural line width in the acid solution.

Ionization in aqueous nitric acid solutions and interaction between ions in aqueous solutions of nitrates have received considerable attention. Many studies have established that, of the common cations, the NH_4^+ ion perturbs the water structure and the nitrate ion the least.²⁻⁶ Ions such as NH_4^+ and H_3O^+ , because of their tetrahedral structure, can fit into the water structure with minimum disturbance of the solvent shell of the anion.² Ammonium nitrate solutions should then be the best choice of reference system for which to determine the band width of an infrared absorption band of a long-lived nitrate ion in surroundings which, except for possibility of the exchange reaction, resemble closely those existing in nitric acid solution. Experimental conditions do not allow the ideal condition of very dilute solutions to be attained in aqueous infrared studies.

Experimental Section

Aqueous solutions are notoriously difficult to examine by infrared methods in dilute concentration and, because the one suitable absorption band for the study of the nitrate ion, that near 830 cm^{-1} , is not a strong band, rather concentrated solutions (3 *M* and greater) supported as capillary films of undetermined thickness between AgCl plates were necessarily examined. Spectra were recorded using grating instruments, a Beckman IR9 and a Herscher instrument, with slit widths of 1.5 cm^{-1} or less, i.e., sufficiently narrow to avoid significant error in the directly recorded band widths (width at half the peak intensity) which ranged between 7 and 17 cm^{-1} . The linear absorbance mode of operation used in conjunction with absorbance scale expansion facilitated the measurements.

Raman band width measurements were made, using a Hilger photoelectric recording instrument, on the 1050-cm^{-1} band of the nitrate ion. Since effective slit widths were necessarily comparable in magnitude to the band widths a correction procedure was used^{7,8} to obtain true band widths.

- (1) M. M. Kreevoy and C. A. Mead, *J. Am. Chem. Soc.*, **84**, 4596 (1962).
- (2) H. S. Frank and A. L. Robinson, *J. Chem. Phys.*, **8**, 933 (1940).
- (3) K. Fajans and O. Johnson, *J. Am. Chem. Soc.*, **64**, 668 (1942).
- (4) H. S. Frank and M. W. Evans, *J. Chem. Phys.*, **13**, 507 (1945).
- (5) P. M. Vollmar, *ibid.*, **39**, 2236 (1963).
- (6) R. E. Hester and R. A. Plane, *Inorg. Chem.*, **3**, 769 (1964).
- (7) S. Brodersen, *J. Opt. Soc. Am.*, **44**, 22 (1954).

DNO_3 was prepared by treating dried KNO_3 with D_2SO_4 which was prepared from the reaction of SO_3 with D_2O . ND_4NO_3 was prepared by three successive exchanges with D_2O ; the infrared spectrum showed that little H remained.

Results and Discussion

The results of the infrared band-width measurements for aqueous nitric acid and aqueous ammonium nitrate solutions are illustrated in Figure 1 where the band widths at half the peak absorbance are plotted against solution concentration. Each point represents the mean of four or more independent measurements.

The ammonium nitrate solution data show a slight concentration dependence indicating that the NH_4^+ is not without some effect upon the solvent shell or upon the nitrate ion directly. A reasonable extrapolation yields a value of $10.4 \pm 0.5 \text{ cm.}^{-1}$ for the nitrate ion band width in dilute aqueous solution. In 3 *N* HNO_3 , the band width is $12.5 \pm 0.5 \text{ cm.}^{-1}$, and if we accept the difference of $2.1 \pm 1.0 \text{ cm.}^{-1}$ to be the natural line width of the nitrate ion in acid solution, the lifetime of this ion is approximately $3.2 \times 10^{-11} \text{ sec.}$ and the reciprocal of this lifetime is the pseudo-first-order rate constant k_1 for the reaction, nitrate ion \rightarrow acid; $k_1 = 3.2 \times 10^{10} \text{ sec.}^{-1}$. The corresponding approximate value of k_1 in the 3 *N* deuterium acid system, where the band-width difference was determined to be 1.4 cm.^{-1} , is $k_1 = 2.1 \times 10^{10} \text{ sec.}^{-1}$. The isotope ratio of about 1.5 is in accord with the view that reactions of this type are diffusion-controlled reactions whose rates are determined by the exceptionally high mobilities of the proton and deuteron in aqueous solution.⁹ The ratio of proton to deuteron mobilities is 1.47,¹⁰ which is then the predicted ratio of reaction rates.

Raman data for the ν_1 nitrate mode, near 1050 cm.^{-1} , yielded essentially the same result for the nitrate ion lifetime. The band width in ammonium nitrate solutions was found to be independent of concentration within experimental uncertainty, $8.3 \pm 0.5 \text{ cm.}^{-1}$, while the nitric acid solutions showed much wider bands, the band width increasing with concentration at a rate comparable to that observed for the 830-cm.^{-1} infrared band. At 3 *N* the band width was 10.8 cm.^{-1} which gives a natural line width of 2.5 cm.^{-1} .

The band-width increase with acid-concentration increase can probably be almost entirely ascribed to the decreasing lifetime of the nitrate ion. A small part of the change may be due to a specific interaction between ions, such as that which presumably produces the small concentration dependence of the nitrate ion band width in spectra of ammonium nitrate solu-

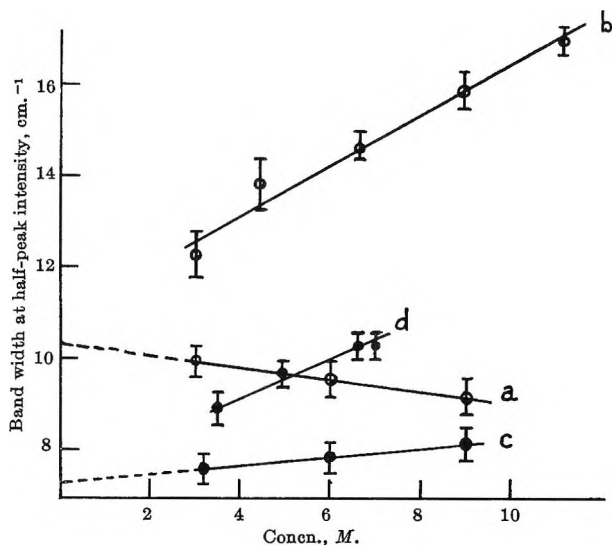


Figure 1. Widths of the 830-cm.^{-1} infrared band of nitrate ion in aqueous solutions: a, NH_4NO_3 in water; b, HNO_3 in water; c, ND_4NO_3 in D_2O ; d, DNO_3 in D_2O .

tions, but if this effect is neglected, the ratio of lifetimes in the deuterium and protium acid solutions is, within the uncertainty of the measurements, independent of concentration and is near 1.5. This dependence of ion lifetime upon concentration is, at least qualitatively, in accord with the proposed mechanism of such exchange reactions.⁹

Solvent Isotope Effect on the 830-cm.^{-1} Infrared Band. Of considerable interest is the marked difference in band widths observed for the 830-cm.^{-1} infrared absorption band of the NO_3^- ion in water and in D_2O . A solvent isotope effect of this type has, to our knowledge, not been reported previously. The band-width values extrapolated to infinite dilution are 10.4 and 7.3 cm.^{-1} in water and D_2O , respectively. The ratio of these values, 1.42 ± 0.15 , is in accord with the following physical picture of the main band-broadening mechanism which is responsible for the observed band width: fluctuations in the interaction between the ion and its solvent shell. The interaction is largely hydrogen bonding between the OH or OD of the water and the $\text{O}^{\delta-}$ atoms of the NO_3^- . The nitrate mode under study, ν_2 , involves the motion of the N atom in a direction perpendicular to the plane of the three O atoms which need move very little, so that the ion-oxygen to water-oxygen distance will vary little during the mode, *i.e.*, the motion within the ion should not affect significantly the main contribution to

(8) J. C. Evans, *J. Opt. Soc. Am.*, **50**, 1337 (1960).

(9) M. Eigen, *Z. Elektrochem.*, **64**, 115 (1960).

(10) G. N. Lewis and T. C. Doody, *J. Am. Chem. Soc.*, **55**, 3504 (1933).

the intermolecular interaction. Perturbations of the vibrational energy levels of the nitrate ion must then arise from fluctuations in its interaction with the solvent shell due to those solvent vibrations which change the hydrogen-bond length. The solvent isotope effect is expected to be determined by the ratio of the root-mean-square amplitudes of the stretching vibrations of the OH and OD groups of water. The effect need not be linearly related to this ratio but the agreement between the observed ratio of 1.42 ± 0.15 and the value calculated for the ratio of the mean-square amplitudes, 1.38, is suggestive. This calculated value is the ratio of the OH to OD stretching frequencies of water which, as Raw and Kuenz¹¹ have demonstrated, is a good approximation to the ratio of mean-square amplitudes of OH and OD stretching. Other modes of the nitrate ion or of other molecules or ions need not, of course, show such a large solvent isotope effect and many are expected to show only a small effect because the fluctuations in the interactions with the solvent during the mode are largely due to the internal motions of the atoms of the molecule itself.

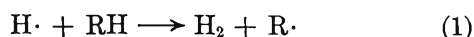
(11) C. J. G. Raw and C. Kuenz, *J. Chem. Phys.*, **35**, 1529 (1961).

Effects of Temperature in the Radiolysis of Methane and Propane¹

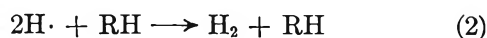
by L. I. Bone² and R. F. Firestone

Department of Chemistry, The Ohio State University, Columbus, Ohio (Received April 8, 1965)

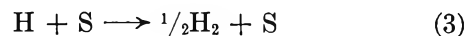
Reactions of H atoms formed in the radiolysis of the lower homologs of the *n*-paraffin series have been a subject of interest since the earliest investigations.^{3,4} Recently, Back⁵ concluded that $G(\text{H}_2)$ decreases rapidly with dosage at very low conversions as a result of H atom scavenging by olefinic products, making it apparent that studies of H atom reactions must be performed in the virtual absence of olefinic impurities and at conversions sufficiently small to prevent scavenging from becoming the predominant reaction. Under such conditions, H atoms may be expected to form H_2 via



and



or



where S represents a surface. There seems to be little doubt that reaction 1 predominates in C_3H_8 near room temperature.⁶ However, in the radiolysis of CH_4 Sieck and Johnsen⁷ hold that reaction 2 predominates while Maurin⁸ contends that abstraction is virtually complete at room temperature. Estimates of k_1 in CH_4 at room temperature range from a low of approximately 10^{-23} cc./molecule sec. ($P = 0.1$, $E = 18$ kcal./mole)⁹ to 10^{-18} cc./molecule sec. ($P = 10^{-5}$, $E = 4.5$ kcal./mole).¹⁰ Thus, the present authors felt that a comparative study of variations of $G(\text{H}_2)$ with respect to temperature at very small conversions in a hydrocarbon in which abstraction is believed to predominate at 25° (C_3H_8) and in CH_4 might provide more definitive insight into the question of methane's apparent inertness to H atom attack.

Experimental Section

All gases used were Phillips Research grade. Ethylene was used without further purification. Propane and methane were purified by trap-to-trap distillation on a vacuum line. Analyses for olefinic impurities were performed by gas chromatography with a 3.66-m., 0.64-cm. copper column packed with 60–80 mesh Chromosorb P coated with a saturated solution of AgNO_3 in propylene glycol at 25° . Other analyses were performed with a 1.53-m., 0.64-cm. copper column packed with silica gel programmed linearly at $9^\circ/\text{min}$. from 25° . Maximum impurities (mole %) in the purified reactants were as follows: for propane: 0.001% CH_4 , 0.1% C_2H_6 , 0.0001% butanes and higher, <0.00001% olefinic impurities; for methane: 0.05% C_2H_6 , 0.001% C_3H_8 , <0.001% olefinic impurities. Mass spectrometric analysis sets an upper limit of 0.1% for CO and O_2 in both CH_4 and C_3H_8 . All C_3H_8 samples and one series of CH_4 samples were irradiated in a 974-cc. cylindrical stainless steel vessel with a mica window 0.008 to 0.313 cm. thick (Muscovite). The window was sealed with Devcon "2-Ton"

(1) This work was partially supported by the U. S. Atomic Energy Commission under Contract No. AT(11-1)-1116.

(2) Capt. U.S.A.F., A.F.I.T. Program, 1962–1964.

(3) S. C. Lind, ACS Monograph No. 151, Reinhold Publishing Corp., New York, N. Y., 1961.

(4) A. J. Swallow, "Radiation Chemistry of Organic Compounds," Pergamon Press Ltd., Oxford, 1960.

(5) R. A. Back, *J. Phys. Chem.*, **64**, 124 (1960).

(6) K. Yang, *ibid.*, **67**, 562 (1963).

(7) L. W. Sieck and R. H. Johnsen, *ibid.*, **67**, 2281 (1963).

(8) J. Maurin, *J. chim. phys.*, **59**, 15 (1962).

(9) E. W. R. Steacie, "Atomic and Free Radical Reactions," 2nd Ed., Reinhold Publishing Corp., New York, N. Y., 1954.

(10) M. J. Berlie and D. J. LeRoy, *Can. J. Chem.*, **32**, 650 (1954).

epoxy cement and held with a brass retaining ring. The neck of the vessel was constructed so that the X-ray cone would not strike steel except at the base of the vessel. The vessel was attached to the vacuum line by a 12/30 stainless steel to glass joint sealed with Apiezon W wax. The stopcock in the filler line was cleaned and regreased with Apiezon M grease, and the sides and base of the vessel were flamed to red heat under vacuum prior to each run. The vessel was irradiated under vacuum for approximately 1 hr. before admission of fresh reactants. A second series of CH_4 samples was irradiated in a 1040-cc. spherical Pyrex vessel with a mica window identical with that in the steel vessel and with a neck designed to enclose the X-ray cone without intercepting any portion of it. All runs at temperatures below room temperature were performed with the irradiation vessel immersed in an appropriate cooling bath. The steel vessel was heated with nichrome heating wire wrapped with asbestos at higher temperatures, and the glass vessel was heated with a 4- π heating mantle. We experienced no difficulty with the window seal on the steel vessel at 150° but were unable to keep a tight window on the Pyrex vessel above 100°. The Machlett OEG-60 beryllium window tube was operated at 50 kv. and 35 ma. in all runs. Hydrocarbon pressures near 1 atm. were maintained in all irradiations (500 to 740 mm.). After irradiation the product gases were diluted with a measured quantity of D_2 , and the resulting mixture was transferred to the gas buret through a liquid nitrogen trap by means of a Toepler pump. The predominantly H_2 - D_2 mixtures were analyzed on a Consolidated 21-620 mass spectrometer modified with a 21-072 isotope ratio accessory and equipped with a metal inlet system and a molecular leak. Samples were expanded into the mass spectrometer through a liquid nitrogen trap. All isotope ratio data were extrapolated to time zero, defined as the time at which gases were admitted to the leak to compensate for fractionation of the sample by the molecular leak, and a calibration sample of approximately the same composition was analyzed immediately before and sometimes immediately after each sample analysis.

Ethylene was employed as a dosimeter, and $G(\text{H}_2)$ from ethylene was assumed to be 1.2 molecules/100 e.v.¹¹ In the glass vessel dosage rates were found to be proportional to gas density in the pressure range 400 to 800 mm. In the steel vessel dosage rates were found to be independent of gas density in this pressure range indicating that a substantial part of the energy deposited in the gas was introduced by very short range photoelectrons ejected from the vessel base of relatively high atomic number and thickness

compared to the glass vessel. For irradiations performed in the steel vessel, the assumption was made that the rate of energy deposition was the same for CH_4 and C_3H_8 as for C_2H_4 . Dosage rates in the glass vessel were computed by assuming that the rate of energy deposition was proportional to the number of electrons per molecule and to the number density of the gaseous contents.

Results and Discussion

It is apparent from the data of Table I that $G(\text{H}_2)$ in propane is independent of temperature between -29° and room temperature. Yang⁶ reports the absence of a temperature coefficient between 50 and 240°. It seems entirely reasonable to conclude that at pressures near 1 atm. reaction 1 consumes essentially all H atoms which escape scavenging in initially pure C_3H_8 between -29 and 240°. The average value for $G(\text{H}_2)$ in the absence of added scavenger is 5.6 ± 0.5 molecules/100 e.v. (extreme deviation from the mean)

Table I: H_2 Yields from CH_4 and C_3H_8

$T, ^\circ\text{C}.$	Mole % C_2H_4 added	$G(\text{H}_2)$, molecules/100 e.v.
Methane irradiations in steel vessel ^a		
-78	None	3.6 ± 0.3^b
-4	None	2.3
29	None	1.9 ± 0.2^c
27	<1	2.2
29	1.1	2.1
29	5.1	1.9
78	2.0	2.2
150	None	2.7 ± 0.4^d
150	1.3	1.9
Methane irradiations in Pyrex vessel ^a		
32	None	3.2 ± 0.1^f
33	2.2	2.0
100	None	3.1 ± 0.1^g
Propane irradiations in steel vessel ^a		
-29	None	5.4 ± 0.5^h
-4	None	5.9
26	None	5.6 ± 0.3^i
28	2.4	1.8

^a Dosage rate assumed equal to that in ethylene dosimeter, 1.1×10^{18} e.v./min., independent of pressure 400 to 800 mm.; all samples irradiated for 20.0 min. ^b Average of three runs, with extreme deviation from mean. ^c Average of five runs. ^d Average of three runs. ^e Dosage rate 7.6×10^{17} e.v./min. at 740 mm.; all samples irradiated for 20.0 min. ^f Average of three runs. ^g Average of two runs. ^h Average of two runs. ⁱ Average of three runs.

(11) M. C. Sauer and L. M. Dorfman, *J. Phys. Chem.*, **66**, 322 (1962).

at 0.01% conversion based on the assumption that $G(-C_3H_8) \simeq 10$ molecules/100 e.v. We estimate that 0.7 of the H_2 is of atomic origin on the basis of $G(H_2) = 1.8$ in the presence of C_2H_4 , in excellent agreement with the anticipated trend between Back's 0.8 at 0.003% conversion⁴ and Yang and Manno's 0.6 at approximately 1% conversion.³

Results of the methane irradiations are more difficult to interpret, particularly so concerning the effects of irradiating in the steel vessel. The observed agreement within 5% for $G(H_2)$ in the presence of added ethylene for the steel and Pyrex vessels indicates, not unexpectedly, that those presumably very fast reactions which produce unscavengeable H_2 are insensitive to the nature of the walls of the vessel and tends to substantiate the validity of our dosage rate computations for the two vessels. Choice of a steel irradiation vessel appears not to have affected the balance between the atomic and ionic yields of H_2 from propane; this is not true in the case of CH_4 .

The data of Table I indicate that about 40% of the H_2 from CH_4 in the Pyrex vessel is scavenged by added ethylene at 32° in agreement with an interpolated value from the data of Sieck and Johnsen at 0.01% conversion.⁷ None of the H_2 formed in the steel vessel at room temperature is scavangeable, and it is necessary to lower the temperature to -78° in order to obtain the normal unscavenged H_2 yield in the steel vessel. Thus, during CH_4 irradiations in the steel vessel, H atoms are removed by a reaction path which is not active during radiolysis of C_3H_8 in the same vessel nor during radiolysis of CH_4 in the Pyrex vessel. A surface reaction is suggested immediately because the observed absence of an effect of choice of vessel in the case of C_3H_8 can be attributed to a high probability that a negligible fraction of the H atoms in C_3H_8 reaches the walls. Even at -29° the rate of abstraction in C_3H_8 is estimated to be about 20 times the rate of removal of H atoms by three-body homogeneous combination, and the ratio increases to 10^3 at room temperature.¹² These estimates serve to make complete abstraction in C_3H_8 credible, but we have no evidence which indicates that H atoms formed in CH_4 reached the walls of the steel vessel. Two pieces of information are merely suggestive, *i.e.*, the observation that hydrogen atoms combine on the walls of vessels of similar dimensions in the radiolysis of H_2O vapor- D_2 mixtures at water vapor pressures near 1 atm. and roughly equal rates of atom formation¹³ and the likelihood that oxides and, possibly, carbonyl compounds on the steel surface are sufficiently reactive toward H atoms to prevent them from combining under certain conditions. One such condition must be a

temperature high enough for activation of the unidentified surface reaction, thus providing a possible explanation for the "normal" H_2 yield at -78° in the steel vessel.

The observation that $G(H_2)$ from CH_4 in the Pyrex vessel is the same at 32° as at 100° demonstrates either that abstraction is complete at both temperatures or that it fails to contribute significantly to the H_2 yield at either temperature. Data obtained at 150° in the steel vessel show that the unscavengeable yield of H_2 is unchanged but that the total yield of H_2 from initially pure CH_4 is about 30% greater than at room temperature in the steel vessel or at 100° in the Pyrex vessel. These observations suggest that the abstraction step does not contribute significantly to the formation of H_2 in the radiolysis of CH_4 between 25 and 100° but that it must be considered in the vicinity of 150° and above.

(12) These estimates are based upon a value of k_1 obtained by extrapolating the expression for k_1 obtained in the range 95 to 170° (H. A. Kazmi, R. J. Diefendorf, and D. J. LeRoy, *Can. J. Chem.*, **41**, 690 (1963)), a value of 2.5×10^{-32} cc.²/molecule² sec. for the three-body rate constant (C. B. Kretschmer and H. L. Peterson, *J. Chem. Phys.*, **39**, 1772 (1963), and W. Steiner, *Trans. Faraday Soc.*, **31**, 623 (1935)), a gross rate of formation equal to the net rate of formation of scavangeable H_2 , and an assumed steady state for H atoms.

(13) R. F. Firestone, *J. Am. Chem. Soc.*, **79**, 5593 (1957).

The Directly Determined Magnetic Susceptibilities of Copper Acetylacetonate and Diphenylpicrylhydrazyl Adsorbed on Silica Gel from 1.40 to 4.2°K.

by K. Kikuchi, H. W. Bernard, J. J. Fritz, and J. G. Aston

Contribution No. 177 from the Cryogenic Laboratory, Department of Chemistry, The Pennsylvania State University, University Park, Pennsylvania (Received May 13, 1966)

It is well known that high specific surface area solids have energetically heterogeneous surfaces. As a result the molecules which go onto the surface first occupy the parts of it that correspond to the lowest energies (higher differential heats of adsorption). It was thought possible that on this account molecules with electron spin moment might, at low coverages, be sufficiently separated to reduce magnetic interactions; thereby systems might behave more closely to the ideal than in the usual crystal. Accordingly, we have made susceptibility measurements of copper acetylac-

tonate and diphenylpicrylhydrazyl adsorbed on silica gel.

The apparatus used was a highly sensitive Faraday balance, a schematic diagram of which is shown in Figure 1. The field gradient is produced by a solenoid of superconducting niobium-zirconium wire containing 25 atomic % of zirconium (10 mils in diameter) wound to produce the largest possible constant field gradient. The critical current is 13.4 amp. and the maximum field with this current is 18 kgauss. The value of $H_z dH_z/dz$ is 5.8×10^7 gauss²/cm. The limiting sensitivity of this balance is 1 μ g.

The sample is suspended inside the field gradient at the end of a fiber which is connected to a Sartorius microbalance. A glass tube which passes through the core of the magnet contains the sample in the same vacuum system as that of the balance. It has been found that at 4°K. and below, exchange gas pressures above 5×10^{-4} mm. and less than 10^{-2} mm. are adequate to obtain thermal equilibrium between the sample and the bath of liquid helium which surrounds the superconducting solenoid and the glass tube. Such pressures do not interfere with the operation of the balance. The liquid helium is contained in a glass dewar and can be pumped to obtain temperatures between 1.3 and 4.2°K. This in turn is surrounded by a dewar of liquid nitrogen. For the time being the balance has been calibrated against a sample of chrome alum.

Figure 2 shows a graph of $1/\chi_M$ (χ_M = molar susceptibility in e.m.u.) against T° K. for polycrystalline copper acetylacetonate for the range between 1.4 and 4.2°K. The points are those obtained by the susceptibility balance while the solid graph is that from Fritz and Taylor.¹

Samples of copper acetylacetonate adsorbed on silica gel were prepared by using a silica gel of specific surface area 400 m.²/g. The samples of approximately 50-mg. weight were prepared by shaking a gel sample with the appropriate concentration of copper acetylacetonate in chloroform. The concentration of copper acetylacetonate on the surface could be ascertained by inspection of the isotherm (surface concentration plotted against the amount of copper acetylacetonate). The isotherm was prepared from a series of spectrophotometric experiments in which the copper acetylacetonate adsorbed from various concentrations of solutions was estimated by measuring the concentration of the solution before and after equilibrium adsorption by the gel.

The results of the magnetic susceptibility measurements on the adsorbed samples are shown in Figure 3, where $1/\chi_M$ is plotted against temperature. There are

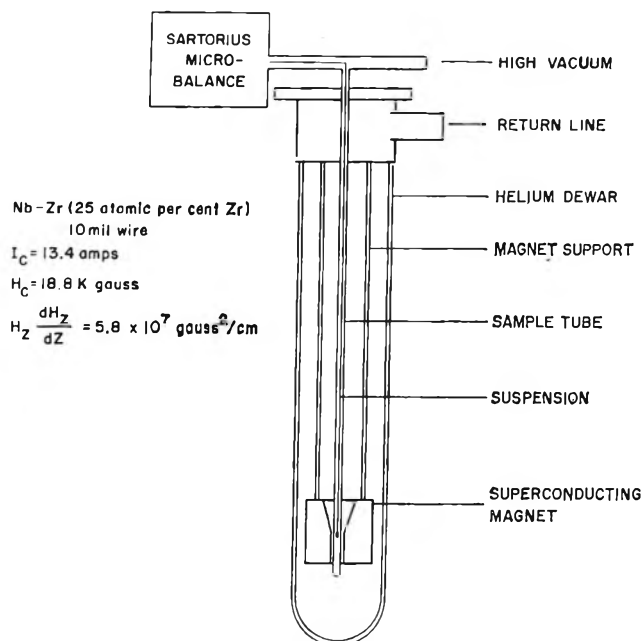


Figure 1. Susceptibility balance.

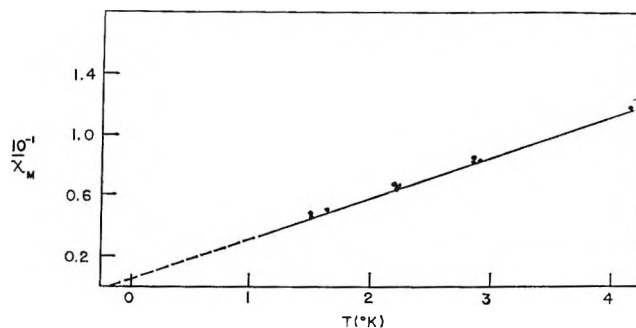


Figure 2. $1/\chi_M$ vs. T for polycrystalline copper acetylacetonate.

graphs for four coverages: 4×10^{-3} , 1×10^{-2} , 5×10^{-2} , and 5×10^{-1} of a monolayer. As can be seen, all of the graphs intersect at a common point at $1/\chi_M = 0$ thus giving the same value of the Weiss δ , namely -0.2° . By comparing with Figure 2 one sees that this is exactly the same Weiss δ obtained for the pure substance.

The surprising fact is that only for the coverage $\theta = 4 \times 10^{-3}$ is the value of χ_M anywhere near equal to that of the pure substance. At this point, as can be seen by comparing Figures 2 and 3, the value is 0.5 that of pure acetylacetonate. For $\theta = 5 \times 10^{-1}$ the susceptibility is less than 0.1 the value of that of the pure substance.

There is only one conclusion to be drawn from these

(1) J. J. Fritz and R. G. Taylor, *J. Am. Chem. Soc.*, 80, 4484 (1958).

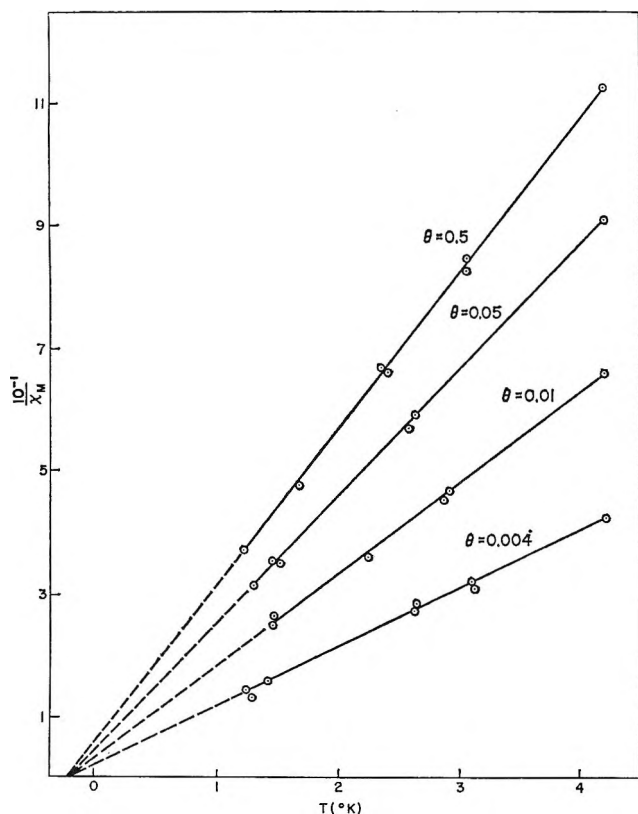


Figure 3. $1/\chi_M$ vs. T for coverages of copper acetylacetonate on silica gel.

results. It must be that the sites of lowest energy (*i.e.*, those occupied first), which must accommodate a square-planar molecule with sides of the order of 10 \AA , are large enough to hold several molecules of the copper acetylacetonate. In such sites the molecules, then, behave like crystalline copper acetylacetonate. It then appears that the rest of the molecules lie on the flat surface in such a way that the molecules are paired off in a similar fashion to the way they are in copper salts of the fatty acids to produce singlet and triplet levels. As a result the paramagnetism decreases rapidly to low values below 90°K .²

Unfortunately, because of the nature of the apparatus, we were not able to carry the measurements above 4°K . The balance will be modified to allow measurements to be taken above the range of temperatures now dictated by the superconducting balance.

The results for fractions of a monolayer of diphenylpicrylhydrazyl confirm the conclusion that molecules go into "holes" on the surface where they behave like crystalline material.

Figure 4 gives a plot of $1/\chi_M$ against T for polycrystalline diphenylpicrylhydrazyl (open circles) for the range between 1.4 and 4.2°K . The Weiss δ ob-

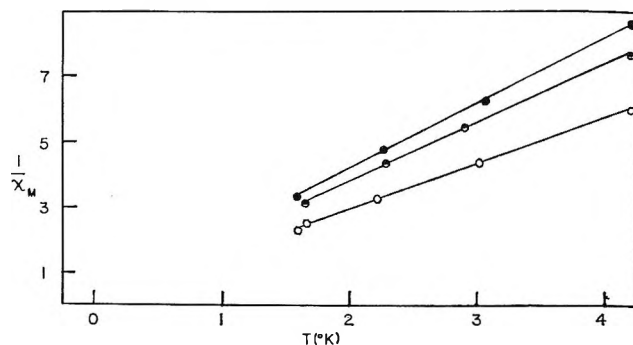


Figure 4. $1/\chi_M$ vs. T for diphenylpicrylhydrazyl and certain coverages.

tained by extrapolation of the straight line through the points to $1/\chi_M = 0$ is -0.1°K , which compares favorably to that obtained previously.³

The half-shaded circles and shaded circles are, respectively, for coverage of 0.05 and 0.02 of a monolayer of diphenylpicrylhydrazyl adsorbed on silica gel of specific surface area $400 \text{ m}^2/\text{g}$.

The samples were prepared by shaking the silica gel samples of approximately 50 mg. with the appropriate amount of the radical in chloroform. The concentration of the radical on the surface was determined by referring to the adsorption isotherm on which the surface concentration against the amount of diphenylpicrylhydrazyl was graphed.

The isotherm was prepared from a series of measurements made with a low-frequency electron spin resonance apparatus.

The curves through the respective points are straight lines intersecting the line for the bulk material at a common point, $1/\chi_M = 0$. Thus all systems give the same Weiss δ of -0.1 . The meaning of this result is quite clear. Evidently when diphenylpicrylhydrazyl is adsorbed, even at low coverages, lateral condensation produces patches which have essentially the properties of the pure substance. It must be, therefore, that these patches consist of more than one monolayer. It will be noticed that the values of χ_M for both coverages are essentially equal to those of pure diphenylpicrylhydrazyl at all temperatures. It has already been noticed that when methane is adsorbed on titanium dioxide⁴ for coverages below the monolayer, there is evidence that below the melting point of methane there are patches of material of at least two or three layers thick. This evidence consists of the fact that

(2) R. L. Martin and H. Waterman, *J. Chem. Soc.*, 2545 (1957).

(3) H. J. Gerritsen, R. Okkes, H. M. Gijsman, and J. van den Handel, *Physica*, 20, 13 (1954).

(4) J. G. Aston, "The Solid Gas Interface," E. A. Flood, Ed., Interscience Publishers, Inc., New York, N. Y., in press.

the n.m.r. line below a monolayer is very similar to that taken on samples with two or three monolayers of methane on the titanium dioxide.

All the values of θ are calculated on the basis of full accessibility (and no more) of the surface to the adsorbate and thus the estimated coverages should be accepted provisionally. The values of χ_M are uncorrected since at these temperatures the correction is negligible.

Acknowledgment. This work was aided by a grant from the National Science Foundation.

Dielectric Constants of

Acetonitrile-Methanol Mixtures

by E. A. S. Cavell, H. G. Jerrard,
B. A. W. Simmonds, and J. A. Speed

*Departments of Chemistry and Physics, The University,
Southampton, England (Received April 23, 1966)*

For the purpose of studying the effect of protic solvents on chemical equilibria or on chemical reaction rates, it is often desirable to be able to vary the proportion of the protic component of a protic-dipolar aprotic solvent mixture without at the same time changing appreciably the static dielectric constant of the system being investigated. Methanol and acetonitrile, which are miscible in all proportions, are convenient for producing a series of almost isodielectric mixtures of variable composition since the change in bulk dielectric constant over the entire range of mixing is never greater than about 12%. This solvent system has the added advantage, as shown by the data reported below, that, to a good approximation, the total polarization of the mixture is a linear function of the mole fraction of methanol.

Experimental Section

Materials. Reagent grade acetonitrile was allowed to stand over anhydrous K_2CO_3 for several days and then fractionated through a column packed with metal gauze rings. The fraction, b.p. 81.5–81.7°, was collected, distilled under reduced pressure over phosphoric oxide to remove the last traces of water, and finally refractionated.

After a preliminary treatment with anhydrous K_2CO_3 , commercial methanol was distilled and then dried by the method of Lund and Bjerrum.¹ It was then fractionated and the fraction with b.p. 64.4–64.6° was collected.

Both solvents contained not more than 0.02% by weight of water, as determined by a Karl Fischer titration, after final purification.

Densities. All mixtures were made up by weight and the densities were determined at 25° by means of an Ostwald-Sprengel pycnometer.

Apparatus and Procedure for Dielectric Constant Measurements. Capacitance measurements were made using a Schering bridge with the liquids contained in a two-terminal test cell. The cell consisted of two stainless steel cylinders, the inner one being solid and the outer one hollow. At the top of the outer cylinder was a plug also of stainless steel and at the bottom a Fluon washer which held the inner cylinder with its axis coincident with that of the outer cylinder. The outer cylinder was surrounded by a jacket through which water controlled to $\pm 0.05^\circ$ was circulated. The Schering bridge was of conventional design. The source was a high-stability oscillator supplying a continuous wave output of about 4 v. r.m.s. A bridge heterodyne detector was used to amplify the out-of-balance signals which were displayed on a cathode ray oscillograph. All components were screened and the bridge was able to measure capacitances up to about 250 pf. and conductances up to 1200 μ mhos. With liquids of low conductance changes of capacitance of 0.01 pf. could be detected but this figure was reduced to 0.2 pf. for high conductances as the conductance approached 10^{-3} μ mhos. All electrical connections within and to the bridge were made by screened cable, the cell being plugged directly into the bridge circuit so as to avoid long leads.

Before measurements were commenced, the cell was leached in a strong caustic soda solution, then washed thoroughly in resin deionized water, and finally dried. The cell was then rinsed out with a small quantity of the liquid under test and then filled. Capacitance measurements were made at 500 kc./sec. since at this frequency it was found that errors due to electrode polarization and lead inductance were negligible.

Results and Discussion

Density values (d) at 25° and dielectric constant values (ϵ) at 25 and 30° are shown in Table I. Values of total polarization $[P_{12}]_{\text{obsd}}$ at 25° were calculated from eq. 1 in which N_1 and N_2 are the mole fractions and M_1 and

$$[P_{12}]_{\text{obsd}} = \frac{(\epsilon - 1) N_1 M_1 + N_2 M_2}{(\epsilon + 2) d} \quad (1)$$

M_2 the molecular weights of the components. Values of $[P_{12}]_{\text{calcd}}$ were found from eq. 2, in which $[P_1]$ and

(1) H. Lund and J. Bjerrum, *Ber.*, **64**, 210 (1931).

$$[P_{12}]_{\text{calcd}} = N_1[P_1] + N_2[P_2] = [P_1] + \{[P_2] - [P_1]\}N_2 \quad (2)$$

$[P_2]$ are the polarizations of the two pure components. The latter values were calculated from the dielectric data taken from the tables of Maryott and Smith.² Comparison of $[P_{12}]_{\text{obsd}}$ and $[P_{12}]_{\text{calcd}}$ in Table I shows little difference so eq. 2 may be used with little error for most practical applications, although it would be unwise to infer from this that intermolecular interactions between methanol and acetonitrile may always be neglected. From eq. 1 it follows that in mixtures of high dielectric constant the density, rather than the dielectric constant, is generally the decisive factor in the determination of the magnitude of the molar polarization. The approximately linear variation of the total polarization $[P_{12}]_{\text{obsd}}$ of the present mixtures with composition could arise principally from the fact that the partial molar volumes of both components vary only slightly over the entire range of composition. Under appropriate circumstances a nitrile can act as an n onium electron donor in Mulliken's classification,³ on account of the presence of a relatively easily ionizable pair of electrons, and there is a certain amount of spectroscopic evidence for the existence of hydrogen bonding between phenols and acetonitrile.⁴

than in liquid acetonitrile. It is probable that the initial addition of acetonitrile to methanol tends to destroy this near order which is manifest in the increased density of the mixture and in the fact that the maximum discrepancy between $[P_{12}]_{\text{obsd}}$ and $[P_{12}]_{\text{calcd}}$ occurs with the mixture having the smallest mole fraction of acetonitrile. Thereafter the effect of the replacement of methanol molecules by the more polar acetonitrile molecules is apparently largely offset by the resultant reduction in short-range order of the system.

The data in Table I also show an apparent anomaly in the change of dielectric constant of the mixture with composition when the concentration of methanol is very small. This was observed for both temperatures, and since it is believed that the uncertainty of the dielectric values is not greater than ± 0.02 , the effect is not attributable to experimental error.

(2) A. A. Maryott and E. R. Smith, "Tables of Dielectric Constants of Pure Liquids," National Bureau of Standards Circular 514, U. S. Government Printing Office, Washington, D. C., 1951.

(3) R. S. Mulliken, *J. Phys. Chem.*, **56**, 814 (1952).

(4) (a) G. L. Caldow and H. W. Thompson, *Proc. Roy. Soc. (London)*, **A254**, 1 (1960); (b) H. Dunken and H. Fritzsche, *Z. Chem.*, **1**, 249 (1961).

(5) H. Muller, *Physik. Z.*, **34**, 689 (1933).

Table I: Dielectric Constant of Methanol-Acetonitrile Mixtures

Acetonitrile, mole fraction	Density at 25°	Dielectric constant		Molar polarization at 25°	
		At 25°	At 30°	$[P_{12}]_{\text{calcd}}$	$[P_{12}]_{\text{obsd}}$
1	0.7769	36.69 ^a	35.93		48.67
0.963	0.7776	36.52	35.75	48.24	48.22
0.918	0.7780	36.52	35.75	47.72	47.68
0.873	0.7784	36.40	35.58	47.20	47.22
0.756	0.7801	36.07	35.25	45.85	45.81
0.602	0.7825	35.75	34.90	44.08	44.01
0.438	0.7845	35.37	34.46	42.18	42.14
0.337	0.7858	34.94	34.04	41.02	40.95
0.210	0.7874	34.26	33.27	39.55	39.47
0.084	0.7889	33.40	32.44	38.10	37.99
0	0.7870	32.63 ^a	31.64		37.13

^a Taken from ref. 2.

In spite of the relatively small value (1.69 D.) of the vapor phase dipole moment of the methanol molecule as compared with 3.94 D. for acetonitrile and of the possible small modification of these moments on solution,⁵ the static dielectric constants of the two pure liquids are nearly equal. This suggests that short-range order is a more important feature in liquid methanol

Decomposition of Hydrogen Peroxide on Glass

by K. B. Keating and A. G. Rozner

Engineering Materials Laboratory, Engineering Research Division, Engineering Department, E. I. du Pont de Nemours & Co., Inc., Wilmington, Delaware (Received April 15, 1966)

Many investigations have been made of the decomposition of hydrogen peroxide on glass, both in the gaseous and liquid states, but substantial disagreement exists in the reported results. The most extensive investigation of this reaction on Pyrex glass has been made by Giguère.¹ In the present study, the catalytic decomposition of a carefully controlled dilute aqueous solution (0.3% by weight) of hydrogen peroxide was observed on a passivated, well-characterized Pyrex glass surface.

The experimental apparatus used in this investigation consisted of a thermostatically controlled constant-temperature water bath in which a 1-l. erlenmeyer flask (Corning Glass Co.) was immersed. The contents of the flask were stirred by a stirrer driven by an

(1) P. A. Giguère, *Can. J. Res.*, **B25**, 135 (1947).

Table I

Investigator	Catalyst surface	H ₂ O ₂ concn., wt. %	State of aggregation	Temp. range, °C.	Activation energy, kcal./mole	Reference
Pana	Glass	0.85	Liquid	40-50	16.8	3
Pana	Glass	2.55	Liquid	40-50	17.0	3
Giguère	Pyrex	95-99	Vapor	140-245	12.6	1
Giguère	Fused Pyrex	95-99	Vapor	240-305	18.7	1
Giguère	Pyrex coated with tin	95-99	Vapor	72-117	13	1
Giguère	Pyrex coated with Al	95-99	Vapor	96-153	12	1
This study	Pyrex	0.3	Liquid	26-54	12.9	...

electrical motor. The velocity of the stirrer (270 r.p.m.), the distance of the stirrer from the bottom of the flask, and the temperature of the bath remained constant during the series of runs. Decomposition runs were made at 26, 37, and 54°. The temperature was controlled to within $\pm 0.15^\circ$. A dark cloth was placed over the whole apparatus during a run to prevent the admission of light.

The hydrogen peroxide obtained from Baker and Adamson (Grade 1802) was a 30% by weight solution in deionized water without any stabilizer or organic matter. The solution was diluted to 0.3% in our laboratory by addition of deionized distilled water whose conductivity was $0.05 \times 10^{-6} \text{ ohm}^{-1} \text{ cm.}^{-1}$. This indicates very pure water, essentially free of ionic contaminants. The solution was protected from light and heat during storage.

All of the glassware contacting hydrogen peroxide was soaked in 35% H₂SO₄ at room temperature for 1 hr., followed by a rinse in distilled water and oven drying at 110° for 3 hr.

The flask containing 500 ml. of 0.3% hydrogen peroxide solution was immersed in the water bath. After 30-45 min., the temperature of the solution reached the desired test temperature. A 10-ml. sample of the H₂O₂ was withdrawn with a pipet for chemical analysis. This sample was then mixed with 10 ml. of a 20% sulfuric acid solution and titrated against a 0.07 N potassium permanganate solution until a pink end point was reached.² The corresponding concentration was recorded as initial concentration C_0 and the time as initial time t_0 . At regular intervals, 10-ml. aliquots were analyzed in identical fashion. Since the mole fraction of H₂O₂ in the vapor space is on the order of 10^{-5} (for the temperature range studied), only an insignificant amount of conversion could occur there.

The decomposition of hydrogen peroxide proceeds in accordance with first-order kinetics.^{1,3} Accordingly, our data were analyzed by plotting $\log C_0/C$ vs. time. The plot in Figure 1 shows the decomposition of hy-

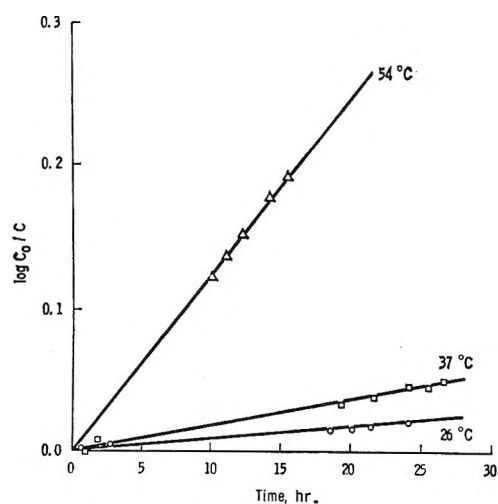


Figure 1. Typical curves for hydrogen peroxide decomposition.

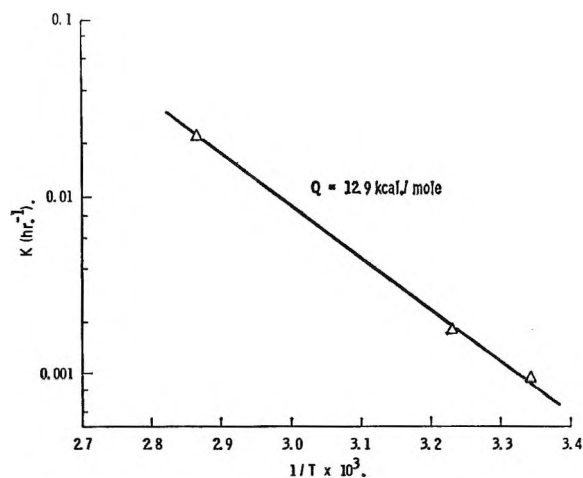


Figure 2. Arrhenius plot for decomposition of H₂O₂ on glass.

(2) C. E. Huckaba and F. G. Keyes, *J. Am. Chem. Soc.*, **70**, 1640 (1948).

(3) C. Pana, *Trans. Faraday Soc.*, **24**, 486 (1928).

drogen peroxide as measured at 26, 37, and 54°. Excellent agreement with the first-order assumption can be seen.

The reaction rate constants are plotted *vs.* $1/T$ in Figure 2; the activation energy for the process is 12.9 kcal./mole.

Table I shows the activation energies obtained by other investigators for the decomposition of H_2O_2 on glass. It is of interest to note the divergence among the results, depending on the various treatments of the glass. The excellent agreement between our value and that of Giguère for Pyrex glass indicates that the mechanism of the heterogeneous decomposition in both the liquid and the vapor phases is the same. This suggestion, based on other considerations, has been made by Roiter and Gaukman,⁴ who compared the activities of several catalytic materials for the decomposition of hydrogen peroxide; they noted that the relative activities of the catalysts studied were about the same in the liquid as in the vapor phase.

(4) V. A. Roiter and S. S. Gaukman, *Russ. J. Phys. Chem.*, **4**, 465 (1933); *Chem. Abstr.*, **28**, 1256 (1934).

Enhanced Oxidation of Platinum in Activated Oxygen. III. Kinetics and Mechanism

by George C. Fryburg

Lewis Research Center, National Aeronautics and Space Administration, Cleveland, Ohio (Received April 23, 1965)

Some time ago we reported¹ that the rate of oxidation of platinum at 1000° was enhanced in activated oxygen. Recent experiments² have confirmed that the enhancement most probably results from the reaction of the normal ³P O atom with the platinum and that the oxide formed is PtO_2 . Since the reaction is now defined, the present communication will discuss the kinetics and the mechanism.

Experimental Section

The oxidation experiments have been extended to other temperatures, and the apparatus has been modified to allow use of more modern methods of O-atom production and detection. A microwave power supply with a slotted wave guide was used to activate the oxygen, and the concentration of O atoms in the oxygen was determined by the NO_2 titration and NO-O afterglow techniques.³ The precision of the results

was increased by using a highly stabilized, solid-state d.c. power supply to heat the platinum specimen and by monitoring the resistance of the specimen with a fast-response digital voltmeter.

The experimental procedure was similar to that employed in ref. 1 except that the arc was stabilized by running for 2 hr. before starting the oxidation run, and the O-atom concentration was measured in the vicinity of the specimen before and after each run. The concentration of O atoms was varied for the different runs by varying the distance between the specimen and the discharge. No effect of flow rate of oxygen on the results could be observed.

Results and Discussion

It was shown previously (Figure 3 of ref. 1) that the oxidation of platinum by both O atoms and O_2 molecules is linear with respect to time. The dependence of the rate of oxidation of a typical specimen (length, 2.9 cm.; width, 0.0287 cm.; thickness, 0.0025 cm.; center section, 1.1 cm.) at different temperatures on the partial pressure of O atoms is shown in Figure 1. The rates are total rates, including oxidation due to both O atoms and O_2 molecules. The intercept on the ordinate is the rate due to O_2 molecules alone at the corresponding temperature. The data at 900

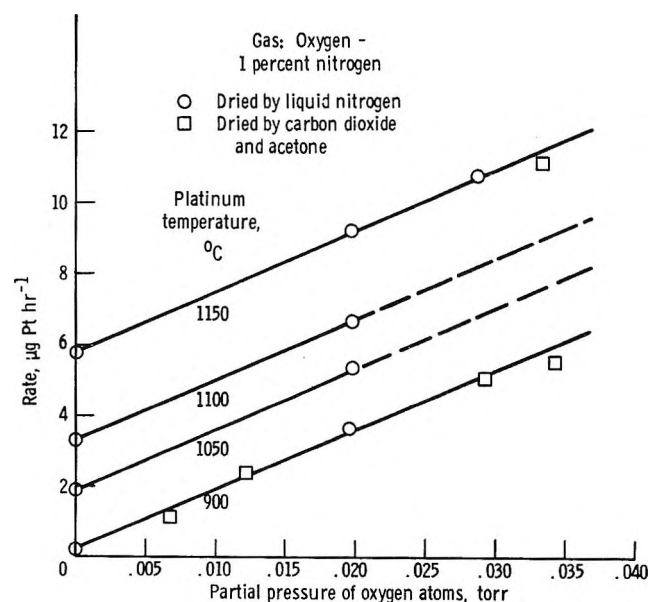


Figure 1. Rate of oxidation of platinum (specimen 19) at various temperatures as a function of partial pressure of oxygen atoms: pressure, 0.5 torr; flow rate, 62.5 cc./min. (STP).

(1) G. C. Fryburg, *J. Chem. Phys.*, **24**, 175 (1956).

(2) G. C. Fryburg, *ibid.*, **42**, 4051 (1965).

(3) F. Kaufman, *Progr. Reaction Kinetics*, **1**, 3 (1961).

and 1150° show that the rate of reaction with O atoms varies as the first power of the O-atom pressure in agreement with our previous work.¹ The data also indicate that the reaction with O atoms occurs with effectively zero activation energy as shown by the fact that the lines at the different temperatures are parallel.

As found before,¹ it appears that the oxidation of the platinum by O₂ molecules and by O atoms occur independently of one another, the oxidation due to a given partial pressure of O atoms merely adding to the oxidation due to the O₂ molecules. The over-all rate may be expressed by an equation analogous to eq. 5 of ref. 1.

$$w_1 = (k_1 + k_2 p_O) t \quad (1)$$

where w_1 is the weight of platinum oxidized from the specimen, k_1 is the temperature-dependent, linear rate constant for the oxidation due to O₂ molecules at the pressure of 0.5 torr, k_2 is the slope of the lines in Figure 1, p_O is the partial pressure of O atoms, and t is the time.

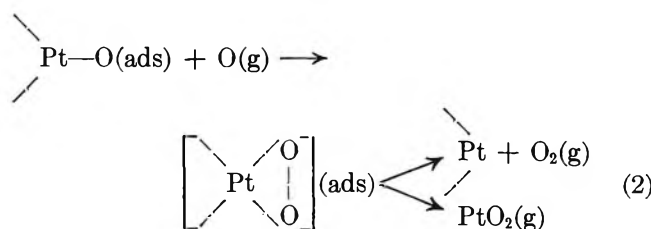
It was shown in ref. 1 that it is possible to calculate the collision efficiency of the O atom in the oxidation reaction, ϵ_0 , from k_2 if the area of the specimen undergoing oxidation is known. With such short specimens (~ 3 cm.) it was anticipated that the area undergoing oxidation would change with temperature due to different cooling effects at the ends. However, it was found that the temperature dependence of the reaction of O₂ molecules with the small ribbons was the same as that obtained with much larger ribbons of well-defined area.⁴ This fact indicated that the area of the small ribbons undergoing oxidation was the same at all temperatures. This area for specimen 19 was calculated from the results given in ref. 4 and found to be 0.077 cm.². Knowing this area, ϵ_0 was calculated from the slope of the lines in Figure 1. From this calculation, $\epsilon_0 = 5 \times 10^{-6}$. This value includes a correction for the escape probability (see ref. 4), which is 0.75 under these experimental conditions, and we have assumed that one O atom reacted for each Pt atom that oxidized (see mechanism in following section). The value of ϵ_0 is independent of the temperature and can be compared to the collision efficiency of the O₂ molecules, ϵ_{O_2} , which varies from 1.8×10^{-8} at 900° to 8.7×10^{-6} at 1500°.⁴ Thus the O atoms are roughly 300 times more reactive than the O₂ molecules at 900° but about equally reactive at 1500°.

Mechanism

We have reported the following observations pertinent to the mechanism of the enhanced oxidation of platinum in activated oxygen. (1) The enhanced

oxidation results from the presence of the normal ³¹P oxygen atom (see ref. 2). (2) The rate of the enhanced oxidation is first order with respect to the O atom (see Figure 1). (3) The energy of activation for the enhanced oxidation is effectively zero (see Figure 1). (4) The oxide formed by reaction with the O atoms is PtO₂ (see ref. 2). (5) The reaction of platinum with O atoms appears to occur independently of the reaction with O₂ molecules (see Figure 1 and eq. 1).

These observations indicate that the enhanced oxidation is an additional oxidation resulting from the reaction of the O atoms with the platinum. The reaction occurs independently of and by a different mechanism from the oxidation by O₂ molecules.⁴ The following mechanism seems most likely. As in the mech-



anism proposed for the oxidation of platinum by O₂ molecules,⁴ the platinum surface is considered to be essentially covered by a tightly bound layer of O atoms and the adsorbed O atom used in the reaction is rapidly replaced by chemisorption. Reaction takes place between a surface Pt atom, with an associated, adsorbed O atom, and a gas phase O atom to form an energy-excess, activated complex. The reaction may proceed along one of two possible paths resulting in merely the recombination of the O atoms or in oxidation of the platinum. The path taken depends on how the excess energy is distributed among the bonds. Since the recombination coefficient for O atoms on hot platinum is probably 10⁻¹ or higher,⁵ and since the collision efficiency for the O atom in the oxidation reaction is only 5 × 10⁻⁶, it is evident that the reaction usually leads to recombination of the O atoms.

The kinetics of atom recombination on surfaces have been considered by Ehrlich⁵ and by Dickens and Sutcliffe.⁶ Our mechanism is compatible with their general conclusions and with the facts known about the recombination of O atoms on platinum, namely, that the recombination is first order with respect to the O

(4) G. C. Fryburg and H. M. Petrus, *J. Electrochem. Soc.*, **108**, 496 (1961).

(5) G. Ehrlich, *J. Chem. Phys.*, **31**, 1111 (1959).

(6) P. G. Dickens and M. B. Sutcliffe, *Trans. Faraday Soc.*, **60**, 1272 (1964).

atoms⁷ and that it occurs with zero activation energy above 800° (see Table II of ref. 1).

Recently, Rosner and Allendorf have shown that the oxidation rate of molybdenum⁸ and tungsten⁹ is also enhanced by O atoms. Their results are very similar to ours, and one would expect that the enhanced oxidation of these metals could be explained by a similar mechanism. There is some difference that results from the difference in stability of the oxides. The PtO₂ is unstable at the temperature of formation and must volatilize in a time comparable to the lifetime of the activated state or decompose. The probability of volatilizing in this short period is small so that the ϵ_0 for platinum is small, 5×10^{-6} . On the other hand, the oxides of tungsten and molybdenum are stable at these temperatures and can exist on the metal surface for some time before volatilizing so that the primary reaction may be between adsorbed MO₂ and a gas phase O atom. This reaction would result in the formation of the trioxide, which is compatible with the fact that metals are usually oxidized to their highest valence state in activated oxygen.²

(7) J. C. Greaves and J. W. Linnett, *Trans. Faraday Soc.*, **54**, 1323 (1958).

(8) D. E. Rosner and H. D. Allendorf, *J. Chem. Phys.*, **40**, 3441 (1964).

(9) D. E. Rosner, private communication.

The Oxygen Electrode in Fused Alkali Nitrates

by R. N. Kust¹

Department of Chemistry, Texas A&M University,
College Station, Texas (Received May 3, 1965)

Several workers have reported on the existence of oxygen gas electrodes reversible to the oxide ion in fused salts.^{2,3} Generally, the solvent used was one containing an oxyanion. However, accurate determinations of standard e.m.f.'s have not been made. Usually, the oxygen electrodes have been used in concentration type cells where the E° 's cancel out. The present author has published a study of the oxygen electrode in fused alkali nitrate solvents⁴ which included the E° for the oxygen electrode against a silver-silver ion glass membrane electrode. The cell reaction could be written



The E° was established by the coulometric addition of oxide ion. Since the quantities of oxide ion generated

were quite small, the oxide ion concentration ranging from about 10^{-5} to $10^{-7} m$, chemical methods of analysis were not employed to determine the oxide ion concentration. The amount of oxide ion added was determined by integration of the time over which a constant current of 10–20 $\mu a.$ was passed through the cell. It was tacitly assumed that the current efficiency was 100%. It has been suggested that the definition of the electrode system would be more reliable if the values for the E° obtained coulometrically could be supported by data obtained from a chemical addition of oxide ion. This note is a report of such data.

Experimental Section

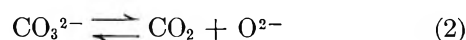
All chemicals used were of reagent grade. The solvent of equimolar sodium-potassium nitrates was prepared by fusing the proper proportions of the two salts and mixing well. Dry nitrogen was bubbled through the melt for 2 hr. The solvent was then filtered through a fine grade fritted glass disk, molded into slugs of about 100 g., and stored over magnesium perchlorate. The sodium carbonate used was dried at 300° for 4 hr.

The reaction vessel and electrode were similar to those previously described.⁴ An oxygen-platinum electrode was used as the indicator electrode and a silver-silver nitrate (1.0 m AgNO₃ in equimolar Na, KNO₃) electrode was used as the reference electrode.

Potential measurements were made with a Leeds and Northrup K-3 universal potentiometer. A Keithley Model 603 electrometer amplifier was connected in series with the electrochemical cell and was used as a null detector.

Results

Small quantities of Na₂CO₃ were added to the electrochemical cell. The oxygen gas passing over the oxygen electrode swept out the CO₂ generated by the dissociation of the carbonate ion according to the reaction



Since oxide ion was the other product of the dissociation, the potential increased with time. The complete dissociation of the carbonate ion was indicated by the halt in the potential rise. The concentration of the oxide ion, calculated from the amount of sodium carbonate added, ranged from 10^{-6} to $10^{-4} m$. Potentiometric readings were made after the e.m.f. had been

(1) Department of Chemistry, University of Utah, Salt Lake City, Utah 84112.

(2) H. Flood and T. Forland, *Acta Chem. Scand.*, **1**, 92 (1947).

(3) B. A. Rose, G. J. Davis, and H. J. T. Ellingham, *Discussions Faraday Soc.*, **4**, 154 (1948).

(4) R. N. Kust and F. R. Duke, *J. Am. Chem. Soc.*, **85**, 3338 (1963).

constant for at least 20 min. The values of E° for the cell reaction were obtained at several temperatures and are listed in Table I. Each value for the E° is the average of at least five and in some cases six measurements of the e.m.f. at known oxide ion concentrations.

Table I: Comparison of the E° Values for the Oxygen Electrode Obtained by Chemical and Coulometric Methods

Temp., °K.	E° , v. (chemical)	E° , v. (coulometric)
536	0.6390	0.6388
543.5	0.6370	0.6369
545	0.6367	0.6365
553	0.6346	0.6345
565	0.6314	0.6314
578	0.6280	0.6281
585	0.6260	0.6263
589	0.6254	0.6253
595	0.6236	0.6238
602	0.6221	0.6220
610	0.6200	0.6200
616	0.6182	0.6185
621	0.6171	0.6173
630	0.6151	0.6150
639	0.6128	0.6127

Discussion

The chemical addition of oxide ion to an equimolar sodium-potassium nitrate melt is complicated by the insolubility of most metallic oxides. Also, the introduction of cations different from the solvent cations would lead to possible complex formation, the formation constants of which would be unknown. Hence, one is limited to either Na_2O or K_2O as a source of oxide ion. It is very difficult to prepare either of these oxides so that they are free from peroxide and superoxide contaminants. However, it has been shown that sodium carbonate has an unusually large dissociation constant in this solvent in the temperature range of interest.⁵ The dissociation constant for reaction 2 is on the order of 10^{-5} at 300° . Thus the addition of Na_2CO_3 to the solvent and the subsequent removal of the CO_2 produced is equivalent to the addition of Na_2O directly. Also, no contamination by peroxides or superoxides is likely to occur.

A comparison of the E° values obtained in this manner to the values obtained by the coulometric generation of oxide ion is given in Table I. In every case the difference between the two values is 0.3 mv. or less. The E° can be calculated for any temperature between 530 and 639°K . from the equation

$$E^\circ (\text{v.}) = 0.7759 - 2.557 \times 10^{-4}T$$

$$530^\circ\text{K.} \leq T \leq 639^\circ\text{K.}$$

With these additional data the oxygen electrode is sufficiently defined to be a useful electrode for electrochemical studies in alkali nitrate solvents.

(5) R. N. Kust, *Inorg. Chem.*, **3**, 1035 (1964).

Aluminum-27 Nuclear Magnetic Resonance of Trialkylaluminum Compounds. II. Variable-Temperature Studies

by Charles P. Poole, Jr., Harold E. Swift, and John F. Itzel, Jr.

Gulf Research & Development Company, Pittsburgh, Pennsylvania (Received May 10, 1966)

In a previous publication¹ several aluminum alkyl compounds were studied by aluminum-27 n.m.r. both in the pure state and dissolved in various solvents. In low-viscosity solvents the line width was found to be proportional to the viscosity times the cube of the molecular radius, and the dominant relaxation mechanism in these solvents was attributed to quadrupolar relaxation through molecular rotation. In high-viscosity solvents the line width became much less dependent on the viscosity.

The present study employed variable-temperature techniques to obtain the temperature dependence of the line width of pure aluminum alkyls and mixtures of triethylaluminum in solution.

Experimental Section

The n.m.r. measurements were made on a Varian V-4200-A wide-line n.m.r. spectrometer equipped with a V-4257 variable-temperature accessory. The experimental arrangement and spectrometer settings were identical with those employed in the room-temperature studies of these same chemical systems.¹ The temperature was monitored by a thermocouple located below the sample, and a correction was made for the temperature difference between the thermocouple position and the actual sample location. The sample tubes used in the variable-temperature studies had inside diameters of 8 mm., whereas the tubes used for the room-temperature studies had inside

(1) C. P. Poole, Jr., H. E. Swift, and J. F. Itzel, Jr., *J. Chem. Phys.*, **42**, 2576 (1965).

diameters of 12 mm. The decrease in the diameter of the tube resulted in a decrease in sensitivity. The sources of the aluminum alkyls were also previously reported.¹

Results and Discussion

The peak-to-peak full line widths of the first derivative n.m.r. spectra obtained from pure triethylaluminum (TEA), tri-*n*-propylaluminum (TNPA), and triisobutylaluminum (TIBA) varied with temperature in the manner shown on Figure 1. Triethylaluminum was dissolved in the four hydrocarbon solvents: isopentane, hexane, cyclohexane, and hexadecane (cetane); and the line widths of the Al²⁷ n.m.r. spectra from these solutions varied with temperature in accordance with Figure 2. Each of these two figures is drawn to the same scale and has the logarithm of the line width ΔH as the ordinate. The data for each system fit straight lines which are almost parallel. One should note that the slopes of the lines in Figure 1 are greater than those in Figure 2. The lowest temperature triisobutylaluminum point in Figure 1 and the lowest temperature hexadecane point in Figure 2 are considerably above their corresponding lines. These two points were obtained from broad weak resonances where the experimental error is large. The resonances of tri-*n*-butylaluminum and tri-*n*-hexylaluminum were too broad to furnish meaningful line widths. All of the spectra recorded in this study contained a single Lorentzian-shaped resonance.

Figures 1 and 2 show that the data fit the relationship²

$$\Delta H = \Delta H_0 e^{\Delta E_{\text{nmr}}/RT} \quad (1)$$

where R is the gas constant, ΔE_{nmr} is the activation energy for nuclear relaxation, and ΔH_0 is a constant. From the data in Figures 1 and 2 the activation energy (ΔE_{nmr}) and pre-exponential constant (ΔH_0) were calculated, and the results are listed in Table I. The three pure aluminum alkyls have the same activation energy (3.4 kcal./mole) while each of the triethylaluminum solutions have an activation energy of about two-thirds of this value. The logarithms of the viscosities, η , of the aluminum alkyls and solvents were plotted against the reciprocal of the absolute temperature, and the resulting straight lines were used to calculate ΔE_{vis} and the pre-exponential viscosity constants η_0 using the equation²

$$\eta = \eta_0 e^{\Delta E_{\text{vis}}/RT} \quad (2)$$

The values of ΔE_{vis} and η_0 are listed in Table I. Viscosity data were not available for tri-*n*-propylaluminum.

It is interesting to note that the exponential tempera-

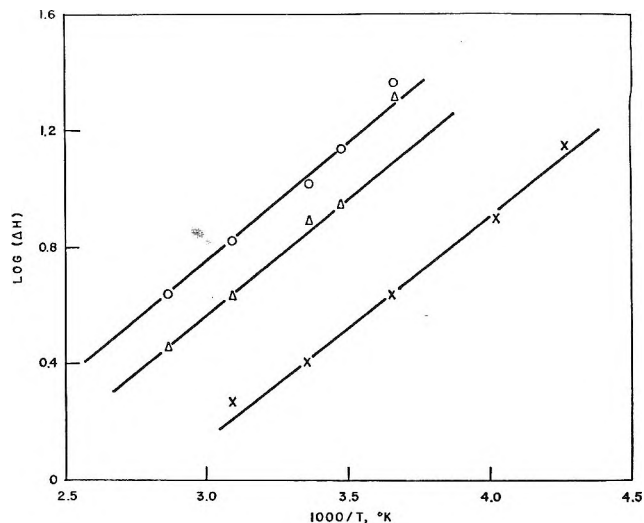


Figure 1. The temperature dependence of the peak-to-peak full line width (ΔH) of pure triethylaluminum (\times), tri-*n*-propylaluminum (O), and triisobutylaluminum (Δ) at 7.2 Mc.

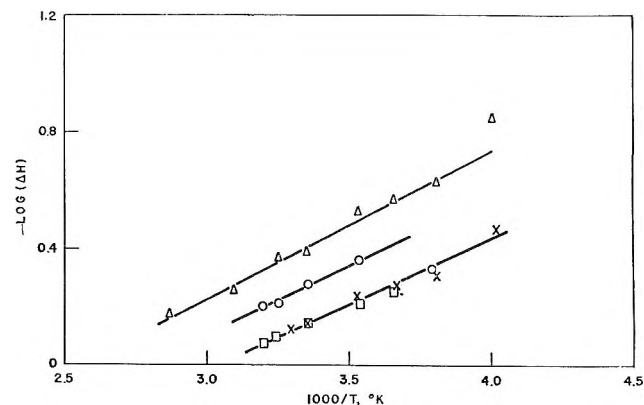


Figure 2. The temperature dependence of the peak-to-peak full line width (ΔH) of triethylaluminum (2 ml.) in various solvents (2 ml.): Δ , hexadecane; O, cyclohexane; \square , hexane; and \times , isopentane.

ture dependence of the line widths of pure TEA is the same as the exponential temperature dependence of the viscosity of TEA resulting in the same values of ΔE_{nmr} and ΔE_{vis} . This agreement for ΔE_{nmr} and ΔE_{vis} does not hold for pure TIBA and the solutions of TEA. O'Reilly and Schacher found ΔE_{vis} to be consistently greater than the ΔE_{nmr} values obtained from Cl³⁵ n.m.r. line widths.

If eq. 1 is divided by eq. 2, then one obtains

$$\Delta H/\eta = \Delta H_0/\eta_0 e^{\Delta E_{\text{nmr}} - \Delta E_{\text{vis}}/RT} \quad (3)$$

(2) D. E. O'Reilly and G. E. Schacher, *J. Chem. Phys.*, 39, 1768 (1963).

From Table I one can see that $\Delta E_{\text{nmr}} = \Delta E_{\text{vis}}$ for pure TEA which means that $\Delta H/\eta$ equals $\Delta H_0/\eta_0$ and, therefore, is independent of temperature. For the other pure aluminum alkyls and TEA solutions $\Delta E_{\text{nmr}} \neq \Delta E_{\text{vis}}$ making the ratio $\Delta H/\eta$ temperature dependent. Triethylaluminum, in isopentane and hexane, has $\Delta E_{\text{nmr}} > \Delta E_{\text{vis}}$ and so for it the ratio $\Delta H/\eta$ decreases with increasing temperature, whereas, pure TIBA and TEA in cyclohexane have $\Delta E_{\text{vis}} > \Delta E_{\text{nmr}}$ and a ratio $\Delta H/\eta$ which increases with increasing temperature.

At high viscosities (large line widths), both the room-temperature¹ and variable-temperature results (Figure 1) indicate a breakdown in the simple Debye theory. The monomeric character of TIBA may be the reason why its values of ΔE_{vis} and η_0 deviate from the others shown in Table I.

We have shown that both ΔE_{nmr} and ΔE_{vis} are nearly the same for TEA in isopentane and *n*-hexane. Therefore, these two systems also have nearly the same value for the ratio $\Delta H_c/\eta a^3$ as determined from eq.

Table I: Values of ΔE_{nmr} , ΔH_0 , ΔE_{vis} , and η_0 for Several Aluminum Alkyls and Hydrocarbons

Aluminum alkyl solute	Concn.	Hydrocarbon solvent	ΔE_{nmr} , kcal./mole	ΔH_0 , gauss $\times 10^2$	ΔE_{vis} , kcal./mole	η_0 , cp. $\times 10^2$
Triethylaluminum ^a	...	None	3.3 \pm 0.2	0.80	3.3	1.5
Tri- <i>n</i> -propylaluminum	...	None	3.4	3.5
Triisobutylaluminum ^a	...	None	3.4	2.3	7.0	0.002
Triethylaluminum	<i>b</i>	Isopentane	2.0	4.6	1.6 ^c	1.3 ^c
Triethylaluminum	<i>b</i>	<i>n</i> -Hexane	2.0	4.7	1.6 ^c	2.0 ^c
Triethylaluminum	<i>b</i>	Cyclohexane	2.4	3.3	3.0 ^c	0.13 ^c
Triethylaluminum	<i>b</i>	Hexadecane	2.4	4.4	2.4 ^c	2.65 ^c

^a Viscosity data furnished by Texas Alkyls Inc. ^b 2 ml. of alkyl + 2 ml. of hydrocarbon solvent. ^c Values apply to the hydrocarbons and not to the alkyl-hydrocarbon mixtures. Viscosity data for the hydrocarbons were obtained from the "American Institute of Physics Handbook" and viscosity data for hexadecane were obtained from "Selected Values of Physical and Thermodynamic Properties of Hydrocarbons and Related Compounds," American Petroleum Institute, Carnegie Press, Pittsburgh, Pa., 1953.

It was previously shown that at room temperature the ratio $\Delta H/\eta a^3$ remained constant for several trialkylaluminum compounds (TEA, TNPA, TNBA, and tri-*n*-hexylaluminum) dissolved in isopentane and normal hexane, where *a* is the effective radius of the trialkylaluminum compounds. It was also found that the ratio $\Delta H/\eta a^3$ was less for TEA dissolved in cyclohexane and hexadecane than for TEA dissolved in isopentane and normal hexane. These room-temperature studies indicated that at low viscosities the Debye relation for the correlation time τ_c

$$\tau_c = \frac{4\pi\eta a^3}{3kT} \quad (4)$$

is a good approximation in these systems. The general correspondence between the n.m.r. and viscosity results shown on Table I for the *n*-trialkylaluminum compounds supports the assumed approximate proportionality between η and τ_c . The C₄ and lower normal aluminum alkyls are predominantly dimeric³ and participate in an alkyl exchange process.^{1,4} The effect of the temperature dependence of this exchange process on the activation energies and pre-exponential constants may be similar for all these compounds.

1 and 2. The ratio $\Delta H/\eta a^3$ calculated from eq. 3 (including the *a* value) at $T = 300^\circ\text{K}$. is over three times as great for TEA in cyclohexane as it is for TEA in isopentane or normal hexane. Thus if the activation energy and pre-exponential term are taken into account, the $\Delta H/\eta a^3$ ratio for TEA in cyclohexane is too large, while if these terms are ignored as was previously done, the ratio is too small. In other words the change in activation energy from one system to another appears to be partially compensated by changes in ΔH_0 and η_0 so that the over-all effect on the ratio $\Delta H/\eta a^3$ is minimized. Values of $\Delta H/\eta a^3$ for the various systems previously reported obtained at various temperatures would give more information about the line-broadening mechanism. A more accurate explanation of the results presented in this paper would take into account the viscosities of the mixtures instead of merely the solvent viscosities.⁵

(3) G. E. Coates, "Organo-Metallic Compounds," John Wiley and Sons, Inc., New York, N. Y., 1956, p. 132.

(4) N. Muller and D. E. Pritchard, *J. Am. Chem. Soc.*, **82**, 248 (1960).

(5) R. W. Mitchell and M. Eisner, *J. Chem. Phys.*, **33**, 86 (1960).

Optical Energy Gaps in the Monoclinic Oxides of Hafnium and Zirconium and Their Solid Solutions¹

by J. G. Bendoraitis and R. E. Salomon

Department of Chemistry, Temple University, Philadelphia, Pennsylvania 19122 (Received June 2, 1965)

Zirconium and hafnium are perhaps the most similar pair of elements with respect to chemical and physical properties. Their compounds are similar in crystal structure, melting point, and solubility. The monoclinic oxides of zirconium and hafnium, in particular, have nearly identical unit cell dimensions,² with the following lattice parameters: $a = 5.1454$, $b = 5.2075$, $c = 5.3107$ Å., $\beta = 99^\circ 14' \pm 0.05$ for ZrO_2 , and $a = 5.1156$, $b = 5.1722$, $c = 5.2948$ Å., $\beta = 99^\circ 11' \pm 0.05$ for HfO_2 . The isomorphous character of these oxides has been demonstrated by the formation of homogeneous solid solutions in all proportions.³

It was of interest to determine the extent of the difference in the optical energy gap of these oxides. Among other things, the energy gap is expected to be sensitive to the type of bonding in the lattice. Although the exact nature of the bonding is not well understood, crystal field studies applied to the optical spectra of the Cr^{+3} ion doped into the monoclinic lattice of ZnO_2 suggest significant covalent contributions.⁴ The estimate is based on the ratio of the Racah B parameter⁵ of the Cr^{+3} ion in the lattice to that of the free ion.

In recent years, diffuse reflectance spectroscopy has been applied as a convenient technique for estimating the width of the energy gap in systems which are not amenable to investigation by transmission measurements.^{6,7} It was felt that the diffuse reflectance spectra of HfO_2 - ZrO_2 solid solutions could be used to demonstrate orbital overlap, since such solutions would be expected to have a behavior which is intermediate between that of a solid solution of weakly interacting organic molecules and strongly interacting atoms in a metallic alloy.

Experimental Section

Low hafnium zirconium oxide, obtained from the TAM Division of National Lead. Co., and hafnium oxide, obtained from Alfa Inorganics, Inc., were purified by forming insoluble chelates with mandelic acid.⁸ Impurities which might mask the onset of the intrinsic oxide absorption in the ultraviolet region were removed in this manner. The diffuse reflectance spectra of the purified oxides are shown in Figure 1.

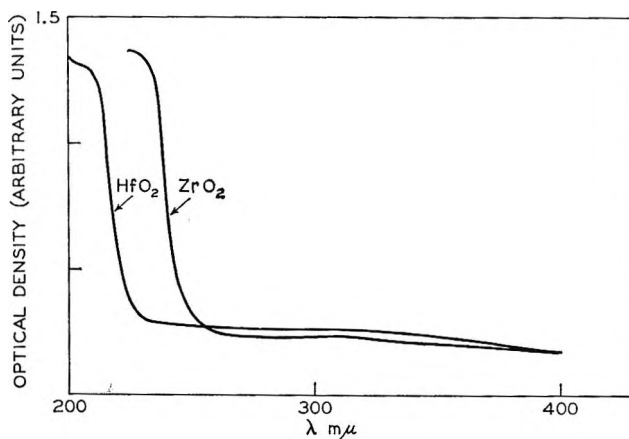


Figure 1. Diffuse reflectance spectra of purified hafnium oxide and zirconium oxide.

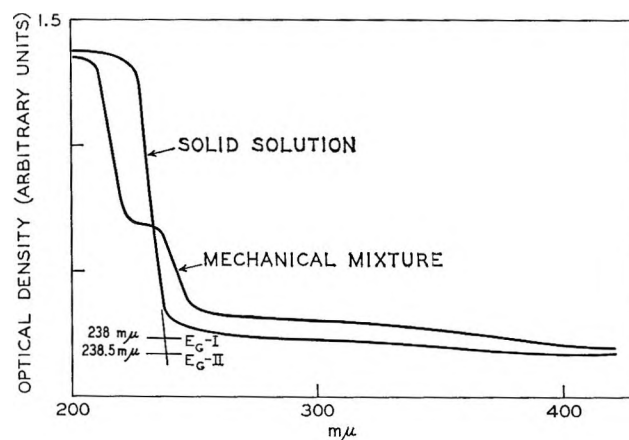


Figure 2. Diffuse reflectance spectra of a mechanical mixture of solid solutions of 40 mole % zirconium oxide in hafnium oxide.

Solid solutions of the oxides were prepared by ignition of the mixed mandelates. Weighed portions of the purified oxides were dissolved in molten sodium bisulfate. After cooling, the resulting melts were dissolved in dilute HCl (1:10). The mixed mandelates then precipitated upon the addition of mandelic acid. These

(1) This work was supported in part by the Socony Mobil Oil Co., Inc., and the U. S. Atomic Energy Commission, Contract No. AT(30-1)-2775, and is from the Ph.D. thesis of J. G. Bendoraitis to be submitted to the Graduate School, Temple University.

(2) J. Adam and M. D. Rogers, *Acta Cryst.*, **12**, 951 (1959).

(3) C. E. Curtis, L. M. Doney, and J. R. Johnson, *J. Am. Ceram. Soc.*, **37**, 458 (1954).

(4) J. P. Meehan, Ph.D. Thesis, Temple University, 1965.

(5) D. L. Wood, J. Ferguson, K. Knox, and J. F. Dillon, *J. Chem. Phys.*, **39**, 890 (1963).

(6) P. D. Fochs, *Proc. Phys. Soc. (London)*, **69**, 70 (1956).

(7) A. L. Companion, *J. Phys. Chem. Solids*, **25**, 357 (1964).

(8) W. B. Blumenthal, "Chemical Behavior of Zirconium," D. Van Nostrand Co. Inc., New York, N. Y., 1958.

precipitates were filtered, washed, and dissolved in dilute ammonium hydroxide to minimize contamination by foreign ions. The mandelates were reprecipitated by the addition of HCl, filtered, and ignited at 1000° for periods ranging from 1 to 100 hr. Typical ignition times were 20 hr. X-Ray powder diffractometer studies showed the resulting solid solutions to be homogeneous and they were invariant in both their optical and X-ray spectra after heating for 1 hr. at 1000°. No evidence of a superlattice structure was observed in the diffraction patterns.

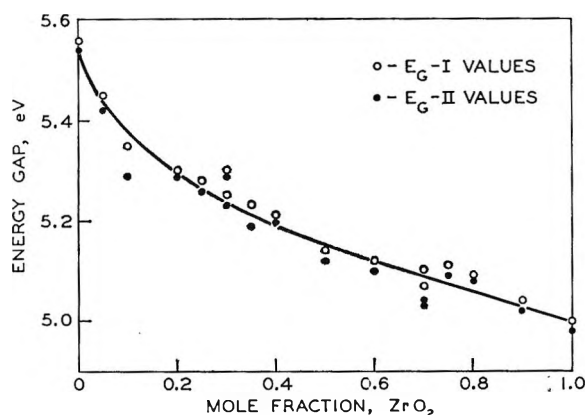


Figure 3. Variation of the optical energy gap with composition in solid solutions of hafnium and zirconium oxides.

Spectra were determined with a Cary Model 14 recording spectrophotometer equipped with a ring collector reflectance attachment calibrated against MgCO_3 (220–700 $m\mu$). Reflectance measurements relative to the standard are given in units of optical density, where $\text{O.D.} = \log (R_{\text{MgCO}_3}/R_{\text{sample}})$. Typical spectra of a 40 mole % mechanical mixture of ZrO_2 in HfO_2 and the corresponding solid solution are shown in Figure 2.

Results

The energy gap is taken as the intercept of the extrapolated linear portion of the absorption edge (region of strong optical absorption) with a base line corresponding to the region of minimum absorption. A band gap obtained in this manner for rutile has been shown by Companion⁹ to be in good agreement with values obtained by transmission measurements. This value is essentially the minimum width between the valence and conduction bands and does not necessarily agree with values based on the long wave length limit of photoconductivity. Such extrapolations, in our case, lead to two values ($E_G\text{-I}$ and $E_G\text{-II}$) of the energy gap depending on the choice of the region of minimum

absorption in the presence of contributions from impurities. The difference in the values of the energy gap obtained in this manner is normally of the order of 0.02 e.v. The observed variation in the energy gap over the concentration range extending from pure HfO_2 (5.55 e.v.) to pure ZrO_2 (4.99 e.v.) is shown in Figure 3. The variation with composition more nearly resembles the behavior of metallic alloys¹⁰ rather than mechanical mixtures or solid solutions of organic molecules.

The nonlinear dependence of band gap on composition can be explained as due to appreciable cation-cation orbital overlap in the solid solution. In the tight binding approximation, the band gap of a solid can be expressed as a linear combination of matrix elements connecting neighboring atomic orbitals.¹¹ The coefficients of these matrix elements depend, among other things, on the crystal symmetry and, for the case of alloys, the degree of order and the composition. In the case of completely disordered alloys, the coefficients of matrix elements connecting functions localized on neighboring cations and anions would be proportional to the mole fraction, whereas the coefficients of matrix elements connecting functions on neighboring cations would be proportional to the square of the mole fraction; i.e., the number of cation-cation pairs is proportional to the square of the mole fractions. The deviation from linearity of the curve in Figure 3 indicates that the matrix element connecting functions centered on adjacent cation sites is of appreciable magnitude, if the tight binding approximation is appropriate.

It is often important to know the magnitude of the extinction coefficient for the purpose of making spectral assignments. In the case of ZrO_2 , diffuse reflectance spectra may be compared with transmission spectra measurements made with stripped anodic films¹² in which one can ascribe the large extinction coefficients below 250 $m\mu$ to transitions from the valence to the conduction band.¹³

The influence of the lattice parameters on the energy gap is not known, although the lattice spacing in these solutions appears to vary linearly with composition (Vegard's law).

(9) A. L. Companion and R. E. Wyatt, *J. Phys. Chem. Solids*, **24**, 1025 (1963).

(10) J. C. Wooley and J. Warner, *Can. J. Phys.*, **42**, 1879 (1964).

(11) F. Seitz and D. Turnbull, "Solid State Physics," Vol. 1, Academic Press, Inc., New York, N. Y., 1955.

(12) R. E. Salomon, W. M. Graven, and G. B. Adams, *J. Chem. Phys.*, **32**, 310 (1960).

(13) R. E. Salomon, G. B. Adams, and W. M. Graven, *J. Electrochem. Soc.*, **110**, 1163 (1963).

Evidence for Nitrogen Trioxide in the Combustion of a Double-Base Propellant

by L. Dauerman, G. E. Salser, and Y. A. Tajima

Department of Chemical Engineering, New York University,
New York, New York 10453 (Received May 3, 1965)

Mass spectrometric evidence has been obtained for the formation of NO_3 during the low pressure combustion of a typical double-base propellant. This has not been suggested by previous studies, *e.g.*, Heller and Gordon, and Brent and Crawford.¹

The composition of the double-base propellant used in the present investigation is given in Table I.

Table I: Composition of Double-Base Propellant

Constituent	Wt. %
Nitrocellulose (12.7% N)	55.5
Nitroglycerin	27.5
Ethyl centralite	2.0
Triacetin	15.0

The propellant strand was burned in a 10 torr helium atmosphere; the helium was flowing through the strand burner to continuously sweep out the combustion products. Radiant heat from an arc source was focused on the end of the strand. Exothermic retrogression of the surface was observed. The surface temperature was measured by means of a recording 0.005-in. chromel-alumel thermocouple. The gas evolved off the surface was continuously sampled into a fast scanning mass spectrometer *via* a conical probe having a 0.051-mm. leak. The leak was 5–10 mm. from the surface and 19 mm. from the electron beam in the ionization chamber of the mass spectrometer. The experimental setup and mass spectrometer are to be described elsewhere. Mass spectra obtained with this instrument are very similar to those from a CEC 21-103. For example, the mass spectra of NO_2 recorded by this instrument and reported in the API tables are given together for comparison in Table II.

Table II: Mass Spectra of NO_2

Source	<i>m/e</i>			
	14	16	30	46
N.Y.U.	12.5	27.4	100	37.9
API	9.6	22.3	100	37.0

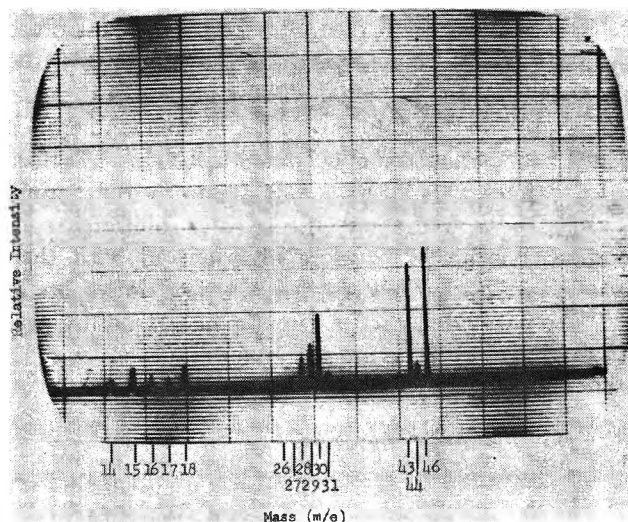


Figure 1. Mass spectrum observed during low-pressure combustion of a double-base propellant—pre-ignition stage.

Evidence for NO_3 and possibly nitrates is especially striking in mass spectra recorded during the pre-ignition stage. A typical spectrum is shown in Figure 1, surface temperature 200° . The major peaks are masses 43 and 46. Since they rise at independent rates as combustion proceeds, they are considered to represent different species. The 46 mass peak is of immediate interest. The 30 and 46 mass peaks rise together. These peaks might be ascribed to NO_2 except for the fact that the 30/46 ratio is inverse to that expected for NO_2 . Peak 46 might be due to formic acid except for the absence of mass 45 peak which for formic acid is almost equivalent to the 46 peak. Similarly, dimethyl ether is eliminated. It might be due to nitroglycerin vaporizing from the propellant. However, the spectrum of nitroglycerin² is totally unlike that observed here. For example, nitroglycerin has a mass 47 peak with intensity equal to that of 46 as well as numerous other strong peaks.

The interdependence of masses 30 and 46 is very strong evidence for a species containing the NO_2 entity. Boschan and Smith³ have studied the mass spectra of a series of nitro compounds, nitrite esters, and nitrate esters. The spectra of two alkyl nitrites, four nitroalkanes, and ethyl nitrate are also given in the API compilation. In the case of all the nitrites and nitro compounds (ten compounds), the 30/46

(1) C. A. Heller and A. S. Gordon, *J. Phys. Chem.*, **59**, 773 (1955); H. A. Brent and B. C. Crawford, *ibid.*, **63**, 941 (1959).

(2) M. King, U. S. Navy Propellant Laboratory, private communication.

(3) R. Boschan and S. R. Smith, "Mass Spectra of Nitrate Esters, Nitrite Esters, Nitro Compounds, and Several Other Nitrogen Compounds," NAVORD Report 5412, U. S. Naval Ordnance Test Station, China Lake, Calif., July 23, 1957.

ratio is much larger than unity as it is for NO_2 . Thus, these classes of NO_2 -containing compounds are virtually eliminated from consideration. The significant feature of the mass spectra of nitrate esters is the mass 46 peak. It is consistently more intense than the 30 peak, *viz.*, 30/46 ratio less than unity. In addition, no peak is observed at mass 62 (NO_3^+). Therefore, the mass spectroscopic data indicate that NO_3 or a nitrate is being observed.

The mass spectra of all the alkyl nitrates including nitroglycerin (nine compounds) show either a significant mass 76 peak ($\text{CH}_2\text{ONO}_2^+$) or a peak corresponding to the ion RCHONO_2^+ . Since these peaks and peaks corresponding to aliphatic fragments which vary in intensity as the 46 peak are not observed, the evidence indicates that NO_3 is the species given off during the low pressure combustion of a typical double-base propellant.

The finding of NO_3 as an intermediate in the combustion of a double-base propellant is also unexpected relative to previously reported mechanisms of the thermal decomposition of simple alkyl nitrates and of pure nitroglycerin. For example, Levy⁴ concludes that NO_2 is formed in the initial step of the decomposition of ethyl nitrate. However, the major product over a temperature range of 161–201° is ethyl nitrite; at 181° a 75% yield of ethyl nitrite is obtained with an 80% conversion of ethyl nitrate. Of greater immedi-

ate relevance is the study by Krastins⁵ of the thermal decomposition of nitroglycerin. He finds that at 150°, vapor phase, the initial product is NO_2 followed almost immediately by formaldehyde. Within a short period, CO , CO_2 , and NO appear simultaneously. N_2O is found late in the course of the reaction. Both Levy and Krastins used static reactors and analyzed samples by infrared spectrometry. Krastins in one series actually ran the pyrolysis in an infrared gas cell and followed the course of reaction by periodically recording infrared spectra. The data from this series appeared to substantiate his findings using the sampled static reactor technique. An interesting point is Krastins' inability to find or detect water although it must be a major reaction product. It appears that the last word has not yet been written on the combustion of nitrate ester propellants.

Acknowledgment. This investigation was supported in part by the Army Materials Command under Contract No. DA-30-069-AMC-122(A). The mass spectrometer was constructed in part by support provided by the Propulsion Research Division, Air Force Office of Scientific Research, under Contract No. AF 49(638)-173.

(4) J. B. Levy, *J. Am. Chem. Soc.*, **76**, 3254 (1954).

(5) G. Krastins, Ph.D. Thesis, University of Connecticut, 1957.

COMMUNICATIONS TO THE EDITOR

Polymorphism in Palladium(II) Chloride

Sir: A structure of PdCl_2 has been established¹ which is often given as an example of a linear, infinite-chain, inorganic molecule.² We present evidence that this structure is of a high temperature polymorph which can exist metastably at room temperature for many months and that a third modification of PdCl_2 exists at still higher temperatures. Structural details of the latter, as well as of the form thermodynamically stable at room temperature, are as yet not known.

Figure 1 shows the differential thermal analysis (d.t.a.) curve of PdCl_2 ³ which clearly indicates three endothermic effects. That at the highest temperature can be attributed to melting and decomposition on the

basis of previous studies⁴ and our confirmation of no significant weight loss below 600° by thermogravimetric analysis. The endotherms centering near 400 and 500° are thus due to crystalline transitions. The d.t.a. curves when heating was stopped at 575°, prior to onset of decomposition, had exotherms during cooling at about 440° caused by reversal of the 500°

(1) A. F. Wells, *Z. Krist.*, **100**, 189 (1939).

(2) See, for example, L. Pauling, "The Nature of the Chemical Bond," 3rd Ed., Cornell University Press, Ithaca, N. Y., 1960, p. 157.

(3) Obtained from J. Bishop & Co., Malvern, Pa., which kindly furnished information that the maximum temperature attained during production of this material is 166°.

(4) F. Pusche, *Ann. Chem.*, **9**, 233 (1938); M. A. Oranskaya and N. A. Mikhailova, *Russ. J. Inorg. Chem.*, **5**, 12 (1960); W. E. Bell, U. Merten, and M. Tagami, *J. Phys. Chem.*, **65**, 510 (1961).

Table I: Comparison of PdCl₂ X-Ray Data

d-spacings calculated from Wells' lattice constants			Powder pattern of intermediate temperature form			Powder pattern of low temperature form		
hkl	d, Å.	F _{calcd} ^a	d, Å. ^b	I ^c	Diff. ^d	d, Å. ^b	I ^c	Diff. ^d
010	11.000	A						
020	5.500	80	5.5	s	-0.0	5.3	s	0.2
100	3.810	A						
030	3.667	A						
110	3.600	96	3.61	s	-0.01			
001	3.340	A				3.28	w	0.06
011	3.196	42	3.21	m	-0.01	3.14	w	0.06
120	3.132	-44	3.15	w	-0.02	3.07 ^f	vw	0.06
021	2.885	A						
040	2.750	28	2.76	vw	-0.01			
130	2.642	57	2.66	w	-0.02			
101	2.512	50	2.48 ^e	s	-0.01 (from			
031	2.469	108			average)			

^a Numerical values are calculated structure factors from Wells' paper; A indicates plane giving no reflection in his study. ^b Cu K α radiation taken as 1.5418 Å. ^c Visual estimates of intensities. ^d d-spacing calculated from Wells' lattice constants minus our measured d-spacing. ^e Remainder of intermediate temperature form pattern had 18 lines in region from 2.29 to 1.24 Å. ^f Remainder of low temperature form pattern had 15 lines in region from 2.38 to 1.12 Å.

transition, but during the remainder of cooling to room temperature *no exotherm corresponding to the transition near 400°* occurred with pure PdCl₂. Accordingly, the intermediate temperature form could be recovered for leisurely study.

The X-ray diffraction powder pattern of our starting material agreed exactly with one published earlier,⁵ whereas that of PdCl₂ heated above 425° and cooled was distinctly different. However, after a month or two at room temperature, the latter samples began to show the strongest X-ray diffraction lines of the low temperature form. This pattern increased gradually in intensity, but complete reversion required at least 5 months.

Inasmuch as the single crystal of PdCl₂ used in the previous structural study¹ was prepared at 600°, it is now of interest to determine which form was studied. Using a Control Data Corporation G-15 computer we calculated from the lattice constants determined by Wells all possible d-spacings in the range of those of our patterns. The first 13 are listed in the second column of Table I, together with their associated hkl values^{6,7} and calculated structure factors from Wells' paper.¹ The powder pattern of the intermediate temperature form of PdCl₂ is seen to agree almost exactly both in d-spacings and intensities, whereas that of the low temperature form shows considerably greater deviations in lines that can be matched, lacks several important diffraction lines to be expected from Wells' structure, and requires one plane (001) whose reflection was absent in the single crystal study. On the basis of these comparisons, the differences in preparative

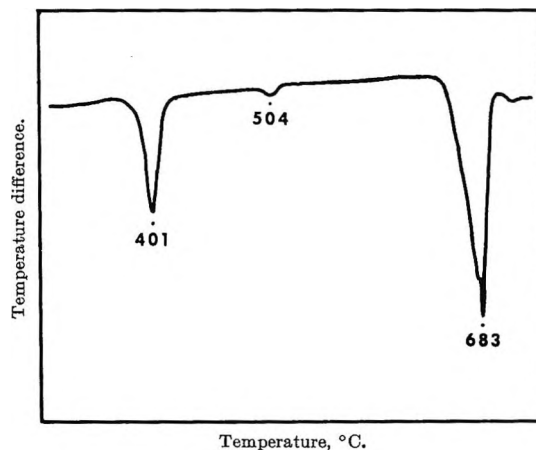


Figure 1. Differential thermal analysis curve of PdCl₂ heated 5°/min. in a nitrogen atmosphere. Deviations downward from base line show endothermic changes.

conditions of the samples, and our findings on the behavior of PdCl₂ polymorphs, we must conclude that the structure Wells determined is that of the intermediate temperature form.

We have investigated the densities and infrared absorption spectra of the low and intermediate temperature forms of PdCl₂. These findings plus more exten-

(5) J. D. Hanawalt, H. W. Rinn, and L. K. Frevel, *Ind. Eng. Chem., Anal. Ed.*, 10, 497 (1938).

(6) In accordance with recent data compilations,⁷ we have reversed the values of lattice constants *b* and *c* from those originally ascribed by Wells, and therefore also of indexes *k* and *l*.

(7) (a) R. W. G. Wyckoff, "Crystal Structures," 2nd Ed., Vol. 1, John Wiley and Sons, New York, N. Y., p. 343; (b) ASTM X-ray Powder Data File, Card No. 1-0228.

sive X-ray work will be reported on in full, together with implications regarding the structures of the several forms and revisions necessary in interpretations of previous work reported on this substance.

Acknowledgments. Partial support of this work by the Office of Naval Research is gratefully acknowledged.

PENNSALT CHEMICALS CORPORATION
TECHNOLOGICAL CENTER
KING OF PRUSSIA, PENNSYLVANIA

J. R. SOULEN
WILLIAM H. CHAPPELL, JR.

RECEIVED JULY 30, 1965

Near-Infrared Spectrum of Liquid Water from 30 to 374°

Sir: Some years ago, the authors obtained the near-infrared spectrum of liquid water over a temperature range of 30 to 374°. Some of the spectra were published as an illustration of the operation of the high temperature cell¹ and as a chapter in a doctoral thesis.²

Recently, much attention has been given to the structure of liquid water.³ Questions have been raised regarding the fraction of monomeric water present in the liquid.

Certain facts clearly emerge from the spectra shown in Figure 1. (1) There is a very strong effect of temperature, since the single band becomes two bands and the frequencies shift. (2) However the structure changes, no totally free water molecules are present since no band is observed at 3750 cm.⁻¹. (3) If the higher frequency band appearing at 200° is assumed to result from nonhydrogen-bonded species, then these results are consistent with the theory of Marchi and Eyring⁴ giving the fraction of monomeric molecules as a function of temperature. (4) On the other hand, these two peaks can also reasonably be explained as ν_3 and ν_1 , since their frequency difference is the same as found for ν_3 and ν_1 in the vapor phase⁵ and in dilute solutions of water in inert organic solvents.^{2,3} This is also consistent with the apparent intensity reversal between ν_3 and ν_1 which takes place on liquefaction. In the gas phase, ν_3 is very much more intense; in the liquid phase, ν_1 is more intense. As the environment of the liquid water becomes more and more like that in the vapor, there is apparently a continuous change in relative intensity, both in pure water, as seen here, and in organic solvents.

Acknowledgment. This research was sponsored in part by the Air Force Office of Scientific Research under Contract No. AF 49(638)-3 and the French Atomic Energy Commission.

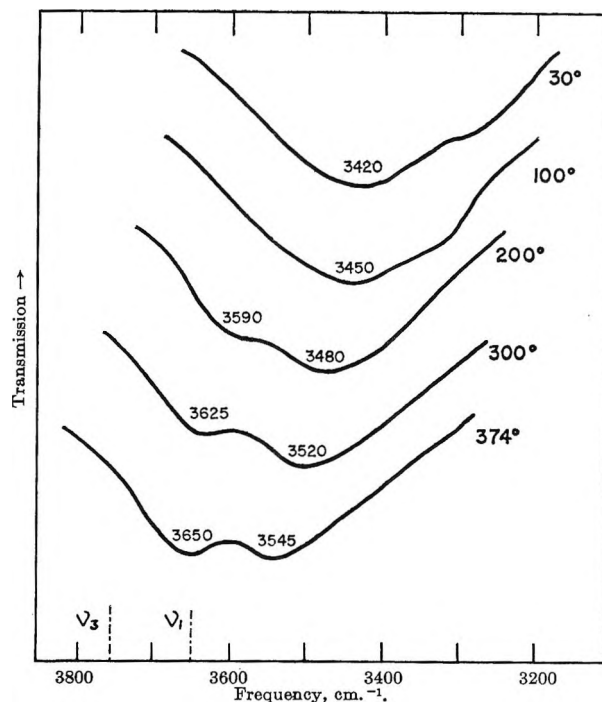


Figure 1. Infrared absorption of liquid water in the hydroxyl stretching region at different temperatures. ν_3 and ν_1 , indicated in the figure, are the vapor phase values of these frequencies shown for comparison.

- (1) E. Fishman, *Appl. Opt.*, **1**, 493 (1962).
- (2) P. Saumagne, Thesis, University of Bordeaux, 1961.
- (3) D. P. Stevenson, *J. Phys. Chem.*, **69**, 2145 (1965), with references to previous literature.
- (4) R. P. Marchi and H. Eyring, *ibid.*, **68**, 221 (1964). Their eq. 10 for the fraction of monomeric molecules yields 7% at 200°, where the high-frequency shoulder just appears, to 41% at 374°, where the two peaks have nearly equal intensity.
- (5) G. Herzberg, "Infrared and Raman Spectra of Polyatomic Molecules," D. Van Nostrand Co., Inc., New York, N. Y., 1945, p. 281. The antisymmetric and symmetric stretching vibrations of water, ν_3 and ν_1 , are given as 3756 and 3652 cm.⁻¹, respectively. The difference of 104 cm.⁻¹ is within experimental error of the differences between the two peaks at each temperature shown in Figure 1.

DEPARTMENT OF CHEMISTRY
SYRACUSE UNIVERSITY
SYRACUSE, NEW YORK

ERWIN FISHMAN

UNIVERSITY OF BREST
BREST, FRANCE

PIERRE SAUMAGNE

RECEIVED AUGUST 2, 1965

Gas Phase Charge-Transfer Complexes

Sir: One major difficulty in comparing the experimental data for charge-transfer (c.t.) molecular complexes with theoretical predictions has been that of properly assessing the role of solvent. Existing spectro-

photometric data have been almost exclusively obtained from solutions.¹ Solvent interactions generally^{2,3} have been ignored in the evaluation of the equilibrium constant, extinction coefficient, and thermodynamic constants describing the c.t. complex equilibrium. Further, existing theories of solvent peak shifts for pure compounds do not correctly predict the gas phase peaks,⁴ while in the case of c.t. complexes there has been no real test of these theories owing to the absence of gas phase data.

We recently have observed strong absorption spectra in gas phase mixtures of aromatic hydrocarbons and tetracyanoethylene (TCNE) which are analogous to the corresponding c.t. spectra observed in solution. These c.t. spectra are completely free from overlapping by the spectra of the parent molecules, and this makes the analysis of the data unambiguous. In the present communication we present preliminary results on the TCNE-*p*-xylene system. A portion of the observed spectral data appears in Figure 1. The occurrence of a double peak is equally characteristic of the spectrum in the gas phase and in solution.

The spectrophotometric measurements were made using a Warren Spectracord modified to accommodate cells 100 cm. in length within an oven which can be maintained within $\pm 0.5^\circ$ over the length of the tube. The cells (of known volume) were fitted with break-seals containing accurately weighed amounts of the compounds to be studied and then evacuated. A base line was then determined for the evacuated cells and the break-seals were broken. Spectrograms were recorded for the temperature range 97–162°. The

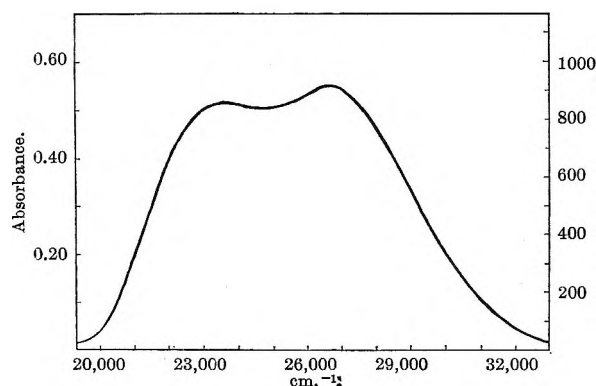


Figure 1. Absorption spectrum of c.t. complex of TCNE and *p*-xylene. The left-hand ordinate is for 5.687×10^{-5} M TCNE and 4.987×10^{-3} M *p*-xylene at 97° , while the right-hand ordinate is the extinction coefficient, ϵ (l. mole⁻¹ cm.⁻¹), as computed from the Benesi-Hildebrand equation.

data for nine concentrations were fitted by least squares to the Benesi-Hildebrand equation.⁵ The resulting values of ϵ and K are listed in Table I, together with observed thermodynamic constants and corresponding solution data where available.

As can be seen from Table I, the equilibrium constant appears to have increased by a factor of ~ 35 and the extinction coefficient to have decreased by a factor of ~ 3 in going from solution to the gas phase. The splitting of the double peak is constant at 3100 ± 200 (cm.⁻¹), in both the gaseous and condensed phases. This supports the belief² that this splitting of peaks is due to the expected splitting in *p*-xylene of the ionization energies of the π -orbitals which in benzene are degenerate.

Table I

	Gas phase		Solution (CH ₂ Cl ₂) (ref. 2)
	ν , peak A, cm. ⁻¹	ν , peak B, cm. ⁻¹	$\nu_A - \nu_B$, cm. ⁻¹
ϵ_{\max} , l. mole ⁻¹ cm. ⁻¹	910 \pm 100		2770
K_c 295°K., l. mole ⁻¹	275		7.64
K_c 398°K., l. mole ⁻¹	11.6		...
ΔH_f° , kcal. mole ⁻¹	-7.2 \pm 1		-3.37
ΔS , e.u.	-13.1 \pm 1.6		-7.38
f , osc. strength	0.032		...
Gas phase	26,600	23,500	3100
C ₇ F ₁₆	25,800	22,900	2900
C ₇ H ₁₆	25,100	22,000	3100
CCl ₄	24,500	21,300	3200
CH ₂ Cl ₂ (ref. 2)	24,100	21,700	2400

Acknowledgment. This work was supported by a grant from the National Science Foundation, NSF GP 3427 Research.

- (1) F. T. Lang and R. L. Strong, *J. Am. Chem. Soc.*, **87**, 2345 (1965).
- (2) R. E. Merrifield and W. D. Phillips, *ibid.*, **80**, 2778 (1958).
- (3) S. Carter, J. N. Murrell, and E. J. Rosch, *J. Chem. Soc.*, 2048 (1965).
- (4) (a) E. A. Bovey and S. S. Yanari, *Nature*, **186**, 1042 (1960); (b) O. Sverdlova, *Opt. Spectry. (USSR)*, **6**, 223 (1959).
- (5) H. A. Benesi and J. H. Hildebrand, *J. Am. Chem. Soc.*, **71**, 2703 (1949).

LABORATORY OF MOLECULAR STRUCTURE
AND SPECTRA
DEPARTMENT OF PHYSICS
UNIVERSITY OF CHICAGO
CHICAGO, ILLINOIS 60637

M. KROLL
M. L. GINTER

RECEIVED AUGUST 10, 1965